Environmental Chemistry for a Sustainable World

Saravanan Rajendran
Mu. Naushad
Kumar Raju
Rabah Boukherroub *Editors*

Emerging Nanostructured Materials for Energy and Environmental Science

Springer

Environmental Chemistry for a Sustainable World

Volume 23

Other Publications by the Editors

Books
Environmental Chemistry
http://www.springer.com/978-3-540-22860-8

Organic Contaminants in Riverine and Groundwater Systems
http://www.springer.com/978-3-540-31169-0

Sustainable Agriculture
Volume 1: http://www.springer.com/978-90-481-2665-1
Volume 2: http://www.springer.com/978-94-007-0393-3

Book series
Environmental Chemistry for a Sustainable World
http://www.springer.com/series/11480

Sustainable Agriculture Reviews
http://www.springer.com/series/8380

Journals
Environmental Chemistry Letters
http://www.springer.com/10311

Agronomy for Sustainable Development
http://www.springer.com/13593

More information about this series at http://www.springer.com/series/11480

Saravanan Rajendran • Mu. Naushad
Kumar Raju • Rabah Boukherroub
Editors

Emerging Nanostructured Materials for Energy and Environmental Science

Springer

Editors
Saravanan Rajendran
Faculty of Engineering, Department of Mechanical Engineering
University of Tarapacá
Arica, Chile

Mu. Naushad
Chemistry Department, College of Science
King Saud University
Riyadh, Saudi Arabia

Kumar Raju
Energy Materials
CSIR Materials Science and Manufacturing
Pretoria, South Africa

Rabah Boukherroub
Univ. Lille, CNRS, Centrale Lille, ISEN, Univ. Valenciennes, UMR 8520 – IEMN
Lille, France

ISSN 2213-7114 ISSN 2213-7122 (electronic)
Environmental Chemistry for a Sustainable World
ISBN 978-3-030-04473-2 ISBN 978-3-030-04474-9 (eBook)
https://doi.org/10.1007/978-3-030-04474-9

Library of Congress Control Number: 2018968082

This Springer imprint is published by the registered company Springer Nature Switzerland AG.
The registered company address is: Gewerbestrasse 11, 6330 Cham, Switzerland

Preface

The ever-increasing energy consumption and environmental pollution are the major obstacles in the modern day society. Hence, this could be altered by an innovative and contemporary approach globally to make ease of the rapid growing energy hassles with zero environmental pollution. Advanced technologies exploiting the fascinating properties of nanostructured materials and nanoscale engineering have been widely accepted to revolutionize the performance of electrocatalyst platforms, energy storage and conversion systems, photocatalysts, efficient adsorption technology, and carbon capturing systems. A massive amount of research has been devoted on nanomaterials in the recent past to achieve sustainable development in clean energy and environmental protection. Also, for competent dealing with pollutants, identifying unique materials having inherent advantages like superior structure and function as an active catalyst, electrode materials, and adsorbents remains a key challenge. Besides, fundamental understanding of their structural properties and operating principles is equally important to design the state-of-the-art nanomaterials for very specific challenges. This book describes the fundamental aspects of diverse range of nanomaterials for energy and environmental applications in a comprehensive manner from the specialists who are at the forefront of research in the field of energy and environmental science. As these two topics are tremendously broad, and to summarize the recent developments and future perspectives, we have chosen the chapters carefully to cover the important aspects of energy and environmental field, especially an efficient utilization of nanomaterials to deliver solutions for the public consciousness.

Arica, Chile — Saravanan Rajendran
Riyadh, Saudi Arabia — Mu. Naushad
Pretoria, South Africa — Kumar Raju
Lille, France — Rabah Boukherroub

Acknowledgments

First and foremost, we would like to thank Almighty God for the completion of this book. We are grateful to the series editor, Eric Lichtfouse, for his support, encouragement, and trust during the process of writing this book. His observations, remarks, and eagerness have helped to improve the quality of this book. We would also like to express our gratitude to the publisher, Springer, for accepting this book as part of the series Environmental Chemistry for a Sustainable World.

This book is the outcome of the remarkable contribution of experts from various interdisciplinary fields of science and covers the most comprehensive, in-depth, and up-to-date research and reviews. We are thankful to all the contributing authors and their coauthors for their esteemed work. We would like to express our gratitude to all the authors, publishers, and other researchers for granting us the copyright permissions to use their illustrations. Although, every effort has been made to obtain the copyright permissions from the respective owners to include citation with the reproduced materials. We would still like to offer our deep apologies to any copyright holder if unknowingly their right is being infringed.

Saravanan Rajendran would like to thank the SERC (CONICYT/FONDAP/15110019), FONDECYT, Government of Chile (Project No.: 11170414), and School of Mechanical Engineering (EUDIM), University of Tarapaca, Arica, Chile, which made it possible to edit this book. Further, my sincere gratitude to Prof. Francisco Gracia (DIQBT, University of Chile), Prof. Lorena Cornejo Ponce (EUDIM, University of Tarapaca), and Prof. Rodrigo Palma (Director, SERC) for their continuous support, motivation, moral guidance, enthusiasm, and immense knowledge which helped me at the time of research and editing of this book.

Mu. Naushad would like to express his deep gratitude to the Chairman, Department of Chemistry, College of Science, King Saud University, Saudi Arabia, for his valuable suggestions and constant inspiration. He is also thankful to the Deanship of Scientific Research at King Saud University for the support.

R. Boukherroub gratefully acknowledges the financial support from the Centre National de la Recherche Scientifique (CNRS), the University of Lille, and the Hauts-de-France region.

Saravanan Rajendran
Mu. Naushad
Kumar Raju
Rabah Boukherroub

Contents

About the Editors

Dr. Saravanan Rajendran has received his Ph.D. in Physics-Material Science in 2013 from the Department of Nuclear Physics, University of Madras, Chennai, India. He was awarded the University Research Fellowship (URF) during 2009–2011 by the University of Madras. After working as an Assistant Professor in Dhanalakshmi College of Engineering, Chennai, India, during 2013–2014, he was awarded SERC and CONICYT-FONDECYT postdoctoral fellowship (2014–2017) by the University of Chile, Santiago. He has worked (2017–2018) in the research group of Professor John Irvine, School of Chemistry, University of St. Andrews, UK, as a Postdoctoral Research Fellow within the framework of an EPSRC Global Challenges Research Fund for the removal of blue-green algae and their toxins. Currently, he is working as a Research Scientist, in the School of Mechanical Engineering (EUDIM), University of Tarapaca, Arica, Chile. He has published several international peer-reviewed journals and book chapters. His work interest includes nanoporous and nanomaterial-based catalysts for renewable energy and wastewater purification.

Dr. Mu. Naushad is presently working as an Associate Professor in the Department of Chemistry, College of Science, King Saud University (KSU), Riyadh, Kingdom of Saudi Arabia. He obtained his M.Sc. and Ph.D. degrees in Analytical Chemistry from Aligarh Muslim University, Aligarh, India, in 2002 and 2007, respectively. He has a vast research experience in the multidisciplinary fields of analytical chemistry, materials chemistry, and environmental science. He holds several US patents, over 250 publications in the international journals of repute, 15 book chapters, and several books published by renowned international publishers. He has >5800 citations with a Google Scholar H-Index >47. He has successfully run several research projects funded by National Plan for Science, Technology, and Innovation (NPSTI) and King Abdulaziz City for Science and Technology (KACST), Kingdom of Saudi Arabia. He is the Editor/Editorial Member of several reputed journals like *Scientific Reports* (Nature), *Process Safety and Environmental Protection* (Elsevier), *Journal of Water Process Engineering* (Elsevier), and *International Journal of Environmental*

Research and Public Health (MDPI). He is also the Associate Editor of *Environmental Chemistry Letters* (Springer) and *Desalination and Water Treatment* (Taylor & Francis). He has been awarded the Scientist of the Year Award (2015) by the National Environmental Science Academy, New Delhi, India, and Almarai Award (2017), Saudi Arabia.

Dr. Kumar Raju received his Ph.D. degree in Chemistry (Chemistry-Energy Interdisciplinary) from the University of Madras, India. He was awarded Junior and Senior Research Fellowships by the DST and CSIR, India, during his Ph.D. tenure, and then he joined as a Postdoctoral Fellow (2012) in Hanyang University, South Korea. After that, he joined the Council for Scientific and Industrial Research (CSIR), South Africa, in 2013 as Postdoctoral Fellow. Currently, he is a Senior Researcher at the CSIR. He is the author of several research publications, 2 book chapters, and 2 patents. His research interest focusses on the electrochemical materials science and developing advanced materials for energy storage and conversion devices.

Dr. Rabah Boukherroub received his Ph.D. in Chemistry from the University of Paul Sabatier in Toulouse, France. He is currently a CNRS Research Director and a Group Leader at the Institute of Electronics, Microelectronics and Nanotechnology (IEMN), University of Lille, France. He is Associate Editor for *ACS Applied Materials & Interfaces*. He is also a Guest Professor in the China University of Petroleum, Qingdao, China. His research interests are in the area of nanostructured functional materials, surface chemistry, and photophysics of semiconductor/metal nanostructures with emphasis on biosensors, nanomedicine, photocatalysis, and energy-related applications. He is the author of 490+ research publications and wrote 33 book chapters in subjects related to nanotechnology, materials chemistry, and biosensors. He has 11 patents or patents pending.

Contributors

Soosaimanickam Ananthakumar Crystal Growth Centre, Anna University, Chennai, India

Instituto de Ciencia de los Materiales (ICMUV), Universidad de Valencia, Valencia, Spain

Sridharan Moorthy Babu Crystal Growth Centre, Anna University, Chennai, India

Jesudas Balasubramanian Department of Pharmacology and Environmental Toxicology, Dr. ALM PGIBMS, University of Madras, Chennai, India

Joyita Banerjee Department of Chemical Engineering, University of Pittsburgh, Pittsburgh, PA, USA

Abdulhakeem Bello Department of Materials Science and Engineering, African University of Science and Technology (AUST), Abuja, Nigeria

Rosalin Beura Centre for Nanoscience and Technology, Pondicherry University, Puducherry, India

Pankaj Bharali Department of Chemical Sciences, Tezpur University, Napaam, Assam, India

Arulvasu Chinnasamy Department of Zoology, University of Madras, Chennai, India

K. Chitrarasu Centre for Nanoscience and Technology, Pondicherry University, Puducherry, India

Bhugendra Chutia Department of Chemical Sciences, Tezpur University, Napaam, Assam, India

Raghunath Das Department of Applied Chemistry, University of Johannesburg, Johannesburg, South Africa

Kingshuk Dutta Department of Materials Science and Engineering, Cornell University, Ithaca, NY, USA

Pravin K. Dwivedi Polymer and Advanced Materials Laboratory, Physical & Material's Chemistry Division, CSIR-National Chemical Laboratory, Pune, India

Duncan Paul Fagg Nanoengineering Research Group, Department of Mechanical Engineering, University of Aveiro, Aveiro, Portugal

Gajalakshmi Selvaraj Sustainable Fuel Cells Laboratory, Centre for Pollution Control & Environmental Engineering, Pondicherry University, Pondicherry, India

Babu Gajendran Department of Biology and Chemistry, The Key Laboratory of Chemistry for Natural Products of Guizhou Province and Chinese Academy of Sciences, Guiyang, Guizhou, China

State Key Laboratory of Functions and Applications of Medicinal Plants, Guizhou Medical University, Guiyang, China

Chiranjita Goswami Department of Chemical Sciences, Tezpur University, Napaam, Assam, India

Mounika Gudeppu Department of Pharmacology and Environmental Toxicology, Dr. ALM PGIBMS, University of Madras, Chennai, India

Mpitloane J. Hato Department of Chemistry, School of Physical and Mineral Sciences, University of Limpopo (Turfloop), Polokwane, South Africa

Wilson Henao Quality, Metrology and Production Research Group, Instituto Tecnológico Metropolitano, Campus Robledo, Medellín, Colombia

Leyla Y. Jaramillo Quality, Metrology and Production Research Group, Instituto Tecnológico Metropolitano, Campus Robledo, Medellín, Colombia

Facultad de Ingeniería, Tecnológico de Antioquia, Medellín, Colombia

S. Joicy Centre for Nanoscience and Technology, Pondicherry University, Puducherry, India

Sathish-Kumar Kamaraj Laboratorio de Cultivo de Tejidos Vegetales, Instituto Tecnológico El Llano (ITEL)/Tecnológico Nacional de México (TecNM), El Llano, Aguascalientes, Mexico

Jeyagopal Ram Kumar Crystal Growth Centre, Anna University, Chennai, India

Department of Physics, Faculty of Physical and Mathematical Sciences, University of Concepcion, Concepcion, Chile

Pushpendra Kumar Polymer and Advanced Materials Laboratory, Physical & Material's Chemistry Division, CSIR-National Chemical Laboratory, Pune, India

Vignesh Kumaravel Department of Environmental Science, School of Science, Institute of Technology Sligo, Sligo, Ireland

Gunaseelan Kuppurangam Sustainable Fuel Cells Laboratory, Centre for Pollution Control & Environmental Engineering, Pondicherry University, Pondicherry, India

Krishnamoorthy Lalitha Department of Chemistry, School of Chemical and Biotechnology, SASTRA Deemed University, Thanjavur, Tamil Nadu, India

Yanmei Li Department of Biology and Chemistry, The Key Laboratory of Chemistry for Natural Products of Guizhou Province and Chinese Academy of Sciences, Guiyang, Guizhou, China

State Key Laboratory of Functions and Applications of Medicinal Plants, Guizhou Medical University, Guiyang, China

Arjun Maity Department of Applied Chemistry, University of Johannesburg, Johannesburg, South Africa

DST/CSIR National Center for Nanostructured Materials, Council for Scientific and Industrial Research (CSIR), Pretoria, South Africa

Katlego Makgopa Department of Chemistry, Faculty of Science, Tshwane University of Technology (Acardia Campus), Pretoria, South Africa

Kwena D. Modibane Department of Chemistry, School of Physical and Mineral Sciences, University of Limpopo (Turfloop), Polokwane, South Africa

Subbiah Nagarajan Department of Chemistry, School of Chemical and Biotechnology, SASTRA Deemed University, Thanjavur, Tamil Nadu, India

Department of Chemistry, National Institute of Technology Warangal (Institute of National Importance), Warangal, Telangana, India

Narendar Nasani Centre for Materials for Electronics Technology, Pune, Maharashtra, India

Kamya Parashar Department of Applied Chemistry, University of Johannesburg, Johannesburg, South Africa

Kriveshini Pillay Department of Applied Chemistry, University of Johannesburg, Johannesburg, South Africa

D. Pukazhselvan Nanoengineering Research Group, Department of Mechanical Engineering, University of Aveiro, Aveiro, Portugal

Kumar Raju Energy Materials, CSIR Materials Science and Manufacturing, Pretoria, South Africa

Thirumurugan Ramasamy Laboratory of Aquabiotics/Nanoscience, Department of Animal Science, Bharathidasan University, Tiruchirappalli, Tamil Nadu, India

Dipak Rana Department of Chemical and Biological Engineering, Industrial Membrane Research Institute, University of Ottawa, Ottawa, ON, Canada

Manuel Romero-Sáez Quality, Metrology and Production Research Group, Instituto Tecnológico Metropolitano, Campus Robledo, Medellín, Colombia

J. Santhosh Kumar Centre for Nanoscience and Technology, Pondicherry University, Puducherry, India

Manjusha V. Shelke Polymer and Advanced Materials Laboratory, Physical & Material's Chemistry Division, CSIR-National Chemical Laboratory, Pune, India

S. K. Singh Department of Physics, D.C.R. University of Science and Technology, Murthal, Haryana, India

Sivaraman Somasundaram Department of Chemistry, Kongju National University, Gongju, Republic of Korea

Ayyapillai Thamizhanban Department of Chemistry, School of Chemical and Biotechnology, SASTRA Deemed University, Thanjavur, Tamil Nadu, India

P. Thangadurai Centre for Nanoscience and Technology, Pondicherry University, Puducherry, India

Sumathi Thangarajan Department of Medical Biochemistry, Dr. ALM PGIBMS, University of Madras, Chennai, India

Unai de la Torre Department of Chemical Engineering, Faculty of Science and Technology, Universidad del País Vasco-UPV/EHU, Leioa, Bizkaia, Spain

Krishnapriya Madhu Varier Department of Medical Biochemistry, Dr. ALM PGIBMS, University of Madras, Chennai, India

Department of Zoology, University of Madras, Chennai, India

Vignesh Venkatasamy Animal Quarantine and Certification Service, Department of Animal Husbandry, Dairying and Fisheries, Ministry of Agriculture & Farmers Welfare, Mumbai, India

Poonam Yadav Polymer and Advanced Materials Laboratory, Physical & Material's Chemistry Division, CSIR-National Chemical Laboratory, Pune, India

---

The original version of this book was revised. A correction to this chapter can be found at https://doi.org/10.1007/978-3-030-04474-9_14

Chapter 1
Emerging Nanomaterials in Energy and Environmental Science: An Overview

P. Thangadurai, S. Joicy, Rosalin Beura, J. Santhosh Kumar, and K. Chitrarasu

Contents

Abstract Materials play a huge role in the development of human lifestyle at all ages. By the emergence of nanomaterials, a new field of science and technology was born, known as "nanoscience and nanotechnology." This is mainly because of the peculiar characteristics of the nanomaterials that are applied in modern science and technology. Nowadays there are mainly two major global threats, namely, (i) energy and (ii) environment cleanliness. Most of the energy used these days are from fossil fuels, and this energy is running out, and therefore there is a huge hunt for new sources of energy; mostly they are renewable energy and that should be environment-friendly. Energy generation and storage are big challenges and can be done via solar cells, fuel cells, and batteries. The next issue of environmental

P. Thangadurai (✉) · S. Joicy · R. Beura · J. Santhosh Kumar · K. Chitrarasu
Centre for Nanoscience and Technology, Pondicherry University, Kalapet, Puducherry, India
e-mail: thangaduraip.nst@pondiuni.edu.in

R. Saravanan et al. (eds.), *Emerging Nanostructured Materials for Energy and Environmental Science*, Environmental Chemistry for a Sustainable World 23,
https://doi.org/10.1007/978-3-030-04474-9_1

pollution is mainly from the enormously developing industries. Most of these industries discharge effluents (mainly from textile and tanning industries) into the mainstream water bodies, leading to a polluted water for supply. This particular issue, depending on the type of chemicals/dyes/organics that it contains, is very harmful to the living things, including human beings. The level of danger can go to the extent of inducing cancer. These effluents have to be treated properly and converted into harmless products (such as water, CO_2, etc.) before letting them into water. Process like advanced oxidation process assisted by photocatalyst can be a good solution for cleaning the industrial wastes. Ability of the photocatalyst with appropriate characteristics is very crucial for this particular application. Another category of threat to environment is the corrosion caused by the electrochemical reactions when the metal/structure interacts with their surroundings. What is more importantly required to meet out the energy and environment issues is to develop better performing materials that can improve the working efficiency of solar cells, batteries, and photocatalysts for photocatalysis. Boon for this is the blooming of "nanomaterials" that come with improved properties compared to their bulk counterpart. Development of nanomaterials is enormous in all these fields of applications. In this aspect, this chapter describes the applications of nanomaterials in the fields of energy (solar cells, batteries, and fuel cells) and environment issues (gas sensing, photocatalysts in photocatalysis, and corrosion). The emergence of these nanomaterials for these applications is discussed in this chapter.

1.1 Introduction

Entering into the twenty-first century, energy and environmental issues have demanded urgent attention to solve the major challenges on a global scale. The major challenge is the problem of global warming where these energy-related problems are themselves an environmental problem. Hence, while tackling the energy issues, it is also required to meet the economic factors as well as to take care of the long-term environmental concerns. A massive growth of the world's population accompanied by the substantial development of industry has brought about enormous increasing demand for global energy consumption (Hoffert et al. 1998). In the beginning, world energy consumption was mainly relied on the combustion of nonrenewable fossil fuels (oil, coal, and natural gas). With the exhaustion of these nonrenewable resources, more effort has been paid toward clean, renewable, and environmentally benign energy sources including hydro, wind, solar, nuclear, etc. Out of them solar cells have attracted much attention because of the huge amount of solar energy available in nature and that can be tapped without harming the environment. Followed by the solar cells, the energy-generating and storage devices, batteries, have been a great boon to the society. As an alternate to the combustion engines that uses fossil fuels, fuel cells are also considered and strongly researched a lot for energy applications.

In addition to energy issues, environmental issues, like water pollution, air pollution, etc., have become important issues to be tackled. Pollution becomes unavoidable in the recent lifestyle due to the faster industrial and technological development. Water pollution is the most concerned one. In the global scenario, the textile industry is considered as one of the largest water polluters by releasing huge amounts of dyes/organics into a water system. The biggest challenge in this issue is that these dyes or organic molecules are highly stable and remain unaffected even after chemically and biologically treated (Chong et al. 2010). Various methods, such as adsorption on activated carbon, ultrafiltration, reverse osmosis, chlorination, advanced oxidation processes (AOPs), etc. (Kulkar and Thakur 2014; Mills et al. 1993; Rajeshwar et al. 2008), have been used for the treatment of these dyes. The air pollution can be avoided by sensing the unwanted gas molecules present in air/atmosphere, and therefore gas sensing is a good method for this particular application. The environment is also damaged by a most important phenomenon called as "corrosion" when structural materials are in contact with air/wet/hot environment, and protection from corrosion becomes significant.

All these issues discussed above have been addressed by many researchers around the globe for quite long time. Especially evolution of nanoscience, nanomaterials, and nanotechnology and their robustness have helped scientists to find appropriate solution for those issues. This chapter addresses these issues and focuses on various nanomaterials that have been successfully used for energy applications majorly in three fields such as (i) solar cells, (ii) fuel cells, and (iii) batteries and for environmental applications in the fields such as (i) photocatalysis for water pollution, (ii) corrosion, and (iii) gas sensing.

1.2 Nanomaterials

Materials are classified basically into crystalline and amorphous based on the type of atomic arrangement in their lattice. They can be further classified into single crystalline, microcrystalline, and nanocrystalline materials. Single crystals are the materials that keep their atomic order the same throughout the crystal, whereas the microcrystalline materials have grains of size a few micrometer separated by grain boundaries. When the size of the grain lies typically in the range of 1–100 nm ($1\ \text{nm} = 10^{-9}\ \text{m}$), those materials are called as nanocrystalline materials. In a broad sense, they are called as nanomaterials as there is no compulsion that they should be crystalline. When their size is reduced to this order, their surface becomes too sensitive with many defects, dangling bonds formed, or significantly altered the electronic structure. They can be crystalline, amorphous, and polymeric, but the only thing is that one of their physical dimensions has to lie in the range from 1 to 100 nm. Many of the physical and chemical properties are significantly altered when the dimension of the materials reduced to the nanometer scale (Gleiter 1989; Suryanarayana 1995). For example, electrical conductivity will go down due to the scattering of electrons in the grain boundary atoms, and at the same time

mechanical properties are improved due to the fact that the defects such as stacking faults dissolve into the grain boundary (Tian 2017). Another property such as melting point will be decreased in nanomaterials, and the magnetic properties such as superparamagnetism are shown by the nanomaterials (Li et al. 2016d; Mikhaylova et al. 2004). More significantly, the bandgap of the nanomaterials is strongly dependent on their size; in a region below a critical dimension called as Bohr's excitonic radius (in semiconductor), their bandgap is increased, and this region is known as "strongly confined region." As far as chemical activity is concerned, due to the large surface area of the nanomaterials (specifically surface-to-volume ratio), they are very active, and their activity will be much enhanced compared to their bulk counterpart.

As far as optical properties are concerned, the photoluminescence emission, optical absorption, and optical bandgap are strongly dependent on the size of the nanomaterials. In most of the cases, by tuning the size of the nanomaterial, many of their properties can be tuned, and this is the big advantage of the nanomaterials for different applications. It is to be noted that they are used and made breakthrough developments in many fields such as energy generation and energy storage by means of batteries, fuel cells, solar cells, etc. In environmental applications, they found applications such as photocatalysis to photodegrade many of the industrial-based dyes/organic molecules (Mondal and Sharma 2016; Sandroni et al. 2018), detecting harmful gases through gas sensors (Amutha et al. 2015) and increasing corrosion resistance when coated on metal substrates (Gnedenkov et al. 2015; Liu et al. 2015a). In microelectronic and nanoelectronics, the metal nanoparticles are used to enhance the charge storage of metal-oxide-semiconductor (MOS) capacitors (Luo et al. 2008; Ye et al. 2007). Taking into consideration of the peculiar properties of nanomaterials, this chapter discusses their application in the field of energy and environment applications.

1.3 Nanomaterials for Energy

1.3.1 Solar Cells

Among myriad possible renewable clean energy resources, solar energy stands out as one of the highly promising sustainable options in terms of its availability, accessibility, affordability, and huge potential. In this regard, many research activities have been employed to utilize the natural light energy effectively through developing solar cells/panels with high power conversion efficiency. At present, the solar photovoltaic (PV) device is the third most important clean sustainable energy technology which directly converts the renewable light radiation into electricity with the use of semiconductor that exhibits the photovoltaic effect. In 1839, the photovoltaic effect was first witnessed by Alexandre-Edmond Becquerel. Later, first modern silicon solar cell was patented by Russell Ohl in 1946. The first practical silicon solar cell with the power efficiency of 6% was demonstrated in 1954 (Chapin

et al. 1954). In a typical photovoltaic device, free carriers (in inorganics such as GaAs and Si) or excitons (in organics) are generated in a semiconductor material by absorbing photons with energies exceeding their bandgap (carbon nanotubes (inorganic) are exempted from the above rule because they create excitons upon photoexcitation owing to their one-dimensional (1D) nature). Further, these separated charge carriers are swept across the device by built-in electric field and extracted at the contact ends, which provide useful electric current. Over the years, improvement of the solar PV technology has undergone various modifications in fabrication leading to the device being categorized into four different generations according to the material used in the absorber layers. They are first generation (high cost/high efficiency), second generation (low cost/low efficiency), third generation (low cost/high efficiency), and fourth generation (low cost/high efficiency/flexible). An illustration of the different generations is presented in Fig. 1.1 (Jayawardena et al. 2013).

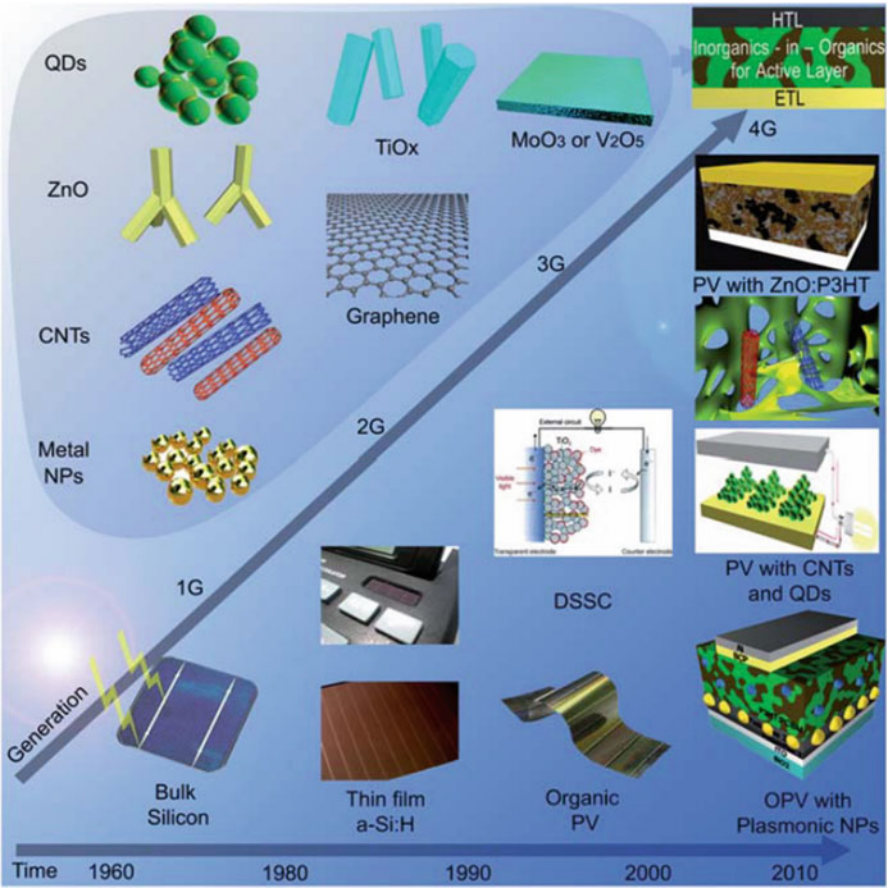

Fig. 1.1 Timeline of the four generations of photovoltaic devices, illustrating the changes from the first generation (1G) to fourth generation (4G) with associated nanomaterial components that comprise half of the 4G devices. (Reprinted with permission from Jayawardena et al. 2013)

First-generation (1G) solar devices (conventional and commercial solar cells) were based on Si wafer, start with Si single crystals, and further use bulk polycrystalline Si with higher conversion efficiency up to 25% (Zhao et al. 1998). However, these 1G devices suffered from high fabrication and installation costs.

Consequently, second-generation (2G) solar cells have been established with the aim of reducing the cost through utilization of thin film technology, and this technology includes amorphous silicon, cadmium telluride (CdTe) (Lin et al. 2012), and copper indium gallium selenide (CuInGaSe) (Shigeru et al. 2010) as light-absorber material. These devices are considerably less expensive than that of 1G solar cells because of the reduced amount of materials for manufacturing and processing cost; nevertheless, these solar cells possess lesser conversion efficiency than those of traditional bulk single crystalline PV cells. Developing plentiful electrical power from the sunlight at the moderate device cost is a tough challenge to meet the global energy demand. Nanotechnology has facilitated new opportunities to design next-generation solar cells through utilization of nanostructured semiconductor to accomplish higher solar energy conversion efficiencies at lower construction costs. Currently, third generation (3G) of solution-processed PV technology is an alternative to fabricate promising PV devices based on nanostructured materials with the aim to enhance the electrical performance of the solar cells, which was poor in the prior 2G technology (thin film), and, at the same time, maintain the lower construction costs. This technology mainly involves dye-sensitized solar cell (DSSC), quantum dot-sensitized solar cell (QDSSC), hybrid organic solar cell, perovskite solar cells, etc. (discussed below).

1.3.2 Dye-Sensitized Solar Cells

In 1991, Brian O'Regan and Michael Gratzel have published a work in the journal *Nature* entitled "A low cost and high-efficiency solar cell based on dye-sensitized colloidal TiO_2 films" with the power conversion efficiency (PCE) of 7.1–7.9% (O'Regan and Grätzel 1991). Later this device was recognized as DSSC or Gratzel cells. The DSSC is mainly based on photoexcitation of dye molecules on the surface of metal-oxide nanostructured semiconductors as a photoanode. In DSSC devices, TiO_2 is the dominant nanostructured semiconductor even though there is a development of various semiconductors such as ZnO (Shinde et al. 2010), SnO_2 (Birkel et al. 2012), WO_3 (Patil et al. 2005), Nb_2O_5 (Ghosh et al. 2011), and CuO (Guo and Yin 2014). Different nano-architectures of TiO_2, including nanoparticles, nanotubes, nanorods, nanowires, nanosheets, mesoporous, etc., have been reported for making more efficient DSSC device because the nanomaterials with different morphology will perform in a different way. Most of these nanostructures offer considerably improved power efficiency than that of a spherical one. For instance, densely aligned porous rutile TiO_2 nanorod arrays with the large internal surface area on a fluorine-doped tin oxide (FTO) substrate with the record PCE of 7.91% were developed (Lv et al. 2013). Also, three-dimensional (3D) hierarchical TiO_2 nanostructure was

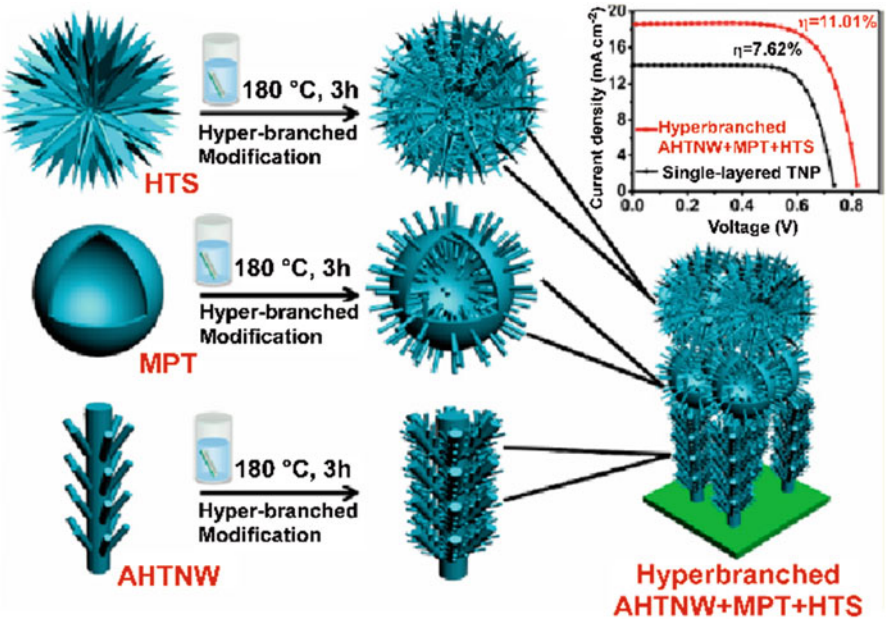

Fig. 1.2 A schematic illustration of hyperbranched modification of parental hierarchical TiO_2 microspheres (HTS), microporous TiO_2 hollow sphere (MPT), and anatase hierarchical TiO_2 nanowires (AHTNW) to form HTS branches, MPT branches, and AHTNW branches. (Reprinted with permission of Ref. Wu et al. 2014)

prepared and showed considerable improvement in efficiency from 6.64% to 8.50% due to the large surface area (104.5 $m^2\ g^{-1}$) of those nanostructures and great light-scattering ability (Ye et al. 2013). In another case, it was also attempted to design the DSSC device with multi-stack configuration of anatase TiO_2 nanowires (hyperbranched tree-like morphology, underlayer), TiO_2 hollow submicrometer-sized spheres (hierarchical rambutan-like morphology, intermediate layer), and TiO_2 microspheres (hyperbranched urchin-like morphology, top layer) on a FTO glass substrate (Fig. 1.2), boosted overall PCE up to 11.06% which is greater than single-layered TiO_2 nanoparticles (PCE 7.62%) (Wu et al. 2014). Also, recent studies have shown that hybrid structured photoanode by modifying the TiO_2 surface with a high conduction band edge semiconducting layer materials, such as ZnO (Boro et al. 2018; Diamant et al. 2004), ZrO_2 (Diamant et al. 2004; Luan and Wang 2014), SiO_2 (Maçaira et al. 2017), Ga_2O_3 (Chandiran et al. 2012), In_2O_3 (Brennan et al. 2013), Nb_2O_5 (Chen et al. 2001; Diamant et al. 2004), or SnO_2 (Desai et al. 2013; Diamant et al. 2004), or an insulating materials like Al_2O_3 (Diamant et al. 2004; Kim et al. 2010), MgO (Jung et al. 2005), or $BaCO_3$ (Wu et al. 2007) can effectively improve the power efficiency of DSSC by reducing exciton recombination rate. Besides, it has been revealed that incorporation of carbon-based materials, such as carbon nanotubes, multiwall carbon nanotubes (MWCNTs), graphene, etc., into the semiconductor photoanodes has the capability of improving charge

collection efficiency of photogenerated electrons leading to increased DSSC performance (Kim et al. 2015; Shih et al. 2016). For example, the DSSCs fabricated with the MWCNT-TiO_2 photoanode yielded PCE as high as 9.0% due to increased electron lifetime and reduced charge recombination (Dembele et al. 2013). The DSSCs made with graphene/N-doped TiO_2 composite photoelectrode showed the maximum efficiency of 9.32% (Kim et al. 2015).

1.3.3 Quantum Dot-Sensitized Solar Cell (QDSSC)

In recent years, QDSSCs are perceived as the most promising technology as 3G photovoltaics using inorganic QDs as nanoscale photon harvester due to their distinguished characteristics such as tunable optical bandgap, high optical absorption coefficient, and multiple exciton generation characteristics (Joicy et al. 2017, 2018). In QDSSC, the semiconductor QDs as an essential part should possess two important characteristics: (i) appropriate optical bandgap to maximize the harvesting efficiency of incident photons and (ii) high absorption coefficient. Over the years, many research efforts have been employed to develop the QDs with suitable bandgap as a photon sensitizer in QDSSC. Figure 1.3a summarizes the energy level diagram of some representative QD sensitizers applied in QDSSC (Ye et al. 2017). Cadmium chalcogenide QDs (such as CdS, CdSe, and CdTe) are the most preferably used ones as sensitizer because of their high stability in QDSSC. The most commonly used QD sensitizer can be classified into three categories: (i) cadmium chalcogenide QDs such as CdS (Li et al. 2011), CdSe (Gao et al. 2014), and CdTe (Yang and Zhong 2016), (ii) lead chalcogenide QDs including PbS (Heo et al. 2017) and PbSe (Zhang et al. 2014b), and (iii) antimony sulfide Sb_2S_3 (Hsieh et al. 2015). At the same time, another type of QDs with narrow bandgaps including Ag_2S (Chen et al. 2011), InAs (Yu et al. 2006), PbS, and PbSe has also been extensively applied in DSSCs owing to their ability to absorb the light energy in near-infrared (NIR) region of the electromagnetic spectrum. Furthermore, combining two kinds of chalcogenides in core-shell architecture as co-sensitizer is also well developed to further enhance the device performance by reducing exciton recombination rate and extending the absorption range to harvest the light energy. Recently, alloying chalcogenides (such as $CdSe_xTe_{1-x}$ (Du et al. 2016b), $CdSe_xS_{1-x}$ (Lan et al. 2018), $CuInSe_xS_{2-x}$ (McDaniel et al. 2013), ZnCuInSe (Du et al. 2016a), etc.) with metal including have proven to be a more significant way to enhance the power efficiency. For instance, CdSeTe QDSSCs with mesoporous carbon/Ti used as counter electrode have shown an extraordinary conversion efficiency of 11.16% with short circuit current density of $J_{SC} = 20.68$ mA/cm^2 by extending absorption edge to the NIR region (Du et al. 2016b). Again a higher certified PCE of 11.61% was reported when the QDSSC is made with ZnCuInSe alloyed QDs (Du et al. 2016a).

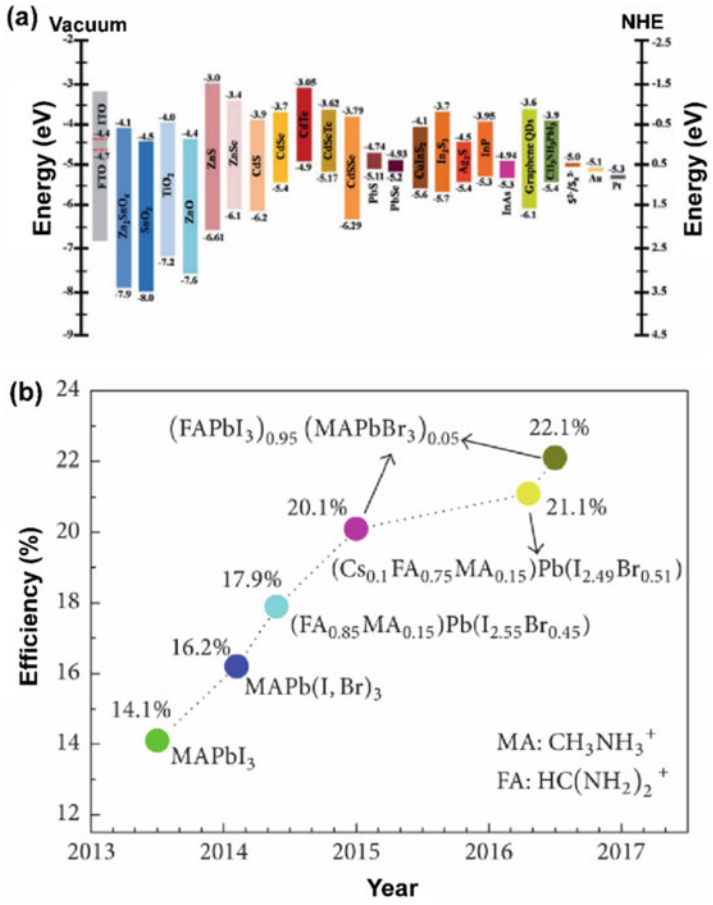

Fig. 1.3 (**a**) A summarized energy level diagram of some representative materials applied in QDSSCs. (Reprinted with permission of Ye et al. 2017). (**b**) The best efficiency of perovskite solar cells certified by NREL. (Reprinted from Zhou et al. 2017)

1.3.4 Perovskite-Sensitized Solar Cell

In the present decade, perovskite materials have emerged as a promising candidate for large-scale solar power generation owing to their excellent properties, such as large optical absorption coefficient (up to 10^4 cm^{-1}), lower exciton binding energy, large dielectric constant, cubic lattice-nested octahedral layered structure, etc. The first perovskite-sensitized solar cell was reported in 2009, which yielded the power efficiency of only 3.81% for $CH_3NH_3PbI_3$ (Kojima et al. 2009). Over the years, the most common perovskites used for solar cell application are organometallic halide perovskites such as $CH_3NH_3PbI_3$ (Ball et al. 2013), $CH_3NH_3PbBr_3$ (Kojima et al. 2009), and the mixed halide system $CH_3NH_3PbI_{3-x}Cl_x$ (Zhou et al. 2014).

Figure 1.3b represents the best efficiency of perovskite solar cells certified by the National Renewable Energy Laboratory (NREL) (Zhou et al. 2017). Within a few years, the certified PCE of perovskite solar cells have been rapidly boosted from 3.81% (Kojima et al. 2009) to 22.1% (Green et al. 2016). The highest PCE of 22.1% in perovskite solar cell has been attained on an aperture area of 0.046 cm^2. However, for more realistic PV performance evaluation, the measured power efficiency for cell area $\geq$1 cm^2 is encouraged. Very recently, perovskite/silicon tandems were fabricated by combining an infrared-tuned silicon heterojunction bottom cell with caesium formamidinium lead halide perovskite, and the highest certified PCE of 23.6% has been achieved on an area of 1 cm^2 (Bush et al. 2017). A review article on Inorganics-in-organics: Recent developments and the outlook for 4G polymer solar cells (Jayawardena et al. 2013) has outlined the 4G solar cells based on inorganic-in-organics which combine low cost/flexibility of polymer thin film with the stability of novel organic nanostructures (CNT, graphene, metal nanoparticles, and metal oxides).

1.4 Emerging Materials for Fuel Cell and Battery Application

Fuel cells and batteries are almost similar in a way that both are electrochemical cells containing two electrodes with an electrolyte sandwiched between them. Both of them use oxidation-reduction reactions to convert chemical energy into electrical energy. The difference however lies in the composition and the role of the electrode used. While battery uses electrodes that are typically metals immersed in mild acids, in fuel cells, the electrodes consist of proton-conducting media, carbon-supported catalyst, and electron-conducting fibers. Batteries are used for energy storage and conversion, whereas fuel cells are used only for energy conversion (Sharaf and Orhan 2014).

1.4.1 Fuel Cells

With a potential to reduce the environmental impact and geopolitical consequence with the use of fossil fuels, fuel cells have emerged to be an exciting alternative to combustion engines. Fuel cell is a device that directly converts the chemical energy into electrical energy, offering higher efficiency (50–70%) compared to conventional technologies like internal combustion engines (35% efficiency). Similar to combustion engines, fuel cell uses chemical fuel as its energy source, but like a battery, it directly converts the chemical energy into electrical energy without any relatively inefficient combustion step. Having a high energy conversion efficiency, low emissions, fuel flexibility, and zero noise pollution, these fuel cells have been considered

a promising technology to the future energy crisis and environmental issues (Haile 2003; Sharaf and Orhan 2014).

The active components of the fuel cells generally consist of an ion-conducting electrolyte sandwiched between an oxidant electrode (cathode) and a fuel electrode (anode), which is together referred as a membrane electrode assembly (MEA). Oxidation of the fuels like hydrogen, methanol, ethanol, methane, etc. occurs at the anode; reduction to oxygen, air, etc. occurs at the cathode; and a current is set up between the electrodes by the transport of ions present in the electrolyte (e.g., a proton-conducting membrane, ionic conductive doped ceria). There are various types of fuel cells that are categorized based on the nature of the electrolytes they employ. This categorization determines the kind of electrochemical reactions taking place in the cell, catalyst required, operating temperature range, and fuel required for the most suitable application. But basically they are categorized as low- (ca. <200 °C) and high-temperature (ca. >450 °C) fuel cells. Different fuel cell types are classified as proton-exchange membrane fuel cells (PEMFCs), direct methanol fuel cells (DMFCs), phosphoric acid fuel cells (PAFCs), alkaline fuel cells (AFCs), molten carbonate fuel cells (MCFCs), biofuel cells, polymer electrolyte fuel cells (PEFCs), and solid oxide fuel cells (SOFCs) (Abdalla et al. 2018). Among these, AFC, PEMFC, DMFC, and PAFCs are typical low-temperature fuel cells, whereas MCFC and SOFC belong to the high-temperature fuel cells. All these varieties of fuels are simultaneously under development for their respective application, and each category has its own merits and demerits. Each category of the fuel cell can be briefly described as below:

Alkaline fuel cell (AFC) is one of the fuel cell technologies developed and widely used in the US space program. Here, KOH in water is used as the electrolyte, and a variety of non-precious metals are used as the catalyst at the anode and the cathode along with an acid membrane. The key challenge of this type of fuel cell is its susceptibility to CO_2 poisoning which affects the cell performance and durability due to the carbonate formation. The PEMFC delivers high power density and also offers the benefit of low weight and volume compared with the other fuel cells. They only need hydrogen, oxygen from air, and water to operate at relatively low temperature, thus requiring low warm-up time. These are primarily used for the transportation and stationary applications. The DMFCs are powered by pure methanol which is mixed with water and that is fed directly to the fuel cell anode. The DMFCs do not have many of the fuel storage problems like other fuel cells since methanol has high energy density than hydrogen. These cells are mostly used for portable fuel cell applications like cell phones or laptop computers.

The PAFC is considered the "first generation" of modern fuel cells and one of the most mature fuel cells and first to be commercially used. The cell uses liquid phosphoric acid as an electrolyte which is contained in a Teflon-bonded silicon carbide matrix and porous carbon electrodes containing platinum catalyst. The efficiency of PAFC is only slightly greater than that of the combustion-based power plants. The PAFCs are less powerful than other fuel cells and are typically large, heavy, and also expensive. The SOFCs use a hard, nonporous ceramic compound as the electrolyte which is around 60% efficient at converting fuel to

Table 1.1 Chronological order of development taken place in sthe field of fuel cell technology (Sharaf and Orhan 2014)

Year(s)	Milestone
1839	W.R. Grove and C.F. Schönbein separately demonstrate the principals of a hydrogen fuel cell
1889	L. Mond and C. Langer develop porous electrodes, identify carbon monoxide poisoning, and generate hydrogen from coal
1893	F.W. Ostwald describes the functions of different components and explains the fundamental electrochemistry of fuel cells
1896	W.W. Jacques builds the first fuel cell with a practical application
1933–1959	F.T. Bacon develops AFC technology
1937–1939	E. Baur and H. Preis develop SOFC technology
1950	Teflon is used with platinum/acid and carbon/alkaline fuel cells
1955–1958	T. Grubb and L. Niedrach develop PEMFC technology at General Electric
1958–1961	G.H.J. Broers and J.A.A. Ketelaar develop MCFC technology
1960	NASA uses AFC technology based on Bacon's work in its Apollo space program
1961	G.V. Elmore and H.A. Tanner experiment with and develop PAFC technology
1962–1966	The PEMFC developed by General Electric is used in NASA's Gemini space program
1968	DuPont introduces Nafions
1992	Jet Propulsion Laboratory develops DMFC technology
1990s	Worldwide extensive research on all fuel cell types with a focus on PEMFCs
2000s	Early commercialization of fuel cells

electricity. These are the most sulfur-resistant fuel cells, which can tolerate sulfur to several orders of magnitude and also the carbon monoxide. The high operating temperature of the SOFCs requires material with high durability, which has been the key challenge faced. Presently, enormous research is being carried out to develop SOFCs with low operating temperature so as to increase the durability as well as reduce the cost of the cell. Development in the field of fuel cell technology is summarized in Table 1.1.

The SOFCs, because of their modularity and electrical efficiency, have a wide range of applications and are thus an important fuel cell. The SOFC consists of two porous components (anode and cathode) separated by a highly dense component (electrolyte). Yttria-stabilized zirconia (YSZ) or gadolinium-/samarium-doped ceria (GDC/SDC) has been successfully used as the electrolyte material because of their fast ionic conduction. Similarly, $La_{0.8}Sr_{0.2}MnO_3$ (LSM) has been successfully employed as the cathode material for high-temperature SOFCs. Anode material utilizes about 95% of the material used in the anode-supported cells. A cermet of nickel and YSZ have been the most widely used anode material for SOFCs. In order to overcome the problem of carbon deposition on the electrode, nickel is replaced with copper.

The performance and stability of intermediate-temperature SOFCs (IT-SOFCs) are very sensitive to impurities in the gas stream like sulfur, thus leading to degradation in activity of conventional IT-SOFC anodes like Ni/YSZ and

Ni/GDC. Meng et al. (Li et al. 2016a) have reported about enhancing the sulfur tolerance of Ni-based cermet anodes by ytterbium-doped barium cerate (BCYb) infiltration. In this work, the BCYb was impregnated into the conventional Ni/GDC cermet anode, and the cell performance in both pure H_2- and H_2S-containing fuels was investigated. It was observed that addition of BCYb has improved the initial cell performance in both H_2 and 500 ppm H_2S/H_2 fuels. Particularly, it enhanced the resistance to sulfur poisoning by increasing the water adsorption and dissociation that effectively removed the absorbed sulfur via oxidation reaction, thus releasing the active sites.

Nickel-free alternative materials like $BaZr_{0.1}Ce_{0.7}Y_{0.2-x}Yb_xO_{3-\delta}$ (Liu et al. 2009), yttrium-doped $SrTiO_3$ (Kurokawa et al. 2007b), $(La_{0.75}Sr_{0.25})(Cr_{0.5}Mn_{0.5})O_3$ (LSCM) (Kim et al. 2011; Lu and Zhu 2007; Zha et al. 2005), $La_{0.7}Sr_{0.3}VO_3$ (Cheng et al. 2006), $Sr_2MgMoO_{6-\delta}$ (Huang et al. 2006), $Ce_{0.9}Sr_{0.1}$ VO_x (Danilovic et al. 2009), and $La_{0.8}Sr_{0.2}Cr_{1-x}Ru_xO_{3-\delta}$-$Gd_{0.1}Ce_{0.9}O_{1.95}$ (Kobsiriphat et al. 2009) have been examined as a sulfur-tolerant anodes as well as alleviate carbon buildup problems. But these ceramic oxides have relatively low electronic conductivity compared to Ni. There are certain other ways adopted to boost the sulfur tolerance in the ceramic anodes like addition of nanosized particles like ceria (He et al. 2005; Kurokawa et al. 2007a), $Ce_{0.8}Sm_{0.2}O_2$ (Yun et al. 2011), and Pd (Babaei et al. 2012; Nabae and Yamanaka 2009; Ye et al. 2008; Zheng et al. 2012) to porous electrodes. Introduction of nanosized electrocatalysts can significantly promote the electrochemical activity of conventional Ni-based anodes toward the oxidation of hydrogen and hydrocarbon fuels and thus suppresses carbon cracking and sulfur poisoning. It is also (Kurokawa et al. 2007a) showed that a ceria nanocoating produced by infiltration of Ni-based SOFC has led to a stable performance that delivered more than 200–240 $mWcm^{-2}$ at 0.6 V for at least 500 h, with humidified hydrogen that contains a significant concentration of sulfur. Further (Yun et al. 2011), the effect of ceria and ceria-based oxides on sulfur poisoning was investigated where the anode surface was modified by coating porous ceria and a $Sm_{0.2}Ce_{0.8}O_2$ (SDC) thin layer on its pore wall surface (Fig. 1.4). Cell performance has been increased by 20% and 50% for ceria- and SDC-modified anode. There was no formation of bulk Ni_3S_2 at 700 °C and up to 100 ppm of H_2S, thus confirming that sulfur poisoning of Ni occurred through sulfur adsorption on the Ni surface. The thin layer of SDC in Ni/YSZ anode pore acted as a sulfur sorbent as well as provided additional TPB (triple boundary phase, electrode-electrolyte-gas phase) area; otherwise, ceria mainly acted as a sorbent for sulfur at high H_2S concentration (>60 ppm). Illustrations for triple boundary phase and gas phase diffusion are given clearly in Fig. 1.4. Due to the difference in density of cerium oxysulfide (6.1 g/cm^3) and ceria (7.7 g/cm^3), the pore size and porosity of the anode decrease that leads to the increase in the gas diffusion resistance. The mechanism for gas diffusion at the anode during H_2S poisoning is illustrated in Fig. 1.5. In order to investigate the anode performance, impedance spectra of anode-supported button cell were analyzed (Fig. 1.5). It was observed that polarization resistance was least for SDC-modified anode (1.0 Ωcm^2) when compared to ceria-modified anode (1.5 Ωcm^2) and unmodified Ni/YSZ (1.9 Ωcm^2). This was because at low oxygen partial pressure, Ce^{4+} is likely to be

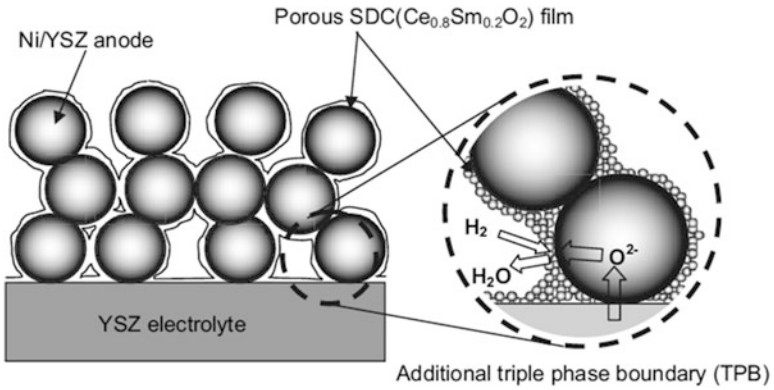

Fig. 1.4 Controlling anode microstructure using SDC coating on the Ni/YSZ anode pore structure. (Reprinted with permission from Yun et al. 2011)

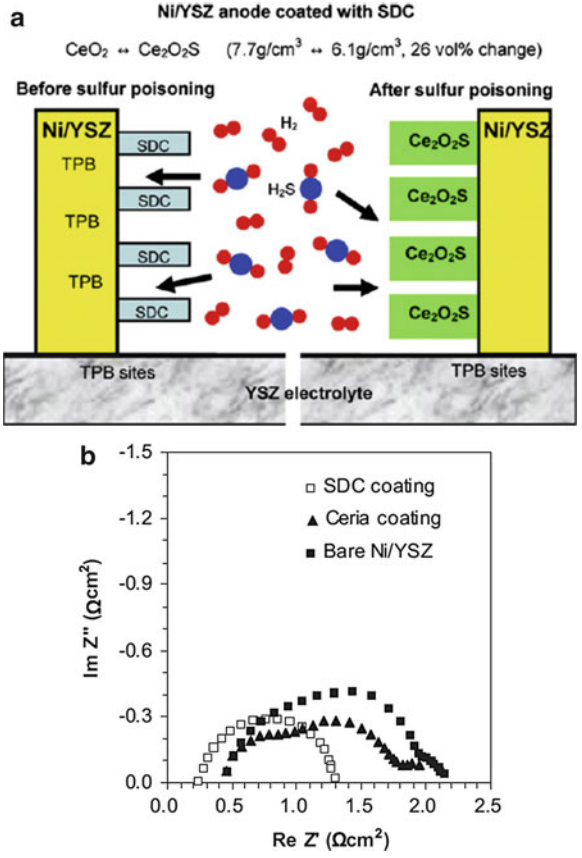

Fig. 1.5 (**a**) Illustration of gas phase diffusion in SDC-coated Ni/YSZ anode during H_2S poisoning. (**b**) Comparison of polarization resistance by coating of ceria and SDC in Ni/YSZ pore wall surface without H_2S at 700 °C. (Reprinted with permission from Yun et al. 2011)

reduced to Ce^{3+} by doping trivalent oxides such as Sm^{3+} that leads to increase in the oxygen ion defects. As a result, the ionic conductivity of oxygen ions is increased in doped ceria, leading to cell performance improvement.

A comparative study on the electrode behavior and performance of Ni/GDC as a function of Pd nanoparticle impregnation in a H_2S-containing H_2 fuel with H_2S concentration varied from 5 to 700 ppm at 800 °C is reported (Zheng et al. 2012). Results showed that the Pd nanoparticle impregnation has substantially enhanced the sulfur tolerance of Ni/GDC anodes. This is because the impregnated Pd nanoparticles on the electrode are associated with hydrogen dissociation and diffusion and reduced detrimental effects on the morphology and microstructure of Ni and GDC phases. The electrochemical performance of Pd-impregnated Ni/GDC anode for the oxidation reaction of methane, methanol and ethanol fuels was also studied (Babaei et al. 2012). Results showed that the impregnation of Pd nanoparticles has substantially reduced the electrode polarization resistance and overpotentials of the oxidation reaction of the fuel such as methanol and ethanol. The incorporation of Pd nanoparticles on the Ni/GDC has reduced the activation energy for methanol oxidation reaction over the use of pure Ni/GDC anode electrode. That is, the activation energy has decreased from 154 to 101 kJ mol^{-1} for a reaction on 0.15 mg cm^{-2} PdO-impregnated Ni/GDC anode. This is because Pd nanoparticles not only accelerate the oxidation reaction but also reduce the energy barrier of the oxidation reaction. The effect of adding dopant levels of precious metals (PM: Pt, Rh, or Pd) on cell performance of the SOFC anodes is based on carbon, ceria and YSZ (Steven et al. 2003). It was observed that PM-doped anodes remained stable in dry CH_4 and *n*-butane over a period of at least 24 h. The maximum power density for H_2 and *n*-butane has increased almost by a factor of 2 upon addition of PM, while the maximum power density for CH_4 has increased by a factor of almost 10 over that measured on a Cu-ceria-YSZ anode to 280 mW/cm^2 at 973 K. The metal nanoparticle (Pt, Pt-Ru)-decorated polypyrrole (PPy)-carbon nanotube composites are synthesized and used as catalysts for methanol oxidation (Selvaraj and Alagar 2007). The cyclic voltammetric response revealed that methanol oxidation current of the Pt (or Pt-Ru)/PPy-CNT/graphite electrodes is higher than that of Pt/PPy/graphite electrodes. This is because of the following reasons such as (i) increase in the electrochemically accessible surface areas due to the combined effect of polymers and carbon nanotubes, (ii) electronic conductivity and efficient charge transfer at polymer/electrolyte interfaces allowing dispersion, and (iii) unique relationship between the peak current and peak current densities. In addition to that, the Pt-Ru catalyst showed a better long-term cycling stability compared to pure Pt nanoparticles.

The most important factor that influences the performance of fuel cells is the materials that are used as a catalyst. The presence of the catalyst speeds up the reaction, thereby increasing the efficiency of the fuel cell. The electrodes consist of a porous material that is covered with a layer of catalysts. The efficiency of the fuel cells can be improved with the use of catalysts, and noble metals have a good catalytic efficiency. However, use of noble metals is highly expensive, which imposes a huge obstacle for fuel cell commercialization. Hence, it demands the

development of new catalysts improving the oxidation-reduction reaction (ORR) of the electrode. Further, in order to reduce the amount of platinum metal used in the electrode and make sure the activity and stability of the catalyst kept at a high level, various methods, like use of CNT as support material (Luo et al. 2015), noble metal alloy, no noble metal-containing catalysts (Sheng et al. 2014), etc., have been developed. The Pt electrode exhibits the highest electrocatalytic activity among all the metal catalysts used for anode and cathode reactions. In spite of its excellent properties, Pt has certain disadvantages that limit its application in fuel cell. First is the self-poisoning originating from strong CO adsorption on the surface of Pt, second is the reduction in the ORR performance, and third is the limited reserve of it in nature which results in high cost, thus hindering the wide commercialization. A comprehensive review on graphene-supported nanoelectrocatalysts for fuel cell application is presented (Liu et al. 2014). The review summarized the synthesis techniques and applications of doped graphene and graphene-supported nanoelectrocatalysts in fuel cells as anode and cathode catalyst. Figure 1.6 illustrates

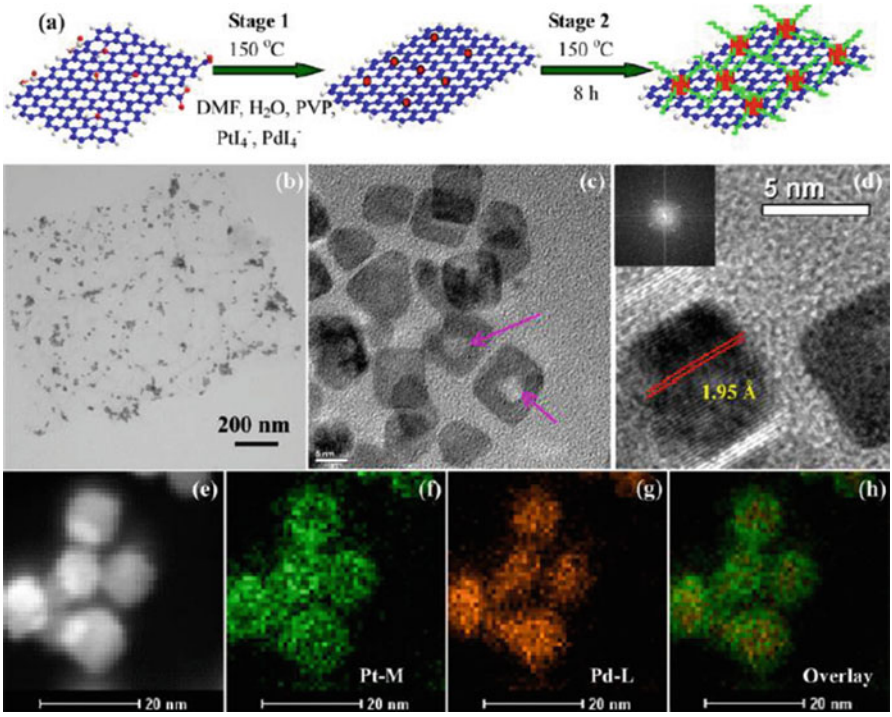

Fig. 1.6 (**a**) Schematic illustration of the one-pot hydrothermal synthesis of PtPd alloy nanocubes supported on rGO. (**b**) TEM and (**c**, **d**) HRTEM images of the PtPd alloy nanocubes dispersed on rGO at different magnifications. The inset in (**d**) shows the FFT pattern of an individual PtPd nanocrystal. (**e**) The high-angle annular dark-field (HAADF)-STEM image of PtPd/rGO and the corresponding elemental mapping of (**f**) Pt, (**g**) Pd, and (**h**) the overlay. (Reprinted with permission from Lu et al. 2013)

the one-pot hydrothermal method used to synthesize PtPd nanocubes supported on graphene for methanol electrooxidation (Lu et al. 2013).

In order to overcome the problem of high-cost and energy-demanding manufacturing processes of the advanced ceramics (YSZ), the self-supported 3% yttria-stabilized zirconia (3YSZ) electrolyte is printed using stereo-lithography 3D printer (Masciandaro et al. 2017). The functionality of the honeycomb-shaped 3YSZ membrane has been evaluated in terms of ionic conductivity and gas tightness, where they obtained an ionic conductivity of 0.022 S/cm at 900 °C. Under fuel cell operation conditions, the open circuit voltage of 1.14 ± 0.05 V at 800 °C was measured that perfectly matched with the theoretical values for their application in fuel cells. An excellent review (Antolini 2010) has been published on composite materials as an emerging class of fuel cell catalyst supports. Generally, highly dispersed platinum or platinum-based catalysts on conductive support are commonly used as electrode materials in low-temperature fuel cells where the performance of the cell strongly depends on the characteristic of the support material. The main requirements for a suitable fuel cell catalyst are high surface area for high metal dispersion, suitable porosity to boost gas flow, high electrical conductivity, and high stability under fuel cell operating conditions. Since the use of plain carbon, ceramic, or polymer materials was not completely satisfactory, use of hybrid polymer-carbon, ceramic-carbon, and polymer-ceramic materials have been proposed where the synergistic effect has shown improved characteristics than the bare components. Recent review has summarized various materials and their operational related issues (of anode, cathode, electrolyte, sealant, and interconnects) (Fig. 1.7) for the selection of high-performance SOFC, which shows that there are vast research opportunities in the field of SOFC (Mahato et al. 2015).

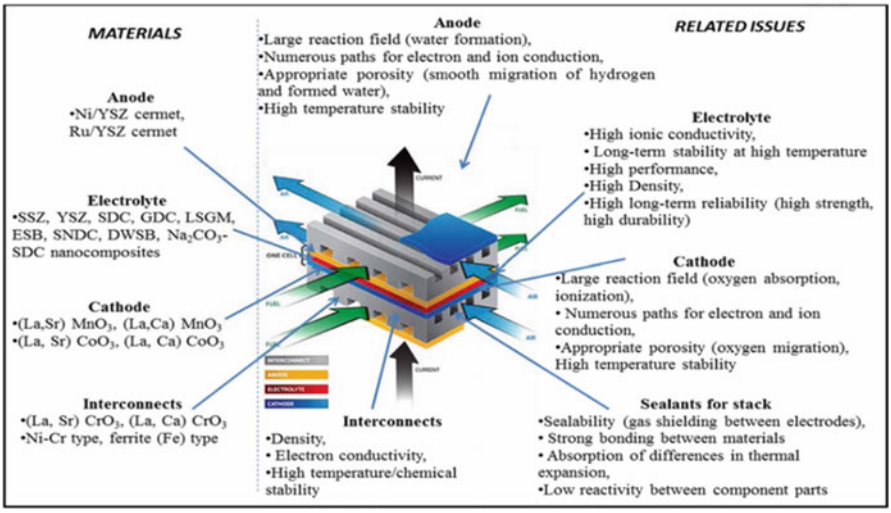

Fig. 1.7 Some of the materials and related issues with SOFC. (Reprinted with permission from Mahato et al. 2015)

It is also worth to note that the microbial-based fuel cells are also coming up as a new technology for energy production (Logan and Regan 2006). In a typical microbial fuel cell, chemical energy is converted into electrical energy by the chemical reaction catalyzed by bacteria. Of course, the appropriate selection of anode and cathode materials and electrolytes is very important. The main requirement is that the surface area of the anode and cathode is to be very high so that the one made with nanomaterials can be a good option.

1.4.2 Batteries

Batteries are in general classified as primary and secondary batteries. The primary batteries convert chemical energy into electricity as long as the chemical reactions are happening, that is, once the chemicals are over by the reaction, then it stops supplying electrical current. On the other hand, the secondary batteries are the ones that can be recharged once it is over, by external power supply so that it can be repeatedly used. Evolution of battery has started right from Luigi Galvani, Alessandro Volta, Gaston Plante, Gratzel, and so on, and it happened in various stages. It started from Volta's wet pile, lead-acid, Leclanche to the very heavily used one, Li-ion batteries. Owing to the unmatched volumetric energy density and high charge-discharge current rates, rechargeable lithium ion (LIB) batteries have been found to be very promising and dominated the portable electronic industries. It was first commercialized by Sony Corporation for the application of different portable electronic devices. Lithium, as the most electropositive element and the lightest metal, is a unique element for the design of high-density energy storage system. Materials involved in Li-ion batteries consist of carbon which is porous in nature, usually graphite as the anode and metal oxides as a cathode. Working principle includes the storage of lithium in the anode terminal and its transportation to the cathode terminal by the electrolyte. The choice of the electrode depends upon their electrochemical potential values as well as the position of relative to HOMO-LUMO energy gap of the electrolyte. The roadmap showing the development of the anode and cathode materials for the Li-ion batteries is presented in Fig. 1.8 (Marom et al. 2011).

The most common cathode components are lithium nickel, manganese cobalt oxide, nickel oxide, cobalt oxide, manganese spinel, iron phosphate, and titanates. Among them lithium nickel and manganese cobalt oxide have a higher energy density and cell voltage. The other cathode materials are $LiCoO_2$, $LiNiO_2$, $LiMn_2O_4$, partial substitution of cobalt for nickel ($Li_xNi_{1-x}O$), LiV_3O_8, $LiMPO_4$, and $LiFePO_4$ (Rozier and Tarascon 2015). Three categories of materials, i.e., Li [MnFe]PO_4, Li_2MnO_3, Li[MnNiCo]O_2, and $LiMn_{1.5}Ni_{0.5}O_4$, have shown prospects for practical development, and it is expected that a successful implementation of any of these compounds as cathode materials could take Li-ion technology well beyond its current limits (Marom et al. 2011).

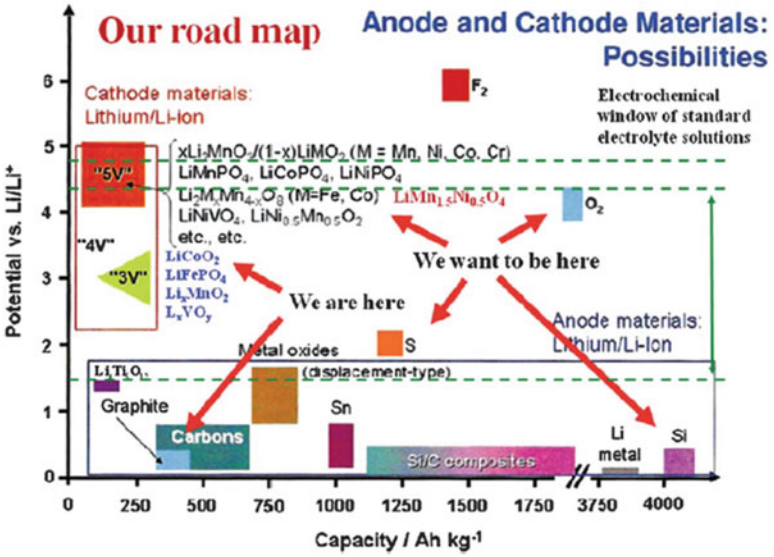

Fig. 1.8 The roadmap for R&D of new electrode materials, compared to today's state of the art. The *y*- and *x*-axes are voltage and specific capacity, respectively. (Reprinted with permission from Marom et al. 2011)

The anode material of Li-ion batteries consists of four most promising groups of materials, i.e., (i) carbonaceous materials/graphite, (ii) Sn- and Si-based alloys and composites (Chen et al. 2010), (iii) metal oxides (Amine et al. 2010), and (iv) Li_xTiO_y (Park et al. 2010)-based electrodes. A synthetic route to obtain Sn-sandwiched composite nanoparticles by ball milling with rigid SiC nanocores to form a SiC@Sn core-shell nanocomposite and then carbon coating the SiC@Sn nanoparticles with graphite to produce SiC@Sn@C nanoparticles is developed (Chen et al. 2010). The Sn-sandwiched nanoparticles exhibited a considerable high Li storage with the capacity of ~600 mA h g^{-1} and an excellent cycling stability with ~90% retention capacity at 100 cycles, showing a prospect for practical lithium battery applications.

Miniaturization of the electrodes in LIBs is a smart approach to store as much energy in a small volume in order to address the huge energy demand. Therefore, enormous research is being done in nanostructured anode materials that are more effective for fast Li intercalation-de-intercalation reactions, short Li^+ diffusion path length, and fast transportation to the current collector. The particle size effect of nickel oxide nanoparticles as anode for lithium ion battery is studied (Cheng et al. 2014b). It is observed that NiO nanoparticles synthesized in confined space of ordered mesoporous silica showed anomalously high capacity and higher energy efficiency compared to the submicron-sized NiO. This higher energy efficiency was due to the reduction of the hysteresis loop between charge and discharge voltage

plateaus. The main drawback of the conversion reaction-type Li-ion battery anode materials is that they usually show higher hysteresis. There are certain disadvantages with the use of nanoparticles as anode materials, such as loose contact between the nanoparticles and the poor electronic/ionic transportation by random walk, thereby limiting the electron collection efficiency in the current collector. Subsequently, the 1D nanostructures have been considered superior to the nanoparticles due to their directional electronic transportation resulting in high electron collection efficiency. It is also demonstrated how the pulverization effect and the capacity fading issues are circumvented by silicon nanowires (Chan et al. 2007). The silicon nanowires can accommodate large strain without pulverization, provide good electronic contact and conduction, and display short lithium insertion distance, by which they maintain a discharge capacity close to 75% of this maximum. Hollow sphere and core-shell nanostructures of the same or different materials were also considered as alternative for stable nanostructured anode. An interesting approach is reported for efficient synthesis of SnO_2 hollow sphere inside mesoporous silica nanoreactors (Fig. 1.9) (Ding et al. 2011). Lithium ion storage properties were compared with SnO_2 solid particles, and the SnO_2 hollow nanosphere showed the highest discharge capacity of 1571 mA h g^{-1}.

Carbonaceous materials were the first commercially used successful anode materials in LIBs. Their different forms are categorized as graphite/graphitized material and non-graphitized soft carbon and hard carbon, each of them having different structures as well as electrochemical properties. It is demonstrated that the

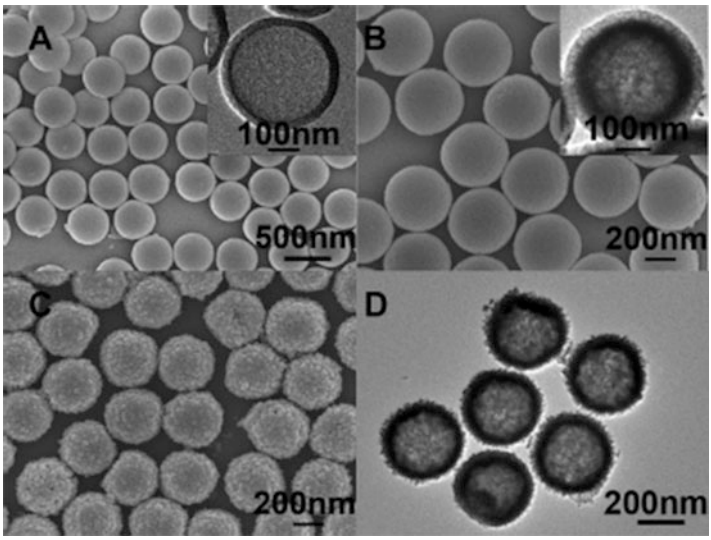

Fig. 1.9 (**a**) SEM and TEM (inset) images of mesoporous silica hollow spheres with a diameter of 400 nm; (**b**) SEM and TEM (inset) images of SnO_2@silica double shells; (**c**, **d**) SEM and TEM images of SnO_2 hollow spheres, which are prepared by removing silica with 2 wt % HF solution for 30 min. (Reprinted with permission from Ding et al. 2011)

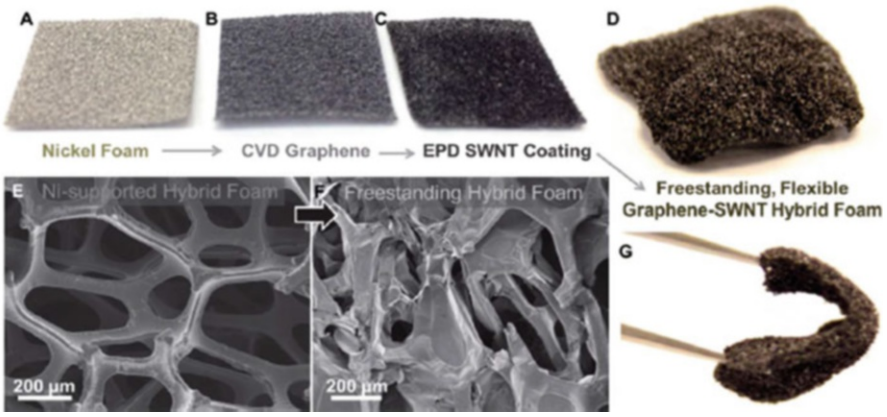

Fig. 1.10 (**a**–**d**) Pictures of the materials formed during steps associated with the fabrication of 3D freestanding hybrid graphene-SWNT foams starting from (**a**) nickel foam, (**b**) nickel foam after CVD coating of graphene, (**c**) the graphene/nickel foam material after EPD of a thin layer of SWNTs, and (**d**) the freestanding graphene-SWNT foam after dissolution of Ni in HCl. (**e**, **f**) SEM images of (**e**) nickel foam-supported graphene-SWNT hybrid materials and (F) freestanding graphene-SWNT hybrid materials. (**g**) Photograph showing the flexure of a foam material at over a 90° angle, emphasizing the mechanical rigidity and flexibility of the material. (Reprinted with permission from Cohn et al. 2014)

fabrication of 3D freestanding foams (Fig. 1.10) of hybrid graphene-single-walled carbon nanotube materials with reversible capacities of 2640 mA h g^{-1} at 0.186 A g^{-1} maintains an excellent rate performance of 236 mA h g^{-1} at 27.9 A g^{-1} (Cohn et al. 2014). These materials are promising to achieve simultaneously 10X greater capacity and over 10X faster charging rate than that can be achieved with conventional battery technology.

Certain disadvantages of using graphite such as low lithiation potential can be avoided by using spinel-structured $Li_4Ti_5O_{12}$ (LTO). The LTO works at a potential of 1.5 V vs. Li/Li^+, and thereby the solid electrolyte interface (SEI) layer formation can be avoided. The SEI, if grows, depletes the available Li ions for further reaction. LTO hollow microspheres were synthesized with the shell consisting of nanosheets exhibiting high reversible capacity and superior rate performance even at a very high rate (131 $mAhg^{-1}$ at 50 °C) (Tang et al. 2009). However, the LTO material suffers from limitations related to poor intrinsic electron conductivity as well as moderate ionic conductivity. Recently, a number of targeted fundamental strategies were put forward for controllably tuning (i) morphology, (ii) attachment modalities of carbon, and (iii) ion doping of the LTO material in order to achieve improved high-rate performance (Wang et al. 2018).

The third and very important component in LIB is the electrolytes. Electrolytes that are active at room-temperature Li-based batteries are classified into five types: (i) nonaqueous electrolytes, (ii) aqueous solutions, (iii) ionic liquids, (iv) polymer electrolytes, and (v) hybrid electrolytes (Li et al. 2016b). The most commonly used

electrolyte comprises of lithium salt, and they are listed such as lithium hexafluorophosphate ($LiPF_6$) dissolved in organic carbonates, particularly mixture of ethylene carbonate (EC) with dimethyl carbonate (DMC), propylene carbonate (PC), diethyl carbonate (DEC), and/or ethyl methyl carbonate (EMC). Organic fluoro-compounds are also one of the most promising electrolyte solvents for high voltage condition, because the fluorinated molecules have higher oxidation potentials due to a strong electron-withdrawing effect of the fluorine atom. However, the poor safety characteristics have been the major bottleneck for the widespread development of this technology. It is also reported that a novel nonaqueous $Li_2B_{12}F_{12-x}H_x$ electrolyte, using lithium difluoro(oxalato)borate as an electrolyte additive, has superior performance than the conventional $LiPF_6$-based electrolyte with regard to cycle life and safety, including tolerance to both overcharge and thermal abuse (Chen et al. 2013). Cells were tested with the $Li_2B_{12}F_9H_3$-based electrolyte that maintained about 70% initial capacity even when cycled at 55 °C for 1200 cycles, and the intrinsic overcharge protection mechanism was active up to 450 overcharge abuse cycles.

In addition to lithium ion batteries (LIB), Li-S batteries have been thought as one of the most promising batteries because of their overwhelming advantage in energy density (2600 Wh kg^{-1} in theory) that is up to five times that of commercial LIBs. Unfortunately, since the Li-S cell uses organic electrolytes, it usually shows poor cycle performances and low Coulombic efficiencies due to the formation of various lithium polysulfide species. Hence, there comes a necessity for searching more suitable nonaqueous electrolytes for Li-S batteries. It is reported how the shuttle factor of polysulfide can be mediated from 0.02 to 0.99 by matching the electrolyte/sulfur loading in Li-S batteries (Cheng et al. 2014a). A Li-S cell with a high initial discharge capacity of 1053 mAh g^{-1} at a high rate of 1C and an ultralow decay rate of 0.049%/per cycle during 1000 cycles was obtained by using carbon nanotube@sulfur cathode, and polysulfide shuttle was suppressed to a shuttle factor of 0.02.

Polymer electrolytes provide a solution to low mechanical strength and safety issues of the liquid electrolytes. Polyethylene oxide has been the common solid electrolyte for battery with a drawback of low ionic conductivity that limits the application. Addition of lithium salt and ceramic particles have been adopted to overcome these problems. It is reported that ceramic fillers can facilitate the formation ionic conduction network in polymer-based solid electrolytes whereby the ionic conductivity has been increased by a magnitude of three orders (Liu et al. 2015b). Polyacrylonitrile-$LiClO_4$ incorporated with 15 wt% $Li_{0.33}La_{0.557}TiO_3$ nanowire composite electrolyte exhibited an unprecedented ionic conductivity of 2.4×10^{-4} S cm^{-1} at room temperature.

It is to be noted that besides lithium-based system, there are also sodium, magnesium, calcium, zinc, and aluminum ion-based batteries available, and a lot of research is being carried out on them to outperform the existing battery technology such as LIB, but only future will decide on it.

1.5 Nanomaterials for Environmental Remediation and Monitoring

1.5.1 Photocatalysis

Discharge from industries into the water stream is a big social issue that has to be tackled. Mostly they are the dyestuffs released from textile industrial sector, containing many types of organic dye molecules that are threat to clean environment. Removal of organic dyes from the contaminated water body or industrial effluents is a very important environmental issue (Chan et al. 2011). Different types of conventional methods such as coagulation, microbial degradation, adsorption on activated carbon, incineration, biosorption, filtration, and sedimentation have been used to degrade the dye molecules from the contaminated water. In certain cases, where the wastewater contains particles in colloidal form, coagulation process is used to clean it up. In this process, coagulant salts are added to the wastewater which forms micro flocs and promotes faster settling of the colloidal pollutants which can be easily separated. This process can achieve the efficiency only up to 60–70% (Ayekoe et al. 2017). The microbial method is meant to remove the dissolved organic compounds from industrial effluents. Many microbes, including bacteria, fungi, and actinomycetes, have been developed for their ability to decolorize the dyes. This method is not suitable to degrade all types of dye molecules (Han et al. 2009). Activated carbon is the commonly used adsorbent material for the removal of organic compounds from the industrial/textile wastes. All these conventional methods are expensive, and the final by-products usually are left with a large amount of residues, which creates the secondary level of land pollution (Rashed et al. 2017). These methods mostly transfer the pollutants from one phase to another phase and are also very slow and ineffective process. Therefore, economic and harmless removal of the organic dyes is still a significant research problem. In order to overcome the demerits of these conventional methods, advanced oxidation processes (AOPs) have proven to be a very useful method. This method is comparatively new and promising technique, which can completely degrade the dye molecules into harmless products like CO_2 and H_2O under mild conditions (Beura et al. 2018). When light source (ultraviolet/visible) with energy equal to or greater than the bandgap energy is irradiated on the photocatalyst, electrons in the valence band get energy and become excited. These excited electrons (e^-) are promoted to the conduction band, thereby creating positive holes in the valence band (h^+). The conduction band electrons and valence band holes then migrate to the surface of the photocatalyst generating a redox environment for the photocatalytic degradation of the dye molecule to occur. The conduction band electrons react with the oxygen to produce a superoxide radicals ($^{\bullet}O^-_2$). The valence band holes (h^+) will react with OH^- to form $^{\bullet}OH$ radicals. These $^{\bullet}O^-_2$ and $^{\bullet}OH$ radicals further react with the dye molecules and effectively degrade them into harmless, simple molecules, such as CO_2 and H_2O. The AOP generates very reactive species such as hydroxyl radicals, which further activate the oxidation reaction to degrade the organic dye molecules into harmless mineralization. It has

several advantages like fast, nondestructive, inexpensive, complete mineralization, and low-temperature process (can happen at room temperature) (Nageswara Rao et al. 2009). Numbers of nanostructured homogeneous metal oxides, such as titanium dioxide (TiO_2), zinc oxide (ZnO), tungstate (WO_3), vanadate (VO_4), molybdate (MoO_4), etc., have been reported to be photocatalysts (Khataee and Kasiri 2010) through AOP. The metal oxides are the most attractive photocatalysts in environmental cleaning because they are nontoxic, have high photocatalytic activity and photochemical stability, and are low cost and environment-friendly (Han et al. 2009; Lv et al. 2017). However, properties such as fast recombination rate of photogenerated charge carriers, active mainly in the UV region (because sunlight contains less than the 5% of UV light), have inhibited metal oxides from its strong use as photocatalyst (Inturi et al. 2014). Therefore, many researches have been carried out to improve and to make them active in visible light region. Sometimes decorating the surface of metal oxides with noble metal nanoparticles (Deng et al. 2012; Inturi et al. 2014; Jin et al. 2015; Naik et al. 2013; Yin et al. 2014) (such as Au, Pt, Ag, and Pd) and developing hetero-structures could be an effective approach to improve the photocatalytic activity of the metal oxide photocatalyst (Dai et al. 2014; Su et al. 2011; Zou et al. 2010).

A simple metal oxide ZnO with hierarchical microstructures was prepared by hydrothermal method, and their photocatalytic degradation of methylene blue (MB) under UV light irradiation was evaluated. The photocatalytic activity was investigated as a function of different morphologies such as porous flower, porous microsphere structure, and branchy structure (Wang et al. 2017) where the degradation efficiency for MB was obtained to be 90.15, 86.11 and 58.57%, respectively, under 180 min of UV irradiation. The maximum degradation efficiency was exhibited with ZnO porous structure, compared with pure ZnO, which was due to possessing high surface area and large amount of oxygen vacancies (Wang et al. 2017). Another interesting choice of the materials than using just the simple metal oxides is that to use the metal oxides with their surface decorated with metal nanoparticles. In many cases, the surface plasmon resonance (SPR) of the metal nanoparticles would assist and enhance the photocatalytic activity. The Au nanoparticle-dispersed Co_3O_4 composite films were made by spin-coating method and used for the degradation of Congo red dye (CR) under visible light irradiation (Wang and Zhang 2013). The SPR peak of Au nanoparticles has appeared at 630 nm in the Au-CoO_3 composite films (Fig. 1.11). Pure Co_3O_4 film degraded the CR to 17% in 60 min under visible light, whereas the 40% Au nanoparticles containing CoO_3 had degraded the CR to 81% in the same time period of irradiation. The photocatalytic mechanism taking place in the Au-CoO_3 nanocomposite composite films with the SPR-assisted visible light photocatalysis is thoroughly explained with a schematic (see Fig. 1.8 of Wang and Zhang 2013). The SPR effect of Au has strongly enhanced the efficiency of Au-dispersed Co_3O_4 in the degradation of CR dye under visible light (Wang and Zhang 2013).

Recently, the Pd nanoparticles that decorated BiOBr by two-step synthesis method were developed: first the BiOBr was prepared by hydrothermal method and then followed by the photodeposition of the Pd nanoparticles on BiOBr (Meng

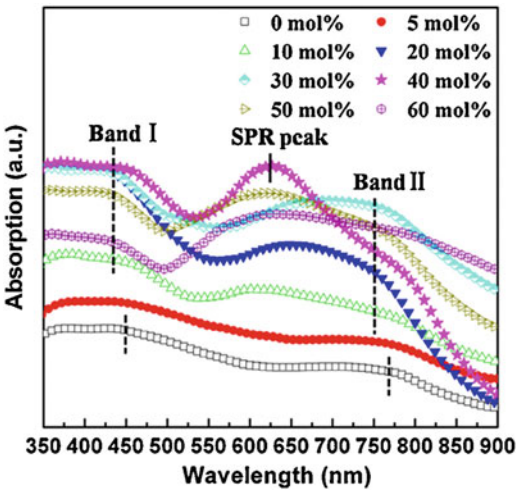

Fig. 1.11 Optical absorption spectra of Co_3O_4 and Au/Co_3O_4 thin films with various Au contents. (Reprinted with permission from Wang and Zhang 2013)

et al. 2018). Photocatalytic activity of pure and Pd-BiOBr was studied for the degradation of phenol under visible light irradiation. Figure 1.12 shows the SEM micrographs of pure BiOBr and Pd-BiOBr, where a platelet-like structure of BiOBr is well noticed (Fig. 1.12). The Pd particles that decorate the surface of the BiOBr are clearly seen in Fig. 1.12d. The photocatalytic efficiency of pure BiOBr was 67% over 300 min, whereas the Pd-BiOBr showed better activity due to the improved harvesting capacity of visible light photons via the SPR of Pd. Figure 1.13 shows the photocurrent measurement of Pd-BiOBr and BiOBr: the photocurrent response of Pd-BiOBr is five times better than the pure BiOBr because of the enhanced electron-hole pair recombination rate and improved visible light absorption (SPR effect). This activity was found to be Pd content-dependent; when the Pd content was increased from 0.1% to 0.5%, the photocatalytic efficiency for phenol degradation has increased from 77% to 100% under visible light (Meng et al. 2018).

The Ag/ZnO nanocomposite was prepared by thermal decomposition method for the first time with varying content of Ag, and their photocatalytic activity was evaluated against model organic dyes MB and MO (Saravanan et al. 2013a). Their activity was also checked on the real industrial effluents collected from the industry. It was clearly observed that the Ag-decorated ZnO has photodegraded much efficiently than the pure ZnO under visible light. More importantly, the activity has been shifted from UV region to visible region by dispersing Ag nanoparticles with ZnO. Parameters such as optimum Ag content (10 wt%) and surface area were found to be the reasons for the improved visible light photocatalytic activity. The same author has done the photocatalytic work with the pure ZnO (Saravanan et al. 2013b), ZnO/CuO (Saravanan et al. 2015a), and ZnO/Ag/CdO (Saravanan et al. 2015b) nanostructures on the photodegradation of textile effluents under visible light irradiation.

The Au-decorated TiO_2 (Au/TiO_2) nanoforests with anatase/rutile phase junctions with controlled locations of Au nanoparticles were fabricated for photocatalytic

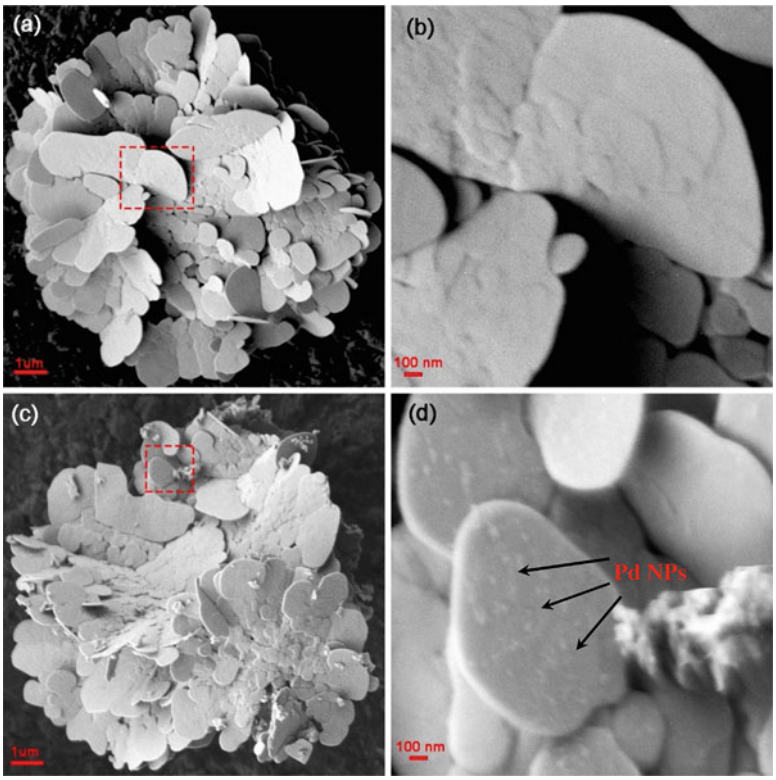

Fig. 1.12 SEM micrographs of BiOBr at (**a**) low and (**b**) high magnification, 0.5 Pd-BiOBr at (**c**) low and (**d**) high magnification for pure BiOBr and 0.5 Pd-BiOBr. (Reprinted with permission from Meng et al. 2018)

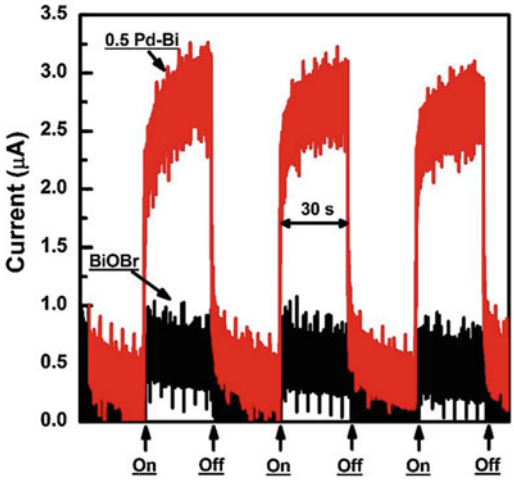

Fig. 1.13 The transient photocurrent responses of the BiOBr and Pd-BiOBr electrodes (Reprinted with permission from Meng et al. 2018)

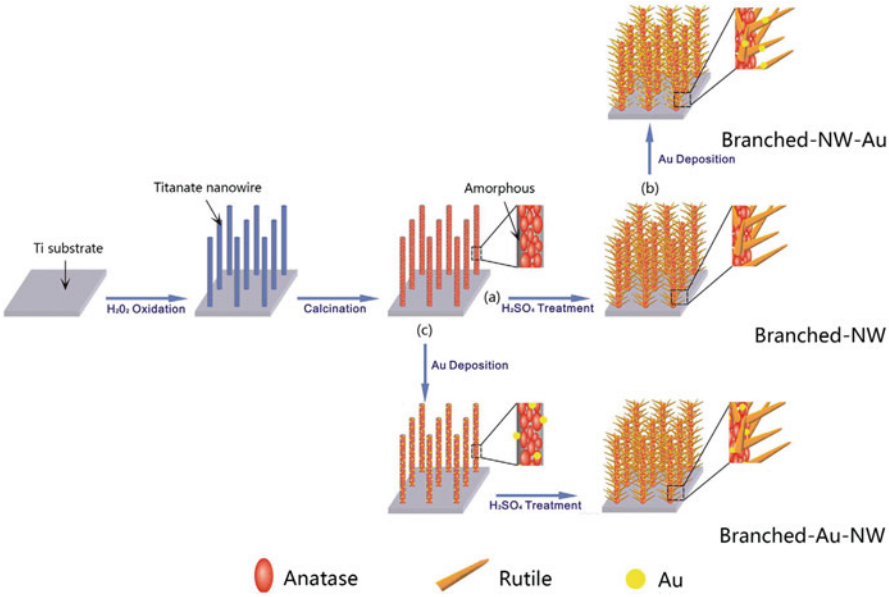

Fig. 1.14 A schematic diagram showing the formation of the branched TiO_2 nanowires (**a** Branched-NW), those after the Au loading (**b** Branched-NW-Au), and the branched TiO_2 nanowires with an intermediate Au loading (**c** Branched-Au-NW). (Reprinted with permission from Yu et al. 2017)

degradation of three dyes, namely, p-nitrophenol, phenol, and rhodamine B (Rh-B) (Yu et al. 2017). The Au decoration has increased the photocatalytic activity because of the beneficial effects of either electron trapping or localized surface plasmon resonance (LSPR) under the irradiation of either UV or visible light. Gold nanoparticles located preferably at the interface of anatase/rutile led to a further enhanced photocatalytic activity. Figure 1.14 shows a scheme of growing TiO_2 nanowires, and the microstructure of TiO_2 nanowires decorated with Au nanoparticles (NPs) on its surface is shown in Fig. 1.15. The Au nanoparticles are seen with the dark contrast (as spots) along with the TiO_2 nanowires. The rate constant of photocatalysis for the photodegradation of Rh-B has increased from 0.86×10^{-2} min^{-1} for the Au-TiO_2 nanowire to 4×10^{-2} min^{-1} for the just branched TiO_2 nanowire. There is a clear fivefold increase in the reaction rate when the branched TiO_2 nanowire is decorated with Au nanoparticles. The Au-decorated photocatalyst shows a better photocatalytic activity under the UV light irradiation, because of its SPR effect (Yu et al. 2017).

The other way is to alter the photocatalytic activity of the photocatalyst by doping them with appropriate ions. Most of the times, they change the bandgap of the photocatalyst so that it will become active in the visible region. One such photocatalyst, nanostructured ZnO with vanadium doping (0–15%) was prepared by sol-gel method, and their photocatalytic activity in the degradation of methylene

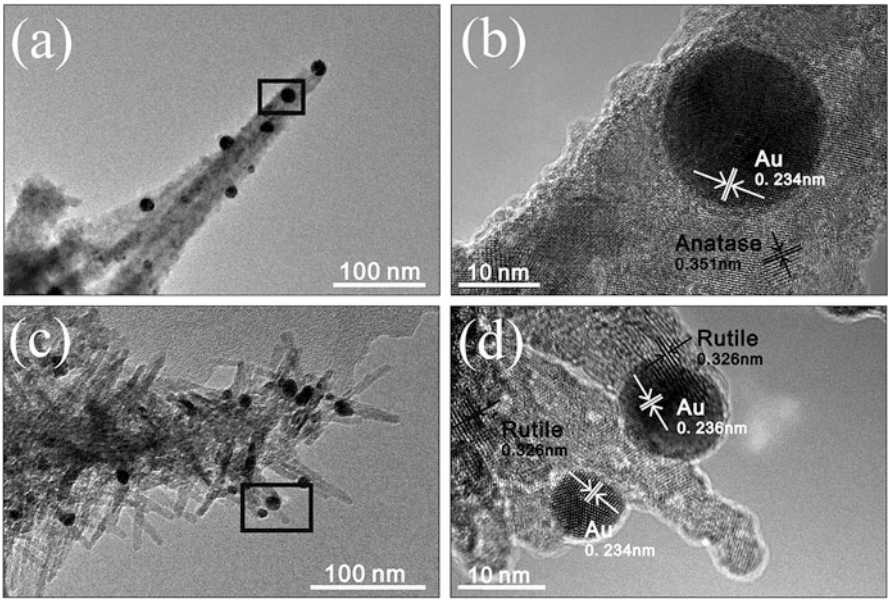

Fig. 1.15 (**a**, **b**) TEM and HRTEM images of the Au-decorated nanowires just before the final H_2SO_4 treatment; (**c**, **d**) TEM and HRTEM images of the Branched-NW-Au. (Reprinted with permission from Yu et al. 2017)

blue was tested under visible light illumination. The maximum degradation efficiency was exhibited by 10% V-doped ZnO, compared to pure ZnO (Slama et al. 2011). The Ag^+ (10, 15, 20, and 25%)-doped $BiVO_4$ microspheres had been prepared by hydrothermal method, and their photocatalytic activity on MB, Rh-B, and 2,4-dinitrophenol (DNP) was studied under the UV and visible light irradiation (Zhu et al. 2016). The pure $BiVO_4$ photocatalyst showed 100% degradation of MB in 50 min of UV irradiation. The 15% $Ag^+/BiVO_4$ showed 97% in 20 min of irradiation, which is the highest performance, whereas the 15% $Ag^+/BiVO_4$ also showed a 94% of MB degradation in 120 min of under visible light irradiation. Similarly, the 5% $Ag^+/BiVO_4$ photocatalyst has degraded Rh-B to 91% in 50 min of UV irradiation. The content of the doping ion is crucial in this case as the 15% Ag performed the best in this particular case.

Another research group has fabricated TiO_2 films on ITO glass substrate by doctor blade technique and Au/Pd-modified TiO_2 films by sputtering method on the same substrate. The degradation efficiency of them on MB was tested under UV light irradiation. The Au/Pd-modified TiO_2 films had performed better. Addition of noble metals improved the electron-hole recombination rate and therefore efficiency from 23% to 43% in 45 min (Quiñones et al. 2010). The other research group (Kerkez-Kuyumcu et al. 2015) has prepared the transition metal (Cr, Mn, Fe, Co, Ni, and Cu)-doped TiO_2 nanoparticles by modified precipitation method and evaluated their photocatalytic degradation of MB and MO dyes under visible light

irradiation. Pure TiO_2 showed 44% and 27% degradation of MB and MO, respectively, under visible light irradiation. The Cu-doped TiO_2 revealed the highest efficiency for both dyes (81% and 44% for MB and MO, respectively) compared to other metal doping. Pure ZnO, In_2O_3/ZnO, and In_2O_3/ZnO@Ag nanowire ternary composites have been studied for the degradation of methyl orange (MO) and 4-nitrophenol (4NP) under visible light irradiation (Liu et al. 2017). The SEM micrographs (see Fig. 2 of Liu et al. 2017) of In_2O_3/ZnO and In_2O_3/ZnO@Ag photocatalysts show well-dispersed In_2O_3 nanoparticles on the surface of the ZnO. The pure ZnO, In_2O_3/ZnO, and In_2O_3/ZnO@Ag photocatalysts have degraded MO with efficiency of 10, 43, and 67% in 90 min, respectively, and the same for 4NP increases to 40%, 44%, 68%, and 92% in 240 min with Ag/ZnO, In_2O_3/ZnO/Ag, ZnO/In_2O_3, and In_2O_3/ZnO@Ag under visible light irradiation, respectively. The photocatalytic activity enhancement was attributed to the widened region of visible light absorption by Ag nanowires and the close hetero-structure formation by the matched band structures of In_2O_3 and ZnO (Liu et al. 2017). The possible mechanism of the photocatalysis based on band structure alignment and the active species experimental results obtained by scavenging experiments is discussed well (see Fig. 1.9 of Liu et al. 2017). The active species that participated in the photocatalytic reaction were proposed to be mainly $\cdot O_2^-$ and h^+.

It was reported that the nanocomposites of ZnO-graphene oxide (ZnO-GO) with different weight ratios of ZnO to GO (0.95:0.05–0.70:0.30) and with their surface decorated with Pd NPs (Zhang et al. 2014a) were prepared and their photocatalytic activity was studied. The ZnO-GO (0.85:0.15) photocatalyst showed the highest degradation efficiency 93% of MB in 60 min compared to pure ZnO and other photocatalysts. Beura et al. have developed different concentrations of Sn^{4+} (1–30%)-doped ZnO nanostructures and tested their activity on MO under UV light irradiation (Beura et al. 2018). Figure 1.16 summarizes the results including the set of UV absorption spectra (Fig. 1.16a), the corresponding C_t/C_0 curves (Fig. 1.16b), and the reaction rate constants (Fig. 1.16d). The rate constants are 0.0076, 0.0188, 0.0137, 0.0090, 0.0032, 0.0027, and 0.0010 min^{-1} for ZnO with 1, 5, 10, 15, 20, and 30% Sn doping. The optimum Sn^{4+} content to achieve the highest photocatalytic activity (98.3%) was reported to be 1%. The enhanced photocatalytic activity was attributed to the decreased bandgap, enhanced PL lifetime, and increased electrical conductivity (Beura et al. 2018). Also graphene-ZnO composite was made for the degradation of MO under UV light and direct sunlight, and in both the cases, the degradation was about 97% and 98%, respectively, by the 5 wt% ZnO-graphene nanocomposite (Beura and Thangadurai 2017).

1.5.2 Corrosion

Corrosion is defined as the natural deterioration of materials caused by the electrochemical reaction with the environment. In order to rectify the corrosion issues, it is important to understand its types. In a broad sense, corrosion can be divided into

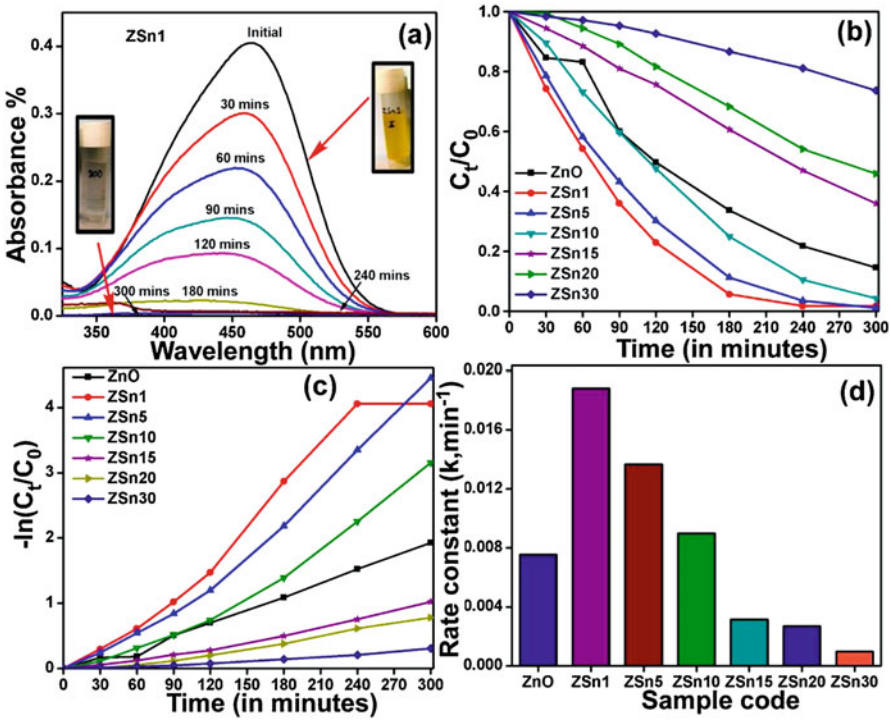

Fig. 1.16 (**a**) UV absorption spectra of MO in the presence of the photocatalyst ZSn1 (ZnO doped with 1% of Sn^{4+}) under UV light irradiation of various irradiation times, (**b**) concentration-time profile of photodegraded MO by pure and Sn^{4+}-doped ZnO under UV light, (**c**) reaction kinetics curve for the same photocatalytic degradation, and (**d**) the corresponding rate constant, k, for all the samples. (Reprinted with permission from Beura et al. 2018)

two: (i) the first one is the wet corrosion that occurs when the metals/alloys are exposed to the liquid electrolyte environment and (ii) the second is the dry corrosion that occurs when metals/alloys are exposed to the normal atmosphere or the high-temperature environment and does not necessitate the presence of humid/wet environment. Corrosion can occur in different forms such as uniform corrosion, where the thickness of the metals/alloys decreases without any localized attack. Rusting of iron, tarnishing of silverware, and corrosion of automobile bodies are the best example of this form of corrosion. The other forms of corrosions are galvanic corrosion, dezincification, crevice corrosion, pitting corrosion, intergranular corrosion, stress corrosion cracking, corrosion fatigue, and fretting corrosion. Out of them, the pitting corrosion is very important as it occurs in highly localized regions.

Corrosion is one of the prime causes of material and energy loss, accounting for 20% of global energy use. Shockingly, 4.2% of the gross national product (GNP) is lost annually due to corrosion-related issues (Metroke et al. 2001). The corrosion cost loss is mainly allocated to the inspection of corroded structures, repair of the corroded structures, and discarding the potentially hazardous waste materials

(Vazirinasab et al. 2017). Steel, copper (Cu), aluminum (Al), magnesium (Mg), and their alloys are common structural metals used in a variety of applications such as marine, industrial, aeronautical, and construction. Deterioration of metals due to corrosion leads to the premature failure of components, economic losses, environmental pollution, as well as injury or death (Ejenstam et al. 2013). Therefore, saving these metals/alloys from corrosion is an important environmental protection.

1.5.2.1 Nanomaterials on Corrosion Control

Nanocrystalline materials are highly distinct from its bulk counterpart due to its defective core structure, which is caused by the incorporation of dislocations, vacancies, and grain/interphase boundaries (Nalwa 2000). In general, grain boundary sites are more active and subjected to preferential corrosion/cracking. The increased grain boundary fraction in nanocrystalline materials makes more anodic sites for nucleation of corrosion. Grain boundaries are always associated with higher electrical resistivity and high diffusivity. The positive characteristic of grain boundaries is providing faster diffusion paths of ions from the interior to the surface and favors the formation of a protective passive layer. This passive layer in the nanomaterials is favorable for corrosion resistance.

Grain refinement in metals and alloys leads to the improvement in mechanical properties such as hardness, stiffness, wear, and ductility without modifications of the alloy chemistry. The relation between the mechanical properties and grain size is given by the well-known Hall-Petch equation. As far as corrosion is concerned, the direct relationship between grain size and corrosion resistance is yet to be determined. On the other hand, it is difficult to study the effect of grain size on corrosion resistance because any processing route to achieve different grain sizes will lead to other microstructure changes, which will influence the corrosion resistance of alloys (Atrens et al. 2015; Gupta and Birbilis 2015). However, many reports suggest the enhancement of corrosion resistance when the size goes down (Ambat et al. 2000; Ralston et al. 2011; Ralston and Birbilis 2010), and it is attributed to the fact that nanocrystalline (NC) alloys/metals possess higher grain boundary density. In general grain boundaries of any system will have different atomic coordination, diffusion rate, and reactivity compared to their bulk. It is reported that the corrosion resistance in nanocrystalline Fe_{32}-Ni_{36}-Cr_{14}-P_{12}-B_6 is improved than its amorphous counterpart (Thorpe et al. 1988). The improvement was attributed to rapid interphase boundary diffusion of Cr which in turn leads to the Cr enrichment on the surface. A study on the corrosion resistance of NC-Fe-8 wt% Al in Na_2SO_4 solution has reported (Zeiger et al. 1995) the defect density (density of grain boundaries) promotes Al dissolution leading to form an oxide film which provides protection against corrosion. The corrosion behavior of nanocrystalline nickel in H_2SO_4 in deaerated media has been found to be enhanced (Rofagha et al. 1991). It was found that the corrosion potential of NC nickel was about 200 mV anodically shifted than that of their bulk counterpart. It also showed that NC processing of nickel reduces kinetics of passivation, catalyzes hydrogen reduction processes, and compromises passive film stability.

1.5.2.2 Protective Coatings

One of the most effective ways to prevent corrosion is to coat the base material by protective thin films. Coatings can protect a substrate by decoupling the metal from its environment. Nanostructured metals are expected to be harder, stronger, and tougher, which can be coated to be corrosion resistant. These nano-metallic coatings are used in aerospace components, medical devices, defense armor, sports equipment, etc. Apart from metallic coatings, ceramics and polymer coatings have also exhibited to enhance the corrosion resistance of structural materials. Ceramics and polymers take advantage of higher electrical resistance and can provide better corrosion resistance than metals. Nanocoatings can be fabricated by a variety of vacuum and non-vacuum techniques such as sol-gel dip coating, magnetron sputtering, electro-spark deposition, electrodeposition laser beam surface treatment, atomic layer deposition (ALD), high-velocity oxy-fuel thermal spray, electron beam evaporation, chemical vapor deposition (CVD), etc. The Al coating on AZ31 magnesium alloy was fabricated by magnetron sputtering technique and found higher corrosion resistance than the bare AZ31 magnesium alloy (Wu et al. 2008). The enhanced corrosion resistance was attributed to the barrier effect of Al and cathodic protection of magnesium alloy. The nano TiO_2 (15–18 nm) coated on 316L stainless steel (SS) fabricated by sol-gel and dip-coating method was found to exhibit self-cleaning hydrophobic property (Shen et al. 2005). These self-cleaning coatings cause liquid droplets to roll off from the surface without wetting and pick up surface contaminants which substantially increase resistance to corrosion in wet environments. Recent study has reported the fabrication of nano Nb_2O_5 thin films on AISI 316 SS by reactive DC magnetron sputtering technique (Fuser Pillis et al. 2015). Two different thicknesses of films, such as 36 and 70 nm, were achieved by employing two deposition times such as 15 and 30 mins, respectively. The coatings exhibited higher corrosion resistance than the bare. The corrosion current density was increased, and the charge transfer resistance was decreased with the increase in the thickness of the Nb_2O_5 coatings. It is also reported that the 36-nm-thick film provided the effective protection against localized corrosion. Sol-gel method was employed to fabricate ZrO_2 films on 304 SS with different thicknesses varying from 150 to 280 nm achieved by introducing different number of layers of ZrO_2 (Zhang et al. 2015). The 280-nm-thick film exhibited optimal structure characteristics of dense and uniform surface morphology, which provided better corrosion resistance than the other films and bare 304 SS substrate in acidic media at room temperature. It was explored that the 2D nanostructure graphene is a protective layer for corrosion resistance in metals (Fig. 25). The atomically thin layer of graphene was initially grown on copper by CVD and mechanically transferred on to pristine nickel. The thickness of the graphene is varied by transferring two and four layers of graphene successively onto the nickel substrate. The corrosion resistance of copper films coated with graphene in an aerated Na_2SO_4 solution is seven times higher than the bare copper. Striking results were that the corrosion resistance of four layers of graphene transferred mechanically to nickel surface is 20 times higher than the bare

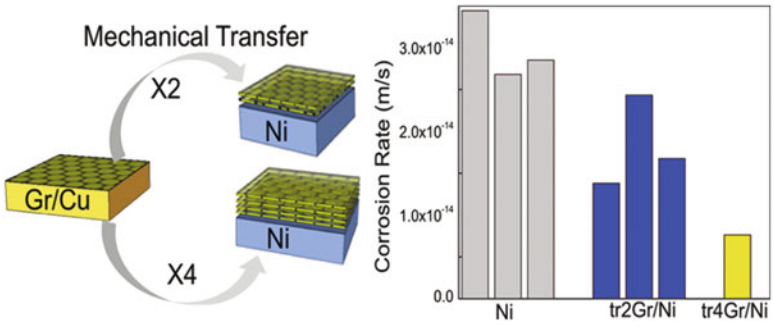

Fig. 1.17 Schematic of chemical vapor deposited graphene layer mechanically transferred from Cu substrate to nickel substrate and histogram representing their corrosion rate comparison. (Reprinted with permission from Prasai et al. 2012)

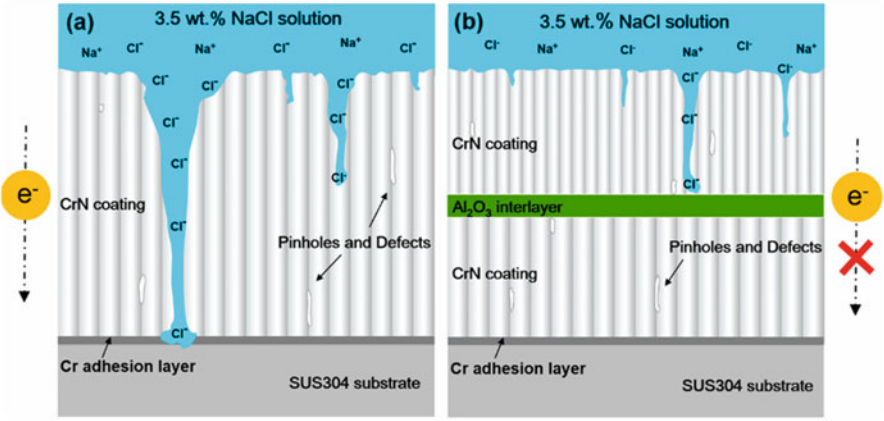

Fig. 1.18 Schematic representation of corrosion behavior of the (**a**) CrN coating and (**b**) CrN-Al_2O_3 coating in 3.5 wt % NaCl solution. (Reprinted with permission from Wan et al. 2015)

nickel. A schematic of the graphene transfer and the rate of corrosion of graphene-coated Ni is shown in Fig. 1.17.

There was new approach adopted to enhance the corrosion resistance of 304 SS (Wan et al. 2015). The hard CrN coatings fabricated by hybrid deposition process involving high-power impulse magnetron sputtering (HiPIMS) with nano Al_2O_3 layer insertion by atomic layer deposition are employed. The long-term corrosion durability and corrosion resistance were significantly increased by the insertion of nano Al_2O_3 interlayer, which was due to the good insulating nature of Al_2O_3 and acts as a barrier for the diffusion of corrosive species, such as Cl-ions. It is also demonstrated that increasing the thickness of Al_2O_3 interlayer from 5 to 10 nm and shifting its position toward the surface of CrN coatings further enhanced the corrosion resistance (see Fig. 1.18).

A facile electrochemical approach was employed for the development of graphene nanosheets coated on to the copper substrate (Sahu et al. 2013). The electrochemical deposition by chronoamperometry (i–t) technique was employed to coat graphene on copper substrate, followed by a chemical reduction. The graphene-coated copper substrate exhibited higher corrosion resistance than the bare copper with the inhibition efficiency (ratio of difference in current density of coatings and substrate to the current density of substrate) of above 94.3%. Silicate-aluminate-based nanocomposite coating on AZ91D magnesium alloy (Wang et al. 2015) was fabricated, and the effect of incorporation on nano-SiC on the composite coating was studied. It was found that the incorporation of nano-SiC into the electrolyte enhanced the corrosion resistance of the nanocomposite-coated magnesium alloy. The polarization resistance of these nanocomposite coatings with nano-SiC was 18.7% higher than the coatings without nano-SiC. It was attributed to the better barrier protective by the dense structure of the nano-SiC incorporated nanocomposite coating. The $CuAlO_2$ films of two different thicknesses, such as 100 and 200 nm, were deposited by radio-frequency (RF) magnetron sputtering on 316L SS for biomedical applications (Chang et al. 2014). The corrosion resistance of this coated 316L is higher than the bare substrate. Furthermore, the 100-nm-thick $CuAlO_2$-coated 316L SS provided better protection than the 200-nm-thick $CuAlO_2$ coating. The better corrosion protection was attributed to the fact that ceramic materials with low conductivity, better passivity, and good tribological properties provide better resistance to corrosion than metallic substrates. An eco-friendly silane coating incorporated with nanoclay (sodium montmorillonite particles) on SS was made by sol-gel method (Ansari et al. 2015). The effect of incorporation of different concentrations of nanoclay, such as 500, 1000, 2000, and 5000 ppm, was studied. The nanocomposite coating consisting of 1000 ppm of clay nanoparticles offered superior resistance to corrosion to the SS in 3.5% NaCl solution. BinSabt reported the fabrication of nanocubed ZnS quantum dots (NCQDs)/polyvinyl alcohol (PVA) nanocomposite coating on SS for corrosion studies (BinSabt et al. 2016). Initially, NCQDs/PVA was prepared by hydrothermal method and coated on to the SS substrate by dip-coating method. The nanocomposite coating has improved the corrosion protection of SS in saline water. Further, the inhibition efficiency has increased from 67% to 94% for the PVA coatings and PVA/ZnS-NCQDs nanocomposite coatings. Thus, presence of ZnS-NCQDs in the coatings provided better corrosion resistance to the SS. The influence of incorporation of SiO_2 nanoparticles on the electroless Ni-P coating on AZ91 magnesium alloy against corrosion resistance was reported (Sadreddini et al. 2015) that revealed that the presence of SiO_2 nanoparticles on the coating has influenced positively to the enhancement in the corrosion resistance of AZ91 magnesium alloy. It was also illustrated that the increase in the quantity of SiO_2 nanoparticles from 0 to 4.62 wt% in the coating favored the corrosion resistance improvement. Thin films of monolithic titanium nitride, monolithic titanium, and titanium nitride with intercalated titanium on Si wafer were fabricated by magnetron sputtering technique, and influence of thickness of intercalation layer, such as 20 and 60 nm, was studied. It was found that the intercalation of titanium in titanium nitride exhibited higher

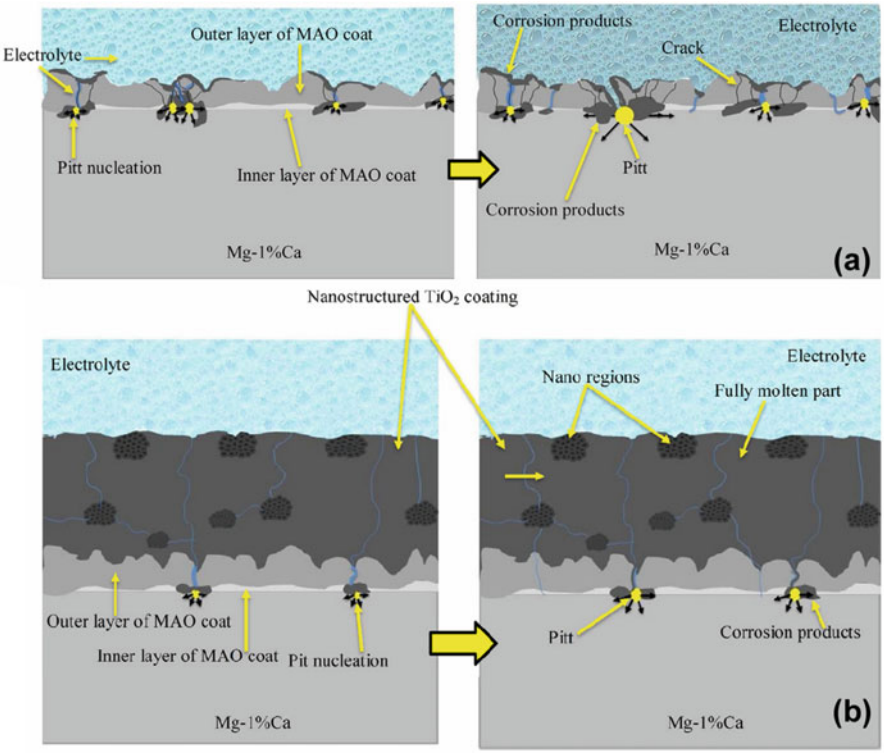

Fig. 1.19 (**a**) Schematic illustration of the corrosion mechanism of the MAO-coated Mg alloy in 3.5 wt.% NaCl solution. (**b**) The same of the composite (MAO/APS TiO_2)-coated Mg alloy in 3.5 wt.% NaCl solution. (Reprinted with permission from Daroonparvar et al. 2015)

corrosion resistance than the monolithic counterparts. It was attributed to the presence of comparatively lower defective and compact Ti intercalated layer that effectively blocks the corrosive species from the substrate. The duplex coating consisting of micro-arc oxidation layer and air plasma sprayed (APS) nanostructure TiO_2 coating on the Mg-1%Ca alloy (Daroonparvar et al. 2015) exhibited higher corrosion resistance than the single MAO (micro-arc oxidation) layer, and it was attributed to effective sealing of porous MAO layer by nanostructured TiO_2 topcoat which showed compact and dense structure along with nano regions. Further, it was also found that the bond coat prevented the formation of galvanic cell at the interface during corrosion. It is explained schematically in Fig. 1.19a, b.

Alumina was effectively used as a corrosion protective layer for SS (Diaz et al. 2011). Thin films of alumina (10, 50, and 100 nm) were coated on SS by ALD. The lowest thick alumina (10 nm) coating was found to be more defective, and further increase in the thickness has sealed the defective layer providing excellent protection against corrosion. Further, the corrosion rate was found to decrease by one, two, and four orders of magnitude for the 10-, 50-, and 100-nm-thick Al_2O_3 coatings,

respectively. The Al_2O_3 was also coated on AISI 316L SS by ALD with two different thicknesses (34 and 84 nm), and their barrier properties against corrosion were investigated (Fedel and Deflorian 2016). These alumina films were fabricated by employing different self-terminating gas-surface reactions, such as 500 and 1000 cycles, in the ALD chamber. Their electrochemical properties investigated for prolonged immersion (in NaCl) time (1000 h) revealed that the higher thickness coatings provided better corrosion resistance than the thinner and bare 314 L SS substrate. The investigation of the coatings after the immersion in NaCl electrolyte suggested that these facts are attributed to a lower tendency to be permeated by water and a lower susceptibility to crack formation of the thicker coating compared to the thinner ones.

1.5.3 Emerging Nanomaterials for Sensing Application

Sensors have become increasingly more significant in a world where there is a demand of technological advances for various categories (Akyildiz et al. 2002). In an environment, especially where people work in a harmful environment such as mines, it becomes important to be alert on what types of gases are there in it so that casualties can be avoided. Gases such as methane, ammonia, and cooking gas are supposed to be under control, and sensing of them is an environmental issue. There are three main factors required to be satisfied by a material to be a good sensor, and they are high sensitivity, good selectivity, and fast response time. Moreover, for large-scale production, ease of fabrication and low material cost are also required to make a good sensor. Nanotechnology is facilitating production of the efficient sensor for large-scale application with low cost. In recent years, numerous nanomaterials have been developed for sensor application due to their inherent properties including high surface-to-volume ratio, smaller size, target-binding characteristics, etc. (Goldoni et al. 2018; Gupta Chatterjee et al. 2015; Toda et al. 2015). Especially, nanomaterials are growing attention in the field of molecular diagnosis because of their comparable size to the size of chemical and biological species being sensed. On the basis of different detecting targets, the sensor is referred to the optical sensor, gas sensor, biosensor, electrical sensor, etc.

In recent years, metal-oxide semiconductor (SnO_2 (Das and Jayaraman 2014; Li et al. 2016c), ZnO (Quy et al. 2018), TiO_2 (Bai and Zhou 2014), WO_3 (Moon et al. 2013), CuO (Zhang et al. 2008), etc.)-based gas sensors have recently gained attracted attention due to their high stability, sensitivity, fast response, and low cost. As reviewed in different references, nanostructured metal oxides (in the form of nanoparticles, nanorods, nanowires, or nano-heterojunction) have shown to be mainly suitable for gas sensing application (Comini 2016; Li et al. 2015; Miller et al. 2014). For instance, a review focused on TiO_2 nanomaterials for gas sensor applications (Bai and Zhou 2014) provides a detailed listing of various synthesis routes leading to different TiO_2 morphologies, as well as wide range of sensing devices (gas sensing, chemical oxygen demand (COD), and biosensing).

Very recently, plate-like nanostructures of ZnO with an average diameter and thickness of less than 100 and 10 nm, respectively, were prepared (Quy et al. 2018). Further, they were treated by thermal treatment at various temperatures ranging from 500 to 700 °C. The sample treated at 600 °C showed a higher response to ethanol and NO_2 sensing. Three different nanostructures of CuO (wires, platelets, and spindles) were prepared for glucose sensing application (Zhang et al. 2008). These CuO nanostructures showed their electron transfer ability in the following order: nanospindles> nanowires> nanoplatelets. The CuO with nanospindle structures exhibits excellent sensing performance toward glucose (sensitivity of 5.5675×10^{-6} A/μmol L^{-1}). Recently, graphene-SnO_2 nanocomposites developed by microwave-assisted synthesis method were found to have selectively sense NO_2 gas than other gases such as NH_3, SO_2, and ethanol (Kim et al. 2017). This nanocomposite showed an outstanding sensitivity toward very low concentration (1–5 ppm) of gases.

Metal oxides and carbon materials are excellent complementary materials. The shortcoming of these single components can be enhanced by a hybrid of carbon-metal oxide composite nanostructures. A review on advanced promising routes to carbon/metal oxide hybrids in sensors was contributed to research society (Goldoni et al. 2018). This comprehensive review article describes the already existing carbon/metal oxide-based hybrid sensors for improved gas sensing application. The ultrafast and highly sensitive WO_3 hemitube nanostructure-assisted O_2 plasma surface modification with functionalization of graphene-based material was developed for the detection of hydrogen sulfide and acetone (Choi et al. 2014). The fabrication process of this nanostructure is presented in Fig. 1.20. Graphene oxide (0.1 wt %) and thin-layered graphite (0.1 wt%)-WO_3 hemitube composites showed

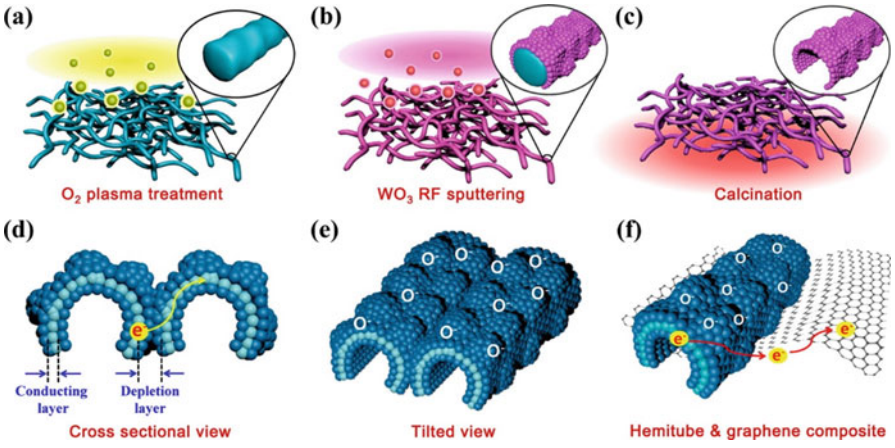

Fig. 1.20 Schematic illustration of fabrication process: (**a**) surface modification of electrospun polymeric fiber template by O_2 plasma treatment, (**b**) WO_3 coating using RF sputtering, and (**c**) high-temperature calcination by decomposing the inner polymeric fiber template. (**d**, **e**) Homojunction between pristine WO_3 hemitubes and (**f**) a heterojunction between a graphene-based material and a WO_3. (Reprinted with permission from Choi et al. 2014)

the response time of 11.5 s and 13.5 s to 1 ppm acetone as well as 12.5 s and 10 s to 1 ppm of H_2S, respectively.

Methane gas sensors were fabricated by using SnO_2 nanorods (Amutha et al. 2015) and SnO_2 thin films (Amutha et al. 2016). The SnO_2 nanorods were prepared by hydrothermal method (at a reaction temperature of 180 °C), whereas the thin films were fabricated by thermal evaporation of Sn metal followed by post-oxidation under O_2 gas flow. The nanorods have shown the sensitivity at a relatively low operating temperature (100 °C) with a response time of 13 s (Amutha et al. 2015), and the maximum response was achieved at the operating temperature of 175 °C. In the case of SnO_2 thin films (Amutha et al. 2016), due to its ultra-small thickness of 7 nm and well-oriented grains that shows the higher sensitivity that is better than the reported values in the literature (Chakraborty et al. 2006; Haridas and Gupta 2012).

1.6 Conclusion

Many reports discussed here indicate that the nanomaterials and nanotechnology provide significant contribution either directly or indirectly in the enhancement of their properties so that they can be used very well in the applications such as solar cells, batteries, fuel cells, sensors, photocatalysis for water purification, and corrosion resistant for metals and alloys. Significance of the nanomaterials for energy and environmental applications is discussed in detail. Evolution of solar cells and its four generations have been discussed. How these four generations have been dependent on the type of materials used and evolution in the efficiency with the development of nanomaterials was given. The DSSCs have shown the maximum efficiency of 9.32% whereas the QDSSCs have shown the efficiency of 11.61%. At the same time by using perovskite-structured nanomaterials, the photovoltaic conversion efficiency of the solar cell has been recently reported to be 23.6%, which is because of the nanomaterial's usage in them. Energy important materials for the applications of fuel cells and batteries were discussed. In both cases, the appropriate parameters for the materials to act a role of anode, cathode, and electrolytes were discussed. In particular, materials that have been evolved to nanomaterials for this application in Li-ion batteries are discussed thoroughly. New generation of materials for flexible batteries is also presented.

The importance of photocatalysis in keeping the environment clean is presented along with the necessary requirements of suitable photocatalysts. Photocatalysis carried out by nanomaterials of simple oxides, metal oxide-metal oxide nanocomposites, metal nanoparticle-decorated oxides, metal ion-doped oxides, and mixed oxides for the photodegradation of industrial dyes such as methylene blue, methyl orange, rhodamine B, and Congo red has been discussed. In many cases, the synergistic effect between the nanomaterials had improved the photocatalytic activity. The surface plasmon resonance of metal nanoparticles that decorate the surface of oxide nanostructures has also played a key role in improving the photocatalytic activity of the materials. As corrosion is an important phenomenon in destructing the

structures, the significance of its prevention is also dealt with. Ways of protecting the surface by coating appropriate materials (many of the cases, it is ceramic material) and the parameters are presented. Coating methods like thermal evaporation, electron beam evaporation, and ALD were used to coat a thin/thick film as corrosion protective coatings. In some cases, inclusion of nanoparticles into the thin films had improved the corrosion resistance. Gas sensors by using nanomaterials such as ZnO, SnO_2, TiO_2, WO_3, etc. have been described. And, nanocomposites of oxides with graphene for gas sensing are also given. The SnO_2 for methane gas sensing with nanorod and thin film structure have shown better parameters like high sensitivity at relatively lower operating temperatures such as 175 °C. In summary, the evolution made by nanomaterials for energy and environmental application is addressed in detail in this section.

Acknowledgment The DST-SERB (EMR/2016/005795), India, and UGC-DAE-CSR, India (CSR-KN/CRS-89/2016-17/1130), are acknowledged for the research grants.

References

Abdalla AM, Hossain S, Azad AT, Petra PM, Begum F, Eriksson SG, Azad AK (2018) Nanomaterials for solid oxide fuel cells: a review. Renew Sust Energ Rev 82:353–368. https://doi.org/10.1016/j.rser.2017.09.046

Akyildiz IF, Su W, Sankarasubramaniam Y, Cayirci E (2002) A survey on sensor networks. IEEE Commun Mag 40:102–114. https://doi.org/10.1109/MCOM.2002.1024422

Ambat R, Aung NN, Zhou W (2000) Evaluation of microstructural effects on corrosion behaviour of AZ91D magnesium alloy. Corros Sci 42:1433–1455. https://doi.org/10.1016/S0010-938X(99)00143-2

Amine K, Belharouak I, Chen Z, Tran T, Yumoto H, Ota N, Myung S, Sun Y (2010) Nanostructured anode material for high-power battery system in electric vehicles. Adv Mater 22:3052–3057. https://doi.org/10.1002/adma.201000441

Amutha A, Amirthapandian S, Prasad AK, Panigrahi BK, Thangadurai P (2015) Methane gas sensing at relatively low operating temperature by hydrothermally prepared SnO_2 nanorods. J Nanopart Res 17:289. https://doi.org/10.1007/s11051-015-3089-z

Amutha A, Amirthapandian S, Sundaravel B, Prasad AK, Panigrahi BK, Thangadurai P (2016) Structural and gas sensing properties of ex-situ oxidized Sn grown by thermal evaporation. Appl Surf Sci 360:731–737. https://doi.org/10.1016/j.apsusc.2015.11.054

Ansari F, Naderi R, Dehghanian C (2015) Improvement in the corrosion resistance of stainless steel 304L in sodium chloride solution by a nanoclay incorporated silane coating. RSC Adv 5:706–716. https://doi.org/10.1039/C4RA10332G

Antolini E (2010) Composite materials: an emerging class of fuel cell catalyst supports. Appl Catal B Environ 100:413–426

Atrens A, Song G-L, Liu M, Shi Z, Cao F, Dargusch MS (2015) Review of recent developments in the field of magnesium corrosion. Adv Eng Mater 17:400–453. https://doi.org/10.1002/adem.201400434

Ayekoe CYP, Robert D, Lanciné DG (2017) Combination of coagulation-flocculation and heterogeneous photocatalysis for improving the removal of humic substances in real treated water from Agbô River (Ivory-Coast). Catal Today 281:2–13. https://doi.org/10.1016/j.cattod.2016.09.024

Babaei A, Zhang L, Liu E, Jiang SP (2012) Performance and carbon deposition over Pd nanoparticle catalyst promoted Ni/GDC anode of SOFCs in methane, methanol and ethanol fuels. Int J Hydrog Energy 37:15301–15310. https://doi.org/10.1016/j.ijhydene.2012.07.089

Bai J, Zhou B (2014) Titanium dioxide nanomaterials for sensor applications. Chem Rev 114:10131–10176. https://doi.org/10.1021/cr400625j

Ball JM, Lee MM, Hey A, Snaith HJ (2013) Low-temperature processed meso-superstructured to thin-film perovskite solar cells. Energy Environ Sci 6:1739–1743. https://doi.org/10.1039/c3ee40810h

Beura R, Thangadurai P (2017) Structural, optical and photocatalytic properties of graphene-ZnO nanocomposites for varied compositions. J Phys Chem Solids 102:168–177. https://doi.org/10.1016/j.jpcs.2016.11.024

Beura R, Pachaiappan R, Thangadurai P (2018) A detailed study on Sn^{4+} doped ZnO for enhanced photocatalytic degradation. Appl Surf Sci 433:887–898. https://doi.org/10.1016/j.apsusc.2017.10.127

BinSabt M, Nazeer AA, Madkour M, Al-Sagheer F (2016) Hydrothermally modified PVA/ZnS-NCQD nanocoating for stainless steel corrosion protection in saline water. RSC Adv 6:6888–6895. https://doi.org/10.1039/C5RA26581A

Birkel A, Lee Y-G, Koll D, Meerbeek XV, Frank S, Choi MJ, Kang YS, Char K, Tremel W (2012) Highly efficient and stable dye-sensitized solar cells based on SnO_2 nanocrystals prepared by microwave-assisted synthesis. Energy Environ Sci 5:5392–5400. https://doi.org/10.1039/C1EE02115J

Boro B, Gogoi B, Rajbongshi BM, Ramchiary A (2018) Nano-structured TiO_2/ZnO nanocomposite for dye-sensitized solar cells application: a review. Renew Sust Energ Rev 81:2264–2270

Brennan TP, Tanskanen JT, Roelofs KE, To JW, Nguyen WH, Bakke JR, Ding I, Hardin BE, Sellinger A, McGehee MD, Bent SF (2013) TiO_2 conduction band modulation with In_2O_3 recombination barrier layers in solid-state dye-sensitized solar cells. J Phys Chem C 117:24138–24149. https://doi.org/10.1021/jp406789k

Bush KA, Palmstrom AF, Yu ZJ, Boccard M, Cheacharoen R, Mailoa JP, McMeekin DP, Hoye RL, Bailie CD, Leijtens T, Peters IM, Minichetti MC, Rolston N, Prasanna R, Sofia S, Harwood D, Ma W, Moghadam F, Snaith HJ, Buonassisi T, Holman ZC, Bent SF, McGehee MD (2017) 23.6%-efficient monolithic perovskite/silicon tandem solar cells with improved stability. Nat Energy 2:17009

Chakraborty S, Sen A, Maiti HS (2006) Selective detection of methane and butane by temperature modulation in iron doped tin oxide sensors. Sensors Actuators B Chem 115:610–613. https://doi.org/10.1016/j.snb.2005.10.046

Chan C, Peng H, Liu G, McIlwrath K, Zhang XF, Huggins RA, Cui Y (2007) High-performance lithium battery anodes using silicon nanowires. Nat Nanotechnol 3:31–35. https://doi.org/10.1038/nnano.2007.411

Chan SHS, Wu TY, Juan JC, Teh CY (2011) Recent developments of metal oxide semiconductors as photocatalysts in advanced oxidation processes (AOPs) for treatment of dye waste-water. J Chem Technol Biotechnol 86:1130–1158. https://doi.org/10.1002/jctb.2636

Chandiran AK, Tetreault N, Humphry-baker R, Kessler F, Baranoff E, Yi C, Nazeeruddin MK, Grätzel M (2012) Sub-nanometer Ga_2O_3 tunnelling layer by atomic layer deposition to achieve 1.1V open-circuit potential in dye-sensitized solar cells. Nano Lett 12:3941. https://doi.org/10.1021/nl301023r

Chang S-H, Chen J-Z, Hsiao S-H, Lin G-W (2014) Nanohardness, corrosion and protein adsorption properties of $CuAlO_2$ films deposited on 316L stainless steel for biomedical applications. Appl Surf Sci 289:455–461. https://doi.org/10.1016/j.apsusc.2013.11.004

Chapin DM, Fuller CS, Pearson GL (1954) A new silicon p-n junction photocell for converting solar radiation into electrical power. J Appl Phys 25:676–677. https://doi.org/10.1063/1.1721711

Chen SG, Chappel S, Diamant Y, Zaban A (2001) Preparation of Nb_2O_5 coated TiO_2 nanoporous electrodes and their application in dye-sensitized solar cells. Chem Mater 13:4629–4634. https://doi.org/10.1021/cm010343b

Chen Z, Cao Y, Qian J, Aia X, Yang H (2010) Facile synthesis and stable lithium storage performances of Sn-sandwiched nanoparticles as a high capacity anode material for rechargeable Li batteries. J Mater Chem 20:7266–7271. https://doi.org/10.1039/c0jm00829j

Chen C, Xie Y, Ali G, Yoo SH, Cho SO (2011) Improved conversion efficiency of Ag_2S quantum dot-sensitized solar cells based on TiO_2 nanotubes with a ZnO recombination barrier layer. Nanoscale Res Lett 6:462. https://doi.org/10.1186/1556-276X-6-462

Chen Z, Ren Y, Jansen AN, Lin CK, Weng W, Amine K (2013) New class of nonaqueous electrolytes for long-life and safe lithium-ion batteries. Nat Commun 4:1513. https://doi.org/10.1038/ncomms2518

Cheng Z, Zha SW, Aguilar L, Wang D, Winnick J, Liua M (2006) A solid oxide fuel cell running on H_2S/CH_4 fuel mixtures. Electrochem Solid-State Lett 9:A31–A33. https://doi.org/10.1149/1.2137467

Cheng XB, Huang JQ, Peng HJ, Nie JQ, Liu XY, Zhang Q, Wei F (2014a) Polysulfide shuttle control: towards a lithium-sulfur battery with superior capacity performance up to 1000 cycles by matching the sulfur/electrolyte loading. J Power Sources 253:263–268. https://doi.org/10.1016/j.jpowsour.2013.12.031

Cheng M-Y, Ye Y-S, Chiu T-M, Pan C-J, Hwang B-J (2014b) Size effect of nickel oxide for lithium ion battery anode. J Power Sources 253:27–34. https://doi.org/10.1016/j.jpowsour.2013.12.037

Choi SJ, Fuchs F, Demadrille R, Grévin B, Jang BH, Lee JS, Lee JH, Harry L, Tuller HL, Kim ID (2014) Fast responding exhaled-breath sensors using WO_3 hemitubes functionalized by graphene-based electronic sensitizers for diagnosis of diseases. ACS Appl Mater Interfaces 6:9061–9070. https://doi.org/10.1021/am501394r

Chong MN, Jin B, Chow CWK, Saint C (2010) Recent developments in photocatalytic water treatment technology: a review. Water Res 44:2997–3027. https://doi.org/10.1016/j.watres.2010.02.039

Cohn AP, Oakes L, Carter R, Chatterjee S, Westover AS, Share K, Pint CL (2014) Assessing the improved performance of freestanding, flexible graphene and carbon nanotube hybrid foams for lithium ion battery anodes. Nanoscale 6:4669–4675. https://doi.org/10.1039/C4NR00390J

Comini E (2016) Metal oxide nanowire chemical sensors: innovation and quality of life. Mater Today 19:559–567. https://doi.org/10.1016/j.mattod.2016.05.016

Dai K, Li D, Lu L, Liu Q, Changhao L, Lv J, Zhu G (2014) Plasmonic TiO_2/AgBr/Ag ternary composite nanosphere with heterojunction structure for advanced visible light photocatalyst. Appl Surf Sci 314:864–871. https://doi.org/10.1016/j.apsusc.2014.06.183

Danilovic N, Luo JL, Chuang KT, Sanger AR (2009) $Ce_{0.9}Sr_{0.1}VO_x$ (x = 3, 4) as anode materials for H_2S-containing CH_4 fueled solid oxide fuel cells. J Power Sources 192:247–257. https://doi.org/10.1016/j.jpowsour.2009.03.045

Daroonparvar M, Azizi M, Yajid M, Yusof NM, Bakhsheshi-rad HR, Hamzah E, Mardanikivi T (2015) Deposition of duplex MAO layer/nanostructured titanium dioxide composite coatings on Mg-1% Ca alloy using a combined technique of air plasma spraying and micro arc oxidation. J Alloys Compd 649:591–605. https://doi.org/10.1016/j.jallcom.2015.07.200

Das S, Jayaraman V (2014) SnO_2: a comprehensive review on structures and gas sensors. Prog Mater Sci 66:112–255. https://doi.org/10.1016/j.pmatsci.2014.06.003

Dembele KT, Selopal GS, Soldano C, Nechache R, Rimada JC, Concina I, Sberveglieri G, Rosei F, Vomiero A (2013) Hybrid carbon nanotubes–TiO_2 photoanodes for high efficiency dye-sensitized solar cells. J Phys Chem C 117:14510–14517. https://doi.org/10.1021/jp403553t

Deng Q, Duan X, Ng DHL, Tang H, Yang Y, Kong M, Wu Z, Cai W, Wang G (2012) Ag nanoparticle decorated nanoporous ZnO microrods and their enhanced photocatalytic activities. ACS Appl Mater Interfaces 4:6030–6037. https://doi.org/10.1021/am301682g

Desai UV, Xu C, Wu J, Gao D (2013) Hybrid TiO_2–SnO_2 nanotube arrays for dye-sensitized solar cells. J Phys Chem C 117:3232–3239. https://doi.org/10.1021/jp3096727

Diamant Y, Chappel S, Chen SG, Melamed O, Zaban A (2004) Core–shell nanoporous electrode for dye sensitized solar cells: the effect of shell characteristics on the electronic properties of the electrode. Coord Chem Rev 248:1271–1276. https://doi.org/10.1016/j.ccr.2004.03.003

Diaz B, Harkonen E, Swiatowska J, Maurice V, Seyeux A, Marcus P, Ritala M (2011) Low-temperature atomic layer deposition of Al_2O_3 thin coatings for corrosion protection of steel: surface and electrochemical analysis. Corros Sci 53:2168–2175. https://doi.org/10.1016/j.corsci.2011.02.036

Ding S, Chen JS, Qi G, Duan X, Wang Z, Giannelis EP, Archer LA, Lou XW (2011) Formation of SnO_2 hollow nanospheres inside mesoporous silica nanoreactors. J Am Chem Soc 133:21–23. https://doi.org/10.1021/ja108720w

Du J, Du Z, Hu J-S, Pan Z, Shen Q, Sun J, Long D, Dong H, Sun L, Zhong X, Wan LJ (2016a) Zn–Cu–In–Se quantum dot solar cells with a certified power conversion efficiency of 11.6%. J Am Chem Soc 138:4201–4209. https://doi.org/10.1021/jacs.6b00615

Du Z, Pan Z, Fabregat-Santiago F, Zhao K, Long D, Zhang H, Zhao Y, Zhong X, Yu JS, Bisquert J (2016b) Carbon counter-electrode-based quantum-dot-sensitized solar cells with certified efficiency exceeding 11%. J Phys Chem Lett 7:3103–3111. https://doi.org/10.1021/acs.jpclett.6b01356

Ejenstam L, Ovaskainen L, Rodriguez-Meizoso I, Wågberg L, Pan J, Swerin A, Claesson PM (2013) The effect of superhydrophobic wetting state on corrosion protection – the AKD example. J Colloid Interface Sci 412:56–64. https://doi.org/10.1016/j.jcis.2013.09.006

Fedel M, Deflorian F (2016) Electrochemical characterization of atomic layer deposited Al_2O_3 coatings on AISI 316L stainless steel. Electrochim Acta 203:404–415. https://doi.org/10.1016/j.electacta.2016.02.107

Fuser Pillis M, Altomari Geribola G, Scheidt G, De Araújo ED, Lopes de Oliveira MC, Antunes RA (2015) Corrosion of thin, magnetron sputtered Nb_2O_5 films. Corros Sci 102:317–325. https://doi.org/10.1016/j.corsci.2015.10.023

Gao B, Shen C, Zhang B, Zhang M, Yuan S, Yang Y, Chen G (2014) Green synthesis of highly efficient CdSe quantum dots for quantum-dots-sensitized solar cells. J Appl Phys 115:193104. https://doi.org/10.1063/1.4876118

Ghosh R, Brennaman MK, Uher T, Ok M-R, Samulski ET, McNeil LE, Meyer TJ, Lopez R (2011) Nanoforest Nb_2O_5 photoanodes for dye-sensitized solar cells by pulsed laser deposition. ACS Appl Mater Interfaces 3:3929–3935. https://doi.org/10.1021/am200805x

Gleiter H (1989) Nanocrystalline materials. Prog Mater Sci 33:223–315. https://doi.org/10.1016/0079-6425(89)90001-7

Gnedenkov SV, Sinebryukhov SL, Mashtalyar DV, Imshinetskiy IM, Gnedenkov AS, Samokhin AV, Tsvetkov YV (2015) Protective composite coatings obtained by plasma electrolytic oxidation on magnesium alloy MA8. Vacuum 120:107–114. https://doi.org/10.1016/j.vacuum.2015.02.004

Goldoni A, Alijani V, Sangaletti L, D'Arsiè L (2018) Advanced promising routes of carbon/metal oxides hybrids in sensors: a review. Electrochim Acta 266:139–150. https://doi.org/10.1016/j.electacta.2018.01.170

Green MA, Emery K, Hishikawa Y, Warta W, Dunlop ED (2016) Solar cell efficiency tables (version 48). Prog Photovolt Res Appl 24:905–913. https://doi.org/10.1002/pip.2788

Guo E, Yin L (2014) Nitrogen doped TiO_2-Cu_xO core-shell mesoporous spherical hybrids for high-performance dye-sensitized solar cells. Phys Chem Chem Phys 17:563–574. https://doi.org/10.1039/c4cp03132f

Gupta RK, Birbilis N (2015) The influence of nanocrystalline structure and processing route on corrosion of stainless steel: a review. Corros Sci 92:1–15. https://doi.org/10.1016/j.corsci.2014.11.041

Gupta Chatterjee S, Chatterjee S, Ray AK, Chakraborty AK (2015) Graphene-metal oxide nanohybrids for toxic gas sensor: a review. Sensors Actuators B Chem 221:1170–1181. https://doi.org/10.1016/j.snb.2015.07.070

Haile SM (2003) Fuel cell materials and components. Acta Mater 51:5981–6000

Han F, Kambala VSR, Srinivasan M, Rajarathnam D, Naidu R (2009) Tailored titanium dioxide photocatalysts for the degradation of organic dyes in wastewater treatment: a review. Appl Catal A Gen 359:25–40. https://doi.org/10.1016/j.apcata.2009.02.043

Haridas D, Gupta V (2012) Enhanced response characteristics of SnO_2 thin film based sensors loaded with Pd clusters for methane detection. Sensors Actuators B Chem 166–167:156–164. https://doi.org/10.1016/j.snb.2012.02.026

He H, Gorte RJ, Vohs JM (2005) Highly sulfur tolerant cu-ceria anodes for SOFCs. Electrochem Solid-State Lett 8:A279. https://doi.org/10.1149/1.1896469

Heo JH, Jang MH, Lee MH, Shin DH, Kim DH, Moon SH, Kim SW, Park BJ, Im SH (2017) High-performance solid-state PbS quantum dot-sensitized solar cells prepared by introduction of hybrid perovskite interlayer. ACS Appl Mater Interfaces 9:41104–41110. https://doi.org/10.1021/acsami.7b12046

Hoffert MI, Caldeira K, Jain AK, , Haites EF, Harvey LD, Potter SD, Schlesinger ME, Schneider SH, Watts RG, Wigley TM, Wuebbles DJ (1998) Energy implications of future stabilization of atmospheric CO_2 content. Nature 395:881

Hsieh Y, Lee M, Wang G (2015) Sb_2S_3 quantum-dot sensitized solar cells with silicon nanowire photoelectrode. Int J Photoenergy 2015:1–10. https://doi.org/10.1155/2015/213858

Huang Y-H, Dass RI, Denyszyn JC, Goodenough JB (2006) Synthesis and characterization of $Sr_2MgMoO_{6-\delta}$: an anode material for the solid oxide fuel cell. J Electrochem Soc 153:A1266–A1272. https://doi.org/10.1149/1.2195882

Inturi SNR, Boningari T, Suidan M, Smirniotis PG (2014) Visible-light-induced photodegradation of gas phase acetonitrile using aerosol-made transition metal (V, Cr, Fe, Co, Mn, Mo, Ni, Cu, Y, Ce, and Zr) doped TiO_2. Appl Catal B Environ 144:333–342. https://doi.org/10.1016/j.apcatb.2013.07.032

Jayawardena KDGI, Rozanski LJ, Mills CA, Beliatis MJ, Nismy NA, Silva RP (2013) 'Inorganics-in-Organics': recent developments and outlook for 4G polymer solar cells. Nanoscale 5:8411. https://doi.org/10.1039/c3nr02733c

Jin YX, Xi JB, Zhang ZY, Xiao JW, Xiao F, Qian LH, Wang S (2015) An ultra-low Pd loading nanocatalyst with efficient catalytic activity. Nanoscale 7:5510–5515. https://doi.org/10.1039/c5nr00599j

Joicy S, Mahesh A, Asokan V, Vaseeharan B, Arunkumar D, Thangadurai P (2017) Phosphine-free, highly emissive, water-soluble Mn:ZnSe/ZnS Core–Shell Nanorods: synthesis, characterization, and in vitro bioimaging of HEK293 and HeLa cells. ACS Appl Nano Mater acsanm.7b00218. https://doi.org/10.1021/acsanm.7b00218

Joicy S, Arun M, Vaseeharan B, Arunkumar D, Thangadurai P (2018) Colloidal gradated alloyed (Cu)ZnInS/ZnS core/shell nanocrystals with tunable optical properties for live cell optical imaging. Chem Select 3:5993–6008. https://doi.org/10.1002/slct.201800742

Jung HS, Lee J-K, Nastasi M, Lee SW, Kim JY, Park JS, Hong KS, Shin H (2005) Preparation of nanoporous MgO-coated TiO_2 nanoparticles and their application to the electrode of dye-sensitized solar cells. Langmuir 21:10332–10335. https://doi.org/10.1021/la051807d

Kerkez-Kuyumcu Ö, Kibar E, Dayıoğlu K, Gedik F, Akın AN, Özkara-Aydınoğlu S (2015) A comparative study for removal of different dyes over M/TiO_2 (M = Cu, Ni, Co, Fe, Mn and Cr) photocatalysts under visible light irradiation. J Photochem Photobiol A Chem 311:176–185. https://doi.org/10.1016/j.jphotochem.2015.05.037

Khataee AR, Kasiri MB (2010) Photocatalytic degradation of organic dyes in the presence of nanostructured titanium dioxide: influence of the chemical structure of dyes. J Mol Catal A Chem 328:8–26. https://doi.org/10.1016/j.molcata.2010.05.023

Kim J-Y, Kang SH, Kim HS, Sung Y-E (2010) Preparation of highly ordered mesoporous Al_2O_3/TiO_2 and its application in dye-sensitized solar cells. Langmuir 26:2864–2870. https://doi.org/10.1021/la902931w

Kim JS, Nair VV, Vohs JM, Gorte RJ (2011) A study of the methane tolerance of LSCM-YSZ composite anodes with Pt, Ni, Pd and ceria catalysts. Scr Mater 65:90–95. https://doi.org/10.1016/j.scriptamat.2010.06.016

Kim SB, Park JY, Kim CS, Okuyama K, Lee SE, Jang HD, Kim TO (2015) Effects of graphene in dye-sensitized solar cells based on nitrogen-doped TiO_2 composite. J Phys Chem C 119:16552–16559. https://doi.org/10.1021/acs.jpcc.5b02309

Kim HW, Na HG, Kwon YJ, Kang SY, Choi MS, Bang JH, Wu P, Kim SS (2017) Microwave-assisted synthesis of graphene–SnO_2 nanocomposites and their applications in gas sensors. ACS Appl Mater Interfaces 9:31677–31682. https://doi.org/10.1021/acsami.7b02533

Kobsiriphat W, Madsen BD, Wang Y, Marks LD, Barnett SA (2009) $La_{0.8}Sr_{0.2}Cr_{1-x}Ru_xO_{3-\delta}$-$Gd_{0.1}Ce_{0.9}O_{1.95}$ solid oxide fuel cell anodes: Ru precipitation and electrochemical performance. Solid State Ionics 180:257–264. https://doi.org/10.1016/j.ssi.2008.12.022

Kojima A, Teshima K, Shirai Y, Miyasaka T (2009) Organometal halide perovskites as visible-light sensitizers for photovoltaic cells. J Am Chem Soc 131:6050–6051. https://doi.org/10.1021/ja809598r

Kulkar M, Thakur P (2014) Photocatalytic degradation and mineralization of reactive textile azo dye using semiconductor metal oxide nano particles. Int J Eng Res Gen Sci 2:245–254

Kurokawa H, Sholklapper TZ, Jacobson CP, De Jonghe LC, Visco SJ (2007a) Ceria Nanocoating for sulfur tolerant Ni-based anodes of solid oxide fuel cells. Electrochem Solid-State Lett 10: B135–B138. https://doi.org/10.1149/1.2748630

Kurokawa H, Yang L, Jacobson CP, De Jonghe LC, Visco SJ (2007b) Y-doped $SrTiO_3$ based sulfur tolerant anode for solid oxide fuel cells. J Power Sources 164:510–518. https://doi.org/10.1016/j.jpowsour.2006.11.048

Lan Z, Chen X, Zhang S, Wu J (2018) $CdSe_xS_{1-x}$/CdS-cosensitized 3D TiO_2 hierarchical nanostructures for efficient energy conversion. J Solid State Electrochem 22:347–353. https://doi.org/10.1007/s10008-017-3748-3

Li L, Yang X, Gao J, Tian H, Zhao J, Hagfeldt A, Sun L (2011) Highly efficient CdS quantum dot-sensitized solar cells based on a modified polysulfide electrolyte. J Am Chem Soc 133:8458–8460. https://doi.org/10.1021/ja201841p

Li T, Zeng W, Wang Z (2015) Quasi-one-dimensional metal-oxide-based heterostructural gas-sensing materials: a review. Sensors Actuators B Chem 221:1570–1585. https://doi.org/10.1016/j.snb.2015.08.003

Li W, Cai X, Ma S, Zhan X, Lan F, Wu Y, Gu Z (2016a) Synthesis of amphipathic superparamagnetic Fe_3O_4 Janus nanoparticles via a moderate strategy and their controllable self-assembly. RSC Adv 6:40450–40458. https://doi.org/10.1039/C6RA04648G

Li Q, Chen J, Fan L, Kong X, Lu Y (2016b) Progress in electrolytes for rechargeable Li-based batteries and beyond. Green Energy Environ 1:18–42. https://doi.org/10.1016/j.gee.2016.04.006

Li M, Hua B, Luo JL, Jiang SP, Pu J, Chi B, Li J (2016c) Enhancing sulfur tolerance of Ni-based cermet anodes of solid oxide fuel cells by ytterbium-doped barium cerate infiltration. ACS Appl Mater Interfaces 8:10293–10301. https://doi.org/10.1021/acsami.6b00925

Li T, Zeng W, Long H, Wang Z (2016d) Nanosheet-assembled hierarchical SnO_2 nanostructures for efficient gas-sensing applications. Sensors Actuators B Chem 231:120–128. https://doi.org/10.1016/j.snb.2016.03.003

Lin H, Irfan XW, Wu HN, Gao Y, Tang CW (2012) MoO_x back contact for CdS/CdTe thin film solar cells: preparation, device characteristics, and stability. Sol Energy Mater Sol Cells 99:349–355. https://doi.org/10.1016/j.solmat.2012.01.001

Liu M, Yang L, Wang S, Blinn K, Liu M, Liu Z, Cheng Z (2009) Enhanced sulfur and coking tolerance of a mixed ion conductor for SOFCs: $BaZr_{0.1}Ce_{0.7}Y_{0.2-X}Yb_xO_{3-\delta}$. Science 326:126–129. https://doi.org/10.1126/science.1174811

Liu M, Zhang R, Chen W (2014) Graphene-supported nanoelectrocatalysts for fuel cells: synthesis, properties, and applications. Chem Rev 114:5117–5160

Liu Q, Chen D, Kang Z (2015a) One-step electrodeposition process to fabricate corrosion-resistant Superhydrophobic surface on magnesium alloy. ACS Appl Mater Interfaces 7:1859–1867. https://doi.org/10.1021/am507586u

Liu W, Liu N, Sun J, Hsu PC, Li Y, Lee HW, Cui Y (2015b) Ionic conductivity enhancement of polymer electrolytes with ceramic nanowire fillers. Nano Lett 15:2740–2745. https://doi.org/10.1021/acs.nanolett.5b00600

Liu H, Hu C, Zhai H, Yang J, Liu X, Jia H (2017) Fabrication of In_2O_3/ZnO@Ag nanowire ternary composites with enhanced visible light photocatalytic activity. RSC Adv 7:37220–37229. https://doi.org/10.1039/C7RA04929C

Logan BE, Regan JM (2006) Microbial fuel cells—challenges and applications. Environ Sci Technol 40:5172–5180. https://doi.org/10.1021/es0627592

Lu XC, Zhu JH (2007) Cu(Pd)-impregnated $La_{0.75}Sr_{0.25}Cr_{0.5}Mn_{0.5}O_{3-\delta}$ anodes for direct utilization of methane in SOFC. Solid State Ionics 178:1467–1475. https://doi.org/10.1016/j.ssi.2007.09.001

Lu Y, Jiang Y, Wu H, Chen W (2013) Nano-PtPd cubes on graphene exhibit enhanced activity and durability in methanol electrooxidation after CO stripping-cleaning. J Phys Chem C 117:2926–2938. https://doi.org/10.1021/jp3116726

Luan X, Wang Y (2014) Ultrathin exfoliated TiO_2 nanosheets modified with ZrO_2 for dye-sensitized solar cells. J Phys Chem C 118:18917–18923. https://doi.org/10.1021/jp5052112

Luo XF, Yuan CL, Zhang ZR (2008) Synthesis, photoluminescence and charge storage characteristics of isolated silver nanocrystals embedded in Al_2O_3 gate dielectric. Thin Solid Films 516:7675–7679. https://doi.org/10.1016/j.tsf.2008.03.017

Luo C, Xie H, Wang Q, Luo G, Liu C (2015) A review of the application and performance of carbon nanotubes in fuel cells. J Nanomater 2015:1–10

Lv M, Zheng D, Ye M, Xiao J, Guo W, Lai Y, Sun L, Lin C, Zuo J (2013) Optimized porous rutile TiO_2 nanorod arrays for enhancing the efficiency of dye-sensitized solar cells. Energy Environ Sci 6:1615–1622. https://doi.org/10.1039/c3ee24125d

Lv J, Dai K, Zhang J, Lu L, Liang C, Geng L, Wang Z, Yuan G, Zhu G (2017) In situ controllable synthesis of novel surface plasmon resonance-enhanced Ag_2WO_4/Ag/Bi_2MoO_6 composite for enhanced and stable visible light photocatalyst. Appl Surf Sci 391:507–515. https://doi.org/10.1016/j.apsusc.2016.05.001

Maçaira J, Andrade L, Mendes A (2017) Highly efficient SiO_2/TiO_2 composite photoelectrodes for dye-sensitized solar cells. Sol Energy 158:905–916. https://doi.org/10.1016/j.solener.2017.10.056

Mahato N, Banerjee A, Gupta A, Omar S, Balani K (2015) Progress in material selection for solid oxide fuel cell technology: a review. Prog Mater Sci 72:141–337

Marom R, Amalraj SF, Leifer N, Jacob D, Aurbach D (2011) A review of advanced and practical lithium battery materials. J Mater Chem 21:9938–9954. https://doi.org/10.1039/c0jm04225k

Masciandaro S, Torrell M, Leone P, Tarancón A (2017) Three-dimensional printed yttria-stabilized zirconia self-supported electrolytes for solid oxide fuel cell applications. J Eur Ceram Soc https://doi.org/https://doi.org/10.1016/j.jeurceramsoc.2017.11.033

McDaniel H, Fuke N, Pietryga JM, Klimov VI (2013) Engineered CuInSe_xS_{2-x} quantum dots for sensitized solar cells. J Phys Chem Lett 4:355–361. https://doi.org/10.1021/jz302067r

Meng X, Li Z, Chen J, Xie H, Zhang Z (2018) Enhanced visible light-induced photocatalytic activity of surface-modified BiOBr with Pd nanoparticles. Appl Surf Sci 433:76–87. https://doi.org/10.1016/j.apsusc.2017.09.103

Metroke TL, Parkhill RL, Knobbe ET (2001) Passivation of metal alloys using sol–gel-derived materials-a review. Prog Org Coat 41:233–238. https://doi.org/10.1016/S0300-9440(01)00134-5

Mikhaylova M, Kim DK, Bobrysheva N, Osmolowsky M, Semenov V, Tsakalakos T, Muhammed M (2004) Superparamagnetism of magnetite nanoparticles: dependence on surface modification. Langmuir 20:2472–2477. https://doi.org/10.1021/la035648e

Miller DR, Akbar SA, Morris PA (2014) Nanoscale metal oxide-based heterojunctions for gas sensing: a review. Sensors Actuators B Chem 204:250–272. https://doi.org/10.1016/j.snb.2014.07.074

Mills A, Davies RH, Worsley D (1993) Water purification by semiconductor photocatalysis. Chem Soc Rev 22:417–425. https://doi.org/10.1039/CS9932200417

Mondal K, Sharma A (2016) Recent advances in the synthesis and application of photocatalytic metal-metal oxide core-shell nanoparticles for environmental remediation and their recycling process. RSC Adv 6:83589–83612. https://doi.org/10.1039/C6RA18102C

Moon HG, Choi YR, Shim YS, Choi KI, Lee JH, Kim JS, Yoon SJ, Park HH, Kang CY, Jang HW (2013) Extremely sensitive and selective NO probe based on villi-like WO_3 nanostructures for application to exhaled breath analyzers. ACS Appl Mater Interfaces 5:10591–10596. https://doi.org/10.1021/am402456s

Nabae Y, Yamanaka I (2009) Alloying effects of Pd and Ni on the catalysis of the oxidation of dry CH_4 in solid oxide fuel cells. Appl Catal A Gen 369:119–124. https://doi.org/10.1016/j.apcata.2009.09.007

Nageswara Rao A, Sivasankar B, Sadasivam V (2009) Kinetic study on the photocatalytic degradation of salicylic acid using ZnO catalyst. J Hazard Mater 166:1357–1361. https://doi.org/10.1016/j.jhazmat.2008.12.051

Naik GK, Mishra PM, Parida K (2013) Green synthesis of Au/$TiO_2$for effective dye degradation in aqueous system. Chem Eng J 229:492–497. https://doi.org/10.1016/j.cej.2013.06.053

Nalwa HS (2000) Handbook of nanostructured materials and nanotechnology. Academic, Burlington

O'Regan B, Grätzel M (1991) A low-cost, high-efficiency solar cell based on dye-sensitized colloidal TiO_2 films. Nature 353:737

Park C-M, Kim J-H, Kim H, Sohn H-J (2010) Li-alloy based anode materials for Li secondary batteries. Chem Soc Rev 39:3115–3141. https://doi.org/10.1039/b919877f

Patil PS, Mujawar SH, Inamdar AI, Shinde PS, Deshmukh HP, Sadale SB (2005) Structural, electrical and optical properties of TiO_2 doped WO_3 thin films. Appl Surf Sci 252:1643–1650. https://doi.org/10.1016/j.apsusc.2005.03.074

Prasai D, Tuberquia JC, Harl RR, Jennings GH, Bolotin KI (2012) Graphene: corrosion-inhibiting coating. ACS Nano 6:1102–1108. https://doi.org/10.1021/nn203507y

Quiñones C, Ayala J, Vallejo W (2010) Methylene blue photoelectrodegradation under UV irradiation on Au/Pd-modified TiO_2 films. Appl Surf Sci 257:367–371. https://doi.org/10.1016/j.apsusc.2010.06.079

Quy CT, Thai NX, Hoa ND, Thanh Le DT, Hung CH, Duy NV, Hieu NV (2018) C_2H_5OH and NO_2 sensing properties of ZnO nanostructures: correlation between crystal size, defect level and sensing performance. RSC Adv 8:5629–5639. https://doi.org/10.1039/C7RA13702H

Rajeshwar K, Osugi ME, Chanmanee W, Chenthamarakshan CR, Zanoni MVB, Kajitvichyanukul P, Krishnan-Ayer R (2008) Heterogeneous photocatalytic treatment of organic dyes in air and aqueous media. J Photochem Photobiol C: Photochem Rev 9:171–192. https://doi.org/https://doi.org/10.1016/j.jphotochemrev.2008.09.001

Ralston KD, Birbilis N (2010) Effect of grain size on corrosion. Corrosion 66:1–4. https://doi.org/10.5006/1.3462912

Ralston KD, Fabijanic D, Birbilis N (2011) Effect of grain size on corrosion of high purity aluminium. Electrochim Acta 56:1729–1736. https://doi.org/10.1016/j.electacta.2010.09.023

Rashed MN, Eltaher MA, Abdou ANA (2017) Adsorption and photocatalysis for methyl orange and Cd removal from wastewater using TiO_2/sewage sludge-based activated carbon nanocomposites. R Soc Open Sci 4:170834. https://doi.org/10.1098/rsos.170834

Rofagha R, Langer R, El-Sherik AM, Erb U, Palumbo G, Aust KT (1991) The corrosion behaviour of nanocrystalline nickel. Scr Metall Mater 25:2867–2872. https://doi.org/10.1016/0956-716X(91)90171-V

Rozier P, Tarascon JM (2015) Review-Li-rich layered oxide cathodes for next-Generation Li-ion batteries: chances and challenges. J Electrochem Soc 162:A2490–A2499. https://doi.org/10.1149/2.0111514jes

Sadreddini S, Salehi Z, Rassaie H (2015) Characterization of Ni–P–SiO_2 nano-composite coating on magnesium. Appl Surf Sci 324:393–398

Sahu SC, Samantara AK, Seth M, Parwaiz S, Singh BP, Rath PC, Jena BK (2013) A facile electrochemical approach for development of highly corrosion protective coatings using graphene nanosheets. Electrochem Commun 32:22–26. https://doi.org/10.1016/j.elecom.2013.03.032

Sandroni M, Gueret R, Wegner KD, Reiss P, Fortage J, Aldakov D, Collomb MN (2018) Cadmium-free $CuInS_2$/ZnS quantum dots as efficient and robust photosensitizers in combination with a molecular catalyst for visible light-driven H_2 production in water. Energy Environ Sci. https://doi.org/10.1039/C8EE00120K

Saravanan R, Karthikeyan N, Gupta VK, Thirumal E, Thangadurai P, Narayanan V, Stephen A (2013a) ZnO/Ag nanocomposite: an efficient catalyst for degradation studies of textile effluents under visible light. Mater Sci Eng C 33:2235–2244. https://doi.org/10.1016/j.msec.2013.01.046

Saravanan R, Thirumal E, Gupta VK, Narayanan V, Stephen A (2013b) The photocatalytic activity of ZnO prepared by simple thermal decomposition method at various temperatures. J Mol Liq 177:394–401. https://doi.org/10.1016/j.molliq.2012.10.018

Saravanan R, Gracia F, Khan MM, Poornima V, Gupta VK, Narayanan V, Stephen A (2015a) ZnO/CdO nanocomposites for textile effluent degradation and electrochemical detection. J Mol Liq 209:374–380. https://doi.org/10.1016/j.molliq.2015.05.040

Saravanan R, Mansoob Khan M, Gupta VK, Mosquera E, Gracia F, Narayanan V, Stephen A (2015b) ZnO/Ag/CdO nanocomposite for visible light-induced photocatalytic degradation of industrial textile effluents. J Colloid Interface Sci 452:126–133. https://doi.org/10.1016/j.jcis.2015.04.035

Selvaraj V, Alagar M (2007) Pt and Pt-Ru nanoparticles decorated polypyrrole/multiwalled carbon nanotubes and their catalytic activity towards methanol oxidation. Electrochem Commun 9:1145–1153. https://doi.org/10.1016/j.elecom.2007.01.011

Sharaf OZ, Orhan MF (2014) An overview of fuel cell technology: fundamentals and applications. Renew Sust Energ Rev 32:810–853

Shen GX, Chen YC, Lin L, Lin CJ, Scantlebury D (2005) Study on a hydrophobic nano-TiO2 coating and its properties for corrosion protection of metals. Electrochim Acta 50:5083–5089. https://doi.org/10.1016/j.electacta.2005.04.048

Sheng X, Wouters B, Breugelmans T, Hubin A, Vankelecom IFJ, Pescarmona PP (2014) Cu/Cu_xO and Pt nanoparticles supported on multi-walled carbon nanotubes as electrocatalysts for the reduction of nitrobenzene. Appl Catal B Environ 147:330–339. https://doi.org/10.1016/j.apcatb.2013.09.006

Shigeru N, Miguel C, Ingrid R, Michael P, Katsumi K, Shogo I, Koji M (2010) CIGS absorbers and processes. Prog Photovolt Res Appl 18:453–466. https://doi.org/10.1002/pip.969

Shih Y-C, Yeh C-W, Lin K-F (2016) Photovoltaic performance enhancement of dye-sensitized solar cells by incorporating poly(sodium-4-styrenesulfonate)-physisorbed MWCNTs into photoelectrode. Mater Chem Phys 171:352–358. https://doi.org/10.1016/j.matchemphys.2016.01.028

Shinde SS, Patil PS, Gaikwad RS, Mane RS, Pawar BN, Rajpure KY (2010) Influences in high quality zinc oxide films and their photoelectrochemical performance. J Alloys Compd 503:416–421. https://doi.org/10.1016/j.jallcom.2010.05.019

Slama R, Ghribi F, Houas A, Barthou C, Mir LE (2011) Visible photocatalytic properties of vanadium doped zinc oxide aerogel nanopowder. Thin Solid Films 519:5792–5795. https://doi.org/10.1016/j.tsf.2010.12.197

Steven M, Vohs JM, Gorte RJ (2003) Effect of precious-metal dopants on SOFC anodes for direct utilization of hydrocarbons. Electrochem Solid-State Lett 6:A240–A243. https://doi.org/10.1149/1.1613231

Su J, Zou X-X, Li G-D, Wei X, Yan C, Wang Y, Zhao J, Zhou L, Chen JS (2011) Macroporous $V_2O_5-BiVO_4$ composites: effect of heterojunction on the behavior of Photogenerated charges. J Phys Chem C 115:8064–8071. https://doi.org/10.1021/jp200274k

Suryanarayana C (1995) Nanocrystalline materials. Int Mater Rev 40:41–64. https://doi.org/10.1179/imr.1995.40.2.41

Tang Y, Yang L, Fang S, Qiu Z (2009) $Li_4Ti_5O_{12}$ hollow microspheres assembled by nanosheets as an anode material for high-rate lithium ion batteries. Electrochim Acta 54:6244–6249. https://doi.org/10.1016/j.electacta.2009.05.092

Thorpe SJ, Ramaswami B, Aust KT (1988) Corrosion and auger studies of a nickel-base metal-metalloid glass. J Electrochem Soc 135:2170–2179. https://doi.org/10.1149/1.2096234

Tian L (2017) Metallurgy and metal physics a short review on mechanical behavior of Nanocrystalline materials. Tian Int J Met Met Phys 2:008

Toda K, Furue R, Hayami S (2015) Recent progress in applications of graphene oxide for gas sensing: a review. Anal Chim Acta 878:43–53. https://doi.org/10.1016/j.aca.2015.02.002

Vazirinasab E, Jafari R, Momen G (2017) Application of superhydrophobic coatings as a corrosion barrier: a review. Surf Coat Technol 341:40–56. https://doi.org/10.1016/j.surfcoat.2017.11.053

Wan Z, Zhang TF, Lee H-B-R, Yang JH, Choi WC, Han B, Kim KH, Kwon SH (2015) Improved corrosion resistance and mechanical properties of CrN hard coatings with an atomic layer deposited Al_2O_3 interlayer. ACS Appl Mater Interfaces 7:26716–26725. https://doi.org/10.1021/acsami.5b08696

Wang S, Zhang B (2013) SPR propelled visible-active photocatalysis on Au-dispersed Co_3O_4 films. Appl Catal A Gen 467:585–592. https://doi.org/10.1016/j.apcata.2013.07.021

Wang S, Si N, Xia Y, Liu L (2015) Influence of nano-SiC on microstructure and property of MAO coating formed on AZ91D magnesium alloy. Trans Nonferrous Metals Soc China 25:1926–1934. https://doi.org/10.1016/S1003-6326(15)63800-6

Wang C, Gao Y, Wang L, Li P (2017) Morphology regulation, structural, and photocatalytic properties of ZnO hierarchical microstructures synthesized by a simple hydrothermal method. Phys Status Solidi Appl Mater Sci 214. doi: https://doi.org/10.1002/pssa.201600876

Wang L, Tang C, Takeuchi KJ, Takeuchi ES, Marschilok AC (2018) Synthesis and characterization of $Li_4Ti_5O_{12}$ anode materials with enhanced high-rate performance in lithium-ion batteries. MRS Adv 3:575–580. https://doi.org/10.1557/adv.2018.247

Wu XM, Wang LD, Luo F, Ma BB, Zhan C, Qiu Y (2007) $BaCO_3$ modification of TiO_2 electrodes in quasi-solid-state dye-sensitized solar cells: performance improvement and possible mechanism. J Phys Chem C 111:8075–8079. https://doi.org/10.1021/Jp0706533

Wu G, Zeng X, Yuan G (2008) Growth and corrosion of aluminum PVD-coating on AZ31 magnesium alloy. Mater Lett 62:4325–4327. https://doi.org/10.1016/j.matlet.2008.07.014

Wu W-Q, Xu Y-F, Rao H-S, Su C-Y, Kuang D-B (2014) Multistack integration of three-dimensional hyperbranched anatase titania architectures for high-efficiency dye-sensitized solar cells. J Am Chem Soc 136:6437–6445. https://doi.org/10.1021/ja5015635

Yang J, Zhong X (2016) CdTe based quantum dot sensitized solar cells with efficiency exceeding 7% fabricated from quantum dots prepared in aqueous media. J Mater Chem A 4:16553–16561. https://doi.org/10.1039/C6TA07399A

Ye Y, He T, Li Y, Tang EH, Reitz TL, Jiang SP (2008) Pd-promoted $La_{0.75}Sr_{0.25}Cr_{0.5}Mn_{0.5}O_3$/YSZ composite anodes for direct utilization of methane in SOFCs. J Electrochem Soc 155:B811–B818. https://doi.org/10.1149/1.2931518

Ye M, Chen C, Lv M, Zheng D, Guo W, Lin C (2013) Facile and effective synthesis of hierarchical TiO_2 spheres for efficient dye-sensitized solar cells. Nanoscale 5:6577–6583. https://doi.org/10.1039/c3nr01604h

Ye M, Gao X, Hong X, Liu Q, He C, Liu X, Lin C (2017) Recent advances in quantum dot-sensitized solar cells: insights into photoanodes, sensitizers, electrolytes and counter electrodes. Sustain Energy Fuels 1:1217–1231. https://doi.org/10.1039/C7SE00137A

Yin H, Yu K, Song C, Huang R, Zhu Z (2014) Synthesis of Au-decorated V_2O_5@ZnO heteronanostructures and enhanced plasmonic photocatalytic activity. ACS Appl Mater Interfaces 6:14851–14860. https://doi.org/10.1021/am501549n

Yu P, Zhu K, Norman AG, Ferrere S, Frank AJ, Nozik AJ (2006) Nanocrystalline TiO_2 solar cells sensitized with InAs quantum dots. J Phys Chem B 110:25451–25454. https://doi.org/10.1021/jp064817b

Yu Y, Wen W, Qian XY, Liu JB, Wu JM (2017) UV and visible light photocatalytic activity of Au/TiO_2 nanoforests with anatase/rutile phase junctions and controlled Au locations. Sci Rep 7:1–13. https://doi.org/10.1038/srep41253

Yuan CL, Lee PS, Ye SL (2007) Formation, photoluminescence and charge storage characteristics of Au nanocrystals embedded in amorphous Al_2 O_3 matrix. EPL (Europhys Lett) 80:67003

Yun JW, Yoon SP, Park S, Kim HS, Nam SW (2011) Analysis of the regenerative H2S poisoning mechanism in $Ce_{0.8}Sm_{0.2}O_{2-\delta}$ coated Ni/YSZ anodes for intermediate temperature solid oxide fuel cells. Int J Hydrog Energy 36:787–796. https://doi.org/10.1016/j.ijhydene.2010.10.060

Zeiger W, Schneider M, Scharnweber D, Worch H (1995) Corrosion behaviour of a nanocrystalline FeA18 alloy. Nanostruct Mater 6:1013–1016. https://doi.org/10.1016/0965-9773(95)00234-0

Zha S, Tsang P, Cheng Z, Liu M (2005) Electrical properties and sulfur tolerance of $La_{0.75}Sr_{0.25}Cr_{1-x}Mn_xO_3$ under anodic conditions. J Solid State Chem 178:1844–1850. https://doi.org/10.1016/j.jssc.2005.03.027

Zhang X, Wang G, Liu X, Wu J, Li M, Gu J, Liu H, Fang B (2008) Different CuO nanostructures: synthesis, characterization, and applications for glucose sensors. J Phys Chem C 112:16845–16849

Zhang L, Du L, Yu X, Tan S, Cai X, Yang P, Gu Y, Mai W (2014a) Significantly enhanced photocatalytic activities and charge separation mechanism of Pd-decorated ZnO-graphene oxide nanocomposites. ACS Appl Mater Interfaces 6:3623–3629. https://doi.org/10.1021/am405872r

Zhang J, Gao J, Church CP, Miller EM, Luther JM, Klimov VI, Beard MC (2014b) PbSe quantum dot solar cells with more than 6% efficiency fabricated in ambient atmosphere. Nano Lett 14:6010–6015. https://doi.org/10.1021/nl503085v

Zhang W, Ji G, Bu A, Zhang B (2015) Corrosion and tribological behavior of ZrO_2 films prepared on stainless steel surface by the sol–gel method. ACS Appl Mater Interfaces 7:28264–28272. https://doi.org/10.1021/acsami.5b07915

Zhao J, Wang A, Green MA, Ferrazza F (1998) 19.8% efficient "honeycomb" textured multicrystalline and 24.4% monocrystalline silicon solar cells. Appl Phys Lett 73:1991–1993. https://doi.org/10.1063/1.122345

Zheng LL, Wang X, Zhang L, Wang JY, Jiang SP (2012) Effect of Pd-impregnation on performance, sulfur poisoning and tolerance of Ni/GDC anode of solid oxide fuel cells. Int J Hydrog Energy 37:10299–10310. https://doi.org/10.1016/j.ijhydene.2012.03.105

Zhou H, Chen Q, Li G, Luo S, Song T, Duan HS, Hong Z, You J, Liu Y, Yang Y (2014) Interface engineering of highly efficient perovskite solar cells. Science 345:542–546. https://doi.org/10.1126/science.1254050

Zhou D, Zhou T, Tian Y, Zhu X, Tu Y (2017) Perovskite-based solar cells: materials, methods, and future perspectives. J Nanomater 2018:1–15. https://doi.org/10.1155/2018/8148072

Zhu S, Li Q, Li F, Cao W, Li T (2016) One-pot synthesis of Ag^+ doped $BiVO_4$ microspheres with enhanced photocatalytic activity via a facile hydrothermal method. J Phys Chem Solids 92:11–18. https://doi.org/10.1016/j.jpcs.2016.01.009

Zou CW, Rao YF, Alyamani A, Chu W, Chen MJ, Patterson DA, Emanuelsson AC, Gao W (2010) Heterogeneous lollipop-like V_2O_5/ZnO array: a promising composite nanostructure for visible light photocatalysis. Langmuir 26:11615–11620. https://doi.org/10.1021/la101324e

Chapter 2
Carbon Nanomaterials in Renewable Energy Production and Storage Applications

Joyita Banerjee, Kingshuk Dutta, and Dipak Rana

Contents

Abstract With the increase in worldwide consumption of nonrenewable energy resources (i.e., fossil fuels) and emission of toxic gases, it is our foremost concern to concentrate our research on sustainable and renewable energy. This motive paved the way to develop several renewable energy production and storage systems, like solar cells, supercapacitors, fuel cells, and lithium-ion batteries. These devices, with high specific power, long cycle life, portability, and ease of fabrication, have been

J. Banerjee
Department of Chemical Engineering, University of Pittsburgh, Pittsburgh, PA, USA

K. Dutta (✉)
Department of Materials Science and Engineering, Cornell University, Ithaca, NY, USA
e-mail: kd426@cornell.edu

D. Rana (✉)
Department of Chemical and Biological Engineering, Industrial Membrane Research Institute, University of Ottawa, Ottawa, ON, Canada
e-mail: rana@uottawa.ca

R. Saravanan et al. (eds.), *Emerging Nanostructured Materials for Energy and Environmental Science*, Environmental Chemistry for a Sustainable World 23,
https://doi.org/10.1007/978-3-030-04474-9_2

able to secure worthy positions in the field of energy science and technology. Over the last decades, attempts have been taken to use nanostructured carbon-based materials, like graphene and carbon nanotubes (CNTs), with the aim of improving the efficiency of the abovementioned energy storage systems.

In this book chapter, focus has been directed toward the recent progress and advancement on the efficiency of the electrode materials of these renewable energy storage systems via application of CNTs, graphene, or nanohybrid fillers. The ability of these materials to exhibit superior capacity toward photon absorption, capability toward generation of photocarriers, photovoltaic properties, and separation of charge carriers to form heterojunctions makes them ideal applicants in solar cells. The capacitance of a supercapacitor varied with the specific surface area, synthetic approach, pore size, pore size distribution, and posttreatment of these materials. Moreover, high electron conductivity and high surface area of these nanomaterials led to improvements in (a) electrode reaction rates in fuel cells, lithium-ion batteries, and supercapacitors and (b) charge storage capability of supercapacitors and lithium-ion batteries.

2.1 Introduction

2.1.1 Background and Significance

The enormous global consumption of energy and significant emission of carbon dioxide have led to a new frontier for research in the field of nanotechnology. Nowadays, the most important challenge that engages human civilization is to restore renewable energy and to achieve a sustainable society free of environmental pollution. Different forms of renewable energies like geothermal, solar, wind power, biofuel, and hydropower have been nurtured by human being. In this context, carbon nanomaterials, like carbon nanotubes (CNTs) (Banerjee et al. 2015; Kim et al. 2010; Kanninen et al. 2014) and graphene (Wang and Kumta 2010; Tung et al. 2009; Jafri et al. 2010; Jiang et al. 2012), and in some cases polymer nanocomposites have been recognized as ideal candidates for utilization in advanced energy storage devices.

Carbon nanomaterials have found application in energy storage systems owing to their ability to store charges with good electrical and mechanical properties. Carbon nanostructures have been used as electrodes for fuel cells, solar cells, lithium-ion (Li-ion) batteries, and supercapacitors (Gong et al. 2009; Du et al. 2012; Landi et al. 2009). It has been reported that 2.5% of the total power delivered in the USA has been used for storage purposes, whereas the level of energy storage in Europe and Japan are 10% and 15%, respectively (EPRI-DOE 2003).

The first solar cell was introduced by Bell executives in 1954. The first fuel cell was invented in 1838, and it was commercialized after a century by NASA for use in power supply for satellites in space. Up until now, batteries have been used as efficient electrical energy storage devices with good portability, excellent energy

power supply over a prolong time scale, and high energy density. The advent of Li-ion batteries has resulted in overcoming certain limitations, such as resistance toward sudden power surge (Goodenough and Mizuchima 1981; Yazami and Reynier 2002; Nagaura and Tozawa 1990). In 1991, the first Li-ion battery was discovered through the work of Goodenough, Yazami, and others (EPRI-DOE 2003; Goodenough and Mizuchima 1981). In subsequent years, several studies were carried out to develop Li-ion batteries with high capacity. However, there still exist certain limitations for these batteries. In order to improve the capability of the electrical energy storage, supercapacitors or ultracapacitors have been developed with exceptionally high charge/discharge rates. General Electric Co., in 1957, was the first to file a patent on the concept of supercapacitors using carbon, with a high specific surface area, for the electrode and using sulfuric acid as the electrolyte. The first low resistance supercapacitor was commercialized by Pinnacle Research Institute (PRI) in 1982 for military applications. Supercapacitors usually store energy by polarizing an electrolyte solution, whereas dielectric capacitors perform energy storage in the form of separated electrical charges (Conway 1999; Aricò et al. 2005). Supercapacitors produce two orders of magnitude higher power than that of fuel cells and higher efficiency and ability to withstand larger numbers of charge/discharge cycles, adverse temperature, and environmental conditions.

2.1.2 Broader Context

Figure 2.1 presents the progressive increase over the years in the application of CNTs in solar cells, supercapacitors, Li-ion batteries, and fuel cells. It can be observed from the figure that the use of CNTs in the field of energy has increased over the years, and their application is much more prominent in the field of fuel cells as compared to other devices. The extraordinary properties of CNTs, such as excellent electrical conductivity, high entanglements, good thermal conductivity,

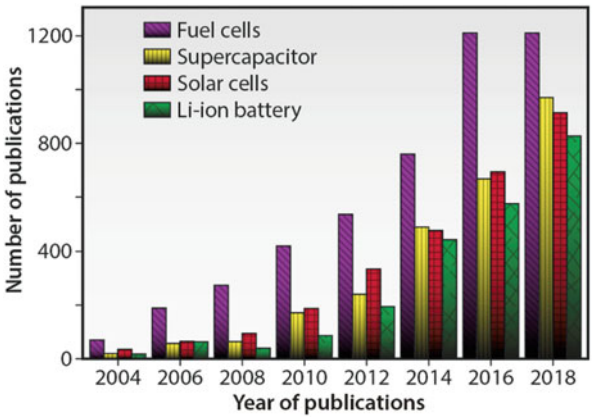

Fig. 2.1 The progressive increase in the number of publications over the years in the field of application of CNTs in different types of electrochemical storage devices

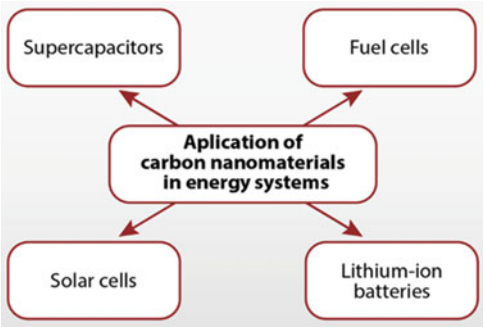

Fig. 2.2 A schematic illustration exhibiting the application of carbon nanomaterials in various energy storage systems

and high resilience, have resulted in extensive application as catalyst-supporting materials in fuel cells (Dutta and Kundu 2014; Dutta et al. 2015a, b; Das et al. 2015a). These nanomaterials have been used for improving the energy efficiency or enhancing the power output of several new devices for energy storage applications (Baughman et al. 2002). Recent research activities include the generation of steam from solar energy, a highly engineered polymer matrix used for high-efficiency light bulbs, generating electricity from waste materials and storing hydrogen for fuel cell-powered cars.

Nanostructured materials have increasingly found application in electrochemical energy storage devices. It is to be mentioned here that it is beyond the scope of this chapter to give a comprehensive summary of the energy storage or energy conversion materials used in the present day or in the future. Instead, an attempt has been made to highlight the application of carbon nanomaterials in the field of Li-ion batteries, supercapacitors, fuel cells, and solar cells. Figure 2.2 elaborates the use of carbon nanomaterials in four essential energy storage systems, which are considered to be the most promising devices to store renewable energy.

2.2 General Discussion on Renewable Energy Devices

2.2.1 Supercapacitors

In this new era, development of highly efficient supercapacitors has been one of the most promising fields of research in academia as well as in industry. At present, extensive research work is being focused on the use of carbon nanomaterials as electrodes in supercapacitors. Similar to other capacitors, supercapacitors also consist of two solid/porous electrodes, which remain in contact with a separator and an electrolyte. A schematic diagram of a supercapacitor is presented in Fig. 2.3. While an electrolytic capacitor accumulates charges on the two conductors, which are separated by a dielectric, a supercapacitor stores charges at the interfacial region between the electrolyte solution and the electrode. It can be observed from Fig. 2.3 that there exist porous dielectric materials which prevent the transport of charges

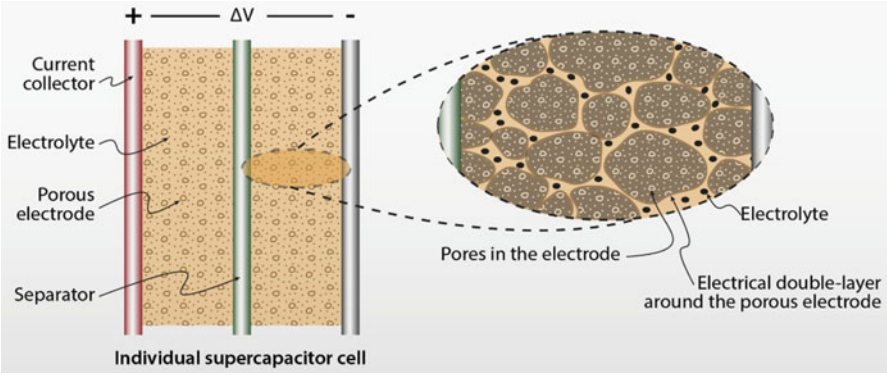

Fig. 2.3 A schematic illustration of a supercapacitor. (Reproduced after modification from Pan et al. 2010, Courtesy of Springer. Originally figure from the Wikipedia: http://en.wikipedia.org/wiki/Supercapacitor)

between the electrodes. Usually, supercapacitors can be divided into two classes – (a) pseudocapacitors and (b) electrical double-layer capacitors (ELDC) (Pan et al. 2010). The basic difference between these two types of capacitors is in their charge transfer and storage aspects, i.e., a pseudocapacitor follows faradaic charge-transfer laws, whereas an ELDC obeys the non-faradaic charge-transfer mechanism. It was found that in case of ELDC, the storage of electrical energy remains electrostatic without any electron transfer, resulting in the formation of a Helmholtz layer (Emmenegger et al. 2003). However, there are some exceptions, including several carbon electrodes with high specific surface area, which showed pseudocapacitance due to the presence of redox-active moieties (Gong et al. 2009). ELDC comprises an electrochemical redox reaction between the electrodes and the electrolytes, which involves charge transfer. Hence, the capacitance of EDLC is much higher than that of the pseudocapacitors.

Figure 2.4 depicts the comparison (from Ragone plot) of the power and the volumetric specific energy densities of a supercapacitor, an electrolytic capacitor, a microsupercapacitor based on activated carbon (AC), and a lithium thin-film battery. In general, it is observed that for a supercapacitor, the negatively charged ions present within the electrolyte migrate toward the positively charged electrode and the positively charged ions move toward the negatively charged electrode, forming two layers of capacitive storage. This gives an added advantage for the two capacitors present in series over the single capacitor, and hence, the capacitance of the cell is given by:

$$(C_{\text{Cell}})^{-1} = {C_1}^{-1} + {C_2}^{-1} \tag{2.1}$$

where C_{cell} represents the overall capacitance value of the two terminal devices and C_1 and C_2 are the individual capacitance values of the two electrodes (Pandolfo and Hollenkamp 2006; Wang et al. 2012; Frackowiak and Béguin 2001).

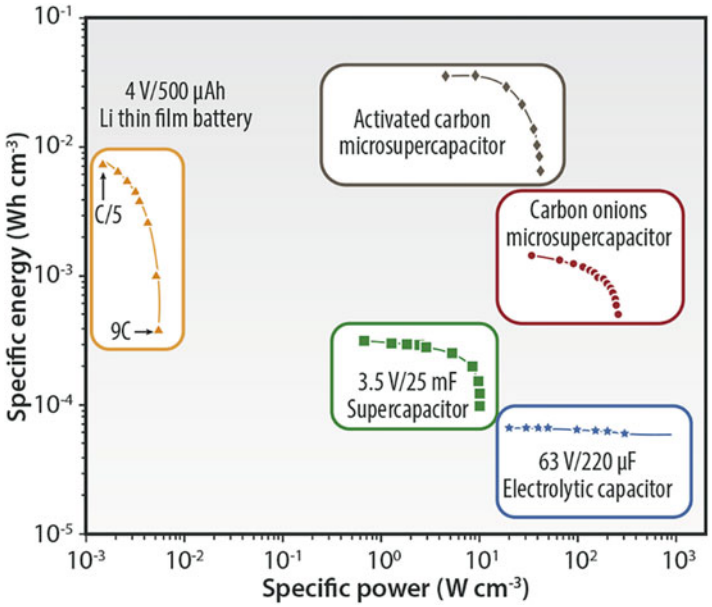

Fig. 2.4 Comparative Ragone plot of the specific energy and power density (per cm^3 of stack) of a Li thin-film battery, a supercapacitor, an electrolytic capacitor, and activated carbon and carbon onion microsupercapacitors. (Reproduced after modification from Pech et al. 2010, with permission from Macmillan Publishers Limited)

The electrical energy stored within the supercapacitor is given by Pech et al. (2010):

$$E = \frac{CV^2}{2} = \frac{QV}{2} \tag{2.2}$$

where E stands for the accumulated electrical energy, Q is the stored charge, V represents the voltage, and C stands for the capacitance of the cell.

It has been suggested that the charge stored by the cell and the cell capacitance are dependent upon the electrode material, whereas the operating voltage depends simply on the stability window of the electrolyte (Nagaura and Tozawa 1990). Although supercapacitors possess high power owing to the presence of the double-layer system, their output power density remains low due to the series resistance. The energy density (E, $Whkg^{-1}$) of a supercapacitor is given by:

$$E = \frac{C_{\text{cell}} V^2}{2m} \tag{2.3}$$

The power density (P) of a supercapacitor can be presented as:

$$P = \frac{E}{\Delta T} \tag{2.4}$$

The maximum power density produced by a supercapacitor can be presented as:

$$P_{\max} = \frac{V^2}{4mR_s} \tag{2.5}$$

where $P_{\max}$ is the maximum power output by the supercapacitor, m stands for the mass of the active material, Δt represents the discharge time, and R_s is the equivalent resistance in series (ESR).

When the internal resistance of the cell becomes equal to its load resistance, then the device (any energy storage device) achieves the maximum power output. The power and energy densities of the cell depend on the volumetric capacitance, the ESR, and the cell voltage of the device. The ESR consists of the electrolyte resistance, the mass transfer resistance toward the movement of ions through the pores present within the matrix, the internal resistance of the electrode matrix, and various other types of resistances existing within the cell (Aricò et al. 2005). The performance of a supercapacitor mainly depends on its self-discharge rate and leakage current, whereas its cyclic stability depends on the nature and chemistry of the electrode materials. Thermodynamically, a fully charged supercapacitor possesses higher free energy as compared to a discharged one. Therefore, it is the general tendency of a supercapacitor to self-discharge in order to equilibrate with the environment. There exist three types of materials that can be utilized for fabricating the electrodes. They are high surface area AC materials, oxides of transition metals, and electroactive polymers.

2.2.2 *Fuel Cells*

Fuel cells are environmentally friendly energy-storing devices, possessing low or no emission threat and high energy conversion and power density (Dutta et al. 2015b). The polymer electrolyte membrane (PEM) fuel cell is mainly used for low-temperature mobile applications (Dutta et al. 2014a, b; Kundu and Dutta 2016). Their slow electrode kinetics resulted in a significant amount of costly and scarce catalyst materials (especially Pt metal) being used (Kumar et al. 2014a). Similar to batteries, fuel cells also convert chemical energy to electrical energy producing heat and water as a by-product (Dutta et al. 2016a, b). In the case of fuel cells, the fuel is fed to the anode side of the cell, while the oxidant is fed at the cathode side of the cell (Kumar et al. 2014b); electrochemical reactions take place at the two electrodes (Das et al. 2015b). Electrons are generated at the anode and are then transferred to the cathode through the external circuit to produce electricity. The electrolyte also plays a crucial role in the operation of the fuel cell (Dutta et al.

2014c, 2015c). It helps in the transportation of the generated protons from the anode to the cathode side and prevents mixing of the contents of the anode and the cathode chambers (Dutta et al. 2014d, 2016c). In the last few decades, several attempts have been made to improve the efficiency of fuel cells by using innovative and other catalysts in place of the state-of-the-art Pt metal. This is owing to the fact that Pt is extremely costly and scarce, thus hindering commercialization of the fuel cell devices (Das et al. 2015c, 2016). Several new catalyst supports have also been developed in place of traditionally used carbon black. These include carbon nanomaterials, like CNTs and graphene, as well as other nanomaterials that help in improving the capability of the catalyst (Landi et al. 2009; EPRI-DOE 2003; Goodenough and Mizuchima 1981; Yazami and Reynier 2002; Das et al. 2015a). Other worth-mentioning materials used as a support matrix are mesoporous carbon materials (Chang et al. 2007; Chai et al. 2004), carbon nanocoils (Sevilla et al. 2007), and mesocarbon microbeads (Bai et al. 2007). It is important to mention here that the performance of a catalyst improves with the increase in its surface area. However, there is evidence which shows that a decrease in the efficiency of metal nanoparticles with a decrease in the particle size occurs due to particle-size effect (Kinoshita 1990; Yahikozawa et al. 1991; Kabbabi et al. 1994). Therefore, in order to improve the performance of the catalyst, it is supported on materials possessing high surface area. Porous materials possessing high mesoporous characteristics and good electrical conductivity for easy flow of electrons are ideal for being used as supports. Proper and uniform dispersion of the catalyst on the supporting material is the primary concern in improving the catalytic activity of the catalyst. Several studies have revealed that the mere decoration of the external and the internal walls of CNTs with active materials, like Ru, Pt, and Ru-Pt alloy, leads to an increase in the catalytic activity of the catalyst (Debe 2012; Liu et al. 2002; Lordi et al. 2001; Che et al. 1998, 1999; Planeix et al. 1994).

CNTs-based fuel cells have been found to possess high catalytic activity and high quality of transmission and production of large current densities (Yoshitake et al. 2002; Li et al. 2005; Mink and Hussain 2013). CNTs have been applied as supporting materials for both the anode and the cathode of the fuel cells (Liu et al. 2002; He et al. 2004a, b; Guo and Li 2004). There are several aspects that make CNTs a more preferred candidate over other materials, which include higher crystalline nature, higher chemical stability, better electrical and thermal properties, and a 3D structure favoring sufficient space for reaction. Moreover, the absence of impurities in purified CNTs helps in inhibiting the formation of any toxic intermediate(s) (Hamon et al. 1999). Figure 2.5 displays a schematic diagram of a typical fuel cell.

2.2.3 Solar Cells

Solar cell devices are those which use solar energy as the only fuel and produce electrical charges by photovoltaic effect, so that these can move freely in semiconductors and finally through an electric load (motor or bulb) (McEvoy et al. 2012).

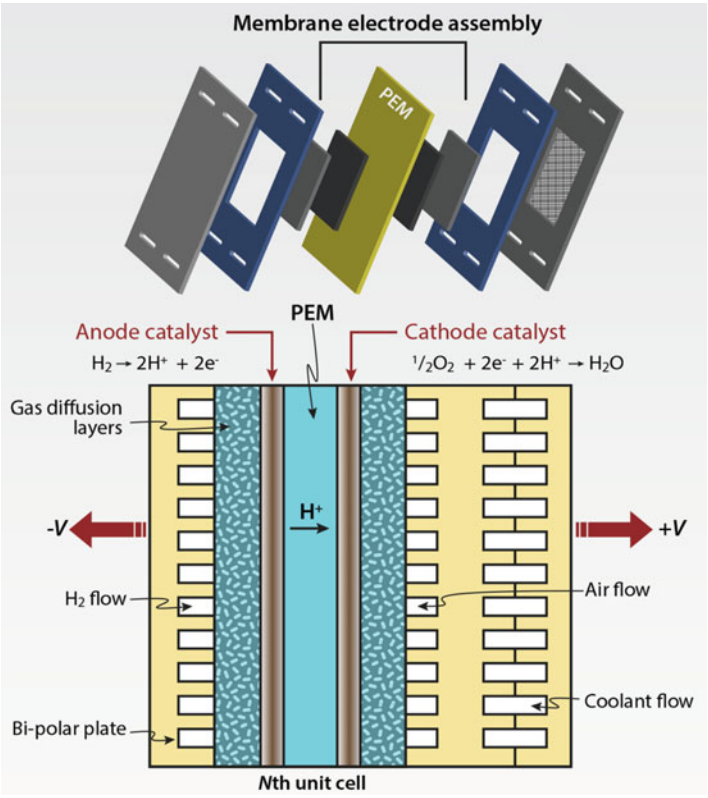

Fig. 2.5 A schematic illustration of a fuel cell. (Reproduced after modification from Debe 2012, with permission from Macmillan Publishers Limited)

A solar cell involves direct harvesting of sunlight into solar energy using small photovoltaic cells (Fahrenbruch and Bube 1983). From the advent of the first solar cell, which was a silicon (Si)-based cell (Yadav and Kumar 2015), this has gained enormous attention from research communities (Castellano 2010). The first generation of solar cells was produced on silicon wafers either using monocrystalline or polycrystalline silicon crystals (Srinivas et al. 2015; Würfel and Würfel 2009; Dmitrijev 2006; Saga 2010; Jayakumar 2009). Usually, silicon wafers have a thickness of 350 μm, whereas the second-generation thin-film solar cells possess a thickness of 1 μm. The second-generation solar cells are amorphous silicon, CdTe, and copper indium gallium diselenide (CIGS) (Naghavi et al. 2003; Li et al. 2014b; Goswami and Kreith 2007; Luque and Hegedus 2003; Elsabawy et al. 2012; Razykov et al. 2011). The most recent and promising generation of solar cells consists of concentrated solar cells, polymer-based solar cells, dye-sensitized solar cells, nanocrystal-based solar cells, and perovskite-based solar cells. Over the last decades, organic materials like conducting polymers have been used as ideal candidates for the photovoltaics in solar cells. It has been found that organic

semiconductors have the potential to absorb solar energy within a few thin layers. However, there exist some limitations in using organic photovoltaics. In order to improve the efficiency of polymer photovoltaics, CNTs have been used. CNTs help in improving the charge conduction, the optoelectronic properties, and the thermal and chemical properties of the cells (Candelaria et al. 2012; Wang et al. 2004). In this chapter, the application of various carbon nanomaterials in photovoltaic solar cells, organic solar cells, dye-sensitized solar cells (DSSC), quantum dot-sensitized solar cells (QDSC), and silicon-based solar cells has been highlighted. DSSCs are defined as photoelectrochemical solar cell devices which involve absorption of solar energy by dyes and transferring it to the semiconductor oxide present within the cell. Figure 2.6a shows a schematic of the currently used p-n junction photovoltaic cells. This PEC DSSC consists of a semiconductor, assembled with a working electrode and a conducting transparent substrate. Figure 2.6b presents porous TiO_2 nanostructures, with a coating of dye on it, assembled with CNTs. The dye molecule assembled with TiO_2 absorbs photonic energy which is then transmitted onto the surface of nanocrystalline TiO_2 with a porous structure. This results in excitation of an electron from the ground to an excited state, presumably to the conduction band of TiO_2. This electron, excited from the absorbed photon energy, after passage through the TiO_2 layer, forms the first layer of transparent conducting layer as the anode and the second layer as the cathode. This phenomenon is depicted in Fig. 2.6c (Yan et al. 2013).

Silicon has long been considered as an ideal candidate for electrode material in solar technology. However, high cost and low stability limit the application of

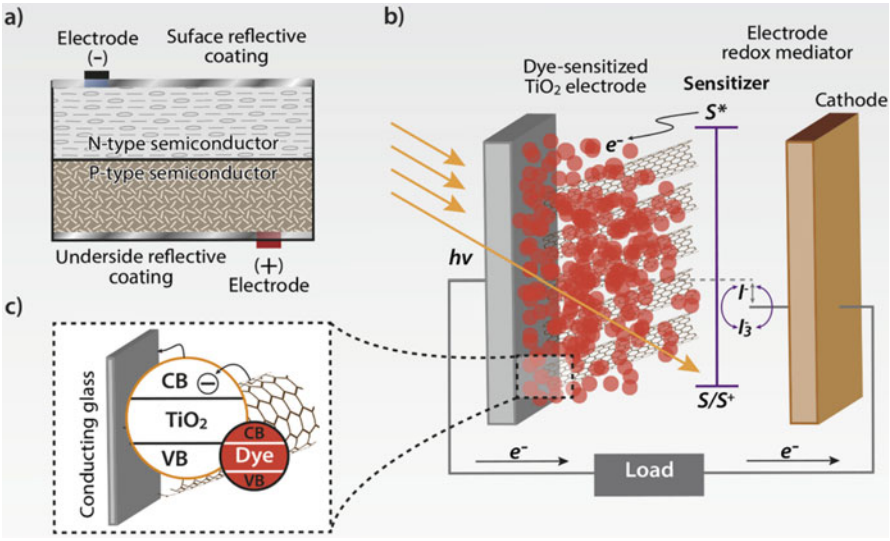

Fig. 2.6 (**a**) The p-n junction in solar cells, (**b**) the working principle of DSSC, and (**c**) electrons' transportation route in dye-sensitized TiO_2 electrode. (Reproduced after modification from Yan et al. 2013, with permission from Elsevier)

silicon in solar cells. In this context, carbon nanomaterials play an important role in increasing the commercialization potential of solar cells. CNTs find application as heterojunctions in solar cells and also as windows/back electrodes. Semiconducting CNTs possess a direct bandgap which facilitates optical transition without the intervention of photons. Stewart and Léonard (2004) have reported that the photoresponse generated at the p-n junction of CNTs have unusual behavior, i.e., appearance of multiple sharp peaks in visible, ultraviolet, and infrared regions. In addition, it has been found that there exists a size effect at this nanoscale region where photocurrent scales linearly and starts oscillating with the length of the devices. Moreover, it was suggested that even bundled CNTs and CNT films were also able to produce photocurrent (Wei et al. 2006; Lu and Panchapakesan 2006; Itkis et al. 2006; Lien et al. 2006). Another application of CNTs in solar cells is their use as windows/back electrodes. It has been demonstrated that a thin layer composed of metallic CNTs performs electrical conductivity along the lateral direction and collects current from the front surface of the thin-film solar cells. Studies have proved that CNTs circuits and coatings act as an efficient alternative to traditional conductive materials, like fluorine-doped tin oxide (FTO), indium tin oxide (ITO), cadmium sulfide, or zinc oxide. It has been found that the performance of solar cells depends on the type of CNTs employed. Attempts have been taken to synthesize single-walled carbon nanotubes (SWCNTs) and double-walled carbon nanotubes (DWCNTs) from cheap petroleum coke as the carbon source using an arc-discharge method (Xu et al. 2014). SWCNTs-based solar cells exhibit better performance under LED illumination in the range of 400–940 nm as compared to DWCNTs-based solar cells under 1310 nm infrared light LED illumination.

2.2.4 Lithium-Ion Batteries

In order to keep pace with the advancement of computers, the battery technology has also improved a lot from nickel cadmium (NiCd) used for wireless communications and mobile computing to nickel metal hydride (NiMH) and finally to Li-ion batteries with high capacity (Banerjee and Dutta 2017). The challenge for developing new generation Li-ion batteries depends on the advancement of electrodes and electrolytes which can withstand hundreds of charge-discharge cycles with minimum capacity fading. The Li-ion battery cell (Fig. 2.7) involves intercalation and de-intercalation of Li-ions into the electrodes (anode and cathode) depending on charging or discharging. The process of charging or discharging depends on the mobility of the Li-ions exchanged between the electrodes through electrolytes followed by the flow of electrons in the external circuits. The increasing demand of Li-ion battery emerges from its high volumetric energy, high power density, minimal self-discharge, and long cycle life (Etacheri et al. 2011; Armand and Tarascon 2008; Scrosati and Garche 2010; Nazri and Pistoia 2003). Figure 2.8

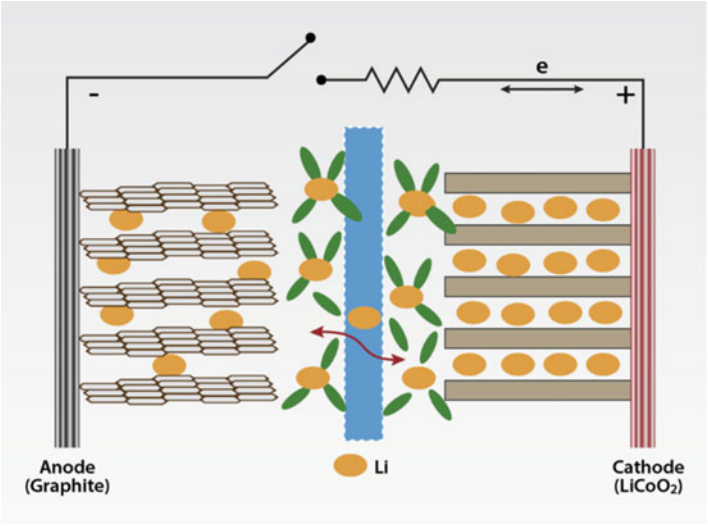

Fig. 2.7 A schematic representation of the lithium insertion/de-insertion mechanism for current rechargeable lithium battery. (Reproduced after modification from Goriparti et al. 2014, Courtesy of Elsevier)

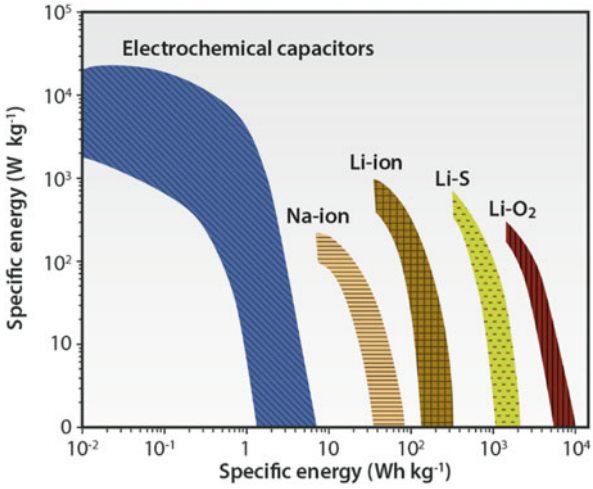

Fig. 2.8 Distribution of the different electrochemical energy storage performances. (Reproduced after modification from Yuan et al. 2016b, with permission from the Royal Society of Chemistry)

shows the power and energy densities of Li-ion, Li-S, and Li-O_2 batteries. However, there remain some problems with each of these three types of batteries (Yuan et al. 2016b).

It has been found that conventional cathodes like $LiCoO_2$, $LiFePO_4$, $Li_3V_2(PO_4)_3$, and $LiMn_2O_4$ and anodes like graphite, silicon, and tin based and even oxides possess respective drawbacks. Metallic oxides have good cycle stability with high reversible capacity loss. Besides, carbon-based materials exhibit high

cycle performance; however, they lack efficiency. Electrodes comprised of conventional materials undergo subsequent expansion and contraction, leading to damage of the electrodes. This can be overcome by using carbon nanomaterials like CNTs and graphene, which possess high conductivity, high electron mobility, and superconductivity, along with less resistive heating, and, therefore, can be operated at low temperatures. It has been further studied that Li-ions insert within the defects of CNTs present on the surface and even between the layers (Goriparti et al. 2014). This incorporation of Li^+ within the defects of CNTs leads to production of further defects, which is followed by deepening and shortening of the diffusion path for Li-ions (Han et al. 2012; Wu et al. 1999).

It is now important to think about the reason behind the improvement in the performance of the energy storage devices using nanomaterials. The significant increase in the efficiency of the energy storage or conversion devices upon a change from bulk to nanoscale materials is due to the increase in electrode/electrolyte contact area, which improves the rate of electrode reactions (Aricò et al. 2005). Increase in interfacial area and grain boundaries leads to increase in the density of mobile defects at the space charge region, which eventually imparts excellent electrochemical properties to the nanomaterials.

2.3 Application of Carbon Nanomaterials

2.3.1 Supercapacitors

The porous structures of graphene and CNTs were studied in order to improve the energy storage capability of supercapacitors. Freestanding mats of entangled multiwalled carbon nanotubes (MWCNTs), with H_2SO_4 electrolyte, have shown significant improvement in the specific capacitance of the electrodes of supercapacitors (Niu et al. 1997). Attempts have been made to study the effect of vertically aligned and random CNTs on the specific capacitance of the supercapacitor electrodes (An et al. 2001; Futaba et al. 2006). It has been demonstrated that Au-MnO_2/CNT coaxial electrodes, prepared by a complex process, exhibit an energy density value of 4.5 $Whkg^{-1}$ and a specific capacitance of 68 Fg^{-1} in an aqueous electrolyte (Reddy et al. 2010). CNTs-implanted mesoporous carbon spheres as the electrode in an aqueous electrolyte have been fabricated in order to provide additional porosity and to improve the electrical conductivity of the carbon spheres (Yi et al. 2011). These mesoporous carbon spheres possessed a diameter of approximately 0.5–1.0 mm, an average pore size of 3.9 nm and a specific surface area of 284 $m^2\ g^{-1}$. This electrode produced an ESR value of 0.83 Vcm^2, a maximum specific capacitance value of 189 Fg^{-1} and a power density value of 8.7 $kWkg^{-1}$ at an energy density value of 6.6 $Whkg^{-1}$. Random SWCNTs networks have also shown significant value of specific capacitance in the presence of KOH electrolyte with a power density of 20 $kWkg^{-1}$ and an energy density of 10 $Whkg^{-1}$ (Chen and Dai 2013). An MnO_2-based nanocomposite, formed by electrophoretic

deposition of exfoliated CNTs on nickel foam followed by deposition of nanoparticles, like Pt, Pd, or Au, led to the generation of a hybrid supercapacitor exhibiting a specific capacitance value of 559.1 Fg^{-1} (Zhao et al. 2013). This electrode displayed extremely good conducting and 3D porous structure for easy electrolyte penetration and ion delivery in the presence of 1-butyl-3-methylimidazolium hexafluorophosphate (BMIM-PF6)/N,N-dimethylformamide (DMF) electrolyte. Xiao et al. have assembled a supercapacitor composed of functionalized freestanding CNTs as the positive electrode and freestanding CNT/MoO_{3-x} as the negative electrode with a high volumetric capacitance value of 3.0 Fcm^{-3} and high power and energy densities of 4.2 Wcm^{-3} and 1.5 $mWhcm^{-3}$, respectively, with a stable operation window between 0 and 1.9 V (Xiao et al. 2014).

Polypyrrole (PPy)/CNT composite was prepared by utilizing CVD-grown CNTs on ceramic foam, followed by PPy coating by chemical polymerization (Lee et al. 2011a). It was observed that PPy not only acted as a binder but also helped in interconnecting the CNTs agglomerates, thus helping in retaining the capacitance of the electrode after 5000 redox cycles. Polyaniline (PAni), with carbon porous material having a high surface area, exhibited a high specific capacitance and an improved cycle life. PAni composites, i.e., PAni/graphene, PAni/carbon nanofibers (CNFs), and PAni/CNT, produced higher specific capacitance values compared to PAni (Wang et al. 2013a; Luo et al. 2013; Yang et al. 2013; Dong et al. 2007). PAni/longitudinally unzipped CNTs composites, synthesized by an in situ chemical oxidation process, have shown 81% retention in capacitance even after 1000 cycles and improved cyclability (Fathi et al. 2014). The electrochemical analysis revealed that PAni/partially unzipped carbon nanotubes (UCNTs) composites produced a much higher specific capacitance value of 762 Fg^{-1}, compared to that exhibited by pure PAni (i.e., 295 Fg^{-1}), at a scan rate of 30 mVs^{-1}. Cheng et al. (2014) have analyzed the properties of nickel oxide (NiO_x)-based nanoparticles, which were formed by the process of self-assembly on poly(ethylene imine) (PEI)-CNTs composites as substrate with the aid of microwave radiation. These nanoparticles possessed a particle size of 2–3 nm. In addition, the synergistic effect arising between the homogeneously dispersed nanoparticles and PEI-CNTs composites resulted in improvement in the electrocatalytic performance of the electrode. It can be inferred from Fig. 2.9 that with an increase in the number of nanoparticles, the particle size increased along with an increase in the density. PEI-functionalized CNTs proved to be effective in facilitating the uniform dispersion of nanoparticles on CNTs.

The thermally decomposed NiO has, however, shown the presence of large-size particles due to heat treatment at high temperature. The electrochemical performance of the electrode has been studied through cyclic voltammetry (CV), which showed that the anodic and cathodic peaks were symmetric in nature, suggesting reversibility of the process. Moreover, it was also found that the specific capacitance value of NiO_x/PEI-CNTs was much higher compared to that of unsupported NiO (i.e., 2584 Fg^{-1}) and NiO/PEI-CNTs mixture (i.e., 276 Fg^{-1} based on active materials). It has also been reported that controlled KOH activation and nitrogen doping with melamine improved the specific capacitance, the specific surface area of CNTs, as well as the rate performance along with a stable performance even after 1000 cycles

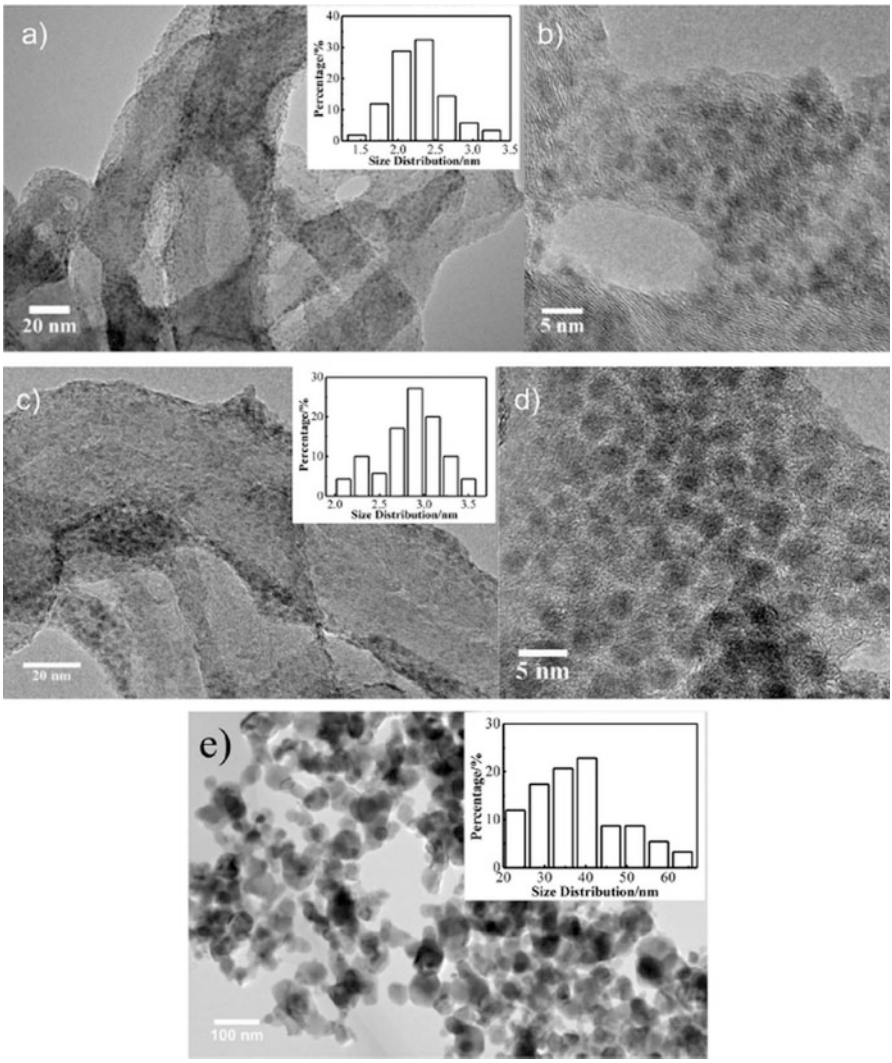

Fig. 2.9 TEM images and histograms of particle-size distribution of (**a**, **b**) 12.5% NiO_x/PEI-CNTs, (**c**, **d**) 25% NiO_x/PEI-CNTs, and (**e**) NiO. (Reproduced after modification from Cheng et al. 2014, with permission from Elsevier)

(Yun et al. 2014). Supercapacitors comprised of these modified CNTs exhibited a specific power of 1750 Wkg^{-1} and a high specific energy of 59 $Whkg^{-1}$ over the voltage range of 0–3.5 V. SWCNTs-coated mesoporous cellulose fibers prepared by "dip-absorption-polymerization" method followed by infiltration and in situ polymerization of aniline have been used as an electrode in supercapacitors (Ge et al. 2015). This flexible, foldable, and lightweight electrode composed of wrapped SWCNTs around interpenetrating cellulose fibers and PAni, formed through in

situ polymerization within SWCNTs network, showed excellent mechanical properties even after 1000 cycles of folding/unfolding with 35% capacitance retention. This hybrid material displayed good volumetric and areal capacitance of 40.5 Fcm^{-3} and 0.33 Fcm^{-2}, respectively. CNTs with high electrical conductivity and surface area were found to enhance the energy storage capacity of the electrode. Successful attempts have been made to develop a supercapacitor having volume power and energy densities in the order of 10 Wcm^{-3} and 10^{-3} $Whcm^{-3}$, respectively (Liu et al. 2015a). This device comprised of a conductive DWCNTs film as a current collector and a 1:1 mixture of graphene and MWCNTs films as an electrode. These two carbon films were coated on a PET paper, with a gelled electrolyte to bind them. Recently, thin freestanding CNT sheets obtained from thick CNT sheets fabricated by an inverse order process exhibited stable electrochemical and improved capacitance properties (Koo et al. 2015). It was further observed that the specific capacitance of the CNT sheets depends on the number of layers of the thin CNT sheets. The smaller the number of layers of CNT sheets, the larger is the specific capacitance of the electrode. Other nanocomposites that find application in supercapacitors are $Na_{0.35}MnO_2$/CNT (Zhang et al. 2014a), MnO_2/CNTs (Li et al. 2014a), $NiCo_2O_4$/CNTs CNFs (Iqbal et al. 2016), and CNTs/$NiCo_2S_4$ (Li et al. 2016a). Porous structure of CNTs aerogel increases the specific surface area of CNTs modified carbon from 123 to 629 m^2g^{-1} (Ciszewski et al. 2016). It was found to minimize the materials shrinkage and improve the specific capacity of the electrode as compared to carbon aerogel. Schopf and Es-Souni (2016) had studied the effect of porous-structured PVDF-MWCNT nanocomposite films on the specific capacitance of the electrode (increased of specific capacitance from 80 to 120 Fg^{-1}). Nanoclay-based polyindole/CNT composites synthesized via facile in situ and ex situ processes have been used as self-assembled ternary electrodes for a supercapacitor with enhanced electrochemical properties (Oraon et al. 2016). It has been reported that CuS/CNT preparation by a solvothermal process involves multi-directional growth of hexagonal covellite CuS over the CNTs surface. Polyimidazole/CuS/CNT composites have been used as electrodes with areal capacitance of 1.51 Fcm^{-2} at a current density of 5 $mAcm^{-2}$ (higher compared to CuS/CNT electrode) (Ravi et al. 2016).

Recently, it has been found that high contact resistance existing between CNT electrodes and their low reactivity toward electrolyte lead to some limitations in their application in the field of supercapacitors. Moreover, restrictions in scaling up of the production of CNTs limit this commercialization. Recent investigations revealed that exfoliated GO processed through solution and even edge-functionalized graphene hold potential in replacing CNTs as carbon-based electrodes in supercapacitors (Van Noorden 2011; Park and Ruoff 2009; Jeon et al. 2012, 2013; Dai 2013; Liu et al. 2012a; Bag et al. 2016). A double-layer capacitor, composed of graphene electrode, has shown a higher specific capacitance of 550 Fg^{-1}, and in some case, it also has showed compared to that of the CNT electrodes (Xia et al. 2009; Liu et al. 2010). Although graphene sheets have higher specific surface area, the presence of π-π forces often leads to restacking of the graphene sheets. The graphene electrode has showed good cyclic stability (97% of capacitance) even after 5000 cycles (Bag et al. 2016).

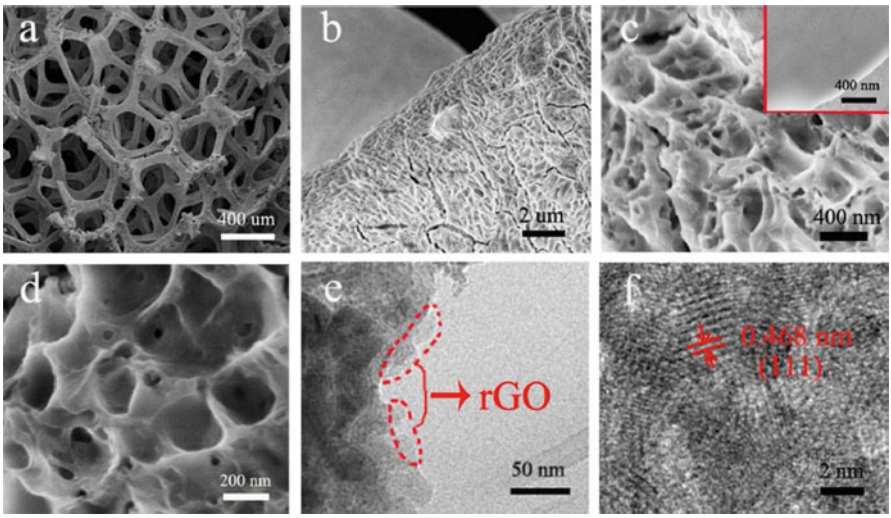

Fig. 2.10 Characterization of $NiCo_2O_4$-rGO composite: (**a**–**d**) SEM images (the inset of c shows the SEM image of pure $NiCo_2O_4$), (**e**) TEM images, and (**f**) high-resolution TEM images. (Reproduced after modification from Luo et al. 2014, with permission from Elsevier)

It has been reported that holey graphene nanosheets (GNS), prepared by ultrarapid heat treatment during thermal reduction/exfoliation of graphene oxide (GO), have shown 49% higher specific capacitance (i.e., 211 Fg^{-1} at 0.5 Ag^{-1}) than non-holey GNS (Peng et al. 2015). A composite of GO/PPy/MWCNTs has been reported by Wang et al. (2015). It was found that the incorporation of GO and MWCNTs formed 3D networks within the composites, while the PPy formed a bridge between GO and MWCNTs particles, resulting in improved conductivity of the composites. The capacitance retention of the composites remained at 92% even after 1000 cycles. Independently, PAni/reduced GO composites, prepared by in situ polymerization, exhibited high specific capacitance values (Wang et al. 2010; Yuan et al. 2011). Porous-structured nanocomposites comprised of $NiCo_2O_4$ and reduced graphene oxide (rGO), supported on nickel foam, have been employed as binder-free electrodes for supercapacitors (Luo et al. 2014). These composites retained about 87.6% of their capacitance upon increasing the current density from 1 to 20 Ag^{-1}. Figure 2.10 presents the scanning electron microscopy (SEM) and the transmission electron microscopy (TEM) images of $NiCo_2O_4$-rGO composite. An irregular porous network structure can be clearly observed from the Fig. 2.10a–d. The inset of Fig. 2.10c displays the SEM images for pure $NiCo_2O_4$ nanoparticles. TEM micrograph in Fig. 2.10e revealed uniform dispersion of $NiCo_2O_4$ nanoparticles on the surface of rGO. The high-resolution TEM micrograph in Fig. 2.10f showed that the interspace between adjacent stacks was 0.468 nm, which is close to the interspace present in pure $NiCo_2O_4$.

Highly uniform thick rGO synthesized by reducing GO by metallic copper at ambient temperature has shown excellent electrochemical properties in a neutral

Li_2SO_4 aqueous solution along with improved conductivity (Li and Yang 2014). Graphene-based electrodes synthesized by laser reduction of graphene oxide have shown specific capacitance 81 Fg^{-1} at 1000 mVs^{-1} and 130 Fg^{-1} at 5 mVs^{-1} (Yang and Bock 2017). It was observed that the value of specific capacitance of the electrode depends on irradiation time and laser energy. It was found that the growth of PAni on graphene depends on its functionality and the most negatively charged graphene is able to produce neat and vertical growth of PAni. The performance of the graphene-based supercapacitor depends on the size of graphene. It has been observed that reducing the graphene size from a micrometer to hundreds of nanometers leads to increase in energy density and power storage (Lu et al. 2016). However, further decrease in size of graphene into tens of nanometers minimizes both the energy density and power storage. It is postulated that the high resistance of defective edge regions and the increase in frequency of charge transfer lead to this effect. CNTs grown on copper substrate, using an alumina buffer layer between the components, have been reported to show excellent performance as electrodes in supercapacitors. CNTs have been grown on radio frequency (RF)-plasma treated copper substrate followed by hydrogen treatment on the copper substrate to restrict the copper oxide formation. $LiClO_4$was used as an electrolyte. Al_2O_3 not only acted as a diffusive layer for the reactant gas to react with the catalyst but also inhibited catalyst agglomeration. $Ni(OH)_2$-graphene sheet-CNTs composites, prepared by solvothermal procedure, have also been used as an effective electrode for supercapacitors. It was reported that the specific surface area of the graphene sheet increased due to the addition of CNTs, which inhibited the restacking of the graphene sheets (Liu et al. 2015c).

Nitrogen doping has been found to enhance the performance of the graphene-based electrodes for supercapacitors. It has been reported that the doping of nitrogen in graphene helps in enhancement of the electron transfer and, thus, helps in improving the performance of the graphene-based electrodes (Wei and Kivioja 2013; Sun et al. 2011b, 2012; Chen et al. 2012a; Wen et al. 2012). However, the unspecified distribution of nitrogen and agglomeration of N-doped graphene limit its application. Different materials used for fabricating supercapacitor electrodes and their associated properties have been presented in Table 2.1.

2.3.2 Fuel Cells

Researchers have studied the role of carbon nanomaterials, like CNTs and graphene, in enhancing the performance of fuel cells (Gharibi et al. 2013; Wu and Shaw 2005; Huang et al. 2012; Liu et al. 2014). Microbial fuel cells (MFCs), i.e., electrochemical devices that convert energy stored within organic wastes into useful electrical energy, composed of an anode and a cathode separated by a cation-specific membrane (Nandy et al. 2015). At the anode, the microbes oxidize the organic fuel to generate protons which transfer to the cathode through a membrane, and the electrons passes through the anode to an external circuit to produce current (Das

Table 2.1 Different materials used for fabricating supercapacitor electrodes and their associated properties

Materials used for electrode	Properties reported	References
H_2SO_4 treated MWCNTs	Specific capacitance = 102 Fg^{-1}	Niu et al. (1997)
Random SWCNTs in the presence of KOH electrolyte	Specific capacitance = 180 Fg^{-1}	Chen and Dai (2013)
CNT-implanted mesoporous carbon spheres with aqueous electrolyte	Maximum specific capacitance of 189 Fg^{-1} with a measured power density of 8.7 $kWkg^{-1}$ at energy density of 6.6 $Whkg^{-1}$	Yi et al. (2011)
PAni/UCNTs composites	Specific capacitance = 762 Fg^{-1}	Fathi et al. (2014)
GO/PPy/MWCNTs	High capacitance of 406.7 Fg^{-1} at current density of 0.5 Ag^{-1}	Wang et al. (2015)
$NiCo_2O_4$/rGO nanocomposite	Specific capacitance = 777.1 Fg^{-1} at 5 Ag^{-1}	Luo et al. (2014)
$MnFe_2O_4$/graphene/PAni nanocomposites	Maximum specific capacitance = 48.5 Fg^{-1}	Sankar and Selvan (2015)
PPy/CNTs composite	Specific capacitance = 152.78 Fg^{-1} at 1 g^{-1}	Lee et al. (2011a)
Graphene nanowalls	Specific capacitance = 991.6 Fg^{-1}	Yen et al. (2015)
$Ni(OH)_2$-graphene sheet-CNT composite	Specific capacitance = 1170.38 Fg^{-1} at 0.2 Ag^{-1}	Liu et al. (2015c)
$Na_{0.35}MnO_2$/CNT	Specific capacitance = 135 Fg^{-1} at 1 Ag^{-1}	Zhang et al. (2014a)
MnO_2/CNT	Specific capacitance = 201 Fg^{-1} at 1 Ag^{-1}	Li et al. (2014a)
$NiCo_2O_4$/CNTs CNFs	Specific capacitance = 220 Fg^{-1} at 1 Ag^{-1}	Iqbal et al. (2016)
CNTs/$NiCo_2S_4$	Specific capacitance = 1537 Fg^{-1} at 1 Ag^{-1}	Gong et al. (2009)
3D graphene/graphite paper	Specific capacitance = 260 Fg^{-1} at 1 Ag^{-1}	Ramadoss et al. (2017)
PAni/GS	Specific capacitance = 49.03 Fg^{-1}	Liu et al. (2015b)
MoS_2/RGO/MoS_2 (MRMS) nanostructured composite	Specific capacitance = 455.3 Fg^{-1} at 20 $mAcm^{-2}$	Zhang et al. (2016)
CeO_2/CNTs	Specific capacitance = 260 Fg^{-1} at 1 Ag^{-1}	Luo et al. (2017)
CNT/GNF/Fe_2O_3 ternary composites	Specific capacitance = 307 Fg^{-1} at 10 mVs^{-1}	Ramli et al. (2018)
PEDOT/CNTs sponge	Specific capacitance = 147 Fg^{-1} at 0.5 Ag^{-1}	He et al. (2018)
MnO_2/CNT films	Specific capacitance = 1980 Fm^{-2} at 10 Ag^{-1}	Qi et al. (2017)
CNTs/C/$NiMoO_4$	Specific capacitance = 1037 Fg^{-1} at 1 Ag^{-1}	Xuan et al. (2018)

et al. 2018a; Dutta and Kundu 2018). These MFCs are used for wastewater treatment, desalination, hydrogen production, and generation of electricity (Kundu and Dutta 2018; Liu et al. 2004; Cao et al. 2009). It has been reported that macroporous structure is formed in sponge/CNTs composites produced by coating sponge with CNTs. This sponge/CNTs composite electrode has low internal resistance and high chemical stability. A maximum volumetric power density value of 182 Wm^{-3} and a maximum areal power density value of 1.24 Wm^{-2} were obtained by using this electrode (Xie et al. 2012). A significant improvement in the performance of MFC has also been observed where CNTs-doped PAni has been used as the anode (Qiao et al. 2007), as compared to the MFC based on neat PAni. It has also been reported that an MFC has shown an improved power density as compared to graphite, using nanofluids and a CNT-based electrode (Sharma et al. 2008). The nanofluid was composed of dispersed nanocrystalline Pt anchored with CNTs in water.

Direct methanol fuel cells (DMFCs) are studied for their various applications in automobile industries and do not even require a separate hydrogen generation system. A DMFC is an electrochemical device that converts energy stored within the chemical bonds of the fuel (methanol) into useful electrical energy. The wide availability, low cost, and easy processability of methanol (which is used as a fuel) make DMFC an attractive fuel cell system (Liu et al. 2006; Lim et al. 2008). In general, Pt has been used as an electrode for methanol oxidation. However, the formation of the intermediate CO species leads to poisoning of the Pt catalyst (Kumar et al. 2014c). Therefore, binary, ternary, and quaternary catalyst systems have been developed to overcome this serious issue (Das et al. 2018b; EPRI-DOE 2003; Yazami and Reynier 2002). Another approach to minimize this poisoning effect is to select an appropriate catalyst-supporting material. The primary goals for a catalyst support are to (a) stabilize the catalyst particles, (b) assist in exposing a high active surface area of the deposited catalyst, (c) take part in the electrode reactions, (d) mitigate the catalyst surface from poisoning, and (e) improve the mass transfer. In this context, conductive polymers have found potential applications as catalyst-supporting matrices (Kundu and Dutta 2016; Dutta and Kundu 2014; Wang et al. 2010, 2015; Kristian et al. 2009; Ishikawa et al. 2000). Studies have revealed that the employment of conducting polymers as host matrices for metal nanoparticles for the uniform distribution of nanoparticles is one of the foremost criteria for the better performance of fuel cells. This assists in electrooxidation of small organic molecules, like formic acid, methanol, and hydrogen, in the presence of metal nanoparticle catalysts (Qu et al. 2010; Chen et al. 2006; Huang et al. 2011). Prasad et al. (2012) have demonstrated that the electrolytic activity of the Pt-MWCNTs/PAni catalyst system is higher than the individual Pt-MWCNTs and Pt catalyst systems. Besides, PAni- and PPy-modified CNTs have also been the focus of research as catalyst supports for fuel cells (Selvaraj and Alagar 2007). Zhao et al. (2009) have studied the effect of co-deposited PtCo bimetallic nanoparticles on PPy-MWCNTs composites. This anode support was found to display stable methanol electrooxidation and improved catalytic activity. It was further revealed that over-oxidation leads to alteration of the structure and arrangement of the PPy matrix, which helps in the exposure of more PtCo nanoparticles on the catalyst surface. This,

in turn, increases the utilization of Pt. Studies revealed that Pt-CeO_2/CNTs composites improved the catalytic activity of the Pt catalyst and also helped in the stripping of CO at lower potentials (Wang et al. 2007).

Nitrogen-containing CNTs, synthesized by reacting toluene with acrylonitrile produced by the CVD process on silicon wafer followed by impregnation with iron-tetramethoxyphenylporphyrin chloride (including a heat treatment step), led to a new cathode for the oxygen reduction reaction (ORR) in PEM fuel cells (PEMFCs) (Prehn et al. 2009). It has been reported that the fabrication of sulfonated poly(ether ether ketone) with modified cast-drop technique and the addition of iron-tetramethoxyphenylporphyrin chloride led to an improvement in the electroactivity of the catalyst and enhanced utilization in fuel cells. Chen et al. (2013) have observed an improvement in absorption kinetics of Mg along with faster hydriding kinetics up to 6.6 wt% only in 1 min at 150 °C in the presence of ball-milled CNTs. Graphite/polypropylene composite bipolar plates have been prepared using 304 stainless steel as a support and CNTs as a conducting interlayer by Lee et al. (2011c). The addition of CNTs to the composite has not only enhanced its efficiency up to 91% compared to the graphite bipolar plate but also has improved the mechanical and the electrical properties of the composites. CNTs produced by a facile method, using Fe-containing hexagonal mesoporous silica as catalyst templates, have been used for the fabrication of Pt/CNT anodic electrocatalysts for DMFC applications and methanol oxidation reaction (Lo et al. 2011). It has been realized that the diameter of CNTs plays a significant role in dispersing Pt nanoparticles and even on the performance of the electrocatalyst. For example, Pt/MWCNTs electrocatalyst, with CNTs having a diameter greater than 8 nm, exhibited better electrocatalytic performance than that of the conventional Pt/Vulcan XC-72 carbon and Pt/SWCNT catalysts. Catalysts PtRu/CNTs and PtRuMo/CNTs, synthesized by microwave-assisted technique and used as anode for DMFC, have been studied by Chen et al. (2010b). The authors inferred that the incorporation of Mo helped in decreasing the energy of each of the Pt sites. The performance of DMFC was found to improve with increasing temperature. This observation was attributed to a corresponding increase in the ion conductivity within the membrane electrode assembly (MEA), leading to an enhancement of the catalyst efficiency. PtCo/PPy-MWCNTs cathode catalysts, synthesized by the one-pot synthetic route with two active sites Pt and CoN_x, have been used for ORR in fuel cells (Zhao et al. 2012). The second transition metal helped in improving the performance of the catalyst through synergistic effect.

Pt/CNTs catalysts for PEMFCs, with stable electrochemical properties, have been the center of research for the last decade (Shao et al. 2006; Wang et al. 2006; Li et al. 2003; Wu et al. 2005). Due to the highly inert nature of CNTs, it is difficult to deposit Pt on them, resulting in separation during ultrasonication. Therefore, He et al. (2011) have used PAni as a bridge between Pt and CNTs, which resulted in improved interfacial interaction between Pt and CNTs. It was observed that PAni forms a wrapping layer on CNTs through π-π interaction. In addition, the electron pair present on nitrogen atoms in PAni forms a coordination complex with the space orbital of Pt. PAni also helps in transferring electrons from Pt to CNTs, thus

Fig. 2.11 A schematic diagram illustrating the preparation of PtRu/PAni/MWCNT catalysts. (Reproduced after modification from Lee et al. 2011b, with permission from the American Chemical Society)

inhibiting the agglomeration of Pt nanoparticles. This results in improving the stability and the performance of Pt in acidic conditions, which is considered to be the most effective condition for PEMFC operations.

Pt is the most commonly used electrocatalyst, especially at low-temperature PEMFC operations, both for the anodic oxidation and the cathodic reduction reactions (Steele and Heinzel 2001; Aricò et al. 2001). PtRu/PAni/MWCNT catalysts, prepared by chemical reduction of H_2PtCl_6 and $RuCl_3$ by $NaBH_4$, possessing a particle size range of 2–4 nm, have shown an improved activity, enhanced Pt utilization, higher specific surface area, and lower methanol oxidation potential as compared to the catalyst based on bare MWCNTs (Lee et al. 2011b).

Figure 2.11 presents a schematic diagram describing the preparation of the PtRu/PAni/MWCNT catalyst. Microscopic studies have revealed that the bimetallic particles of PtRu form homogeneous dispersion on PAni/MWCNTs composite with a "fiber in a jacket" nanostructure. It has been observed that the addition of PAni was responsible for generating the hydrophilicity of the CNTs surface and, thus, facilitated the homogeneous dispersion of PtRu particles. Indium tin oxide (ITO) and CNTs hybrid catalysts have been used as a support for Pd catalyst deposition, using microwave-assisted polyol method with different concentrations of ITO (Qu et al. 2014). It has been found that the addition of ITO has improved the activity and the stability of formic acid oxidation on this supported catalyst due to the interaction between Pd and ITO (substantiated by XPS analysis). Experimental results have revealed that the peak current density obtained for the electrooxidation of formic acid on the ITO/Pd-CNTs catalyst system was 1.5 times and 2 times higher than Pd/CNTs and Pd/ITO catalyst systems, respectively. Liu et al. (2007) studied the mechanical and performance improvement of Pt/CNTs by introducing a novel sandwich structure comprising a Pt/CNTs layer sandwiched between two Nafion layers. This Pt/CNTs layer between two Nafion layers helped in catalytic recombination of gaseous hydrogen and oxygen permeating through the PEM from the

anode to the cathode sides. Joo et al. (2008) observed that functionalization of CNTs by poly(arylenesulfone) (PAS) enhanced the performance of DMFCs. PtRu/CNT-sulfonated PAS (sPAS) composite has low-ohmic resistance, high mechanical strength, high power densities, and high durability as compared to pristine sPAS membrane.

It has also been reported that CNTs are applicable even as a bioanode for a glucose/O_2 biofuel cell (BFC). This novel anode consisted of CNTs-immobilized mediator and silk film (SF)-immobilized glucose oxidase (GOD) (Liu et al. 2012b). The resulting bioanode showed an excellent stability and improved catalytic activity, producing a current density of 0.51 $mAcm^{-2}$ for 0.07 M glucose at 0.01 Vs^{-1}. Successful attempts have been performed by Jin et al. (2014) to generate a metal-free cathode catalyst by using nitrogen-doped CNTs obtained by CVD process. This cathode catalyst exhibited improved catalytic activity with no cyclophosphamide (CYC) toxicity toward SPCA-1 cells. Different materials used for fabricating fuel cell electrodes and their observed characteristics are presented in Table 2.2.

2.3.3 Solar Cells

In this modern era, DSSC and QDSC are the most promising technologies in the field of solar cells due to their flexibility, ease of fabrication, and effectiveness in absorbing diffused sunlight. CNTs have been used in photoanodes of DSSC and QDSC due to their high specific surface area and enhanced charge transport (Chan et al. 2013; Sun et al. 2011a; Dembele et al. 2013; Chen et al. 2010a; Lee et al. 2008; Dang et al. 2011). MWCNTS/Si heterojunctions exhibited linear characteristics for a light-doped p-Si and a rectifying I–V behavior for high-doped p-Si (Hu et al. 1999; Kawano et al. 2006). Other such examples are SWCNTs which form Schottky contact on Si (Behnam et al. 2008), DWCNT/Si (Wei et al. 2007; Jia et al. 2008), and vertically aligned CNTs/Si, which exhibits rectifying characteristics (Tzolov et al. 2004a, b). N-GaAs also forms heterojunction with CNTs (Liang and Roth 2008). Researchers have investigated the role of carbon nanomaterials, like CNTs and graphene, in enhancing the performance of solar cells (Fan et al. 2008; Hong et al. 2008; Li and Mitra 2007; Somani et al. 2008; Xiao et al. 2013; Wang et al. 2008a; Li et al. 2015b).

TiO_2 is the most well-known photoanode used in DSSC, owing to its high specific surface area. However, the grain boundaries present in the porous structure of TiO_2 impart entrapment of electrons, limiting the performance of TiO_2 as a photoanode (Law et al. 2005; Joshi et al. 2010; Grätzel 2001). There are other drawbacks as well regarding the usage of TiO_2 as a photocatalyst, such as (a) the slow rate of electron-hole recombination and the photoscattering of the material itself which limits its photoefficiency and (b) the very high bandgap for electron transition of the material which requires UV light. These drawbacks have necessitated exploitation of other materials which can be used either individually or in combination with TiO_2. Recently, it has been demonstrated that coupling of CNTs

Table 2.2 Different materials used for fabricating fuel cell electrodes and their observed characteristics

Electrodes used	Characteristics observed	References
CNTs sponge	It was observed that the areal power densities for this electrode is more in HMFCs than in PEMFCs for glucose and wastewater	Xie et al. (2012)
Pt_{disk}/Pt-MWCNT	This electrode at the catalyst loading of 0.02 mg had shown a charge exchange of 1.45 mC during electro-adsorption of hydrogen with real surface area of 34.52 m^2g^{-1} obtained electrochemically	Prasad et al. (2012)
Pt_{disk}/PAni/Pt-MWCNT	This electrode at the catalyst loading of 0.02 mg had shown a charge exchange of 2.17 mC during electro-adsorption of hydrogen with real surface area of 58.88 m^2g^{-1} obtained electrochemically	
CNT-based electrode for MFC	CNTs nanofluid-based electrodes had shown sixfold higher power density as compared to graphite electrodes (386 mWm^{-2})	Sharma et al. (2008)
Pt supported on MWCNTs with doped nitrogen	Used as cathode for DFMCs showed higher power density of 0.78 $mWcm^{-2}$ as compared to Pt supported MWCNTs electrode	Kanninen et al. (2014)
Nitrogen-doped graphene nanoplatelets	Used as an electrode for PEM with higher power density (4400 Wcm^{-2}) as compared to electrode composed of graphene nanoplatelets	Jafri et al. (2010)
Vertically aligned nitrogen-doped CNTs	Observed to catalyze a four-electron ORR with much higher performance, catalytic activity, lower overpotential, and longtime operation stability as compared to other conventional fillers	Gong et al. (2009)
Pd_3Co/MWCNT	Possess higher catalytic activity of 2.53 $mWcm^{-2}$ as compared to Pd/MWCNTs catalyst	Gharibi et al. (2013)
PET/PVdF/CNTs	Used as bipolar plates for PEM with excellent strength and conductivity along with triple continuous structure	Wu and Shaw (2005)
PtPb/MnOx-CNTs	It displayed three times higher specific activity of 140.9 $mAcm^{-2}$ and lower onset potential as compared to Pt/CNTs catalysts for methanol electrooxidation	Huang et al. (2012)
Phosphorus-doped CNTs supported low Pt-containing catalyst	It exhibited good electrocatalytic activity toward the ORR and weak methanol oxidation activity in acidic medium	Liu et al. (2014)
3D $PAni_{1600}$@CNTs	The Nafion/Lac/PAni1600@CNTs/GCE electrode exhibited efficient catalytic reduction of O_2 in the presence of ABTS. A glucose/O_2 EBFC consisting of the fabricated bioanode and biocathode outputted a maximum power density of 1.12 $mWcm^{-2}$ at 0.45 V	Kang et al. (2018)

(continued)

Table 2.2 (continued)

Electrodes used	Characteristics observed	References
PtCoN nanoparticles supported on TiN-carbon nanotubes (CNTs)	The ORR onset potential of $Pt_{0.3}CoN$/TiN-CNT (0.812 V vs. RHE) is higher than that of 40 wt% commercial Pt/C (0.789 V vs. RHE) due to the synergistic effect between nano-platinum particles and metal nitrides. The TiN-coated CNT support provided high electron transfer rate and catalytic tolerance in methanol solution	Chen et al. (2018)
Sulfonated poly(ether ether ketone) grafted on graphene oxide	Highly sulfonated poly(ether ether ketone) (PEEK) polymer is hydrogenated and then readily grafted on GO to provide nanohybrid material GO-g-SPEEK. Has much more water uptake but less water swelling compared with Nafion® and an excellent proton conductivity of 0.219 Scm^{-1} at 90 °C. Then, it demonstrates a peak power density of 112 $mWcm^{-2}$ when utilized in a H_2/air fuel cell at circumstance temperature	Gao et al. (2018)

with semiconductors leads to an improvement in the efficiency of the photoanodes due to synergistic effect. Zhang et al. (2013) have reported that the conversion efficiency of a photoanode composite, composed of CNTs and porous TiO_2 prepared by gel chapping method, is 2.6 times higher than TiO_2 nanocrystalline films.

The liquid electrolyte used in DSSC suffers from evaporation and leaking. Hence, in order to overcome this challenge, solid and quasi-solid electrolytes are being used. These types of electrolytes involve polymers, gel electrolytes, ionic liquids, and conductors (Kumara et al. 2002; Papageorgiou et al. 1996; Wang et al. 2003; Longo et al. 2003; Kim et al. 2004; Murai et al. 2002). Introduction of CNTs in poly (ethylene oxide) (PEO) matrix, in the case of PEO/CNTs composite electrolyte, resulted in improving the performance of a solid-state DSSC in terms of conductivity and various other aspects (Akhtar et al. 2010). Ionic liquid-based polymer electrolyte, composed of PEO and 1-methyl-3-propyl imidazolium iodide (prepared by casting technique), used in DSSC has shown an energy conversion efficiency of 0.81% at 100 $mWcm^{-2}$ (Singh et al. 2009). The short-circuit current density (J_{SC}) for both the DSSC and the QDSC increased with the increasing concentration of CNTs, and the improvement was found to be more prominent for the QDSC (Golobostanfard and Abdizadeh 2015). Composites of molybdenum disulfide/CNTs (MoS_2/CNTs), prepared by glucose aided in situ hydrothermal route, have also been used as a catalyst for solar cells (Yue et al. 2013). It has been reported that the electrocatalytic behavior of the catalyst was improved in the presence of CNTs. The DSSC assembled with this novel electrode exhibited a high power conversion efficiency of 7.92% under an illumination of 100 $mWcm^{-2}$. This result was comparable to that obtained for the DSSC fabricated with a Pt electrode (i.e., a conversion efficiency of 7.11%). A novel photoanode was prepared by depositing a layer of TiO_2-MWCNT nanocomposite on a mesoporous P25-TiO_2 film, using layer-by-

layer deposition by spin coating with a compact sol-gel deposited TiO_2 layer underneath. This novel photoanode produced a solar energy conversion of $7.0 \pm 0.3\%$, i.e., a 27% increase was obtained upon the addition of MWCNTs (Yao and Hang 2014). This improvement in the efficiency of the solar cell was attributed to the presence of MWCNTs, which was supported by electrochemical impedance spectroscopy (EIS). It was observed that CNTs exhibit p-type FET characteristic due to the adsorption of O_2 layer which was facilitated by the transference of electron from oxygen to CNTs. However, spin coating a layer of amine-based polymer, like PEI, on the SWCNTs led to the formation of n-type SWCNTs (Yao and Hang 2014; Shim et al. 2001). Other heterojunctions based on CNTs include SWCNTs/SiC, CNF/SiC, single C/CN_x-MWCNT, and BCN/C nanotube (Hu et al. 2004; Yang et al. 2003; Zhang et al. 1999; Kang et al. 2007).

Organic solar cells, consisting of polymers, possess flexibility, low cost, and ease of fabrication and are disposable. Polymers, like poly(3-octylthiophene) (P3OT) and poly(3-hexylthiophene) (P3HT), are the most investigated materials in solar cells. Moreover, the work function (φ) of CNTs (i.e., 4.5–5.1 eV) is close to the valence band of P3OT/P3HT. CNTs help in providing transportation of holes and electrons by improving exciton dissociation (Kanai and Grossman 2008). Polyvinyl alcohol (PVA)/CNTs composites have been utilized by Jia et al. as a substrate to deposit ZnSe thin film by using electrochemical atomic deposition (EC-ALD) (Jia et al. 2013) along with varying the proportion of Zn and Se ($x = 0.33$, 0.5, and 0.67). ZnSe was considered as a p-type semiconductor which possessed good solar energy absorption properties. PVA/MWCNT/PAni hydrogel has been recently investigated as an efficient material in DSSCs. This hydrogel was prepared by sandwiching gel electrolyte I^-/I_3^- between FTO glass and Pt electrodes (Nath et al. 2014). This fabrication includes the in situ polymerization of PAni on the surface of PVA/MWCNTs composites, leading to the formation of a gel electrolyte. It was found that the electrical conductivity and the thermal stability of the gel electrolyte increased with increasing MWCNTs content. The diffusion impedance value decreased in PVA/MWCNTs owing to the restriction imposed on the ion migration in the electrolyte and the electrode. However, optimized addition of MWCNTs was found to help in increasing the surface area, which consequently improved the migration of ions (I^-/I_3^-) in the electrolyte and the charge-transfer processes at the TiO_2 and the Pt counter electrodes. At a high concentration of CNTs (1 wt%), the formation of a solid network of CNTs with counter electrode decreased the surface area available, thus restricting the charge transfer. It was further suggested from CV results (Fig. 2.12) that the peak current increased with increase in CNTs content, which eventually suggested that the catalytic activity of the electrode had increased.

Figure 2.13 shows the working principle of CNT-based solar cells. It involves the use of CNTs as p-type semiconductor and silicon as n-type semiconductor, such that electron and hole transition can occur due to the establishment of a bandgap (Kumar et al. 2016). The emergence of solar energy leads to excite the holes in silicon, and electron transfer takes place from silicon to CNTs, and the photoenergy is stored in the batteries. Bai et al. have reported that "web-cob"-structured CNT/ZnO/TiO_2 nanocomposite, prepared by hydrothermal process followed by acid treatment and

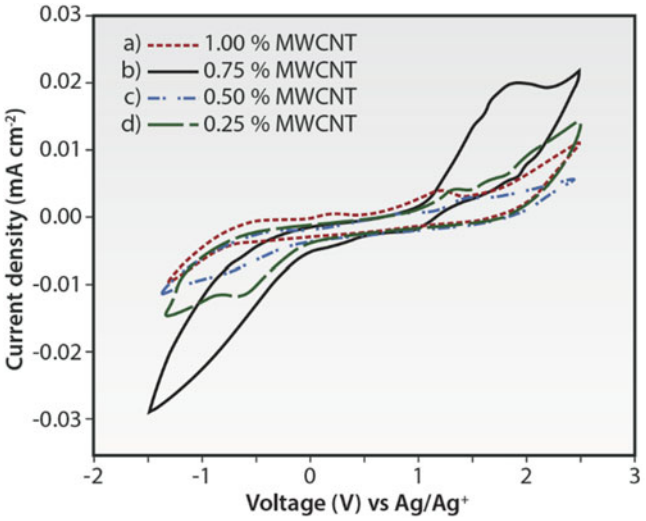

Fig. 2.12 Cyclic voltammograms of (**a**) PVA/(1%) MWCNT/PAni, (**b**) PVA/(0.75%) MWCNT/PAni, (**c**) PVA/(0.50%) MWCNT/PAni, and (**d**) PVA/(0.25%) MWCNT/PAni. (Reproduced after modification from Nath et al. 2014, with permission from Elsevier)

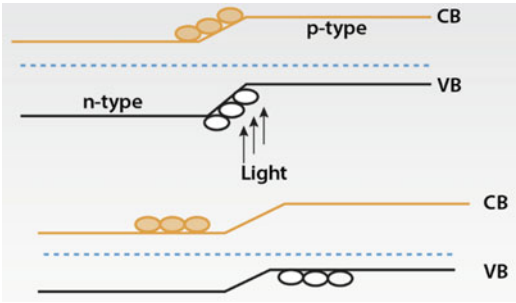

Fig. 2.13 Working principle of solar cells; CNTs was used as a p-type semiconductor, while silica was used as an n-type semiconductor to form the heterojunction. (Reproduced after modification from Kumar et al. 2016, with permission from Springer)

ultrasonication, exhibited high mechanical strength and improved photocatalytic efficiency to produce clean water with low-fouling properties (Bai et al. 2015).

It has been found that the type of CNT also influences the efficiency of solar cells, which can be evidenced from the difference from the efficiency values obtained (Abdullah et al. 2014). MWCNTs-ZnO-based DSSC possessed the highest longest electron lifetime and slowest electron diffusion as compared to ZnO and SWNTs-ZnO-based DSSC. Hollow $CoFe_2O_4$/CNTs composites prepared by hydrothermal process coupled with in situ CVD along with PPy showed good higher electrocatalytic performance than s-$CoFe_2O_4$, h-$CoFe_2O_4$, s-$CoFe_2O_4$/CNTs, and pure CNTs (Yuan et al. 2016a). Addition of PPy nanoparticles improved the conductivity of the h-$CoFe_2O_4$/CNTs/PPy-3 composites. CNT/TiO_2 nanocomposites produced by sol-gel method exhibited high solar energy conversion of 5.23% at 750 °C, and the value of photo-conversion efficiency was found to be

dependent on annealing temperature (Razali et al. 2015). From XRD and SEM analysis, it was evidenced that the film of CNT/TiO_2 nanocomposite was non-crackable, compact, and of high porosity. The annealing temperature of 750 °C produced composites with the highest solar energy conversion. A hybrid colloidal quantum dot was prepared under ambient temperature using layer-by-layer deposition method and involves insertion of graphene layers in between multilayer stacks of PbS (Kim et al. 2016). It was postulated that the introduction of a graphene layer leads to an increase in power conversion efficiency by 9.18% with enhancement of current efficiency from 19.58 ± 0.40 to 24.09 ± 0.46 $mAcm^{-2}$. Researchers have also used CNTs as a hole conductor in methyl ammonium lead bromide ($MAPbBr_3$) perovskite solar cells instead of expensive hole-transporting materials (Li et al. 2016b). The efficiency of this tandem solar cell is further improved by PMMA coating on CNTs to 5.28%.

Graphene possesses high specific surface area, strength, and inertness toward water vapor and oxygen and has thus found promising applications in solar cells (Wang et al. 2008b). A thin film of graphene was utilized as a window electrode for organic solar cells. This solar cell showed a J_{sc} value of 0.36 $mAcm^{-2}$, a V_{oc} value of 0.38, an FF value of 0.25, and a η value of 0.29, under the influence of solar energy. Graphene composites with P3OT and P3HT have also exhibited significant efficiency improvement in organic solar cells (Liu et al. 2008b). Functionalized graphene was successfully applied as a new acceptor for solar cells with a configuration of ITO/poly(3,4-ethylenedioxythiophene) poly(styrenesulfonate) (PEDOT:PSS)/P3HT/graphene/LiF/Al (Liu et al. 2008a). This cell produced a J_{sc} value of 4 $mAcm^{-2}$, a V_{oc} value of 0.72 V, and a Z value of 1.1% at AM1.5. Wu et al. (2008) have reported the fabrication, as well as the performance of a novel cell consisting of graphene/copper phthalocyanine (CuPc)/C_{60}/bathocuproine (BCP)/Ag layered structure. This cell exhibited lower FF and I_{sc} values than that of ITO. GO sheets with oxygen functionalities have shown good catalytic activity toward I^-/I_3^- but have low conductivity due to the presence of many lattice defects. GO sheets, when reduced by hydrazine, form rGO sheets. It has been postulated that rGO sheets showed a lower oxidation capability than GO at the same oxygen concentration (Mattevi et al. 2009; Roy-Mayhew et al. 2010). However, the intensive π-π interactions between graphene sheets lead to restacking (Yen et al. 2011). Researchers have reported that doping graphene with nitrogen influences the spatial electronic distribution of the attached carbon ("activation zone"), which affects the electrical conductivity and consequently helps in improving the electrocatalytic activity of the catalyst (Groves et al. 2009; Zhang and Xia 2011). It has been further found that N-doping of CNTs requires high temperatures, whereas N-doping of graphene sheets can be achieved at low temperatures (Ju et al. 2013; Xue et al. 2012). N-doped graphene/CNTs composite on fluorine-doped SnO_2 substrate, with a 3D "brick-like structure," has been used as a counter electrode in solar cells (Ma et al. 2015). This counter electrode has produced a high efficiency of 6.74% as compared to Pt electrode (i.e., 6.89%), as well as good catalytic activity. It was further found that an increase in the ratio of graphene to CNTs led to an increase in the particle size and a decrease in the electrical conductivity. Studies confirmed that spider web CNTs,

produced by CVD process and embodied with continuous graphene sheet, led to improvement of the electrical conductivity of graphene in the presence of CNTs (Shi et al. 2015). Apart from this, the coexistence of CNT-Si and graphene-Si junctions resulted in the improvement of power conversion efficiency by 15.2% as compared to that obtained by using only graphene. Kavan et al. (2016) have discovered the use of an FTO and Pt-free graphene cathode for co-mediated dye-sensitized solar cells, in the presence of an acetonitrile-free electrolyte solution. It has been found that the diffusion coefficient of $Co(bpy)_3^{3+}$ is smaller in propionitrile mixed with sulfolane or with EMI TCB ionic liquid than in acetonitrile. Agresti et al. (2016) had recently studied the effect of 2D nanomaterials like graphene on the performance of perovskite solar cells. By applying graphene-doped mesoporous TiO_2 as an electron transporting photoelectrode, a conversion efficiency of 18.2% was achieved. The photoanode used graphene oxide as the interlayer between perovskite and 2,2′,7,7-′-tetrakis-(N,N-di-4-methoxyphenylamino)-9,9′-spirobifluorene (spiro-OMeTAD) hole-transport layer (HTL). PEDOT:PSS nanocomposites with hybrid filler GO used for a perovskite solar cells produced higher photoenergy conversion than PEDOT:PSS nanocomposites. Moreover, UV-reduced PEDOT:PSS/GO nanocomposites showed higher efficiency than the PEDOT:PSS/GO nanocomposites. The presence of GO was inferred to improve the charge transport of the solar cells (Giuri et al. 2016). Graphene/Si solar cells prepared at room temperature led to an increase in photoenergy conversion from 5.95% to 13.02% by introducing a spiro-OMeTAD as an interlayer (p-type organic hole-transporting layer) for the solar cells (Xu et al. 2016).

Further studies revealed that incorporation of CNTs and graphene within conventional silicon wafers may lead to solar cells with improved power conversion efficiency, antireflection, and self-cleansing properties. The anti-reflectance property stems from the suppression of reflection of substrate due to suitable optical path difference (Li et al. 2010; Sun et al. 2005). On the other hand, the presence of a high fraction of entrapped air between arrays leads to self-cleansing properties of ARCs arrays. A photovoltaic cell, composed of silicon-PEDOT:PSS-CNT-poly(styrene), with a conversion efficiency of 8.7%, has been identified as an efficient ARC (Yu et al. 2015). Shi et al. (2012) have observed a 15% increase in the efficiency using TiO_2 antireflective coating and CNTs doped with chemical oxidant. Different materials used for fabricating solar cell electrodes, the obtained efficiency and their associated significance, have been presented in Table 2.3.

2.3.4 Lithium-Ion Batteries

The basic requirements for an electrode for advanced LiBs are (Yuan et al. 2016b) (a) high electrical conductivity (low electrical conductivity will diminish the operating voltage, power density, and energy density; moreover, incorporation of conductive additives leads to increase in weight of the electrodes. The full charge and discharge of Li-ion will be difficult owing to hindrance in transportation), (b) high

Table 2.3 Different materials used for fabricating solar cell electrodes, the obtained efficiency and their associated significance

Solar cells used	η (%)	Significance	References
MWCNTs/PEDOT-PSS (DSSC)	6.5	Used as photovoltaic cell	Fan et al. (2008)
SWCNTs/TiO_2	0.13	Efficiency is improved due to its nanostructure	
Graphene/PEDOT-PSS	4.5	Formed by deposition of composite on ITO and used as counter electrode for DSSC	Hong et al. (2008)
PAni/MWCNT	6.24	Polymer-based cells for photovoltaic cells	Xiao et al. (2013)
Transparent graphene thin films	1.53	Used as a window electrode in organic solar cells	
RGO platelets	0.26	TiO_2 photoanodes with a thickness of 2–3 μm	Wang et al. (2008a)
GNF	3.6	Used graphite film as counter electrode and I^-/I^{-3} as electrolyte for a DSSC	Li et al. (2015b)
GNS	2.99		
MWCNT-P3OT/n-Si	0.175	Used in silicon-based DSSC	Somani et al. (2008)
P3HT/C60-CNTs	0.75	Based on fullerene-CNTs complex used as photovoltaic cells	Li and Mitra (2007)
h-$CoFe_2O_4$/CNTs/PPy-3	6.55	Counter electrode for DSSC	Yuan et al. (2016a)
ZnO-SWCNTs/N719	0.65	Used as photoanodes	Abdullah et al. (2014)
$CuMnSnS_4$ microspheres/CNTs	8.97	Prepared by in situ solvothermal route and served as counter electrode (CE) for dye-sensitized solar cells (DSSCs)	Liu et al. (2017)
Graphene transparent conductive electrodes doped with graphene quantum dots (GQDs)-mixed silver nanowires (Ag NWs) on polyethylene terephthalate substrates	3.66	Graphene quantum dots-mixed silver nanowires acts as protecting layer for flexible organic solar cell, and it showed only loss of 14% of their initial PCEs after being kept at 25 °C and 40% humidity for 10 days	Shin et al. (2018)
CNTs	29.18	CNTs used as a semitransparent layer as charge collector with greater area of charge collection on the surface of solar cells and also helps in improving the conductivity	Singh et al. (2017)

(continued)

Table 2.3 (continued)

Solar cells used	η (%)	Significance	References
CNTS/ZnS/Zn (O, S)/FTO	17.06	The performance of CNTS-based solar cell is mainly dependent on absorber layer thickness and on absorber doping concentration. The optimal thickness that was for CNTS absorber layer is found to be 4 μm, and optimal doping concentration is 4×10^{18} cm^{-3}	Khattak et al. (2018)
A hybrid PEDOT:PSS-CNT/n-Si solar cells	10.2	Heterojunction formed between n-type monocrystalline silicon substrates coated with a thin p-type layer, such as CNTs, conductive polymer, or their composites	Fan et al. (2017)
CNTs/VS_2	7.72%	CNTs/VS_2 counter electrode shows more excellent conductivity, electrocatalytic ability, and charge-transfer resistance	Yue et al. (2017)

surface area (the availability of more surface area would lead to more active sites, enhancing the rate of surface reaction), and (c) microstructure of the electrode (the porous structure of the electrode also influences the performance and the efficiency of the electrode). A macroporous structure leads to efficient Li-ion diffusion and mass transfer, whereas a mesoporous structure shortens the distance for lithium transport. It has been suggested that in spite of providing high specific surface area, a significant section of it remains inaccessible to the electrolyte.

Researchers investigated the role of carbon nanomaterials, like CNTs and graphene, in enhancing the performance of Li-ion batteries (Tao et al. 2012; Kim et al. 2006; Bak et al. 2011; Cao and Wei 2013; Sivakumar and Kim 2007; Lian et al. 2010). It is well-established that CNTs may exist in three forms in the electrodes – discontinuous CNTs, CNT arrays, and binder-free CNT network. However, in most of the cases, the discontinuous CNTs are preferred for enhancing the performance of electrodes. Wu and coworkers have synthesized electrodes out of LFP/C/CNTs composites (Wu et al. 2013), such that the CNTs network can be efficiently used to decrease the internal resistance and thus enhancing the performance of the electrode. $ZnFe_2O_4$-C/LFP-CNT electrode had shown excellent performance even after 10,000 cycles (Varzi et al. 2014). Hou et al. (2013) have reported that Sn-filled CNTs electrode showed a capacity of 1000 $mAhg^{-1}$ at a current density of 100 mAg^{-1}. For example, Si/C/CNTs composites have been used as anode materials for Li-ion batteries. PEI has been used as a binder for Si/CNTs anode material. The electron donating group, i.e., imine, of PEI undergoes charge-transfer physisorption with the sidewalls of the CNTs (Bae et al. 2013). Additionally, incorporation of CNTs uniformly within the interspaces of graphite and silicon in Si/graphite/CNTs composites led to alleviation of the SEI formation (Li et al. 2015a). Addition of CNTs to lithium titanium oxide (LTO) resulted in an LTO/TiO_2/C/CNTs composite

with improved electrochemical performance within a voltage window of 1.0–2.5 V (Wang et al. 2014). Fe_3O_4/CNTs composites, prepared by in situ filling of MWCNTs with ultrafine Fe_3O_4 nanoparticles, have exhibited remarkable improvement in capacity, cyclic stability, and performance as compared to commercial Fe_3O_4 as anode materials in Li-ion batteries (Gao et al. 2015). $ZnSO_4$/CNTs composites have also been investigated as anode materials in which CNTs form a 3D electrically percolating network spanning within the $ZnSO_4$ matrix (Qin et al. 2016). Studies have also focused on the SnSb alloy-coated MWCNTs synthesized by reductive precipitation process as an anode material (Park et al. 2007).

Graphene finds application both as active material and as catalyst in metal-air batteries. As an active material, it may act as hosting ions or to store electrostatic charges for electrochemical double-layer capacitors. Reduced graphene oxide (RGO) is considered to be the most common material for Li-ion storage, and it exhibits high capacity values as compared to single-layer graphene (Vargas et al. 2012). However, this charge is not fully released during de-lithiation due to the irreversibility of the process. The efficiency of the RGO electrode also depends on the extent of defects in layers which are responsible for the low Coulombic efficiency in the first cycle. Holey graphene synthesized by ultrasonication and nitric acid etching of GO and followed by thermal exfoliation/reduction have been reported to increase the high rate performance of Li-ion batteries (Zhao et al. 2011). Solid hybrid polymer electrolytes, based on triethylsulfonium-bis (trifluorosulfonyl) imide (S_2TFSI), PEO, and lithium TFSI, have exhibited a reversible cathodic stability more than 4.5 V along with long-term cycle stability against metallic lithium for Li-ion batteries (Fisher et al. 2011). Nowadays, graphene-based materials find application in ultrathin flexible Li-ion batteries with high charge mobility and good mechanical properties (Pushparaj et al. 2007; Mao et al. 2015). Graphene papers have found application as a conducting agent and also as a current collector. Graphene composites with high specific surface area, high conductivity, and high mechanical properties, along with high lithium storage capacity (744 $mAhg^{-1}$), have also found application as anode materials (Rao et al. 2012). $LiFePO_4$/graphene nanocomposites prepared by sol-gel method (used as a cathode) have been observed to possess electrical conductivity six times higher than that of pure $LiFePO_4$, along with improved rate capability and cyclic stability (Dhindsa et al. 2013). SEM micrographs have revealed that each particle of $LiFePO_4$ is surrounded by graphene, forming a 3D network for efficient electrical conductivity. Graphene-coated SnO_2 has exhibited improved cycling stability owing to the addition of graphene (Zhu et al. 2014; Jiang et al. 2014). Zhang et al. (2014c) have also studied in situ Li^+ storage capacity enhancement of MnO nanowire/GNS composites, along with improved electrochemical performance. This self-enhancement has been attributed to the strong interphase interaction between MnO and graphene flakes. GNS acts as a buffering agent for the Sn-based electrode and helps in relieving the stress during the charge/discharge process. Moreover, the functionalities present on the surface of GNS act as a 2D substrate, assisting the anisotropic growth of Sn-based material. Sn/graphene nanocomposites, synthesized by a combination of a microwave hydrothermal and one-step hydrogen gas reduction

processes, have found application as anodes for Li-ion batteries (Chen et al. 2012b). Sn particles having a size range of 10–20 nm exhibited higher capacity and cycle stability as compared to an anode comprised of Sn particles having a size range of 60–120 nm. Recently, graphene-based magnesium-ion batteries have also been reported. Although the electrochemical properties of this battery were poor, still it is the first attempt to use graphene as cathode materials in magnesium-ion batteries (Wang et al. 2013b). Moreover, graphene also improved the efficiency of vanadium redox-flow batteries (VRFBs) (Weber et al. 2011). It has also been studied that the performance of rutile TiO_2 nanoneedle/graphene composites with a combination of 1D and 2D properties possessed a unique microstructure which is responsible for its outstanding electrochemical properties. The 1D structure of rutile TiO_2 shortens the Li-ion transportation pathway, improving the diffusion rate, while the 2D structure of graphene nanosheet imparts good electrical conductivity to the electrode (Gan et al. 2015). Different materials used for fabricating electrodes of Li-ion batteries and their performance details are presented in Table 2.4. Currently, scientists have focused on a new type of commercialized Na-S batteries, and with a mere change in their structural and mechanical design, low-cost devices for grid storage application and redox-flow batteries can be produced (Dunn et al. 2011). It is now recognized that this type of new battery technology is going to replace the existing Li-ion battery technology.

Renewable sources of energy will be able to replenish nonrenewable sources of energy to satisfy the various needs of society. However, there are barriers to the commercialization of renewable energy storage devices. In order to overcome the barriers to commercialization of projects related to nonrenewable energy, financial strategies require flexibility and innovation. The factors that affect the commercialization of renewable energy technologies are as follows: high capital for operation and maintenance costs, high project development to investment cost ratio, small total investment requirement, inaccurate perception of risk, difficulty guaranteeing project cash flow, weak basis for nonrecourse financing, and weak project developers. In the present scenario, 80% of the world's energy consumption is supplied by fossil fuels because of their low cost and high availability. However, in recent years, the cost advantage of renewable sources of energy is increasing over that of fossil fuels (Timmons et al. 2014). Moreover, it is expected that the prices of renewable sources are going to decrease with the passage of time, and hence, it can be inferred that financial strategies will lead to incline the research trends toward renewable energy sources. Researchers have studied the process-based cost model (PBCM) along with the design of experiments to analyze the economy of the batteries. It was revealed that the cost of MWCNTs and process yield have a profound effect on the unit cost for satellite batteries, whereas the unit cost of a computer depends on the process yield and cycle time (Hakimian et al. 2015). It was shown that the addition of CNTs increases the charge and discharge cycle for Li-ion batteries which essentially help decrease cycle time for CNT-based batteries. As the specific energy, battery life, and run-time increase, the overall cost of production also increases due to incorporation of MWCNTs in the batteries.

Table 2.4 Different materials used for fabricating electrodes of Li-ion batteries and their performance details

Materials used for electrode	Performance details	References
Mn_3O_4/graphene	Used as anode synthesized by hydrothermal process with spinel structure. It showed a capacity discharge of 900 $mAhg^{-1}$ and a capacity of 390 $mAhg^{-1}$ after 100 cycles	Tao et al. (2012)
$LiMn_2O_4$/graphene	Used as cathode showed reversible capacities of 117 $mAhg^{-1}$ and 101 $mAhg^{-1}$ at 50 °C and 100 °C	Bak et al. (2011)
PAN/CNTs	Showed a discharge capacity of 86 $mAhg^{-1}$ at the 80th cycle along with efficiency retention of 98%	Sivakkumar and Kim (2007)
$LiNi_{1/3}Mn_{1/3}Co_{1/3}O_2$/graphene	Used as a cathode prepared by mechanical mixing; it displayed a capacity of 115 $mAhg^{-1}$ at 6 °C	Jiang et al. (2012)
Nanocrytalline Si on CNTs	High reversible capacity of 2050 $mAhg^{-1}$ and capacity reduced about 20% after 20 cycles	Wang and Kumta (2010)
Co_3O_4/graphene	Used as anode prepared by solvent method; it exhibited a discharge capacity of 1826 $mAhg^{-1}$ after 40 cycles	Lian et al. (2010)
V_2O_5/SWNT	Used as cathode with high rate capacity of 548 $mAhg^{-1}$ at the discharge rate of 1 °C	Cao and Wei (2013)
FeF_3 functionalized CNTs	Exhibited a specific capacity of 210 $mAhg^{-1}$ at a current rate of 20 mAg^{-1}	Kim et al. (2010)
$ZnFe_2O_4$-C/LFP-CNT	Gravimetric energy of 202 $Whkg^{-1}$ and power density values of 3.72 Wkg^{-1}	Vazri et al. (2014)
Fe_3O_4/C-rGO	Specific discharge capacity of 952 $mAhg^{-1}$	Li et al. (2011)
N-doped C/graphene/$LiFePO_4$	Specific capacity of 171.9 $mAhg^{-1}$ at 0.1 °C	Zhang et al. (2015)
TiO_2-CNTs grown on titanium	Used as anode. The assembled coin cell increases its discharge capacity to 201 $mAhg^{-1}$ measured after the 20th cycle at a discharge rate of 0.2 °C, as opposed to the value of 69 $mAhg^{-1}$ when without the addition of CNTs	Lo et al. (2018)
$CuMn_2O_4$/graphene nanosheets	A high discharge specific capacity of 935 $mAhg^{-1}$ after 150 cycles at a current density of 50 mAg^{-1}	Li et al. (2018)
Si-CNT/PAni	Reversible capacity of 2430 $mAhg^{-1}$ with good capacity retention over 500 cycles	Xiao et al. (2017)
Polyanthraquinone/CNT	Specific capacity (233 $mAhg^{-1}$) within 100 cycles	Tang et al. (2018)
Nanocubic $CoFe_2O_4$/graphene	Specific capacity of 1109 $mAhg^{-1}$ after 100 cycles at 0.2 Ag^{-1} and 835 $mAhg^{-1}$ after 200 cycles at 1 Ag^{-1}	Yang et al. (2018)
Ultrathin MoS_2/graphene composite	Reversible capacity of 1229 $mAhg^{-1}$ in the initial cycle and restores 942.6 $mAhg^{-1}$ even after 50 cycles	Chen et al. (2016)
TiO_2/graphene composite	High reversible capacity retention after 300 cycles, i.e., 84% at 150 mAg^{-1}	Zhang et al. (2012)
Graphene/CoO/C composite	Cycling stability after 352 cycles of 690 $mAhg^{-1}$ at 500 mAg^{-1} and rate capability of 400 $mAhg^{-1}$ at 2 Ag^{-1}	Zhang et al. (2014b)

(continued)

Table 2.4 (continued)

Materials used for electrode	Performance details	References
Exfoliated GO/iron (II) oxide composite	Reversible capacity of 857 $mAhg^{-1}$ at a current density of 50 mAg^{-1}, along with excellent capacity retention even after 60 cycles	Petnikota et al. (2015)
Sn nanoparticle/GNS composite	Reversible capacity of 838.4 $mAhg^{-1}$ even after 100 cycles	Zhou et al. (2014)

2.4 Conclusions and Future Perspectives

The upsurge in the requirement for clean and renewable energy for the next generation of sustainable society led to the development of new advanced energy storage devices, like supercapacitors, fuel cells, solar cells, and Li-ion batteries. Carbon nanomaterials, like CNTs and graphene, and even conducting polymers have been able to secure a significant position in order to meet diverse applications in the field of energy storage devices. However, there exist a great deal of difficulties in scaling up and commercializing these energy production and storage devices with the inclusion of nanomaterials. Therefore, recent research has been focused to improve the efficiency and performance of these devices using CNTs and graphene. CNTs- and graphene-based conducting polymer composites are considered to be a potential candidate for future generation solar cells. These polymer composites are flexible and low cost and can be easily produced; however, the acceptor-donor problem in the case of conducting polymers is currently restricting their application in solar cells. The efficient photon-absorbing capacity, capability to generate photocarriers, good photovoltaic properties, and their ability to separate charge carriers to form heterojunctions with conducting polymers make CNTs and graphene ideal candidates for application in solar cells. Supercapacitors have high power densities; however, their energy densities are lower compared to conventional batteries. The capacitance of a supercapacitor has been found to not only depend on the specific surface area of CNTs but also on several other factors, such as synthesis of CNTs, pore size, pore size distribution, and posttreatment of CNTs. This chapter also described the use of carbon nanostructured materials as supporting matrices for catalysts or even as catalysts for several types of fuel cells. It has also been found that carbon nanomaterials play a significant role in producing electrodes for Li-ion batteries. High electron conductivity and high surface area of these nanomaterials lead to improved rate capability and charge storage. It can be assumed that owing to all the abovementioned outstanding properties of CNTs and graphene, they represent ideal candidates for fabricating such challenging devices. However, the high cost of these materials is still limiting their commercial application. Therefore, reduction in materials and production costs should be achieved in order to attain fruitful market penetration for these prospective energy storage devices.

Acknowledgments KD is thankful to the Science and Engineering Research Board (SERB) [Department of Science and Technology (DST), Govt. of India] and the Indo-US Science and Technology Forum (IUSSTF) for the Indo-US Postdoctoral Fellowship (Award No. 2017/8-Kingshuk Dutta).

References

Abdullah H, Omar A, Razali MZ, Yarmo MA (2014) Photovoltaic properties of ZnO photoanode incorporating with CNTs for dye-sensitized solar cell application. Ionics 20:1023–1030. https://doi.org/10.1007/s11581-013-1038-3

Agresti A, Pescetelli S, Taheri B, Del Rio Castillo AE, Cinà L, Bonaccorso F, Di Carlo A (2016) Graphene-perovskite solar cells exceed 18% efficiency: a stability study. ChemSusChem 9:2609–2619. https://doi.org/10.1002/cssc.201600942

Akhtar MS, Park J-G, Lee H-C, Lee S-K, Yang O-B (2010) Carbon nanotubes-polyethylene oxide composite electrolyte for solid-state dye-sensitized solar cells. Electrochim Acta 55:2418–2423. https://doi.org/10.1016/j.electacta.2009.11.062

An KH, Kim WS, Park YS, Moon JM (2001) Electrochemical properties of high-power supercapacitors using single-walled carbon nanotube electrodes. Adv Funct Mater 11:387–392. https://doi.org/10.1002/1616-3028(200110)11:5<387::AID-ADFM387>3.0.CO;2-G

Aricò AS, Srinivasan S, Antonucci V (2001) DMFCs: from fundamental aspects to technology development. Fuel Cells 1:133–161. https://doi.org/10.1002/1615-6854(200107)1:2<133::AID-FUCE133>3.0.CO;2-5

Aricò AS, Bruce P, Scrosati B, Tarascon J-M, van Schalkwijk W (2005) Nanostructured materials for advanced energy conversion and storage devices. Nat Mater 4:366–377. https://doi.org/10.1038/nmat1368

Armand M, Tarascon JM (2008) Building better batteries. Nature 451:652–657. https://doi.org/10.1038/451652a

Bae J, Cha S-H, Park J (2013) A new polymeric binder for silicon-carbon nanotube composites in lithium ion battery. Macromol Res 21:826–831. https://doi.org/10.1007/s13233-013-1089-3

Bag S, Samanta A, Bhunia P, Raj CR (2016) Rational functionalization of reduced graphene oxide with imidazolium-based ionic liquid for supercapacitor application. Int J Hydrog Energy 41:22134–22143. https://doi.org/10.1016/j.ijhydene.2016.08.041

Bai Y, Li J, Qiu X, Wu J, Wang J, Xi J, Zhu W, Chen L (2007) Mesocarbon microbeads supported PtSn catalysts for electrochemical oxidation of ethanol. J Mater Sci 42:4508–4512. https://doi.org/10.1007/s10853-006-0559-9

Bai H, Zan X, Zhang L, Sun DD (2015) Multi-functional CNT/ZnO/TiO_2 nanocomposite membrane for concurrent filtration and photocatalytic degradation. Sep Purif Technol 156:922–930. https://doi.org/10.1016/j.seppur.2015.10.016

Bak S-M, Nam K-W, Lee C-W, Kim K-H, Jung H-C, Yang X-Q, Kim K-B (2011) Spinel $LiMn_2O_4$/reduced graphene oxide hybrid for high rate lithium ion batteries. J Mater Chem 21:17309–17315. https://doi.org/10.1039/C1JM13741G

Banerjee J, Dutta K (2017) Materials for electrodes of Li-ion batteries: issues related to stress development. Crit Rev Solid State Mater Sci 42:218–238. https://doi.org/10.1080/10408436.2016.1173011

Banerjee J, Panwar AS, Mukhopadhyay K, Saxena AK, Bhattacharyya AR (2015) Deagglomeration of multi-walled carbon nanotubes via an organic modifier: structure and mechanism. Phys Chem Chem Phys 17:25365–25378. https://doi.org/10.1039/C5CP03736K

Baughman RH, Zakhidov AA, de Heer WA (2002) Carbon nanotubes – the route toward applications. Science 297:787–792. https://doi.org/10.1126/science.1060928

Behnam A, Johnson JL, Choi Y, Ertosun MG, Okyay AK, Kapur P, Saraswat KC, Ural A (2008) Experimental characterization of single-walled carbon nanotube film-Si Schottky contacts using metal-semiconductor-metal structures. Appl Phys Lett 92:243116 (1–3). https://doi.org/10.1063/1.2945644

Candelaria SL, Shao Y, Zhou W, Li X, Xiao J, Zhang J-G, Wang Y, Liu J, Li J, Cao G (2012) Nanostructured carbon for energy storage and conversion. Nano Energy 1:195–220. https://doi.org/10.1016/j.nanoen.2011.11.006

Cao Z, Wei B (2013) V_2O_5/single-walled carbon nanotube hybrid mesoporous films as cathodes with high-rate capacities for rechargeable lithium ion batteries. Nano Energy 2:481–490. https://doi.org/10.1016/j.nanoen.2012.11.013

Cao X, Huang X, Liang P, Xiao K, Zhou Y, Zhang X, Logan BE (2009) A new method for water desalination using microbial desalination cells. Environ Sci Technol 43:7148–7152. https://doi.org/10.1021/es901950j

Castellano R (2010) Solar panel processing. Old City Publishing, Philadelphia

Chai GS, Yoon SB, Yu J-S, Choi J-H, Sung Y-E (2004) Ordered porous carbons with tunable pore sizes as catalyst supports in direct methanol fuel cell. J Phys Chem B 108:7074–7079. https://doi.org/10.1021/jp0370472

Chan Y-F, Wang C-C, Chen B-H, Chen C-Y (2013) Dye-sensitized TiO_2 solar cells based on nanocomposite photoanode containing plasma-modified multi-walled carbon nanotubes. Prog Photovolt Res Appl 21:47–57. https://doi.org/10.1002/pip.2174

Chang H, Joo SH, Pak C (2007) Synthesis and characterization of mesoporous carbon for fuel cell applications. J Mater Chem 17:3078–3088. https://doi.org/10.1039/B700389G

Che G, Lakshmi BB, Fisher ER, Martin CR (1998) Carbon nanotubule membranes for electrochemical energy storage and production. Nature 393:346–349. https://doi.org/10.1038/30694

Che G, Lakshmi BB, Martin CR, Fisher ER (1999) Metal-nanocluster-filled carbon nanotubes: catalytic properties and possible applications in electrochemical energy storage and production. Langmuir 15:750–758. https://doi.org/10.1021/la980663i

Chen T, Dai L (2013) Carbon nanomaterials for high-performance supercapacitors. Mater Today 16:272–280. https://doi.org/10.1016/j.mattod.2013.07.002

Chen Z, Xu L, Li W, Waje M, Yan Y (2006) Polyaniline nanofibre supported platinum nanoelectrocatalysts for direct methanol fuel cells. Nanotechnology 17:5254–5259. https://doi.org/10.1088/0957-4484/17/20/035

Chen J, Li C, Zhao DW, Lei W, Zhang Y, Cole MT, Chu DP, Wang BP, Cui YP, Sun XW, Milne WI (2010a) A quantum dot sensitized solar cell based on vertically aligned carbon nanotube template ZnO arrays. Electrochem Commun 12:1432–1435. https://doi.org/10.1016/j.elecom.2010.08.001

Chen S, Ye F, Lin W (2010b) Effect of operating conditions on the performance of a direct methanol fuel cell with PtRuMo/CNTs as anode catalyst. Int J Hydrog Energy 35:8225–8233. https://doi.org/10.1016/j.ijhydene.2009.12.085

Chen L-F, Zhang X-D, Liang H-W, Kong M, Guan Q-F, Chen P, Wu Z-Y, Yu S-H (2012a) Synthesis of nitrogen-doped porous carbon nanofibers as an efficient electrode material for supercapacitors. ACS Nano 6:7092–7102. https://doi.org/10.1021/nn302147s

Chen S, Wang Y, Ahn H, Wang G (2012b) Microwave hydrothermal synthesis of high performance tin-graphene nanocomposites for lithium ion batteries. J Power Sources 216:22–27. https://doi.org/10.1016/j.jpowsour.2012.05.051

Chen B-H, Kuo C-H, Ku J-R, Yan P-S, Huang C-J, Jeng M-S, Tsau F-H (2013) Highly improved with hydrogen storage capacity and fast kinetics in Mg-based nanocomposites by CNTs. J Alloys Compd 568:78–83. https://doi.org/10.1016/j.jallcom.2013.02.062

Chen L, Yang Y, Gao Y, Tronganh N, Chen F, Lu M, Jiang Y, Jiao Z, Zhao B (2016) Facile synthesis of ultrathin, undersized MoS_2/graphene for lithium-ion battery anodes. RSC Adv 6:99833–99851. https://doi.org/10.1039/C6RA19601B

Chen S, Huang Q, Yang W, Zou H, Mai H, Wang JH (2018) Pt-CoN supported on TiN-modified carbon nanotubes (Pt-CoN/TiN-CNT) as efficient oxygen reduction reaction catalysts in acidic medium. Int J Hydrog Energy 43:14337–14346. https://doi.org/10.1016/j.ijhydene.2018.06.003

Cheng Y, Shen PK, Jiang SP (2014) NiOx nanoparticles supported on polyethylenimine functionalized CNTs as efficient electrocatalysts for supercapacitor and oxygen evolution reaction. Int J Hydrog Energy 39:20662–20670. https://doi.org/10.1016/j.ijhydene.2014.06.156

Ciszewski M, Szatkowska E, Koszorek A, Majka M (2016) Carbon aerogels modified with graphene oxide, graphene and CNT as symmetric supercapacitor electrodes. J Mater Sci Mater Electron 28:4897–4903. https://doi.org/10.1007/s10854-016-6137-2

Conway BE (1999) Electrochemical supercapacitors: scientific fundamentals and technological application. Springer, New York

Dai L (2013) Functionalization of graphene for efficient energy conversion and storage. Acc Chem Res 46:31–42. https://doi.org/10.1021/ar300122m

Dang X, Yi H, Ham M-H, Qi J, Yun DS, Ladewski R, Strano MS, Hammond PT, Belcher AM (2011) Virus-templated self-assembled single-walled carbon nanotubes for highly efficient electron collection in photovoltaic devices. Nat Nanotechnol 6:377–384. https://doi.org/10.1038/nnano.2011.50

Das S, Dutta K, Shul YG, Kundu PP (2015a) Progress in developments of inorganic nanocatalysts for application in direct methanol fuel cells. Crit Rev Solid State Mater Sci 40:316–357. https://doi.org/10.1080/10408436.2015.1030493

Das S, Dutta K, Hazra S, Kundu PP (2015b) Partially sulfonated poly(vinylidene fluoride) induced enhancements of properties and DMFC performance of Nafion electrolyte membrane. Fuel Cells 15:505–515. https://doi.org/10.1002/fuce.201500018

Das S, Dutta K, Kundu PP (2015c) Nickel nanocatalysts supported on sulfonated polyaniline: potential toward methanol oxidation and as anode materials for DMFCs. J Mater Chem A 3:11349–11357. https://doi.org/10.1039/C5TA01837D

Das S, Dutta K, Kundu PP (2016) Sulfonated polypyrrole matrix induced enhanced efficiency of Ni nanocatalyst for application as an anode material for DMFCs. Mater Chem Phys 176:143–151. https://doi.org/10.1016/j.matchemphys.2016.03.046

Das S, Dutta K, Rana D (2018a) Polymer electrolyte membranes for microbial fuel cells: a review. Polym Rev. https://doi.org/10.1080/15583724.2017.1418377

Das S, Dutta K, Kundu PP, Bhattacharya SK (2018b) Nanostructured polyaniline: an efficient support matrix for platinum-ruthenium anode catalyst in direct methanol fuel cell. Fuel Cells 18:369–378. https://doi.org/10.1002/fuce.201700201

Debe MK (2012) Electrocatalyst approaches and challenges for automotive fuel cells. Nature 486:43–51. https://doi.org/10.1038/nature11115

Dembele KT, Selopal GS, Soldano C, Nechache R, Rimada JC, Concina I, Sberveglieri G, Rosei F, Vomiero A (2013) Hybrid carbon nanotubes-TiO_2 photoanodes for high efficiency dye-sensitized solar cells. J Phys Chem C 117:14510–14517. https://doi.org/10.1021/jp403553t

Dhindsa KS, Mandal BP, Bazzi K, Lin MW, Nazri M, Nazri GA, Naik VM, Garg VK, Oliveira AC, Vaishnava P, Naik R, Zhou ZX (2013) Enhanced electrochemical performance of graphene modified $LiFePO_4$ cathode material for lithium ion batteries. Solid State Ionics 253:94–100. https://doi.org/10.1016/j.ssi.2013.08.030

Dmitrijev S (2006) Principles of semiconductor devices. Oxford University Press, Oxford

Dong B, He B-L, Xu C-L, Li H-L (2007) Preparation and electrochemical characterization of polyaniline/multi-walled carbon nanotubes composites for supercapacitor. Mater Sci Eng B 143:7–13. https://doi.org/10.1016/j.mseb.2007.06.017

Du H-Y, Wang C-H, Hsu H-C, Chang S-T, Huang H-C, Chen L-C, Chen K-H (2012) Graphene nanosheet-CNT hybrid nanostructure electrode for a proton exchange membrane fuel cell. Int J Hydrog Energy 37:18989–18995. https://doi.org/10.1016/j.ijhydene.2012.09.130

Dunn B, Kamath H, Tarascon J-M (2011) Electrical energy storage for the grid: a battery of choices. Science 334:928–935. https://doi.org/10.1126/science.1212741

Dutta K, Kundu PP (2014) A review on aromatic conducting polymers-based catalyst supporting matrices for application in microbial fuel cells. Polym Rev 54:401–435. https://doi.org/10.1080/15583724.2014.881372

Dutta K, Kundu PP (2018) Ch 1: Introduction to microbial fuel cells. In: Kundu PP, Dutta K (eds) Progress and recent trends in microbial fuel cells. Elsevier, Amsterdam, pp 1–6. https://doi.org/10.1016/B978-0-444-64017-8.00001-4

Dutta K, Kumar P, Das S, Kundu PP (2014a) Utilization of conducting polymers in fabricating polymer electrolyte membranes for application in direct methanol fuel cells. Polym Rev 54:1–32. https://doi.org/10.1080/15583724.2013.839566

Dutta K, Kundu PP, Kundu A (2014b) Fuel cells – exploratory fuel cells | micro-fuel cells. In: Reedijk J (ed) Reference module in chemistry, molecular sciences and chemical engineering. Elsevier, Amsterdam. https://doi.org/10.1016/B978-0-12-409547-2.10975-8

Dutta K, Das S, Kundu PP (2014c) Low methanol permeable and highly selective membranes composed of pure and/or partially sulfonated PVdF-co-HFP and polyaniline. J Membr Sci 468:42–51. https://doi.org/10.1016/j.memsci.2014.05.049

Dutta K, Das S, Kumar P, Kundu PP (2014d) Polymer electrolyte membrane with high selectivity ratio for direct methanol fuel cells: a preliminary study based on blends of partially sulfonated polymers polyaniline and PVdF-*co*-HFP. Appl Energy 118:183–191. https://doi.org/10.1016/j.apenergy.2013.12.029

Dutta K, Das S, Kundu PP (2015a) Synthesis, preparation, and performance of blends and composites of π-conjugated polymers and their copolymers in DMFCs. Polym Rev 55:630–677. https://doi.org/10.1080/15583724.2015.1028631

Dutta K, Das S, Rana D, Kundu PP (2015b) Enhancements of catalyst distribution and functioning upon utilization of conducting polymers as supporting matrices in DMFCs: a review. Polym Rev 55:1–56. https://doi.org/10.1080/15583724.2014.958771

Dutta K, Das S, Kundu PP (2015c) Partially sulfonated polyaniline induced high ion-exchange capacity and selectivity of Nafion membrane for application in direct methanol fuel cells. J Membr Sci 473:94–101. https://doi.org/10.1016/j.memsci.2014.09.010

Dutta K, Das S, Kundu PP (2016a) Effect of the presence of partially sulfonated polyaniline on the proton and methanol transport behavior of partially sulfonated PVdF membrane. Polym J 48:301–309. https://doi.org/10.1038/pj.2015.106

Dutta K, Das S, Kundu PP (2016b) Highly methanol resistant and selective ternary blend membrane composed of sulfonated PVdF-co-HFP, sulfonated polyaniline and nafion. J Appl Polym Sci 133:43294 (1–10). https://doi.org/10.1002/app.43294

Dutta K, Das S, Kundu PP (2016c) Polyaniline nanowhiskers induced low methanol permeability and high membrane selectivity in partially sulfonated PVdF-*co*-HFP membranes. RSC Adv 6:107960–107969. https://doi.org/10.1039/c6ra24090a

Elsabawy KM, El-Hawary WF, Refat MS (2012) Advanced synthesis of titanium-doped-tellerium-cadmium mixtures for high performance solar cell applications as one of renewable source of energy. Int J Chem Sci 10:1869–1879 http://www.sadgurupublications.com/ContentPaper/2012/10_1689_10(4)2012.pdf

Emmenegger C, Mauron P, Sudan P, Wenger P, Hermann V, Gallay R, Züttel A (2003) Investigation of electrochemical double-layer (ECDL) capacitors electrodes based on carbon nanotubes and activated carbon materials. J Power Sources 124:321–329. https://doi.org/10.1016/S0378-7753(03)00590-1

EPRI-DOE Handbook of energy storage for transmission and distribution applications. (Report # 1001834, Electric Power Research Institute (EPRI), Palo Alto, CA, and the US Department of Energy, Washington, DC2003). http://www.sandia.gov/ess/publications/ESHB%201001834%20reduced%20size.pdf

Etacheri VK, Marom R, Elazari R, Salitra G, Aurbach D (2011) Challenges in the development of advanced Li-ion batteries: a review. Energy Environ Sci 4:3243–3262. https://doi.org/10.1039/C1EE01598B

Fahrenbruch AL, Bube RH (1983) Fundamentals of solar cells. Academic, New York

Fan B, Mei X, Sun K, Ouyang J (2008) Conducting polymer/carbon nanotube composite as counter electrode of dye-sensitized solar cells. Appl Phys Lett 93:143103 (1–3). https://doi.org/10.1063/1.2996270

Fan Q, Zhang Q, Zhou W, Xia X, Yang F, Zhang N, Xiao S, Li K, Gu X, Xiao Z, Chen H, Wang Y, Liu H, Zhou W, Xie S (2017) Novel approach to enhance efficiency of hybrid silicon-based solar cells via synergistic effects of polymer and carbon nanotube composite film. Nano Energy 33:436–444. https://doi.org/10.1016/j.nanoen.2017.02.003

Fathi M, Saghafi M, Mahboubi F, Mohajerzadeh S (2014) Synthesis and electrochemical investigation of polyaniline/unzipped carbon nanotube composites as electrode material in supercapacitors. Synth Met 198:345–356. https://doi.org/10.1016/j.synthmet.2014.10.033

Fisher AS, Khalid MB, Widstrom M, Kofinas P (2011) Solid polymer electrolytes with sulfur based ionic liquid for lithium batteries. J Power Sources 196:9767–9773. https://doi.org/10.1016/j.jpowsour.2011.07.081

Frackowiak E, Béguin F (2001) Carbon materials for the electrochemical storage of energy in capacitors. Carbon 39:937–950. https://doi.org/10.1016/S0008-6223(00)00183-4

Futaba DN, Hata K, Yamada T, Hiraoka T, Hayamizu Y, Kakudate Y, Tanaike O, Hatori H, Yumura M, Iijima S (2006) Shape-engineerable and highly densely packed single-walled carbon nanotubes and their application as super-capacitor electrodes. Nat Mater 5:987–994. https://doi.org/10.1038/nmat1782

Gan Y, Zhu L, Qin H, Xia Y, Xiao H, Xu L, Ruan L, Liang C, Tao X, Huang H, Zhang W (2015) Hybrid nanoarchitecture of rutile TiO_2 nanoneedle/graphene for advanced lithium-ion batteries. Solid State Ionics 269:44–50. https://doi.org/10.1016/j.ssi.2014.11.017

Gao G, Zhang Q, Cheng XB, Shapter JG, Yin T, Sun R, Cui D (2015) Ultrafine ferroferric oxide nanoparticles embedded into mesoporous carbon nanotubes for lithium ion batteries. Sci Rep 5:17553 (1–13). https://doi.org/10.1038/srep17553

Gao S, Xu H, Fang Z, Ouadah A, Chen H, Chen X, Shi L, Ma B, Jing C, Zhu C (2018) Highly sulfonated poly(ether ether ketone) grafted on graphene oxide as nanohybrid proton exchange membrane applied in fuel cells. Electrochim Acta 283:428–437. https://doi.org/10.1016/j.electacta.2018.06.180

Ge D, Yang L, Fan L, Zhang C, Xiao X, Gogotsi Y, Yang S (2015) Foldable supercapacitors from triple networks of macroporous cellulose fibers, single-walled carbon nanotubes and polyaniline nanoribbons. Nano Energy 11:568–578. https://doi.org/10.1016/j.nanoen.2014.11.023

Gharibi H, Golmohammadi F, Kheirmand M (2013) Palladium/cobalt coated on multi-walled carbon nanotubes as an electro-catalyst for oxygen reduction reaction in passive direct methanol fuel cells. Fuel Cells 13:987–1004. https://doi.org/10.1002/fuce.201200220

Giuri A, Masi S, Colella S, Listorti A, Rizzo A, Gigli G, Liscio A, Treossi E, Palermo V, Rella S, Malitesta C, Corcione CE (2016) UV reduced graphene oxide PEDOT:PSS nanocomposite for perovskite solar cells. IEEE Trans Nanotechnol 15:725–730. https://doi.org/10.1109/TNANO.2016.2524689

Golobostanfard MR, Abdizadeh H (2015) Comparing incorporation of carbon nanotubes in hierarchical porous photoanodes of quantum dot and dye sensitized solar cells. Ceram Inter 41:497–504. https://doi.org/10.1016/j.ceramint.2014.08.097

Gong K, Du F, Xia Z, Durstock M, Dai L (2009) Nitrogen-doped carbon nanotube arrays with high electrocatalytic activity for oxygen reduction. Science 323:760–764. https://doi.org/10.1126/science.1168049

Goodenough JB, Mizuchima K (1981) Electrochemical cell with new fast ion conductors. US Patent 4302518

Goriparti S, Miele E, Angelis FD, Fabrizio E, Zaccaria RP, Capigli C (2014) Review on recent progress of nanostructured anode materials for Li-ion batteries. J Power Sources 257:421–443. https://doi.org/10.1016/j.jpowsour.2013.11.103

Goswami DY, Kreith F (2007) Handbook of energy efficiency and renewable energy. CRC Press, Boca Raton

Grätzel M (2001) Photoelectrochemical cells. Nature 414:338–344. https://doi.org/10.1038/35104607

Groves M, Chan ASW, Malardier-Jugroot C, Jugroot M (2009) Improving platinum catalyst binding energy to graphene through nitrogen doping. Chem Phys Lett 481:214–219. https://doi.org/10.1016/j.cplett.2009.09.074

Guo DJ, Li HL (2004) High dispersion and electrocatalytic properties of Pt nanoparticles on SWNT bundles. J Electroanal Chem 573:197–202. https://doi.org/10.1016/j.jelechem.2004.07.006

Hakimian A, Kamarthi S, Erbis S, Abraham KM, Cullinane TP, Isaacs JA (2015) Economic analysis of CNT lithium-ion battery manufacturing. Environ Sci Nano 2:463–476. https://doi.org/10.1039/C5EN00078E

Hamon MA, Chen J, Hu H, Chen Y, Itkis ME, Rao AM, Eklund PC, Haddon RC (1999) Dissolution of single-walled carbon nanotubes. Adv Mater 11:834–840. https://doi.org/10.1002/(SICI)1521-4095(199907)11:10<834::AID-ADMA834>3.0.CO;2-R

Han X, Qing G, Sun J, Sun T (2012) How many lithium ions can be inserted onto fused C6 aromatic ring systems? Angew Chem Int Ed 51:5147–5151. https://doi.org/10.1002/anie.201109187

He Z, Chen J, Liu D, Tang H, Deng W, Kuang Y (2004a) Deposition and electrocatalytic properties of platinum nanoparticles on carbon nanotubes for methanol electrooxidation. Mater Chem Phys 85:396–401. https://doi.org/10.1016/j.matchemphys.2004.01.030

He Z, Chen J, Liu D, Zhou H, Kuang Y (2004b) Electrodeposition of Pt-Ru nanoparticles on carbon nanotubes and their electrocatalytic properties for methanol electrooxidation. Diam Relat Mater 13:1764–1770. https://doi.org/10.1016/j.diamond.2004.03.004

He D, Zeng C, Xu C, Cheng N, Li H, Mu S, Pan M (2011) Polyaniline-functionalized carbon nanotube supported platinum catalysts. Langmuir 27:5582–5588. https://doi.org/10.1021/la2003589

He X, Yang W, Mao X, Xu L, Zhou Y, Chen Y, Zhao Y, Yang Y, Xu J (2018) All-solid state symmetric supercapacitors based on compressible and flexible free-standing 3D carbon nanotubes (CNTs)/poly(3,4-ethylenedioxythiophene) (PEDOT) sponge electrodes. J Power Sources 376:138–146. https://doi.org/10.1016/j.jpowsour.2017.09.084

Hong W, Xu Y, Lu G, Li C, Shi G (2008) Transparent graphene/PEDOT-PSS composite films as counter electrodes of dye-sensitized solar cells. Electrochem Commun 10:1555–1558. https://doi.org/10.1016/j.elecom.2008.08.007

Hou X, Jiang H, Hu Y, Li Y, Huo J, Li C (2013) In situ deposition of hierarchical architecture assembly from Sn-filled CNTs for lithium-ion batteries. ACS Appl Mater Interfaces 5:6672–6677. https://doi.org/10.1021/am401442v

Hu J, Ouyang M, Yang P, Lieber CM (1999) Controlled growth and electrical properties of heterojunctions of carbon nanotubes and silicon nanowires. Nature 399:48–51. https://doi.org/10.1038/19941

Hu P, Xiao K, Liu Y, Yu G, Wang X, Fu L, Cui G, Zhu D (2004) Multiwall nanotubes with intramolecular junctions (CNx/C): preparation, rectification, logic gates, and application. Appl Phys Lett 84:4932–4934. https://doi.org/10.1063/1.1760212

Huang YF, Lin CW, Chang CS, Ho MJ (2011) Alternative platinum electrocatalyst supporter with micro/nanostructured polyaniline for direct methanol fuel cell applications. Electrochim Acta 56:5679–5685. https://doi.org/10.1016/j.electacta.2011.04.026

Huang Y, Cai J, Guo Y (2012) Roles of Pb and MnOx in PtPb/MnOx-CNTs catalyst for methanol electro-oxidation. Int J Hydrog Energy 37:1263–1271. https://doi.org/10.1016/j.ijhydene.2011.10.002

Iqbal N, Wang X, Babar AA, Yu J, Ding B (2016) Highly flexible $NiCo_2O_4$/CNTs doped carbon nanofibers for CO_2 adsorption and supercapacitor electrodes. J Colloid Interf Sci 476:87–93. https://doi.org/10.1016/j.jcis.2016.05.010

Ishikawa Y, Liao M-S, Cabrera CR (2000) Oxidation of methanol on platinum, ruthenium and mixed Pt-M metals (M=Ru, Sn): a theoretical study. Surf Sci 463:66–80. https://doi.org/10.1016/S0039-6028(00)00600-2

Itkis ME, Borondics F, Yu A, Haddon RC (2006) Bolometric infrared photo-response of suspended single-walled carbon nanotube films. Science 312:413–416. https://doi.org/10.1126/science.1125695

Jafri RI, Rajalakshmi N, Ramaprabhu S (2010) Nitrogen doped graphene nanoplatelets as catalyst support for oxygen reduction reaction in proton exchange membrane fuel cell. J Mater Chem 20:7114–7117. https://doi.org/10.1039/C0JM00467G

Jayakumar P (2009) Solar energy resource assessment handbook. Renewable Energy Corporation Network for the Asia Pacific Centre for Transfer of Technology (APCTT) of the United Nations. doi: http://apctt.org/recap/sites/all/themes/recap/pdf/SOLAR.pdf

Jeon I-Y, Shin Y-R, Sohn G-J, Choi H-J, Bae S-Y, Mahmood J, Jung S-M, Seo J-M, Kim M-J, Chang DW, Dai L, Baek J-B (2012) Edge-carboxylated graphene nanosheets via ball milling. Proc Natl Acad Sci U S A 09:5588–5593. https://doi.org/10.1073/pnas.1116897109

Jeon I-Y, Choi H-J, Jung S-M, Seo J-M, Kim M-J, Dai L, Baek J-B (2013) Large-scale production of edge-selectively functionalized graphene nanoplatelets via ball milling and their use as metal-free electrocatalysts for oxygen reduction reaction. J Am Chem Soc 135:1386–1393. https://doi.org/10.1021/ja3091643

Jia Y, Wei J, Wang K, Cao A, Shu Q, Gu X, Zhu Y, Zhuang D, Zhang G, Ma B, Wang L, Liu W, Wang Z, Luo J, Wu D (2008) Nanotube-silicon heterojunction solar cells. Adv Mater 20:4594–4598. https://doi.org/10.1002/adma.200801810

Jia L, Kou H, Jiang Y, Yu S, Li J, Wang C (2013) Electrochemical deposition semiconductor ZnSe on a new substrate CNTs/PVA and its photoelectrical properties. Electrochim Acta 107:71–77. https://doi.org/10.1016/j.electacta.2013.06.004

Jiang K-C, Xin S, Lee J-S, Kim J, Xiao X-L, Guo Y-G (2012) Improved kinetics of $LiNi_{1/3}Mn_{1/3}Co_{1/3}O_2$ cathode material through reduced graphene oxide networks. Phys Chem Chem Phys 14:2934–2939. https://doi.org/10.1039/C2CP23363K

Jiang S, Zhao B, Ran R, Cai R, Tadé MO (2014) A freestanding composite film electrode stacked from hierarchical electrospun SnO_2 nanorods and graphene sheets for reversible lithium storage. RSC Adv 4:9367–9371. https://doi.org/10.1039/C3RA47840H

Jin H, Zhu L, Bing N, Wang L, Wang L (2014) No cytotoxic nitrogen-doped carbon nanotubes as efficient metal-free electrocatalyst for oxygen reduction in fuel cells. Solid State Sci 30:21–25. https://doi.org/10.1016/j.solidstatesciences.2014.01.002

Joo SH, Pak C, Kim EA, Lee YH, Chang H, Seung D, Choi YS, Park J-B, Kim TK (2008) Functionalized carbon nanotube-poly(arylenesulfone) composite membranes for direct methanol fuel cells with enhanced performance. J Power Sources 180:63–70. https://doi.org/10.1016/j.jpowsour.2008.02.014

Joshi P, Zhang L, Davoux D, Zhu Z, Galipeau D, Fong H, Qiao Q (2010) Composite of TiO_2 nanofibers and nanoparticles for dye-sensitized solar cells with significantly improved efficiency. Energy Environ Sci 3:1507–1510. https://doi.org/10.1039/C0EE00068J

Ju MJ, Kim JC, Choi H-J, Choi IT, Kim SG, Lim K, Ko J, Lee J-J, Jeon I-Y, Baek J-B, Kim HK (2013) N-doped graphene nanoplatelets as superior metal-free counter electrodes for organic dye-sensitized solar cells. ACS Nano 7:5243–5250. https://doi.org/10.1021/nn4009774

Kabbabi A, Gloaguen F, Andolfatto F, Durand R (1994) Particle size effect for oxygen reduction and methanol oxidation on Pt/C inside a proton exchange membrane. J Electrochem Soc 373:251–254. https://doi.org/10.1016/0022-0728(94)03503-2

Kanai Y, Grossman JC (2008) Role of semiconducting and metallic tubes in P3HT/carbon-nanotube photovoltaic heterojunctions: density functional theory calculations. Nano Lett 8:908–912. https://doi.org/10.1021/nl0732777

Kang SJ, Kocabas C, Ozel T, Shim M, Pimparkar N, Alam MA, Rotkin SV, Rogers JA (2007) High-performance electronics using dense, perfectly aligned arrays of single-walled carbon nanotubes. Nat Nanotechnol 2:230–236. https://doi.org/10.1038/nnano.2007.77

Kang Z, Jiao K, Cheng J, Peng R, Jiao S, Hu Z (2018) A novel three-dimensional carbonized $PANI_{1600}$@CNTs network for enhanced enzymatic biofuel cell. Biosens Bioelectron 101:60–65. https://doi.org/10.1016/j.bios.2017.10.008

Kanninen P, Borghei M, Sorsa O, Pohjalainen E, Kauppinen EI, Ruiz V, Kallio T (2014) Highly efficient cathode catalyst layer based on nitrogen-doped carbon nanotubes for the alkaline direct methanol fuel cell. Appl Catal B 156–157:341–349. https://doi.org/10.1016/j.apcatb.2014.03.041

Kavan L, Liska P, Zakeeruddin SM, Grätzel M (2016) Low-temperature fabrication of highly-efficient, optically-transparent (FTO-free) graphene cathode for co-mediated dye-sensitized solar cells with acetonitrile-free electrolyte solution. Electrochim Acta 195:34–42. https://doi.org/10.1016/j.electacta.2016.02.097

Kawano T, Christensen D, Chen S, Cho CY, Lin L (2006) Formation and characterization of silicon/carbon nanotube/silicon heterojunctions by local synthesis and assembly. Appl Phys Lett 89:163510 (1–3). https://doi.org/10.1063/1.2364151

Khattak YH, Baig F, Soucase BM, Beg S, Gillani SR, Ahmed S (2018) Efficiency enhancement of novel CNTS/ZnS/Zn (O, S) thin film solar cell. Optik 171:453–462. https://doi.org/10.1016/j.ijleo.2018.06.001

Kim YJ, Kim JH, Kang M-S, Lee MJ, Won J, Lee JC, Kang YS (2004) Supramolecular electrolytes for use in highly efficient dye-sensitized solar cells. Adv Mater 16:1753–1757. https://doi.org/10.1002/adma.200306664

Kim H-S, Kim S-I, Kim W-S (2006) A study on electrochemical characteristics of $LiCoO_2$/$LiNi_{1/3}Mn_{1/3}Co_{1/3}O_2$ mixed cathode for Li secondary battery. Electrochim Acta 52:1457–1461. https://doi.org/10.1016/j.electacta.2006.02.045

Kim S-W, Seo D-H, Gwon H, Kim J, Kang K (2010) Fabrication of FeF_3 nanoflowers on CNT branches and their application to high power lithium rechargeable batteries. Adv Mater 22:5260–5264. https://doi.org/10.1002/adma.201002879

Kim B-S, Neo DCJ, Hou B, Park JB, Cho Y, Zhang N, Hong J, Pak S, Lee S, Sohn JI, Assender HE, Watt AAR, Cha SN, Kim JM (2016) High performance PbS quantum dot/graphene hybrid solar cell with efficient charge extraction. ACS Appl Mater Interfaces 8:13902–13908. https://doi.org/10.1021/acsami.6b02544

Kinoshita K (1990) Particle size effects for oxygen reduction on highly dispersed platinum in acid electrolytes. J Electrochem Soc 137:845–848. https://doi.org/10.1149/1.2086566

Koo Y, Shanov VN, Yarmolenko S, Schulz M, Sankar J, Yun Y (2015) Inverse-ordered fabrication of free-standing CNT sheets for supercapacitor. Langmuir 31:7616–7622. https://doi.org/10.1021/acs.langmuir.5b00891

Kristian N, Yu Y, Gunawan P, Xu R, Deng W, Liu X, Wang X (2009) Controlled synthesis of Pt-decorated Au nanostructure and its promoted activity toward formic acid electro-oxidation. Electrochim Acta 54:4916–4924. https://doi.org/10.1016/j.electacta.2009.04.018

Kumar P, Dutta K, Das S, Kundu PP (2014a) An overview of unsolved deficiencies of direct methanol fuel cell technology: factors and parameters affecting its widespread use. Int J Energy Res 38:1367–1390. https://doi.org/10.1002/er.3163

Kumar P, Dutta K, Das S, Kundu PP (2014b) Membrane prepared by incorporation of crosslinked sulfonated polystyrene in the blend of PVdF-*co*-HFP/Nafion: a preliminary evaluation for application in DMFC. Appl Energy 123:66–74. https://doi.org/10.1016/j.apenergy.2014.02.060

Kumar P, Dutta K, Kundu PP (2014c) Enhanced performance of direct methanol fuel cells: a study on the combined effect of various supporting electrolytes, flow channel designs and operating temperatures. Int J Energy Res 38:41–50. https://doi.org/10.1002/er.3034

Kumar U, Sikarwar S, Sonker RK, Yadav BC (2016) Carbon nanotube: synthesis and application in solar cells. J Inorg Organomet Polym Mater 26:1231–1242. https://doi.org/10.1007/s10904-016-0401-z

Kumara GRA, Konno A, Shiratsuchi K, Tsukahara J, Tennakone K (2002) Dye-sensitized solid-state solar cells: use of crystal growth inhibitors for deposition of the hole collector. Chem Mater 14:954–955. https://doi.org/10.1021/cm011595f

Kundu PP, Dutta K (2016) Ch 6: Hydrogen fuel cells for portable applications. In: Ball M, Basile A, Veziroglu TN (eds) Compendium of hydrogen energy, vol 4. Hydrogen use, safety and the

hydrogen economy, Woodhead Publishing Series in Energy # 86. Elsevier, Amsterdam, pp 111–131. https://doi.org/10.1016/B978-1-78242-364-5.00006-3

Kundu PP, Dutta K (2018) Progress and recent trends in microbial fuel cells, 1st edn. Elsevier, Amsterdam. https://doi.org/10.1016/C2016-0-04695-8

Landi BJ, Ganter MJ, Cress CD, DiLeo RA, Raffaelle RP (2009) Carbon nanotubes for lithium ion batteries. Energy Environ Sci 2:638–654. https://doi.org/10.1039/B904116H

Law M, Greene LE, Johnson JC, Saykally R, Yang P (2005) Nanowire dye-sensitized solar cells. Nat Mater 4:455–459. https://doi.org/10.1038/nmat1387

Lee K-M, Hu C-W, Chen H-W, Ho K-C (2008) Incorporating carbon nanotube in a low-temperature fabrication process for dye-sensitized TiO_2 solar cells. Solar Energy Mater Solar Cells 92:1628–1633. https://doi.org/10.1016/j.solmat.2008.07.012

Lee H, Kim H, Cho MS, Choi J, Lee Y (2011a) Fabrication of polypyrrole (PPy)/carbon nanotube (CNT) composite electrode on ceramic fabric for supercapacitor applications. Electrochim Acta 56:7460–7466. https://doi.org/10.1016/j.electacta.2011.06.113

Lee H-Y, Vogel W, Chu PP-J (2011b) Nanostructure and surface composition of Pt and Ru binary catalysts on polyaniline-functionalized carbon nanotubes. Langmuir 27:14654–14661. https://doi.org/10.1021/la202169j

Lee Y-B, Lee C-H, Kim K-M, Lim D-S (2011c) Preparation and properties on the graphite/polypropylene composite bipolar plates with a 304 stainless steel by compression molding for PEM fuel cell. Int J Hydrog Energy 36:7621–7627. https://doi.org/10.1016/j.ijhydene.2011.03.108

Li C, Mitra S (2007) Processing of fullerene-single wall carbon nanotube complex for bulk heterojunction photovoltaic cells. Appl Phys Lett 91:253112 (1–3). https://doi.org/10.1063/1.2827189

Li W, Yang YJ (2014) The reduction of graphene oxide by elemental copper and its application in the fabrication of graphene supercapacitor. J Solid State Electrochem 18:1621–1626. https://doi.org/10.1007/s10008-014-2391-5

Li W, Liang C, Zhou W, Qiu J, Zhou Z, Sun G, Xin Q (2003) Preparation and characterization of multiwalled carbon nanotube-supported platinum for cathode catalysts of direct methanol fuel cells. J Phys Chem B 107:6292–6299. https://doi.org/10.1021/jp022505c

Li W, Wang X, Chen Z, Waje M, Yushan (2005) Carbon nanotube film by filtration as cathode catalyst support for proton-exchange membrane fuel cell. Langmuir 21:9386–9389. https://doi.org/10.1021/la051124y

Li Y, Zang J, Yang B (2010) Antireflective surfaces based on biomimetic nanopillared arrays. Nano Today 5:117–127. https://doi.org/10.1016/j.nantod.2010.03.001

Li B, Cao H, Shao J, Qu M (2011) Enhanced anode performances of the Fe_3O_4-carbon-rGO three dimensional composite in lithium ion batteries. Chem Commun 47:10374–10376. https://doi.org/10.1039/C1CC13462K

Li C, Wu Y, Poplawsky J, Pennycook TJ, Paudel N, Yin W, Haigh SJ, Oxley MP, Lupini AR, Al-Jassim M, Pennycook SJ, Yan Y (2014a) Grain-boundary-enhanced carrier collection in CdTe solar cells. Phys Rev Lett 112:156103 (1–5). https://doi.org/10.1103/PhysRevLett.112.156103

Li L, Hu ZA, An N, Yang YY, Li ZM, Wu HY (2014b) Facile synthesis of MnO_2/CNTs composite for supercapacitor electrodes with long cycle stability. J Phys Chem C 118:22865–22872. https://doi.org/10.1021/jp505744p

Li X, Zhang G, Zhang L, Zhong M, Yuan X (2015a) Silicon/graphite/carbon nanotubes composite as anode for lithium ion battery. Int J Electrochem Sci 10:2802–2811. https://doi.org/10.1016/j.electacta.2006.01.043

Li YY, Li CT, Yeh MH, Huang KC, Chen PW, Vittal R, Ho KC (2015b) Graphite with different structures as catalysts for counter electrodes in dye-sensitized solar cells. Electrochim Acta 179:211–219. https://doi.org/10.1016/j.electacta.2015.06.007

Li D, Gong Y, Pan C (2016a) Facile synthesis of hybrid CNTs/$NiCo_2S_4$ composite for high performance supercapacitors. Sci Rep 6:29788 (1–7). https://doi.org/10.1038/srep29788

Li Z, Boix PP, Xing G, Fu K, Kulkarni SA, Batabyal SK, Xu W, Cao A, Sum TC, Mathews N, Wong LH (2016b) Carbon nanotubes as an efficient hole collector for high voltage methylammonium lead bromide perovskite solar cells. Nanoscale 8:6352–6360. https://doi.org/10.1039/C5NR06177F

Li L, Jiang G, Ma J (2018) $CuMn_2O_4$/graphene nanosheets as excellent anode for lithium-ion battery. Mater Res Bull 104:53–59. https://doi.org/10.1016/j.materresbull.2018.03.051

Lian P, Zhu X, Liang S, Li Z, Yang W, Wang H (2010) Large reversible capacity of high quality graphene sheets as an anode material for lithium-ion batteries. Electrochim Acta 55:3909–3912. https://doi.org/10.1016/j.electacta.2010.02.025

Liang C-W, Roth S (2008) Electrical and optical transport of GaAs/carbon nanotube heterojunctions. Nano Lett 8:1809–1812. https://doi.org/10.1021/nl0802178

Lien DH, Hsu WK, Zan HW, Tai NH, Tsai CH (2006) Photocurrent amplification at carbon nanotube-metal contacts. Adv Mater 18:98–103. https://doi.org/10.1002/adma.200500912

Lim D-H, Lee W-D, Lee H-I (2008) Highly dispersed and nano-sized Pt based electrocatalysts for low-temperature fuel cells. Catal Surv Jpn 12:310–325. https://doi.org/10.1007/s10563-008-9059-z

Liu Z, Lin X, Lee JY, Zhang W, Han M, Gan LM (2002) Preparation and characterization of platinum-based electrocatalysts on multiwalled carbon nanotubes for proton exchange membrane fuel cells. Langmuir 18:4054–4060. https://doi.org/10.1021/la0116903

Liu H, Ramnarayanan R, Logan BE (2004) Production of electricity during wastewater treatment using a single chamber microbial fuel cell. Environ Sci Technol 38:2281–2285. https://doi.org/10.1021/es034923g

Liu H, Song C, Zhang L, Zhang J, Wang H, Wilkinson DP (2006) A review of anode catalysis in the direct methanol fuel cell. J Power Sources 155:95–110. https://doi.org/10.1016/j.jpowsour.2006.01.030

Liu Y-H, Yi B, Shao Z-G, Wang L, Xing D, Zhang H (2007) Pt/CNTs-Nafion reinforced and self-humidifying composite membrane for PEMFC applications. J Power Sources 163:807–813. https://doi.org/10.1016/j.jpowsour.2006.09.065

Liu Q, Liu Z, Zhang X, Zhang N, Yang L, Yin S, Chen Y (2008a) Organic photovoltaic cells based on an acceptor of soluble graphene. Appl Phys Lett 92:223303 (1–3). https://doi.org/10.1063/1.2938865

Liu Z, Liu Q, Huang Y, Ma Y, Yin S, Zhang X, Sun W, Chen Y (2008b) Organic photovoltaic devices based on a novel acceptor material: graphene. Adv Mater 20:3924–3930. https://doi.org/10.1002/adma.200800366

Liu C, Yu Z, Neff D, Zhamu A, Jang BZ (2010) Graphene-based supercapacitor with an ultrahigh energy density. Nano Lett 10:4863–4868. https://doi.org/10.1021/nl102661q

Liu J, Xue Y, Zhang M, Dai L (2012a) Graphene-based materials for energy applications. MRS Bull 37:1265–1272. https://doi.org/10.1557/mrs.2012.179

Liu J, Zhang X, Pang H, Liu B, Zou Q, Chen J (2012b) High-performance bioanode based on the composite of CNTs-immobilized mediator and silk film-immobilized glucose oxidase for glucose/O_2 biofuel cells. Biosens Bioelectron 31:170–175. https://doi.org/10.1016/j.bios.2011.10.011

Liu Z, Shi Q, Zhang R, Wang Q, Kang G, Peng F (2014) Phosphorus-doped carbon nanotubes supported low Pt loading catalyst for the oxygen reduction reaction in acidic fuel cells. J Power Sources 268:171–175. https://doi.org/10.1016/j.jpowsour.2014.06.036

Liu J, Mirri F, Notarianni M, Pasquali M, Motta N (2015a) High performance all-carbon thin film supercapacitors. J Power Sources 274:823–830. https://doi.org/10.1016/j.jpowsour.2014.10.104

Liu X, Zheng Y, Wang X (2015b) Controllable preparation of polyaniline–graphene nanocomposites using functionalized graphene for supercapacitor electrodes. Chem Eur J 21:10408–10415. https://doi.org/10.1002/chem.201501245

Liu YF, Yuan GH, Jiang ZH, Yao ZP, Yue M (2015c) Preparation of $Ni(OH)_2$-graphene sheet-carbon nanotube composite as electrode material for supercapacitors. J Alloys Compd 618:37–43. https://doi.org/10.1016/j.jallcom.2014.08.167

Liu X, Gao L, Yue G, Zheng H, Zhang W (2017) Efficient dye-sensitized solar cells incorporating hybrid counter electrode of $CuMnSnS_4$ microsperes/carbon nanotubes. Sol Energy 158:952–959. https://doi.org/10.1016/j.solener.2017.10.057

Lo A-Y, Yu N, Huang S-J, Hung C-T, Liu S-H, Lei Z, Kuo C-T, Liu S-B (2011) Fabrication of CNTs with controlled diameters and their applications as electrocatalyst supports for DMFC. Diam Relat Mater 20:343–350. https://doi.org/10.1016/j.diamond.2011.01.002

Lo W-C, Su S-H, Chu H-J, He J-L (2018) TiO_2-CNTs grown on titanium as an anode layer for lithium-ion batteries. Surf Coat Technol 337:544–551. https://doi.org/10.1016/j.surfcoat.2018.01.029

Longo C, Freitas J, De Paoli M-A (2003) Performance and stability of TiO_2/dye solar cells assembled with flexible electrodes and a polymer electrolyte. J Photochem Photobiol A 159:33–39. https://doi.org/10.1016/S1010-6030(03)00106-0

Lordi V, Yao N, Wei J (2001) Method for supporting platinum on single-walled carbon nanotubes for a selective hydrogenation catalyst. Chem Mater 13:733–737. https://doi.org/10.1021/cm000210a

Lu SX, Panchapakesan B (2006) Photoconductivity in single wall carbon nanotube sheets. Nanotechnology 17:1843–1850. https://doi.org/10.1088/0957-4484/17/8/006

Lu L, Li W, Zhou L, Zhang Y, Zhang Z, Chen Y, Liu J, Liu L, Chen W, Zhang Y (2016) Impact of size on energy storage performance of graphene based supercapacitor electrode. Electrochim Acta 219:463–469. https://doi.org/10.1016/j.electacta.2016.10.020

Luo Y, Kong D, Jia Y, Luo J, Lu Y, Zhang D, Qiu K, Li CM, Yu T (2013) Self-assembled graphene@PANI nanoworm composites with enhanced supercapacitor performance. RSC Adv 3:5851–5859. https://doi.org/10.1039/C3RA00151B

Luo Y, Zhang H, Guo D, Ma J, Li Q, Chen L, Wang T (2014) Porous $NiCo_2O_4$-reduced graphene oxide (rGO) composite with superior capacitance retention for supercapacitors. Electrochim Acta 132:332–337. https://doi.org/10.1016/j.electacta.2014.03.179

Luo Y, Yang T, Zhao Q, Zhang M (2017) CeO_2/CNTs hybrid with high performance as electrode materials for supercapacitor. J Alloys Compd 729:64–70. https://doi.org/10.1016/j.jallcom.2017.09.165

Luque A, Hegedus S (2003) Handbook of photovoltaic science and engineering, 2nd edn. Wiley, Hoboken

Ma J, Li C, Yu F, Chen J (2015) "Brick-like" N-doped graphene/carbon nanotube structure forming three-dimensional films as high performance metal-free counter electrodes in dye-sensitized solar cells. J Power Sources 273:1048–1055. https://doi.org/10.1016/j.jpowsour.2014.10.003

Mao M, Hu J, Liu H (2015) Graphene-based materials for flexible electrochemical energy storage. Int J Energy Res 39:727–740. https://doi.org/10.1002/er.3256

Mattevi C, Eda G, Agnoli S, Miller S, Mkhoyan KA, Celik O, Mastrogiovanni D, Granozzi G, Garfunkel E, Chhowalla M (2009) Evolution of electrical, chemical, and structural properties of transparent and conducting chemically derived graphene thin films. Adv Funct Mater 19:2577–2583. https://doi.org/10.1002/adfm.200900166

McEvoy AJ, Castañer L, Markvart T (2012) Solar cells: materials, manufacture and operation, 2nd edn. Elsevier, Oxford

Mink JE, Hussain MM (2013) Sustainable design of high-performance microsized microbial fuel cell with carbon nanotube anode and air cathode. ACS Nano 7:6921–6927. https://doi.org/10.1021/nn402103q

Murai S, Mikoshiba S, Sumino H, Hayase S (2002) Quasi-solid dye-sensitized solar cells containing chemically cross-liked gel: how to make gels with a small amount of gelator. J Photochem Photobiol A 148:33–39. https://doi.org/10.1039/B412462F

Nagaura T, Tozawa K (1990) Lithium ion rechargeable battery. In: Kozawa A (ed) Progress in batteries and solar cells, vol 9. JEC Press, Brunswick, pp 209–217 ISSN: 0198-7259

Naghavi N, Spiering S, Powalla M, Cavana B, Lincot D (2003) High-efficiency copper indium gallium diselenide (CIGS) solar cells with indium sulfide buffer layers deposited by atomic layer chemical vapor deposition (ALCVD). Prog Photovolt Res Appl 11:437–443. https://doi.org/10.1002/pip.508

Nandy A, Kumar V, Mondal S, Dutta K, Salah M, Kundu PP (2015) Performance evaluation of microbial fuel cells: effect of varying electrode configuration and presence of a membrane electrode assembly. New Biotechnol 32:272–281. https://doi.org/10.1016/j.nbt.2014.11.003

Nath BC, Gogoi B, Boruah M, Sharma S, Khannam M, Ahmed GA, Dolui SK (2014) High performance polyvinyl alcohol/multi walled carbon nanotube/polyaniline hydrogel (PVA/MWCNT/PAni) based dye sensitized solar cells. Electrochim Acta 146:106–111. https://doi.org/10.1016/j.electacta.2014.08.134

Nazri G-A, Pistoia G (eds) (2003) Lithium batteries: science and technology. Springer, Boston

Niu CM, Sichel EK, Hoch R, Moy D, Tennent H (1997) High power electrochemical capacitors based on carbon nanotube electrodes. Appl Phys Lett 70:1480–1482. https://doi.org/10.1063/1.118568

Oraon R, De Adhikari A, Tiwari SK, Bhattacharyya S, Nayak GC (2016) Hierarchical self-assembled nanoclay derived mesoporous CNT/polyindole electrode for supercapacitors. RSC Adv 6:64271–64284. https://doi.org/10.1039/C6RA12938B

Pan H, Li J, Feng YP (2010) Carbon nanotubes for supercapacitor. Nanoscale Res Lett 5:654–668. https://doi.org/10.1007/s11671-009-9508-2

Pandolfo AG, Hollenkamp AF (2006) Carbon properties and their role in supercapacitors. J Power Sources 157:11–27. https://doi.org/10.1016/j.jpowsour.2006.02.065

Papageorgiou N, Athanassov Y, Armand M, Bonhôte P, Pettersson H, Azam A, Grätzel M (1996) The performance and stability of ambient temperature molten salts for solar cell applications. J Electrochem Soc 143:3099–3108. https://doi.org/10.1149/1.1837171

Park S, Ruoff RS (2009) Chemical methods for the production of graphenes. Nat Nanotechnol 4:217–224. https://doi.org/10.1038/nnano.2009.58

Park C-M, Yoon S, Lee S-I, Kim J-H, Jung J-H, Sohn H-J (2007) High-rate capability and enhanced cyclability of antimony-based composites for lithium rechargeable batteries. J Electrochem Soc 154:A917–A920. https://doi.org/10.1149/1.2761829

Pech D, Brunet M, Durou H, Huang P, Mochalin V, Gogotsi Y, Taberna P-L, Simon P (2010) Ultrahigh-power micrometre-sized supercapacitors based on onion-like carbon. Nat Nanotechnol 5:651–654. https://doi.org/10.1038/nnano.2010.162

Peng Y-Y, Liu Y-M, Chang J-K, Wu C-H, Ger M-D, Pu N-W, Chang C-L (2015) A facile approach to produce holey graphene and its application in supercapacitors. Carbon 81:347–356. https://doi.org/10.1016/j.carbon.2014.09.067

Petnikota S, Marka SK, Banerjee A, Reddy MV, Srikanth VVSS, Chowdari BVR (2015) Graphenothermal reduction synthesis of 'exfoliated graphene oxide/iron (II) oxide' composite for anode application in lithium ion batteries. J Power Sources 293:253–263. https://doi.org/10.1016/j.jpowsour.2015.05.075

Planeix JM, Coustel N, Coq B, Brotons V, Kumbhar PS, Dutartre R, Geneste P, Bernier P, Ajayan PM (1994) Application of carbon nanotubes as supports in heterogeneous catalysis. J Am Chem Soc 116:7935–7936. https://doi.org/10.1021/ja00096a076

Prasad AM, Santhosh C, Grace AN (2012) Carbon nanotubes and polyaniline supported Pt nanoparticles for methanol oxidation towards DMFC applications. Appl Nanosci 2:457–466. https://doi.org/10.1007/s13204-012-0061-4

Prehn K, Warburg A, Schilling T, Bron M, Schulte K (2009) Towards nitrogen-containing CNTs for fuel cell electrodes. Compos Sci Technol 69:1570–1579. https://doi.org/10.1016/j.compscitech.2008.09.006

Pushparaj VL, Shaijumon MM, Kumar A, Murugesan S, Ci L, Vajtai R, Linhardt RJ, Nalamasu O, Ajayan PM (2007) Flexible energy storage devices based on nanocomposite paper. Proc Natl Acad Sci U S A 104:13574–13577. https://doi.org/10.1073/pnas.0706508104

Qi W, Li X, Wu Y, Zeng H, Kuang C, Zhou S, Huang S, Yang Z (2017) Flexible electrodes of MnO_2/CNTs composite for enhanced performance on supercapacitors. Surf Coat Technol 320:624–629. https://doi.org/10.1016/j.surfcoat.2016.10.038

Qiao Y, Li CM, Bao S-J, Bao Q-L (2007) Carbon nanotube/polyaniline composite as anode material for microbial fuel cells. J Power Sources 170:79–84. https://doi.org/10.1016/j.jpowsour.2007.03.048

Qin L, Liang S, Pan A, Tan X (2016) Zn_2SnO_4/carbon nanotubes composite with enhanced electrochemical performance as anode materials for lithium-ion batteries. Mater Lett 164:44–47. https://doi.org/10.1016/j.matlet.2015.10.125

Qu B, Xu Y-T, Lin S-J, Zheng Y-F, Dai L-Z (2010) Fabrication of Pt nanoparticles decorated Ppy-MWNTs composites and their electrocatalytic activity for methanol oxidation. Synth Met 160:732–742. https://doi.org/10.1016/j.synthmet.2010.01.012

Qu W-L, Gu D-M, Wang Z-B, Zhang J-J (2014) High stability and high activity Pd/ITO-CNTs electrocatalyst for direct formic acid fuel cell. Electrochim Acta 137:676–684. https://doi.org/10.1016/j.electacta.2014.06.064

Ramadoss A, Yoon K-Y, Kwak M-J, Kim S-I, Ryu S-T, Jang J-H (2017) Fully flexible, lightweight, high performance all-solid-state supercapacitor based on 3-Dimensional-graphene/graphite-paper. J Power Sources 337:159–165. https://doi.org/10.1016/j.jpowsour.2016.10.091

Ramli NIT, Rashid SA, Mamat MS, Sulaiman Y, Krishnan S (2018) Incorporation of iron oxide into CNT/GNF as a high-performance supercapacitor electrode. Mater Chem Phys 212:318–324. https://doi.org/10.1016/j.matchemphys.2018.03.044

Rao CNR, Maitra U, Matte HSSR (2012) Synthesis, characterization, and selected properties of graphene. In: Rao CNR, Sood AK (eds) Graphene: synthesis, properties and phenomena. Wiley-VCH Verlag GmbH & Co. KGaA, Weinheim, pp 1–47. https://doi.org/10.1002/9783527651122.ch1

Ravi S, Gopi CVVM, Kim HJ (2016) Enhanced electrochemical capacitance of polyimidazole coated covellite CuS dispersed CNT composite materials for application in supercapacitors. Dalton Trans 45:12362–12371. https://doi.org/10.1039/C6DT01664B

Razali MZ, Abdullah H, Asaahari I (2015) Morphological effect of CNT/TiO_2 nanocomposite photoelectrodes dye-sensitized solar cell on photovoltaic performance with various annealing temperatures. Int J Photoenergy 2015:501978 (1–12). https://doi.org/10.1155/2015/501978

Razykov TM, Ferekides CS, Morel D, Stefanakos E, Ullal HS, Upadhyaya HM (2011) Solar photovoltaic electricity: current status and future prospects. Sol Energy 85:1580–1608. https://doi.org/10.1016/j.solener.2010.12.002

Reddy ALM, Shaijumon MM, Gowda SR, Ajayan PM (2010) Multisegmented Au-MnO_2/carbon nanotube hybrid coaxial arrays for high-power supercapacitor applications. J Phys Chem C 114:658–663. https://doi.org/10.1021/jp908739q

Roy-Mayhew JD, Bozym DJ, Punckt C, Aksay IA (2010) Functionalized graphene as a catalytic counter electrode in dye-sensitized solar cells. ACS Nano 4:6203–6211. https://doi.org/10.1021/nn1016428

Saga T (2010) Advances in crystalline silicon solar cell technology for industrial mass production. NPG Asia Mater 2:96–102. https://doi.org/10.1038/asiamat.2010.82

Sankar KV, Selvan RK (2015) The ternary $MnFe_2O_4$/graphene/polyaniline hybrid composite as negative electrode for supercapacitors. J Power Sources 275:399–407. https://doi.org/10.1016/j.jpowsour.2014.10.183

Schopf D, Es-Souni M (2016) Supported porous carbon and carbon-CNT nanocomposites for supercapacitor applications. Appl Phys A 122:203 (1–7). https://doi.org/10.1007/s00339-016-9730-6

Scrosati B, Garche J (2010) Lithium batteries: status, prospects and future. J Power Sources 195:2419–2430. https://doi.org/10.1016/j.jpowsour.2009.11.048

Selvaraj V, Alagar M (2007) Pt and Pt-Ru nanoparticles decorated polypyrrole/multiwalled carbon nanotubes and their catalytic activity towards methanol oxidation. Electrochem Commun 9:1145–1153. https://doi.org/10.1016/j.elecom.2007.01.011

Sevilla M, Lota G, Fuertes AB (2007) Saccharide-based graphitic carbon nanocoils as supports for PtRu nanoparticles for methanol electrooxidation. J Power Sources 171:546–551. https://doi.org/10.1016/j.jpowsour.2007.05.096

Shao Y, Yin G, Gao Y, Shi P (2006) Durability study of Pt/C and Pt/CNTs catalysts under simulated PEM fuel cell conditions. J Electrochem Soc 153:A1093–A1097. https://doi.org/10.1149/1.2191147

Sharma T, Reddy ALM, Chandra TS, Ramaprabhu S (2008) Development of carbon nanotubes and nanofluids based microbial fuel cell. Int J Hydrog Energy 33:6749–6754. https://doi.org/10.1016/j.ijhydene.2008.05.112

Shi E, Zhang L, Li Z, Li P, Shang Y, Jia Y, Wei J, Wang K, Zhu H, Wu D, Zhang S, Cao A (2012) TiO_2-coated carbon nanotube-silicon solar cells with efficiency of 15%. Sci Rep 2:884 (1–5). https://doi.org/10.1038/srep00884

Shi E, Li H, Xu W, Wu S, Wei J, Fang Y, Cao A (2015) Improvement of graphene-Si solar cells by embroidering graphene with a carbon nanotube spider-web. Nano Energy 17:216–223. https://doi.org/10.1016/j.nanoen.2015.08.018

Shim M, Javey A, Kam NWS, Dai H (2001) Polymer functionalization for air-stable n-type carbon nanotube field-effect transistors. J Am Chem Soc 123:11512–11513. https://doi.org/10.1021/ja0169670

Shin DH, Seo SW, Kim JM, Lee HS, Choi S-H (2018) Graphene transparent conductive electrodes doped with graphene quantum dots-mixed silver nanowires for highly-flexible organic solar cells. J Alloys Compd 744:1–6. https://doi.org/10.1016/j.jallcom.2018.02.069

Singh PK, Kim K-W, Rhee H-W (2009) Ionic liquid (1-methyl 3-propyl imidazolium iodide) with polymer electrolyte for DSSC application. Polym Eng Sci 49:862–865. https://doi.org/10.1002/pen.21212

Singh KJ, Singh TJ, Chettri D, Sarkar SK (2017) A thin layer of carbon nano tube (CNT) as semi-transparent charge collector that improve the performance of the GaAs solar cell. Optik Int J Light Electron Opt 135:256–270. https://doi.org/10.1016/j.ijleo.2017.01.090

Sivakkumar SR, Kim D-W (2007) Polyaniline/carbon nanotube composite cathode for rechargeable lithium polymer batteries assembled with gel polymer electrolyte. J Electrochem Soc 154:A134–A139. https://doi.org/10.1149/1.2404901

Somani SP, Somani PR, Umeno M (2008) Carbon nanotube incorporation: a new route to improve the performance of organic-inorganic heterojunction solar cells. Diam Relat Mater 17:585–588. https://doi.org/10.1016/j.diamond.2008.01.084

Srinivas B, Balaji S, Babu MN, Reddy YS (2015) Review on present and advance materials for solar cells. Int J Eng Res 3:178–182 http://www.ijoer.in/Special%20Issue-Vol.3.Issue.1.2015/178-182%20B.SRINIVAS.pdf

Steele BCH, Heinzel A (2001) Materials for fuel-cell technologies. Nature 414:345–352. https://doi.org/10.1038/35104620

Stewart DA, Léonard F (2004) Photocurrents in nanotube junctions. Phys Rev Lett 93:107401 (1–4)

Sun T, Feng L, Gao X, Jiang L (2005) Bioinspired surfaces with special wettability. Acc Chem Res 38:644–652. https://doi.org/10.1021/ar040224c

Sun S, Gao L, Liu Y (2011a) Optimization of the cutting process of multi-wall carbon nanotubes for enhanced dye-sensitized solar cells. Thin Solid Films 519:2273–2279. https://doi.org/10.1016/j.tsf.2010.11.008

Sun Y, Wu Q, Shi G (2011b) Graphene based new energy materials. Energy Environ Sci 4:1113–1132. https://doi.org/10.1039/C0EE00683A

Sun L, Wang L, Tian C, Tan T, Xie Y, Shi K, Li M, Fu H (2012) Nitrogen-doped graphene with high nitrogen level via a one-step hydrothermal reaction of graphene oxide with urea for superior capacitive energy storage. RSC Adv 2:4498–4506. https://doi.org/10.1039/C2RA01367C

Tang D, Zhang W, Qiao Z-A, Liu Y, Wang D (2018) Polyanthraquinone/CNT nanocomposites as cathodes for rechargeable lithium ion batteries. Mater Lett 214:107–110. https://doi.org/10.1016/j.matlet.2017.11.119

Tao L, Zai J, Wang K, Zhang H, Xu M, Shen J, Su Y, Qian X (2012) Co_3O_4 nanorods/graphene nanosheets nanocomposites for lithium ion batteries with improved reversible capacity and cycle stability. J Power Sources 202:230–235. https://doi.org/10.1016/j.jpowsour.2011.10.131

Timmons D, Harris JM, Roach B (2014) The economics of renewable energy. Global Development and Environment Institute, Tufts University, Medford http://www.ase.tufts.edu/gdae/education_materials/modules/RenewableEnergyEcon.pdf

Tung VC, Allen MJ, Yang Y, Kaner RB (2009) High-throughput solution processing of large-scale graphene. Nat Nanotechnol 4:25–29. https://doi.org/10.1038/nnano.2008.329

Tzolov M, Chang B, Yin A, Straus D, Xu JM, Brown G (2004a) Electronic transport in a controllably grown carbon nanotube-silicon heterojunction array. Phys Rev Lett 92:075505 (1–4). https://doi.org/10.1103/PhysRevLett.92.075505

Tzolov MB, Chang B, Straus D, Yin A, Xu J (2004b) Carbon nanotube-silicon heterojunction diode array – integration on silicon and rectifying characteristics. Nontraditional Approaches to Patterning 141–143; Symposium on Nontraditional Approaches to Patterning held at the 2003 MRS Fall Meeting, Boston, MA, December 1–5, 2003

Van Noorden R (2011) Chemistry: the trials of new carbon. Nature 469:14–16. https://doi.org/10.1038/469014a

Vargas COA, Caballero Á, Morales J (2012) Can the performance of graphene nanosheets for lithium storage in Li-ion batteries be predicted? Nanoscale 4:2083–2092. https://doi.org/10.1039/C2NR11936F

Varzi A, Bresser D, von Zamory J, Müller F, Passerini S (2014) $ZnFe_2O_4$-C/$LiFePO_4$-CNT: a novel high-power lithium-ion battery with excellent cycling performance. Adv Energy Mater 4:1400054 (1–9). https://doi.org/10.1002/aenm.201400054

Wang W, Kumta PN (2010) Nanostructured hybrid silicon/carbon nanotube heterostructures: reversible high-capacity lithium-ion anodes. ACS Nano 4:2233–2241. https://doi.org/10.1021/nn901632g

Wang P, Zakeeruddin SM, Comte P, Exnar I, Grätzel M (2003) Gelation of ionic liquid-based electrolytes with silica nanoparticles for quasi-solid-state dye-sensitized solar cells. J Am Chem Soc 125:1166–1167. https://doi.org/10.1021/ja029294+

Wang C, Guo Z-X, Fu S, Wu W, Zhu D (2004) Polymers containing fullerene or carbon nanotube structures. Prog Polym Sci 29:1079–1141. https://doi.org/10.1016/j.progpolymsci.2004.08.001

Wang X, Li W, Chen Z, Waje M, Yan Y (2006) Durability investigation of carbon nanotube as catalyst support for proton exchange membrane fuel cell. J Power Sources 158:154–159. https://doi.org/10.1016/j.jpowsour.2005.09.039

Wang J, Xi J, Bai Y, Shen Y, Sun J, Chen L, Zhu W, Qiu X (2007) Structural designing of Pt-CeO_2/CNTs for methanol electro-oxidation. J Power Sources 164:555–560. https://doi.org/10.1016/j.jpowsour.2006.11.041

Wang X, Zhi L, Müllen K (2008a) Transparent, conductive graphene electrodes for dye-sensitized solar cells. Nano Lett 8:323–327. https://doi.org/10.1021/nl072838r

Wang X, Zhi L, Tsao N, Tomović Ž, Li J, Müllen K (2008b) Transparent carbon films as electrodes in organic solar cells. Angew Chem Int Ed 47:2990–2992. https://doi.org/10.1002/anie.200704909

Wang H, Hao Q, Yang X, Lu L, Wang X (2010) Effect of graphene oxide on the properties of its composite with polyaniline. ACS Appl Mater Interfaces 2:821–828. https://doi.org/10.1021/am900815k

Wang G, Zhang L, Zhang J (2012) A review of electrode materials for electrochemical supercapacitors. Chem Soc Rev 41:797–828. https://doi.org/10.1039/C1CS15060J

Wang L, Ye Y, Lu X, Wen Z, Li Z, Hou H, Song Y (2013a) Hierarchical nanocomposites of polyaniline nanowire arrays on reduced graphene oxide sheets for supercapacitors. Sci Rep 3:3568 (1–9). https://doi.org/10.1038/srep03568

Wang Y, Zhamu A, Jang BZ (2013b) Rechargable magnesium-ion cell having a high-capacity cathode. US Patent 2013/0302697

Wang L, Zhang H, Deng Q, Huang Z, Zhou A, Li J (2014) Superior rate performance of $Li_4Ti_5O_{12}$/TiO_2/C/CNTs composites via microemulsion-assisted method as anodes for lithium ion battery. Electrochim Acta 142:202–207. https://doi.org/10.1016/j.electacta.2014.07.072

Wang B, Qiu J, Feng H, Sakai E (2015) Preparation of graphene oxide/polypyrrole/multi-walled carbon nanotube composite and its application in supercapacitors. Electrochim Acta 151:230–239. https://doi.org/10.1016/j.electacta.2014.10.153

Weber AZ, Mench MM, Meyers JP, Ross PN, Gostick JT, Liu Q (2011) Redox flow batteries: a review. J Appl Electrochem 41:1137–1164. https://doi.org/10.1007/s10800-011-0348-2

Wei D, Kivioja J (2013) Graphene for energy solutions and its industrialization. Nanoscale 5:10108–10126. https://doi.org/10.1039/C3NR03312K

Wei JQ, Sun JL, Zhu JL, Wang KL, Wang ZC, Luo JB, Wu DH, Cao AY (2006) Carbon nanotube macrobundles for light sensing. Small 2:988–993. https://doi.org/10.1002/smll.200600191

Wei J, Jia Y, Shu Q, Gu Z, Wang K, Zhuang D, Zhang G, Wang Z, Luo J, Cao A, Wu D (2007) Double-walled carbon nanotube solar cells. Nano Lett 7:2317–2321. https://doi.org/10.1021/nl070961c

Wen Z, Wang X, Mao S, Bo Z, Kim H, Cui S, Lu G, Feng X, Chen J (2012) Crumpled nitrogen-doped graphene nanosheets with ultrahigh pore volume for high-performance supercapacitor. Adv Mater 24:5610–5616. https://doi.org/10.1002/adma.201201920

Wu M, Shaw LL (2005) A novel concept of carbon-filled polymer blends for applications in PEM fuel cell bipolar plates. Int J Hydrog Energy 30:373–380. https://doi.org/10.1016/j.ijhydene.2004.08.005

Wu GT, Wang CS, Zhang XB, Yang HS, Qi ZF, He PM, Li WZ (1999) Structure and lithium insertion properties of carbon nanotubes. J Electrochem Soc 146:1696–1701. https://doi.org/10.1149/1.1391828

Wu G, Chen Y-S, Xu B-Q (2005) Remarkable support effect of SWNTs in Pt catalyst for methanol electrooxidation. Electrochem Commun 7:1237–1243. https://doi.org/10.1016/j.elecom.2005.07.015

Wu J, Becerril HA, Bao Z, Liu Z, Chen Y, Peumans P (2008) Organic solar cells with solution-processed graphene transparent electrodes. Appl Phys Lett 92:263302 (1–3). https://doi.org/10.1063/1.2924771

Wu X-L, Guo Y-G, Su J, Xiong J-W, Zhang Y-L, Wan L-J (2013) Carbon-nanotube-decorated nano-$LiFePO_4$ @C cathode material with superior high-rate and low-temperature performances for lithium-ion batteries. Adv Energy Mater 3:1155–1160. https://doi.org/10.1002/aenm.201300159

Würfel P, Würfel U (2009) Physics of solar cells: from basic principles to advanced concepts. Wiley, Hoboken

Xia J, Chen F, Li J, Tao N (2009) Measurement of the quantum capacitance of graphene. Nat Nanotechnol 4:505–509. https://doi.org/10.1038/nnano.2009.177

Xiao Y, Lin J-Y, Wu J, Tai S-Y, Yue G, Lin T-W (2013) Dye-sensitized solar cells with high-performance polyaniline/multi-wall carbon nanotube counter electrodes electropolymerized by a pulse potentiostatic technique. J Power Sources 233:320–325. https://doi.org/10.1016/j.jpowsour.2013.01.116

Xiao X, Li T, Peng Z, Jin H, Zhong Q, Hu Q, Yao B, Luo Q, Zhang C, Gong L, Chen J, Gogotsi Y, Zhou J (2014) Freestanding functionalized carbon nanotube-based electrode for solid-state asymmetric supercapacitors. Nano Energy 6:1–9. https://doi.org/10.1016/j.nanoen.2014.02.014

Xiao L, Sehlleier YH, Dobrowolny S, Mahlendorf F, Heinzel A, Schulz C, Wiggers H (2017) Novel Si-CNT/polyaniline nanocomposites as lithium-ion battery anodes for improved cycling performance. Mater Today: Proc 4:S263–S268. https://doi.org/10.1016/j.matpr.2017.09.197

Xie X, Ye M, Hu L, Liu N, McDonough JR, Chen W, Alshareef HN, Criddle CS, Cui Y (2012) Carbon nanotube-coated macroporous sponge for microbial fuel cell electrodes. Energy Environ Sci 5:5265–5270. https://doi.org/10.1039/C1EE02122B

Xu K, Li Y, Yang F, Yang W, Zhang L, Xu C, Kaneko T, Hatakeyama R (2014) Controllable synthesis of single- and double-walled carbon nanotubes from petroleum coke and their application to solar cells. Carbon 68:511–519. https://doi.org/10.1016/j.carbon.2013.11.028

Xu D, Yu X, Gao D, Mu X, Zhong M, Yuan S, Xie J, Ye W, Huang J, Yang D (2016) Room-temperature processed, air-stable and highly efficient graphene/silicon solar cells with an organic interlayer. J Mater Chem A 4:11284–11291. https://doi.org/10.1039/C6TA03759C

Xuan H, Xu Y, Zhang Y, Li H, Han P, Du Y (2018) One-step combustion synthesis of porous CNTs/C/$NiMoO_4$ composites for high-performance asymmetric supercapacitors. J Alloys Compd 745:135–146. https://doi.org/10.1016/j.jallcom.2018.02.172

Xue Y, Liu J, Chen H, Wang R, Li D, Qu J, Dai L (2012) Nitrogen-doped graphene foams as metal-free counter electrodes in high-performance dye-sensitized solar cells. Angew Chem Int Ed 51:12124–12127. https://doi.org/10.1002/anie.201207277

Yadav A, Kumar P (2015) Enhancement in efficiency of PV cell through P&O algorithm. Int J Eng Res Technol 2:2642–2644

Yahikozawa K, Fujii Y, Matsuda Y, Nishimura K, Takasu Y (1991) Electrocatalytic properties of ultrafine platinum particles for oxidation of methanol and formic acid in aqueous solutions. Electrochim Acta 36:973–978. https://doi.org/10.1016/0013-4686(91)85302-N

Yan J, Uddin MJ, Dickens TJ, Okoli OI (2013) Carbon nanotubes (CNTs) enrich the solar cells. Sol Energy 96:239–252. https://doi.org/10.1016/j.solener.2013.07.027

Yang D, Bock C (2017) Laser reduced graphene for supercapacitor applications. J Power Sources 337:73–81. https://doi.org/10.1016/j.jpowsour.2016.10.108

Yang X, Guillorn MA, Austin D, Melechko AV, Cui H, Meyer HM III, Merkulov VI, Caughman JBO, Lowndes DH, Simpson ML (2003) Fabrication and characterization of carbon nanofiber-based vertically integrated Schottky barrier junction diodes. Nano Lett 3:1751–1755. https://doi.org/10.1021/nl0346631

Yang JE, Jang I, Kim M, Baeck SH, Hwang S, Shim SE (2013) Electrochemically polymerized vine-like nanostructured polyaniline on activated carbon nanofibers for supercapacitor. Electrochim Acta 111:136–143. https://doi.org/10.1016/j.electacta.2013.07.183

Yang Z, Huang Y, Hu J, Xiong L, Luo H, Wan Y (2018) Nanocubic $CoFe_2O_4$/graphene composite for superior lithium-ion battery anodes. Synth Met 242:92–98. https://doi.org/10.1016/j.synthmet.2018.05.010

Yao P-C, Hang S-T (2014) Enhancing photovoltaic performances of dye-sensitized solar cells by multi-layered nanostructured titanium oxide photoelectrode. Sol Energy 108:322–330. https://doi.org/10.1016/j.solener.2014.07.020

Yazami R, Reynier YF (2002) Mechanism of self-discharge in graphite-lithium anode. Electrochim Acta 47:1217–1223. https://doi.org/10.1016/S0013-4686(01)00827-1

Yen M-Y, Teng C-C, Hsiao M-C, Liu P-I, Chuang W-P, Ma C-CM, Hsieh C-K, Tsai M-C, Tsai C-H (2011) Platinum nanoparticles/graphene composite catalyst as a novel composite counter electrode for high performance dye-sensitized solar cells. J Mater Chem 21:12880–12888. https://doi.org/10.1039/C1JM11850A

Yen H-F, Horng Y-Y, Hu M-S, Yang W-H, Wen J-R, Ganguly A, Tai Y, Chen K-H, Chen L-C (2015) Vertically aligned epitaxial graphene nanowalls with dominated nitrogen doping for superior supercapacitors. Carbon 82:124–134. https://doi.org/10.1016/j.carbon.2014.10.042

Yi B, Chen X, Guo K, Xu L, Chen C, Yan H, Chen J (2011) High-performance carbon nanotube-implanted mesoporous carbon spheres for supercapacitors with low series resistance. Mater Res Bull 46:2168–2172. https://doi.org/10.1016/j.materresbull.2011.01.018

Yoshitake T, Shimakawa Y, Kuroshima S, Kimura H, Ichihashi T, Kubo Y, Kasuya D, Takahashi K, Kokai F, Yudasaka M, Iijima S (2002) Preparation of fine platinum catalyst supported on single-wall carbon nanohorns for fuel cell application. Physica B 323:124–126. https://doi.org/10.1016/S0921-4526(02)00871-2

Yu L, Tune DD, Shearer CJ, Shapter JG (2015) Application of polymer interlayers in silicon-carbon nanotube heterojunction solar cells. ChemNanoMat 1:115–121. https://doi.org/10.1002/cnma.201400005

Yuan CZ, Gao B, Shen LF, Yang SD, Hao L, Lu XJ, Zhang F, Zhang XG (2011) Hierarchically structured carbon-based composites: design, synthesis and their application in electrochemical capacitors. Nanoscale 3:529–545. https://doi.org/10.1039/C0NR00423E

Yuan H, Jiao Q, Zhang S, Zhao Y, Wu Q, Li H (2016a) In situ chemical vapour deposition growth of carbon nanotubes on hollow $CoFe_2O_4$ as an efficient and low cost counter electrode for dye-sensitized solar cells. J Power Sources 325:417–426. https://doi.org/10.1016/j.jpowsour.2016.06.052

Yuan W, Zhang Y, Cheng L, Wu H, Zheng L, Zhao D (2016b) The applications of carbon nanotubes and graphene in advanced rechargeable lithium batteries. J Mater Chem A 4:8932–8951. https://doi.org/10.1039/C6TA01546H

Yue G, Zhang W, Wu J, Jiang Q (2013) Glucose aided synthesis of molybdenum sulfide/carbon nanotubes composites as counter electrode for high performance dye-sensitized solar cells. Electrochim Acta 112:655–662. https://doi.org/10.1016/j.electacta.2013.09.019

Yue G, Liu X, Mao Y, Zheng H, Zhang W (2017) A promising hybrid counter electrode of vanadium sulfide decorated with carbon nanotubes for efficient dye-sensitized solar cells. Mater Today Energy 4:58–65. https://doi.org/10.1016/j.mtener.2017.03.007

Yun YS, Yoon G, Kang K, Jin H-J (2014) High-performance supercapacitors based on defect-engineered carbon nanotubes. Carbon 80:246–254. https://doi.org/10.1016/j.carbon.2014.08.063

Zhang L, Xia Z (2011) Mechanisms of oxygen reduction reaction on nitrogen-doped graphene for fuel cells. J Phys Chem C 115:11170–11176. https://doi.org/10.1021/jp201991j

Zhang Y, Ichihashi T, Landree E, Nihey F, Iijima S (1999) Heterostructures of single-walled carbon nanotubes and carbide nanorods. Science 285:1719–1722. https://doi.org/10.1126/science.285.5434.1719

Zhang X, Kumar PS, Aravindan V, Liu HH, Sundaramurthy J, Mhaisalkar SG, Duong HM, Ramakrishna S, Madhavi S (2012) Electrospun TiO_2-graphene composite nanofibers as a highly durable insertion anode for lithium ion batteries. J Phys Chem C 116:14780–14788. https://doi.org/10.1021/jp302574g

Zhang M, Zhao N, Li W, He C, Li J, Shi C, Liu E (2013) A novel synthesis of CNTs/TiO_2 nanocomposites with enhanced performance as photoanode of solar cell. Mater Lett 109:240–242. https://doi.org/10.1016/j.matlet.2013.07.036

Zhang BH, Yu F, Zhang L, Wang X, Wen Z, Wu YP, Holze R (2014a) $Na_{0.35}MnO_2$/CNT nanocomposite from a hydrothermal method as electrode material for aqueous supercapacitors. Z Anorg Allg Chem 640:2908–2913. https://doi.org/10.1002/zaac.201400344

Zhang M, Yan F, Tang X, Li Q, Wang T, Cao G (2014b) Flexible CoO-graphene-carbon nanofiber mats as binder-free anodes for lithium-ion batteries with superior rate capacity and cyclic stability. J Mater Chem A 2:5890–5897. https://doi.org/10.1039/C4TA00311J

Zhang S, Zhu L, Song H, Chen X, Zhou J (2014c) Enhanced electrochemical performance of MnO nanowire/graphene composite during cycling as the anode material for lithium-ion batteries. Nano Energy 10:172–180. https://doi.org/10.1016/j.nanoen.2014.09.012

Zhang K, Lee J-T, Li P, Kang B, Kim JH, Yi G-R, Park JH (2015) Conformal coating strategy comprising N-doped carbon and conventional graphene for achieving ultrahigh power and cyclability of $LiFePO_4$. Nano Lett 15:6756–6763. https://doi.org/10.1021/acs.nanolett.5b02604

Zhang Y, Ju P, Zhao C, Qian X (2016) In-situ grown of MoS_2/RGO/MoS_2@Mo nanocomposite and its supercapacitor performance. Electrochim Acta 219:693–700. https://doi.org/10.1016/j.electacta.2016.10.072

Zhao H, Yang J, Li L, Li H, Wang J, Zhang Y (2009) Effect of over-oxidation treatment of Pt-Co/polypyrrole-carbon nanotube catalysts on methanol oxidation. Int J Hydrog Energy 34:3908–3914. https://doi.org/10.1016/j.ijhydene.2009.02.079

Zhao X, Hayner CM, Kung MC, Kung HH (2011) Flexible holey graphene paper electrodes with enhanced rate capability for energy storage applications. ACS Nano 5:8739–8749. https://doi.org/10.1021/nn202710s

Zhao H, Pan L, Jin J, Li L, Xu J (2012) PtCo/polypyrrole-multiwalled carbon nanotube complex cathode catalyst containing two types of oxygen reduction active sites used in direct methanol fuel cells. Fuel Cells 12:876–882. https://doi.org/10.1002/fuce.201100194

Zhao D, Zhao Y, Zhang X, Xu C, Peng Y, Li H, Yang Z (2013) Application of high-performance MnO_2 nanocomposite electrodes in ionic liquid hybrid supercapacitors. Mater Lett 107:115–118. https://doi.org/10.1016/j.matlet.2013.05.053

Zhou X, Zou Y, Yang J (2014) Periodic structures of Sn self-inserted between graphene interlayers as anodes for Li-ion battery. J Power Sources 253:287–293. https://doi.org/10.1016/j.jpowsour.2013.12.034

Zhu J, Zhang G, Yu X, Li Q, Lu B, Xu Z (2014) Graphene double protection strategy to improve the SnO_2 electrode performance anodes for lithium-ion batteries. Nano Energy 3:80–87. https://doi.org/10.1016/j.nanoen.2013.10.009

Chapter 3
Nanostructured Materials for Li-Ion Battery Applications

Pushpendra Kumar, Pravin K. Dwivedi, Poonam Yadav, and Manjusha V. Shelke

Contents

P. Kumar · P. K. Dwivedi · P. Yadav · M. V. Shelke (✉)
Polymer and Advanced Materials Laboratory, Physical & Material's Chemistry Division, CSIR-National Chemical Laboratory, Pune, India
e-mail: mv.shelke@ncl.res.in

R. Saravanan et al. (eds.), *Emerging Nanostructured Materials for Energy and Environmental Science*, Environmental Chemistry for a Sustainable World 23,
https://doi.org/10.1007/978-3-030-04474-9_3

Abstract As a consequence to the remarkable development of the science and technology, an exponential demand for energy leads to the exploitation of nonrenewable energy sources including fossil fuel paves the way to stern environmental crises. Global warming is one of the principal threats, due to the accumulation of greenhouse gases, resulting from the use of fossil fuels. Because of limited availability, the fossil fuels have been rapidly exhausting, compelling researchers to accelerate the search for environment-friendly, renewable, and sustainable energy sources like the solar cell, wind, and electrochemical energy storage systems. Electrochemical energy storage systems (EESs), more specifically rechargeable batteries and supercapacitors being efficient alternatives, have attracted tremendous attention. Rechargeable batteries not only serve as energy storage devices but also capable of providing the dispatchable energy for transportation, i.e., electrical vehicles (EVs and hybrid EVs).

Although LIBs possess energy densities higher than those of the conventional batteries, their lower power densities and poor cycling lives are critical challenges for their applications in electric vehicles (EVs) and grid-scale storage. The present book chapter is an attempt to provide a detailed description of several aspects of the development of Li-ion battery, i.e., preferred electrode (cathode as well as the anode) materials, separators, electrolyte media, and their additives with associated challenges. This chapter spotlights the mechanism for Li-ion storage (lithiation/delithiation processes) with various vital parameters that determine the overall performance of a battery including the shape and size of electrode materials. The recent advancement in designing several nanostructures for high-energy electrodes are highlighted in detail.

3.1 Introduction

The ever-increasing energy demands continuously stimulate enormous depletion of fossil fuels. The emergent need of renewable, safer, and sustainable energy resources is considered as one of the primary issues. Production and storage of renewable energy to control the global warming while effectively containing the emission of greenhouse gases are widely discussed topics. As a result, solar, water, wind, and geothermal energies are being considered as potential resources for renewable energy to replace the existing use of fossil fuels. Conversely, these resources for renewable energy are also constrained by several climate conditions. Thus, sustainable, safer, and economical energy conversion and storage have become an important research area from the last 20 years. Additionally, with the revolution in portable digital electronics, safer, sustainable, and high-energy storage systems are in great demand. EESs, (i.e., rechargeable batteries) which are not only capable of energy storing but also can provide detachable energy sources for transportation such as electrical vehicles (EVs) and hybrid EVs (HEVs), have received significant attention (Dunn et al. 2011; Banerjee and Dutta 2016; Mukhopadhyay and Jangid 2018; Etacheri et al. 2011; Lowe et al. 2010). Recently, a large number of studies have been devoted to understand and manipulate the electrochemical properties of these EESs and to enhance the specific capacity of the potential electrode materials for them.

Rechargeable batteries such as lead-acid batteries have long been used to power stationary as well as mobile electronics and automobiles (Armand and Tarascon 2008; Yang et al. 2011; Ruetschi 1977). An EES (i.e., rechargeable or secondary battery), including Li-ion, Li-S, Li-O_2, Na-ion, Na-S, Li-O_2, Mg-ion, Mg-S, Al-ion, etc., can reversibly convert electrical and chemical energy via redox reactions as a consequence of storing the energy in the form of chemical potential. Since the introduction of first commercial rechargeable Li-ion battery (LIB) in 1991 by SONY, it has established as one of the most effective electrochemical devices for energy storage. In the last two decades, with the emergence of portable, digital electronics including mobile phones and laptop computers, rechargeable batteries (specifically Li-ion) have progressed rapidly with improved energy density and cyclability (Ruetschi 1977; Larcher and Tarascon 2014; Aurbach et al. 2007; Soloveichik 2011).Therefore, rechargeable batteries including Li-ion (Owen 1997; Nitta et al. 2015; Goodenough 2013), Na-ion (Yabuuchi et al. 2014; Han et al. 2015; Slater et al. 2012), Mg-ion (Aurbach et al. 2007; Saha et al. 2014; Huie et al. 2015), and Al-ion (Li and Bjerrum 2002; Lin et al. 2015) based on insertion/extraction or intercalation/deintercalation mechanism of the respective ions in electrodes have increasingly being researched. However, Na, Mg, and Al (−2.71, −2.37, and −1.66 V vs. standard hydrogen electrode (SHE), respectively) possess lesser reducing effect as well as low gravimetric capacities (1165, 2046, and 2978 $mAhg^{-1}$, respectively) as compared with −3.04 V, 3850 mAh g^{-1} of lithium (Li). Therefore, devices based on metals other than Li (e.g., Na, Mg, or Al) anodes suffer lower operating voltages and insignificant energy densities (Slater et al. 2012; Saha et al. 2014; Li and Bjerrum 2002). Similarly, a cathode with high electrochemical potential can be utilized to fabricate a device with superior energy density when assembled

with a high capacity anode as the overall energy/power density of a device is evaluated based on the specific capacity of electrode materials and the working voltage (differential electrochemical potentials between the cathode and anode) (Goodenough 2013; Goodenough and Park 2013). Favorable crystal structures of electrode materials with significant mobile ion-storing sites are the required properties to fabricate a stable and high-energy device (Han et al. 2015; Whittingham 2004). Therefore, the fabrication of electrode materials with desirable architectures and optimized properties has proven to be an effective way leading to anticipated rechargeable batteries. Nanostructured materials have adequately addressed the critical issues, e.g., capacity fading and stability. The nanostructures promise to facilitate large surface area that provides more reaction sites while shortening the diffusion distance for lithium ions during the insertion/extraction (Bruce et al. 2008; Kumar et al. 2016). As a result, shorter Li-ion diffusion route reduces the energy consumption and internal resistance. The proposed mechanism by Kumar and Hu (2018) provides detailed insights to understand the stability of the nanostructure while providing the higher specific capacity.

This chapter covers substantial scientific developments and key technological challenges for the commercialization of LIBs including performance characteristics and topical advancement of several cathodes as well as anode materials. Although the development of nanostructured electrode materials still faces some challenges such as poor rate performance, low cycling stability, and energy density, it has been regarded as the most promising alternatives to replace current commercially available state-of-the-art electrodes. The cost reduction and availability of electrode materials to design the futuristic cells with theoretical aspects are discussed in detail.

3.1.1 Working Principle and Configuration of Rechargeable Batteries

Even after significant advancement, the basic configuration of a rechargeable battery remained unchanged (Akira 2012). Rechargeable batteries consist of two electrodes, "anode" and "cathode," separated by an insulating polymer membrane called "separator" while immersed in an electrolyte. A typical representation of a rechargeable or secondary battery is shown in Fig. 3.1. The redox reactions at the electrode-electrolyte interface and the metal-ion diffusion (Li-ion for the present case) for conventional batteries are quite similar, yet there are notable differences between them. In typical conventional or sometimes termed as galvanic batteries, the redox reactions progressed simultaneously with the declining or evolving electrode surfaces, without affecting the chemical composition or solid-state mass diffusion (Bottone 2010). On the contrary, a heterogeneous redox reaction takes place in

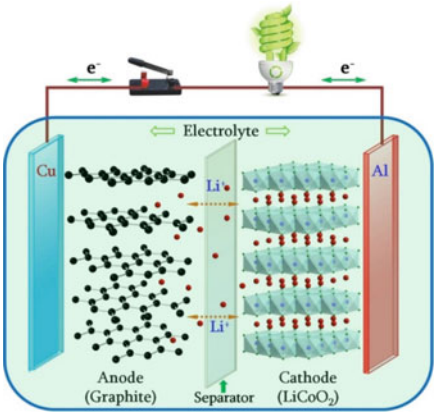

Fig. 3.1 The schematic representation of chargeable Li-ion battery in a full-cell configuration. (This figure was obtained from Liu et al. 2016a; https://doi.org/10.1016/j.mattod.2015.10.009)

Li-ion batteries supplemented by solid-state mass diffusion as well as volume change of electrode surfaces.

In LIBs, Li-ions are responsible for all electrochemical conversion, transferred forth and back between electrodes (anode and cathode) through separator membrane in electrolyte media, leaving their concentration almost constant irrespective of the degree of charge/discharge, while varies at the cathode and anode with the charge/discharge states. In general practice, the electrode materials either cathode or anode are tested concerning the metallic Li which is called half-cell configuration of a battery. In a half-cell configuration (electrode either cathode or anode material vs. metallic lithium), during the charging process, Li-ions are extracted from the electrodes and deposited to the lithium surface while inserted into the host electrode during discharge. However, in a full-cell configuration, Li-ions are extracted from the cathode and inserted into the anode during the charging process, and reverse phenomenon takes place during discharge.

3.2 Electrode Materials

Based on the Li-ion storage mechanism and subsequent electrochemical reactions, the electrode materials can be broadly categorized into three types: (1) insertion or intercalation/deintercalation electrode such as graphite, $LiCoO_2$, and V_2O_5 (Goriparti et al. 2014; Martin et al. 1999; Wang and Cao 2006); (2) alloying-type electrodes like silicon (Si) and tin (Sn) (Obrovac and Chevrier 2014; Wu and Cui 2012; Zhang et al. 2015b); and (3) conversion electrodes, e.g., CuO and SnO_2 (Goriparti et al. 2014). For a detailed understanding, a schematic is presented in Fig. 3.2.

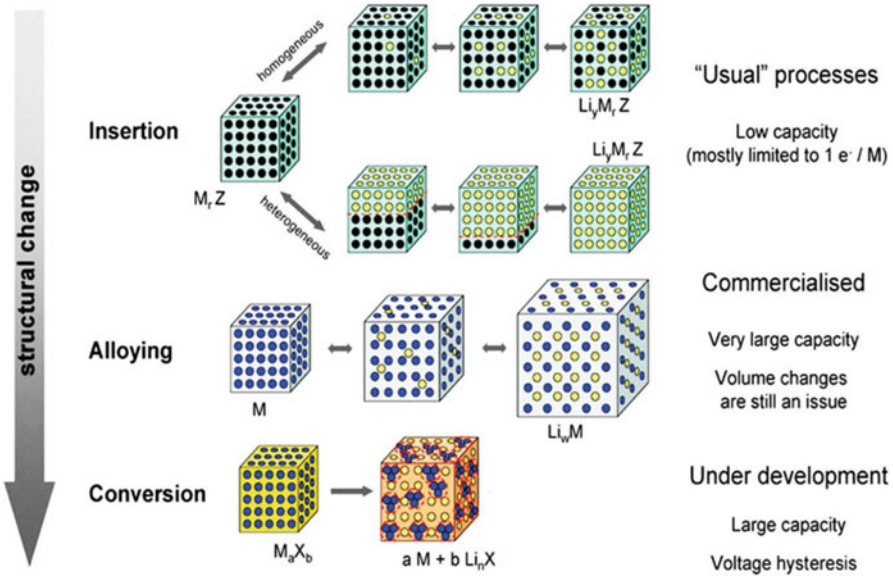

Fig. 3.2 A schematic representation of the different reaction mechanisms, namely, (1) insertion, (2) alloying, and (3) conversion observed in electrode materials for Li-ion batteries. Black circles represent the voids in the crystal structure; blue corresponds to metal and yellow dots for lithium. (This figure was obtained from Palacin 2009; https://doi.org/10.1039/B820555H)

3.2.1 Insertion/Extractions or Intercalation/Deintercalation Electrodes

It is well known that the Li-ion batteries are very aggressive/explosive due to the use of metallic Li and highly inflammable electrolytes while abused or mishandled. The stability of LIBs greatly depends on the thermodynamic stability of electrodes as well as electrolytes. Thus, careful selection of all necessary components (electrodes and electrolytes) to operate at adequate voltage windows promises enhanced safety. Intercalation/deintercalation is defined as the reversible mechanism of a molecule (or ion) into materials with layered structures. Based on ease of insertion/extractions or intercalation/deintercalation mechanism, anodes, such as graphite (Noel and Suryanarayanan 2002; Roberts et al. 2014), and cathodes, including $LiCoO_2$ (Antolini 2004), V_2O_5 (Martin et al. 1999), and $LiFePO_4$ (Wang and Sun 2015; Yuan et al. 2011), are widely used for LIB application. Insertion/extractions of Li-ion at inherited vacancies in electrode structure called as intercalation result in superior rate capability, improved cyclic life, better stability, and safer battery operation (Biao et al. 2015; Licht et al. 2016). For intercalation, the host electrode must provide sufficient sites to facilitate Li as well as multivalent ions for a balanced reaction to take place. The transition metal alloys with layered, spinel, or olivine structures are most commonly and widely used host for Li-ion intercalation

(Whittingham 2004; Koksbang et al. 1996). All three basic components (a cathode, an anode, and an electrolyte) are crucial in determining the overall performance of a rechargeable LIB. Intercalation/insertion processed either through heterogeneous insertion where potential remains unchanged during the reaction or via homogenous insertion when composition and voltage change simultaneously provides superior structural stability with faster kinetics (Palacin 2009). Though homogeneous or heterogeneous intercalation is not an intrinsic property of any electrode, it can be bartered by amending the ion ordering or controlling the size of the host materials (Gibot et al. 2008). Intercalation is more obvious in cathode materials; however, carbon- and titanium (Ti)-based materials serving as anodes also undergo similar reaction (Wang et al. 2009b; Youn et al. 2016; Zhang et al. 2016). Carbon- and Ti-based anodes are reported to provide faster Li-ion intercalation by conducting Li-ions unidirectionally while keeping the structures/volume almost unchanged due to their open framework (Tang et al. 2015). These systems offer limited capacities because of finite sites available for ion accommodation, as only one electron can be stored per ionic center (Martin et al. 1999). The governing factors for Li-ion storage through intercalation in electrodes are (i) the availability of sites to accommodate Li-ions, (ii) the capability of the host electrode to change the valence states, and (iii) the reversibility of host materials for Li-ion intercalation/deintercalation. Most commonly used intercalation cathodes include lithium iron phosphate ($LiFePO_4$), lithium cobalt oxide ($LiCoO_2$), lithium nickel cobalt manganese oxide ($LiNiMnCoO_2$), lithium nickel cobalt aluminum oxide ($LiNiCoAlO_2$) as cathode, and lithium titanium oxide ($Li_4Ti_5O_{12}$) as an anode.

3.2.2 *Alloying Electrodes*

Li metal is one of the highly reactive materials and can alloy with different metals and semimetals. During the alloying process, insertion/extraction of Li into the crystal structure of the electrodes takes places. As a result, phase change of the host material after lithiation takes place as presented below:

$$\mathrm{Li} + \mathrm{xM} \Leftrightarrow \mathrm{LiM_x} \tag{3.1}$$

where M represents the metals/semimetals and LiM_x is entirely different from the parent phase of the host materials. As a result of lithiation, substantial volume expansion (more than 100% of lithiated materials) takes place which is a drawback of this reaction (Wu and Cui 2012; Zhang et al. 2013b). Li-ion insertion/extraction in the metals like Si, Ge, Al, Sn, Sb, etc., chalcogenides (S, Se, Te,), and metal halides (F, Cl, Br, I) takes place through the alloying process. Alloying systems are considered as the most promising electrodes for next-generation LIB application due to their exceptionally high specific capacity such as alloying with Si which can deliver up to 8.5 Ah cm^{-1} or 4.2 Ah g^{-1} (Higgins et al. 2016), lower cost, and safer operation potentials. However, practical utilization of alloying electrodes in LIBs is

primarily hindered by the several inherent disadvantages including short cycle life due to volume expansion during Li-ion insertion with high irreversible capacity (Minsub et al. 2015), e.g., the lithium alloying with Si and Sn results in 300–400% volume increase based on the number of atoms/ions participated yielding the formation of $Li_{4.4}Sn$ and $Li_{4.4}Si$ and poor cyclic life (Klavetter et al. 2015). Due to their low cost, natural abundance, and high theoretical capacities, numerous efforts have been devoted in fabricating alloying-based electrode (Pharr et al. 2016) while improving their stability and cyclability without compromising the overall capacity (Anton et al. 2016; Tadhg et al. 2016). Keeping in mind that alloying highly active material with less or inactive systems can significantly reduce volume expansion, Si and Sn composites are being used as potential and safer anodes possessing better rate performance and extended cyclic life. Recently, nanostructures of some of the well-known transition metal chalcogenide (TMCs) including MoS_2, WS_2, VS_2, VSe_2, VSe_4, cobalt sulfide, cobalt selenide, etc. and their composites had attracted tremendous attention due to their unmatched physical/chemical properties with diverse potential applications including energy storage (Kumar et al. 2016; Kumar and Hu 2018). A comparative study on LIB performance of TMCs and their composites has been summarized by Kumar and Hu in a recent report (Kumar and Hu 2018). Among several, cobalt selenides, a crucial, half-metallic metal chalcogenide, exhibiting various phases (e.g., $CoSe_2$, CoSe and $Co_{0.85}Se$, Co_3Se_4, Co_2Se_3, and Co_9Se_8 (Kumar and Hu 2018), has been reported as potential anode materials for LIB application with significantly low volume expansion and irreversibility as compared to other alloying materials.

3.2.3 Conversion Electrodes

Mostly, transition metal compounds with compositional formulation M_aX_b, (where M = metal, X = O, S, F, P, N, etc.) are classified as conversion-type electrodes. During conversion reactions, the electrode materials get reduced by Li-ions (metals are reduced to their zero oxidation state) delivering an excellent capacity, followed by the equation:

$$M_a + X_b + zLi \rightarrow M_0 + yLi_{\frac{a}{b}}X \tag{3.2}$$

During discharge, conversion anodes, e.g., metal oxides (M_xO_y), react with Li-ions and get reduced to M_0 forming metal nano-domains distributed in the Li_2O matrix. While during charging, M_0 oxidizes and develops a metal oxide (M_xO_y) (Rowsell et al. 2001).

Generally, metal oxides serve as conversion anode, while metal fluorides behave like conversion cathodes (Li et al. 2012a; Wang et al. 2010a). Even though conversion-type electrodes provide higher specific capacity and energy density, they suffer with poor cycle life because of limited irreversibility due to significant

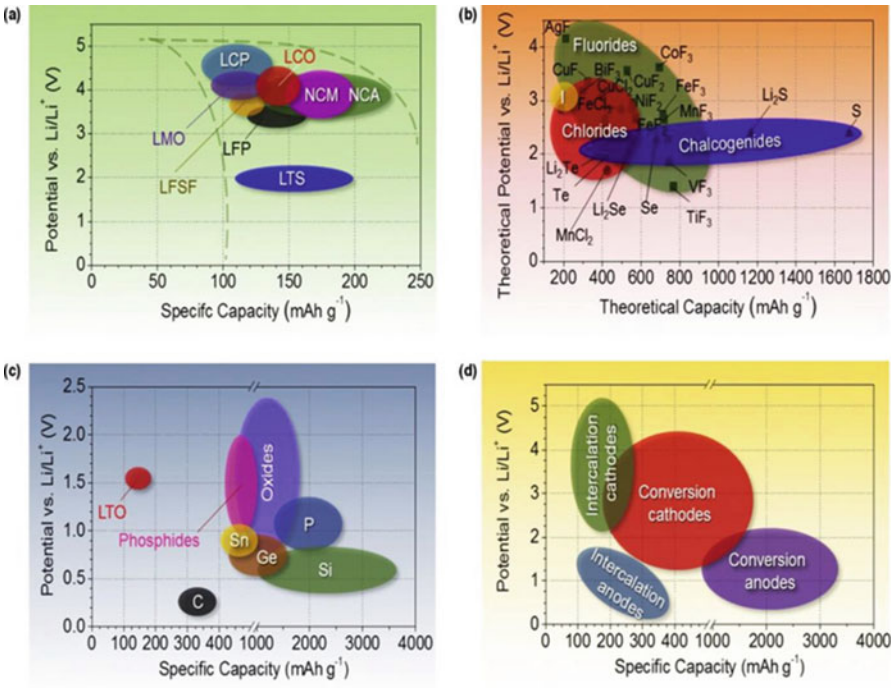

Fig. 3.3 (**a**) Intercalation-type cathodes (experimental), (**b**) conversion-type cathodes (theoretical), (**c**) conversion-type anodes (experimental), and (**d**) an overview of the average discharge potentials and specific capacities for all types of electrodes. (This figure was obtained from Nitta et al. 2015; https://doi.org/10.1016/j.mattod.2014.10.040)

voltage hysteresis (Aricò et al. 2005; Li et al. 2016). During cycling the said voltage hysteresis increases resulting in poor energy efficiency (Taberna et al. 2006). For few initial cycles, voltage hysteresis is more prominent as the crystallinity plays a critical role (Khatib et al. 2013) and, however, decreases as cycling progresses due to the formation of amorphous phase as a result of oxidation of M_aX_b (G. Gallagher et al. 2013).

Recently, doping M_aX_b with highly conductive metals or introducing conductive matrix as well as the development of nanostructured electrode has been reported to boost the overall performance of the battery. Considerable research attention has been dedicated in achieving superior specific capacity and excellent cyclability with improved high rate performance (Bonaccorso et al. 2015; Liu et al. 2014a; Mai et al. 2014; Uchaker and Garcia 2014; Whittingham 2014). Detailed information illustrating average electrode potential, theoretical/experimental specific capacity, and energy density of various cathodes, as well as anodes and their combinations, are summarized in Fig. 3.3. Furthermore, the selection of suitable current collector, preferable additives, and favorable electrolytes for the desired electrode materials cans also be carried out from Fig. 3.3.

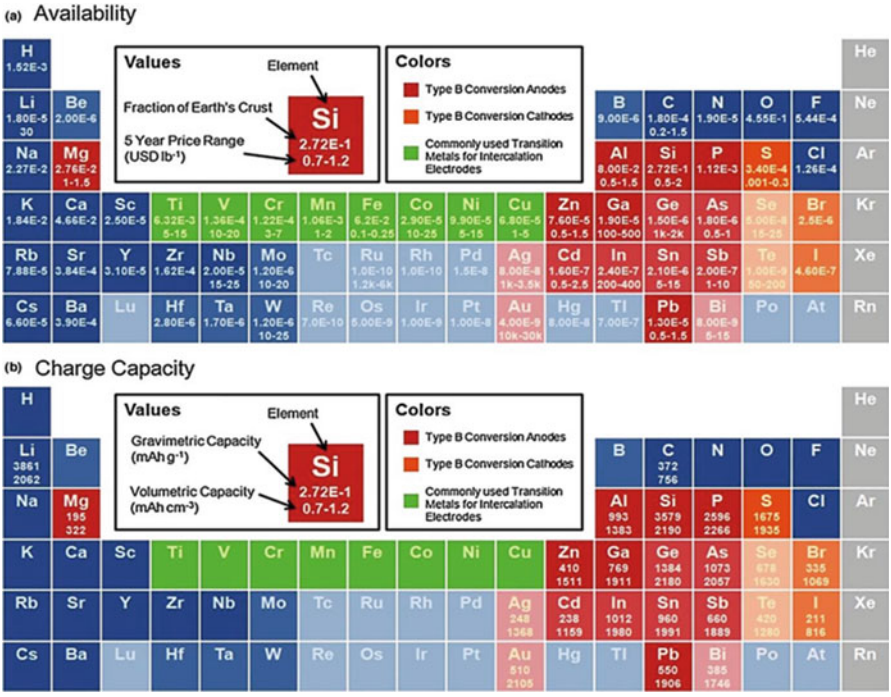

Fig. 3.4 (**a**) Availability and (**b**) capacities of elements that may host Li as electrodes for a rechargeable Li-ion battery application. (This figure was obtained from Nitta et al. 2015; https://doi.org/10.1016/j.mattod.2014.10.040)

Figure 3.4 provides the detailed information on the availability and price as well as the volumetric and gravimetric capacity of various materials suitable for Li-ion battery application. The information of cell voltage and electrochemical potentials of electrodes can provide better insight for designing and fabricating batteries with high-energy density fulfilling the futuristic energy needs.

3.2.4 Cell Voltage or Potential Window of a Battery

The operating voltage of a battery (cell voltage) is usually determined by the whole system, including the anode, cathode, and electrolyte. The evaluation of the cell voltage is rather straightforward and simple; it is defined by the difference of chemical potentials between anode and cathode, also termed as the open-circuit voltage, V_{OC} (Goodenough and Park 2013; Yuan et al. 2011):

$$V_{OC} = V_{Anode} - \frac{V_{Cathode}}{P_e} \tag{3.3}$$

where V_{Anode} is the voltage of anode, $V_{Cathode}$ is the voltage of cathode, and P_e represents the magnitude of the electronic charge. However, the open-circuit voltage, V_{OC}, is limited by the potential window of the electrolyte. Therefore, the selection of electrolyte compatible to electrodes is equally important and crucial to fabricate a stable, longer life battery device. Improper selection of the electrolyte may lead to electrolyte reduction on the anode or oxidation on the cathode resulting in the formation of parasitic solid electrolyte interphase (SEI) film (Goodenough and Kim 2010; Nazri and Pistoia 2003) which may hinder the overall performance while increasing the internal resistance of the battery. The SEI film is also known to consume part of the Li-ions participating in the electrochemical reaction for battery operation leading to capacity and power loss (Park 2012). Nevertheless, it is worth noticing that the SEI layer promotes Li-ion diffusion through it, at a constant electric field, and helps to reduce the over potential (Park 2012). Thus, the SEI film not only inhibits the aggregation of the electrochemically active participant but also supports maintaining a constant chemical composition at the electrode surfaces. Recently, SEI layer has been reported efficiently preventing the exfoliation of graphite during the lithium ion intercalation/deintercalation (Agubra and Fergus 2014).

3.2.5 *Potential Hysteresis*

The potential hysteresis is one of the most common phenomena observed during battery operation and persists in all charge/discharge measurements of electrodes. During a complete charge-discharge cycle, the energy consumed during charging is slightly higher than conveyed during discharge which is the source of the potential gap and commonly termed as potential hysteresis between the charge-discharge curves.

A representative schematic of potential hysteresis for a rechargeable battery during charge-discharge process, assembled with an ideal intercalation electrode material, is depicted in Fig. 3.5 (Liu et al. 2016a). The observed electrochemical potential is a result of the energy difference from phase transitions during the charge-discharge operation. The observed potential hysteresis can be explained in two ways:

1. Goodenough and co-worker postulated that the higher charge potential than discharge (as shown in Fig. 3.5a) is due to the polarization resulting from the internal resistance of the electrode materials (Goodenough and Park 2013). Goodenough et al. also observed further that the polarization decreases the discharge potential below V_{OC} and vice versa to reverse the chemical reaction. Additionally, the authors concluded that the internal resistance drop (IR drop)

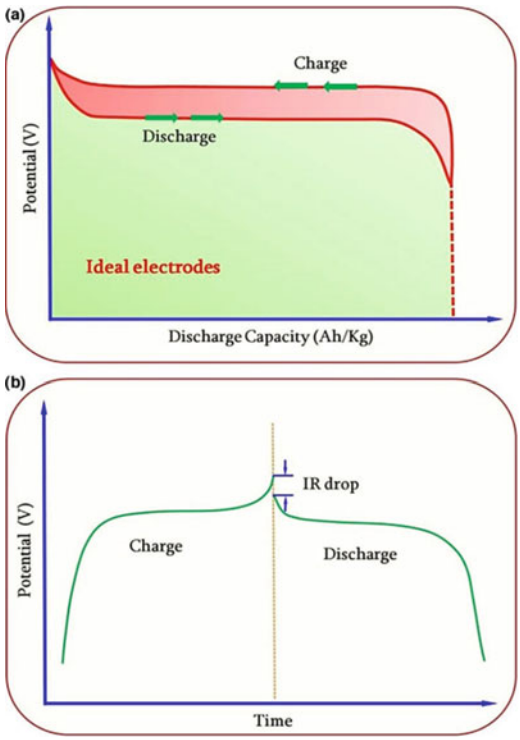

Fig. 3.5 (**a**) Schematic of potential hysteresis during charge/discharge procedure and (**b**) illustration of the potential drop in the interval between charge and discharge. (This figure was obtained from Liu et al. 2016a; https://doi.org/10.1016/j.mattod.2015.10.009)

also contributes to the potential reduction during charge-discharge process more specifically at the end of charging and the beginning of discharge as shown in Fig. 3.5b.

2. Others believe that the overpotential is the critical factor getting inspired from electrochemical phase transitions in insertion-type electrodes (Tang et al. 2010). As is well accepted, the phase transitions during charging are accomplished by extracting the Li-ions from the host lattice while balancing the electrochemical reaction by draining the electrons from the "d" orbitals of transition metal ions. Reversible reaction takes place during the discharge process; the Li-ions and electrons are implanted back to their relative lattice positions and electronic orbitals. However, noticeable change in the resultant energy difference during this reversible phase transition is observed. The mechanism can be justified by considering that during discharge, Li-ions are accommodated to the interstitial sites of the host lattice while transferring the balance electrons to the transition metal's "d" orbital, resulting in the lower energy and phase stabilization. However, during charging, in a reverse process, higher energy is consumed as ions and electrons have to be stimulated from the lower-energy states.

The main reason for IR drop is the change of internal resistance including resistance from electrode materials and electrolyte media. As IR drop comprises energy, this leads to a drop in the battery efficiency and releases heat that may cause

safety concerns. However, these issues can be hampered or eliminated by adopting effective approaches including conductive coating (Su et al. 2011).

3.3 Selection of Electrode Materials and Current Collectors

The selection of active electrode materials and appropriate current collector is made concerning several prospects of LIB including technical, economic, and societal.

3.3.1 Electrode Materials

For the choice of electrode materials, an element or compound must be naturally abundant, eco-friendly, and recyclable as well as suitable for industrial applications with low cost. Along with this, ideal electrode materials must retain a competitively high reversible storage capacity at the anticipated potential window. Detailed information on the specific capacity, availability, and cost of various materials suitable for Li-ion battery application is already discussed and tabulated in Fig. 3.4 (Nitta et al. 2015). The calculation of theoretical capacity of an electrode material can be made based on the number of electrons participating in the reaction and the molar weight of the electrode materials and can be expressed by the equation as below (Zhi et al. 2013):

$$C_t = \frac{nF}{3.6} \times M \tag{3.4}$$

where C_t is theoretical capacity, n stands for the number of reactive electrons per unit formula, M represents the molar weight of active materials, and F is the Faraday constant. The electrons participating in the electrochemical reaction are directly correlated with the number of Li-ions hosted by the electrode. Furthermore, this equation provides information that lesser molecular weight providing more sites to accommodate higher number of electrons per formula unit can result in higher theoretical capacity (Nitta et al. 2015). Even though lighter elements are always a preferred choice for electrodes because of their higher specific capacities, the selection of transition metal oxides as cathodes is also incomparable because of their variable valence electron-storing sites (Nitta et al. 2015).

3.3.2 Current Collectors

A typical Li-ion battery is composed of positive and negative electrodes (the cathode and the anode) (Wagemaker and Mulder 2013; Tang et al. 2015; Goodenough and Park 2013; Vanchiappan et al. 2015) which are in the form of thin film, sandwiching an electrically insulating porous polypropylene separator membrane in a

nonaqueous, organic electrolyte media containing Li salts as presented in Fig. 3.1. The desired active (electrode) materials possessing diffusion channels for Li-ions are applied (coated) on the current collectors in the form of thin films. Al metal foil is a most common choice as the current collector for the positive electrode (cathode) and Cu foil for the negative electrode (anode) (Myung et al. 2011; Sa and Wang 2012; Kim et al. 2008; Guo et al. 2010). During the battery operation, Li-ions migrate from the cathode to the anode and vice versa, via electrolyte media through separator on the application of potential difference between the positive and negative electrodes. It has recently been proved that the current collectors play an extremely crucial role in the overall performance and safety of rechargeable LIB technology (Sa and Wang 2012; Kim et al. 2008; Guo et al. 2010). Inherited physical-chemical properties of a current collector can have a deep impact on the performance of LIBs. Ideally, a current collector must be chemically and electrochemically stable during charge-discharge process between certain potential windows of the active electrode when in contact with the cell components. Selection of diverse current collectors may result in significant variation in the overall performances of the battery (Sa and Wang 2012; Kim et al. 2008; Guo et al. 2010).

The inappropriate choice may result in the corrosion of current collector materials at a certain electrochemical potential during battery operation. There are several reports stating corrosion of the current collectors, as the degradation of battery components is preordained over long-term use. It is well understood that the chemical composition and additives of electrolytes have a profound effect on the overall cell performance including cyclability, rate capability, capacity retention, and stability of the battery. Widely used lithium hexafluorophosphate ($LiPF_6$), lithium nitrate ($LiNO_3$), lithium bis(trifluoromethylsulfonyl)imide (LiTFSI, $LiN(SO_2CF_3)_2$), etc. may have an adverse effect on the stability of the current collectors. For example, the presence of a minimal amount of water in commercial LiPF6 accelerates its decomposition even at elevated temperatures (>40 °C) or at high potentials (>4 V vs. Li/Li^+) because of the production of HF as a by-product (Myung et al. 2011; Aurbach 1989). Thus, formed HF reacts with the positive electrodes and causes poor cell performance and unstable system while rusting the current collector. Corrosion of the current collector leads to the increase in internal resistance, resulting in gradual capacity fade, instability of the battery, and sometimes short circuits. However, there are strategies to minimize the abovementioned risks, including the coating of a protective, conductive, thick, passive layer on the current collector (metal) surface. Depending on the active battery components (including electrolyte salts and additives), different types of conductive, passivating films can be coated to protect the current collector against corrosion. In recent years, along with the traditionally used (Cu and Al) current collectors, several conductive, i.e., two-dimensional (2-D) planar and three dimensional (3-D) porous substrates have been successfully used as the efficient current collectors to construct a battery with superior stability and enhanced performance (Whitehead and Schreiber 2005). Customized design of a current collector can also play a crucial role in restricting corrosion (Wang et al. 2017).

3.4 State-of-the-Art Cathode Designing

3.4.1 Bulk Cathode

In general bulk materials are prepared by solid-state reaction at higher temperatures. The thermodynamically more stable microcrystalline material is obtained adopting this reaction mechanism. Due to undesired aspect ratio, low surface-to-volume ratio, and substantial Li-ion diffusion path length in the solid electrode, bulk materials are not suitable for high rate capability and stability. By decreasing the average diffusion path length and keeping the mass constant, the surface area of the electrode can be increased; current density can be lowered. Because of this, concentration polarization can be delayed, and rate capability can be improved. So, different nanostructured materials came into the picture.

3.4.2 Families of Cathode Materials

In Li-ion battery, Li-ion is the guest, and cathode acts as solid host network. How many Li-ions can be hosted by cathode material decides the storage capacity of the cathode material. Structure/morphology and operating potential of the cathode are two crucial parameters which determine the battery performance. Structure/morphology determines the cyclic stability. Energy stored in the Li-ion battery depends upon the potential operating limit. Mainly cathode material's operating potential is the limiting factor for high-energy density. Starting from the use of TiS_2 by Whittingham and Thompson (1975), more promising $LiCoO_2$ by Mizushima et al. (1980), to $LiNi_{0.8}Co_{0.15}Al_{0.05}O_2$ Ohzuku and Makimura (2001a), many materials have been explored to extend the upper limit of operating potential of the cathode and, in turn, the energy stored in the battery.

3.4.2.1 Layered Compounds

Layered compounds with the formula $LiMO_2$ (M= Co, Ni, Mn) are the most widely used cathode, and $LiCoO_2$ were first commercialized by Sony in 1990 (Nishi 2001). At higher temperature, $LiCoO_2$ forms layered trigonal phase which shows better electrochemical performance in comparison to low-temperature cubic phase (Czyżyk et al. 1992). The unit cell of $LiCoO_2$ consists of three layers of CoO_6 octahedra (transition metal layer or TM layer) separated by interstitial layers of Li (as shown in Fig. 3.6). With the removal of Li from the crystal structure, the material forms a nonstoichiometric compound. Due to structural limitation, only 50% of total Li can be extracted.

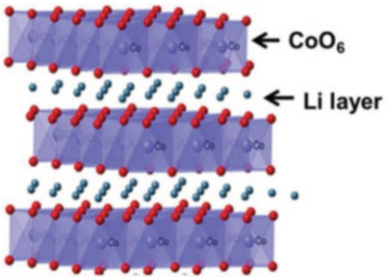

Fig. 3.6 Structure of layered $LiCoO_2$ cathode. (This figure was obtained from Daniel et al. 2014; https://doi.org/10.1063/1.4878478)

This structural instability leads to the maximum practical capacity of 140 mAh/g in comparison to the theoretical capacity of about 280 mAh/g. The specific capacity calculation is shown in the following equations using the example of $LiCoO_2$:

$$LiCoO_2 \leftrightarrow xLi^+ + xe^- + Li_{1-x}CoO_2$$

$$C_{specific} = \frac{xF}{M} = \frac{1^*\left(96485\frac{C}{mol}\right)}{1^*\left(98\frac{g}{mol}\right)*3.6} = 273 \ \ mAhg^{-1}(For \ \ x = 1)$$

Due to structural limitation and the high cost of Co, $LiNiO_2$ (isostructural to $LiCoO_2$) came in to picture. Even though $LiNiO_2$ was cheaper and has high capacity, reproducibility in the synthesis was an issue as the migration of Li into TM layer was unavoidable (Dahn et al. 1990). Ozhuku et al. put forwarded another approach by forming $LiNi_{0.5}Mn_{0.5}O_2$, and it showed the capacity of 200 mAh/g with operating potential in the range of 3.6–4.3 V (Ohzuku and Makimura 2001b). However, detailed characterization reveals that the Li-ion migration into TM layer, and the presence of Ni ions in the Li-ion later leads to the blocking of lithium diffusion. Similar ionic radii of Li and Ni ions were the reason for the Li/Ni ion migration. Further Ozhuku reported oxide with three transition metals in equal amount with the composition $LiCo_{1/3}Ni_{1/3}Mn_{1/3}O_2$. This compound showed a capacity of 160 mAh/g in the range of 2.5 V–4.4 V and 200 mAh/g in the range of 2.8–4.6 V. Elemental doping such as Al, Fe, Zr cation, and F-anion doping can reduce the cation mixing in layered oxide cathodes. In this direction, $LiNi_xCo_yAl_{1-x-y}O_2$ is another very promising material for high capacity (Nitta et al. 2015).

3.4.2.2 Spinel

Compared to layered oxide materials, spinel $LiMn_2O_4$ compounds are cheaper and environment-friendly (Thackeray et al. 1983). Structure of $LiMn_2O_4$ is shown in Fig. 3.7. Unique framework of MnO_6 octahedra provides 3-D diffusion pathway for Li-ion migration which in turn gives excellent rate capability. But the dissolution of Mn^{+3} in the electrolyte by H^+corrosion and formation of Mn^{+2} and Mn^{+4} by

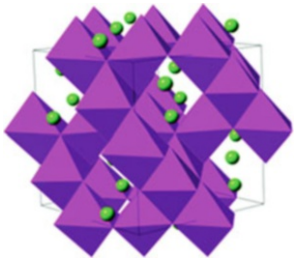

Fig. 3.7 Structure of spinel $LiMnO_4$ cathode. (This figure was obtained from Islam and Fisher 2014; https://doi.org/10.1039/C3CS60199D)

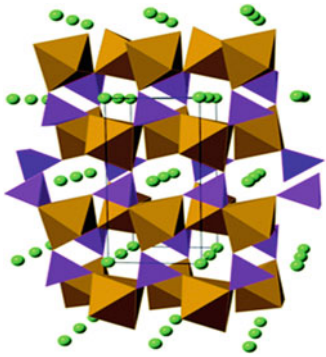

Fig. 3.8 Structure of olivine $LiFePO_4$ cathode. (This figure was obtained from Islam and Fisher 2014; https://doi.org/10.1039/C3CS60199D)

disproportionation reaction lead to capacity fading at elevated temperature (Aurbach et al. 1999). Doping with other metal cations such as Ni, Mg, and Al was expected to suppress the Mn dissolution. In this direction, materials like $LiNi_{0.5}Mn_{1.5}O_4$ came into the picture. The $LiNi_{0.5}Mn_{1.5}O_4$ showed the capacity of 140 mAh/g which is close to its theoretical capacity of 147 mAh/g (Gummow et al. 1994). Ni doping widens the operating potential up to 4.7 V.

3.4.2.3 Olivine

$LiFePO_4$ is a typical example of an olivine-type compound. It has many merits like high capacity, low volume expansion, and low capacity fading. Structure of $LiFePO_4$ is shown in Fig. 3.8. One FeO_6 octahedra share edge with two LiO_6 octahedra and one PO_4 tetrahedron. $LiFePO_4$ shows functional capacity near to theoretical capacity of 170 mAh/g with flat discharge plateau around 3.4 V. Due to the close hexagonal packing of oxygen atoms, there is slow 1-D Li-ion diffusion which leads to low conductivity (Chung et al. 2002). Mainly three approaches used to improve the conductivity of $LiFePO_4$ are: reduction of particle/grain size (Herle et al. 2004), application of a conductive layer on $LiFePO_4$ particles (Zaghib et al. 2008), and doping of Fe with other elements (Sobkowiak et al. 2013). $LiMnPO_4$ and $LiCoPO_4$ are other examples of olivine-type structure.

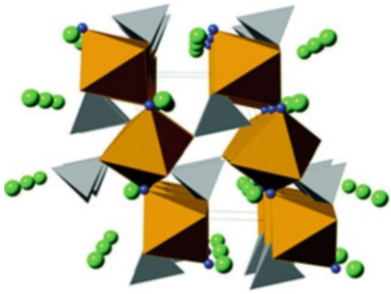

Fig. 3.9 Structure of tavorite $LiFeSO_4F$ cathode. (This figure was obtained from Islam and Fisher 2014; https://doi.org/10.1039/C3CS60199D)

Table 3.1 Providing the information about crystal structure, capacity, and voltage of different cathodes

Crystal structure	Compound	Specific capacity($mAhg^{-1}$) (C^{th}/C_{exp})	Voltage(V)
Layered	$LiCoO_2$	274/148	3.8
	$LiNiO_2$	275/150	3.8
	$LiMnO_2$	285/140	3.3
	$LiNi_{0.33}Mn_{0.33}Co_{0.33}O_2$	280/160	3.7
	$LiNi_{0.8}Co_{0.15}Al_{0.05}O_2$	279/199	3.7
Spinel	$LiMn_2O_4$	148/120	4.1
	$LiCo_2O_4$	142/84	4.0
Olivine	$LiFePO_4$	170/165	3.4
	$LiMnPO_4$	171/168	3.8
	$LiCoPO_4$	167/125	4.2
Tavorite	LiFeSO4F	151/120	3.7

This table was obtained from Nitta et al. (2015); https://doi.org/10.1016/j.mattod.2014.10.040

3.4.2.4 Tavorite

$LiFeSO_4F$ is the example of tavorite-type cathode material (Sobkowiak et al. 2013). It has high cell voltage and better conductivity with reasonable specific capacity. The structure consists of distorted $Fe^{2+}O_4F_2$ oxyfluoride octahedra connected by F vertices in the transposition (Fig. 3.9). Tavorite structure shows 1-D diffusion channel with low activation energy which leads to charge and discharges at very high rates. Comparison of performance of different nanostructured cathode materials is presented in Table 3.1.

Regardless of the development of different cathodes, there are still many issues like structural stability, lower rate capability, and low capacity in comparison to anode materials. Several material design strategies have been introduced like size reduction, surface coatings, core-shell structure and hierarchical structure, and mixed strategies.

3.4.3 Nanostructured Cathodes

To improve the electrochemical properties of cathode, materials with different dimensions such as 0-D, 1-D, 2-D, and 3-D have been utilized.

3.4.3.1 0-D Nanoparticles

Synthesis approaches like grinding, hot-injection, and sol-gel have been used to prepare nanoparticles in the nano-regime. Reduction in size can reduce the diffusion path length and increases the electrode/electrolyte contact area. Gaberscek et al. concluded that the decrease in particle size leads to the increase in the capacity of $LiFePO_4$ (Gibot et al. 2008). Nanosized $LiFePO_4$ is more structurally stable to anti-site defects. Morphology and stability of $LiFePO_4$ are shown in Fig. 3.10a–c. In case of $LiNi_{0.5}Mn_{1.5}O_4$, ordered spinel structure found to favor stability, and showed good rate capability. Structure and electrochemical performance of $LiNi_{0.5}Mn_{1.5}O_4$ are shown in Fig. 3.10d–f (Zhang et al. 2013c).

3.4.3.2 1-D Nanowires/Nanorods

One-dimensional nanostructures like nanowires, nanorods, and nanotubes have been explored widely due to fast electron transfer along one direction and short diffusion path length along that direction. Hosono et al. (2009) reported single crystalline $LiMn_2O_4$ nanowires (Fig. 3.11a, b) with high temperature stability and excellent battery performance at higher current density. It was found that the nanowire structure resists the aggregation and grain growth at a higher temperature. Single crystalline $LiMn_2O_4$ showed flat discharge plateau, and higher stability reason may be clean facet planes in nanowire morphology than $LiMn_2O_4$ nanorod morphology. The capacity reported was 118 $mAhg^{-1}$ at 0.1 Ag^{-1} (Fig. 3.11c). Another nanowire-structured cathode FeF_3 was reported by (Li et al. 2012b) for the first time by dehydrating the α-$FeF_3 \cdot 3H_2O$ precursor NWs. FeF_3 showed first discharge capacity of 543 $mAhg^{-1}$ and 223 $mAhg^{-1}$ after 20 cycles at 50 mAg^{-1}. Higher capacity is attributed to higher surface area and favorable morphology to accommodate the strain developed during the charge-discharge process.

Ding et al. (2011a) reported $LiMn_2O_4$ nanotubes with 600 nm diameter and 1–4 μm length. $LiMn_2O_4$ nanotubes were synthesized by chemically transforming self-sacrificial [001]-oriented α-MnO_2 template to [110]-oriented $LiMn_2O_4$. Electrochemical performance was studied, and first discharge capacity was found to be 115 $mAhg^{-1}$. The $LiMn_2O_4$ nanotubes exhibited high rate performance showing 94% capacity retention at 3C rate for 100 cycles and 80% capacity retention at 5C

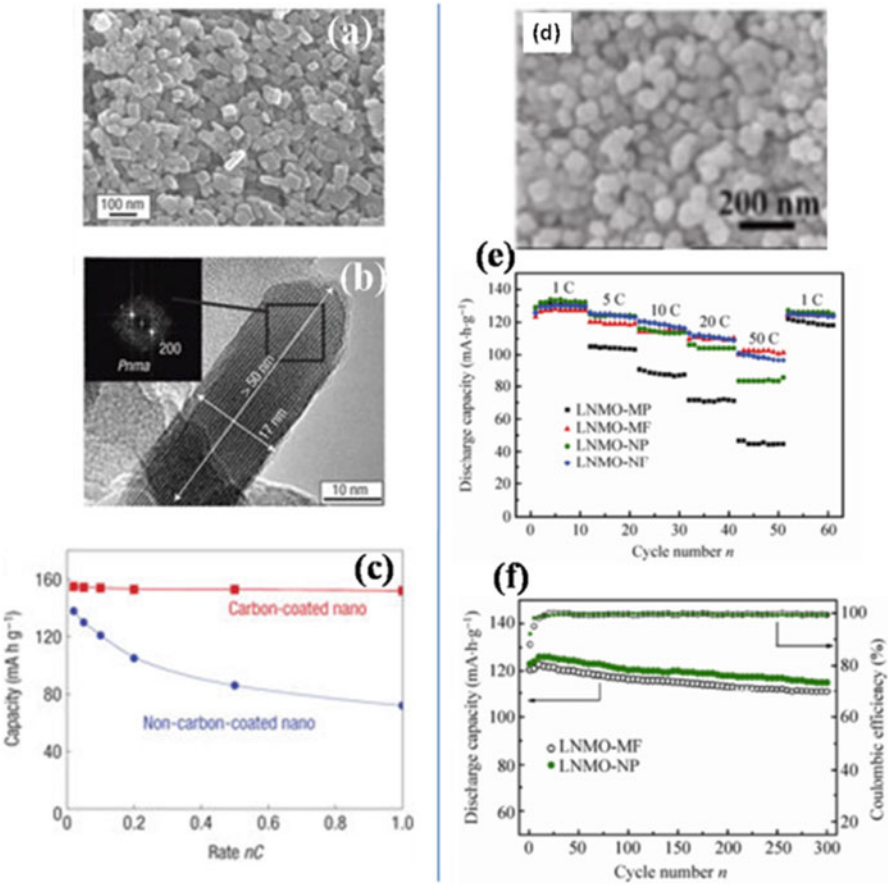

Fig. 3.10 (**a**–**c**) $LiFePO_4$ morphology and electrochemical performance. ((**a**–**c**) was obtained from Gibot et al. 2008; https://www.nature.com/articles/nmat2245), $LiNi_{0.5}Mn_{1.5}O_4$ (**d**–**f**) morphology, and electrochemical performance. ((**d**–**f**) was obtained from Yang et al. 2013; https://doi.org/10.1007/s12274-013-0343-5)

rate for another 100 cycles (Fig. 3.11d–f). Zhang et al. (2013c) reported one-dimensional porous $LiNi_{0.5}Mn_{1.5}O_4$ nanorods. The porous $LiNi_{0.5}Mn_{1.5}O_4$ delivered the capacities of 140 and 109 mAh g^{-1} at 1 and 20 °C rates, respectively (Fig. 3.11i). Capacity retention of 91% was obtained at 5C rate after 500 cycles. The excellent performance can be attributed to the porous 1-D channel morphology that can accommodate strain relaxation by slippage at the subunit wall boundaries and provide short Li-ion diffusion distance along the confined dimension.

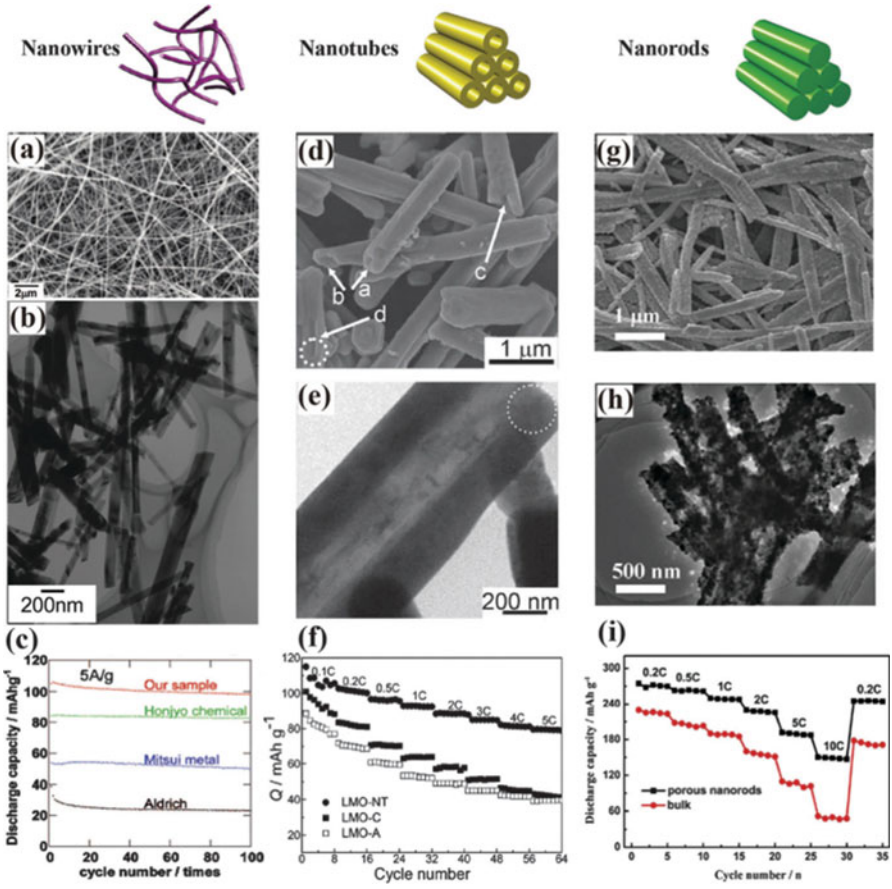

Fig. 3.11 (**a–c**) $LiMn_2O_4$ nanowire. ((**a–c**) was obtained from Hosono et al. 2009; https://pubs.acs.org/doi/abs/10.1021/nl803394v), (**d–f**) $LiMn_2O_4$ nanotubes. ((**d–f**) was obtained from Yuan-Li et al. 2010; https://doi.org/10.1002/adfm.201001448), (**g–i**) $0.2Li_2MnO_3.0.8LiNi_{0.5}Mn_{0.5}O_2$ nanorods. ((**g–i**) was obtained from Zhang et al. 2013c; https://pubs.acs.org/doi/abs/10.1021/nl401072x)

3.4.3.3 2-D Nanosheets/Nanoplates

Sheets which possess thicknesses on the order of nanometers and lateral dimensions of submicro- to micrometers are called as a new class of two-dimensional (2-D) materials (Zhang et al. 2013c). They are material of interest owing to their exotic electronic properties and high specific surface areas compared with the corresponding bulk materials. It was proven by simulation and experiments that Li-ions can diffuse along (010) plane or b-axis in orthorhombic crystal structure of $LiMPO_4$. So, ultrathin 2-D $LiMPO_4$ (M = Fe, Mn, Co) nanosheets with exposed facets have been explored and found to be very promising materials in terms of Li-ion insertion/extraction mechanism at higher rates (Rui et al. 2013) (Fig. 3.12).

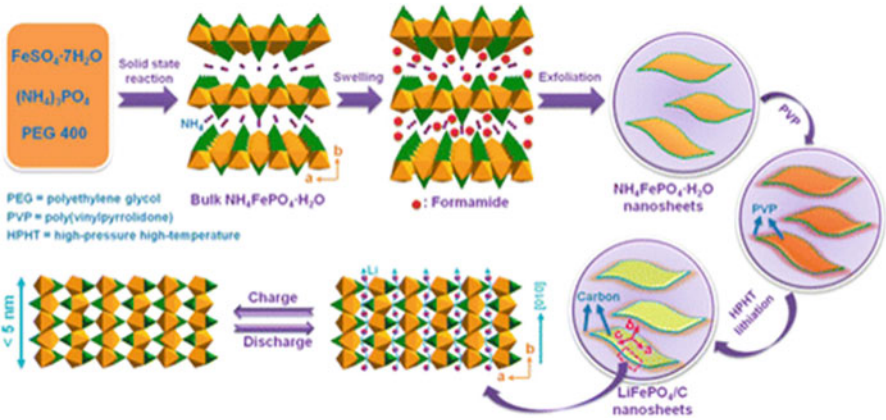

Fig. 3.12 Synthesis and crystal structure of olivine-type $LiFePO_4$. (This figure was obtained from Rui et al. 2013; https://pubs.acs.org/doi/abs/10.1021/nn4022263)

The nanosheets $LiFePO_4$, $LiMnPO_4$, and $LiCoPO_4$ showed fast lithium transport. The estimated diffusion time for Li^+ over a [010] thickness of <5 nm was calculated to be less than 25, 2.5, and 250 μs for $LiFePO_4$, $LiMnPO_4$, and $LiCoPO_4$ nanosheets, respectively. The values are about five orders of magnitude lower than the corresponding bulk materials. The authors further synthesize $LiFePO_4$/C, $LiMnPO_4$/C, and $LiCoPO_4$/C nanosheets delivering initial discharge capacities of 164, 157, and 153 mAh g^{-1} and reversible capacities of 163, 147, and 136 $mAhg^1$ after 50 cycles at 0.2C rate. However, the bulk counterparts showed lower initial discharge capacity values of 134, 130, and 124 $mAhg^{-1}$, respectively. The difference can be related to the much longer diffusion distance for the Li-ion and electron transportation in the bulk. High electrochemical performance in 2-D materials can be assigned to large surface area exposed to the electrolyte, better interface, and interlayer spaces to accommodate volume expansion and faster charge transfer kinetics.

3.4.3.4 3-D Hierarchical Structure

Although 0-D, 1-D, and 2-D materials showed good electrochemical performance, some issues like low packing density and several side reactions remain the problem. By assembling hollow nanoparticles, $LiNi_{0.5}Mn_{1.5}O_4$ microspheres and microcubes have been successfully synthesized. The 3-D hollow structures delivered a discharge capacity of 118 $mAhg^{-1}$ at 1C and 104 $mAhg^{-1}$ at 20C. Core-shell structure is another promising example of 3-D nanostructured cathodes. The core plays a role in Li insertion and extraction, and the shell helps in providing structural integrity. Carbon-coated $LiMn_2O_4$ clusters consisting of many single-crystal nanoparticles have shown ultrahigh rate capability. Morphology and stability of Li $[Ni_{0.60}Co_{0.15}Mn_{0.25}]O_2$ are shown in Fig. 3.13a–c. found to favor stability, and showed good rate capability. Structure and electrochemical performance of $LiMn_{0.85}Fe_{0.15}PO_4$ are shown in Fig. 3.13d, e (Zhang et al. 2013c).

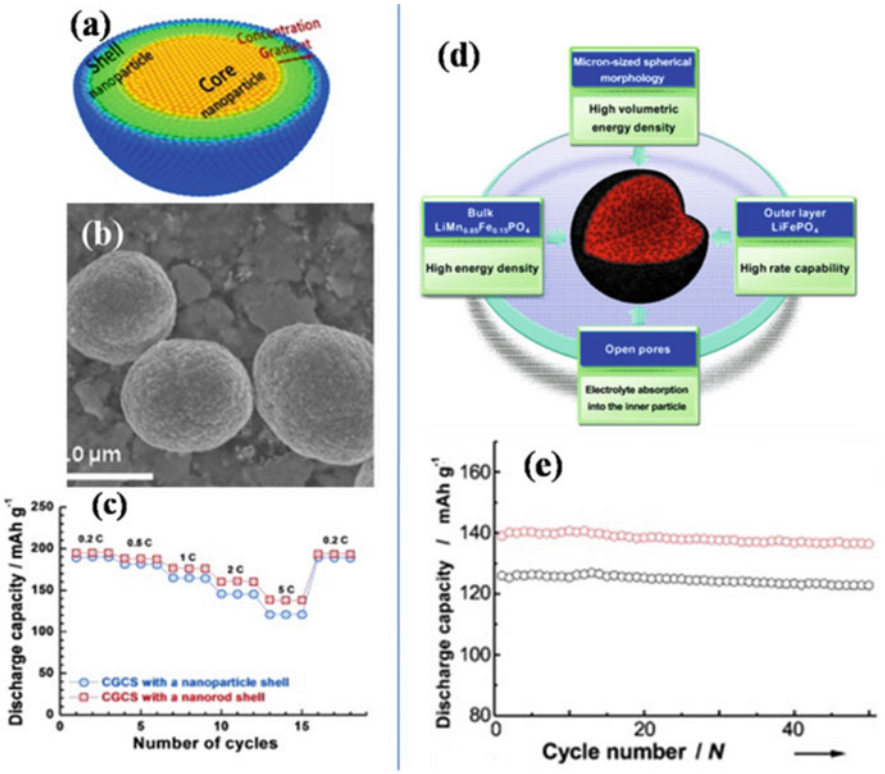

Fig. 3.13 (**a**–**c**) Morphology and electrochemical performance of $Li[Ni_{0.60}Co_{0.15}Mn_{0.25}]O_2$. ((**a**–**c**) was obtained from Yoon et al. 2014; https://doi.org/10.1002/cssc.201402389), (**d**–**e**) $LiMn_{0.85}Fe_{0.15}PO_4$. ((**d**, **e**) was obtained from Oh et al. 2012; https://doi.org/10.1002/anie.201107394)

3.5 State-of-the-Art Anode Designing

The selection of anode materials for the LIB application mostly depends on crystal structure and inherited properties including specific capacity, electrical conductivity, intercalation, reversibility, mechanical stability, etc. Size and shape of electrode materials are also critical parameters which affect the LIB performance. Diffusivity is the crucial factor responsible for lithiation/delithiation kinetics of electrode material, which is related to the Li-ion diffusion coefficient (D_{Li}) and diffusion path length L_{ion}. In an indirect way, diffusivity or diffusion length (τ) is represented as (Bruce et al. 2008):

$$\tau = \frac{Li_{ion}^2}{D_{Li}}$$

where L_{ion} is the diffusion length and depends upon the material size and D_{Li} is the diffusion coefficient and relies on the nature of the material. For example, rutile TiO_2 with low diffusion coefficient of 1015 cm^2 s^{-1} is believed to accommodate a negligible amount of Li-ions at room temperature. However, significant changes can be observed for 5–15-nm-sized rutile TiO_2 nanoparticles with full loading of lithium (x >1 in Li_xTiO_2) and about 0.7 Li per rutile TiO_2 insertion-extraction in subsequent cycles (Hu et al. 2006; Jiang et al. 2006).

3.5.1 Li Metal Anode

Li metal anode has long been considered as the "holy grail" of battery innovations, due to its lightweight (0.53 gcm^{-3}), high specific capacity (3860 $mAhg^{-1}$), and lower anodic potential (3.04 V vs. SHE) (Liang et al. 2016). In the conventional graphite-based battery, the requirement of copper current collectors (9 gcm^{-3}) can be excluded adopting Li metal anodes that can significantly diminish the overall weight of the cell (Liang et al. 2016; Lin et al. 2017). Hence, Li metal has been considered as a most favorable aspirant to be utilized as an anode in profoundly promising, next-generation energy storage devices like Li-ion, Li-sulfur, and Li-air batteries. Nevertheless, uncontrolled dendrite formation during electroplating induces safety issue in Li metal batteries and has become an obstacle in real-life applications of Li metal-based batteries (Lin et al. 2017). During cycling, Li dendrite can penetrate through the separator and provoke internal short circuit. There are two primary challenges associated with the use of Li metal anode: (i) the occurrence of enormous relative volume expansion during cycling and (ii) high chemical reactivity (Liu and Cui 2017). So, the massive volume change during charge-discharge process can rupture the fragile solid electrolyte interphase (SEI) layer, and subsequently, uneven Li-ion flux induces the dendrite formation. Also, the high reactivity of Li metal anode leads to the rebuilding of the ruptured SEI layer which favors the continuous parasitic reaction with electrolyte and rapid capacity fade during cycling (Lin et al. 2016; Liu et al. 2016b). Several investigations have been carried out to stabilize the SEI layer by acquainting with different electrolyte additives and discussed hereafter. These electrolyte additives associated with Li metal can form a protective layer on the electrode surface. A schematic representation in Fig. 3.14 shows the formation of Li dendrite structure on Li metal surface.

3.5.2 Lithiated Anode

Pre-lithiation of active anode materials is a more efficient method to compensate active lithium loss which mainly occurs in the first few cycles of LIBs, due to electrolyte decomposition and SEI formation at the surface of the anode, which

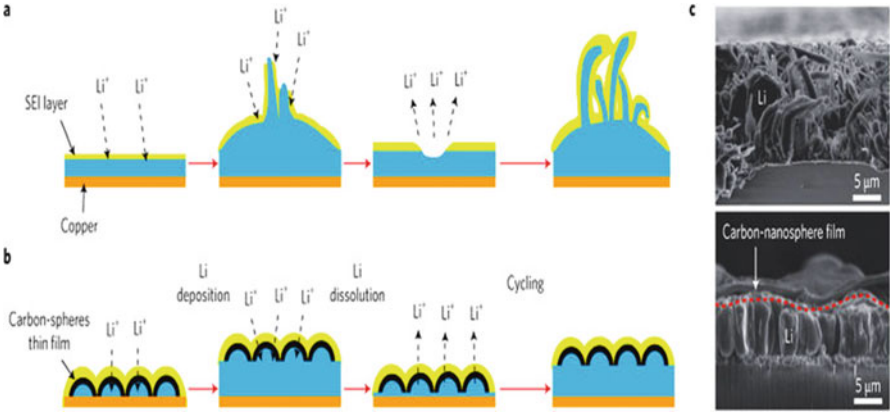

Fig. 3.14 (**a**) Schematic of the growth of the SEI layer lithium (blue) surface. (**b**) Schematic of stabilizing the SEI layer with hollow carbon nanosphere coating. (**c**) Cross-section SEM images of the lithium metal on Cu substrates without/with carbon nanosphere layer. (This figure was obtained from Zheng et al. 2014a; https://doi.org/10.1038/nnano.2014.152)

increased the reversible specific capacity and energy density (Holtstiege et al. 2018). There are several strategies to lithiate the anode electrode (Holtstiege et al. 2018).

- Pre-lithiation of the anode via a short circuit or an external current in combination with a locally separated, thus, not the anode contacting lithium metal electrode
- Pre-lithiation by incorporation of a lithium reservoir
- Pre-lithiation with lithium silicide inside the anode as a pre-lithiation reagent
- Pre-lithiation of the anode by the inclusion of lithium providing additives to the cathode like Li_5FeO_4, Li_5ReO_6, or LiF/Co
- Pre-lithiation by direct contact of the anode and lithium metal

Pre-lithiation time is also an essential parameter for the battery performance. Cyclability performance of 20-min pre-lithiated Si-NWs shows better performance as compared to 60-min pre-lithiated Si-NWs (Liu et al. 2011). Lithium-rich electrode additives and protected lithium particles are also used in pre-lithiation techniques, but these are not much stable in the more humid area (Cao et al. 2016).

3.5.3 Nanostructured Anode Materials

3.5.3.1 Nanoparticles

In the past few years, nanomaterials with different morphologies have been investigated for their applications as anodes in LIBs. Miniaturization of electrode materials allows a large surface area in contact with the electrolyte, resulting in higher charge-discharge rates (Aricò et al. 2005; Goriparti et al. 2014). However, reduction of the material size has not been found to be beneficial always. The very fast Li-ion intercalation-deintercalation often leads

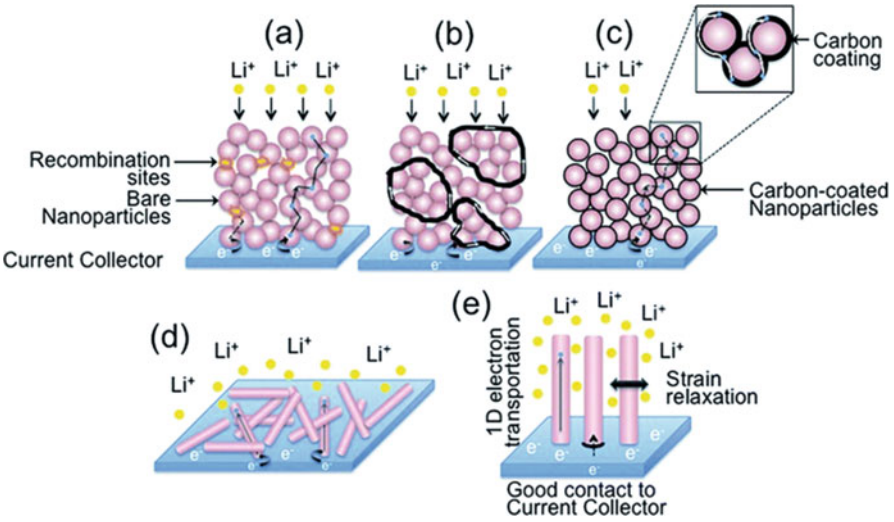

Fig. 3.15 Schematic diagram of electronic transportation through 0-D, 1-D nanostructures: (**a**–**c**) electron random walk through grain boundaries of bare nanoparticles (**a**), through carbon binders blended with nanoparticles (**b**), and through carbon coating onto the nanoparticles (**c**); (**d** and **e**) 1-D electron transportation through randomly distributed nanorods (**d**) and directly grown nanorods (**e**) onto the current collector. (This figure was obtained from Roy and Srivastava 2015; https://doi.org/10.1039/C4TA04980B)

to undesirable side reactions and can damage battery electrode. Although zero-dimensional nanoparticles are very effective anodes for LIB, there are several factors limiting battery performance. Exceptional volume changes during cycling, which pulverize the nanoparticles on repeated Li-ion insertion/extraction, are the primary issue (Bruce et al. 2008). Transportation of electron and Li-ions through nanoparticulate layers can be limited due to random walk as shown in Fig. 3.15. Additionally, voids present in between the nanoparticles and grain boundaries lower the electrical conductivity and hinder the electrochemical performance. There are secondary reactions as well occurring during lithiation/delithiation resulting in poor performance.

Formation of SEI layer onto the anode guzzles excessive charge from the cathode which causes low coulombic efficiency and rapid capacity fade (Bruce et al. 2008; Guo et al. 2008). There are several strategies, which can improve the electrochemical performance of nanoparticle anode material.

1. Conductive carbon or polymers (such as polythiophene, polypyrrole, and polyaniline) covering on nanoparticles can enhance the electronic and ionic conductivity (Li and Zhou 2012). This will allow transportation of electrons or ions through the conductive boundary of nanoparticles avoiding the interfacial resistance in among nanoparticles, though conductive coating of the NPs can stabilize the SEI layer of anode material which inhibits direct contact of the electroactive region of the anode with electrolytes and avoid the pulverization of the electrodes resulting in improved rate and stability performance (Guo et al.

2008). However, addition of a conductive binder leads to the poor packing density of electrodes, limiting the volumetric energy density (Guo et al. 2008).
2. Coating of different metals like Ni, Co Cu, Ag, and Al will improve the electrical conductivity, and these metal-coated nanoparticles exhibit increased exchange current density, high Li-ion diffusion coefficients, fewer surface films, and charge transfer resistance compared to the bare graphite (Shi et al. 2001; Nobili et al. 2009; Kim et al. 2001; Mei et al. 2012; Guo et al. 2007). For example, SnO_2 nanoparticles with Co metal deposition exhibit excellent reversible specific capacity of 810 $mAhg^{-1}$ over 50 cycles.
3. Apart from the metal coating, a coating of electronically conductive metal oxides shows high capacity and excellent power performance, like a coating of RuO_2 on TiO_2 nanoparticles (Lee et al. 2003).
4. Encapsulation of NPs with hollow spherical carbon is also a fascinating approach for LIB anode materials which prevents the agglomeration of NPs and exhibits long cycle life with high volumetric energy density (Wen et al. 2009).

3.5.3.2 Nanorods, Nanotubes, and Nanowires

To overcome the issues related to nanoparticles, anisotropic nanostructures can be a potential candidate (Bruce et al. 2008). One-dimensional nanostructure like nanowires, nanorods, and nanotubes showed directional electronic and ionic transportation providing superior mechanical stability while enhancing Li-ion storage capacity as well as long cycle life (Chan et al. 2007). Cui and co-workers reported self-supported Si nanowires grown onto stainless steel current collectors by the vapor-liquid-solid growth method serving as excellent LIB anode (Chan et al. 2007) exhibiting 4277 $mAhg^{-1}$ of specific capacity for the first cycle. Similarly, mesoporous Co_3O_4 NW arrays grown on a Ti foil exhibit reversible capacity of 700 $mAhg^{-1}$ at 1C which is much better than the commercial Co_3O_4 powders and non-self-supported NWs (Li et al. 2008a). Porosity in branched nanowires is also reported to increase the cycle life and rate capability of electrode material. Similarly, several other 1-D nanostructures of SnO_2 and TiO_2 and dendrites like hierarchical forms of MnO_2 nanowires and Mn_3O_4 nanorods with graphene exhibit improved capacity and longer cycle life (Kim et al. 2009; Armstrong et al. 2006; Cheng et al. 2006; Sayle et al. 2009). The polycrystalline α-Fe_2O_3 nanotubes (diameter, 50–200 nm; shell thickness, 10–20 nm) are reported to deliver specific capacity around 1000 $mAhg^{-1}$, almost double that of Fe_2O_3 nanoparticles (Wang et al. 2010b) (Fig. 3.16).

3.5.3.3 Core-Shell Nanostructures

Material with a hollow sphere and core-shell morphology is another impressive alternative for stable and high-performance LIB anodes. The inner void present in hollow structure provides sufficient space to accommodate volume expansion during lithiation/delithiation process, whereas the outer shell of the core-shell structure provides mechanical stability during volume change of the inner core material

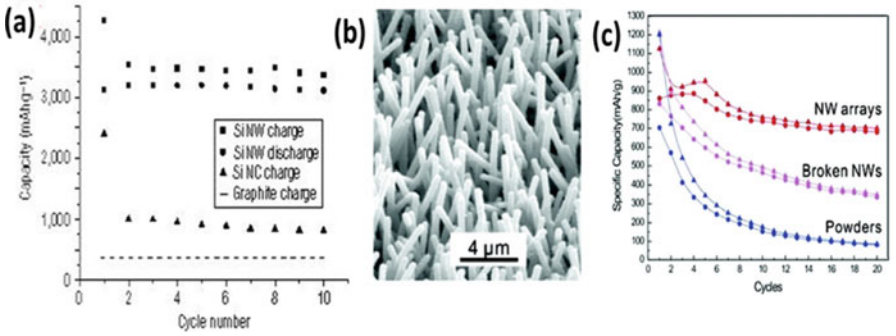

Fig. 3.16 0-D vs. 1-D nanostructures. (**a**) Capacity versus cycle number for the Si nanowires and Si nanocrystals at a rate of C/20. ((**a**) was obtained from Chan et al. 2007; https://www.nature.com/articles/nnano.2007.411), (**d**) SEM images of Co_3O_4 NW arrays growing on Ti foil by ammonia-evaporation-induced method; (**e**) comparative study of specific capacity of the Co_3O_4 NW arrays on Ti foil, non-self-supported NWs, and commercial powders as a function of the cycle number at a current rate of 1C (inset: corresponding capacity retention percentages as a function of the current rate). ((**b**, **c**) was obtained from Li et al. 2008a; https://pubs.acs.org/doi/abs/10.1021/nl0725906)

(Chen et al. 2009; Wang et al. 2010c). Template-assisted synthesis is a most widely used technique to fabricate hollow and core-shell nanostructure with tunable size and shape (Lu et al. 2008; Wang et al. 2011a-c). Lou et al. synthesized the hollow nanospheres of SnO_2 by using mesoporous silica as a template (Fig. 3.17a) (Ding et al. 2011b; Lou et al. 2009) delivering higher specific capacity of 750 $mAhg^{-1}$ at 160 $mAg^{-1}$for 20 cycles as compared to solid spheres and nanoparticles. Further extension of this work by designing SnO_2@carbon coaxial spheres (Fig. 3.17b) has shown enhanced Li-ion diffusion and stable rate performance with longer cycle life (500 $mAhg^{-1}$ at 625 mAg^{-1} of current density for 200 cycles). Several other core-shell structures like SnO_2 hollow nanobox with Cu_2O nanocubes, α-Fe_2O_3@SnO_2 rattle-type hollow structures (Fig. 3.17d), Co_3O_4/NiO core-shell nanowire arrays (Fig. 3.17f), 3-D self-assembled porous NiO-coated ZnO nanorods, TiO_2-C/MnO_2 core-double-shell nanowire arrays, etc. show excellent electrochemical performance and enhanced rate capability with longer cycle life (Wang et al. 2011b-c; Wu et al. 2012, 2013; Xia et al. 2012; Liao et al. 2013; Wu and Chang 2013). Figure 3.17 represents various examples of hollow spheres and core-shell nanostructure LIB anodes.

3.5.3.4 Nano-heterogeneous

Hybrid branched nanostructural morphology is highly intriguing for LIB applications. Tuneable 3-D morphology, homo- or heterogeneous junction, and interface electronic alignment represent unique features suitable for anode application (Cheng and Fan 2012; Jian et al. 2012). For example, interconnected porous MnO nanoflakes were grown on nickel foam (Li et al. 2012c) and α-Fe_2O_3 nanorod branches grown epitaxial on SnO_2 nanowire stems (Zou et al. 2011) and used as

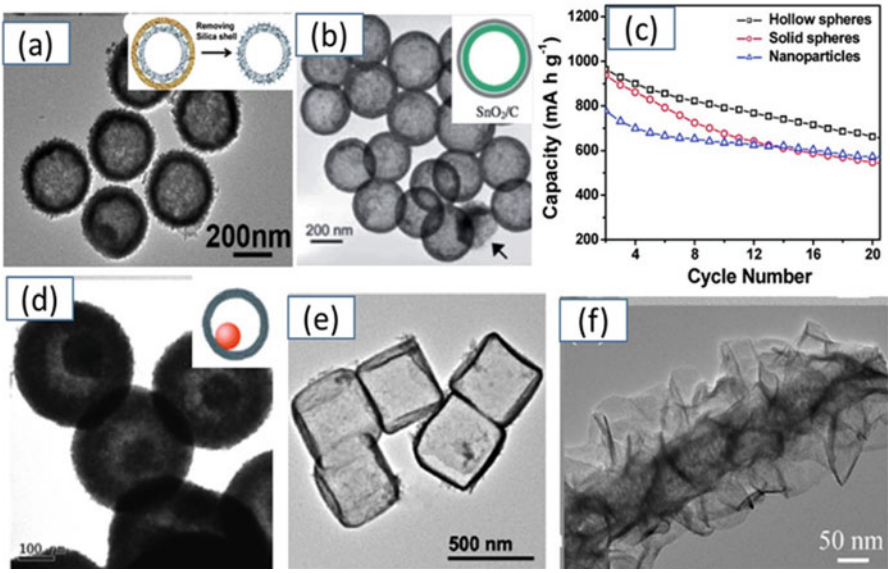

Fig. 3.17 (**a**–**f**) TEM images of (**a**) SnO_2 hollow sphere. ((**a**) was obtained from Ding et al. 2011b; https://pubs.acs.org/doi/abs/10.1021/ja108720w), (**b**) SnO_2/C hollow spheres. ((**b**) was obtained from Lou et al. 2009; https://doi.org/10.1002/adma.200803439), (**d**) α-Fe_2O_3@SnO_2 nano-rattles. ((**d**) was obtained from Chen et al. 2009; https://doi.org/10.1039/b9nr00102f), (**e**) TEM image of as-prepared SnO_2 nanoboxes. ((**e**) was obtained from Wang et al. 2011c; https://pubs.acs.org/doi/abs/10.1021/ja2004329), (**f**) Co_3O_4/NiO core-shell nanowire. ((**f**) was obtained from Xia et al.; https://pubs.acs.org/doi/abs/10.1021/nn301454q), (**c**) Comparison of cycling performances of SnO_2 hollow spheres, solid spheres, and nanoparticles at a current rate of 160 mAg^{-1} with a voltage window of 0.01–2.0 V. ((**c**) was obtained from Ding et al. 2011b; https://pubs.acs.org/doi/abs/10.1021/ja108720w)

LIB anode. Another very promising hetero-nanostructure is Si-coated $TiSi_2$ nanonets reported by Wang et al. as shown in Fig. 3.18, where Si acts as an active material to store and release Li^+ ions and $TiSi_2$ serves as the inactive component to support Si and to facilitate charge transport. The hetero-nanostructure showed remarkable performance with specific capacities of >1000 $mAhg^{-1}$ at 8.4 Ag^{-1} of current density with long cycle life up to 100 cycles (Zhou et al. 2010).

3.5.4 Carbon-Based Anode Materials

Carbon-based materials are well-known commercial anodes because of their excellent electrochemical performance such as electronic conductivity, favorable hierarchical structure to help Li-ion intercalation, low cost, readily availability, and more negative redox potentials compared to metal oxides, chalcogenides, and polymers (Martin et al. 1999). All the carbonaceous material can be classified into two

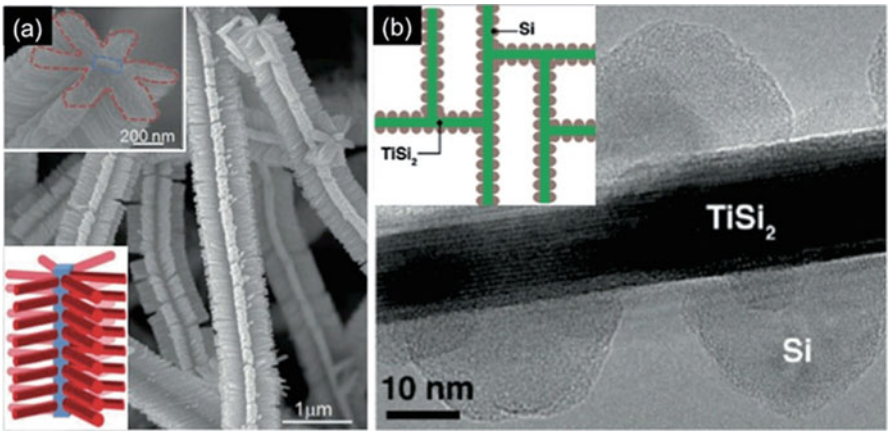

Fig. 3.18 (**a**) SEM image of a-Fe_2O_3/SnO_2 branched nanostructures (inset: TEM image (top), schematic (below) of the branched structure). ((**a**) was obtained from Weiwei et al. 2011; https://doi.org/10.1002/adfm.201100088), (**b**) TEM image of Si nanoparticles deposited on the $TiSi_2$ core (inset: schematic of the heterostructure). ((**b**) was obtained from Zhou et al. 2010; https://pubs.acs.org/doi/abs/10.1021/nl903345f)

categories: (i) graphitic carbon (soft carbon, crystalline nature) and (ii) non-graphitic (hard carbon, amorphous nature). Individual carbon has different structural arrangements and specific electrochemical properties. Graphite-based materials have layered structures which consist of an orderly arrangement of sp^2/sp^3 hybridized carbon network. The ideal defect-free graphitic structure is very hard to find, so researchers have developed highly ordered pyrolytic graphite (HOPG), which is very close to graphite structure and polycrystalline (Su et al. 2005). During lithiation process, six graphitized carbon atoms form LiC_6 alloy with one Li-ion in a completely reversible process and lead to a theoretical capacity of 372 $mAhg^{-1}$. The lithium insertion/extraction mechanism of the carbon material anode can be described as:

$$Li_xC_n \leftrightarrow xLi^+ + xe^- + C_n \ (n = 6)$$

However, during lithiation/delithiation process, SEI layer formation and insertion of solvated lithium into the graphene layers affect the reversible nature on cycling (Martin et al. 1999). However, the hard carbon is known as high specific charge carbonaceous material having x~1.2–5 in Li_xC_6 with a high Li-storage capacity value of 200–600 $mAhg^{-1}$ (Martin et al. 1999). The poor electrical conductivity and large irreversible capacity limit their extensive use as an anode material in LIBs. Lithium diffusion facilitated by defective sites present in the structural arrangements of carbon material (Persson et al. 2010) drives the use of nano-carbons including carbon nanotubes (CNTs), carbon nanofibers (CNFs), graphene nanosheets, and porous carbon with pore sizes in the nanoscale range.

3.5.4.1 1-D Carbon Nanostructure

Carbon nanotubes (CNTs) are widely known potential LIB anodes due to their high surface area providing faster one-dimensional ion transportation and higher conductivity (Futaba et al. 2006; Wang et al. 2007; Eom et al. 2006, 2004; Gao et al. 2000; Yang et al. 2002; Ji et al. 2011). High electronegativity of CNTs facilitates more intercalation of Li-ions, which also increase its reversible capacity to 1116 $mAhg^{-1}$. During lithiation, an inter-wall distance of MWCNTs can hold an excess of Li-ions and during delithiation act as a barrier to release Li-ions, which increase the more irreversible capacity and decrease the coulombic efficiency (Eom et al. 2004; Frackowiak et al. 1999). Hence, the hybrid materials of CNTs with other materials like different carbons, metal oxides (Xia et al. 2010; Wen et al. 2013), and chalcogenides (Shi et al. 2013; Bindumadhavan et al. 2013) can help to overcome these issues. Carbon nanofibers (CNF) are also reported as anode material for LIB application. CNFs exhibit more stable rate capability and longer cycle life due to the presence of surface and lattice defects which shorten the lithium diffusion path length (Wu et al. 2013; Luo et al. 2013; Subramanian et al. 2006). Also, synthesis of nanocomposites of CNFs with other electroactive material improves the battery performances such as high reversible capacity and adequate stability.

3.5.4.2 2-D Carbon Nanostructure

The 2-D graphene nanosheets (solely or in hybrid form) (Novoselov et al. 2004; Geim and Novoselov 2007) are most useful anode material for LIB application (Ji et al. 2011). However, graphene nanosheets exhibit an unavoidable irreversible capacity and low coulombic efficiency due to unwanted chemical reactions of Li-ions with oxygen-containing functional groups and trigger the formation of SEI on the defect sites. Furthermore, electrolyte diffusion along with the Li-ions in between the layers also causes irreversible capacity loss (Wu et al. 2013; Guo et al. 2009). The interlayer spacing between the graphene layers and functional groups attached to the nanosheet surface fluctuates the storage capacity of electrode materials (Pan et al. 2009). The presence of oxygen-containing moieties in graphene decreases the Li-ion storage capacity sometimes even less than natural graphites (Pan et al. 2009; Wang et al. 2009a). Sometimes, graphene oxide (GO) nanosheets show only 335 $mAhg^{-1}$ of specific capacity, whereas (reduced graphene oxide) r-GO exhibits increased capacity ~1000 $mAhg^{-1}$ with better capacity retention. Yoo et al. reported that the graphene nanosheets with ~4 Å of interlayer spacing show high reversible capacity because of more available sites for Li-ion accommodation (Yoo et al. 2008). Nanocomposites of graphene with CNTs, C_{60}, Si, and Sn show enhanced electrochemical performance with high and stable reversible capacity for LIB application (Chou et al. 2010; Wang et al. 2009c). Additionally, nanostructures of transition metal oxides such as Co_3O_4, TiO_2, Fe_3O_4, Mn_3O_4, CuO, NiO, and SnO_2

anchored on the graphene nanosheets efficiently reduce the irreversible capacity loss during lithiation-delithiation due to the synergistic effect (Wu et al. 2010; Peng et al. 2012; Yue et al. 2012; Wang et al. 2012; Xin et al. 2012; Zhu et al. 2011; Li et al. 2011; Behera 2011; Lian et al. 2010; Zhang et al. 2010a; Zou et al. 2011; Chen et al. 2013; Wang et al. 2010a; Lei et al. 2013; Zhou et al. 2012). In these composites, graphene nanosheets provide high surface area and greater ionic conductivity while preventing the agglomeration and facilitating lithium storage to a greater extent.

3.5.4.3 3-D Porous Carbon Nanostructure

Porous carbon nanostructures are an up-and-coming candidate for LIB applications. Pore size distribution of porous carbons can be classified as microporous (<2 nm), mesoporous (2–50 nm), and macroporous (>50 nm) (Lei et al. 2013; Wang et al. 2010c; Zhou et al. 2012; Zhang et al. 2010a). Porosity of electrode enhances the electrochemical properties due to the interconnected carbon networks and also helps to accommodate volume expansion during the intercalation/deintercalation process (Ji et al. 2011). The porous carbon can easily avoid the irreversible capacity loss as compared to 1-D or 2-D carbonaceous material by the facilitation of ionic and electronic transport through interconnected porous network. Zhou et al. reported a porous carbon structure with uniform pore size of 3.9 nm exhibiting excellent reversible capacity of 1000 $mAgh^{-1}$ at 0.1 Ag^{-1} with good capacity retention over 20 cycles (Wang et al. 2010b). Takeuchi et al. develop highly porous carbonaceous materials, which showed very high irreversible capacity loss from ~3500 to ~500 $mAhg^{-1}$ in the first cycle. Pint and co-workers prepared a 3-D foam of free-standing and flexible graphene and CNT hybrid which showed very high reversible capacities of 2640 $mAhg^{-1}$ at a current rate of 186 mAg^{-1}. It is interesting to see that the hybrid structure showed excellent battery performance (Cheng et al. 2008). However, sometimes very high surface area of electrode material can increase irreversible capacity loss due to the electrolyte decomposition and SEI formation onto the electrode surface. Hence, different hybrid composites of carbon with other material may be promising candidates for LIB applications.

3.5.5 Spinel-Structured $Li_4Ti_5O_{12}$

Thackeray's group has reported a spinel-structured $Li_4Ti_5O_{12}$, as an anode material in 1994 (Ferg et al.1994). Unlike graphite, working potential of $Li_4Ti_5O_{12}$ is 1.5 V vs. Li/Li^+ so that the high working potential can avoid SEI layer formation on the electrode surface. Because of negligible volume expansion during lithiation-delithiation, $Li_4Ti_5O_{12}$ exhibits high specific capacity (170 $mAhg^{-1}$) and longer cyclic stability (Yin et al. 2009). However, poor electronic conductivity (10^{-13} S cm^{-1}) of $Li_4Ti_5O_{12}$ and a moderate Li^+ diffusion coefficient (10^{-9}–10^{-13} cm^2 s^{-1}) limit the performance, which up to a certain extent can be overcome

by reducing the size and conductive coating (Yonggang et al. 2008; Wang et al. 2009d; Borghols et al. 2009). Jaiswal et al. have fabricated the $Li_4Ti_5O_{12}$ with two different size distributions of 50 nm and 200 nm by pyrolysis and exhibited charge capability of ~148 and 138 $mAhg^{-1}$ at C/25 and 5C, respectively. Other than nanoparticles, $Li_4Ti_5O_{12}$ in the form of hollow microspheres and nanowire structures also deliver high performance, with more than 90% capacity retention (Jaiswal et al. 2009). Besides fabrication of nanostructured $Li_4Ti_5O_{12}$, conductive coating with carbon or surface nitridation was also found to be fruitful for further improvement in their performances (Park et al. 2008). Ionic liquids, containing C, H, and N elements, are commonly used precursors for N-doped carbon coating onto the surface of $Li_4Ti_5O_{12}$, as they can penetrate porous material quickly due to their fluidic properties (Hongsen et al. 2013).

3.5.6 Transition Metal Oxides

Transition metal oxides (TMOs) undoubtedly bring out a new pathway for the development of electrode materials because of their relatively high capacity and excellent cyclability but also are cheap and readily available. However, high working potential, low coulombic efficiency, and sizeable potential hysteresis between anodic and cathodic regions are hard to handle for TMO anodes. Basically, two types of electrochemical reaction occur in TMOs: (i) insertion reaction and (ii) conversion reaction (Poizot et al. 2000). Moreover, the different structural morphology in nanoscale level plays a crucial role in the performance of LIBs. Because of smaller size and higher volume-to-surface ratio, significant amount of lithium can react with the electrode matrix. TMOs exhibit high theoretical capacity as transference of multiple electrons per unit of the metal atom in conversion reaction. However, in this process, forward reaction is thermodynamically favored, whereas backward reaction is an unfavorable process which is facilitated by formed metal nanoparticles (M) during the reaction (Wu et al. 2012). Hence, reversibility of conversion mechanism is well maintained in the nanoscale region. Among all TMOs, due to its high theoretical capacity of 790 $mAhg^{-1}$, tin oxide (SnO_2) is the primary choice anode material (Idota et al. 1997; Song and Lou 2013). However, significantly large Li-ion irreversibility leads to rapid capacity fade (Demir-Cakan et al. 2008). It is worth noting that hollow spheres and core-shell or mesoporous structures of SnO_2 can accommodate the volume change, whereas SnO_2 in the form of nanowires and nanorods provides the mechanical support to last through several cycles of the intercalation-deintercalation process (Demir-Cakan et al. 2008; Wen et al. 2009). Also, the porous nature not only helps the faster lithium intercalation-deintercalation but also provides a good network system, making the surfaces available for electrolytes.

Manganese oxides (MnO_x) also exhibit very high theoretical specific capacity in different oxide forms such as MnO_2 (1230 $mAhg^{-1}$), Mn_3O_4 (936 $mAhg^{-1}$), and MnO (755 $mAhg^{-1}$), respectively. However, volume expansion and aggregation during charge-discharge result in poor electrical conductivity and severe capacity fade (Lei et al. 2013; Lai et al. 2012). Cui and co-workers have developed r-GO@Mn_3O_4 nanocomposite delivering

four times higher reversible capacity compared to Mn_3O_4 nanoparticles with longer cycle life. The r-GO help in overcoming the insulating nature of Mn_3O_4 NPs (Wang et al. 2010b). Various other MnO_x-C nanocomposites like Mn_3O_4 nanorods dispersed on a graphene nanosheet, a hierarchical structure of graphene-wrapped MnO_2-graphene nanoribbons, MnO_2 nanoflakes coated on carbon nanohorns (CNHs), etc. have been utilized as an anode electrode for LIB applications (Lei et al. 2013; Lai et al. 2012). Co_3O_4 is another promising TMOs exhibiting twofold capacity (700 $mAhg^{-1}$) compared to graphite and maintained 93.4% of capacity retention after 100 cycles (Chou et al. 2010). Furthermore, composites with other active materials like CNTs-Co_3O_4 nanospheres, porous $CuCo_2O_4$ nanocubes wrapped by r-GO nano-paper, and CoO-NiO-C exhibit enhanced electrochemical performance for LIBs (Wang et al. 2009c; Wu et al. 2010; Peng et al. 2012). Iron oxides such as hematite (α-Fe_2O_3), magnetite (Fe_3O_4), and ferrous oxide (FeO) are more popular TMO anodes, exhibiting tremendously high theoretical capacity (1007 $mAhg^{-1}$) (Lai et al. 2012; Larcher et al. 2003).

Fe_2O_3nanostructures grown directly onto conductive substrates (Cu or Ti foil) are preferred due to their direct attachment to the current collector, avoiding the use of additives and thereby facilitating the electron collection efficiency. α-Fe_2O_3 nanoflakes are grown on Cu foil synthesized by Chowdari and co-workers by radio-frequency (rf) magnetron sputtering which showed the stable capacity of 700 $mAhg^{-1}$ at 65 mAg^{-1} with very less capacity loss. Nanocomposites of α-Fe_2O_3 with different metal oxides like Co_3O_4, SnO_2, or TiO_2 as hetero-nanostructures in the form of core-shell, branched structures, etc. have found to be an excellent anode for LIB application due to the synergistic effect (Chen et al. 2009; Weiwei et al. 2011; Lai et al. 2012; Larcher et al. 2003). TiO_2 is another typical TMO with various forms like rutile, anatase, TiO_2 (B), and so on which can be used as anode material. Several other TMOs like NiO, ZnO, etc. have been utilized as an anode material for LIBs (Wu et al. 2012). Very recently, spinel structures (AB_2O_4) of ternary metal oxides have attracted great research attention. In AB_2O_4, two transition metals A and B present with +2 and +3 oxidation states, respectively (Shakir 2014; Zheng et al. 2014b; Linlin et al. 2013; Longwei et al. 2014; Wu et al. 2014). Ajayan and co-workers have reported the anisotropic, hollow, and porous nanostructure of $Zn_xCo_{3-x}O_4$ which is an effective anode material in LIBs, with high reversible capacity value ~1000 $mAhg^{-1}$ at 1C rate for 50 cycles (Wu et al. 2014). A summary of synthesis and electrochemical properties of transition metal oxide-based anodes for rechargeable LIB application is presented in Table 3.2.

3.5.7 Alloyed Compounds

Nanostructures of Si, Sn, and Ge and their alloys are new-generation LIB electrodes because of very high theoretical capacity (two to ten times of graphite), greater energy density, and power density. However, huge volume expansions (400%) during the charge-discharge process and poor electrical conductivities increase the irreversible capacity loss

Table 3.2 Synthetic strategies and electrochemical properties of transition metal oxide-based anodes for rechargeable LIB application

S. no	Electrode	Morphology	Method	Specific capacity	Current density	Stability (cycles)	References
1	Si-NWs	NWs	Vapor-liquid-solid growth method	3541 $mAhg^{-1}$	C/20	10	Chan et al. (2007)
2	Co_3O_4	NWs	Ammonia-evaporation induced	774 $mAhg^{-1}$	1C	20	Li et al. (2008a)
3	α-Fe_2O_3	Nanotubes	Template-engaged precipitation	1000 $mAhg^{-1}$	0.5C	–	Wang et al. (2011)
4	Mn_3O_4/ graphene	Nanorods	Hydrothermal	100 Fg^{-1}	5 Ag^{-1}	10,000	Sayle et al. (2009)
5	Mesoporous SnO_2	Microspheres	Hydrothermal	370 $mAhg^{-1}$	1 Ag^{-1}	100	Ding et al. (2011b)
6	SnO_2	Nanowires	Vapor-liquid-solid method	>700 $mAhg^{-1}$	782 mAg^{-1}	50	Kim et al. (2009)
7	SnO_2	Hollow nanoboxes	Template-engaged synthesis	570 $mAhg^{-1}$	0.2C	40	Wang et al. (2011)
8	SnO_2@carbon	Hollow nanospheres	Hard template and hydrothermal synthesis	>460 $mAhg^{-1}$	0.8C	100	Lou et al. (2009)
9	α-Fe_2O_3@SnO_2	Nano-rattles	Hydrothermal	419 $mAhg^{-1}$	200 mAg^{-1}	30	Chen et al. (2009)
10	Co_3O_4/NiO	Core-shell nanowire	Hydrothermal	853 Fg^{-1}	1 Ag^{-1}	6000	Xia et al. (2012)
11	TiO_2-C/MnO_2	Core-double-shell nanowire	Hydrothermal and layer-by-layer deposition method	471 $mAhg^{-1}$	0.1C	100	Liao et al. (2013)
12	MnO/nickel foam	Nanoflakes	Hydrothermal	700 $mAhg^{-1}$	246 mAg^{-1}	200	Li et al. (2012c)
13	α-Fe_2O_3/SnO_2	Nanorod branches/ nanowire	Chemical vapor deposition	1167 $mAhg^{-1}$	1000 mAg^{-1}	30	Zou et al. (2011)

(continued)

Table 3.2 (continued)

S. no	Electrode	Morphology	Method	Specific capacity	Current density	Stability (cycles)	References
14	$TiSi_2$/Si	Nanonets	Chemical vapor deposition method	>1000 $mAhg^{-1}$	8.2 Ag^{-1}	100	Zhou et al. (2010)
15	Co3O4/Fe2O3	Branched nanowires	Hydrothermal	1000 $mAhg^{-1}$	100 mAg^{-1}	60	Zheng et al. (2013)
16	$Zn_xCo_{3-x}O_4$	Hollow and porous nanostructure	Template-assisted coprecipitation method	1000 $mAhg^{-1}$	1C	50	Wu et al. (2014)

and limit their practical (Lee et al. 2011). Numerous strategies have been developed like controlled morphology, hybrid nanostructures, coatings, and doping with carbon, highly conductive, hard, and inactive metals and void engineered structures to accommodate the volume changes (Zhang et al. 2010b). Moreover, electrochemically active binary metal alloys at the nanoscale are more useful to improve the reversible capacity as well as long cycle life. Several electroactive metals including Si, Sn, Al, Ge, Pb, and Sb are most widely used matrix metals (Lee et al. 2011; Xu et al. 2013; Wen et al. 1979; Saint et al. 2005; Wang et al. 1986). Among all electroactive metals, Si is the most studied anode material which forms alloys with Li metal such as $Li1_2Si_7$, Li_7Si_3, $Li_{13}Si_4$, and $Li_{22}Si_5$ (crystalline to amorphous phase) as follows (Wen and Huggins 1981; Limthongkul et al. 2003; Wang et al. 2013b).

During discharge:

$$\begin{aligned}\mathrm{Si(Crystalline)} + \mathrm{xLi^+} + \mathrm{xe^-} &\rightarrow \mathrm{Li}_x\mathrm{Si\ (Amorphous)} \\ +(3.75 - x)\mathrm{Li^+} + (3.75 - 5)e^- &\rightarrow \mathrm{Li_{15}Si_4(Crystalline)}\end{aligned}$$

And while charging:

$$\mathrm{Li_{15}Si_4(Crystalline)} + \mathrm{Si\ (Amorphous)} + \mathrm{yLi^+} + \mathrm{ye^-} \rightarrow \mathrm{Li_{15}Si_4(Residual)}$$

Similarly, Si and Sn metal forms alloy with Li with different Li-Sn phases such as Li_2Sn_5, LiSn, Li_7Sn_3, Li_5Sn_2, $Li_{13}Sn_5$, Li_7Sn_2, and $Li_{22}Sn_5$ conversion. The most lithium-rich Sn-Li alloy, $Li_{22}Sn_5$, can accommodate 4.5 atoms of Li per Sn atom, delivering a capacity value of 959.5 $mAhg^{-1}$ at a working potential of 0.5 V vs. Li/Li^+ (Yoon et al. 2008). However, inhomogeneous volume changes by the different intermetallic Li-Sn phase formation cause the poor capacity retention which can be improved by using the oxide form of Sn. Ge also form an alloy with Li and shows the high theoretical specific capacity of 1568 $mAhg^{-1}$($Li_{17}Ge_4$), favored as an anode due to fast Li-ion diffusivity compared to Si (Fuller and Severiens 1954). Mg or Ag-silicides are known Si-based intermetallic alloy compounds with Mg and Ag as electroactive elements. The complicated lithiation process involves the formation of both binary and ternary metal alloys Li-Si, Li-Mg, and Li_xMg_2S (Kim et al. 1999). Other than graphite matrix, several other active-inactive matrices including SnSb, SbAl, Mg_2Si, etc. and inactive matrices including metals like Fe, Cu, and Nb and alloys like $FeSi_2$ and oxides like Al_2O_3 and Li_2O have been explored.

3.5.8 *Layered Metal Dichalcogenides and Their Composites*

Transition metal dichalcogenides (TMDs/MX_2) are emerging anode materials for the next-generation LIBs (Kumar et al. 2016). In MX_2, the metal atoms are sandwiched in between two hexagonally arranged chalcogenide layers in the form of X-M-X arrangement, which is attached to another unit through weak van der Waals

forces (Zhang et al. 2013a). So, interstitial sites (tetrahedral or octahedral) present in layered stacking arrangement accommodate li-ions during intercalation. Also, the octahedral site is more energetically favored for Li-ion accommodation (Silbernagel 1975). Moreover, a complete charge transfer occurs during Li-ion intercalation in MX_2 by reduction of M^{4+} to M^{3+}, along with Li^+ ion diffusion in the van der Waals gap, resulting in volume expansion. Depending upon the lithiation potential values, metal sulfides MS_2 of M = Fe, Ti, Co, Ni, and Cu are considered as a cathode material, whereas M = Mo, W, Ga, Nb, and Ta are known to be used as anode materials in LIBs. Molybdenum disulfides (MoS_2) undergo lithiation at a relatively high potential value of ~2 V and were used as the anode, paired with a high-voltage lithiated cathode (~4 V). The theoretical capacity value for MoS_2 is >670 $mAhg^{-1}$, accommodating 4 mol of Li^+ ions per unit, according to the following electrochemical reaction (Wang et al. 2013a):

$$MoS_2 + 4Li^+ + 4e^- \leftrightarrow Mo + 2Li_2S$$

However, Li_2S, formed during the reaction, is very reactive with electrolyte forming the SEI on the surface of the electrode material affecting the cyclic stability and rate capability. Among others, WS_2, $SnSe_2$, ZrS_2, CoSe, CoS, TiS_2, and their hybrids with carbonaceous materials are also found to be very promising anode materials for LIBs (Kartick et al. 2013, 2014; Kumar and Hu 2018; Choi et al. 2011; Jang et al. 2011). The layered structure of TiS_2 can also serve as a suitable host for lithium intercalation resulting in Li_xTiS_2 ($x = 0.12 < 0.52 > 1.0$) as an intercalated compound (Jun et al. 2003; Tao et al. 2004; Whittingham 1978). Table 3.3 provides the information for the synthesis and electrochemical properties of transition metal dichalcogenide-based anode materials used for LIB application.

3.6 Conductive Additives and Binders

3.6.1 Conductive Additives

To ensure uniform conductivity of electrode materials during electrochemical processes, conductive additives are required. Ideally a conductive additive should promise superior conductivity, compatibility with electrode materials, with low cost. However, the choice of the conductive additive is based on several parameters including better chemical and electrochemical stability in the battery environment, enabling good dispersion, and must be readily accessible for ions as well as the electrolyte. Several commercial carbons, e.g., super-P, C-45, MCMB, carbon nanotubes, graphene, graphene oxides, etc., are promising conductive additive for electrode materials. There are some non-carbon, conductive additives as well being considered as potential candidates for electrode fabrication.

Table 3.3 Synthetic strategies and electrochemical properties of transition metal dichalcogenide-based anode materials in lithium ion rechargeable batteries

S.N.	Electrode	Morphology	Methods	Specific capacity ($mAhg^{-1}$)	Current density (mAg^{-1})	Stability (cycles)	References
1	MoS_2	Hollow nanoparticles	Solvothermal	902	100	80	Wang et al. (2013a, b)
2	MoS_2-MWCNT	Hybrid materials	Grinding	>1100	100	30	–
3	WS_2	Nanotubes	Sintering method	600	–	20	–
4	WS_2	Ordered mesoporous	Vacuum-assisted impregnation	805	100	100	–
5	WS_2-SWCNT	Lamellar porous nanocomposite	Vacuum filtration	821	100	50	Liu et al. (2014b)
6	ZrS_2	Nanodiscs	Surfactant-assisted chemical synthesis	600	69	50	Jang et al. (2011)
7	TiS_2-MWCNT	Hybrid material	Grinding method	340	100	20	Kartick et al. (2013)

3.6.2 Binders

A binder is a necessary component to fabricate rechargeable battery electrodes. Binder is mandatory to stabilize the electrode components and to retain sufficient contact between the electrode materials and the current collector. An ideal binder must be conductive and chemically and electrochemically stable and must possess an excellent dispersion and easy access to the electrolyte media. A binder should have excellent ability to hold active/electrode materials to prevent their migration. Therefore, the selection of an appropriate binder in accordance with the electrode and electrolyte media plays a crucial role in the overall performance and stability of the electrodes and battery as well. However, recently there are several reposts on the fabrication of binder-free electrodes.

3.6.2.1 Content and Nature of the Binders

The ideal binder for battery electrode fabrication must possess better electrochemical stability and conductivity in electrolyte media. It must be eco-friendly and stable at a temperature range and should not swell/decompose to the electrolyte. Polyvinylidene fluoride (PVDF) is an extensively used binder for electrode fabrication. Sometimes, PVDF is being used as reference when the properties of new binders are explored (Bao et al. 2013; He et al. 2011; Zhang et al. 2012). Even though PVDF is a commonly used binder for electrode fabrication at laboratory scale, it is not the optimal choice for commercial applications because of the use of the toxic N-methyl-2-pyrrolidone (NMP) solvent. Recently, Lacey et al. (2014b) reported that the amount of binder is also crucial for electrode fabrication. An excessive amount of PDVF leads to the electrode pore blockage, limiting the access of electrolyte to active material resulting in poor specific capacity (Lacey et al. 2014a).There are reports strongly suggesting that the appropriate amount of the binder helps to get superior specific capacity, improved coulombic efficiency, and good cycling performance, further arguing that the observed performance strongly depends on the amount of electrolyte and the concentration of lithium salt (Urbonaite and Novák 2014). To avoid the use of nontoxic solvents, hampering solubility while improving the mechanical stability of the binder as well as active electrode materials in the electrolyte, the use of water-based binders has gained considerable interest. Polyethylene oxide (PEO) is another choice as potential binder for electrode fabrication; however, it can swell in the electrolyte. Recent studies suggested that the mixture of PEO and polyvinylpyrrolidone (PVP) works well as effective binder for electrode preparation (Lacey et al. 2014a). Poly(acrylamide-*co*-diallyldimethylammonium chloride) (AMAC) is also reported as a potential binder candidate utilizing nontoxic solvents (Zhang 2012). AMAC-based electrodes are proved to be more mechanically stable as compared to PEO-based as AMAC-based binder didn't swell in electrolyte media (Zhang 2012). Similarly, carboxymethyl cellulose (CMC) and styrene-butadiene rubber (SBR) are also reported to serve as efficient binders for battery electrode (Urbonaite and Novák, 2014; Lacey et al. 2014a).

3.6.3 Binder-Free Electrodes

As discussed, the choice and amount of binder directly affect the overall performance of the battery. The electrochemical and mechanical stability of a binder, for longer cycle life of electrode materials, is always an issue. Therefore, research on designing the alternative, binder-free electrode to avoid the limitations associated with binder increased recently. Several metal oxides have been intensively researched out as potential alternatives to commercialized electrodes for high-performance materials (Jian et al. 2012; Reddy et al. 2013; Jordi et al. 2010; Croguennec and Palacin 2015). Designing self-supported metal oxide nanostructure arrays as a potential binder-free electrode promises unique benefits over slurry-cast electrodes including superior charge transfer efficiency with improved gravimetric capacity. Inspiring from the several likelihood, the design and fabrication of binder-free, self-supported electrode utilizing highly conductive substrates/current collector have gained significant research attention in recent years (Jiang et al. 2011; Ellis et al. 2014; Zhao et al. 2015; Liaoyong et al. 2015; Wang et al. 2016; Feng and Limin 2016).

There are several reports documenting the use of activated carbon fiber (ACF) cloth (Ran et al. 2011), CNT matrix (Jin et al. 2013), graphene/graphene oxide paper, and mixture of graphene-CNT to fabricate two-dimensional (or 2-D planar substrates) or three-dimensional (3-D porous substrates) to grow metal oxide nanoarray for binder-free, self-supported battery electrodes (Feng and Limin 2016). Binder-free, self-supported electrodes have many advantages including higher surface area, improved charge transfer efficiency, superior electron transportation, and free space to alleviate volume expansion during battery operation while preventing severe aggregation (Feng and Limin 2016).

3.7 Electrolyte and Electrolyte Additives

The compact shape, customized size, lighter weight, and feasibility, makes Li-ion batteries remarkably accessible and suitable power sources for the applications in portable digital electronics and customized devices including mobile phones, laptops, digital cameras, electric vehicles (EV), and hybrid electric vehicles (HEV). To fulfill the demand for higher energy, electrode materials with high specific capacities are under development. At high rate or higher electrochemical potential, battery components including electrodes and electrolytes are prone to decompose because of the increase in internal temperature. As a result the device may short-circuit or explode. Therefore, battery components for long-term stability and high rate applications are under surveillance. In addition to the binder, the electrolytes are essential components of rechargeable LIB. An electrolyte is composed of Li-salt dissolved in nonaqueous, organic liquids. The role of electrolytes in all electrolytic cells including batteries, capacitors, and fuel cells is the same: to provide a medium for charge (ions) to shuttle between electrodes. Ideally, an electrolyte must undergo no net mass or chemical changes during the battery

operation, while all Faradaic reactions are anticipated to take place within the electrodes. Therefore, the electrochemical stability of the electrolytes is crucial and often challenged by the strong reducing and oxidizing nature of the battery electrodes. The severity of the challenges amplified with the quest of the systems providing higher energy densities, as they utilize more oxidizing cathode and reducing anode, thus pushing the requirement for further improvements in electrolyte stability. Similar to the electrode materials, the potencies and the stability of an electrolyte can be quantified by the range in volts between its oxidative and reductive decomposition limits, generally referred to as the "electrochemical window." To enable a rechargeable battery operation, it is necessary that the redox potential of electrodes (cathode and anode) must lie within the electrochemical window. The electrochemical stability of an electrolyte is the only prime requirement. Universal requirements for an ideal electrolyte for LIB application are:

1. It must possess an extensive electrochemical window to hamper the electrolyte degradation within the working range of electrodes.
2. It must retain excellent ionic conductivity and electronically insulating nature so that it can provide maximum ion transport and minimum self-discharge.
3. An ideal electrolyte should be inactive to other cell components such as cell separators, electrode substrates, and cell packaging materials for better stability, longer life, and safety. (iv) Electrolyte and its ingredients (salt, solvents, and additives) should be environment-friendly and electrically, thermally, and mechanically stable (Xu 2004).

Due to their aggressive nature, reduction of electrolytes takes place resulting in the formation of a thin passive film, generally termed as SEI on electrode surface during the first cycle of battery operation. These interfaces between electrodes and the electrolyte decide the fate of the performance and stability of the battery. The formation of SEI layer in LIB technology has gained considerable research interest in recent years. A good SEI layer is believed to prevent further electrolyte degradation by blocking the electron transport while allowing lithium ions migration through it during repetitive cycling (Ehrlich 2002; Haregewoin et al. 2016).

For improved stability and reduced risk of explosion, several additives are suggested to add to the functional electrolytes. Recently, some non-flammable electrolytes with flame-retardant (FR) additive to hinder electrolyte flammability have been reported (Xiao et al. 2004; Xu et al. 2002; Yao et al. 2005). However, the FR additives have adverse effects on battery performance (Xiao et al. 2004; Xu et al. 2002; Yao et al. 2005). It is well understood that the battery performance and safety are directly related to the physical as well as electrochemical properties of the electrolyte. So it is urgent and obligatory to study safer and more stable electrolytes for LIB application. Besides, the increasing demand for different electrolytes obliges a much better understanding to achieve superior performance and more reliable LIB. Based on the physical and chemical appearance, electrolytes generally can be categorized in the liquid, gel, and solid phase. The next section provides a detailed information on the electrolytes and their properties.

3.7.1 Liquid Electrolytes

An ideal electrolyte should not only maintain excellent electrochemical and thermal stability but also must offer suitable ionic conduction and compatibility with electrode materials. The roles of electrolytes in LIBs are to support Li-ion transport during charging and discharging. The majority of the electrolytes are electrolytic solution consisting electrolyte solutes known as "salts" dissolved in nonaqueous organic solvents and are in a liquid state at the ambient temperature range (Ehrlich 2002; Haregewoin et al. 2016). The most commonly available and commercially used LIB electrolytes are based on lithium salts ($LiPF_6$) (1.0 M) dissolved in ethylene carbonate (EC) and ethyl methyl carbonate (EMC) (EC/EMC; 1:1, v/v) or diethyl carbonate (DEC) (EC/DEC; 1:1, v/v). Some other commonly used LIB electrolytes consist of one or more lithium salts including $LiClO_4$, $LiAsF_6$, $LiBF_4$, etc. dissolved in a single or mixtures of organic solvent. However, most of the organic electrolyte solvents are highly reactive, flammable, and corrosive, which may cause short circuit or explosion (Ehrlich 2002; Haregewoin et al. 2016). To ensure the better performance and improved stability with superior cycle life, minimal amounts of additives are introduced to the functional electrolytes. There is significant progress on the development of better and safer electrolyte with the help of several electrolyte additives (Ehrlich 2002; Haregewoin et al. 2016). Some functional electrolyte additives such as vinylene carbonate (VC) (Aurbach et al. 2002; Yoshimoto et al. 2006), vinyl acetate (VA) (Abe et al. 2004; Santner et al. 2003), vinyl ethylene carbonate (VEC) (Hu et al. 2004), ethylene sulfite (ES) (Itagaki et al. 2005; Wrodnigg et al. 2001), trimethyl phosphate (TMP) (Yoshimoto et al. 2006), triphenyl phosphate (TPP), and propylene sulfite (PS) (Wrodnigg et al. 1999) have been intensively investigated in the recent years (Shim et al. 2007).

3.7.2 Gel Electrolytes

Due to the excellent ionic conductivity and virtuous acquaintances with electrodes, liquid electrolytes have played crucial roles in the development of electrochemical energy storage devices (i.e., rechargeable batteries). Frequently used liquid electrolytes for the current state of the art LIBs are composed of the lithium salt in a mixture of organic solvents. However, the organic solvents are highly oxidizing, corrosive, and flammable which may lead to thermal decomposition due to local overheating during battery operation, resulting in thermal runaway, short circuiting, or sometimes explosions of the device. Unavoidable Li dendritic growth triggered by the nonuniform applied current during charging is another severe issue associated with

the use of liquid electrolytes in LIBs. Therefore, LIBs based on liquid electrolyte have multiple risks associated with them and are not preferred choice for further development of flexible and wearable electronics (Finegan et al. 2015; Huang et al. 2015). Solid electrolytes are reported to provide promising opportunity to tackle the safety issues while inhibiting the growth of Li dendrites but suffer low ionic conductivities and deprived interfaces with electrodes, resulting in poor cycle performance (Irene et al. 2016; Jeong et al. 2013; Julian et al. 2015; Shi et al. 2014). To overcome these issues, more reliable and sustainable electrolyte systems are in great demand. Combining the advantage (better ionic conductivity of liquid electrolyte and safety of solid electrolyte), gel electrolytes (GEs) are suggested to provide safer and sustainable battery operation and have attracted considerable research interest (Arya and Sharma 2017; Irene et al. 2016; Zhang et al. 2014). The adjustable shapes and highly flexible nature of GEs are the most suited choices for the portable and wearable electronics (Cui et al. 2017; Wei et al. 2015; Ye et al. 2015). Due to the high flexibility, GEs remain stable in the course of the volume change of electrodes and restrict the Li dendritic growth during charge/discharge process (Hu et al. 2017; Porcarelli et al. 2016; Qingwen et al. 2017; Takeda et al. 2016). Therefore, due to toughness (Chen et al. 2006), stretchability (Zhao et al. 2013), and compressibility (Yan et al. 2017), GEs are the most anticipated substitutes among liquid and solid electrolytes for the range of electrochemical energy storage devices (Hongcai et al. 2015; Jin et al. 2012; Lee et al. 2010). GEs are reported to provide excellent ionic conductivity and better interfacial adhesion to electrodes resulting in deteriorated solvent leakage and improved safety (Hassoun et al. 2007; Song et al. 1999). Ideally, a polymeric matrix providing (i) high mechanical integrity; (ii) superior thermal, chemical, electrochemical stability; (iii) better ionic conductivity; (iii) wide electrochemical window; and (iv) excellent segmental motion of polymer chain and salt dissolution is preferred to serve as GE host framework (Berthier et al. 1983; Grünebaum et al. 2014; Meyer 1999; Marcinek et al. 2015; Michel 2004). Generally, GEs can be classified into four categories including (i) proton based (Hao et al. 2016), (b) alkaline based (Qiao et al. 2010), (c) conducting salts, and (d) ionic liquid (IL) based (Lu et al. 2008).

To fabricate GEs, both the host polymer matrix and electrolytic salts are dissolved in the organic/aqueous solvents providing a medium for ionic conduction. Commonly used Li-ion conducting GEs are prepared by using polyethylene oxide (PEO), polyvinylidene fluoride (PVDF), polyvinylidene fluoride-co-hexafluoropropylene (PVDF-HEP), polyvinyl alcohol (PVA), polyacrylonitrile (PAN), polymethylmethacrylate (PMMA), Nafion, and the combination of two or more abovementioned polymer hosts. Most commonly used organic solvents to prepare GEs include ethylene carbonate (EC), propylene carbonate (PC), diethyl carbonate (DEC), ethyl methyl carbonate (EMC), dimethyl carbonate (DMC), dimethylformamide (DMF), tetrahydrofuran (THF), and dimethyl sulfoxide. Some of the copolymers prepared using *N*-isopropylacrylamide (NIPAM) and acrylic acid (AA) is also reported to serve as GEs for LIB application. Thermally responsive poly (benzyl methacrylate) (PBMA) in 1-ethyl-3-methylimidazolium bis

(trifluoromethanesulfonyl) imide [EMIM][TFSI] was reported successfully inhibiting Li dendritic growth during LIB at elevated temperatures (Kelly et al. 2015). GEs can be fabricated adopting different methodologies including casting (Mohamed and Arof 2004; Sung et al. 1998), in situ polymerization (Kim and Moon 2005; Xu and Ye 2005), extraction-activation (Tarascon et al. 1996), and phase inversion mechanism (Du Pasquier et al. 2000; Gu et al. 2007; Manuel Stephan and Teeters 2003; Pu et al. 2006; Young and Chen 1995; Li et al. 2008b) to ensure superior performance. A variety of inorganic/organic fillers or plasticizers had been reported to improve GE performance by enhancing their mechanical properties and thermal stability. The commonly used filler includes TiO_2, Al_2O_3, SiO_2, Li_3N, $LiAlO_2$, and $BaTiO_3$ (Itoh et al. 2003; Kalyana Sundaram and Subramania 2007; Magistris et al. 2000; Kim et al. 2003; Liu et al. 2003). The performances of the device using GEs strongly depend on the morphology (Capiglia et al. 2002), size (Kumar and Scanlon 1994), crystallinity (Wen et al. 2000), and surface modification (Kim et al. 2003; Liu et al. 2002; Xi and Tang 2004; Zoulalian et al. 2006) of the filler. Inorganic fillers including TiO_2 (Chen et al. 2015; Kurc 2014; Zhang et al. 2015c) and Al_2O_3 (Jeong et al. 2010; Li et al. 2005) nanoparticle usually show better thermal stability compared with organic. A sol-gel type electrolyte composed of thermally responsive poly(*N*-isopropylacrylamide-*co*-acrylamide) including PEG-borate ester and polyvinylidene fluoride-graft-polyacrylonitrile (PVDF-g-PAN) using TiO_2 nanoparticle filler is reported as an excellent choice for LIB application (Hui et al. 2015). Recently, PVDF-HFP/PMMA-based gel polymer electrolyte comprising TiO_2 nanoparticles was developed providing good cyclability, improved rate performance, excellent chemical/mechanical stability, and decent wettability (Song et al. 2015). However, their drawbacks such as low thermal and electrochemical stability and poor cyclic and rate performances have limited their further applications.

3.7.3 Solid Electrolytes

Rechargeable Li-ion batteries based on liquid electrolyte are dangerous as they can leak and ignite rapidly if overheated or abused during operation. Solid-state electrolytes (SSEs) currently become very attractive and progressive field for LIB application due to superior thermal and mechanical stability, improved safety, and flexibility. Moreover, SSEs provide much reliable ion transport as compared to the liquid electrolytes leading to the uniform electrodeposition, resulting in high stability and stable battery performance. Therefore, SSEs are the preferred choice to replace liquid electrolytes. The developments of SSEs for LIBs have explicitly focused on oxide and thiophosphate compounds. The oxide-based SSEs possess moderate Li-ion conductivity; on the other hand, thiophosphates, such as $Li_{10}GeP_2S_{12}$ and Li_2S-P_2S_5, deliver conductivities comparable to liquid electrolytes at room temperature (Takada 2013; Thangadurai et al. 2014; Bron et al. 2013; Hori et al. 2014; Kamaya et al. 2011; Kuhn et al. 2013; Seino et al. 2014). Even though some scientific challenges have been recognized for these systems including limited

chemical and electrochemical interfacial stability with electrodes (Kato et al. 2016; Mo et al. 2012; Sakuda et al. 2010; Shin et al. 2014; Wenzel et al. 2016), significant improvements with new solutions have proven an absolute success. Recently complex hydrides, e.g., $LiBH_4$, were discovered to provide good ionic conductivity and exceptional stability at a higher temperature. For instance, the Li-ion conductivity of $LiBH_4$ increases abruptly to $>1 \times 10^{-3}$ S cm^{-1} above 100 °C due to a structural phase transition (Matsuo et al. 2007). Furthermore, this high-temperature, superionic phase is reported to stabilize at room temperature by the integration of Li-halides ($LiBH_4$-LiX, where X = Cl, Br, I). Among all, Li iodide (Li-I) exhibits the highest ionic conductivity (~10^{-5} S cm^{-1}) at room temperature (Maekawa et al. 2009). Very recently, the conductivity of the $Li(BH_4)_{1-x}(NH_2)_x$ system is reported to reach around 10^{-4} Scm^{-1} near room temperature (Mohtadi et al. 2016; Matsuo et al. 2009; Mohtadi and Orimo 2016). However, SSE-based Li-ion batteries have not yet reached the performance level of their liquid counterparts. Even after considerable success, before commercialization, SSEs need to overcome poor ionic conductivity, low mechanical strength, inferior interfacial properties, and ambiguity in fabrication.

3.8 Separators

The last two decades has witnessed tremendous development and application of LIBs in digital, handy, customized, and futuristic electronic systems. Safety and reliability are the crucial issues to be considered with the rechargeable LIBs. The separator is one of the necessary and essential components of the rechargeable batteries. The separator is a thin insulating porous membrane, physically separating battery electrodes (anode and cathode) while facilitating ion transport. An ideal battery separator must be highly stable, chemically inert, and mechanically robust while providing excellent porosity and ion transport properties. The insulating separator membrane must be as thin as possible and highly porous to provide obstruct-free ionic conductivity (Huang and Hitt 2013). During battery operation, the overall electrochemical process is exothermic (Zhang et al. 2015a). Even at normal working conditions (at ambient temperature), the heat transfer from internal battery components to cell case took place simultaneously to counterbalance the internal heat generation (Zhang et al. 2015b; Wang et al. 2017). Sometimes, during commercial/lab-scale packaging, the battery cell is abused mechanically due to inappropriate handling; as a result the separator membrane can rupture leaving electrodes (cathode and anode) in direct physical contact, leading to uncontrolled discharge or short circuit. For this type of cell assembly, under battery operation, the local internal temperature can rise up to 100–120 °C within few seconds, triggering exothermic chemical and electrochemical reactions resulting in thermal runaway or explosion (Wang et al. 2012) as most of the electrolytes contain highly flammable organic solvents (Hu et al. 2013), which may undergo combustion. In the case of the small-sized Li-ion battery pack (e.g., CR-2023 and smaller), the surface-to-volume

ratio is high; the temperature change is a repeatedly trifling result worsening the situation (Wang et al. 2017).

3.8.1 The Role and Characteristics of an Ideal Separator Membrane

A battery separator allows Li-ions to migrate through it via electrolyte during the charging, from the cathode to anode. A reverse reaction takes place during discharge when Li-ions transport from anode to cathode. During whole battery operation (charging-discharging process), the electrons are transported through the external circuit. Selection of the suitable battery separator is based on the following factors:

1. A separator membrane must provide good electronic insulation with negligible electrolyte (ionic) resistance and should allow easy handling.
2. An ideal separator membrane should own sufficient physical, mechanical strength and excellent thermal stability.
3. The separator should be chemically resistant to the degradation by the internal battery components including electrode materials, electrolyte media, their by-products, and impurities.
4. A separator must efficiently prevent migration of intermediate by-products or soluble species resulting from the reaction of electrode and electrode.
5. A separator must be readily wettable by electrolyte while procuring uniform thickness (Arora and Zhang 2004).

3.8.2 Separators for Li-Ion Batteries

Most commonly used LIB separators are made of very simple plastic films inheriting porosity allowing ions to travel through while restricting the other battery components. An ideal battery separator must be absorbent and thin enough to allow the Li-ions to migrate through it without any static hindrance while limiting itself to the least possible space. Additionally, a battery separator must remarkably oppose penetration to intercept any possible physical contact of electrodes. Polypropylene (PP), polyethylene (PE), and ceramic-embedded battery separators are reported delivering excellent porosity, high mechanical strength, and durability, as well as low cost. Separators made up from the single polyolefins layer are commercially available for small batteries. However, many multilayer separators where two of the layers have different phase transition temperatures, specially designed with a shut-down feature, are also being used to ensure safer battery operation at higher temperature. As the internal temperature of the battery increases during operation, a separator layer with the lower melting point melts and fills the pores to stop ion transport resulting in the shutting off of the device. Commonly used separators designed for small rechargeable LIBs are approximately 25 μm thick, possess 40%

Table 3.4 List of various separators commercially available. The specification is provided from the datasheet of the respective product

	Celgard	Entek	Degussa	Exxon
Product	2325	Tecklon	Separion	Tonen
Thickness	25	25	25	25
Single/multilayer	Trilayer	Single	Trilayer	Single
Composition	PE-PP-PE	PE	Ceramic-PE-ceramic	PE
Porosity (%)	41	38	>40	36
Melting temperature	134–166 °C	135 °C	220 °C	135 °C

porosity and low ionic resistivity (1.5–2.5 Ω-cm^2), and have bulk puncture strengths >300 g/mil (Arora and Zhang 2004; Linden and Reddy 2002; Zhang 2007). Ideally, a separator must be much thinner than 25 μm for better performance, but with issues related to stability, mechanical robustness arises due to downsizing (Arora and Zhang 2004; Linden and Reddy 2002; Zhang 2007).

Recently, there are reports on successful development of composite separators fabricated using γ-$LiAlO_2$, Al_2O_3, and MgO ceramics with PVDF binder (Prosini et al. 2002). Soon after this, several researchers started following while integrating other ceramic composites including $CaCO_3$@polytetrafluoroethylene (PTFE) and TiO_2@PVdF (Kim et al. 2006; Zhang et al. 2003). The first ever successfully commercialized composite separator "Separion" was composed of a three-layer membrane system introducing two layers of ceramics (SiO_2/Al_2O_3) sandwiched between porous polyethylene terephthalate (PET) films (Augustin et al. 2002). This composite separator was highly stable as compared to commonly used polyolefin membranes (>220 °C) due to the higher melting points of its ingredients ensuring excellent battery safety. Later on, Al_2O_3, ZrO_2, SiO_2, etc. along with polymers including polyethylene (PE), polypropylene (PPE), PET, and PVdF have been reported (Cho et al. 2010; Jeong et al. 2010; Bruce et al. 2008) to fabricate composite separators. A list summarizing commercially available separators and their properties is presented in Table 3.4.

3.9 Summary and Perspectives

Even after the great success in the development of state-of-the-art design and flourishing commercialization of LIBs, their accomplishment is not up to the mark because of some bottlenecks including insignificant energy/power density, large irreversible capacity, and poor cycle life. The deployment of nanostructured electrode is suggested to be one of the most effective solutions to these issues, promising high specific capacity. However, some of the hitches, e.g., exponential volume change during lithiation resulting in capacity decay and poor charge transfer kinetics, prominently obstruct LIB applications. Coating of thin passive protective layers

(e.g., metal oxide Al_2O_3, TiO_2, carbon, conductive polymers, etc.) on the electrode surface is an advantageous strategy to improve the cycling stability. Recently, considerable interest is spotted in growing different nanostructures including 0-D (nanoparticles), 1-D (nanowires, nanorods, nanobelts, and nanotubes), 2-D (nanoflakes, nanosheets, nanoplates, and nanowalls), and 3-D (flower-like or hierarchical) directly on different 2-D/3-D planner conductive substrates, e.g., copper, titanium, and stainless steel foils, to serve as binder-free electrodes with superior performance. As compared to the bulk counterpart, nanostructured electrode materials provide higher surface area, which is easily accessible for electrolyte and ions, while shortening the diffusion lengths, leading to improved energy storage and superior performance for LIB application. A number of strategies for synthesizing energy storage materials have been reported till date. The use of micro-/nanostructured or, nanomaterials with hollow and core-shell architectures as potential electrode materials for Li-ion batteries results in enhanced Li-ion kinetics resulting in improved rate capability and cycling performance. Interestingly, heterostructured nanoarrays have shown unrivaled possibilities to generate hybrid nanoarray electrodes with superior capacity, improved cyclability, and enhanced rate capability due to synergistic effects. Nevertheless, insignificant active electrode mass results in poor areal capacity and energy density. It is still challenging to realize thick layer of nanostructured active materials providing superior battery performance. Furthermore, the research directions toward nanostructured electrode designing have set the future research area to realize high energy and power density, better cyclability, and safer LIB operation. The design of nano-heterostructure assembly helps to overcome the low coulombic efficiency, exhibiting enhanced thermodynamic stability. Hollow and core-shell nanostructured electrode materials have demonstrated superior rate capability and improved cycling stability. Furthermore, optimization for the development of unique and high-energy, stable electrode materials can still be achieved through the synergy of several strategies resulting in high capacity, longer cycling life, and improved safety electrode materials to facilitate wider application.

Acknowledgments We acknowledge the Department of Science & Technology-Science, Engineering Research Board (DST-SERB) and the Council of Scientific & Industrial Research (CSIR), New Delhi, India, for providing financial support.

References

Abe K, Yoshitake H, Kitakura T, Hattori T, Wang H, Yoshio M (2004) Additives-containing functional electrolytes for suppressing electrolyte decomposition in lithium-ion batteries. Electrochim Acta 49(26):4613–4622. https://doi.org/10.1016/j.electacta.2004.05.016

Agubra VA, Fergus JW (2014) The formation and stability of the solid electrolyte interface on the graphite anode. J Power Sources 268:153–162. https://doi.org/10.1016/j.jpowsour.2014.06.024

Akira Y (2012) The birth of the lithium-ion battery. Angew Chem Int Ed 51(24):5798–5800. https://doi.org/10.1002/anie.201105006

Antolini E (2004) LiCoO2: formation, structure, lithium and oxygen nonstoichiometry, electrochemical behaviour and transport properties. Solid State Ionics 170(3):159–171. https://doi.org/10.1016/j.ssi.2004.04.003

Anton T, Ravi K, Chunzeng L, Stephen M, Xingcheng X, Sheldon WB (2016) Control and optimization of the electrochemical and mechanical properties of the solid electrolyte interphase on silicon electrodes in Lithium ion batteries. Adv Energy Mater 6(8):1502302. https://doi.org/10.1002/aenm.201502302

Aricò AS, Bruce P, Scrosati B, Tarascon J-M, van Schalkwijk W (2005) Nanostructured materials for advanced energy conversion and storage devices. Nat Mater 4:366. https://doi.org/10.1038/nmat1368

Armand M, Tarascon J-M (2008) Building better batteries. Nature 451:652. https://doi.org/10.1038/451652

Armstrong G, Armstrong AR, Bruce PG, Reale P, Scrosati B (2006) TiO_2(B) nanowires as an improved anode material for Lithium-ion batteries containing $LiFePO_4$ or $LiNi_{0.5}Mn_{1.5}O_4$ cathodes and a polymer electrolyte. Adv Mater 18(19):2597–2600. https://doi.org/10.1002/adma.200601232

Arora P, Zhang Z(J) (2004) Battery separators. Chem Rev 104(10):4419–4462. https://doi.org/10.1021/cr020738u

Arya A, Sharma AL (2017) Polymer electrolytes for lithium ion batteries: a critical study. Ionics 23(3):497–540. https://doi.org/10.1007/s11581-016-1908-6

Augustin S, Hennige V, Hörpel G, Hying C (2002) Ceramic but flexible: new ceramic membrane foils for fuel cells and batteries. Desalination 146(1):23–28. https://doi.org/10.1016/S0011-9164(02)00465-4

Aurbach D (1989) The electrochemical behavior of lithium salt solutions of γ-butyrolactone with noble metal electrodes. J Electrochem Soc 136(4):906–913. https://doi.org/10.1149/1.2096876

Aurbach D, Levi MD, Gamulski K, Markovsky B, Salitra G, Levi E, Oesten R (1999) Capacity fading of $LixMn_2O_4$ spinel electrodes studied by XRD and electroanalytical techniques. J Power Sources 81–82:472–479. https://doi.org/10.1016/S0378-7753(99)00204-9

Aurbach D, Gamolsky K, Markovsky B, Gofer Y, Schmidt M, Heider U (2002) On the use of vinylene carbonate (VC) as an additive to electrolyte solutions for Li-ion batteries. Electrochim Acta 47(9):1423–1439. https://doi.org/10.1016/S0013-4686(01)00858-1

Aurbach D, Suresh GS, Levi E, Mitelman A, Mizrahi O, Chusid O, Brunelli M (2007) Progress in rechargeable magnesium battery technology. Adv Mater 19(23):4260–4267. https://doi.org/10.1002/adma.200701495

Banerjee J, Dutta K (2016) Materials for electrodes of Li-ion batteries: issues related to stress development. Crit Rev Solid State Mater Sci 42:218–238

Bao W, Zhang Z, Gan Y, Wang X, Lia J (2013) Enhanced cyclability of sulfur cathodes in lithium-sulfur batteries with Na-alginate as a binder. J Energy Chem 22(5):790–794. https://doi.org/10.1016/S2095-4956(13)60105-9

Behera SK (2011) Enhanced rate performance and cyclic stability of Fe3O4-graphene nanocomposites for li ion battery anodes. Chem Commun 47(37):10371–10373. https://doi.org/10.1039/C1CC13218K

Berthier C, Gorecki W, Minier M, Armand MB, Chabagno JM, Rigaud P (1983) Microscopic investigation of ionic conductivity in alkali metal salts-poly(ethylene oxide) adducts. Solid State Ionics 11(1):91–95. https://doi.org/10.1016/0167-2738(83)90068-1

Biao Z, Matei GC, Christel L, Cathie V, Jean-Marie T (2015) Correlation between microstructure and Na storage behavior in hard carbon. Adv Energy Mater 6(1):1501588. https://doi.org/10.1002/aenm.201501588

Bindumadhavan K, Srivastava SK, Mahanty S (2013) MoS2-MWCNT hybrids as a superior anode in lithium-ion batteries. Chem Commun 49(18):1823–1825. https://doi.org/10.1039/C3CC38598A

Bonaccorso F, Colombo L, Yu G, Stoller M, Tozzini V, Ferrari AC, Pellegrini V (2015) Graphene, related two-dimensional crystals, and hybrid systems for energy conversion and storage. Science 347(6217):1246501. https://doi.org/10.1126/science.1246501

Borghols WJH, Wagemaker M, Lafont U, Kelder EM, Mulder FM (2009) Size effects in the $Li_{4+x}Ti_5O_{12}$ spinel. J Am Chem Soc 131(49):17786–17792. https://doi.org/10.1021/ja902423e

Bottone SR (2010) Galvanic batteries, their theory, construction and use, comprising primary, single and double fluid cells. Secondary and gas batteries. Nabu Press, Charleston

Bron P, Johansson S, Zick K, Schmedt auf der Günne J, Dehnen S, Roling B (2013) Li10SnP2S12: an affordable Lithium superionic conductor. J Am Chem Soc 135(42):15694–15697. https://doi.org/10.1021/ja407393y

Bruce PG, Scrosati B, Tarascon J-M (2008) Nanomaterials for rechargeable lithium batteries. Angew Chem Int Ed 47(16):2930–2946. https://doi.org/10.1002/anie.200702505

Cao Z, Xu P, Zhai H, Du S, Mandal J, Dontigny M, Zabhib K, Yang Y (2016) Ambient-air stable lithiated anode for rechargeable Li-ion batteries with high energy density. Nano Lett 16 (11):7235–7240. https://doi.org/10.1021/acs.nanolett.6b03655

Capiglia C, Yang J, Imanishi N, Hirano A, Takeda Y, Yamamoto O (2002) Composite polymer electrolyte: the role of filler grain size. Solid State Ionics 154–155:7–14. https://doi.org/10.1016/S0167-2738(02)00448-4

Chan CK, Peng H, Liu G, McIlwrath K, Zhang XF, Huggins RA, Cui Y (2007) High-performance lithium battery anodes using silicon nanowires. Nat Nanotechnol 3:31. https://doi.org/10.1038/nnano.2007.411

Chen J, Asano M, Yamaki T, Yoshida M (2006) Preparation and characterization of chemically stable polymer electrolyte membranes by radiation-induced graft copolymerization of four monomers into ETFE films. J Membr Sci 269(1):194–204. https://doi.org/10.1016/j.memsci.2005.06.035

Chen JS, Li CM, Zhou WW, Yan QY, Archer LA, Lou XW (2009) One-pot formation of SnO2 hollow nanospheres and [small alpha]-Fe2O3@SnO2 nanorattles with large void space and their lithium storage properties. Nanoscale 1(2):280–285. https://doi.org/10.1039/B9NR00102F

Chen L, Wang Z, He C, Zhao N, Shi C, Liu E, Li J (2013) Porous graphitic carbon nanosheets as a high-rate anode material for lithium-ion batteries. ACS Appl Mater Interfaces 5(19):9537–9545. https://doi.org/10.1021/am402368p

Chen W, Liu Y, Ma Y, Yang W (2015) Improved performance of lithium ion battery separator enabled by co-electrospinning polyimide/poly(vinylidene fluoride-co-hexafluoropropylene) and the incorporation of TiO2-(2-hydroxyethyl methacrylate). J Power Sources 273:1127–1135. https://doi.org/10.1016/j.jpowsour.2014.10.026

Cheng C, Fan HJ (2012) Branched nanowires: synthesis and energy applications. Nano Today 7 (4):327–343. https://doi.org/10.1016/j.nantod.2012.06.002

Cheng F, Zhao J, Song W, Li C, Ma H, Chen J, Shen P (2006) Facile controlled synthesis of MnO_2 nanostructures of novel shapes and their application in batteries. Inorg Chem 45(5):2038–2044. https://doi.org/10.1021/ic051715b

Cheng F, Tao Z, Liang J, Chen J (2008) Template-directed materials for rechargeable Lithium-ion batteries. Chem Mater 20(3):667–681. https://doi.org/10.1021/cm702091q

Cho T-H, Tanaka M, Ohnishi H, Kondo Y, Yoshikazu M, Nakamura T, Sakai T (2010) Composite nonwoven separator for lithium-ion battery: development and characterization. J Power Sources 195(13):4272–4277. https://doi.org/10.1016/j.jpowsour.2010.01.018

Choi J, Jin J, Jung IG, Kim JM, Kim HJ, Son SU (2011) SnSe2 nanoplate-graphene composites as anode materials for lithium ion batteries. Chem Commun 47(18):5241–5243. https://doi.org/10.1039/C1CC10317B

Chou S-L, Wang J-Z, Choucair M, Liu H-K, Stride JA, Dou S-X (2010) Enhanced reversible lithium storage in a nanosize silicon/graphene composite. Electrochem Commun 12 (2):303–306. https://doi.org/10.1016/j.elecom.2009.12.024

Chung S-Y, Bloking JT, Chiang Y-M (2002) Electronically conductive phospho-olivines as lithium storage electrodes. Nat Mater 1:123. https://doi.org/10.1038/nmat732

Croguennec L, Palacin MR (2015) Recent achievements on inorganic electrode materials for Lithium-ion batteries. J Am Chem Soc 137(9):3140–3156. https://doi.org/10.1021/ja507828x

Cui Y, Chai J, Du H, Duan Y, Xie G, Liu Z, Cui G (2017) Facile and reliable in situ polymerization of poly(ethyl cyanoacrylate)-based polymer electrolytes toward flexible lithium batteries. ACS Appl Mater Interfaces 9(10):8737–8741. https://doi.org/10.1021/acsami.6b16218

Czyżyk MT, Potze R, Sawatzky GA (1992) Band-theory description of high-energy spectroscopy and the electronic structure of ${\mathrm{ LiCoO}}_{2}$. Phys Rev B 46(7):3729–3735. https://doi.org/10.1103/PhysRevB.46.3729

Dahn JR, von Sacken U, Michal CA (1990) Structure and electrochemistry of $Li_{1\pm y}NiO_2$ and a new Li_2NiO_2 phase with the $Ni(OH)_2$ structure. Solid State Ionics 44(1):87–97. https://doi.org/10.1016/0167-2738(90)90049-W

Daniel C, Mohanty D, Li J, Wood DL (2014) AIP Conference Proceedings 1597:26. https://doi.org/10.1063/1.4878478

Demir-Cakan R, Hu Y-S, Antonietti M, Maier J, Titirici M-M (2008) Facile one-pot synthesis of mesoporous SnO_2 microspheres via nanoparticles assembly and lithium storage properties. Chem Mater 20(4):1227–1229. https://doi.org/10.1021/cm7031288

Ding YL, Zhao X-B, Xie J, Cao G-S, Zhu TJ, Yu HM, Sun CY (2011a) Double-shelled hollow microspheres of $LiMn_2O_4$ for high-performance lithium-ion batteries. J Mater Chem 21(26):9475–9479. https://doi.org/10.1039/C1JM10924C

Ding S, Chen JS, Qi G, Duan X, Wang Z, Giannelis EP, Lou XW (2011b) Formation of SnO_2 hollow nanospheres inside mesoporous silica nanoreactors. J Am Chem Soc 133(1):21–23. https://doi.org/10.1021/ja108720w

Du Pasquier A, Warren PC, Culver D, Gozdz AS, Amatucci GG, Tarascon JM (2000) Plastic PVDF-HFP electrolyte laminates prepared by a phase-inversion process. Solid State Ionics 135(1):249–257. https://doi.org/10.1016/S0167-2738(00)00371-4

Dunn B, Kamath H, Tarascon J-M (2011) Electrical energy storage for the grid: a battery of choices. Science 334(6058):928 LP-–935. https://doi.org/10.1126/science.1212741

Ehrlich GM (2002) Chapter 35. In: Linden D, Reddy TB (eds) Handbook of batteries. McGraw-Hill, New York, pp 35.31–35.94

Ellis BL, Philippe K, Thierry D (2014) Three-dimensional self-supported metal oxides for advanced energy storage. Adv Mater 26(21):3368–3397. https://doi.org/10.1002/adma.201306126

Eom JY, Kwon HS, Liu J, Zhou O (2004) Lithium insertion into purified and etched multi-walled carbon nanotubes synthesized on supported catalysts by thermal CVD. Carbon 42(12):2589–2596. https://doi.org/10.1016/j.carbon.2004.05.039

Eom J, Kim D, Kwon H (2006) Effects of ball-milling on lithium insertion into multi-walled carbon nanotubes synthesized by thermal chemical vapour deposition. J Power Sources 157(1):507–514. https://doi.org/10.1016/j.jpowsour.2005.08.024

Etacheri V, Marom R, Elazari R, Salitra G, Aurbach D (2011) Challenges in the development of advanced Li-ion batteries: a review. Energy Environ Sci 4(9):3243–3262. https://doi.org/10.1039/C1EE01598B

Feng Z, Limin Q (2016) Recent progress in self-supported metal oxide nanoarray electrodes for advanced Lithium-ion batteries. Adv Sci 3(9):1600049. https://doi.org/10.1002/advs.201600049

Ferg E, Gummow RJ, de Kock A, Thackeray MM (1994) Spinel anodes for lithium-ion batteries. J Electrochem Soc 141(11):L147–L150. https://doi.org/10.1149/1.2059324

Finegan DP, Scheel M, Robinson JB, Tjaden B, Hunt I, Mason TJ et al (2015) In-operando high-speed tomography of lithium-ion batteries during thermal runaway. Nat Commun 6:6924. https://doi.org/10.1038/ncomms7924

Frackowiak E, Gautier S, Gaucher H, Bonnamy S, Beguin F (1999) Electrochemical storage of lithium in multiwalled carbon nanotubes. Carbon 37(1):61–69. https://doi.org/10.1016/S0008-6223(98)00187-0

Fuller CS, Severiens JC (1954) Mobility of impurity ions in germanium and silicon. Phys Rev 96(1):21–24. https://doi.org/10.1103/PhysRev.96.21

Futaba DN, Hata K, Yamada T, Hiraoka T, Hayamizu Y, Kakudate Y, Iijima S (2006) Shape-engineerable and highly densely packed single-walled carbon nanotubes and their application as super-capacitor electrodes. Nat Mater 5:987. https://doi.org/10.1038/nmat1782

Gallagher K, Croy J, Balasubramanian M, Bettge M, Abraham DK, Burrell A, Thackeray M (2013) Correlating hysteresis and voltage fade in lithium- and manganese-rich layered transition-metal oxide electrodes. Electrochem Commun 33:96–98. https://doi.org/10.1016/j.elecom.2013.04.022

Gao B, Bower C, Lorentzen JD, Fleming L, Kleinhammes A, Tang XP, Zhou O (2000) Enhanced saturation lithium composition in ball-milled single-walled carbon nanotubes. Chem Phys Lett 327(1):69–75. https://doi.org/10.1016/S0009-2614(00)00851-4

Geim AK, Novoselov KS (2007) The rise of graphene. Nat Mater 6:183. https://doi.org/10.1038/nmat1849

Gibot P, Casas-Cabanas M, Laffont L, Levasseur S, Carlach P, Hamelet S et al (2008) Room-temperature single-phase Li insertion/extraction in nanoscale LixFePO4. Nat Mater 7:741. https://doi.org/10.1038/nmat2245

Goodenough JB (2013) Evolution of strategies for modern rechargeable batteries. Acc Chem Res 46(5):1053–1061. https://doi.org/10.1021/ar2002705

Goodenough JB, Kim Y (2010) Challenges for rechargeable li batteries. Chem Mater 22 (3):587–603. https://doi.org/10.1021/cm901452z

Goodenough JB, Park K-S (2013) The Li-ion rechargeable battery: a perspective. J Am Chem Soc 135(4):1167–1176. https://doi.org/10.1021/ja3091438

Goriparti S, Miele E, De Angelis F, Di Fabrizio E, Proietti Zaccaria R, Capiglia C (2014) Review on recent progress of nanostructured anode materials for Li-ion batteries. J Power Sources 257:421–443. https://doi.org/10.1016/j.jpowsour.2013.11.103

Grünebaum M, Hiller MM, Jankowsky S, Jeschke S, Pohl B, Schürmann T et al (2014) Synthesis and electrochemistry of polymer based electrolytes for lithium batteries. Prog Solid State Chem 42(4):85–105. https://doi.org/10.1016/j.progsolidstchem.2014.04.004

Gu M, Zhang J, Xia Y, Wang X (2007) Poly(vinylidene fluoride) crystallization behavior and membrane structure formation via thermally induced phase separation with benzophenone diluent. J Macromol Sci B 47(1):180–191. https://doi.org/10.1080/00222340701748628

Gummow RJ, de Kock A, Thackeray MM (1994) Improved capacity retention in rechargeable 4 V lithium/lithium-manganese oxide (spinel) cells. Solid State Ionics 69(1):59–67. https://doi.org/10.1016/0167-2738(94)90450-2

Guo Y-G, Hu Y-S, Sigle W, Maier J (2007) Superior electrode performance of nanostructured mesoporous TiO_2 (Anatase) through efficient hierarchical mixed conducting networks. Adv Mater 19(16):2087–2091. https://doi.org/10.1002/adma.200602828

Guo YG, Hu JS, Wan LJ (2008) Nanostructured materials for electrochemical energy conversion and storage devices. Adv Mater 20(15):2878–2887. https://doi.org/10.1002/adma.200800627

Guo P, Song H, Chen X (2009) Electrochemical performance of graphene nanosheets as anode material for lithium-ion batteries. Electrochem Commun 11(6):1320–1324. https://doi.org/10.1016/j.elecom.2009.04.036

Guo J, Sun A, Wang C (2010) A porous silicon–carbon anode with high overall capacity on carbon fiber current collector. Electrochem Commun 12(7):981–984. https://doi.org/10.1016/j.elecom.2010.05.006

Han MH, Gonzalo E, Singh G, Rojo T (2015) A comprehensive review of sodium layered oxides: powerful cathodes for Na-ion batteries. Energy Environ Sci 8(1):81–102. https://doi.org/10.1039/C4EE03192J

Hao S, Xuemei F, Songlin X, Yishu J, Huisheng P (2016) Electrochemical capacitors with high output voltages that mimic electric eels. Adv Mater 28(10):2070–2076. https://doi.org/10.1002/adma.201505742

Haregewoin AM, Wotango AS, Hwang B-J (2016) Electrolyte additives for lithium ion battery electrodes: progress and perspectives. Energy Environ Sci 9(6):1955–1988. https://doi.org/10.1039/C6EE00123H

Hassoun J, Reale P, Scrosati B (2007) Recent advances in liquid and polymer lithium-ion batteries. J Mater Chem 17(35):3668–3677. https://doi.org/10.1039/B707040N

He M, Yuan L-X, Zhang W-X, Hu X-L, Huang Y-H (2011) Enhanced cyclability for sulfur cathode achieved by a water-soluble binder. J Phys Chem C 115(31):15703–15709. https://doi.org/10.1021/jp2043416

Herle PS, Ellis B, Coombs N, Nazar LF (2004) Nano-network electronic conduction in iron and nickel olivine phosphates. Nat Mater 3:147. https://doi.org/10.1038/nmat1063

Higgins TM, Park S-H, King PJ, Zhang CJ, McEvoy N, Berner NC et al (2016) A commercial conducting polymer as both binder and conductive additive for silicon nanoparticle-based lithium-ion battery negative electrodes. ACS Nano 10(3):3702–3713. https://doi.org/10.1021/acsnano.6b00218

Holtstiege F, Schmuch R, Winter M, Brunklaus G, Placke T (2018) New insights into the pre-lithiation kinetics of graphite anodes via nuclear magnetic resonance spectroscopy. J Power Sources 378:522–526. https://doi.org/10.1016/j.jpowsour.2017.12.069

Hongcai G, Bingkun G, Jie S, Kyusung P, Goodenough JB (2015) A composite gel–polymer/glass–fiber electrolyte for sodium-ion batteries. Adv Energy Mater 5(9):1402235. https://doi.org/10.1002/aenm.201402235

Hongsen L, Laifa S, Jie W, Bing D, Ping N, Guiyin X, Xiaogang Z (2013) Design of a nitrogen-doped, carbon-coated $Li_4Ti_5O_{12}$ nanocomposite with a core–shell structure and its application for high-rate lithium-ion batteries. ChemPlusChem 79(1):128–133. https://doi.org/10.1002/cplu.201300316

Hori S, Suzuki K, Hirayama M, Kato Y, Saito T, Yonemura M, Kanno R (2014) Synthesis, structure, and ionic conductivity of solid solution, Li10+[small delta]M1+[small delta]P2-[small delta]S12 (M = Si, Sn). Faraday Discuss 176(0):83–94. https://doi.org/10.1039/C4FD00143E

Hosono E, Kudo T, Honma I, Matsuda H, Zhou H (2009) Synthesis of single-crystalline spinel LiMn2O4 nanowires for a lithium-ion battery with high power density. Nano Lett 9 (3):1045–1051. https://doi.org/10.1021/nl803394v

Hu Y, Kong W, Li H, Huang X, Chen L (2004) Experimental and theoretical studies on reduction mechanism of vinyl ethylene carbonate on graphite anode for lithium ion batteries. Electrochem Commun 6(2):126–131. https://doi.org/10.1016/j.elecom.2003.10.024

Hu Y-S, Kinley L, Guo Y-G, Maier J (2006) High lithium electro activity of nanometer-sized rutile TiO2. Adv Mater 18(11):1421–1426. https://doi.org/10.1002/adma.200502723

Hu L, Zhang Z, Amine K (2013) Fluorinated electrolytes for Li-ion battery: an FEC-based electrolyte for high voltage LiNi0.5Mn1.5O4/graphite couple. Electrochem Commun 35:76–79. https://doi.org/10.1016/j.elecom.2013.08.009

Hu J, Tian J, Li C (2017) Nanostructured carbon nitride polymer-reinforced electrolyte to enable dendrite-suppressed lithium metal batteries. ACS Appl Mater Interfaces 9(13):11615–11625. https://doi.org/10.1021/acsami.7b00478

Huang X, Hitt J (2013) Lithium ion battery separators: development and performance characterization of a composite membrane. J Membr Sci 425–426:163–168. https://doi.org/10.1016/j.memsci.2012.09.027

Huang P, Wang Q, Li K, Ping P, Sun J (2015) The combustion behavior of large scale lithium titanate battery. Sci Rep 5:7788. https://doi.org/10.1038/srep07788

Hui Y, Zhiyuan L, Chandran BK, Jiyang D, Jiancan Y, Dianpeng Q et al (2015) Self-protection of electrochemical storage devices via a thermal reversible sol–gel transition. Adv Mater 27 (37):5593–5598. https://doi.org/10.1002/adma.201502484

Huie MM, Bock DC, Takeuchi ES, Marschilok AC, Takeuchi KJ (2015) Cathode materials for magnesium and magnesium-ion based batteries. Coord Chem Rev 287:15–27. https://doi.org/10.1016/j.ccr.2014.11.005

Idota Y, Kubota T, Matsufuji A, Maekawa Y, Miyasaka T (1997) Tin-based amorphous oxide: a high-capacity lithium-ion-storage material. Science 276(5317):1395 LP–-1397. https://doi.org/10.1126/science.276.5317.1395

Irene O, de Henrik V, Bruno S, Stefano P (2016) Ionic-liquid-based polymer electrolytes for battery applications. Angew Chem Int Ed 55(2):500–513. https://doi.org/10.1002/anie.201504971

Islam MS, Fisher CAJ (2014) Chem Soc Rev 43:185–204

Itagaki M, Kobari N, Yotsuda S, Watanabe K, Kinoshita S, Ue M (2005) LiCoO2 electrode/electrolyte interface of Li-ion rechargeable batteries investigated by in situ electrochemical impedance spectroscopy. J Power Sources 148:78–84. https://doi.org/10.1016/j.jpowsour.2005.02.007

Itoh T, Miyamura Y, Ichikawa Y, Uno T, Kubo M, Yamamoto O (2003) Composite polymer electrolytes of poly(ethylene oxide)/BaTiO3/Li salt with hyperbranched polymer. J Power Sources 119–121:403–408. https://doi.org/10.1016/S0378-7753(03)00261-1

Jaiswal A, Horne CR, Chang O, Zhang W, Kong W, Wang E, Doeff MM (2009) Nanoscale LiFePO4 and Li4Ti5O12 for high rate Li-ion batteries. J Electrochem Soc 156(12):A1041–A1046. https://doi.org/10.1149/1.3223987

Jang J, Jeong S, Seo J, Kim M-C, Sim E, Oh Y, Cheon J (2011) Ultrathin zirconium disulfide nanodiscs. J Am Chem Soc 133(20):7636–7639. https://doi.org/10.1021/ja200400n

Jeong H-S, Kim D-W, Jeong YU, Lee S-Y (2010) Effect of phase inversion on microporous structure development of Al2O3/poly(vinylidene fluoride-hexafluoropropylene)-based ceramic composite separators for lithium-ion batteries. J Power Sources 195(18):6116–6121. https://doi.org/10.1016/j.jpowsour.2009.10.085

Jeong PM, Ilyoung C, Jaewan H, Onnuri K (2013) Polymer electrolytes integrated with ionic liquids for future electrochemical devices. J Appl Polym Sci 129(5):2363–2376. https://doi.org/10.1002/app.39064

Ji L, Lin Z, Alcoutlabi M, Zhang X (2011) Recent developments in nanostructured anode materials for rechargeable lithium-ion batteries. Energy Environ Sci 4(8):2682–2699. https://doi.org/10.1039/C0EE00699H

Jian J, Yuanyuan L, Jinping L, Xintang H, Changzhou Y, Lou XW(D) (2012) Recent advances in metal oxide-based electrode architecture design for electrochemical energy storage. Adv Mater 24(38):5166–5180. https://doi.org/10.1002/adma.201202146

Jiang C, Hosono E, Zhou H (2006) Nanomaterials for lithium-ion batteries. Nano Today 1 (4):28–33. https://doi.org/10.1016/S1748-0132(06)70114-1

Jiang J, Li Y, Liu J, Huang X (2011) Building one-dimensional oxide nanostructure arrays on conductive metal substrates for lithium-ion battery anodes. Nanoscale 3(1):45–58. https://doi.org/10.1039/C0NR00472C

Jin J, Wen Z, Liang X, Cui Y, Wu X (2012) Gel polymer electrolyte with ionic liquid for high performance lithium sulfur battery. Solid State Ionics 225:604–607. https://doi.org/10.1016/j.ssi.2012.03.012

Jin K, Zhou X, Zhang L, Xin X, Wang G, Liu Z (2013) Sulfur/carbon nanotube composite film as a flexible cathode for Lithium–sulfur batteries. J Phys Chem C 117(41):21112–21119. https://doi.org/10.1021/jp406757w

Jordi C, Laure M, Dominique L, Rosa PM (2010) Beyond intercalation-based Li-ion batteries: the state of the art and challenges of electrode materials reacting through conversion reactions. Adv Mater 22(35):E170–E192. https://doi.org/10.1002/adma.201000717

Julian K, Gebresilassie EG, Dominic B, Stefano P (2015) Safer electrolytes for Lithium-ion batteries: state of the art and perspectives. ChemSusChem 8(13):2154–2175. https://doi.org/10.1002/cssc.201500284

Jun C, Zhan-Liang T, Suo-Long L (2003) Lithium intercalation in open-ended TiS2 nanotubes. Angew Chem Int Ed 42(19):2147–2151. https://doi.org/10.1002/anie.200250573

Kalyana Sundaram NT, Subramania A (2007) Nano-size LiAlO2 ceramic filler incorporated porous PVDF-co-HFP electrolyte for lithium-ion battery applications. Electrochim Acta 52 (15):4987–4993. https://doi.org/10.1016/j.electacta.2007.01.066

Kamaya N, Homma K, Yamakawa Y, Hirayama M, Kanno R, Yonemura M et al (2011) A lithium superionic conductor. Nat Mater 10:682. https://doi.org/10.1038/nmat3066

Kartick B, Srivastava SK, Mahanty S (2013) TiS2–MWCNT hybrid as high performance anode in lithium-ion battery. J Nanopart Res 15(9):1950. https://doi.org/10.1007/s11051-013-1950-5

Kartick B, Srivastava SK, Mahanty S (2014) Tungsten disulfide-multiwalled carbon nanotube hybrid anode for lithium-ion battery. J Nanosci Nanotechnol 14(5):3758–3764. https://doi.org/10.1166/jnn.2014.8737

Kato Y, Hori S, Saito T, Suzuki K, Hirayama M, Mitsui A et al (2016) High-power all-solid-state batteries using sulfide superionic conductors. Nat Energy 1:16030. https://doi.org/10.1038/nenergy.2016.30

Kelly JC, Degrood NL, Roberts ME (2015) Li-ion battery shut-off at high temperature caused by polymer phase separation in responsive electrolytes. Chem Commun 51(25):5448–5451. https://doi.org/10.1039/C4CC10282G

Khatib R, Dalverny A-L, Saubanère M, Gaberscek M, Doublet M-L (2013) Origin of the voltage hysteresis in the CoP conversion material for Li-ion batteries. J Phys Chem C 117(2):837–849. https://doi.org/10.1021/jp310366a

Kim H-S, Moon S-I (2005) Synthesis and electrochemical performances of di(trimethylolpropane) tetraacrylate-based gel polymer electrolyte. J Power Sources 146(1):584–588. https://doi.org/10.1016/j.jpowsour.2005.03.148

Kim H, Choi J, Sohn H, Kang T (1999) The insertion mechanism of lithium into Mg_2Si anode material for Li-ion batteries. J Electrochem Soc 146(12):4401–4405. https://doi.org/10.1149/1.1392650

Kim S-S, Kadoma Y, Ikuta H, Uchimoto Y, Wakihara M (2001) Electrochemical performance of natural graphite by surface modification using aluminum. Electrochem Solid-State Lett 4(8): A109–A112. https://doi.org/10.1149/1.1379829

Kim J-W, Ji K-S, Lee J-P, Park J-W (2003) Electrochemical characteristics of two types of PEO-based composite electrolyte with functional SiO2. J Power Sources 119–121:415–421. https://doi.org/10.1016/S0378-7753(03)00263-5

Kim KM, Park N-G, Ryu KS, Chang SH (2006) Characteristics of PVdF-HFP/TiO2 composite membrane electrolytes prepared by phase inversion and conventional casting methods. Electrochim Acta 51(26):5636–5644. https://doi.org/10.1016/j.electacta.2006.02.038

Kim Y-L, Sun Y-K, Lee S-M (2008) Enhanced electrochemical performance of silicon-based anode material by using current collector with modified surface morphology. Electrochim Acta 53 (13):4500–4504. https://doi.org/10.1016/j.electacta.2008.01.050

Kim Y-D, Kang J-G, Park J-G, Lee S, Kim D-W (2009) Self-supported SnO_2 nanowire electrodes for high-power lithium-ion batteries. Nanotechnology 20(45):455701. https://doi.org/10.1088/0957-4484/20/45/455701

Klavetter KC, Pedro de Souza J, Heller A, Mullins CB (2015) High tap density microparticles of selenium-doped germanium as a high efficiency, stable cycling lithium-ion battery anode material. J Mater Chem A 3(11):5829–5834. https://doi.org/10.1039/C5TA00319A

Koksbang R, Barker J, Shi H, Saïdi MY (1996) Cathode materials for lithium rocking chair batteries. Solid State Ionics 84(1):1–21. https://doi.org/10.1016/S0167-2738(96)83001-3

Kuhn A, Duppel V, Lotsch BV (2013) Tetragonal Li10GeP2S12 and Li7GePS8 – exploring the li ion dynamics in LGPS li electrolytes. Energy Environ Sci 6(12):3548–3552. https://doi.org/10.1039/C3EE41728J

Kumar P, Hu LH (2018) Mater Res Express 5(2018):075510

Kumar B, Scanlon LG (1994) Polymer-ceramic composite electrolytes. J Power Sources 52 (2):261–268. https://doi.org/10.1016/0378-7753(94)02147-3

Kumar P, Ming J, Li. M, Wahyudi W, Li LJ (2016) ECS- J Solid State Sci Technol 2016 5:Q3021–Q3025

Kurc B (2014) Gel electrolytes based on poly(acrylonitrile)/sulfolane with hybrid TiO2/SiO2 filler for advanced lithium polymer batteries. Electrochim Acta 125:415–420. https://doi.org/10.1016/j.electacta.2014.01.117

Lacey MJ, Jeschull F, Edström K, Brandell D (2014a) Functional, water-soluble binders for improved capacity and stability of lithium–sulfur batteries. J Power Sources 264:8–14. https://doi.org/10.1016/j.jpowsour.2014.04.090

Lacey MJ, Jeschull F, Edström K, Brandell D (2014b) Porosity blocking in highly porous carbon black by PVdF binder and its implications for the li–S system. J Phys Chem C 118 (45):25890–25898. https://doi.org/10.1021/jp508137m

Lai H, Li J, Chen Z, Huang Z (2012) Carbon nanohorns as a high-performance carrier for MnO2 anode in lithium-ion batteries. ACS Appl Mater Interfaces 4(5):2325–2328. https://doi.org/10.1021/am300378w

Larcher D, Tarascon J-M (2014) Towards greener and more sustainable batteries for electrical energy storage. Nat Chem 7:19. https://doi.org/10.1038/nchem.2085

Larcher D, Masquelier C, Bonnin D, Chabre Y, Masson V, Leriche J-B, Tarascon J-M (2003) Effect of particle size on lithium intercalation into α-Fe_2O_3. J Electrochem Soc 150(1):A133–A139. https://doi.org/10.1149/1.1528941

Lee KT, Jung YS, Oh SM (2003) Synthesis of tin-encapsulated spherical hollow carbon for anode material in Lithium secondary batteries. J Am Chem Soc 125(19):5652–5653. https://doi.org/10.1021/ja0345524

Lee S-Y, Ogawa A, Kanno M, Nakamoto H, Yasuda T, Watanabe M (2010) Nonhumidified intermediate temperature fuel cells using protic ionic liquids. J Am Chem Soc 132 (28):9764–9773. https://doi.org/10.1021/ja102367x

Lee SW, McDowell MT, Choi JW, Cui Y (2011) Anomalous shape changes of silicon nanopillars by electrochemical Lithiation. Nano Lett 11(7):3034–3039. https://doi.org/10.1021/nl201787r

Lei L, Raji AR, Tour JM (2013) Graphene-wrapped MnO_2–graphene nanoribbons as anode materials for high-performance lithium ion batteries. Adv Mater 25(43):6298–6302. https://doi.org/10.1002/adma.201302915

Li Q, Bjerrum NJ (2002) Aluminum as anode for energy storage and conversion: a review. J Power Sources 110(1):1–10. https://doi.org/10.1016/S0378-7753(01)01014-X

Li H, Zhou H (2012) Enhancing the performances of Li-ion batteries by carbon-coating: present and future. Chem Commun 48(9):1201–1217. https://doi.org/10.1039/C1CC14764A

Li Z, Su G, Wang X, Gao D (2005) Micro-porous P(VDF-HFP)-based polymer electrolyte filled with Al2O3 nanoparticles. Solid State Ionics 176(23):1903–1908. https://doi.org/10.1016/j.ssi.2005.05.006

Li Y, Tan B, Wu Y (2008a) Mesoporous Co_3O_4 nanowire arrays for Lithium ion batteries with high capacity and rate capability. Nano Lett 8(1):265–270. https://doi.org/10.1021/nl0725906

Li ZH, Zhang P, Zhang HP, Wu YP, Zhou XD (2008b) A lotus root-like porous nanocomposite polymer electrolyte. Electrochem Commun 10(5):791–794. https://doi.org/10.1016/j.elecom.2008.02.036

Li B, Cao H, Shao J, Qu M (2011) Enhanced anode performances of the Fe_3O_4-carbon-rGO three dimensional composite in lithium ion batteries. Chem Commun 47(37):10374–10376. https://doi.org/10.1039/C1CC13462K

Li L, Meng F, Jin S (2012a) High-capacity Lithium-ion battery conversion cathodes based on Iron fluoride nanowires and insights into the conversion mechanism. Nano Lett 12(11):6030–6037. https://doi.org/10.1021/nl303630p

Li L, Yu Y, Meng F, Tan Y, Hamers RJ, Jin S (2012b) Facile solution synthesis of α-FeF3·3H2O nanowires and their conversion to α-Fe2O3 nanowires for photoelectrochemical application. Nano Lett 12(2):724–731. https://doi.org/10.1021/nl2036854

Li X, Li D, Qiao L, Wang X, Sun X, Wang P, He D (2012c) Interconnected porous MnO nanoflakes for high-performance lithium ion battery anodes. J Mater Chem 22(18):9189–9194. https://doi.org/10.1039/C2JM30604B

Li L, Jacobs R, Gao P, Gan L, Wang F, Morgan D, Jin S (2016) Origins of large voltage hysteresis in high-energy-density metal fluoride lithium-ion battery conversion electrodes. J Am Chem Soc 138(8):2838–2848. https://doi.org/10.1021/jacs.6b00061

Lian P, Zhu X, Xiang H, Li Z, Yang W, Wang H (2010) Enhanced cycling performance of Fe3O4–graphene nanocomposite as an anode material for lithium-ion batteries. Electrochim Acta 56 (2):834–840. https://doi.org/10.1016/j.electacta.2010.09.086

Liang Z, Lin D, Zhao J, Lu Z, Liu Y, Liu C, Cui Y (2016) Composite lithium metal anode by melt infusion of lithium into a 3D conducting scaffold with lithiophilic coating. Proc Natl Acad Sci U S A 113(11):2862 LP–2867. https://doi.org/10.1073/pnas.1518188113

Liao J-Y, Higgins D, Lui G, Chabot V, Xiao X, Chen Z (2013) Multifunctional TiO2–C/MnO2 Core–double-Shell nanowire arrays as high-performance 3D electrodes for lithium ion batteries. Nano Lett 13(11):5467–5473. https://doi.org/10.1021/nl4030159

Liaoyong W, Zhijie W, Yan M, Rui X, Shu-Hong Y, Yong L (2015) Designing heterogeneous 1D nanostructure arrays based on AAO templates for energy applications. Small 11 (28):3408–3428. https://doi.org/10.1002/smll.201500120

Licht S, Douglas A, Ren J, Carter R, Lefler M, Pint CL (2016) Carbon nanotubes produced from ambient carbon dioxide for environmentally sustainable lithium-ion and sodium-ion battery anodes. ACS Cent Sci 2(3):162–168. https://doi.org/10.1021/acscentsci.5b00400

Limthongkul P, Jang Y-I, Dudney NJ, Chiang Y-M (2003) Electrochemically-driven solid-state amorphization in lithium-silicon alloys and implications for lithium storage. Acta Mater 51 (4):1103–1113. https://doi.org/10.1016/S1359-6454(02)00514-1

Lin M-C, Gong M, Lu B, Wu Y, Wang D-Y, Guan M, Dai H (2015) An ultrafast rechargeable aluminium-ion battery. Nature 520:324. https://doi.org/10.1038/nature14340

Lin D, Liu Y, Liang Z, Lee H-W, Sun J, Wang H, Cui Y (2016) Layered reduced graphene oxide with nanoscale interlayer gaps as a stable host for lithium metal anodes. Nat Nanotechnol 11:626. https://doi.org/10.1038/nnano.2016.32

Lin D, Liu Y, Cui Y (2017) Reviving the lithium metal anode for high-energy batteries. Nat Nanotechnol 12(3):194–206. https://doi.org/10.1038/nnano.2017.16

Linden D, Reddy TB (2002) Handbook of batteries, 3rd edn. McGraw-Hill, New York

Linlin L, Shengjie P, Yanling C, Peifen T, Jin W, Grace W, Madhavi S (2013) Electrospun porous $NiCo_2O_4$ nanotubes as advanced electrodes for electrochemical capacitors. Chem Eur J 19 (19):5892–5898. https://doi.org/10.1002/chem.201204153

Liu Y, Cui Y (2017) Lithium Metal Anodes: Recipe Prot Joule 1:643–650. https://doi.org/10.1016/j.joule.2017.12.001

Liu Y, Lee JY, Hong L (2002) Functionalized SiO2 in poly(ethylene oxide)-based polymer electrolytes. J Power Sources 109(2):507–514. https://doi.org/10.1016/S0378-7753(02)00167-2

Liu Y, Lee JY, Hong L (2003) Morphology, crystallinity, and electrochemical properties of in situ formed poly(ethylene oxide)/TiO2 nanocomposite polymer electrolytes. J Appl Polym Sci 89 (10):2815–2822. https://doi.org/10.1002/app.12487

Liu N, Hu L, McDowell MT, Jackson A, Cui Y (2011) Prelithiated silicon nanowires as an anode for lithium-ion batteries. ACS Nano 5(8):6487–6493. https://doi.org/10.1021/nn2017167

Liu H, Su D, Wang G, Qiao SZ (2012) An ordered mesoporous WS_2 anode material with superior electrochemical performance for lithium ion batteries. J Mater Chem 22(34):17437–17440. https://doi.org/10.1039/c2jm33992g

Liu N, Li W, Pasta M, Cui Y (2014a) Nanomaterials for electrochemical energy storage. Front Phys 9(3):323–350. https://doi.org/10.1007/s11467-013-0408-7

Liu Y, Wang W, Huang H, Gu L, Wang Y, Peng X (2014b) The highly enhanced performance of lamellar WS_2 nanosheet electrodes upon intercalation of single-walled carbon nanotubes for supercapacitors and lithium ions batteries. Chem Commun 50(34):4485–4488

Liu C, Neale ZG, Cao G (2016a) Understanding electrochemical potentials of cathode materials in rechargeable batteries. Mater Today 19(2):109–123. https://doi.org/10.1016/j.mattod.2015.10.009

Liu Y, Lin D, Liang Z, Zhao J, Yan K, Cui Y (2016b) Lithium-coated polymeric matrix as a minimum volume-change and dendrite-free lithium metal anode. Nat Commun 7:10992. https://doi.org/10.1038/ncomms10992

Longwei Y, Zhiwei Z, Zhaoqiang L, Fengbin H, Qun L, Chengxiang W, Yongxin Q (2014) Spinel ZnMn2O4 nanocrystal-anchored 3D hierarchical carbon aerogel hybrids as anode materials for lithium ion batteries. Adv Funct Mater 24(26):4176–4185. https://doi.org/10.1002/adfm.201400108

Lou XW, Li CM, Archer LA (2009) Designed synthesis of coaxial SnO2@carbon hollow nanospheres for highly reversible lithium storage. Adv Mater 21(24):2536–2539. https://doi.org/10.1002/adma.200803439

Lowe M, Tokuoka S, Trigg T, Gereffi G (2010) Lithium-ion batteries for electric vehicles: the US value chain. Center on Globalization, Governance & Competitiveness Duke University, Durham

Lu W, Henry K, Turchi C, Pellegrino J (2008) Incorporating ionic liquid electrolytes into polymer gels for solid-state ultracapacitors. J Electrochem Soc 155(5):A361–A367. https://doi.org/10.1149/1.2869202

Luo W, Schardt J, Bommier C, Wang B, Razink J, Simonsen J, Ji X (2013) Carbon nanofibers derived from cellulose nanofibers as a long-life anode material for rechargeable sodium-ion batteries. J Mater Chem A 1(36):10662–10666. https://doi.org/10.1039/C3TA12389H

Maekawa H, Matsuo M, Takamura H, Ando M, Noda Y, Karahashi T, Orimo S (2009) Halide-stabilized LiBH4, a room-temperature lithium fast-ion conductor. J Am Chem Soc 131 (3):894–895. https://doi.org/10.1021/ja807392k

Magistris A, Mustarelli P, Quartarone E, Tomasi C (2000) Transport and thermal properties of (PEO)n–LiPF6 electrolytes for super-ambient applications. Solid State Ionics 136–137:1241–1247. https://doi.org/10.1016/S0167-2738(00)00594-4

Mai L, Tian X, Xu X, Chang L, Xu L (2014) Nanowire electrodes for electrochemical energy storage devices. Chem Rev 114(23):11828–11862. https://doi.org/10.1021/cr500177a

Manuel Stephan A, Teeters D (2003) Characterization of PVdF-HFP polymer membranes prepared by phase inversion techniques I. morphology and charge–discharge studies. Electrochim Acta 48(14):2143–2148. https://doi.org/10.1016/S0013-4686(03)00197-X

Marcinek M, Syzdek J, Marczewski M, Piszcz M, Niedzicki L, Kalita M et al (2015) Electrolytes for Li-ion transport – review. Solid State Ionics 276:107–126. https://doi.org/10.1016/j.ssi.2015.02.006

Martin W, Besenhard JO, Spahr ME, Petr N (1999) Insertion electrode materials for rechargeable lithium batteries. Adv Mater 10(10):725–763. https://doi.org/10.1002/(SICI)1521-4095(199807)10:10<725:AID-ADMA725>3.0.CO;2-Z

Matsuo M, Nakamori Y, Orimo S, Maekawa H, Takamura H (2007) Lithium superionic conduction in lithium borohydride accompanied by structural transition. Appl Phys Lett 91(22):224103. https://doi.org/10.1063/1.2817934

Matsuo M, Remhof A, Martelli P, Caputo R, Ernst M, Miura Y et al (2009) Complex hydrides with (BH4)− and (NH2)− anions as new lithium fast-ion conductors. J Am Chem Soc 131 (45):16389–16391. https://doi.org/10.1021/ja907249p

Mei L, Li C, Qu B, Zhang M, Xu C, Lei D, Wang T (2012) Small quantities of cobalt deposited on tin oxide as anode material to improve performance of lithium-ion batteries. Nanoscale 4 (18):5731–5737. https://doi.org/10.1039/C2NR31307C

Meyer WH (1999) Polymer electrolytes for lithium-ion batteries. Adv Mater 10(6):439–448. https://doi.org/10.1002/(SICI)1521-4095(199804)10:6<439:AID-ADMA439>3.0.CO;2-I

Michel A (2004) Polymers with ionic conductivity. Adv Mater 2(6–7):278–286. https://doi.org/10.1002/adma.19900020603

Minsub O, Sekwon N, Chang-Su W, Jun-Ho J, Sung-Soo K, Alicja B et al (2015) Observation of electrochemically driven elemental segregation in a Si alloy thin-film anode and its effects on cyclic stability for Li-ion batteries. Adv Energy Mater 5(22):1501136. https://doi.org/10.1002/aenm.201501136

Mizushima K, Jones PC, Wiseman PJ, Goodenough JB (1980) $LixCoO_2$ (0<x<−1): a new cathode material for batteries of high energy density. Mater Res Bull 15(6):783–789. https://doi.org/10.1016/0025-5408(80)90012-4

Mo Y, Ong SP, Ceder G (2012) First principles study of the Li10GeP2S12 Lithium super ionic conductor material. Chem Mater 24(1):15–17. https://doi.org/10.1021/cm203303y

Mohamed NS, Arof AK (2004) Investigation of electrical and electrochemical properties of PVDF-based polymer electrolytes. J Power Sources 132(1):229–234. https://doi.org/10.1016/j.jpowsour.2003.12.031

Mohtadi R, Orimo S (2016) The renaissance of hydrides as energy materials. Nat Rev Mater 2:16091. https://doi.org/10.1038/natrevmats.2016.91

Mohtadi R, Remhof A, Jena P (2016) Complex metal borohydrides: multifunctional materials for energy storage and conversion. J Phys Condens Matter 28(35):353001. https://doi.org/10.1088/0953-8984/28/35/353001

Mukhopadhyay A, Jangid MK (2018) Li metal battery, healthy self. Science 359:1463

Myung S-T, Hitoshi Y, Sun Y-K (2011) Electrochemical behavior and passivation of current collectors in lithium-ion batteries. J Mater Chem 21(27):9891–9911. https://doi.org/10.1039/C0JM04353B

Nazri GA, Pistoia P (2003) Lithium batteries: science and technology. Kluwer Academic Publishers, Boston

Nishi Y (2001) Lithium ion secondary batteries; past 10 years and the future. J Power Sources 100 (1):101–106. https://doi.org/10.1016/S0378-7753(01)00887-4

Nitta N, Wu F, Lee JT, Yushin G (2015) Li-ion battery materials: present and future. Mater Today 18(5):252–264. https://doi.org/10.1016/j.mattod.2014.10.040

Nobili F, Dsoke S, Mancini M, Marassi R (2009) Interfacial properties of copper-coated graphite electrodes: coating thickness dependence. Fuel Cells 9(3):264–268. https://doi.org/10.1002/fuce.200800087

Noel M, Suryanarayanan V (2002) Role of carbon host lattices in Li-ion intercalation/de-intercalation processes. J Power Sources 111(2):193–209. https://doi.org/10.1016/S0378-7753(02)00308-7

Novoselov KS, Geim AK, Morozov SV, Jiang D, Zhang Y, Dubonos SV, Firsov AA (2004) Electric field effect in atomically thin carbon films. Science 306(5696):666 LP-–669. https://doi.org/10.1126/science.1102896

Obrovac MN, Chevrier VL (2014) Alloy negative electrodes for Li-ion batteries. Chem Rev 114 (23):11444–11502. https://doi.org/10.1021/cr500207g

Oh SM, Myung ST, Park JB, Scrosati B, Amine K, Sun YK (2012) Angew Chem Int Ed 51 (8):1853–1856. https://doi.org/10.1002/anie.201107394

Ohzuku T, Makimura Y (2001a) Layered lithium insertion material of $LiCo_{1/3}Ni_{1/3}Mn_{1/3}O_2$ for lithium-ion batteries. Chem Lett 30(7):642–643. https://doi.org/10.1246/cl.2001.642

Ohzuku T, Makimura Y (2001b) Layered lithium insertion material of $LiNi_{1/2}Mn_{1/2}O_2$: a possible alternative to $LiCoO_2$ for advanced lithium-ion batteries. Chem Lett 30(8):744–745. https://doi.org/10.1246/cl.2001.744

Owen JR (1997) Rechargeable lithium batteries. Chem Soc Rev 26(4):259–267. https://doi.org/10.1039/CS9972600259

Palacin MR (2009) Recent advances in rechargeable battery materials: a chemist's perspective. Chem Soc Rev 38(9):2565–2575. https://doi.org/10.1039/B820555H

Pan D, Wang S, Zhao B, Wu M, Zhang H, Wang Y, Jiao Z (2009) Li storage properties of disordered graphene nanosheets. Chem Mater 21(14):3136–3142. https://doi.org/10.1021/cm900395k

Park JK (2012) Principles and applications of lithium secondary batteries. Wiley-VCH, Weinheim

Park K-S, Benayad A, Kang D-J, Doo S-G (2008) Nitridation-driven conductive Li4Ti5O12 for lithium ion batteries. J Am Chem Soc 130(45):14930–14931. https://doi.org/10.1021/ja806104n

Peng C, Chen B, Qin Y, Yang S, Li C, Zuo Y, Yang J (2012) Facile ultrasonic synthesis of CoO quantum dot/graphene nanosheet composites with high lithium storage capacity. ACS Nano 6 (2):1074–1081. https://doi.org/10.1021/nn202888d

Persson K, Sethuraman VA, Hardwick LJ, Hinuma Y, Meng YS, van der Ven A, Ceder G (2010) Lithium diffusion in graphitic carbon. J Phys Chem Lett 1(8):1176–1180. https://doi.org/10.1021/jz100188d

Pharr M, Choi YS, Lee D, Oh KH, Vlassak JJ (2016) Measurements of stress and fracture in germanium electrodes of lithium-ion batteries during electrochemical lithiation and delithiation. J Power Sources 304:164–169. https://doi.org/10.1016/j.jpowsour.2015.11.036

Poizot P, Laruelle S, Grugeon S, Dupont L, Tarascon J-M (2000) Nano-sized transition-metal oxides as negative-electrode materials for lithium-ion batteries. Nature 407:496. https://doi.org/10.1038/35035045

Porcarelli L, Gerbaldi C, Bella F, Nair JR (2016) Super soft all-ethylene oxide polymer electrolyte for safe all-solid Lithium batteries. Sci Rep 6:19892. Retrieved from. https://doi.org/10.1038/srep19892

Prosini PP, Villano P, Carewska M (2002) A novel intrinsically porous separator for self-standing lithium-ion batteries. Electrochim Acta 48(3):227–233. https://doi.org/10.1016/S0013-4686(02)00601-1

Pu W, He X, Wang L, Jiang C, Wan C (2006) Preparation of PVDF–HFP microporous membrane for Li-ion batteries by phase inversion. J Membr Sci 272(1):11–14. https://doi.org/10.1016/j.memsci.2005.12.038

Qiao J, Fu J, Lin R, Ma J, Liu J (2010) Alkaline solid polymer electrolyte membranes based on structurally modified PVA/PVP with improved alkali stability. Polymer 51(21):4850–4859. https://doi.org/10.1016/j.polymer.2010.08.018

Qingwen L, Yan-Bing H, Qipeng Y, Baohua L, Valentino KY, Youwei Y et al (2017) Dendrite-free, high-rate, long-life lithium metal batteries with a 3D cross-linked network polymer electrolyte. Adv Mater 29(13):1604460. https://doi.org/10.1002/adma.201604460

Ran E, Gregory S, Arnd G, Alexander P, Doron A (2011) Sulfur-impregnated activated carbon Fiber cloth as a binder-free cathode for rechargeable li-S batteries. Adv Mater 23 (47):5641–5644. https://doi.org/10.1002/adma.201103274

Reddy MV, Subba Rao GV, Chowdari BVR (2013) Metal oxides and oxysalts as anode materials for li ion batteries. Chem Rev 113(7):5364–5457. https://doi.org/10.1021/cr3001884

Roberts AD, Li X, Zhang H (2014) Porous carbon spheres and monoliths: morphology control, pore size tuning and their applications as Li-ion battery anode materials. Chem Soc Rev 43 (13):4341–4356. https://doi.org/10.1039/C4CS00071D

Rowsell JLC, Pralong V, Nazar LF (2001) Layered lithium Iron nitride: a promising anode material for Li-ion batteries. J Am Chem Soc 123(35):8598–8599. https://doi.org/10.1021/ja0112745

Roy P, Srivastava SK (2015) J Mater Chem A 3:2454. https://doi.org/10.1039/c4ta04980b

Ruetschi P (1977) Review on the lead—acid battery science and technology. J Power Sources 2 (1):3–120. https://doi.org/10.1016/0378-7753(77)85003-9

Rui X, Zhao X, Lu Z, Tan H, Sim D, Hng HH, Yan Q (2013) Olivine-type nanosheets for lithium-ion battery cathodes. ACS Nano 7(6):5637–5646. https://doi.org/10.1021/nn4022263

Sa Q, Wang Y (2012) Ni foam as the current collector for high capacity C–Si composite electrode. J Power Sources 208:46–51. https://doi.org/10.1016/j.jpowsour.2012.02.020

Saha P, Datta MK, Velikokhatnyi OI, Manivannan A, Alman D, Kumta PN (2014) Rechargeable magnesium battery: current status and key challenges for the future. Prog Mater Sci 66:1–86. https://doi.org/10.1016/j.pmatsci.2014.04.001

Saint J, Morcrette M, Larcher D, Tarascon JM (2005) Exploring the Li–Ga room temperature phase diagram and the electrochemical performances of the LixGay alloys vs. Li. Solid State Ionics 176(1):189–197. https://doi.org/10.1016/j.ssi.2004.05.021

Sakuda A, Hayashi A, Tatsumisago M (2010) Interfacial observation between LiCoO2 electrode and Li2S−P2S5 solid electrolytes of all-solid-state lithium secondary batteries using transmission electron microscopy. Chem Mater 22(3):949–956. https://doi.org/10.1021/cm901819c

Santner HJ, Möller K-C, Ivančo J, Ramsey MG, Netzer FP, Yamaguchi S, Winter M (2003) Acrylic acid nitrile, a film-forming electrolyte component for lithium-ion batteries, which belongs to the family of additives containing vinyl groups. J Power Sources 119–121:368–372. https://doi.org/10.1016/S0378-7753(03)00268-4

Sayle TXT, Maphanga RR, Ngoepe PE, Sayle DC (2009) Predicting the electrochemical properties of MnO2 nanomaterials used in rechargeable li batteries: simulating nanostructure at the atomistic level. J Am Chem Soc 131(17):6161–6173. https://doi.org/10.1021/ja8082335

Seino Y, Ota T, Takada K, Hayashi A, Tatsumisago M (2014) A sulphide lithium super ion conductor is superior to liquid ion conductors for use in rechargeable batteries. Energy Environ Sci 7(2):627–631. https://doi.org/10.1039/C3EE41655K

Shakir I (2014) High performance flexible pseudocapacitor based on nano-architectured spinel nickel cobaltite anchored multiwall carbon nanotubes. Electrochim Acta 132:490–495. https://doi.org/10.1016/j.electacta.2014.03.138

Shi L, Wang Q, Li H, Wang Z, Huang X, Chen L (2001) Electrochemical performance of Ni-deposited graphite anodes for lithium secondary batteries. J Power Sources 102(1):60–67. https://doi.org/10.1016/S0378-7753(01)00773-X

Shi Y, Wang Y, Wong JI, Tan AYS, Hsu C-L, Li L-J, Yang HY (2013) Self-assembly of hierarchical MoSx/CNT nanocomposites (2<x<3): towards high performance anode materials for lithium ion batteries. Sci Rep 3:2169. https://doi.org/10.1038/srep02169

Shi T, J. JY, R ZZ, Yong Y (2014) Recent progress in research on high-voltage electrolytes for lithium-ion batteries. ChemPhysChem 15(10):1956–1969. https://doi.org/10.1002/cphc.201402175

Shim E-G, Nam T-H, Kim J-G, Kim H-S, Moon S-I (2007) Effects of functional electrolyte additives for Li-ion batteries. J Power Sources 172(2):901–907. https://doi.org/10.1016/j.jpowsour.2007.04.089

Shin BR, Nam YJ, Oh DY, Kim DH, Kim JW, Jung YS (2014) Comparative study of TiS2/li-in all-solid-state Lithium batteries using glass-ceramic Li3PS4 and Li10GeP2S12 solid electrolytes. Electrochim Acta 146:395–402. https://doi.org/10.1016/j.electacta.2014.08.139

Silbernagel BG (1975) Lithium intercalation complexes of layered transition metal dichalcogenides: an NMR survey of physical properties. Solid State Commun 17(3):361–365. https://doi.org/10.1016/0038-1098(75)90312-9

Slater MD, Donghan K, Eungje L, Johnson CS (2012) Sodium-ion batteries. Adv Funct Mater 23 (8):947–958. https://doi.org/10.1002/adfm.201200691

Sobkowiak A, Roberts MR, Younesi R, Ericsson T, Häggström L, Tai C-W, Björefors F (2013) Understanding and controlling the surface chemistry of LiFeSO4F for an enhanced cathode functionality. Chem Mater 25(15):3020–3029. https://doi.org/10.1021/cm401063s

Soloveichik GL (2011) Battery technologies for large-scale stationary energy storage. Annu Rev Chem Biomol Eng 2(1):503–527. https://doi.org/10.1146/annurev-chembioeng-061010-114116

Song CJ, Lou XW(D) (2013) SnO2-based nanomaterials: synthesis and application in lithium-ion batteries. Small 9(11):1877–1893. https://doi.org/10.1002/smll.201202601

Song JY, Wang YY, Wan CC (1999) Review of gel-type polymer electrolytes for lithium-ion batteries. J Power Sources 77(2):183–197. https://doi.org/10.1016/S0378-7753(98)00193-1

Song D, Xu C, Chen Y, He J, Zhao Y, Li P, Fu F (2015) Enhanced thermal and electrochemical properties of PVDF-HFP/PMMA polymer electrolyte by TiO2 nanoparticles. Solid State Ionics 282:31–36. https://doi.org/10.1016/j.ssi.2015.09.017

Su F, Zeng J, Bao X, Yu Y, Lee JY, Zhao XS (2005) Preparation and characterization of highly ordered graphitic mesoporous carbon as a Pt catalyst support for direct methanol fuel cells. Chem Mater 17(15):3960–3967. https://doi.org/10.1021/cm0502222

Su L, Jing Y, Zhou Z (2011) Li ion battery materials with core-shell nanostructures. Nanoscale 3 (10):3967–3983. https://doi.org/10.1039/C1NR10550G

Subramanian V, Zhu H, Wei B (2006) High rate reversibility anode materials of lithium batteries from vapor-grown carbon nanofibers. J Phys Chem B 110(14):7178–7183. https://doi.org/10.1021/jp057080j

Sung H, Wang Y, Wan C (1998) Preparation and characterization of poly(vinyl chloride-co-vinyl acetate)-based gel electrolytes for Li-ion batteries. J Electrochem Soc 145(4):1207–1211. https://doi.org/10.1149/1.1838440

Taberna PL, Mitra S, Poizot P, Simon P, Tarascon J-M (2006) High rate capabilities Fe3O4-based Cu nano-architectured electrodes for lithium-ion battery applications. Nat Mater 5:567. https://doi.org/10.1038/nmat1672

Tadhg K, Michael B, Ryan KM (2016) Advances in the application of silicon and germanium nanowires for high-performance lithium-ion batteries. Adv Mater 28(27):5696–5704. https://doi.org/10.1002/adma.201503978

Takada K (2013) Progress and prospective of solid-state lithium batteries. Acta Mater 61 (3):759–770. https://doi.org/10.1016/j.actamat.2012.10.034

Takeda Y, Yamamoto O, Imanishi N (2016) Lithium dendrite formation on a lithium metal anode from liquid, polymer and solid electrolytes. Electrochemistry 84(4):210–218. https://doi.org/10.5796/electrochemistry.84.210

Tang M, Carter WC, Chiang Y-M (2010) Electrochemically driven phase transitions in insertion electrodes for lithium-ion batteries: examples in lithium metal phosphate olivines. Annu Rev Mater Res 40(1):501–529. https://doi.org/10.1146/annurev-matsci-070909-104435

Tang Y, Zhang Y, Li W, Ma B, Chen X (2015) Rational material design for ultrafast rechargeable lithium-ion batteries. Chem Soc Rev 44(17):5926–5940. https://doi.org/10.1039/C4CS00442F

Tao Z-L, Xu L-N, Gou X-L, Chen J, Yuan H-T (2004) TiS2 nanotubes as the cathode materials of Mg-ion batteries. Chem Commun 18:2080–2081. https://doi.org/10.1039/B403855J

Tarascon J-M, Gozdz AS, Schmutz C, Shokoohi F, Warren PC (1996) Performance of Bellcore's plastic rechargeable Li-ion batteries. Solid State Ionics 86–88:49–54. https://doi.org/10.1016/0167-2738(96)00330-X

Thackeray MM, David WIF, Bruce PG, Goodenough JB (1983) Lithium insertion into manganese spinels. Mater Res Bull 18(4):461–472. https://doi.org/10.1016/0025-5408(83)90138-1

Thangadurai V, Narayanan S, Pinzaru D (2014) Garnet-type solid-state fast Li ion conductors for Li batteries: critical review. Chem Soc Rev 43(13):4714–4727. https://doi.org/10.1039/C4CS00020J

Uchaker E, Garcia B (2014) Mesocrystals as electrode materials for lithium-ion batteries. Nano Today 9:499–524. https://doi.org/10.1016/j.nantod.2014.06.004

Urbonaite S, Novák P (2014) Importance of "unimportant" experimental parameters in Li–S battery development. J Power Sources 249:497–502. https://doi.org/10.1016/j.jpowsour.2013.10.095

Vanchiappan A, Yun-Sung L, Srinivasan M (2015) Research progress on negative electrodes for practical Li-ion batteries: beyond carbonaceous anodes. Adv Energy Mater 5(13):1402225. https://doi.org/10.1002/aenm.201402225

Wagemaker M, Mulder FM (2013) Properties and promises of nanosized insertion materials for Li-ion batteries. Acc Chem Res 46(5):1206–1215. https://doi.org/10.1021/ar2001793

Wang Y, Cao G (2006) Synthesis and enhanced intercalation properties of nanostructured vanadium oxides. Chem Mater 18(12):2787–2804. https://doi.org/10.1021/cm052765h

Wang J, Sun X (2015) Olivine $LiFePO_4$: the remaining challenges for future energy storage. Energy Environ Sci 8(4):1110–1138. https://doi.org/10.1039/C4EE04016C

Wang J, Raistrick ID, Huggins RA (1986) Behavior of some binary lithium alloys as negative electrodes in organic solvent-based electrolytes. J Electrochem Soc 133(3):457–460. https://doi.org/10.1149/1.2108601

Wang GX, Bewlay S, Yao J, Liu H-K, Dou SX (2004) Tungsten disulfide nanotubes for lithium storage. Electrochem Solid-State Lett 7(10):A321–A323

Wang XX, Wang JN, Chang H, Zhang YF (2007) Preparation of short carbon nanotubes and application as an electrode material in Li-ion batteries. Adv Funct Mater 17(17):3613–3618. https://doi.org/10.1002/adfm.200700319

Wang C, Li D, Too CO, Wallace GG (2009a) Electrochemical properties of graphene paper electrodes used in Lithium batteries. Chem Mater 21(13):2604–2606. https://doi.org/10.1021/cm900764n

Wang D, Choi D, Li J, Yang Z, Nie Z, Kou R et al (2009b) Self-assembled TiO2–graphene hybrid nanostructures for enhanced Li-ion insertion. ACS Nano 3(4):907–914. https://doi.org/10.1021/nn900150y

Wang G, Wang B, Wang X, Park J, Dou S, Ahn H, Kim K (2009c) Sn/graphene nanocomposite with 3D architecture for enhanced reversible lithium storage in lithium ion batteries. J Mater Chem 19(44):8378–8384. https://doi.org/10.1039/B914650D

Wang Y, Liu H, Wang K, Eiji H, Wang Y, Zhou H (2009d) Synthesis and electrochemical performance of nano-sized $Li_4Ti_5O_{12}$ with double surface modification of Ti(III) and carbon. J Mater Chem 19(37):6789–6795. https://doi.org/10.1039/B908025B

Wang B, Wu X-L, Shu C-Y, Guo Y-G, Wang C-R (2010a) Synthesis of CuO/graphene nanocomposite as a high-performance anode material for lithium-ion batteries. J Mater Chem 20(47):10661–10664. https://doi.org/10.1039/C0JM01941K

Wang H, Cui L-F, Yang Y, Sanchez Casalongue H, Robinson JT, Liang Y, Dai H (2010b) Mn_3O_4−graphene hybrid as a high-capacity anode material for Lithium ion batteries. J Am Chem Soc 132(40):13978–13980. https://doi.org/10.1021/ja105296a

Wang Y, Li H, He P, Hosono E, Zhou H (2010c) Nano active materials for lithium-ion batteries. Nanoscale 2(8):1294–1305. https://doi.org/10.1039/C0NR00068J

Wang F, Robert R, Chernova NA, Pereira N, Omenya F, Badway F et al (2011a) Conversion reaction mechanisms in lithium ion batteries: study of the binary metal fluoride electrodes. J Am Chem Soc 133(46):18828–18836. https://doi.org/10.1021/ja206268a

Wang Z, Luan D, Madhavi S, Ming Li C, Lou XW(D) (2011b) α-Fe_2O_3 nanotubes with superior lithium storage capability. Chem Commun 47(28):8061–8063. https://doi.org/10.1039/C1CC12111A

Wang Z, Luan D, Boey FYC, Lou XW(D) (2011c) Fast formation of SnO_2 nanoboxes with enhanced lithium storage capability. J Am Chem Soc 133(13):4738–4741. https://doi.org/10.1021/ja2004329

Wang Q, Ping P, Zhao X, Chu G, Sun J, Chen C (2012) Thermal runaway caused fire and explosion of lithium ion battery. J Power Sources 208:210–224. https://doi.org/10.1016/j.jpowsour.2012.02.038

Wang M, Li G, Xu H, Qian Y, Yang J (2013a) Enhanced lithium storage performances of hierarchical hollow MoS_2 nanoparticles assembled from Nanosheets. ACS Appl Mater Interfaces 5(3):1003–1008. https://doi.org/10.1021/am3026954

Wang Z, Gu M, Zhou Y, Zu X, Connell JG, Xiao J, Gao F (2013b) Electron-rich driven electrochemical solid-state amorphization in Li–Si alloys. Nano Lett 13(9):4511–4516. https://doi.org/10.1021/nl402429a

Wang Z, Cao D, Xu R, Qu S, Wang Z, Lei Y (2016) Realizing ordered arrays of nanostructures: a versatile platform for converting and storing energy efficiently. Nano Energy 19:328–362. https://doi.org/10.1016/j.nanoen.2015.11.032

Wang M, Le AV, Shi Y, Noelle DJ, Wu D, Fan J, Qiao Y (2017) Sigmoidal current collector for lithium-ion battery. J Appl Phys 121(1):15303. https://doi.org/10.1063/1.4973585

Wei W, Qian S, Ye Z, Sisi H, Qingqing W, Jue D, Huisheng P (2015) A gum-like lithium-ion battery based on a novel arched structure. Adv Mater 27(8):1363–1369. https://doi.org/10.1002/adma.201405127

Weiwei Z, Chuanwei C, Jinping L, Yan TY, Jian J, Xingtao J, Jin FH (2011) Epitaxial growth of branched α-Fe_2O_3/SnO_2 nano-heterostructures with improved lithium-ion battery performance. Adv Funct Mater 21(13):2439–2445. https://doi.org/10.1002/adfm.201100088

Wen CJ, Huggins RA (1981) Chemical diffusion in intermediate phases in the lithium-silicon system. J Solid State Chem 37(3):271–278. https://doi.org/10.1016/0022-4596(81)90487-4

Wen CJ, Boukamp BA, Huggins RA, Weppner W (1979) Thermodynamic and mass transport properties of "LiAl". J Electrochem Soc 126(12):2258–2266. https://doi.org/10.1149/1.2128939

Wen Z, Itoh T, Ikeda M, Hirata N, Kubo M, Yamamoto O (2000) Characterization of composite electrolytes based on a hyperbranched polymer. J Power Sources 90(1):20–26. https://doi.org/10.1016/S0378-7753(00)00442-0

Wen LX, Ming LC, Archer LA (2009) Designed synthesis of coaxial SnO2@carbon hollow nanospheres for highly reversible lithium storage. Adv Mater 21(24):2536–2539. https://doi.org/10.1002/adma.200803439

Wen Z, Ci S, Mao S, Cui S, He Z, Chen J (2013) CNT@TiO2 nanohybrids for high-performance anode of lithium-ion batteries. Nanoscale Res Lett 8(1):499. https://doi.org/10.1186/1556-276X-8-499

Wenzel S, Randau S, Leichtweiß T, Weber DA, Sann J, Zeier WG, Janek J (2016) Direct observation of the interfacial instability of the fast ionic conductor Li10GeP2S12 at the lithium metal anode. Chem Mater 28(7):2400–2407. https://doi.org/10.1021/acs.chemmater.6b00610

Whitehead AH, Schreiber M (2005) Current collectors for positive electrodes of lithium-based batteries. J Electrochem Soc 152(11):A2105–A2113. https://doi.org/10.1149/1.2039587

Whittingham MS (1978) Chemistry of intercalation compounds: metal guests in chalcogenide hosts. Prog Solid State Chem 12(1):41–99. https://doi.org/10.1016/0079-6786(78)90003-1
Whittingham MS (2004) Lithium batteries and cathode materials. Chem Rev 104(10):4271–4302. https://doi.org/10.1021/cr020731c
Whittingham MS (2014) Ultimate limits to intercalation reactions for lithium batteries. Chem Rev 114(23):11414–11443. https://doi.org/10.1021/cr5003003
Whittingham MS, Thompson AH (1975) Intercalation and lattice expansion in titanium disulfide. J Chem Phys 62(4):1588. https://doi.org/10.1063/1.430581
Wrodnigg GH, Wrodnigg TM, Besenhard JO, Winter M (1999) Propylene sulfite as film-forming electrolyte additive in lithium ion batteries. Electrochem Commun 1(3):148–150. https://doi.org/10.1016/S1388-2481(99)00023-5
Wrodnigg GH, Besenhard JO, Winter M (2001) Cyclic and acyclic sulfites: new solvents and electrolyte additives for lithium ion batteries with graphitic anodes? J Power Sources 97–98:592–594. https://doi.org/10.1016/S0378-7753(01)00536-5
Wu M-S, Chang H-W (2013) Self-assembly of NiO-coated ZnO nanorod electrodes with core–shell nanostructures as anode materials for rechargeable lithium-ion batteries. J Phys Chem C 117 (6):2590–2599. https://doi.org/10.1021/jp3079327
Wu H, Cui Y (2012) Designing nanostructured Si anodes for high energy lithium ion batteries. Nano Today 7(5):414–429. https://doi.org/10.1016/j.nantod.2012.08.004
Wu Z-S, Ren W, Wen L, Gao L, Zhao J, Chen Z, Cheng H-M (2010) Graphene anchored with Co_3O_4 nanoparticles as anode of Lithium ion batteries with enhanced reversible capacity and cyclic performance. ACS Nano 4(6):3187–3194. https://doi.org/10.1021/nn100740x
Wu HB, Chen JS, Hng HH, Lou XW(D) (2012) Nanostructured metal oxide-based materials as advanced anodes for lithium-ion batteries. Nanoscale 4(8):2526–2542. https://doi.org/10.1039/C2NR11966H
Wu Y, Reddy MV, Chowdari BVR, Ramakrishna S (2013) Long-term cycling studies on electrospun carbon nanofibers as anode material for lithium ion batteries. ACS Appl Mater Interfaces 5(22):12175–12184. https://doi.org/10.1021/am404216j
Wu R, Qian X, Zhou K, Wei J, Lou J, Ajayan PM (2014) Porous spinel ZnxCo3–xO4 hollow polyhedra templated for high-rate lithium-ion batteries. ACS Nano 8(6):6297–6303. https://doi.org/10.1021/nn501783n
Xi J, Tang X (2004) Enhanced lithium ion transference number and ionic conductivity of composite polymer electrolyte doped with organic–inorganic hybrid P123@SBA-15. Chem Phys Lett 400 (1):68–73. https://doi.org/10.1016/j.cplett.2004.10.094
Xia H, Lai M, Lu L (2010) Nanoflaky MnO_2/carbon nanotube nanocomposites as anode materials for lithium-ion batteries. J Mater Chem 20(33):6896–6902. https://doi.org/10.1039/C0JM00759E
Xia X, Tu J, Zhang Y, Wang X, Gu C, Zhao X, Fan HJ (2012) High-quality metal oxide core/shell nanowire arrays on conductive substrates for electrochemical energy storage. ACS Nano 6(6):5531–5538. https://doi.org/10.1021/nn301454q
Xiao L, Ai X, Cao Y, Yang H (2004) Electrochemical behavior of biphenyl as polymerizable additive for overcharge protection of lithium ion batteries. Electrochim Acta 49(24):4189–4196. https://doi.org/10.1016/j.electacta.2004.04.013
Xin X, Zhou X, Wu J, Yao X, Liu Z (2012) Scalable synthesis of TiO2/graphene nanostructured composite with high-rate performance for lithium ion batteries. ACS Nano 6(12):11035–11043. https://doi.org/10.1021/nn304725m
Xu K (2004) Nonaqueous liquid electrolytes for lithium-based rechargeable batteries. Chem Rev 104(10):4303–4418. https://doi.org/10.1021/cr030203g
Xu JJ, Ye H (2005) Polymer gel electrolytes based on oligomeric polyether/cross-linked PMMA blends prepared via in situ polymerization. Electrochem Commun 7(8):829–835. https://doi.org/10.1016/j.elecom.2005.04.034

Xu K, Ding MS, Zhang S, Allen JL, Jow TR (2002) An attempt to formulate nonflammable lithium ion electrolytes with alkyl phosphates and phosphazenes. J Electrochem Soc 149(5):A622–A626. https://doi.org/10.1149/1.1467946

Xu L, Kim C, Shukla AK, Dong A, Mattox TM, Milliron DJ, Cabana J (2013) Monodisperse Sn nanocrystals as a platform for the study of mechanical damage during electrochemical reactions with Li. Nano Lett 13(4):1800–1805. https://doi.org/10.1021/nl400418c

Yabuuchi N, Kubota K, Dahbi M, Komaba S (2014) Research development on sodium-ion batteries. Chem Rev 114(23):11636–11682. https://doi.org/10.1021/cr500192f

Yan H, Ming Z, Fukuan S, Xiaoying L, Zijie T, Yukun W, Chunyi Z (2017) An intrinsically stretchable and compressible supercapacitor containing a polyacrylamide hydrogel electrolyte. Angew Chem Int Ed 56(31):9141–9145. https://doi.org/10.1002/anie.201705212

Yang Z, Wu H-Q, Simard B (2002) Charge–discharge characteristics of raw acid-oxidized carbon nanotubes. Electrochem Commun 4(7):574–578. https://doi.org/10.1016/S1388-2481(02)00384-3

Yang Z, Zhang J, Kintner-Meyer MCW, Lu X, Choi D, Lemmon JP, Liu J (2011) Electrochemical energy storage for green grid. Chem Rev 111(5):3577–3613. https://doi.org/10.1021/cr100290v

Yang J, Han X, Zhang X, Cheng F, Chen J (2013) Nano Res 6(9):679–687. https://doi.org/10.1007/s12274-013-0343-5

Yao XL, Xie S, Chen CH, Wang QS, Sun JH, Li YL, Lu SX (2005) Comparative study of trimethyl phosphite and trimethyl phosphate as electrolyte additives in lithium ion batteries. J Power Sources 144(1):170–175. https://doi.org/10.1016/j.jpowsour.2004.11.042

Ye Z, Yang Z, Xunliang C, Wei W, Jing R, Xin F et al (2015) Realizing both high energy and high power densities by twisting three carbon-nanotube-based hybrid fibers. Angew Chem Int Ed 54(38):11177–11182. https://doi.org/10.1002/anie.201506142

Yin SY, Song L, Wang XY, Zhang MF, Zhang KL, Zhang YX (2009) Synthesis of spinel Li4Ti5O12 anode material by a modified rheological phase reaction. Electrochim Acta 54(24):5629–5633. https://doi.org/10.1016/j.electacta.2009.04.067

Yonggang W, Yarong W, Eiji H, Kaixue W, Haoshen Z (2008) The design of a LiFePO4/carbon nanocomposite with a core–shell structure and its synthesis by an in situ polymerization restriction method. Angew Chem Int Ed 47(39):7461–7465. https://doi.org/10.1002/anie.200802539

Yoo E, Kim J, Hosono E, Zhou H, Kudo T, Honma I (2008) Large reversible Li storage of graphene nanosheet families for use in rechargeable lithium ion batteries. Nano Lett 8(8):2277–2282. https://doi.org/10.1021/nl800957b

Yoon S, Park C-M, Sohn H-J (2008) Electrochemical characterizations of germanium and carbon-coated germanium composite anode for lithium-ion batteries. Electrochem Solid-State Lett 11(4):A42–A45. https://doi.org/10.1149/1.2836481

Yoon SJ, Myung ST, Noh HJ, Lu J, Amine K, Sun YK (2014) ChemSusChem 7(12):3295–3303

Yoshimoto N, Niida Y, Egashira M, Morita M (2006) Nonflammable gel electrolyte containing alkyl phosphate for rechargeable lithium batteries. J Power Sources 163(1):238–242. https://doi.org/10.1016/j.jpowsour.2006.02.090

Youn DH, Meyerson ML, Klavetter KC, Friedman KA, Coffman SS, Lee J-W et al (2016) Mixing super P-Li with N-doped mesoporous templated carbon improves the high rate performance of a potential lithium ion battery anode. J Electrochem Soc 163(6):A953–A957. https://doi.org/10.1149/2.0771606jes

Young T-H, Chen L-W (1995) Pore formation mechanism of membranes from phase inversion process. Desalination 103(3):233–247. https://doi.org/10.1016/0011-9164(95)00076-3

Yuan L-X, Wang Z-H, Zhang W-X, Hu X-L, Chen J-T, Huang Y-H, Goodenough JB (2011) Development and challenges of $LiFePO_4$ cathode material for lithium-ion batteries. Energy Environ Sci 4(2):269–284. https://doi.org/10.1039/C0EE00029A

Yuan-Li D, Jian X, Gao-Shao C, Tie-Jun Z, Hong-Ming Y, Xin-Bing Z (2010) Single-crystalline $LiMn_2O_4$ nanotubes synthesized via template-engaged reaction as cathodes for high-power lithium-ion batteries. Adv Funct Mater 21(2):348–355. https://doi.org/10.1002/adfm.201001448

Yue W, Lin Z, Jiang S, Yang X (2012) Preparation of graphene-encapsulated mesoporous metal oxides and their application as anode materials for lithium-ion batteries. J Mater Chem 22 (32):16318–16323. https://doi.org/10.1039/C2JM30805C

Zaghib K, Mauger A, Gendron F, Julien CM (2008) Surface effects on the physical and electrochemical properties of thin LiFePO4 particles. Chem Mater 20(2):462–469. https://doi.org/10.1021/cm7027993

Zhang SS (2007) A review on the separators of liquid electrolyte Li-ion batteries. J Power Sources 164(1):351–364. https://doi.org/10.1016/j.jpowsour.2006.10.065

Zhang SS (2012) Binder based on polyelectrolyte for high capacity density lithium/sulfur battery. J Electrochem Soc 159(8):A1226–A1229. https://doi.org/10.1149/2.039208jes

Zhang SS, Xu K, Jow TR (2003) Alkaline composite film as a separator for rechargeable lithium batteries. J Solid State Electrochem 7(8):492–496. https://doi.org/10.1007/s10008-003-0375-y

Zhang L-S, Jiang L-Y, Yan H-J, Wang WD, Wang W, Song W-G, Wan L-J (2010a) Mono dispersed SnO_2 nanoparticles on both sides of single layer graphene sheets as anode materials in Li-ion batteries. J Mater Chem 20(26):5462–5467. https://doi.org/10.1039/C0JM00672F

Zhang M, Lei D, Yin X, Chen L, Li Q, Wang Y, Wang T (2010b) Magnetite/graphene composites: microwave irradiation synthesis and enhanced cycling and rate performances for lithium ion batteries. J Mater Chem 20(26):5538–5543. https://doi.org/10.1039/C0JM00638F

Zhang Z, Bao W, Lu H, Jia M, Xie K, Lai Y, Li J (2012) Water-soluble Polyacrylic acid as a binder for sulfur cathode in lithium-sulfur battery. ECS Electrochem Lett 1(2):A34–A37. https://doi.org/10.1149/2.009202eel

Zhang K, Kim H-J, Shi X, Lee J-T, Choi J-M, Song M-S, Park JH (2013a) Graphene/acid coassisted synthesis of ultrathin MoS_2 nanosheets with outstanding rate capability for a lithium battery anode. Inorg Chem 52(17):9807–9812. https://doi.org/10.1021/ic400735f

Zhang Q, Uchaker E, Candelaria SL, Cao G (2013b) Nanomaterials for energy conversion and storage. Chem Soc Rev 42(7):3127–3171. https://doi.org/10.1039/C3CS00009E

Zhang X, Cheng F, Yang J, Chen J (2013c) LiNi0.5Mn1.5O4 porous nanorods as high-rate and long-life cathodes for Li-ion batteries. Nano Lett 13(6):2822–2825. https://doi.org/10.1021/nl401072x

Zhang J, Sun B, Huang X, Chen S, Wang G (2014) Honeycomb-like porous gel polymer electrolyte membrane for lithium ion batteries with enhanced safety. Sci Rep 4:6007. https://doi.org/10.1038/srep06007

Zhang J, Ge H, Li Z, Ding Z (2015a) Internal heating of lithium-ion batteries using alternating current based on the heat generation model in frequency domain. J Power Sources 273:1030–1037. https://doi.org/10.1016/j.jpowsour.2014.09.181

Zhang M, Wang T, Cao G (2015b) Promises and challenges of tin-based compounds as anode materials for lithium-ion batteries. Int Mater Rev 60(6):330–352. https://doi.org/10.1179/1743280415Y.0000000004

Zhang S, Cao J, Shang Y, Wang L, He X, Li J, Wang Y (2015c) Nanocomposite polymer membrane derived from nano TiO2-PMMA and glass fiber nonwoven: high thermal endurance and cycle stability in lithium ion battery applications. J Mater Chem A 3(34):17697–17703. https://doi.org/10.1039/C5TA02781K

Zhang B, Dugas R, Rousse G, Rozier P, Abakumov AM, Tarascon J-M (2016) Insertion compounds and composites made by ball milling for advanced sodium-ion batteries. Nat Commun 7:10308. Retrieved from. https://doi.org/10.1038/ncomms10308

Zhao C, Wang C, Yue Z, Shu K, Wallace GG (2013) Intrinsically stretchable supercapacitors composed of polypyrrole electrodes and highly stretchable gel electrolyte. ACS Appl Mater Interfaces 5(18):9008–9014. https://doi.org/10.1021/am402130j

Zhao H, Zhou M, Wen L, Lei Y (2015) Template-directed construction of nanostructure arrays for highly-efficient energy storage and conversion. Nano Energy 13:790–813. https://doi.org/10.1016/j.nanoen.2015.02.024

Zheng GY et al (2014a) Interconnected hollow carbon nanospheres for stable lithium metal anodes. Nat Nanotechnol 9:618–623. https://doi.org/10.1038/nnano.2014.152

Zheng F, Zhu D, Chen Q (2014b) Facile fabrication of porous NixCo3–xO4 nanosheets with enhanced electrochemical performance as anode materials for Li-ion batteries. ACS Appl Mater Interfaces 6(12):9256–9264. https://doi.org/10.1021/am501512j

Zhi M, Xiang C, Li J, Li M, Wu N (2013) Nanostructured carbon-metal oxide composite electrodes for supercapacitors: a review. Nanoscale 5(1):72–88. https://doi.org/10.1039/C2NR32040A

Zhou S, Liu X, Wang D (2010) Si/TiSi2 hetero nanostructures as high-capacity anode material for Li-ion batteries. Nano Lett 10(3):860–863. https://doi.org/10.1021/nl903345f

Zhou G, Wang D-W, Yin L-C, Li N, Li F, Cheng H-M (2012) Oxygen bridges between NiO nanosheets and graphene for improvement of lithium storage. ACS Nano 6(4):3214–3223. https://doi.org/10.1021/nn300098m

Zhu X, Zhu Y, Murali S, Stoller MD, Ruoff RS (2011) Nanostructured reduced graphene oxide/Fe2O3 composite as a high-performance anode material for lithium ion batteries. ACS Nano 5 (4):3333–3338. https://doi.org/10.1021/nn200493r

Zou Y, Kan J, Wang Y (2011) Fe2O3-graphene rice-on-sheet nanocomposite for high and fast lithium ion storage. J Phys Chem C 115(42):20747–20753. https://doi.org/10.1021/jp206876t

Zoulalian V, Monge S, Zürcher S, Textor M, Robin JJ, Tosatti S (2006) Functionalization of titanium oxide surfaces by means of poly(alkyl-phosphonates). J Phys Chem B 110 (51):25603–25605. https://doi.org/10.1021/jp066811s

Chapter 4
Nanomaterials for CO_2 Hydrogenation

Manuel Romero-Sáez, Leyla Y. Jaramillo, Wilson Henao, and Unai de la Torre

Contents

M. Romero-Sáez (✉) · W. Henao
Quality, Metrology and Production Research Group, Instituto Tecnológico Metropolitano, Campus Robledo, Medellín, Colombia
e-mail: manuelromero@itm.edu.co; wilsonhenao176510@correo.itm.edu.co

L. Y. Jaramillo
Quality, Metrology and Production Research Group, Instituto Tecnológico Metropolitano, Campus Robledo, Medellín, Colombia

Facultad de Ingeniería, Tecnológico de Antioquia, Medellín, Colombia
e-mail: leyla.jaramillo@tdea.edu.co

U. de la Torre
Department of Chemical Engineering, Faculty of Science and Technology, Universidad del País Vasco-UPV/EHU, Leioa, Bizkaia, Spain
e-mail: unai.delatorre@ehu.eus

R. Saravanan et al. (eds.), *Emerging Nanostructured Materials for Energy and Environmental Science*, Environmental Chemistry for a Sustainable World 23,
https://doi.org/10.1007/978-3-030-04474-9_4

Abstract The use of fossil fuels such as coal, oil, and natural gas has allowed a fast and unprecedented development of human society. However, this has led to a continuous increase in anthropogenic CO_2 emissions, which affect human life and the ecological environment through global warming and climate changes. There are various strategies to mitigate the atmospheric concentration of CO_2, such as capture, separation, and utilization. Among them, CO_2 hydrogenation to obtain different products through catalytic processes is a strategy of great interest. Thus, the catalytic combination of CO_2 and hydrogen not only mitigates anthropogenic emissions into Earth's atmosphere, but it also produces carbon compounds that can be used as fuel or precursors for the production of different chemicals.

This chapter reviews the use of different nanomaterials for CO_2 hydrogenation. Three different processes are distinguished, depending on the final product: (i) CO_2 hydrogenation to carbon monoxide, (ii) methanol production by CO_2 hydrogenation, and (iii) CO_2 hydrogenation to methane. It has been included both nanomaterials that act as support and those that can replace the active metal phase. Concerning CO_2 hydrogenation to CO, one-dimensional transition metal carbides have received increasing attention because their unique electronic structure allows similar catalytic properties to the expensive noble metals. Attending the high thermal requirements of CO synthesis, emerging metal oxides nanocatalysts are focused to prevent the metal sintering by increasing the metal-support interactions. Controlling the support's morphology at nanoscale can enhance both catalytic activity and stability at high temperatures up to twice with respect to those conventional micro-sized catalysts. Regarding to methanol production, the nanomaterials most commonly used as supports are those based on carbon, e.g., carbon nanotubes, carbon nanofibers, and graphene oxide. The main advantage of using these materials is their high surface area, which improves metallic phase dispersion, higher thermal and electrical conductivities, and greater mechanical resistance. In addition, the use of intermetallic nanoparticles as an active phase is very promising. The combination of two metals in the same nanoparticle greatly increases the interface between components, which clearly leads to a synergistic effect between them. The use of these nanomaterials improves the activity and selectivity to methanol between 2 and ~50%, compared with classical catalysts. Moreover, similar strategies are equally valid in methane production. Catalysts based on nanoparticles, such as Ni or NiO, supported on traditional metal oxides have been recently reported to improve catalytic activity in CO_2 methanation with high resistance to coke deposition. Other supports, such as carbon nanofibers and carbon nanotubes previously mentioned, have shown excellent results, with CO_2 conversions higher than 90% and complete selectivity to methane. Finally, TiO_2-based catalysts are a promising solution for methane production by the still undeveloped photocatalytic reduction. This reaction can be performed under mild temperatures and pressure conditions, which is a clear advantage for methane synthesis.

Abbreviations

CNF	Carbon nanofiber
CNT	Carbon nanotube
GO	Graphene oxide
rGO	Reduced graphene oxide
RWGS	Reverse water-gas shift
TMC	Transition metal carbide

4.1 Introduction

In recent centuries, the utilization of carbon-rich fossil fuels, such as oil, coal, and natural gas, has allowed an unprecedented era of prosperity and advancement for human development (Olah et al. 2008). As a consequence, the levels of CO_2 in the atmosphere are growing steadily year after year. Before the industrial revolution, the carbon dioxide concentration was ~280 ppm, while in February 2018 it increased to ~408 ppm (NOAA 2018). If this growth rate is maintained, the concentration of atmospheric CO_2 is estimated to reach ~570 ppm by the end of the twenty-first century (Xiaoding and Moulijn 1996). The said increase in atmospheric CO_2 concentration contributes to the global warming through the "greenhouse effect," and it is one of the most important environmental concerns nowadays. Therefore, the development of appropriate strategies to capture or use CO_2 is an interesting alternative for current energy and environmental problems (Kim et al. 2018).

Among the different alternatives for the use of CO_2, as capture, sequestration, conversion, etc., hydrogenation has been an effective method for CO_2 consumption (Saeidi et al. 2014). The combination with hydrogen allows this pollutant to be used as an economical, safe, and renewable carbon source, turning it out to be an attractive C1 building block for producing organic chemicals, materials, and carbohydrates (Song 2006; Ramachandriya et al. 2013).

The main products obtained from CO_2 hydrogenation can be grouped into two categories: fuels and chemicals. Within fuels, methane stands out in a very important way because it is the main component of natural gas and an actual energy compound widely used (Miguel et al. 2015). On the other hand, methanol is currently synthesized almost exclusively from fossil fuels, such as coal or natural gas, but it can be obtained from almost any carbon source, such as CO_2. This compound is a common solvent and one of the most important organic feedstock in the chemical industry (Goeppert et al. 2014). However, methanol is also an alternative fuel that offers a convenient solution for efficient energy storage (Kiss et al. 2016; Ali et al. 2015). Among the chemicals obtained by hydrogenation of CO_2, CO stands out for its importance in the chemical industry. This compound is, along with hydrogen, the main component of the synthesis gas, which is used for the production of different

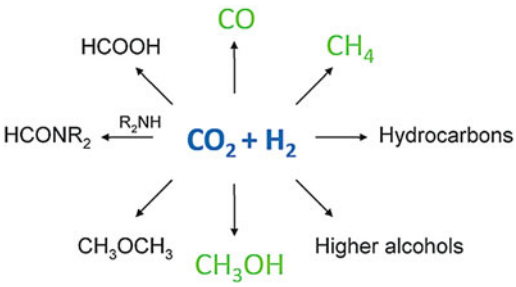

Fig. 4.1 Possible products that can be obtained from the reaction between CO_2 and H_2. The products covered in this chapter are indicated in green

products, such as methanol, ammonia, methane, ethanol, toluene, and aromatic olefins, among others (Centi et al. 2013).

Therefore, the hydrogenation of CO_2 to different products will not only help to reduce the concentration of this compound in the atmosphere and mitigate global warming, but it will also produce chemical compounds that can be used as fuels or as chemical intermediates in several applications or synthesis processes.

These products can be synthesized from CO_2 and hydrogen using two different methods, such as electrochemical and thermocatalytic reduction. In both cases, the selection of the catalyst is critical, since it will determine the activity and the selectivity of the reaction to the desired product. As shown in Fig. 4.1, several products can be formed from the reaction between CO_2 and H_2, whose separation in practical applications can be very expensive (Kattel et al. 2017).

For that reason, for CO_2 conversion, the selectivity is equally or maybe even more important than the activity. There are several factors that determine the catalytic behavior of a metal/support system, such as its specific surface area, nature and dispersion of the active metal phase, nature of the support, and interaction between the metal and the support at their interface.

During the last years, new strategies have been explored to incorporate nanomaterials into different processes and find active, selective, robust, and low-cost catalysts. Specifically, they seek to replace classic supports, such as Al_2O_3 or SiO_2, with nanomaterials that offer better physical, chemical, and thermal properties. In addition, some studies have evaluated the effect of substituting the metallic phase incorporated by classical methods (e.g., impregnation or ion exchange) with multimetallic or monodisperse nanoparticles (Shui et al. 2015; Bhanja et al. 2018; Chesnokov et al. 2017).

Recently, several research papers have reported the use of nanomaterials as supports and/or the active phase of catalysts used in CO_2 hydrogenation. This review summarizes their results and focuses on the role of different nanomaterials in the hydrogenation reaction as well as their advantages over conventional catalysts.

4.2 Synthesis of Carbon Monoxide

Carbon monoxide, a compound of great industrial interest, is the simplest C1 product that can be obtained by CO_2 reduction. Along with hydrogen, it comprises the reactive syngas mixture (CO + H_2), and it is used as a precursor for manufacturing a wide range of chemicals and fuels (Kattel et al. 2017). The typical thermochemical route to convert CO_2 into CO is the reverse water-gas shift (RWGS) reaction, in which CO_2 is reduced to reversibly produce CO and H_2O, as shown in Eq. (4.1).

$$CO_2 + H_2 \leftrightarrows CO + H_2O \; \Delta H^{\circ}_{298K} = S + 41 \text{ kJ/mol} \tag{4.1}$$

Due to the relative chemical stability of CO_2, the conversion into CO via RWGS is an energy intensive reaction. The endothermic nature of this reaction limits the equilibrium of RWGS and, consequently, CO production is favored when the temperature and H_2/CO_2 ratio are increased (Pastor-Pérez et al. 2017). RWGS is an important reaction that occurs in many processes where CO_2 and H_2 are present as a reactive gas mixture. Indeed, besides the generation of CO, RWGS is useful as an integrated reaction to the Fischer-Tropsch process to obtain several hydrocarbon fuels such as diesel, gasoline, and alcohols (Pöhlmann and Jess 2016).

In industrial applications, the high-temperature requirements of RWGS (~400 to 800 °C) demand the use of high thermal stability catalysts with large activity and selectivity to CO. On this subject, numerous efforts have focused on the development of high-performance catalysts that enable a more favorable energy consumption with high CO_2 conversion. For decades, several transition metals (e.g., Cu, Fe, Ni, Co) and noble metals (e.g., Pt, Rh, Ru, Au) supported either on active or inert oxides (e.g., SiO_2, CeO_2, ZrO_2, TiO_2, Al_2O_3) have been evaluated as heterogeneous catalysts for CO_2 reduction to CO (Daza and Kuhn 2016; Su et al. 2017).

Among them, Cu-based catalysts have been the most commonly used in low-temperature RWGS reactions, because they provide both high CO_2 conversion and CO selectivity (Jurković et al. 2017). However, under high-temperature conditions, copper tends to decrease its activity by sintering phenomena due to its low melting point. To improve the thermal stability and prevent metal sintering, doping with more stable agents has proven to be an alternative solution. In this respect, the following order has been suggested to select the doping metal according to its thermal stability: Au < Pd < Fe < Ni < Co < Pt < Rh < Ru < Ir < Os < Re (Bartholomew 2001). In addition to copper, iron-based catalysts are also used. Recently, unsupported Fe_xO_y nanoparticles have been reported to be notably stable, maintaining high catalytic activity for RWGS reaction during 19 h at 600 °C (Kim et al. 2015).

Nevertheless, the good performance of a catalyst in this reaction goes beyond its stability at high temperatures and, therefore, is necessary a synergistic effect between metals dispersion (active phase), the surface chemistry of the support (oxygen vacancies, acidity, basicity, surface area), and the metal-support interaction.

4.2.1 Metal Oxide Nanoparticles as Support for CO_2 Reduction to CO

The precise design of catalysts with integrated properties for CO_2 reduction to CO remains a great challenge. In recent years, diverse nanostructured materials have been proposed for CO production via RWGS. Table 4.1 summarizes them, as well as the type of catalyst used and its preparation method, the reaction conditions and results of CO_2 conversion and CO selectivity. In these catalysts, not only the metals are in the nanoscale but also the material that serves as support, which represents an advantage over conventional alternatives whose support is usually micro-sized. In that sense, understanding the way the size and morphology of catalysts can affect their performance in the generation of CO is greatly important.

Dou et al. (2017) demonstrated the key role of particle size control in optimizing the catalytic performance of mesoporous silica nanowires with encapsulated Ru nanoparticles, Ru@mSiO_2. They found that, by modifying the metal particle size, it was possible to direct the CO_2 hydrogenation toward a particular product, namely, CO or CH_4. Thus, encapsulated 1–3 nm Ru nanoparticles showed high selectivity to CO, while larger (5–20 nm) Ru nanoparticles favored the production of CH_4. This singular behavior was attributed to the formation of different intermediates on the catalysts surface, CO-Ru^{n+} on 1–3 nm Ru@mSiO_2 and formate species on 5–20 nm Ru@mSiO_2, as shown in Fig. 4.2. By controlling the Ru particle size and using SiO_2 nanowires as support, the average CO_2 conversion and CO selectivity was enhanced by 8.0% and 36.5%, respectively, compared to a conventional Ru/silica gel catalyst. In addition, Ru@mSiO_2 also showed high stability during RWGS reaction at 400 °C for 50 h.

Changes in the dimensions and morphology of supports can influence the performance of a catalyst. Kovacevic et al. (2016) evaluated the catalytic performance of CeO_2 nanoparticles with different morphologies, such as cubes, rods, and sphere-like particles, in reverse water-gas shift reaction. Cerium oxide nanocubes exhibited two times higher activity per surface area compared to rods and sphere-like nanoparticles. These authors suggest that the superior activity of CeO_2 nanocubes is due to the greater reactivity of (100) crystal planes enclosing the cubes, contrary to the less reactive (111) facets exposed in rods and sphere-like nanoparticles. In a similar study, Liu et al. (2016) maintain that the exposed active planes in Ni/CeO_2 nanocubes can promote the oxygen-ion conductivity and the formation of surface oxygen vacancy, which are efficient active sites for CO_2 hydrogenation.

Unsupported hematite nanosheets, nanowires, and nanoparticles have been evaluated as well to catalyze the RWGS reaction under atmospheric pressure. Fishman et al. (2017) found that materials with a lower band gap, such as hematite nanowires and nanosheets, exhibit higher reactivity at lower temperatures compared to nanoparticles, which have a higher band gap.

Core-shell nanoparticles are another type of emerging nanomaterial for the synthesis of CO. Yin et al. (2018) studied nanochains of Co@CoO core-shell catalysts for CO generation under mild conditions and found a synergistic effect

Table 4.1 Nanomaterial description and respective catalyst, preparation method, and reaction conditions and results for different studies on CO_2 reduction to CO

Nanomaterial description	Catalyst	Preparation method	T, °C	H_2: CO_2 ratio	CO_2 conversion, %	CO selectivity, %	Reference
Unsupported nanoparticles	Fe_xO_y	Coprecipitation of Fe^{II} and Fe^{III} solutions	600	1:1	38	85	Kim et al. (2015)
Mesoporous silica nanowires with encapsulated Ru nanoparticles	$Ru@mSiO_2$	Simultaneous soft-templating and encapsulation of pre-synthesized Ru nanoparticles	400	4:1	23	83.5	Dou et al. (2017)
Impregnated Cu nanoparticles over ceria nanospheres	Cu/CeO_2	Microemulsion method followed by incipient wetness impregnation	450	5:1	42	n/a	Lin et al. (2018)
Impregnated Cu nanoparticles over ceria nanorods	Cu/CeO_2	Hydrothermal route followed by incipient wetness impregnation	450	5:1	51	n/a	Lin et al. (2018)
Nanocubes	CeO_2	Hydrothermal route	750	1:1	36	100	Liu et al. (2016)
Nanorods	CeO_2	Hydrothermal route	750	1:1	34	100	Liu et al. (2016)
Nanooctahedra	CeO_2	Hydrothermal route	750	1:1	27	100	Liu et al. (2016)
Impregnated Ni nanoparticles over ceria nanocubes	Ni/CeO_2	Hydrothermal route followed by incipient wetness impregnation	750	1:1	45	100	Liu et al. (2016)
Hematite nanoparticles	Fe_2O_3	Hydrolysis of acidic solution of Fe^{III} salt	600	1:1	9	n/a	Fishman et al. (2017)
Hematite nanosheets	Fe_2O_3	Hard templating	550	1:1	30	n/a	

(continued)

Table 4.1 (continued)

Nanomaterial description	Catalyst	Preparation method	T, °C	H_2: CO_2 ratio	CO_2 conversion, %	CO selectivity, %	Reference
							Fishman et al. (2017)
Hematite nanowires	Fe_2O_3	Precipitation under inert atmosphere	850	1:1	55	n/a	Fishman et al. (2017)
Cobalt nanochains	Co	Direct current arc-discharge method	250	2:5	6	96	Yin et al. (2018)
Core-shell catalyst with nanochains structure	Co@CoO	Direct current arc-discharge method	250	2:5	14	>99	Yin et al. (2018)
N-doped core-shell catalyst with nanochains structure	Co@CoO-N	Direct current arc-discharge method	250	2:5	19	>99	Yin et al. (2018)
Hierarchical porous Cu/Zn-nanoparticle@carbon material	Cu/Zn@C	Pyrolysis of a Cu-based metal-organic framework	500	3:1	5	100	Zhang et al. (2017a, b)
Nanoparticles hexagonal crystal structure	β-Mo_2C	Coprecipitation followed by temperature-programmed carburization	300	2:1	8.7	14.5	Porosoff et al. (2014)
Nanoparticles hexagonal crystal structure	Co/β-Mo_2C	Coprecipitation followed by temperature-programmed carburization	300	2:1	9.5	51.3	Porosoff et al. (2014)
Nanowires with cubic crystal structure	α-MoC_{1-x}	Coprecipitation followed by thermal treatment	600	4:1	>60	100	Gao et al. (2016)
	β -MoC_{1-x}		600	4:1	>60	100	

Nanowires with hexagonal crystal structure		Coprecipitation followed by thermal treatment					Gao et al. (2016)
Nanoparticles with hexagonal crystal structure	β-Mo_2C	Coprecipitation followed by temperature-programmed carburization	200	5:1	6	39	Xu et al. (2015)
Nanoparticles with hexagonal crystal structure	Cu/β-Mo_2C	Coprecipitation followed by temperature-programmed carburization	200	5:1	4	44	Xu et al. (2015)
Nanoparticles with hexagonal crystal structure	Ni/β-Mo_2C	Coprecipitation followed by temperature-programmed carburization	200	5:1	8	37	Xu et al. (2015)
Nanoparticles with hexagonal crystal structure	Co/β-Mo_2C	Coprecipitation followed by temperature-programmed carburization	200	5:1	9	31	Xu et al. (2015)
Nanoparticles with hexagonal crystal structure	Co/β-Mo_2C	Coprecipitation followed by temperature-programmed carburization	600	2:1	47.7	99.2	Zhang et al. (2017a, b)

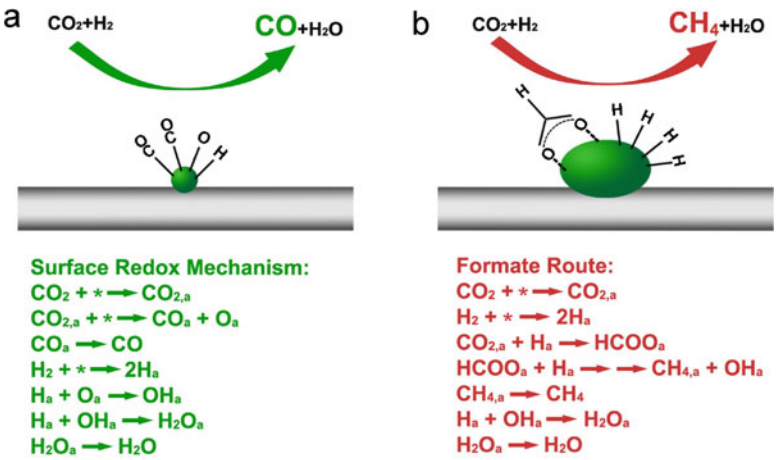

Fig. 4.2 Proposed reaction pathways. (**a**) Surface redox mechanism the 1–3 nm Ru@mSiO$_2$ nanocatalyst and (**b**) formate route of the 5–20 nm Ru@mSiO$_2$ nanocatalysts, for the selective reduction of CO_2 to CO and CH_4, respectively. Note that particle size has a great influence on the selectivity of a catalyst for a desirable product. (Reprinted with permission from Dou et al. 2017. Copyright (2017), with permission from Elsevier)

between the metallic Co and the encapsulating coordinatively unsaturated CoO species. As shown in Fig. 4.3, the catalytic performance of the Co-base catalyst was improved by a high H_2 activation in Co nanoparticles and the adsorption-activation of CO_2 by the defective CoO in the shell. In addition, the incorporation of N dopant in the shell allows increase the nanomaterial surface electron density and modulate CO_2 adsorption, which further promote the catalytic efficiency.

On the other hand, Zhang et al. (2017a) found that the encapsulation of Cu/Zn nanoparticles into a porous carbon matrix of Cu/Zn@C prevents the nanoparticles sintering, leading to superior stability of the catalysts in the RWGS reaction. The high activity of the catalyst was attributed to a synergistic effect between Cu and Zn metals and the carbon in the shell.

4.2.2 Transition Metal Carbides for CO_2 Reduction via RWGS

Noble metals, such as Pt, Pd, Ru, and Au, are commonly used as catalysts for RWGS, due to their high thermal stability and deactivation resistance (Su et al. 2017). However, for large-scale CO_2 utilization, the amounts of said metals must be minimized because they increase the manufacturing costs of the catalysts and, therefore, make the entire process less sustainable. In this regard, transition metal carbides (TMC) of Co, Ni, Mo, Zr, Hf, Nb, and Ta have drawn attention for CO_2 reduction, either as active phases or supports, because their properties are similar to

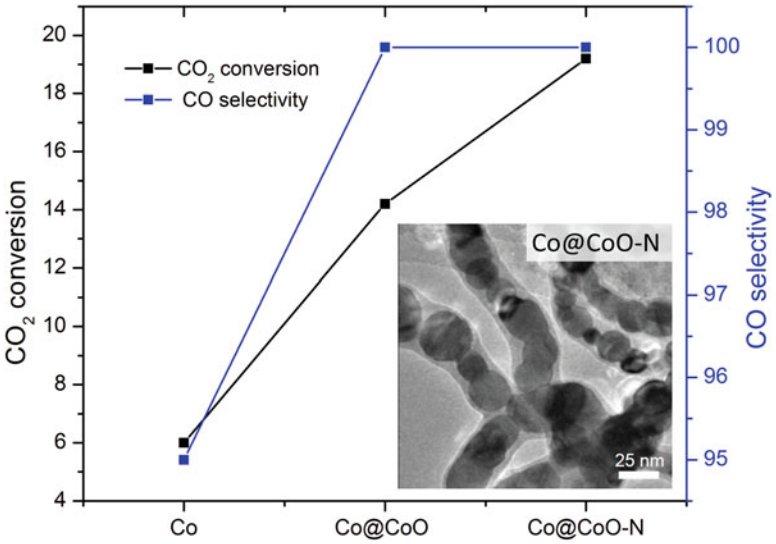

Fig. 4.3 Catalytic activity of different core-shell nanochains for conversion of CO_2 to CO. The use of Co@CoO nanochains resulted in an improvement of both CO_2 conversion and CO selectivity, with respect to the Co-based catalyst. Reaction conditions: GHSV: 42,000 ml/(g h), 250 °C for 8 h. (Modified after Yin et al. 2018)

those of noble metals (Kunkel et al. 2016). Typically, these materials are synthesized by a nanocasting process using mesoporous silicas as template. First, the metal precursor is infiltrated into the silica pores. Then, by a thermal treatment, the precursor becomes solid, and the carburization reaction is carried out. Afterward, the removal of the template results in the formation of metal carbides nanowires with diameters close to those of the parent porous template.

In comparison with their parent metals, the high activity of TMCs is caused by carbon atoms that modify the electronic metal properties, affecting the binding strength and the reactivity of adsorbates such as CO_2 and H_2 (Posada-Pérez et al. 2014). Commonly, the interaction between transition metals and some adsorbates is excessively strong to be useful in catalysis, because the desorption of products becomes a rate-limiting step of reaction. An attractive advantage of transition metal carbides is that the carbon included in the metal crystal lattice not only improve the thermal stability of catalyst, but it also moderates the chemical reactivity of metal, which results in a material with great potential for catalytic processes (Posada-Pérez et al. 2015). Another remarkable feature of TMCs is that they combine the conductivity of transition metals, the structural coordination and high melting point of ionic solids, and the hardness of covalent solids (Quesne et al. 2018).

Among transition metal carbides, molybdenum carbide (Mo_xC_y) has been considered a promising catalyst for RWGS due to its low cost, dual functionality for H_2 dissociation and C=O bond scission, and a similar behavior to reducible oxides

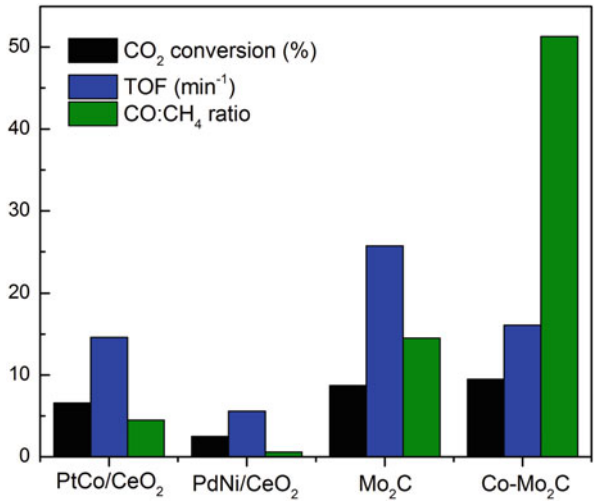

Fig. 4.4 Catalytic performance comparison of Mo_2C and some bimetallic nanoparticles supported on CeO_2 in terms of CO_2 conversion, turnover frequency (TOF), and CO:CH_4 ratio. Note that molybdenum carbides, Mo_2C and Co- Mo_2C, show improved activity and CO selectivity over the other catalyst. Reaction conditions: 300 °C, H_2:CO_2 ratio 3:1, 0.1 MPa. (Modified after Porosoff et al. 2014)

(Porosoff et al. 2016). Figure 4.4 compares the catalytic performance of Mo_2C and some bimetallic Pt-based nanoparticles supported on CeO_2. The use of Mo_2C provided an increase in CO_2 conversion and CO selectivity, with respect to conventional Pt-based catalysts. Thus, the addition of a small amount of Co to Mo_2C improved the CO:CH_4 ratio from 15 to 51 (Porosoff et al. 2014). In a recent work, the same author pointed out that K-promoted Mo_2C (KMo_2C/γ-Al_2O_3) was found to be an active and selective catalyst for CO_2 conversion (~40%) at a relatively high temperature of 450 °C (Porosoff et al. 2017).

β-Mo_2C enables a good dispersion and stabilization of copper nanoparticles, thus preventing their sintering at high temperatures (Zhang et al. 2017b). Under optimal reaction conditions (600 °C, WHSV = 300,000 ml/(g h)), highly dispersed copper nanoparticles over β-Mo_2C showed higher activity and stability than traditional Pt nanoparticles supported on oxides for RWGS reaction. After a detailed characterization, the authors found that the strong interaction between copper nanoparticles and the hexagonal β-Mo_2C nanowires substrate was responsible for the extraordinary performance of this novel catalyst.

On the other hand, Rodriguez et al. (2013) found a strong dependence between the catalytic activity of some metals, such as Au, Cu, or Ni, and the (001) surface of TiC carbide. The highest catalytic activity was achieved with small two-dimensional nanoparticles or metal clusters in close contact with TiC(001). Furthermore, the catalytic activity of TiC-supported metals was significantly higher than those of unsupported Au, Cu, or Ni.

4.3 Synthesis of Methanol

The synthesis of CH_3OH from CO_2 is given by Eq. (4.2). Methanol is a common solvent, a starting material in chemical industry and an alternative fuel. As an alternative feedstock, CO_2 has replaced CO and is considered an effective way for CO_2 utilization in methanol production (Sakakura et al. 2007; Ma et al. 2009).

$$CO_2 + 3H_2 \leftrightarrows CH_3OH + H_2O \quad \Delta H_{298K} = -49.5\ \text{kJ/mol} \tag{4.2}$$

Attending to the thermodynamics of the reaction, it should be noted that this is reversible, and the optimal reaction conditions to shift the equilibria toward the formation of methanol require high pressures and low temperatures according to Le Chatelier's principle. However, during the hydrogenation reaction of CO_2, other by-products such as CO, hydrocarbons, and higher alcohols are formed (Hu et al. 2018). Therefore, catalysts should be not only active but also selective to methanol, which allows to avoid the formation of undesired by-products. Among the many materials that have been studied, oxide-supported metals have emerged as promising catalysts, and the metal/oxide interfaces have been identified to play a critical role in controlling the activity and selectivity of CH_3OH synthesis by CO_2 hydrogenation (Martin et al. 2016). Although numerous catalysts based on different metals have been tested, Cu, along with different modifiers (Zn, Zr, Ce, Al, Si, V, Ti, Ga, B, Cr, etc.), remains their main active component in this reaction (Samei et al. 2012). Other active metals used in this process are Ni, Pd, Ag, or Au (Saeidi et al. 2014).

Selecting an appropriate support is very important for different reasons. On the one hand, the support affects the formation and stabilization of the catalyst active phase and is capable of tuning the interactions between the major component and promoter. On the other hand, support also determines the characteristics of the final catalyst, i.e., basicity, acidity, or surface area (Hartadi et al. 2015).

In this regard, in recent years a variety of nanomaterials have been used as supports in this reaction with different objectives, such as improving the dispersion of metals, promoting the reduction of metal oxides, or increasing the surface area. Table 4.2 shows some recent studies in which nanomaterials are used as supports in the production of methanol by hydrogenation of CO_2, as well as some cases in which intermetallic nanoparticles are used as the active phase of the catalyst.

4.3.1 Carbon Nanotube-Supported Catalysts

One of the nanomaterials used in CO_2 hydrogenation to methanol are carbon nanotubes (CNT). CNTs were discovered by Sumio Iijima in 1991 (Iijima 1991) and can be defined as graphite sheets rolled into seamless hollow cylinders. The two main types of CNT that exist are based on the number of graphite layers that make up their walls. Thus, single-wall carbon nanotubes consist of one tube of graphite, while

Table 4.2 Studies on methanol production by CO_2 hydrogenation using different nanomaterials

Nanomaterial description	Catalyst	Preparation method	T, °C	H_2: CO_2 ratio	CO_2 conv., %	CH_3OH select., %	Reference
Pd nanoparticles supported inside of CNTs	Pd/CNTs-in	Acetone-based incipient wetness impregnation over commercial CNTs	250	3:1	0.77	48.8	Wang et al. (2015)
Pd nanoparticles supported outside of CNTs	Pd/CNTs-out	Dimethybenzene-based incipient wetness impregnation over commercial CNTs	250	3:1	0.61	13.4	Wang et al. (2015)
Long CNTs intercrossed Cu/Zn/Al/Zr catalyst	Cu-Zn-Al-Zr/CNTs	Floating catalyst process followed by deposition coprecipitation	240	3:1	21.5	n/a	Zhang et al. (2010)
Pd-ZnO catalysts supported on "herringbone-type" MWCNTs	Pd_x-Zn_y/CNTs (h-type)	Catalytic decomposition of CH_4 followed by stepwise incipient wetness	250	3:1	6.3	99.6	Liang et al. (2009)
Pd-ZnO catalysts supported on "parallel-type" MWCNTs	Pd_x-Zn_y/CNTs (p-type)	Catalytic disproportionation of CO followed by stepwise incipient wetness	250	3:1	6.2	95.2	Liang et al. (2009)
Commercial herringbone CNFs supported bimetallic copper/zirconia	Cu-ZrO_2/CNFs	Deposition precipitation method	180	3:1	14.0	n/a	Ud Din et al. (2015)
Nb_2O_5-doped Cu/ZrO2/CNF catalyst	Nb_2O_5-Cu-ZrO_2 /CNFs	Deposition precipitation method	180	3:1	9.0	87.0	Ud Din et al. (2016)
Fishbone CNFs supported bimetallic palladium/zinc	$PdZn_x$/CNF-(fishbone)	Chemical vapor deposition followed by wet impregnation	225	9:1	2.7	12.5	Díez-Ramírez et al. (2016)
Platelet CNFs supported bimetallic palladium/zinc	$PdZn_x$/CNF-(Platelet)	Chemical vapor deposition followed by wet impregnation	275	9:1	3.3	12.1	Díez-Ramírez et al. (2016)
Graphene oxide supported CuO-ZnO-ZrO_2 catalyst	CuO-ZnO-ZrO_2/GO	Modified Hummer's method followed by reverse coprecipitation method	240	3:1	15.6	34.6	Witoon et al. (2018)
Reduced graphene oxide supported CuO-ZnO-ZrO_2-Al_2O_3 catalyst	CuO-ZnO-ZrO_2-Al_2O_3/rGO	Hummer's method followed by coprecipitation	240	3:1	14.7	78.0	Fan and Wu (2016)
Supported Cu-Zn/reduced graphene oxide	Cu-Zn/rGO	Modified Hummer's method followed by incipient wetness impregnation	250	3:1	26.0	5.1	Deerattrakul et al. (2016)

SiO_2 nanospheres supported intermetallic Ni_xGa_y compounds	Ni_xGa_y/SiO_2	Sol-gel method followed by incipient wetnessimpregnation	205	3:1	n/a	98.5	Sharafutdinov et al. (2014)
Hydrotalcite-derived supported PdZn intermetallic nanoparticles	PdZnAl hydrotalcite-like	Coprecipitation method	250	3:1	0.6	60.0	Ota et al. (2012)
Hydrotalcite-derived supported Pd_2Ga intermetallic nanoparticles	PdMgGa hydrotalcite-like	Coprecipitation method	250	3:1	1.0	47.0	Ota et al. (2012)
Hydrotalcite-derived supported PdMgAl intermetallic nanoparticles	PdMgAl hydrotalcite-like	Coprecipitation method	250	3:1	0.3	4.0	Ota et al. (2012)
Hydrotalcite-derived supported CuZnAl intermetallic nanoparticles	CuZnAl hydrotalcite-like	Coprecipitation method	250	3:1	1.3	82.0	Ota et al. (2012)
Pd-promoted Ga_2O_3 nanorods	Pd/β-Ga_2O_3 rodlike	Hydrothermal route followed by impregnation wetness	250	3:1	11.0	41.3	Qu et al. (2014)
Pd-promoted Ga_2O_3 nanoplates	Pd/β-Ga_2O_3 platelike	Solid-state synthesis followed by impregnation wetness	250	3:1	17.3	51.6	Qu et al. (2014)

multiwall carbon nanotubes consist of a number of concentric tubes, cylinders inside the other cylinders (Sinnott and Andrews 2001). CNTs have a high aspect ratio, with a few tens of atoms in circumference and many microns in length. For this reason, they are often referred to as one-dimensional materials (Dresselhaus and Eklund 2000). Due to its particular morphology, these nanomaterials have high surface area, thermal stability, unique electronic properties and chemical inertness, and high mechanical strength (Romero-Sáez et al. 2018).

The inclusion of CNT in the catalysts formulation allows to reduce the concentration of the metallic active phase, which in many cases entails a high cost, and to maintain or even improve the catalytic behavior. The metal active phase dispersion in a CNT matrix enables higher dispersion and smaller particle sizes of the metal phase, which results in a better catalytic performance. An example of this behavior was observed in the study conducted by Liang et al. (2009) with carbon nanotube-supported Pd-ZnO catalyst. CNTs were found to play dual roles: catalyst support and a promoter. When CNT were employed as support, the results of metallic Pd exposed area were 9.3% and 19.7% higher than those observed while using activated carbon and γ-Al_2O_3, respectively. This change caused an almost twofold increase in the activity and a 100% selectivity to methanol in CO_2 hydrogenation products.

On the other hand, recent studies by the same authors took a step beyond in explaining the reason for the best behavior of CNT-supported catalysts in methanol production by CO_2 hydrogenation (Liang et al. 2015). In this case, the promoter action by 5%Pd/CNTs was mainly in providing the sp^2-C surface sites for H_2 adsorption-activation. Simultaneously, the molar percentage of the catalytically active species (Pd^0 in the form of PdZn-alloys) increased. In addition, it was observed that CNT-supported catalysts did not suffer deactivation during long reaction times, since their activity and selectivity were not affected after 200 h time on stream.

The electron density distortion of carbon atoms is another important characteristic to consider when using CNTs as support. This is because their tube structure could induce a difference in the electronic environment between the inside and outside of CNTs that can affect the catalytic performance of the metal inside and outside CNTs. This phenomenon was observed in Pd nanoparticles, since an important difference in the catalytic behavior was found between a disposition inside or outside the CNTs (Wang et al. 2015). Thus, the CO_2 conversion obtained with the Pd nanoparticles inside CNT was 1.3 times higher than that observed with the Pd nanoparticles outside. In addition, the selectivity of methanol by the catalyst with the Pd nanoparticles inside the CNT was even higher, 3.6 times in this case.

The characterization of the catalysts revealed that the surface of the Pd nanoparticles inside the CNTs existed mainly as $Pd^{\delta+}$ species, thus forming more Pd_n^0-$Pd^{\delta+}$ sites, which were proposed as responsible for methanol synthesis from CO_2 hydrogenation. Thus, in the reaction mechanism proposed by the authors (Fig. 4.5), the reaction route of methanol production by CO_2 hydrogenation is the formate pathway. The Pd_n^0-$Pd^{\delta+}$ sites have a dual effect, since Pd^0 activates H_2 and $Pd^{\delta+}$ activates CO_2. The activated species first form HCOO*, which is further hydrogenated to HCOOH* and then to H_2COOH*. This H_2COOH* itself forms

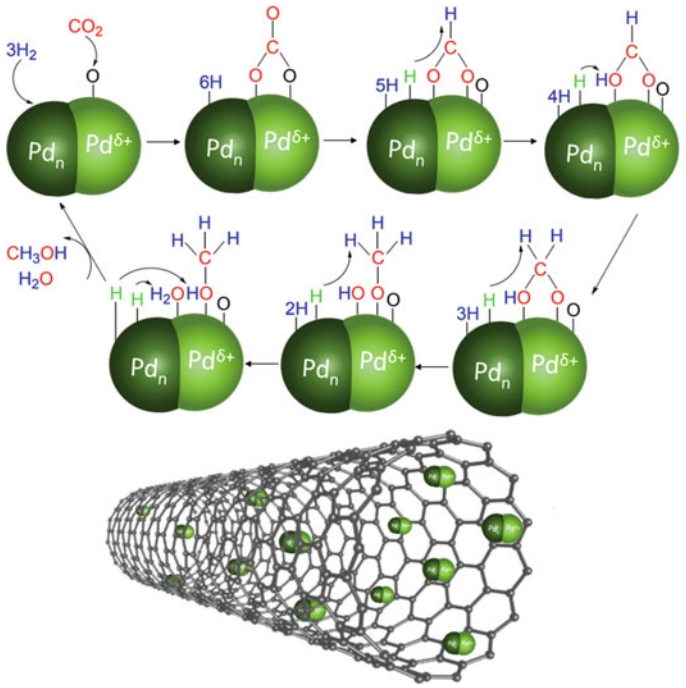

Fig. 4.5 Proposed mechanism for CO_2 hydrogenation to methanol on Pd/CNTs catalysts, when Pd nanoparticles are located inside CNT. (Modified after Wang et al. 2015)

H_2CO^* by splitting off an OH group. Subsequent hydrogenation produces H_3CO^*, which is the final intermediate for the formation of CH_3OH^* and, subsequently, CH_3OH.

Therefore, the authors proposed that the active sites for methanol production were Pd_n^0-$Pd^{\delta+}$ sites. In this regard, the presence of CNT as support was important, since their channels could stabilize Pd^0 to $Pd^{\delta+}$ species on the surface of the Pd nanoparticles inside CNTs and form coexisting Pd_n^0-$Pd^{\delta+}$ active sites.

On the other hand, the thermal conductivity of the catalyst is a very important aspect in catalytic reactions. In the event that the reaction heat is difficult to be transferred, hot spots could be created in the fixed bed. Consequently, a higher temperature will be necessary to achieve good conversion, and catalyst deactivation could increase due to the higher temperature areas. Carbon nanotubes were found to have excellent thermal conduction properties. For example, the calculated axial thermal conductivity of CNTs was extremely high, about 2000 W/m K or more than 3000 W/m K in multiwalled CNTs, and even higher in single-walled CNTs (Berber et al. 2000).

This positive effect was observed when unsupported and supported Cu/Zn/Al/Zr catalysts on long carbon nanotubes were compared (Zhang et al. 2010). The thermal conductivity rose from 0.4 to 20 W/m K, thus eliminating the hot spot in the catalyst

and preventing catalyst deactivation. As a result, the activity of the catalyst in CO_2 hydrogenation to methanol increased by 7% compared to Cu/Zn/Al/Zr catalyst without CNTs. Additionally, high Cu/Zn dispersion was observed due to the use of long CNTs.

In addition to hydrogenation, CNTs have also been used in the production of methanol from CO_2 through other processes. Electrochemical reduction is one of them. The electrochemical production of methanol occurs at room temperature, and it generally requires an overpotential to reduce CO_2 on a metal electrode of more than 1 V (Albo and Irabien 2016).

More specifically, in the study conducted by Qu et al. (2005), RuO_2/TiO_2 nanoparticles and nanotubes composite electrodes were prepared by loading RuO_2 on TiO_2 nanoparticles and nanotubes, respectively. The efficiency of the electrochemical reduction of CO_2 to CH_3OH on the RuO_2/TiO_2 nanoparticles modified with the Pt electrode was 40.2%, and it increased to 60.5% when RuO_2/TiO_2 NTs were used. Therefore, these results clearly suggest that the nanotubes composite modified electrode provides better electrochemical conditions for CO_2 reduction. This is mainly due to the fact that the dispersion of RuO_2 on the surface of TiO_2 nanotubes with higher surface area could create more active sites, which favors the diffusion of reacting species and reactions for CO_2 reduction.

4.3.2 Carbon Nanofiber-Supported Catalysts

Carbon nanofibers (CNFs) are another type of nanomaterial recently used for CO_2 hydrogenation to methanol. These structures consist of a stack of different graphite sheets oriented at an angle with respect to the fiber axis, without an open tubule in the middle. Their characteristics produce a high length-to-diameter ratio, high external surface area, and the absence of any 2D porosity material. CNFs are of great technological and industrial importance because of their comprehensive properties such as high electrical and thermal conductivity, very high strength-to-weight ratio, and excellent chemical resistance (Zhang et al. 2014). These nanomaterials have been applied as promising materials in many fields, such as gas adsorption/storage, energy conversion and storage, water treatment, reinforcement of composites, and self-sensing devices (Feng et al. 2014). In catalytic applications, this material could lead to new electronic interactions and higher accessibility of the reactants to the deposited active phase (Ledoux and Pham-Huu 2005).

Some authors have investigated the use of CNFs in methanol production by CO_2 hydrogenation in different conditions. Ud Din et al. (2015, 2017) evaluated Cu/Zr catalysts supported on CNFs in slurry reactors. The special physiochemical characteristics of CNFs, like higher surface area, higher mechanical strength, and surface defects for holding catalyst particles, make them a suitable choice as catalyst supports. In addition, the use of CNFs in slurry-phase reactors is more advantageous due to their mesoporous nature. Furthermore, since CNFs lack any 2D porosity,

accessibility of the reacting molecules to the active sites is enhanced, which improves the catalyst activity profile (Ud Din et al. 2015).

In another work, the activity of Cu/Zr/CNF catalyst was compared with recently reported data of various catalysts (Ud Din et al. 2017). They found that the activity of a CNF-supported catalytic system was comparatively better than other recently reported catalysts in similar reaction conditions, such as Ag/ZrO_2, Ag/ZnO, $Cu/Zn/Al_2O_3$, Cu/SiO_2, or $Cu/Zn/Cr_2O_3$. On the other hand, the said catalyst is much more active than the carbon nanotube-supported Pd/ZnO catalysts reported by Liang et al. (2009) studied for CO_2 hydrogenation to methanol.

In addition to studying the hydrogenation of CO_2 to methanol in gas phase, Ud Din et al. (2016) also delved into this reaction in liquid phase. They selected CNFs as support due to their high surface area and hydrophobic nature. Besides, Nb_2O_5 was incorporated into the catalyst formulation, resulted in $Cu/ZrO_2/Nb_2O_5$/CNF, with the aim of facilitating copper reduction. Comparing CO_2 conversion and methanol production results with other studies, CNF-supported catalysts revealed a better catalytic performance than many other alternatives, such as $Au/ZnO/ZrO_2$, $Ag/ZnO/ZrO_2$, $Pd/ZnO/Al_2O_3$, or Pd/ZnO supported on activated carbon.

Variation in the conditions of CNF preparation produces materials with a different structure. This is the case of the study carried out by Díez-Ramírez et al. (2016), who prepared carbon nanofibers with different crystalline structures by catalytic decomposition of ethylene over a Ni/SiO_2 catalyst. Afterward, when the preparation temperature was 600 °C, fishbone-type nanofiber was obtained, while at 450 °C the structure of the CNFs was platelet-type.

The evaluation of CNF-supported PdZn catalysts showed that the carbon nanofiber structure has an influence on the nature of the PdZn alloy that is formed and, therefore, on the catalytic performance. Thus, the platelet-type CNF-supported catalyst was observed to have higher activity and selectivity toward methanol at higher temperatures. This was attributed to different factors, such as a higher reactant adsorption, different Pd/Zn ratios in the resulting alloy, and a greater metal-support interaction due to the different orientation of the graphene sheets.

4.3.3 *Use of Graphene Oxide in CO_2 Hydrogenation to Methanol*

A third kind of carbon-based nanomaterials used in CO_2 hydrogenation to methanol is graphene oxide (GO). Graphene is a one-atom thick sheet constituted by sp^2-hybridized carbons in hexagonal arrangement. Recently, it has been considered a support material for various applications, such as environmental pollution treatment, electrochemical biosensors, or computing and electronic devices, owing to its extraordinary electronic properties and electron transport capabilities, unprecedented pliability and impermeability, strong mechanical strength, and excellent thermal and electrical conductivities (Li et al. 2017; Balakumar and Prakash 2016; Chen et al.

2018). From the catalytic point of view, it shows high specific surface area of about 2500 m^2/g and strong interaction with supported metal nanoparticles as consequence of the favorable overlap of the extended π orbital of graphene with the d orbitals of the metal atoms, which makes it a very good potential support for this type of applications (Chabot et al. 2014).

Currently, the number of works about the use GO to obtain methanol by CO_2 hydrogenation is limited. One of them was recently produce by Witoon et al. (2018), who investigated the effect of adding graphene oxide to CuO-ZnO-ZrO_2 catalyst on the catalytic performance of this reaction. They prepared GO-supported CuO-ZnO-ZrO_2 catalysts with different amounts of GO (0.5–2.5 wt%). In all cases, a higher space-time yield of methanol (compared to the GO-free catalyst) was achieved due to the increase in number of active sites for CO_2 and H_2 adsorption. However, when the GO content was higher than 2.5 wt%, it interrupted the coprecipitation of mixed metal oxides, thus causing the formation of isolated metal oxides particles, as well as a considerable increase in CuO crystallite size. The result of these two factors was a lower space-time yield of methanol compared to the GO-free catalyst.

This remarkable enhancement of CO_2 hydrogenation and methanol selectivity can be due to the fact that the GO nanosheet could serve as a bridge between mixed metal oxides. It is known that the correct hydrogenation of formate species to methanol, avoiding CO production, is the rate-determining step for methanol synthesis. Thus, H_2 dissociates on copper surface. In the absence of GO, the atomic hydrogen that is not in close contact with the metal oxides cannot be associated with the carbon species adsorbed on them. However, the GO surface can bridge this atomic hydrogen, thus facilitating the hydrogenation of the formate and other intermediate species adsorbed on the surface of metal oxides that are not in direct contact with the copper surface. This leads to a more effective use of the active sites than in a GO-free catalyst (Fig. 4.6).

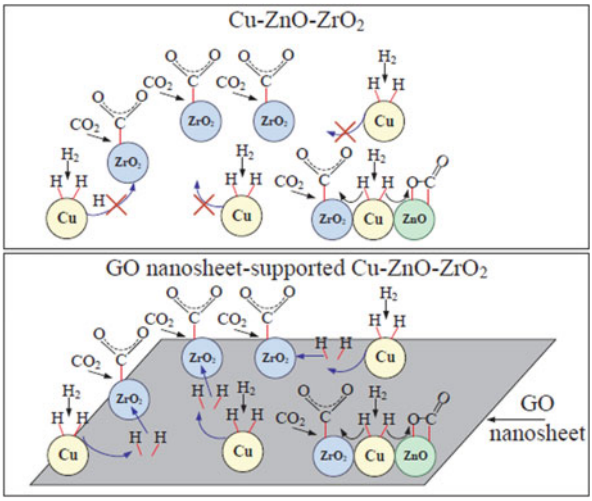

Fig. 4.6 Graphene oxide nanosheet as a bridge promoting hydrogen spillover from the surface of copper to the surface of other metal oxides. (Reprinted with permission from Witoon et al. 2018. Copyright (2018), with permission from Elsevier)

Besides the aforementioned, other recent studies have used graphene oxide as support for this reaction; however, in those cases, GO was subjected to a previous reduction (rGO). This is the case of the work conducted by Fan and Wu (2016), in which GO was reduced by chemical treatment. They evaluated the effect of rGO by comparing the performance of a CuO ZnO-ZrO_2-Al_2O_3/rGO (20/80 wt.%) catalyst with its rGO-free counterpart. The former showed higher CO_2 conversion (1.5%) and methanol yield (2%), even though the metal content was only 20%. This superior catalytic performance observed when rGO is present in the catalyst could be attributed to its higher surface area, high H_2 and CO_2 adsorption capacity, and higher dispersion of active copper species. These characteristics prevent the catalyst from sintering and lead to a higher CO_2 conversion and methanol selectivity.

On the other hand, Deerattrakul et al. (2016) also evaluated the effect of rGO on this reaction. In their case, GO was previously reduced by chemical treatment with hydrazine. Cu-Zn catalyst was used, and samples with different metal phase/rGO ratios were produced. The tested samples revealed that the catalyst with the highest CO_2 conversion and space-time yield to methanol was 10 wt.%CuZn/rGO. The authors pointed out that by increasing the metal loading beyond 10 wt.%, the CO_2 conversion and methanol yield decreased because of the agglomeration of active metals. This agglomeration led to reduced copper oxides, which is a crucial active metal for methanol synthesis. Therefore, the presence of rGO nanosheets and their high surface area could greatly enhance the catalytic performance by helping the dispersion of bimetallic compounds Cu-Zn particles. In addition, the nitrogen atoms bonded to the rGO can reduce the energy barrier of H_2 dissociation, which also promotes CO_2 conversion to methanol. It is also important to note that 10 wt.% CuZn/rGO catalyst provides much better results than similar alternatives on classical supports, such as Cu-ZnO/Al_2O_3, Cu-Zn/SiO_2, and Cu/ZnO/ZrO_2, and even when CNT is used as support.

4.3.4 *Intermetallic Nanoparticles for CO_2 Hydrogenation to Methanol*

Except for compounds based on carbon, the main group of nanomaterials used in CO_2 hydrogenation to methanol is composed of metallic nanoparticles. In previous decades, different types of metallic nanoparticles and their combinations with several supports have been evaluated in this reaction. Usually, in conventional catalysts, the metal nanoparticle plays a role in the reaction mechanism, while the activity of the support complements it. Thus, the activation and conversion of CO_2 can be achieved on multifunctional catalytic sites available at the metal/oxide interface by harnessing the synergy between the metal nanoparticles and the oxide support (Rodriguez et al. 2015; Kattel et al. 2017).

In recent years, several efforts have been aimed at the production of intermetallic nanoparticles, which combine the benefits of two metals to obtain better results and

might represent attractive alternatives to conventional catalysts in terms of cost, activity, stability, and selectivity. The unique properties of said nanoparticles are attributed to their electronic and geometric structure, which might be very different compared to their monometallic counterparts (Sharafutdinov et al. 2014).

Most studies in this field are focus on the production of Pd-Ga or Ni-Ga intermetallic nanoparticles by different methods, such as synthesis of the bulk phase from pure metals, preparation of unsupported nanoparticles by grinding the bulk phase, coprecipitation, impregnation, and a colloidal approach (Fiordaliso et al. 2015).

Depending on the conditions of their preparation, intermetallic nanoparticles with different Ni-Ga ratios can be produced; they can be richer in nickel, gallium, or the same amount of both metals (Sharafutdinov et al. 2014). Recently, a computational screening study has shown the theoretical activity of different Ni-Ga bimetallic catalysts in methanol synthesis from CO_2 and H_2 (Fig. 4.7). According to it, Ni_3Ga with the same sites of both elements and Ni_5Ga_3 rich in nickel are the formulations with the greatest theoretical activity. These theoretical results have been experimentally confirmed by CO_2 hydrogenation to methanol over supported Ni-Ga catalysts (Studt et al. 2014; Sharafutdinov et al. 2014). These studies also suggest that, at pressures close to atmospheric, the specific activity and selectivity toward methanol of Ni-Ga bimetallic nanoparticles were very close to those of conventional $Cu/ZnO/Al_2O_3$ catalysts (Kurtz et al. 2003).

However, the main problem of using Ni-Ga bimetallic nanoparticles is that nickel sites become poisoned by adsorbed CO and, eventually, by carbon formation. As an alternative, Pd-Ga intermetallic nanoparticles also exhibited high activity and selectivity to methanol, as well as a greater resistance to carbon poisoning. Among the different types of Pd-Ga nanoparticles prepared by different methods, the $GaPd_2$ phase has been reported as more active and selective in this reaction (Oyola-Rivera et al. 2015; Ota et al. 2012). The reaction mechanism proposed for methanol

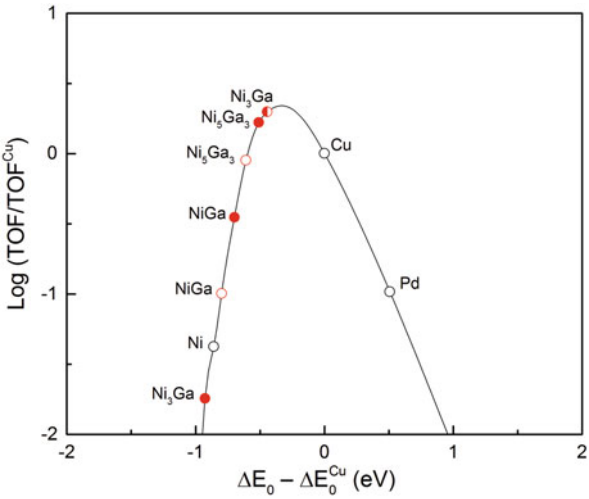

Fig. 4.7 Theoretical activity of different Ni-Ga intermetallic nanoparticles in CO_2 hydrogenation to methanol. Black open circles indicate pure elements; red solid circles, nickel-rich sites; red open circles, gallium-rich sites; and red half-open circles, mixed sites. (Modified after Studt et al. 2014)

production that takes place in this type of particles is very similar to that reported for catalysts based on Pd nanoparticles supported on gallium oxides (Collins et al. 2004, 2012; Qu et al. 2014). The production of methanol takes place via a bifunctional pathway. CO_2 is adsorbed on gallium oxide, and, as result, bicarbonate, bidentate, and polydentate carbonate species are formed on its surface. Subsequently, the active atomic hydrogen is generated on the metallic Pd, and, afterward, it spills to the gallium oxide surface to hydrogenate of all the carbon-containing species bonded to it. Therefore, the use of this type of intermetallic nanoparticles is very promising, since it reduces the size of the active phases to near atomic levels, thus increasing the interface between the components of the catalyst (Fiordaliso et al. 2015).

4.4 Synthesis of Methane

Nowadays, methane is an energy carrier of great importance for the industry, energy, and transportation sectors worldwide (Rönsch et al. 2016). Furthermore, due to the existing distribution infrastructure in many countries, it is a constitutive element of modern economies. Although most methane used in the industry comes from fossil natural gas resources, the debate over the use of fossil resources and climate change caused the research expenses related to the production of catalytic and biological methane from carbon oxide-rich gases (methanation) increase in recent years.

Through the process of methanation, H_2 and CO_2 are converted to CH_4 and H_2O. The process can be carried out chemically or biologically (Rönsch et al. 2016). In the biological route for the production of biogas, two main reaction pathways can be distinguished: acetoclastic methanogenesis and hydrogenotrophic methanogenesis (Thauer et al. 2008; Pavlostathis and Giraldo-Gomez 1991). The last route results in CH_4 production from CO_2 and H_2 in stirred tank reactors or trickle-bed reactors (Thauer et al. 2008; Seifert et al. 2014; Götz et al. 2015). Biological methanation has positive characteristics, such as operation at moderate temperatures (<70 °C) and atmospheric pressure, as well as a high tolerance to contaminants in the feedstream (Peillex et al. 1988; Wilhelm et al. 1977; Nishimura et al. 1992). However, poor mass transfer, slow kinetics, and low flexibility are the main disadvantages of this process.

On the contrary, catalytic methanation needs to occur above 250 °C, predominantly in fixed-bed reactors. The reaction equation of the chemical methanation (hereinafter called methanation) of CO_2 is expressed as follows in Eq. (4.3), using carbon dioxide and hydrogen as reagents. When H_2 derived from electrolysis is supplied as a reactant (PtG – power-to-gas), methanation of CO_2 enables the chemical storage of electricity (Götz et al. 2015; Hashimoto et al. 1999; Lefebvre et al. 2015).

$$CO_2 + 4H_2 \leftrightarrows CH_4 + 2H_2O \quad \Delta H_{298K} = -164\ \mathrm{kJ/mol} \tag{4.3}$$

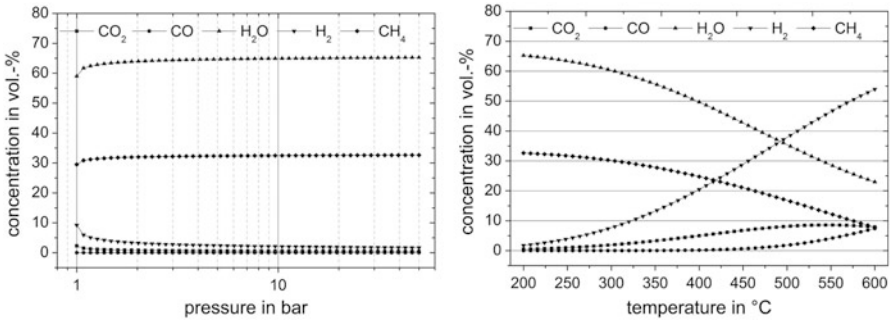

Fig. 4.8 Pressure and temperature influence on the equilibrium composition of CO_2 methanation and water-gas shift reaction (left: 300 °C, right: 1 bar). Reactant gas composition: $y_{H_2} = 0.8$, $y_{CO_2} = 0.2$. (Reprinted with permission from Rönsch et al. 2016. Copyright (2016), with permission from Elsevier)

CO_2 methanation is principally exothermic. The conversion of CO_2 releases 164 kJ per mole, and each 1 m^3 methane, at standard conditions for temperature and pressure, produced per hour corresponds to 1.8 kW heat. In addition, the reaction is characterized by a volume reduction of 40% of the reacting gases (Ghaib and Ben-Fares 2018).

The equilibrium of the reaction is influenced by temperature and pressure. Detailed studies on the dependence of methanation with pressure and temperature can be found in scientific literature (Gao et al. 2012; Seemann 2006; Sahebdelfar and Ravanchi 2015), which are based on thermodynamic equilibrium models available in commercial process simulation software. In this thermodynamic equilibrium, high pressures favor methane production, while high temperatures restrict methane formation. However, a high operation pressure is not economical, and a low-operating temperature requires a highly active catalyst, which is currently one of the challenges to develop catalysts for methanation. The influence of temperature and pressure on the equilibrium composition of CO_2 methanation and water-gas shift reaction is presented in Fig. 4.8.

CO_2 methanation process was first discovered by Sabatier and Sanderens in 1902 (Sabatier and Senderens 1902) and it has been investigated and developed for more than 100 years (Fig. 4.9). Developments of CO_2 methanation process are based mainly on CO methane research but were driven by the desire to use alternative exhaust gases. Basic studies on CO_2 methanation processes were conducted in the 1980s (Weatherbee and Bartholomew 1981), focusing on the use of coke oven gas or blast furnace gas for downstream methanation. However, due to the high efforts required for the purification of these gases (Hiller and Reimert 2006), only some of these concepts reached commercial scale.

In the 1970s and 1980s, CO_2 methanation processes gained new attention in the industry and research institutions due to the increasing demand for electricity storage, caused by increasing shares of wind and solar power (known as power-to-gas). As early as in the 1980s and 1990s, a combination of seawater electrolysis and

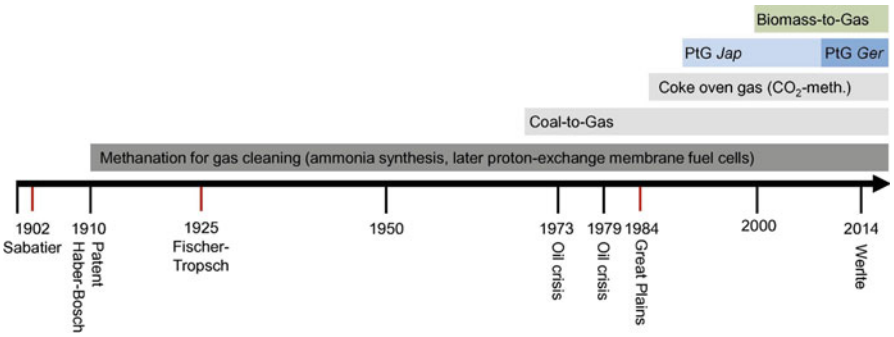

Fig. 4.9 History of methanation (Jap, Japan; Ger, Germany). (Reprinted with permission from Rönsch et al. 2016. Copyright (2016), with permission from Elsevier)

CO_2 methanation was proposed by Hashimoto et al. (1999), as a possibility to recycle CO_2 and prevent global warming. The idea was finally revived in 2009 by Sterner (2009), who focused on the climate change prevention and the electric energy storage.

Nowadays, CO_2 methanation research focuses on the optimization of processes developed in the 1970s and 1980s. New methods such as microreactor manufacturing (Schubert et al. 2001; Brooks et al. 2007; Liu et al. 2012b) and materials properties as advanced heat transfer fluids (Götz et al. 2013) release a potential for optimization and adaptation of last century's latest technologies to meet the new requirements of an increasingly decentralized energy system.

A high heat of reaction and sensitive catalysts make methanation a challenging process with a long history of development and research. The reduction of the fully oxidized carbon (+4) to methane (−4) is an eight-electron reaction. Consequently, there is a high kinetic barrier, and efficient and effective catalysts, providing high thermal stability as well as good resistance to coke formation, are needed for the reaction (Ghaib and Ben-Fares 2018). Sabatier discovered in one of his early works that Ni-based catalysts were able to catalyze the reaction between carbon monoxide and hydrogen to form methane and water (Sterner 2009). Nowadays, many metals, mainly in groups 8–10, have been found to be active for methanation reaction. According to Mills and Steffgen (1974), the active metals can be listed as follows:

Activity: Ru > Fe > Ni > Co > Mo
Selectivity: Ni > Co > Fe > Ru

Ni/Al_2O_3 results in the most widely used catalyst in CO_2 methanation. In addition to providing high activity and CH_4 selectivity, Ni is relatively cheap. However, its main drawback is its high propensity to get oxidized in oxidizing atmospheres, similar to other non-noble metals, such as Fe and Co (Götz et al. 2015; Lunde and Kester 1974). Additionally, toxic compounds for the human body, such as nickel carbonyl, can be formed (Lunde and Kester 1974). On the other hand, Co shows lower activity and is more expensive than Ni (Rönsch et al. 2016; Kao et al. 2014),

while Fe shows low CH_4 selectivity (Rönsch et al. 2016). Finally, Ru offers positive characteristics such as high activity, low-temperature CH_4 selectivity, and high resistance to oxidizing atmospheres (Brooks et al. 2007; Mills and Steffgen 1974; Habazaki et al. 1998). Nevertheless, its main disadvantage is its high price, which limits its application.

Support material also influences the activity of a catalyst system (Hu et al. 2007). As already mentioned, due to its ability to disperse metal species and its relatively low price, Al_2O_3 is the common support. However, other supports are being studied nowadays, such as Ce-Zr binary oxides, as one of the most promising catalyst supports for methanation thanks to their advantages, which include excellent thermal stability, sintering resistance, and special redox properties (Ghaib et al. 2016; Kang et al. 2011; Ocampo et al. 2011). In order to enhance the performance of catalysts, promoters are added to modify the surface basicity (decreasing activation energy) and the metal-carrier interface (better resistance to extreme conditions) as well as to improve metal dispersion.

4.4.1 Nanoparticles for CO_2 Methanation Catalysts

Another alternative for CO_2 methanation is the use of nanoparticles as catalysts. Nickel dispersion and particle size are frequently mentioned as factors that influence CO/CH_4 selectivity of CO_2 methanation (Aziz et al. 2014; Du et al. 2007; Wu et al. 2015; He et al. 2013; Kwak et al. 2013). It has been reported that small Ni^0 nanoparticles result in low selectivity to CH_4, due to the high rate of CO formation (Kesavan et al. 2017; Kwak et al. 2013a). This observation is a consequence of the different reaction pathways for the hydrogenation of CO_2 as a function of the Ni^0 particles size. With small and large Ni^0 nanoparticles, mHCOO is the key intermediate, formed from co-adsorbed H_2 and CO_2. Meanwhile, in small Ni^0 particles, mHCOO is decomposed to CO, to be further hydrogenated to CH_4, following a consecutive reaction path. However, the low H_2 coverage on small Ni^0 particles favors the CO formation. On the contrary, mHCOO intermediate can be directly hydrogenated to CH_4 over large Ni^0 particles due to the large H_2 surface coverage and a higher CH_4 production rate that is obtained compared to the CO production rate.

On the other hand, small Ni^0 crystals have also suppressed carbon deposition in CO_2 dry reforming (Luisetto et al. 2015; Hou et al. 2007), being the C formation speed, due to CH_4 dehydrogenation, lower than its oxidative removal by CO_2 on small Ni^0 particles. Then, small Ni^0 nanoparticle-supported catalysts may be useful for methanation process with anti-coking properties.

Other authors (Kesavan et al. 2018) have recently investigated the effect of the size of nickel nanoparticles on the catalytic properties for CO_2 methanation of several Ni/YSZ samples with different Ni^0 particle sizes but the same nickel loading (10 wt%). In summary, the catalytic performance for CO_2 methanation over Ni/YSZ catalysts mainly depends on the Ni^0 particles size and morphology, while Ni/YSZ

prepared by wet impregnation with $Ni(EDTA)^{2-}$ complex resulted the most efficient catalyst, in terms of CO_2 conversion and CH_4 selectivity, due to its high Ni^0 dispersion (Ni^0 particle size 19 nm).

Kesavan et al. (2018) also focused their research in different methodologies for Ni/YSZ catalysts preparation, by five different procedures. On one hand, two catalysts were prepared by typically used wetness impregnation method, varying Ni precursor. On the other hand, two additional catalysts were prepared by mechanical mixing of the support and NiO nano- or microparticles, which required a previous calcination at 1000 °C to increase their particle size. However, a third catalyst was also prepared by novel electroless plating method, which showed good activity in comparison with the rest of the catalysts.

Other authors (Mutz et al. 2018) have recently synthetized methanation catalysts based on Ni nanoparticles supported on alumina prepared by homogeneous deposition-precipitation with urea as precipitation agent. These catalysts showed, regardless the Ni concentration, nanoparticles around 3 nm as well as a high catalytic activity in the methanation of CO_2.

Song et al. (2017) prepared a well-dispersed Ni/Al_2O_3 catalyst with a microwave-assisted method, which showed high catalytic activity and stability for the CO_2 methanation. Ultrasonic techniques have been extensively used as an efficient method for preparation of homogenous and dispersed nanoparticles (Bang and Suslick 2010; Prasad et al. 2010; Khorasani-Motlagh et al. 2012). In addition, preparation by ultrasound irradiations produces free radicals which increase reaction rates at ambient temperatures. As a consequence, these unique conditions lead to the formation of homogenous nanoscale particles with high surface area (Bang and Suslick 2010; Pendashteh et al. 2014).

Vargas et al. (2016) reported a two-step ultrasonic procedure for synthesizing and supporting nickel nanoparticles on m-ZrO_2 to produce versatile and effective low-cost nanocatalysts active in CO_2 methanation. The supported samples showed high activity for CO_2 conversion, although the CH_4 selectivity strongly depended on the nickel particle size. The $NiZrO_2$ nanocatalyst with a 3 nm Ni particle size presented higher activity for CO_2 conversion (70%) than a 40 nm Ni size catalyst (50%) and also 90% CH_4 selectivity at 450 °C.

Another highly innovative catalysts preparation method for CO_2 methanation process is the Ni nanoparticles deposition on silica microspheres. Gac et al. (2018) prepared nickel catalysts supported on silica microspheres by the application of porous resin beads (Amberlite XAD7HP) as hard template using different order of nickel nitrate and tetraethoxysilane (TEOS) introduction. Summarizing, they were able to control the size of the prepared Ni nanoparticles varying the preparation order, and it was stated that the activity and selectivity of catalysts in the CO_2 methanation reaction were related to the active surface area and the size of nickel nanoparticles. In fact, an increase in CO_2 conversion and selectivity to CH_4 at low temperatures (220–350 °C) with an increase in active surface area and decrease in nickel crystallite size were observed.

Mutz et al. (2018) also studied CO_2 methanation activity and possible deactivation pathways over alumina-supported Ni catalysts, using Ni nanoparticles as active

phase. Three different Ni-based catalyst systems with metal nanoparticles around 3 nm were presented: 5 wt.% Ni/Al_2O_3, 5 wt.% Ni_3Fe/Al_2O_3, and 3.4 wt.% $NiRh_{0.1}$. Ni_3Fe catalyst exhibited its best catalytic performance in the mid-temperature range at 300–350 °C, while the Ni catalyst achieved the highest conversion and CH_4 production at 400 °C. $NiRh_{0.1}$ catalyst was less active compared to the Ni and Ni_3Fe systems in the whole temperature range. In deactivation terms, the three Ni-based catalyst systems showed similar behavior in carbon formation and reactivation, with only minor deviations among them. Other studies concentrated on the preparation of the nanomaterials and nanostructured supported metal catalysts hold that the homogenous dispersion of nanoparticles enhances the activity of catalyst by imparting a large number of active centers and enhances the stability by prevention of coke deposition (Sepehri and Rezaei 2015; Park and McFarland (2009).

In addition to Ni-based systems, other catalysts, such as magnetic zinc and manganese ferrite nanophase-based catalysts, have been tested for CO_2 methanation (Chiang et al. 2017). After the decomposition activity was stabilized, the CO_2 decomposition rate of a $ZnFe_2O_4$ catalyst was found to reach almost 99%, while it was about 88% in the $MnFe_2O_4$ counterpart.

4.4.2 *Carbon Nanofibers as Support for CO_2 Methanation Catalysts*

Different supports, such as carbon nanofibers, could be an alternative to classical ones (alumina, silica, TiO_2, etc.) that have been widely studied in the literature, due to their excellent characteristics. The said features include high mechanical strength, high purity of the material, and mesopore nature, which result in low internal mass transfer resistances (Díaz-Taboada et al. 2009). Jiménez et al. (2010) investigated the catalytic performance of Ru-based catalyst for selective CO_x methanation using different types of carbon nanofibers (platelet, fishbone, and ribbon). Results of the study suggest that the catalytic performance and selectivity to reaction products over Ru catalysts supported on different types of CNFs strongly depend on the experimental conditions used. In CO_2 methanation, catalytic performance is not affected by the nature of the CNFs used as support. Among the various Ru/CNFs catalysts investigated, optimal results (almost 60% CO_2 conversion) were obtained over the Ru/ribbon catalyst.

A recent study delved into CO_2 methanation over SiC foam catalysts impregnated with the same amount of active phase (Ni + Ru) and with different coatings: carbon nanofibers (CNF), ceria-zirconia (CZ), and the combination of both (Frey et al. 2015). The main objective of this work was to develop a catalyst with enough catalytic activity at temperatures below 250 °C. CNF washcoat was able to increase the low specific surface area of the foam up to 50 m^2/g. Besides, combining the positive effect of ceria-zirconia and carbon nanofibers gave the best productivity results (85% CO_2 conversion at 350 °C).

The high electronic and thermal conductivity of CNFs are also quite important and enable their use as electrodes or catalyst electrodes. A research by Jiménez et al. (2011) studied composite electrodes based on Ni or Ru impregnated with carbon nanofibers deposited on an Y_2O_3-stabilized ZrO_2 solid electrolyte. They concluded that CNF or CNF–YSZ composite electrodes are stable in an oxidizing environment at temperatures up to 450 °C, exhibiting satisfactory conductivity and are usable as electrodes in solid oxide YSZ cells. Also, it was determined that composite catalyst electrodes show better performance in the CO_2 methanation than the corresponding dispersed catalysts. In fact, Ru-based catalysts achieved up to 76% CH_4 selectivity. Finally, electrochemical promotion can be obtained for the CO_2 hydrogenation reaction. The application of potential or current changes slightly the catalytic activity of composite CNF electrodes. The behavior is electrophilic, i.e., the rate increases with negative potential.

4.4.3 Carbon Nanotubes and Other Nanomaterials as Support for CO_2 Methanation Catalysts

Apart from carbon nanofibers, well-defined and activated carbon nanotubes are today also well-established supports for a wide variety of applications, e.g., the Fischer-Tropsch synthesis (Bahome et al. 2005) and other hydrogenation reactions, including CO_2 hydrogenation (Liang et al. 2009; Romero-Sáez et al. 2018). Compared to a classical support like γ-Al_2O_3, the turnover frequency of CO_2 hydrogenation on CNT-supported catalysts is roughly 1.2 times higher. A recent study compared the CO_2 hydrogenation behavior of catalysts containing 1.5–35 wt% Co supported on CNTs and CNFs (Tursunov and Tilyabaev 2017). Although the Co catalyst supported on CNTs showed catalytic inactivity due to the amorphous state of the metal, it was possible to activate it during Co crystallization after thermal treatment. In fact, 35% Co-loaded catalyst supported on CNT and doped with Nb_2O_5 achieved 93% CO_2 conversion and 100% CH_4 selectivity at mid-temperature.

Other studies, as carried out by Wang et al. (2016), proposed a mechanism of the CO_2 methanation on catalysts supported on CNT (Fig. 4.10). In this work, catalysts containing 12 wt% Ni supported on multiwalled CNTs promoted with cerium (0–6 wt%) were evaluated. They proposed that the cerium promoter, together with the CNTs, donated electrons and facilitated their transfer from the support to the metallic nickel nanoparticles and absorbed CO_2. This improved the dissociation of molecular hydrogen to atomic hydrogen and the CO_2 activation. Then, the activated CO_2 was dissociated on the Ni surface, forming carbonate intermediate species. Finally, CH_4 was formed through the reaction between these carbonate species and the atomic hydrogen, while CO could be produced as by-product during this process.

Rh, Au, and Au-Rh bimetallic clusters supported on titanate nanotubes, titanate nanowire, and TiO_2 have also been studied for CO_2 hydrogenation (Tóth et al. 2012). It was concluded that the simultaneous deposition of gold and rhodium on

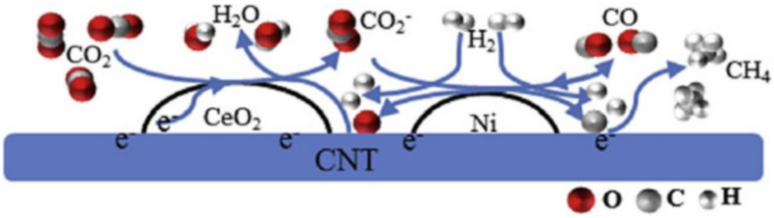

Fig. 4.10 CO_2 methanation mechanism on the cerium promoted nickel catalyst supported on CNTs. (Reprinted with permission from Wang et al. 2016. Copyright (2016), with permission from Elsevier)

titania and titanate nanowire and nanotube supports resulted in highly dispersed gold particles on the catalytic surface. The CO_2 methanation followed at 493 K on these catalysts by gas chromatography showed that CH_4 was the main product in all cases.

In addition to CNT, there are many other CO_2 conversion methods, such as biotransformation (Jacob-Lopes et al. 2010), thermal-assisted catalysis (Zhu et al. 2016), and plasma reduction (Jwa et al. 2013) that use nanomaterials. Indeed, plasma-deposited novel nanocatalysts for CO_2 methanation were studied on wire gauzes made from kanthal steel (FeCrAl) (Kierzkowska-Pawlak et al. 2017). Series of thin films of active phase were prepared by plasma-enhanced metalorganic chemical vapor deposition, containing cobalt spinel (Co_3O_4), ruthenium oxide (RuO_2), mixed oxides, and iron oxide (Fe_2O_3). RuO_2-based catalyst revealed the highest yield of methane and reaction rate, while Fe_2O_3-based catalyst promoted CO production through reverse water-gas shift reaction.

4.4.4 Photocatalytic Reduction

Another method for CO_2 removal is photocatalytic reduction (Low et al. 2015; Jin et al. 2015; Mao et al. 2013). Photocatalysis emerged as an economical technology for CO_2 conversion because it uses solar energy to trigger the photochemical reduction of CO_2 in order to produce hydrocarbon fuels. Compared with other methods, photocatalytic conversion of CO_2 can be carried out under mild temperature and pressure (Mao et al. 2012). Although the application of this area is very broad, the current efficiency of the photocatalyst toward CO_2 adsorption and conversion remains very low, which is the biggest obstacle for the transformation of carbonaceous resources.

Semiconductor materials such as TiO_2, ZnO, ZrO_2, CdS, Fe_2O_3, SiC, and WO_3 and various combinations have been applied to the photocatalytic conversion of CO_2. Considering their commercial availability, suitable optical/electronic qualities, and chemical stability, TiO_2 nanomaterials appear to be promising candidates. In fact, as small TiO_2 particles absorb more photoenergy, higher yields of methane over TiO_2 nanoparticles are certified as the particle size is reduced down to 14 nm (Liu et al. 2012a).

Table 4.3 CO_2 photocatalysts in the presence of doped/undoped TiO_2 nanotube, nanorod, and nanoribbons

Photocatalyst	Reductant	Light source	Reference
Multiwalled carbon nanotube-supported TiO_2	Water	15 W UV lamp $\lambda = 365$ nm	Xia et al. (2007)
Pt/titania nanotubes	Hydrogen	FT-IR spectra study	Yu et al. (2008)
Pt/TiO_2 nanotubes	Water vapor	300 W Hg lamp $\lambda = 365$ nm	Zhang et al. (2009)
TiO_2 nanotubes	Water vapor	Water vapor UV lamp with a 100 W mercury vapor bulb $\lambda = 365$ nm 1000 W Xe arc lamp	Schulte et al. (2010)
Titania nanotubes/ nanorod	Water vapor	A 100 W Hg lamp, $\lambda = 365$ nm density ~110 mW/cm^2	Vijayan et al. (2010)
TiO_2 nanotubes	1.0 M $NaHCO_3$	150 W xenon lamp	La Tempa et al. (2012)
Cu-TiO_2 nanorod	Water	8 W UVA	Tan et al. (2012)
MgO/TiO_2 nanotube filmss	Water vapor	Hg lamp with 300 W	Li et al. (2014)

Titania is a suitable photocatalyst that provides sufficiently negative and positive redox potentials. Therefore, new TiO_2 nanoarchitectures have been developed for CO_2 methanation, such as the nanoparticles previously mentioned or nanoparticles dispersed on support materials, nanotubes, and nanoribbons. Table 4.3 shows CO_2 photocatalysts in the presence of doped/undoped TiO_2 nanotube, nanorod, and nanoribbons.

Simple and promising strategies to achieve good CH_4 productions include tuning the crystal phase, morphology, crystal facet and size, forming defects/Ti^{3+}, employing good supports, and modifying the catalyst surface. One of the highest CH_4 productivities in CO_2 methanation by photocatalytic reduction was achieved with MgO/TiO_2 nanotube films (Li et al. 2014), where MgO played an important role by keeping the nanotubular morphology. The basic MgO is prone to adsorption of CO_2 molecules and to form the magnesium carbonate species, whose reactivity is higher than that of the linear CO_2 molecule. Then, the magnesium carbonate methanation proceeds by reacting with atomic H supplied from H_2O. The increase of MgO loading improved the photoreduction activity, while the highest production of CH_4 was obtained on the 0.01 MgO-loaded films. Besides, adding Pt nanoparticles also enhanced the photocatalytic activity remarkably (CH_4 generation = 100.22 ppm/(h cm^2)).

Recently, graphene and other 2D-related materials have been successfully employed not only as support but also as additive in catalysts for photocatalytic

CO_2 reduction (Low et al. 2015). A recent study (Mateo et al. 2018) proved that NiO/Ni nanoparticles supported on graphene constitute a suitable photocatalyst to perform methanation of CO_2 at relatively low temperature (~200 °C). Furthermore, specific CH_4 formation rates of 642 μmol g/(Ni h) were achieved, which double the calculation for Ni nanoparticles supported on silica-alumina with a high surface area. This positive effect of graphene seems to be due to the photoinduced electron transfer from excited NiO/Ni nanoparticles to the graphene sheet.

Also, CH_4 selectivity has been improved by a photoinduced CO_2 reduction on carbon dots through the modification of nitrogen-containing groups and graphitization (Liu et al. 2018). In summary, highly graphitized carbon dots prepared from graphene oxide with plenty of nitrogen-containing groups can exhibit up to 74.8% electronic selectivity of methane.

4.5 Conclusion

This chapter contains an elaborate review that analyzes the current use and trend of nanomaterials in CO_2 hydrogenation. Among the products that can be obtained from CO_2 hydrogenation, this work focuses on those that enjoy widespread use nowadays as fuels and/or chemicals, such as carbon monoxide, methanol, and methane. Employing nanomaterials to convert CO_2 into these high valuable compounds is a promising strategy to reduce CO_2 emissions and mitigate their environmental impact. However, since direct conversion of CO_2 is, in some cases, thermodynamically limited, the current challenge for large-scale CO_2 utilization is designing materials that can achieve high product selectivity and conversion rates.

Recently, nanomaterials have attracted special attention due to their unique properties compared to their micro-sized counterparts. Emergent nanomaterials with diverse morphologies, such as nanosheets, nanowires, nanotubes, nanofibers, as well as intermetallic compounds, metal oxides, and other carbon-based nanomaterials, have been studied either as supports or active phases for CO_2 hydrogenation reactions. They show interesting characteristics to be used as catalysts, e.g., high surface area, thermal stability and conductivity, and active interface regions. This review summarizes the results of recent studies on the role of different nanomaterials in the CO_2 hydrogenation reaction and the advantage of their use over conventional catalysts.

As main aspects, the use of nanomaterials in CO_2 hydrogenation to carbon monoxide seeks to prevent metal sintering and to replace expensive noble metals without compromising the activity and selectivity of the catalyst. On the other hand, methanol production research aims at increasing the catalysts' surface area, metallic phase dispersion, and thermal and electrical conductivities by employing carbon-based nanomaterials, such as carbon nanotubes, nanofibers, or graphene oxide. Finally, the investigations in CO_2 methanation tend to the production of metal nanoparticles to avoid coking, as well as to the use of new formulations, such as TiO_2-based catalysts.

Acknowledgments U. de la Torre is grateful to Universidad del País Vasco/EHU (Postdoctoral Project ESPDOC16/69).

References

Albo J, Irabien A (2016) Cu_2O-loaded gas diffusion electrodes for the continuous electrochemical reduction of CO_2 to methanol. J Catal 343:232–239. https://doi.org/10.1016/j.jcat.2015.11.014

Ali KA, Abdullah AZ, Mohamed AR (2015) Recent development in catalytic technologies for methanol synthesis from renewable sources: a critical review. Renew Sustain Energ Rev 44:508–518. https://doi.org/10.1016/j.rser.2015.01.010

Aziz MAA, Jalil AA, Triwahyono S, Mukti RR, Taufiq-Yap YH, Sazegar MR (2014) Highly active Ni-promoted mesostructured silica nanoparticles for CO_2 methanation. Appl Catal B Environ 147:359–368. https://doi.org/10.1016/j.apcatb.2013.09.015

Bahome MC, Jewell LL, Hildebrandt D, Glasser D, Covillle NJ (2005) Fischer–Tropsch synthesis over iron catalysts supported on carbon nanotubes. Appl Catal A Gen 287:60–67. https://doi.org/10.1016/j.apcata.2005.03.029

Balakumar V, Prakash P (2016) A facile in situ synthesis of highly active and reusable ternary Ag-PPy-GO nanocomposite for catalytic oxidation of hydroquinone in aqueous solution. J Catal 344:795–805. https://doi.org/10.1016/j.jcat.2016.08.010

Bang JH, Suslick KS (2010) Applications of ultrasound to the synthesis of nanostructured materials. Adv Mater 22:1039–1059. https://doi.org/10.1002/adma.200904093

Bartholomew CH (2001) Mechanisms of catalyst deactivation. Appl Catal A Gen 212(1–2):17–60. https://doi.org/10.1016/S0926-860X(00)00843-7

Berber S, Kwon Y-K, Tománek D (2000) Unusually high thermal conductivity of carbon nanotubes. Phys Rev Lett 84(20):4613–4616. https://doi.org/10.1103/PhysRevLett.84.4613

Bhanja P, Modak A, Bhaumik A (2018) Supported porous nanomaterials as efficient heterogeneous catalysts for CO_2 fixation reactions. Chem Eur J. https://doi.org/10.1002/chem.201800075

Brooks KP, Hu J, Zhu H, Kee RJ (2007) Methanation of carbon dioxide by hydrogen reduction using the Sabatier process in microchannel reactors. Chem Eng Sci 62:1161–1170. https://doi.org/10.1016/j.ces.2006.11.020

Centi G, Quadrelli EA, Perathoner S (2013) Catalysis for CO_2 conversion: a key technology for rapid introduction of renewable energy in the value chain of chemical industries. Energy Environ Sci 6(6):1711–1731. https://doi.org/10.1039/c3ee00056g

Chabot V, Higgins D, Yu A, Xiao X, Chen Z, Zhang J (2014) A review of graphene and graphene oxide sponge: material synthesis and applications to energy and the environment. Energy Environ Sci 7:1564–1596. https://doi.org/10.1039/c3ee43385d

Chen L, Li Y, Chen L, Li N, Dong C, Chen Q, Liu B, Ai Q, Si P, Feng J, Zhang L, Suhr J, Lou J, Ci L (2018) A large-area free-standing graphene oxide multilayer membrane with high stability for nanofiltration applications. Chem Eng J 345:536–544. https://doi.org/10.1016/j.cej.2018.03.136

Chesnokov VV, Podyacheva OY, Richards RM (2017) Influence of carbon nanomaterials on the properties of Pd/C catalysts in selective hydrogenation of acetylene. Mater Res Bull 88:78–84. https://doi.org/10.1016/j.materresbull.2016.12.013

Chiang CL, Lin KS, Hsu PJ, Lin YG (2017) Synthesis and characterization of magnetic zinc and manganese ferrite catalysts for decomposition of carbon dioxide into methane. Inter J Hydro Energy 42:22123–22137. https://doi.org/10.1016/j.ijhydene.2017.06.033

Collins SE, Baltanás MA, Bonivardi AL (2004) An infrared study of the intermediates of methanol synthesis from carbon dioxide over Pd/β-Ga_2O_3. J Catal 226(2):410–421. https://doi.org/10.1016/j.jcat.2004.06.012

Collins SE, Delgado JJ, Mira C, Calvino JJ, Bernal S, Chiavassa DL, Baltanás MA, Bonivardi AL (2012) The role of Pd–Ga bimetallic particles in the bifunctional mechanism of selective

methanol synthesis via CO_2 hydrogenation on a Pd/Ga_2O_3 catalyst. J Catal 292:90–98. https://doi.org/10.1016/j.jcat.2012.05.005

Daza YA, Kuhn JN (2016) CO_2 conversion by reverse water gas shift catalysis: comparison of catalysts, mechanisms and their consequences for CO_2 conversion to liquid fuels. RSC Adv 6 (55):49675–49691. https://doi.org/10.1039/C6RA05414E

Deerattrakul V, Dittanet P, Sawangphruk M, Kongkachuichay P (2016) CO_2 hydrogenation to methanol using Cu-Zn catalyst supported on reduced graphene oxide nanosheets. J CO_2 Util 16:104–113. https://doi.org/10.1016/j.jcou.2016.07.002

Díaz-Taboada C, Batista J, Pintar A, Levec J (2009) Preparation, characterization and catalytic properties of carbon nanofiber-supported Pt, Pd, Ru monometallic particles in aqueous-phase reactions. Appl Catal B Environ 89:375–382. https://doi.org/10.1016/j.apcatb.2008.12.016

Díez-Ramírez J, Sánchez P, Rodríguez-Gómez A, Valverde JL, Dorado F (2016) Carbon nanofiber-based palladium/zinc catalysts for the hydrogenation of carbon dioxide to methanol at atmospheric pressure. Ind Eng Chem Res 55(12):3556–3567. https://doi.org/10.1021/acs.iecr.6b00170

Dou J, Sheng Y, Choong C, Chen L, Zeng HC (2017) Silica nanowires encapsulated Ru nanoparticles as stable nanocatalysts for selective hydrogenation of CO_2 to CO. Appl Catal B Environ 219:580–591. https://doi.org/10.1016/j.apcatb.2017.07.083

Dresselhaus MS, Eklund PC (2000) Phonons in carbon nanotubes. Adv Phys 49(6):705–814. https://doi.org/10.1080/000187300413184

Du G, Lim S, Yang Y, Wang C, Pfefferle L, Haller G (2007) Methanation of carbon dioxide on Ni-incorporated MCM-41 catalysts: the influence of catalyst pretreatment and study of steady-state reaction. J Catal 249:370–379. https://doi.org/10.1016/j.jcat.2007.03.029

Fan YJ, Wu SF (2016) A graphene-supported copper-based catalyst for the hydrogenation of carbon dioxide to form methanol. J CO2 Util 16:150–156. https://doi.org/10.1016/j.jcou.2016.07.001

Feng L, Xie N, Zhong J (2014) Carbon nanofibers and their composites: a review of synthesizing, properties and applications. Materials 7(5):3919–3945. https://doi.org/10.3390/ma7053919

Fiordaliso EM, Sharafutdinov I, Carvalho HW, Grunwaldt JD, Hansen TW, Chorkendorff I, Wagner JB, Damsgaard CD (2015) Intermetallic $GaPd_2$ nanoparticles on SiO_2 for low-pressure CO_2 hydrogenation to methanol: catalytic performance and in situ characterization. ACS Catal 5(10):5827–5836. https://doi.org/10.1021/acscatal.5b01271

Fishman ZS, He Y, Yang KR, Lounsbury A, Zhu J, Tran TM, Zimmerman JB, Batista VS, Pfefferle LD (2017) Hard templating ultrathin polycrystalline hematite nanosheets: effect of nanodimension on CO_2 to CO conversion via the reverse water shift reaction. Nanoscale 9:12984–12995. https://doi.org/10.1039/C7NR03522E

Frey M, Édouard D, Roger AC (2015) Optimization of structured cellular foam-based catalysts for low-temperature carbon dioxide methanation in a platelet milli-reactor. C R Chim 18:283–292. https://doi.org/10.1016/j.crci.2015.01.002

Gac W, Zawadzki W, Słowik G, Sienkiewicz A, Kierys A (2018) Nickel catalysts supported on silica microspheres for CO_2 methanation. Microporous Mesoporous Mater 272:79–91. https://doi.org/10.1016/j.micromeso.2018.06.022

Gao J, Wang Y, Ping Y, Hu D, Xu G, Gu F, Su F (2012) A thermodynamic analysis of methanation reactions of carbon oxides for the production of synthetic natural gas. RSC Adv 2:2358–2368. https://doi.org/10.1039/c2ra00632d

Gao J, Wu Y, Jia C, Zhong Z, Gao F, Yang Y, Liu B (2016) Controllable synthesis of α-MoC_{1-x} and β-Mo_2C nanowires for highly selective CO_2 reduction to CO. Catal Commun 84(5):147–150. https://doi.org/10.1016/j.catcom.2016.06.026

Ghaib K, Ben-Fares FZ (2018) Power-to-methane: a state-of-the-art review. Renew Sustain Energ Rev 81:433–446. https://doi.org/10.1016/j.rser.2017.08.004

Ghaib K, Nitz K, Ben-Fares FZ (2016) Chemical methanation of CO_2: a review. Chem Bio Eng Rev 3(6):266–275. https://doi.org/10.1002/cben.201600022

Goeppert A, Czaun M, Jones JP, Prakash GS, Olah GA (2014) Recycling of carbon dioxide to methanol and derived products – closing the loop. Chem Soc Rev 43(23):7995–8048. https://doi.org/10.1039/c4cs00122b

Götz M, Ortloff F, Reimert R, Basha O, Morsi BI, Kolb T (2013) Evaluation of organic and ionic liquids for three-phase methanation and biogas purification processes. Energy Fuel 27 (8):4705–4716. https://doi.org/10.1021/ef400334p

Götz M, Lefebvre J, Mörs F, McDaniel Koch A, Graf F, Bajohr S, Reimert R, Kolb T (2015) Renewable power-to-gas: a technological and economic review. Renew Energy 85:1371–1390. https://doi.org/10.1016/j.renene.2015.07.066

Habazaki H, Yamasaki M, Zhang B, Kawashima A, Kohno S, Takai T, Hashimoto K (1998) Co-methanation of carbon monoxide and carbon dioxide on supported nickel and cobalt catalysts prepared from amorphous alloys. Appl Catal A Gen 172(1):131–140. https://doi.org/10.1016/S0926-860X(98)00121-5

Hartadi Y, Widmann D, Behm RJ (2015) CO_2 hydrogenation to methanol on supported au catalysts under moderate reaction conditions: support and particle size effects. ChemSusChem 8 (3):456–465. https://doi.org/10.1002/cssc.201402645

Hashimoto K, Yamasaki M, Fujimura K, Matsui T, Izumiya K, Komori M, El-Moneim AA, Akiyama E, Habazaki H, Kumagai N, Kawashima A, Asami A (1999) Global CO_2 recycling – novel materials and prospect for prevention of global warming and abundant energy supply. Mater Sci Eng A 267(2):200–206. https://doi.org/10.1016/S0921-5093(99)00092-1

He S, Li C, Chen H, Su D, Zhang B, Cao X, Wang B, Wei M, Evans DG, Duan X (2013) A surface defect-promoted Ni nanocatalyst with simultaneously enhanced activity and stability. Chem Mater 25:1040–1046. https://doi.org/10.1021/cm303517z

Hiller H, Reimert R (2006) Types of gases. In: Ullmann's encyclopedia of industrial chemistry. Wiley-VCH Verlag GmbH & Co. KGaA, Weinheim, p 10

Hou Z, Gao J, Guo J, Liang D, Lou H, Zheng X (2007) Deactivation of Ni catalysts during methane autothermal reforming with CO_2 and O_2 in a fluidized-bed reactor. J Catal 250(2):331–341. https://doi.org/10.1016/j.jcat.2007.06.023

Hu J, Brooks KP, Holladay JD, Howe DT, Simon TM (2007) Catalyst development for microchannel reactors for martian in situ propellant production. Catal Today 125 (1–2):103–110. https://doi.org/10.1016/j.cattod.2007.01.067

Hu B, Yin Y, Liu G, Chen S, Hong X, Tsang SCE (2018) Hydrogen spillover enabled active Cu sites for methanol synthesis from CO_2 hydrogenation over Pd doped CuZn catalysts. J Catal 359:17–26. https://doi.org/10.1016/j.jcat.2017.12.029

Iijima S (1991) Helical microtubules of graphitic carbon. Nature 354:56–58. https://doi.org/10.1038/354056a0

Jacob-Lopes E, Scoparo CHG, Queiroz MI, Franco TT (2010) Biotransformations of carbon dioxide in photobioreactors. Energy Convers Manag 51(5):894–900. https://doi.org/10.1016/j.enconman.2009.11.027

Jiménez V, Sánchez P, Panagiotopoulou P, Valverde JL, Romero A (2010) Methanation of CO, CO_2 and selective methanation of CO, in mixtures of CO and CO_2, over ruthenium carbon nanofibers catalysts. Appl Catal A Gen 390(1–2):35–44. https://doi.org/10.1016/j.apcata.2010.09.026

Jiménez V, Jiménez-Borja C, Sánchez P, Romero A, Papaioannou EI, Theleritis D, Souentie S, Brosdac S, Valverde JL (2011) Electrochemical promotion of the CO_2 hydrogenation reaction on composite Ni or Ru impregnated carbon nanofiber catalyst-electrodes deposited on YSZ. Appl Catal B Environ 107(1–2):210–220. https://doi.org/10.1016/j.apcatb.2011.07.016

Jin J, Yu J, Cui C, Ho W (2015) A hierarchical Z-scheme CdS–WO_3 photocatalyst with enhanced CO_2 reduction activity. Small 11(39):5262–5271. https://doi.org/10.1002/smll.201500926

Jurković DL, Pohar A, Dasireddy DBC, Likozar B (2017) Effect of copper-based catalyst support on reverse water-gas shift reaction (RWGS) activity for CO_2 reduction. Chem Eng Technol 40 (5):973–980. https://doi.org/10.1002/ceat.201600594

Jwa E, Lee SB, Lee HW, Mok YS (2013) Plasma-assisted catalytic methanation of CO and CO_2 over Ni–zeolite catalysts. Fuel Process Technol 108:89–93. https://doi.org/10.1016/j.fuproc.2012.03.008

Kang SH, Ryu JH, Kim JH, Seo SJ, Yoo YD, Prasad PSS, Lim H-J, Byun C-D (2011) Co-methanation of CO and CO_2 on the Nix-Fe_{1-x}/Al_2O_3 catalysts; effect of Fe contents. Korean J Chem Eng 28(12):2282–2286. https://doi.org/10.1007/s11814-011-0125-2

Kao YL, Lee PH, Tseng YT, Chien IL, Ward JD (2014) Design, control and comparison of fixed-bed methanation reactor systems for the production of substitute natural gas. J Taiwan Inst Chem E 45(5):2346–2357. https://doi.org/10.1016/j.jtice.2014.06.024

Kattel S, Liu P, Chen JG (2017) Tuning selectivity of CO_2 hydrogenation reactions at the metal/oxide interface. J Am Chem Soc 139(29):9739–9754. https://doi.org/10.1021/jacs.7b05362

Kesavan JK, Luisetto I, Tuti S, Meneghini C, Battocchio C, Iucci G (2017) Ni supported on YSZ: XAS and XPS characterization and catalytic activity for CO_2 methanation. J Mater Sci 57 (17):10331–10340. https://doi.org/10.1007/s10853-017-1179-2

Kesavan JK, Luisetto I, Tuti S, Meneghini C, Iucci G, Battocchio C, Mobilio S, Casciardi S, Sisto R (2018) Nickel supported on YSZ: the effect of Ni particle size on the catalytic activity for CO_2 methanation. J CO_2 Util 23:200–211. https://doi.org/10.1016/j.jcou.2017.11.015

Khorasani-Motlagh M, Noroozifar M, Ahanin-Jan A (2012) Ultrasonic and microwave-assisted co-precipitation synthesis of pure phase $LaFeO_3$ perovskite nanocrystals. J Iran Chem Soc 9 (5):833–839. https://doi.org/10.1007/s13738-012-0100-9

Kierzkowska-Pawlak H, Tracz P, Redzynia W, Tyczkowski J (2017) Plasma deposited novel nanocatalysts for CO_2 hydrogenation to methane. J CO2 Util 17:312–319. https://doi.org/10.1016/j.jcou.2016.12.013

Kim DH, Han SW, Yoon HS, Kim YD (2015) Reverse water gas shift reaction catalyzed by Fe nanoparticles with high catalytic activity and stability. J Ind Eng Chem 23:67–71. https://doi.org/10.1016/j.jiec.2014.07.043

Kim SM, Abdala PM, Broda M, Hosseini D, Copéret C, Müller CR (2018) Integrated CO_2 capture and conversion as an efficient process for fuels from greenhouse gases. ACS Catal 8:2815–2823. https://doi.org/10.1021/acscatal.7b03063

Kiss AA, Pragt JJ, Vos HJ, Bargeman G, de Groot MT (2016) Novel efficient process for methanol synthesis by CO_2 hydrogenation. Chem Eng J 284:260–269. https://doi.org/10.1016/j.cej.2015.08.101

Kovacevic M, Mojet BL, Van Ommen JG, Lefferts L (2016) Effects of morphology of cerium oxide catalysts for reverse water gas shift reaction. Catal Lett 146(4):770–777. https://doi.org/10.1007/s10562-016-1697-6

Kunkel C, Viñes F, Illas F (2016) Transition metal carbides as novel materials for CO_2 capture, storage, and activation. Energy Environ Sci 9(1):141–144. https://doi.org/10.1039/C5EE03649F

Kurtz M, Wilmer H, Genger T, Hinrichsen O, Muhler M (2003) Deactivation of supported copper catalysts for methanol synthesis. Catal Lett 86(1–3):77–80. https://doi.org/10.1023/A:1022663125977

Kwak JH, Kovarik L, Szanyi J (2013) CO_2 reduction on supported Ru/Al_2O_3 catalysts: cluster size dependence of product selectivity. ACS Catal 3(11):2449–2455. https://doi.org/10.1021/cs400381f

Kwak JH, Kovarik L, Szanyi J (2013a) Heterogeneous catalysis on atomically dispersed supported metals: CO_2 reduction on multifunctional Pd catalysts. ACS Catal 3:2094–2100. https://doi.org/10.1021/cs4001392

La Tempa TJ, Rani S, Bao N, Grimes CA (2012) Generation of fuel from CO_2 saturated liquids using a p-Si nanowire k n-TiO_2 nanotube array photoelectrochemical cell. Nanoscale 4 (7):2245–2250. https://doi.org/10.1039/c2nr00052k

Ledoux MC, Pham-Huu C (2005) Carbon nanostructures with macroscopic shaping for catalytic applications. Catal Today 102–103:2–14. https://doi.org/10.1016/j.cattod.2005.02.036

Lefebvre J, Götz M, Bajohr S, Reimert R, Kolb T (2015) Improvement of three-phase methanation reactor performance for steady-state and transient operation. Fuel Process Technol 132:83–90. https://doi.org/10.1016/j.fuproc.2014.10.040

Li Q, Zong L, Li C, Yang J (2014) Photocatalytic reduction of CO_2 on MgO/TiO_2 nanotube films. Appl Surf Sci 314:458–463. https://doi.org/10.1016/j.apsusc.2014.07.019

Li M, Zhou S, Xu M (2017) Graphene oxide supported magnesium oxide as an efficient cathode catalyst for power generation and wastewater treatment in single chamber microbial fuel cells. Chem Eng J 328:106–116. https://doi.org/10.1016/j.cej.2017.07.031

Liang XL, Dong X, Lin G-D, Zhang H-B (2009) Carbon nanotube-supported Pd–ZnO catalyst for hydrogenation of CO_2 to methanol. Appl Catal B Environ 88(3–4):315–322. https://doi.org/10.1016/j.apcatb.2008.11.018

Liang XL, Xie J-R, Liu Z-M (2015) A novel Pd-decorated carbon nanotubes-promoted Pd-ZnO catalyst for CO_2 hydrogenation to methanol. Catal Lett 145(5):1138–1147. https://doi.org/10.1007/s10562-015-1505-8

Lin L, Yao S, Liu Z, Zhang F, Na L, Vovchok D, Martínez-Arias A, Castañeda R, Lin J, Senanayake SD, Su D, Ma D, Rodriguez JA (2018) In-situ characterization of Cu/CeO_2 nanocatalysts during CO_2 hydrogenation: morphological effects of nanostructured ceria on the catalytic activity. J Phys Chem C 122(24):12934–12943. https://doi.org/10.1021/acs.jpcc.8b03596

Liu G, Hoivik N, Wang K, Jakobsen H (2012a) Engineering TiO_2 nanomaterials for CO_2 conversion/solar fuels. Sol Energy Mater Sol Cells 105:53–68. https://doi.org/10.1016/j.solmat.2012.05.037

Liu Z, Chu B, Zhai X, Jin Y, Cheng Y (2012b) Total methanation of syngas to synthetic natural gas over Ni catalyst in a micro-channel reactor. Fuel 95:599–605. https://doi.org/10.1016/j.fuel.2011.12.045

Liu Y, Li Z, Xu H, Han Y (2016) Reverse water-gas shift reaction over ceria nanocube synthesized by hydrothermal method. Catal Commun 76(3):1–6. https://doi.org/10.1016/j.catcom.2015.12.011

Liu Z, Wang Z, Qing S, Xue N, Jia S, Zhang L, Li L, Li N, Shi L, Chen J (2018) Improving methane selectivity of photo-induced CO_2 reduction on carbon dots through modification of nitrogen-containing groups and graphitization. Appl Catal B Environ. https://doi.org/10.1016/j.apcatb.2018.03.045

Low J, Yu J, Ho W (2015) Graphene-based photocatalysts for CO_2 reduction to solar fuel. J Phys Chem Lett 6(21):4244–4251. https://doi.org/10.1021/acs.jpclett.5b01610

Luisetto I, Tuti S, Battocchio C, Lo Mastro S, Sodo A (2015) $Ni/CeO_2–Al_2O_3$ catalysts for the dry reforming of methane: the effect of $CeAlO_3$ content and nickel crystallite size on catalytic activity and coke resistance. Appl Catal A Gen 500:12–22. https://doi.org/10.1016/j.apcata.2015.05.004

Lunde PJ, Kester FL (1974) Carbon dioxide methanation on a ruthenium catalyst. Ind Eng Chem Proc Des Dev 13(1):27–33. https://doi.org/10.1021/i260049a005

Ma J, Sun NN, Zhang XL, Zhao N, Mao FK, Wei W, Sun YH (2009) A short review of catalysis for CO_2 conversion. Catal Today 148(3–4):221–231. https://doi.org/10.1016/j.cattod.2009.08.015

Mao J, Peng TY, Zhang XH, Li K, Ye LQ, Zan L (2012) Selective methanol production from photocatalytic reduction of CO_2 on $BiVO_4$ under visible light irradiation. Catal Commun 28:38–41. https://doi.org/10.1016/j.catcom.2012.08.008

Mao J, Peng TY, Zhang XH, Li K, Ye LQ, Zan L (2013) Effect of graphitic carbon nitride microstructures on the activity and selectivity of photocatalytic CO_2 reduction under visible light. Cat Sci Technol 3(5):1253–1260. https://doi.org/10.1039/c3cy20822b

Martin O, Mondelli C, Cervellino A, Ferri D, Curulla-Ferre D, Perez-Ramirez J (2016) Operando synchrotron X-ray powder diffraction and modulated-excitation infrared spectroscopy elucidate the CO_2 promotion on a commercial methanol synthesis catalyst. Angew Chem Int Ed 55(37):11031–11036. https://doi.org/10.1002/anie.201603204

Mateo D, Albero J, García H (2018) Graphene supported NiO/Ni nanoparticles as efficient photocatalyst for gas phase CO_2 reduction with hydrogen. Appl Catal B Environ 224:563–571. https://doi.org/10.1016/j.apcatb.2017.10.071

Miguel CV, Soria MA, Mendes A, Madeira LM (2015) Direct CO_2 hydrogenation to methane or methanol from post-combustion exhaust streams – a thermodynamic study. J Nat Gas Sci Eng 22:1–8. https://doi.org/10.1016/j.jngse.2014.11.010

Mills GA, Steffgen FW (1974) Catalytic methanation. Catal Rev 8:159–210. https://doi.org/10.1080/01614947408071860

Mutz B, Sprenger P, Wang W, Wang D, Kleist W, Grunwaldt JD (2018) Operando Raman spectroscopy on CO_2 methanation over alumina-supported Ni, Ni_3Fe and $NiRh_{0.1}$ catalysts: role of carbon formation as possible deactivation pathway. Appl Catal A Gen 556:160–171. https://doi.org/10.1016/j.apcata.2018.01.026

Nishimura N, Kitaura S, Mimura A, Takahara Y (1992) Cultivation of thermophilic methanogen KN-15 on H_2-CO_2 under pressurized conditions. J Ferment Bioeng 73(6):477–480. https://doi.org/10.1016/0922-338X(92)90141-G

NOAA – National Oceanic and Atmospheric Administration (2018) Recent monthly average Mauna Loa CO_2. Available online at https://www.esrl.noaa.gov/gmd/webdata/ccgg/ trends/co2_trend_mlo.pdf. Accessed Mar 2018

Ocampo F, Louis B, Kiwi-Minsker L, Roger A-C (2011) Effect of Ce/Zr composition and noble metal promotion on nickel based $Ce_xZr_{1-x}O_2$ catalysts for carbon dioxide methanation. Appl Catal A Gen 392(1–2):36–44. https://doi.org/10.1016/j.apcata.2010.10.025

Olah GA, Goeppert A, Prakash GS (2008) Chemical recycling of carbon dioxide to methanol and dimethyl ether: from greenhouse gas to renewable, environmentally carbon neutral fuels and synthetic hydrocarbons. J Organomet Chem 74(2):487–498. https://doi.org/10.1021/jo801260f

Ota A, Kunkes EL, Kasatkin I, Groppo E, Ferri D, Poceiro B, Navarro Yerga RM, Behrens M (2012) Comparative study of hydrotalcite-derived supported Pd_2Ga and PdZn intermetallic nanoparticles as methanol synthesis and methanol steam reforming catalysts. J Catal 293:27–38. https://doi.org/10.1016/j.jcat.2012.05.020

Oyola-Rivera O, Baltanás MA, Cardona-Martínez N (2015) CO_2 hydrogenation to 1methanol and dimethyl ether by Pd–Pd_2Ga catalysts supported over Ga_2O_3 polymorphs. J CO_2 Util 9:8–15. https://doi.org/10.1016/j.jcou.2014.11.003

Park JN, McFarland EW (2009) A highly dispersed Pd-Mg/SiO_2 catalyst active for methanation of CO_2. J Catal 266(1):92–97. https://doi.org/10.1016/j.jcat.2009.05.018

Pastor-Pérez L, Baibars F, Le Sache E, Arellano-García H, Gu S, Reina TR (2017) CO_2 valorisation via reverse water-gas shift reaction using advanced Cs doped Fe-Cu/Al_2O_3 catalysts. J CO_2 Util 21:423–428. https://doi.org/10.1016/j.jcou.2017.08.009

Pavlostathis SG, Giraldo-Gomez E (1991) Kinetics of anaerobic treatment: a critical review. Crit Rev Environ Control 21(5–6):411–490. https://doi.org/10.1080/10643389109388424

Peillex JP, Fardeau ML, Boussand R, Navarro JM, Belaich JP (1988) Growth of Methanococcus thermolithotrophicus in batch and continuous culture on H_2 and CO_2: influence of agitation. Appl Microbiol Biotechnol 29(6):560–564. https://doi.org/10.1007/BF00260985

Pendashteh A, Rahmanifar MS, Mousavi MF (2014) Morphologically controlled preparation of CuO nanostructures under ultrasound irradiation and their evaluation as pseudocapacitor materials. Ultrason Sonochem 21(2):643–652. https://doi.org/10.1016/j.ultsonch.2013.08.009

Pöhlmann F, Jess A (2016) Influence of syngas composition on the kinetics of Fischer-Tropsch synthesis of using cobalt as catalyst. Energy Technol 4(1):55–64. https://doi.org/10.1002/ente.201500216

Porosoff MD, Yang X, Boscoboinik JA, Chen JG (2014) Molybdenum carbide as alternative catalysts to precious metals for highly selective reduction of CO_2 to CO. Angew Chem Int Ed 53(26):6705–6709. https://doi.org/10.1002/anie.201404109

Porosoff MD, Yan B, Chen JG (2016) Catalytic reduction of CO_2 by H_2 for synthesis of CO, methanol and hydrocarbons: challenges and opportunities. Energy Environ Sci 9(1):62–73. https://doi.org/10.1039/C5EE02657A

Porosoff MD, Baldwin JW, Peng X, Mpourmpakis G, Willauer HD (2017) Potassium-promoted molybdenum carbide as a highly active and selective catalyst for CO_2 conversion to CO. ChemSusChem 10(11):2408–2415. https://doi.org/10.1002/cssc.201700412

Posada-Pérez S, Viñes F, Ramirez PJ, Vidal AB, Rodriguez JA, Illas F (2014) The bending machine: CO_2 activation and hydrogenation on δ-MoC(001) and β-Mo_2C(001) surfaces. Phys Chem Chem Phys 16(28):14912–14921. https://doi.org/10.1039/C4CP01943A

Posada-Pérez S, Viñes F, Rodriguez JA, Illas F (2015) Fundamentals of methanol synthesis on metal carbide based catalysts: activation of CO_2 and H_2. Top Catal 58(2–3):159–173. https://doi.org/10.1007/s11244-014-0355-8

Prasad K, Pinjari DV, Pandit AB, Mhaske ST (2010) Synthesis of titanium dioxide by ultrasound assisted sol-gel technique: effect of amplitude (power density) variation. Ultrason Sonochem 17:697–703. https://doi.org/10.1016/j.ultsonch.2010.01.005

Qu J, Zhang X, Wang Y, Xie C (2005) Electrochemical reduction of CO_2 on RuO_2/TiO_2 nanotubes composite modified Pt electrode. Electrochim Acta 50(16–17):3576–3580. https://doi.org/10.1016/j.electacta.2004.11.061

Qu J, Zhou X, Xu F, Gong XQ, Tsang SCE (2014) Shape effect of Pd-promoted Ga_2O_3 nanocatalysts for methanol synthesis by CO_2 hydrogenation. J Phys Chem C 118 (42):24452–24466. https://doi.org/10.1021/jp5063379

Quesne MG, Roldan A, de Leeuw NH, Catlow CRA (2018) Bulk and surface properties of metal carbides: implications for catalysis. Phys Chem Chem Phys 20:6905–6916. https://doi.org/10.1039/C7CP06336A

Ramachandriya KD, Kundiyana DK, Wilkins MR, Terrill JB, Atiyeh HK, Huhnke RL (2013) Carbon dioxide conversion to fuels and chemicals using a hybrid green process. Appl Energy 112:289–299. https://doi.org/10.1016/j.apenergy.2013.06.017

Rodriguez JA, Evans J, Feria L, Vidal AB, Liu P, Nakamura K, Illas F (2013) CO_2 hydrogenation on Au/TiC, Cu/TiC, and Ni/TiC catalysts: production of CO, methanol, and methane. J Catal 307:162–169. https://doi.org/10.1016/j.jcat.2013.07.023

Rodriguez JA, Liu P, Stacchiola DJ, Senanayake SD, White MG, Chen JG (2015) Hydrogenation of CO_2 to methanol: importance of metal–oxide and metal–carbide interfaces in the activation of CO_2. ACS Catal 5(11):6696–6706

Romero-Sáez M, Dongil AB, Benito N, Espinoza-González R, Escalona N, Gracia F (2018) CO_2 methanation over nickel-ZrO_2 catalyst supported on carbon nanotubes: a comparison between two impregnation strategies. Appl Catal B Environ 237:817–825. https://doi.org/10.1016/j.apcatb.2018.06.045

Rönsch S, Schneider J, Matthischke S, Schlüter M, Götz M, Lefebvre J, Prabhakaran P, Bajohr S (2016) Review on methanation – from fundamentals to current projects. Fuel 166:276–296. https://doi.org/10.1016/j.fuel.2015.10.111

Sabatier P, Senderens JB (1902) New synthesis of methane. Compt Rend 134:514–516

Saeidi S, Amin NAS, Rahimpour MR (2014) Hydrogenation of CO_2 to value-added products – a review and potential future developments. J CO_2 Util 5:66–81. https://doi.org/10.1016/j.jcou.2013.12.005

Sahebdelfar S, Ravanchi MT (2015) Carbon dioxide utilization for methane production: a thermodynamic analysis. J Pet Sci Eng 134:14–22. https://doi.org/10.1016/j.petrol.2015.07.015

Sakakura T, Choi J-C, Yasuda H (2007) Transformation of carbon dioxide. Chem Rev 107 (6):2365–2387. https://doi.org/10.1021/cr068357u

Samei E, Taghizadeh M, Bahmani M (2012) Enhancement of stability and activity of Cu/ZnO/Al_2O_3 catalysts by colloidal silica and metal oxides additives for methanol synthesis from a CO_2-rich feed. Fuel Process Technol 96:128–133. https://doi.org/10.1016/j.fuproc.2011.12.028

Schubert K, Brandner J, Fichtner M, Linder G, Schygulla U, Wenka A (2001) Microstructure devices for application in thermal and chemical process engineering. Microscale Thermophys Eng 5(1):17–39. https://doi.org/10.1080/108939501300005358

Schulte KL, DeSario PA, Gray KA (2010) Effect of crystal phase composition on the reductive and oxidative abilities of TiO_2 nanotubes under UV and visible light. Appl Catal B Environ 97 (3–4):354–360. https://doi.org/10.1016/j.apcatb.2010.04.017

Seemann L (2006) Methanation of biosyngas in a fluidized bed reactor – development of a one-step synthesis process, featuring simultaneous methanation, watergas shift and low temperature tar reforming. PhD thesis. ETH Zurich

Seifert AH, Rittmann S, Herwig C (2014) Analysis of process related factors to increase volumetric productivity and quality of biomethane with Methanothermobacter marburgensis. Appl Energy 132:155–162. https://doi.org/10.1016/j.apenergy.2014.07.002

Sepehri S, Rezaei M (2015) Preparation of highly active nickel catalysts supported on mesoporous nanocrystalline gamma-Al_2O_3 for methane autothermal reforming. Chem Eng Technol 38 (9):1637–1645. https://doi.org/10.1002/ceat.201400566

Sharafutdinov I, Elkjær CF, de Carvalho HWP, Gardini D, Chiarello GL, Damsgaard CD, Wagner JB, Grunwaldt JD, Dahl S, Chorkendorff I (2014) Intermetallic compounds of Ni and Ga as catalysts for the synthesis of methanol. J Catal 320:77–88. https://doi.org/10.1016/j.jcat.2014.09.025

Shui J, Wang M, Du F, Dai L (2015) N-doped carbon nanomaterials are durable catalysts for oxygen reduction reaction in acidic fuel cells. Sci Adv 1(1):e1400129. https://doi.org/10.1126/sciadv.1400129

Sinnott SB, Andrews R (2001) Carbon nanotubes: synthesis, properties, and applications. Crit Rev Solid State 26(3):145–249. https://doi.org/10.1080/20014091104189

Song C (2006) Global challenges and strategies for control, conversion and utilization of CO_2 for sustainable development involving energy, catalysis, adsorption and chemical processing. Catal Today 115(1–4):2–32. https://doi.org/10.1016/j.cattod.2006.02.029

Song F, Zhong Q, Yu Y, Shi M, Wu Y, Hu J, Song Y (2017) Obtaining well-dispersed Ni/Al_2O_3 catalyst for CO_2 methanation with a microwave-assisted method. Int J Hydrog Energy 42 (7):4174–4183. https://doi.org/10.1016/j.ijhydene.2016.10.141

Sterner M (2009) Bioenergy and renewable power methane in integrated 100% renewable energy systems – limiting global warming by transforming energy systems. PhD thesis. University of Kassel

Studt F, Sharafutdinov I, Abild-Pedersen F, Elkjær CF, Hummelshøj JS, Dahl S, Chorkendorff I, Nørskov JK (2014) Discovery of a Ni-Ga catalyst for carbon dioxide reduction to methanol. Nat Chem 6(4):320–324. https://doi.org/10.1038/nchem.1873

Su X, Yang X, Zhao B, Huang Y (2017) Designing of highly selective and high-temperature endurable RWGS heterogeneous catalysts: recent advances and the future directions. J Energy Chem 26(5):854–867. https://doi.org/10.1016/j.jechem.2017.07.006

Tan JZY, Fernandez Y, Liu D, Maroto-Valer M, Bian J, Zhang X (2012) Photo-reduction of CO_2 using copper-decorated TiO_2 nanorod films with localized surface plasmon behavior. Chem Phys Lett 531:149–154. https://doi.org/10.1016/j.cplett.2012.02.016

Thauer RK, Kaster AK, Seedorf H, Buckel W, Hedderich R (2008) Methanogenic archaea: ecologically relevant differences in energy conservation. Nat Rev Microbiol 6:579–591. https://doi.org/10.1038/nrmicro1931

Tóth M, Kiss J, Oszkó A, Pótári G, László B, Erdőhelyi A (2012) Hydrogenation of carbon dioxide on Rh, Au and Au–Rh bimetallic clusters supported on titanate nanotubes, nanowires and TiO_2. Top Catal 55(11–13):747–756. https://doi.org/10.1007/s11244-012-9862-7

Tursunov O, Tilyabaev Z (2017) Hydrogenation of CO_2 over Co supported on carbon nanotube, carbón nanotube-Nb_2O_5, carbon nanofiber, low-layered graphite fragments and Nb_2O_5. J Energy Inst. https://doi.org/10.1016/j.joei.2017.12.004

Ud Din I, Shaharun MS, Subbarao D, Naeem A (2015) Synthesis, characterization and activity pattern of carbon nanofibers based copper/zirconia catalysts for carbon dioxide hydrogenation to methanol: influence of calcination temperature. J Power Sources 274:619–628. https://doi.org/10.1016/j.jpowsour.2014.10.087

Ud Din I, Shaharun MS, Subbarao D, Naeem A, Hussain F (2016) Influence of niobium on carbon nanofibres based Cu/ZrO_2 catalysts for liquid phase hydrogenation of CO_2 to methanol. Catal Today 259(2):303–311. https://doi.org/10.1016/j.cattod.2015.06.019

Ud Din I, Shaharun MS, Naeem A, Tasleem S, Johan MR (2017) Carbon nanofiber-based copper/zirconia catalyst for hydrogenation of CO_2 to methanol. J CO_2 Util 21:145–155. https://doi.org/10.1016/j.jcou.2017.07.010

Vargas E, Romero-Saéz M, Denardin JC, Gracia F (2016) The ultrasound-assisted synthesis of effective monodisperse nickel nanoparticles: magnetic characterization and its catalytic activity in CO_2 methanation. New J Chem 40:7307–7310. https://doi.org/10.1039/C6NJ01574C

Vijayan B, Dimitrijevic NM, Rajh T, Gray K (2010) Effect of calcination temperature on the photocatalytic reduction and oxidation processes of hydrothermally synthesized titania nanotubes. J Phys Chem C 114(30):12994–13002. https://doi.org/10.1021/jp104345h

Wang J, Lu S, Li J, Li C (2015) Remarkable difference in CO_2 hydrogenation to methanol on Pd nanoparticles supported inside and outside of carbon nanotubes. Chem Commun 51 (99):17615–17618. https://doi.org/10.1039/C5CC07079A

Wang W, Chu W, Wang N, Yang W, Jiang C (2016) Mesoporous nickel catalyst supported on multi-walled carbon nanotubes for carbon dioxide methanation. Int J Hydrog Energy 41:967–975. https://doi.org/10.1016/j.ijhydene.2015.11.133

Weatherbee GD, Bartholomew CH (1981) Hydrogenation of CO_2 on group VIII metals: I. specific activity of Ni/SiO_2. J Catal 68(1):67–76. https://doi.org/10.1016/0021-9517(81)90040-3

Wilhelm E, Battino R, Wilcock RJ (1977) Low-pressure solubility of gases in liquid water. Chem Rev 77(2):219–262. https://doi.org/10.1021/cr60306a003

Witoon T, Numpilai T, Phongamwong T, Donphai W, Boonyuen C, Warakulwit C, Chareonpanich M, Limtrakul J (2018) Enhanced activity, selectivity and stability of a CuO-ZnO-ZrO_2 catalyst by adding graphene oxide for CO_2 hydrogenation to methanol. Chem Eng J 334:1781–1791. https://doi.org/10.1016/j.cej.2017.11.117

Wu HC, Chang YC, Wu JH, Lin JH, Lin IK, Chen CS (2015) Methanation of CO_2 and reverse water gas shift reactions on Ni/SiO_2 catalysts: the influence of particle size on selectivity and reaction pathway. Cat Sci Technol 5(8):4154–4163. https://doi.org/10.1039/C5CY00667H

Xia X, Jia Z, Yu Y, Liang Y, Wang Z, Ma L (2007) Preparation of multi-walled carbon nanotube supported TiO_2 and its photocatalytic activity in the reduction of CO_2 with H_2O. Carbon 45 (4):717–721. https://doi.org/10.1016/j.carbon.2006.11.028

Xiaoding X, Moulijn JA (1996) Mitigation of CO_2 by chemical conversion: plausible chemical reactions and promising products. Energ Fuels 10(2):305–325. https://doi.org/10.1021/ef9501511

Xu W, Ramírez PJ, Stacchiola D, Brito JL, Rodriguez JA (2015) The carburization of transition metal molybdates (M_xMoO_4, M = Cu, Ni or Co) and the generation of highly active metal/carbide catalysts for CO_2 hydrogenation. Catal Lett 145(7):1365–1373. https://doi.org/10.1007/s10562-015-1540-5

Yin G, Yuan X, Du X, Zhao W, Bi Q, Huang F (2018) Efficient reduction of CO_2 to CO using cobalt–cobalt oxide core–shell catalysts. Chem Eur J 24(9):2157–2163. https://doi.org/10.1002/chem.201704596

Yu KP, Yu WY, Kuo MC, Liou YC, Chien SH (2008) Pt/titania-nanotube: a potential catalyst for CO_2 adsorption and hydrogenation. Appl Catal B Environ 84(1–2):112–118. https://doi.org/10.1016/j.apcatb.2008.03.009

Zhang QH, Han WD, Hong YJ, Yu JG (2009) Photocatalytic reduction of CO_2 with H_2O on Pt-loaded TiO_2 catalyst. Catal Today 148(3–4):335–340. https://doi.org/10.1016/j.cattod.2009.07.081

Zhang Q, Zuo Y-Z, Han M-H, Wang J-F, Jin Y, Wei F (2010) Long carbon nanotubes intercrossed Cu/Zn/Al/Zr catalyst for CO/CO_2 hydrogenation to methanol/dimethyl ether. Catal Today 50 (1–2):55–60. https://doi.org/10.1016/j.cattod.2009.05.018

Zhang L, Aboagye A, Kelkar A, Lai C, Fong H (2014) A review: carbon nanofibers from electrospun polyacrylonitrile and their applications. J Mater Sci 49:463–480. https://doi.org/10.1007/s10853-013-7705-y

Zhang J, An B, Hong Y, Meng Y, Hu X, Wang C, Lin J, Lin W, Wang Y (2017a) Pyrolysis of metal–organic frameworks to hierarchical porous Cu/Zn-nanoparticle@carbon materials for efficient CO_2 hydrogenation. Mater Chem Front 1:2405–2409. https://doi.org/10.1039/C7QM00328E

Zhang X, Zhu X, Lin L, Yao S, Zhang M, Liu X, Wang X, Li Y, Shi C, Ma D (2017b) Highly dispersed copper over β-Mo_2C as an efficient and stable catalyst for the reverse water gas shift (RWGS) reaction. ACS Catal 7(1):912–918. https://doi.org/10.1021/acscatal.6b02991

Zhu X, Qu X, Li X, Liu J, Liu J, Zhu B, Shi C (2016) Selective reduction of carbon dioxide to carbon monoxide over Au/CeO_2 catalyst and identification of reaction intermediate. Chin J Catal 37(12):2053–2058. https://doi.org/10.1016/S1872-2067(16)62538-X

Chapter 5
Metal Oxide Additives Incorporated Hydrogen Storage Systems: Formation of In Situ Catalysts and Mechanistic Understanding

D. Pukazhselvan, Narendar Nasani, S. K. Singh, and Duncan Paul Fagg

Contents

Abstract Hydrogen storage is a critical bottleneck to hydrogen economy. Presently none of the solid-state hydrogen storage materials (metal hydrides) reaches the capacity vs performance target (6.5 wt.% at 85 °C/5-12 bar, 1500 cycles) for the commercialization of light duty H_2 fuel cell vehicles. A few reversible hydrogen storage materials (e.g. MgH_2, $LiBH_4/MgH_2$ composite) possess adequate capacity, but their performance needs to be improved significantly. Metal oxide additives improve the hydrogen storage performance of metal hydrides, but the additive-hydride reaction mechanism remains not well understood. In this context, the present chapter discusses how various metal oxide additives interact with metal hydrides and

D. Pukazhselvan (✉) · D. P. Fagg
Nanoengineering Research Group, Department of Mechanical Engineering, University of Aveiro, Aveiro, Portugal
e-mail: dpuksel@gmail.com

N. Nasani
Centre for Materials for Electronics Technology, Pune, Maharashtra, India

S. K. Singh
Department of Physics, D.C.R. University of Science and Technology, Murthal, Haryana, India

R. Saravanan et al. (eds.), *Emerging Nanostructured Materials for Energy and Environmental Science*, Environmental Chemistry for a Sustainable World 23,
https://doi.org/10.1007/978-3-030-04474-9_5

facilitate the low temperature de/ab-sorption of hydrogen. The metal oxide additives may either directly catalyze the reaction without making any chemical changes or they catalyze indirectly by making active in situ products. In this chapter, various oxides and hydride combinations of the latter category are analyzed, and factors governing the improved hydrogen ab-/desorption performance are highlighted.

5.1 Introduction

Nanoparticles exhibit significantly improved electronic and surface chemical properties as compared to their bulk counterparts (Kelly et al. 2003; Sapra and Sarma 2004). Gold nanoparticles are the simplest example, for which size-dependent properties offer a wide diversity of potential applications, e.g., electronic circuits, sensors, probes, diagnostics, therapy, and catalysis (Daniel and Astruc 2004; Eustis and El-Sayed 2006; Haruta 2002). For a detailed explanation regarding the synthesis, characterization, and application of nanomaterials, the reader is directed to material-specific, in-depth studies reported in the literature (Bruce et al. 2008; Cao 2004; Chen and Mao 2007; Schwarz et al. 2004). In the present chapter, our interest is metal oxide nanoparticles, especially for catalytic applications. Since surface chemical features such as oxidation/reduction, gas ad-/ab-/desorption, complexation, and ion exchange properties determine the system performance, oxides are naturally the main choice as additives/catalysts and templates/supports in heterogeneous catalysis. There are various specific reasons why oxide surfaces are unique for catalytic applications: (i) the presence of cations and anions in a certain ratio that is relevant for influencing another species existing in chemical proximity, (ii) existence of bonding sites, (iii) existence of surface fields due to the coulombic nature of the ionic lattice, (iv) presence of charged adsorbed species, (v) presence of surface acidity or basicity, (vi) cationic/anionic vacancies, (vii) ability of cations to undergo oxidation/reduction reaction, (viii) ease of surface bridging with functional groups, (ix) high mobility of lattice oxygen and the possibility of oxygen-oxygen hopping, (x) creation of surface oxygen derived free radicals, etc. These properties are relevant for a wide variety of surface/bulk reactions, such as redox, oxidative Mannich reactions, condensation, deprotection, alkylation/hydroxylation, cycloaddition, dehydration, de-/re-hydrogenation, transesterification, organosynthesis, etc. Especially, in the case of metal-hydrogen interaction systems, when high-capacity metal hydrides exhibit thermodynamic and/or kinetic limitations, incorporation of suitable additives yield significantly improved hydrogenation/dehydrogenation performance (Zaluska et al. 2001; Zaluski et al. 1997).

A general universal classification of oxides is given in Fig. 5.1. Note that only transition metal oxides receive significant accolades for catalysis because the existence of partially filled d-shells of the metal ions and oxide ligands influences the neighboring atoms/molecules (Kung 1989). Usually binary/ternary metal oxides are routinely used in heterogeneous catalysis; however, mixed metal oxides, the oxygen-containing combinations of two or more metallic ions in a specific stoichiometry, are

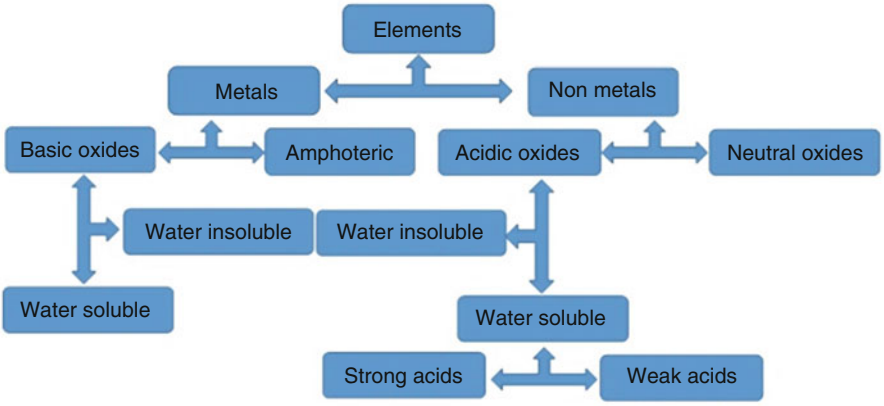

Fig. 5.1 Classification of oxides derived from the metals and non-metals

also useful additives under various circumstances (Gawande et al. 2012; Yuan et al. 2014). Especially for hydrogen storage systems, a wide variety of binary, ternary, and mixed metal oxides were employed as additives, and significant performance improvements have been reported. In the present chapter, we highlight how various metal oxides interact with the host hydride particles and mediate the reversible gas-solid surface interaction. The present chapter is organized as follows. Initially, by reciting the energy-wave vector/density of states (DOS) relationship for bulk, nano 3D, 2D, 1D, and 0D materials, the quantization effect implied by crystal dimension is highlighted. This section is followed by a brief summary to highlight a few classes of important metal oxides normally used for catalytic applications. Characteristics of oxide additives loaded hydrides belonging to few important categories, such as aluminates, binary hydrides, reactive hydride composites (RHC), and amide/imides, are reviewed. Catalysts existing without any structural/chemical changes throughout the reaction process are routinely reported in the literature. Therefore, in the present chapter, the main focus is on additives that undergo phase/chemical transformation to enhance the recycling performance of hydrogen storage systems. Some recent works performed by the authors in this line specifically on the promising hydrogen storage materials MgH_2 and $NaAlH_4$ are also highlighted in this respect.

5.2 Role of Size Effects

In heterogeneous catalysis, the size of the catalyst and the host particles are important factors influencing their interaction. Since sensitive electronic properties such as redox behavior/ionization and conductivity are strongly affected by domain size of the solid matter (particle/crystallite size) (Norris and Bawendi 1996; Zhang et al. 2009), for the understanding of readers, in the following, a brief explanation regarding the size-energy relationship is provided. A free electron existing in a

bulk 3D space (crystal structure) is free to move and no boundary conditions apply on the electron wave function. The energy-wave vector relation in this case is given by the relation,

$$E = \frac{\hbar^2 k^2}{2m} \tag{5.1}$$

As there are no restrictions, wave vector k is continuous and correspondingly energy values are continuous as shown in Fig. 5.2. On the other hand, when an electron is forced to confine in a 3D space, due to the potential barrier (V) existing at the boundaries of confined space "a," boundary conditions ("$\pm a$") apply. Therefore, the corresponding wave equation becomes solvable only for specific values of k and the derived value of k is given by the relation $k_n = n\frac{\pi}{a}$. Note that when "a" is high, the k_n values are small; hence the E vs k profile looks continuous. However, for the small values of "a," wave vector is bound to exhibit a substantial separation and since the wave vector is related with energy by a square function, the $E-k$ diagram shows an energy quantization effect. The corresponding $E-k$ diagram shown in Fig. 5.2 (top) is a simplest direct illustration that "confinement effect induces a circumstance called quantization." This quantization, how differs with a nanostructure where special restrictions exist in one or more directions, i.e., 2D, 1D, and quantum dots (OD), can be explained with the help of density of states (DOS) and energy relationships. For a 3D structure (nano), the density of states is given by the relation,

$$\mathrm{DOS}_{3\mathrm{D}} = \frac{8\pi\sqrt{2}}{\boldsymbol{h}^3} m^{\frac{3}{2}}\sqrt{E} \tag{5.2}$$

where m is mass of electrons ($9.109{*}10^{-31}$ kg), h is Planck's constant (6.626×10^{-34} J.s), $\hbar = h/2\pi$, and E is the energy accountable for the concerned states. Note that the $\mathrm{DOS}_{3\mathrm{D}}$ is directly proportional to the square root of energy as shown in the $\mathrm{DOS}_{3\mathrm{D}}$ vs energy profile of Fig. 5.2. In this case, although the electrons are confined than in the bulk material due to quantization, they have reasonable freedom to choose the states. On the other hand, when the structure is 2D, further confinement is forced due to the $\mathrm{DOS}_{2\mathrm{D}}$-energy relationship as shown by the expression:

$$\mathrm{DOS}_{2\mathrm{D}} = \frac{4\pi m}{\boldsymbol{h}^2} \tag{5.3}$$

In this case, the DOS is not proportional to energy (or proportional to E^0); hence, the DOS vs energy relation follows a step profile as shown in the figure. It means that only at specific energy values a significant number of states available for charge carriers when one degree of freedom is restricted. This situation, unlike the nano 3D case, forces electrons to occupy only certain states, ensuring higher confinement. When the movement of electrons is restricted in two directions, the $\mathrm{DOS}_{1\mathrm{D}}$ vs energy relation is given by,

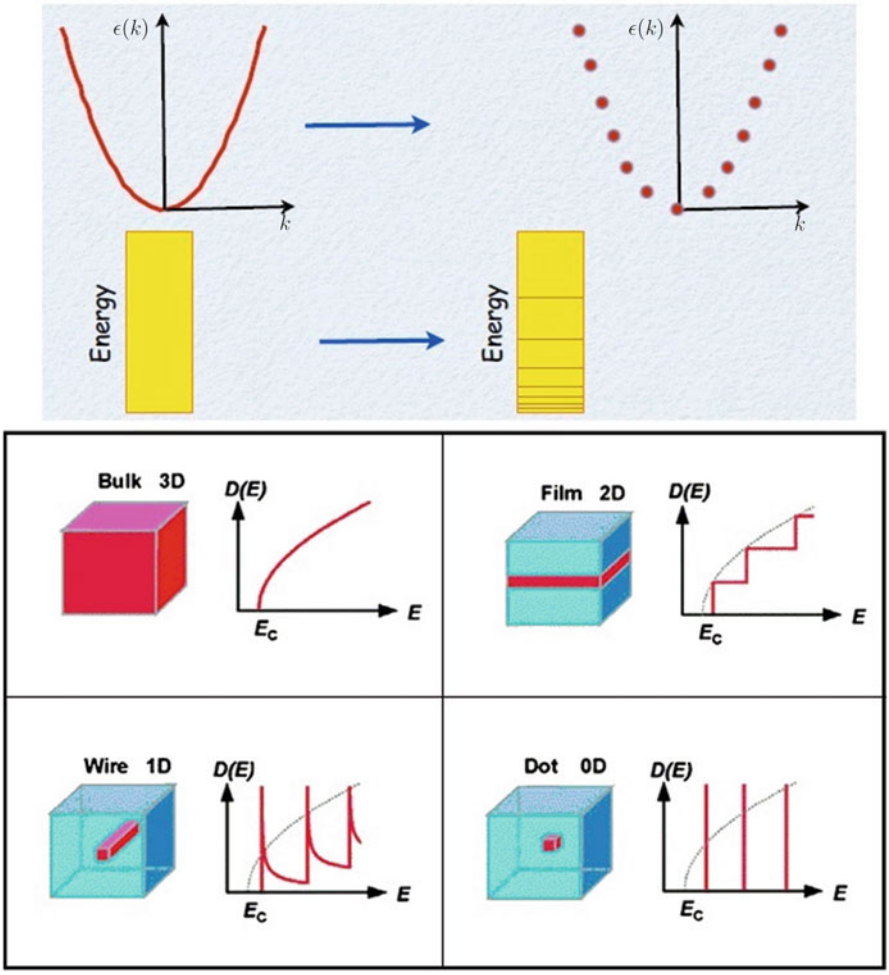

Fig. 5.2 Top: energy-wave vector diagram (*E-k* diagram) for a typical bulk and nano-3D structure. Bottom: density of states (DOS) vs energy profiles for dimension-controlled solid-state materials. (Adapted with permission from Handelman et al. 2012. Copyright © 2012, Royal Society of Chemistry)

$$\mathrm{DOS}_{1\mathrm{D}} = \frac{2\sqrt{2m^{\frac{1}{2}}}}{\sqrt{E}} \tag{5.4}$$

In this case the DOS is inversely proportional to the square root of energy, which implies a sharp decrease of states after a specific energy value. For the 0D materials, i.e., quantum dots, the $\mathrm{DOS}_{0\mathrm{D}}$ is a delta function as given in the following relation:

$$\mathrm{DOS}_{0\mathrm{D}} = 2\delta(E) \tag{5.5}$$

This relationship suggests that only with specific energy values, states can be accessed and everywhere except these is forbidden for electrons, ensuring high degree of confinement. The representation by Eqs. (5.1), (5.2), (5.3), (5.4) and (5.5), thus, provides a brief fundamental quantum mechanical explanation for readers regarding the origin of nanoconfinement. For a more detailed overview of mathematical expressions, the reader is directed to comprehensive quantum mechanical chapters discussed in the literature (Yu and Cardona 1996). In the case of metal oxides, apart from the naturally occurring size-dependent confinement effects (3D, 2D, 1D, or 0D structure), the surface chemical composition also significantly contributes to catalytic activity (Henrich and Cox 1996).

5.3 Metal Oxides for Catalytic Applications

Oxides commonly studied as catalysts/additives belong to the structural classes of corundum, rock salt, wurtzite, spinel, perovskite, rutile, and anatase structures. Table 5.1 summarizes these structure classes with a few examples. In fact there is no rule for the structural choice of oxides for catalytic applications. However, under certain circumstances, certain unique properties of a particular class of oxides look relevant for specific applications, and the catalyst is chosen accordingly.

Metal oxides are proven to be influential additives for almost every class of metal hydride systems. However, based upon the observations made for one hydride, the catalytic reaction mechanism cannot be generalized for every metal hydride systems. The oxide additive may be generated in situ or externally added, and the oxide may directly or indirectly catalyze the reaction. One interesting example for the in situ generated oxide additive that indirectly influences the metal-hydrogen interaction is lanthanum oxide existing in the $LaNi_5$ intermetallic/hydride system. The surface studies by spectroscopic methods clearly indicate a strong surface enrichment of oxidized La in $LaNi_5$ powder. When the intermetallic alloy $LaNi_5$ is exposed for a short time either in air or hydrogen gas (consisting oxygen impurities), oxidized La and Ni clusters are incorporated in the surface by the following reaction:

$$2\mathrm{LaNi}_5 + 1.5\,\mathrm{O}_2 \rightarrow \mathrm{La}_2\mathrm{O}_3 + 10\mathrm{Ni}. \tag{5.6}$$

A few authors have also identified the presence of $La(OH)_3$ and Ni clusters (Wallace et al. 1979). In either case, chemisorption of H_2 by Ni clusters was confirmed, as the studies identified a fermi surface at the top of the Ni 3D-derived states (Schlapbach 1981; Weaver et al. 1980). After breaking the H-H bond, the La oxide and Ni cluster interface act as a gateway for the diffusion of hydrogen inside the bulk $LaNi_5$. The same happens in the reverse direction during hydrogen release (Wallace et al. 1979). This is one of the simplest examples for in situ generated oxide

Table 5.1 Summary of common metal oxides used for catalytic applications (Categorized based upon crystal structure)

Crystal type	Lattice	Specific examples	Remarks
Corundum	Hexagonal	Al_2O_3, Ti_2O_3, V_2O_3, α-Fe_2O_3	General formula: M_2X_3
			Cations occupy distorted octahedral sites surrounded by six O legends
Rock salt	Face centered cubic	MgO, CaO, CoO, MnO, FeO, NiO	General formula: MX, where M at (0, 0, 0) and O at (1/2, 1/2, 1/2)
Wurtzite	Hexagonal	ZnO, β-$LiGaO_2$, β-$AgGaO_2$	General formula: MX
			Where M is at (1/3, 2/3, z) for z ~0.0 and is at (1/3, 2/3, z) for z ~0.38
Spinel	Cubic	$MgAl_2O_4$, Pb_3O_4 $CoFe_2O_4$, Na_2WO_4.	General formula: MM'_2X_4
			M and M′ are tetrahedrally and octahedrally coordinated cations
Perovskites	Simple cubic	$CaTiO_3$, BiF_2O_3, $BaZrO_3$, $LaAlO_3$	General formula: M′M″X
			M″ at cube corner positions (0, 0, 0), whereas M′ at (1/2, 1/2, 1/2) and O at face-centered positions (1/2, 1/2, 0)
Rutile	Tetragonal	TiO_2, V_2O_4, CrO_2, GeO_2, MoO_2, PbO_2	General formula MX_2 if the radius ratio r-/r+ exceeds ~1.37 MX2 favors rutile structure
			M at (0 0 0) and X at (x, x, 0) x~0.3
Anatase	Tetragonal	TiO_2, SnO_2	General formula MX_2
			M at (0 0 0) and X at (0 0 x) x~0.21

*Note: There is considerable confusion in the literature regarding the use of the word "catalysts" and "additives" for hydrogen storage systems. In general, catalysts take part in the chemical reaction but do not get consumed and hence not play any role in the thermodynamics of the system. Additives, on the other hand, may or may not get consumed in the reaction and may take part a role in the thermodynamics of the system. An additive may act as a catalyst, hence, when the role of the catalyst is not well understood, it is often safer to call it an additive

additives and their indirect effect on H sorption performance. In the case of high-capacity complex hydrides and binary hydrides, an external additive needs to be incorporated as hydrogen is strongly bonded with metal atoms. A large number of metal oxide additives and interesting materials aspects have been presented in the literature. In the following sections, we present a few metal oxide additives loaded hydrogen storage systems that are significant for commercial applications.

5.4 Metal Oxide Additives for High-Capacity Hydrogen Storage Systems

A few most important metal oxide additives studied in recent times is summarized in Table 5.2. When applying an oxide additive for improving the performance of a hydride, one may come across any of the following observations:

Table 5.2 Summary of a few most successful metal oxide additives studied for important high-capacity hydrogen storage systems

Hydride category	Specific example	Best oxide additives
Complex hydrides	$NaAlH_4$, $LiAlH_4$, $Mg(AlH_4)_2$	TiO_2, CeO_2, Nb_2O_5, $Ti(OBu)_4$
Binary hydrides	MgH_2, AlH_3	Nb_2O_5, r-GO, TiO_2, V_2O_5, Cr_2O_3, Fe_3O_4
Reactive hydride composites	MgH_2+2$LiBH_4$, $Ca(BH_4)_2$ + MgH_2	Sc_2O_3, Nb_2O_5, TiO_2/Ti_2O_3
Amide/imides	$LiNH_2$/2LiH, $Mg(NH_2)_2$/2LiH	K_2CO_3, K_3PO_4, $LiTi_2O_4$

(i) The additive remains chemically unchanged and provides consistently better system performance.
(ii) The additive reduces while mixing with hydride and improves the performance of the system.
(iii) The additive remains intact in the first cycle (or the first few cycles) but reduces during repeated cycles, improving the performance of the hydride.
(iv) The additive reduces during cycling runs but degrades the performance of the system.
(v) The additive gets reduced and makes new in situ catalysts, and the stable in situ catalyst improves the performance of the system for the long-term.
(vi) The additive makes a new in situ catalyst and provides better system performance, but the performance degrades due to slow compositional changes occurring to the catalyst. Whereas case (i) is straightforward, any of the situations (i)–(vi) can occur when an oxide additive is incorporated with a hydride.

In experimental context, our requirement is to obtain higher system performance, no matter whatever mechanistic category, among (i)–(vi), the additive/catalyst undertakes.

5.4.1 Metal Oxides Loaded Aluminates

Owing to the good H/M ratio, lightweight aluminates ($MAlH_4$ and $M'(AlH_4)_2$, M = Li, Na, K and M′ = Ca, Mg) receive considerable interest for hydrogen storage applications (Orimo et al. 2007). Among all the aluminates, good reversibility is reported only for two aluminates, $NaAlH_4$ and $KAlH_4$ (Bogdanović and Sandrock 2011; Morioka et al. 2003; Pukazhselvan et al. 2012, 2015), and their working temperature range is identified to be 180–350 °C. By incorporating additives, better performance can be achieved, but the mechanism of hydrogen release/reabsorption is not well understood (Bogdanović et al. 2007). In order to successfully tailor new promising reversible complex hydrides, it is necessary to understand the exact mechanism of H de-/absorption promoted by additives. Since sodium alanate ($NaAlH_4$) is the best model system in the category of aluminates, for mechanistic

studies, researchers prefer $NaAlH_4$ over other aluminates (later on the acquired knowledge can be extended to other aluminates). Since aluminum contains only three valence electrons for covalent bonding with hydrogen, the stable existence of Al-H covalently bonded $[AlH_4]^-$ tetrahedral complex relies on its ionic bond strength with Na^+ ion. The catalyst/additive should stimulate the antibonding between Na^+ and $[AlH_4]^-$ ions for the liberation of hydrogen atoms. The circumstance of the additive/catalyst may correspond to any of the cases (i)–(vi) mentioned above (Sect. 5.4), but antibonding will be stimulated only when the additive/catalyst possesses appropriate electronic features for depleting the stabilizing electron from the complex $[AlH_4]^-$. It is interesting that, in the literature, additives falling across all the categories (i)–(vi) have been reported for $NaAlH_4$/$LiAlH_4$. A few of them are discussed below.

Lee et al. (2007b) performed a comparative study for 10 wt.% lanthanide oxides, La_2O_3, CeO_2, Sm_2O_3, and Gd_2O_3 mixed $NaAlH_4$ and suggested that all these oxides trigger higher kinetics at lower dehydrogenation temperatures as compared to neat $NaAlH_4$. XRD investigation suggested that except CeO_2 additive which transforms to cerium hydride, all other oxides remain unchanged. Among these oxides, Sm_2O_3 additive was found to be the best for improving the reaction kinetics, reversibility, and cyclic stability. Xuanhui et al. (Rafi ud et al. 2012) used Nb_2O_5, TiO_2, and Cr_2O_3 nanoparticle additives for $NaAlH_4$ and found that TiO_2 and Nb_2O_5 are better than Cr_2O_3. The authors observed the reduction of TiO_2 and Nb_2O_5 in the first cycle itself. Xuanhui et al. (Rafi ud et al. 2011) also tested the dehydrogenation behavior of Nb_2O_5 and Cr_2O_3 additives loaded $LiAlH_4$ and found that both additives improve the desorption of hydrogen at lower temperatures as compared to additive-free samples but Nb_2O_5 is the best among these additives. After ball milling with $LiAlH_4$ for 30 min, both Nb_2O_5 and Cr_2O_3 additives remain chemically unchanged. However, the powder tested after dehydrogenation measurements suggests that whereas Cr_2O_3 remains chemically unchanged Nb_2O_5 additive reduces during the first cycle dehydrogenation. Apparently, the existence of three different Nb variants, NbO_2, NbH, and $LiNbO_3$, was identified, but it is not exactly clear which product among these was responsible for catalytic activity. Notwithstanding, the authors suggested that the variable valence states of Nb incorporated in the powder may be a prime reason for the catalytic activity. Although such a claim requires further verification, it is interesting that the reduction of additive and the subsequent formation of multiple in situ additive(s) helps to destabilize the complex hydride. In another study, Li et al. (2013) used $NiFe_2O_4$ additive for $LiAlH_4$ and found that the additive interacts with $LiAlH_4$ during ball milling itself and forms $LiFeO_2$ and Al-Ni alloy (Al_4Ni_3). During dehydrogenation, these in situ products further interact chemically and produce $LiAlO_2$ and $Al_{1.1}Ni_{0.9}$ products. The authors suggested that the synergetic effect of these products is the reason behind the superior performance of the system.

In one of the authors' earlier studies (Pukazhselvan et al. 2010), the hydrogen storage behavior of metal oxide nanoparticle additives such as TiO_2, CeO_2, La_2O_3, Pr_2O_3, Nd_2O_3, Sm_2O_3, Eu_2O_3, and Gd_2O_3 loaded $NaAlH_4$ was tested, and it was found that TiO_2 is the most effective additive. This observation is in agreement with the findings of Lee et al. (2008) who used 2 mol.% TiO_2 nanopowder for catalyzing

$NaAlH_4$. The thermodynamic calculations of Lee et al. further revealed that titania reacts with $NaAlH_4$ to form an intermetallic phase $TiAl_3$ in the mixture. Usually pure $NaAlH_4$ releases 5.5 wt.% hydrogen through a two-step decomposition reaction, first step at 180 °C and second step at 230 °C, as given by the reaction (5.7):

$$3NaAlH_4 \leftrightarrow Na_3AlH_6 + 2Al + 3H_2 \leftrightarrow 3NaH + 3Al + 4.5H_2. \quad (5.7)$$

As per the thermodynamic calculations of Lee et al., 2 mol.% TiO_2 reacts with $NaAlH_4$ by the following reaction:

$$0.98NaAlH_4 + 0.02TiO_2 \rightarrow 0.859NaAlH_4 + 0.073Na_3AlH_6 + 0.011Al_2O_3 + 0.013TiAl_3 + 0.044H_2 \quad (5.8)$$

The 1.3 mol.% $TiAl_3$ derived from 2 mol.% TiO_2 catalyzes the remaining 85.9 mol.% $NaAlH_4$ and 7.3 mol.% Na_3AlH_6 and lowers the H desorption temperature by at least 30–50 °C while also appreciably increasing the reaction kinetics. The existence of 1.1 mol.% alumina is believed to have no impact as alumina is not a fine catalyst for $NaAlH_4$ (Ma et al. 2012). Another study that directly employs mechanochemically synthesized $TiAl_3$ as catalyst proves that $TiAl_3$ exhibits a pronounced catalytic activity for $NaAlH_4$ (Lee et al. 2007a). It may herewith be recalled that the well-studied $TiCl_3$ additive also makes $TiAl_3$ by the following reaction:

$$0.98NaAlH_4 + 0.02TiCl_3 \rightarrow 0.916NaAlH_4 + 0.025Na_3AlH_6 + 0.010NaCl + 0.013TiAl_3 + 0.036H_2 \quad (5.9)$$

Various forms of Ti-based additives, Ti nanoparticles (Fichtner et al. 2003), chlorides/fluorides (Majzoub and Gross 2003), and oxides/alkoxides (Bogdanović et al. 2003; Pukazhselvan 2012), were tried for $NaAlH_4$, and formation of in situ Ti_xAl_y intermetallic alloy was identified for many of these cases. The chemical state of reduced titanium and its coordination in the Ti_xAl_y alloy were well studied by various researchers (Bogdanović et al. 2007; Léon et al. 2004), and it is concluded that Ti exists in zerovalent state that does not change by hydrogenation/dehydrogenation cycles. Felderhoff et al. (2004) identified slight structural changes for Ti_xAl_y alloy during charging/discharging cycles, but the zero valence of Ti is always maintained. Following these observations, Pukazh et al. tested a 10 mol.% TiO_2 loaded $NaAlH_4$ powder and explored further details regarding the reduction of titania and the Ti_xAl_y in situ additive (Pukazhselvan 2012). The results are demonstrated by XRD as shown in Fig. 5.3.

The existence of anatase titania peak in profile “a” of Fig. 5.3 suggests that although a partial reduction may be possible during mechanical milling, a major portion of the titania additive remains unreacted. Profile “b” suggests that reduction of TiO_2 takes place during the first de-/re-hydrogenation cycle, but a smaller part still

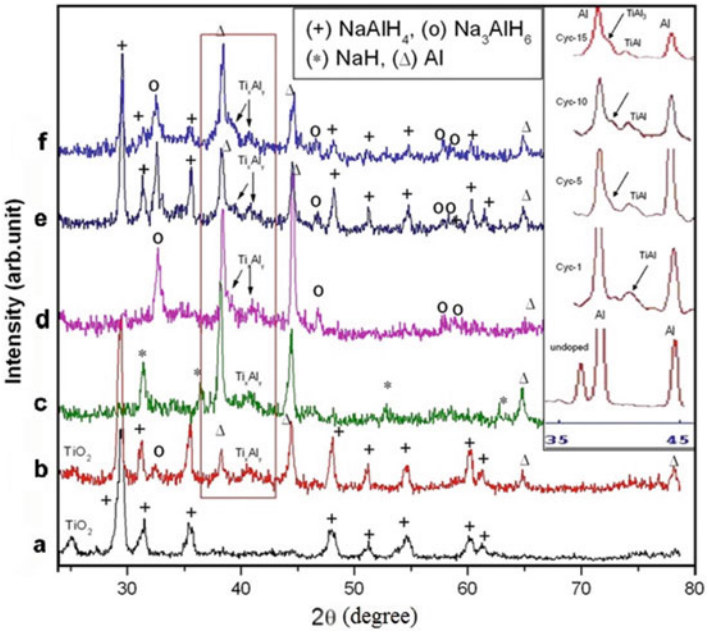

Fig. 5.3 XRD profiles of 10 wt.% titania additive mixed $NaAlH_4$ tested for various cycles. (**a**) 10 mol% TiO_2 (25 nm):$NaAlH_4$ ball milled (1 h) starting material. (**b**) Re-hydrogenated powder of the 1st cycle dehydrogenated material, (**c**) 2nd cycle dehydrogenated powder, (**d**) 6th cycle dehydrogenated (to 1st step), (**e**) 10th cycle hydrogenated, and (**f**) 15th cycle hydrogenated. (Reproduced with permission from Pukazhselvan 2012, Copyright © 2012 Hydrogen Energy Publications. Elsevier.

Note* The existence of Ti_xAl_y alloy in the Ti/Ti variant additives loaded $NaAlH_4$ powder was a chapter of intense debate in the literature. In the early days of research, its presence could not be confirmed due to two reasons: (i) The size of Ti_xAl_y crystallites is too small; hence when a small concentration of additive is used, its XRD peaks get hindered by the background noise (in some cases amorphous Ti_xAl_y is also reported). (ii) The peak position of Ti_xAl_y alloy is closer to the peak position of Al(111) peak; hence it is discernible only as a shoulder to the Al (111) peak (in the Ti_xAl_y alloy family, several alloy combinations show XRD reflections in the range 39–44° 2θ, and among these $TiAl_3$ is a widely known alloy whose peak position is too close to Al(111) for simple deconvolution. Using higher additive concentrations is therefore recommended for characterization studies; however, for hydrogen storage studies, the additive concentration should be as little as possible)

remains unreacted at the end of first cycle. The XRD profiles corresponding to cycles 2 and 6 (profiles "c" and "d," respectively) show no presence of TiO_2. It is clear from these results that titania reduces completely during the second cycle and the reduced Ti combines with Al (Ti_xAl_y phase peak position, 40.8°). Upon cycling the sample further, as revealed by comparing profiles "d," "e," and "f," the formation of another phase of Ti_xAl_y alloy (Schoenitz et al. 2004) is also identified (position 39.9°, right-side shoulder to Al(111) peak. For clarity, this is highlighted in the inset). This observation possibly indicates the transformation of one Ti_xAl_y phase to another

during repeated H ab-/desorption cycles. Further studies may provide more clarity for these observations. However, these observations are enough to conclude that in certain cases, metal oxides get reduced and make new in situ products, and the in situ product itself get chemically and/or structurally modified upon catalyzing the reaction. It is therefore a challenge for material scientists to identify the most promising composition for most active catalytic performance and retain the optimum catalyst concentration/structure during cyclic studies. Presently although the actual chemical species (Ti_xAl_y) responsible for catalytic activity is confirmed, further studies are required to know how it influences the ionic $Na^+ - [AlH_4]^-$ and covalent Al-H bonds. Extensive theoretical studies for understanding the electronic structure of Ti_xAl_y will throw further light on the bond breaking/making mechanism of $NaAlH_4$.

5.4.2 Metal Oxides Loaded Magnesium Hydride

The high capacity reversible binary hydride, MgH_2 (7.6 wt.% and 110 g/L), is another potential solid-state system for hydrogen storage. However, owing to the high enthalpy of formation ($\Delta H = -76$ kJ/mol), MgH_2 requires temperature over 300 °C for the release of hydrogen at 1 bar equilibrium pressure (Pukazhselvan et al. 2012). Extensive research works have, thus, been conducted for enhancing the hydrogen storage performance of MgH_2 through various strategies (Kalidindi and Jagirdar 2009; Pukazhselvan et al. 2014b; Zhao-Karger et al. 2010; Zlotea et al. 2015), e.g., (i) size tailoring, (ii) nanoconfinement, (iii) chemical modification, (iv) additive loading, etc. Nevertheless, considering the context of the present chapter, we restrict our discussion to category "iv," especially on metal oxide additives. Various metal oxides, transition metal oxides (Jung et al. 2006), rare earth oxides (Sadhasivam et al. 2013), mixed ternary oxide phases (Patah et al. 2009; Rahman et al. 2011), and rock salt oxides (Pukazhselvan et al. 2014a) were used by researchers for improving the dehydrogenation of MgH_2. It is widely agreed that metal oxide additives are the best for MgH_2, but the catalytic reaction mechanism of metal oxides added MgH_2 remains a chapter of intense debate. In this context, by referring some significant results reported in the literature, we attempt to provide a reasonable understanding regarding the mechanistic role of best metal oxide additives for MgH_2.

The formation enthalpy of MgO, −601 kJ/mol, is a much higher value than the formation enthalpy of MgH_2, i.e., −76 kJ/mol. Therefore, naturally the tendency of Mg oxidation is higher when the system contains oxygen impurities. Formation of MgO as a result of oxidation of Mg in the surface of Mg/MgH_2 is believed to be a serious contamination effect that impedes the Mg-H sorption interaction. Therefore, the additive/catalytic selectivity steers two considerations: (i) additives that incorporate surface oxide contaminants need to be avoided, and (ii) additives that offer clean surface and facilitating Mg-H interaction need to be deployed. In order to protect the Mg/MgH_2 surface from oxygen/moisture, some methods have been suggested in the literature, such as embedding MgH_2 on gas-selective polymers (e.g., PMMA) or encapsulating with graphene or graphene oxide layers. These

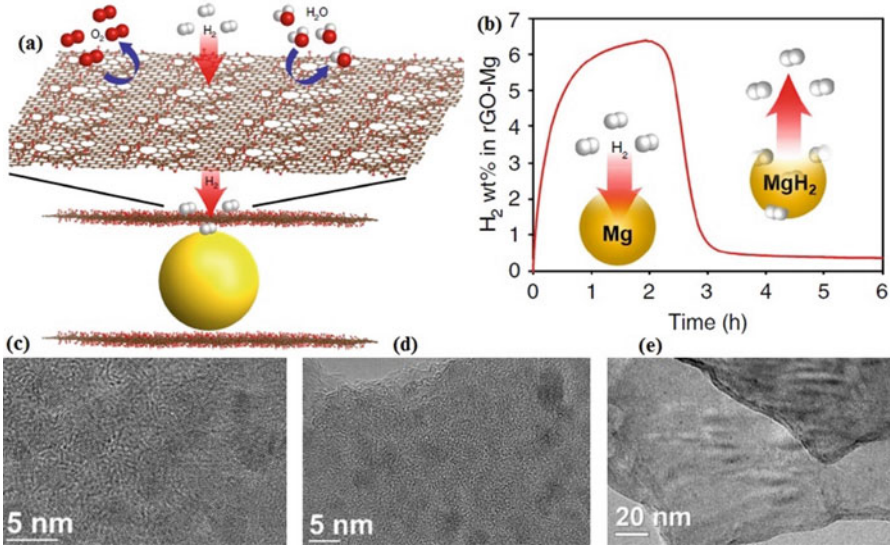

Fig. 5.4 (**a**) Pictorial representation of Mg laminated by rGO, (**b**) hydrogen ab-/desorption kinetics profile of Mg crystals laminated by rGO sheets, (**c**) HRTEM image of as-prepared Mg-rGO laminates, (**d**) HRTEM image of Mg-rGO laminates after hydrogenation, and (**e**) overview of one portion of the rGO-laminated MgH_2 sample. (Reproduced from the work of Cho et al. 2016 Copyright © 2016, Springer Nature)

surface protectors prevent the intrusion of larger molecules, such as O_2, N_2, and H_2O, while facilitating the permeation of hydrogen (Jeon et al. 2011; Kim et al. 2013). Recently Cho et al. (2016) have demonstrated a method to laminate Mg nanoparticles by using reduced graphene oxide (rGO) and suggested that it is a good method for preventing surface oxidation. As shown in the pictorial representation (Fig. 5.4a), Cho et al. showed that about 3.3 nm sized Mg nanocrystals can be laminated by large sheets of rGO by complexing GO with bis(cyclopentadienyl) magnesium and then reducing it by treating with lithium naphthalenide solution. As shown in Fig. 5.4b, the rGO-laminated Mg instantly absorbs (200 °C/15 bar H_2 pressure) over 6 wt.% H_2 and desorbs all hydrogen (300 °C/vacuum). Moreover, the results are consistent even after 3 months of exposure in air. The HRTEM images shown in Fig. 5.4c and d, respectively, correspond to rGO-laminated Mg and its hydrogenated counterpart. Figure 5.4e represents the overview of one portion of the rGO-laminated MgH_2 sample. The data shown in Fig. 5.4 clearly reveals that Mg/MgH_2 nanoparticles are well confined and stable over the conditions applied for recycling tests. Based upon DFT studies and Mg K-edge X-ray absorption spectra, Wan et al. (2017) have recently explored that when MgO nanoparticles are sealed by rGO, the outermost atomic layer of Mg gets slightly oxidized and forms a monolayer honeycomb MgO. Whereas the bulk MgO rock salt is known as a potential H diffusion barrier, the monolayer MgO formed as a result of interaction with rGO provides no barrier and in fact works similarly to a clean Mg surface. It is

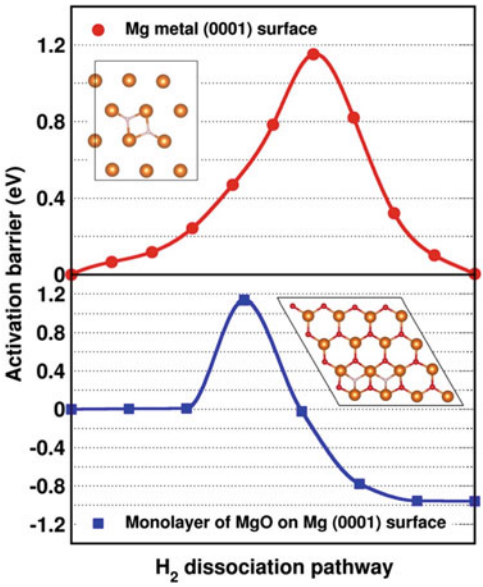

Fig. 5.5 Hydrogen molecular dissociation energy profile for clean Mg surface and monolayer MgO covered Mg surface. (Reproduced with permission from Wan et al. 2017. Copyright © 2017, American Chemical Society)

also in agreement with the work of Kobayashi et al. (Kobayashi et al. 1994) that suggested that thin MgO substrates exhibit suitable electronic structure for the chemisorption of hydrogen molecules.

By applying density functional theory, Wan et al. calculated the H_2 dissociation energy profile for clean Mg surfaces and monolayer MgO covered Mg surfaces as demonstrated in Fig. 5.5. As seen, the H_2 dissociation energy is the same value (1.14 eV) for both surfaces. Nonetheless, once the H-H bond is broken, the MgO-layered system relaxes to a much lower energy state, roughly about 1 eV lower than the initial H_2 physisorbed state at a distance of 2.9 Å away from the surface. Note that when a few layers of such honeycomb structured MgO deposits over another, it results to the formation of a bulk rock salt MgO structure, which is well known as hydrogen diffusion barrier. Hence, from the understanding gained from this study, a valid question arises that whether the proven best oxide additives play a role to restrict the growth of the MgO and lead to a circumstance as presented in Fig. 5.5. Moreover, there are also convincing data that supports (Wu et al.) that the energy required to break the dihydrogen bond on the MgO surface varies depending on the sites where H_2 faces the MgO surface (Wu et al. 2009). In another work, Borgschulte et al. (2008) investigated the surface composition and chemical state of ball-milled MgH_2 by XPS and H/D exchange experiments. This study confirms the existence of MgO wrapped surfaces with cationic vacancies having catalytic tendencies. These studies give us two interesting pieces of information: (i) not all the MgO surfaces are inactive for Mg-H interaction, and (b) tuning the chemistry of the MgO surface may be a critical step in the process of catalysis for reducible metal oxide additives loaded MgH_2 system.

Proceeding with the above information, in the following, we reviewed a few important results reported for various metal oxide additives loaded MgH_2. In some of these studies, the existence of oxidized Mg surfaces was proven, but the catalytic contribution of this oxidized Mg surface was considered insignificant. Hanada et al. (2009) used 1 mol % of transition metal oxide nanoparticle additives such as Nb_2O_5, V_2O_5, and TiO_2 and showed that all these products after dehydrogenation show the coexistence of Mg and MgO without any traces of intact additives. The K-edge XANES spectra revealed the existence of the used additives in partially reduced state. Based upon these observations, the authors concluded that improved hydrogen sorption is due to the formation of reduced oxides. However, in this study it was not detailed how influential was the existence of an oxidized Mg surface. Oelerich et al. (2001b) investigated the hydrogen absorption/desorption behavior of MgH_2 by incorporating a range of metal oxide additives, such as Sc_2O_3, TiO_2, V_2O_5, Cr_2O_3, Mn_2O_3, Fe_3O_4, CuO, Al_2O_3, and SiO_2. By this comparative study, the authors categorized the additives from most effective to the least effective. For example, for hydrogen absorption, a nearly similar effect was observed for TiO_2, V_2O_5, Cr_2O_3, Mn_2O_3, Fe_3O_4, and CuO additives. On the other hand, for dehydrogenation, Fe_3O_4 and V_2O_5 show comparable effects, followed by Mn_2O_3, Cr_2O_3, and TiO_2 additives. It was shown that only 0.2 mol.% of the additive is sufficient for providing fast sorption kinetics. However, details regarding why certain oxides are better than others for MgH_2 were not explored.

Oelerich et al. (2001a) made a comparative hydrogen storage test for MgH_2 using various forms of vanadium additives, such as V, V_2O_5, VN, and VC. This study confirms that vanadium oxide is better than other forms of vanadium additives. Further studies revealed that V_2O_5 gets reduced during processing the powder toward H ab-/desorption measurements. Porcu et al. (2008) observed that the Nb_2O_5 additive reacts with MgH_2 and oxidizes a significant portion of MgH_2. Polanski et al. (Polanski and Bystrzycki 2009) performed comparative hydrogen storage measurements for Cr_2O_3, TiO_2, Fe_3O_4, Fe_2O_3, In_2O_3, and ZnO additives mixed MgH_2 and suggested that Cr_2O_3, TiO_2, Fe_3O_4, and Fe_2O_3 additives are better than indium and zinc oxides for improving the dehydrogenation of MgH_2. Later on, Polanski et al. (2011) used Cr_2O_3 nanoparticle additive for MgH_2, and an ab-/desorption study for 150 cycles revealed that reduction of Cr_2O_3 leads to the formation of Cr and MgO. A substantial capacity reduction was observed due to the loss of Mg as MgO and the consequent microstructural changes. Patah et al. (2009) observed that co-catalyzing MgH_2 by Nb_2O_5 and Cr_2O_3 provides better effect than when these additives were incorporated separately. The authors suggested the generation of diffusion paths as the reason for the result; however, no further information was added how the diffusion pathways are generated by mixing together the Nb_2O_5 and Cr_2O_3 additives. Croston et al. (2010) used titania additive for improving the dehydrogenation of MgH_2 and suggested that titania is reduced by its interaction with MgH_2. Huang et al. (2006) used oxides of iron, such as Fe_2O_3 and Fe_3O_4 as additives for MgH_2 and found that during heating, both iron oxides reduce to pure Fe. For both samples, there were no substantial differences in catalytic activity in terms of decreasing the desorption temperature and increasing the reaction

kinetics. However, a slightly higher loss of capacity for Fe_2O_3 additive loaded sample as compared to Fe_3O_4 additive loaded sample was observed. The authors suggested the capacity, especially for $MgH_2 + Fe_2O_3$ composite, to be a result of the reduction reaction, as more magnesium is lost to MgO in this mixture. In these studies, the role of MgO is ignored, at times referring this as an unintended reaction product and a potential barrier layer incorporated in the system by consuming useful magnesium. Friedrichs et al. (2006c) observed that the Mg/MgH_2 samples exhibit a strong tendency for surface oxidation and an oxide passivation layer, size 3–4 nm, forms instantly in MgH_2/Mg samples upon the availability of oxygen impurities. This study further revealed that once the surface is neatly covered by a thin layer of MgO, further oxidation does not occur. These studies necessitate an in-depth study for exploring the details of oxide-MgH_2 chemical interaction and its role on the catalysis of the system. The information observed through these studies suggest that the MgO layer existing in oxide additives loaded MgH_2 cannot be ignored as a barrier layer as was thought previously.

Among all the metal oxide additives reported in the literature, Nb_2O_5 is the most widely investigated additive for MgH_2. Barkhordarian et al. (2003) revealed that Nb_2O_5 additive loaded MgH_2 at the reaction temperature of 300 °C releases about 7 wt.% hydrogen within 130 s and reabsorbs it within 60 s. Friedrichs et al. (2006a) used 15 nm- and 100 nm-sized Nb_2O_5 additives for MgH_2 and observed that, whereas both sizes are beneficial, smaller particles strongly enhance the kinetics of the reaction. In another study Hanada et al. (2005) showed that in the case of a 1 mol. % Nb_2O_5 admixed material, the required dehydrogenation temperature is reduced by at least 50 °C in the second cycle as compared to the first cycle. Note that the performance improvement during cycling measurements is a sign for the formation of modified in situ additives. Although all these results are in good agreement with each other, regarding mechanistic understanding, considerable anomalies exist in the literature. Aguey-Zinsou et al. (2007) suggested that Nb_2O_5 acts as lubricant, dispersing and/or cracking agent during milling and helping to further reduce MgH_2 particle size, while no chemical changes occur to Nb_2O_5 during cyclic measurements. Further exemplary studies, however, revealed that Nb_2O_5 in fact gets reduced chemically and a significant amount of oxidized Mg gets incorporated in the powder.

Presently it is clear that some of the best metal oxide additives reported for MgH_2, for example, Nb_2O_5 and TiO_2, involve a chemical interaction with MgH_2 to make active in situ catalysts. However, there are contradictory opinions in the literature regarding the exact chemical composition of the reduced in situ catalyst. Ma et al. reported that Nb nanocrystals of size ~10 to 20 nm are the apparent reaction product when ball milling MgH_2/Nb_2O_5 mixture and these nanocrystals may be responsible for the catalytic activity (Ma et al. 2013). Friedrichs et al. (2006a) suggested the formation of oxygen deficient magnesium niobate ($MgNb_2O_{3.67}$) in the Nb_2O_5 added MgH_2 samples. However, their further study suggested the composition to be $Mg_xNb_{0.8(1-x)}O$ (Friedrichs et al. 2007). By an in situ X-ray diffraction study, Nielsen and Jensen identified that Nb dissolved MgO forms during the dehydrogenation of Nb_2O_5 additive loaded MgH_2 (Nielsen and Jensen 2012). Recently Pukazh

et al. employed Nb_2O_5 and TiO_2 additives for MgH_2 and showed that metals substituted MgO rock salt products, typified by $Mg_xNb_yO_{x+y}$/$Mg_xTi_yO_{x+y}$ form as a result of chemical interaction between the additives with MgH_2, and this rock salt is responsible for the catalytic activity (Pukazhselvan et al. 2016a, 2017a). Recent theoretical calculations of Sandhya et al. by DFT modeling also support these observations (Pukazhselvan et al. 2017b; Sandhya et al. 2016).

Pukazh et al. made composite mixtures of MgH_2+nNb_2O_5 (n = 0.083, 0.10, 0.123, 0.167, 0.25, 0.50, 1.0, and 1.5) and tested the mechanochemical reaction products for three sets of reaction times, such as 1 h, 10 h, and 30 h (totally 24 samples) (Pukazhselvan et al. 2016a). The best composition out of these 24 samples, i.e., MgH_2+0.167Nb_2O_5, was then studied by varying the reaction time, i.e., 2 min, 5 min, 15 min, 30 min, 45 min, 1 h, 2 h, 5 h, 10 h, 15 h, 20 h, 25 h, and 30 h (Pukazhselvan et al. 2016d). The corresponding XRD profiles of these samples are shown in Fig. 5.6. As seen at the initial stage (15 min to 5 h) of mechanochemical

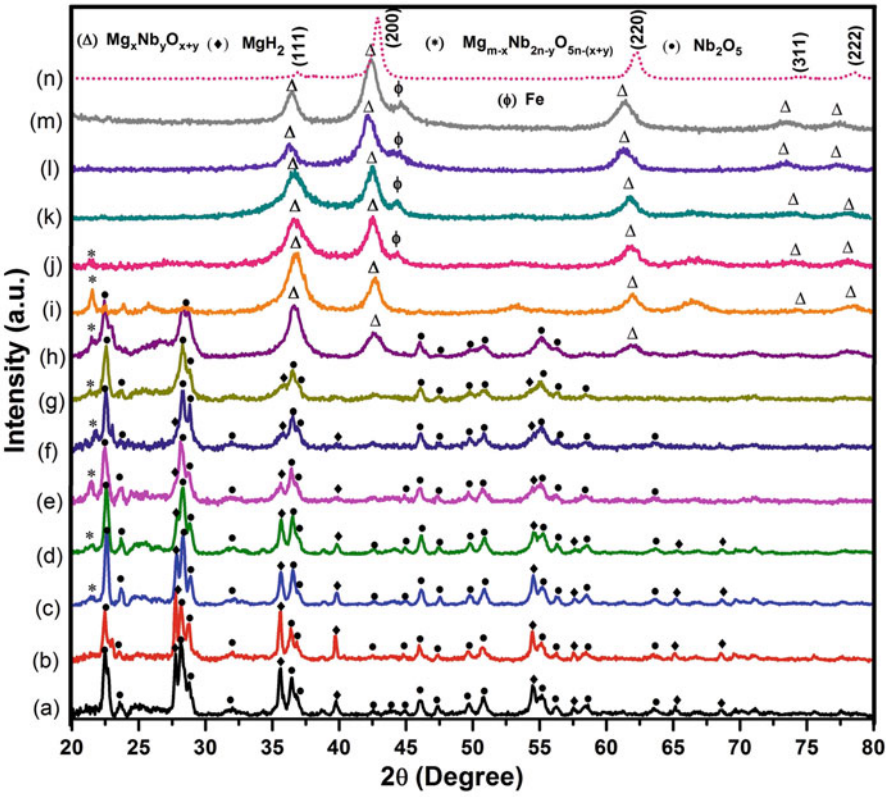

Fig. 5.6 Mechanochemically reacted MgH_2+0.167Nb_2O_5 powder for (**a**) 2 min, (**b**) 5 min, (**c**) 15 min, (**d**) 30 min, (**e**) 45 min, (**f**) 1 h, (**g**) 2 h, (**h**) 5 h, (**i**) 10 h, (**j**) 15 h, (**k**) 20 h, (**l**) 25 h, and (**m**) 30 h and (**n**) standard MgO rock salt. (Reproduced with permission from Pukazhselvan et al. 2016d, Copyright © 2015, John Wiley and Sons)

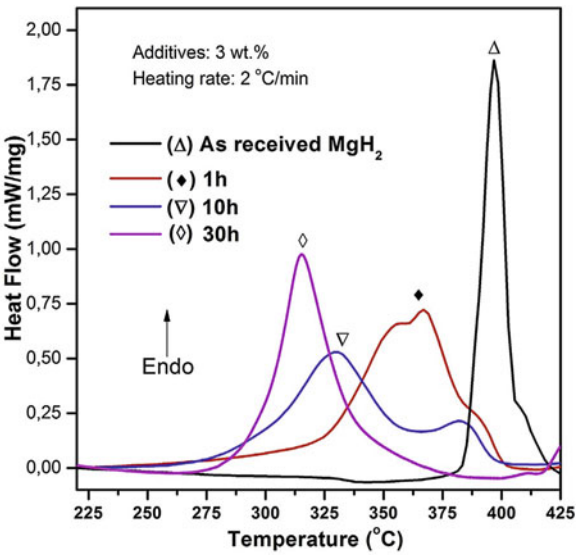

Fig. 5.7 DSC profiles of MgH_2 added with a 3 wt.% of 1h, 10h and 30h reacted additive (MgH_2+0.167Nb_2O_5). Symbols: (▯) as-received MgH_2; (◆)1 h reacted additive powder mixed with MgH_2; (▿)10 h reacted additive powder mixed with MgH_2; (◊)30 h reacted additive powder mixed with MgH_2. (Reproduced with permission from Pukazhselvan et al. 2016a. Copyright © 2015 Hydrogen Energy Publications, LLC. Elsevier)

reaction, MgH_2 disappears gradually, and an unidentified phase (indexed by * symbol) forms in minor quantities. During 5–15 h of reaction, dominant existence of a monophase rock salt product with characteristic (111), (200), and (220) reflections can be noticed. Upon further increasing the milling time up to 30 h, a monophase with visibly unchanged XRD features after 25 h, having close crystallographic resemblance with MgO rock salt is observed. Further spectroscopic/microscopic studies suggested that the product existing in 30 h reacted material is actually Nb incorporated MgO, typified by a general formula, $Mg_xNb_yO_{x+y}$. Samples taken from 1 h, 10h, and 30h reacted powders were used as additives (3 wt.%) for MgH_2, and the DSC profiles were recorded. The DSC profiles demonstrated by Fig. 5.7 show a systematic shift toward lower temperatures with a series, 30 h > 10 h > 1 h > no additive. This result shows that the rock salt product $Mg_xNb_yO_{x+y}$ possesses a significant catalytic behavior for the low-temperature dehydrogenation of MgH_2. Following this study, Pukazh et al. explored a similar observation for titania added MgH_2 through an XRD/in situ XRD study performed for a 10 wt.% titania loaded MgH_2 (Pukazhselvan et al. 2017a). As it can be seen in the in situ XRD shown in Fig. 5.8, reduction of titania resulting to evolution of a new phase closer to the peak position of MgO can be observed (compare the MgO peak position from Fig. 5.6) upon increasing the temperature. Further characterization studies by XRD, HRTEM, and elemental chemical mapping techniques revealed the existence of homogeneously distributed Ti in a crystalline rock salt matrix ($Mg_xTi_yO_{x+y}$) which is similar to that observed for the Nb_2O_5 loaded MgH_2 system. Note that MgO and metals dissolved MgO (e.g., $Mg_xTi_yO_{x+y}$/ $Mg_xNb_yO_{x+y}$) exhibit almost identical crystallographic features; hence its existence is usually overlooked by many researchers. Sandhya et al. (2016) recently revealed that incorporation of Nb in the Mg site of

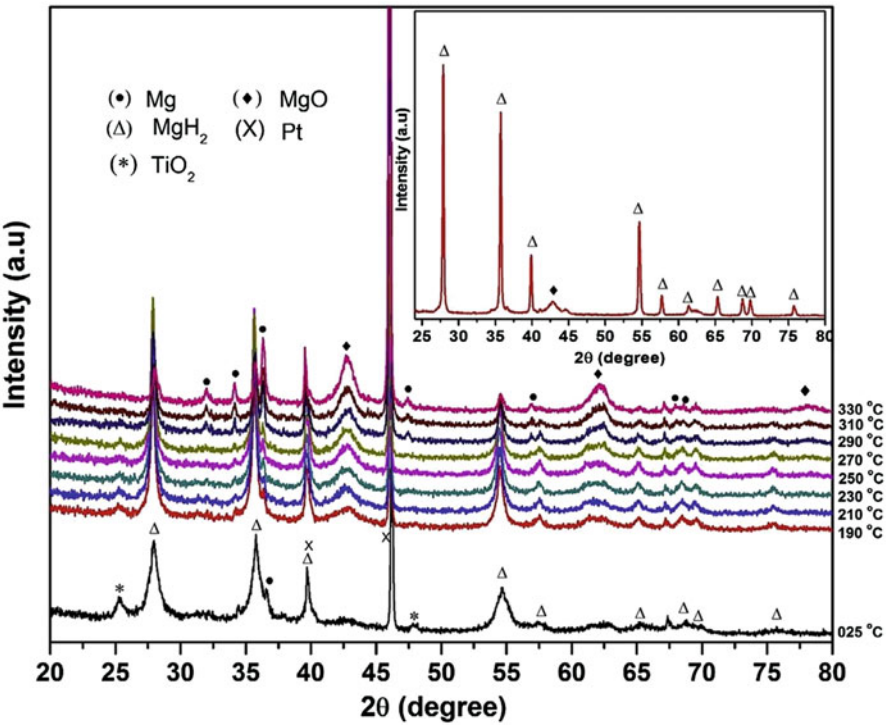

Fig. 5.8 In situ XRD patterns of 10 wt.% TiO_2 added MgH_2 (5 h milling). Inset shows the XRD of the re-hydrogenated sample. (Reproduced with permission from Pukazhselvan et al. 2017a, Copyright © 2017 Elsevier)

MgO rock salt structure results in an improved electronic behavior and hence is very active for catalytic interaction with MgH_2 and H_2.

From these understandings, a surface reaction model shown in Fig. 5.9 (Pukazhselvan et al. 2016c) seems to be a logically valid model for Nb_2O_5 loaded MgH_2. As shown in Fig. 5.9a, the commercial Mg/MgH_2 samples usually contain thin MgO rock salt layers in the surface. When the surface MgO rock salt layer is thick as shown in Fig. 5.9b, the system requires high operating conditions because of the high diffusion barrier caused by MgO. On the other hand, when Nb replaces few Mg spots (i.e., $Mg_xNb_yO_{x+y}$), the rock salt layer becomes catalytically active because of modifications in its electronic structure. Earlier in Fig. 5.6, it was shown that $Mg_xNb_yO_{x+y}$ forms from the reaction between MgH_2 and Nb_2O_5 additive. Hence the MgH_2 particles sealed by $Mg_xNb_yO_{x+y}$ shells as shown in Fig. 5.9c seems to be apparently a valid model for Nb_2O_5 loaded MgH_2. Note that the insertion of Nb, having a slightly higher ionic size than Mg, may also make fractures in the rock salt lattice. Moreover, since XPS study (Pukazhselvan et al. 2016b) proves the existence of a small amount of Nb-O secondary phase(s) other than $Mg_xNb_yO_{x+y}$, the presence of $NbO_x/Mg_xNb_yO_{x+y}/Nb$ interface cannot be

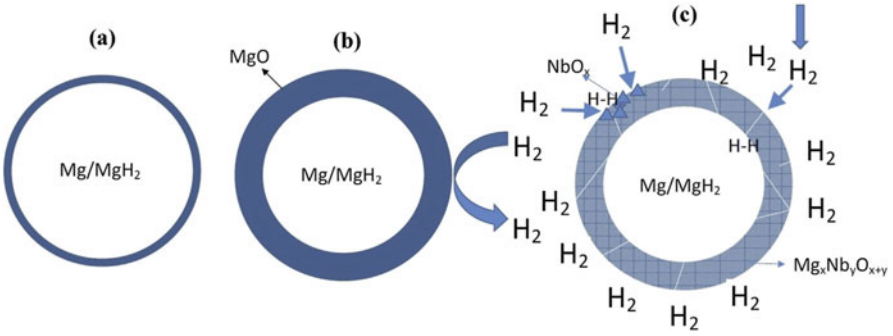

Fig. 5.9 Schematic representation for enhanced diffusion of hydrogen across the MgO shells, (**a**) thin MgO shell in commercial MgH_2 samples, (**b**) surface passivated Mg/MgH_2 particles due to thick MgO shells, and (**c**) active Nb dissolved MgO surface/interface layer. (Reproduced with permission from Pukazhselvan et al. 2016c. Copyright © 2016 Hydrogen Energy Publications. Elsevier)

ruled out. The $NbO_x/Mg_xNb_yO_{x\ +\ y}$/Nb interface, fractures, and the modified electronic structure of rock salt phase may all contribute the high H_2 diffusion/surface interaction in the system. A widely accepted similar mechanism was earlier proposed by Wallace et al. for $LaNi_5$ intermetallic hydride (Wallace et al. 1979).

5.4.3 *Reactive Hydride Composites, Amide/Imides, and Other High-Capacity Systems*

An oxide composition with a specific stoichiometry may be catalytically active for various metal hydride systems, but the mechanism of dehydrogenation through additive-host interaction is not necessarily the same for each system. For example, $LiTi_2O_4$ additive is found to be effective for improving the dehydrogenation of both MgH_2, $LiAlH_4$ and $LiNH_2$ + LiH systems, but the mechanism is believed to be substantially different for each system (Zhang et al. 2014b). It was reported by Zheng et al. that the crystal structure of $LiTi_2O_4$ additive play a key role in enhancing the H ab-/desorption kinetics of $LiNH_2$ + LiH hydrogen storage system. Since the diffusion rate of Li cations is high (108 cm^2/s) for $LiTi_2O_4$ spinal structure (Johnson 1964), its admixing with $LiNH_2$ + LiH is expected to assist the overall cationic mobility (Li^+) under lower temperatures. This "mobile" effect may apparently influence the hydrogen transport within the solid-state admixture. The authors did not comment whether the same holds true for $LiAlH_4$ and MgH_2. Particularly for MgH_2, since it is categorically a different hydride, further studies are necessary to ascertain whether the cationic mobility within the crystal structure of the additive provide bond breaking/making effects.

Chemical transformation of additive was suggested to be a main cause of catalysis in some cases. Recently, Puszkiel et al. (2017) employed lithiated titania (Li_xTiO_2) as additive for the promising reactive hydride composite (RHC), $2LiBH_4 + MgH_2$. In this case, the additive plays a key role in "reaction route modification" that results to equilibrium condition at shorter reaction time. Note that $LiBH_4$ is an irreversible complex hydride that releases hydrogen through the following reaction (ΔH=75 kJ/mol H_2):

$$LiBH_4 \rightarrow LiH + B + 1.5H_2 \tag{5.10}$$

In order to restore $LiBH_4$, the LiH + B mixture requires to be placed under a hydrogen atmosphere at 600 °C and 350 bar pressure. Hence, $LiBH_4$ is generally categorized as an irreversible hydride. However, when $LiBH_4$ is reacted with MgH_2 in 2:1 molar ratio, a reversible reaction occurs as shown in (5.11):

$$2LiBH_4 + MgH_2 \rightarrow 2LiH + MgB_2 + 4H_2 \tag{5.11}$$

This RHC reaction exhibits enthalpy 46 kJ/mol.H_2 with a theoretical hydrogen capacity of 11.4 wt%, which is 29 kJ/mol.H_2 lower in comparison with pure $LiBH_4$. However, under standard reaction conditions with a few bars of overpressure, instead of evolving to MgB_2, the decomposition of $LiBH_4$ and MgH_2 occurs separately with the imminent formation of unintended intermediate products. For example, at 400–450 °C with an overpressure of 3–5 bar pressure, initially, MgH_2 decomposes to Mg and H_2. $LiBH_4$ proceeds with an unintended slow kinetic intermediate reaction (5.12) before ending with reaction products as given in (5.11),

$$2LiBH_4 \rightarrow (1/6)Li_2B_{12}H_{12} + (5/3)LiH + (13/6)H_2 \tag{5.12}$$

A few researchers suggest that the $Li_2B_{12}H_{12}$ formation can be suppressed by making the reaction at pressure higher than 10 bar. On the other hand, lithiated TiO_2 (Li_xTiO_2) additive loaded RHC proceeds to reaction (5.11) at low back pressures (3 bar) without any signs of $Li_2B_{12}H_{12}$ intermediate in the reaction. An experimental evidence indicating the modification of reaction route when adding lithiated titania additive with $LiBH_4/MgB_2$ RHC is demonstrated by Fig. 5.10. The profiles (a) and (b), respectively, show the isothermal dehydrogenation kinetics recorded at 425 °C at 3 bar H_2 pressure (temperature program: heating with 10 °C/min to the target temperature). As seen, in the RHC sample that contains no additive, among the total capacity (11.4 wt.%, normalized in the figure), about 60–70% is liberated in the first step with fast kinetics, whereas the remaining hydrogen releases with very slow kinetics. On the other hand, in the lithiated titania loaded RHC sample, among the total hydrogen capacity (8 wt.%, normalized in the figure), although about a 20% is released during heating the sample (probably due to a premature release from MgH_2 but is usually expected), comparatively a much better kinetics can be achieved. When samples taken from two different stages of desorption (marked in the figure) were tested by Raman spectroscopy, the existence of $Li_2B_{12}H_{12}$ complex can be

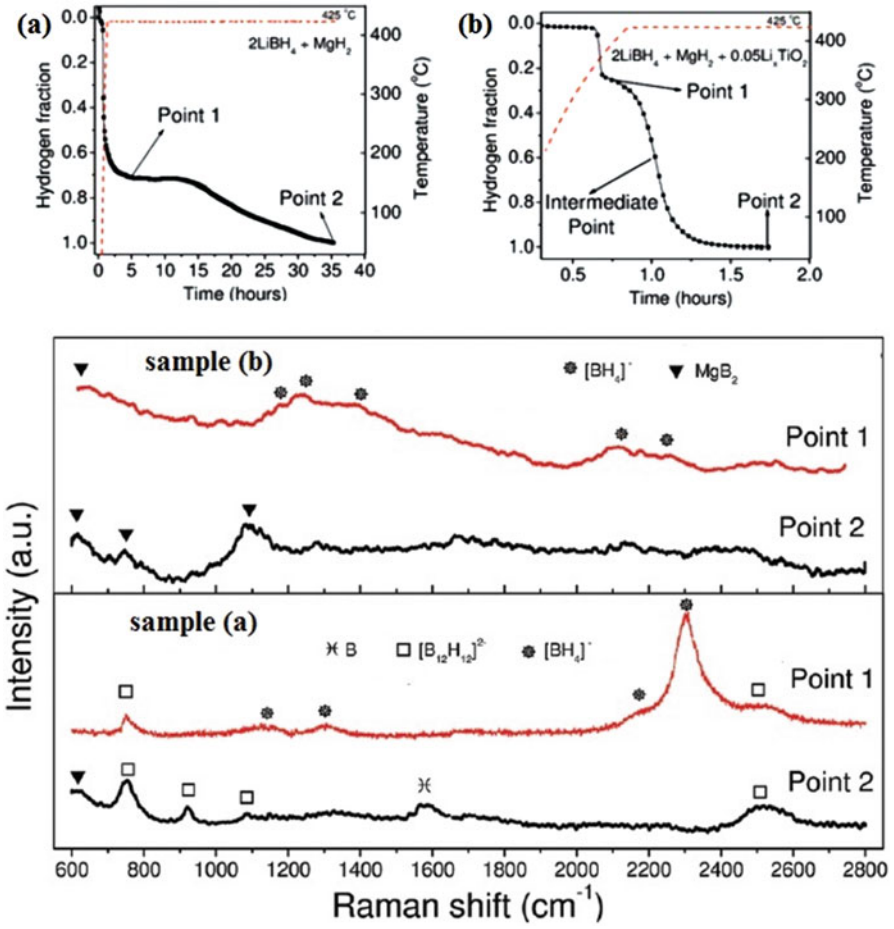

Fig. 5.10 (**a**) Isothermal dehydrogenation kinetics at 425 °C/3 bar H_2 pressure for $2LiBH_4$+MgH_2 sample, (**b**) kinetics at 425 °C/3 bar H_2 pressure for $2LiBH_4 + MgH_2 + 0.5Li_xTiO_2$ sample, (**c**) Raman spectra of both samples "a" and "b" taken from two reaction stages (marked as point 1/point 2 in both samples). (Adopted with permission from Puszkiel et al. 2017 Copyright © 2017, Royal Society of Chemistry)

proved only in the additive-free RHC sample (taken at state 2 of the sample). The Raman spectral data shown in Fig. 5.10 further reveals that transformation of boron atoms from $[BH_4]^-$ complex to make MgB_2 occurs only in the additive loaded sample under identical experimental conditions. Further studies reveal that when a 5 mol.% lithiated titania ($Li_{0.59}TiO_2$) admixed $2LiBH_4 + MgH_2$ is dehydrogenated, the additive initially reacts with $LiBH_4$ as shown in (5.13),

$$LiBH_4 + Li_{0.59}TiO_2 \rightarrow LiTiO_2 + 0.59LiH + B + 1.705H_2 \quad (5.13)$$

Subsequently, formation of MgB_2 seeds occurs from the partly decomposed Mg and B, and it defies the formation of $Li_2B_{12}H_{12}$ intermediate. The MgB_2 seeds provide coherent interfaces to promote the heterogeneous nucleation and the further growth of hexagonal MgB_2. Interestingly, apart from contributing the formation of MgB_2, the additive also contributes for the formation of LiH through reaction (5.14).

$$LiTiO_2 + 0.205H_2 \rightarrow Li_{0.59}TiO_2 + 0.41LiH. \quad (5.14)$$

When the MgB_2+LiH mixture is hydrogenated, formation of $LiTiO_2$ occurs again. The entire reaction system in the above experiments suggest that when $Li_{0.59}TiO_2$ additive was incorporated with the $2LiBH_4$+MgH_2 composite, the additive undergoes a chemical transformation and reversibly mediates the entire reaction by suppressing the undesired reaction products. Note that there were metals, chlorides, fluorides, and various other classes of materials tested for $2LiBH_4$+MgH_2 and it would be interesting to know how different the reaction mechanism of those systems are in contrast with the lithiated titania. Extensive theoretical investigations focused to extracting the transition states and the corresponding energetics will give interesting clues to understand the generalized mechanism of RHC reaction (5.11) improved by additives.

In another work, Fan et al. (2008) used Nb_2O_5 additive for catalyzing the RHC reaction (5.11) and observed that Nb_2O_5 transforms to NbH_2, initially during ball milling the $LiBH_4$/MgH_2 with Nb_2O_5 additive and subsequently by the dehydrogenation experiment. In this case a temperature reduction of at least 50 °C with significantly improved kinetics was reported, and there was no identification of intermediate phase(s) during the desorption measurements. Moreover, the product forms the RHC again, and the NbH_2 remains without further chemical modification. It obviously suggests that the way Nb_2O_5 catalyzes the RHC is different as compared to lithiated titania discussed above, but the role seems to be suppressing the intermediate phase(s). Reports in the literature suggest that $LiBH_4$ itself can be separately catalyzed by metal oxide additives for low-temperature hydrogen release. In this case the catalytic reaction is found to be redox-type chemical reaction, as depicted by $LiBH_4$+$MO_x \rightarrow LiMO_x$+B+$2H_2$ (Yu et al. 2009). Nonetheless, the reaction is not reversible, and addition of MgH_2 is necessary for driving reversibility.

Another distinct example regarding the superior role of metal oxides as additives is the catalytically enhanced hydrogen evolution reaction in ammonia borane (AB) system (Bluhm et al. 2006). Ammonia borane is known as an irreversible high-capacity hydrogen storage system (hydrogen capacity, 20 wt.%). In order to release hydrogen from AB, one has to either thermally decompose it (thermolysis) or react it with water (hydrolysis). In the process of thermolysis, hydrogen is liberated in three steps at temperatures 100 °C, 150 °C, and 500 °C. By hydrolysis on the other hand, desorption can be achieved at lower temperatures, but the reaction kinetics is poor (<1 wt.%/day) due to high activation barriers. Lapin and D'yankova (Lapin and

D'yankova 2013) showed that oxides of certain metals, especially Co_3O_4 substantially decrease the activation energy barrier from 100 kJ/mol.H_2 to 48 kJ/mol.H_2. The authors tested a number of metal oxide additives and noted that the catalytic activity of ZnO, CdO, TiO_2, MnO_2, Cr_2O_3, and WO_3 is negligible whereas Cu_2O, CuO, MoO_3, V_2O_5, Co_3O_4, and $Fe_2O_3.nH_2O$ yield moderate improvement. These observations suggest that an active oxide additive known for one metal hydride may be passive for another metal hydride.

Lithium amide/imide is another promising hydrogen storage system for which metal oxides were proven to be effective for improving the reaction kinetics (Zhang et al. 2014a). Chen et al. was the first to report that lithium nitride (Li_3N) absorbs 10.4 wt.% of hydrogen reversibly (Chen et al. 2002) through a two-step reaction as shown in (5.15) and (5.16).

$$Li_3N + H_2 \leftrightarrow Li_2NH + LiH \tag{5.15}$$

$$Li_2NH + H_2 \leftrightarrow LiNH_2 + LiH \tag{5.16}$$

The enthalpy of these two reactions, respectively, −165 kJ/mol.H_2 and −44.55 kJ/mol.H_2. Due to the low enthalpy, only the second reaction (capacity, 6.5 wt.%) is considered viable for hydrogen storage applications. However, one of the important issues is that usually $LiNH_2$ releases ammonia at 300 °C by following reaction (5.17).

$$2LiNH_2 \rightarrow Li_2NH + NH_3 \tag{5.17}$$

Lchikawa et al. (Ichikawa et al. 2004) showed that the release of NH_3 depends on how intimately LiH binds with $LiNH_2$. The poorly bound powder releases ammonia as per reaction (5.17), whereas the closely bound mixture releases hydrogen as per reaction (5.16). Therefore, one of the important roles of additive in this case is believed to be shielding the reactants so as to offer a better surface contact.

Later developments in lithium amide hydrogen storage system suggested that Li can be substituted by Mg and better performance and higher capacity can be achieved (Janot et al. 2007; Li et al. 2014). For further understanding regarding the hydrogen storage aspects of amide-imide systems, the reader is directed to references (David et al. 2007; Miwa et al. 2005). The work of Anton et al. (2011) on MgH_2 + $LiNH_2$ hydrogen storage system identified that by incorporation of defects through ball milling, the release of ammonia can be controlled and better reaction kinetics can be achieved. When the additives V_2O_5 and Fe_2O_3 were employed, the authors observed controlled release of ammonia and faster kinetics. From these observations, it was concluded that the role of oxide additives is to incorporate more defects in the system. Yuan et al. (2012) employed various metal oxide nanoparticle additives such as CeO_2, TiO_2, Fe_2O_3, Co_3O_4, and SiO_2 for improving the hydrogen storage performance of another mixed hydride system $LiBH_4/2LiNH_2/MgH_2$. Based upon the improved desorption performance, they

have categorized the catalytic activity with a series, $Fe_2O_3 > Co_3O_4 > CeO_2 > TiO_2 > SiO_2$.

Numerous examples are available in the literature regarding the superior effect of metal oxides as additives for many other hydrogen storage materials. For further information, the reader is directed to material specific journal articles regularly updated in the literature.

5.5 Summary and Outlook

The above discussions suggest that the best metal oxide additive known for one metal hydride is not necessarily a best for another hydride and also the additive-hydride interaction cannot be generalized. Likewise, for a particular metal hydride, many oxide additives may be proven active, but the interaction need not remain the same. However, since bond breaking/making is the end result of each catalytic reaction, catalytically enhanced common bonding/antibonding mechanism do exist, and it should be well understood for optimizing any system for commercial applications. In this connection, for understanding the catalytic mechanism, the details regarding how a hydride chemically interacts with various oxide additives should be well studied. In the literature, by performing comparative studies, researchers categorize the effectiveness of oxide additives from most effective to least effective. On many occasions, whereas extensive characterization studies are performed on the most effective oxide additive, the least effective oxides are ignored without further scrutiny. Nonetheless, it is also necessary to identify what makes an additive least effective for formulating a general catalytic mechanism for the system. Moreover, note that any comparison of additives made in the literature without taking into account the size effect may not be accurate. There are materials known to be less active in bulk scale that become very active when scaled down to nano-order. This suggests that any comparative studies reported in the literature with no reference to size effects may have erroneous conclusions. As we decrease the size of the particles, the number of atoms in direct chemical contact with the surrounding species increases significantly. Apart from this, in the case of metal oxides, the exposed atoms in the surface usually do not reflect the correct stoichiometry of the compound as the surface cation/anion ratio is significantly different as compared to the overall ionic ratio and bulk stoichiometry. The distinct valence states and vacancies existing at the surface of oxide nanoparticles substantially influence their chemical proximity as compared to the bulk structure. When two non-reducible oxide samples with the same size and chemical composition but exhibiting different crystal structure are used as additives for a hydride, the result may not remain the same, because the surface cation/anion ratio is different for different crystal structures. Considering all these aspects, in order to understand the mechanism of a catalytic reaction, it is necessary to correctly test the interaction of various metal oxides with a hydride and understand what common observation connects all these oxides. Such a study will be helpful for making a generalized

mechanism for understanding catalytically improved reactions. In this connection, the interesting literature data supports compiled in this chapter may guide readers for understanding the various possibilities of additive-hydride interaction.

5.6 Conclusions

The additives that catalyze a metal hydride by making in situ catalysts through a chemical reaction with the hydride are the most suitable for high enthalpy hydrides. Due to the formation of in situ catalyst, tuning the thermodynamics of the hydride is likely, at least a small extent. Maintaining the stability of the in situ catalysts is one challenge presently, but further research in this direction will bring revolutions for sustainable energy development.

References

Aguey-Zinsou KF, Ares Fernandez JR, Klassen T, Bormann R (2007) Effect of Nb2O5 on MgH2 properties during mechanical milling. Int J Hydrog Energy 32:2400–2407. https://doi.org/10.1016/j.ijhydene.2006.10.068

Anton DL, Price CJ, Gray J (2011) Affects of mechanical milling and metal oxide additives on sorption kinetics of 1:1 LiNH2/MgH2 mixture. Energies 4:826

Barkhordarian G, Klassen T, Bormann R (2003) Fast hydrogen sorption kinetics of nanocrystalline Mg using Nb2O5 as catalyst. Scr Mater 49:213–217. https://doi.org/10.1016/S1359-6462(03)00259-8

Bluhm ME, Bradley MG, Butterick R, Kusari U, Sneddon LG (2006) Amineborane-based chemical hydrogen storage: enhanced ammonia borane dehydrogenation in ionic liquids. J Am Chem Soc 128:7748–7749. https://doi.org/10.1021/ja062085v

Bogdanović B, Sandrock G (2011) Catalyzed complex metal hydrides. MRS Bull 27:712–716. https://doi.org/10.1557/mrs2002.227

Bogdanović B et al (2003) Investigation of hydrogen discharging and recharging processes of Ti-doped NaAlH4 by X-ray diffraction analysis (XRD) and solid-state NMR spectroscopy. J Alloys Compd 350:246–255. https://doi.org/10.1016/S0925-8388(02)00953-2

Bogdanović B, Eberle U, Felderhoff M, Schüth F (2007) Complex aluminum hydrides. Scr Mater 56:813–816. https://doi.org/10.1016/j.scriptamat.2007.01.004

Borgschulte A, Bielmann M, Züttel A, Barkhordarian G, Dornheim M, Bormann R (2008) Hydrogen dissociation on oxide covered MgH2 by catalytically active vacancies. Appl Surf Sci 254:2377–2384. https://doi.org/10.1016/j.apsusc.2007.09.069

Bruce PG, Scrosati B, Tarascon JM (2008) Nanomaterials for rechargeable lithium batteries. Angew Chem Int Ed 47:2930–2946. https://doi.org/10.1002/anie.200702505

Cao G (2004) Nanostructures & nanomaterials: synthesis, properties & applications. Imperial College Press, London

Chen X, Mao SS (2007) Titanium dioxide nanomaterials: synthesis, properties, modifications, and applications. Chem Rev 107:2891–2959. https://doi.org/10.1021/cr0500535

Chen P, Xiong Z, Luo J, Lin J, Tan KL (2002) Interaction of hydrogen with metal nitrides and imides. Nature 420:302. https://doi.org/10.1038/nature01210 https://www.nature.com/articles/nature01210#supplementary-information

Cho ES, Ruminski AM, Aloni S, Liu Y-S, Guo J, Urban JJ (2016) Graphene oxide/metal nanocrystal multilaminates as the atomic limit for safe and selective hydrogen storage. Nat Commun 7:10804. https://doi.org/10.1038/ncomms10804 https://www.nature.com/articles/ncomms10804#supplementary-information

Croston DL, Grant DM, Walker GS (2010) The catalytic effect of titanium oxide based additives on the dehydrogenation and hydrogenation of milled MgH2. J Alloys Compd 492:251–258. https://doi.org/10.1016/j.jallcom.2009.10.199

Daniel M-C, Astruc D (2004) Gold nanoparticles: assembly, supramolecular chemistry, quantum-size-related properties, and applications toward biology, catalysis, and nanotechnology. Chem Rev 104:293–346. https://doi.org/10.1021/cr030698+

David WIF, Jones MO, Gregory DH, Jewell CM, Johnson SR, Walton A, Edwards PP (2007) A mechanism for non-stoichiometry in the lithium amide/lithium imide hydrogen storage reaction. J Am Chem Soc 129:1594–1601. https://doi.org/10.1021/ja066016s

Eustis S, El-Sayed MA (2006) Why gold nanoparticles are more precious than pretty gold: noble metal surface plasmon resonance and its enhancement of the radiative and nonradiative properties of nanocrystals of different shapes. Chem Soc Rev 35:209–217. https://doi.org/10.1039/B514191E

Fan M-Q, Sun L-X, Zhang Y, Xu F, Zhang J, H-l C (2008) The catalytic effect of additive Nb2O5 on the reversible hydrogen storage performances of LiBH4–MgH2 composite. Int J Hydrog Energy 33:74–80. https://doi.org/10.1016/j.ijhydene.2007.09.012

Felderhoff M et al (2004) Combined TEM-EDX and XAFS studies of Ti-doped sodium alanate. Phys Chem Chem Phys 6:4369–4374. https://doi.org/10.1039/B403657N

Fichtner M, Fuhr O, Kircher O, Rothe J (2003) Small Ti clusters for catalysis of hydrogen exchange in NaAlH4. Nanotechnology 14:778

Friedrichs O, Klassen T, Sánchez-López JC, Bormann R, Fernández A (2006a) Hydrogen sorption improvement of nanocrystalline MgH2 by Nb2O5 nanoparticles. Scr Mater 54:1293–1297. https://doi.org/10.1016/j.scriptamat.2005.12.011

Friedrichs O, Sánchez-López JC, López-Cartes C, Dornheim M, Klassen T, Bormann R, Fernández A (2006b) Chemical and microstructural study of the oxygen passivation behaviour of nanocrystalline Mg and MgH2. Appl Surf Sci 252:2334–2345. https://doi.org/10.1016/j.apsusc.2005.04.018

Friedrichs O et al (2006c) MgH2 with Nb2O5 as additive, for hydrogen storage: chemical, structural and kinetic behavior with heating. Acta Mater 54:105–110. https://doi.org/10.1016/j.actamat.2005.08.024

Friedrichs O, Martínez-Martínez D, Guilera G, Sánchez López JC, Fernández A (2007) In situ energy-dispersive XAS and XRD study of the superior hydrogen storage system MgH2/Nb2O5. J Phys Chem C 111:10700–10706. https://doi.org/10.1021/jp0675835

Gawande MB, Pandey RK, Jayaram RV (2012) Role of mixed metal oxides in catalysis science-versatile applications in organic synthesis. Cat Sci Technol 2:1113–1125. https://doi.org/10.1039/C2CY00490A

Hanada N, Ichikawa T, Fujii H (2005) Catalytic effect of Ni nano-particle and Nb oxide on H-desorption properties in MgH2 prepared by ball milling. J Alloys Compd 404–406:716–719. https://doi.org/10.1016/j.jallcom.2004.12.166

Hanada N et al (2009) X-ray absorption spectroscopic study on valence state and local atomic structure of transition metal oxides doped in MgH2. J Phys Chem C 113:13450–13455. https://doi.org/10.1021/jp901859f

Handelman A, Beker P, Amdursky N, Rosenman G (2012) Physics and engineering of peptide supramolecular nanostructures. Phys Chem Chem Phys 14:6391–6408. https://doi.org/10.1039/c2cp40157f

Haruta M (2002) Catalysis of gold nanoparticles deposited on metal oxides. Cattech 6:102–115

Henrich VE, Cox PA (1996) The surface science of metal oxides. Cambridge university press, Cambridge

Huang ZG, Guo ZP, Calka A, Wexler D, Lukey C, Liu HK (2006) Effects of iron oxide (Fe2O3, Fe3O4) on hydrogen storage properties of Mg-based composites. J Alloys Compd 422:299–304. https://doi.org/10.1016/j.jallcom.2005.11.074

Ichikawa T, Isobe S, Hanada N, Fujii H (2004) Lithium nitride for reversible hydrogen storage. J Alloys Compd 365:271–276. https://doi.org/10.1016/S0925-8388(03)00637-6

Janot R, Eymery J-B, Tarascon J-M (2007) Investigation of the processes for reversible hydrogen storage in the Li–Mg–N–H system. J Power Sources 164:496–502. https://doi.org/10.1016/j.jpowsour.2006.11.046

Jeon K-J, Moon HR, Ruminski AM, Jiang B, Kisielowski C, Bardhan R, Urban JJ (2011) Air-stable magnesium nanocomposites provide rapid and high-capacity hydrogen storage without using heavy-metal catalysts. Nat Mater 10:286. https://doi.org/10.1038/nmat2978 https://www.nature.com/articles/nmat2978#supplementary-information

Johnson OW (1964) One-dimensional diffusion of Li in rutile. Phys Rev 136:A284–A290

Jung KS, Lee EY, Lee KS (2006) Catalytic effects of metal oxide on hydrogen absorption of magnesium metal hydride. J Alloys Compd 421:179–184. https://doi.org/10.1016/j.jallcom.2005.09.085

Kalidindi SB, Jagirdar BR (2009) Highly monodisperse colloidal magnesium nanoparticles by room temperature digestive ripening. Inorg Chem 48:4524–4529. https://doi.org/10.1021/ic9003577

Kelly KL, Coronado E, Zhao LL, Schatz GC (2003) The optical properties of metal nanoparticles: the influence of size, shape, and dielectric environment. J Phys Chem B 107:668–677. https://doi.org/10.1021/jp026731y

Kim HW et al (2013) Selective gas transport through few-layered graphene and graphene oxide membranes. Science 342:91

Kobayashi H, Salahub DR, Ito T (1994) Dissociative adsorption of hydrogen molecule on MgO surfaces studied by the density functional method. J Phys Chem 98:5487–5492. https://doi.org/10.1021/j100072a015

Kung HH (1989) Transition metal oxides: surface chemistry and catalysis, vol 45. Elsevier, Amsterdam

Lapin NV, D'yankova NY (2013) Hydrogen evolution kinetics during transition metal oxide-catalyzed ammonia borane hydrolysis. Inorg Mater 49:975–979. https://doi.org/10.1134/s0020168513100063

Lee G-J, Kim JW, Shim J-H, Cho YW, Lee KS (2007a) Synthesis of ultrafine titanium aluminide powders and their catalytic enhancement in dehydrogenation kinetics of NaAlH4. Scr Mater 56:125–128. https://doi.org/10.1016/j.scriptamat.2006.09.027

Lee G-J, Shim J-H, Whan Cho Y, Sub Lee K (2007b) Reversible hydrogen storage in NaAlH4 catalyzed with lanthanide oxides. Int J Hydrog Energy 32:1911–1915. https://doi.org/10.1016/j.ijhydene.2006.10.023

Lee G-J, Shim J-H, Cho YW, Lee KS (2008) Improvement in desorption kinetics of NaAlH4 catalyzed with TiO2 nanopowder. Int J Hydrog Energy 33:3748–3753. https://doi.org/10.1016/j.ijhydene.2008.04.035

Léon A, Kircher O, Rothe J, Fichtner M (2004) Chemical state and local structure around titanium atoms in NaAlH4 doped with TiCl3 using x-ray absorption spectroscopy. J Phys Chem B 108:16372–16376. https://doi.org/10.1021/jp048615w

Li P, Li Z, Zhai F, Wan Q, Li X, Qu X, Volinsky AA (2013) NiFe2O4 nanoparticles catalytic effects of improving LiAlH4 dehydrogenation properties. J Phys Chem C 117:25917–25925. https://doi.org/10.1021/jp408364p

Li C, Liu Y, Ma R, Zhang X, Li Y, Gao M, Pan H (2014) Superior dehydrogenation/hydrogenation kinetics and long-term cycling performance of K and Rb Cocatalyzed Mg(NH2)2-2LiH system. ACS Appl Mater Interfaces 6:17024–17033. https://doi.org/10.1021/am504592x

Ma J, Li J, Tang RY, Li WZ, Chen QY (2012) Effects of porous Al_2O_3/SiO_2 on hydrogen storage capacities of NaAlH_4-Tm_2O_3 system [J]. Chin J Nonferrous Met 6:017

Ma T, Isobe S, Wang Y, Hashimoto N, Ohnuki S (2013) Nb-gateway for hydrogen desorption in Nb2O5 catalyzed MgH2 nanocomposite. J Phys Chem C 117:10302–10307. https://doi.org/10.1021/jp4021883

Majzoub EH, Gross KJ (2003) Titanium–halide catalyst-precursors in sodium aluminum hydrides. J Alloys Compd 356–357:363–367. https://doi.org/10.1016/S0925-8388(03)00113-0

Miwa K, Ohba N, Towata S-i, Nakamori Y, Orimo S-i (2005) First-principles study on lithium amide for hydrogen storage. Phys Rev B 71:195109

Morioka H, Kakizaki K, Chung S-C, Yamada A (2003) Reversible hydrogen decomposition of KAlH4. J Alloys Compd 353:310–314. https://doi.org/10.1016/S0925-8388(02)01307-5

Nielsen TK, Jensen TR (2012) MgH2–Nb2O5 investigated by in situ synchrotron X-ray diffraction. Int J Hydrog Energy 37:13409–13416. https://doi.org/10.1016/j.ijhydene.2012.06.082

Norris DJ, Bawendi M (1996) Measurement and assignment of the size-dependent optical spectrum in CdSe quantum dots. Phys Rev B 53:16338

Oelerich W, Klassen T, Bormann R (2001a) Comparison of the catalytic effects of V, V2O5, VN, and VC on the hydrogen sorption of nanocrystalline Mg. J Alloys Compd 322:L5–L9. https://doi.org/10.1016/S0925-8388(01)01173-2

Oelerich W, Klassen T, Bormann R (2001b) Metal oxides as catalysts for improved hydrogen sorption in nanocrystalline Mg-based materials. J Alloys Compd 315:237–242. https://doi.org/10.1016/S0925-8388(00)01284-6

Orimo S-i, Nakamori Y, Eliseo JR, Züttel A, Jensen CM (2007) Complex hydrides for hydrogen storage. Chem Rev 107:4111–4132. https://doi.org/10.1021/cr0501846

Patah A, Takasaki A, Szmyd JS (2009) Influence of multiple oxide (Cr2O3/Nb2O5) addition on the sorption kinetics of MgH2. Int J Hydrog Energy 34:3032–3037. https://doi.org/10.1016/j.ijhydene.2009.01.086

Polanski M, Bystrzycki J (2009) Comparative studies of the influence of different nano-sized metal oxides on the hydrogen sorption properties of magnesium hydride. J Alloys Compd 486:697–701. https://doi.org/10.1016/j.jallcom.2009.07.042

Polanski M, Bystrzycki J, Varin RA, Plocinski T, Pisarek M (2011) The effect of chromium (III) oxide (Cr2O3) nanopowder on the microstructure and cyclic hydrogen storage behavior of magnesium hydride (MgH2). J Alloys Compd 509:2386–2391. https://doi.org/10.1016/j.jallcom.2010.11.026

Porcu M, Petford-Long AK, Sykes JM (2008) TEM studies of Nb2O5 catalyst in ball-milled MgH2 for hydrogen storage. J Alloys Compd 453:341–346. https://doi.org/10.1016/j.jallcom.2006.11.147

Pukazhselvan D (2012) Effect of crystallite size of Al on the reversible hydrogen storage of NaAlH4 and few aspects of catalysts and catalysis. Int J Hydrog Energy 37:9696–9705. https://doi.org/10.1016/j.ijhydene.2012.03.098

Pukazhselvan D, Hudson MSL, Sinha ASK, Srivastava ON (2010) Studies on metal oxide nanoparticles catalyzed sodium aluminum hydride. Energy 35:5037–5042. https://doi.org/10.1016/j.energy.2010.08.015

Pukazhselvan D, Kumar V, Singh SK (2012) High capacity hydrogen storage: basic aspects, new developments and milestones. Nano Energy 1:566–589. https://doi.org/10.1016/j.nanoen.2012.05.004

Pukazhselvan D, Antunes I, Lo Russo S, Perez J, Fagg DP (2014a) Synthesis of catalytically active rock salt structured MgxNb1−xO nanoparticles for MgH2 system. Int J Hydrog Energy 39:18984–18988. https://doi.org/10.1016/j.ijhydene.2014.08.138

Pukazhselvan D, Capurso G, Maddalena A, Lo Russo S, Fagg DP (2014b) Hydrogen storage characteristics of magnesium impregnated on the porous channels of activated charcoal scaffold. Int J Hydrog Energy 39:20045–20053. https://doi.org/10.1016/j.ijhydene.2014.10.038

Pukazhselvan D, Fagg DP, Srivastava ON (2015) One step high pressure mechanochemical synthesis of reversible alanates NaAlH4 and KAlH4. Int J Hydrog Energy 40:4916–4924. https://doi.org/10.1016/j.ijhydene.2015.01.186

Pukazhselvan D, Bdikin I, Perez J, Carbó-Argibay E, Antunes I, Stroppa DG, Fagg DP (2016a) Formation of Mg–Nb–O rock salt structures in a series of mechanochemically activated MgH2 + nNb2O5 (n = 0.083–1.50) mixtures. Int J Hydrog Energy 41:2677–2688. https://doi.org/10.1016/j.ijhydene.2015.12.077

Pukazhselvan D, Nasani N, Pérez J, Hortigüela MJ, Yang T, Bdikin I, Fagg DP (2016b) Two step mechanochemical synthesis of Nb doped MgO rock salt nanoparticles and its application for hydrogen storage in MgH2. Int J Hydrog Energy 41:11716–11722. https://doi.org/10.1016/j.ijhydene.2015.11.175

Pukazhselvan D, Otero-Irurueta G, Pérez J, Singh B, Bdikin I, Singh MK, Fagg DP (2016c) Crystal structure, phase stoichiometry and chemical environment of MgxNbyOx+y nanoparticles and their impact on hydrogen storage in MgH2. Int J Hydrog Energy 41:11709–11715. https://doi.org/10.1016/j.ijhydene.2016.04.029

Pukazhselvan D, Perez J, Nasani N, Bdikin I, Kovalevsky AV, Fagg DP (2016d) Formation of MgxNbyOx+y through the mechanochemical reaction of MgH2 and Nb2O5, and its effect on the hydrogen-storage behavior of MgH2. Chem Phys Chem 17:178–183. https://doi.org/10.1002/cphc.201500620

Pukazhselvan D, Nasani N, Correia P, Carbó-Argibay E, Otero-Irurueta G, Stroppa DG, Fagg DP (2017a) Evolution of reduced Ti containing phase(s) in MgH2/TiO2 system and its effect on the hydrogen storage behavior of MgH2. J Power Sources 362:174–183. https://doi.org/10.1016/j.jpowsour.2017.07.032

Pukazhselvan D, Nasani N, Sandhya KS, Singh B, Bdikin I, Koga N, Fagg DP (2017b) Role of chemical interaction between MgH2 and TiO2 additive on the hydrogen storage behavior of MgH2. Appl Surf Sci 420:740–745. https://doi.org/10.1016/j.apsusc.2017.05.182

Puszkiel JA et al (2017) Changing the dehydrogenation pathway of LiBH4-MgH2via nanosized lithiated TiO2. Phys Chem Chem Phys 19:7455–7460. https://doi.org/10.1039/C6CP08278E

Rafi ud d, Xuanhui Q, Ping L, Zhang L, Ahmad M (2011) Hydrogen sorption improvement of LiAlH4 catalyzed by Nb2O5 and Cr2O3 nanoparticles. J Phys Chem C 115:13088–13099. https://doi.org/10.1021/jp202969y

Rafi ud d et al (2012) Superior catalytic effects of Nb2O5, TiO2, and Cr2O3 nanoparticles in improving the hydrogen sorption properties of NaAlH4. J Phys Chem C 116:11924–11938. https://doi.org/10.1021/jp302474c

Rahman MW, Livraghi S, Dolci F, Baricco M, Giamello E (2011) Hydrogen sorption properties of Ternary Mg–Nb–O phases synthesized by solid–state reaction. Int J Hydrog Energy 36:7932–7936. https://doi.org/10.1016/j.ijhydene.2011.01.053

Sadhasivam T, Sterlin Leo Hudson M, Pandey SK, Bhatnagar A, Singh MK, Gurunathan K, Srivastava ON (2013) Effects of nano size mischmetal and its oxide on improving the hydrogen sorption behaviour of MgH2. Int J Hydrog Energy 38:7353–7362. https://doi.org/10.1016/j.ijhydene.2013.04.040

Sandhya KS, Pukazhselvan D, Fagg DP, Koga N (2016) Interaction of magnesium hydride clusters with Nb doped MgO additive studied by density functional calculations. RSC Adv 6:61200–61206. https://doi.org/10.1039/C6RA11281A

Sapra S, Sarma DD (2004) Evolution of the electronic structure with size in II-VI semiconductor nanocrystals. Phys Rev B 69:125304

Schlapbach L (1981) XPS/UPS study of the oxidation of La and LaNi5 and of the electronic structure of LaNi5. Solid State Commun 38:117–123. https://doi.org/10.1016/0038-1098(81)90802-4

Schoenitz M, Zhu X, Dreizin EL (2004) Mechanical alloys in the Al-rich part of the Al-Ti binary system. J Metastable Nanocryst Mater 20–21, 455–461. Trans Tech Publ

Schwarz JA, Contescu CI, Putyera K (2004) Dekker encyclopedia of nanoscience and nanotechnology, vol 3. CRC press, Boca Raton

Wallace WE, Karlicek RF, Imamura H (1979) Mechanism of hydrogen absorption by lanthanum-nickel (LaNi5). J Phys Chem 83:1708–1712. https://doi.org/10.1021/j100476a006

Wan LF et al (2017) Atomically thin interfacial suboxide key to hydrogen storage performance enhancements of magnesium nanoparticles encapsulated in reduced graphene oxide. Nano Lett 17:5540–5545. https://doi.org/10.1021/acs.nanolett.7b02280

Weaver JH, Franciosi A, Wallace WE, Smith HK (1980) Electronic structure and surface oxidation of LaNi5, Er6Mn23, and related systems. J Appl Phys 51:5847–5851. https://doi.org/10.1063/1.327544

Wu G, Zhang J, Wu Y, Li Q, Chou K, Bao X (2009) Adsorption and dissociation of hydrogen on MgO surface: a first-principles study. J Alloys Compd 480:788–793. https://doi.org/10.1016/j.jallcom.2009.02.086

Yu PY, Cardona M (1996) Fundamentals of semiconductors: physics and materials properties. Springer, Heidelberg

Yu XB, Grant DM, Walker GS (2009) Dehydrogenation of LiBH4 destabilized with various oxides. J Phys Chem C 113:17945–17949. https://doi.org/10.1021/jp906519p

Yuan H et al (2012) Influence of metal oxide on LiBH4/2LiNH2/MgH2 system for hydrogen storage properties. Int J Hydrog Energy 37:3292–3297. https://doi.org/10.1016/j.ijhydene.2011.11.065

Yuan C, Wu HB, Xie Y, Lou XW (2014) Mixed transition-metal oxides: design, synthesis, and energy-related applications. Angew Chem Int Ed 53:1488–1504. https://doi.org/10.1002/anie.201303971

Zaluska A, Zaluski L, Ström-Olsen J (2001) Structure, catalysis and atomic reactions on the nano-scale: a systematic approach to metal hydrides for hydrogen storage. Appl Phys A 72:157–165

Zaluski L, Zaluska A, Ström-Olsen JO (1997) Nanocrystalline metal hydrides. J Alloys Compd 253–254:70–79. https://doi.org/10.1016/S0925-8388(96)02985-4

Zhang M, Li J, Li H, Li Y, Shen W (2009) Morphology-dependent redox and catalytic properties of CeO2 nanostructures: nanowires, nanorods and nanoparticles. Catal Today 148:179–183

Zhang T, Isobe S, Wang Y, Hashimoto N, Ohnuki S (2014a) A homogeneous metal oxide catalyst enhanced solid–solid reaction in the hydrogen desorption of a lithium–hydrogen–nitrogen system. ChemCatChem 6:724–727. https://doi.org/10.1002/cctc.201301068

Zhang T, Isobe S, Wang Y, Oka H, Hashimoto N, Ohnuki S (2014b) A metal-oxide catalyst enhanced the desorption properties in complex metal hydrides. J Mater Chem A 2:4361–4365. https://doi.org/10.1039/C3TA15294D

Zhao-Karger Z, Hu J, Roth A, Wang D, Kubel C, Lohstroh W, Fichtner M (2010) Altered thermodynamic and kinetic properties of MgH2 infiltrated in microporous scaffold. Chem Commun 46:8353–8355. https://doi.org/10.1039/C0CC03072D

Zlotea C, Oumellal Y, Hwang S-J, Ghimbeu CM, de Jongh PE, Latroche M (2015) Ultrasmall MgH2 nanoparticles embedded in an ordered microporous carbon exhibiting rapid hydrogen sorption kinetics. J Phys Chem C 119:18091–18098. https://doi.org/10.1021/acs.jpcc.5b05754

Chapter 6
Nanostructured Metal Oxides for Supercapacitor Applications

Katlego Makgopa, Abdulhakeem Bello, Kumar Raju, Kwena D. Modibane, and Mpitloane J. Hato

Contents

Abstract The fundamental properties of supercapacitors (SCs) with descriptions restricted to the metal oxides systems and the effect on the electrochemical performance and synthesis are described in this chapter. Metal oxides such as manganese oxide (MnO), vanadium oxide (V_2O_5) and ruthenium oxide (RuO) have

K. Makgopa (✉)
Department of Chemistry, Faculty of Science, Tshwane University of Technology (Acardia Campus), Pretoria, South Africa
e-mail: makgopak@tut.ac.za

A. Bello
Department of Materials Science and Engineering, African University of Science and Technology (AUST), Abuja, Nigeria

K. Raju
Energy Materials, CSIR Materials Science and Manufacturing, Pretoria, South Africa

K. D. Modibane · M. J. Hato
Department of Chemistry, School of Physical and Mineral Sciences, University of Limpopo (Turfloop), Polokwane, South Africa

R. Saravanan et al. (eds.), *Emerging Nanostructured Materials for Energy and Environmental Science*, Environmental Chemistry for a Sustainable World 23,
https://doi.org/10.1007/978-3-030-04474-9_6

demonstrated great potential in the field of energy storage due to their structural as well as electrochemical properties, thus attracting huge attention in the past decade and in recent years. The major contributing factor to the electrochemical properties is their capability to achieve relatively high pseudocapacitive performance derived from their theoretical values resulting from their multiple valence state changes. The developments of the metal oxide (MO)-based electrode materials and their composites are being explored from the synthetic point of view as well as their emerging applications as energy storage materials. Therefore, the need to further exploration of MO-based electrodes is motivated by their considerably low-cost and environmentally friendly nature as compared to other supercapacitive electrode materials. This chapter accounts to the overview of various nanostructured metal oxide materials for application as energy storage materials in supercapacitors.

6.1 Introduction

Today's society and particularly the developing countries rely heavily on fossil fuels as the primary source of energy since they are cheap and also exhibits high specific energy and power per weight (or per volume) output. The growing world population and increasing standard of life-style exerted much pressure on the deliverance of energy, and as a result, these have led to a rapidly increasing energy demand over a period of time (Poizot and Dolhem 2011). In addition, the fast-growing interest in portable electronic devices and electric vehicles has stimulated extensive research in high-performance energy storage devices. The above reasons are justified by the projections stated in the *International Energy Outlook 2017* (IEO 2017 https://www.eia.gov/outlooks/ieo/) reference case, which shows that the total world energy consumption continues to rise from 575 quadrillion British thermal units (Btu) in 2015 to 736 quadrillion Btu in 2040, indicating an increase of 28% (IEA 2014). The incineration of fossil fuels results in severe environmental pollution and contributes to greenhouse effect, which is harmful to the environment while also placing many countries at disadvantage as the rate of coal depletion exceeds that of its production. The development of technology that is compatible with the resources provided by nature is essential in order to reduce the uprising malice to the environment by fossil fuel energy sources worldwide and also to meet the high energy demands resulting from the growth in civilization. Renewable energy has shown to be the escalating solution towards mitigating this energy crisis, and currently, they are the world's fastest-growing energy source, with consumption increasing by an average 2.3%/year between 2015 and 2040 (Bang et al. 2000; UNEP 2013). As much as renewable energy resources (i.e. photovoltaics, wind turbines, geothermal heat, etc.) have displayed great potential to be employed as the alternative energy sources to fossil fuels globally, their success is still limited by their inability to store the harvested energy and a lack of a quick transmission of the same energy (Hatzell et al. 2015).

Thus, the market for energy storage applications becomes an integrated critical component in clean energy development and sustainability. Electrochemical energy storage systems (EES) have emerged as an established, valuable approach for improving the reliability and overall use of the advantages of renewable energy resources (Béguin et al. 2014). An energy storage device is an apparatus used to store electrical energy when needed and releases the stored energy when required. The role of the technology involving energy storage device in the fields such as renewable energy generation and electric/hybrid electric automobile systems has become increasingly important in modern society as a measure of checking the ever-increasing global warming and other matters related to the energy crisis. Therefore, in consideration of reliable, stable and sustainable large-scale use of renewables, electrochemical capacitors (ECs) and batteries play a fundamental role in advanced and highly efficient energy storage and management. Lithium–ion batteries (LIBs) can store large amount of energy as high as 150–200 Wh kg^{-1} but are confined to their low-power density (below 1000 W kg^{-1}) and poor cycle life (usually less than 1000 cycles) (Thackeray et al. 2012; Béguin et al. 2014). In comparison with batteries, electrochemical capacitors (ECs) vastly known as supercapacitors have demonstrated to be the competing measures with regards to storing energy output that can be delivered at the faster rate without the loss of the device efficiency (Burke et al. 2014). This electrochemical energy storage device has great potential in energy applications that require peak power pulses. The ability of the ECs to serve as a gap between conventional capacitors (that display great power output but limited energy storage output) and batteries (with great energy storage output but limited power deliverance) places this electrochemical energy storage device at the much added advantage. The advantages of ECs arise from their energy storage mechanism, which involves physical storage of energy through dielectric polarization or electronic double layer of ions and electrons (surface phenomenon). There are two types of fundamental storage mechanisms involved in ECs, viz. (a) 'electrochemical double layer capacitor' (EDLC) that uses nanocarbons as the main electrode materials for supercapacitors, and there are many abundant sources of nanocarbons with facile processes for the fabrication of cheap electrodes (Ghosh and Lee 2012) and (b) 'pseudocapacitor'. The operation mechanism of the EDLC involves the non-faradaic separation of charges at the 'double layer (i.e. electrode/electrolyte interface), while pseudocapacitor involves fast faradaic, redox reaction of electroactive materials at the interface (Béguin et al. 2014). A Ragone chart in Fig. 6.1 shows the power and energy densities of various energy storage and conversion devices.

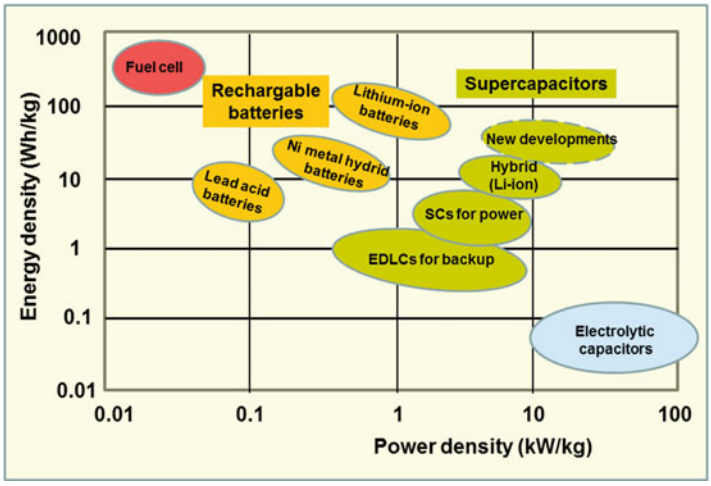

Fig. 6.1 Ragone chart showing energy density as a function of power density of various capacitors and batteries

6.1.1 Electrochemical Capacitors as an Energy Storage Solution

The concept of the electrochemical double-layer capacitance dates back to a German physicist, Hermann von Helmholtz, in 1853 (Conway 1999). In 1957, General Electric Company filed the earliest ECs patented based on the double-layer capacitance structure. However, not until the 1990s did EC technology begin to draw some attention in the field of hybrid electric vehicles (Burke 2000). It was found that the main function of ECs could promote the electrochemical performance of a battery or fuel cell in a hybrid electric vehicle by providing necessary power for acceleration and recuperating brake energy (Toupin et al. 2004). Thus, the capacitor technology is regarded as a promising means for storing electricity (Jiang et al. 2013). The early electrochemical capacitors (ECs) were rated at a few volts and had capacitance values measured from fractions of farads up to several farads. Today's trend is for cells with the size ranging from small millifarad-sized devices with exceptional pulse power performance up to devices rated at several kilo farads. The technology is experiencing increasingly broader use especially originating from the 'humble' beginning, both replacing batteries in some cases and in others complementing their performance (Miller and Burke 2008). Due to the intrinsic properties occurring at the electrode/electrolyte interface of an EC device, understanding of the materials used for fabricating the device is of great importance especially for the enhancement of the electrochemical performance of the EC device (Conway 1999; Béguin et al. 2009). Figure 6.2 shows the composition and working principle of an ideal parallel plate capacitor. In a charged capacitor, the metal plates are oppositely charged, and an electric field is formed in the dielectric medium (Thomas and Floyd 2009).

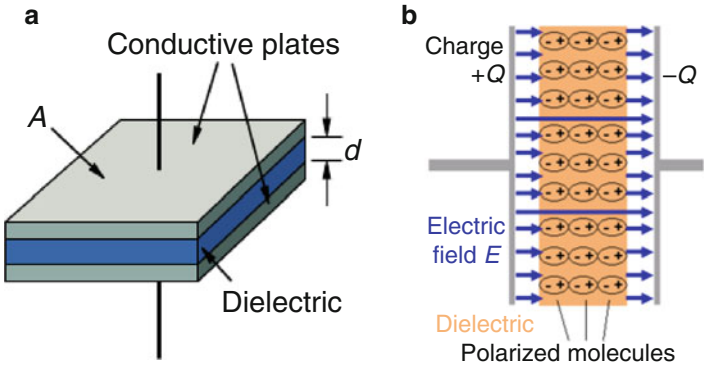

Fig. 6.2 Schematic diagrams of (**a**) the design of a parallel plate capacitor (with permission of Yuan et al. 2012) and (**b**) a charged parallel plate capacitor (With permission of Vol'fkovich et al. 2002)

Generally, to improve on the electrochemical performance of ECs, electroactive materials that provide supercapacitive effect contributing to the total double-layer capacitance are considered. Pseudocapacitance originates from electrochemical reduction-oxidation (Redox) reaction due to faradic transfer that occurs in the active electrode materials. This phenomenon is similar to the chemical reaction that occurs in many rechargeable batteries; therefore, the reaction must be reversible or quasi-reversible for optimum/efficient electrochemical performance. Taking into account a uniform distribution of the redox-based material on the electrodes, the redox process is governed by the reaction below (Yu et al. 2013a):

$$O_X + n_e^- X \leftrightarrow R_D \tag{6.1}$$

where n is the number of electrons transferred and O_X and R_D represent the oxidized and reduced species, respectively.

The electrochemical potential arising from Eq. 6.1 has been described by the Nernst equation:

$$E = E^0_{O_X/R_d} + \frac{\mathrm{RT}}{\mathrm{nF}} \ln\left(\frac{C_{O_X}}{C_{R_d}}\right) \tag{6.2}$$

The faradaic reaction in Eq. 6.1 corresponds to a reversible pseudocapacitance (per/vol) given by Eq. 6.3 for an ideal system.

$$C_{pc}(E) = \frac{idt}{dE} = \frac{i}{v} = \frac{n^2\mathrm{F}^2}{RT} dC^0_{O_x} \frac{\exp\left(\frac{n\mathrm{F}}{\mathrm{RT}}\left(E^0_{O_X/R_d} - E\right)\right)}{\left[1 + \exp\left(\frac{n\mathrm{F}}{\mathrm{RT}}\left(E^0_{O_X/R_d} - E\right)\right)\right]^2} \tag{6.3}$$

However, taking into account the irregularities in the matrix structure of the electrodes leads to uneven distribution of the redox centres and therefore leads to a quasi-reversible reaction and can be resolved by introducing a lateral interaction energy ($-g\frac{C_{O_X}}{C^0_{O_X}}$) term, and Eq. 6.3 can then be modified to Eq. 6.4 as shown below (Yu et al. 2013a).

$$C_{\mathrm{pc}}(E) = \frac{n^2F^2}{\mathrm{RT}}\mathrm{dC}^0_{O_x}\frac{\exp\left(\frac{nF}{RT}\left(E^0_{O_X/R_d}-E\right)+g\frac{C_{O_X}}{C^0_{O_X}}\right)}{\left[1+\exp\left(\frac{nF}{RT}\left(E^0_{O_X/R_d}-E\right)+g\frac{C_{O_X}}{C^0_{O_X}}\right)\right]^2+g\exp\left(\frac{\mathrm{nF}}{RT}\left(E^0_{O_X/R_d}-E\right)+g\frac{C_{O_X}}{C^0_{O_X}}\right)} \tag{6.4}$$

Equation 6.4 holds for a completely reversible redox reaction system when $g = 0$ and quasi-reversible reaction when $g > 0$. The capacitance defined by Eq. 6.4, which is a function of electrode potential, is known as the momentary capacitance. The intrinsic pseudocapacitance (C_{sp}, measured in F/g) of the redox reaction is expressed by Eq. 6.5:

$$C_{pc} = \frac{\mathrm{AM_{mw}}}{m}\sum_{j=1(E_{\mathrm{on}})}^{j=n(E_{\mathrm{off}})}C_{pc}(E_j) = \frac{n^2}{mRT}\frac{F^2}{}\mathrm{AdM_{mw}}C^0_{O_X}\frac{\exp\left(\frac{nF}{RT}\left(E^0_{O_X/R_d}-E\right)+g\frac{C_{O_X}}{C^0_{O_X}}\right)}{\left[1+\exp\left(\frac{nF}{RT}\left(E^0_{O_X/R_d}-E\right)+g\frac{C_{O_X}}{C^0_{O_X}}\right)\right]^2+g\exp\left(\frac{nF}{RT}\left(E^0_{O_X/R_d}-E\right)+g\frac{C_{O_X}}{C^0_{O_X}}\right)} \tag{6.5}$$

where A is the electrode geometric area (cm^2), d is the thickness of the electrode layer, M_{mw} is the molecule weight of the redox material (g), m is the weight of redox material inside the entire electrode layer (g) and E_{on} and E_{off} are the onset and offset potentials.

The incorporation or combination of electrodes having double layer and pseudocapacitance leads to a coupling effects between the two materials taking advantage of the synergy to enhance the total capacitance of the electrodes. Thus, for an ideal condition, the total capacitance (C_T) of an electrode must be the sum of electrochemical double-layer capacitance (C_{dl}) and pseudocapacitance (C_{pc}) which is expressed in Eq. 6.6:

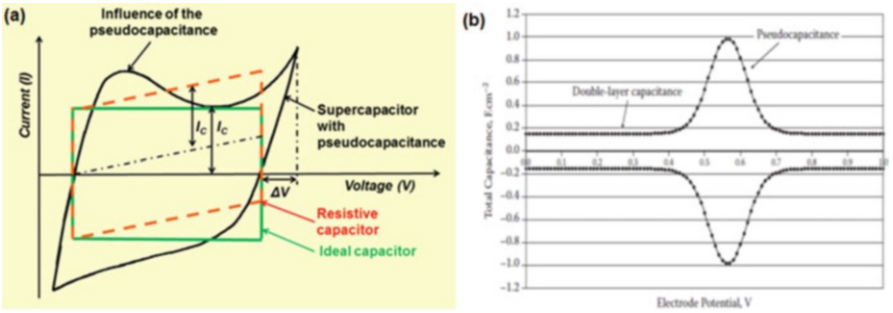

Fig. 6.3 (**a**) CV curves showing fundamental differences between static capacitance (rectangular) and pseudo-/faradaic capacitance (curved) and (**b**) shows the calculated total capacitance as a function of electrode potential reflecting the double-layer capacitance and the pseudocapacitance contribution (Yu et al. 2013a)

$$
\begin{aligned}
C_T &= C_{\mathrm{dl}} + C_{pc}(E) \\
&= C_{\mathrm{dl}} + \frac{n^2F^2}{\mathrm{RT}} dC^0_{O_X} \\
&\quad \times \frac{\exp\left(\frac{nF}{\mathrm{RT}}\left(E^0_{O_X/R_d} - E\right) + g\frac{C_{O_X}}{C^0_{O_X}}\right)}{\left[1 + \exp\left(\frac{nF}{\mathrm{RT}}\left(E^0_{O_X/R_d} - E\right) + g\frac{C_{O_X}}{C^0_{O_X}}\right)\right]^2 + g\exp\left(\frac{nF}{\mathrm{RT}}\left(E^0_{O_X/R_d} - E\right) + g\frac{C_{O_X}}{C^0_{O_X}}\right)}
\end{aligned}
\tag{6.6}
$$

Figure 6.3 is a reversible cyclic voltammetry of an electrode showing the total computed capacitance against the potential. This capacitance clearly shows the double-layer capacitance and the huge contribution from the pseudocapacitive components, indicating that materials that exhibit pseudocapacitance would significantly contribute to the development of supercapacitor technology.

Different faradaic mechanisms can occur in electrochemical charge storage in pseudocapacitors, and these include electrosorption (underpotential deposition), reduction-oxidation reactions (redox pseudocapacitance) and intercalation (intercalation pseudocapacitance). These processes are illustrated in Fig. 6.4 (Augustyn et al. 2013).

Underpotential deposition occurs when the onset of deposition of metal adatoms (adsorbed atom) at various types of substrates in potential ranges positive to the reversible equilibrium potential (also referred to as the Nernst potential). A classic example of underpotential deposition is the deposition of lead (Pb) on the surface of a gold (Au) electrode (Sudha and Sangaranarayanan 2002). While redox pseudocapacitance occurs when the electrochemical adsorption of ions near surface or onto the surface of a material with a concomitant faradaic charge transfer (Augustyn et al. 2014), e.g. surface redox reactions as in RuO_X (Augustyn et al. 2013). Intercalation pseudocapacitance occurs when ions intercalate into the pores or layers

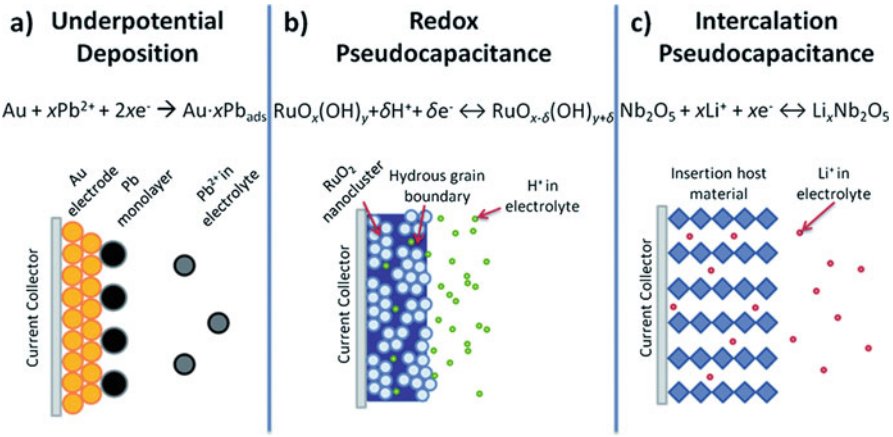

Fig. 6.4 Schematic showing different types of reversible redox mechanisms that give rise to pseudocapacitance (With permission of Augustyn et al. 2014)

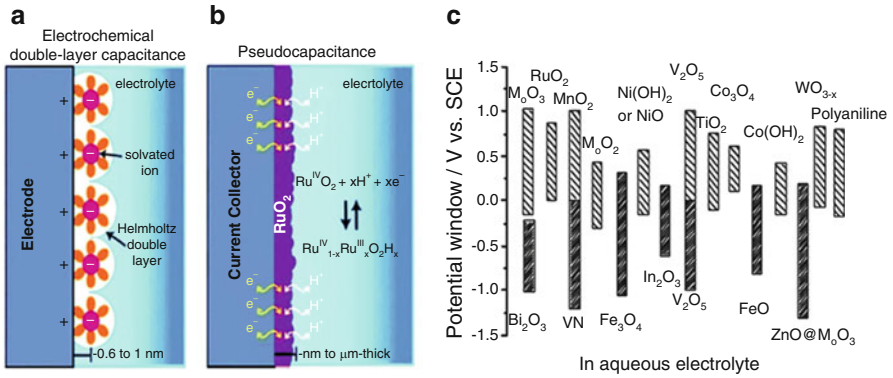

Fig. 6.5 Schematic representation of the mechanism in (**a**) double capacitors, (**b**) pseudocapacitors, (With permission of Zhang et al. (2016a) and (**c**) the working potential windows of various pseudocapacitve-type materials in aqueous electrolyte (With permission of Qu et al. 2011))

of a redox active material accompanied by a faradaic charge transfer with no crystallographic phase change (Augustyn et al. 2014). Underpotential deposition and redox pseudocapacitance represent charge storage on the surface; however, in intercalation pseudocapacitance, charge storage does not occur on the surface but in the bulk material (Augustyn et al. 2013). Figure 6.5 shows the schematics of the double capacitors, the pseudocapacitance and the working potential windows of many oxide materials in aqueous electrolyte with the average working potential of above 0 V vs. SCE.

6.1.2 *Design and Synthesis of the Transition Metal-Oxides-Based Materials for Application in Supercapacitors (SCs)*

In order to keep the effectiveness of the electrochemical energy storage technology to improve the advancement of renewable energy sources, several important requirements should be considered during the design and selection of the suitable electrode material. These desired requirements include (1) high stability in various types of electrolyte solution, (2) high resistance against electrochemical corrosion and (3) good electronic conductivity. Nanomaterials of about the length scale of less than 100 nm have received increasing interest, owing to their fundamental scientific significance as well as their potential applications that is derived from their fascinating electrical, magnetic and catalytic properties (Burda et al. 2005; Tan et al. 2011). As compared to the bulk active electrode materials, the corresponding nanomaterials possess outstanding electrochemical activity, such as higher capacitance, larger surface areas and relatively good conductivity; thereby, nanomaterials have vast potential application in the electrochemistry field. Many transition metal oxides (TMOs) and metal hydroxide (Johan E. ten Elshof et al. 2016) give rise to faradaic reaction that offers high specific capacity and high energy densities due to their rich electrochemistry and have been extensively explored as supercapacitive materials due to their high power and energy output through nanostructuring and materials engineering. Consequently, metal oxides (MOs) with various chemistries (i.e. simple, double or mixed metal oxides, nanostructures, composites, etc.) have been investigated as high-performance electrode materials for pseudocapacitive application. The studied MOs in this chapter include RuO_2 (Xia et al. 2012), MnO_2 (Bello et al. 2013b; Makgopa et al. 2015), SnO_2 (Yan et al. 2010), V_2O_5 (Wei et al. 2012), Fe_2O_3 (Zhou et al. 2012), Fe_3O_4 (Wu et al. 2003), Bi_2O_3 (Gujar et al. 2006), WO_3 (Deb 2008; Zheng et al. 2011) and In_2O_3 (Chang et al. 2008). Conducting polymers (CPs) have also attracted attention and are among the most promising pseudocapacitor materials for flexible supercapacitors, motivating the existing energy storage devices towards the future advanced flexible electronic applications due to their high redox active-specific capacitance and inherent elastic polymeric nature (Shown et al. 2015). Similarly, metal nitrides/oxynitrides have shown emerging properties compared to the metal oxide and in some cases show better and interesting result and therefore have attracted attention as an emerging supercapacitor electrode beyond oxide (Ghosh et al. 2018).

6.1.2.1 Ruthenium Oxide (RuO_x)

At the early stages of exploring MOs as suitable electrode material for supercapacitor applications, RuO_2 emerged as a promising and predominant candidate in energy storage due to its excellent electrical characteristics, thermal stability and other unique electrochemical properties such as high specific capacitance.

Therefore, the above-mentioned properties made RuO_2 to be one of the most extensively studied electrode materials for supercapacitor applications. Ruthenium is a multivalence rare metal element, hard, brittle and light grey in colour (Zheng et al. 1995; Li et al. 2018). As a group of multifunctional material, Ru-based materials family include ruthenium dioxide (RuO_2), hydrous ruthenium dioxide ($RuO_2{\cdot}xH_2O$), ruthenium oxide (RuO_x), ruthenium (Ru) and their composites (Vijayabala et al. 2018). There are two phases of RuO_2: a crystal phase (RuO_2, rutile phase) and an amorphous hydrous phase ($RuO_2{\cdot}xH_2O$). The efficiency of Ru-based materials depends on variety of factors, but their overall performance strongly rests with the surface area that can result from the careful selection of the method of preparing the desired material (Wang et al. 2016a; Li and He 2018). The synthesis of Ru-based nanomaterials has been achieved via various synthetic routes such as wet chemical, vapour phase, hydrothermal and biological and also through various synthetic methods such as thermal decomposition, sol–gel process, electrostatic spray deposition and electrodeposition, among others (Hu et al. 2006; Yin et al. 2012; Park et al. 2015; Li et al. 2018; Vijayabala et al. 2018). From the above synthetic methods, the hydrothermal technique displayed several advantages, such as one-step synthesis method, low aggregation level and narrow crystallite size distribution, over the other synthetic methods (Yin et al. 2012). In addition, the high purity and excellent control over the morphology and size of the particle have been achieved by control of the nucleation and growth owing to its surfactant or protective agent (Park et al. 2015; Vijayabala et al. 2018). During this process, surfactants such as cetyltrimethylammonium bromide (CTAB), hexamethylenetetramine (HMT), polyethylene glycol (PEG), citric acid, citrate potassium, ethylenediamine (EDA) or polyethylene glycol (PEG) are used to control the morphology of the materials (Vijayabala et al. 2018). Several architectures of different morphologies of Ru-based material ranging from one-dimensional (1D) nanostructures, nanorods and nanosheets were synthesized in the presence and absence of the surfactant. The quest for other suitable and cheaper electrode materials with excellent electrochemical properties similar to RuO_2 has been explored. In addition, these RuO_2 capacitor-type materials are only suitable for aqueous electrolytes, thus limiting the nominal cell voltage to 1.0 V. In order to manipulate the morphology of RuO_2, the annealing temperature is a key factor affecting the morphology, which exists usually in the form of nanostructure such as nanoparticle, nanorod and nanofiber. High annealing temperature, for example, from 300 to 800 °C, leads to the crystalline phase of RuO_2 and less water content, resulting in the change of the number of active reaction sites, as well as the electron and proton conductivity (Park et al. 2015). Synthesis of the RuO_2 nanocatalyst is shown in Fig. 6.6. A schematic diagram for the fabrication of RuO_2 nanowires and 3D RuO_2 branched Au-TiO_2 nanostructure can be clearly observed in Fig. 6.6a, and the above results were supported by the top-view SEM images of RuO_2 nanowires and 3D branched nanostructures (Fig. 6.6b, c). A simple and cheap way of synthesising RuO_2 nanocatalyst with various morphologies can be obtained by following the route in Fig. 6.6d, e).

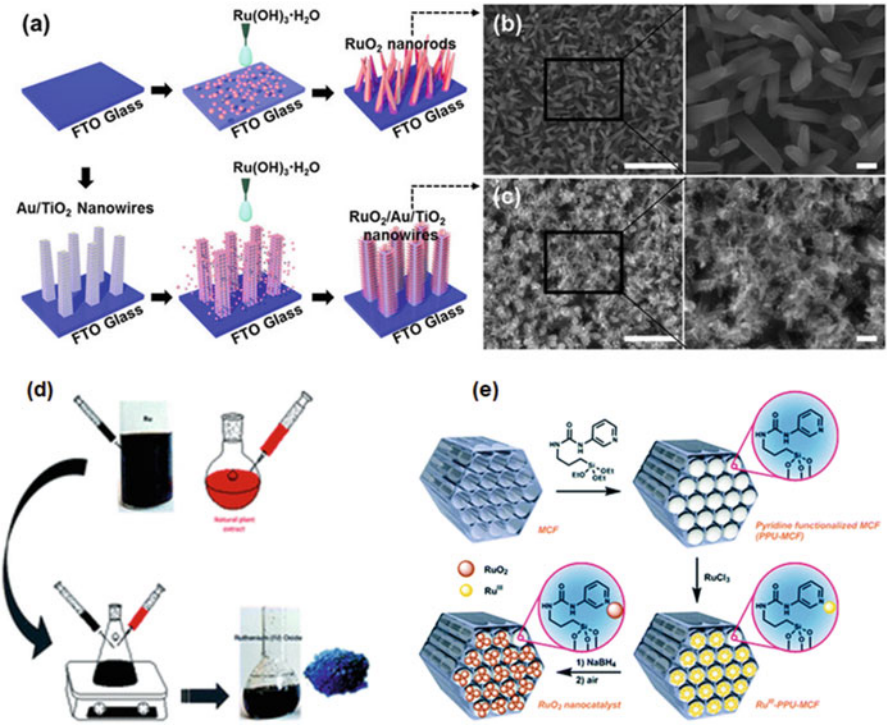

Fig. 6.6 (**a**) Schematic diagram for the fabrication of RuO_2 nanowires and 3D RuO_2 branched Au-TiO_2 nanostructure, (**b, c**) top-view SEM images of RuO_2 nanowires and 3D branched nanostructures (scale bars in the left and right images, 1 μm and 100 nm, respectively) (With permission of Park et al. 2015) and (**d, e**) synthesis of the RuO_2 nanocatalyst ((**d**), with permission of Li et al. 2018, and (**e**), with permission of Gustafson et al. 2017)

It is well known that RuO_2 is a good cathode material for electrochemical capacitors due to the fact that its hydrous form can reversibly store 150–260 F cm^{-2} in aqueous electrolytes or approximately ten times the double-layer capacity of carbon (Zheng et al. 1995). This material stores charge by reversibly accepting and donating protons from an aqueous electrolyte governed by the potential dependent equilibrium of Eq. 6.7.

$$RuO_2 + \delta H^+ + \delta e^- \leftrightarrow RuO_{2-\delta}(OH)_\delta; 0 \leq \delta \leq 2 \tag{6.7}$$

Due to the lack of abundance and the expensive cost of the noble metallic element ruthenium (Ru), there are drawbacks for its commercial application in supercapacitors (SCs), leading to the reduced use of this electrode for SC applications. However, in order to improve the electrochemical properties of other materials that have limited application in energy storage, Ru-based nanomaterials are being explored resulting in Ru-based composites. Miller and co-workers (Miller 1997)

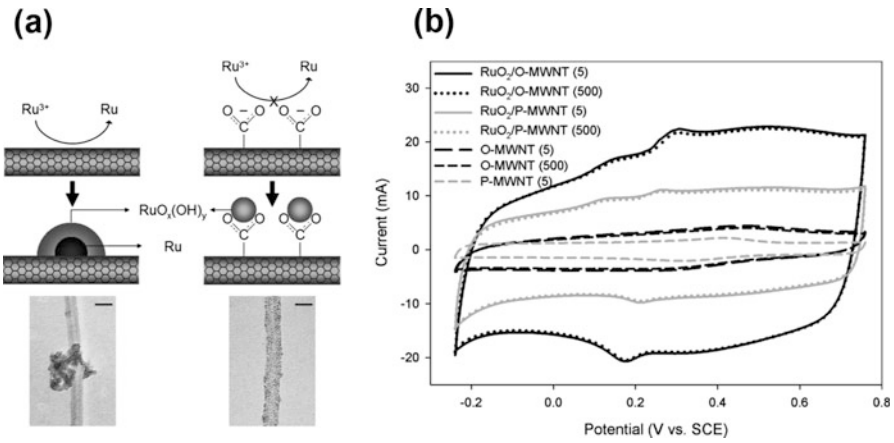

Fig. 6.7 (**a**) Schematic diagram of the different formation mechanisms of RuO_2 on P-MWNT and O-MWNT in the preparation process and their actual TEM images (scale bar = 20 nm) and (**b**) cyclic voltammograms in 1 M H_2SO_4 electrolyte with a scan rate of 20 mV s^{-1} (With permission of Kim and Mitani 2006)

have demonstrated the specific capacitance of ruthenium nanoparticles deposited on the surface of the carbon aerogels to be 330 F g^{-1}, while Zheng and co-workers (Zheng et al. 1995) have reported values as high as 768 F g^{-1} in the early and mid-1990s. Other researchers explored various synthetic routes of making Ru-based nanocomposites by using functionalized carbon nanotubes as supports to these nanoparticles. The surface carboxyl groups from the acid-functionalized carbon nanotubes (CNTs) are able to protect against spontaneous reduction into disadvantageous Ru metal through blocking the contact between MWCNT surfaces and Ru ions by certain bond formation. The as-mentioned mechanism above is presented in schematic form in Fig. 6.7a. The electrochemical performance of the synthesized Ru-Carbon nanocomposite shown in Fig. 6.7b exhibits quite large difference in capacitance behaviour between RuO_2/P-MWNT and RuO_2/O-MWNT, with capacitance values of 182 and 304 F g^{-1}, respectively. The results obtained in this study are lower than other Ru-based results obtained from the literature. However, the ability to reduce the usage of Ru alone but substitute it with other cheap materials and yet obtain such promising capacitive performance emphasizes the promise that lies ahead in terms of developing cheap yet effective Ru-C composite SC devices.

Hwang and co-workers (2015) demonstrated a simple one-step process for the synthesis and processing of laser-scribed graphene (LSG) and RuO_2 nanocomposites fabricated into electrodes that exhibit ultrahigh energy and power densities. The high voltage asymmetric electrochemical capacitors made-up of LSG/RuO_2 as positive electrode and AC as negative electrode showed improved electrochemical performance as shown in Fig. 6.8. The asymmetric electrochemical capacitor demonstrated extremely high energy density of 55 Wh kg^{-1} at a power density of 12 kW kg^{-1}, placing it among the best-performing hybrid electrochemical capacitors.

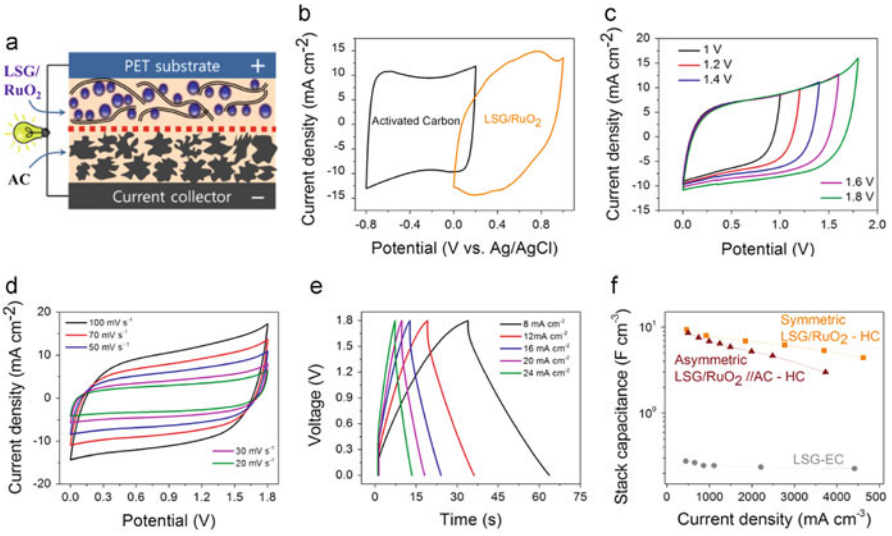

Fig. 6.8 Electrochemical performance of an asymmetric LSG/RuO_2//AC SCs. (**a**) Illustration of the structure of asymmetric SCs assembled with LSG/RuO_2 +ve electrode and activated carbon −ve electrode. (**b**) CV curves comparing the electrochemical properties of the +ve and −ve electrodes in their stable operating voltage windows, obtained at 70 mV s^{-1}. (**c**) CV curves of the asymmetric SCs at increasing voltage window from 1.0 to 2.0 V, all acquired at 70 mV s^{-1}. (**d**) CV performance of the asymmetric supercapacitor at different scan rates tested at a maximum voltage of 1.8 V. (**e**) Galvanostatic charge and discharge curves of the asymmetric supercapacitor collected at different current densities. (**f**) Evolution of the capacitance of the cell stack (including the current collector, active material, electrolyte and separator) as a function of the applied specific current for symmetric LSG/RuO_2, asymmetric LSG/RuO_2//AC and LSG SCs (With permission of Hwang et al. 2015)

Recently, Jiang and co-worker (2018) have managed to integrate the Ru nanoparticles on the 2D transition metal carbides and nitrides, known as MXenes instead of the carbon nanomaterials employed in the literature and tested them for SC applications (Fig. 6.9). They have demonstrated that the hydrophilicity of MXenes combined with their metallic conductivity and surface redox reactions which is the key for high-rate pseudocapacitive energy storage in MXene electrodes can be used to support electrode materials that have good theoretical capacitive performance but yet limited in applications due to the poor conductivity. Their study utilized titanium carbide MXene ($Ti_3C_2T_x$) as negative electrode in acidic electrolyte while ruthenium oxide (RuO_2) as positive electrode. The asymmetric device operated at a voltage window of 1.5 V and managed to deliver an energy density of 37 μW h cm^{-2} at a power density of 40 mW cm^{-2}, with 86% capacitance retention after 20,000 charge–discharge cycles.

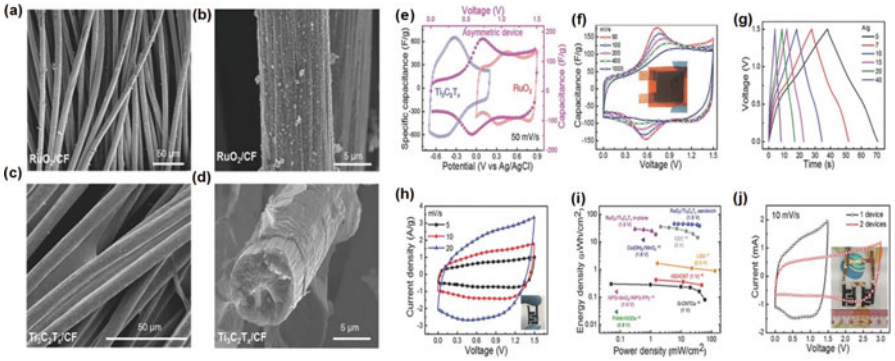

Fig. 6.9 (**a**) Low- **and** (**b**) high-magnification FESEM images of RuO_2/CF. (**c**) Low-magnification SEM image showing uniform coating of $Ti_3C_2T_x$ on carbon fibres. (**d**) Wrapped $Ti_3C_2T_x$ flakes over an individual fibre of the carbon fabric. (**e**) CVs of RuO_2/CF, $Ti_3C_2T_x$/CF and the asymmetric device at a scan rate of 50 mV s^{-1}. (**f**) CVs of RuO_2//$Ti_3C_2T_x$ asymmetric sandwich device at different scan rates, inset shows the digital photograph of the asymmetric device. (**g**) Galvanostatic charge–discharge curves at different current densities. (**h**) CVs of asymmetric in-plane device; inset shows optical image for the in-plane solid-state device attached to polypropylene substrate. (**i**) Ragone plot displays real energy and power densities of RuO_2//$Ti_3C_2T_x$ device in comparison with the other state-of-the-art microsupercapacitors, square represents carbon-based microsupercapacitors, triangle represents pseudocapacitive asymmetric microsupercapacitors. (**j**) Cyclic voltammograms of the RuO_2//$Ti_3C_2T_x$ tandem in-plane devices at scan rate of 10 mV s^{-1} (inset shows that two devices connected in series can power up a green LED during the discharge state) (With permission of Jiang et al. 2018)

6.1.2.2 Manganese Oxide (Mn_xO_y)

Manganese oxide (Mn_xO_y)-based electrode materials (i.e. MnO_2, Mn_3O_4, Mn_2O_3 and MnO) and its derivatives have been studied as the alternative electrode material in supercapacitors due to their contrasting properties as compared to RuO_2. The Mn_xO_y-based electrode materials and their derivatives have demonstrated to be environmentally friendly while being relatively cheap and abundant in nature. Apart from the socio-economic benefits of the Mn_xO_y-based materials and their derivatives, these electrode materials are also characterized by their relatively high theoretical specific surface area (i.e. MnO_2, 1370 m^2 g^{-1}), multiple crystal phases, high theoretical capacitance and good electrochemical response (Subramanian et al. 2005; Yan et al. 2009; Wu et al. 2010; Wang et al. 2012c; Yu et al. 2013b; Jafta et al. 2013; Chidembo et al. 2014; Borgohain et al. 2014). Manganese oxide displays various oxidation states and phases, and the most often studied phases of Mn_xO_y-based materials are MnO_2 having an oxidation state of +4, Mn_2O_3 having an oxidation state of +3 and Mn_3O_4 having an oxidation state of both +2 and +3. The MnO_2 nanomaterials further exhibit various crystallographic forms depending on the types of structural phases (i.e. -, -, γ-, -, ε- and -types) that are dominant during synthesis, as shown in Fig. 6.10 (Xiao et al. 2009). They can also be identified in their various mineral forms such as birnessite, hausmannite, pyrolusite, manganite,

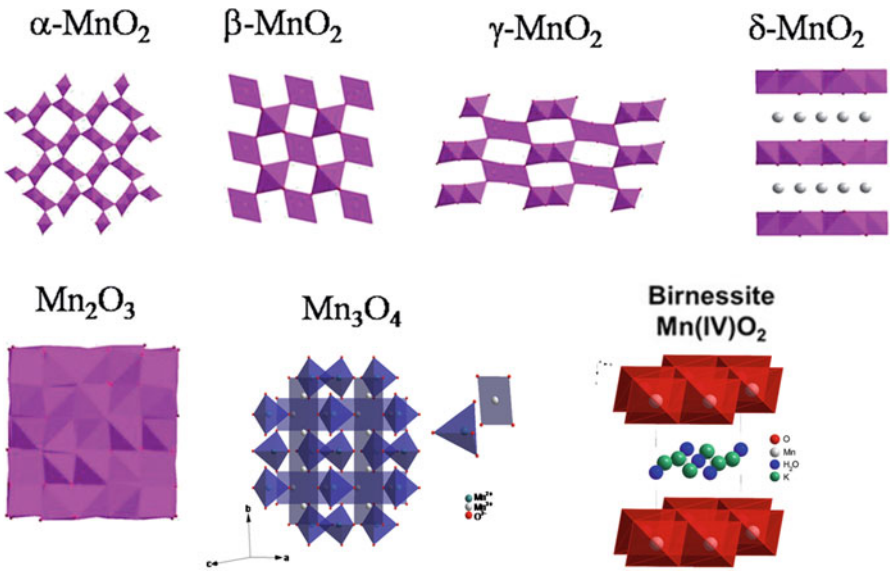

Fig. 6.10 Different Mn_xO_y crystal structures With permission of Liu et al. 2015c)

manganosite and psilomelane (Potter and Rossman 1979; Fan and Yang 1999; Wei et al. 2011). Several structural forms of MnO_2 with different nanoarchitectures such as nanowires (Wang et al. 2014; Yin et al. 2014), nanorods (Wu et al. 2013), single crystal nanotubes (Xiao et al. 2009), nanourchins (Xu et al. 2007) and amorphous (Hatzell et al. 2014) have been synthesized using hydrothermal techniques. Some other techniques used for the synthesis of MnO_2 nanostructures include thermal decomposition, co-precipitation (Lee and Goodenough 1999; Brousse et al. 2006; Nam et al. 2010), simple reduction (Ni et al. 2009; Ragupathy et al. 2009), sol–gel (Wang et al. 2005, 2007), solid-state process and microwave process (Meher and Rao 2012; Ming et al. 2012; Bello et al. 2013a). The other rising Mn_xO_y material in the literature is manganese (II, III) oxide with the chemical formula Mn_3O_4. It is found in nature as the mineral hausmannite and is made of a spinel structure with tetragonal distortion elongated along the c-axis due to Jahn-Teller effect on the Mn^{3+} ion. Manganese ions occupy the octahedral B-site (Mn^{3+}) and tetrahedral A-site (Mn^{2+}) corresponding to a normal spinel structure (Fig. 6.10). Several studies have been conducted in order to improve Mn_3O_4 electrode materials in SC application. Subsequently, to improve the electrochemical capacitive behaviour of Mn_3O_4, the nanosized particles of Mn_3O_4 have been prepared by various methods such as successive ionic layer adsorption and reaction (SILAR) (Dubal and Holze 2013), hydrothermal (Yang et al. 2015), solution combustion (Gao et al. 2011), chemical bath deposition (Xu et al. 2006), sonochemical (Baykal et al. 2010) and microwave techniques (Zhou et al. 2011; Sankar et al. 2012). Different nanoarchitectures of Mn_3O_4 particles such as single crystals, nanocrystals, nanocubics, nanorods, microspheres and interlocked cubes have been successfully synthesized and tested for SC

application (Dubal et al. 2009, 2010; Sankar et al. 2012; Wang et al. 2012; Lee et al. 2012; Dong et al. 2013). Manganese (III) oxide, Mn_2O_3, and manganese (II) oxide, MnO, are other types of the oxides of the Mn_xO_y-based derivatives. The Mn_2O_3 type exists in two recognizable forms, α-Mn_2O_3 and γ-Mn_2O_3. The α-Mn_2O_3 has the cubic bixbyite structure, while pure Mn_2O_3 has an orthorhombic structure, and γ-Mn_2O_3 has a structure related to the spinel structure of Mn_3O_4 with the oxide ions closely packed in cubic form (Wells 1984). A MnO, just like any monoxides, adopts the rock salt structure, with anions and cations being both octahedrally coordinated (Greenwood 1997). Just as much as any manganese oxide material, Mn_2O_3 nanospheres have been synthesized using hydrothermal and sonochemical techniques by Nathan et al. as an EC electrode material (Nathan et al. 2008). Chen et al. has successfully synthesized γ-Mn_2O_3 nanowire bundles (Chen et al. 2005). Recently, Li et al. synthesized nanocubic Mn_2O_3 using hydrothermal technique for the EC application (Li et al. 2015). Nano-sized manganese oxide (Mn_2O_3) was synthesized by Chiang et al. using a solvothermal technique (Chiang et al. 2006). There is a limited literature on the synthesis of Mn_2O_3 for EC application even though several of these materials have been widely synthesized using various techniques such as chemical oxidation (Chen et al. 1997), calcination of MnO_2 and hydrothermal (He et al. 2003).

Several studies on electrochemical behaviour of MnO_2-based materials and its derivatives in an aqueous electrolyte have been conducted in order to better understand their mechanism of charge storage on the surface of the electrode. Hydrated manganese oxides exhibit specific capacitances within the range of 100–200 F g^{-1} in alkaline electrolyte. The surface reaction occurring at the MnO_2 electrode involves the adsorption of electrolyte cations (C+ = H+, Li+, Na+ and K+) on the MnO_2-based materials, whereas the bulk faradaic reaction relies on the intercalation or de-intercalation of electrolyte cations in the bulk of the manganese oxide and is illustrated by Eqs. 6.7 and 6.8, respectively, (Toupin et al. 2004; Yang et al. 2014):

$$(MnO_2)_{surface} + C + + e^- \leftrightarrow (MnO_2{}^- C^+)_{surface} \tag{6.8}$$

$$MnO_2 + C^+ + e^- \leftrightarrow MnOOC \tag{6.9}$$

In the established charge storage mechanisms, a redox reaction between the III and IV oxidation states of Mn ions occurs (Yang et al. 2014). Dedicated approach on the synthesis of MnO_2-based materials and the electrolyte type played a major role on the electrochemical outcome of its SC applications. An amorphous hydrous manganese oxide (α-$MnO_2{\cdot}nH_2O$) was anodically deposited onto a graphite substrate showing an improved maximum specific capacitance of 330 F g^{-1} and 320 F g^{-1} achieved from cyclic voltammetry and galvanostatic charge-discharge measurements, respectively, using Na_2SO_4 (0.1 M) as electrolyte (Hu and Tsou 2002). However, due to the high resistivity of α-$MnO_2{\cdot}nH_2O$, a conducting additive, such as carbon materials, CNTs or graphene and OLCs, is required for the realization of EC electrodes (Cottineau et al. 2006; Sharma et al. 2007). As a result, α-MnO_2 has been decorated on the SWCNT by a simple precipitation technique with good cycle

power at the specific current of 2 A g^{-1} (Subramanian et al. 2006). Ma et al. (2008) synthesized a birnessite-type MnO_2 coated uniformly on multi-walled carbon nanotubes (CNTs) with specific surface area of 200 m^2 g^{-1} by using a spontaneous direct redox reaction between the multi-walled CNTs and permanganate ions (MnO_4^-) with a high specific capacitance of the MnO_2/CNT nanocomposite in an organic electrolyte of ca. 250 F g^{-1} at a high specific current of 1 A g^{-1}. Jafta et al. (2013) synthesized α-MnO_2 from the raw electrolytic manganese dioxide (EMD) using hydrothermal technique in the presence of a sodium dodecyl sulphate (SDS) surfactant and decorated them on the surface of the graphene oxide (GO). The electrochemical properties of nanostructured α-MnO_2/GO composite fabricated in an aqueous asymmetric electrochemical capacitor exhibited high energy density of 35 Whkg^{-1} and specific capacitance of 280 F g^{-1} at high voltage window of 1.8 V using 1 M Li_2SO_4 as electrolyte. The electrochemical behaviour of vertical graphene nanosheets (VGNs) and MnO_2 was also investigated; the VGNs provide controlled porous structure and high electrolyte accessible surface area for multiple pathways for ion transport. The charge storage behaviour of the MnO_2/VGNs was excellent exhibiting a high areal capacitance of 5.6 mF/cm^2, which is 110 times higher than that of VGNs (51.95 μF/cm^2) at 50 mV s^{-1}. The enhanced capacitance is attributed to the highly conductive 3D network of VGNs which provide fast electron and ion transport and also a large pseudocapacitance from MnO2 coating (Ghosh et al. 2016). Makgopa et al. (2015) showed that the use of birnessite-type MnO_2 decorated on highly graphitized onion-like carbon (OLC) can improve the electrochemical performance of the MnO_2. The nanocomposite of OLC/MnO_2 shown by the FESEM images (Fig. 6.11a, b) displayed better interaction and was fabricated on a symmetrical two-electrode device using the Ni foam as a current collector (Fig. 6.11c, d,) and exhibited a large specific capacitance of 254 F g^{-1} and a remarkably high power density of 74.8 kW kg^{-1}. The surface morphologies of OLC/MnO_2 nanohybrid are shown in Fig. 6.11a (FESEM) and in Fig. 6.11b (TEM) which indicates clear interactions of the precursor material with each other for good capacitive performance. The SAED pattern in the inset (Fig. 6.11b) shows lattice fringes for crystalline MnO_2 and circular lattice shells for OLC confirming the synergistic effect from the nanocomposites.

Manganese (II, III) oxide (Mn_3O_4) as a potential electrode material for ECs showed up just after the researchers discovered MnO_2 as pseudocapacitive electrode material. In 2003, a thin film Mn_3O_4 electrode material was reported to have displayed specific capacitance of 92 F g^{-1} in aqueous electrolyte and 58 F g^{-1} in organic electrolyte from cyclic voltammetry at the scan rate of 20 mV s^{-1} (Jiang and Kucernak 2002). Wu and Hu (2005) studied a mixture, consisting of Mn_3O_4 and MnOOH crystals and reported specific capacitance ranging between 45 and 71 F g^{-1}, and Djurfors et al. (Djurfors et al. 2005) showed that Mn_3O_4 film prepared by either thermal or electrochemical oxidation of Mn/MnO films has an effect on the capacitive performance of the electrode material. Nagarajan et al. (2006) later followed the principle of Djurfors et al. to form a spinel Mn_3O_4 phase at 300 °C with an improved specific capacitance value of 445 F g^{-1} in Na_2SO_4 electrolyte. As a race in finding a stable and suitable electrode derived from the Mn_3O_4 material,

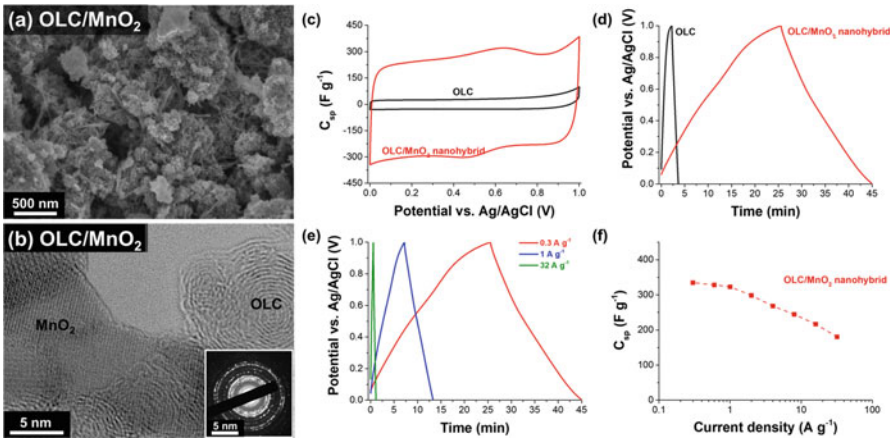

Fig. 6.11 (**a**) SEM (**b**) TEM images of the OLC/MnO_2 nanohybrid (the inset is the corresponding SAED pattern of (**b**)), (**c**) cyclic voltammograms at 5 mV s^{-1} and (**d**) galvanostatic charge–discharge curves at 0.3 A g^{-1} comparing OLC and the OLC/MnO_2 nanohybrid, (**e**) galvanostatic charge–discharge curves for the OLC/MnO_2 nanohybrid at various current densities and (**f**) C_{sp} vs. current densities of the OLC/MnO_2 nanohybrid. Three-electrode configuration with nickel foam as the current collector. Electrolyte: aqueous 1 M Na_2SO_4 (With permission of Makgopa et al. 2015)

researchers developed composites of this material from carbon templates. In 2008, Mn_3O_4/MWCNT composite was examined using cyclic voltammetry and obtained a maximum specific capacitance of 330 F g^{-1} (An et al. 2008). Wang et al. (2010) later used graphene sheet as a template for decoration of Mn_3O_4 by mixing graphene suspension in ethylene glycol with MnO_2 organosol, followed by subsequent ultrasonication processing and heat treatment. The as-prepared Mn_3O_4/graphene nanocomposite gave a specific capacitance of 175 F g^{-1} in Na_2SO_4 electrolyte and 256 F g^{-1} in KOH electrolyte. The higher result obtained in the alkaline medium is due to the higher ionic conductivity of the electrolyte compared with the neutral electrolyte. As it has been shown from the literature, the hydrated ion size (3.31 Å for K^+ and 3.58 Å for Na^+) and ionic conductivity (73.5 S cm^2 mol^{-1} for K^+ compared to 50.11 S cm^2 mol^{-1} for Na^+) play a crucial role in electrochemical performance of carbon electrode materials (Zhong et al. 2015). Similarly, the ionic radius of the hydrated negatively charged anions contributes to the EDL behaviour via electroadsorption, and the sizes are in the following order OH^- (3.00 Å) < NO_3^- (3.35 Å) < SO_4^{2-} (5.33 Å) (Zhong et al. 2015). Hence, the alkaline electrolyte is expected to give the best electrochemical performance taking into account electrode that could easily accommodate the smaller size of K^+ and the electroadsorption of the negatively charge anions (OH^-), coupled with it better conductivity and ionic mobility. Qiao et al. (2015) synthesized micro/nanostructured Mn_3O_4 with an open 3D flower-like morphology by a facile solvothermal approach using hexadecyltrimethylammonium bromide as a surfactant and ethanol as a solvent. The Mn_3O_4 microspheres used exhibited electrochemical performance with a

specific capacitance of 286 F g^{-1} at a low specific current (0.5 A g^{-1}) and still retained 80% (230 F g^{-1}) and 73% (210 F g^{-1}) at higher current densities of 5 A g^{-1} and 10 A g^{-1}, respectively. The enhanced capacitive performance of Mn_3O_4/graphene nanocomposites was attributed to the nanoparticulate nature of Mn_3O_4 nanoparticles and functional groups attached to graphene nanosheets. Recently, Makgopa et al. (2017) reported on the electrochemical performance of the tetragonal hausmannite Mn_3O_4, when embedded on various carbon materials to form OLC/Mn_3O_4, CNT/Mn_3O_4, GO/Mn_3O_4 and AC/Mn_3O_4 nanohybrids, and investigated as electrode material for symmetric, as shown in Fig. 6.12, and asymmetric pseudocapacitor device. The nanohybrid electrode materials demonstrated higher electrochemical performance (in terms of specific capacitance and rate capability as energy storage devices) compared to the pure Mn_3O_4. The OLC/Mn_3O_4 nanohybrid was shown to be the best-performing symmetric pseudocapacitor device, and it exhibited higher specific capacitance of 195 F g^{-1}, specific energy of 4.3 Wh kg^{-1} and power density of 52 kW kg^{-1} compared to other carbon nanohybrid materials studied. When it was tested as a high-voltage asymmetric pseudocapacitor device, the OLC/Mn_3O_4 nanohybrid displayed maximum energy and power densities of ca. 19 Wh kg^{-1} (at 0.1 A g^{-1}) and 45 kW kg^{-1} (at 10 A g^{-1}), respectively. The high performance of the OLC-based system compared to the other carbon systems is ascribed to the combined unique intrinsic properties of the OLC, high electrical conductivity, highly accessible outer surface and large interparticle pore volumes. The above properties have ensured OLC/Mn_3O_4 nanohybrid as a suitable candidate for the high-voltage asymmetric pseudocapacitor device.

To the best of our knowledge, there is no much literature on the use of Mn_2O_3 and MnO as SC applications. The study of Mn_2O_3 as electrode material for supercapacitors surfaced at around 2006, when Chiang et al. (2006) reported on the synthesis and the examination of the nanoparticles of Mn_2O_3 as a potential SC electrode material. The electrode material exhibited a maximum specific capacitance of about 197 F g^{-1} from cyclic voltammetry at the scan rate of 10 mV s^{-1}. Yu et al. (2008) reported on the synthesis of Mn_2O_3 particles that were made of micropores having a specific capacitance of 350 F g^{-1}. The improved performance was attributed to the relatively high specific surface area of 283 m^2 g^{-1}. Zhang et al. (2009) reported on the nano-sized Mn_2O_3 which was homogenously incorporated on a mesoporous carbon template exhibiting an improved specific capacitance of 600 F g^{-1}. In 2011, Wang et al. (2011) reported a composite of Mn_2O_3 and carbon aerogel microbead (CAMB), a maximum specific capacitance of 368 F g^{-1}, and it was emphasized the fact that this type of manganese oxide material is well suited for EC applications. Li et al. (2015) developed porous Mn_2O_3 nanocubins through hydrothermal technique that was followed by calcination in the air which exhibited a specific capacitance of 191 F g^{-1} at a specific current of 0.1 A g^{-1}. This electrode material showed relatively high rate capability at high specific current of 5.0 A g^{-1} and excellent long-term cycle stability even after 3000 cycles. The enhanced rate capability of this material was associated with the improved porosity. Mn_2O_3-based electrode materials are potentially useful as supercapacitor electrode materials, albeit its growth or attention has been dramatically slow compared to other manganese

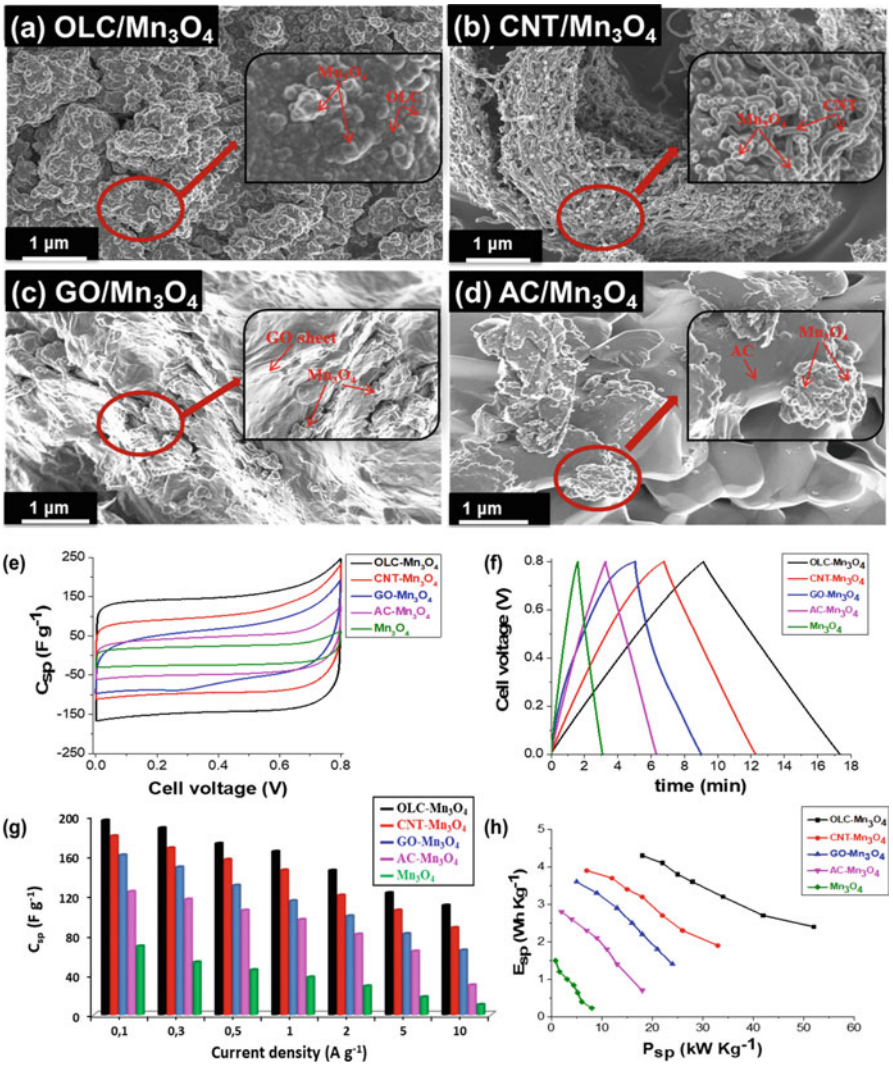

Fig. 6.12 SEM images of (**a**) OLC/Mn_3O_4, (**b**) CNT/Mn_3O_4, (**c**) GO/Mn_3O_4 and (**d**) AC/Mn_3O_4 nanohybrids. Inset in (**a**–**d**) is the high-magnification SEM image of respective nanohybrids. Comparative (**e**) cyclic voltammograms at 5 mV s^{-1}, (f) galvanostatic charge-discharge curves at 0.3 A g^{-1}, (**g**) Csp vs. specific current plot and (**h**) energy vs. power densities, for OLC/Mn_3O_4, CNT/Mn_3O_4, GO/Mn_3O_4, AC/Mn_3O_4 nanohybrids and Mn_3O_4 in aqueous 1 M Na_2SO_4 (With permission of Makgopa et al. 2017)

oxide-based electrode such as MnO_2 and Mn_3O_4. To the best of our knowledge, there is no literature on the use of manganese mono-oxide (MnO) as an electrode material for SC application. For more information on this Mn_xO_y-based electrode material, the reader is referred to the book chapter by Makgopa et al. (2016).

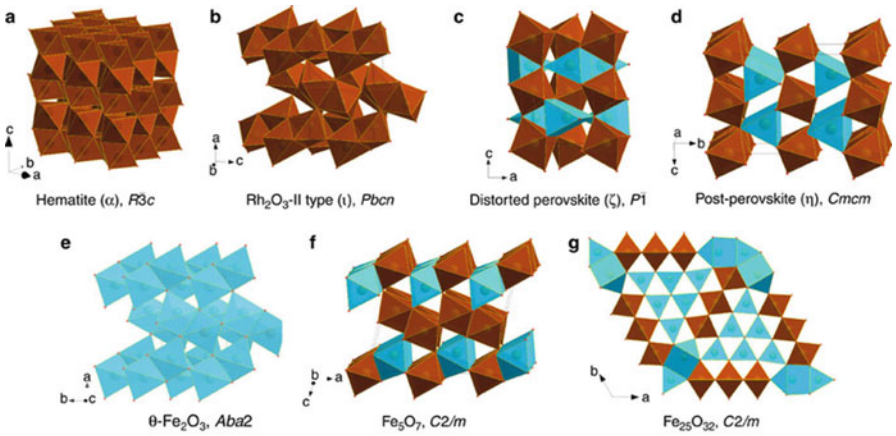

Fig. 6.13 Crystal structures of iron oxide phases. Building blocks are octahedral (brown) and trigonal prisms (blue) (With permission of Bykova et al. 2016)

6.1.2.3 Iron Oxide (Fe_xO_y)

Iron oxide (Fe_3O_4) is another cheap alternative to RuO_x and has attracted attention in several fields of application due to its favourable magnetic, electric and optical properties (Ozkaya et al. 2009) and has been chosen as a potential electrode material in energy storage due to its high theoretical capacity (924 mA h g^{-1}), natural abundance, low cost, good chemical stability, environmental friendliness and cost-effectiveness (Wang et al. 2008). Similar to the manganese discussed above, different crystal structures can easily lead to pathway for the synthesis of these materials. Figure 6.13 shows the various enigmatic structural, electronic and magnetic transformations at high pressures and high temperatures.

They have been predominantly investigated as anode in Li-ion batteries, showing high- performance capability when the morphologically or compositionally is properly engineered (Luo et al. 2013). For SC applications, they are suitable as negative electrodes for hybrid devices due to their broad potential window of operation (1–1.2 V) in aqueous solutions (Qu et al. 2011). The preliminary evaluations revealed that the relatively low electrical conductivity of these oxides requires the introduction of conductive additive such as CB to increase its conductivity and boost its capacitance. In addition, it has been already demonstrated in several studies that combining these oxide materials with carbonaceous materials leads to high values of conductivity and can improve the overall electrochemical behaviour due to synergistic effects between the oxide and the carbon material. The capacitive nature of Fe_3O_4 has been investigated by Wu et al. (2003) in various electrolytes, and it was shown with a high capacitance value of 510 F g^{-1}. Similarly, it has been shown that Fe_2O_3 can operate in a wide negative potential window of 0 to −1.35 V; such an excellent supercapacitive performance makes it a perfect anode electrode material (Tang et al. 2015). The reaction governing the performance of aqueous electrolytes

such as Na_2SO_3, Na_2SO_4 and KOH (Wang et al. 2006) was established using an electrochemical quartz crystal microbalance and X-ray photoelectron spectroscopy. It was found that the capacitance of Fe_3O_4 in the Na_2SO_3 electrolyte arises due to the combination of both the EDLC and pseudocapacitor involving the reduction/oxidation of specifically adsorbed sulphite anions given by the equations below. In the Na_2SO_4 solution, the performance was due to the formation of a double layer, and in the KOH, the performance arises due to partial surface oxidization of the oxide electrode.

$$2SO_3^2 + 3H_2O + 4e \leftrightarrow S_2O_3^2 + 6OH \tag{6.10}$$

$$2SO_3^2 + 3H_2O + 8e \leftrightarrow 2S^2 + 6OH \tag{6.11}$$

Quite a number of Fe_3O_4 electrodes have been reported, for example, Fe_3O_4 films made by electroplating technique exhibited a specific capacitance of 170 F g^{-1} in Na_2SO_3 (Wang et al. 2006), and Fe_3O_4 nanoparticles with a specific capacitance of 185 F g^{-1} was reported via a sol–gel technique (Mitchell et al. 2014). However, the capacitance reported is far below the theoretical value, which is because of low electronic conductivity, and morphology collapse, which often leads to low electrochemical performance and poor cycling performance. To build on the exhibiting and maximize the performance of SCs, it is necessary to develop hybrid electrode materials, combining electric double-layer capacitive materials and pseudocapacitive materials such as Fe_3O_4. Thus, Fe_3O_4 has been included in many carbon matrices to improve the overall capacitance of the system because of the good electrical conductivity and excellent electrochemical stability (Sevilla and Mokaya 2014; Meng et al. 2014). These Fe_3O_4–carbon composites showed improved electrochemical performance compared to the individual components due to a positive synergy between Fe_3O_4 and carbon materials, and their charge storage arises from both the double-layer and faradaic reactions. For example, cubic Fe_3O_4 and graphene layer assembled into a symmetric supercapacitor device with the specific capacitance ~782 F g^{-1} at a specific current of 3 A g^{-1} (Xu et al. 2008). An Fe_2O_3 decorated with single-walled carbon nanotubes (SWCNT) as flexible anodes in LIBs with a discharge capacity of 801 mA h g^{-1} after 90 cycles was reported by Zhou et al. (2012). The excellent result obtained was attributed to the conductivity of the SWCNT. Min et al. (2017) reported a facile and efficient technique to synthesize porous iron oxide coated with graphene as was tested as electrode materials for lithium–ion batteries and supercapacitors. The encapsulation of porous Fe_2O_3 and Fe_3O_4 nanorods by graphene is directly carried out from FeOOH/GO colloids by taking advantage of an electrostatic self-assembly method, owing to the positively charged surface of FeOOH and the negatively charged surface of GO. This combination leads to multifunctional features of the electrode materials as follows: (1) An enhanced electrical conductivity makes the electrodes serve as the current collectors; (2) reinforced softness of the electrodes accommodates the large volume changes during charge–discharge cycles; (3) improved high specific surface area of the electrodes increases the accessibility of the active electrode materials to electrolyte;

(4) the pores formed by graphene and iron oxide particles facilitate ion transportation; and (5) iron oxide particles separate graphene and prevent their restacking or agglomeration and vice versa, thus improving the immersion and splitting of electrolyte into and out of the electroactive material. Consequently, the porous iron oxide/graphene hybrid nanocomposites deliver a good performance in the electrochemical energy storage. As expected, the incorporation of Fe_3O_4 in carbon matrix can greatly improve the electrochemical performance by inducing some vigorous redox reactions. Similarly, Kim et al. reported that composites of multi-walled carbon nanotubes and Fe_3O_4 exhibited specific capacitances of 165 F g^{-1} at a specific current of 0.2 A g^{-1} (Kim and Park 2011). The Fe_3O_4 and CNT together formed an interpenetrating network that provided a high specific capacitance and better cycling stability. An ultrathin nanoporous Fe_3O_4/carbon nanosheets with surface areas of 229 m^2 g^{-1} was reported by Liu et al.; the composite exhibited specific capacities of 163.4 F g^{-1} at a specific current of 1 A g^{-1}. An optimum Fe_3O_4 content in a Fe_3O_4/SiCF feeding ratio of 1.5:1 (SiCF/Fe_3O_4(1.5)) exhibited a high charge storage capacity, showing a specific capacitance of 423.2 F g^{-1} at a scan rate of 5 mV s^{-1} with a 81.8% rate performance from 5 to 500 mV s^{-1} in 1 M KOH aqueous electrolyte (Kim and Kim 2017). These results indicate the potential and advantages of iron-based materials for use as a high-energy and high power density supercapacitor electrode. Furthermore, an optimized electrochemical performance of electrode structures with proper control of the metal oxide/carbon was produced as shown in the scheme in Fig. 6.14. The morphology shows a hierarchical graphite

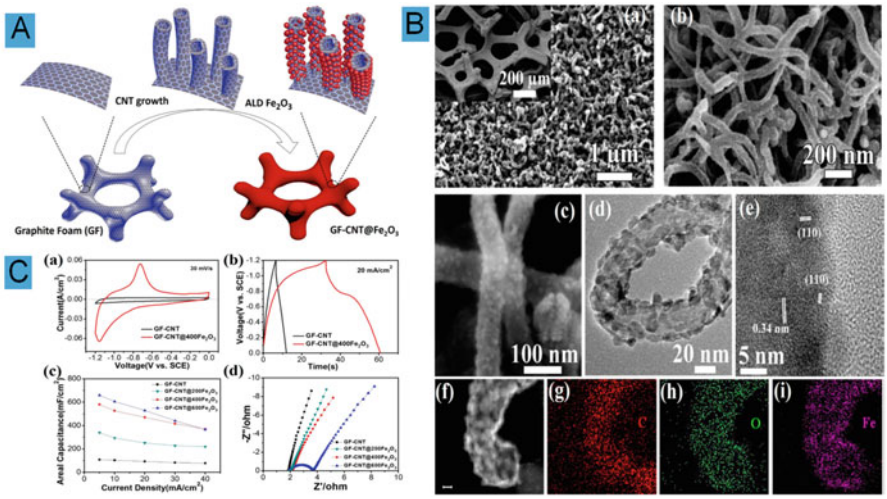

Fig. 6.14 (**a**) Schematic representation of the growth procedure of GF-CNT@Fe_2O_3 starting from graphite foam. (**b**) SEM and TEM characterization of GF-CNT@Fe_2O_3, (**a**–**c**) SEM and (**d**, **e**) HRTEM images of GF-CNT@Fe_2O_3, (f) HAADF-STEM image of a single CNT@Fe_2O_3 and (g–**i**) the corresponding STEM element mapping. The scale bar in (**f**) is 10 nm. (**c**) Electrochemical analysis, (**a**) CV curves and (**b**) charge-discharge curves of GF-CNT@400Fe_2O_3 and GF-CNT. (**c**) Rate properties and (**d**) EIS of four samples (With permission of Guan et al. 2015)

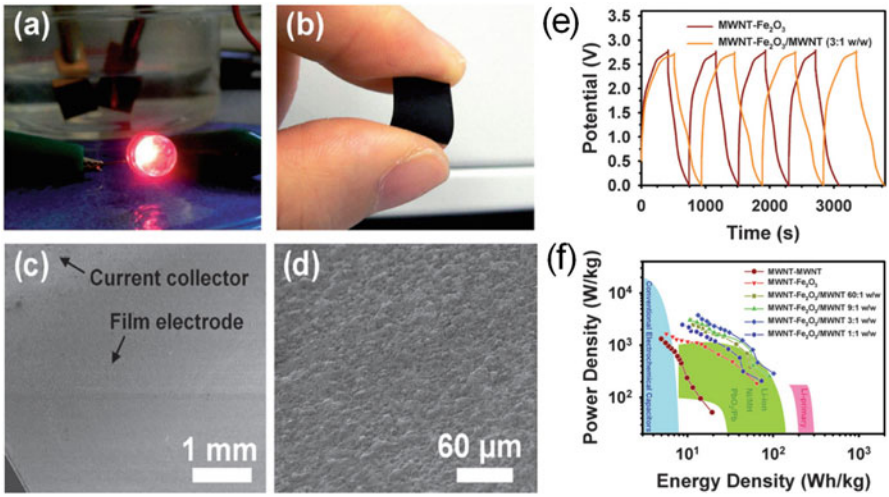

Fig. 6.15 (**a**) an optical image showing that a LED was lit brightly even after 300 cycles of the MWNT-α-Fe_2O_3/MWNT, (**b**) an optical image, (**c**, **d**) SEM images of the top surface of a α-Fe_2O_3/MWNT composite anode after 600 cycles and then bending, (**e**) galvanostatic charging/discharging behaviour of α-Fe_2O_3 and α-Fe_2O_3/MWNT composite as anode (MWNT as cathode) and (**f**) Ragone plot of MWNT cathode and various anode arrangements, together with other energy storage technologies (With permission of Zhao et al. 2009)

foam–carbon nanotube framework with thin layer of iron oxide coating on the surface to form (GF–CNT@Fe2O3) composite. Anode cells fabricated based on this material displayed a high energy of ~74.7 Wh/kg at a power of ~1400 W/kg and ~95.4% capacitance retention after 50,000 cycles of charge–discharge. This performance is superior to the results obtained by the GF-CNT alone and to many different forms of metal oxide-based supercapacitors, making it a promising candidate for the next generation of high-performance electrochemical energy storage.

Similarly, the spray deposition method was used for the fabrication of a flexible supercapacitor based on thin film of multi-walled carbon nanotube (MWNT) cathodes and hematite (α-Fe_2O_3)/MWNT composite anodes. The device fabricated provided a very high specific energy density of 50 Wh kg^{-1} at a power density of 1000 W kg^{-1} with potential window of 0–2.8 V, this energy value was eight times bigger than that fabricated for symmetric supercapacitors based on MWNT electrodes under the same conditions. The excellent performance of the hybrid devices was attributed to the incorporation of MWNTs into the α-Fe_2O_3 anodes, which leads to a decrease of internal resistance and an improvement in both the ion diffusion behaviour and the integrity of the α-Fe_2O_3 containing films (Zhao et al. 2009) (Fig. 6.15).

6.1.2.4 Vanadium Oxide (V_2O_5)

Vanadium oxide is gaining considerable research interest as suitable electrodes for supercapacitor owing to their low cost, layered structure and its ability to exist in variable oxidation states (e.g. V_2O_5, V_2O_3 and V_4O_7) (Wei et al. 2012; Saravanakumar et al. 2012; Li et al. 2013; Cao et al. 2014). The electronic structure, charge density, transport properties and phase transitions of different vanadium oxides are expected to vary with the composition. Vanadium pentoxide, V_2O_5, possesses the unique advantages of high-energy density (Yang et al. 2011b), and wide potential window arising from its variable oxidation states (Choi et al. 2006) makes it suitable as electrode material for supercapacitors. Different nanostructures of V_2O_5 such as nanowires (Wang et al. 2015), nanotubes (Yu et al. 2012), nanorods (Tien and Chen 2013), nanofibers (Wee et al. 2010), hollow spheres (Yang et al. 2013) and V_2O_5 nanosheets constructing 3D architectures (Xiong et al. 2008) have been synthesized using techniques such as hydrothermal (Xiong et al. 2008), electrospining (Wee et al. 2010; Yu et al. 2011), template-assisted growth (Cheng et al. 2008) and various other methods are used to produce these unique nanostructures. For example, Zhang et al. (Zhang et al. 2016b) reported three different structures of V_2O_5 (nanobelts, nanoparticles and microspheres) by a simple hydrothermal route, and the combination of calcination and the electrochemical results obtained indicate that microspheres lead to a significant improvement of storage capacity with a specific capacitance of 308 F g^{-1} in 1.0 M $LiNO_3$ electrolyte. Figure 6.16 shows the processing of bulk V_2O_5 into nanosheets of V_2O_5 of 4 nm and lateral dimension of up to micrometres via hydrothermal system and characterized with the various state-of-the-art facilities such as TEM, SEM and STEM (Fig. 6.16b). The active electrode material displayed excellent specific capacitance of 451 F g^{-1} in a neutral aqueous Na_2SO_4 electrolyte, as the 3D architectures are utilized for energy storage, with capacitance retention after 4000 cycles is more than 90%, and the energy density is up to 107 W·h·kg^{-1} at a high power density of 9.4 kW kg^{-1} (Zhu et al. 2013). The performance was due to the unique 3D V_2O_5 architecture that provides high surface area for enhanced electrolyte/electrode interaction and also reduces the diffusion path both for electrons and ions.

Nanoporous V_2O_5 network was prepared via a capping agent-assisted technique and examined the effect of annealing on the morphology, electrochemical and structural properties (Saravanakumar et al. 2012). The electrode fabricated exhibited a specific capacitance of 316 F g^{-1}, which is attributed to the creation of facile nanochannels for ion diffusion and facilitates the easy accessibility of ions. Nevertheless, despite the high capacitance values recorded for V_2O_5 nanostructures, their poor electronic conductivity and high dissolution issues in liquid electrolyte due to phase changes upon cycling, which gradually erodes the quantity of electrochemically active materials, are detrimental to high-rate, long-term cycling and mechanical stability (Qu et al. 2012). Thus, the combination of V_2O_5 with carbon-based material or doping of the V_2O_5 has been demonstrated to be an effective strategy to improve electronic transport (Chen et al. 2009, 2011b). As such, various composites have

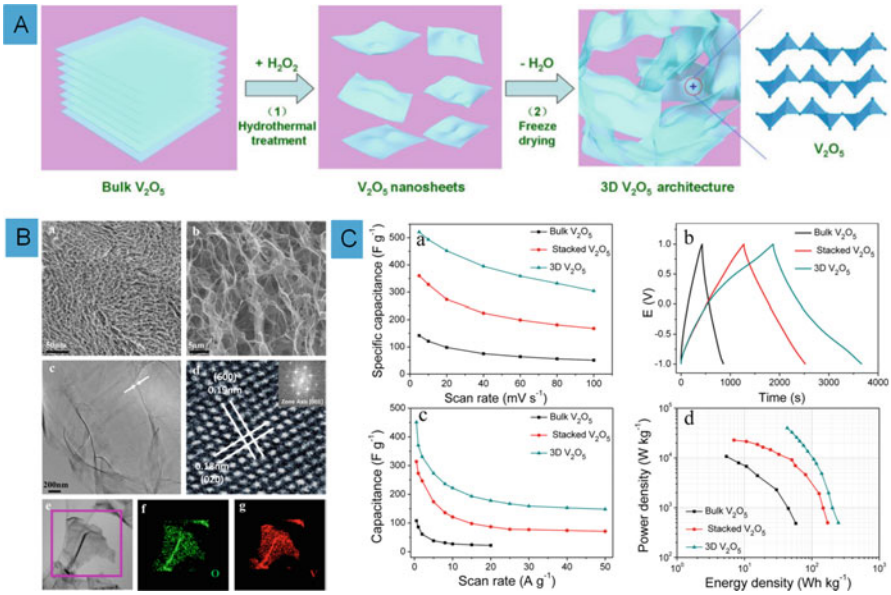

Fig. 6.16 (**a**) Schematics of the fabrication steps of the 3D V_2O_5 architectures: (1) producing thin and flexible V_2O_5 nanosheets via the hydrothermal treatment of V_2O_5 powder with H_2O_2 at 190 °C; (2) removal of water from the as-prepared V_2O_5 nanosheet samples via freeze-drying. (B) Characterization of the 3D V_2O_5 constructs, (**a**, **b**) FESEM; (**c**, **d**) TEM images (FFT, inset); (**e**–**g**) STEM image and corresponding elemental mapping of (**f**) oxygen and (**g**) vanadium. (**c**) Electrochemical performance of 3D V_2O_5 (**a**) Specific capacitances from CV. (**b**) Galvanostatic charge/discharge (GCD) at a specific current of 0.5 A·g^{-1}. (**c**) Specific capacitances from GCD (With permission of Zhu et al. 2013)

been investigated, for example, W-doped V_2O_5 nanobelts were prepared and exhibited specific capacitance of 407 F g^{-1} at 0.5 A g^{-1}. Similarly, V_2O_5/reduced graphene oxide (rGO) hybrid nanostructures are fabricated and showed a higher specific capacitance (484 F g^{-1} at 0.5 A g^{-1}), rate capacity (251 Fg^{-1} at 10 A g^{-1}) and cyclic stability (83% up to 1000 cycles) (Saravanakumar et al. 2016). The improved capacitive performance was due to the high conductivity of rGO and electrochemical activity of V_2O_5. Similarly, an effective facile electrochemical oxidation method was reported to significantly boost the durability and capacitance of VO_x through tuning the valence state of vanadium (Yu et al. 2015). Figure 6.17 shows the SEM, TEM and the electrochemical performance of V_2O_3 nanorods. The valence state of vanadium is optimized through a very facile electrochemical oxidation method, with morphological characterization revealing porous tubular structures (Fig. 6.17a, b). A superior electrochemical performance with rectangular cyclic voltammograms (Fig. 6.17c) and a long stability after 100,000 cycles (Fig. 6.17h) for the prepared electrodes was demonstrated with an in-depth study on the variation for the valence state of vanadium during the oxidation process, and the cyclic

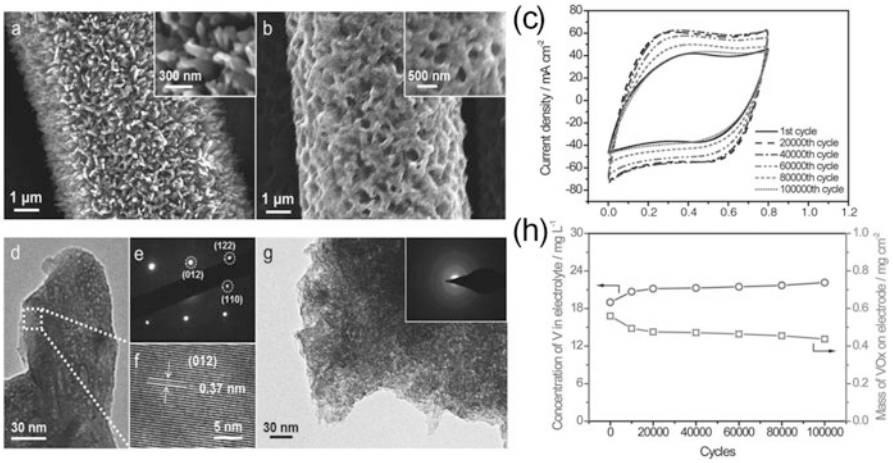

Fig. 6.17 SEM images of as-prepared (**a**) V_2O_3 and (**b**) VO_x samples. (**c**) CV curves collected at 100 mV s^{-1} of VO_x electrode after different cycles. (**d**) TEM image, (**e**) SAED pattern, and (**f**) HRTEM images of a V_2O_3 nanorods. (**g**) TEM image and corresponding SAED pattern of a VO_x sample. (**h**) The concentration of V element in the electrolyte and the mass loading of active materials remained in electrode after different cycles (With permission of Yu et al. 2015)

stability indicates that the long cyclic stability has an important relationship with the distribution of the valence state of vanadium (Yu et al. 2015).

The electrochemical co-deposition of vanadium oxide and polypyrrole was also explored for high-performance supercapacitor devices as shown in Fig. 6.18. The V_2O_5–PPy composite exhibited fibre-like morphology (Fig. 6.18a), and due to the organic-inorganic synergistic effect, the composite exhibits good charge storage properties with a large potential window from −1.4 to 0.6 V vs SCE in a three-electrode configuration, exhibiting a specific capacitance of 412 F g^{-1} at 4.5 mA cm^{-2} (Fig. 6.18b) with good capacitance retention as shown in Fig. 6.18c. The device assembled based on this V_2O_5–PPy composite displayed a high operating voltage of 2 V and a high energy density of 82 Wh kg^{-1} (at the power density of 800 W kg^{-1}) (Bai et al. 2014). The results demonstrate the development of vanadium-based electrode materials as a low-cost strategy towards the advancement of high-performance supercapacitors.

Similarly, VO and VO_2 have also been explored and have demonstrated excellent results, for example, VO coupled with amorphous vanadium covalent bonds (VO_x) was incorporated into carbon nanofibres (VO/VOx/CNF) by electrospinning and heat treatment. The VO/VOx/CNF electrode displayed specific capacitance of 325.7 F g^{-1} at a specific current of 1 A g^{-1} and maintaining 92% of its initial capacitance after 5000 cycles at a specific current of 4 A g^{-1} in a 6 M KOH. The superior electrochemical performance of VO/VOx/CNF was attributed for two reasons, namely, the enhanced conductivity brought upon the incorporation of quasi-metallic VO ($\sim$ 102 Ω^{-1} cm^{-1}) and the network of nanowire and secondly the rapid ion transfer rate caused by the rich vanadium redox couples VO/VOx as

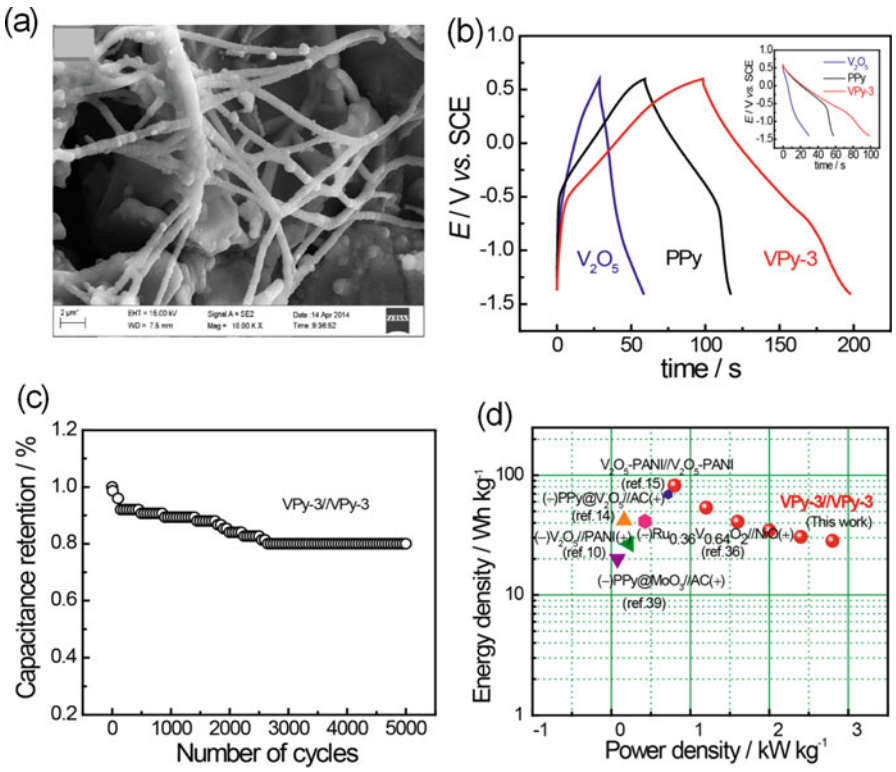

Fig. 6.18 (**a**) SEM images of VPy-3 deposited on carbon cloth substrate, (**b**) galvanostatic charge−discharge profiles of VPy-3, V_2O_5 and PPy collected at a specific current of 4.5 mA cm^{-2}, (**c**) cycling stability of VPy-3//VPy-3 collected by galvanostatic charge−discharge experiments at a specific current of 9 mA cm^{-2} and (**d**) Ragone plots of VPy-3//VPy-3, the values reported for other supercapacitors are included for comparison (With permission of Bai et al. 2014)

well as the developed pore structure (Tang et al. 2016). VO_2 has also been studied as a potential electrode material for supercapacitors, and they have shown a great promise for potential application (Yan et al. 2016), for example, Rakhi et al. reported VO_2 nanosheet electrodes in organic gel electrolyte for supercapacitor applications by hydrothermal method, and the electrodes exhibited a specific capacitance of 405 F g^{-1} at a specific current of 1 A g^{-1} (Rakhi et al. 2016). Also, Deng et al. prepared hybrid of graphene/VO_2 (RG/VO_2) for supercapacitors by hydrothermal reduction method, and the material exhibited a specific capacitance of 225 F g^{-1} at a specific current of 0.25 A g^{-1} in 0.5 MK_2SO_4 aqueous solution (Deng et al. 2013).

6.1.2.5 Tin Oxide (SnO_2)

Tin oxide, SnO_2, is an n-type wide band gap semiconducting material not only with the direct band gap energy of 3.5–3.9 eV (Spence 1967; Arlinghaus 1974) but also with the indirect band gap energy of around 2.6 eV (Kawasaki et al. 1970). The SnO_2 possess the advantages of being inexpensive, efficient semiconducting in nature, environmentally safe, high electrical and optical properties and high chemical stability. These properties have made SnO_2 to be widely explored in many applications such as electrochemical sensors, transistors, catalysts, energy storage and conversions (Yan et al. 2010; Chen et al. 2011a; Zhang et al. 2011; Hou et al. 2013). The interest in the electrochemical energy storage such as SCs and batteries is due to its relative abundance, high theoretical specific capacity (782 mAh g^{-1}) and chemical stability (Tang et al. 2013).

The nanostructures of SnO_2 can also be synthesized via different techniques such as pulsed laser deposition (Pham et al. 2014), co-precipitation (Du et al. 2012), SILAR (Yıldırım et al. 2012), chemical bath deposition (Pusawale et al. 2013), electrodeposition (Yang et al. 2011a), hydrothermal (Hui-Chi Chiu 2007) and thermal evaporation (Kim et al. 2006). The SnO_2 nanoparticles synthesized by co-precipitation technique were evaluated and tested for SC application and displayed a maximum specific capacitance of 122 F g^{-1} at a scan rate of 2 mV s^{-1} (Manikandan et al. 2016). Hierarchical SnO_2 nanostructures (HTNs) prepared by hydrothermal method and characterized revealed a crystalline tetragonal rutile structure of SnO_2 as shown in Fig. 6.18 (Liu et al. 2014). The morphologies of the prepared SnO_2 revealed hierarchical flower shapes in very high density (Fig. 6.18b). The typical diameter of a single hierarchical flower-shaped morphology was $\sim 3 \pm 1$ μm. It was also observed that the hierarchical flower-shaped structures are made of ultrathin nanosheets of ~20 nm in size, which intermingled with each other leading to triangular nanostructures. The HRTEM images (Fig. 6.18e, f) show well defined lattice fringes with lattice spacing of 0.337 and 0.265 nm, corresponding to the (110) and (101) lattice planes of SnO_2, respectively. The SAED pattern shown as inset confirmed the prepared SnO_2 nanosheet crystalline. The electrochemical performance of the SnO_2 structures was evaluated in three-electrode configuration using 1 M Na_2SO_4 aqueous electrolyte. A specific capacitance of 187.7 F g^{-1} was obtained at a specific current of 1 A g^{-1} and was attributed to the hierarchical nature and thin thickness of the nanosheets. Semiconductor quantum dots (QDs) play a vital role in technological and biological applications; SnO_2 QDs exhibit a typical behaviour in comparison with their bulk counterparts due to high surface to volume ratio and excitonic confinement effects (Chen et al. 2005, 2011b). Thus, it is important to understand this distinct nature of QDs such that it can be used more effectively in applications. Bonu et al. carried out electrochemical supercapacitor performance of SnO_2 quantum dots, and it was shown that (QDs) can significantly improve the understanding on the reasons behind the better performance, and it will also help in using QDs or smaller size nanoparticles (NPs) more efficiently in supercapacitors (Bonu et al. 2016). The specific capacitance of the stable SnO_2 QDs showed only 9%

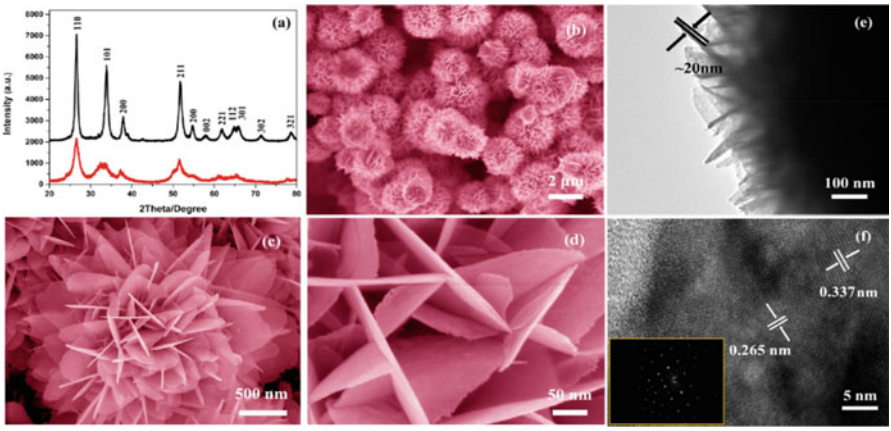

Fig. 6.19 XRD patterns of the prepared SnO_2 nanostructures before (red line) and after calcination (black line); (**b**–**d**) FESEM images, (**e**) low-magnification TEM image and (**f**) high-resolution TEM (HRTEM) image of the prepared hierarchical SnO_2 nanostructures. Inset in (**f**) exhibits the typical corresponding SAED pattern (With permission of Liu et al. 2014)

loss while increasing the scan rate from 20 to 500 mV/S, and the capacitance loss for the QDs is less than 2% after 1000 cycles of charging/discharging, whereas for the 25 nm SnO_2 NPs, the capacitance loss is 8% after 1000 cycles. The new findings about the SnO_2 QDs can be helpful supercapacitors (Fig. 6.19).

Velmurugan et al. (2016) further studied graphene-doped SnO_2 and showed the overall specific capacitance of the composite electrode (SnO_2/graphene) corresponds to the combined contribution from electrochemical double-layer charging and pseudocapacitive behaviour of the composite. The resultant specific capacitance was 50 F g^{-1} for the pristine SnO_2 and 100 F g^{-1} for SnO_2/graphene composite at a high scan rate of 50 mV s^{-1}. The specific capacitance of 470 and 818 F g^{-1} was obtained at low scan rates. A pulse microwave-assisted deposition technique was also explored to grow SnO_2 crystals with homogeneously distribution on rGO sheets to form a composite of SnO_2/rGO composites as shown in Fig. 6.20.

The specific capacitance of the devices fabricated from the composite exhibited specific capacitance of 348 F g^{-1} at a specific current of 50 mA g^{-1}, maximum energy density of 32.2 Wh kg^{-1} with a power density of 1000 W kg^{-1}. The improved capacitance and energy values were attributed to the fact that the SnO_2 crystals not only serve as spacers to create more active sites on the rGO surface but also maximized the fraction of hydrophilic surface, which is more accessible for the formation of the electric double layer (Hsieh et al. 2014). Similarly, SnO_2 was also decorated onto Ti_3C_2 by an efficient and simple microwave irradiation method to form SnO_2-Ti_3C_2 nanocomposite. Figure 6.21a–c showed the layered structure of the Ti_3C_2 with the SnO_2 intercalated into the layer of the Ti_3C_2 to prevent stacking of the layers. The composite exhibited an ideal capacitive behaviour from the CV at different scan rates and GCD at different specific current densities presented in Fig. 6.21d, e. The high specific capacitance of 126 F g^{-1} at 1 A g^{-1} and 100 F g^{-1}

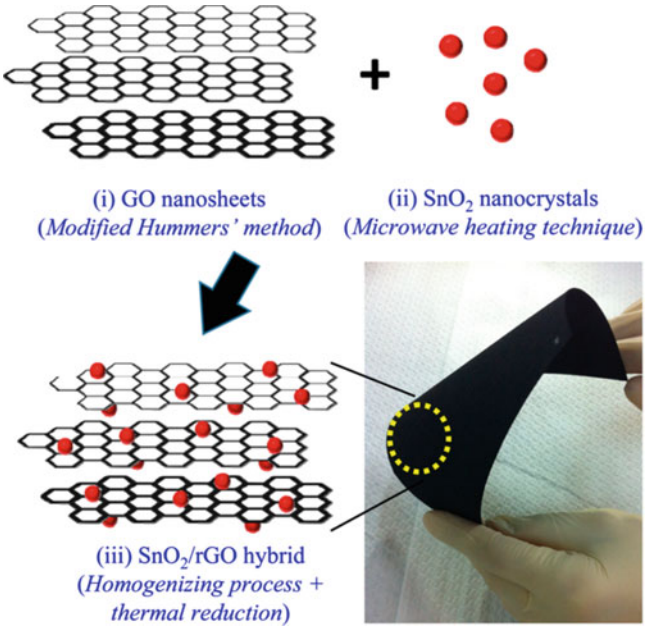

Fig. 6.20 Schematic diagram for growing SnO_2/rGO composites through the following steps: (i) GO sheets by the Hummers' method, (ii) SnO_2 nanocrystals by microwave heating technique and (iii) homogenizing dispersion and thermal reduction. The bottom right photo shows as-prepared flexible SnO_2/rGO CP electrode sheets (With permission of Hsieh et al. 2014)

at 10 A g^{-1} specific current was obtained for the composite. The composite material showed an improved electrochemical performance compared to its precursors (Fig. 6.21f). The composites retained almost 82% of its initial capacitance after 8000 cycles at a specific current of 3 A g^{-1} (Fig. 6.21g). The improved performance observed was due to the intercalation of the Sn^{2+} into the layers of the Ti_3C_2 and also prevent the stacking of Ti_3C_2 layer (Zheng et al. 2017).

6.1.2.6 Tungsten Oxide (W_xO_y)

Tungsten trioxide (WO_3) semiconductor having an indirect band gap of 2.5–2.8 eV has also emerged as a promising material for electrochemical applications due to its low cost, high electrical conductivity, good chemical stability in acidic aqueous solution and high theoretical capacity (Zheng et al. 2011). The interest for this material in electrochemical energy storage is due to its efficient charge storage/delivery dynamic and its reversible valence change (i.e. change of oxidation state between W^{6+} and W^{5+} centres) (Deb 2008; Zheng et al. 2011). Pseudocapacitive charge storage behaviour in highly conductive ordered mesoporous tungsten oxide electrodes was reported by Jo et al. (2011). They observed a voltage rise of the m-WO_{3-X} electrode, which is similar to the EDLC, displayed a high rate capability,

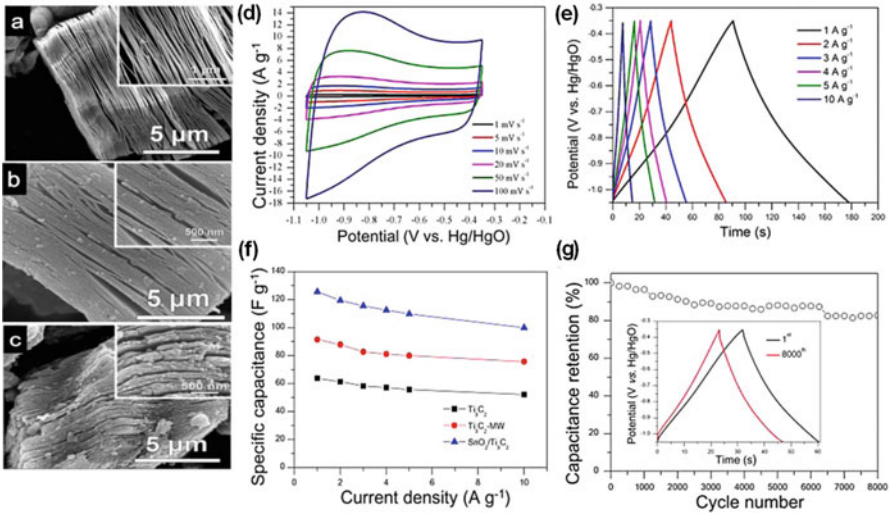

Fig. 6.21 SEM images for (**a**) Ti_3C_2, (**b**) Ti_3C_2-MW and (**c**) SnO_2-Ti_3C_2, (**d**) CV curves of SnO_2-Ti_3C_2 electrode at various scan rates, (**e**) GCD curves of SnO_2-Ti_3C_2 electrodes, (**f**) the plots of the specific capacitance of the three electrodes under different specific current and (**g**) capacitance retention (the inset shows charge-discharge curves before and after 8000 cycles), of SnO_2-Ti_3C_2 electrode after 8000 GCD cycles at 3 A g^{-1} (With permission of Zheng et al. 2017)

which was attributed to its fast proton diffusion within the metal oxide wall and the short path of electrolyte transport through the well-ordered mesopores. Thus, the proposed Fig. 6.22 explained the possible mechanism in the m-WO_{3-X} electrode.

As shown in Fig. 6.22, the three phases within the WO_{3-X} wall were separated. The tungsten metal has two oxidation states of W^{5+} and W^{6+}, and the proton is obtained from the electrolyte phase (Jo et al. 2011). An interphase is assumed to exist between electrode and electrolyte, where the faradaic reaction takes place. Using a simple calculation to estimate the total charge (q*t = 67 C g^{-1}) in cyclic voltammetry (CV) measurement, leads to a charge utilization of 15,533 C mol^{-1}(67 C g^{-1} X 231.84 g mol^{-1}), which indicated that only 16% of W atoms of the m-WO_{3-X} electrode. When the electrode potential increases to 0.6 V, most of the W^{5+} species oxidizes to the W^{6+} state. This oxidation state leads to a decrease in the conductivity, and the charge transfer resistance (R_{ct}) becomes larger. When the potential is lowered to 0 V, the state of the interphase is reduced to W^{5+} and also leads to an increase in the electrical conductivity (lower resistance) of the electrodes. However, WO_3 is suitable as a negative electrode material, and recently, Qiu's group reported the flower-like nanostructures of WO_3 as negative electrode in solid-state asymmetric supercapacitors and exhibited a specific capacitance of 196 F g^{-1} at a scan rate of 10 mV s^{-1} (Qiu et al. 2016). Upadhyay et al. synthesized nanochannel layers of WO_3 by electrochemical anodization in orthophosphoric acid (o-H_3PO_4) (Upadhyay et al. 2017). The cross-sectional SEM images (Fig. 6.23a–c) show nanochannel layers of WO_3.

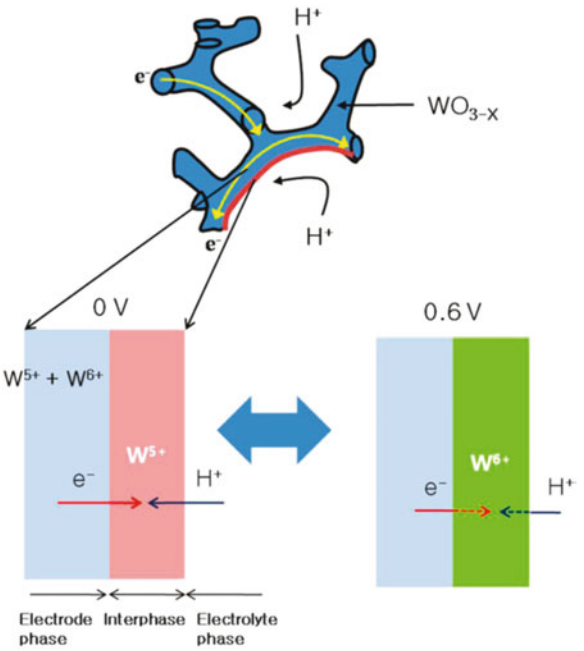

Fig. 6.22 Schematic illustration of the pseudocapacitive charge storage mechanism in the m-WO_{3-X} electrode. Upper part is for the schematic transport of electron and proton within m-WO_{3-X}. Bottom part indicates a schematic change of the oxidation state during pseudocapacitive charging/discharging. Note that transports of electron (e^-) and proton (H^+) within the interphase at 0 V became sluggish at 0.6 V vs Ag/AgCl (With permission of Jo et al. 2011)

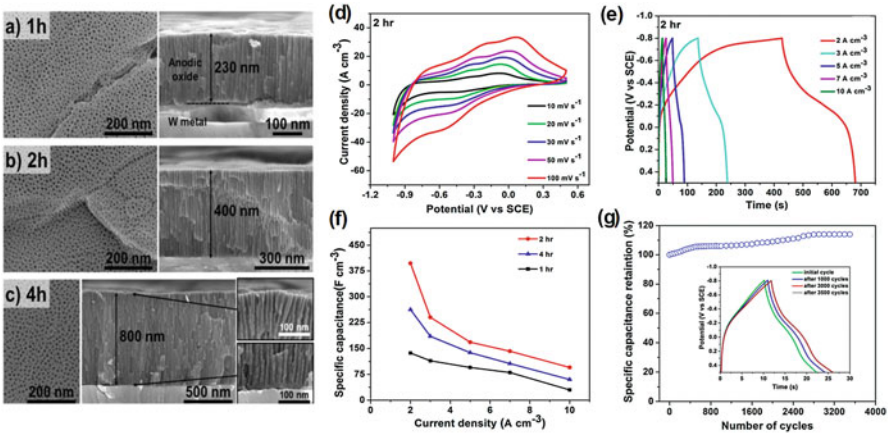

Fig. 6.23 (**a**–**c**) Top-view (left) and cross-sectional(right) SEM images of WO3 nanochannel layers formed by self-organizing electrochemical anodization of W foils in pure hot H_3PO_4 (100 C 5 V) for different times: (**a**) 1 h, (**b**) 2 h and (**c**) 4 h, (**d**–**e**) CV and galvanostatic charge-discharge plot of 2 h. anodized sample at different scan rates and current densities, respectively, (**f**) specific capacitance vs. current densities for all the samples and (**g**) capacitance retention up to 3500 cycles at 10 A cm^{-3} (inset: charge discharge plots over time). All the experiments were performed with annealed sample (450 C, air, 1 h) (With permission of Upadhyay et al. 2017)

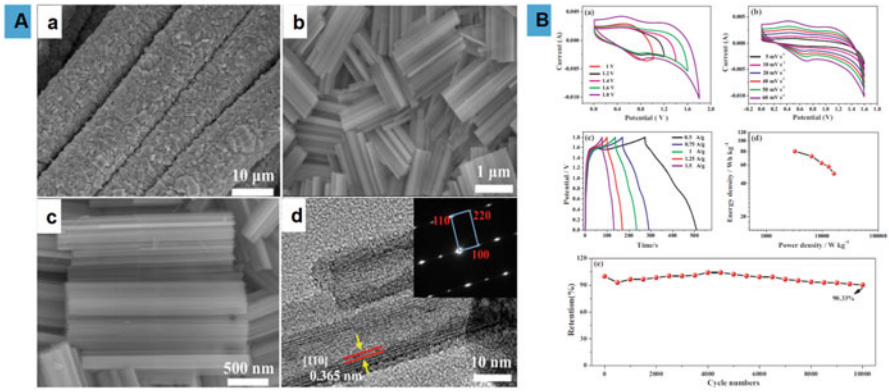

Fig. 6.24 (**a**) SEM and TEM images, (**a**)–(**c**) SEM images of the as-prepared product of WO_3 nanotube bundle, (**d**) the corresponding HRTEM image. (**b**) Electrochemical analysis: (**a**) CV curves in different potential windows at 60 mV s^{-1}, (**b**) CV curves of the as-fabricated ASC device at various scan rates from 5 to 60 mV/s in 1.8 V potential window, (**c**) galvanostatic charging/discharging curves of ASC device at different current densities, (**d**) Ragone plots of ASC device and (**e**) cycling performance at constant specific current of 5 A/g (With permission from Wu and Yao 2017)

The top surface of the layers is homogeneous and shows the open pores, with inner diameter of ca. 10 nm. The cross-sectional SEM images (right) show clearly that the anodic WO_3 has a nanochannel structure, with aligned vertically oriented channels that extend from the top surface of the anodic film to the oxide-metal interface. These channels are open at the top surface and remain open (with inner diameter of ca. 10 nm) across the entire channel length, regardless of the anodic oxide thickness. These layers show remarkable pseudocapacitive behaviour within the potential window of −0.8–0.5 V in 1 M Na_2SO_4 as shown in Fig. 6.23d–g.

A higher capacitance was obtained for the WO_3 structures grown for 2 h when compared to the other samples, i.e. 397 F cm^{-3} at 2 A cm^{-3} in a potential range of 1.3 V, and displayed an excellent capacitance retention up to 3500 cycles at 10 A cm^{-3} as shown in Fig. 6.23g. The cyclic stability showed that the returned 27% of the total capacitance originated from surface adsorption/desorption process, while the remaining 73% originated from a diffusion-controlled process. The WO_3 nanotube bundles made by Wu and co-workers (Wu and Yao 2017) and used as a negative electrode in an asymmetric device against PANI as a positive electrode. As shown in Fig. 6.24a (a–d), the SEM and TEM images revealed the bundles of the WO_3 nanotubes, and the electrochemical performance of the assembled pseudocapacitor device (Fig. 6.24b (a–e) showed that this electrode material could be a potential candidate in energy storage application.

An area capacitance of 2575.3 mF cm^{-2} at a specific current of 3 mA cm^{-2} and a specific capacitance of 615.7 F g^{-1} at a specific current of 1 A g^{-1} were obtained in a three-electrode configuration, respectively. The asymmetrical device fabricated displayed a wide voltage window of 1.8 V from the CV and GCD presented in

Fig. 6.24b (c). A high energy densities of 80.1 W h kg^{-1} and 49.5 W h kg^{-1} were obtained at power densities of 3240 W kg^{-1} and 16,200 W kg^{-1}, respectively.

6.1.2.7 Bismuth Oxide (Bi_xO_y)

Bismuth oxide, Bi_2O_3, also exhibits intrinsic properties such as refractive index, energy bandgap (2.8 eV), dielectric constant and photoconductivity similar to many semiconductors. This metal oxide is suitable for large-range applications such as sensors, catalysis, energy storage and conversion. Recently, this metal oxide has emerged as good electrode material for energy storage applications in SCs due to its high theoretical capacity (690 mAh g^{-1} and 6280 mAh cm^{-3}) and electrochemical stability (Gujar et al. 2006; Liu et al. 2012, 2015b). The structure of the Bi_2O_3 can be described as a sequence of alternating layers of bismuth atoms parallel to the (100) plane of the cell and oxide ions in the c-axis direction (Michel Drache et al. 2007). The electrode made up of Bi_2O_3 thin film grown on copper substrates at room temperature via electrodeposition from an aqueous alkaline nitrate has been fabricated and tested for supercapacitor application by Gujar et al. (2006). The supercapacitor device made from this electrode displayed good electrochemical performance and durability, with specific capacitance of 98 F g^{-1} reported. Similarly, electrode potential oscillations have been used for the synthesis of hierarchical rippled Bi_2O_3 nanobelts, and the electrodes fabricated exhibited excellent stability and electrochemical performance (Zheng et al. 2010). Based on the reported electrochemical energy storage capabilities of Bi_2O_3, there is no doubt that this material has potential for application in SCs. Nevertheless, this metal oxide still suffers from low abundance and poor conductivity and rate capability, thus limiting its application. Due to the mentioned challenges, researchers have explored the use of carbon-based materials with Bi_2O_3 either in composite form or in asymmetric configuration to improve the electrochemical performance of the SC device taking advantage of the properties offered by both materials. Senthilkumar et al. (2014) fabricated asymmetric device based on Bi_2O_3 and activated carbon (AC) in redox additive aqueous electrolyte and achieved remarkable energy density of 35.4 Wh kg^{-1} (Senthilkumar et al. 2014). Ng and co-workers studied Bi_2O_3 temperature effects in a bismuth oxide/manganese oxide (Bi_2O_3/MnO_2) SCs. An improved electrochemical performance was achieved judging from the CV curves shown in Fig. 6.25 for the Bi_2O_3 measured at 60 °C displaying larger area compared to those at 30 and 0 °C, which corresponds to a high specific capacitance of 150.2 F g^{-1} at a scan rate of 2 mV s^{-1}. The increase in capacitance was attributed to the enhanced ion mobility at elevated temperature, which prompted greater charge transfer and storage capability. Furthermore, the evaporation of electrolyte at a high temperature could induce the physisorption of electrolyte ions and give rise to faradaic currents, which enhanced the capacitance performance. The GCD also shown in Fig. 6.25 displayed evidence that the application of temperature stimulated electrochemical activation, leading to high capacitance performance compared to that at 0 °C. The linear voltage−time profiles at 60 °C compared to those at 30 and 0 °C from the prolonged discharge time

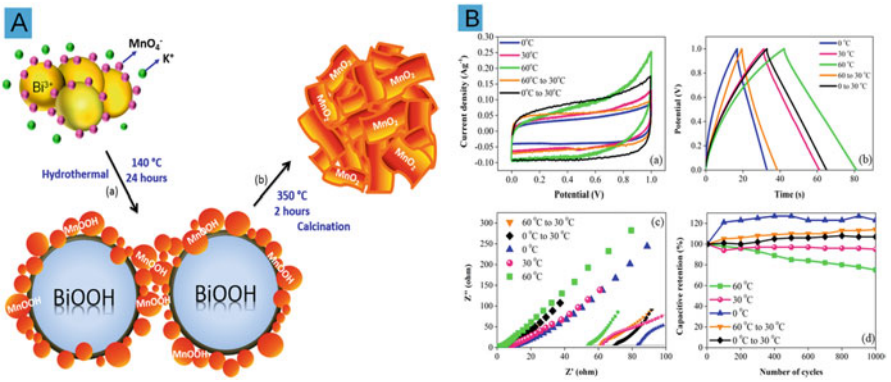

Fig. 6.25 (**a**) Schematic representation of the plausible growth mechanism of Bi_2O_3/MnO_2 on nickel foam substrate during hydrothermal process. (**b**) Electrochemical analysis: (**a**) Cyclic voltammogram, (**b**) galvanostatic charge/discharge, (**c**) Nyquist plot and (**d**) life cycle of Bi_2O_3/MnO_2 supercapacitors at different temperatures. Inset shows the magnified EIS spectra of Bi_2O_3/MnO_2 supercapacitors at different temperatures (With permission of Ng et al. 2018)

indicated a good capacitive behaviour and better charge storage capability at elevated temperature. An energy and power densities of 9.5 Wh kg^{-1} and 102.6 W kg^{-1} were obtained at 60 °C, respectively, which shows a great improvement to values obtained at 0 °C and 30 °C. The Nyquist plot (Fig. 6.25c) shows a slightly higher resistance at 0 °C than that at 30 and lower resistance values at 60 °C which is believed to be due to the expansion of the matrix, which facilitated the diffusion of electrolyte ions. Moreover, the SC device achieved energy densities of 4.9 and 6.9 Wh kg^{-1} and power densities of 53.8 and 74.8 W kg^{-1} at 0 and 30 °C, respectively. The Bi_2O_3/MnO_2 composite exhibited a superior stability retaining 95% of the original capacitance at 30 °C and > 75% at the high temperature of 60 °C (Ng et al. 2018).

The synergistic effect between the Bi_2O_3 and MnO_2 materials enhanced the electrochemical performances of the composite electrodes and dramatically improved the cyclic reversibility, sustainability and stability of the Bi_2O_3/MnO_2 supercapacitor, regardless of the temperature influence. These results showed that the device with a longer defrosting period possessed better electrolyte ion diffusivity, which therefore leads to enhanced capacitive performances and show that the Bi_2O_3 is suitable for use in the automotive sector.

6.1.2.8 Indium Oxide (In_2O_3)

Nanostructured In_2O_3, a transparent conductive oxide with a wide bandgap (Eg∼3.65 eV), has recently attracted attention due to its high electrical conductivity, high optical transmittance and excellent luminescence. Because of these fascinating properties, In_2O_3 has been used for applications such as antireflection coatings

(Wang et al. 2016b), gas sensors (Zheng et al. 2015), lithium–ion batteries (Osiak et al. 2013) and supercapacitors (Bastakoti et al. 2013) and has been produced using different methods such as spray pyrolysis (Korotcenkov et al. 2002), chemical vapour deposition (CVD) (Tuzluca et al. 2017), pulsed laser deposition (PLD), thermal evaporation (Liu et al. 2015a), carbothermal methods (Huang et al. 2007) and hydrothermal synthesis (Padmanathan et al. 2016). The interest in electrochemical capacitors is based on the reversible reaction below (equation xx) which gives rise to high theoretical specific capacity ~580 mAh g^{-1}.

$$\mathrm{In} + \mathrm{xLi}^{+} + \mathrm{xe}^{-} \leftrightarrow \mathrm{Li}_x\mathrm{In}\ (0 \leq x \leq 3) \tag{6.12}$$

The In_2O_3 nanostructures can exhibit different morphologies, which are suitable as electrodes for materials for supercapacitors. For example, 1-D single crystal In_2O_3 nanotowers, nanobouquets, nanocones and nanowires were synthesized using the CVD system over different temperature regions (1000, 900, 800, 700 and 600 °C) as shown in Fig. 6.26. The interests of this work displayed the relationship between the size and shape of In_2O_3 nanostructures to the electrochemical properties. The synthesized materials were explored as electrodes for electrochemical capacitors, and the In_2O_3 nanowires displayed the highest areal capacitance of 16.6 mF cm^{-2} with cycle stability of 66.8% after 10,000 cycles (Tuzluca et al. 2018). The morphology of these various shapes of In_2O_3 nanostructures indicated on FESEM image and line scanning and point EDS analyses of the sample, attesting that nanobouquets had In and O atoms at their main trunks and tips, are shown in Fig. 6.26. As it was also shown, the absence of Au at the tips of nanobouquets designates that the growth mechanism of these nanobouquets is via the growth path rather than the VLS growth pathway.

The electrochemical performance of the In_2O_3 nanostructure presented in Fig. 6.27 displayed the highest areal capacitance value obtained from In_2O_3 nanowires due to the fact that the nanoscale wires have high surface area to volume ratio compared to the nanostructures. The observed result is because electrode materials with nanowire morphology have a higher capacitance and amount of charge storage. It is known that the increase in surface area of an electrode makes ionic diffusion paths to become shorter during reactions due to the synergistic effect arising from both the electrode and electrolyte. Thus, electrode materials with nanowire morphology can increase the electrochemical performance of supercapacitors. The CV and GCD curves (Fig. 6.27b, c) taken in the potential range of 0–0.8 V and 0 to (−0.6) V, respectively, indicated the electrochemical behaviour similar to the ones observed in the literature. Figure 6.27b shows the CV curves of the sample and the bare Si substrate at 10 mV s^{-1} scan rate. An areal capacitance values of 10.1, 5.7, 4.2 and 3.7 mF cm^{-2} were obtained for sample A (nanotowers); 6.7, 4.5, 3.5 and 3 mF cm^{-2} for sample B (nanotowers); 12.5, 10.8, 9.6 and 8.2 mF cm^{-2} for sample C (nanobouquets); 4.9, 4.1, 3 and 2.7 mF cm^{-2} for sample D (nanocones); and 16.6, 14, 12.3 and 11.3 mF cm^{-2} for sample E (nanowires) (Fig. 6.27d) at a specific current of 0.04, 0.06, 0.08 and 0.1 mA cm^{-2}.

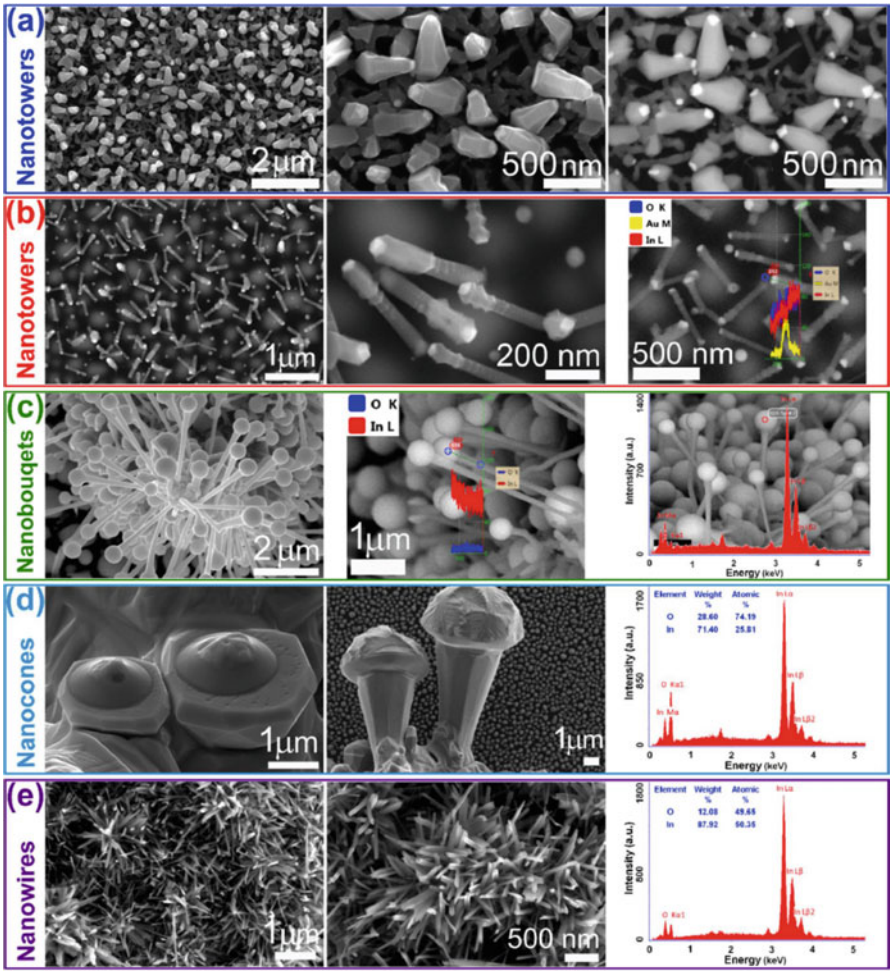

Fig. 6.26 (**a**) Low- and high-magnification FESEM images of In_2O_3 nanotowers grown in sample A and their backscattered electron image; (**b**) low- and high-magnification FESEM images of In_2O_3 nanotowers grown in sample B and their line scanning EDS analysis; (**c**) FESEM images of In_2O_3 nanobouquets grown in sample C and their line scanning and point EDS analyses; (**d**) FESEM images of In_2O_3 nanocones with complete and incomplete growth in sample D and their EDS analysis; (**e**) low- and high-magnification FESEM images of In_2O_3 nanowires grown in sample E and their EDS analysis (With permission of Tuzluca et al. 2018)

As noted, nanostructured and three-dimensional nanorod of In_2O_3 deposited on stainless steel (SS) by a novel potentiodynamic method at a high scan rate of 200 mV s^{-1} exhibited high specific capacitance, high power density and long-term stability when used as active electrode materials for redox supercapacitors

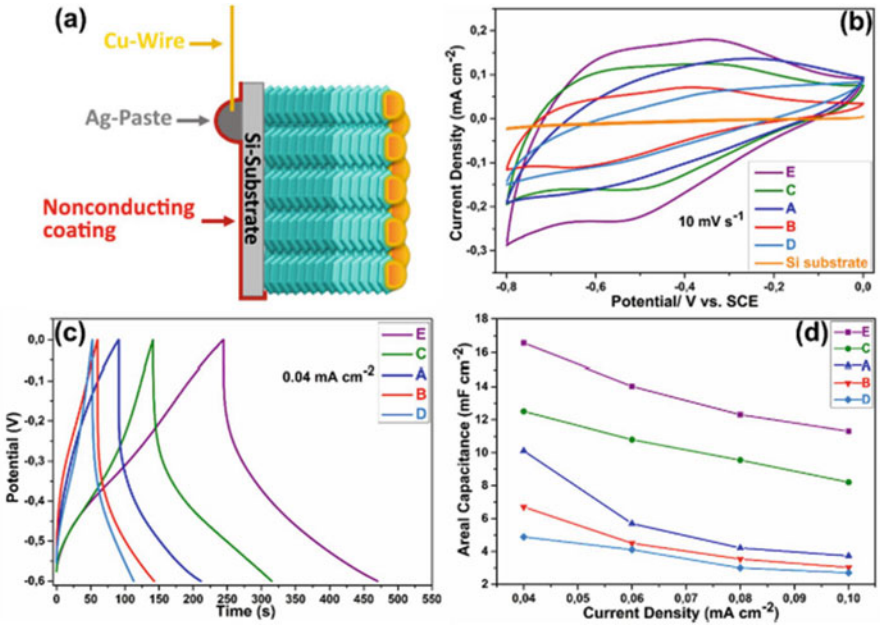

Fig. 6.27 (**a**) The schematic indicating the fabrication process of samples for electrochemical analyses; (**b**) Si substrate material and CV curves of all samples obtained at 10 mV s^{-1}; (**c**) GCD curves of all samples at 0.04 mA cm^{-2}; (**d**) Areal capacitance values of all samples at the current densities of 0.04, 0.06, 0.08, and 0.1 mA cm^{-2} (With permission of Tuzluca et al. 2018)

(Kalakodimi Rajendra Prasad et al. 2004). In_2O_3 nanowires exhibited better electrochemical performance. It is also worth stating that an increase in the surface area of an electrode leads to decrease in the ionic diffusion paths; thus, electrode materials with nanowire morphology can increase the electrochemical performance of supercapacitors.

Carbon-based materials were also used to improve on the electrochemical performance of In_2O_3-based electrodes and have shown great improvements. Fine In_2O_3 nanoparticles were successfully synthesized within the mesopores by thermal decomposition of a metal source. The obtained metal oxide-impregnated mesoporous carbon was effectively utilized for the enhancement of capacitive performance through a combination of both faradaic and non-faradaic processes, and the composite exhibited a high capacitance of 275 F g^{-1} in 1 M Na_2SO_4 (Bastakoti et al. 2013), demonstrating an addition of carbon materials as a strategy to improving energy density of supercapacitors. Table 6.1 summarizes the electrochemical performances of some transition metal oxide-based materials for application in supercapacitors (SCs) obtained from the literature.

Table 6.1 Summary of electrochemical performances of some transition metal oxide-based materials for application in supercapacitors (SCs)

Electrode material	Cell voltage (V)	Cell configuration	Aqueous electrolyte	Specific capacitance	Specific current/scan rate	Energy density (Wh kg^{-1})	Power density (kW kg^{-1})	Capacitance retention	References
RuO_2	1.6	2-electrode, symmetric	1 M Na_2SO_4	53.0 F g^{-1}	0.625 A g^{-1}	18.8	10.0	92% (2000 cycles)	Xia et al. (2012)
RuO_2//MXene	1.5	2-electrode, asymmetric	1 M H_2SO_4	93.0 F g^{-1}	50 mV s^{-1}	29.0	26.0	86% (20 000)	Jiang et al. (2018)
LSG/RuO_2// AC	1.8	2-electrode, asymmetric	1 M Na_2SO_4	8.6 F cm^{-3}	0.5 Acm^{-3}	55.3	81.4	–	Hwang et al. (2015)
RuO_2-Gr	1.5	2-electrode, symmetric	2 M Li_2SO_4	140 F g^{-1}	1.0 A g^{-1}	43.8	37.5	93% (10,000 cycles)	Li and He (2018)
OLC/MnO_2	0.8	2-electrode, symmetric	1 M Na_2SO_4	254 F g^{-1}	0.1 A g^{-1}	5.6	74.8	–	Makgopa et al. (2015)
$MnO_{2(SDS)}$/ GO//GO	1.8	2-electrode, asymmetric	1 M Li_2SO_4	280 F g^{-1}	0.5 A g^{-1}	35.0	7.2	70% (1000 cycles)	Jafta et al. (2013)
GF/MnO_2	1.0	2-electrode, symmetric	1 M Na_2SO_4	240 F g^{-1}	0.1 A g^{-1}	34	20	100% (1000 cycles).	Bello et al. (2013b)
SnO_2/MnO_2	1.0	2-electrode, symmetric	1 M Na_2SO_4	800 F g^{-1}	1 A g^{-1}	35.4	25	99% (2000 cycles)	Yan et al. (2010)
rGO/Mn_2O_3/ Mn_3O_4//rGO	1.4	2-electrode, asymmetric	1 M Na_2SO_4	133 F g^{-1}	0.2 A g^{-1}	9.1	26.4	83% (1000 cycles)	Chidembo et al. (2014)
MnO_2-NW/Gr// Gr	2.0	2-electrode, asymmetric	1 M Na_2SO_4	32.0 F g^{-1}	0.5 A g^{-1}	30.4	5.0	79% (1000 cycles)	Wu et al. (2010)
MnO_2/OLC	0.8	3-electrode	1 M Na_2SO_4	177.5 F g^{-1}	2 A g^{-1}	–	–	101% (1000 cycles)	Wang et al. (2012c)
NW-MnO_2	0.8	3-electrode	Gel electrolyte (3 wt.% SiO_2)	151 F g^{-1}	100 mV s^{-1}	–	–	–	Nam et al. (2010)
MnO_2	1.0	3-electrode	1 M LiOH	317 F g^{-1}	0.1 A g^{-1}	–	–	80% (2000 cycles)	Wang et al. (2007)

$MnO_2.nH_2O$	1.2	3-electrode	2 M KCl	200 F g^{-1}	2 mA/cm^2	–	–	100% (100 cycles)	Lee and Goodenough (1999)
MnO_2/NF-Gr	1.0	3-electrode	1 M Na_2SO_4	305 F g^{-1}	1 A g^{-1}	–	–	80% (1000 cycles)	Bello et al. (2013a)
Birnessite-type MnO_2	0.8	3-electrode	1 M Na_2SO_4	210 F g^{-1}	0.2 A g^{-1}	–	–	98% (300 cycles)	Ming et al. (2012)
α-MnO_2	1.0	3-electrode	1 M Na_2SO_4	146 F g^{-1}	16.0 A g^{-1}	–	–	91% (400 cycles	Meher and Rao (2012)
Mn_3O_4/CNTs	1.0	3-electrode	1 M Na_2SO_4	498 F g^{-1}	5.0 mV s^{-1}	–	–	90% (2000 cycles)	Dubal and Holze (2013)
Porous Mn_3O_4	1.0	3-electrode	1 M Na_2SO_4	233 F g^{-1}	0.5 A g^{-1}	–	–	78% (5000 cycles)	Yang et al. (2015)
Mn_3O_4/MC	1.0	3-electrode	6 M KOH	266 F g^{-1}	1.0 mV s^{-1}	–	–	74% (1000 cycles)	Zhou et al. (2011)
Gr/Mn_3O_4	1.0	3-electrode	1 M Na_2SO_4	121 F g^{-1}	0.5 A g^{-1}	–	–	100% (10,000 cycles)	Lee et al. (2012)
Mn_3O_4/Gr	0.9	3-electrode	2 M KOH	237 F g^{-1}	1.0 A g^{-1}	12.0	5.4	93.68% (1000 cycles)	Wang et al. (2012)
Mn_2O_3	0.8	3-electrode	0.5 M Na_2SO_4	191 F g^{-1}	0.1 A g^{-1}	–	–	108% (3000 cycles)	Li et al. (2015)
Mn_3O_4/OLC	2.0	2-electrode, asymmetric	1 M Na_2SO_4	–	–	19.0	45.0	–	Makgopa et al. (2017)
NiO//Fe_2O_3/CFP	1.35	2-electrode, asymmetric	2 M KOH	908 F g^{-1}	2 A g^{-1}	105	12.7	–	Tang et al. (2015)
Fe_3O_4	0.7	3-electrode	1 M Na_2SO_3	170 F g^{-1}	2.0 mV s^{-1}	–	–	–	Wang et al. (2006)
Fe_3O_4/Carbon	1.0	3-electrode	1 M KOH	139 F g^{-1}	0.5 A g^{-1}	–	–	83.3% (4000 cycles)	Meng et al. (2014)
	1.0	3-electrode	1 M Na_2SO_3	165 F g^{-1}	0.2 A g^{-1}	–	–		

(continued)

Table 6.1 (continued)

Electrode material	Cell voltage (V)	Cell configuration	Aqueous electrolyte	Specific capacitance	Specific current/scan rate	Energy density (Wh kg^{-1})	Power density (kW kg^{-1})	Capacitance retention	References
Fe_3O_4/MWCNT								85.1% (1000 cycles)	Kim and Park (2011)
SiCF/Fe_3O_4	1.2	3-electrode	1 M KOH	423 F g^{-1}	5 mV s^{-1}	–	–	90.3% (5000 cycles)	Kim and Kim (2017)
GF/CNT@Fe_2O_3//GF/$CoMoO_4$	1.6	2-electrode, asymmetric	2 M KOH	210 F g^{-1}	–	74.7	11.2	95.4% (50,000 cycles)	Guan et al. (2015)
V_2O_5/TiO_2-NT	0.8	3-electrode	0.1 M $HClO_4$	220 F g^{-1}	0.2 mA/cm^2	19.56	–	–	Yang et al. (2011b)
V_2O_5-NW	1.2	3-electrode	1 M $LiNO_3$	351 F g^{-1}	2 A g^{-1}	–	–	–	Wang et al. (2015)
V_2O_5/PPY	1.0	3-electrode	5 M $LiNO_3$	559 F g^{-1}	3 A g^{-1}	–	–	70% (100 cycles.)	Yang et al. (2013)
3D V_2O_5	2.0	2-electrode, symmetric	1 M Na_2SO_4	451 F g^{-1}	0.5 A g^{-1}	107	9.4	90% (4000 cycles)	Zhu et al. (2013)
V_2O_5	0.9	2-electrode, symmetric	2 M KCl	190 F g^{-1}	0.1 A g^{-1}	578	−1.8	–	Wee et al. (2010)
	3.0		1 M $LiClO_4$ in PC	250 F g^{-1}					
V_2O_5/PANI	2.0	2-electrode, symmetric	5 M LiCl	412 F g^{-1}	4.5 mA/cm^2	82	0.8	80% (5000 cycles)	Bai et al. (2014)
VO/VO_x/CNF	1.0	2-electrode, symmetric	6 M KOH	326 F g^{-1}	1 A g^{-1}	10	0.96	92% (5000 cycles)	Tang et al. (2016)
2D VO_2-NS	1.4	2-electrode, symmetric	1 M $LiClO_4$ in PC	405 F g^{-1}	1 A g^{-1}	46	1.4	95% (6000 cycles)	Rakhi et al. (2016)
Gr/VO_2//Gr	1.7	2-electrode, asymmetric	0.5 M K_2SO_4	225 F g^{-1}	–	22.8	8.5	81% (1000 cycles)	Deng et al. (2013)

SnO_2/rGO	1.0	3-electrode,	1 M H_2SO_4	348 F g^{-1}	0.5 A g^{-1}	32.2	1.0	–	Hsieh et al. (2014)
SnO_2/Ti_3C_2	0.7	3-electrode	6 M KOH	126 F g^{-1}	1 A g^{-1}	–	–	82% (8000 cycles)	Zheng et al. (2017)

Key: *Gr* graphene, *NF* nickel foam, *GF* graphene foam, *CNT* carbon nanotube, *MWCNT* multi-walled carbon nanotube, *OLCs* onion-like carbons, *PDDA* polydiallyldimethylammonium, *rG* reduced graphene, *MC* mesoporous carbon, *CFP* carbon fibre paper, *CNF* carbon nanofibre

6.2 Summary and Future Prospects

It is evident that significant progress has been made in SC applications, which has generated worldwide attention in these energy storage/conversion devices due to the need to resolve high demands for clean and sustainable energy followed by the fact that fossil fuels have shown potential threat to the environment and thereby deemed unreliable. The advantages of SC systems account to their high power density, high efficiency and long-life expectancy. However, the development of these energy storage devices depends upon the innovative ways of fine-tuning their electrode materials. Metal oxide nanostructured materials with their interesting properties such as low cost, good electrochemical response, various oxidation states and availability have proven themselves as attractive electrode materials for energy storage applications since they can be easily synthesized from various synthetic routes even though their synthesis and application are still restricted to the lab-scale production. Much of the limitation of the use of metal-oxides in SCs could be attributed to the low conductivity and agglomeration upon rapid cycling, which limits their electrochemical performance to match their theoretical estimation, thus hindering their commercial applications. Intensive work has been devoted in mitigating the above limitation by incorporation of highly conductive materials such as carbon allotropes and recently MXENES to make composite materials with an improved electrochemical performance and stability upon long-time cycling. The approach of discovering new materials that boosts the properties of metal oxides has drastically improved the rapid use of these nanostructured materials as EC electrode materials. Therefore, the innovation that further improves the existing metal oxide electrodes while also promoting their novel composites that results in stable fabrication in order to meet the market demand of EC technology is of great importance. From the literature and data presented in this work, it is very clear that the performance of metal-based oxides for supercapacitor applications has increased exponentially over the last decade and continues to improve. Specific capacitance, energy and power density values continue to improve, while the storage mechanisms of most of the oxide-based supercapacitors continue to be widely studied and understood. Efforts to produce SCs from renewable materials also encourage optimism that such an environmentally friendly option may soon be feasible for use on a larger scale. Currently, supercapacitors are being used for some small applications, and with the rapid improvement of their energy densities, it is only a matter of time before their industrial applications become common. The future of supercapacitor research is endlessly promising; however, there are certain things that should be taken into account in order to ensure that all future research can be used fully. One of the challenges is that results are communicated in multiple different ways, and this can make it difficult to compare different studies. Most studies choose to express their results in terms of specific capacitance, $F \cdot g^{-1}$, measured at different scan rates, $mV \cdot s^{-1}$ and/ or specific current, $A \cdot g^{-1}$. Some papers, however, choose to express

specific current in $mA \cdot cm^{-2}$, and specific capacitance in $mF \cdot cm^{-2}$, making it difficult to compare the performance of the subject material to that of others in the literature when additional information, such as the density of the material, is not provided. However, F/cm^2 is justified while the mass of electrode materials is beyond the measurable limit and as well for micro-supercapacitor. Therefore, it is recommended that for future studies, a standard be developed for such aspects of the research so that all materials may be accurately compared. The recent upsurge in the quantity of research carried out on the various oxide-based supercapacitors, as well as the quality of SCs being produced, has well-established their position in the field of energy storage. In order to fully succeed on the generation of the reliable, efficient and effective technology that can mitigate the global energy demand, more conductive materials obtained from different sources and various synthetic routes should be explored and be incorporated on these metal oxides. Another major drawback in the development of supercapacitor technology is the relatively high cost associated with it when compared to other energy devices. Thus, future research should be invested towards the development of fascinating transition metal oxide nanomaterials exhibiting a high charge capacity while demonstrating a minimum electronic and electrolytic resistance in a very cost-effective manner. As research advances, and improvements continue to be made, it is certain that the future held for supercapacitors is an auspicious one.

Appendix

Potentiostat – A potentiostat is the electronic hardware required to control electrochemical cell and run most electroanalytical experiments.

Cell potential – The overall electrical potential of an electrochemical cell. It is the sum of the reduction potential of the cathode and the oxidation potential of the anode.

Electrolytic cell – A cell that consumes electrical energy to drive a non-spontaneous redox reaction.

Charge (Q) – The quantity of unbalanced electricity in a body such as an electron or an ion.

Charge density (q) – The measure of charge Q and electrode area A, i.e. $q = Q/A$.

Chronoamperometry – The techniques and methodology of studying current as a function of time.

Current (I) – The rate of charge flow or passage, i.e. $I = (dQ/dt)$.

Specific current – The measure of current I and electrode mass g, i.e. $i = I/g$.

Cyclic voltammogram (CV) – A plot of current on the y-axis against potential on the x-axis during a voltammetric experiment in which the potential is ramped twice, once forward to the switch potential and then back again.

Electrochemical area – The area of an electrode; the area that an electrode is 'perceived' to have.

Electrochemical cell – An electrochemical cell typically consists of two electronic conductors (also called electrodes) – An ionic conductor (called an electrolyte).

Electrode – A conductor employed either to determine an electrode potential (at zero current, i.e. for potentiometric experiments) or to determine current during a dynamic electroanalytical measurement. The electronic conductivity of most electrodes is metallic.

A reaction is classified as oxidation or reduction depending on the direction of electron transfer. There are two fundamental types of half-cell reactions: – Oxidation reactions – Reduction reactions

Oxidation – Involves the loss of an electron and involves the transfer of electrons from the species to the electrode $R = O + ne$

Reduction – Involves the gain of an electron and involves the transfer of electrons from the electrode to the species $O + ne = R$.

Electrode at which the oxidation reaction occurs is called the anode.

Electrode at which the reduction reaction occurs is called the cathode.

Anodic current – An anodic current is the flow of electrical charge (usually carried by electrons) into a working electrode from a second phase (usually an electrolyte solution) as a result of the oxidation of one or more species in the second phase.

Cathodic current – A cathodic current is the flow of electrical charge (usually carried by electrons) out of a working electrode into a second phase (usually an electrolyte solution) leading to the reduction of one or more species in the second phase.

The electrode at which the reaction of interest occurs is called the working electrode.

The electrode at which the other (coupled) reaction occurs is called the counter electrode.

A third electrode, called the reference electrode, may also be used. An ideal reference electrode is one that maintains a constant potential irrespective of the amount of current (if any) that is passed through it.

Electrode potential – The electrode potential for a reaction is derived directly from the free energy change for that reaction $\Delta G = -NFE$. The standard oxidation potential is equal in magnitude but opposite in sign to the std. reduction potential.

Electrolyte – An ionic salt to be dissolved in a solvent or the solution formed by dissolving an ionic salt in a solvent.

Electrolytic processes – Reactions in which chemical changes occur on the passage of an electrical current.

Galvanic or voltaic processes – Chemical reactions that result in the production of electrical energy.

References

An G, Yu P, Xiao M et al (2008) Low-temperature synthesis of Mn_3O_4 nanoparticles loaded on multi-walled carbon nanotubes and their application in electrochemical capacitors. Nanotechnology 19:275709. https://doi.org/10.1088/0957-4484/19/27/275709

Arlinghaus FJ (1974) Energy bands in stannic oxide (SnO_2). J Phys Chem Solids 35:931–935. https://doi.org/10.1016/S0022-3697(74)80102-2

Augustyn V, Come J, Lowe MA et al (2013) High-rate electrochemical energy storage through Li^+ intercalation pseudocapacitance. Nat Mater 12:518–522. https://doi.org/10.1038/nmat3601

Augustyn V, Simon P, Dunn B (2014) Pseudocapacitive oxide materials for high-rate electrochemical energy storage. Energy Environ Sci 7:1597. https://doi.org/10.1039/c3ee44164d

Bai MH, Bian LJ, Song Y, Liu XX (2014) Electrochemical codeposition of vanadium oxide and polypyrrole for high-performance supercapacitor with high working voltage. ACS Appl Mater Interfaces 6:12656–12664. https://doi.org/10.1021/am502630g

Bang H, Ellinger AE, Hadjimarcou J, Traichal PA (2000) Consumer concern, knowledge, belief, and attitude toward renewable energy: an application of the reasoned action theory. Psychol Mark 17:449–468

Bastakoti BP, Oveisi H, Hu C-C et al (2013) Mesoporous carbon incorporated with In_2O_3 nanoparticles as high-performance supercapacitors. Eur J Inorg Chem 2013:1109–1112. https://doi.org/10.1002/ejic.201201311

Baykal A, Kavas H, Durmuş Z et al (2010) Sonochemical synthesis and chracterization of Mn_3O_4 nanoparticles. Cent Eur J Chem 8:633–638. https://doi.org/10.2478/s11532-010-0037-8

Béguin F, Raymundo-Piñero E, Frackowiak E (2009) Electrical double-layer capacitors and pseudocapacitors. CRC Press, Boca Raton

Béguin F, Presser V, Balducci A, Frackowiak E (2014) Carbons and electrolytes for advanced supercapacitors. Adv Mater 26:2219–2251., 2283. https://doi.org/10.1002/adma.201304137

Bello A, Fashedemi OO, Fabiane M et al (2013a) Microwave assisted synthesis of MnO_2 on nickel foam-graphene for electrochemical capacitor. Electrochim Acta 114:48. https://doi.org/10.1016/j.electacta.2013.09.134

Bello A, Fashedemi OO, Lekitima JN et al (2013b) High-performance symmetric electrochemical capacitor based on graphene foam and nanostructured manganese oxide. AIP Adv 3:82118

Bonu V, Gupta B, Chandra S et al (2016) Electrochemical supercapacitor performance of SnO_2 quantum dots. Electrochim Acta 203:230–237. https://doi.org/10.1016/J.ELECTACTA.2016.03.153

Borgohain R, Selegue JP, Cheng Y-T (2014) Ternary composites of delaminated-MnO_2 /PDDA/functionalized-CNOs for high-capacity supercapacitor electrodes. J Mater Chem A 2:20367–20373. https://doi.org/10.1039/C4TA04439H

Brousse T, Toupin M, Dugas R et al (2006) Crystalline MnO_2 as possible alternatives to amorphous compounds in electrochemical supercapacitors. J Electrochem Soc 153:A2171. https://doi.org/10.1149/1.2352197

Burda C, Chen X, Narayanan R, El-Sayed MA (2005) Chemistry and properties of nanocrystals of different shapes. Chem Rev 105:1025–1102

Burke A (2000) Ultracapacitors: why, how, and where is the technology. J Power Sources 91:37–50. https://doi.org/10.1016/S0378-7753(00)00485-7

Burke A, Liu Z, Zhao H (2014, December) Present and future applications of supercapacitors in electric and hybrid vehicles. https://doi.org/10.1109/IEVC.2014.7056094 Conference: IEEE International Electric Vehicle Conference 2014, Florence 17–19

Bykova E, Dubrovinsky L, Dubrovinskaia N et al (2016) Structural complexity of simple Fe_2O_3 at high pressures and temperatures. Nat Commun 7:10661. https://doi.org/10.1038/ncomms10661

Cao L, Zhu J, Li Y et al (2014) Ultrathin single-crystalline vanadium pentoxide nanoribbon constructed 3D networks for superior energy storage. J Mater Chem A 2:13136–13142. https://doi.org/10.1039/C4TA02229G

Chang J, Lee W, Mane RS et al (2008) Morphology-dependent electrochemical supercapacitor properties of indium oxide. Electrochem Solid-State Lett 11:A9. https://doi.org/10.1149/1.2805996

Chen Z, Zhang S, TAn S et al (1997) Preparation and electron spin resonance effect of nanometer-sized Mn_2O_3. J Cryst Growth 180:280–283. https://doi.org/10.1016/S0022-0248(97)00215-7

Chen X, Li X, Jiang Y et al (2005) Rational synthesis of MnO_2 and Mn_2O_3 nanowires with the electrochemical characterization of MnO_2 nanowires for supercapacitor. Solid State Commun 136:94–96. https://doi.org/10.1016/j.ssc.2005.06.033

Chen Z, Qin Y, Weng D et al (2009) Design and synthesis of hierarchical nanowire composites for electrochemical energy storage. Adv Funct Mater 19:3420–3426. https://doi.org/10.1002/adfm.200900971

Chen JS, Archer LA, Wen (David) Lou X (2011a) SnO_2 hollow structures and TiO_2 nanosheets for lithium-ion batteries. J Mater Chem 21:9912. https://doi.org/10.1039/c0jm04163g

Chen Z, Augustyn V, Wen J et al (2011b) High-performance supercapacitors based on intertwined CNT/V_2O_5 nanowire nanocomposites. Adv Mater 23:791–795. https://doi.org/10.1002/adma.201003658

Cheng H-W, Zhou C, Mai L et al (2008) Field emission from $V_2O_5nH_2O$ Nanorod arrays. J Phys Chem C 112:2262–2265. https://doi.org/10.1021/JP0766151

Chiang NK, Clokec M, Chena GZ et al (2006) Nano-sized Mn_2O_3 preparedby a novel solvolysis route as an electrochemical capacitor. Inst Eng Malaysia 69:31–36

Chidembo AT, Aboutalebi SH, Konstantinov K et al (2014) In situ engineering of urchin-like reduced graphene oxide–Mn_2O_3–Mn_3O_4 nanostructures for supercapacitors. RSC Adv 4:886–892. https://doi.org/10.1039/c3ra44973d

Choi D, Blomgren GE, Kumta PN (2006) Fast and reversible surface redox reaction in nanocrystalline vanadium nitride supercapacitors. Adv Mater 18:1178–1182

Conway BE (1999) Electrochemical supercapacitors: scientific fundamentals and technological applications. Kluwer Academic/Plenum, New York

Cottineau T, Toupin M, Delahaye T et al (2006) Nanostructured transition metal oxides for aqueous hybrid electrochemical supercapacitors. Appl Phys A Mater Sci Process 82:599–606

Deb SK (2008) Opportunities and challenges in science and technology of WO_3 for electrochromic and related applications. Sol Energy Mater Sol Cells 92:245–258. https://doi.org/10.1016/J.SOLMAT.2007.01.026

Deng L, Zhang G, Kang L et al (2013) Graphene/VO_2 hybrid material for high performance electrochemical capacitor. Electrochim Acta 112:448–457. https://doi.org/10.1016/J.ELECTACTA.2013.08.158

Djurfors B, Broughton JN, Brett MJ, Ivey DG (2005) Electrochemical oxidation of Mn/MnO films: formation of an electrochemical capacitor. Acta Mater 53:957–965. https://doi.org/10.1016/j.actamat.2004.10.041

Dong R, Ye Q, Kuang L et al (2013) Enhanced supercapacitor performance of Mn_3O_4 nanocrystals by doping transition-metal ions. ACS Appl Mater Interfaces 5:9508–9516

Drache M, Roussel P, Wignacourt J-P (2007) Structures and oxide mobility in Bi−Ln−O materials: heritage of Bi_2O_3. Chem Rev 107:80–96. https://doi.org/10.1021/CR050977S

Du Y, Yan J, Meng Q et al (2012) Fabrication and excellent conductive performance of antimony-doped tin oxide-coated diatomite with porous structure. Mater Chem Phys 133:907–912. https://doi.org/10.1016/J.MATCHEMPHYS.2012.01.115

Dubal DP, Holze R (2013) A successive ionic layer adsorption and reaction (SILAR) method to induce Mn_3O_4 nanospots on CNTs for supercapacitors. New J Chem 37:403–408. https://doi.org/10.1039/c2nj40862g

Dubal DP, Dhawale DS, Salunkhe RR et al (2009) A novel chemical synthesis of interlocked cubes of hausmannite Mn_3O_4 thin films for supercapacitor application. J Alloys Compd 484:218–221. https://doi.org/10.1016/j.jallcom.2009.03.135

Dubal DP, Dhawale DS, Salunkhe RR et al (2010) Chemical synthesis and characterization of Mn_3O_4 thin films for supercapacitor application. J Alloys Compd 497:166–170. https://doi.org/10.1016/j.jallcom.2010.02.182

Fan D, Yang P (1999) Introduction to and classification of manganese deposits of China. Ore Geol Rev 15:1–13

Gao W, Ye S, Shao M (2011) Solution-combusting preparation of mono-dispersed Mn_3O_4 nanoparticles for electrochemical applications. J Phys Chem Solids 72:1027–1031. https://doi.org/10.1016/j.jpcs.2011.05.015

Ghosh A, Lee YH (2012) Carbon-based electrochemical capacitors. ChemSusChem 5:480–499. https://doi.org/10.1002/cssc.201100645

Ghosh S, Gupta B, Ganesan K et al (2016) MnO_2-vertical graphene nanosheets composite electrodes for energy storage devices. Mater Today Proc 3:1686–1692. https://doi.org/10.1016/J.MATPR.2016.04.060

Ghosh S, Jeong SM, Polaki SR (2018) A review on metal nitrides/oxynitrides as an emerging supercapacitor electrode beyond oxide. Korean J Chem Eng 35:1389–1408. https://doi.org/10.1007/s11814-018-0089-6

Greenwood N (1997) Chemistry of the elements, 2nd edn. Heinemann, Butterworth

Guan C, Liu J, Wang Y et al (2015) Iron oxide-decorated carbon for supercapacitor anodes with ultrahigh energy density and outstanding cycling stability. ACS Nano 9:5198–5207. https://doi.org/10.1021/acsnano.5b00582

Gujar TP, Shinde VR, Lokhande CD, Han S-H (2006) Electrosynthesis of Bi_2O_3 thin films and their use in electrochemical supercapacitors. J Power Sources 161:1479–1485. https://doi.org/10.1016/J.JPOWSOUR.2006.05.036

Gustafson KPJ, Shatskiy A, Verho O et al (2017) Water oxidation mediated by ruthenium oxide nanoparticles supported on siliceous mesocellular foam. Cat Sci Technol 7:293–299. https://doi.org/10.1039/C6CY02121B

Hatzell KB, Fan L, Beidaghi M et al (2014) Composite manganese oxide percolating networks as a suspension electrode for an asymmetric flow capacitor. ACS Appl Mater Interfaces 6:8886–8893. https://doi.org/10.1021/am501650q

Hatzell KB, Boota M, Kumbur EC, Gogotsi Y (2015) Flowable conducting particle networks in redox-active electrolytes for grid energy storage. J Electrochem Soc 162:A5007–A5012. https://doi.org/10.1149/2.0011505jes

He W, Zhang Y, Zhang X et al (2003) Low temperature preparation of nanocrystalline Mn_2O_3 via ethanol-thermal reduction of MnO_2. J Cryst Growth 252:285–288. https://doi.org/10.1016/S0022-0248(03)00937-0

Hou X, Liu B, Wang X et al (2013) SnO_2-microtube-assembled cloth for fully flexible self-powered photodetector nanosystems. Nanoscale 5:7831. https://doi.org/10.1039/c3nr02300a

Hsieh C-T, Lee W-Y, Lee C-E, Teng H (2014) Electrochemical capacitors fabricated with tin oxide/graphene oxide nanocomposites. J Phys Chem C 118:15146–15153. https://doi.org/10.1021/jp502958w

Hu C, Tsou T (2002) Ideal capacitive behavior of hydrous manganese oxide prepared by anodic deposition. Electrochem Commun 4:105–109

Hu C-C, Chang K-H, Lin M-C, Wu Y-T (2006) Design and tailoring of the nanotubular arrayed architecture of hydrous RuO_2 for next generation supercapacitors. Nano Lett 6:2690–2695

Huang Z, Chai C, Tan X et al (2007) Photoluminescence properties of the In_2O_3 octahedrons synthesized by carbothermal reduction method. Mater Lett 61:5137–5140. https://doi.org/10.1016/J.MATLET.2007.04.062

Hui-Chi Chiu C-SY (2007) Hydrothermal synthesis of SnO_2 nanoparticles and their gas-sensing of alcohol. J Phys Chem C 111:7256–7259. https://doi.org/10.1021/JP0688355

Hwang JY, El-Kady MF, Wang Y et al (2015) Direct preparation and processing of graphene/RuO_2 nanocomposite electrodes for high-performance capacitive energy storage. Nano Energy 18:57–70. https://doi.org/10.1016/j.nanoen.2015.09.009

IEA (2014) With projections to 2040. In: Int. Energy Outlook 2014

Jafta CJ, Nkosi F, le Roux L et al (2013) Manganese oxide/graphene oxide composites for high-energy aqueous asymmetric electrochemical capacitors. Electrochim Acta 110:228–233. https://doi.org/10.1016/j.electacta.2013.06.096

Jiang J, Kucernak A (2002) Electrochemical supercapacitor material based on manganese oxide: preparation and characterization. Electrochim Acta 47:2381–2386. https://doi.org/10.1016/S0013-4686(02)00031-2

Jiang H, Lee PS, Li C (2013) 3D carbon based nanostructures for advanced supercapacitors. Energy Environ Sci 6:41–53

Jiang Q, Kurra N, Alhabeb M et al (2018) All pseudocapacitive MXene-RuO_2 asymmetric supercapacitors. Adv Energy Mater 1703043:1703043. https://doi.org/10.1002/aenm.201703043

Jo C, Hwang I, Lee J et al (2011) Investigation of pseudocapacitive charge-storage behavior in highly conductive ordered mesoporous tungsten oxide electrodes. J Phys Chem C 115:11880–11886. https://doi.org/10.1021/jp2036982

Johan E. ten Elshof, Yuan H, Gonzalez Rodriguez P (2016) Two-dimensional metal oxide and metal hydroxide nanosheets: synthesis, controlled assembly and applications in energy conversion and storage. Adv Energy Mater 6:1600355. https://doi.org/10.1002/aenm.201600355

Kawasaki BS, Garside BK, Shewchun J (1970) Electron beam luminescence of SnO_2. Proc IEEE 58:179–180. https://doi.org/10.1109/PROC.1970.7583

Kim M, Kim J (2017) Synergistic interaction between pseudocapacitive Fe_3O_4 nanoparticles and highly porous silicon carbide for high-performance electrodes as electrochemical supercapacitors. Nanotechnology 28:195401. https://doi.org/10.1088/1361-6528/aa6812

Kim Y-T, Mitani T (2006) Oxidation treatment of carbon nanotubes: an essential process in nanocomposite with RuO_2 for supercapacitor electrode materials. Appl Phys Lett 89:033107. https://doi.org/10.1063/1.2221872

Kim Y-H, Park S-J (2011) Roles of nanosized Fe_3O_4 on supercapacitive properties of carbon nanotubes. Curr Appl Phys 11:462–466. https://doi.org/10.1016/J.CAP.2010.08.018

Kim HW, Shim SH, Lee C (2006) SnO2 microparticles by thermal evaporation and their properties. Ceram Int 32:943–946. https://doi.org/10.1016/J.CERAMINT.2005.06.015

Korotcenkov G, Brinzari V, Cerneavschi A et al (2002) Crystallographic characterization of In2O3 films deposited by spray pyrolysis. Sensors Actuators B Chem 84:37–42. https://doi.org/10.1016/S0925-4005(02)00008-4

Lee HY, Goodenough JBJB (1999) Supercapacitor behavior with KCl electrolyte. J Solid State Chem 144:220–223. https://doi.org/10.1006/jssc.1998.8128

Lee JW, Hall AS, Kim J-D, Mallouk TE (2012) A facile and template-free hydrothermal synthesis of Mn_3O_4 Nanorods on graphene sheets for supercapacitor electrodes with long cycle stability. Chem Mater 24:1158–1164. https://doi.org/10.1021/cm203697w

Li M, He H (2018) Nickel-foam-supported ruthenium oxide/graphene sandwich composite constructed via one-step electrodeposition route for high-performance aqueous supercapacitors. Appl Surf Sci 439:612–622. https://doi.org/10.1016/j.apsusc.2018.01.064

Li Y, Yao J, Uchaker E et al (2013) Leaf-like V_2O_5 Nanosheets fabricated by a facile green approach as high energy cathode material for Lithium-ion batteries. Adv Energy Mater 3:1171–1175. https://doi.org/10.1002/aenm.201300188

Li W, Shao J, Liu Q et al (2015) Facile synthesis of porous Mn_2O_3 nanocubics for high-rate supercapacitors. Electrochim Acta 157:108–114. https://doi.org/10.1016/j.electacta.2015.01.056

Li Q, Zheng S, Xu Y et al (2018) Ruthenium based materials as electrode materials for supercapacitors. Chem Eng J 333:505–518. https://doi.org/10.1016/j.cej.2017.09.170

Liu F-A, Yang Y-C, Liu J et al (2012) Preparation of Bi_2O_3@Bi_2S_3 core–shell nanoparticle assembled thin films and their photoelectrochemical and photoresponsive properties. J Electroanal Chem 665:58–62. https://doi.org/10.1016/J.JELECHEM.2011.11.015

Liu Y, Jiao Y, Zhang Z et al (2014) Hierarchical SnO_2 nanostructures made of intermingled ultrathin nanosheets for environmental remediation, smart gas sensor, and supercapacitor applications. ACS Appl Mater Interfaces 6:2174–2184. https://doi.org/10.1021/am405301v

Liu J, Huang S, He L (2015a) Metal-catalyzed growth of In_2O_3 nanotowers using thermal evaporation and oxidation method. J Semicond 36:123007. https://doi.org/10.1088/1674-4926/36/12/123007

Liu T, Zhao Y, Gao L, Ni J (2015b) Engineering Bi_2O_3-Bi_2S_3 heterostructure for superior lithium storage. Sci Rep 5:9307. https://doi.org/10.1038/srep09307

Liu Y, Wei J, Tian Y, Yan S (2015c) The structure–property relationship of manganese oxides: highly efficient removal of methyl orange from aqueous solution. J Mater Chem A 3:19000–19010. https://doi.org/10.1039/C5TA05507E

Luo J, Liu J, Zeng Z et al (2013) Three-dimensional graphene foam supported Fe_3O_4 lithium battery anodes with long cycle life and high rate capability. Nano Lett 13:6136–6143. https://doi.org/10.1021/nl403461n

Ma S-B, Nam K-W, Yoon W-S et al (2008) Electrochemical properties of manganese oxide coated onto carbon nanotubes for energy-storage applications. J Power Sources 178:483–489. https://doi.org/10.1016/j.jpowsour.2007.12.027

Makgopa K, Ejikeme PM, Jafta CJ et al (2015) A high-rate aqueous symmetric pseudocapacitor based on highly graphitized onion-like carbon/birnessite-type manganese oxide nanohybrids. J Mater Chem A 3:3480–3490

Makgopa K, Ejikeme PM, Ozoemena KI (2016) Nanostructured manganese oxides in supercapacitors. In: KOzoemena KI, Chen S (eds) Nanomaterials in advanced batteries and supercapacitors. Springer, New York, pp 345–376

Makgopa K, Raju K, Ejikeme PM, Ozoemena KI (2017) High-performance Mn_3O_4/onion-like carbon (OLC) nanohybrid pseudocapacitor: unravelling the intrinsic properties of OLC against other carbon supports. Carbon 117:20–32. https://doi.org/10.1016/j.carbon.2017.02.050

Manikandan K, Dhanuskodi S, Maheswari N, Muralidharan G (2016) SnO_2 nanoparticles for supercapacitor application. In: AIP conference proceedings. AIP Publishing LLC, p 050048

Meher SK, Rao GR (2012) Enhanced activity of microwave synthesized hierarchical MnO_2 for high performance supercapacitor applications. J Power Sources 215:317–328. https://doi.org/10.1016/J.JPOWSOUR.2012.04.104

Meng W, Chen W, Zhao L et al (2014) Porous Fe_3O_4/carbon composite electrode material prepared from metal-organic framework template and effect of temperature on its capacitance. Nano Energy 8:133–140. https://doi.org/10.1016/J.NANOEN.2014.06.007

Miller JM (1997) Deposition of ruthenium nanoparticles on carbon aerogels for high energy density supercapacitor electrodes. J Electrochem Soc 144:L309. https://doi.org/10.1149/1.1838142

Miller JRJ, Burke AFA (2008) Electrochemical capacitors: challenges and opportunities for real-world applications. Electrochem Soc Interface 17:53

Min J, Kierzek K, Chen X et al (2017) Facile synthesis of porous iron oxide/graphene hybrid nanocomposites and potential application in electrochemical energy storage. New J Chem 41:13553–13559. https://doi.org/10.1039/C7NJ03416D

Ming B, Li J, Kang F et al (2012) Microwave–hydrothermal synthesis of birnessite-type MnO_2 nanospheres as supercapacitor electrode materials. J Power Sources 198:428–431. https://doi.org/10.1016/j.jpowsour.2011.10.003

Mitchell E, Gupta RK, Mensah-Darkwa K et al (2014) Facile synthesis and morphogenesis of superparamagnetic iron oxide nanoparticles for high-performance supercapacitor applications. New J Chem 38:4344–4350. https://doi.org/10.1039/C4NJ00741G

Nagarajan N, Humadi H, Zhitomirsky I (2006) Cathodic electrodeposition of MnO_x films for electrochemical supercapacitors. Electrochim Acta 51:3039–3045. https://doi.org/10.1016/j.electacta.2005.08.042

Nam HS, Kwon JS, Kim KM et al (2010) Supercapacitive properties of a nanowire-structured MnO_2 electrode in the gel electrolyte containing silica. Electrochim Acta 55:7443–7446. https://doi.org/10.1016/j.electacta.2010.02.027

Nathan T, Cloke M, Prabaharan SRS (2008) Electrode properties of Mn2O3 nanospheres synthesized by combined sonochemical/solvothermal method for use in electrochemical capacitors. J Nanomater 1: https://doi.org/10.1155/2008/948183

Ng CH, Lim HN, Hayase S et al (2018) Effects of temperature on electrochemical properties of bismuth oxide/manganese oxide pseudocapacitor. Ind Eng Chem Res 57:2146–2154. https://doi.org/10.1021/acs.iecr.7b04980

Ni J, Lu W, Zhang L et al (2009) Low-temperature synthesis of monodisperse 3D manganese oxide nanoflowers and their pseudocapacitance properties. J Phys Chem 113:54–60. https://doi.org/10.1021/jp806454r

Osiak M, Khunsin W, Armstrong E et al (2013) Epitaxial growth of visible to infra-red transparent conducting In_2O_3 nanodot dispersions and reversible charge storage as a Li-ion battery anode. Nanotechnology 24:065401. https://doi.org/10.1088/0957-4484/24/6/065401

Ozkaya T, Toprak MS, Baykal A et al (2009) Synthesis of Fe_3O_4 nanoparticles at 100°C and its magnetic characterization. J Alloys Compd 472:18–23. https://doi.org/10.1016/J.JALLCOM.2008.04.101

Padmanathan N, Shao H, McNulty D et al (2016) Hierarchical NiO–In_2O_3 microflower (3D)/nanorod (1D) hetero-architecture as a supercapattery electrode with excellent cyclic stability. J Mater Chem A 4:4820–4830. https://doi.org/10.1039/C5TA10407F

Park J, Lee JW, Ye BU et al (2015) Structural evolution of chemically-driven RuO_2/ nanowires and 3-dimensional design for photo-catalytic applications. Sci Rep 5:1–10. https://doi.org/10.1038/srep11933

Pham DP, Phan BT, Hoang VD et al (2014) Control of preferred (222) crystalline orientation of sputtered indium tin oxide thin films. Thin Solid Films 570:16–19. https://doi.org/10.1016/J.TSF.2014.08.041

Poizot P, Dolhem F (2011) Clean energy new deal for a sustainable world: from non-CO_2 generating energy sources to greener electrochemical storage devices. Energy Environ Sci 4:2003. https://doi.org/10.1039/c0ee00731e

Potter R, Rossman G (1979) The tetravalent manganese oxides: identification , hydration , and structural relationships by infrared spectroscopy. Am Mineral 64:1199–1218

Prasad KR, Koga K, Miura N (2004) Electrochemical deposition of nanostructured indium oxide: high-performance electrode material for redox supercapacitors. Chem Mater 16:1845–1847. https://doi.org/10.1021/CM0497576

Pusawale SN, Deshmukh PR, Gunjakar JL, Lokhande CD (2013) SnO_2–RuO_2 composite films by chemical deposition for supercapacitor application. Mater Chem Phys 139:416–422. https://doi.org/10.1016/J.MATCHEMPHYS.2012.12.059

Qiao Y, Sun Q, Cui H et al (2015) Synthesis of micro/nano-structured Mn_3O_4 for supercapacitor electrode with excellent rate performance. RSC Adv. https://doi.org/10.1039/C4RA04783D

Qiu M, Sun P, Shen L et al (2016) WO_3 nanoflowers with excellent pseudo-capacitive performance and the capacitance contribution analysis. J Mater Chem A 4:7266–7273. https://doi.org/10.1039/C6TA00237D

Qu Q, Yang S, Feng X (2011) 2D Sandwich-like sheets of iron oxide grown on graphene as high energy anode material for supercapacitors. Adv Mater 23:5574–5580. https://doi.org/10.1002/adma.201103042

Qu Q, Zhu Y, Gao X, Wu Y (2012) Core-shell structure of polypyrrole grown on V_2O_5 nanoribbon as high performance anode material for supercapacitors. Adv Energy Mater 2:950–955. https://doi.org/10.1002/aenm.201200088

Ragupathy P, Park DH, Campet G et al (2009) Remarkable capacity retention of nanostructured manganese oxide upon cycling as an electrode material for supercapacitor. J Phys Chem C 113:6303–6309. https://doi.org/10.1021/jp811407q

Rakhi RB, Nagaraju DH, Beaujuge P, Alshareef HN (2016) Supercapacitors based on two dimensional VO_2 nanosheet electrodes in organic gel electrolyte. Electrochim Acta 220:601–608. https://doi.org/10.1016/J.ELECTACTA.2016.10.109

Sankar KV, Senthilkumar ST, Berchmans LJ et al (2012) Effect of reaction time on the synthesis and electrochemical properties of Mn_3O_4 nanoparticles by microwave assisted reflux method. Appl Surf Sci 259:624–630. https://doi.org/10.1016/j.apsusc.2012.07.087

Saravanakumar B, Purushothaman KK, Muralidharan G (2012) Interconnected V_2O_5 Nanoporous network for high-performance supercapacitors. ACS Appl Mater Interfaces 4:4484–4490. https://doi.org/10.1021/am301162p

Saravanakumar B, Purushothaman KK, Muralidharan G (2016) Fabrication of two-dimensional reduced graphene oxide supported V_2O_5 networks and their application in supercapacitors. Mater Chem Phys 170:266–275. https://doi.org/10.1016/J.MATCHEMPHYS.2015.12.051

Senthilkumar ST, Selvan RK, Ulaganathan M, Melo JS (2014) Fabrication of Bi_2O_3||AC asymmetric supercapacitor with redox additive aqueous electrolyte and its improved electrochemical performances. Electrochim Acta 115:518–524. https://doi.org/10.1016/J.ELECTACTA.2013.10.199

Sevilla M, Mokaya R (2014) Energy storage applications of activated carbons: supercapacitors and hydrogen storage. Energy Environ Sci 7:1250–1280. https://doi.org/10.1039/C3EE43525C

Sharma RK, Oh H-S, Shul Y-G, Kim H (2007) Carbon-supported, nano-structured, manganese oxide composite electrode for electrochemical supercapacitor. J Power Sources 173:1024–1028. https://doi.org/10.1016/j.jpowsour.2007.08.076

Shown I, Ganguly A, Chen L-C, Chen K-H (2015) Conducting polymer-based flexible supercapacitor. Energy Sci Eng 3:2–26. https://doi.org/10.1002/ese3.50

Spence W (1967) The uv absorption edge of tin oxide thin films. J Appl Phys 38:3767–3770. https://doi.org/10.1063/1.1710208

Subramanian V, Zhu H, Vajtai R et al (2005) Hydrothermal synthesis and pseudocapacitance properties of MnO2 nanostructures. J Phys Chem B 109:20207–20214

Subramanian V, Zhu H, Wei B (2006) Synthesis and electrochemical characterizations of amorphous manganese oxide and single walled carbon nanotube composites as supercapacitor electrode materials. Electrochem Commun 8:827–832. https://doi.org/10.1016/j.elecom.2006.02.027

Sudha V, Sangaranarayanan MV (2002) Underpotential deposition of metals: structural and thermodynamic considerations. J Phys Chem B 106:2699–2707. https://doi.org/10.1021/jp013544b

Tan Y, Meng L, Peng Q, Li Y (2011) One-dimensional single-crystalline Mn_3O_4 nanostructures with tunable length and magnetic properties of Mn3O4 nanowires. Chem Commun (Camb) 47:1172–1174. https://doi.org/10.1039/c0cc00978d

Tang Y, Wu D, Chen S et al (2013) Highly reversible and ultra-fast lithium storage in mesoporous graphene-based TiO_2/SnO_2 hybrid nanosheets. Energy Environ Sci 6:2447. https://doi.org/10.1039/c3ee40759d

Tang Q, Wang W, Wang G (2015) The perfect matching between the low-cost Fe_2O_3 nanowire anode and the NiO nanoflake cathode significantly enhances the energy density of asymmetric supercapacitors. J Mater Chem A 3:6662–6670. https://doi.org/10.1039/C5TA00328H

Tang K, Li Y, Li Y et al (2016) Self-reduced VO/VO_x/carbon nanofiber composite as binder-free electrode for supercapacitors. Electrochim Acta 209:709–718. https://doi.org/10.1016/J.ELECTACTA.2016.05.051

Thackeray MM, Wolverton C, Isaacs ED (2012) Electrical energy storage for transportation—approaching the limits of, and going beyond, lithium-ion batteries. Energy Environ Sci 5:7854. https://doi.org/10.1039/c2ee21892e

Thomas L, Floyd DB (2009) Electronics fundamentals: circuits, devices & applications, 6th edn. Prentice Hall Press, Upper Saddle River

Tien L-C, Chen Y-J (2013) Influence of growth ambient on the surface and structural properties of vanadium oxide nanorods. Appl Surf Sci 274:64–70. https://doi.org/10.1016/J.APSUSC.2013.02.092

Toupin M, Brousse T, Be D (2004) Charge storage mechanism of MnO_2 electrode used in aqueous electrochemical capacitor. Chem Mater 16:3184–3190

Tuzluca FN, Yesilbag YO, Akkus T, Ertugrul M (2017) Effects of graphite on the synthesis of 1-D single crystal In_2O_3 nanostructures at high temperature. Mater Sci Semicond Process 66:62–68. https://doi.org/10.1016/J.MSSP.2017.04.007

Tuzluca FN, Yesilbag YO, Ertugrul M (2018) Synthesis of In_2O_3 nanostructures with different morphologies as potential supercapacitor electrode materials. Appl Surf Sci 427:956–964. https://doi.org/10.1016/J.APSUSC.2017.08.127

UNEP (2013) Green economy and trade – trends, challenges and opportunities. In: United Nations Environmental Program

Upadhyay KK, Altomare M, Eugénio S et al (2017) On the supercapacitive behaviour of anodic porous WO3-based negative electrodes. Electrochim Acta 232:192–201. https://doi.org/10.1016/J.ELECTACTA.2017.02.131

Velmurugan V, Srinivasarao U, Ramachandran R et al (2016) Synthesis of tin oxide/graphene (SnO_2/G) nanocomposite and its electrochemical properties for supercapacitor applications. Mater Res Bull 84:145–151. https://doi.org/10.1016/J.MATERRESBULL.2016.07.015

Vijayabala V, Senthilkumar N, Nehru K, Karvembu R (2018) Hydrothermal synthesis and characterization of ruthenium oxide nanosheets using polymer additive for supercapacitor applications. J Mater Sci Mater Electron 29:323–330. https://doi.org/10.1007/s10854-017-7919-x

Vol'fkovich YM, Serdyuk TM, Vol YM (2002) Electrochemical capacitors. Russ J Electrochem 38:935–959

Wang X, Wang X, Huang W et al (2005) Sol-gel template synthesis of highly ordered MnO_2 nanowire arrays. J Power Sources 140:211–215. https://doi.org/10.1016/j.jpowsour.2004.07.033

Wang S-Y, Ho K-C, Kuo S-L, Wu N-L (2006) Investigation on capacitance mechanisms of Fe_3O_4 electrochemical capacitors. J Electrochem Soc 153:A75. https://doi.org/10.1149/1.2131820

Wang X, Yuan A, Wang Y (2007) Supercapacitive behaviors and their temperature dependence of sol-gel synthesized nanostructured manganese dioxide in lithium hydroxide electrolyte. J Power Sources 172:1007–1011. https://doi.org/10.1016/j.jpowsour.2007.07.066

Wang L, Yu Y, Chen PC et al (2008) Electrospinning synthesis of C/Fe_3O_4 composite nanofibers and their application for high performance lithium-ion batteries. J Power Sources 183:717–723. https://doi.org/10.1016/j.jpowsour.2008.05.079

Wang B, Park J, Wang C et al (2010) Mn_3O_4 nanoparticles embedded into graphene nanosheets: preparation, characterization, and electrochemical properties for supercapacitors. Electrochim Acta 55:6812–6817

Wang X, Liu L, Wang X et al (2011) Mn_2O_3/carbon aerogel microbead composites synthesized by in situ coating method for supercapacitors. Mater Sci Eng B Solid-State Mater Adv Technol 176:1232–1238. https://doi.org/10.1016/j.mseb.2011.07.003

Wang D, Li Y, Wang Q, Wang T (2012) Facile synthesis of porous Mn_3O_4 nanocrystal-graphene nanocomposites for electrochemical supercapacitors. Eur J Inorg Chem:628–635. https://doi.org/10.1002/ejic.201100983

Wang Y, Yu SF, Sun CY et al (2012c) MnO_2/onion-like carbon nanocomposites for pseudocapacitors. J Mater Chem 22:17584–17588. https://doi.org/10.1039/c2jm33558a

Wang HY, Xiao FX, Yu L et al (2014) Hierarchical α-MnO_2 nanowires@$Ni_{1-x}Mn_xO_y$ nanoflakes core-shell nanostructures for supercapacitors. Small 10:3181–3186. https://doi.org/10.1002/smll.201303836

Wang N, Zhang Y, Hu T et al (2015) Facile hydrothermal synthesis of ultrahigh-aspect-ratio V_2O_5 nanowires for high-performance supercapacitors. Curr Appl Phys 15:493–498. https://doi.org/10.1016/J.CAP.2015.01.026

Wang P, Liu H, Xu Y et al (2016a) Supported ultrafine ruthenium oxides with specific capacitance up to 1099 F g-1for a supercapacitor. Electrochim Acta 194:211–218. https://doi.org/10.1016/j.electacta.2016.02.089

Wang Y-C, Chen C-Y, Kuo C-W et al (2016b) Low-temperature grown indium oxide nanowire-based antireflection coatings for multi-crystalline silicon solar cells. Phys Status Solidi 213:2259–2263. https://doi.org/10.1002/pssa.201600005

Wee G, Soh HZ, Cheah YL et al (2010) Synthesis and electrochemical properties of electrospun V2O5 nanofibers as supercapacitor electrodes. J Mater Chem 20:6720. https://doi.org/10.1039/c0jm00059k

Wei W, Cui X, Chen W, Ivey DG (2011) Manganese oxide-based materials as electrochemical supercapacitor electrodes. Chem Soc Rev 40:1697–1721. https://doi.org/10.1039/c0cs00127a

Wei D, Scherer MRJ, Bower C et al (2012) A nanostructured electrochromic supercapacitor. Nano Lett 12:1857–1862. https://doi.org/10.1021/nl2042112

Wells AF (1984) Structural inorganic chemistry, 5th edn. Science Publications, Oxford

Wu Y-T, Hu C-C (2005) Aspect ratio controlled growth of MnOOH in mixtures of Mn_3O_4 and MnOOH single crystals for supercapacitors. Electrochem Solid-State Lett 8:A240–A244

Wu X, Yao S (2017) Flexible electrode materials based on WO_3 nanotube bundles for high performance energy storage devices. Nano Energy 42:143–150. https://doi.org/10.1016/J.NANOEN.2017.10.058

Wu N-L, Wang S-Y, Han C-Y et al (2003) Electrochemical capacitor of magnetite in aqueous electrolytes. J Power Sources 113:173–178. https://doi.org/10.1016/S0378-7753(02)00482-2

Wu Z-S, Ren W, Wang D et al (2010) High-energy MnO_2 nanowire/graphene and graphene asymmetric electrochemical capacitors. ACS Nano 4:5835–5842. https://doi.org/10.1021/nn101754k

Wu J, Huang H, Yu L, Hu J (2013) Controllable hydrothermal synthesis of MnO_2 nanostructures. Adv Mater Phys Chem 3:201–205

Xia H, Shirley Meng Y, Yuan G et al (2012) A symmetric RuO_2/RuO_2 supercapacitor operating at 1.6 V by using a neutral aqueous electrolyte. Electrochem Solid-State Lett 15:A60–A63. https://doi.org/10.1149/2.023204esl

Xiao W, Xia H, Fuh JYH, Lu L (2009) Growth of single-crystal-MnO_2 nanotubes prepared by a hydrothermal route and their electrochemical properties. J Power Sources 193:935–938. https://doi.org/10.1016/j.jpowsour.2009.03.073

Xiong C, Aliev AE, Gnade B, Balkus KJ (2008) Fabrication of silver vanadium oxide and V_2O_5 nanowires for electrochromics. ACS Nano 2:293–301. https://doi.org/10.1021/nn700261c

Xu HY, Le XS, Li XD et al (2006) Chemical bath deposition of hausmannite Mn_3O_4 thin films. Appl Surf Sci 252:4091–4096. https://doi.org/10.1016/j.apsusc.2005.06.011

Xu M, Kong L, Zhou W, Li H (2007) Hydrothermal synthesis and pseudocapacitance properties of Î±-MnO_2 hollow spheres and hollow urchins. J Phys Chem C 111:19141–19147

Xu L, Ding Y, Chen C, Zhao L (2008) 3D flowerlike α-nickel hydroxide with enhanced electrochemical activity synthesized by microwave-assisted hydrothermal method. Chem Mater 20:308–316. https://doi.org/10.1021/cm702207w

Yan D, Cheng S, Zhuo RF et al (2009) Nanoparticles and 3D sponge-like porous networks of manganese oxides and their microwave absorption properties. Nanotechnology 20:105706–105717. https://doi.org/10.1088/0957-4484/20/10/105706

Yan J, Khoo E, Sumboja A, Lee PS (2010) Facile coating of manganese oxide on tin oxide nanowires with high-performance capacitive behavior. ACS Nano 4:4247–4255. https://doi.org/10.1021/nn100592d

Yan Y, Li B, Guo W et al (2016) Vanadium based materials as electrode materials for high performance supercapacitors. J Power Sources 329:148–169. https://doi.org/10.1016/J.JPOWSOUR.2016.08.039

Yang J, Li X, Bai SL et al (2011a) Electrodeposition and electrocatalytic characteristics of porous crystalline SnO_2 thin film using butyl-rhodamine B as a structure-directing agent. Thin Solid Films 519:6241–6245. https://doi.org/10.1016/J.TSF.2011.03.119

Yang Y, Kim D, Yang M, Schmuki P (2011b) Vertically aligned mixed V_2O_5–TiO_2 nanotube arrays for supercapacitor applications. Chem Commun 47:7746. https://doi.org/10.1039/c1cc11811k

Yang J, Lan T, Liu J et al (2013) Supercapacitor electrode of hollow spherical V_2O_5 with a high pseudocapacitance in aqueous solution. Electrochim Acta 105:489–495. https://doi.org/10.1016/J.ELECTACTA.2013.05.023

Yang P, Ding Y, Lin Z et al (2014) Low-cost high-performance solid-state asymmetric supercapacitors based on MnO2 nanowires and Fe_2O_3 nanotubes. Nano Lett 14:731–736. https://doi.org/10.1021/nl404008e

Yang F, Zhao M, Sun Q, Qiao Y (2015) A novel hydrothermal synthesis and characterisation of porous Mn_3O_4 for supercapacitors with high rate capability. RSC Adv 5:9843–9847. https://doi.org/10.1039/C4RA10175H

Yıldırım MA, Akaltun Y, Ateş A (2012) Characteristics of SnO_2 thin films prepared by SILAR. Solid State Sci 14:1282–1288. https://doi.org/10.1016/J.SOLIDSTATESCIENCES.2012.07.012

Yin AX, Liu WC, Ke J et al (2012) Ru nanocrystals with shape-dependent surface-enhanced raman spectra and catalytic properties: controlled synthesis and DFT calculations. J Am Chem Soc 134:20479–20489. https://doi.org/10.1021/ja3090934

Yin B, Zhang S, Yang J et al (2014) Facile synthesis of ultralong MnO_2 nanowires as high performance supercapacitor electrodes and photocatalysts with enhanced photocatalytic activities. CrystEngComm 16:9999–10005. https://doi.org/10.1039/C4CE01302F

Yu C, Zhang L, Shi J et al (2008) A simple template-free strategy to synthesize nanoporous manganese and nickel oxides with narrow pore size distribution, and their electrochemical properties. Adv Funct Mater 18:1544–1554. https://doi.org/10.1002/adfm.200701052

Yu D, Chen C, Xie S et al (2011) Mesoporous vanadium pentoxide nanofibers with significantly enhanced Li-ion storage properties by electrospinning. Energy Environ Sci 4:858–861. https://doi.org/10.1039/C0EE00313A

Yu M, Liu X, Wang Y et al (2012) Gas sensing properties of p-type semiconducting vanadium oxide nanotubes. Appl Surf Sci 258:9554–9558. https://doi.org/10.1016/J.APSUSC.2012.05.120

Yu A, Chabot V, Zhang J (2013a) Electrochemical supercapacitors for energy storage and delivery: fundamentals and applications. CRC Press

Yu Z, Duong B, Abbitt D, Thomas J (2013b) Highly ordered MnO_2 nanopillars for enhanced supercapacitor performance. Adv Mater 25:3302–3306. https://doi.org/10.1002/adma.201300572

Yu M, Zeng Y, Han Y et al (2015) Valence-optimized vanadium oxide supercapacitor electrodes exhibit ultrahigh capacitance and super-long cyclic durability of 100 000 cycles. Adv Funct Mater 25:3534–3540. https://doi.org/10.1002/adfm.201501342

Yuan L, Xiao X, Ding T et al (2012) Paper-based supercapacitors for self-powered nanosystems. Angew Chem Int Ed 51:4934–4938. https://doi.org/10.1002/anie.201109142

Zhang LL, Wei T, Wang W, Zhao XS (2009) Manganese oxide – carbon composite as supercapacitor electrode materials. Microporous Mesoporous Mater 123:260–267

Zhang Z, Zou R, Song G et al (2011) Highly aligned SnO_2 nanorods on graphene sheets for gas sensors. J Mater Chem 21:17360. https://doi.org/10.1039/c1jm12987b

Zhang X, Cheng X, Zhang Q (2016a) Nanostructured energy materials for electrochemical energy conversion and storage: a review. J Energy Chem 25:967–984. https://doi.org/10.1016/j.jechem.2016.11.003

Zhang Y, Zheng J, Zhao Y et al (2016b) Fabrication of V_2O_5 with various morphologies for high-performance electrochemical capacitor. Appl Surf Sci 377:385–393. https://doi.org/10.1016/J.APSUSC.2016.03.180

Zhao X, Johnston C, Grant PS (2009) A novel hybrid supercapacitor with a carbon nanotube cathode and an iron oxide/carbon nanotube composite anode. J Mater Chem 19:8755. https://doi.org/10.1039/b909779a

Zheng JP, Cygan PJ, Jow TR (1995) Hydrous ruthenium oxide as an electrode material for electrochemical capacitors. J Electrochem Soc 142:2699–2703

Zheng F-L, Li G-R, Ou Y-N et al (2010) Synthesis of hierarchical rippled Bi_2O_3 nanobelts for supercapacitor applications. Chem Commun 46:5021. https://doi.org/10.1039/c002126a

Zheng H, Ou JZ, Strano MS et al (2011) Nanostructured tungsten oxide – properties, synthesis, and applications. Adv Funct Mater 21:2175–2196. https://doi.org/10.1002/adfm.201002477

Zheng ZQ, Zhu LF, Wang B (2015) In_2O_3 nanotower hydrogen gas sensors based on both schottky junction and thermoelectronic emission. Nanoscale Res Lett 10:293. https://doi.org/10.1186/s11671-015-1002-4

Zheng W, Zhang P, Tian W et al (2017) Microwave-assisted synthesis of SnO_2-Ti_3C_2 nanocomposite for enhanced supercapacitive performance. Mater Lett 209:122–125. https://doi.org/10.1016/J.MATLET.2017.07.131

Zhong C, Deng Y, Hu W et al (2015) A review of electrolyte materials and compositions for electrochemical supercapacitors. Chem Soc Rev 44:7484–7539. https://doi.org/10.1039/c5cs00303b

Zhou T, Mo S, Zhou S et al (2011) Mn_3O_4/worm-like mesoporous carbon synthesized via a microwave method for supercapacitors. J Mater Sci 46:3337–3342. https://doi.org/10.1007/s10853-010-5221-x

Zhou G, Wang D-W, Hou P-X et al (2012) A nanosized Fe_2O_3 decorated single-walled carbon nanotube membrane as a high-performance flexible anode for lithium ion batteries. J Mater Chem 22:17942. https://doi.org/10.1039/c2jm32893c

Zhu J, Cao L, Wu Y et al (2013) Building 3D structures of vanadium pentoxide nanosheets and application as electrodes in supercapacitors. Nano Lett 13:5408–5413. https://doi.org/10.1021/nl402969r

Chapter 7
Third-Generation Solar Cells: Concept, Materials and Performance - An Overview

Soosaimanickam Ananthakumar, Jeyagopal Ram Kumar, and Sridharan Moorthy Babu

Contents

S. Ananthakumar (✉)
Crystal Growth Centre, Anna University, Chennai, India

Instituto de Ciencia de los Materiales (ICMUV), Universidad de Valencia, Calle Catedratico Jose Beltran, Valencia 46980, Spain
e-mail: soosaima@uv.es

J. R. Kumar
Crystal Growth Centre, Anna University, Chennai, India

Department of Physics, Faculty of Physical and Mathematical Sciences, University of Concepcion, Concepcion, Chile

S. M. Babu
Crystal Growth Centre, Anna University, Chennai, India

R. Saravanan et al. (eds.), *Emerging Nanostructured Materials for Energy and Environmental Science*, Environmental Chemistry for a Sustainable World 23,
https://doi.org/10.1007/978-3-030-04474-9_7

Abstract The large scarcity of natural fuels in earth crust has triggered to search alternative energy reservoirs for the future generation of human life. Because of large abundancy, solar energy is considered as big hope for the future generation energy utilization for commercial as well as home applications. The scientific revolution achieved in synthesis and processing of semiconductor nanomaterials, organic conducting polymers have led into new dimension in fabrication of future-generation solar cells. Reduction in the dimension of semiconductor nanomaterials significantly influences on their structural and optical properties which is helpful for the excellent photon harvesting. Also, their large surface area is further favourable to assist with the attachment of several organic or inorganic compounds in order to functionalize them effectively. Developments that have been made in semiconducting organic polymers still encourage the fabrication of highly efficient, flexible solar cell devices on conducting substrates. Formation of nanocomposites, hybrids, alloy system, doping, etc. are successfully carried out on different kinds of inorganic semiconductor nanomaterials for the photovoltaic applications. The day-by-day improvement in terms of efficiency and new materials development predicts that the breakthrough to achieve highly stable, high-efficiency solar cell is about the near future. In this aspect, this chapter summarizes the development in the solar cells research of each category with general aspects. The important parameters and process that affects the performance of each category is outlined.

7.1 Introduction to Semiconductor Photovoltaics

The current energy crisis in the world has made a great attention on the photovoltaic (PV) energy conversion technology. Photovoltaic is a very promising technology to produce the electricity from sunlight. The advantages of this technology include many features such as pollution free, easy maintenance, long lifetime, etc. An hour

of solar energy radiation on earth is about 14TW which is enough to tackle the yearly usage of global electricity. Hence, materials harvesting solar energy are becoming great interest of study. The key requirement of an ideal solar cell material includes (Chopra et al. 2004; Goetzberger et al. 2002) (i) it should have the bandgap between 1.1 and 1.7 eV, (ii) it should possess direct band structure, (iii) it should be non-toxic in nature, (iv) it should obey with the reproducible deposition techniques and suitable for the large area photovoltaic applications, and (v) it should give good photovoltaic conversion efficiency and long-term stability.

7.2 Development of Solar Cells

Development of solar cells and solar cell materials can be classified into three categories. All these are briefly explained as below.

7.2.1 First-Generation Solar Cells

First-generation solar cells are the crystalline silicon-based solar cells. It is a known fact that still the current solar energy market is dominated by crystalline silicon solar cells (over 90%). The high efficiency observed based on these single crystalline silicon solar cells is about 25%. Due to the high-cost expensive manufacturing of crystalline silicon from sand, attempts were made to develop new materials with low-cost fabrication technology.

7.2.2 Second-Generation Solar Cells

Second-generation solar cells were fabricated by cheaper technologies compared to the first-generation solar cells. Copper indium gallium selenide (CIGS), cadmium telluride (CdTe), amorphous silicon (a-Si) and nanocrystalline silicon (nc-Si) are the most commonly used materials. Due to their high absorption coefficient than silicon, only a thin layer (i.e. it reduces the amount of material used) is enough to harvest a large amount of photons. The highest confirmed efficiencies obtained for CIGS, CdTe, a-Si cell and nc-Si are 20.1%, $16.7 \pm 0.5\%$, $9.5 \pm 0.3\%$ and $10.1 \pm 0.2\%$, respectively. Though they could able to fabricate by cheaper methods, the performance of these solar cells are not higher than the first-generation solar cells.

7.2.3 *Third-Generation Solar Cells*

These solar cells are targeted to achieve both high efficiency and low cost. Novel approaches using semiconductor nanoparticles were utilized in this type of solar cells. Since semiconductor nanoparticles could produce high current using the novel concepts like impact ionization, devices using this concept are highly interesting. The thermodynamic energy conversion limit of solar cells varies from 31% to 41% which is termed as Shockley-Queisser efficiency limit, and it is expected that this limit can be overcome by using the semiconductor nanoparticles (Beard et al. 2014; Rao and Friend 2017). The categories of third-generation solar cells include dye-sensitized solar cells (DSSCs), quantum dot-sensitized solar cells (QDSSCs), organic solar cells and currently emerging hybrid perovskite solar cells. In the first two cases, a mesoporous Titania (TiO_2) layer is sensitized by ruthenium complex dye and semiconductor quantum dots (QDs) respectively, to enhance the optical absorption. The high efficiency achieved so far has reached about 14% in DSSCs, and for the QDSSCs, about 8–10% has been achieved (Low and Lai 2018). Still, the ongoing efforts to achieve higher efficiency using novel dyes, counter electrodes and electrolytes are believed that this will lead into highly stable, low-cost, higher efficiency devices. In case of organic solar cells, a potential organic donor and acceptor molecules are playing in the active layer either as bilayer or bulk heterojunction constructed through solution-based deposition approaches. Till date, about 10–15% of efficiency has been achieved (Li et al. 2018). The recently emerged perovskite solar cells (PSCs) with hybrid organic-inorganic perovskite halides, $CH_3NH_3PbX_3$ (X = Cl, Br, I) as the active layer, have generated over 20% efficiency (Dubey et al. 2018; Anaraki et al. 2018; Saliba et al. 2018). In additional, hot carrier cells, multiband cells and tandem solar cells are also emerged as potential concepts to improve the photocurrent as well as efficiency.

7.3 Solar Cell Parameters

Solar cell efficiency is measured by using various parameters. The photo conversion efficiency (PCE) of solar cell is generally defined as the percentage of maximum output of electrical power to the incident light power. It can be represented by using the following formula (Hagfeldt et al. 2010; Zhou et al. 2010),

$$\mathrm{PCE} = \frac{P_m}{P_{\mathrm{in}}} = \frac{J_{\mathrm{sc}} \times V_{\mathrm{oc}} \times \mathrm{FF}}{P_{\mathrm{in}}}$$

where;

P_m is maximum power point.

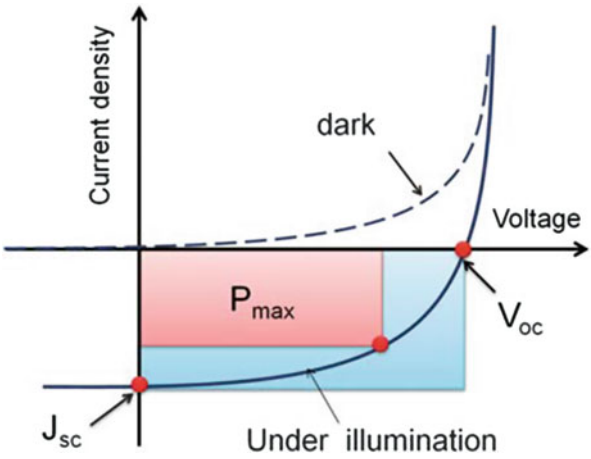

Fig. 7.1 Current density-voltage (I–V) characteristic of a typical solar cell in the dark and under illumination. (Reprinted with permission from Zhou et al. Copyright@2010, Royal Society of Chemistry)

P_{in} is the incident light intensity.
J_{sc} is the short-circuit current density.
V_{oc} is the open-circuit voltage, i.e. the maximum voltage available from a solar cell at zero current.

FF is the fill factor, which is defined as the ratio of maximum power point (P_m) to the product of short-circuit current density (J_{sc}) and open-circuit voltage (V_{oc}). The fill factor is represented by Eq. (7.1), and Fig. 7.1 shows the J-V curve of a solar cell under dark and light.

$$\mathrm{FF} = \frac{P_m}{J_{sc} \times V_{oc}} \tag{7.1}$$

A typical I-V curve of a solar cell is given in Fig. 7.1.

7.4 Important Materials Properties Controlling Efficiency

Some of the important properties associated with the efficiency of solar cells are described as below.

7.4.1 Trap States

Trap states are one of the major candidates in influencing the performance of solar cells. According to classical semiconductor physics, trap states are defined as energy

sites located in the energy gap of the semiconductor (Stephen et al. 2017). Apparently, trap states are playing crucial role in all kind of modern solar cells. In nanoparticles, trap states are also called as defects, and these are employing important role in charge recombination process. The electron transport is greatly hindered by trap states in the nanoparticle-based solar cells such as hybrid solar cells, DSSCs, QDSSCs and perovskite solar cells. In case of organic solar cells, trap states are forming near the interface and monomolecular and bimolecular recombination mechanisms are dealing about such processes.

7.4.2 Morphology of the Active Layer

Morphology of the active layer invariantly influence on the final efficiency of the solar cells. A pinhole-free, smooth active layer is very important in case of organic, hybrid and perovskite solar cells. Different polar and non-polar solvents, additives and other physical parameters are greatly involving in optimizing such kind of morphology. In case of DSSCs and QDSSCs, the proper adsorption of dyes or QDs on the photoanode is important, and this essentially reflects on the efficiency. Moreover, different morphologies of the nanoparticles such as spherical, nanoplate, nanorod and nanowire shapes significantly influence on the final morphology of the active layer.

7.4.3 Solubility

Solubility of active layer materials in the single solvent or mixture of solvents affects the performance of device. In particular, organic solar cells, hybrid solar cells and perovskite solar cells are mostly depending on the solvent-based fabrication procedures. Polar solvents such as chlorobenzene, chloroform, dimethyl sulfoxide (DMSO) and dimethylformamide (DMF) are mostly used for the dissolution of precursors. For hybrid solar cells, non-polar solvent such as n-hexane also found to be as efficient (Celik et al. 2012). In case of DSSCs and QDSSCs, single solvent or mixture of solvents is used to dissolve dyes or to redisperse the nanoparticles. For the perovskite solar cells, DMSO and DMF are the widely used solvents to achieve the pinhole-free active layer.

7.5 Organic Solar Cells

7.5.1 Semiconducting Polymers for Organic Solar Cells

The invention of different varities of organic semiconducting polymers had opened a new pathway in the development of organic solar cells. The salient features of organic semiconducting polymers over crystalline silicon such as high optical absorption coefficient (~10^5 cm^{-1}) which need a very thin layer (~100 nm) to harvest large amount of photons, tunable bandgap in the entire visible range, high yield of charge generation when coupled with the electron acceptor molecules have turned huge interest (Günes et al. 2007). Typically, an ideal semiconducting polymer for solar cells should have a low bandgap in order to harvest large amount of photons. When light strikes on the active layer, the exciton which generated in donor polymer can diffuse up to ~5 to 10 nm (Li et al. 2012). This length is defined as exciton diffusion length of a polymer, and this plays major role in the construction of an efficient organic solar cell. On the other hand, the exciton binding energy of a semiconducting organic polymer is quite higher than inorganic semiconducting materials. This is one of the most important parameter of organic polymers which influence on the efficiency of a solar cell. These polymers can be deposited on the flexible substrates like polyethylene terephthalate (PET), biocompatible silk fibroin, etc. There are two types of device structures that can be made using organic semiconducting donor polymers and acceptor molecules, namely, bilayer configuration and bulk heterojunction-type configuration. Both these configurations have contributed a lot in the fabrication of high-efficiency organic solar cells.

7.5.2 Construction of Organic Solar Cells

In bulk heterojunction configuration, both acceptor and donor compounds are mixed in a suitable solvent system and then deposited on the conducting substrate. The typical organic solar cell or plastic solar cell consists of a transparent conducting oxide substrate (usually indium-coated tin oxide (ITO)), hole transporting layer (HTL), active layer, electron transporting layer (ETL) and cathode. The different configurations of organic solar cell are schematically given in Fig. 7.2. Efficiency of an organic solar cell depends upon several factors which include nature of the donor and acceptor components used in the active layer, method of deposition, annealing, solvents used for deposition and work function of the cathode electrode. Spin coating is the mostly adopted process to deposit the active layers of the organic solar cell. Semiconducting polymers such as poly-3-hexyl-thiophene (P3HT) and poly(2-methoxy-5-(3′,7′-dimethyloctyloxy)-1,4-phenylenevinylene) (MDMO-PPV) are used as the donor, and compounds such as PCBM and fullerene derivatives are used as the acceptor molecules in organic solar cell. Non-fullerene acceptors such as naphthalene diimide (NDI), phthalimide (PhI), perylene diimide (PDI) and

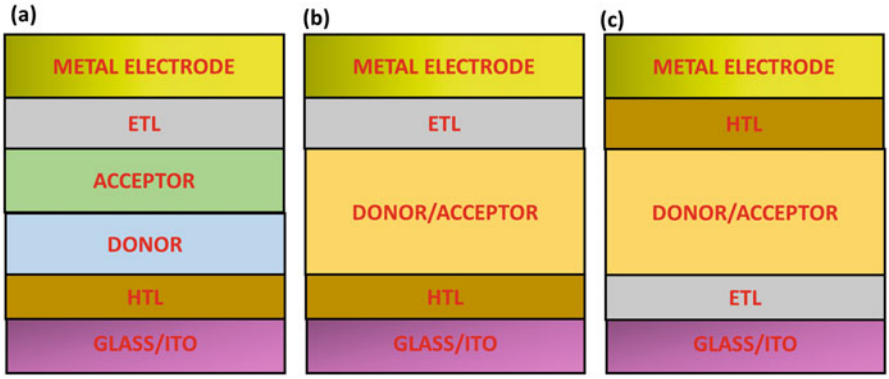

Fig. 7.2 Schematic diagram of various kinds of organic solar cells (**a**) bilayer heterojunction, (**b**) bulk heterojunction and (**c**) inverted bulk heterojunction (*ITO* indium tin oxide, *HTL* hole transport layer, *ETL* electron transport layer)

diketopyrrolopyrrole (DPP) which also have emerged as potential candidates for organic solar cells to reach the efficiency ~13 to 14% (Chang et al. 2018; Liu et al. 2018). The domain formation between organic donor and acceptor components in the active layer influence significantly on the final performance of an organic solar cell. Therefore, the ratio of donor and acceptor molecules, nature of solvents used for the blend formation, method of forming layers, temperature used to evaporate the solvent, etc. are the major factors to obtain a smooth film of active layer. The average efficiency of the organic solar cell lie in the range of around 8–10% (Scharber and Sariciftci 2013). Approaches such as inverted solar cell, tandem configuration and fabrication with extremely low-bandgap polymers were also utilized to improve the device performance (Chen et al. 2009; Kouijzer et al. 2012; You et al. 2013). In terms of stability, organic solar cells suffer much due to the oxidation nature of most of the semiconducting polymers. Also, incorporation of oxygen and water from the moisture, poorly fabricated morphology of the active layer, diffuse of electrode element and PEDOT:PSS into the active layer, photo-oxidation due to the irradiation of active layers under prolonged time, heating of active layer under uncontrolled conditions and mechanical stress are the main factors that affect the stability of the fabricated organic solar cells (Jørgensen et al. 2008; Cheng and Zhan 2016). Formation of charge transfer complexes was confirmed when P3HT was interacting with oxygen (Abdou et al. 1997). These are acting as the traps in the electron transfer process and hence finally decrease the efficiency. Though effective sealants are used to protect from the oxidation and to avoid this problem, still the lifetime of an organic solar cell is a challenging issue. However, the limitations of the materials, mainly the degradation of polymer have been a major setback in commercializing the organic solar cells.

7.5.3 Future of Organic Solar Cells

Though organic solar cells are fabricated advanced techniques such as roll-to-roll fabrication and inkjet printing, their commercialization is still a challenging effort due to their stability issues. For the future consideration, coupling organic solar cells together with the emerging solar cell technology such as perovskite solar cells would be beneficial for the space and other kind of applications (Cardinaletti et al. 2018). Recently, constructing a four-terminal tandem solar cell based on inorganic $CsPbBr_3$ perovskite solar cell together with organic solar cell has delivered about 14.03% efficiency (Chen et al. 2018). Moreover, enhanced fill factor value (about 80%) has been observed in the integrated P-I-N-type perovskite/bulk heterojunction organic solar cell architecture (Kim et al. 2016). Since most of the organic semiconducting polymers used in organic solar cells can also be used for the perovskite solar cells, these kinds of efforts with new materials would lead this field into new arena.

7.6 Hybrid Solar Cells

7.6.1 Basic Introduction of Hybrid Solar Cells

Important features such as low fabrication cost, easy fabrication methods, less weight, etc. are the main advantages of the third-generation solar cells. In this view, hybrid solar cells are believed as potential device configuration to improve the efficiency. The term 'hybrid' denotes the association of at least two components distinctly different chemical nature, whose molecular level distribution is achieved either by simple mixing or by linking both components together via specific interactions (Reiss et al. 2011). The core concept of hybrid solar cells is adopted from organic solar cells where the acceptor component of the active layer is replaced by the inorganic semiconductor nanoparticles. The role of semiconductor nanoparticles with organic semiconducting polymer is notable due to their interesting size-dependent optical properties. The binding energy of organic semiconductors is much higher (200–400 meV) than the inorganic semiconductors (20–40 meV) (Freitas et al. 2018; Zhao et al. 2010). So, the photo-generated exciton (electron-hole pair) is a strongly bounded one. Hence, the inbuilt electric field is essential to dissociate the excitons. Further, the charge-carrier mobility of the organic semiconductors also in the range of $\sim 10^{-3}$ m $s^{-1}V^{-1}$ is about five times higher than the silicon. The charge transfer between organic polymer and inorganic nanoparticles takes place in about picoseconds of time scale. Depending upon the structure of the nanoparticles (e.g. QDs, nanorods, tetrapods, etc.), this time scale would differ. Also, the phase separation of the polymer and inorganic nanoparticles in the active layer forms a nanosize of domains which is much smaller or comparable to the exciton diffusion length of the semiconducting polymer (approximately about

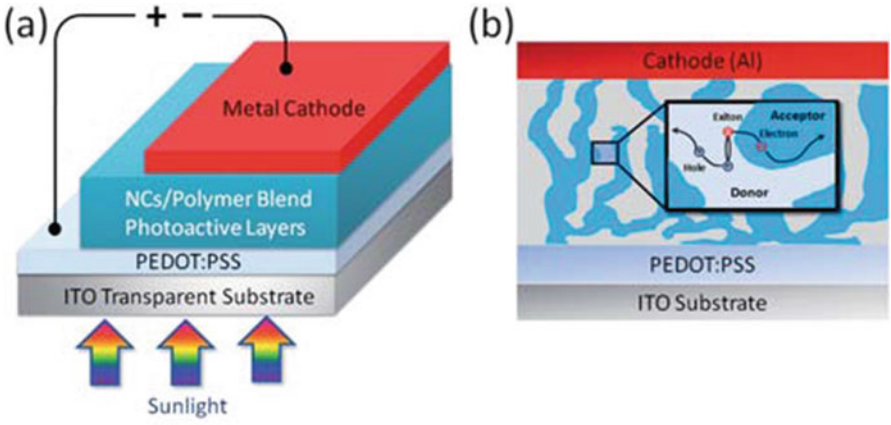

Fig. 7.3 (**a**) Schematic structure of a typical NC/polymer hybrid solar cell. (**b**) Illustration of the bulk heterojunction composite structure. (Reprinted with permission from Zhou et al. Copyright@2010, Royal society of chemistry)

10–20 nm). This phase separation process of active layer is very important parameter which affects the final performance of device.

7.6.2 Construction of Hybrid Solar Cells

A typical hybrid solar cell consists of the following device structure. This consists of a transparent conducting oxide-coated glass substrate (FTO(fluorine doped tin oxide)/glass) or a flexible polymer substrate which is functioning as an anode, and a hole transport layer, usually polyethylene-dioxy polythiophene-poly styrene sulphonate, PEDOT: PSS is preferred. The photoactive layer is made like a sandwitch type of structure between the two electrodes. The deposition of hole transport layer (HTL) and active layer is carried out by spin-coating method. The active layer is configured either a bilayer structure or a bulk heterojunction structure. Finally, the cathode material aluminium is deposited through thermal evaporation process. The typical hybrid solar cell structure is given in Fig. 7.3.

7.6.3 Materials in Hybrid Solar Cells

Several varieties of the nanoparticle structures like quantum dots, nanorods, nanotubes and tetrapods were analysed to improve the efficiency of the hybrid solar cells. Materials like silicon (Si) quantum dots, II-VI group semiconductor nanoparticles and metal oxides such as ZnO and TiO_2 have widely studied for the acceptor molecules. So far, the highest efficiency of the organic-inorganic hybrid

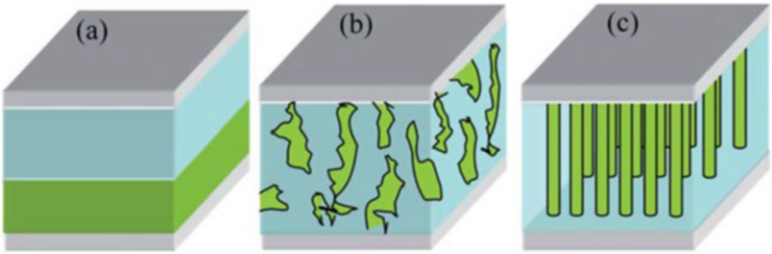

Fig. 7.4 Three different configurations of polymer-inorganic hybrid solar cells: (**a**) bilayer heterojunction, (**b**) bulk heterojunction and (**c**) ordered heterojunction. (Reprinted with permission from Xu and Qiao Copyright@ 2011, Royal Society of Chemistry)

solar cells has reached about 4–5% (Jianyu Yuan et al. 2015). The first report of hybrid solar cell was based on the poly [2-methoxy-5-(2′-ethyl-hexoxy)-p-phenylenevinylene) MEH-PPV polymer by Greenham et al. (1996) which produced about only 0.2% efficiency. But with different morphologies of nanoparticles like rods, tetrapods, the enhanced power conversion efficiency was achieved. The polyphenylene vinylene derivatives were widely studied for hybrid solar cells with various nanoparticles. Perhaps, the mostly used polymer for the hybrid solar cells was poly-3-hexyl-thiophene (P3HT) although other systems such as poly-3-octylthiophene (P3OT), PCPDTBT, etc. have also seen studied. Different architectures such as nanorods, tetrapods, nanowires and nanoparticles semiconductor nanoparticles were fabricated with P3HT polymer, and their efficiency was analysed (Wright and Uddin 2012). In the inorganic nanostructures, long-chain insulating ligands attached on the surface considerably affect the efficiency parameters, and there are interesting studies exploring the crucial role of organic ligands and their replacement from the surface (Said et al. 2010; Moule et al. 2012; Greaney et al. 2012; Liu et al. 2008). The self-organizing crystal structure, high optical absorption, good matching bandgap (~1.9 eV) with energy levels of semiconductor nanoparticles and high-hole mobility of P3HT have made as a benchmark polymer for the organic and hybrid solar cell applications. The basic criteria of the semiconducting donor polymer in hybrid solar cell are having a bandgap of around ~1.5 to 1.6 eV, and the occurrence of its LUMO (lowest unoccupied molecular orbital) is above the inorganic conduction band (CB). The ideal configuration of a hybrid solar cell may be within the three different categories, namely, a bilayer heterojunction, bulk heterojunction (the interpenetrating network of organic and inorganic components) and an ordered heterojunction. This device architecture is schematically given in Fig. 7.4.

7.6.4 Preparation and Factors Affecting Hybrids in Active Layer of Solar Cells

There are different methods followed to prepare semiconductor nanoparticles/organic polymer hybrid for the active layer of hybrid solar cells. These include:

- Blending of non-functionalized polymers with nanoparticles capped with initial ligand

This process involves the direct blending of the as-synthesized nanoparticles with sterically hindering bulky ligands. Mostly this kind of approach results less efficiency in solar cell applications. But, after treating with small length organic molecule that has similar interaction with the nanoparticles surface, the efficiency could be improved. For example, solar cells made by TOPO-capped CdSe nanoparticles/P3HT hybrid have shown very less efficiency in comparing to the pyridine-treated CdSe nanoparticles/P3HT hybrids (Reiss et al. 2011).

- Capping effect of the nanocrystals surface with the conjugated macromolecules anchoring groups

Here, the synthesized nanoparticles with initial ligand are treated or ligand exchanged with solvents like pyridine and blended with the macromolecule polymer with high anchoring groups. Though pyridine treatment could able produce the enhanced power conversion efficiency, its demerits such as incomplete ligand exchange, co-solvent requirement to obtain a good stable colloidal solutions, influencing organic conducting polymer, etc. have to be accounted.

- Covalent grafting of conjugated macromolecules and nanocrystals capped with functionalized ligands

Here, the hybrids are made by either the ligand-exchange process followed by grafting of the conjugated polymer or a one-step process using a bifunctional linker ligand in the nanocrystal synthesis.

- Through non-covalent interactions

Here, the nanoparticles with suitable capping agents are assembled within the polymer matrix to make a homogenous interpenetrating network formation.

- In-situ growth of nanoparticles in a conjugated polymer matrix

In this method, the precursor solutions of the nanoparticles are dissolved in the presence of polymer, and growth of the nanoparticles takes place within the polymer matrix.

7.6.5 *Role of Solvents and Working Mechanism of Hybrid Solar Cells*

Solvents play a major role in the preparation of hybrid blend for the active layer of hybrid solar cells (Thomas et al. 2013; Wang et al. 2007). Chloroform ($CHCl_3$) and chlorobenzene (C_6H_5Cl) are found to be most versatile solvents for such applications. The addition of second solvent, also called as 'co-solvent', improves the morphology of the active layer effectively. By carefully optimizing the morphology, formation of interpenetrating network can be obtained (Gur et al. 2007). Chloroform with pyridine or chlorobenzene with pyridine in suitable proportion have been found as ideal solvent mixture for the hybrid solar cells applications (Zhou et al. 2012). To find out the charge transfer between organic and inorganic components in a hybrid, methods such as cyclic voltammetry and photoluminescence analysis are widely followed. Moreover, electrochemical, spectro-electrochemical and photoelectron spectroscopic studies are necessary to find the energy level position of the hybrid constituents. The energy levels of various inorganic semiconductor nanoparticles and organic polymer are given in Fig. 7.5.

The mechanism involving in the operation of organic-inorganic hybrid solar cell can be described as follows: when light falls on the active layer, the charge generation or photo-induced electron transfer occurs in the donor polymer from HOMO to LUMO level. This electron-hole pair should eventually diffuse towards the donor-acceptor interface. The diffusion length of the semiconducting polymers is very short one. For the polyphenylene vinylene (PPV), it is about 5–10 nm, and for the polythiophenes, it is about ~5 nm. Hence, the effective charge separation should occur within this distance in order to avoid the efficiency loss in the device. The interface of the organic-inorganic hybrid system is very crucial. At the interface, dissociation of the charges takes place which then ultimately move towards their opposite electrodes (Fig. 7.6).

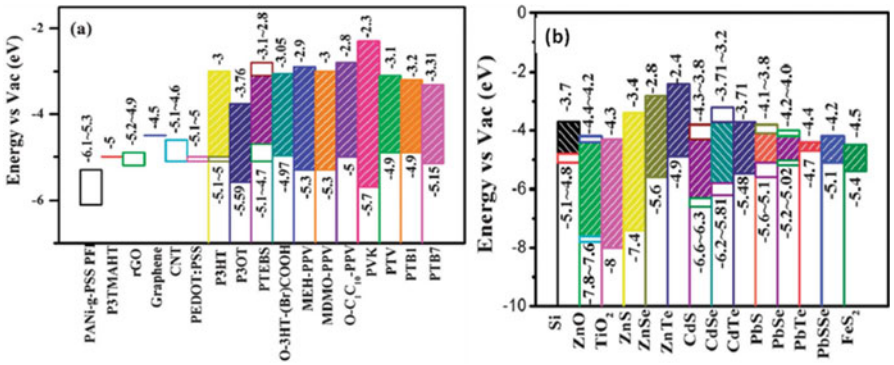

Fig. 7.5 Schematics of energy bands of frequently used (**a**) organic polymers and (**b**) inorganic semiconductor materials. (Reprinted with permission from Fan et al. Copyright@2013, Royal Society of Chemistry)

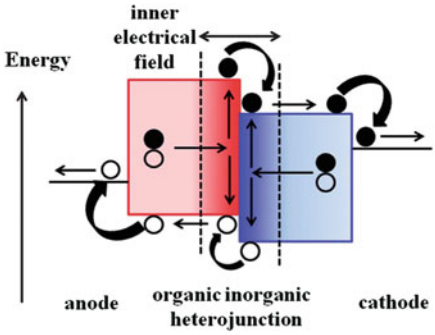

Fig. 7.6 Charge transfer process in organic-inorganic hybrid solar cells. (Reprinted with permission from Fan et al. Copyright@ 2013, Royal Society of Chemistry)

7.6.6 Advantages and Disadvantages of Hybrid Solar Cells

The major advantages and disadvantages of hybrid solar cells are given below (Moule et al. 2012).

Advantages

(a) Both electron donor polymer (P3HT) and acceptor nanoparticle (CdSe) components contribute to light absorption.
(b) Identity of the inorganic component can be altered.
(c) Shape of the nanoparticles can be modified in order to increase the surface area.
(d) Fabrication process is extremely simple with both components spin-coated from a common solution, and morphology is self-assembled.
(e) Deposition of large surface, cheap substrates are possible using suitable solvents and reaction parameters.

Disadvantages

(a) Phase separation in self-assembled morphologies is usually appeared as too large.
(b) Solubility of nanoparticles is very limited. Not all solvents are useful for the deposition process.
(c) Ligands that provide solubility for the nanoparticles are usually insulating in nature. This strongly affects the charge conduction process.

The most frequently used semiconducting polymers in hybrid solar cell are given in Fig. 7.7.

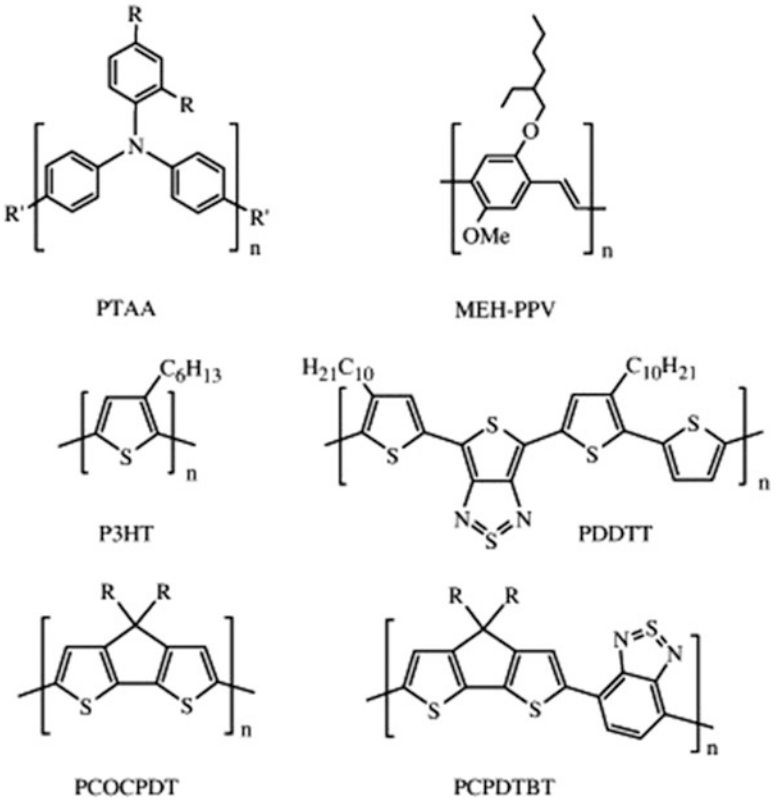

Fig. 7.7 Semiconducting polymers used in the active layer of hybrid solar cells. (Reprinted with permission from Saunders et al. Copyright@ 2008, Elsevier)

7.6.7 Stability and Future of Hybrid Solar Cells

On comparing with organic acceptor molecules, inorganic semiconducting nanoparticles significantly offer a good stability. However, because of similar device configuration, hybrid solar cells also have problematic stability issues like organic solar cells. In terms of efficiency, it still lacks due to the less developed donor and acceptor components. Materials which absorb large amount of photons are required in order to achieve higher efficiency in this category. Since most of the nanoparticles are with heavy metals, environmentally benign nanomaterials should also be developed and studied for the hybrid solar cell applications. Also, multi-junction approaches with new materials would also be a better way in order to improve the efficiency from the present level.

7.7 Dye-Sensitized Solar Cells (DSSCs)

7.7.1 Principle and Working Mechanism of DSSCs

Dye-sensitized solar cells are considered as a new paradigm for the low-cost and high-efficiency solar cells. The seminal report of O'Regan and Gratzel (1991) triggered much intensive research in this field. This device structure consists of totally four components, namely, photoanode, sensitizer, electrolyte and a counter electrode. A photoanode is typically a nanocrystalline titanium dioxide (TiO_2) coated (about 1–10 μm) on the conducting glass substrate (generally FTO). Various morphologies of TiO_2 nanomaterials such as spherical, rod, hierarchical and tubular were analysed effectively for the photoanode applications. These structures strongly affect the light harvesting, charge injection and charge-collecting properties of the DSSCs. Since TiO_2 is a wide-bandgap material ($E_g = 3.2$ eV for anatase phase), its absorption range is limited only up to the UV region. To improve the light absorption in the visible region, organometallic ruthenium-based dyes are used as effective sensitizers. Upon illumination of the dye, electron from the highest occupied molecular orbital (HOMO) transfers to lowest unoccupied molecular orbital (LUMO) which then transfers into the photoanode in a femtosecond time scale. Ruthenium-based molecular sensitizers such as cis-di(thiocyanato)bis(2,2′-bipyridyl)-4,4′-dicarboxylate)ruthenium(II) (termed as N3 or N-719 dye) which absorbs photons in the wavelength of 400–800 nm are extremely versatile for DSSCs. These dyes have good anchoring groups like -COOH in its side chain which helps them to get better adsorption with surface of the highly mesoporous TiO_2 layer. Other than ruthenium dyes, potential compounds such as osmium (II) complex, metal-free dyes, organic dyes and porphyrin dyes were also analysed (Wu et al. 2012; Chaurasia and Lin 2016; Blaszczyk 2018; Higashino and Imahori 2015). Natural dyes are another group of dyes frequently used to construct low-cost DSSCs, but still the performance of natural dyes are very low compared with the ruthenium-based molecular dyes.

Methods like incorporation of energy relay dyes, co-sensitization have been observed as suitable ways to enhance the efficiency of the DSSCs. To regenerate oxidized dye molecule, a redox electrolyte system is used which complete the external circuit. Generally, iodine/tri-iodide (I^-/I_3^-) electrolyte system is used for this process though other compounds such as Br^-/Br_3^-, $SCN^-/(SCN)_3^-$ and $SeCN^-/(SeCN)_3^-$ were also analysed (Wu et al. 2015). For the solid-state dye-sensitized solar cells, Spiro-OMeD was widely used as a better hole-transporting material. Ionic liquids (ILs) have also emerged as the potential electrolytes for DSSCs. For the counter electrode, platinum-coated FTO is used. In recent years, replacing platinum with low-cost good electrocatalytic materials has turned as new interest among researchers. The best efficiency of DSSCs was in between 10% and 12% in the last decade, and recently it has been upgraded over 14% (Kakiage et al. 2015). The basic device configuration and energy level diagram of a DSSC are given in Fig. 7.8.

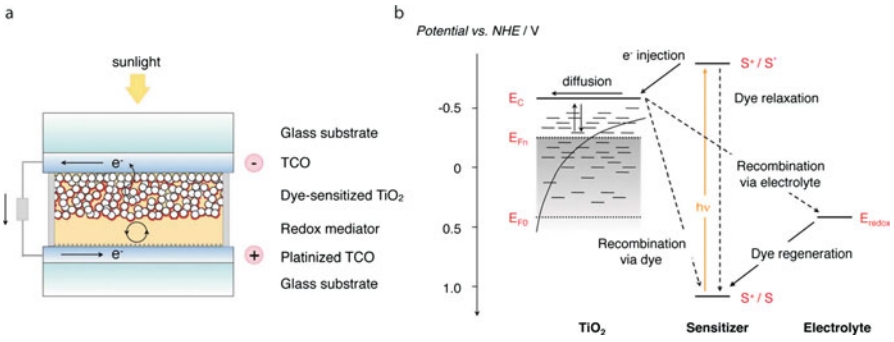

Fig. 7.8 (**a**) Basic structure of a DSSC and (**b**) illustration of the typical energy diagram of DSSC. (Reprinted with permission from Tetreault and Gratzel, Copyright@ 2012, Royal Society of Chemistry)

Some of the interesting process and facts associated with the dye-sensitized solar cells are given below (Hagfeldt et al. 2010).

- Under working conditions, there are about ten electrons present per TiO_2 nanoparticle.
- More than 90% of electrons in TiO_2 nanoparticles are trapped, and <10% are in the conduction band.
- There are ~10,000 adsorption sites available for H^+ on an 18 nm (diameter) size of TiO_2 nanoparticle.
- A TiO_2 nanoparticle (18 nm) has the capability of having ~600 dye molecules on its surface with suitable functional group attachment.
- Under the optimized conditions, each dye molecule effectively absorbs a photon once per second.
- The flux of electron injection into the TiO_2 nanoparticle is estimated as ~600 s^{-1}.
- Under working conditions, it is observed that about 1 dye per 150 TiO_2 nanoparticles is in its oxidized state.
- The total volume fraction of the solutes present in the electrolyte is calculated as about ~10 to 20%.
- In the pore volume around the TiO_2 nanoparticle, it is estimated that there will be ~1000 I^- and 200 I_3^- ions.
- The concentration of iodine, I_2, is <1 μM, that is, about 1 free iodine is available per 10,000 TiO_2 nanoparticles.

7.7.2 Role of Counter Electrode and Its Replacement

Once the electrons from photoexcited dye are injected into the TiO_2 layer, it's oxidized by the receiving electrons from redox electrolyte. Hence, the redox electrolyte should get reduced by the electrons from the external circuit (Fig. 7.9). In this

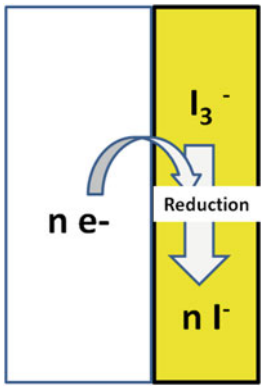

Fig. 7.9 Schematic diagram of reduction of electrolyte at the counter electrode of DSSC

stage, the counter electrode plays a major role in injecting electrons to redox electrolyte. The suitable counter electrode material for DSSC is identified based on its ability to reduce the over potential. The intrinsic catalytic activity of the counter electrode material functioning as effectively to regenerate the redox electrolyte (Faber and Jin 2014). A counter electrode material should also be a low cost, highly conductive, easy scalable, chemical and electrochemical stable. The most commonly used counter electrode material for the DSSCs is a noble metal, platinum. Since platinum is a high-cost material, development of the low-cost counter electrode material which is equal or surpasses the catalytic activity of platinum is indispensable. Also, for the quantum dot-sensitized solar cells, the platinum electrode is strongly affected by the polysulphide redox electrolyte which reduces its performance. Many compounds/nanocomposites including carbon-based materials, conducting polymers, metal sulphide, metal oxide materials, transition metal nitrides and carbides have been analysed for the counter electrode applications which is shown in Fig. 7.10 (Theerthagiri et al. 2015; Yun et al. 2014; Wu et al. 2017). But the earthy abundant materials with good electrocatalytic activity have generated large interest among researchers. Recently emerging copper-based binary, ternary and quaternary sulphide/selenide nanomaterials have shown promising results for the counter electrode applications. The so far achieved results clearly predict that these materials are almost equal or superior performance in solar cells. Methods such as electrodeposition, doctor blade, spray deposition and spin coating are being followed for the preparation of counter electrode materials on conducting substrate for DSSC applications. Optimization of thickness of the depositing layers is trivial, and these techniques immensely help to achieve high electrocatalytic activity of counter electrode through meticulous tuning of various parameters.

Stability of DSSCs is also a critical issue to handle since the organometallic dyes and electrolytes are not quite stable for a long time. Contamination of photocathode, incorporation of oxygen and moisture from atmosphere, desorption and degradation of dyes, degradation of all components by UV light irradiation from the sunlight and thermal stress, etc. are the major existing challenges in improving the stability (Castro-Hermosa et al. 2016). Electrolytes may leak from the device, and hence proper sealants like Surlyn, Bynel or certain kind of resins are required to protect

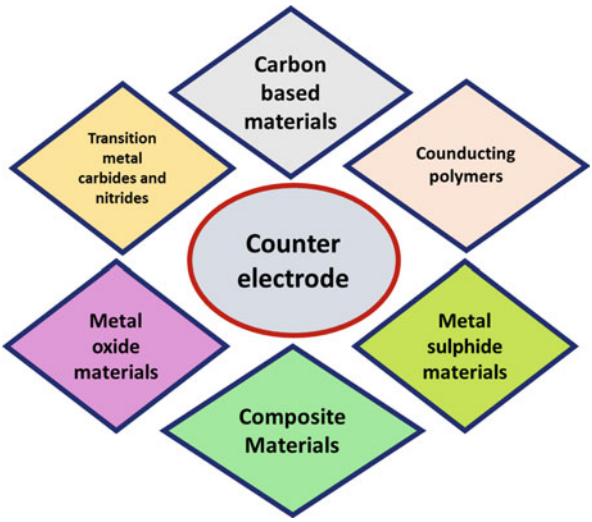

Fig. 7.10 Wide variety of materials used for the counter electrode applications of DSSC. (Adapted from Theerthagiri et al. 2015)

it. All these factors should be considered for the large module production of DSSCs, and hence proper outdoor tests with suitable materials would alleviate the existing obstacles in the near future.

7.7.3 Future of Dye-Sensitized Solar Cells

Development of new dyes and new inorganic nanomaterials will have new possibilities in improving the efficiency of DSSCs. Also, exploration of methods to improve dye loading, stability will also help some extent. Two terminal tandem architectures of silicon together with a DSSC have been reported as exceeding 18% efficiency with high V_{oc} of 1.36 V (Kwon et al. 2016), and this kind of approach with new molecular dyes would deliver higher efficiency. New potential direction such as solar hydrogen production using DSSCs is also a promising method, and several research findings are discussing about this approach (Ajayi et al. 2010; Sabatini et al. 2014; Cecconi et al. 2016). Also, integrated device approaches of DSSCs with perovskite solar cells also seem to be another interesting technology for the construction of future generation devices (Yun et al. 2018).

7.8 Quantum-Dot Sensitized Solar Cells (QDSSCs)

7.8.1 Basic Introduction of QDSSCs

Quantum dot-sensitized solar cells (QDSSCs) are nowadays a promising third-generation solar cell technology due to advantages of QDs like light-absorbing

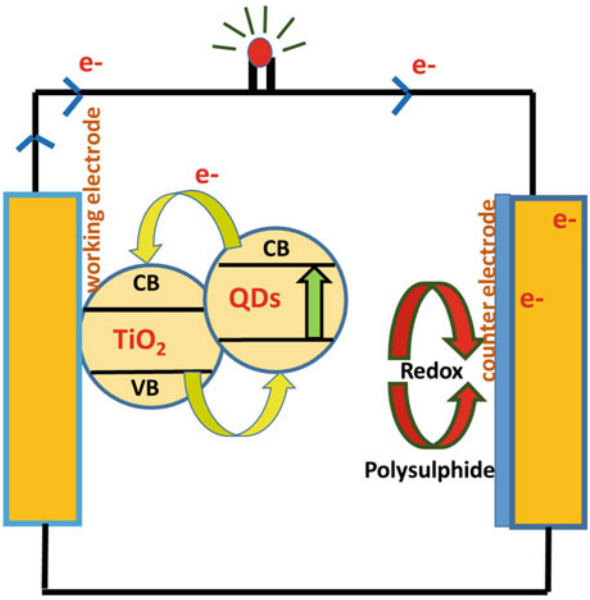

Fig. 7.11 Schematic diagram of basic device structure of a QDSSC

ability towards infrared (IR) region, hot electron injection, good photochemical stability over dyes and the increasing efficiency through multiple electron generation (MEG) (Kamat 2013). The extremely promising optical, structural properties of QDs have shown good assurance for the future generation solar cells. Importantly, MEG phenomena has been experimentally proved in the PbS and PbSe QDs by prominent research groups. For example, Ellingson et al. (2005) have experimentally proved that a 3.9 nm diameter of PbSe nanoparticle produced 300% quantum yield when irradiated by photon energy which is equal to four times of its bandgap. The basic device structure of QDSSCs is adopted from the DSSCs where the dye is replaced by QDs for the sensitization. The energy difference between QDs and metal oxide (mostly TiO_2 nanoparticles) facilitates the driving force for the efficient electron transfer. The QDs may be a bimetallic nanoparticles or with core-shell structure of another compound. The device structure consists of working electrode, QDs, electrolyte and counter electrode. The schematic diagram of basic assembly of a QDSSC is given in Fig. 7.11.

7.8.2 Materials, Methods and Working Mechanism of QDSSCs

Several inorganic semiconductor sensitizers like CdS, CdTe, CdSe, PbS, PbSe, SnS and SnSe were studied either individually or with core-shell-like structures for QDSSC applications. Because of limitation of the materials, higher power

conversion efficiency was achieved within the best structure of these materials with best available approaches. The major steps occurring in the QDSSCs can be described as (i) charge separation, (ii) charge recombination, (iii) charge regeneration and (iv) charge transport. When light strikes on the active layer, as a first step, photoexcitation takes place. After photoexcitation, charge separation takes place at the interface of QD and metal oxide. This process takes place if only the energy level of QDs and metal oxide is energetically favourable. Then, finally the oxidized nanoparticles are balanced by the redox electrolyte (polysulphide). All these process are extremely sensitive to the solvents, materials and fabrication procedures followed. Though the structure of QDSSC is similar to DSSC, there are notable differences between these two technologies. For example, depending on the composition of the solar cell, a photo-induced band-edge shift may occur in QDSSCs (Albero et al. 2014). Also, because of incompatibility, in QDSSCs, the traditional redox electrolyte iodide/triiodide couple used in DSSCs is replaced by the polysulphide electrolyte (S^{2-}/S_x^{2-}).

The most important challenge exists in the fabrication of a QDSSC is formation of crack-free layer of nanocrystalline particles. Importantly, meticulous observation is required to achieve such kind of film quality and solvents and deposition cycles; ligands used for the exchange process severely affect the formation of thin film of nanoparticles. As we know that metal chalcogenide nanoparticles have many defect centres on their surface, the role of organic ligands is very important in reducing them effectively. These defects are serving as recombination centres during charge transfer process, but efficient passivation has been proved to be an excellent way in suppressing it. Short chain ligand-like mercaptopropionic acid (MPA) capped metal chalcogenide nanoparticles are found to be very effective in producing higher efficiency under various conditions. When nanoparticles are synthesized through high temperature reaction using trioctyl phosphine (TOP), oleylamine (OLAm) as ligands, MPA is found to be successful in the ligand-exchange process (Feng et al. 2016). Here, the finally formed nanocrystalline films are treated with the alcoholic solution (usually methanol or ethanol) of MPA to remove the native ligands. The interparticle distance of nanoparticles is significantly reduced after this process, and improved charge transport is feasible. Other than MPA, ligands such as hydrazine (Semonin et al. 2011), halide ions (Crisp et al. 2015) and amines (Law et al. 2008) also found to be useful for the surface treatment processes. Surprisingly, it is found that treatment of nanoparticles using these ligands converts the nanoparticles conductivity to either p- or n-type (Law et al. 2008). Chemical bath deposition (CBD), successive ionic layer absorption and reaction (SILAR), ex situ grown QDs deposition are widely followed to sensitize the QDs on working electrode. The physical and chemical parameters of these methods are very important, and they are the deciding factors for the high efficiency while fabricating solar cells. In SILAR, the photoanode is immersed in the precursor solutions of cationic and anionic sources at different cycles and time intervals. Optimization of layer thickness through different deposition cycles assures the photon harvesting ability of layers and efficiency. In case of CBD, the basic principle is when ionic product exceeds solubility product, precipitation takes place in solution. Unlike SILAR, both anionic and cationic

Table 7.1 Factors affecting the performance of QDSSCs and their analysing methods

Property	Related solar cell parameters	Testing method
Carrier mobility	J_{sc}, FF	CELIV, TOF, transient decay
Trap density	V_{oc}, J_{sc}, FF	V_{oc} transient decay
Doping density	V_{oc}, FF	Capacitance-voltage, FET
Carrier life time	J_{sc}, FF	V_{oc} transient decay
Diffusion length	J_{sc}, FF	Photoluminescence quenching

J_{sc} short-circuit current, V_{oc} open-circuit voltage, *FF* fill factor, *CELIV* carrier extraction by linearly increasing voltage, *TOF* time of flight, *FET* field effect transistor. (Adapted from Carey et al. 2015)

precursors are taken in the same beaker for the CBD process. Both these methods are well analysed to fabricate highly efficient QDSSCs with different structural configurations. Other than these two, ex-situ methods such as direct linker-assisted deposition of QDs on metal oxide substrate (Wang et al. 2012) and electrophoretic deposition of QDs (Salant et al. 2010) were also analysed. Because of precise particles controlling ability, SILAR is the mostly followed method over other methods.

The important parameters affect the device performance in QDSSCs are carrier mobility, doping density, trap density and diffusion length in nanocrystalline films which are tabulated in Table 7.1 (Carey et al. 2015). Analysis of the interface between TiO_2/QDs/electrolyte in QDSSCs reveals the cause of recombination which helps to improve the efficiency of the device. In a recent report, about 8% efficiency is achieved through intensive research since the last decade (Zhao et al. 2015). Though the device architecture is almost the same for both DSSC and QDSSCs, the counter electrode is very sensible with the quantum dots and electrolyte, and hence nature of platinum may be affected. Thus, most of the cases, the platinum-free electrodes have been reported with high efficiency in QDSSCs.

7.8.3 Future Direction of QDSSCs

Materials, method of sensitization and developments in sensitizers, electrolyte and counter electrode have been a keen interest among researchers in this area, and intensive investigation is ongoing in different disciplines of this field. Though the attained efficiency is reasonable compared with its previous level, collection of multiply excited carriers through MEG is very less (about 4%) and this to be enhanced. However, lead chalcogenide nanomaterials are showing extremely promising stability (over 1000 h under continuous illumination) (Luther et al. 2010) over other nanoparticles, and suitable technology of utilizing led them for long-term use to be scrutinized. By reducing surface recombination processes, it is expected that inorganic nanoparticle-based solar cells could surpass the efficiency reached by the same materials in bulk thin film structure. The photon-absorbing ability of nanocrystalline thin films should also be enhanced further through necessary surface

engineering process. Recently, luminescent solar concentrators associated with the QDSSCs, constructing inverted structures, are identified as promising way to achieve high efficiency (Wang et al. 2018; Brennan et al. 2018; Wu et al. 2018). Such kind of efforts are expected to pave a new platform in this area.

7.9 Organic-Inorganic Hybrid Perovskite Solar Cells (OIHPSCs)

7.9.1 Introduction of OIHPSCS

Hybrid perovskites are having the common structure of ABX_3 in which A is organic cation(s) (e.g. $CH_3NH_3^+$, $C_2H_5NH_3^+$, etc.), B is the metal ion(s) (Pb^{2+}, Sn^{2+}, Bi^{2+}, etc.) and X is halide ion(s) (Cl^-, Br^-, I^-). Perovskite solar cells are currently hot area of research because of their impressive efficiency record within the short span of time. Organo-methyl ammonium lead halides ($CH_3NH_3PbX_3$, X= Cl^-, Br^-, I^- are a class of perovskites that are analysed for potential photovoltaic applications in the last couple of years. The large number of scientific publications with impressive results in this field boosts this hope additionally. The outstanding scientific contributions of Miyasaka (2017), Snaith (2013) and Park (2015) in the organometal halide perovskite solar cells have strengthen the significant achievement in the near future. Mesoscopic perovskite solar cells are much investigated in the last few years because of their promising avenue of increasing the efficiency. Having the common structural formula of ABX_3 (where A, B are cations and X = halogens), the high absorption coefficient of organometal halide perovskites in the visible region (from 10^4 to 10^5 cm^{-1}) particularly, $CH_3NH_3PbI_3$, has shown the excellent light harvesting ability, high charge-carrier mobility, more conductive (10^{-3} S cm^{-1}), large exciton diffusion length (about 1 μm) and well-matched energy band level with the commonly used electron transport and hole transport materials (Snaith 2013). The bandgap of $CH_3NH_3PbI_3$ is around 1.55 eV which could be tuned through the replacement of halogen I by Cl, Br. This kind of halide-based tuning of optical properties is one of the most advantages of hybrid as well as pure-inorganic lead halide perovskite materials. Moreover, organo-lead perovskites have very unusual open-circuit voltage (V_{oc}~1 to 1.5 V) which reveals the low thermodynamic loss in the system (Edri et al. 2013; Liang et al. 2018). The most striking material property of this organo-lead halide perovskite is having an ambipolar behaviour (i.e. working as both electron and hole transporter). Further, the electron diffusion coefficient of the perovskite-sensitized TiO_2 has been found to be higher than organic dye-sensitized TiO_2 photoanode. This predicts the high charge transport of perovskite over dyes. Moreover, the deposition of layers during the fabrication of perovskite solar cells is carried out using low temperature solution methods like spin coating. All these advantages have promoted OIHPSCs as important subject of study.

7.9.2 Device Structure, Materials of OIHPSCs

The device structure of OIHPSCs have emerged with various forms at different periods. At first, the common device structure of perovskites-sensitized/perovskites-infiltrated solar cell was given as glass/FTO/TiO_2/$CH_3NH_3PbI_3$/HTM/Ag or Au. Later, the device structure was framed with different configurations, namely, planar and mesoporous architectures and is given in Fig. 7.12. In the mesoporous-type structure, a porous layer of metal oxide is employed in order to adsorb the perovskites, and this is eliminated in the planar-type structure. Other than these configurations, an aluminium oxide (Al_2O_3) photoanode-based perovskite solar cell, called meso-superstructured solar cells (MSSCs) also successfully demonstrated. In the porous architecture, for the electron transport layer, other than TiO_2, tin oxide (SnO_2) and zinc oxide (ZnO) are also employed. It was Kojima et al. (2009) who fabricated the first perovskite-sensitized solar cell using traditional iodine/tri-iodide redox couple electrolyte with 3.8% efficiency. Due to the limitation and drawbacks with the liquid electrolytes, the scenario of the hole conductor has changed from liquid to solid state. Different hole transport materials (HTMs) such as PEDOT:PSS, P3HT, PCPDTBT, PCDTBT, poly-triarylamine (PTAA), $CsSnI_3$ and spiro-OMeTAD were studied with $CH_3NH_3PbI_3$ in device performance. Even though spiro-OMeTAD was studied much (since the redox potential of spiro-OMeTAD fits better with organic dyes) for HTM, a recent analysis demonstrated using PTAA which function as best HTM with improved efficiency ($\eta = 12\%$) and high-hole mobility ($\sim 1 \times 10^{-2}$ to $\sim 1 \times 10^{-3}$ cm^2 V^{-1} s^{-1}), high work function than spiro-OMeTAD. Other than organic HTMs, p-type inorganic semiconductor materials such as CuSCN, PbS, Cu_2O and CuO were also successfully used. Starting the efficiency from 3.8% (2009), about 22.1% (2017) of efficiency has reached so far within a short period in perovskite solar cells (Yang et al. 2017). When the TiO_2

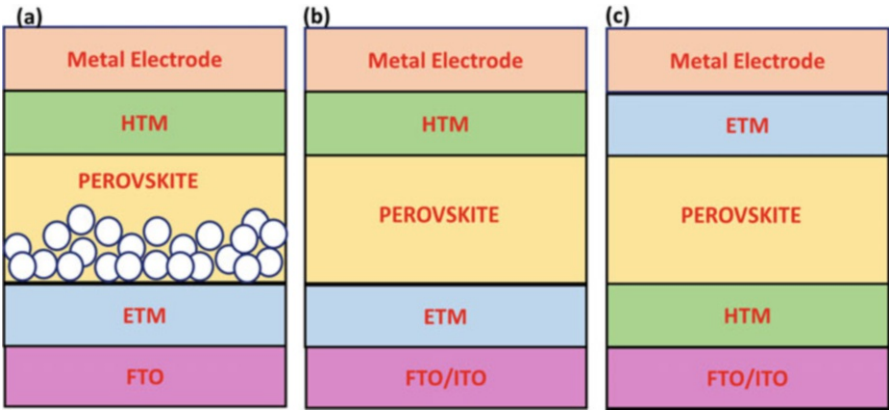

Fig. 7.12 Basic device structure of perovskite solar cell with different configuration (**a**) mesoporous (**b**) planar n-i-p (regular) structure and (**c**) planar p-i-n (inverted) structure. (Adapted from Bai et al. 2018)

layer was replaced by the insulating Al_2O_3 layer, an enhanced efficiency ($\eta = 12.3\%$) was found due to the direct transfer of electron from perovskite to contact electrode. Thus, Al_2O_3 was simply functioned as 'scaffold' for the perovskite sensitization in these kind of MSSCs. Recently, over 15% efficiency has achieved through the sequential deposition and vapour phase deposition technique which is a remarkable record in the hybrid organic-inorganic solar cell research field (Seok et al. 2018). The fundamental working mechanism of perovskite-sensitized solar cell is yet to understand and there are several proposed theories describing about the possible operation. Moreover, processes such as ion migration and hysteresis are still under intensive study. But the obtained results clearly predict the possibility towards attaining more than 25% efficiency in the near future.

Interestingly, the application of perovskite has also been coupled with the quantum dot-sensitized solar cells, where PbS nanoparticles are covered by a perovskite layer which made a core-shell arrangement and enhancing considerable photovoltaic performance (Seo et al. 2014). Apart from photovoltaics, the possibility of applying $CH_3NH_3PbX_3$ has also successfully extended to gas sensor applications to detect gases, e.g. NH_3 (Zhao and Zhu 2014). The possible prediction of expanding the direction from current single cell to tandem perovskite architecture has also stimulated large interest (Sobus and Ziolek 2014). Besides, the nanowire structure formation of template-directed synthesis of perovskites has turned to future motivation for the next-generation photovoltaic applications (Rauda et al. 2013). The day-by-day improvements of materials modification, device architecture and the method of fabrication of active layer and playing with the electrode modification via active materials have stimulated huge interest for the last couple of years. Both planar and sensitized architecture of hybrid perovskite solar cells are actively moving with their own record-breaking results. The effort on up-scaling of solid-state perovskite solar cell modules (Matteocci et al. 2014) has also given a big hope on its future progress. The improvement in materials and methods in perovskite solar cells lead to the successful demonstration of flexible type of perovskite solar cells (Susrutha et al. 2015). It is expected that future approaches in fabrication of devices will help to reach the higher efficiency. In recent years, because of the toxicity of lead, 'lead-free' perovskite solar cell materials have developed which also showing promising efficiencies. Elements such as tin (Sn), bismuth (Bi) and stibium (Sb) were used in place of Pb, and their performance was also evaluated. A planar-type configured $FASnI_3$ solar cell has reached about 9% efficiency recently (Shao et al. 2017). However, poor stability and high number of defects associated with lead have not admitted to improve the efficiency further. Similarly, though Bi-based perovskite solar cells show impressive stability over lead counterpart, the presently achieved highest efficiency is 3.17% only (Jain et al. 2018).

7.9.3 Stability and Future Direction of OIHPSCs

Stability of perovskite solar cells is strongly affected by water, moisture and UV light. When the humidity is high, it has been found that about 55% of $MAPbI_3$ start to decompose (Noh et al. 2013). In this process, the initially formed degradation components are CH_3NH_3I and PbI_2. This CH_3NH_3I further degrade into two components, namely, methylamine (CH_3NH_2) and hydriodic acid (HI) (Niu et al. 2015). The finally formed HI also decomposes into H_2O and I_2. All these indications can be observed through the change of colour of the perovskite film from dark black to yellow. The stability of perovskite structures has been showing decreasing trend moving towards from I^- to Cl^-. Though tin-based hybrid perovskites showing extremely less stability, interestingly, it is found that incorporation of appropriate percentage of Pb atoms significantly improve the stability in addition with large spectral absorption (Ogomi et al. 2014). Also, addition of rubidium (Rb^+) and Cs^+ ions helped to reach the hybrid solar cells efficiency to 21.6% (Saliba et al. 2016). These kinds of modifications in the composition with new perovskite materials could deliver promising performances in the near future. For the future consideration, theoretical and experimental approaches of developing new perovskite structure materials are necessary in order to move ahead from the present level. Approach such as multi-junction (tandem) architecture of perovskite solar cells seems to be more promising. A four-terminal Si-perovskite-based solar cell has been demonstrated with over 20% efficiency (Quiroz et al. 2018). Both wide-bandgap and narrow bandgap perovskite materials are being analysed as top cell in this concept. It is predicted by theoretically that Si-perovskite tandem architecture could reach the efficiency of up to 31% which is a positive indication to commercializing the product (Leijtens et al. 2018). Certainly says, reliable deposition methods, fabricating high-quality stable layers, new material compositions and novel tandem approaches will bring this field into new direction in near future.

7.10 Colloidal Semiconductor Nanoparticles: Properties and Synthesis in Aqueous Medium

For the most of the above discussed solar cell applications, inorganic semiconductor nanomaterials are synthesized through colloidal method. Colloidally synthesized nanoparticles are useful for the applications of hybrid solar cells and quantum dot-sensitized solar cells. Semiconductor nanoparticles are the small crystalline particles having the sizes around 1–100 nm. When the dimension of these nanoparticles is lesser than the Bohr exciton radius (i.e. the average distance between the e^-s in the conduction band and the hole it leaves behind in the valence band), the optical properties of these nanoparticles vary due to the formation of discrete energy levels which is useful for many applications. Compared to other methods, colloidal method of synthesizing nanoparticles has many advantages. The resultant

nanoparticles after purification can be applied through spin coating, drop casting and ink jet printing for the potential applications such as light-emitting diodes (LED), solar cells, etc. (Talapin et al. 2010). Moreover, colloidal synthesized semiconductor nanoparticles can be utilized for solar cell applications by dispersing in the conjugated polymer (hybrid solar cells) or directly applied for the sensitization of metal oxide photoelectrode (QDSSCs), etc. During the year 1993, Murray et al. (1993) report on organometallic solvent (usually trioctyl phosphine (TOP) combined with trioctyl phosphine oxide (TOPO))-based synthesis of semiconductor nanoparticles had initiated a platform in this area. The kinetics of semiconductor nanoparticles growth can be explained through La-Mer plot (Lesnyak et al. 2013). The synthesis is carried out either hot-injection method or heating-up method. In hot-injection, the growth of the nanoparticles takes place during the thermal decomposition of cationic precursor molecules at higher temperature followed by the injection of anionic precursor. In heating-up method, all reagents are mixed together and heated controllably to initiate the nucleation and growth of the nanoparticles (Embden et al. 2015). When the precursor concentration reaches below the critical concentration, no nucleus is formed. Growth of nanoparticles takes place at this stage through Ostwald ripening process when the temperature increases. The nanoparticles shape and size can be regulated by the kinetic control of growth process and nucleation in the presence of suitable surfactants or ligands. Size distribution of nanoparticles can also be controlled by temperature, injection temperature of reactant, solvent and pH, etc. (Chang and Waclawik 2014). Moreover, size selective precipitation of the prepared nanoparticles by suitable solvent gives uniform size distribution. The typical experimental arrangement for the synthesis of semiconductor nanoparticles through colloidal method is given in Fig. 7.13. To overcome tedious processes associated with the organometallic approach, aqueous-based synthesis of semiconductor nanomaterials has become much interested.

II-VI group semiconductor nanoparticles such as CdS, CdSe and CdTe are widely synthesized using aqueous-based approach in the presence of water-soluble thiol ligands. Advantages of aqueous synthesis over organometallic synthesis include (i) environmental friendly, biocompatible nature of water, (ii) inert atmosphere is

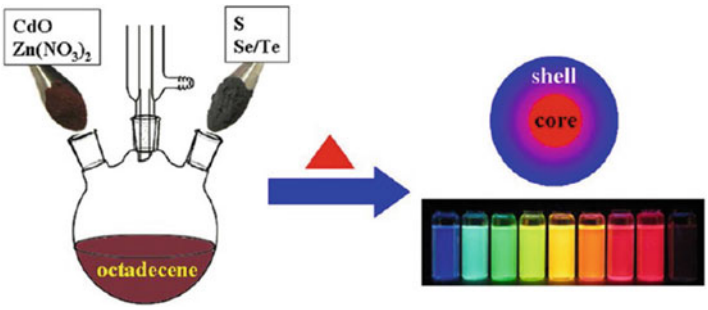

Fig. 7.13 (**a**) Schematic diagram of experimental arrangement of colloidal synthesis of core/shell QDs. (Reprinted with permission from Zhang et al. Copyright@2012 American Chemical Society)

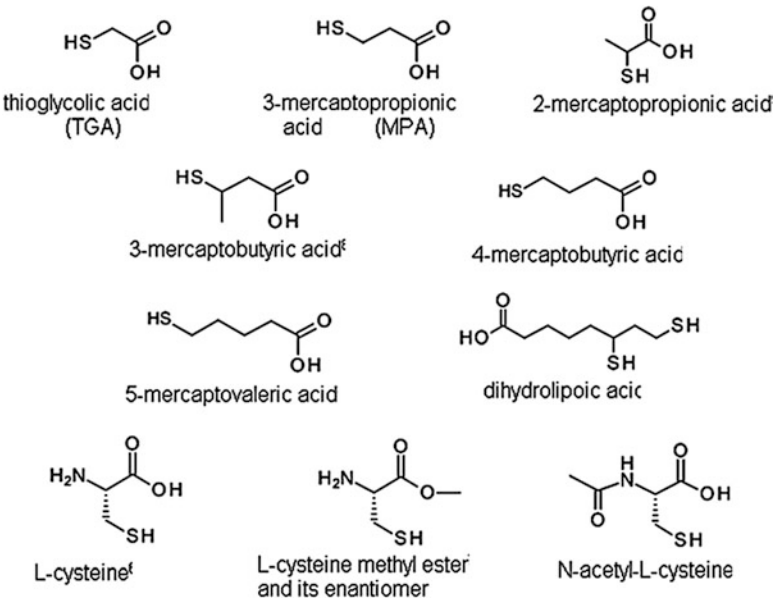

Fig. 7.14 Chemical structures of some of the thiol group ligands used in the synthesis of semiconductor nanoparticles in aqueous medium. (Reprinted with permission from Lesnyak et al. Copyright@2013 Royal Society of Chemistry)

not a mandate, (iii) easily up-scalable and (iv) adoptable for the functionalization etc. (Lesnyak et al. 2013; Murray et al. 2000). Moreover, the thiol ligands could potentially make M-SR bond (M=Cd, Zn, Hg etc., SR=thiols) on the surface of the nanoparticles, which strongly prevents the uncontrollable growth and stabilize the synthesized nanoparticles. From visible to near infrared (NIR)-emitting nanoparticles (like PbS, PbSe) are prepared using aqueous-based synthetic approach. Some of the promising ligands used in the aqueous synthesis of nanoparticles are given in Fig. 7.14.

Organic ligands such as thioglycolic acid (TGA) and 3-mercaptopropionic acid (MPA) are widely used to prepare the water-soluble semiconductor nanoparticles. The nature of ligands differs not only in their structural aspects but also in their physical and chemical properties. For example, the pK_{COOH} value of TGA is 3.53, and it is 4.32 for MPA. Replacing existing ligand from the surface of the nanoparticles also strongly reflects in the photoluminescence properties. The typical steps involving in the preparation of thiol-capped nanoparticles are listed out below (Lesnyak et al. 2013):

1. Formation of metal-thiol complexes with adjustment of pH
2. Injection of chalcogen source into the metal-thiol mixture
3. Nucleation and growth of nanoparticles by refluxing the entire mixture

Post-preparative treatment such as ligand exchange is followed to make dispersion of the nanoparticles from aqueous to organic media. Thiols like 1-dodecanethiol has been used to treat the nanoparticles surface using this strategy. Also, inclusion of additives after synthesis has been found to help in improving the photoluminescence properties of as-synthesized nanoparticles. These kinds of post-treatment processes are removing surface defects associated with the as-synthesized nanoparticles and improve their optical properties significantly.

7.11 Conclusion, Summary and Future Scope

The concepts discussed regarding third-generation solar cells are seeming to overtake the current scenario solar energy market. From the discussed point of view, it is clear that newly emerging nanomaterials flourish the ongoing research to achieve highly efficient, low-cost solar cells. Perhaps the existing challenges are tackled by the scientific community through various ways, it is seen that there should be a strong platform to be launched in order to develop solar cells using nanomaterials. The remarkable efficiency improvement in perovskite solar cells research area clearly reveals the promising path to high efficiency large area modules in near future. Perhaps setbacks regarding the high cost of raw materials should be dealt severely. Flexible substrates are often costly in nature, and this affects constructing new-generation solar cells with low-cost expenses. Industrial approaches such as roll-to-roll fabrication and inkjet printing of different layers are to be enlarged with new materials so that the possibilities of expanding it for commercialization can be assured. Also, new materials that harvest up to near infrared (NIR) region are required in order to improve the efficiency. Development of such new materials for highly efficient solar cells can be accomplished through colloidal synthesis route. The future of this field clearly predicts that it is still possible to reach the goal of harvesting huge amount of photons by functionalizing different kinds of inorganic semiconductor nanomaterials, organic polymers and dyes with suitable molecules.

Acknowledgements The authors sincerely acknowledge DST (DST/TMC/SERI/FR/90), Govt. of India and DST-PURSE for funding the research.

References

Abdou MSA, Orfino FP, Son Y, Holdcroft S (1997) Interaction of oxygen with conjugated polymers: charge transfer complex formation with poly(3-alkylthiophenes). J Am Chem Soc 119:4518–4524. https://doi.org/10.1021/ja964229j

Ajayi FF, Kim K-Y, Chae K-J, Choi M-J, Chang IS, Kim IS (2010) Optimization studies of bio-hydrogen production in a coupled microbial electrolysis-dye sensitized solar cell system. Photochem Photobiol Sci 9:349–356. https://doi.org/10.1039/B9PP00097F

Albero J, Clifford JN, Palomares E (2014) Quantum dot based molecular solar cells. Coord Chem Rev 263–264:53–64. https://doi.org/10.1016/j.ccr.2013.07.005

Anaraki EH, Kermanpur A, Mayer MT, Steier L, Ahmed T, Turren-Cruz S-H, Seo J, Luo J, Zakeeruddin SM, Tress WR, Edvinsson, Gratzel M, Hagfeldt A, Correa-Baena JP (2018) Low-temperature Nb-doped SnO_2 electron-selective contact yields over 20% efficiency in planar perovskite solar cells. ACS Energ Lett 3(4):773–778. https://doi.org/10.1021/acsenergylett.8b00055

Bai Y, Meng X, Yang S (2018) Interface engineering for highly efficient and stable planar p-i-n perovskite solar cells. Adv Energy Mater 8:1701883. https://doi.org/10.1002/aenm.201701883

Beard MC, Luther JM, Nozik AJ (2014) The promise and challenge of nanostructured solar cells. Nat Nanotechnol 9:951–954. https://doi.org/10.1038/nnano.2014.292

Blaszczyk A (2018) Strategies to improve the performance of metal-free dye-sensitized solar cells. Dyes Pigments 149:707–718. https://doi.org/10.1016/j.dyepig.2017.11.045

Brennan LJ, Purcell-Milton F, McKenna B, Watson TM, Gun'ko YK, Evans RC (2018) Large area quantum dot luminescent solar concentrators for use with dye-sensitized solar cells. J Mater Chem A 6:2671–2680. https://doi.org/10.1039/C7TA04731B

Cardinaletti I, Vangerven T, Nagels S, Cornelissen R, Schreurs D, Hruby J, Vodnik J, Devisscher D, Kesters J, D'Haen J, Franquet A, Spampinato V, Conard T, Maes W, Deferme W, Manca JV (2018) Organic and perovskite solar cells for space applications. Solar Energ Mater Solar Cells 182:121–127. https://doi.org/10.1016/j.solmat.2018.03.024

Carey GH, Abdelhady AL, Ning Z, Thon SM, Bakr OM, Sargent EH (2015) Colloidal quantum dot solar cells. Chem Rev 115:12732–12763. https://doi.org/10.1021/acs.chemrev.5b00063

Castro-Hermosa S, Yadav SK, Vesce L, Guidobaldi A, Reale A, Di Carlo A, Brown TM (2016) Stability issues pertaining large area perovskite and dye-sensitized solar cells and modules. J Phys D Appl Phys 50:033001. https://doi.org/10.1088/1361-6463/50/3/033001

Cecconi B, Manfredi N, Montini T, Fornasiero P, Abbotto A (2016) Dye-sensitized solar hydrogen production: the merging role of metal-free organic sensitizers. Eur J Org Chem 2016:5194–5215. https://doi.org/10.1002/ejoc.201600653

Celik D, Krueger M, Veit C, Schleiermacher HF, Zimmermann B, Allard S, Dumsch I, Scherf U, Rauscher, Niyamakom P (2012) Performance enhancement of CdSe nanorod-polymer based hybrid solar cells utilizing a novel combination of post-synthetic nanoparticle surface treatments. Solar Energ Mat Solar Cells 98:433–440. https://doi.org/10.1016/j.solmat.2011.11.049

Chang J, Waclawik ER (2014) Colloidal semiconductor nanocrystals: controlled synthesis and surface chemistry in organic media. RSC Adv 4:23505–23527. https://doi.org/10.1039/C4RA02684E

Chang P, Li G, Zhan X, Yang Y (2018) Next-generation organic photovoltaics based on non-fullerene acceptors. Nat Photonics 12:131–142. https://doi.org/10.1038/s41566-018-0104-9

Chaurasia S, Lin JT (2016) Metal-free sensitizers for dye-sensitized solar cells. Chem Rec 16 (3):2016. https://doi.org/10.1002/tcr.201500288

Chen H-Y, Hou J, Zhang S, Liang Y, Yang G, Yang Y, Yu L, Wu Y, Li G (2009) Polymer solar cells with enhanced open-circuit voltage and efficiency. Nat Photon 3:649–653. https://doi.org/10.1038/nphoton.2009.192

Chen W, Zhang J, Xu G, Xue R, Li Y, Zhou Y, Hou J, Li Y (2018) A semitransparent inorganic perovskite film for overcoming ultraviolet light instability of organic solar cells and achieving 14.03% efficiency. Adv Mater 30:1800855 (1–10). https://doi.org/10.1002/adma.201800855

Cheng P, Zhan X (2016) Stability of organic solar cells: challenges and strategies. Chem Soc Rev 45:2544–2582. https://doi.org/10.1039/C5CS00593K

Chopra KL, Paulson PD, Dutta V (2004) Thin film solar cells: an overview. Prog Photovolt 12 (2–3):69–92. https://doi.org/10.1002/pip.541

Crisp RW, Kroupa DM, Marshall AR, Miller EM, Zhang J, Beard MC, Luther JM (2015) Metal halide solid-state surface treatment for high efficiency PbS and PbSe QD solar cells. Sci Rep 5:9945(1–6). https://doi.org/10.1038/srep09945

Dubey A, Adhikari N, Mabrouk S, Wu F, Chen K, Yang S, Qiao Q (2018) A strategic review on processing routes towards highly efficient perovskite solar cells. J Mater Chem A 6:2406–2431. https://doi.org/10.1039/C7TA08277K

Edri E, Kirmayer S, Cahen D, Hodes G (2013) High open-circuit voltage solar cells based on organic-inorganic lead bromide perovskite. J Phys Chem Lett 4(6):897–902. https://doi.org/10.1021/jz400348q

Ellingson RJ, Beard MC, Johnson JC, Yu P, Micic OI, Nozik AJ, Shabaev A, Efros AL (2005) Highly efficient multiple exciton generation in colloidal PbSe and PbS quantum dots. Nano Lett 5:865–871. https://doi.org/10.1021/nl0502672

Embden J, Chesman ASR, Jasieniak JJ (2015) The heat-up synthesis of colloidal nanocrystals. Chem Mater 27(7):2246–2285. https://doi.org/10.1021/cm5028964

Faber MS, Jin S (2014) Earth-abundant inorganic electrocatalysts and their nanostructures for energy conversion applications. Energy Environ Sci 7:3519–3542. https://doi.org/10.1039/C4EE01760A

Fan X, Zhang M, Wang X, Yang F, Meng X (2013) Recent progress in organic-inorganic hybrid solar cells. J Mater Chem A l:8694–8709. https://doi.org/10.1039/C3TA11200D

Feng W, Li Y, Du J, Wang W, Zhong X (2016) Highly efficient and stable quasi-solid-state quantum dot-sensitized solar cells based on a superabsorbent polyelectrolyte. J Mater Chem A 4:1461–1468. https://doi.org/10.1039/C5TA08209A

Freitas JN, Alves JPC, Nogueira AF (2018) Hybrid solar cells:effects of incorporation of inorganic nanoparticles into bulk heterojunction organic solar cells. In: Souza F, Leite E (eds) Nanoenergy. Springer, Cham, pp 1–68. https://doi.org/10.1007/978-3-319-62800-4_1

Goetzberger A, Luther J, Willeke G (2002) Solar cells: past, present, future. Sol Energ Mat Sol Cells 74(1–4):1–11. https://doi.org/10.1016/S0927-0248(02)00042-9

Greaney MJ, Das S, Webber DH, Bradforth SE, Brutchey RL (2012) Improving open circuit potential in hybrid P3HT:CdSe bulk heterojunction solar cells via colloidal tert-butylthiol ligand exchange. ACS Nano 6(5):4222–4230. https://doi.org/10.1021/nn3007509.

Greenham NC, Peng X, Alivisatos AP (1996) Charge separation and transport in conjugated polymer/semiconductor nanocrystal composites studied by photoluminescence quenching and photoconductivity. Phys Rev B 54:17628–17637. https://doi.org/10.1103/PhysRevB.54.17628

Gunes S, Neugebauer H, Sariciftci NS (2007) Conjugated polymer-based organic solar cells. Chem Rev 107(4):1324–1338. https://doi.org/10.1021/cr050149z

Gur I, Fromer NA, Chen C-P, Kanaras AG, Alivisatos AP (2007) Hybrid solar cells with prescribed nanoscale morphologies based on hyperbranched semiconductor nanocrystals. Nano Lett 7 (2):409–414. https://doi.org/10.1021/nl062660t

Hagfeldt A, Boschloo G, Sun L, Kloo L, Pettersson H (2010) Dye-sensitized solar cells. Chem Rev 110:6595–6663. https://doi.org/10.1021/cr900356p

Higashino T, Imahori H (2015) Porphyrins as excellent dyes for dye-sensitized solar cells: recent developments and insights. Dalton Trans 44:448–463. https://doi.org/10.1039/C4DT02756F

Jain SM, Phuyal D, Davies ML, Li M, Philippe B, Castro CD, Qiu Z, Kim J, Watson T, Tsoi WC, Karis O, Rensmo H, Boschloo G, Edvinsson T, Durrant JR (2018) An effective approach of vapour assisted morphological tailoring for reducing metal defect sites in lead-free (CH3NH3) 3Bi2I9 bismuth-based perovskite solar cells for improved performance and long-term stability. Nano Energ 49:614–624. https://doi.org/10.1016/j.nanoen.2018.05.003

Jorgensen M, Norrman K, Krebs FC (2008) Stability/degradation of polymer solar cells. Solar Energ Mater Solar Cells 92:686–714. https://doi.org/10.1016/j.solmat.2008.01.005

Kakiage K, Aoyama Y, Yano T, Oya K, Fujisawa JI, Hanaya M (2015) Highly-efficient dye-sensitized solar cells with collaborative sensitization by silyl-anchor and carboxy-anchor dyes. Chem Commun 51:15894–15897. https://doi.org/10.1039/C5CC06759F

Kamat PV (2013) Quantum dot solar cells. The next big thing in photovoltaics. J Phys Chem Lett 4:908–918. https://doi.org/10.1021/jz400052e

Kim J, Kim G, Back H, Kong J, Hwang I-W, Kim TK, Kwon S, Lee J-H, Lee J, Yu K, Lee C-L, Kang H, Lee K (2016) High-performance integrated perovskite and organic solar cells with

enhanced fill factors and near-infrared harvesting. Adv Mater 28:3159–3165. https://doi.org/10.1002/adma.201504555

Kojima A, Teshima K, Shirai Y, Miyasaka T (2009) Organometal halide perovskites as visible-light sensitizers for photovoltaic devices. J Am Chem Soc 131(17):6050–6051. https://doi.org/10.1021/ja809598r.

Kouijzer S, Esiner S, Frijters CH, Turbiez M, Wienk MM, Janssen RAJ (2012) Efficient inverted tandem polymer solar cells with a solution-processed recombination layer. Adv Ener Mater 2:945–949. https://doi.org/10.1002/aenm.201100773

Kwon J, Im MJ, Kim CU, Won SH, Kang SB, Kang SH, Choi IT, Kim HK, Kim IH, Park JH, Choi KJ (2016) Two-terminal DSSC/silicon tandem solar cells exceeding 18% efficiency. Energy Environ Sci 9:3657–3665. https://doi.org/10.1039/C6EE02296K

Law M, Beard MC, Choi S, Luther JM, Hanna MC, Nozik AJ (2008) Determining the internal quantum efficiency of PbSe nanocrystal solar cells with aid of an optical model. Nano Lett 8:3904–3910. https://doi.org/10.1021/nl802353x

Leijtens T, Bush KA, Prasanna R, McGehee MD (2018) Opportunities and challenges for tandem solar cells using metal halide perovskite semiconductors. Nat Energ. https://doi.org/10.1038/s41560-018-0190-4

Lesnyak V, Gaponik N, Eychmuller A (2013) Colloidal semiconductor nanocrystals: the aqueous approach. Chem Soc Rev 42:2905–2929. https://doi.org/10.1039/C2CS35285K

Li G, Zhu R, Yang Y (2012) Polymer solar cells. Nat Photonics 6:153–161. https://doi.org/10.1038/nphoton.2012.11

Li Y, Xu G, Cui C, Li Y (2018) Flexible and semitransparent organic solar cells. Adv Energy Mater 8:1701791(1–28). https://doi.org/10.1002/aenm.201701791

Liang Y, Wang Y, Mu C, Wang S, Wang X, Xu D, Sun L (2018) Achieving high open-circuit voltages upto 1.57 V in hole-transport-material-free $MAPbBr_3$ solar cells with carbon electrodes. Adv Energy Mater 8(4):1701159. https://doi.org/10.1002/aenm.201701159

Liu J, Wang W, Yu H, Wu Z, Peng J, Cao Y (2008) Surface ligand effects in MEH-PPV/TiO_2 hybrid solar cells. Sol Energ Mat Sol Cells 92(11):1403–1409. https://doi.org/10.1016/j.solmat.2008.05.017

Liu F, Hou T, Xu X, Sun L, Zhou J, Zhao X, Zhang S (2018) Recent advances in nonfullerene acceptors for organic solar cells. Macromol Rapid Commun 39:1700555(1–54). https://doi.org/10.1002/marc.201700555

Low FW, Lai CW (2018) Recent developments of graphene-TiO_2 composite nanomaterials as efficient photoelectrodes in dye-sensitized solar cells: a review. Renew Sust Energ Rev 82 (1):103–125. https://doi.org/10.1016/j.rser.2017.09.024

Luther JM, Gao J, Lloyd MT, Semonin OE, Beard MC, Nozik AJ (2010) Stability assessment on a 3% bilayer PbS/ZnO quantum dot heterojunction solar cell. Adv Mater 22:3704–3707 (2010). https://doi.org/10.1002/adma.201001148

Matteocci M, Razza S, Giacomo FD, Casaluci S, Mincuzzi G, Brown TM, D'Epifanio A, Licoccia S, Carlo DA (2014) Solid-state solar modules based on mesoscopic organometal halide perovskite: a route towards the up-scaling process. Phys Chem Chem Phys 16:3918–3923. https://doi.org/10.1039/C3CP55313B

Miyasaka T (2017) Evolution of organic and hybrid photovoltaics on interdiscipline of science. Electrochemistry 85(5):221. https://doi.org/10.5796/electrochemistry.85.221

Moule AJ, Chang L, Thambidurai C, Vidu R, Stroeve P (2012) Hybrid solar cells: basic principles and the role of ligands. J Mater Chem 22:2351–2368. https://doi.org/10.1039/C1JM14829J

Murray CB, Kagan CR, Bawendi MG (2000) Synthesis and characterization of monodisperse nanocrystals and close-packed nanocrystal assemblies. Ann Rev Mater Sci 30:545–610. https://doi.org/10.1146/annurev.matsci.30.1.545

Murray CB, Norris DJ, Bawendi MG (1993) Synthesis and characterization of nearly monodisperse CdE (E= S, Se, Te) semiconductor nanocrystallites. J Am Chem Soc 115:8706–8715. https://doi.org/10.1021/ja00072a025

Niu G, Guo X, Wang L (2015) Review of recent progress in chemical stability of perovskite solar cells. J Mater Chem A 3:8970–8980. https://doi.org/10.1039/C4TA04994B

Noh JH, Im SH, Heo JH, Mandal TN, Seok S (2013) Chemical management for colourful. efficient, and stable inorganic-organic hybrid nanostructured solar cells. Nano Lett 13:1764–1769. https://doi.org/10.1021/nl400349b

O'Regan B, Gratzel M (1991) A low-cost, high-efficiency solar cell based on dye-sensitized colloidal TiO_2 films. Nature 353:737–740. https://doi.org/10.1038/353737a0

Ogomi Y, Morita A, Tsukamoto S, Saitho T, Fujikawa N, Shen Q, Toyoda T, Yoshino K, Pandey SS, Ma T, Hayase S (2014) $CH_3NH_3Sn_xPb_{1-x}I_3$ perovskite solar cells covering up to 1060 nm. J Phys Chem Lett 5:1004–1011. https://doi.org/10.1021/jz5002117

Park N-G (2015) Perovskite solar cells: an emerging photovoltaic technology. Mater Today 18 (2):65–72. https://doi.org/10.1016/j.mattod.2014.07.007

Quiroz COR, Shen Y, Salvador M, Forberich K, Schrenker N, Spyropoulos GD, Heumuller T, Wilkinson B, Kirchartz T, Spiecker E, Verlinden PJ, Zhang X, Green MA, Baillie AH, Brabec CJ (2018) Balancing electrical and optical losses for efficient 4-terminal Si-perovskite solar cells with solution processed percolation electrodes. J Mater Chem A 6:3583–3592

Rao A, Friend RH (2017) Harnessing singlet exciton fission to break the Shockley-queisser limit. Nat Rev Mater 2:17063. https://doi.org/10.1038/natrevmats.2017.63

Rauda IE, Senter R, Tolbert SH (2013) Directing anisotropic charge transport of layered organic-inorganic hybrid perovskite semiconductors in porous templates. J Mater Chem C 1:1423–1427. https://doi.org/10.1039/C2TC00239F

Reiss P, Couderc E, Girolamo JD, Pron A (2011) Conjugated polymers/semiconductor nanocrystals hybrid materials-preparation, electrical transport properties and applications. Nanoscale 3:446–489. https://doi.org/10.1039/C0NR00403K

Sabatini RP, Eckenhoff WT, Orchard A, Liwosz KR, Detty MR, Watson DF, McCamant DW, Eisenberg R (2014) From seconds to femtoseconds: solar hydrogen production and transient absorption of chalcogenorhodamine dyes. J Am Chem Soc 136:7740–7750. https://doi.org/10.1021/ja503053s

Said AJ, Poize G, Martini C, Ferry D, Marine W, Giorgio S, Fages F, Hocq J, Boucle J, Nelson J, Durrant JR, Ackerman J (2010) Hybrid bulk heterojunction solar cells based on P3HT and porphyrin-modified ZnO nanorods. J Phys Chem C 114(25):11273–11278. https://doi.org/10.1021/jp911125w

Salant A, Shalom M, Hod I, Faust A, Zaban A, Banin U (2010) Quantum dot sensitized solar cells with improved efficiency prepared using electrophoretic deposition. ACS Nano 4:5962–5968. https://doi.org/10.1021/nn1018208

Saliba M, Matsui T, Domanski K, Seo J-Y, Ummadisingu A, Zakeeruddin SM, Correa-Baena JP, Tress WR, Abate A, Hagfeldt A, Gratzel M (2016) Incorporation of rubidium cations into perovskite solar cells improves photovoltaic performance. Science 354:206–209. https://doi.org/10.1126/science.aah5557

Saliba M, Correa-Baena J-P, Gratzel M, Hagfeldt A, Abate A (2018) Perovskite solar cells: from the atomic level to film quality and device performance. Angew Chem Int Ed 57:2554–2569. https://doi.org/10.1002/anie.201703226

Saunders BR, Turner ML (2008) Nanoparticle-polymer photovoltaic cells. Adv Colloid Inter Sci 138(1):1–23. https://doi.org/10.1016/j.cis.2007.09.001

Scharber MC, Sariciftci NS (2013) Efficiency of bulk-heterojunction organic solar cells. Prog Polymer Sci 38:1929–1940. https://doi.org/10.1016/j.progpolymsci.2013.05.001

Semonin OE, Luther JM, Choi S, Chen H-Y, Gao J, Nozik AJ, Beard MC (2011) Peak external photocurrent quantum efficiency exceeding 100% via MEG in a quantum dot solar cell. Science 334:1530–1533. https://doi.org/10.1126/science.1209845

Seo G, Seo J, Ryu S, Yin W, Ahn TK, Seok S II (2014) Enhancing the performance of sensitized solar cells with $PbS/CH_3NH_3PbI_3$ core/shell quantum dots. J Phys Chem Lett 5(11):2015–2020. https://doi.org/10.1021/jz500815h

Seok S, Gratzel M, Park N-G (2018) Methodologies toward highly efficient perovskite solar cells. Small 4:1704177 (1–17). https://doi.org/10.1002/smll.201704177
Shao S, Liu J, Portale G, Fang H-H, Blake GR, Brink GH, Koster LJA, Loi MA (2017) Highly reproducible Sn-based hybrid perovskite solar cells with 9% efficiency. Adv Energy Mater 8:1702019. https://doi.org/10.1002/aenm.201702019
Snaith HJ (2013) Perovskites: the emergence of a new era for low-cost, high-efficiency solar cells. J Phys Chem Lett 4(21):3623–3630. https://doi.org/10.1021/jz4020162
Sobus J, Ziolek M (2014) Optimization of absorption bands of dye-sensitized and perovskite tandem solar cells based on loss-in-potential values. Phys Chem Chem Phys 16:14116–14126. https://doi.org/10.1039/C4CP01937G
Stephen M, Genevicius K, Juska G, Arlauskas K, Hiorns RC (2017) Charge transport and its characterization using photo-CELIV in bulk heterojunction solar cells. Polym Int 66:13–25. https://doi.org/10.1002/pi.5274
Susrutha B, Giribabu L, Singh SP (2015) Recent advances in flexible perovskite solar cells. Chem Commun 51:14696–14707. https://doi.org/10.1039/C5CC03666F
Talapin DV, Lee J-S, Kovalenko MV, Shevchenko EV (2010) Prospects of colloidal nanocrystals for electronic and optoelectronic applications. Chem Rev 110(1):389–458. https://doi.org/10.1021/cr900137k
Tetreault N, Gratzel M (2012) Novel nanostructures for next generation dye-sensitized solar cells. Energ Enviorn Sci 5:8506–8516. https://doi.org/10.1039/C2EE03242B
Theerthagiri J, Senthil AR, Madhavan J, Maiyalagan T (2015) Recent progress in non-platinum counter electrode materials for dye-sensitized solar cells. ChemElectroChem 2:928–945. https://doi.org/10.1002/celc.201402406
Thomas JP, Zhao L, McGillivray D, Leung KT (2013) High-efficiency hybrid solar cells by nanostructural modification in PEDOT:PSS with co-solvent addition. J Mater Chem A 2:2383–2389. https://doi.org/10.1039/C3TA14590E.
Wang L, Liu YS, Jiang X, Qin DH, Cao Y (2007) Enhancement of photovoltaic characteristics using a suitable solvent in hybrid polymer/multiarmed CdS nanorods solar cells. J Phys Chem C 111(26):9538–9542. https://doi.org/10.1021/jp0715777
Wang H, Luan C, Xu X, Kershaw SV, Rogach AL (2012) In situ versus ex situ assembly of aqueous-based thioacid capped CdSe nanocrystals within mesoporous TiO2 films for quantum dot sensitized solar cells. J Phys Chem C 116:484–489. https://doi.org/10.1021/jp209987q
Wang R, Wu X, Xu K, Zhou W, Shang Y, Tang H, Chen H, Ning Z (2018) Highly efficient inverted structural quantum-dot solar cells. Adv Mater 30(7):1704882. https://doi.org/10.1002/adma.201704882
Wright M, Uddin A (2012) Organic-inorganic hybrid solar cells: a comparative review. Sol Energ Mater Sol Cells 107:87–111. https://doi.org/10.1016/j.solmat.2012.07.006
Wu K-L, Ho S-T, Chou C-C, Chang Y-C, Pan H-A, Chi Y, Chou P-T (2012) Engineering of osmium (II) based light absorbers for dye-sensitized solar cells. Angew Chem Int Ed 51 (23):5642–5646. https://doi.org/10.1002/anie.201200071
Wu J, Lan Z, Lin J, Huang M, Huang Y, Fan L, Luo G (2015) Electrolytes in dye-sensitized solar cells. Chem Rev 115(5):2136–2173. https://doi.org/10.1021/cr400675m
Wu J, Lan Z, Lin J, Huang M, Huang Y, Fan L, Luo G, Lin Y, Xie Y, Wei Y (2017) Counter electrodes in dye-sensitized solar cells. Chem Soc Rev 46:5975–6023. https://doi.org/10.1039/C6CS00752J
Xu T, Qiao Q (2011) Conjugated polymer–inorganic semiconductor hybrid solar cells. Energy Environ Sci 4:2700–2720. https://doi.org/10.1039/C0EE00632G
Yang WS, Park B-W, Jung EH, Jeon NJ, Kim YC, Lee DU, Shin SS (2017) Iodide management in formamidinium-lead-halide-based perovskite layers for efficient solar cells. Science 356 (6345):1376–1379. https://doi.org/10.1126/science.aan2301
You J, Dou L, Yoshimura K, Kato T, Ohya K, Moriarty T, Emery K, Chen CC, Gao J, Li G, Yang Y (2013) A polymer tandem solar cell with 10.6% power conversion efficiency. Nat Commun 4:1–10. https://doi.org/10.1038/ncomms2411.

Yuan J, Gallagher A, Liu Z, Sun Y, Ma W (2015) High-efficiency polymer-PbS hybrid solar cells via molecular engineering. J Mater Chem A 3:2572–2579. https://doi.org/10.1039/C4TA03995E

Yun S, Hagfledt A, Ma T (2014) Pt-free counter electrode for dye-sensitized solar cells with high efficiency. Adv Mater 26(36):6210–6237. https://doi.org/10.1002/adma.201402056

Yun S, Qin Y, Uhi AR, Vlachopoulos N, Yin M, Li D, Han X, Hagfeldt A (2018) New-generation integrated devices based on dye-sensitized and perovskite solar cells. Energy Environ Sci 11:476–526. https://doi.org/10.1039/C7EE03165C.

Zhang W, Zhang H, Feng Y, Zhong X (2012) Scalable single-step noninjection synthesis of high-quality core/shell quantum dots with emission tunable from violet to near infrared. ACS Nano 6 (12):11066–11073

Zhao Y, Zhu K (2014) Optical bleaching of perovskite (CH_3NH_3)PbI_3 through room-temperature phase transformation induced by ammonia. Chem Commun 50:1605–1607. https://doi.org/10.1039/C3CC48522F

Zhao L, Wang J, Lin Z (2010) Semiconducting nanocrystals, conjugated polymers, and conjugated polymer/nanocrystal nanohybrids and their usage in solar cells. Front Chem China 5:33–44. https://doi.org/10.1007/s11458-009-0112-x

Zhao K, Pan Z, Mora-Sero I, Canovas E, Wang H, Song Y, Gong X, Wang J, Bonn M, Bisquert J, Zhong X (2015) Boosting power conversion efficiencies of quantum-dot-sensitized solar cells beyond 8% by recombination control. J Am Chem Soc 137:5602–5609. https://doi.org/10.1021/jacs.5b01946

Zhou Y, Eck M, Kruger M (2010) Bulk-heterojunction hybrid solar cells based on colloidal nanocrystals and conjugated polymers. Energy Environ Sci 3:1851–1864. https://doi.org/10.1039/C0EE00143K

Zhou R, Zheng Y, Qian L, Yang Y, Holloway PH, Xue J (2012) Solution-processed, nanostructured hybrid solar cells with broad spectral sensitivity and stability. Nanoscale 4:3507–3514. https://doi.org/10.1039/C2NR30210A

Chapter 8
An Overview of Current Trends in Emergence of Nanomaterials for Sustainable Microbial Fuel Cells

Gunaseelan Kuppurangam, Gajalakshmi Selvaraj, Thirumurugan Ramasamy, Vignesh Venkatasamy, and Sathish-Kumar Kamaraj

Contents

G. Kuppurangam · G. Selvaraj
Sustainable Fuel Cells Laboratory, Centre for Pollution Control & Environmental Engineering, Pondicherry University, Puducherry, India

T. Ramasamy
Laboratory of Aquabiotics/Nanoscience, Department of Animal Science, Bharathidasan University, Tiruchirappalli, Tamil Nadu, India

V. Venkatasamy
Animal Quarantine and Certification Service, Department of Animal Husbandry, Dairying and Fisheries, Ministry of Agriculture & Farmers Welfare, Mumbai, Maharashtra, India

Sathish-KumarKamaraj (✉)
Laboratorio de Cultivo de Tejidos Vegetales, Instituto Tecnológico El Llano (ITEL)/ Tecnológico Nacional de México (TecNM), El Llano, Aguascalientes, México
e-mail: sathish.bot@gmail.com

R. Saravanan et al. (eds.), *Emerging Nanostructured Materials for Energy and Environmental Science*, Environmental Chemistry for a Sustainable World 23,
https://doi.org/10.1007/978-3-030-04474-9_8

Abstract Microbial fuel cell (MFC) technologies have been globally noticed as one of the most promising sources for alternative renewable energy, due to its capability of transforming the organics in the wastewater directly into electricity through catalytic reactions of microorganisms under anaerobic conditions. In this chapter, the state of the art of review on the various emerging technological aspects of nanotechnology for the development of nanomaterials to make the existing

microbial fuel cell technology as more sustainable and reliable in order to serve the growing energy demand. Initially, a brief history of the development and the current trends of the microbial fuel cells along with its basic working mechanism, basic designs, components, fascinating derivative forms, performance evaluation, challenges and synergetic applications have been presented. Then the focus is shifted to the importance of incorporation of the nanomaterials for the sustainable development of MFC technology by means of advancements through anode, cathode, and proton exchange membranes modifications along with the various ultimate doping methods. The possibilities of applied nanomaterials and its derivatives in various places in MFCs are discussed. The nanomaterials in MFCs have a significant contribution to the increased power density, treatment efficiency, durability, and product recovery due to its higher electrochemical surface area phenomenon, depending on the fuel cell components to get modified. The promising research results open the way for the usage of nanomaterials as a prospective material for application and development of sustainable microbial fuel cells. Though the advances in nanomaterials have opened up new promises to overcome several limitations, but challenges still remain for the real-time and large-scale applications. Finally, an outlook for the future development and scaling up of sustainable MFCs with the nanotechnology is presented with some suggestions and limitations.

8.1 Introduction

The demand for energy, globally, continues to grow faster than predicted, thereby leading to the energy crisis and environmental pollution. Due to the availability of fossil fuels in the range of finite and depleting amount, it became an unsustainable and unreliable source of energy. Nowadays research has been targeted toward the alternative, renewable, and carbon-neutral sources of energy, which are the need of the hour for economic and sustainable development (Parkash 2016).

With this backdrop, microbial fuel cell (MFC) technologies have been universally observed as one of the most promising substitute sources of renewable energy (Xia et al. 2018).

The technology of generating electricity through bacteria was found 100 years ago, but it did not gain much attention due to the production very less power (Rabaey et al. 2004; Reguera et al. 2006). Because of its ability in converting available chemical energy into electrical energy, MFCs got several applications such as wastewater treatment, electricity generation, biosensor, resource recovery, biohydrogen generation, etc. (Logan et al. 2005, 2006; Reguera et al. 2006). Consequently, the number of research studies in the area of MFCs became greater than before since the early 1990s (Xia et al. 2018).

The innovative idea of employing microbes to generate electricity was conceived and attributed to Potter in 1911 (Potter 1911); moreover, the concept of "animal electricity" dates back to the eighteenth century when Galvani was experimenting with frog legs for electricity generation (Piccolino 2008). Later on, the concepts and

practical improvements were explored since, with Cohen's 35-unit setup in 1931. The investigations on the development of the catalyst in the 1960s by Karube et al. (1976) and more in the recent times of the 1980s–1990s, with the work of Bennetto et al. on synthetic mediators gave rise to the development of the so-called analytical MFC that is still in use to date. From those primary instances, major progress on the understanding of electron transfer mechanisms, improvement of efficient bioelectrocatalytic interfaces, and development of unique, low-cost, and durable electrode materials has been attained; however, ample room for improvement and work have to be done for the industrialization of MFCs (Rahimnejad et al. 2015; Santoro et al. 2017a; Trapero et al. 2017).

There has been a substantial shift of focus toward the renewable energy technologies for many decades like wind, wave, solar, and also nuclear technology.

As a promising alternative to the other potential area of renewable energy sources, MFCs has resurfaced in recent times as modern technology which accommodate and exhibit potential for generating power using bacterial populations (Juan and Nixon 2013).

The emerging areas of science are nanoscience and nanotechnology playing a lead role in diversified fields like electrical, environmental engineering, medical etc., due to technological and scientific upgradation. Nanoscience is a study of atoms, molecules, and objects which possess size on the nanometer level. In nanotechnology, the manipulation of matter for a specific application with the help of nano-sized dimensions in the range of 1–100 nm with the peculiar features through physical and chemical processes is explored. The nanotechnological approaches can be incorporated in various forms in order to increase the overall performance of the microbial fuels, which may satisfy the energy needs of the electrical appliances.

The enormous significance is being provided by human beings to generate energy in many ways, which is considered as the main resource for human activities. Due to the substantial growth in the global human population, there is no hope for the decrease in the energy demand other than the drastic increase in the need. For the futuristic energy needs, the modern nanotechnology is one of the promising solutions to gain a more effective and efficient procedure to generate more energy.

Furthermore, huge importance should be given to nanotechnology in the microbial fuel cells energy systems in order to attain greater energy production with high efficiency, lower production cost, and ease during real-time applications.

8.2 MFCs' Working Principle, Components, and Designs

8.2.1 Working Principle of MFC

Microbial fuel cell (MFC) is a bioreactor incorporated with an electrochemical system that converts chemical energy in the chemical bonds in organic pollutants in the wastewater to electrical energy through catalytic reactions of microorganisms under anaerobic conditions (Fig. 8.1).

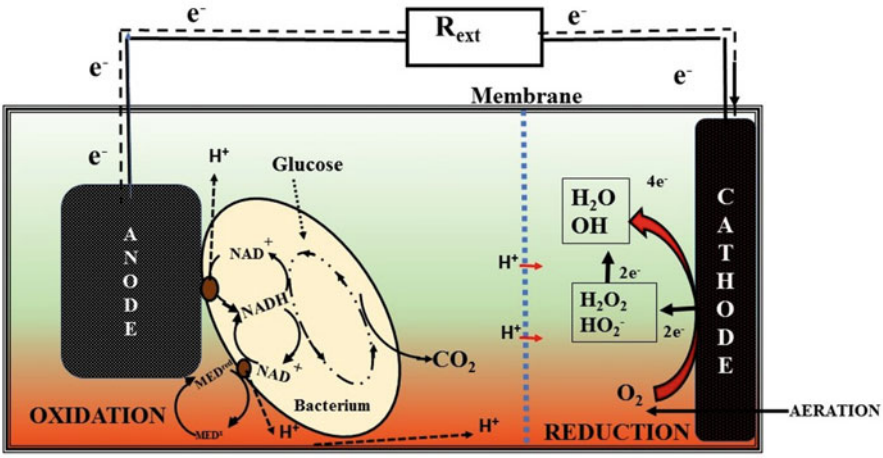

Fig. 8.1 Schematic view of dual chambered microbial fuel cell

MFC can be constructed using a variety of materials and in an ever-increasing diversity of configurations.

In the bioreactor, the bacterial populations will oxidize the provided wastewater as substrates in the anodic chamber to produce free electrons and protons, while carbon dioxide will be an oxidation product. Electrons attached on the anode (negative terminal) flow to the cathode (positive terminal) through an external circuit. Free protons migrate across the proton/cation exchange membrane to combine with electrons to form water if oxygen is provided or to form ferrocyanide if ferricyanide is provided (Xia et al. 2018).

8.2.2 Electron Transport Mechanism (ETM) in MFCS

Electron transport mechanism in microbial fuel cell deals with the transfer of liberated electrons from the degraded organic matter to the electrodes through several irreversible and reversible electrochemical reactions of the electron transport chain and finally ends up with the generation of electricity by transferring those electrons from cell to MFC circuit (Busalmen et al. 2008; Bhunia and Dutta 2018).

In order to achieve the reversible interfacial reactions at the anode surface, the electrons have to depend on shuttles such as cytochromes, proteins (such as PQQ), and bound or soluble redox mediators to reach at least within a proximity of 10 A°~ near the anode (Labelle and Bond 2009; Bhunia and Dutta 2018).

The proposed three pathways like (i) direct membrane complex mediated electron transfer (Bond and Lovley 2003), (ii) Indirect or redox shuttle mediated electron transfer (Rabaey et al. 2005a), and (iii) electron transfer through conductive pili or

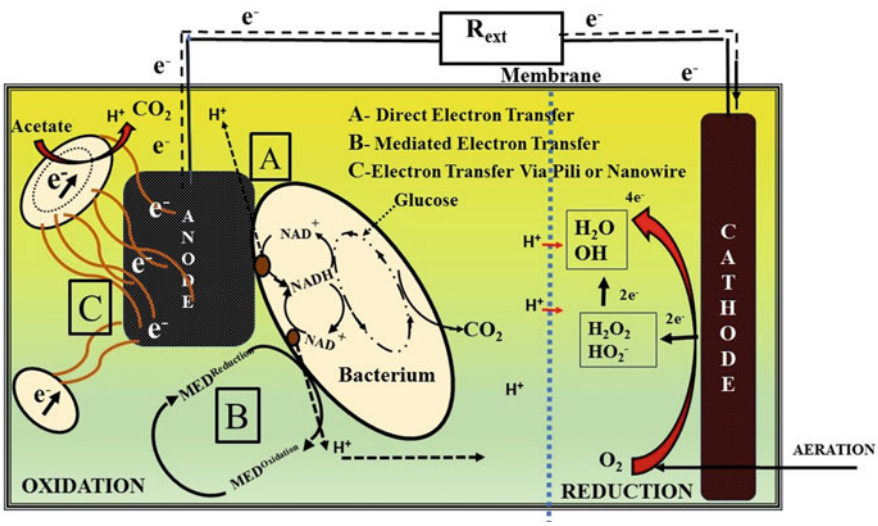

Fig. 8.2 Schematic view of electron transfer mechanism

nanowires (Reguera et al. 2005) are the very often reported modes of electron transport (Fig. 8.2).

8.2.2.1 Direct Electron Transfer

In the direct electron transport mechanism, a monolayer of microorganisms will be formed over the anode surface, which permits a direct transfer of electrons to the anode surface through a cell membrane or a membrane organelle.

Notably, certain Fe (III)-reducing bacteria (*S. putrefaciens*) would be able to transfer electrons to the electrode even with the absence of synthetic mediators (Mahadevan et al. 2014; Bhunia and Dutta 2018).

It is evident that the presence of cytochrome (a redox protein) over the outer membrane of the cell might be responsible for direct electron transfer through a reduction of the water-soluble Fe (III). As a consequence, due to the negligible gap between the microbes and the electrode, this phenomenon results in the lowest extracellular potential losses (Bhunia and Dutta 2018).

The direct transport mechanism through the cytochrome has been clearly demonstrated with mutants of *G. suilfurreducens* through experiments wherein the gene encoding for the cytochrome C proteins has been deleted or overexpressed (Lovley 2006a; Santoro et al. 2017a).

Bond and Lovley (2003) reported that cathodephillic microorganisms such as *Thiobacillus ferrooxidans* which forms a biofilm over the cathode and finally the cathode act as the electron donor. These microbes results with a potential difference

in cathode driving to a suitable reaction at the anode by acidophilic microorganisms to generate the electricity (Tekle and Demeke 2015).

8.2.2.2 Indirect or Mediated Electron Transfer

The extensive study about an indirect or mediated electron transport mechanism is being carried out for electricity production in MFCs due to the sufficient weakness of the direct electron transport mechanism (Schröder 2007; Bhunia and Dutta 2018).

The mechanism of transporting electrons by artificial mediators is referred to as electron shuttles. These chemical compounds offer the opportunity for microorganisms to produce the reduced products that are more electrochemically active than utmost fermentation products. These electron shuttles or mediators are usually capable of crossing cell membranes, accepting electrons from one or more electron carriers within the cell, exiting the cell in the reduced form, and then transferring electrons onto the electrode surface (Lovley 2006b; Tekle and Demeke 2015).

In an indirect or mediated electron transfer mechanism, the microbes produce/require indigenous soluble organic redox mediators (quinone and flavin) or artificial exogenous mediators (dye or toxic metal complexes) to transport electron between terminal respiratory enzyme and anode surface (Park and Zeikus 2000; Das and Mangwani 2010).

To enhance the mediated electron transfer mechanism, there is a wide range of mediators like microbial electroactive metabolic mediators and synthetic mediators which are categorized and listed in the following section (Bhunia and Dutta 2018).

The redox mediators like phenazines, phenothiazines, phenoxazines, and quinones will be employed initially to conduct electron transfer mechanism in MFCs. The active microorganisms release the electroactive metabolites in bulk solution/over the formed biofilm and finally interact at the electrode surface (Bhunia and Dutta 2018).

Most remarkably, the primary metabolites like H_2 and H_2S generated through microbial catabolic oxidation of fuel (anaerobic respiration and fermentation) have been productively used as redox mediators (Straub et al. 2004; Sekoai and Gueguim Kana 2014) (Fig. 8.3). Some of the secondary metabolites, namely, phenazine-1-carboxamide, pyocyanine (*Pseudomonas aeruginosa*), neutral red, humic acid, anthraquinone-2,6-disulfonate (AQDS), thionine, methyl viologen, methyl blue, and 2-amino-3-carboxy-1,4-naphthoquinone (ACNQ) (*Bifidobacterium longum*), are extensively involved in indirect electron transfer mechanism in MFCs (Mahadevan et al. 2014; Bhunia and Dutta 2018).

The synthetic mediators like methylene blue, neutral red, thionine, Meldola's blue, and Fe (III) EDTA possess high redox potentials, but the problem is their toxicity which limits their use in MFCs (Davis and Higson 2007). In the current state of knowledge, cyclic voltammetry (CV) study can reveal the mechanism of electron transfer that takes place through redox enzymes, namely, ferricyanide reductase and lactate dehydrogenase, at the outer membrane of the microbial cell, whether it is a

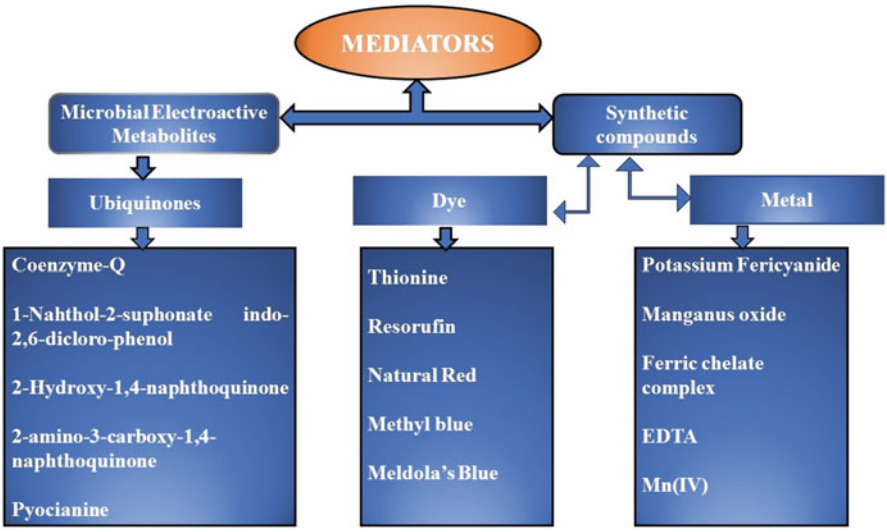

Fig. 8.3 Schematic representation of various types of mediators

mobile redox shuttles transfer or direct electrons transfer mechanism through the membrane-associated compounds (Mahadevan et al. 2014; Bhunia and Dutta 2018).

8.2.2.3 Electron Transfer via Conductive Pili or Nanowires

The mechanism of electron transfer to the anode surface by bacteria requires physical contact with the electrode's surface which involves outer membrane-bound cytochromes or putative conductive pili called nanowires (Coates and Wrighton 2009; Das and Mangwani 2010).

More remarkably in 2005, an additional type of electron transfer mimicking the direct electron transport mechanism has been described, which proceeds via extracellular conductive connections called the conductive pili or bacterial nanowires (Reguera et al. 2005; Santoro et al. 2017a).

In a study, *Geobacter sulfurreducens* with its electrically conductive bacterial appendages named as pili or nanowires have been revealed to be electrically conductive through scanning tunneling electron microscopy (Reguera et al. 2005; Bhunia and Dutta 2018).

These nanowires are a flexible structure made with proteins, which assist the bacteria to hold the surface of the anode and as distinguished materials in its surroundings. The internal networks of conductive pilus may overcome the restrictions of the earlier discussed direct electron transfer mechanism. More specifically, the pili consist of a cluster of aromatic acids and subunit of proteins, which permit them to play a significant role in electrical conductivity (Reguera et al. 2005; Bhunia and Dutta 2018).

Surprisingly, *Shewanella oneidensis* involves in the direct electron transfer mechanism as well as conductive pilus-like nanowires for electron transfer through the c-type cytochrome (Reguera et al. 2005; Bhunia and Dutta 2018).

The conductivity of the nanowire can be measured through the equation as given:

$$\boldsymbol{\sigma = G\ (2a/gL)}$$

where **G** is the conductance of the biofilm, **L** is the length of the electrode, **g** is the biofilm thickness, and **a** is the nonconducting gap width between two working electrodes (anode) (Malvankar et al. 2011; Bhunia and Dutta 2018).

On the other hand, bacterial nanowires are positive findings toward a long range of electron transfer on the electrode, but the attractive feature of the pili that eases metallike conductivity, notably other microbial species, does not possess this provisions, and still in-depth investigations are needed (Mahadevan et al. 2014).

8.2.3 Adequate Components of MFC

An ideal MFC reactor may consist of two chambers (anodic and cathodic) made with polycarbonate, polyacrylic sheet, or glass, with the desired electrodes like graphite felt, carbon paper, graphite, carbon cloth, reticulated vitreous carbon (RVC), carbon black, etc. Both these chambers will be separated by proton exchange membrane (PEM) like Nafion® or Ultrex® with the phenomenon of only permitting the ions to get diffused than the substrate crossover (Fig. 8.4 and Table 8.1). The organic

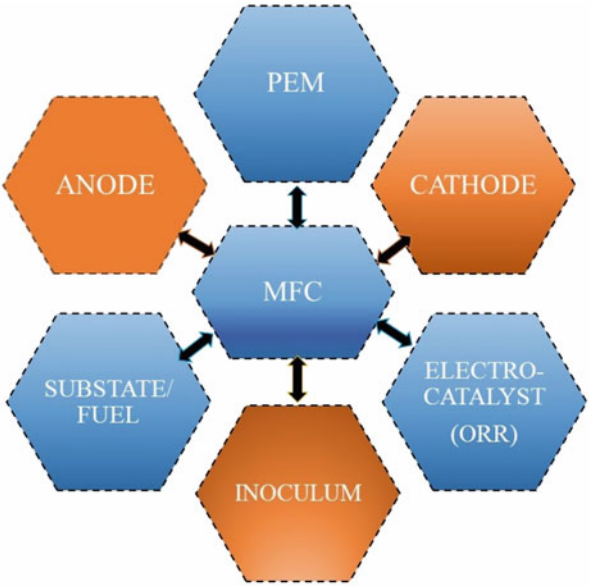

Fig. 8.4 Schematic representation of components of MFC

Table 8.1 Materials for construction of MFCs

Items	Materials
Anode	Graphite, graphite felt, carbon felt, carbon fiber, carbon paper, carbon cloth, Pt, Pt black, reticulated vitreous carbon (RVC), granulated activated carbon (GAC), SS wire mesh, etc.
Cathode	Graphite, graphite felt, carbon felt, carbon fiber, carbon paper, carbon cloth, Pt, Pt black, reticulated vitreous carbon (RVC)
Anodic chamber	Glass, polycarbonate, plexiglass or polyacrylics, earthenware etc.
Cathode chamber	Glass, polycarbonate, plexiglass
Proton exchange system	Nafion cation-exchange membrane (CEM), Ultrex anion-exchange membrane (AEM), ultrafiltration membrane (UFM), microfiltration membranes (MFM), bipolar membranes (BPM), salt bridges, glass fibers, porous fabrics, polystyrene-co-divinylbenzene, porcelain septum, ceramic membrane, etc.
Electrode catalyst	Pt, Pt black, MnO_2, Fe^{3+}, polyaniline, electron mediators, etc.
Catholyte	Ferricyanide, permanganate, hypochlorite, etc.

substrates are filled in the anodic chamber employed with the microbes for degradation of organics and production of free electrons and protons; on the other side, the cathode chamber is filled with a potential electron acceptor to complete the circuit and get the electricity. An ideal electron acceptor like oxygen can be used as a preferred oxidizing reagent due to its nontoxic effect and simplified operation. For the very high performance with optimal power density, ferricyanide can be used as the potential electron acceptor. The various designs of the MFC are only dependent on the assembly of anode and cathode chambers. Besides the simple MFC prototypes like two-chamber or single chamber, numerous alterations have been made to obtain other prototypes of MFC design and structure (Das and Mangwani 2010).

8.2.3.1 Biocatalysts for Substrate Utilization and Electricity Generation

Generally, the microbial cells facilitate the electron transfer from the substrate to the electrode through the mechanism of electron shuttling; this effect is called as bioelectrocatalysis.

Our understanding regarding the electrochemically active exoelectrogenic microbes is still in its beginning, but evidently, a whole new field of microbial ecology is getting developed that is based on the knowledge about the anodophilic bacteria and its potential interspecies electron transfer mechanism. These bacteria with the ability to release the electrons exocellularly are called as exoelectrogens (Table 8.2). Earlier an understanding of electron transfer mechanism by bacteria to electrodes came to light from the studies of dissimilatory metal-reducing bacteria such as *Geobacter* and *Shewanella* species, which can generate electricity in MFCs (Bond and Lovley 2003; Gil et al. 2003). Various genetic and biochemical

Table 8.2 Reported microbes in microbial fuel cells

Microbes	Fuel/substrate	Mediators	References
Streptococcus lactis	Glucose	Ferric chelate complex	Vega and Fernandez (1987)
Shewanella putrefaciens	Lactate, pyruvate, acetate, and glucose	Mn(IV)	Park and Zeikus (2003)
Aeromonas hydrophila	Glucose and acetate	Neutral red or thionine	Pham et al. (2003)
Escherichia coli	Glucose and sucrose	Methylene blue	Schroder et al. (2003)
Proteus mirabilis	Glucose	Thionin	Choi et al. (2003)
Clostridium butyricum	Starch, glucose, lactate, molasses	Sulfate/sulfide	Niessen et al. (2006)
Geobacter sulfurreducens	Acetate	Nanowires	Bond and Lovley (2005)
Rhodoferax ferrireducens	Glucose, xylose, sucrose, altose	Mediator-less	Liu et al. (2005b)
Geobacter metallireducens	Acetate	Mediator-less	Min et al. (2005)
Klebsiella pneumoniae	Glucose	Biomineralized manganese	Veluchamy et al. (2006)
Shewanella oneidensis	Lactate	Anthraquinone-2,6-disulfonate (AQDS)	Ringeisen et al. (2006)
Consortium—wastewater inoculum	Acetate, glucose, and xylose	Humic acid	Thygesen et al. (2009)
Bifidobacterium longum	Bacto Peptone medium	2-amino-3-carboxy-l,4-naphthoquinone	Kano et al. (1999)

characterizations directed that outer membrane cytochromes can be involved in exogenous electron transfer (Myers and Myers 2001). Furthermore, some microbes may produce and use soluble electron shuttles which exclude the need for direct contact between the cell and an electron acceptor (Turick et al. 2002; Logan and Regan 2006).

The substrate is also the key factor for an efficient production of electricity from an MFC: from the range of simple to a complex mixture of organic matters present in the substrate/wastewater can be employed. The simple mixture substrate like acetate and glucose are most recommended for immediate output and the complex mixtures substrate for the growth of diverse active microbial populations. Another promising and most used substrate is brewery wastewater with growth-promoting organic matter and lacking inhibitory substances (Feng et al. 2008). Other unconventional substrates like synthetic wastewater, landfill leachates, and dye wastewater are used for the generation of electricity (Das and Mangwani 2010; Pant et al. 2010).

8.2.3.2 Electrocatalyst for Oxygen Reduction Reaction (ORR)

The role of the electrocatalyst is very crucial in the cathode chamber, where the synthesized free protons and electrons recombine and reduce an electron acceptor to end up the electrical circuit. Oxygen is the paramount suitable electron acceptor for an MFC owing to its high oxidation potential, abundance, low cost, sustainability, and the lack of a chemical waste product (water is formed as the only end product). However, the reaction is very slow with the oxygen as an electron acceptor; hence the need for a catalyst arises. Most of the MFCs use platinum as the catalyst; on the other hand, this is exceptionally expensive. Chemical electron acceptors like ferricyanide and potassium permanganate have been used effectively with results similar to those achieved with platinum. These chemicals are far less expensive than platinum, but the disadvantage is that they are much toxic and getting consumed in the reaction (He and Angenent 2006). Due to the abovementioned drawbacks, which affect the viability of the MFC directly, these chemicals should be avoided by replacing them with an equally efficient but less expensive catalyst through extensive research (Tekle and Demeke 2015).

8.3 Designs of MFC

8.3.1 Dual Compartment MFC System

Generally, this dual compartment MFC system has an anodic and cathodic compartment connected by a proton exchange membrane (PEM) that mediates only the transfer of free protons from the anode to cathode compartment while blocking the diffusion of oxygen into the anode and also the crossover of the substrate into the cathode compartment (Fig. 8.5). This type of MFC is commonly employed for treatment of wastewater with simultaneous electricity generation. But scaling up of

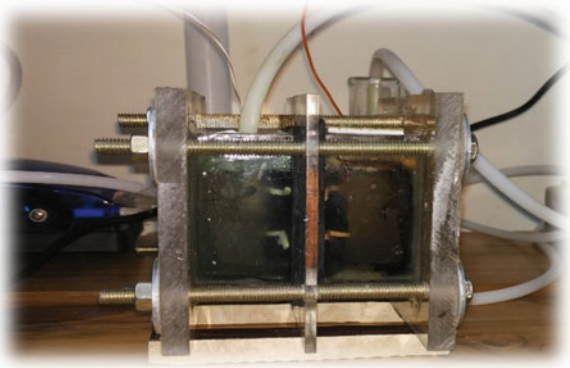

Fig. 8.5 Typical dual chamber MFC

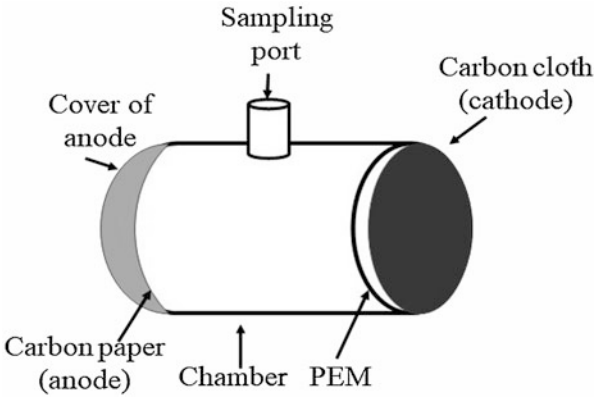

Fig. 8.6 Air-cathode chamber MFC. (Figure drawn with modifications after Liu and Logan 2004; Du et al. 2007)

this MFC system to industrial size is quite challenging, due to the necessity of aeration in the cathodic chamber.

The mode of operation of the double chamber MFC system will be batch and fed-batch mode (Parkash 2016).

8.3.2 Single Air-Cathode Chamber MFC System

The earliest single air-cathode chamber MFC system was designed and reported the possibility that an oxygen gas diffusion electrode could be used as a cathode in a bioelectrochemical fuel cell (Liu et al. 2005a). However, initially, this single air-cathode setup has not drawn much attention in MFC research until Liu reported the air-cathode MFC possibly will generate much greater power than typical dual chamber aqueous-cathode MFCs (Fig. 8.6). They advanced the air-cathode configuration with and without the PEM, reported with the maximum power output of 262 mW/m^2 using glucose with PEM and 494 mW/m^2 without PEM (Liu et al. 2005a; Parkash 2016).

Furthermore, Liu et al.'s study was attempted with acetate and butyrate in the same reactor in the absence of the CEM. Other studies have also been performed to examine the power outputs in single air-cathode MFCs, and shown the power density results in 506 mW/m^2 with acetate and 305 mW/m^2 for butyrate in the same air-cathode setup without any membrane (Liu et al. 2005a).

The single air-cathode MFCs design is expected to optimize some of the characteristics of dual chamber MFCs, such as high cost of cathode catalysts, less relative power output and energy requirement for intensive air/oxygen sparing. An additional advantage of the single air-cathode MFCs over the dual chamber is the reduction of the high internal resistance of MFCs, which is a significant factor to improve electricity production (Parkash 2016).

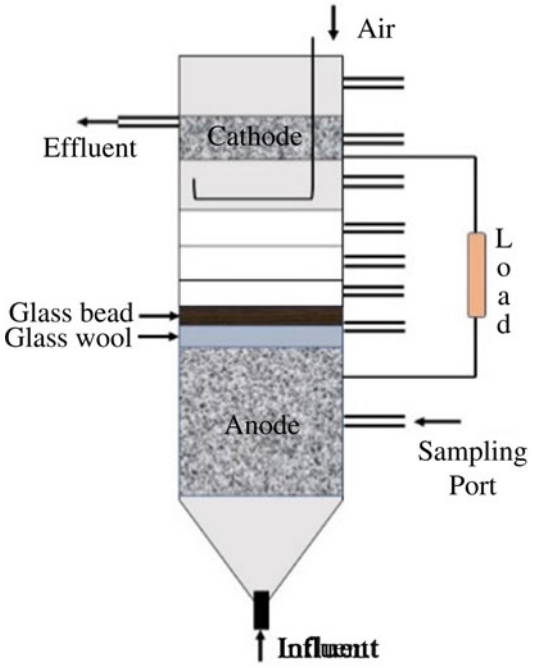

Fig. 8.7 Typical upflow MFC. (Figure drawn with modifications after Jang et al. 2004)

8.3.3 Tubular/Upflow MFC System

The generated voltage by MFCs remained limited and unable to exceed theoretical open circuit voltage of 1.14 V as based on the NADH (−0.32 V) and pure oxygen (+0.82) redox potentials even ignoring the internal resistances (Logan and Regan 2006). Tubular/upflow architecture is the well-known and highly optimized MFCs setup (Cheng and Hamelers 2008). Chang et al. (2006) have designed a tubular reactor MFC setup working in continuous flow mode; the flow was moving through an anode chamber and then directed up into the cathode chamber in the same column (Fig. 8.7). They claimed that the upflow reactor had several advantages over other conventional designs, on the basis of higher affinity for oxygen with cathode (Lovley 2006a), combining the benefits of the upflow anaerobic sludge blanket system with two-chamber MFC (Parkash 2016).

8.3.4 Stacks

The idea of connecting several microbial fuel cells in series may result in the added voltages, whereas connecting several MFCs in parallel may result in the enhanced

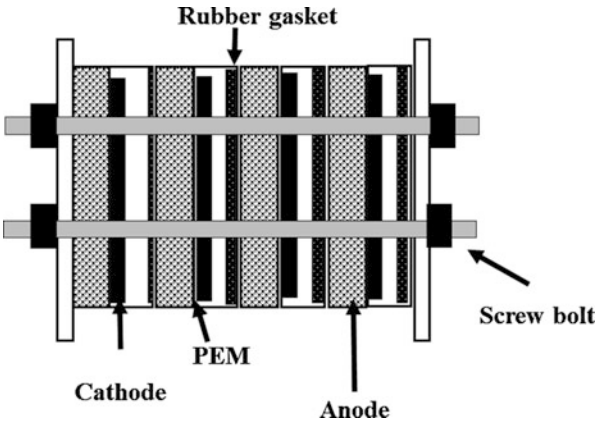

Fig. 8.8 Typical stack MFC. (Figure drawn with modifications after Aelterman et al. 2006)

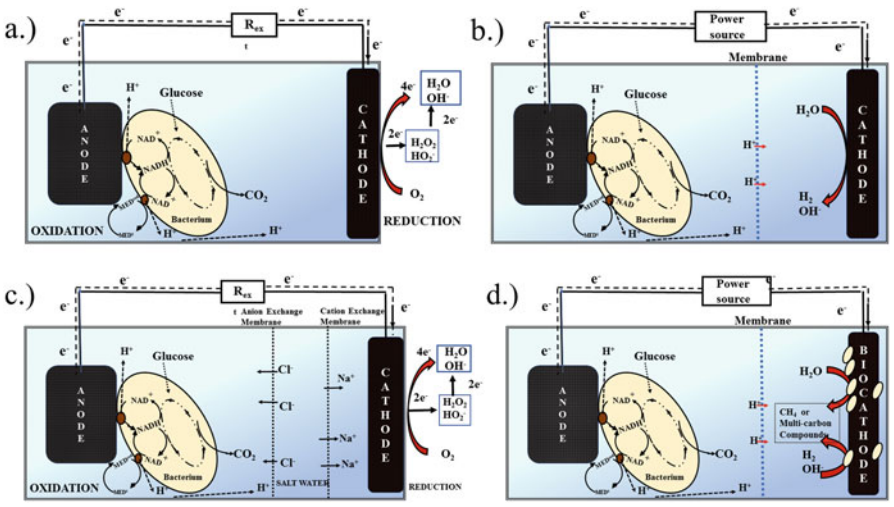

Fig. 8.9 Schematics of microbial fuel cell (**a**), microbial electrolysis cell (**b**), microbial desalination fuel cell (**c**), and microbial electrosynthesis cell (**d**)

current outputs. Due to these reasons, the existence of the stacked MFCs came into practice (Fig. 8.8). The application of the stacked MFCs for the treatment of the wastewater treatment can result in the improved chemical oxygen demand removal when compared to the single MFC (Fig. 8.9a). This type of MFC setup also got optimized at the level of configurations and components aimed at the reduced internal resistance and increased cell power outputs (Chae et al. 2009; Parkash 2016).

8.4 Advancements and Fascinating Derivative Forms of MFC

Microbial fuel cells (MFCs) are comparatively unique bioelectrochemical systems (BESs) that directly transform microbial metabolic energy into electricity (ElMekawy et al. 2017).

There are numerous forms of bioelectrochemical systems (BESs) that have been proposed, and they are classified on the basis of their applications. Most of the BESs can be employed to extract the chemical energy from the provided complex organic substrates in the anodic chamber and transform it into useful electrical energy. Other forms of the BESs have been developed to generate valuable products like hydrogen gas (Escapa et al. 2016; Kadier et al. 2016), acetate (Xafenias and Mapelli 2014), methane gas (Villano et al. 2011; Babanova et al. 2017), formate (Nevin et al. 2010), desalinate water (Cao et al. 2009), etc. other than generating the electricity from the wastewater (Werner et al. 2013; Watson et al. 2015; Santoro et al. 2017a).

8.4.1 Microbial Electrolysis Cell (MEC)

Among the BESs, one of the most remarkable and well investigated is the microbial electrolysis cell (MEC), which was first introduced in 2005 and related publications on MEC increased over time (Santoro et al. 2017a). MFC is a galvanic process that generates electricity, while MEC is an electrolytic process which requires extra potential. This process occurs in a device similar to that of the microbial fuel cell (MFC) (Rozenfeld et al. 2018).

An illustration of the working principle of the microbial electrolysis cell is presented (Fig. 8.9b). MEC is of a specific interest ever since hydrogen is an expensive gas produced and essentially needed for the upcoming hydrogen energy economy (Winter 2005; Rizzi et al. 2014).

MEC consist of a single- or dual-glass compartment separated by a proton exchange membrane. The anode chamber contains exoelectrogenic bacterial cells which oxidize organic material to free electrons and protons which recombine on the cathode to produce biohydrogen.

However, since the overall free energy of this process is positive, the MEC device operates under a low external voltage of about 0.15–0.8 V, which is much lower than the theoretical and practical values of 1.5 and above in the general water electrolysis system (Liu et al. 2010).

Numerous progress and developments in relation to the increase in production of hydrogen gas, improvements in aspects of cell design, membrane removal and replacement, and utilization of microbial catalysts in the optimal amount or Pt-free catalysts have been productively revealed. Notable work was reported with the scale-up studies dealing with the hydrogen gas production from industrial winery wastewater and other sources of wastewater (Santoro et al. 2017a).

These scale-up studies on production of hydrogen gas from the industrial wastewater clearly signposted the intentions of the scientists taking this technology to the next level by researching on the limitations related to the increase in reactor's working volume (Santoro et al. 2017a).

8.4.2 Microbial Desalination Cell (MDC)

Remarkably, microbial desalination cell (MDC) has been magnificently advanced in the longtime objectives of treating wastewater, desalinating water, and generating electricity simultaneously (Cao et al. 2009; Santoro et al. 2017a).

A general schematic of the microbial desalination cell is here presented (Fig. 8.9c). There are numerous research works reported on the main configurations adopted in microbial desalination cells, along with the implementation of air-breathing cathodes, biocathodes, and osmotic membranes (Santoro et al. 2017a).

There is a rising attention in developing innovative processes to reduce the energy and chemical costs connected with the conventional nitrification-denitrification process. The very first proof of concept study proved that ANAMMOX mechanism can be advantageous to deliver simultaneous removal of carbon and nitrogen compounds from the source wastewater in MDCs along with bioelectricity generation (Kokabian et al. 2018).

This ANAMMOX mechanism is considered as ideal candidates which significantly reduce the required energy and chemical inputs. Anammox bacteria are much capable of attaining anaerobic ammonia oxidation (ANAMMOX) which results in the anaerobic transformation of ammonium to nitrogen gas resulting in the substantial energy and cost savings (Kokabian et al. 2018).

The electrons produced from the oxidation of wastewater at the anode chamber will be utilized by a biocathode to drive the nitrite/nitrate reduction. The MDC is gaining huge interests in the recent years for addressing water and energy nexus issues in a single process configuration potentially. This system can be adapted for treating the wastewater, water reuse, and desalination in water-scarce regions (Kokabian et al. 2018).

The important parameters such as recirculating anolyte and catholyte, stacking the cells, and using capacitive materials for deionization were investigated for improving the performance of the microbial desalination cells. A pilot-scale MDC system of 105 L was also presented in the recent (Santoro et al. 2017a).

8.4.3 Microbial Electrosynthesis Device (MES)

With the results of recent research, BESs have been presented with the as microbial electrosynthesis device, where the specific bacterial population or operating conditions can be utilized for the production of highly valuable resources as the products

from CO_2 or other compounds, including gas transformation or reduction (Fig. 8.9d). This absolute new direction is of high interest due to the possible utilization of renewable energy when separated from the main power lines distribution.

Fascinatingly, this MEC device can utilize the CO_2, and it can be converted to methane (Rabaey and Rozendal 2010; Lu and Ren 2016), acetate (Rabaey and Rozendal 2010), formate (Srikanth et al. 2014), and other compounds (Rabaey and Rozendal 2010; Roy et al. 2015; ElMekawy et al. 2016; Huang et al. 2016; Bajracharya et al. 2017). While the feasibility of the process has been reported in several cases, numerous challenges have yet to be overcome.

The most challenging problems to address are selectivity of the product, product separation from the solution, low reaction kinetics, and cell design. Regardless of these challenges, the results are quite promising and deserve further investigations (Santoro et al. 2017a).

8.5 Performance Evaluation by Electrochemical and Electroanalytical Techniques

8.5.1 Power/Voltage Generation

Power density is one of the normalized characteristic of the reactor in order to make it possible to compare the power output of the various types of fuel cells systems. The choice of the parameter that is generally used for the normalization depends on the application. Generally, the power output is usually normalized to three ways, the power density (P_{An}, W/m ^{2}) based on the projected anode surface area (A_{An}) (Park et al. 1999; Park and Zeikus 2003; Liu et al. 2004; Rabaey et al. 2004).

$$\mathbf{P_{an}=E^2_{cell}/A_{An}R_{ext}}$$

The power density in the case of anode consists of a material which can be challenging to express the surface area of the granular material (Rabaey et al. 2005b) instead the area of the cathode (A_{Cat}) can alternatively be used to obtain a power density (P_{Cat}).

$$\mathbf{P_{Cat}=E^2_{cell}/C_{Cat}R_{ext}}$$

In order to perform engineering calculations for size and costing of reactors, the power is normalized to the reactor volume, or where PV is the volumetric power (W/m^3) (Bullen et al. 2006),

$$\mathbf{P_v = E^2_{cell}/vR_{ext}}$$

8.5.2 Coulombic Efficiency

The coulombic efficiency (CE) is known as the ratio of total coulombs actually transferred to the anode against that theoretically present in the organic substrate for current generation over the time period. The energy conversion efficiency of MFCs describes which region of the energy present in the provided organic substrate ends up as an electrical energy.

$$\varepsilon \mathrm{cb} = \frac{M \int_o^{T_b} \mathrm{Idt}}{\mathrm{FbV_{AN}\Delta COD}}$$

The total coulombs obtained are determined by integrating the current over time, so that the coulombic efficiency for an MFC run in fed-batch mode, $\boldsymbol{\varepsilon c_b}$, evaluated over a period of time t_b, is calculated (Rabaey et al. 2005b; Cheng et al. 2006), where **M** is the molecular weight of oxygen, **F** is Faraday's constant, b is the number of electrons exchanged (4) per mole of oxygen, $\mathbf{v_{An}}$ is the volume of liquid in the anode compartment, and **ΔCOD** is the change in COD over time $\mathbf{(t_b)}$. In the case of continuous flow through the system, the coulombic efficiency **(εcb or CE) is calculated** on the basis of current generated under steady conditions as where q is the volumetric influent flow rate and **ΔCOD** is the difference in the influent and effluent COD (Logan et al. 2006).

8.5.3 Electrokinetics and Mass Transfers

The examination of electron transfer kinetics is not only great interest but also even greater complexity. The kinetic parameters can be identified from the separation of the peak potentials and peak currents of a redox system as functions of the applied scan rate by using the cyclic voltammetry (CV), and the electron transfer rate constant can also be gained from Tafel plots at zero current (open circuit potential) (Harnisch and Freguia 2012).

8.5.3.1 Cyclic Voltammetry (CV)

The most common and direct technique for the determination of the mechanisms of electrode reactions underlying oxidation or reduction reactions can be done by using

CV, which requires a three-electrode configuration to obtain accurate results (Zhao et al. 2009).

It is comparatively easy to find using CV whether a chemical system under study is reversible or irreversible. MFC studies employing CV generally use forward and backward voltage sweeps with rates in the range of 1–100 mV s^{-1}. Multiple peaks in the cyclic voltammograms of the bioelectrochemical system can be witnessed due to multistep parallel or consecutive (series) mechanisms, or to the presence of several different redox species (Zhao et al. 2009).

In MFC electrochemical studies, CV experiments have been extensively used to (i) examine the mechanisms of electrode reactions involving both direct and indirect electron transfer between the biofilm and the electrode, (ii) examine the redox potentials of the chemical or biological species involved at the anode or cathode (for a reversible redox couple, the average of the cathodic and anodic peak gives the reversible potential for that couple referenced against the RE being employed), and (iii) evaluate the performance of the catalysts being studied (Zhao et al. 2009).

Even though CV is a simple technique and the results are obtained in a relatively short time, the background experiments (with blank electrolyte) are mandatory for high excellence mechanistic studies.

8.5.3.2 Rotating Ring Disk Electrode (RRDG) and Rotating Disk Electrode (RDE)

In electrochemical experiments where mass transfer is sensibly controlled and crucial for studying the precise kinetic parameters of electron transfer, detailed probing of electrochemical reaction mechanisms including enzyme electrodes can be done by using the hydrodynamic techniques, namely, RDE and RRDE.

These techniques have been used in the evaluation of catalyst or modified electrode performances and for quantifying the number of electrons involved in ORR (Bard et al. 2000). The desired cathode process is the full ($4e^-$) reduction of oxygen to water, but partial ($2e^-$) ORR will occur on carbon-based electrodes and results in the generation of substantial quantities of highly reactive hydrogen peroxide (H_2O_2), which might affect the microbial metabolism (Zhao et al. 2009).

RRDE studies take in an RDE with an additional ring electrode (separately poised at a controlled potential—hence it needs a biopotentiostat) to identify the products (including peroxides) of the electrochemical reactions occurring on the central disk electrode. Very small rotating disk electrodes can be used to find an expression of linear sweep voltammograms (LSV) in a most precise manner.

However, these techniques cannot always be used to probe the electrochemical manners of biofilms on electrode surfaces as the biofilm can be fragile and likely to be destroyed under the conditions of high-speed rotation. An additional possibility that will permit experiments with the rapid mass transfer is to design experiments, which can study the electrochemistry of a single microbe on some form of electrochemically inactive but electronically conductive electrode surface. The hydrogen

oxidation reaction can be studied over electrode tips containing single Pt nanoparticles of defined size (Chen and Kucernak 2004; Zhao et al. 2009).

8.5.3.3 Differential Pulse Voltammetry (DPV)

DPV is also a voltammetry method with an improved sensitivity when compared to CV and LSV methods. A significant limitation of both CV and LSV is the substantial background levels from capacitive to non-Faradaic currents. Enhanced discrimination of Faradaic currents (electron transfer to and from an electrode) can be acquired using DPV, where the potential disconcertion consisting of small pulses will be superimposed upon a staircase waveform. DPV studies can also provide and improve the selectivity for observing different redox processes compared with CV and LSV (Zhao et al. 2009).

8.5.4 Electron Impedance Spectroscopy

Electrochemical impedance spectroscopy technique has a larger potential to examine and study the intricate impedance characteristics of microbial fuel cells (Ramaraja and Ramasamy 2013).

It is one of the most powerful tools for examining chemical and physical processes in solutions, at solid-solid interfaces and at solid-liquid interfaces as it permits the separation of the different voltage loss phenomena (Ramaraja and Ramasamy 2013).

With EIS technique the conductivity of electrode materials and membranes can also be measured easily. Above all, the way of nondestructive measurements makes EIS, a highly fascinating tool for studying the MFC performance without troubling its operation (Ramaraja and Ramasamy 2013).

Even after all the advantages, the knowledge of impedance from EIS alone is not enough, because this technique is only applicable to linear or quasi-linear system, but combining the EIS with the other electrochemical and biochemical techniques could make it better in understanding the performance of the bioelectrochemical systems (Ramaraja and Ramasamy 2013; Kashyap et al. 2014).

EIS of a system can be understood by two common graphical representations:

(i) *Nyquist plots*: The main limitation of Nyquist plots is that they will not show the frequency denoted by each data point (each point being a depiction of the impedance vector in the complex plane at a particular frequency).
(ii) *Bode plots*: This shows the frequency information as they are plots of the magnitude and phase angle of the impedance vector (Zhao et al. 2009).

In a microbial fuel cell, the bacterial populations will synthesize an endogenous mediator which may facilitate the electron transfer in the intracellular environment. The microorganisms adhere to the electrode surface and favor electron transfer,

whereas the other microbes may secrete soluble mediators for electron transfer shuttles that is electron from bacteria to the electrode and vice versa (Kashyap et al. 2014).

EIS has been magnificently exploited to find the response of such mediators on charge transfer resistance. The charge transfer reaction and the bioelectrochemical reaction provide high impedance and mostly observed from mid- to high-frequency region in the Nyquist plot.

8.6 Challenges and Influencing Factors Defining the Performance of MFCs

There are numerous hurdles remaining to get overcome for MFCs to get adopted widely. One of the main disadvantages in the MFCs operation is the poor power output, which edges the performance of MFCs to drive electronic devices. The power output of MFCs cannot achieve the high-power level as like other sources of renewable energy, such as solar power, tidal power, nuclear power, wind power, and others for industrial applications (Xia et al. 2018).

More than all the material cost of the electrode, PEM and catalyst result in reducing the economic competitive scopes when compared with other sources of energy (Xia et al. 2018).

So far, the performances of the laboratory MFCs are still much lower than the ideal performance due to its operating condition effects. The power generation of an MFC is influenced by various factors including the type of microbes, organic substrate's concentration, pH, temperature, ionic strength, and reactor configuration (Liu et al. 2005a; Du et al. 2007).

With a given MFC system, the following influencing parameters can be controlled to decline the polarizations in order to improve the performance of an MFC.

8.6.1 Voltage Reversal

The phenomena named voltage reversal and power overshoot are frequently witnessed in microbial fuel cell (MFC) systems, which results in the decline of the MFC's performance (An et al. 2016).

One in four microbial fuel cell (MFC) units undergoes the issues of power overshoot. Series connection and stacks of the MFC unit to a high-current generating unit showed significant current loss of 57% owing to power overshoot and the resultant voltage reversal (Zhu et al. 2011; An et al. 2016).

The doubling back of power (or current) in a high-overvoltage region (i.e., power overshoot) is related with a drop in the current production rate below a specific working voltage. Researchers have reported that anode malfunctions may lead to

power overshoot instigated by the population of the anodic bacterial community, rate of substrate utilization by the anode bacteria, and the maturity of the anodic biofilm (An et al. 2016; Sugnaux et al. 2017).

Peng et al. (2013b) claimed that the nonexistence of anodic abiotic capacitance might be a reason for power overshoot in MFCs.

Based on the literature survey, it was supposed that the power overshoot happened due to the lack of electrons (i.e., oxidation current), and it might be removed by supplying electrons to the anode of the MFC unit that experiences the power overshoot issue (An et al. 2016).

Zhu et al. (2013) stated that enhancement and acclimation of anode bacteria with a higher anode onset potential may possibly lead to increasing the maximum current of MFCs and be effective for reducing power overshoot related to the performance at a low anode onset potential.

The current loss for series connection of the two parallel-connected MFCs was reported by An et al. (2016) as small as 3%, and it clearly shows that series connection of parallel-connected MFCs might be a readily appropriate way for concurrently controlling the power overshoot and voltage reversal in MFC systems.

The challenges due to voltage reversals are resolvable, and optimal power generation is possible by using an MFC stack with shared anolyte was demonstrated by the most convenient techniques like electrical circuit alternation in the serial MFC stack, fast electrostimulation of biofilm growth, higher nutrient concentrations, and anolyte recirculation postponed voltage reversals, while the asymmetry of voltages in the stack endured and the power output persisted well below a balanced state (Sugnaux et al. 2017).

An interesting study demonstrated by Zhu et al. (2011) that stacked MFCs connected with reverse diodes, the voltages of each unit MFC almost equal their open circuit voltages (~0.75 V) and the voltage reversal occurs in the unit MFC with reverse diodes at the cathode end only. It clearly indicates that the imbalanced consumption of electrons in MFCs units, and the potential changes of a specific electrode directly result in voltage reversal.

8.6.2 Effect of Electrode Materials

Electrode modification studies are being actively investigated by several research groups to advance the MFC performances. In order to improve the performance of the MFC, the better performing electrodes should be used, because the anode materials may end up with the various potential losses mainly the activation which occurs during the transfer of electrons from or compound reacting at the electric surfaces and the concentration losses caused by rate of mass transport of a species to and from the electrode surface (Du et al. 2007).

Pt and Pt black electrodes are superior to other electrode materials like graphite plate, graphite felt, and carbon cloth electrodes for both anode and cathode constructions, due to its higher catalytic activity with regard to oxygen than graphite

material, but their costs are high. MFCs with Pt or Pt-coated cathodes material may produce high-power densities than with graphite or graphite felt cathodes (Jang et al. 2004; Oh et al. 2004; Moon et al. 2006; Du et al. 2007).

Generally, the electrode in the MFC will have a certain resistance; therefore, the most efficient one should have the very least resistive (Liu et al. 2013a).

As the use of highly efficient electrode materials (i.e. platinum) is not economically feasible for large-scale applications, studies on exploring more cost-effective alternatives are in the priority in MFC research (Wei et al. 2011).

The role of the nanomaterials may pave the way for making the electrode materials more efficient with the characteristics like active electron transfer with high conductivity and mechanical strength. There is no requirement for bacteria adhesion on the electrode as well. The high performance, sustainable, scalable, and cost-effective MFC can be made only with the incorporation of the nanomaterials in the system (Juan and Nixon 2013).

8.6.3 pH Buffer and Electrolyte

The role of the electrolyte's pH is very crucial in the proper functioning of the MFCs. If there is no pH buffer solution used in a working MFC, there will be a huge pH difference between both the chambers of the MFC reactor. Ideally there will be no shift in the pH, when the reaction rate of protons, electrons and oxygen at the cathode equals the production rate of protons at the anode. But this may lead to cause the transport barrier in the PEM during cross-membrane diffusion of the protons; proton transport through the membrane is slower than its production rate in the anode and, finally, results with the developed high pH level in the anodic chamber (Gil et al. 2003).

8.6.4 Proton Exchange Membrane System

Proton exchange membrane system is able to affect an MFC system's internal resistance, concentration, and polarization loss; finally they will have the influence over the power output of the MFC. Nafion (DuPont, Wilmington, Delaware) is the most popular and commonly used PEM, because of its highly selective permeability of protons (Juan and Nixon 2013).

Nafion is still the outstanding PEM membrane in the market, despite the attempts by researchers to develop less expensive and more durable substitutes for it (Juan and Nixon 2013). As it is very expensive with another side effect like the cations, transport through the membrane is inevitable during the MFC operation.

In a batch mode accumulative system, the transportation of cation species other than protons through the Nafion dominates the charge balance between the anodic

and cathodic chambers because its huge concentrations of Na^+, K^+, NH^{4+}, Ca^{2+}, and Mg^{2+} are much higher than the proton concentrations in the anolyte and catholyte (Logan et al. 2006).

Due to this, Nafion and other PEMs used in the MFCs are not necessarily proton-specific membranes but actually cation-specific membranes.

To ensure the optimum power output, the ratio of PEM surface area to system volume is very important. The PEM surface area has a huge impact on maximum power output if the power output is lower than a critical threshold. Eventually, the MFC internal resistance decreases with the increase of PEM surface area over a relatively larger range (Oh and Logan 2006). The phenomenon of the larger surface area in the PEM can be achieved with the usage of nanomaterials with the very high surface area.

8.6.5 *Anodic Chamber Operating Conditions*

The anodic chamber of the MFC directly relies on the important factors like the substrate/fuel type, pH, concentration, and feed rate. Even with the employed microbial consortium for the purpose of substrate degradation, power generation varies with the different fuels provided (Juan and Nixon 2013).

Various studies have shown that electricity production is mostly dependent on fuel concentration, in both the batch and fed-batch mode of operations. Generally in a wide concentration range of higher fuel concentration, a higher-power output is achieved (Juan and Nixon 2013). The increased inflow rate of feed is unlikely to affect the flora of microbes grown around the electrodes as biofilms.

The possible reason may be that the high feed rate brings in other alternate electron acceptors competing with the anode to lower the power output of the MFC (Juan and Nixon 2013).

8.6.6 *Cathodic Chamber Operating Conditions*

Oxygen is the most often used electron acceptor in MFCs for the cathodic reduction reaction. The power output of an MFC intensely is influenced by the concentration levels of electron acceptors. Notable, research studies of (Gil et al. 2003; Oh et al. 2004; Pham et al. 2004) had shown that DO was a major limiting factor for the electron acceptors when it remained below the air-saturated level.

Remarkably, a catholyte sparged with pure oxygen resulted with 38 mg/L DO did not further increased the power output, when compared to that of the air-saturated water at 7.9 mg/L DO (Min and Logan 2004; Oh et al. 2004; Pham et al. 2004).

8.7 Synergetic Applications of MFC's

8.7.1 Powering Implanted Medical Devices

Among one of the strange and newly emerging applications of MFC to power the implanted medical devices with glucose and oxygen which are present in the blood, the implanted MFC may deliver power open-endedly and avoids the need for replacing the batteries with surgery (Kerzenmacher et al. 2008).

Due to the growing interests in MFC for powering the implanted devices, the human white blood cells were used as a source of electrons for an anode. This experiment using white blood cells in phosphate-buffered saline solution with a ferricyanide cathode generated a low current level of 1–3 μAcm^2, but it perhaps could not be determined, if electron transported to the anode was through a direct or indirect mediated process (Tekle and Demeke 2015).

Several developments and improvements concerning the increase in the development of MFC for implanted devices are being added up. Scientists forecast that in the future a miniature MFC can be implanted in a human body to power an implantable medical device with the utilization of the nutrients supplied by the human body. This technology is principally favored for sustainable long-term power applications for the implanted devices. Nevertheless, this MFC will be used for this purpose only after studying the potential health and safety issues brought by the microorganisms in the MFC are comprehensively explained (Chia 2002).

8.7.2 Biohydrogen as Secondary Fuel

MFCs can be employed to generate secondary fuel like hydrogen (H_2) as an alternate of electricity (Das and Mangwani 2010). Due to the energy-intensive and sustainable behavior, biological hydrogen (biohydrogen) production processes are found to be advantageous over the thermochemical and electrochemical processes (Parkash 2016).

Biohydrogen can be successfully produced by the dark fermentation produce, but the efficiency is low. For the fermentation of carbohydrate-rich wastewater resulted in the yield of less than 15% (Liu et al. 2005a; Huang et al. 2016). Moreover, the methanogenic depletion of hydrogen in the fermentation process ended with the substrates being majorly converted to acetate or butyrate as by-products (Cheng and Hamelers 2008; Parkash 2016).

An MFC can also be modified to generate the hydrogen gas (H_2) by removing oxygen at the cathode region and the addition of a small voltage by the bioelectrochemically assisted microbial reactor (BEAMR) process or the biocatalyzed electrolysis process (Liu et al. 2005b; Logan and Regan 2006).

Around 8–9 mol-H_2 could be generated in a process that uses glucose as a substrate, where the first-stage fermentation system achieves 2–3 mol-acetate/mol glucose and a second-stage BEAMR process recovers 2.9 mol-H_2/mol-acetate. The

power needed for the second stage is estimated to be equivalent to 0.5 mol-H_2/mol-(Liu et al. 2005b; Logan and Regan 2006).

The production of biohydrogen through the BEAMR process is not restricted to glucose alone. Any biodegradable substrates which produce electricity in an MFC may work in a BEAMR system as well (Heilmann and Logan 2006; Logan and Regan 2006).

Through extensive study, Liu et al. (2005b) had revealed that the MFCs can produce about 8–9 mol H_2/mol glucose potentially, when related to the typical 4 mol_2/mol glucose achieved in other form of conventional fermentation methods. Consequently, MFCs will provide a renewable hydrogen source that may contribute to the overall hydrogen demand in this current hydrogen economy (Liu et al. 2005b; Tekle and Demeke 2015).

In a recent research work, an exfoliated molybdenum disulfide (MoS_2-EF) catalyst was synthesized, and the obtained particle size was 200 ± 50 nm, 50-fold smaller than the pristine MoS_2 catalyst. Hydrogen production rates in the same MEC with a *Geobacter sulfurreducer* act as a biocatalyst at the anode along with Pt, MoS_2-EF, and the pristine MoS_2 cathodes were 0.106, 0.133, and 0.083 m^3d^{-1} m^{-3}, respectively. This result promoted that MoS_2-EF led to highly purified hydrogen and that this catalyst can serve as an electrochemical active and cost-effective alternative to Pt (Rozenfeld et al. 2018).

8.7.3 Wastewater Treatment

In the earlier 1991 (Habermann and Pommer 1991), the MFCs were employed for treating the municipal or community wastewater which contains a huge amount of organic compounds that can be utilized as the fuel for the MFCs.

The power generated by MFCs through the wastewater treatment process potentially halved the electricity needed in a conventional treatment process that consumes a lot of electric power for aerating in the activated sludge reactors along with the removal of 50–90% less solids (Tekle and Demeke 2015).

The alternate methods to treat wastewater are favored even with the need of high operating cost and huge operating energy. The significant ability of MFCs is to treat wastewater with the benefits of low-energy requirement along with the additional energy generation. The first demonstration of consuming domestic wastewater as the substrate for the generation of electricity by MFC was reported by Liu et al. (2005b) and Parkash (2016).

An MFC would be used in a wastewater treatment system as a substitute for the existing energy-demanding bioreactor like an activated sludge system as a net energy-producing system. On the other hand, economical scale-up of an MFC is yet a challenge, and also the costs should be to replace a conventional treatment system with an MFC-based design (Logan and Regan 2006).

The development of the high internal resistance during the scale-up of the MFC and its high materials costs are the greatest challenges in bringing the MFCs for the real-time application in the wastewater treatment system (Logan and Regan 2006).

8.7.4 Benthic/Sediment Microbial Fuel Cells

Sediment or benthic microbial fuel cells (SMFCs) come under the category of the bioelectrochemical systems (BESs), where this type of BESs comprising an anode embedded in the anoxic sediments and a cathode suspended at the surface of the water column to ensure aerobic condition.

Owing to their exceptional characteristics, SMFCs can be explored as new technology for eliminating organic pollutants from sediments (Yan et al. 2014) and for in situ bioremediation of organic-rich sediment (Zhou et al. 2015) and wastewater (Huang et al. 2011a).

SMFC became an exciting application in the microbial fuel cell research area that is able to generate electricity from the organic matter in aquatic sediments (Liu et al. 2005b). The sediment MFC design can be made to power devices placed on the seafloor or underwater environment, where it will be expensive and technically difficult to exchange traditional batteries routinely, and the sediment MFC is also known as benthic unattended generators (BUGs) (Kim et al. 2003).

Due to the abundance of exoelectrogenic bacteria in the sediments, the sediment MFCs are set to generate electricity. Remarkable works suggested that the sediment-anode united with seawater-cathode configuration harvested high energy from the net oxidation of marine sediment's organic matter (Reimers et al. 2001; Parkash 2016).

The data about the natural environment can be supportive in understanding and modeling ecosystem responses, but the sensors distributed in the natural environment require power for operation. SMFCs can feasibly be used to power such devices, mostly in the river and deep-water environments where it is challenging to routinely access the system to replace the batteries. Sediment fuel cells are being advanced to monitor environmental systems such as creeks, rivers, and the ocean (Logan and Regan 2006).

The developed power densities are low in sediment fuel cells due to the low organic matter concentrations and their high intrinsic internal resistance. SMFCs developed to this date are limited to producing <30 mW/m^2. Nevertheless, the low-power density can be equalized with the energy storage systems that release data in gusts to central sensors (Logan and Regan 2006).

8.8 Importance of Nanomaterials for the Sustainable Development of MFC Technology

Microbial fuel cells (MFCs) are the promising technology to solve the futuristic energy related the issues. The performance levels and unit cost of the MFCs significantly rely on the basis of architecture, choice of materials, and overall geometry. In this endeavor for the enhanced performance either with the readily available or bespoke nanomaterials, a number of researches are continuing in hunt of the optimum combination of "high performance/low cost/multi-functional" materials that can create a formula for easy and economical scale-up of the MFCs (Santoro et al. 2017a).

The limited productivity of MFCs compared to other fuel cell technologies and the high cost of their components are the two major obstacles to commercialization. Since the early emergence of nanomaterial, there has been a great concern in its potential applications due to its excellent conductivity, enormous surface area, and good mechanical strength (ElMekawy et al. 2017).

The application of nanomaterials could help to overcome such challenges while integrating with biocatalysts for the construction of MFCs, either as an anode to enhance the electron transfer efficiency or as a cathode to successfully catalyze the oxygen reduction reaction (ORR) (ElMekawy et al. 2017).

8.8.1 The Ultimate Doping Processes for Nanomaterials

There are quite a remarkable efforts that have been taken for modifying the electrocatalysts to ensure optimum performance of the microbial fuel cell; in that list, the doping of heteroatoms of the approximately the same radius, namely, boron, nitrogen, sulfur, and phosphorous, was substituted over the carbon atoms in the sp^2 network (Zehtab Yazdi et al. 2015).

The O_2 is electrocatalytically reduced on the cathode surface via scavenging the electrons from the anodic region, and thus the oxygen reduction reaction (ORR) efficiency predicts the cell's overall performance (Liu et al. 2013b).

In general, the ORR takes place majorly through the four-electron pathway on platinum group metals (PGMs) as a catalyst (Bing et al. 2010) or two-electron pathway on non-noble materials like carbon black, Vulcan X, and activated carbon (Liu et al. 2013b).

Among the carbon nanomaterials, the metal-free electrocatalysts, namely, graphene, are at the forefront and also the promising alternative to the costlier Pt catalyst. Moreover, the reduced graphene was reported as a competent ORR catalyst which is proven for its fast electron transfer kinetics and excellent electrocatalytic activity (Tang et al. 2009)

8.8.1.1 Chemical Vapor Deposition (CVD)

The chemical vapor deposition (CVD) technique allows the carbon nanotubes (CNT) development in a diversity of forms, namely, powder, thick and thin films, aligned or entangled, straight or coiled, or even a preferred architecture of nanotubes, at predefined sites over a patterned substrate. This technique also offers better control over the growth parameters in contrast to other synthesis approaches. The parameters like atmosphere, carbon source, catalyst, and growth temperature are essential for the development of CNT growth in CVD technique (Koziol et al. 2010).

8.8.1.2 Thermal Catalytic Chemical Vapor Deposition (TCCVD)

The method of chemical vapor deposition (CVD) relies on the pyrolysis of hydrocarbons or other carbon feedstock through the addition of a nitrogen source like nitrogen, amines, ammonia, and nitriles in the furnace system over the surface of metallic catalyst particles, namely, ferrocene, cobaltocene, nickelocene, and others. The different quality of growth products was synthesized on the basis of varied conditions and parameters (Fig. 8.10). It has been recommended that only a minor concentration of nitrogen (<15%) could be introduced into MWNTs (Terrones et al. 1997).

Because of the distinctive properties like high oxygen reduction reaction (ORR) efficiency due to their increased catalytic activity, outstanding reliability, and environmental friendliness, the nitrogen-doped carbon materials have attracted substantial attention (Wen et al. 2014).

In the case of nitrogen doping process, there are two exclusive routes available to the synthesis of nitrogen-doped carbon nanotubes (N-CNTs):

(i) Direct delivery of heteroatoms with the carbon source stream, during the development of the nanotubes.
(ii) Replacement of carbon atoms by heating the nitrogen-comprising compound with CNTs. The operating temperature range of TCVD is 500–1200 °C at atmospheric pressure for the synthesis processes (Koziol et al. 2010).

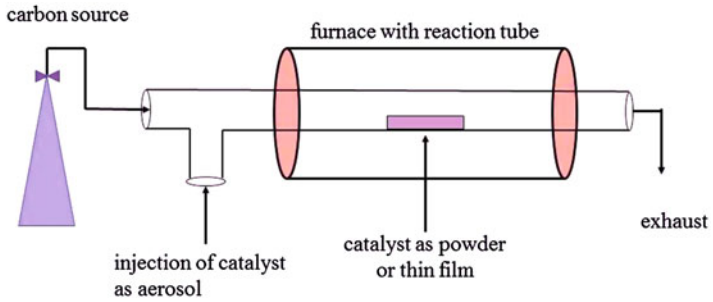

Fig. 8.10 Schematic diagram of thermal catalytic chemical vapor deposition (TCCVD). (Figure drawn with modifications after Koziol et al. 2010)

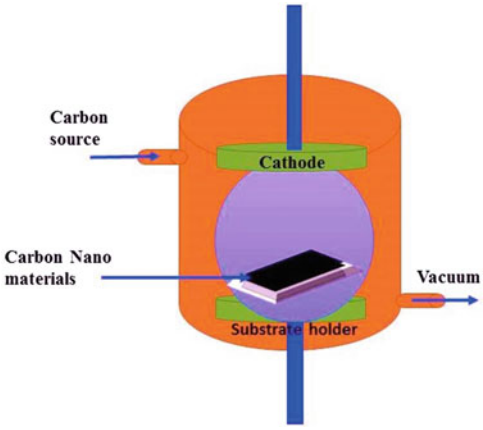

Fig. 8.11 Schematic diagram of plasma-enhanced chemical vapor deposition (PECVD). (Figure drawn with modifications after (Koziol et al. 2010)

A novel low-price, scalable, artificial technique for the preparation of porous nitrogen-doped carbon nanosheet on grapheme (PNCN) is the carbonization of graphite oxide-polyaniline hybrid (GO-PANI), subsequently followed by KOH activation treatment (Wen et al. 2014). Due to its high concentration of nitrogen and high specific surface area, PNCN exhibited an excellent catalytic activity for ORR. As a result, the maximum power density of 1159.34 mW m^{-2} obtained with PNCN catalyst was higher than that of Pt/C catalyst (858.49 mW m^{-2}) in an MFC. Therefore, porous nitrogen-doped carbon nanosheet could be a good alternative to Pt catalyst in MFCs.

The technique of plasma-enhanced CVD (PECVD) can be employed to synthesize carbon nanotubes and nanofibers, where the gaseous form of hydrocarbons will be in an ionized state over the transition metal catalyst, namely, nickel, iron, cobalt, etc. (Fig. 8.11). The electrical self-bias fields from plasma can be used to get the carbon nanotube and nanofiber with the optimum aligned growth which is perpendicular to the substrate (Koziol et al. 2010). There are two types of PECVD available, namely, hot filament PECVD which uses thermal energy for plasma generation and microwave PECVD used for the preparation of diamond films.

During a study, atmospheric pressure plasma jets (APPJs) were used to treat the carbon cloth, which resulted in increased hydrophilic nature of the carbon cloth, and notably no observable cracks or flaws were found. MFCs constructed with APPJ-treated carbon cloth electrodes had shown maximum power density of 7.56 mW m^{-2}, which was superior to that of MFCs configured with untreated carbon cloth electrodes of the maximum power density of 2.38 mW^{-2} (Chang et al. 2016)

8.8.1.3 Hydrothermal/Solvothermal Process

The solvothermal process including the hydrothermal process is one of the oldest methods in the green chemistry (Fig. 8.12). This hydrothermal/solvothermal process

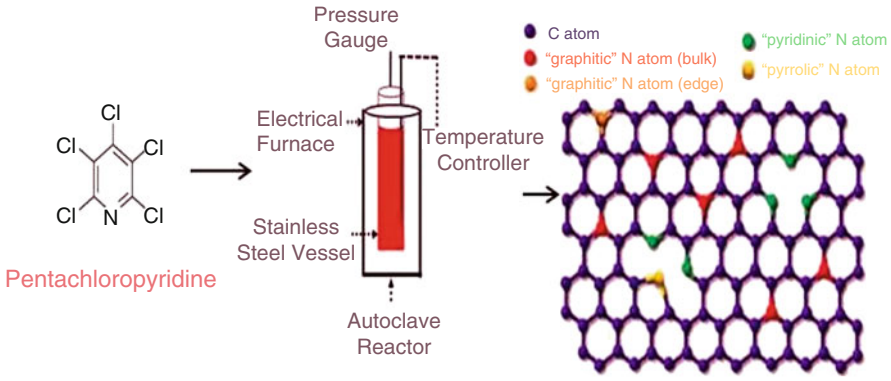

Fig. 8.12 Schematic illustration of the preparation of nitrogen-doped graphene by a solvothermal method in autoclave reactor. (Figure drawn with modifications after Ghanbarlou et al. 2015)

generally called as a green technique due to its closed system conditions available in the hydrothermal reactors is being extensively used for synthesizing quartz and metal oxides and also for growing the single crystals (Komarneni et al. 2010).

With the knowledge of the theoretical studies, it is predicted that graphene doping with nitrogen can alter its electronic properties and chemical reactivity. A novel process of one-pot direct synthesis of N-doped grapheme is through the reaction of tetrachloromethane with lithium nitride under mild conditions, which renders fabrication in gram scale. This new type of solvothermal process had maintained the temperature below 350 °C for the synthesis of N-doped graphene based on the reaction of tetrachloromethane with lithium nitride (Deng et al. 2011).

An innovative nanoflower-like NG with designed nitrogen types was directly produced by a low-temperature solvothermal process, and then Fe, Co, and Fe-Co nanoparticles are precipitated onto the NG using a reformed polyol technique. The electrocatalytic activity was measured by using cyclic voltammetry, electrochemical impedance spectroscopy, and linear sweep voltammetry. The higher electrocatalytic activity was exhibited by M/NG catalysts than NG catalysts. Further, the high stability of the Co/NG catalyst was proven by using the chronoamperometric techniques (Ghanbarlou et al. 2015).

In a recent endeavor, α -MnO_2 nanorods (MN), α-MnO_2 nanorods supported on reduced graphene oxide (MN/rGO), and α -MnO_2 nanorods supported on nitrogen-doped reduced graphene oxide (MN/NrGO) were synthesized through a facile one-step hydrothermal method (Gautam et al. 2016). The synthesized MN/NrGO and MN/rGO electrocatalysts were coated over the cathode of the air-cathode microbial fuel cell for the experimental studies with a very low loading of 0.5 mg/cm^2. The MFCs produced maximum power densities of 135.27 mW m^2 and 85.45 mW m^2, respectively, which was significantly higher as compared to pure rGO (57.63 mW m^2) and MN (45.56 mW m^2). From the experimental results, it was shown that MN/NrGO electrocatalysts are potentially efficient and cost-effective cathode catalysts for the practical application in MFCs.

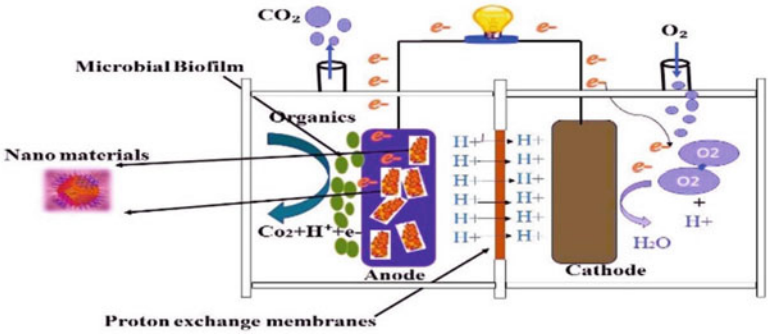

Fig. 8.13 Schematic diagram of anodic modifications with nanomaterials

8.8.2 Advancements in Anode Modifications

Microbial fuel cell (MFC) is one the most capable device, which can yield electrical energy through the conversion of the organic load with the help of microbial populations by the electron transfer mechanism (ETM). The need for the anode modification is very crucial in order to create a platform to permit the optimum level of extracellular electrons transfer (EET). Recently, remarkable levels in anode modifications are available by using the metal oxide nanomaterials due to their unique properties like good chemical stability, eco-friendliness, biocompatibility, etc.

Paramount importance is being provided in the selection of anode materials and architectures, which can directly influence the key performance parameters, namely, adhesion of microbial population, oxidation of organic loads, and electron transfer mechanisms (Fig. 8.13 and Table 8.3). There are several exclusive studies done to provide new knowledge in the area of anode surface modification by using the promising nanocomposite materials like nanometal oxides, nanotubes, nanofibers, nanosheets, etc.

8.8.2.1 Anodic Modifications with Metal Oxides Nanocomposite

The advancements and modifications in the surface of the anode play a vital role in enhancing the overall performance of the MFC and also ensuring the optimal biocatalytic activity. The anode surface can be modified to provide a favorable ambience for the microbial population, which results in the improved electron transfer from the bacterial biofilm to the anodic surfaces. The optimal bacterial population's adhesion over the anode surfaces may result in increased power production with minimal loss. Notably, the performance of TiO_2 nanosheet (TiO_2-NS)-modified carbon paper anode (TiO_2-NSs/CP) in *Shewanella loihica* PV-4 inoculated MFCs was significantly enhanced by intentional N doping of TiO_2-NSs

Table 8.3 A summary of recent studies on anode interface modifications by nanomaterials

Anode modifications			Influent	Configuration	Inoculum	Performance	Reference
	Support	**Method**					
Metal oxide	ITO glass/iron oxide	Chitosan binding	Acetate	Single chamber	*S. loihica* PV-4	35 mA/m^2	Ji et al. (2011)
	Activated carbon/ iron oxide	Rolling-pressing	Acetate	Single chamber	Mixed culture	2000 mA/m^2	Peng et al. (2013a)
	Carbon paper/ TiO2	Soaking, calcination	Lactate	Double chamber	*S. loihica* PV-4	2000 mA/m^2	Fan et al. (2011)
	Carbon paper	Calcination	Domestic wastewater	Double chamber	*Shewanella loihica* PV-4	747 mW/m^2	Yin et al. (2017)
CNT	Carbon cloth	Electrophoresis	Glucose	Double chamber	*P. aeruginosa*	245 mA/m^2	Liu et al. (2012)
	Sponge	Dipping-drying	Glucose	Double chamber	Mixed culture	7200 mA/m^2	Xie et al. (2011)
	Carbon cloth		Human urine	Single chamber	Mixed culture	899.52 mW/m^2	Chen et al. (2018)
	Textile fiber	Dipping-drying	Domestic wastewater	Double chamber	Mixed culture	2400 mA/m^2	Xie et al. (2014)
	Carbon cloth	Electrodeposition	Lactate	Double chamber	*S. oneidensis* MR-1	2650 mA/m^2	Liu et al. (2014)
	Carbon cloth	Pulsed voltage technique	Glucose nutrient solution	Double chamber	Mixed culture	560.40 mW/m^2	Fan et al. (2017)
Nanoarray	Carbon cloth	Polymerization technique	Acetate	Double chamber	Mixed culture	567.2 mW/m^2	Zhang et al. (2017)
	SS plate	In situ polymerization technique	Synthetic wastewater	Single chamber	Mixed culture	0.078 ± 0.011 mW cm^{-2}	Sonawane et al. (2018)

to modify its electronic properties (Yin et al. 2017). TiO_2-NSs/CP was synthesized by calcination alone, respectively.

With NH_3 atmosphere at various temperatures ($T = 400$, 500, 600, and 700 °C, T – temperature) N-doped anode nanocomposite (T-NTiO_2-NSs/CP) was obtained. Out of other nanocomposite materials, the T600C-NTiO_2-NSs/CP electrode had shown the maximal power density output increased by 196% and 50% compared to that from the bare CP and TiO_2-NSs/CP electrodes.

Most fascinatingly, the improvement of electrocatalytic activity of the composite modified electrode was reported through the bioelectrochemical sensing platform with a high potential for the microbial-electrode interactions. It was designed based on decorated graphene oxide (GO) sheet with alumina (Al2O3) nanocrystals to get GO-$Al2O_3$ nanocomposite through the self-assembly of GO and $Al2O_3$ (Hassan et al. 2018). The cell viability was evaluated by monitoring the bioelectrochemical response of the living microbial cells (bacteria and yeast) upon stimulation with carbon source by using the modified GO-$Al2O_3$ electrode nanocomposite.

8.8.2.2 Anodic Modifications with Nanotubes Composite

Anode materials like carbon nanotubes are being considered as the essential component of microbial fuel cells (MFCs), with enormous impacts on power generation performance and general cost. Due to the unique electronic and textural attributes, carbon nanotubes (CNTs) have been recognized as an electrode material with promising prospects with protruding properties of the large specific surface area, the capacity to be modified with various target groups and good chemical stability (Filip and Tkac 2014; Mehdinia et al. 2014). In a versatile study, supercapacitor (SC)-activated carbon (AC)-carbon nanotubes (CNTs) (SC-AC-CNTs) were used first to modify the carbon cloth (CC) anodes of microbial fuel cells (MFCs) and related with that of SC-AC and CC (Zhang et al. 2017). This study reveals that the specific surface area is increased from 219.519 to 283.643 m^2g^{-1} after modifications. The anode's effectiveness was tested in a urine-powered MFC (UMFC) also. The obtained power densities values of the UMFC assembled with SC-AC-CNTs and SC-AC-modified anodes are 899.52 mW m^{-2} and 555.10 mW m^{-2}, which are 2.9 and 1.8 times higher than that of the blank UMFC, respectively.

A simple and effective study was done to illustrate clearly the activity effect of multiwalled carbon nanotubes (MWCNTs) and their functionality on anodic exoelectrogen in microbial fuel cells (Fan et al. 2017). In addition, the growth of *E. coli* and anode biofilm over the MWCNT-, MWCNT-COOH-, and MWCNT-NH_2-modified anodes was related to a bare carbon cloth anode. The MFCs tested with the MWCNT-COOH-modified anode have attained a maximum power density of 560.40 mW/m^2, which was 49% greater than the one gained with pure carbon cloth.

8.8.2.3 Anodic Modifications with Nanoarrays Composite

Modification of the anode surfaces with three-dimension (3D) materials in nanoscale and microscale is also a possible approach to enhance the surface participating in electron transfer and biofilm growth mechanism.

Edifying work was carried to generate brush-like polyaniline (BL-PANI) nanowire arrays over the surface of the Carbon cloth and it was employed as anode material for improving the power output from the MFCs. The pulsed voltage technique was used to fabricate BL-PANI with PANI nanowires of 230 nm in length (Zhang et al. 2017). Due to the BL-PANI modified carbon cloth anode, the power output was enhanced by 58.1% and 36.1% compared to that of plain carbon cloth and PANI-modified carbon cloth with ordinary structure, respectively. The remarkable performance was reported because of the high specific area and capacitive manners caused by superior morphology contributed to higher-power output when compared with normal PANI-modified or plain carbon cloth.

Notably, a facile approach for production of conductive polyaniline (PANI) nanoflower modified carbon cloth electrode was made and employed in the microbial fuel cell for energy production. It was done by simple tuning of aniline monomer's concentration (Sonawane et al. 2018). By in situ polymerization technique, a uniformly distributed PANI nanoflower that was assembled from PANI nanoflakes which got anchored over the surface of carbon cloth electrode was fabricated. Moreover, the electrode modified with PANI nanoflower was employed as the anode of microbial fuel cells (MFC), which generated 2.6 and 6.5 times higher voltage and power output than these of pristine carbon cloth electrode, respectively.

8.8.3 Advancements in Cathode Modifications with Electro Catalyst for Improved Oxygen Reduction Reaction (ORR)

Abiotic catalysts used in MFCs cathodes can be classified in three main categories on the basis of the presence/absence of platinum and the presence/absence of earth-abundant metals. They are: (i) Platinum-based (PGM-based) with a $4e^-$ transport mechanism identified, (ii) Carbonaceous-based (metal-free) with a $2e^-$ transport mechanism identified and (iii) Platinum-group metal-free (PGM-free) with a more complex electron transfer mechanism (Santoro et al. 2017a).

Numerous methods are used to apply or incorporate the catalyst over the cathode surface. These can be based on: (i) Spraying technique, (ii) Doctor blade technique, (iii) Rolling, (iv) Pressing and (v) Drop casting.

In an MFC reactor, the biological oxidation may occur at the anode chamber with the presence of the exoelectrogenic bacterial populations which may produce free electrons and ions (Table 8.4 and Fig. 8.14). Those electrons will flow to the cathode via an external path where oxygen, a terminal electron acceptor get reduced. Even

Table 8.4 A summary of recent studies on cathode interface modifications by nanomaterials

Anode modifications			Influent	Configuration	Inoculum	Performance	References
	Support	**Method**					
Metal oxide	Carbon felt	Press-drying	Glucose	Single chamber	*E. coli*	1520 mA/m^2	Wang et al. (2013)
	Graphite plate	Green facile method	Phosphate buffer solution	Double chamber	Anaerobic tank sludge	220 mW/m^2	Mashkour et al. (2017)
	Carbon felt/ WO3	PTFE-binding	Acetate medium	Single chamber	S. putrefaciens	1100 mA/m^2	Varanasi et al. (2016)
	Carbon felt	In situ polymerization	Acetate medium	Plate MFC	Domesticated sludge	1078.8 mW/m^2	Zhong et al. (2018)
	Cobalt phosphide	Rolling and pressing	Phosphate buffer saline	Single chamber	Domesticated sludge	1914.4 ± 59.7 mW/ m^2	Zou et al. (2016)
CNT	Carbon cloth	Freeze-drying	Lactate	Double chamber	S. putrefaciens CN32	2500 mW/m^2	Zou et al. (2016)
	Carbon paper	Layer-by-layer (LBL) assembly	Sodium acetate medium	Double chamber	Mixed culture	55.5 mW/m^2	Xu et al. (2017)
	Carbon paper	Electrochemical deposition	Lactate	Single chamber	S. oneidensis MR1	1900 01 mA/m^2	Huang et al. (2011b)
	Platinum electrode	In situ method	Glucose medium	Double chamber	Anaerobic sludge	84.01 mA/m^2	Halakoo et al. (2015)
	Graphite felt	Different electrophoretic deposition	Sediment soil and plant leaves	SMFC	Sediment soil	215 ± 9.9 mW/m^2	Zhu et al. (2015)
Graphene	Carbon cloth	PTFE-binding	Glucose	Double chamber	E. coli	550 01 mA/m^2	Zhang et al. (2011)
	Carbon cloth	PTFE-binding	Glucose	Single chamber	Anaerobic sludge	2337 mW/m^2	Gnana kumar et al. (2016)
	Carbon cloth	Nafion-binding	Glucose	Double chamber	Mixed culture	2700 mA/m^2	Xiao et al. (2012)

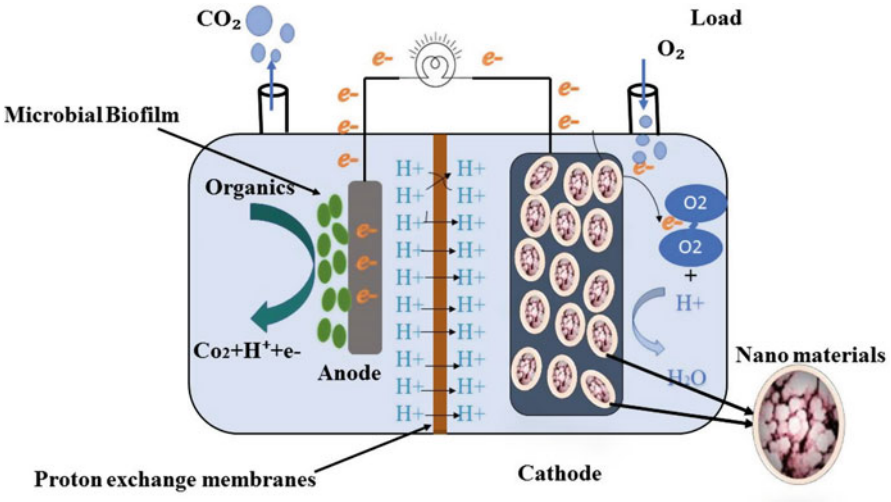

Fig. 8.14 Schematic diagram of cathode modifications with nanomaterials

with the easy availability of Oxygen in the environment as an electron acceptor, the mechanism of oxygen reduction reaction (ORR) is slow and retains high-energy obstruction for its activation, which can be reduced by the usage of a competent catalyst.

8.8.3.1 Cathodic Modifications with Metal Oxides Nanocomposite

There were several studies reported on the development of the noble catalysts to enhance the oxygen reduction reaction (ORR) in the cathode surfaces. Notably, in a study, modified cathodes with titanium dioxide (TiO_2) or hybrid graphene (HG) was employed in the dual-chamber MFC and reported with an enhanced catalytic activity of the cathode surface (Mashkour et al. 2017). A significant enhancement in the MFC performance was noted by calculating the power density value of 80 mW/m^2 for GP-TiO_2 and 220 mW/m^2 for GP-HG compared to 30 mW/m^2 for GP electrode. Furthermore, lower charge transfer resistance (R_{ct}) was revealed by the modified electrodes compared to the bare electrode.

The highly projectable study was done by using the in situ growth and in situ polymerized embedded polyaniline (PANI) inpetaline NiO (NiO@PANI-CF) for electricity generation and dye degradation (Zhong et al. 2018). Due to the high capacitive property of NiO and the high conductivity of PANI reported with the improved electricity generation capacity on basis of its maximum output power density of 1078.8 mW·m^{-2} and less charge transfer resistance of 10.4 Ω. Notably, the color and COD removal capability of Reactive Brilliant Red X-3B attained 95.94% and 64.24% at 48 h, respectively.

A novel and simplistic method were proposed for the first time to fabricate the electrocatalyst for oxygen reduction reaction (ORR) namely the surface-oxidized cobalt phosphide (CoP) nanocrystals (NCs), for electricity generation in microbial fuel cell (MFC). This corallite-like CoP NCs were successfully synthesized by a hydrothermal reaction with subsequent phosphating treatment in the N_2 atmosphere (Zou et al. 2016). The maximum power density of MFC overstated with 10% CoP reached 1914.4 ± 59.7 mW m^{-2}, which is 108.5% higher than the control. Furthermore, characterizations of material pointed out the important and beneficial for ORR due to the surface oxide layer (CoO_x) around the metallic CoP core.

8.8.3.2 Cathodic Modifications with Nanotube Composites

On one side, rigorous studies were attempted to overcome the challenges in making the very efficient electrocatalysts with the high electron transfer's activity rate between anode and electrolyte solution. The carbon nanotubes (CNTs) were used to modify the carbon electrode surface is confirmed to be the efficient catalytic support for several electrochemical applications, due to its exclusive electrical conductivity, large specific surface area, and structural properties.

To improve the reduction of Orange II azo dye in cathode compartment of microbial fuel cells (MFCs) and power generation, through immobilization of redox mediators (RMs) with self-assembled peptide nanotubes (PNTs) as the carrier, a novel cathode modification was done over the carbon paper (CP) (Xu et al. 2017). MFCs loaded with the riboflavin (RF)-/PNT-altered cathode (PNT/RF/CP) or anthraquinone-2,6-disulfonate (AQDS)-/PNT-altered cathode (PNT/AQDS/CP) resulted in an enhanced decolorization rate to Orange II azo dyes, compared with the control electrode, along with 1.3 and 1.2-folds increased by the reduction kinetic constants. In addition, the MFCs with the PNT/AQDS/CP cathode and PNT/RF/CP cathode produced a very higher-power density of 55.5 mW m^{-2} and 72.6 mW m^{-2}, respectively, than the unmodified control electrode (15.5 mW m^{-2}).

To emphasize the remarkable work done on the carbon nanotube platinum (CNT/Pt) nanocomposite was fabricated by using the in situ method, used as a novel cathode catalyst in MFCs, and its performance was compared with platinum in MFC system (Halakoo et al. 2015). The results show that CNT coupled with Pt has reported with better performance than Pt in MFCs, due to better interaction with oxygen in the cathode chamber and high catalytic activity of CNT/Pt for oxygen reduction reaction. The catalytic power of the cathode improved when the quantity of Pt is raised to 0.2 mg/$cm^2$and reached 73.01 mW/m^2 at 246.67 mA/m^2. After that the power density was greater than before slightly and reached to 75.95 (251.58), 77.028 (327.08), and 84.01 mW/m^2 (341 mA/m^2) with the loading rate of 0.3 mg/cm 2, 0.4 mg/cm^2, and 0.5 mg/cm^2, respectively.

Interestingly, the performance of sediment microbial fuel cells (SMFCs) was increased by fabricating it with the multiwalled, carbon nanotube (MWNT)-modified graphite felt (GF) cathode (Zhu et al. 2015). They proposed three types of MWNT-modified GF cathodes prepared by different electrophoretic deposition

(EPD) times of the duration of 10, 30, and 60 min. Notably, the highest-power density of SMFC with MWNT-GF cathode at 60 min EPD was 215 ± 9.9 mW m^2, which was nearly 1.6 times higher than the SMFC with an unmodified control GF cathode.

8.8.3.3 Cathodic Modifications with Graphene Nanocomposites

A novel and environmental-friendly study was proposed to develop a ternary composite containing reduced graphene oxide (rGO), poly(3,4-ethylene dioxythiophene) (PEDOT), and iron oxide (Fe3O4) nanorods. Further, the significant influence of the energy generation through air-cathode microbial fuel cells (ACMFC) was due to the application of competent oxygen reduction reaction (ORR) catalyst (Gnana kumar et al. 2016). Among the prepared composites, rGO/PEDOT/CC showed the ACMFC power and current densities of 2337 mW/$m^2$and 7410 mA/m^2, respectively, with the greater sturdiness of more than 600 h and this behavior is mainly due to its protracted surface area, extraordinary electrical conductivity, and large oxygen adsorption sites.

A versatile work was reported on the viability of graphene-based nanomaterials ($RGO_{HI\text{-}AcOH}$ vs. RGO/Ni nanoparticle composite) as a unique cathode catalyst in single-chamber air-cathode MFCs (Valipour et al. 2016). The prepared RGOHI-A_cOH nanocomposite cathode has shown higher-power densities (>37%) than those with the RGO/Ni nanoparticle cathodes. Furthermore, MFCs with the highest-power density of 1683 ± 23 mW/m^2 (CE ¼72 ± 3%), which covers 77% of that estimated for Pt/C (2201 ± 45 mW/m^2 (CE¼81 ± 4%), were obtained from the double-loading $RGO_{HI\text{-}AcOH}$ cathodes.

Recently, three-dimensional graphene nanosheets (3D-GNS) were synthesized and employed as catalysts over the cathode surface in microbial fuel cells, operating under the neutral conditions (Santoro et al. 2017b). Further, the overall performances in MFCs exhibited that 3D-GNS had the utmost performances with power densities of 2.059 ± 0.003 Wm^{-2}, 1.855 ± 0.007 Wm^{-2}, and 1.503 ± 0.005 Wm^{-2} for loading of 10, 6, and 2 mg/cm^{-2}, respectively.

8.8.4 Recent Trends in the Development of Nanocomposite Electrolyte Membranes

Proton exchange membrane (PEM), as well as other structural materials like electrode and electro catalysts, plays a crucial role in enduring the development of MFCs, especially for the real-time practical implementations (Santoro et al. 2017a).

Most of MFC designs need the separation of the anode and the cathode compartments by a cation exchange membrane (CEM). Exemptions are naturally separated systems such as sediment MFCs (Reimers et al. 2001).

The most commonly used CEM is Nafion (DuPont Co., USA), which is available from numerous suppliers, and other options to Nafion, such as Ultrex CMI-7000 (Membranes International Incorp., Glen Rock, NJ), also are well suited for MFC applications (Rabaey et al. 2004), but all the other types of membranes are significantly more cost-effective than Nafion (Logan et al. 2006).

Initially, various examples focused on the utilization of cation exchange membranes (CEM) (e.g., Nafion) that came from the existing hydrogen proton exchange membrane fuel cell technology (PEMFC) and membrane-based water treatment systems (Santoro et al. 2017a).

In the present endeavor, the market for ion exchange membranes is continually growing, and more systematic studies are necessary to develop the membranes with the nanocomposite electrolyte membranes for the enhanced performance and long-term stability in the MFCs (Logan et al. 2006). Several varieties of the nanocomposite electrolyte membranes can be fabricated on basis of the appropriate carrier polymers and the functional nanocomposites (Table 8.5).

8.8.4.1 Sulfonated Polymer Nanocomposite Electrolyte Membranes

The nanocomposite electrolyte membranes fabricated from the sulfonated groups of metal oxides not only create a path for proton transport but also act as means of transportation due to its negative charge. Both metal oxide (-OH group metal oxide) and water molecule can only create a path for proton transport but cannot act as vehicle due to their neutral charge (Ayyaru and Dharmalingam 2015).

A most promising study was carried with solution cast sulfonated TiO_2 (S-TiO_2)/polystyrene ethylene butylene polystyrene) SPSEBS nanocomposite membranes and the performance was analyzed by using single-chamber microbial fuel cell (SCMFC) (Ayyaru and Dharmalingam 2015). The results exposed that the incorporation of sulfonated TiO_2 composite enhanced the proton conductivity of the SPSEBS membrane efficiently and showed the maximum peak power density of 1345 ± 17 mWm^{-2} for SPSEBS-S-$TiO_2$7.5% when compared to 695 ± 7 $mWm^{-2}$and 835 ± 8 mWm^{-2}obtained for SPSEBS and SPSEBS-TiO_2 membranes, respectively. Furthermore, the prepared SPSEBS-S-$TiO_2$7.5% membrane was also compared to previously reported work with Nafion®(300 ± 10 mWm^{-2}) in MFCs. Interestingly, the composite membrane supplied more than fourfold higher-power density. In addition, the oxygen mass transfer coefficient (K_O) of nanocomposite membranes reduced due to the usage of the sulfonated TiO_2 which in turn improved the columbic efficiency (CE).

The highly projectable study was reported by using nanocomposites QPSU, QPSU/GO, and QPSU/FGO which was fabricated by solvent-casting method (Elangovan and Dharmalingam 2016). The agar plate test confirmed the better antibacterial property of the QPSU/FGO-1.0% membrane among all five different

Table 8.5 A summary of recently reported works on proton exchange membrane modifications (PEM) with nanomaterials

PEM modifications			Influent	Configuration	Inoculum	Performance	References
	Anode	**Cathode**					
Sulfonated polymers	Wetproof carbon cloth	Carbon cloth	Glucose medium	Single chamber	Sewage wastewater	300 ± 10 mW/m^2	Ayyaru and Dharmalingam (2015)
	Wetproof carbon cloth	Carbon cloth	Sodium acetate medium	Single chamber	Sewage wastewater	2880.70 mW/m^2	Elangovan and Dharmalingam (2016)
	Carbon paper	Carbon paper	Sodium acetate medium	Dual chamber	Sewage wastewater	38.38 ± 4.73 mW/m^2	Di Palma et al. (2018)
	Carbon cloth	Carbon cloth	Nutrient broth	Single chamber	Mixed bacterial culture	659.79 mW/m^2	(Papiya et al. (2018)
Non-sulfonated polymers	Carbon cloth	Carbon cloth	Synthetic wastewater	Single chamber and dual chamber	Septic tank sludge	0.80 W/m^3	Khilari et al. (2013)
	SS plate	Carbon cloth		Single chamber	Sodic saline hybrid H-inocula	1053 mW/m^3	Kamaraj et al. (2015)
Natural polymers	Carbon cloth	Carbon cloth	Nutrient broth	Single chamber	*Escherichia coli*	46 mW/m^2	Narayanaswamy Venkatesan and Dharmalingam (2013)
	Graphite felt	Graphite felt	Tryptone medium	Dual chamber	Anaerobic sludge	–	Srinophakun et al. (2017)

composites and also reported with an extreme power density of 1036.15 mW m^{-2} and a current density of 2880.70 mAm^{-2}. Additionally, the outperformed composite membrane was compared with the commercially available anion exchange membranes (AEMs) like AMI-7001, and it reveals that the membrane QPSU/FGO-1.0 wt % had the least resistance with enhanced the anti-biofouling efficiency even for long-term use.

In a recent study, nanocomposite membranes based on polyethersulfone (PES) with different amounts of Fe_3O_4 nanoparticles were synthesized and utilized as proton exchange membranes in a microbial fuel cell (MFC). The maximum power (9.59 ± 1.18 mW m^{-2}) and current density (38.38 ± 4.73 mA m^{-2}) generation were achieved by using a composite with 20 wt% of nanoparticles. The obtained results of mechanical characterization pointed out that increasing the nanoparticles content can compromise the mechanical properties of membranes leading to an extensive brittle behavior, while the tensile strength was found to be appropriate for durable operation of MFC (Di Palma et al. 2018).

This particular study demonstrated the evaluation of synthesized non-noble bimetallic [1:1 nickel (Ni): cobalt (Co)] nanocatalyst supported on sulfonated polyaniline (SPAni) in MFC. Furthermore, in MFC, a maximum power density of ~659.79 mW/m^2 was witnessed with prospective Ni-Co/SPAni catalyst also compared to the corresponding Pt/C catalyst (~483.48 mW/m^2). The results strongly direct the potential application of a conducting polymer such as SPAni as supporting matrix in bimetallic Ni-Co catalyst system that could also alternatively function as an efficient cathode catalyst over the traditionally used costly Pt/C catalyst in MFCs operation (Papiya et al. 2018).

8.8.4.2 Non-sulfonated Polymer Nanocomposite Electrolyte Membranes

Other than the sulfonated polymer, presently the non-sulfonated polymer nanocomposite electrolyte membrane has got remarkable consideration as well. The low-cost non-sulfonated polymer like PVA with the inorganic composite had shown an outstanding dimensional and thermal stabilities, good mechanical stability, controllable physical properties, and good hydrophilic and electrochemical properties, all of which are necessary for ion exchange membranes (Anis et al. 2008).

Noteworthy, a study was presented with the development and application of a proton exchange polymer membrane separator containing of graphene oxide (GO), poly(vinyl alcohol) (PVA), and silicotungstic acid (STA), and it was employed in a single-chamber microbial fuel cell (SMFC) (Khilari et al. 2013). Interestingly, an extreme power density of 1.9 W/m^3 was attained when acetate wastewater was treated in a MFC equipped with a PVA-STA-GO non-sulfonated polymer nanocomposite.

Remarkable work was reported with the fabricated 12-mm-thin nanocomposite fuel cell membranes, where poly(vinylidene fluoride-co-hexafluoropropylene)

(PVDF-HFP) nanofibers are directly electrospunned onto the gas diffusion electrodes (Breitwieser et al. 2017). At the temperature of 120 °C and 35% relative humidity, stoichiometric 1.5/2.5 H_2/airflow and atmospheric pressure, the power density of the DMD fuel cell (0.19 W cm^{-2}), resulted with 1.7 times higher than that of the reference fuel cell (0.11 W cm^{-2}) with Nafion HP membrane and identical catalyst. Additionally, a 100 h accelerated stress test exposed a voltage decline of below 0.8 mV h^{-1}, which is in the range of literature values notably for the thicker reinforced membranes.

8.8.4.3 Natural Polymer Nanocomposite Electrolyte Membranes

Time being we are in the growing need of finding the solution to replace the costlier and not environmental-friendly polymer electrolyte membranes like Nafion® without compromising the maximum power density generation.

An adaptable work reported the influence of multiwalled carbon nanotube (MWCNT) in water absorption, oxygen crossover, and performance of chitosan (CHIT) in single-chamber microbial fuel cell (SCMFC) (Narayanaswamy Venkatesan and Dharmalingam 2013). They also reported the maximum power density yield of CHIT–MWCNT composite membrane, and it was greater compared to that of CHIT membrane with 38.16 mW/m^2 and 46.94 mW/m^2 for CHIT and CHIT–MWCNT, respectively.

A promising study was reported by using a novel quaternized poly(vinyl alcohol)/chitosan/molybdenum disulfide (QPVA/CS/MoS_2) anion exchange membranes (AEMs) prepared with MoS_2 nanosheets (0, 0.1, 0.2, 0.5 and 1 wt%) into QPVA/CS mixture solution. The membrane was cast by the solution casting method and employed in the direct methanol alkaline fuel cell (DMAFC) (Jiang et al. 2018). Notably, with the casted nanocomposite electrolyte membranes of 1.0 wt% MoS_2, the QPVA/CS/MoS_2 was reported with the lowest methanol permeability of 0.210×10^{-7} $cm^2 \cdot s^{-1}$.

For the first time, chitosan nano-ZnO composite film was prepared by a simple one-pot method. The potential applicability of composite films as an efficient antimicrobial packaging material was evaluated, and it exhibited enhanced antimicrobial efficacy as compared with pure chitosan film, and it is linearly related to the amount of ZnO particles in the matrix (Mujeeb Rahman et al. 2018).

8.9 Conclusions

In general, the MFCs exploiting the naturally occurring microbes decomposing the organic materials through the exoelectrogenic pathways are used to both clean water and produce electrical energy by oxidizing the organic materials from the wastewater. Therefore, it has created tremendous attraction to the multidisciplinary researchers. Even though it has many barriers in the power production, it has viable

application with usage of cost-effective materials as a possible future technology in the field of wastewater treatment sector. With the aid of future leading nanotechnology, a great platform can be obtained in terms of maximum power production by minimizing the obstacle in the MFCs operation in various components like anodic and cathodic electrode modification and membrane development. Moreover, with the support of nanotechnology in MFCs, the surface area to volume ratio can be enlarged, for providing an easier and more direct access between microbes and electrodes for a more an efficient transfer of electrons at the anode modification.

Furthermore, modification of cathode with nanomaterials could reduce the potential in the air cathode and creates the opportunities to search for the alternative non-noble metal catalyst. A recent advance in the hybrid bio-supercapacitor with the electrodes modified with the nanomaterials has shown to improve the efficiency of the capacitance behavior and makes the process viable. Moreover, few issues such as biocompatibility, environmental-friendly synthesis, and minimum nanotoxicology effect to the environment could take into account the implementation of nanotechnology in MFCs application.

As afore-discussed elaborately, MFCs can be used potentially for different applications. When used in wastewater treatment, a large surface area is needed for biofilm to build upon the anode. An advanced nanomaterial is needed in creating a less expensive and high-performance MFCs. It is impractical to expect the power density output from an MFC to match the conventional chemical fuel cell like a hydrogen-powered fuel cell. The fuel in an MFC is more often the wastewater treatment in the anodic chamber that has a limited releasable energy and inherent naturally low catalytic rate of the microbes and even at their fastest-growing microbes are relatively slow transformers.

Even with all the abovementioned challenges, the coulombic efficiency of more than 90% has been reported with the MFCs incorporated with nanomaterials. Currently, basic knowledge has been gained through a century of extensive research in the field of MFCs; there is still a lot to be learned about the extensive applications of the nanomaterials for developing MFC to serve the wide-range and large-scale applications. Through all the above-discussed research, MFC can be strongly considered as the promising technology with sustainable materials for the development of the low-cost and futuristic high-performance microbial fuel cells.

References

Aelterman P, Rabaey K, Verstraete W (2006) Continuous electricity generation at high voltages and currents using stacked microbial fuel cells. Environ Sci Technol 40:3388–3394. https://doi.org/10.1021/es0525511

An J, Kim T, Chang IS (2016) Concurrent control of power overshoot and voltage reversal with series connection of parallel-connected microbial fuel cells. Energ Technol 4:729–736. https://doi.org/10.1002/ente.201500466

Anis A, Banthia AK, Bandyopadhyay S (2008) Synthesis & characterization of PVA/STA composite polymer electrolyte membranes for fuel cell application. J Mater Eng Perform 17:772–779. https://doi.org/10.1007/s11665-008-9200-1

Ayyaru S, Dharmalingam S (2015) A study of influence on nanocomposite membrane of sulfonated TiO2and sulfonated polystyrene-ethylene-butylene-polystyrene for microbial fuel cell application. Energy 88:202–208. https://doi.org/10.1016/j.energy.2015.05.015

Babanova S, Carpenter K, Phadke S et al (2017) The effect of membrane type on the performance of microbial electrosynthesis cells for methane production. J Electrochem Soc 164:H3015–H3023. https://doi.org/10.1149/2.0051703jes

Bajracharya S, Srikanth S, Mohanakrishna G et al (2017) Biotransformation of carbon dioxide in bioelectrochemical systems: state of the art and future prospects. J Power Sources 356:256–273. https://doi.org/10.1016/j.jpowsour.2017.04.024

Bard AJ, Faulkner LR, Swain E, Robey C (2000) Electrochemical methods fundamentals and applications

Bhunia P, Dutta K (2018) Biochemistry and electrochemistry at the electrodes of microbial fuel cells. Elsevier B.V

Bing Y, Liu H, Zhang L, Ghosh D, Zhang J (2010) Nanostructured Pt-alloy electrocatalysts for PEM fuel cell oxygen reduction reaction. Chem Soc Rev 39(6):2184

Bond DR, Lovley DR (2003) Electricity production by Geobacter sulfurreducens attached to electrodes electricity production by Geobacter sulfurreducens attached to electrodes. Appl Environ Microbiol 69:1548–1555. https://doi.org/10.1128/AEM.69.3.1548

Bond DR, Lovley DR (2005) Evidence for involvement of an Electron shuttle in electricity generation by Geothrix fermentans evidence for involvement of an Electron shuttle in electricity generation by Geothrix fermentans. Appl Environ Microbiol 71:2186–2189. https://doi.org/10.1128/AEM.71.4.2186

Breitwieser M, Klose C, Klingele M et al (2017) Simple fabrication of 12 μm thin nanocomposite fuel cell membranes by direct electrospinning and printing. J Power Sources 337:137–144. https://doi.org/10.1016/j.jpowsour.2016.10.094

Bullen RA, Arnot TC, Lakeman JB, Walsh FC (2006) Biofuel cells and their development. Biosens Bioelectron 21:2015–2045. https://doi.org/10.1016/j.bios.2006.01.030

Busalmen JP, Esteve-Nuñez A, Feliu JM (2008) Whole cell electrochemistry of electricity-producing microorganisms evidence an adaptation for optimal exocellular electron transport. Environ Sci Technol 42:2445–2450. https://doi.org/10.1021/es702569y

Cao X, Huang X, Liang P et al (2009) A new method for water desalination using microbial desalination cells. Environ Sci Technol 43:7148–7152. https://doi.org/10.1021/es901950j

Chae KJ, Choi MJ, Lee JW et al (2009) Effect of different substrates on the performance, bacterial diversity, and bacterial viability in microbial fuel cells. Bioresour Technol 100:3518–3525. https://doi.org/10.1016/j.biortech.2009.02.065

Chang IS, Moon H, Bretschger O et al (2006) Electrochemically active bacteria (EAB) and mediator-less microbial fuel cells. J Microbiol Biotechnol 16:163–177

Chang SH, Liou JS, Liu JL et al (2016) Feasibility study of surface-modified carbon cloth electrodes using atmospheric pressure plasma jets for microbial fuel cells. J Power Sources 336:99–106. https://doi.org/10.1016/j.jpowsour.2016.10.058

Chen S, Kucernak A (2004) Electrocatalysis under conditions of high mass transport: investigation of hydrogen oxidation on single submicron Pt particles supported on carbon. J Phys Chem B 108:13984–13994. https://doi.org/10.1021/jp048641u

Cheng S, Hamelers HVM (2008) Critical review microbial electrolysis cells for high yield hydrogen gas production from organic matter. 42

Cheng S, Liu H, Logan BE (2006) Increased power generation in a continuous flow MFC with advective flow through the porous anode and reduced electrode spacing. Environ Sci Technol 40:2426–2432. https://doi.org/10.1021/es051652w

Chia MA (2002) Miniatured microbial fuel cell. Technical digest of solid state sensors and actuators workshop, Hilton Head Island, pp 59–60

Choi Y, Jung E, Kim S, Jung S (2003) Membrane fluidity sensoring microbial fuel cell. Bioelectrochemistry 59(1–2):121–127

Coates JD, Wrighton KC (2009) Microbial fuel cells: plug-in and power-on microbiology. Microbe Mag 4:281–287. https://doi.org/10.1128/microbe.4.281.1

Das S, Mangwani N (2010) Recent developments in microbial fuel cells: a review. J Sci Ind Res (India) 69:727–731

Davis F, Higson SPJ (2007) Biofuel cells-recent advances and applications. Biosens Bioelectron 22:1224–1235. https://doi.org/10.1016/j.bios.2006.04.029

De Juan A, Nixon B (2013) Technical evaluation of the microbial fuel cell technology in wastewater applications declaration: 1–18. https://doi.org/10.13140/2.1.4481.0569

Deng D, Pan X, Yu L et al (2011) Toward N-doped graphene via solvothermal synthesis. Chem Mater 23:1188–1193. https://doi.org/10.1021/cm102666r

Di Palma L, Bavasso I, Sarasini F et al (2018) Synthesis, characterization and performance evaluation of Fe3O4/PES nano composite membranes for microbial fuel cell. Eur Polym J 99:222–229. https://doi.org/10.1016/j.eurpolymj.2017.12.037

Du Z, Li H, Gu T (2007) A state of the art review on microbial fuel cells: a promising technology for wastewater treatment and bioenergy. Biotechnol Adv 25:464–482. https://doi.org/10.1016/j.biotechadv.2007.05.004

Elangovan M, Dharmalingam S (2016) A facile modification of a polysulphone based anti biofouling anion exchange membrane for microbial fuel cell application. RSC Adv 6:20571–20581. https://doi.org/10.1039/c5ra21576e

ElMekawy A, Hegab HM, Mohanakrishna G et al (2016) Technological advances in CO2conversion electro-biorefinery: a step toward commercialization. Bioresour Technol 215:357–370. https://doi.org/10.1016/j.biortech.2016.03.023

ElMekawy A, Hegab HM, Losic D et al (2017) Applications of graphene in microbial fuel cells: the gap between promise and reality. Renew Sust Energ Rev 72:1389–1403. https://doi.org/10.1016/j.rser.2016.10.044

Escapa A, Mateos R, Martínez EJ, Blanes J (2016) Microbial electrolysis cells: an emerging technology for wastewater treatment and energy recovery. From laboratory to pilot plant and beyond. Renew Sust Energ Rev 55:942–956. https://doi.org/10.1016/j.rser.2015.11.029

Fan Y, Xu S, Schaller R et al (2011) Nanoparticle decorated anodes for enhanced current generation in microbial electrochemical cells. Biosens Bioelectron 26:1908–1912. https://doi.org/10.1016/j.bios.2010.05.006

Fan M, Zhang W, Sun J et al (2017) Different modified multi-walled carbon nanotube–based anodes to improve the performance of microbial fuel cells. Int J Hydrog Energy 42:22786–22795. https://doi.org/10.1016/j.ijhydene.2017.07.151

Feng Y, Wang X, Logan BE, Lee H (2008) Brewery wastewater treatment using air-cathode microbial fuel cells. Appl Microbiol Biotechnol 78:873–880. https://doi.org/10.1007/s00253-008-1360-2

Filip J, Tkac J (2014) Is graphene worth using in biofuel cells? Electrochim Acta 136:340–354. https://doi.org/10.1016/j.electacta.2014.05.119

Gautam RK, Bhattacharjee H, Venkata Mohan S, Verma A (2016) Nitrogen doped graphene supported α-MnO_2 nanorods for efficient ORR in a microbial fuel cell. RSC Adv 6:110091–110101. https://doi.org/10.1039/C6RA23392A

Ghanbarlou H, Rowshanzamir S, Kazeminasab B, Parnian MJ (2015) Non-precious metal nanoparticles supported on nitrogen-doped graphene as a promising catalyst for oxygen reduction reaction: synthesis, characterization and electrocatalytic performance. J Power Sources 273:981–989. https://doi.org/10.1016/j.jpowsour.2014.10.001

Gil GC, Chang IS, Kim BH et al (2003) Operational parameters affecting the performance of a mediator-less microbial fuel cell. Biosens Bioelectron 18:327–334. https://doi.org/10.1016/S0956-5663(02)00110-0

Gnana kumar G, Joseph Kirubaharan C, Yoo DJ, Kim AR (2016) Graphene/poly(3,4-ethylenedioxythiophene)/Fe3O4nanocomposite – an efficient oxygen reduction catalyst for the continuous

electricity production from wastewater treatment microbial fuel cells. Int J Hydrog Energy 41:13208–13219. https://doi.org/10.1016/j.ijhydene.2016.05.099
Habermann W, Pommer EH (1991) Biological fuel cells with sulphide storage capacity. Appl Microbiol Biotechnol 35(1)
Halakoo E, Khademi A, Ghasemi M et al (2015) Production of sustainable energy by carbon nanotube/platinum catalyst in microbial fuel cell. Procedia CIRP 26:473–476. https://doi.org/10.1016/j.procir.2014.07.034
Harnisch F, Freguia S (2012) A basic tutorial on cyclic voltammetry for the investigation of electroactive microbial biofilms. Chem – Asian J 7:466–475. https://doi.org/10.1002/asia.201100740
Hassan M, Wei H, Qiu H, Su Y, Jaafry SWH, Zhan L, Xie B (2018) Power generation and pollutants removal from landfill leachate in microbial fuel cell: variation and influence of anodic microbiomes. Bioresour Technol 247:434–442
He Z, Angenent LT (2006) Application of bacterial biocathodes in microbial fuel cells. Electroanalysis 18:2009–2015. https://doi.org/10.1002/elan.200603628
Heilmann J, Logan BE (2006) Production of electricity from proteins using a microbial fuel cell. Water Environ Res 78:531–537. https://doi.org/10.2175/106143005X73046
Huang L, Chai X, Chen G, Logan BE (2011a) Effect of set potential on hexavalent chromium reduction and electricity generation from biocathode microbial fuel cells. Environ Sci Technol 45:5025–5031. https://doi.org/10.1021/es103875d
Huang YX, Liu XW, Xie JF et al (2011b) Graphene oxide nanoribbons greatly enhance extracellular electron transfer in bio-electrochemical systems. Chem Commun 47:5795–5797. https://doi.org/10.1039/c1cc10159e
Huang Z, Jiang D, Lu L, Ren ZJ (2016) Ambient CO2capture and storage in bioelectrochemically mediated wastewater treatment. Bioresour Technol 215:380–385. https://doi.org/10.1016/j.biortech.2016.03.084
Jang JK, Pham TH, Chang IS et al (2004) Construction and operation of a novel mediator- and membrane-less microbial fuel cell. Process Biochem 39:1007–1012. https://doi.org/10.1016/S0032-9592(03)00203-6
Ji J, Jia Y, Wu W et al (2011) A layer-by-layer self-assembled Fe2O3nanorod-based composite multilayer film on ITO anode in microbial fuel cell. Colloids Surf A Physicochem Eng Asp 390:56–61. https://doi.org/10.1016/j.colsurfa.2011.08.056
Jiang X, Sun Y, Zhang H, Hou L (2018) Preparation and characterization of quaternized poly(vinyl alcohol)/chitosan/MoS2composite anion exchange membranes with high selectivity. Carbohydr Polym 180:96–103. https://doi.org/10.1016/j.carbpol.2017.10.023
Kadier A, Simayi Y, Abdeshahian P et al (2016) A comprehensive review of microbial electrolysis cells (MEC) reactor designs and configurations for sustainable hydrogen gas production. Alex Eng J 55:427–443. https://doi.org/10.1016/j.aej.2015.10.008
Kamaraj SK, Romano SM, Moreno VC et al (2015) Use of novel reinforced cation exchange membranes for microbial fuel cells. Electrochim Acta 176:555–566. https://doi.org/10.1016/j.electacta.2015.07.042
Kano K et al (1999) Bifidobacterium longum. Biochim Biophys Acta 1428:241–250
Karube I, Matsunaga T, Tsuru S, Suzuki S (1976) Continuous hydrogen production by immobilized whole cells of Clostridium butyricum. Biochim Biophys Acta – Gen Subj 444:338–343. https://doi.org/10.1016/0304-4165(76)90376-7
Kashyap D, Dwivedi PK, Pandey JK et al (2014) Application of electrochemical impedance spectroscopy in bio-fuel cell characterization: a review. Int J Hydrog Energy 39:20159–20170. https://doi.org/10.1016/j.ijhydene.2014.10.003
Kerzenmacher S, Ducrée J, Zengerle R, von Stetten F (2008) Energy harvesting by implantable abiotically catalyzed glucose fuel cells. J Power Sources 182:1–17. https://doi.org/10.1016/j.jpowsour.2008.03.031

Khilari S, Pandit S, Ghangrekar MM et al (2013) Graphene oxide-impregnated PVA-STA composite polymer electrolyte membrane separator for power generation in a single-chambered microbial fuel cell. Ind Eng Chem Res 52:11597–11606. https://doi.org/10.1021/ie4016045

Kim BH, Chang IS, Gil GC et al (2003) Novel BOD (Biochemical Oxygen Demand) sensor using mediator-less microbial fuel cell. Biotechnol Lett 25:541–545. https://doi.org/10.1023/A:1022891231369

Kokabian B, Gude VG, Smith R, Brooks JP (2018) Evaluation of anammox biocathode in microbial desalination and wastewater treatment. Chem Eng J 342:410–419. https://doi.org/10.1016/j.cej.2018.02.088

Komarneni S, Noh YD, Kim JY, et al (2010) ChemInform abstract: solvothermal/hydrothermal synthesis of metal oxides and metal powders with and without microwaves. ChemInform 41:no-no. https://doi.org/10.1002/chin.201043010

Koziol K et al (2010) Synthesis of carbon nanostructures by CVD method. Carbon oxide nanostructures. Adv Struct Mater 5:23–49. https://doi.org/10.1007/8611_2010_12

Labelle E, Bond DR (2009) Cyclic voltammetry for the study of microbial electron transfer at electrodes. Bioelectrochemical Syst Extracell Electron Transf Biotechnol Appl 137–152

Liu H, Logan BE (2004) Electricity generation using an air-cathode single chamber microbial fuel cell in the presence and absence of a proton exchange membrane. Environ Sci Technol 38:4040–4046. https://doi.org/10.1021/es0499344

Liu H, Ramnarayanan R, Logan BE (2004) Production of electricity during wastewater treatment using a single chamber microbial fuel cell. Environ Sci Technol 38:2281–2285. https://doi.org/10.1021/es034923g

Liu H, Cheng SA, Logan BE (2005a) Power generation in fed-batch microbial fuel cells as a function of ionic strength, temperature, and reactor configuration. Environ Sci Technol 39:5488–5493. https://doi.org/10.1021/es050316c

Liu H, Grot S, Logan BE (2005b) Electrochemically assisted microbial production of hydrogen from acetate. Environ Sci Technol 39:4317–4320. https://doi.org/10.1021/es050244p

Liu H, Hu H, Chignell J, Fan Y (2010) Microbial electrolysis: novel technology for hydrogen production from biomass. Biofuels 1:129–142. https://doi.org/10.4155/bfs.09.9

Liu J, Qiao Y, Guo CX et al (2012) Graphene/carbon cloth anode for high-performance mediatorless microbial fuel cells. Bioresour Technol 114:275–280. https://doi.org/10.1016/j.biortech.2012.02.116

Liu L, Tsyganova O, Lee DJ et al (2013a) Double-chamber microbial fuel cells started up under room and low temperatures. Int J Hydrog Energy 38:15574–15579. https://doi.org/10.1016/j.ijhydene.2013.02.090

Liu Y, Liu H, Wang C et al (2013b) Sustainable energy recovery in wastewater treatment by microbial fuel cells: stable power generation with nitrogen-doped graphene cathode. Environ Sci 47:13889–13895

Liu XW, Chen JJ, Huang YX et al (2014) Experimental and theoretical demonstrations for the mechanism behind enhanced microbial electron transfer by CNT network. Sci Rep 4:1–7. https://doi.org/10.1038/srep03732

Logan BE, Regan JM (2006) Microbial fuel cells—challenges and applications. Environ Sci Technol 40:5172–5180. https://doi.org/10.1021/es0627592

Logan BE, Murano C, Scott K et al (2005) Electricity generation from cysteine in a microbial fuel cell. Water Res 39:942–952. https://doi.org/10.1016/j.watres.2004.11.019

Logan BE, Hamelers B, Rozendal R et al (2006) Microbial fuel cells: methodology and technology. Environ Sci Technol 40:5181–5192. https://doi.org/10.1021/es0605016

Lovley DR (2006a) Bug juice: harvesting electricity with microorganisms. Nat Rev Microbiol 4:497–508. https://doi.org/10.1038/nrmicro1442

Lovley DR (2006b) Microbial fuel cells: novel microbial physiologies and engineering approaches. Curr Opin Biotechnol 17:327–332. https://doi.org/10.1016/j.copbio.2006.04.006

Lu L, Ren ZJ (2016) Microbial electrolysis cells for waste biorefinery: a state of the art review. Bioresour Technol 215:254–264. https://doi.org/10.1016/j.biortech.2016.03.034

Mahadevan A, Gunawardena D A, Fernando S (2014) Biochemical and electrochemical perspectives of the anode of a microbial fuel cell. Technol Appl Microb Fuel Cells 13–32. https://doi.org/10.5772/57200

Malvankar NS, Vargas M, Nevin KP et al (2011) Tunable metallic-like conductivity in microbial nanowire networks. Nat Nanotechnol 6:573–579. https://doi.org/10.1038/nnano.2011.119

Mashkour M, Rahimnejad M, Pourali SM et al (2017) Catalytic performance of nano-hybrid graphene and titanium dioxide modified cathodes fabricated with facile and green technique in microbial fuel cell. Prog Nat Sci Mater Int 27:647–651. https://doi.org/10.1016/j.pnsc.2017.11.003

Mehdinia A, Ziaei E, Jabbari A (2014) Multi-walled carbon nanotube/SnO2 nanocomposite: a novel anode material for microbial fuel cells. Electrochim Acta 130:512–518. https://doi.org/10.1016/j.electacta.2014.03.011

Menicucci J, Beyenal H, Marsili E, Veluchamy GD, Lewandowski Z (2006) Procedure for determining maximum sustainable power generated by microbial fuel cells. Environ Sci Technol 40(3):1062–1068

Min B, Logan BE (2004) Continuous electricity generation from domestic wastewater and organic substrates in a flat plate microbial fuel cell. Environ Sci Technol 38:5809–5814. https://doi.org/10.1021/es0491026

Min B, Cheng S, Logan BE (2005) Electricity generation using membrane and salt bridge microbial fuel cells. Water Res 39(9):1675–1686

Moon H, Chang IS, Kim BH (2006) Continuous electricity production from artificial wastewater using a mediator-less microbial fuel cell. Bioresour Technol 97:621–627. https://doi.org/10.1016/j.biortech.2005.03.027

Mujeeb Rahman P, Abdul Mujeeb VM, Muraleedharan K, Thomas SK (2018) Chitosan/nano ZnO composite films: enhanced mechanical, antimicrobial and dielectric properties. Arab J Chem 11:120–127. https://doi.org/10.1016/j.arabjc.2016.09.008

Myers JM, Myers CR (2001) Role for outer membrane cytochromes OmcA and OmcB of Shewanella putrefaciens MR-1 in reduction of manganese dioxide. Appl Environ Microbiol 67:260–269. https://doi.org/10.1128/AEM.67.1.260-269.2001

Narayanaswamy Venkatesan P, Dharmalingam S (2013) Characterization and performance study on chitosan-functionalized multi walled carbon nano tube as separator in microbial fuel cell. J Memb Sci 435:92–98. https://doi.org/10.1016/j.memsci.2013.01.064

Nevin KP, Woodard TL, Franks AE et al (2010) Microbial electrosynthesis: feeding microbes electricity to convert carbon dioxide and water to multicarbon extracellular organic compounds. MBio 1:e00103-10. https://doi.org/10.1128/mBio.00103-10

Niessen J, Harnisch F, Rosenbaum M, Schroder U, Scholz F (2006) Heat treated soil as convenient and versatile source of bacterial communities for microbial electricity generation. Electrochem Commun 8(5):869–873

Oh S-E, Logan BE (2006) Proton exchange membrane and electrode surface areas as factors that affect power generation in microbial fuel cells. Appl Microbiol Biotechnol 70(2):162–169

Oh S, Min B, Logan BE (2004) Cathode performance as a factor in electricity generation in microbial fuel cells. Environ Sci Technol 38:4900–4904. https://doi.org/10.1021/es049422p

Pant D, Van Bogaert G, Diels L, Vanbroekhoven K (2010) A review of the substrates used in microbial fuel cells (MFCs) for sustainable energy production. Bioresour Technol 101:1533–1543. https://doi.org/10.1016/j.biortech.2009.10.017

Papiya F, Pattanayak P, Kumar P et al (2018) Development of highly efficient bimetallic nanocomposite cathode catalyst, composed of Ni:Co supported sulfonated polyaniline for application in microbial fuel cells. Electrochim Acta 282:931–945. https://doi.org/10.1016/j.electacta.2018.07.024

Park DH, Zeikus JG (2000) Electricity generation in microbial fuel cells using neutral red as an electronophore electricity generation in microbial fuel cells using neutral red as an electronophore. Appl Environ Microbiol 66:1292–1297. https://doi.org/10.1128/AEM.66.4.1292-1297.2000.Updated

Park DH, Zeikus JG (2003) Improved fuel cell and electrode designs for producing electricity from microbial degradation. Biotechnol Bioeng 81:348–355. https://doi.org/10.1002/bit.10501

Park DH, Laivenieks M, Guettler MV et al (1999) Microbial utilization of electrically reduced neutral red as the sole electron donor for growth and metabolite production. Appl Environ Microbiol 65:2912–2917

Parkash A (2016) Microbial fuel cells: a source of bioenergy. J Microb Biochem Technol 8:247–255. https://doi.org/10.4172/1948-5948.1000293

Peng X, Yu H, Wang X et al (2013a) Enhanced anode performance of microbial fuel cells by adding nanosemiconductor goethite. J Power Sources 223:94–99. https://doi.org/10.1016/j.jpowsour.2012.09.057

Peng X, Yu H, Yu H, Wang X (2013b) Lack of anodic capacitance causes power overshoot in microbial fuel cells. Bioresour Technol 138:353–358. https://doi.org/10.1016/j.biortech.2013.03.187

Pham CA, Jung SJ, Phung NT, Lee J, Chang IS, Kim BH, Yi H, Chun J (2003) A novel electrochemically active and Fe(III)-reducing bacterium phylogenetically related to, isolated from a microbial fuel cell. FEMS Microbiol Lett 223(1):129–134

Pham TH, Jang JK, Chang IS, Kim BH (2004) Improvement of cathode reaction of a mediatorless microbial fuel cell. J Microbiol Biotechnol 14:324–329

Piccolino M (2008) Visual images in Luigi Galvani's path to animal electricity. J Hist Neurosci 17:335–348. https://doi.org/10.1080/09647040701420198

Potter MC (1911) Electrical effects accompanying the decomposition of organic compounds. Proc R Soc B Biol Sci 84:260–276. https://doi.org/10.1098/rspb.1911.0073

Rabaey K, Rozendal RA (2010) Microbial electrosynthesis – revisiting the electrical route for microbial production. Nat Rev Microbiol 8:706–716. https://doi.org/10.1038/nrmicro2422

Rabaey K, Boon N, Siciliano SD et al (2004) Biofuel cells select for microbial consortia that self-mediate electron transfer biofuel cells select for microbial consortia that self-mediate electron transfer. Appl Environ Microbiol 70:5373–5382. https://doi.org/10.1128/AEM.70.9.5373

Rabaey K, Boon N, Höfte M, Verstraete W (2005a) Microbial phenazine production enhances electron transfer in biofuel cells. Environ Sci Technol 39:3401–3408. https://doi.org/10.1021/es048563o

Rabaey K, Clauwaert P, Aelterman P, Verstraete W (2005b) Tubular microbial fuel cells for efficient electricity generation. Environ Sci Technol 39:8077–8082. https://doi.org/10.1021/es050986i

Rahimnejad M, Adhami A, Darvari S et al (2015) Microbial fuel cell as new technol ogy for bioelectricity generation: a review. Alex Eng J 54:745–756. https://doi.org/10.1016/j.aej.2015.03.031

Ramaraja P, Ramasamy NS (2013) Electrochemical impedance spectroscopy for microbial fuel cell characterization. J Microb Biochem Technol. https://doi.org/10.4172/1948-5948.S6-004

Reguera G, McCarthy KD, Mehta T et al (2005) Extracellular electron transfer via microbial nanowires. Nature 435:1098–1101. https://doi.org/10.1038/nature03661

Reguera G, Nevin KP, Nicoll JS et al (2006) Biofilm and nanowire production leads to increased current in Geobacter sulfurreducens fuel cells. Appl Environ Microbiol 72:7345–7348. https://doi.org/10.1128/AEM.01444-06

Reimers CE, Tender LM, Fertig S, Wang W (2001) Harvesting energy from the marine sediment−water Interface. Environ Sci Technol 35:192–195. https://doi.org/10.1021/es001223s

Ringeisen BR, Henderson E, Peter KW, Pietron J, Ray R, Little B, Biffinger JC, Jones-Meehan JM (2006) High power density from a miniature microbial fuel cell using DSP10. Environ Sci Technol 40(8):2629–2634

Rizzi F, Annunziata E, Liberati G, Frey M (2014) Technological trajectories in the automotive industry: are hydrogen technologies still a possibility? J Clean Prod 66:328–336. https://doi.org/10.1016/j.jclepro.2013.11.069

Roy S, Schievano A, Pant D (2015) Electro-stimulated microbial factory for value added product synthesis. Bioresour Technol 213:129–139. https://doi.org/10.1016/j.biortech.2016.03.052

Rozenfeld S, Teller H, Schechter M et al (2018) Exfoliated molybdenum di-sulfide (MoS2) electrode for hydrogen production in microbial electrolysis cell. Bioelectrochemistry 123:201–210. https://doi.org/10.1016/j.bioelechem.2018.05.007

Santoro C, Arbizzani C, Erable B, Ieropoulos I (2017a) Microbial fuel cells: from fundamentals to applications. Rev J Power Sources 356:225–244. https://doi.org/10.1016/j.jpowsour.2017.03.109

Santoro C, Kodali M, Kabir S et al (2017b) Three-dimensional graphene nanosheets as cathode catalysts in standard and supercapacitive microbial fuel cell. J Power Sources 356:371–380. https://doi.org/10.1016/j.jpowsour.2017.03.135

Schröder U (2007) Anodic electron transfer mechanisms in microbial fuel cells and their energy efficiency. Phys Chem Chem Phys 9:2619–2629. https://doi.org/10.1039/b703627m

Schröder U, Nießen J, Scholz F (2003) A generation of microbial fuel cells with current outputs boosted by more than one order of magnitude. Angew Chem Int Ed 42(25):2880–2883

Sekoai PT, Gueguim Kana EB (2014) Semi-pilot scale production of hydrogen from organic fraction of solid municipal waste and electricity generation from process effluents. Biomass Bioenergy 60:156–163. https://doi.org/10.1016/j.biombioe.2013.11.008

Sonawane JM, Al-Saadi S, Singh Raman RK et al (2018) Exploring the use of polyaniline-modified stainless steel plates as low-cost, high-performance anodes for microbial fuel cells. Electrochim Acta 268:484–493. https://doi.org/10.1016/j.electacta.2018.01.163

Srikanth S, Maesen M, Dominguez-Benetton X et al (2014) Enzymatic electrosynthesis of formate through CO2sequestration/reduction in a bioelectrochemical system (BES). Bioresour Technol 165:350–354. https://doi.org/10.1016/j.biortech.2014.01.129

Srinophakun P, Thanapimmetha A, Plangsri S et al (2017) Application of modified chitosan membrane for microbial fuel cell: roles of proton carrier site and positive charge. J Clean Prod 142:1274–1282. https://doi.org/10.1016/j.jclepro.2016.06.153

Straub KL, Straub KL, Schink B, Schink B (2004) Ferrihydrite-dependent growth of. Society 70:5744–5749. https://doi.org/10.1128/AEM.70.10.5744

Sugnaux M, Savy C, Cachelin CP et al (2017) Simulation and resolution of voltage reversal in microbial fuel cell stack. Bioresour Technol 238:519–527. https://doi.org/10.1016/j.biortech.2017.04.072

Tang L, Wang Y, Li Y et al (2009) Preparation, structure, and electrochemical properties of reduced graphene sheet films. Adv Funct Mater 19:2782–2789. https://doi.org/10.1002/adfm.200900377

Tekle Y, Demeke A (2015) Review on microbial fuel cell. Basic Res J Microbiol 1:1–32

Terrones M, Grobert N, Olivares J, Zhang JP, Terrones H, Kordatos K, Hsu WK, Hare JP, Townsend PD, Prassides K, Cheetham AK, Kroto HW, Walton DRM (1997) Controlled production of aligned-nanotube bundles. Nature 388(6637):52–55

Thygesen A, Poulsen FW, Min B, Angelidaki I, Thomsen AB (2009) The effect of different substrates and humic acid on power generation in microbial fuel cell operation. Bioresour Technol 100(3):1186–1191

Trapero JR, Horcajada L, Linares JJ, Lobato J (2017) Is microbial fuel cell technology ready? An economic answer towards industrial commercialization. Appl Energy 185:698–707. https://doi.org/10.1016/j.apenergy.2016.10.109

Turick CE, Tisa LS, Caccavo F (2002) Melanin production and use as a soluble electron shuttle for Fe (III) oxide reduction and as a terminal electron acceptor by Shewanella algae BrY melanin production and use as a soluble electron shuttle for Fe (III) oxide reduction and as a terminal E. Appl Environ Microbiol 68:2436–2444. https://doi.org/10.1128/AEM.68.5.2436

Valipour A, Ayyaru S, Ahn Y (2016) Application of graphene-based nanomaterials as novel cathode catalysts for improving power generation in single chamber microbial fuel cells. J Power Sources 327:548–556. https://doi.org/10.1016/j.jpowsour.2016.07.099

Varanasi JL, Nayak AK, Sohn Y et al (2016) Improvement of power generation of microbial fuel cell by integrating tungsten oxide electrocatalyst with pure or mixed culture biocatalysts. Electrochim Acta 199:154–163. https://doi.org/10.1016/j.electacta.2016.03.152

Vega CA, Fernández I (1987) Mediating effect of ferric chelate compounds in microbial fuel cells with *Lactobacillus plantarum*, *Streptococcus lactis*, and *Erwinia dissolvens*. Bioelectrochem Bioenerg 17(2):217–222

Villano M, Monaco G, Aulenta F, Majone M (2011) Electrochemically assisted methane production in a biofilm reactor. J Power Sources 196:9467–9472. https://doi.org/10.1016/j.jpowsour.2011.07.016

Wang Y, Li B, Zeng L et al (2013) Polyaniline/mesoporous tungsten trioxide composite as anode electrocatalyst for high-performance microbial fuel cells. Biosens Bioelectron 41:582–588. https://doi.org/10.1016/j.bios.2012.09.054

Watson VJ, Hatzell M, Logan BE (2015) Hydrogen production from continuous flow, microbial reverse-electrodialysis electrolysis cells treating fermentation wastewater. Bioresour Technol 195:51–56. https://doi.org/10.1016/j.biortech.2015.05.088

Wei J, Liang P, Huang X (2011) Recent progress in electrodes for microbial fuel cells. Bioresour Technol 102:9335–9344. https://doi.org/10.1016/j.biortech.2011.07.019

Wen Q, Wang S, Yan J et al (2014) Porous nitrogen-doped carbon nanosheet on graphene as metal-free catalyst for oxygen reduction reaction in air-cathode microbial fuel cells. Bioelectrochemistry 95:23–28. https://doi.org/10.1016/j.bioelechem.2013.10.007

Werner CM, Logan BE, Saikaly PE, Amy GL (2013) Wastewater treatment, energy recovery and desalination using a forward osmosis membrane in an air-cathode microbial osmotic fuel cell. J Memb Sci 428:116–122. https://doi.org/10.1016/j.memsci.2012.10.031

Winter CJ (2005) Into the hydrogen energy economy – milestones. Int J Hydrog Energy 30:681–685. https://doi.org/10.1016/j.ijhydene.2004.12.011

Xafenias N, Mapelli V (2014) Performance and bacterial enrichment of bioelectrochemical systems during methane and acetate production. Int J Hydrog Energy 39:21864–21875. https://doi.org/10.1016/j.ijhydene.2014.05.038

Xia C, Zhang D, Pedrycz W et al (2018) Models for microbial fuel cells: a critical review. J Power Sources 373:119–131. https://doi.org/10.1016/j.jpowsour.2017.11.001

Xiao L, Damien J, Luo J et al (2012) Crumpled graphene particles for microbial fuel cell electrodes. J Power Sources 208:187–192. https://doi.org/10.1016/j.jpowsour.2012.02.036

Xie X, Hu L, Pasta M et al (2011) Three-dimensional carbon nanotube-textile anode for high-performance microbial fuel cells. Nano Lett 11:291–296. https://doi.org/10.1021/nl103905t

Xie X, Zhao W, Lee HR et al (2014) Enhancing the nanomaterial bio-interface by addition of mesoscale secondary features: crinkling of carbon nanotube films to create subcellular ridges. ACS Nano 8:11958–11965. https://doi.org/10.1021/nn504898p

Xu H, Quan X, Xiao Z, Chen L (2017) Cathode modification with peptide nanotubes (PNTs) incorporating redox mediators for azo dyes decolorization enhancement in microbial fuel cells. Int J Hydrog Energy 42:8207–8215. https://doi.org/10.1016/j.ijhydene.2017.01.025

Yan Z, Jiang H, Li X, Shi Y (2014) Accelerated removal of pyrene and benzo[a]pyrene in freshwater sediments with amendment of cyanobacteria-derived organic matter. J Hazard Mater 272:66–74. https://doi.org/10.1016/j.jhazmat.2014.02.042

Yin T, Su L, Li H et al (2017) Nitrogen doping of TiO2nanosheets greatly enhances bioelectricity generation of S. loihica PV-4. Electrochim Acta 258:1072–1080. https://doi.org/10.1016/j.electacta.2017.11.160

Zehtab Yazdi A, Fei H, Ye R et al (2015) Boron/nitrogen co-doped helically unzipped multiwalled carbon nanotubes as efficient electrocatalyst for oxygen reduction. ACS Appl Mater Interfaces 7:7786–7794. https://doi.org/10.1021/acsami.5b01067

Zhang Y, Mo G, Li X et al (2011) A graphene modified anode to improve the performance of microbial fuel cells. J Power Sources 196:5402–5407. https://doi.org/10.1016/j.jpowsour.2011.02.067

Zhang W, Xie B, Yang L et al (2017) Brush-like polyaniline nanoarray modified anode for improvement of power output in microbial fuel cell. Bioresour Technol 233:291–295. https://doi.org/10.1016/j.biortech.2017.02.124

Zhao F, Slade RCT, Varcoe JR (2009) Techniques for the study and development of microbial fuel cells: an electrochemical perspective. Chem Soc Rev 38:1926–1939. https://doi.org/10.1039/b819866g

Zhong D, Liao X, Liu Y et al (2018) Enhanced electricity generation performance and dye wastewater degradation of microbial fuel cell by using a petaline NiO@ polyaniline-carbon felt anode. Bioresour Technol 258:125–134. https://doi.org/10.1016/j.biortech.2018.01.117

Zhou YL, Jiang HL, Cai HY (2015) To prevent the occurrence of black water agglomerate through delaying decomposition of cyanobacterial bloom biomass by sediment microbial fuel cell. J Hazard Mater 287:7–15. https://doi.org/10.1016/j.jhazmat.2015.01.036

Zhu NW, Chen X, Tu LX et al (2011) Voltage reversal during stacking microbial fuel cells with or without diodes. Adv Mater Res 396–398:188–193. https://doi.org/10.4028/www.scientific.net/AMR.396-398.188

Zhu X, Tokash JC, Hong Y, Logan BE (2013) Controlling the occurrence of power overshoot by adapting microbial fuel cells to high anode potentials. Bioelectrochemistry 90:30–35. https://doi.org/10.1016/j.bioelechem.2012.10.004

Zhu D, Wang D-B, Song T et al (2015) Effect of carbon nanotube modified cathode by electrophoretic deposition method on the performance of sediment microbial fuel cells. Biotechnol Lett 37:101–107. https://doi.org/10.1007/s10529-014-1671-6

Zou L, Qiao Y, Wu XS, Li CM (2016) Tailoring hierarchically porous graphene architecture by carbon nanotube to accelerate extracellular electron transfer of anodic biofilm in microbial fuel cells. J Power Sources 328:143–150. https://doi.org/10.1016/j.jpowsour.2016.08.009

Chapter 9
Fluoride Toxicity and Recent Advances in Water Defluoridation with Specific Emphasis on Nanotechnology

Kamya Parashar, Kriveshini Pillay, Raghunath Das, and Arjun Maity

Contents

K. Parashar · K. Pillay · R. Das
Department of Applied Chemistry, University of Johannesburg, Johannesburg, South Africa

A. Maity (✉)
Department of Applied Chemistry, University of Johannesburg, Johannesburg, South Africa

DST/CSIR National Center for Nanostructured Materials, Council for Scientific and Industrial Research (CSIR), Pretoria, South Africa
e-mail: Amaity@csir.co.za

R. Saravanan et al. (eds.), *Emerging Nanostructured Materials for Energy and Environmental Science*, Environmental Chemistry for a Sustainable World 23,
https://doi.org/10.1007/978-3-030-04474-9_9

Abstract Water contamination has been a global challenge for many decades. A variety of inorganic and organic pollutants have indeed degraded the quality of water over the years. Among these various pollutants, fluoride ions stand out as the inorganic pollutants of prime concern in ground- and drinking water since concentrations which exceed 1,5 mg/L can lead to skeleton fluorosis and other bone disorders. The defluoridation of ground- and drinking water has therefore become a topic of great importance. This chapter therefore serves to review the current global distribution of fluoride in ground- and drinking water. Some attention is also paid to the natural and anthropogenic sources of fluoride as well as the chemistry of fluorides which renders them toxic. The various toxic effects of fluoride are highlighted. The defluoridation techniques employed thus far are also critically reviewed and discussed. Much emphasis is devoted to adsorption technology which is currently the most popular technology due to its simplicity and effectiveness and the various adsorbents that have been tested for defluoridation. Each adsorbent is critically analysed with respect to its merits and demerits. Lastly, the benefits of nanotechnology and nanostructured adsorbents are discussed, and future research prospects on the use of such a technology are presented.

9.1 Introduction

9.1.1 Fluoride in Water

Water is professed as one of the most indispensable natural resources for sustaining life. It serves as an engine of growth and development by serving most of the necessary human activities. However, even in the twenty-first century, which is well-thought-out as an era of growth and progress, pure and safe drinking water is still inaccessible to almost one-fifth of the human population across the globe (Mumtaz et al. 2015). An ever-growing human population and rapid industrialisation are two main contributors to environmental pollution in today's world. Such activities are introducing various toxic chemical contaminants into the ecosphere and are thus incessantly deteriorating the quality of various natural resources. As a result, drinking water scarcity has become a most alarming threat that humanity is expected to face in the immediate future, and as per the current scenario, water pollution control has become an earnest subject for research amongst scientists all over the world. Moreover, it is well anticipated that as per the global growth rate, the increase in global population by 74.8 million every year will make the situation worse shortly (Ayoob et al. 2008). Recently, in a world water assessment programme conducted by the United Nations, it was estimated that by the year 2025 the average amount of water available per person would drastically drop down to one-third, and this will put humanity in a precarious condition (Ayoob et al. 2008).

Groundwater constitutes 97% of global freshwater and serves as the leading source of drinking water for half of the global population. It is the most economical,

readily available, and the only source of freshwater that can be availed by rural as well as urban communities of the developing countries for their daily activities (Mumtaz et al. 2015). Surface or groundwater can be put to various usages such as domestic, agricultural or industrial uses depending on their chemical composition. However, over the recent years, various anthropogenic and naturogenic activities have perilously declined the groundwater quality, and along with the scarcity issue, the excessive fluoride concentrations present in the groundwater as a geogenic pollutant have arisen as a key concern due to its severe environmental and health complications. As a 13th most abundant element, fluorine is ubiquitously present in the environment, and being highly electronegative and reactive it mostly exists in an oxidation state of −1 in the form of inorganic and organic fluoride compounds (Jagtap et al. 2012). Comparatively, inorganic fluorides are more abundant in the global environment than organic fluorides. Although both natural and human-originated activities such as weathering of natural mineral rocks, volcanic eruptions, marine aerosols, coal combustion power plants, fertilizer-producing industries, cement- and steel-manufacturing industries, etc. can collectively contribute to excess fluoride in water resources, fluoride in groundwater is mainly geological in origin and results to the dissolution of fluoride from fluoride-rich mineral rocks (Lewandowska et al. 2013). Fluoride in drinking water in the optimum concentration range of 1.0–1.5 mg/L improvises dental and bone health by preventing dental caries and osteoporosis (Mandinic et al. 2010). Various organisations have set different regulatory stipulations for the standard permissible concentration of fluoride in drinking water, and the same is presented in Table 9.1 (Mumtaz et al. 2015). However, exposure to fluoride levels above the recommended range may result in chronic fluoride intoxication which is a state of fluoride toxicity termed as fluorosis.

9.1.2 Global Scenario

Excessive fluoride in drinking water has engulfed several nations across the world. As per World Health Organization (WHO) estimation, several nations across the world with 748 million people still rely on poor-quality freshwater resources to satisfy their water necessities (Mumtaz et al. 2015). Apparently, 200 million people and 27 countries all over the world are exposed to excess fluoride in drinking water, and its severity level depends on the economic status as well as the topographical

Table 9.1 Standard permissible concentration of fluoride in drinking water as set by various health organisations

Agency/organisation	Standard acceptable range (mg/L)
Bureau of Indian Standards (BIS-2012)	1.0–1.5
World Health Organisation (WHO)	0.5–1.5
US Public Health	0.7–1.2

Modified after Mumtaz et al. (2015)

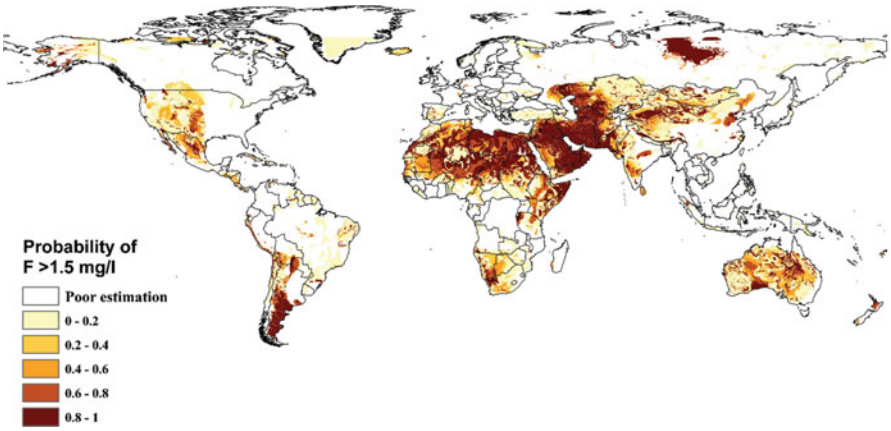

Fig. 9.1 Global prediction of fluoride concentrations exceeding WHO guidelines for drinking water. (Reprinted from Amini et al. 2008)

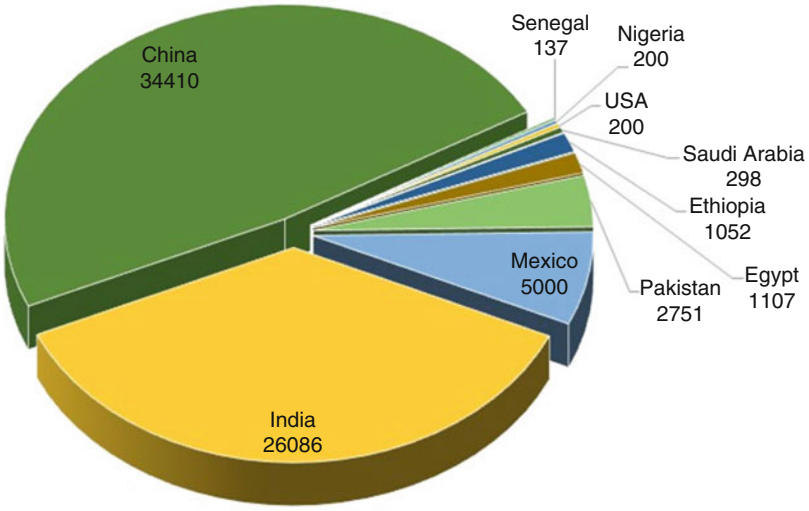

Fig. 9.2 Global projection of population exposed to excess fluoride in selected nations ($\times 10^3$). (Modified after Jadhav et al. 2015)

location of the nations involved (Mumtaz et al. 2015). In 2008, Amini et al. predicted the global occurrence of excess fluoride in groundwater as per the WHO guidelines (Fig. 9.1) (Amini et al. 2008). A more recent statistical depiction of the world's population affected by high fluoride concentration in groundwater was provided by Jadhav et al. as shown in Fig. 9.2 (Jadhav et al. 2015). It is evident from Fig. 9.2 that India and China are the top two countries globally which are severely affected by excess fluoride contamination in groundwater.

Table 9.2 The global scenario of excess fluoride concentrations in groundwater

Affected nations	Reported fluoride levels (mg/L)
Argentina	0.9–18.2
China	Up to 21.5
Ethiopia	1.5–177
India	0.5–69.7
Germany	Up to 8.8
Ghana	0.11–4.6
Turkey	13.7
Norway	0.02–9.48
Nigeria	4.7–6.6
Pakistan	8–13.52
Korea	Higher than 5
South Africa	0.05–13.0
Spain	2.50–4.59
Sri Lanka	Up to 10
Senegal	4.6–7.4
Tanzania	8.0–12.7
USA	1.06–4.07

Modified after Mumtaz et al. (2015)

Moreover, in 2015, Mumtaz et al. statistically assessed the excess fluoride concentration in the groundwater of different nations and found it explicitly in the range of 0.01–48 mg/L (Table 9.2) (Mumtaz et al. 2015). Yellowstone national park of the United States was reported to have a very high fluoride concentration in groundwater which ranged from 25 to 50 mg/L. Other severely fluoride-stricken areas where fluoride toxicity was reported amongst local people were Syria, Jordan, Northern Thailand, Finland, Mexico, arid regions of Northern China, Poland, Southern California Lakeland and many African countries including Ghana, Senegal, Tanzania and South Africa (Ncube and Schutte 2005; Dhillon et al. 2016).

9.2 Sources of Fluoride and Human Exposure

9.2.1 Sources of Fluoride

Fluoride enters the earth's ecosystem through various sources which can be broadly classified as naturogenic and anthropogenic based on their origin. Naturogenic sources also known as geogenic sources are mainly natural or geological in origin and include various natural activities such as weathering of fluoride-containing mineral rocks, gaseous emissions from volcanic eruptions and aerosols produced from marine activities. When fluoride-containing mineral rocks are exposed to weathering agents, a series of chemical processes occur due to which fluoride leaches out and permeates through the earth's crust and infuses to the groundwater.

Sedimentary stones, sandstones and limestones are some fluoride-rich rocks which specifically contain fluorspar (CaF_2) as fluoride mineral, whereas igneous rocks and granite contain cryolite (Na_3AlFPO_6) and fluorapatite ($Ca_5(PO_4)_3F$) (Jagtap et al. 2012). On the contrary, anthropogenic sources are mainly man-made in origin and comprise various human activities such as the combustion of coal in coal-fired plants, industrial wastes from aluminium and steel manufacturing, fertilizer production, ore processing, glass and ceramic manufacturing, nickel and copper production and glue and adhesive-producing industries. Besides, agricultural use of fluoride-containing pesticides, fluorinated pharmaceuticals and addition of fluoride to public water supplies are some other anthropogenic sources of fluoride in water (García and Borgnino 2015).

9.2.2 Pathways to Human Exposure

The major pathways of fluoride exposure to humans are water, air, food, medicaments and cosmetics. Most of the fluoride intake by humans occurs orally through the consumption of fluoride-contaminated water and dietary sources. Human exposure to fluoride through inhalation is almost negligible, except for rare and very specific occupational exposures. A brief overview of the various sources responsible for human exposure to fluoride is detailed as follows:

Water: It is estimated that 60% of the total human exposure to fluoride is through the consumption of fluoride-contaminated drinking water. Fluoride levels in groundwater or surface water are predominantly dependent on the topographical location of the water reservoir and vary according to the physico-chemical parameters such as pH, total dissolved solids, temperature, alkalinity, temperature, total dissolved solids, alkalinity, acidity and porosity of rocks and soil surrounding the water reservoir and its depth (Mandinic et al. 2010).

Food: Small traces of fluoride are present in almost all food items. The fluoride content of vegetables and fruits depends typically on the fluoride content of the soil in which they are grown and the water used for irrigation. Some of the vegetables containing very high levels of fluoride are barley, yams, rice, taro, cassava and tea. Amongst these various types of tea are potentially one of the most hazardous sources of fluoride (Mumtaz et al. 2015). This applies typically to tea plants grown in fluoride rich soils. The fluoride content in fresh meat is usually insignificantly low, but canned fish sometimes contain a high fluoride content (~370 mg/kg) due to the bioaccumulation of fluoride in its bones. Table 9.3 presents the list of different food items with their fluoride content as estimated by researchers (Mumtaz et al. 2015).

Medicaments: The treatment of osteoporosis and rheumatoid arthritis involves the use of sodium fluoride and niflumic acid, respectively. Extended intake of these drugs can lead to chronic fluoride intoxication. Prolonged use of certain fluoride-based mouthwashes is also associated with fluorosis (Tamer 2011; Jagtap et al. 2012).

Table 9.3 Fluoride content of various food products

Food products	Fluoride concentration range (mg/Kg)
Vegetables	0.01–1.34
Fruits and fruit juices	0.01–0.58
Milk and milk products	0.01–0.8
Fats and oils	0.05–0.13
Beverages	0.02–1.28
Tea	0.005–287.9
Sugar and candies	0.01–0.31
Meat and poultry	0.01–1.7
Fishes	0.06–4.57

Modified after Mumtaz et al. (2015)

Air: Aluminium-producing industries use inorganic compounds of fluoride, and fluorides are also released during the synthesis and use of phosphate fertilizers. All such industries which use fluoride compounds in some or the other way lead to its occupational exposure (Jagtap et al. 2012).

Cosmetics: Fluoride-containing dental products such as dentifrices and excessive use of fluoride-containing toothpaste lead to significant ingestion of fluoride and thus known to cause fluorosis. To prevent tooth decay and strengthen dental enamel, fluoridated brands of toothpaste are also available with fluoride content in the range of 1000–4000 mg/L (Tamer 2011; Jagtap et al. 2012).

9.3 Fluoride Toxicity

Fluorosis is the most evident manifestation of chronic fluoride intoxication where the duration of fluoride exposure and the amount ingested play a decisive role in determining its severity (Yang and Liang 2011). Body weight, activity level, nutrition and skeletal growth are some of the crucial factors which primarily control an individual's response to fluoride exposure. In the human body, about 90% of the total ingested fluoride is mainly absorbed through the gastrointestinal tract. Due to the acidic environment (pH 1.5–3.5) in the human stomach, approximately half of the ingested fluoride (~40%) is absorbed in the stomach as hydrofluoric acid (HF), whereas absorption of residual fluoride is independent of the pH and occurs in the intestinal region of the digestive tract (Tamer 2011). Henceforth, the absorbed fluoride undergoes a series of biochemical changes and combines with calcium hydroxyapatite present in teeth and bones to form stable fluorapatite (Fig. 9.3) (Dhillon et al. 2016). Consequently, a significant amount of ingested fluoride binds to mineralized tissues such as teeth and bones, and only a small amount is excreted. Overexposure to fluoride hence results in clinical, developmental alterations in teeth and bones, known as dental and skeletal fluorosis (Jagtap et al. 2012).

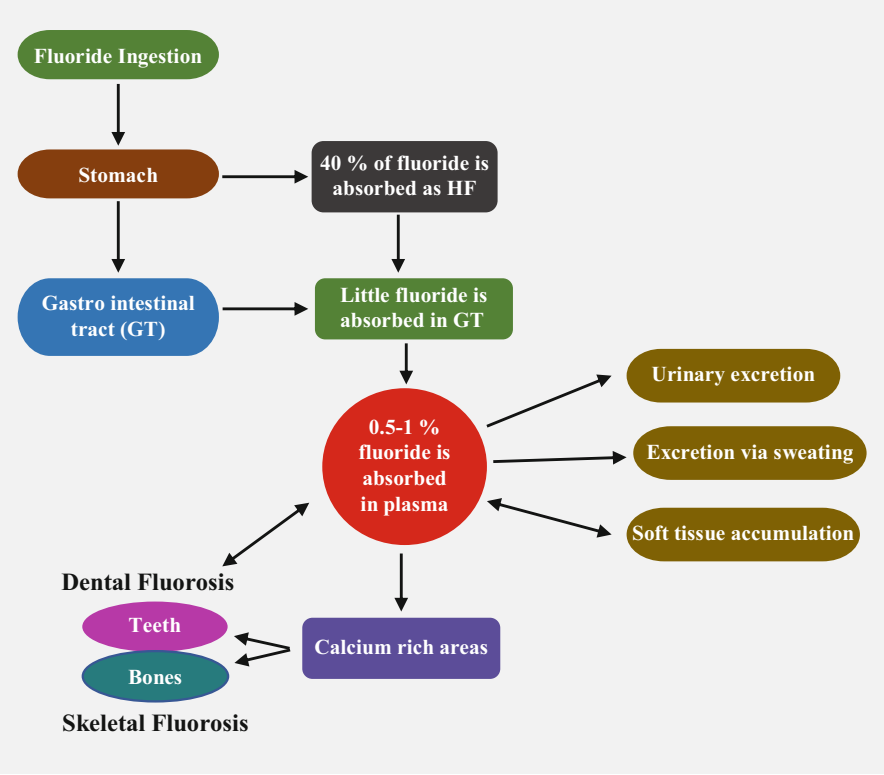

Fig. 9.3 Fluoride metabolism in the human body. (Modified after Dhillon et al. 2016)

Dental fluorosis is the most apparent and readily identified form of fluoride toxicity that affects children during their permanent dentition. Fluoride being highly electronegative readily binds with positively charged calcium ions present in the teeth during the mineralization process of dental enamel. Insoluble fluorapatite appears in the form of white patches on teeth and eventually leads to teeth eruption (Dhillon et al. 2016). However, if permanent dentition has already occurred prior to the exposure to excess fluoride, it becomes difficult to diagnose dental fluorosis clinically; hence no sign of dental fluorosis in an adult does not necessarily assure that the individual is not exposed to excessive fluoride intake (Jagtap et al. 2012). Skeletal fluorosis is a more severe and serious form of fluoride intoxication affecting children and adults alike. However, it is not apparent unless the disease progresses to an advanced stage. The initial symptoms are very much like arthritis such as bone tenderness, joint stiffness, osteoporosis, bone deformation and increased risk of frequent fractures (Jagtap et al. 2012). More precisely, fluoride gets deposited in various parts of the skeletal system and causes abnormal hardening of bones. Increased skeletal density along with excessive mineralization of muscle ligaments and tendons leads to the development of osteosclerosis, making it difficult to walk,

move or bend (Tamer 2011). However, fluoride not only causes health complications related to dental or skeletal fluorosis but can also develop several other nonskeletal manifestations such as neurological disorders, muscular atrophy, gastrointestinal troubles (hydrofluoric acid formed in the stomach destroys gastric mucosa) and fatal conditions like cancer (Fordyce and Survey 2011).

9.4 Water Defluoridation Techniques

Due to the above-mentioned health consequences, it has become mandatory to reduce the fluoride levels to standard allowable limits postulated by various health organisations. Some of the alternatives/methods to prevent fluoride intoxication through water supplies are the utilisation of reliable water sources, the establishment of alternative water sources and reduction of industrial emissions of fluoride. However, when the provision of alternative water sources is practically not feasible, then the development of efficient water defluoridation technologies is the best and only viable option to alleviate excess fluoride from water. A detailed analysis of defluoridation research archives has revealed that precipitation-coagulation, membrane-based processes, ion exchange and adsorption are some of the most widely employed defluoridation technologies for the removal of fluoride from water (Ayoob et al. 2008).

9.4.1 Chemical Precipitation-Coagulation

The chemical precipitation-coagulation technique involves the mixing of two chemicals which results in the formation of solid precipitates of fluorides. As per the operative underlying mechanism, in the first step, negatively charged colloids undergo charge neutralisation by cationic hydrolysis, and in the second step known as sweep flocculation the impurities present in the solution get incorporated in the solid amorphous precipitates of metal hydroxides. Hence, fluoride ions adsorbed on the surface of flocs (amorphous metal hydroxide precipitates) are subsequently removed by sedimentation or microfiltration. As the literature reveals, lime, alum and magnesium oxide are some of the chemicals which have been widely applied as fluoride precipitants in chemical precipitation techniques. Lime ($Ca(OH)_2$) and other calcium salts such as calcium sulphate ($CaSO_4$) and calcium chloride ($CaCl_2$) precipitate fluoride in the form of insoluble calcium fluoride (CaF_2) as shown in the following reaction (Eq. 9.1) (Huang and Liu 1999; Meenakshi and Maheshwari 2006):

$$Ca(OH)_2 + 2F^- \rightarrow CaF_2 + 2OH^- \tag{9.1}$$

However, the major shortcoming associated with lime is that it not only leaves behind a residual concentration of 8.0 mg F^-/L but also elevates the pH of water up

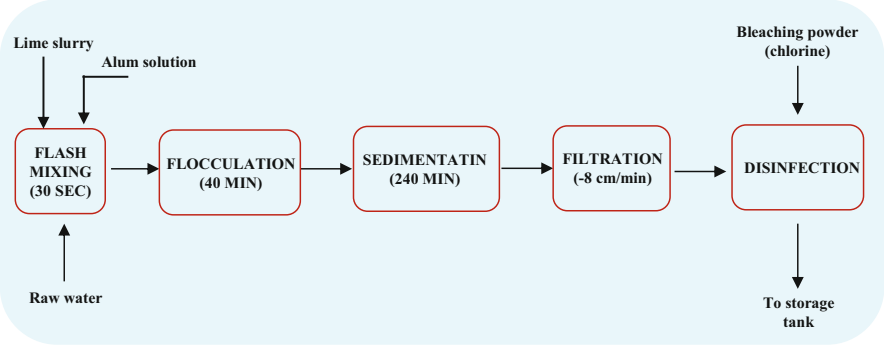

Fig. 9.4 Schematic representation of water defluoridation using the Nalgonda technique. (Modified after Ayoob et al. 2008)

to 11–12 (Jagtap et al. 2012). Hence, lime is best used in combination with an aluminium salt, i.e. alum as a coagulant to ensure best possible fluoride removal (Jadhav et al. 2014). In the first step, lime dosing causes precipitation followed by the second step in which alum is added to carry out coagulation of fluoride. In the 1970s, after extensive research, the Nalgonda technique was developed as the first cost-effective precipitation technique and implemented at pilot scale in Senegal, Tanzania and Kenya. Later on, the National Environmental Engineering Research Institute (NEERI) introduced this technique in Nagpur, India (Ayoob et al. 2008; Jagtap et al. 2012; Jadhav et al. 2015). The Nalgonda technique involves the rapid mixing of raw water with the calculated amount of aluminium salts, lime and bleaching powder, followed by flocculation, sedimentation and finally filtration. The schematic representation of the same is presented in Fig. 9.4.

The amount of lime used is almost 1/20th of the alum, and the residual fluoride concentrations vary between 1 and 1.5 mg/L. Besides lime and alum, magnesium oxide when added as a chemical precipitant to fluoride containing water undergoes hydration to form magnesium hydroxide which on further reaction with fluoride ions forms a precipitate of insoluble magnesium fluoride (Ayoob et al. 2008). Moreover, a more recent and advanced form of traditional chemical coagulation is electrocoagulation that utilises a highly active metal anode to act as a coagulant. This has several advantages over conventional chemical precipitation technique such as easy storage with less space and does not need dilution, pH adjustment or chemical storage (Zhao et al. 2009; Velazquez-Jimenez et al. 2015).

Although chemical precipitation is one of the most established water defluoridation methods which can be widely used in the community as well as household levels, its low efficiency of ~70%, high maintenance cost, prerequisite of massive amounts of chemical reagents (sometimes alum is needed up to 700–1200 mg/L), adverse health impacts due to high residual aluminium in treated water, large sludge generation and hence disposal issues are some of the major shortcomings associated with this technique which makes it less acceptable for large-scale application in real field water defluoridation.

9.4.2 Membrane-Based Separation

In recent years, membrane-based separation processes have drawn great interest and have evolved as innovative, compatible and more modern techniques with regard to defluoridation of industrial wastewater or desalination of seawater. The membrane-based separation technique selectively controls the transport of a material based on its molecular size and shape across a semipermeable membrane. Typically, a chemical potential gradient generated across the membrane as a result of concentration/pressure gradient or by an electric field serves as the driving force for the transport of the material (Ayoob et al. 2008; Shen and Schafer 2014). Based on the membrane porosity and the gradients involved, the membrane separation processes can be categorized as reverse osmosis (RO), nanofiltration (NF) and electrodialysis (ED). Reverse osmosis (RO) is a separation process in which high-purity water is obtained after the removal of anions by applying pressure to the feed water to direct it through the semipermeable membrane as shown in Fig. 9.5 (Velazquez-Jimenez et al. 2015). Reverse osmosis is a complete converse of the natural osmosis process where a pressure much higher than natural osmotic pressure is applied to the concentrated side. RO system operates at a very high pressure where ions of dissolved solids are prominently rejected by a RO membrane referring to their size and electrical charge. Physico-chemical characteristics of raw water, temperature, pressure and membrane maintenance are some of the key parameters which control the operating efficiency of RO systems. The RO separation technique has been effectively employed for the treatment of fluoride-bearing industrial effluents and seawater desalination in many developed countries. Ndiaye et al. applied RO separation process for removal of fluoride from an industrial effluent and obtained a fluoride rejection percentage higher than 98%, provided that RO membranes are completely restored after each experimental analysis (Ndiaye et al. 2005). Although the RO process is highly profound separation system to guarantee steady water quality, there are several disadvantages associated with RO membrane systems such as the requirement of

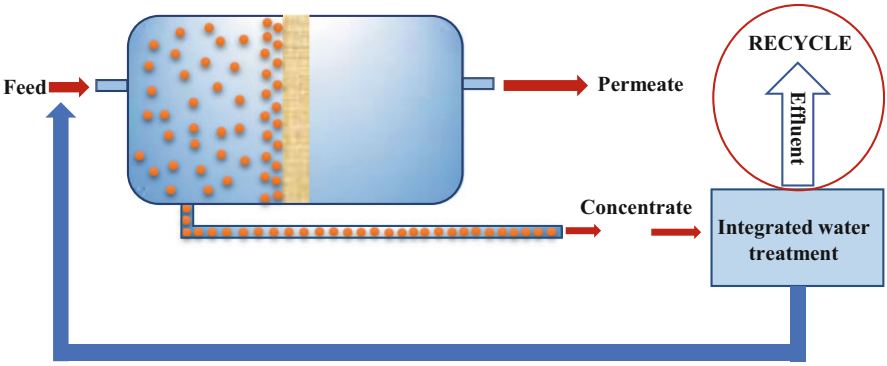

Fig. 9.5 Schematic representation of reverse osmosis (RO). (Modified after Velazquez-Jimenez et al. 2015)

regular disinfection of RO module due to frequent microbial growth, high operational cost and inaccessibility in water scarce arid regions.

Nanofiltration (NF), a relatively newer term, has emerged as a later innovation among available membrane processes for water treatment. An essential difference between NF and RO membrane separation is that NF membranes have comparatively bigger pores than RO membranes and offer less resistance to the transport of solvent as well as solute. Consequently, it requires a much lower pressure and less energy and provides faster flow across the membrane. NF systems predominately remove larger dissolved solids like multivalent ions; however, despite the small size, hydrated F^- ions present in aqueous solution with high charge density are quite efficiently retained in NF membranes due to steric effects. NF separation processes have more permeable membranes than RO systems and thus provide effective defluoridation of drinking water with no need for remineralization. Elazhar et al. obtained 97.8% fluoride rejection with water recovery of 84%, by using NF membranes (Elazhar et al. 2009). Malaisamy et al. developed an eight-bilayer modified NF membrane by assembling polyelectrolytic thin films on a commercial unmodified NF membrane and observed a 30% increase in its fluoride removal efficiency (Malaisamy et al. 2011).

Nasr et al. conducted a selectivity study for commercially available NF membranes in the presence of chloride, sulphate and calcium as naturally coexisting groundwater ions to produce water with a satisfactory chemical composition (Nasr Ben et al. 2013). The experimental results indicated that NF membranes strongly reject divalent ions and smaller ions are preferably retained due to their high solvation energy. Since fluoride ions are more solvated, they are better retained than chloride, sulphate and calcium ions. Furthermore, Chakrabortty et al. applied a cross flow NF membrane system to fluoride-contaminated groundwater and mathematically modelled the transport phenomenon of fluoride ions (Chakrabortty et al. 2013). The nanofiltration membrane in cross flow mode not only removed 98% fluoride from contaminated water but also reduced the high pH of water to the desired level of potable water at quite an affordable cost.

Electrodialysis (ED) is another membrane-based separation process in which instead of pressure, an electric field operates as the driving force for the separation of ionic solutes. Principally, due to the applied electric field, cations move towards cathode through negatively charged cation exchange membranes, and anions move towards anode through positively charged anion exchange membranes. Figure 9.6 represents a schematic layout of an electrodialytic cell (Velazquez-Jimenez et al. 2015). Thus, the concentration of cations and anions increases and decreases throughout the parallelly arranged alternate stacks of membranes, and the salinity of water is eventually reduced to anticipated levels. Sahli et al. conducted a fluoride removal study for significantly brackish Moroccan groundwater by carrying out adsorption on chitosan trailed by electrodialysis using CMX-ACS membranes and effectively reduced the fluoride and total dissolved salt levels to 3 mg/L and 3000 mg/L, respectively (Menkouchi Sahli et al. 2007).

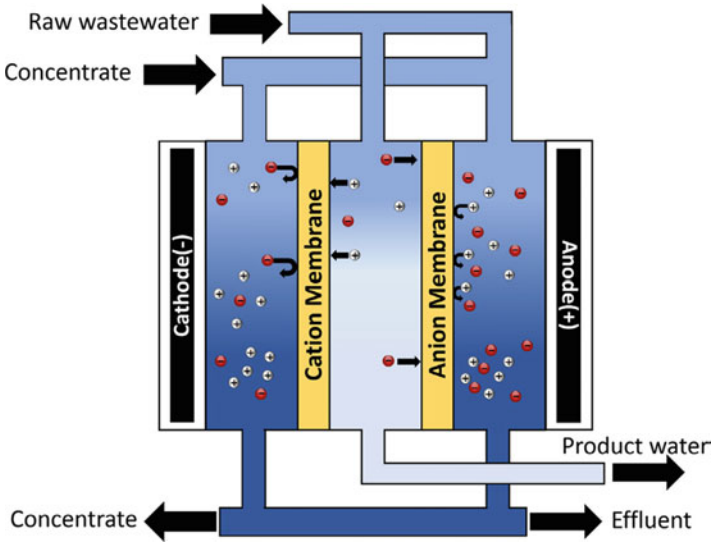

Fig. 9.6 Schematic layout of an electrodialytic cell. (Reprinted from Velazquez-Jimenez et al. 2015)

In 2008, Ergun et al. used an anion exchange membrane SB-6407 for the electrodialytic removal of fluoride and observed a 96% reduction in fluoride concentrations at pH 6 (Ergun et al. 2008). Quite recently, Elazhar et al. conducted a study for defluoridation of groundwater of Morocco utilizing both NF membrane separation process and ED and concluded ED as a more advantageous technique in comparison with NF regarding flexibility (Elazhar et al. 2013). Although the global trend is shifting towards the membrane-based techniques for water defluoridation because of its capability to overcome the shortcomings associated with the chemical processes, its high operational and maintenance cost, skilled labour requirements, poor selectivity and high-energy requirements make it unsuitable to be used in rural or countryside communities (Jagtap et al. 2012). RO is an expensive membrane-based technique and requires regular disinfection of RO modules due to clogging, scaling and fouling problems associated with RO membranes (Velazquez-Jimenez et al. 2015; Dhillon et al. 2016). Moreover, in RO systems, some essential ions are also removed in addition to fluoride, and as a result, continuous remineralization of treated water becomes necessary. Similarly, NF systems have limited membrane reusability due to membrane fouling at the nanoscale. However, though ED systems are more advantageous regarding flexibility as compared to RO and NF, the process is highly energy intensive and highly voltage dependent; thus it cannot be successfully used in rural areas. Besides, the electrodes used undergo frequent polarization and thus require continuous electrodes replacement which is not a cost-effective practice (Dhillon et al. 2016).

9.4.3 Ion-Exchange Technique

Fluoride can also be efficiently removed from water using anion exchange resins containing quaternary ammonium functional groups, and the reaction takes place as per the following Eq. (9.2) (Jagtap et al. 2012; Dhillon et al. 2016):

$$\text{Matrix} - \text{NR}_3{}^{+}\text{Cl}^{-} + \text{F}^{-} \rightarrow \text{Matrix} - \text{NR}_3{}^{+}\text{F}^{-} + \text{Cl}^{-} \tag{9.2}$$

The chloride ions present in the resin are replaced by fluoride ions, and this replacement continues until all the active sites on the anionic resin are occupied by F^- ions (Jagtap et al. 2012). The fluoride-laden resin is then regenerated with a supersaturated solution of sodium chloride salt. The fluoride ions present in the resin are replaced by new chloride ions present in the supersaturated sodium chloride solution triggering the regeneration of the resin and beginning the whole process again. An insight into the literature has revealed that both anionic and cationic synthetic resins were equally employed for fluoride removal. However, Ku et al. in 2002 conducted a study on fluoride removal by Amberlite IR-120 resin and observed that anionic resins display not only poor regeneration potential as compared to cationic resins but also show poor selectivity in the presence of foreign ions (Ku et al. 2002). Singh et al. also presented the following order of anionic selectivity for anion exchange resins: citrate > $SO_4{}^{2-}$ > oxalate > I^- > $NO_3{}^-$ > $CrO_4{}^{2-}$ > Br^- > Cl^- > $HCOO^-$ > CH_3COO^- > F^- (Singh et al. 2014). Viswanathan et al. applied a new approach in ion-exchange techniques to improve the selectivity and efficiency by incorporation of metal ions in the resin matrix (Viswanathan and Meenakshi 2009). For this, Viswanathan and his co-workers developed Na^+ and an Al^{3+} modified Indion FR 10 resin and demonstrated an appreciable increase in the defluoridation potential as compared to unmodified Indion FR 10. More recently, Pan et al. fabricated a hydrous zirconium oxide supported polystyrene anion exchanger D201 and obtained highly efficient fluoride removal results and concluded that ion-exchange resins have enough room for further development to achieve selective fluoride removal (Pan et al. 2013). Although the ion exchange technique is highly efficient and can remove fluoride up to 90–95%, it is less selective in the presence of coexisting ions, highly sensitive to pH changes, and only recommended for small community systems with low total dissolved solids (TDS) and sulphate concentration (Dhillon et al. 2016).

9.4.4 Adsorption

In view of the fact that excessive fluoride problems are mostly found in the countryside, there is a need to adopt low-cost and simple defluoridation techniques. Major hindrances for the global implementation of the above-mentioned defluoridation techniques are their high operational and maintenance costs and the

Table 9.4 Most obvious advantages and disadvantages associated with various water defluoridation technologies

Technologies	Advantages	Disadvantages
Precipitation-coagulation	Established method, widely used at community and household level, commercially available technique	Low efficiency ~70%, high maintenance cost, requires a large dosage of aluminium sulphate up to 700–1200 mg/L, adverse health effects due to high residual aluminium in treated water, cannot remove fluoride below 5 mg/L, large sludge generation and hence disposal issues
Membrane processes	High efficiency, no chemicals required, wide pH range applicability, removes other contaminants as well	Skilled labour requirement, high operational and maintenance cost, poor selectivity, the membrane is pH sensitive and can undergo clogging and fouling, polarization occurs in the case of electrodialysis
Ion exchange	90–95% removal efficiency, taste and colour of water remain intact, offer flexibility in design	Expensive due to resins, vulnerable to coexisting ions (sulphate, phosphate, bicarbonate.), produces toxic liquid waste, highly pH dependant, only recommended for small community systems with low total dissolved solids (TDS) and sulphate concentration
Adsorption	High efficiency, cost-effective, easy operation, highly eco-friendly, availability of a wide range of adsorbents	High pH dependence, interference by other coexisting ions like phosphate and bicarbonates, repeated regeneration is required, disposal of fluoride-laden adsorbent

requirement of expert or skilled manpower. Some of the major advantages and disadvantages associated with these defluoridation techniques in water treatment are depicted in Table 9.4 (Jagtap et al. 2012; Velazquez-Jimenez et al. 2015; Dhillon et al. 2016). However, adsorption has emerged as one of the most preferred water defluoridation techniques in developing countries because of its salient features such as low operational costs (including medium and running costs), greater accessibility, simple design, environmental friendliness, easy handling, easy maintenance, high fluoride removal efficiency, removal even at low fluoride concentrations and possibility of regeneration (Ayoob et al. 2008; Bhatnagar et al. 2011). It is a surface phenomenon that involves the removal of a substance, formally present in one phase by accumulating it at an interface between two phases (gaseous or liquid and solid phase). The reduction in the interfacial surface tension between the two phases is the prime underlying driving force behind the adsorption process (Dhillon et al. 2016). The substance which is adsorbed is termed as the adsorbate, and the adsorbing phase is termed as an adsorbent. Depending upon the type of interactions between adsorbate and adsorbent, adsorption is classified as either "physical adsorption" or "physisorption" and chemical adsorption or "chemisorption". Physisorption

involves van der Waals forces and usually predominates at lower temperatures with low adsorption energy. Conversely, chemisorption occurs at higher temperatures when the adsorbate interacts chemically with adsorbent and exhibit higher adsorption energy (Ayoob et al. 2008; Velazquez-Jimenez et al. 2015).

The efficiency of an adsorption process is primarily dependent on the development of an adsorptive material (adsorbent) and the criteria for selection of suitable adsorbents which include an evaluation of its cost, fluoride adsorption capacity, the potential for its reuse and the possibility of its regeneration. Recently, substantial research has been conducted to study the removal of fluoride by adsorption technology using various materials as adsorbents.

9.5 Adsorbents Used for Water Defluoridation

Fluoride ion adsorption occurs on the adsorbent's surface via a three-step mechanism: (i) bulk transfer of fluoride ions to the surface of adsorbent, (ii) fluoride ion adsorption on particle's external surface and (iii) intraparticle diffusion of fluoride ions from external surface to inside the particles through pores (Jadhav et al. 2015). The assessment of the applicability of an adsorbent involves its adsorption efficiency evaluation in dilute solutions, working pH range, adsorbate uptake rate, reusability potential and its economic feasibility. Several materials with fluoride adsorptive potential have been evaluated in the past to find a competent as well as economical fluoride adsorbent. However, due to different applied experimental conditions, various adsorbents reported in the literature could not be directly compared and weighed against each other to evaluate the best. An array of conventional fluoride adsorbents comprises alumina, activated alumina, activated carbon, clay-based materials, various geomaterials, industrial by-products, biosorbents, metal oxides and their composites (Suriyaraj and Selvakumar 2016).

9.5.1 Conventional Fluoride Adsorbents

9.5.1.1 Alumina-Based Adsorbents

Over the years, aluminium and aluminium-containing sorbents because of their high affinity towards the F^- ion have been considered as substantially important materials for water defluoridation. In early years, Farrah et al. tested the fluoride adsorptive potential of aluminium hydroxide ($Al(OH)_3$) and aluminium oxide (Al_2O_3) over a pH range of 3–8, for F^- concentrations which ranged from 1.9 to 19 mg/L, and obtained a maximum fluoride uptake of 170.98 mg/g in the pH range of 5.5–6.5. Apart from lower fluoride adsorption capacity, almost similar pH trends were observed using α-Al_2O_3 (Mohapatra et al. 2009). Later, alumina was activated by

heating to produce a more efficient adsorbent, activated alumina (AA) through slow decomposition (achieved by steam) of gibbsite ($Al(OH)_3$) (Velazquez-Jimenez et al. 2015). AA is granular and highly porous with surface areas ranging between 200 and 300 m^2/g (Ayoob et al. 2008). Amongst the various forms of activated alumina, γ-Al_2O_3 is used more frequently for water defluoridation due to its high fluoride adsorption capacity (Loganathan et al. 2013).

However, due to the slower fluoride uptake demonstrated by commercial AA, recently, quite a lot of work has been conducted to develop modified AA. In the view of the same, Tripathy et al. achieved 99% fluoride removal using alum impregnated activated alumina (AIAA) at pH 6.5, but then the contact time required for removal of the initial fluoride concentration 20 mg/L was quite high (3 h) (Tripathy et al. 2006). Maliyekkal et al. calcined magnesium hydroxide-impregnated alumina and developed magnesia-amended activated alumina (MAAA) and obtained an adsorption capacity of 10.12 mg/g (Maliyekkal et al. 2008). Rafigue et al. prepared a modified immobilized activated alumina (MIAA) that demonstrated a comparatively faster and 1.35 times better performance than its unmodified form (Rafigue et al. 2013). More recently, Cheng et al. incorporated a rare earth element lanthanum into the activated alumina and prepared La^{3+}-modified activated alumina (La-AA) to further improvise the fluoride adsorption property of AA and obtained a much higher fluoride adsorption capacity (6.70 mg/g) than unmodified AA (2.74 mg/g) (Cheng et al. 2014).

Liu et al. obtained an adsorption capacity of 110 mg/g for fluoride from freshly prepared aluminium hydroxides ($Al_2O_3{\cdot}xH_2O$) (Liu et al. 2011). However, the removal of fluoride by $Al_2O_3{\cdot}xH_2O$ was found to be highly dependent on solution pH with maximum removal obtained in the slightly acidic medium. The efficiency of aluminium-modified iron oxides in a continuous column system for fluoride removal was also successfully evaluated by Sanchez et al. (Garcia-Sánchez et al. 2013). Biswas et al. co-precipitated iron, aluminium and chromium oxides to develop hydrated mixed oxide of Fe(III)-Al(III)-Cr(III) and obtained fluoride removal capacity of 31.89 mg/g at pH 5.6 (Biswas et al. 2010). Later, Zhu et al. co-precipitated a double oxide of Al(III)-Zr(IV), where aluminium and zirconium oxide synergistically interacted to yield a significantly high fluoride removal capacity (114.54 mg/g) (Zhu et al. 2015). Lately, hydroxyl aluminium oxalate (HAO) as a highly efficient fluoride adsorbent with Langmuir capacity 400 mg/g (amongst the highest capacities of fluoride adsorbents known today) at pH 6.5 was synthesized via a simple hydrothermal method by Wu et al.

Although the alumina-based adsorbents have demonstrated excellent fluoride uptake, their expensive nature and reduced performance in the presence of coexisting ions restrict their real field application. Alumina- and aluminium-based adsorbents also pose some limitations such as noteworthy loss of capacity (~30 to 40%) due to the regeneration and highly pH-dependent defluoridation potential. Besides, high residual aluminium (2.0–6.86 mg/L) in the treated water as a result of leached aluminium can cause Alzheimer's disease because of it proven neurotoxic nature (Ayoob et al. 2008).

9.5.1.2 Metal-Based Adsorbents

Metal-based adsorbents have attracted considerable attention in the field of water defluoridation due to their tendencies to acquire positive charge (by donating electrons) and hence electrostatically attract negatively charged fluoride ions. However, so far 15 different metal elements have been used for adsorbent development for various applications (Velazquez-Jimenez et al. 2015). These adsorbents comprise of metal oxides and metal hydroxides also known as hydrous oxides or oxyhydroxides. Metal-based adsorbents which have been utilized thus far as per the literature can be categorized as monometallic, bimetallic and trimetallic adsorbents based on the number of metal elements mixed to form oxides or hydrous oxides. Amongst them alkali metals such as lithium and sodium due to their low electronegativity predominately form covalent bonds with fluoride ions and thus have not been reported as the principal elements in fluoride adsorbents.

Calcium is an alkaline earth metal with a great affinity for fluoride ions, low cost and biocompatibility with the human body. This metal has therefore attracted the considerable interest of researchers for fluoride removal studies. Islam and Patel conducted a fluoride removal study using quick lime (CaO) and concluded that chemisorption along with precipitation is an underlying adsorption mechanism (Islam and Patel 2007). However, quick lime displayed a F^- removal capacity of 16.67 mg/g for initial F^- concentration 10 mg/L and could not effectively reduce the fluoride levels in the water below standard acceptable limits. Calcite ($CaCO_3$) as another calcium adsorbent was applied to remove fluoride from acid-treated fluoride-containing water (Poonam et al. 2014). On addition of calcite to acid-treated fluoride-contaminated water, a large number of Ca^{2+} ions were produced which undergo chemical bond formation with fluoride ions to form CaF_2 precipitate and demonstrated a fluoride removal capacity of 7 mg/g. Gogoi and Dutta obtained a F^- uptake capacity of 6.45 mg/g by using phosphoric acid-modified limestone powder as an adsorbent (Gogoi and Dutta 2016). Sakhare et al. synthesized calcium aluminate (CA) as another highly porous fluoride adsorbent where F^- ions were adsorbed chemically by calcium component and physically by aluminium component of CA, synergistically resulting in 85% F^- removal for initial F^- concentration 8.9 mg/L (Sakhare et al. 2012). More recently, Chaudhary and Prasad carried out fluoride removal study using activated dolomite ($CaCO_3.MgCO_3$) which is a low-cost and readily available calcium mineral of geological origin mainly found in sedimentary rocks and composed of alternate layers of CO_3^{2-}, Ca^{2+} and Mg^{2+} ions. An excellent F^- uptake capacity of 243.25 mg/g was observed for fluoride containing aqueous solution at neutral pH (~7.0) (Chaudhary and Prasad 2015). Labastida et al. conducted a fluoride removal study using limestones from various geological rock formations and established the relationship between fluoride adsorption efficiency and $CaCO_3$ content and particle size (Labastida et al. 2017). However, the study suggested that fluoride retention through adsorption over limestone particles may be an unstable process which is highly dependent on limestone PZC (point of zero charge) and experimental pH values.

Another group of low-cost naturally occurring calcium minerals which has been widely employed as fluoride adsorbents is hydroxyapatite (HAP) with chemical formula $Ca_5(PO_4)_3OH$. It involves the replacement of hydroxyl ions present in its apatite crystal structure by fluoride ions present in contaminated water to form thermodynamically more stable fluorapatite (FA) (Dhillon et al. 2016). Gao et al. prepared synthetic HAP consisting particles of different sizes and comparatively evaluated its fluoride removal efficiency with that of HAP bulk synthesized using conventional solid-state reactions (Gao et al. 2009). It was observed that HAP with smaller particle size demonstrated higher F^- uptake capacity and better effectiveness at lower pH. Recently, several studies have been carried out for surface modification of HAP either by coating or doping with ions like aluminium, magnesium and sulphate into the crystal structure of HAP. In view of the same, Chen et al. fabricated sulphate-doped hydroxyapatite hierarchical hollow microspheres and observed a significant enhancement in fluoride removal efficiency of HAP (F^- removal capacity 28.3 mg/g) after sulphate doping because of the cooperative reinforcement effect between the surface hydroxyl groups and sulphate ions (Chen et al. 2016).

However, despite having a high affinity towards fluoride ions, calcium-based adsorbents still hold some limitations concerning reusability. Adsorption of fluoride ions onto the calcium-based adsorbents occurs via chemisorption (i.e. chemical bond formation) which makes desorption of adsorbed fluoride ions quite tricky during regeneration. The poor regeneration eventually results in drastic reduction in fluoride sorption capacity of calcium based adsorbents after successive adsorption-desorption cycles.

Regarding other metals, transition elements such as zirconium, iron, titanium, cerium and manganese due to their multivalent behaviour and more active adsorption sites have gained greater attention in the field of water defluoridation as compared to alkali and alkaline earth elements. Transition elements being more electronegative show slightly weak electron-transferring interactions with fluoride ions and hence do not tend to precipitate fluoride (Velazquez-Jimenez et al. 2015).

Dou et al. synthesized hydrous zirconium oxide (HZO) by a simple precipitation technique and used this as an adsorbent for the removal of fluoride. HZO demonstrated a reasonably high F^- adsorption capacity of 68 mg/g, which was attributed to its plentiful surface OH groups (due to its hydrous nature) which actively adsorbed F^- ions electrostatically as well as via ion exchange (Dou et al. 2012). Moreover, Saha et al. in their work conducted successful surface modification and functionalization of hydrous zirconium oxide using β-cyclodextrin (CY-HZO) which is a pretty well-documented, inexpensive, non-toxic toroidal oligosaccharide (Saha et al. 2015). As a consequence of the surface modification, the modified adsorbent (CY-HZO) incorporated more surface hydroxyl groups and displayed a reasonably higher F^- uptake capacity (31.45 mg/g) than pristine HZO. Babaeivelni and Khodadoust explored the fluoride removing properties of crystalline TiO_2 and reported optimum F^- uptake in between pH range 2 and 5 (Babaeivelni and Khodadoust 2013). Amongst the p-block elements, only aluminium, tin and bismuth are evidenced to exhibit fluoride-adsorbing properties. Other than tin and bismuth, aluminium has been explored hugely for fluoride removal in the form of alumina and

alumina-containing materials as discussed earlier. Hence, Srivastav et al. synthesized hydrous bismuth oxide (HBO) to evaluate its defluoridation potential and obtained a higher fluoride removal percentage (65%) as compared to commercial Bi_2O_3 (6%) (Srivastav et al. 2013).

However, there are several shortcomings associated with the use of mono metal-based adsorbents such as slow removal, easy deactivation and tedious separation from aqueous solution. Considering these shortcomings, it became essential to try and develop novel and efficient binary metal oxides for water defluoridation. Hence, Dou et al. prepared a granular binary oxide of Zr and Fe (molar ratio 2.3:1), which exhibited F^- adsorption capacity of 9.80 mg/g and exceptionally high mechanical strength and stability assuring better real field feasibility with minimal material loss (Dou et al. 2011). Rare earth metal oxides of cerium (Ce) and lanthanum (La) are strongly basic with relatively small ionic potentials and thus tend to hydrolyse their surface hydroxyl groups into OH^- ions which are readily exchangeable with F^- ions. However, the expensive nature of rare earth metal-based materials makes them less viable as fluoride adsorbents for real field implementation in developing countries with poor economic status. Hence, Tang et al. in this study developed a hybrid binary metal oxide with hierarchical pore structure using Ce(IV) and a cheaper metal Fe(III) which has shown a significant affinity towards fluoride ions in the literature and obtained a F^- adsorption capacity of 60.97 mg/g (Tang and Zhang 2016). Quite recently, Yan et al. synthesized a composite adsorbent made up of La and TiO_2 (TiO_2-La), where $LaCO_3OH$ was properly oriented over the TiO_2 lattice, and the developed TiO_2-La composite removed fluoride optimally in a range of pH 3–9 with adsorption capacity 78.4 mg/g (Yan et al. 2017). Nowadays, substantial work has been directed towards the development of trimetallic adsorbents in continuous efforts for developing highly competent and effective adsorbents for fluoride removal. Accordingly, a trimetal composite comprising Mg/Fe/Al in molar ratio of 25:1:4 was developed by Wang et al. and further calcined at 400 °C (Wang et al. 2015). The as-calcined Mg/Fe/La composite displayed a high F^- removal capacity of 112.17 mg/g due to the addition of La (a rare earth element) which is well known to exhibit specific properties such as multivalence behaviour and high selectivity towards F^- ions. However, it was noted that the addition of rare earth metals not only enhances the fluoride adsorption capacity but also elevates the overall preparation cost of adsorbent; hence in view of the same, Wang et al. fabricated a low-cost Mg-Al-Zr triple-metal composite adsorbent to remove fluoride from aqueous solution where fluoride adsorption capacity was improved by incorporating zirconium instead of high-cost rare earth elements. Nevertheless, Mg-Al-Zr exhibited maximum fluoride uptake of 22.9 mg/g which was still low in comparison with several other zirconium-based fluoride adsorbents as reported in literature (Wang et al. 2017).

9.5.1.3 Activated Carbon-Based Adsorbents

Carbonaceous materials can be utilised as efficient adsorbents when suitably treated and modified. Activated carbon (AC) due to its remarkably high surface area ranged

between 500 and 1500 m^2/g, and highly porous internal framework with the presence of a broad range of functional groups is one of the most extensively used carbon-based adsorbent for removal of toxic water pollutants. However, due to its low pH_{pzc} (~1.6–3.5), it exhibits poor adsorption properties for anionic pollutants. Besides F^- ions also show a weaker affinity towards non-metallic surfaces like activated carbon in comparison with metallic solids. Nevertheless, due to their high surface area, a carbonaceous matrix of AC prevents the metal ion sintering in its porous internal framework and thus can be modified with appropriate metal ions to obtain improvised fluoride adsorption efficiency. Vences-Alvarez et al. developed lanthanum-modified granular activated carbon (GAC-La0.05) as an adsorbent with fluoride adsorption capacity of 9.98 mg/g which is five times higher than commercial GAC (Vences-Alvarez et al. 2015). In another study, Velazquez-Jimenez et al. obtained a fluoride adsorption capacity of 7.40 mg/g by using Zr(IV) impregnated activated carbon (ZrOX-AC) as adsorbent where the size of Zr (IV) particles was controlled by using oxalic acid as a complexing ligand during the synthesis (Velazquez-jimenez et al. 2014). Quite recently, Mullick and Neogi reported the synthesis of a zirconium-impregnated activated carbon composite with ultrasonic assistance using powdered activated carbon and $ZrOCl_2.8H_2O$ as a precursor (Mullick and Neogi 2018). The acoustic cavitation phenomenon as a result of ultrasonication treatment significantly improved the surface area and reduced the particle size of composite and demonstrated the Langmuir adsorption capacity of 5.4 mg/g at pH 4.0.

However, commercially available activated carbon is quite expensive, and its high cost makes the adsorption process less cost-effective. Hence, Yu et al. derived carbon from an alternative cheaper source, i.e. *Sargassum* species (seaweed), and modified it with lanthanum to make lanthanum-modified carbon and applied the same as an adsorbent to obtain F^- adsorption capacity of 94.34 mg/g at neutral pH (Yu et al. 2015). Fluoride adsorption predominantly occurred via outer-sphere complex formation, along with electrostatic attraction and ion-exchange mechanisms. Sivasankar et al. selected starch as the carbon source for the development of Ce dispersed in carbon (CeDC) and at pH 8.02 obtained a maximum F^- uptake of 52 mg/g. However, the proper composite structure of CeDC could not be established which restricted its further scale up for real field studies (Sivasankar et al. 2013). Lately, Ajisha and Rajagopal utilised *Delonix regia* pod to develop an activated carbon without any chemical treatment and utilized the same for water defluoridation to obtain a maximum F^- removal capacity of 33.4 mg/g in acidic pH range (Angelina Thanga Ajisha and Rajagopal 2015). Regardless of demonstrating a significant fluoride adsorption capacity, the adsorbent required lower pH conditions to operate optimally which makes it less feasible for real field groundwater treatment. Very recently, Singh et al. fabricated activated carbon from the shell of *Aegle marmelos* commonly known as bael and employed the same as fluoride adsorbent to obtain a maximum F^- uptake of 1.07 mg/g and 2.4 mg/g for initial F^- concentrations 4 mg/L and 8 mg/L, respectively (Singh et al. 2017). Recently, biowaste coconut husk was identified by Talat et al. as a suitable source to derive activated carbon with mere treatment of KOH (Talat et al. 2018). The obtained highly porous activated

carbon with very high surface area ≈1448 m^2/g provided the dual edge over commercially available high cost ACs. Firstly it resolved the disposal issue of coconut husk waste and secondly served as an excellent low-cost fluoride adsorbent with high adsorption capacity of 6.5 mg/g at pH 5.0.

Although quite a lot of studies have been conducted to develop surface-modified carbonaceous materials, most of the studies are still in the preliminary stages at bench scale and lack information regarding their utilization in fixed-bed continuous column systems for full-scale real field water treatment applications. Moreover, high-quality activated carbons are of high cost with poor selectivity and suffer from regeneration issues, which render their application impractical on a large scale.

9.5.1.4 Low-Cost Materials as Adsorbents

A wide range of fluoride removal studies have been reported on the usage of various naturally existing materials found in abundance at no cost such as locally accessible soil or natural clay and agricultural as well as industrial by-products (Loganathan et al. 2013; Vinati et al. 2015). Chidambaram et al. used natural red soil in a continuous flow column system to defluoridate fluoride-contaminated water and concluded the active involvement of surface hydroxyl groups (Fe-OH and Al-OH) in fluoride adsorption (Chidambaram et al. 2013). Recently, fluoride adsorption on naturally occurring iron-rich lateritic soil of Misiones province of Argentina was studied by Iriel et al. under controlled pH and ionic strength conditions (Iriel et al. 2018). The fluoride adsorption process on lateritic soil particles was mainly physical in nature, and the maximum fluoride uptake capacity was 0.48 mg/g.

Over the past few years, different clay materials have become the subject of substantial research amongst scientists because of their economic viability, ease of availability, enhanced stability, high surface area and useful ion-exchange features. Attapulgite (A) is amongst the well-known clay materials consisting three-dimensional hydrated crystalline magnesium aluminium silicate with the negatively charged surface. Zhang et al. developed zirconium-modified attapulgite (Zr-A) as an adsorbent to further improvise the fluoride adsorptive potential of bare attapulgite (Zhang et al. 2012). Although the adsorbent presented a superior fluoride adsorption as compared to unmodified attapulgite, it also demonstrated poor selectivity in the presence of coexisting anions (SO_4^{2-}, HCO_3^- and PO_4^{3-}).

Another class of low-cost materials is industrial by-products such as red mud, slag materials and fly ash originating, respectively, from mining industries, steel industries and power plant industries as by-products. Amongst them, red mud which is generated as a slurry (waste) in the bauxite industry has gained considerable interest as an adsorbent for fluoride uptake, due to its easy accessibility and cost-effective nature. Its fluoride-adsorbing properties are primarily contributed by its chief components Al and Fe oxides. However, along with Fe and Al oxides, red mud may also be composed of Ti oxides, Si oxides and other metal oxides depending on its origin. To activate the red mud, most of the researchers have used HCl, which as a result reduced the Fe quantity that is required for the fluoride adsorption processes. Henceforth, the effect of

various acid treatments (HCl, HNO_3 and H_2SO_4) on the fluoride adsorption capacity of red mud was evaluated, and it was observed that the treatment of red mud with H_2SO_4 demonstrated the highest fluoride removal by generating $2H^+$ to protonate surface -OH groups present in red mud (Liang et al. 2014).

Bone char is another widely used low-cost fluoride adsorbent which tends to exhibit fluoride uptake capacities in the range of 1–5 mg/g, based on the synthetic conditions and parameters. Hydroxyapatite constitutes main inorganic component (>60%) of the bone char and primarily accounts for it fluoride removal properties. As discussed earlier, several fluoride removal studies have already been conducted using surface-modified hydroxyapatite as an adsorbent. Hence, under the same scenario, Muro et al. reported the new insights in surface modification of the bone char using cerium species where Ce^{4+}-doped bone char offered much better fluoride adsorption capacities of 13.6 mg/g at pH 7.0 as compared to Ce^{3+}-doped bone char as well as other reported commercial bone chars (Zúñiga-Muro et al. 2017).

Moreover, since the last few years, considerable attention has been focussed on agricultural by-products which are now emerging as competitive alternatives to costly synthetic fluoride adsorbents due to their low cost, natural abundance, easy availability and various surface functional groups. Tomar et al. evaluated the fluoride-adsorbing potential of *Citrus limonum* (lemon) leaf as an eco-friendly agricultural by-product and observed profoundly pH-dependent fluoride removal with a maximum F^- adsorption of 70% at pH 2 which decreased with increase in pH of the fluoride solution (Tomar et al. 2014). Paudyal et al. loaded different metal ions (Zr(IV), Ce(IV) and Al(III) on the commercially available agricultural by-product of dried orange juice residue and evaluated their fluoride removal potential (Paudyal et al. 2013). Zr(IV)-loaded dried orange juice residue demonstrated great fluoride adsorption potential with no significant interference of coexisting ions, and the maximum F^- uptake capacity obtained was higher (27.17 mg/g) than Ce(IV)-loaded (23.18 mg/g) as well as Al(III)-loaded (12.73 mg/g) dried orange juice residue. Recently, tea waste is another agricultural by-product which is used as an adsorbent in water defluoridation studies. Cai et al. loaded tea waste with Al/Fe oxides to develop an efficient, low-cost fluoride adsorbent and obtained maximum F^- adsorption capacities as 3.83 mg/g, 10.47 mg/g, 13.79 mg/g and 18.52 mg/g for original tea, Tea-Fe, Tea-Al and Tea-Al-Fe, respectively (Cai et al. 2015). Quite recently, the same authors fabricated a novel fluoride sorbent by loading ball-milled ultrafine tea powder with Zr(IV) and obtained a maximum F^- removal capacity of 12.43 mg/g (Cai et al. 2016). Moreover, Tirkey et al. prepared an inexpensive fluoride adsorbent using readily available biomass, i.e. Jamun leaf (*Syzygium cumini*) (Tirkey et al. 2018). The developed adsorbent mainly comprised of calcium carbonate and calcium oxide/hydroxide and demonstrated the fluoride uptake capacity of 4.56 mg/g at pH 6.5. Amongst available agricultural by-products, exhausted coffee ground wastes have been recently identified as an ideal economical substitute in removal of fluoride from water. Babu et al. developed an economic fluoride adsorbent using acid-activated exhausted coffee grounds and obtained a fluoride adsorption capacity of 9.05 mg/g at pH 4 (Naga Babu et al. 2018). However, the use of low-cost natural materials as fluoride adsorbents is accompanied with several shortcomings such as

poor regeneration leading to poor recyclability, low adsorption capacity, poor selectivity and incapability to work efficiently for lower initial fluoride concentration (Loganathan et al. 2013; Mondal and George 2015).

9.5.1.5 Polymer-Based Adsorbents

Over the recent years, biosorption has established itself as an effective water defluoridation method involving the use of copiously available biomaterials as fluoride adsorbents. Amongst various biomaterials, chitin, chitosan and its derivatives and alginates have gained global recognition as economical fluoride adsorbents with a large number of amino and hydroxyl groups. Chitin is a long chain polymer of a glucose derivative, i.e. N-acetyl glucosamine, primarily found in exoskeletons of various organisms and commercially obtained as a waste product of shellfish processing. Chitosan is a linear polysaccharide obtained by deacetylation of chitin using alkali treatment (NaOH). Chitosan has the highest metal coordinating ability among the available biopolymers due to plentiful amino (NH_2) and hydroxyl (OH) groups in its polymeric chain. Liu et al. explored chitosan for its metal-complexing property and synthesized titanium (IV) hydrate based on a chitosan template as a cost-effective bio-adsorbent for defluoridation of the aqueous solution (Liu et al. 2014). Fluoride adsorption capacity obtained was 16.12 mg/g which declined enormously in the presence of coexisting ions. Prabhu et al. took advantage of the non-leaching behaviour of lanthanum (rare earth metal) and adopted a novel approach to fabricate chitosan-based fluoride adsorbents in which La(III)-Zr(IV) mixed oxide was supported on the chitosan beads (Muthu Prabhu and Meenakshi 2014). However, a significantly low fluoride adsorption capacity was obtained at an extended contact time of 50 min, which prevented its further implementation in technology development. Furthermore, the same group of authors developed another chitosan-based fluoride adsorbent by using chitosan as a template to grow Al and La mixed oxyhydroxides and obtained a selective fluoride uptake with negligible effect of coexisting ions and maximum defluoridation capacity of 49.54 mg/g (at pH 7) (Prabhu et al. 2016). Although it is evident that chitosan can offer satisfactory fluoride uptake after specific modifications, chitosan in powder form is mostly crystalline whereas adsorption predominantly occurs in an amorphous region which limits its adsorption potential.

Alginate (Alg) as a low-cost anionic biopolymer is mainly extracted from brown algae and has a broad spectrum of applications in the field of water treatment. It is composed of mannuronate and guluronate monomeric units with carboxylate groups and thus carries an overall negative charge. However, due to plentiful negatively charged surface carboxylate groups, alginate can be readily cross-linked with multivalent cations to be used as fluoride adsorbents. Kaygusuz et al. synthesized a composite bead of alginate-montmorillonite-clay as fluoride adsorbent, where alginate and montmorillonite were cross-linked by Al(III) aqueous solution (Kaygusuz et al. 2015). Alginate-montmorillonite-clay composite exhibited comparatively higher mechanical strength than pure alginate beads and demonstrated fluoride

adsorption capacity of 31 mg/g which reduced significantly in the presence of SO_4^{2-} ions. Sujana et al. used hydrous ferric oxide (HFO) as a dopant to modify calcium alginate beads and conducted fluoride adsorption studies with HFO-doped Ca-Alg beads (Sujana et al. 2013). Although modified Ca-Alg beads worked well at drinking water pH range and hence do not require pH adjustments, these still demonstrated quite a low F^- uptake capacity (8.9 mg/g) which restricted its large-scale real field application. Besides, zirconium alginate beads fabricated by Quisheng et al. for fluoride removal demonstrated a reasonably good F^- removal capacity (32.797 mg/g) but poor selectivity in the presence of SO_4^{2-}, HCO_3^- and PO_4^{3-} ions (Qiusheng et al. 2015). Hence, it was observed that although the use of biopolymeric adsorbents provides an economical defluoridation method, it is still associated with drawbacks of higher adsorbent dose, long contact time and low selectivity.

Intrinsic conducting polymers (ICPs) are another special class of polymers that have gained considerable attention over the past two decades due to their high electrical conductivity and good environmental stability. These polymers have unlocked numerous pathways to progress and understand physical as well as chemical aspects of conjugated π electron systems. Conjugation comprises of alternate single and double bonds in between the carbon atoms, and as a result polymer backbone of ICPs contains a strong localized σ bond along with a delocalized π bond. Conductivity is imparted to ICPs through the addition of dopant ions as charge carriers in the polymer backbone. ICPs are heavily employed in various fields of applications such as supercapacitors, electrostatic materials, light-emitting diodes, aircraft structures, electrochromic devices, conductive adhesives, biosensors and biomedical devices (Zhang and Bai 2003; Kavitha et al. 2013). Figure 9.7 represents the chemical structures of some commonly used ICPs (Ravichandran et al. 2010).

Amongst the available ICPs, polypyrrole (PPy) and polyaniline (PANI) have attracted an immense interest from researchers in the field of water treatment due to their inexpensive nature, facile synthesis, good biocompatibility and excellent ion-exchange properties (Zhang and Bai 2003; T and Belagali 2015). During the chemical oxidative polymerization of PPy and PANI, the polymer is synthesized in its oxidized form, and as a result, most of the nitrogen atoms present in the polymer backbone are positively charged (Huang et al. 2003; Zhang and Bai 2003). Hence, to neutralize this unstable oxidized backbone, the growing polymer chain of PPy or PANI incorporates counter anions (dopant ions) present in the polymerizing solution.

Due to the high mobility in the polymer backbone and easy exchangeability, these doped counter ions impart ion-exchange properties in PPy or PANI. PPy and PANI can portray either anion- or cation-exchange behaviour depending on the type and size of dopant ions present in the polymerizing solution during the synthesis (Weidlich et al. 2001). As the literature reveals, PPy and PANI primarily demonstrate anion exchange properties when their polymerizing solution contains dopant ions such as chloride (Cl^-), perchlorate (ClO_4^-) or nitrate (NO_3^-). Due to ion-exchange properties PPy and PANI have been extensively studied in various fields of water treatment. However, despite the fact that the positively charged N atoms present in the polymer backbone offer a great possibility for fluoride adsorption, so

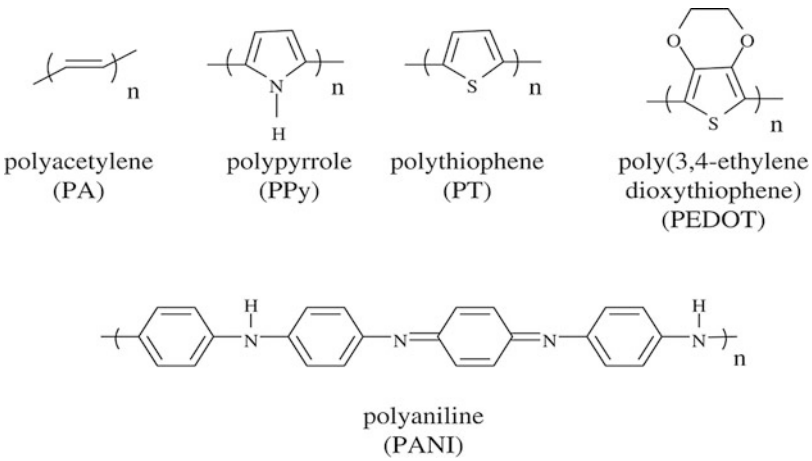

Fig. 9.7 Chemical structures of some commonly used ICPs. (Reprinted from Ravichandran et al. 2010)

far only a few defluoridation studies for PPy and PANI have been reported in the literature. Karthikeyan et al. synthesized PPy and PANI by chemical oxidative polymerization, studied their defluoridation performance for the first time and obtained fluoride adsorption capacities of 6.3 mg/g and 0.78 mg/g, respectively (Karthikeyan et al. 2009b, c). However, PPy and PANI tended to aggregate in irregular morphology because of strong π-π* interactions between the polymeric chains and hence exhibited poor surface area along with poor dispersion in aqueous solution. To alleviate this drawback and to improvise the surface area of PPy and PANI, the same groups of authors tried to incorporate alumina in the polymer matrix and thus fabricated a composite of alumina with PPy and PANI. The alumina composites of PPy and PANI displayed fluoride adsorption capacities of 6.6 mg/g and 8 mg/g, respectively, for PPy/AlO and PANI/AlO. Even though PPy/AlO and PANI/AlO demonstrated better defluoridation performance than unmodified PPy and PANI, it was still not sufficient enough for full-scale defluoridation technology development (Karthikeyan et al. 2009a).

9.5.2 Emerging Nanomaterial-Based Adsorbents

Every adsorbent system requires a real water analysis prior to its field application. Though a number of conventional adsorbents had been developed as cited in this chapter for water defluoridation with their various pros and cons, only a few of them had been successfully scaled up to the real field water defluoridation applications. Over the last decade, nanomaterials due to their minuscule size have become the subject of extensive interest amongst the scientists across the world and are emerging as commercialized commodities due to their wide-range applications. A nanometre

might be represented by the length of ten hydrogen atoms lined up in a row and is one billionth of a metre (10^{-9}). Materials reduced to nanoscale exhibit substantially different physical and chemical characteristics than what they usually tend to show at the microscale or bulk counterparts. However, particles at nanoscale behave differently due to the change in surface to volume ratio which leads to (i) the increase in the number of atoms present on the surface of particle as compared to the inside, (ii) the increased number of surface atoms eventually increases the surface area and (iii) with the increase in surface area, free energy associated with the surface atoms (i.e. surface energy) increases as well. As a consequence due to an increased surface energy, atoms present at the surface of nanosized particles become chemically more active and exhibit entirely different optical, electrical, mechanical and magnetic properties as compared to its macroscopic bulk (Khajeh et al. 2013). Recently, nanomaterials have gained the vast interest of scientists across the world in the form of nanosorbent systems and providing a new direction to the water treatment technologies to overcome the challenges and shortcomings associated with the use of conventional adsorbents. Due to their high porosity, small size, highly active surface, nanosorbents provide not only effective sequestration of water contaminants but also allow industrial processes to consume raw materials efficiently without discharging a toxic payload. Moreover, nanosorbents show commendably rapid adsorption of pollutant ions and exhibit excellent regeneration potential after exhaustion making the overall process more cost-effective. According to the intrinsic surface property and key constituents involved, nanosorbents in fluoride removal can be divided into three broad categories: (i) carbonaceous nanomaterials as adsorbents, (ii) metal-based nanomaterials as adsorbents and (iii) polymer based nanocomposites as adsorbents.

9.5.2.1 Carbonaceous Nanomaterials

Carbonaceous nanomaterials are exclusively made up of carbon atoms and due to their remarkably high surface area exhibit excellent adsorption potential towards water pollutants. Moreover, carbonaceous nanomaterials are intrinsically hydrophobic in nature and thus can be readily functionalized according to the target pollutant ion. Carbon nanotubes (CNTs), graphene with its derivatives, fullerenes and carbon nanofibres are some of the carbonaceous nanomaterials which have gained the massive interest of researchers due to their exceptional one-dimensional (1D) nanostructures; attractive physical, chemical and electronic properties; and remarkably high mechanical strength. Amongst the above-mentioned carbonaceous nanomaterials, carbon nanotubes (CNTs) and graphene are the ones which have been proven to be of great importance and are exclusively used in the field of water defluoridation.

CNTs are hollow cylindrical tubes of graphitic origin with a diameter of nanometre scale, and length ranged from several hundred nanometres to several micrometres (Khajeh et al. 2013). CNTs can be categorized as single-walled (SWCNTs) or multiwalled (MWCNTs) carbon nanotubes depending on the number

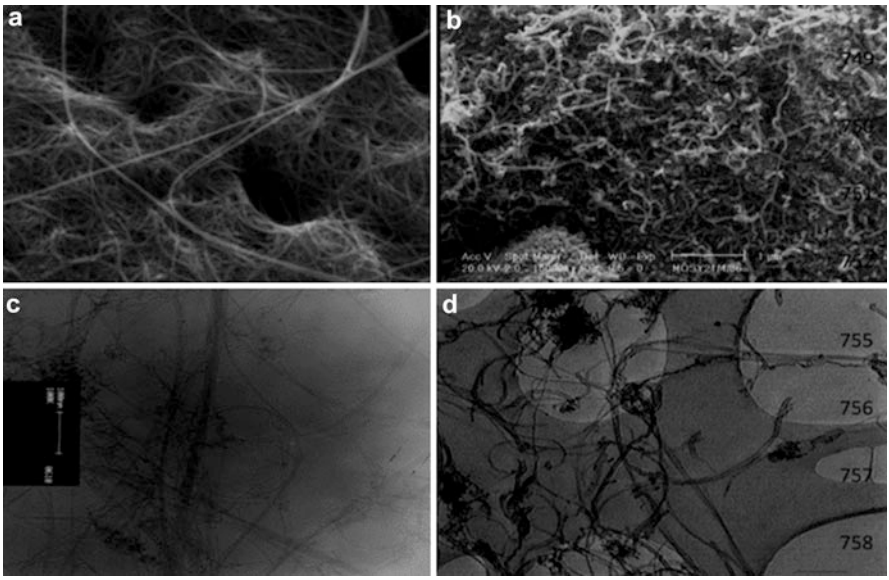

Fig. 9.8 SEM micrographs of (**a**) SWCNTs and (**b**) MWCNTs and TEM micrographs of (**c**) SWCNTs and (**d**) MWCNTs. (Reprinted from Dehghani et al. 2016)

of graphene layers present in the CNTs. Dehghani et al. used high specific surface area CNTs (SWCNTs-700 and MWCNTs-270 m^2/g) porous tubular morphology (Fig. 9.8), for fluoride adsorption from aqueous solution, and obtained maximum F^- uptake of 2.83 mg/g and 2.4 mg/g, for SWCNTs and MWCNTs, respectively (Dehghani et al. 2016).

Sankararamakrishnan et al. synthesized cetyltrimethylammonium bromide (CTAB) grafted multiwalled carbon nanotubes (CGCNTs) as fluoride adsorbents and obtained fluoride uptakes of 20 mg/g (Sankararamakrishnan et al. 2013). However, fluoride adsorption showed a significant reduction (40–60%) in the presence of coexisting anions. Ruan et al. recently developed a novel composite material of hydroxyapatite (HA)-multiwalled carbon nanotubes (MWCNTs) using a simple in situ sol-gel method for fluoride adsorption and achieved maximum fluoride sorption capacity of 17.80 mg/g (Ruan et al. 2017).

Although the application of modified CNTs as an adsorbent for removing fluoride from water is still in its embryonic stage, one of the major concerns, which blocks the large-scale application of CNTs for technology development, is its expensive nature due to underlying high synthesis cost. Moreover, due to human health and safety issues, carbon nanotube toxicity has nowadays become a subject of great concern and has prompted thorough investigations to understand the aftermath of its improper disposal. It has been found that due to improper disposal, CNTs enter the biological systems of human beings either through inhalation or via food chain and can cause detrimental health effects (Dhillon et al. 2016).

Graphene as well as its derivative, i.e. graphene oxide (GO), is another class of carbonaceous materials which exhibits sp^2 hybridized two-dimensional (2D) structure and is well established as an effective nanosorbent in wastewater treatment due to its exceptionally high surface area (~2630 m^2/g) (~100 to 1000 m^2/g), presence of plentiful oxygen-rich functional groups (carboxylic, carbonyl, hydroxyl and epoxy), high thermal conductivity and excellent charge carrier mobility (Suriyaraj and Selvakumar 2016; Dhillon et al. 2016). However, due to inherent hydrophilic nature, GO cannot be collected readily from its aqueous solution which restricts its direct application as an adsorbent. Hence, Li et al. fabricated a hybrid material by coating graphene oxide (GO) with manganese oxide and the developed hybrid materials which when applied as fluoride adsorbents demonstrated a Langmuir sorption capacity of 11.93 mg/g which was 8.34 times higher than that of bare GO (1.43 mg/g) (Li et al. 2011, 2013). Later on, Barathi et al. continued exploring modified GO composites hybrid materials as fluoride adsorbents and synthesized an aluminium oxyhydroxide (AlO(OH)) modified GO composite that displayed a considerably high F^- sorption capacity of 51.42 mg/g (Barathi et al. 2014). Furthermore, Kanrar et al. incorporated iron-aluminium mixed oxide into the support matrix of GO, used the as-synthesized composite for fluoride removal studies and obtained a F^- sorption capacity of 27.8 mg/g (Kanrar et al. 2016). Recently, magnetic separation techniques have gained much attention among researchers due to their preferential advantages over the conventional separation methods. Therefore, nowadays, research is primarily focussed on the development of magnetic adsorbents which can be easily separated from the aqueous phase with the help of an external magnetic field. Liu et al. used GO as a support to anchor iron-aluminium oxide nanoparticles through a co-precipitation technique and used the fabricated magnetic adsorbent for water defluoridation (Liu et al. 2016a). GO and IAO synergistically exhibited a significantly high F^- uptake capacity (64.72 mg/g), with optimum adsorption over a considerably broader pH range (3–9), excellent stability in acidic as well as alkaline medium, superparamagnetism and selective fluoride removal in the presence of most of the coexisting ions except HPO_4^{2-}. Hence, it was concluded that the application of iron-aluminium oxide nanoparticle/graphene oxide magnetic composite as a fluoride adsorbent can be effectively scaled up for technology development for water defluoridation.

Until 2015, only iron, aluminium and manganese oxides were explored to fabricate GO composite materials to be used as adsorbents for water defluoridation, but then Liu et al. developed an akageneite@GO nanocomposite by anchoring akageneite (β-FeOOH) on the support of GO via facile in situ hydrolysis of $FeCl_3$ in the presence of GO, evaluated its performance for fluoride adsorption and obtained a Langmuir F^- adsorption capacity of 17.67 mg/g (Liu et al. 2016b). Morphologically powdered β-FeOOH@rGO displayed rice-spike like nanorods compacted on GO with lengths ranged between 50 and 150 nm (Fig. 9.9). This study elucidated the importance of Cl^- ions in fluoride removal and projected a vital viewpoint of developing metal oxides with a higher content of exchangeable anions besides classical OH^-, to obtain better defluoridation results in the real field.

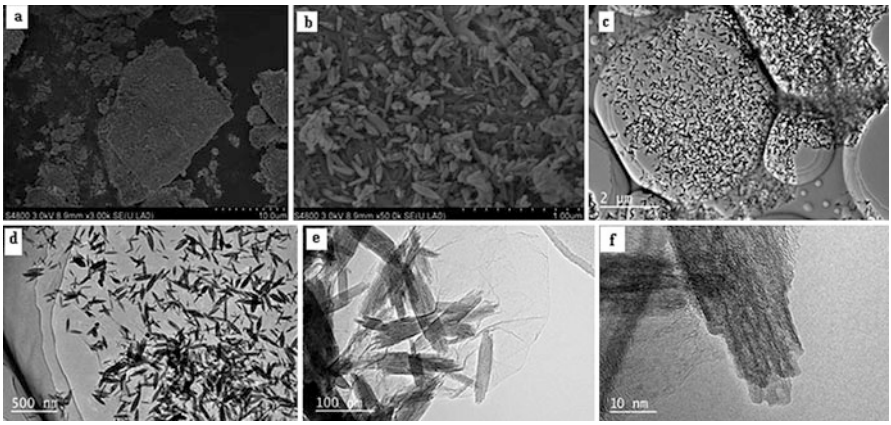

Fig. 9.9 SEM images of β-FeOOH@GO (**a**, **b**) and TEM images of β-FeOOH@GO (**c**–**f**). (Reprinted from Liu et al. 2016b)

Besides aluminium-, magnesium- and iron-modified graphene-based nanocomposites, very recently a reduced graphene oxide (rGO)- and zirconium oxide (ZrO_2)-based nanocomposite was used as a fluoride adsorbent in continuous fixed-bed column study by Mohan et al. (2017), and the maximum fluoride uptake of 45.7 mg/g was achieved. Despite various unique properties which make GO a material of great importance in the research field, most of the defluoridation studies utilizing GO adsorbents are still in the early stage and their further scale up to operate in the real field is still restricted. This is because when GO is applied to continuous flow column systems for real field applications, it undergoes excessive pressure drop. To mitigate the above drawback, Pandi et al. fabricated a composite of GO with alginate beads where GO was dispersed in the polymeric matrix of alginate cross-linked with La(III) ions (Pandi and Viswanathan 2016). Although the developed GO composite was in a usable bead form, it displayed a significantly low defluoridation capacity (6.617 mg/g) for its potential utility in the real field. Hence, concisely it can be concluded that despite being a breakthrough discovery in the field of science and technology, poor separability from aqueous solution due to hydrophilicity and excessive drop in pressure when applied to column systems are some of the drawbacks associated with graphene and its derivatives which limit their further implementation in real field water defluoridation (Barathi et al. 2014; Dhillon et al. 2016).

9.5.2.2 Metal-Based Nanomaterials

Recently, nanosized metal elements such as Fe, Al, Ti, Mg, Zr, Ce, Mn and La and their composites have become the materials of great importance in water treatment applications. However, in the field of water defluoridation, nanosized metal oxides (NMOs) have emerged as most sought after metal based nanomaterials for fluoride removal due to their high stability, excellent fluoride affinity, abundant surface

hydroxyl groups, water insolubility and great regeneration potential. Also, the higher surface area of NMOs and smaller particle size provide faster fluoride adsorption kinetics, since F^- ions experience lesser diffusion resistance and thus reach the active adsorption sites readily (Hua et al. 2012; Velazquez-Jimenez et al. 2015). Ghosh et al. used a simple co-precipitation technique and synthesized nanosized agglomerated hydrous cerium and zirconium mixed oxide with 1:1 molar ratio of Ce/Zr and obtained 19.5 mg/g fluoride adsorption capacity (Ghosh et al. 2014).

Quite recently, a very significant study was conducted by Jia et al., where γ-AlO(OH) mineral (bayerite nanocomposite) used as fluoride adsorbent demonstrated maximum F^- removal capacity of 56.80 mg/g at neutral pH (Jia et al. 2015). A facile one-pot hydrothermal method was applied to develop three-dimensional feather like bayerite/boehmite nanocomposites with nanoplate thickness of about 15–25 nm (Fig. 9.10). Fluoride was predominantly removed due to its ion exchange with surface hydroxyl groups and nitrate ions present in bayerite nanocomposite. Hence, the work presented a critical approach towards the fabrication of NMOs containing surface NO_3^- ions to be exchanged with F^- ions in addition to classical OH^- ion exchange. However, reusability of the synthesized adsorbent was still questionable because its fluoride removal efficiency dropped significantly after five regeneration cycles.

Most of these nanosized metal oxides exhibit low pH_{pzc} (point of zero charge) and hence have a delimitation of narrow working pH range. However, previous studies have revealed that pH_{pzc} of a metal oxide being a surface property can undergo marked change on doping small amounts of ions or atoms in its surface. On the same approach, Chai et al. synthesized sulphate-doped Fe_3O_4/Al_2O_3 nanoparticles which exhibited a wider fluoride-adsorbing pH range due to its exceptionally high $pH_{pzc} \approx 11.2$ as compared to most of the other fluoride adsorbents (Chai et al. 2013) reported in the literature. In addition, sulphate-doped Fe_3O_4/Al_2O_3 nanoparticles displayed a high F^- uptake capacity of 70.4 mg/g at pH 7.0 along with cost-effective and quick magnetic separation. Therefore, sulphate-doped Fe_3O_4/Al_2O_3 nanoparticles as a fluoride adsorbent was found to be potentially efficient for developing a sustainable real field water defluoridation technology. Recently, owing to the large surface area and excellent physical and chemical surface properties of nanostructured adsorbents, considerable efforts have been made towards the fabrication of metal oxide hollow nanospheres. Porous alumina hollow nanospheres fabricated by Zhang et al. via a simple hydrothermal method demonstrated a F^- adsorption capacity of 16.77 mg/g at neutral pH, and the residual concentration of aluminium in treated water was found to be quite low ≈0.16 mg/L (Zhang and Jia 2016).

More recently, Kang et al. fabricated cactus like amorphous alumina (CA-AlOx) microspheres of diameter ~40 μm (Fig. 9.11) by means of a facile solvothermal method without the use of template or surfactant (Kang et al. 2018). The amorphous nature of aluminium oxide phase was well depicted through XRD spectra (Fig. 9.11b) with no obvious crystallization peaks. Moreover, maximum fluoride adsorption capacity of 129.4 mg/g was obtained along with good recyclability and much better real field applicability as compared to other literature-reported alumina-based fluoride adsorbents. Various MgO nanomaterials were also developed to

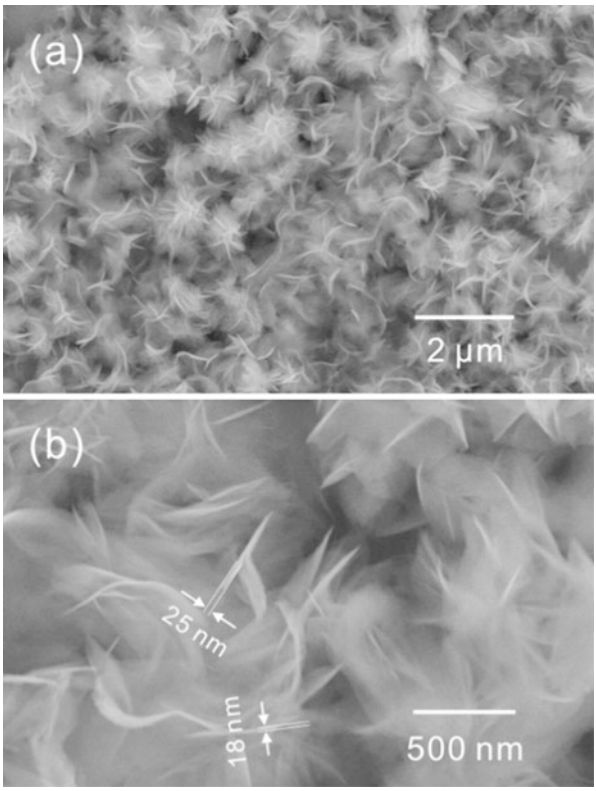

Fig. 9.10 SEM images of the feather-like bayerite/boehmite nanocomposites. (Reprinted from Jia et al. 2015)

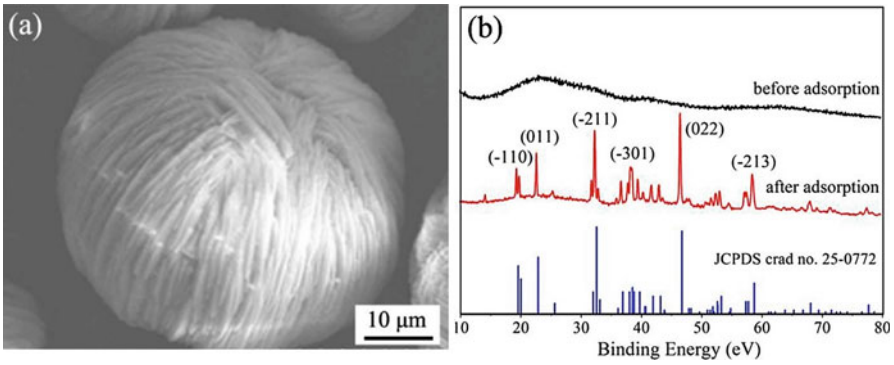

Fig. 9.11 (**a**) SEM image and (**b**) XRD patterns of CA-AlOx microspheres. (Reprinted from Kang et al. 2018)

achieve superior fluoride adsorption capacity as compared to macroscopic MgO particles (Nagappa and Chandrappa 2007; Maliyekkal et al. 2010). Li et al. developed higher surface area (≈130 m^2/g) porous and hollow MgO microspheres

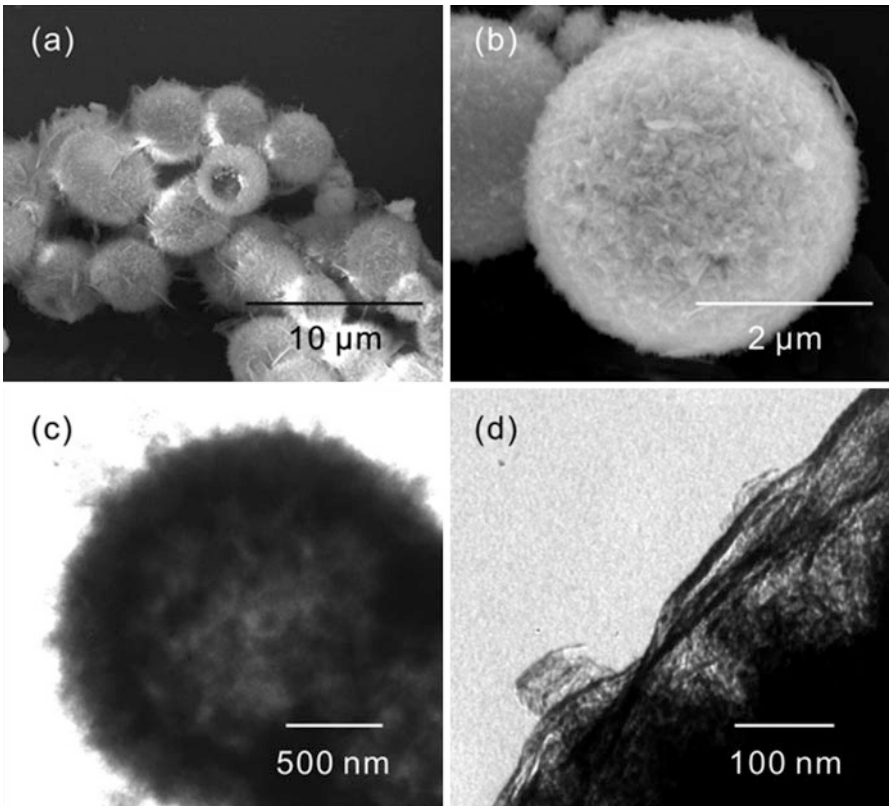

Fig. 9.12 (**a**, **b**) SEM and (**c**, **d**) TEM images of the obtained porous and hollow MgO microspheres. (Reprinted from Li et al. 2014)

consisting MgO nanoparticles (Fig. 9.12) and obtained a defluoridation capacity of 120 mg/g (Li et al. 2014).

Although nanosized MgO displayed great fluoride adsorption properties, its ultrafine size and difficult separability from the treated water created the possibility of secondary pollution. To overcome this drawback, Jin et al. synthesized hierarchically assembled MgO microspheres in the form of porous nanoplates (Fig. 9.13) with micrometre size which demonstrated easy separation from treated water and high F^- adsorption capacity (115.5 mg/g) due to its high porosity with abundant active adsorption sites (Jin et al. 2015). Besides, hierarchical MgO microspheres efficiently removed fluoride over a significantly broad pH range from 2 to 10. Although hydroxyl ion exchange is the most predominant mechanism for fluoride adsorption by MgO, in this study, for the very first time, exchange of surface CO_3^{2-} groups (formed due to the reaction of MgO with atmospheric CO_2) with fluoride ions was reported.

Owing to the high fluoride-adsorbing characteristics of zirconia (ZrO_2), Yu et al. fabricated one-dimensional mesoporous ZrO_2 fibres using electrospinning device,

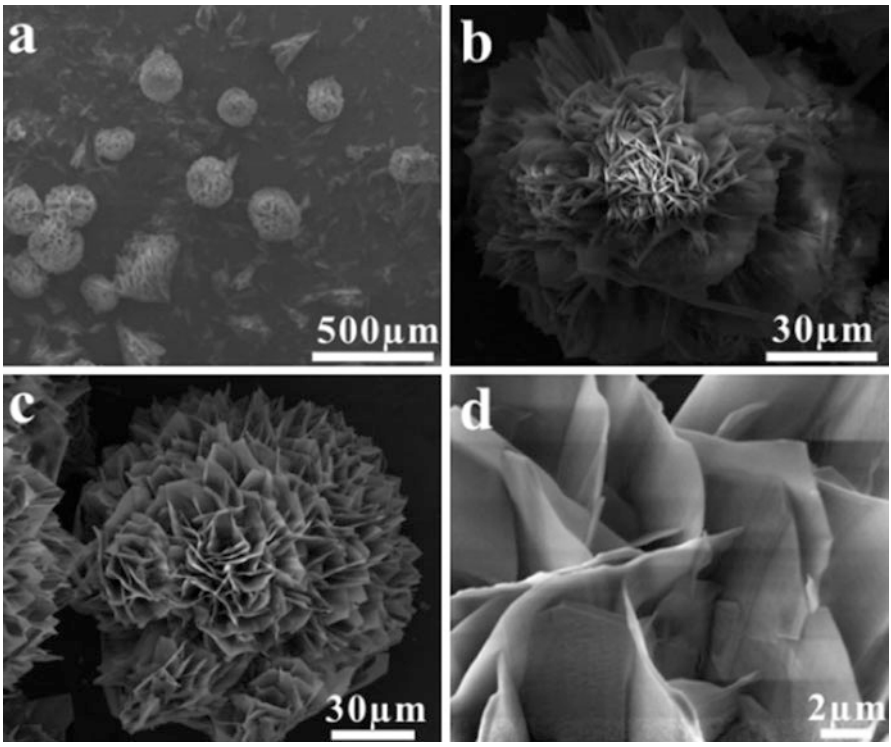

Fig. 9.13 SEM images of the hierarchical MgO microsphere precursors (**a**, **b**) and the corresponding calcined hierarchical MgO microspheres (**c**, **d**) at different magnifications. (Reprinted from Jin et al. 2015)

applied for fluoride removal from water and obtained a significantly high fluoride adsorption capacity of 297.70 mg/g (Yu et al. 2018). The morphology and EDS elemental mapping of prepared ZrO_2 fibres as depicted in Fig. 9.14 clearly demonstrated the complete fibre morphology with smooth surface and uniform distribution of Zr and O in the fibres without agglomeration.

Very recently, another group of researchers, Zhang et al., developed cerium-based uniform-sized $CeCO_3OH$ nanospheres as adsorbent and obtained high F^- removal capacity (45 mg/g) as a result of the involvement of surface OH groups as well as surface CO_3^{2-} ion exchange with F^- ions (Zhang et al. 2016). Due to the accomplishment of high fluoride adsorption efficiency even at low initial F^- concentration along with negligible hindrance due to coexisting ions, it was concluded that application of $CeCO_3OH$ nanospheres as fluoride adsorbents can be efficiently scaled up for water defluoridation technology development.

Furthermore, in the process of synthesis of micro- and nanocrystals with controlled shape and sizes, manganese carbonate ($MnCO_3$) has attracted considerable scientific attention; hence, Zhang and Jia et al. fabricated $MnCO_3$ nanowires and microcubes using controlled synthesis by a simple ethylene glycol mediation

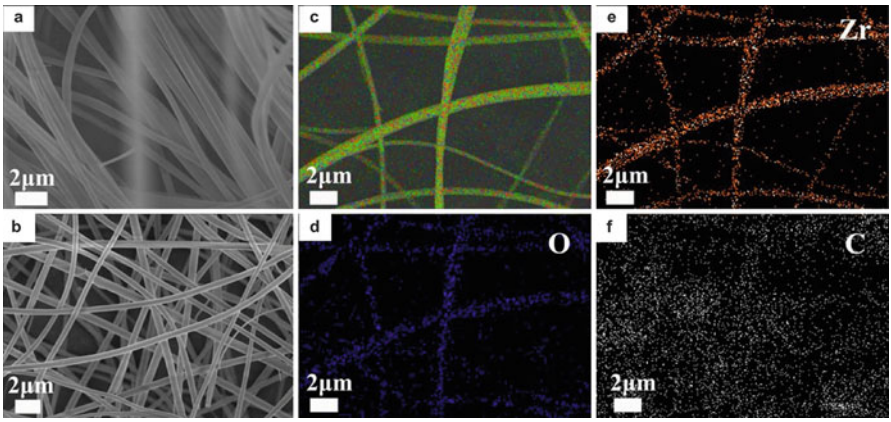

Fig. 9.14 SEM images of ZrO_2 fibres (**a**) precursor (**b**) heat treated at 350 °C and EDS mapping of (**c**) ZrO_2, (**d**) oxygen, (**e**) zirconium and (**f**) carbon. (Reprinted from Yu et al. 2018)

solution method and established the fluoride removal properties of developed $MnCO_3$ products (Zhang and Jia 2018). The maximum adsorption capacity obtained was 46.80 mg/g at pH 7.0 where fluoride adsorption was significantly affected by the presence of bicarbonate and phosphate anions. However, the fluoride removal was attributed to dual ion exchange based on surface hydroxyl groups and carbonate like groups as revealed by FTIR and XPS.

Many research groups have fabricated mixed metal oxide nanosorbents such as Fe-Ti, Ce-Zr, Ce-Fe and Al-Zr to further explore the metal oxides-based adsorbent systems for water defluoridation. Chen et al. synthesized a Fe-Ti oxide nanosorbent (Fe/Ti molar ratio 2:1) by co-precipitation, where Fe and Ti chemically bonded to each other through oxygen synergistically increased the number of surface hydroxyl groups and consequently resulted in high fluoride adsorption capacity of 47.0 mg/g (Chen et al. 2012). However, Fe-Ti oxide nanosorbent synthesis required frequent ethanol washing and microwave drying which restricted its scale up for real field applications. Recently, Wang et al. developed a hollow Fe-Al binary metal oxyhydroxide micro-box (FeAl-OOH MB) adsorbent which effectively reduced the initial F^- concentration of 10 mg/L below the standard permissible limit (<1 mg/g) and displayed a maximum F^- uptake capacity of 146.59 mg/g at optimum pH 5. Besides, Mukhopadhyay et al. synthesized a Ce(IV) incorporated hydrous ferric porous microcrystalline material as a fluoride adsorbent that demonstrated fluoride adsorption capacity of 24.8 ± 0.5 mg/g for 15 mg/L initial F^- concentration in between pH 5 and 7 (Mukhopadhyay et al. 2017). Wang et al. utilized the Kirkendall effect for the development of CeO_2-ZrO_2 nanocages to evaluate its defluoridation performance in the batch adsorption mode and obtained a notably high fluoride adsorption capacity of 175 mg/g at optimum pH 4 (Wang et al. 2013). CeO_2-ZrO_2 nanocages adsorbed fluoride optimally in the pH range of 3–7, and only slight inhibition in its fluoride removal efficiency was observed in the presence of very high concentrations of chloride and arsenate ions. However, several points need

to be assessed prior to the real field implementation of CeO_2-ZrO_2 nanocages as a fluoride adsorbent. Primarily, the adsorbent needs to be embedded in a chitosan matrix through a sol-gel method for improvised mechanical strength. Adsorbent leakage into the treated water can degrade the water quality for drinking purposes; hence leaching studies need to be conducted, and finally, the regular ethanol washing and microwave drying during the synthesis need to be sorted out to scale up its production. Markeb et al. combined the fluoride-adsorbing properties of Ce and Ti along with magnetic Fe_3O_4 nanoparticles and synthesized magnetic core-shell Ce-Ti@Fe_3O_4 nanoparticles which showed high fluoride uptake capacity of 91.04 mg/g at pH 7 and surpassed several reported fluoride adsorbents (Abo Markeb et al. 2017). Moreover, magnetic properties of Ce-Ti@Fe_3O_4 manifested add-on benefit of easy recovery of adsorbent for further reuse. Quite recently in a study reported by Chigodo et al., a series of cerium-magnesium bimetal oxides (different Ce/Mg molar ratios), prepared using simple co-precipitation technique, were applied as adsorbent in fluoride removal from water (Chigondo et al. 2018b). The ideal adsorbent with Ce/Mg molar ratio 1:1 demonstrated quite rapid adsorption kinetics with maximum fluoride adsorption capacity 66.23 mg/g.

Over the past few years, it is presumed that multi-metal mixed oxides might act as great potential key adsorbents in scavenging fluoride from fluoride-rich groundwater. However, so far detailed meticulous studies involving investigation of proper metal combinations and compositions have not been testified. In this context, Zhou et al. fabricated a layered Zr-Al-La trimetal composite for fluoride removal from water, which exhibited maximum fluoride adsorption capacity of 90.48 mg/g at pH 3.0 (Zhou et al. 2018). Adsorption mechanism investigation studies revealed that lanthanum ions (La^{3+}) primarily contributed as main active sites for fluoride adsorption. On the other hand, Thathsara et al. developed a highly efficient trimetallic fluoride adsorbent comprising Fe-La-Ce (Thathsara et al. 2018). Though fluoride adsorption was significantly hindered in the presence of bicarbonate ions, however due to high fluoride adsorption capacities of 303.03 mg/g and 161.29 mg/g at pH 4.00 and pH 7.00, respectively, and excellent regeneration potential with 96.13% desorption, Fe-La-Ce composite stands out as an excellent fluoride adsorbent.

Although NMOs have been found to provide an efficient and specific adsorption towards fluoride ions, several application limitations are associated with them due to their ultrafine microscopic particle size such as tedious separability from aqueous solution, loss of activity due to agglomeration, clogging of filter pores and unwarranted drop in pressure when used in column systems (Khajeh et al. 2013).

9.5.2.3 Polymer-Based Nanocomposites

Polymer-based nanocomposites as adsorbents are gaining more and more recognition worldwide in water treatment applications as new generation adsorbents. Nowadays, polymers are either being used as a porous matrix to implant inorganic

nanoparticles or as a template or a support system to synthesize and grow inorganic nanoparticles. In either case, polymer and inorganic nanoparticles synergistically give rise to hybrid nanocomposites with superior chemical, thermal, mechanical, and adsorption properties. One of the most beneficial aspects of incorporating nanosized metal oxides on the porous polymeric support matrices was to overcome the inability of pristine nanosized metal oxides to be used in continuous flow or plug flow-type column arrangements for water defluoridation due to severe pressure drop and poor durability. Moreover, polymeric hybrid composites exhibit better regeneration potential with excellent reusability, improved chemical stability with wide-range pH applicability, superior fluoride uptake capacities due to the synergistic presence of various functional groups (of the polymer as well as nanosized metal oxide) and surface area-enhanced manifold.

As discussed earlier amongst different types of polymers, chitosan has been identified as an excellent biopolymeric adsorbent because of abundant availability of surface amine and hydroxyl groups to serve as adsorption active sites for various water pollutants. However, being anionic in nature, it has been found to display quite low defluoridation potential on its own. In a study conducted by Prasad et al., a chitosan matrix was used as a support to embed Zr nanoparticles (synthesized from *Aloe vera*) to fabricate *Aloe vera*-mediated nano-Zr chitosan composite (CNZr) (Prasad et al. 2014). As a result, the incorporation of Zr nanoparticles into the polymer matrix of chitosan synergistically resulted in an inorganic/organic hybrid adsorbent with fluoride adsorption capacity manifold enhanced (96.58 mg/g) in comparison with raw chitosan beads (0.052 mg/g). In addition, CNZr composite also exhibited quite high regeneration potential up to ten regeneration cycles with desorption efficiency ranged from 99.10% to 96.81%.

As the defluoridation literature reveals, quite a few researchers have also attempted to improvise the fluoride adsorptive potential of aluminide through synthesizing polymeric composites of aluminide using chitosan. However, the aluminide chitosan composites demonstrated difficult separability in natural water which confined their real field implementation. Hence, Wan et al. developed a pseudo-boehmite and chitosan shell magnetic composite (γ-AlOOH @CS) to provide magnetic separation capabilities and applied the same for defluoridation of drinking water (Wan et al. 2015). γ-AlOOH @CS displayed a rapid fluoride uptake where 80% of F^- was adsorbed within first 20 min and equilibrium was attained in 60 min. Besides, maximum F^- adsorption capacity achieved was (67.5 mg/g) significantly better than most of the chitosan based adsorbents reported in the literature for fluoride removal. However, fluoride adsorption on γ-AlOOH @CS was noticeably reduced in the presence of coexisting ions in the order of $PO_4^{3-} > SO_4^{2-} > NO_3^- > Cl^-$.

Besides separation difficulties, another drawback associated with chitosan is its limited application in acidic media due to its soluble nature in most dilute mineral acids. For this purpose, Teimouri et al. successfully synthesized a series of cross-linked chitosan derivatives by varying the molar concentrations of chitosan,

Fig. 9.15 Optical microscopic picture of Fe-Zr entrapped calcium alginate. (Reprinted from Swain et al. 2013)

montmorillonite and ZrO_2 in different ratios (Teimouri et al. 2015). The optimum molar ratio of chitosan to montmorillonite/ZrO_2 was found to be 1:1, and the optimized nanocomposite demonstrated a better biocompatibility, mechanical and thermal stability as well as better fluoride adsorption capacity (23 mg/g) than its base constituents (chitosan, montmorillonite and ZrO_2). Although it was observed that cross-linking of chitosan to make chitosan derivatives can effectively overcome the problems of acidic and alkaline solubility, the involvement of amino functional groups in cross-linking makes them unavailable for adsorption which eventually results in a reduced fluoride adsorption capacity of cross-linked chitosan derivatives. Swain et al. attempted to synergistically combine the properties of alginate (an anionic biopolymer) and nanosized binary metal oxide and, in the same reference, fabricated an alginate composite material by dispersing Fe(III)/Zr(IV) binary oxide nanoparticles in the matrix of alginate biopolymer (Fig. 9.15) (Swain et al. 2013). Though developed alginate composite, when used as a fluoride adsorbent, displayed a maximum fluoride sorption capacity of 0.981 mg/g at pH 6.0 which was still far from satisfactory however, 89% desorption efficiency was achieved at pH 12 with reusability up to multiple adsorption-desorption cycles.

Later Shen et al. conducted a study in which a chitosan-Ca(II) complex was used as a calcium precursor to develop the well-dispersed monetite bundles inlaid chitosan beads (MONs@CS) as a highly efficient and cost-effective fluoride adsorbent (Shen et al. 2016). Different from the direct mixing of chitosan and metal oxides, MONs@CS was found to be a highly dispersive heterogeneous metal material due to excellent anchoring of calcium in chitosan polymer and hence demonstrated as well as maintained a high maximum adsorption capacity of 50.01 mg/g in a wide pH range of 3–12 unlike other chitosan-based composites. However, recently, to further improve the defluoridation capacity of chitosan-based adsorbents along with easy separation, Hu et al. fabricated novel magnetic beads

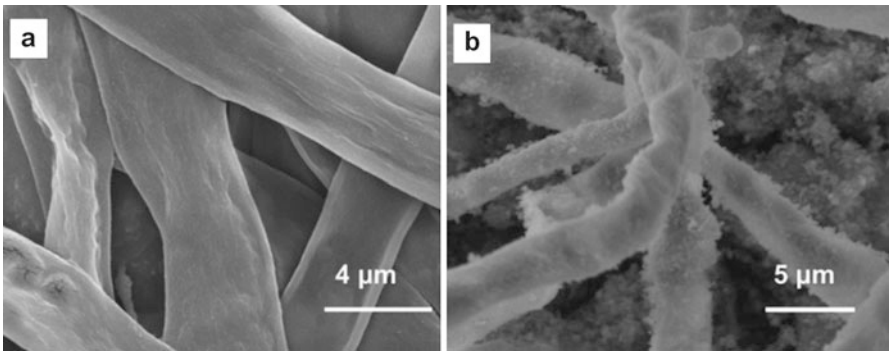

Fig. 9.16 SEM images of (**a**) pure fungus hyphae and (**b**) fungus hyphae-supported alumina. (Reprinted from Yang et al. 2017)

(Fe_3O_4/CS/$Al(OH)_3$) composed of Fe_3O_4, chitosan and $Al(OH)_3$ (Hu et al. 2018). Though Langmuir maximum adsorption capacity obtained was substantially high, 76.63 mg/g, the developed adsorbent displayed poor selectivity in the presence of coexisting anions.

Furthermore, Yang et al. constructed a bio-nanocomposite for water defluoridation by coating nano-alumina on the support matrix of filamentous fungal hyphae (Fig. 9.16) (Yang et al. 2017). The developed biocomposite demonstrated F^- removal capacity (105.60 mg/g) much higher than pristine alumina nanoparticles (50.55 mg/g) and bare fungal hyphae (22.47 mg/g). The enhanced fluoride uptake demonstrated by hybrid biocomposite is attributed to the increased active surface area of nano-alumina coated along fungal hyphae matrix as well as abundant functional groups (−OH, $-NH_2$ and CO) present on the surface of fungal hyphae. Moreover, the developed biocomposite was easily retrievable from water due to microscopic and macroscopic characteristics of filamentous fungal hyphae.

Later, Bhaumik et al. fabricated a magnetic nanocomposite by incorporating iron (III) oxide (Fe_3O_4) nanoparticles into the polymer backbone of PPy and evaluated its fluoride-adsorbing potential (Bhaumik et al. 2011). TEM images of the PPy/Fe_3O_4 nanocomposite demonstrated Fe_3O_4 nanoparticles embedded in the PPy matrix forming a core-shell structure (Fig. 9.17) which displayed significantly enhanced F^- uptake capacity (17.63 mg/g) as compared to unmodified PPy and pristine Fe_3O_4 nanoparticles. Moreover, the magnetic nanocomposite performed well in the presence of coexisting ions and displayed 97% desorption efficiency at pH 12. However, the developed nanocomposite still needs to be evaluated on various other parameters prior to its scale up for real field implementation.

Quite recently, Parashar et al. fabricated a series of polypyrrole/hydrous tin oxide nanocomposites (PPy/HSnO NC 1, 2, 3, 4 and 5) through encapsulating hydrous tin oxide (HSnO) nanoparticles by the growing PPy moieties via an in situ polymerization technique and tested its efficiency as fluoride adsorbent for the first time

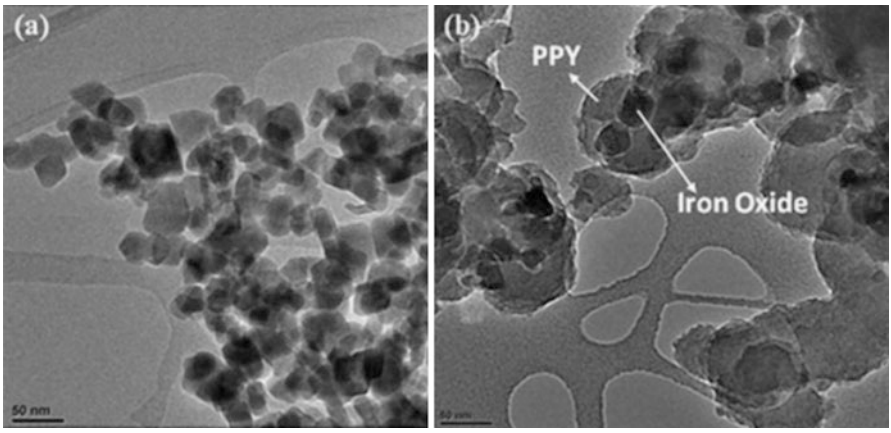

Fig. 9.17 TEM images of (**a**) Fe_3O_4 nanoparticles and (**b**) PPy/Fe_3O_4 nanocomposite. (Reprinted from Bhaumik et al. 2011)

(Parashar et al. 2016a). The optimized adsorbent, i.e. PPy/HSnO NC 3, demonstrated rapid fluoride uptake with maximum adsorption capacity of 26.16 mg/g at pH 6.5 ± 0.1. Moreover, the adsorbent performed very well over a considerably wide pH range of 3.5–8.5 and in the presence of other coexisting ions. However, due to the encouraging results obtained in this study, the same authors further explored and improvised the fluoride removing properties of PPy-based nanocomposites by incorporating hydrous titanium oxide $HTiO_2$ nanoparticles into the PPy matrix (Parashar et al. 2016b). A relatively high specific surface area (98.17 m^2/g) and pH_{pzc} (~8.4) of $HTiO_2$@PPy nanocomposites resulted in its superior fluoride adsorptive properties with maximum adsorption capacity of 31.93 mg/g at pH 6.5 (±0.2).

Furthermore, the same group of authors developed a hybrid material ($HZrO_2$@PANI NFs) comprising one-dimensional PANI nanofibres as support matrix for $HZrO_2$ nanoparticles (Fig. 9.18) and used the same as a fluoride adsorbent (Parashar et al. 2017). The developed hybrid nanocomposite demonstrated a fluoride uptake capacity of 83.23 and 28.77 mg/g at pH 3 and 6.5, respectively, which is superior to most ZrO_2- and PANI-based adsorbents reported in the literature. Additionally, $HZrO_2$@PANI NFs was found to be effective over a wide pH range (3–9) as designated by its high pH_{pzc} ~9.8. Later Rahman and Nasir fabricated Zr(IV)-doped polypyrrole/zirconium (IV) iodate composite for fluoride removal and obtained a fluoride adsorption capacity of 183.5 mg/g at pH 6.8 (Rahman and Nasir 2017). Quite recently, Chigondo et al. fabricated hydrous CeO_2-Fe_2O_3 (HCeFe)-decorated PANI NFs as a novel nanofibrous fluoride adsorbent and obtained a high maximum adsorption capacity of 116.28 mg/g at pH 6.0 ± 0.2 (Chigondo et al. 2018a).

Nevertheless, the application of nanosized metal oxides and conducting polymer (PPy and PANI)-based nanocomposites for fluoride removal is still in the nascent

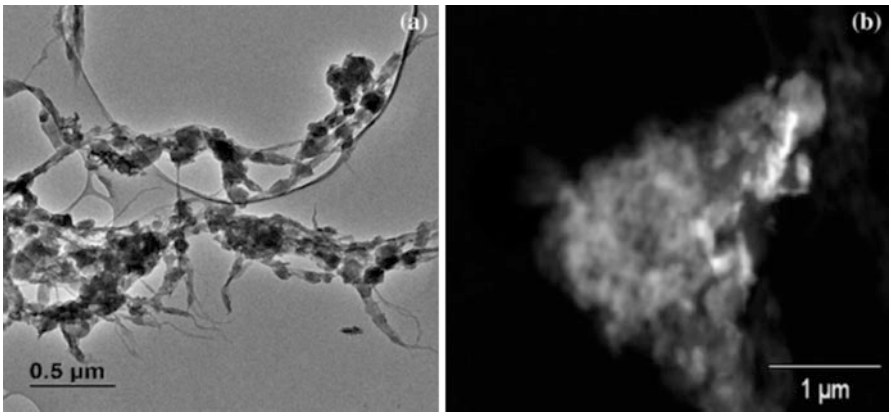

Fig. 9.18 (**a**) TEM and (**b**) STEM images of $HZrO_2$@PANI NFs. (Reprinted from Parashar et al. 2017)

stage and needs further research to thoroughly assess their durability, selectivity, reusability and cost-effectiveness through fixed-bed column dynamic system for the water defluoridation technology development.

9.6 Conclusion and Future Perspectives

Fluoride is omnipresent in the earth's ecosystem, and its concentration usually varies according to the geographical location. Excessive fluoride in drinking water is becoming a subject of leading concern especially for the human population residing in regions where fluoride occurrence exceeds standard allowable limits (1.5 mg/L) has been reported in public water supplies. The primary source of intake of fluoride is fresh groundwater, and hence consumption of groundwater with high fluoride concentrations has been explicitly recognized as the chief contributor for endemic fluorosis and debilitating disease fluorosis. Hence it has become mandatory to alleviate excess fluoride present in drinking water resources. Amongst the different defluoridation technologies, adsorption is the most sought after due to its ease of handling, the simplicity of design, environment-friendly nature and economic viability for most of the population relying on groundwater sources. Although a number of conventional adsorbents had been developed so far as discussed in this chapter for water defluoridation with their various pros and cons, only a few of them have been successfully scaled up to the real field water defluoridation applications. Over the past few years, nanomaterials due to their minuscule size have been the subject of substantial research interest for their widespread applications including water treatment, and therefore recently various nanosorbents have emerged as a potential

material for water defluoridation technology development. The following concluding observations are presented by the literature reviewed for the recent advances in nanotechnology-based adsorptive removal of fluoride from water:

- Among the available carbonaceous nanomaterials, CNTs have shown good defluoridation potential up to some extent, but the high cost of synthesis restricts its application on a larger scale; however, cheaper methods of synthesis are currently under exploration. Additionally, CNTs being toxic in nature have also drawn considerable attention regarding their detrimental health effects. The other class of carbonaceous nanomaterials, i.e. GO, is also associated with a disadvantage of excessive pressure drop when applied to column systems, which blocks its scale up for real field application. To overcome these issues, composites of GO were developed with different inorganic or organic materials and successfully applied to water defluoridation. However, real field implementations of GO composites in column operations and/or pilot-scale studies still need to be explored.
- Among the metallic nanomaterials, nanosized metal oxides are widely explored as highly efficient fluoride adsorbents. They exhibit various advantages such as fast kinetics and commendably high adsorption capacities. Nevertheless, some technical bottlenecks associated with the use of nanosized metal oxides need to be resolved, prior to their practical application in water defluoridation. For instance, when applied in aqueous solution, NMOs tend to aggregate into large-size particles which result in loss of their adsorption capacity. Additionally due to their fine particle size, they clog the filter pores, and thus the efficient separation of the exhausted NMOs from aqueous solution remains a challenging mission. Moreover, when applied to the column, they cause excessive pressure drops.
- Polymer-based nanocomposites are the new-generation adsorbents, which involve the impregnation or coating of inorganic nanomaterials either into or onto the polymer matrix to mutually and synergistically combine the properties of both polymer and inorganic nanoparticles. Fortuitously, the fabrication of new nanosized metal oxide-based nanocomposites seems to be an effective approach in mitigating all the above technical problems associated with the use of pure polymers or nanosized metal oxides. However, the use of nanosized metal oxides and polymer-based nanocomposites is still in the infant stage, and further research is required to prolong the life or regeneration of NCs to make them truly sustainable for successive adsorption cycles without much loss in their original defluoridation efficiency.

Although the in-depth analysis through the defluoridation research annals shows that application of nanosorbents for the fluoride mitigation from water is increasing at a tremendous rate, there are still several loopholes that need to be addressed such as evaluation of their efficiency in real water samples, regeneration studies and continuous flow studies. Despite the various challenges that currently exist with the implementation of nanotechnology in water defluoridation, it is envisioned that nanomaterials will become a critical component of public water treatment.

References

Abo Markeb A, Alonso A, Sánchez A, Font X (2017) Adsorption process of fluoride from drinking water with magnetic core-shell Ce-Ti@Fe_3O_4 and Ce-Ti oxide nanoparticles. Sci Total Environ 598:949–958

Amini M, Mueller K, Abbaspour KC et al (2008) Statistical modeling of global geogenic fluoride contamination in groundwaters. Environ Sci Technol 42:3662–3668

Angelina Thanga Ajisha M, Rajagopal K (2015) Fluoride removal study using pyrolyzed *Delonix regia* pod, an unconventional adsorbent. Int J Environ Sci Technol 12:223–236

Ayoob S, Gupta AK, Bhat VT (2008) A conceptual overview on sustainable technologies for the defluoridation of drinking water. Crit Rev Environ Sci Technol 38:401–470

Babaeivelni K, Khodadoust AP (2013) Adsorption of fluoride onto crystalline titanium dioxide: effect of pH, ionic strength, and co-existing ions. J Colloid Interface Sci 394:419–427

Barathi M, Santhana Krishna Kumar A, Kumar CU, Rajesh N (2014) Graphene oxide-aluminium oxyhydroxide interaction and its application for the effective adsorption of fluoride. RSC Adv 4:53711–53721

Bhatnagar A, Kumar E, Sillanpää M (2011) Fluoride removal from water by adsorption-A review. Chem Eng J 171:811–840

Bhaumik M, Leswifi TY, Maity A et al (2011) Removal of fluoride from aqueous solution by polypyrrole/Fe_3O_4 magnetic nanocomposite. J Hazard Mater 186:150–159

Biswas K, Gupta K, Goswami A, Ghosh UC (2010) Fluoride removal efficiency from aqueous solution by synthetic iron(III)-aluminum(III)-chromium(III) ternary mixed oxide. Desalination 255:44–51

Cai H, Chen G, Peng C et al (2015) Removal of fluoride from drinking water using tea waste loaded with Al/Fe oxides: a novel, safe and efficient biosorbent. Appl Surf Sci 328:34–44

Cai H, Xu L, Chen G et al (2016) Removal of fluoride from drinking water using modified ultrafine tea powder processed using a ball-mill. Appl Surf Sci 375:74–84

Chai L, Wang Y, Zhao N et al (2013) Sulfate-doped Fe_3O_4/Al_2O_3 nanoparticles as a novel adsorbent for fluoride removal from drinking water. Water Res 47:4040–4049

Chakrabortty S, Roy M, Pal P (2013) Removal of fluoride from contaminated groundwater by cross flow nanofiltration: transport modeling and economic evaluation. Desalination 313:115–124

Chaudhary V, Prasad S (2015) Rapid removal of fluoride from aqueous media using activated dolomite. Anal Methods 7:8304–8314

Chen L, He B, He S et al (2012) Fe-Ti oxide nano-adsorbent synthesized by co-precipitation for fluoride removal from drinking water and its adsorption mechanism. Powder Technol 227:3–8

Chen L, Zhang KS, He JY et al (2016) Enhanced fluoride removal from water by sulfate-doped hydroxyapatite hierarchical hollow microspheres. Chem Eng J 285:616–624

Cheng J, Meng X, Jing C, Hao J (2014) La^{3+}-modified activated alumina for fluoride removal from water. J Hazard Mater 278:343–349

Chidambaram S, Manikandan S, Ramanathan A et al (2013) A study on the defluoridation in water by using natural soil. Appl Water Sci 3:741–751

Chigondo M, Kamdem Paumo H, Bhaumik M et al (2018a) Hydrous CeO_2-Fe_3O_4 decorated polyaniline fibers nanocomposite for effective defluoridation of drinking water. J Colloid Interface Sci 532:500–516

Chigondo M, Paumo HK, Bhaumik M et al (2018b) Rapid high adsorption performance of hydrous cerium-magnesium oxides for removal of fluoride from water. J Mol Liq 265:496–509

Dehghani MH, Haghighat GA, Yetilmezsoy K et al (2016) Adsorptive removal of fluoride from aqueous solution using single- and multi-walled carbon nanotubes. J Mol Liq 216:401–410

Dhillon A, Prasad S, Kumar D (2016) Recent advances and spectroscopic perspectives in fluoride removal. Appl Spectrosc Rev 4928:1–56

Dou X, Zhang Y, Wang H et al (2011) Performance of granular zirconium-iron oxide in the removal of fluoride from drinking water. Water Res 45:3571–3578

Dou X, Mohan D, Pittman CU, Yang S (2012) Remediating fluoride from water using hydrous zirconium oxide. Chem Eng J 198–199:236–245
Elazhar F, Tahaikt M, Achatei A et al (2009) Economical evaluation of the fluoride removal by nanofiltration. Desalination 249:154–157
Elazhar F, Tahaikt M, Zouahri A et al (2013) Defluoridation of Moroccan groundwater by nanofiltration and electrodialysis: performances and cost comparison. World Appl Sci J 22:844–850
Ergun E, Tor A, Cengeloglu Y, Kocak I (2008) Electrodialytic removal of fluoride from water: effects of process parameters and accompanying anions. Sep Purif Technol 64:147–153
Fordyce FM, Survey BG (2011) Fluorine: human health risks. pp 776–785
Gao S, Sun R, Wei Z et al (2009) Size-dependent defluoridation properties of synthetic hydroxyapatite. J Fluor Chem 130:550–556
García MG, Borgnino L (2015) Chapter 1. Fluoride in the context of the environment. pp 3–21
García-Sánchez JJ, Solache-Ríos M, Martínez-Miranda V, Solís Morelos C (2013) Removal of fluoride ions from drinking water and fluoride solutions by aluminum modified iron oxides in a column system. J Colloid Interface Sci 407:410–415
Ghosh A, Chakrabarti S, Biswas K, Ghosh UC (2014) Agglomerated nanoparticles of hydrous Ce (IV) + Zr(IV) mixed oxide: preparation, characterization and physicochemical aspects on fluoride adsorption. Appl Surf Sci 307:665–676
Gogoi S, Dutta RK (2016) Fluoride removal by hydrothermally modified limestone powder using phosphoric acid. J Environ Chem Eng 4:1040–1049
Hu H, Yang L, Lin Z et al (2018) Preparation and characterization of novel magnetic Fe_3O_4/chitosan/$Al(OH)_3$ beads and its adsorption for fluoride. Int J Biol Macromol 114:256–262
Hua M, Zhang S, Pan B et al (2012) Heavy metal removal from water/wastewater by nanosized metal oxides: a review. J Hazard Mater 211–212:317–331
Huang CJ, Liu JC (1999) Precipitate flotation of fluoride-containing wastewater from a semiconductor manufacturer. Water Res 33:3403–3412
Huang J, Virji S, Weiller BH, Kaner RB (2003) Polyaniline nanofibers: facile synthesis and chemical sensors. J Am Chem Soc 125:314–315
Iriel A, Bruneel SP, Schenone N, Fernández A (2018) The removal of fluoride from aqueous solution by a lateritic soil adsorption: kinetic and equilibrium studies. Ecotoxicol Environ Saf 149:166–172
Islam M, Patel RK (2007) Evaluation of removal efficiency of fluoride from aqueous solution using quick lime. J Hazard Mater 143:303–310
Jadhav SV, Gadipelly CR, Marathe KV, Rathod VK (2014) Treatment of fluoride concentrates from membrane unit using salt solutions. J Water Process Eng 2:31–36
Jadhav SV, Bringas E, Yadav GD et al (2015) Arsenic and fluoride contaminated groundwaters: a review of current technologies for contaminants removal. J Environ Manag 162:306–325
Jagtap S, Yenkie MK, Labhsetwar N, Rayalu S (2012) Fluoride in drinking water and defluoridation of water. Chem Rev 112:2454–2466
Jia Y, Zhu BS, Jin Z et al (2015) Fluoride removal mechanism of bayerite/boehmite nanocomposites: roles of the surface hydroxyl groups and the nitrate anions. J Colloid Interface Sci 440:60–67
Jin Z, Jia Y, Luo T et al (2015) Efficient removal of fluoride by hierarchical MgO microspheres: performance and mechanism study. Appl Surf Sci 357:1080–1088
Kang D, Yu X, Ge M et al (2018) Insights into adsorption mechanism for fluoride on cactus-like amorphous alumina oxide microspheres. Chem Eng J 345:252–259
Kanrar S, Debnath S, De P et al (2016) Preparation, characterization and evaluation of fluoride adsorption efficiency from water of iron-aluminium oxide-graphene oxide composite material. Chem Eng J 306:269–279
Karthikeyan M, Satheesh Kumar KK, Elango KP (2009a) Conducting polymer/alumina composites as viable adsorbents for the removal of fluoride ions from aqueous solution. J Fluor Chem 130:894–901

Karthikeyan M, Satheeshkumar KK, Elango KP (2009b) Removal of fluoride ions from aqueous solution by conducting polypyrrole. J Hazard Mater 167:300–305
Karthikeyan M, Satheeshkumar KK, Elango KP (2009c) Defluoridation of water via doping of polyanilines. J Hazard Mater 163:1026–1032
Kavitha B, Siva Kumar K, Narsimlu N (2013) Synthesis and characterization of polyaniline nanofibers. Indian J Pure Appl Phys 51:207–209
Kaygusuz H, Çoşkunırmak MH, Kahya N, Erim FB (2015) Aluminum alginate–montmorillonite composite beads for defluoridation of water. Water Air Soil Pollut 226:2257
Khajeh M, Laurent S, Dastafkan K (2013) Nanoadsorbents: classification, preparation, and applications (with emphasis on aqueous media). Chem Rev 113:7728–7768
Ku Y, Chiou H-M, Wang W (2002) The removal of fluoride ion from aqueous solution by a cation synthetic resin. Sep Sci Technol 37:89–103
Labastida I, Armienta MA, Beltrán M et al (2017) Limestone as a sustainable remediation option for water contaminated with fluoride. J Geochem Explor 183:206–213
Lewandowska A, Falkowska L, Jóźwik J (2013) Factors determining the fluctuation of fluoride concentrations in PM10 aerosols in the urbanized coastal area of the Baltic Sea (Gdynia, Poland). Environ Sci Pollut Res 20:6109–6118
Li Y, Zhang P, Du Q et al (2011) Adsorption of fluoride from aqueous solution by graphene. J Colloid Interface Sci 363:348–354
Li Y, Du Q, Wang J et al (2013) Defluoridation from aqueous solution by manganese oxide coated graphene oxide. J Fluor Chem 148:67–73
Li L-X, Xu D, Li X-Q et al (2014) Excellent fluoride removal properties of porous hollow MgO microspheres. New J Chem 38:5445–5452
Liang W, Couperthwaite SJ, Kaur G et al (2014) Effect of strong acids on red mud structural and fluoride adsorption properties. J Colloid Interface Sci 423:158–165
Liu R, Gong W, Lan H et al (2011) Defluoridation by freshly prepared aluminum hydroxides. Chem Eng J 175:144–149
Liu J, Li W, Liu Y et al (2014) Titanium (IV) hydrate based on chitosan template for defluoridation from aqueous solution. Appl Surf Sci 293:46–54
Liu L, Cui Z, Ma Q et al (2016a) One-step synthesis of magnetic iron-aluminum oxide/graphene oxide nanoparticles as a selective adsorbent for fluoride removal from aqueous solution. RSC Adv 6:10783–10791
Liu Y, Lv J, Jin W, Zhao Y (2016b) Defluoridation by rice spike-like akaganeite anchored graphene oxide. RSC Adv 6:11240–11249
Loganathan P, Vigneswaran S, Kandasamy J, Naidu R (2013) Defluoridation of drinking water using adsorption processes. J Hazard Mater 248–249:1–19
Malaisamy R, Talla-Nwafo A, Jones KL (2011) Polyelectrolyte modification of nanofiltration membrane for selective removal of monovalent anions. Sep Purif Technol 77:367–374
Maliyekkal SM, Shukla S, Philip L, Nambi IM (2008) Enhanced fluoride removal from drinking water by magnesia-amended activated alumina granules. Chem Eng J 140:183–192
Maliyekkal SM, Anshup, Antony KR, Pradeep T (2010) High yield combustion synthesis of nanomagnesia and its application for fluoride removal. Sci Total Environ 408:2273–2282
Mandinic Z, Curcic M, Antonijevic B et al (2010) Fluoride in drinking water and dental fluorosis. Sci Total Environ 408:3507–3512
Meenakshi, Maheshwari RC (2006) Fluoride in drinking water and its removal. J Hazard Mater 137:456–463
Menkouchi Sahli MA, Annouar S, Tahaikt M et al (2007) Fluoride removal for underground brackish water by adsorption on the natural chitosan and by electrodialysis. Desalination 212:37–45
Mohan S, Singh DK, Kumar V, Hasan SH (2017) Effective removal of Fluoride ions by rGO/ZrO_2 nanocomposite from aqueous solution: fixed bed column adsorption modelling and its adsorption mechanism. J Fluor Chem 194:40–50

Mohapatra M, Anand S, Mishra BK et al (2009) Review of fluoride removal from drinking water. J Environ Manag 91:67–77

Mondal P, George S (2015) A review on adsorbents used for defluoridation of drinking water. Rev Environ Sci Biotechnol 14:195–210

Mukhopadhyay K, Ghosh A, Das SK et al (2017) Synthesis and characterisation of cerium(iv)-incorporated hydrous iron(iii) oxide as an adsorbent for fluoride removal from water. RSC Adv 7:26037–26051

Mullick A, Neogi S (2018) Acoustic cavitation induced synthesis of zirconium impregnated activated carbon for effective fluoride scavenging from water by adsorption. Ultrason Sonochem 45:65–77

Mumtaz N, Pandey G, Labhasetwar PK (2015) Global fluoride occurrence, available technologies for fluoride removal, and electrolytic defluoridation: a review. Crit Rev Environ Sci Technol 45:2357–2389

Muthu Prabhu S, Meenakshi S (2014) Enriched fluoride sorption using chitosan supported mixed metal oxides beads: synthesis, characterization and mechanism. J Water Process Eng 2:96–104

Naga Babu A, Reddy DS, Kumar GS et al (2018) Removal of lead and fluoride from contaminated water using exhausted coffee grounds based bio-sorbent. J Environ Manag 218:602–612

Nagappa B, Chandrappa GT (2007) Mesoporous nanocrystalline magnesium oxide for environmental remediation. Microporous Mesoporous Mater 106:212–218

Nasr Ben A, Charcosset C, Amar Ben R, Walha K (2013) Defluoridation of water by nanofiltration. J Fluor Chem 150:92–97

Ncube EJ, Schutte CF (2005) The occurrence of fluoride in South African groundwater: a water quality and health problem. Water SA 31:35–40

Ndiaye PI, Moulin P, Dominguez L et al (2005) Removal of fluoride from electronic industrial effluentby RO membrane separation. Desalination 173:25–32

Pan B, Xu J, Wu B et al (2013) Enhanced removal of fluoride by polystyrene anion exchanger supported hydrous zirconium oxide nanoparticles. Environ Sci Technol 47:9347–9354

Pandi K, Viswanathan N (2016) A facile synthesis of metal ion-imprinted graphene oxide/alginate hybrid biopolymeric beads for enhanced fluoride sorption. RSC Adv 6:75905–75915

Parashar K, Ballav N, Debnath S et al (2016a) Rapid and efficient removal of fluoride ions from aqueous solution using a polypyrrole coated hydrous tin oxide nanocomposite. J Colloid Interface Sci 476:103–118

Parashar K, Ballav N, Debnath S et al (2016b) Hydrous TiO_2@polypyrrole hybrid nanocomposite as an efficient selective scavenger for the defluoridation of drinking water. RSC Adv 6:99482–99495

Parashar K, Ballav N, Debnath S et al (2017) Hydrous ZrO_2 decorated polyaniline nanofibres: synthesis, characterization and application as an efficient adsorbent for water defluoridation. J Colloid Interface Sci 508:342–358

Paudyal H, Pangeni B, Inoue K et al (2013) Adsorptive removal of trace concentration of fluoride ion from water by using dried orange juice residue. Chem Eng J 223:844–853

Poonam M, Suja G, Dhiraj M (2014) Use of calcite for defluoridation of drinking water in acidic medium. Res J Chem Sci 4:62–65

Prabhu SM, Subaramanian M, Meenakshi S (2016) A simple one-pot in-situ method for the synthesis of aluminum and lanthanum binary oxyhydroxides in chitosan template towards defluoridation of water. Chem Eng J 283:1081–1089

Prasad KS, Amin Y, Selvaraj K (2014) Defluoridation using biomimetically synthesized nano zirconium chitosan composite: kinetic and equilibrium studies. J Hazard Mater 276:232–240

Qiusheng Z, Xiaoyan L, Jin Q et al (2015) Porous zirconium alginate beads adsorbent for fluoride adsorption from aqueous solutions. RSC Adv 5:2100–2112

Rafigue A, Awan MA, Wasti A et al (2013) Removal of fluoride from drinking water using modifed immobilized activated alumina. J Chem 2013:7

Rahman N, Nasir M (2017) Development of Zr(IV)-doped polypyrrole/zirconium (IV) iodate composite for efficient removal of fluoride from water environment. J Water Process Eng 19:172–184

Ravichandran R, Sundarrajan S, Venugopal JR et al (2010) Applications of conducting polymers and their issues in biomedical engineering. J R Soc Interface 7:S559–S579

Ruan Z, Tian Y, Ruan J et al (2017) Synthesis of hydroxyapatite/multi-walled carbon nanotubes for the removal of fluoride ions from solution. Appl Surf Sci 412:578–590

Saha I, Ghosh A, Nandi D et al (2015) β-Cyclodextrin modified hydrous zirconium oxide: synthesis, characterization and defluoridation performance from aqueous solution. Chem Eng J 263:220–230

Sakhare N, Lunge S, Rayalu S et al (2012) Defluoridation of water using calcium aluminate material. Chem Eng J 203:406–414

Sankararamakrishnan N, Singh N, Gupta A (2013) One pot green synthetic route for the preparation of cetyl trimethyl ammonium bromide grafted multiwalled carbon nanotubes and their application towards defluoridation. RSC Adv 3:22421–22429

Shen J, Schafer A (2014) Removal of fluoride and uranium by nanofiltration and reverse osmosis: a review. Chemosphere 117:679–691

Shen C, Wu L, Chen Y et al (2016) Efficient removal of fluoride from drinking water using well-dispersed monetite bundles inlaid in chitosan beads. Chem Eng J 303:391–400

Singh J, Singh P, Singh A (2014) Fluoride ions vs removal technologies: a study. Arab J Chem 9:815–824

Singh K, Lataye DH, Wasewar KL (2017) Removal of fluoride from aqueous solution by using bael (*Aegle marmelos*) shell activated carbon: kinetic, equilibrium and thermodynamic study. J Fluor Chem 194:23–32

Sivasankar V, Murugesh S, Rajkumar S, Darchen A (2013) Cerium dispersed in carbon (CeDC) and its adsorption behavior: a first example of tailored adsorbent for fluoride removal from drinking water. Chem Eng J 214:45–54

Srivastav AL, Singh PK, Srivastava V, Sharma YC (2013) Application of a new adsorbent for fluoride removal from aqueous solutions. J Hazard Mater 263:342–352

Sujana MG, Mishra A, Acharya BC (2013) Hydrous ferric oxide doped alginate beads for fluoride removal: adsorption kinetics and equilibrium studies. Appl Surf Sci 270:767–776

Suriyaraj SP, Selvakumar R (2016) Advances in nanomaterial based approaches for enhanced fluoride and nitrate removal from contaminated water. RSC Adv 6:10565–10583

Swain SK, Patnaik T, Patnaik PC et al (2013) Development of new alginate entrapped Fe(III)–Zr (IV) binary mixed oxide for removal of fluoride from water bodies. Chem Eng J 216:763–771

T VK, Belagali SL (2015) Characterization of polyaniline for optical and electrical properties. IOSR J Appl Chem Ver II 8:53–56

Talat M, Mohan S, Dixit V et al (2018) Effective removal of fluoride from water by coconut husk activated carbon in fixed bed column: experimental and breakthrough curves analysis. Groundw Sustain Dev 7:48–55

Tamer MN (2011) Fluorosis. pp 786–791

Tang D, Zhang G (2016) Efficient removal of fluoride by hierarchical Ce–Fe bimetal oxides adsorbent: thermodynamics, kinetics and mechanism. Chem Eng J 283:721–729

Teimouri A, Ghanavati Nasab S, Habibollahi S et al (2015) Synthesis and characterization of a chitosan/montmorillonite/ZrO_2 nanocomposite and its application as an adsorbent for removal of fluoride. RSC Adv 5:6771–6781

Thathsara SKT, Cooray PLAT, Mudiyanselage TK et al (2018) A novel Fe-La-Ce tri-metallic composite for the removal of fluoride ions from aqueous media. J Environ Manag 207:387–395

Tirkey P, Bhattacharya T, Chakraborty S (2018) Optimization of fluoride removal from aqueous solution using Jamun (*Syzygium cumini*) leaf ash. Process Saf Environ Prot 115:125–138

Tomar V, Prasad S, Kumar D (2014) Adsorptive removal of fluoride from aqueous media using *citrus limonum* (lemon) leaf. Microchem J 112:97–103

Tripathy SS, Bersillon JL, Gopal K (2006) Removal of fluoride from drinking water by adsorption onto alum-impregnated activated alumina. Sep Purif Technol 50:310–317
Velazquez-jimenez LH, Hurt RH, Matos J, Rangel-mendez JR (2014) Zirconium-Carbon hybrid sorbent for removal of fluoride from water: oxalic acid mediated Zr(IV) assembly and adsorption mechanism. Environ Sci Technol 48:1166–1174
Velazquez-Jimenez LH, Vences-Alvarez E, Flores-Arciniega JL et al (2015) Water defluoridation with special emphasis on adsorbents-containing metal oxides and/or hydroxides: a review. Sep Purif Technol 150:292–307
Vences-Alvarez E, Velazquez-Jimenez LH, Chazaro-Ruiz LF et al (2015) Fluoride removal in water by a hybrid adsorbent lanthanum-carbon. J Colloid Interface Sci 455:194–202
Vinati A, Mahanty B, Behera SK (2015) Clay and clay minerals for fluoride removal from water: a state-of-the-art review. Appl Clay Sci 114:340–348
Viswanathan N, Meenakshi S (2009) Role of metal ion incorporation in ion exchange resin on the selectivity of fluoride. J Hazard Mater 162:920–930
Wan Z, Chen W, Liu C et al (2015) Preparation and characterization of γ-AlOOH@CS magnetic nanoparticle as a novel adsorbent for removing fluoride from drinking water. J Colloid Interface Sci 443:115–124
Wang J, Xu W, Chen L et al (2013) Excellent fluoride removal performance by CeO_2–ZrO_2 nanocages in water environment. Chem Eng J 231:198–205
Wang J, Kang D, Yu X et al (2015) Synthesis and characterization of Mg-Fe-La trimetal composite as an adsorbent for fluoride removal. Chem Eng J 264:506–513
Wang M, Yu X, Yang C et al (2017) Removal of fluoride from aqueous solution by Mg-Al-Zr triple-metal composite. Chem Eng J 322:246–253
Weidlich C, Mangold M, Ju K (2001) Conducting polymers as ion-exchangers for water purification. Electrochim Acta 47:741–745
Yan L, Tu H, Chan T, Jing C (2017) Mechanistic study of simultaneous arsenic and fluoride removal using granular TiO 2 -La adsorbent. Chem Eng J 313:983–992
Yang K, Liang X (2011) Fluoride in drinking water: effect on liver and kidney function. pp 769–775
Yang W, Tian S, Tang Q et al (2017) Fungus hyphae-supported alumina: an efficient and reclaimable adsorbent for fluoride removal from water. J Colloid Interface Sci 496:496–504
Yu Y, Wang C, Guo X, Paul Chen J (2015) Modification of carbon derived from Sargassum sp. by lanthanum for enhanced adsorption of fluoride. J Colloid Interface Sci 441:113–120
Yu Z, Xu C, Yuan K et al (2018) Characterization and adsorption mechanism of ZrO_2 mesoporous fibers for health-hazardous fluoride removal. J Hazard Mater 346:82–92
Zhang X, Bai R (2003) Surface electric properties of polypyrrole in aqueous solutions. Langmuir 19:10703–10709
Zhang Y-X, Jia Y (2016) Preparation of porous alumina hollow spheres as an adsorbent for fluoride removal from water with low aluminum residual. Ceram Int 42:17472–17481
Zhang Y, Jia Y (2018) Fluoride adsorption on manganese carbonate: ion-exchange based on the surface carbonate-like groups and hydroxyl groups. J Colloid Interface Sci 510:407–417
Zhang G, He Z, Xu W (2012) A low-cost and high efficient zirconium-modified-Na-attapulgite adsorbent for fluoride removal from aqueous solutions. Chem Eng J 183:315–324
Zhang K, Wu S, He J et al (2016) Development of a nanosphere adsorbent for the removal of fluoride from water. J Colloid Interface Sci 475:17–25
Zhao HZ, Yang W, Zhu J, Ni JR (2009) Defluoridation of drinking water by combined electrocoagulation: effects of the molar ratio of alkalinity and fluoride to Al(III). Chemosphere 74:1391–1395
Zhou J, Zhu W, Yu J et al (2018) Highly selective and efficient removal of fluoride from ground water by layered Al-Zr-La Tri-metal hydroxide. Appl Surf Sci 435:920–927
Zhu J, Lin X, Wu P et al (2015) Fluoride removal from aqueous solution by Al (III)– Zr (IV) binary oxide adsorbent. Appl Surf Sci 357:91–100
Zúñiga-Muro NM, Bonilla-Petriciolet A, Mendoza-Castillo DI et al (2017) Fluoride adsorption properties of cerium-containing bone char. J Fluor Chem 197:63–73

Chapter 10
Self-Assembled Soft Materials for Energy and Environmental Applications

Ayyapillai Thamizhanban, Krishnamoorthy Lalitha, and Subbiah Nagarajan

Contents

Abstract Molecular gels are ubiquitous soft solids formed by the self-assembly of small building blocks via the weak intermolecular interactions resulting in the formation of 3D nano- or micro fibrous network wherein solvent molecules are trapped that act as an excellent platform for environmental and energy applications. Appropriate molecular modification can alter the nanoscale assembly which could be utilized practically for various applications in the field of biology, medicine, and materials science. The nanofiber formation in gel can be transformed into conducting architectures or metallic nanowires via doping and annealing procedure. Since gels are formed by weak intermolecular interactions, the gel-to-solution transition can be

A. Thamizhanban · K. Lalitha
Department of Chemistry, School of Chemical and Biotechnology, SASTRA Deemed University, Thanjavur, Tamil Nadu, India

S. Nagarajan (✉)
Department of Chemistry, School of Chemical and Biotechnology, SASTRA Deemed University, Thanjavur, Tamil Nadu, India

Department of Chemistry, National Institute of Technology Warangal (Institute of National Importance), Warangal, Telangana, India
e-mail: snagarajan@nitw.ac.in

R. Saravanan et al. (eds.), *Emerging Nanostructured Materials for Energy and Environmental Science*, Environmental Chemistry for a Sustainable World 23,
https://doi.org/10.1007/978-3-030-04474-9_10

triggered by various external stimuli such as temperature, mechanical action, light, ultrasound waves, acids, bases, ions, redox reagents, and biomolecules. However, gel-to-sol phase change associated with stimuli-responsive behavior can be used for tuning the molecular-level behavior. This chapter reviews the various practical applications of molecular gels such as removal of dyes, aromatic compounds, toxic metals, anions, hydrocarbons, crude oil, smart photonics, electrolytes, and artificial light-harvesting devices.

10.1 Introduction

Supramolecular chemistry is an interdisciplinary branch of science that aims at developing complex chemical systems from the spontaneous organization of small molecules interacting with each other via intermolecular interactions (Lehn 1985). Fine-tuning of these interactions crafts supramolecular chemistry as information science by storing the information at molecular level in their structural features which can be retrieved, transferred, and processed at supramolecular level (Lehn 2004). Nature provides us a plenty of biological materials exhibiting flexibility, precision, and self-repairing capacity, which are fabricated by supramolecular self-assembly of small molecules (Zhang 2003). Formation of eggs, teeth, silk, corals, muscle fibers, hemoglobin, membrane channels, and lipid bilayers are few examples (Lehn 1990). Inspired by nature, extensive research work has been carried out to explore molecular or supramolecular assembly to (1) design materials which mimic nature's self-assembling tendency to produce complicated structures with nanoscale precision, (2) reveal and understand the mechanism of biological self-assembly, and (3) create materials with potential applications. Supramolecular chemistry in combination with materials science and biomedicine can be effectively used to produce self-assembled materials of different shape, size, and helicity for potential applications in the field of energy, environment, nanomedicine, and biotechnology (Lin and Mao 2011). In particular, gels play vital role in daily life such as hair gel, jam, cosmetic creams, ointments, etc. (Draper and Adams 2017). Gels are soft supramolecular material formed by the molecular self-assembly of either small molecules or macromolecules resulted in 3D fibrous network via chemical or physical cross-linking, wherein a large volume of liquid entrapped in it (Amabilino et al. 2017; Dastidar et al. 2017). Generally, gels are categorized into two broad types: chemical and physical gel (Sundararajan 2016; Bhattacharya et al. 2006; Fujita and Shinkai 2006). In chemical gel, 3D fibrous network is formed by the covalent linkage, which is generally referred as polymeric gel and is thermo-irreversible in nature, i.e., during the heating-cooling cycles, gel-sol phase transition cannot be achieved (Smith 2008; Krishnan et al. 2010), whereas physical gels are formed by noncovalent intermolecular interactions facilitated by H-bonding, halogen bonding, anion-π interaction, cation-π interaction, π-π stacking, ionic interaction, van der Waals interactions, etc. (Weiss 2014; Zamboulis et al. 2015). Physical gels display

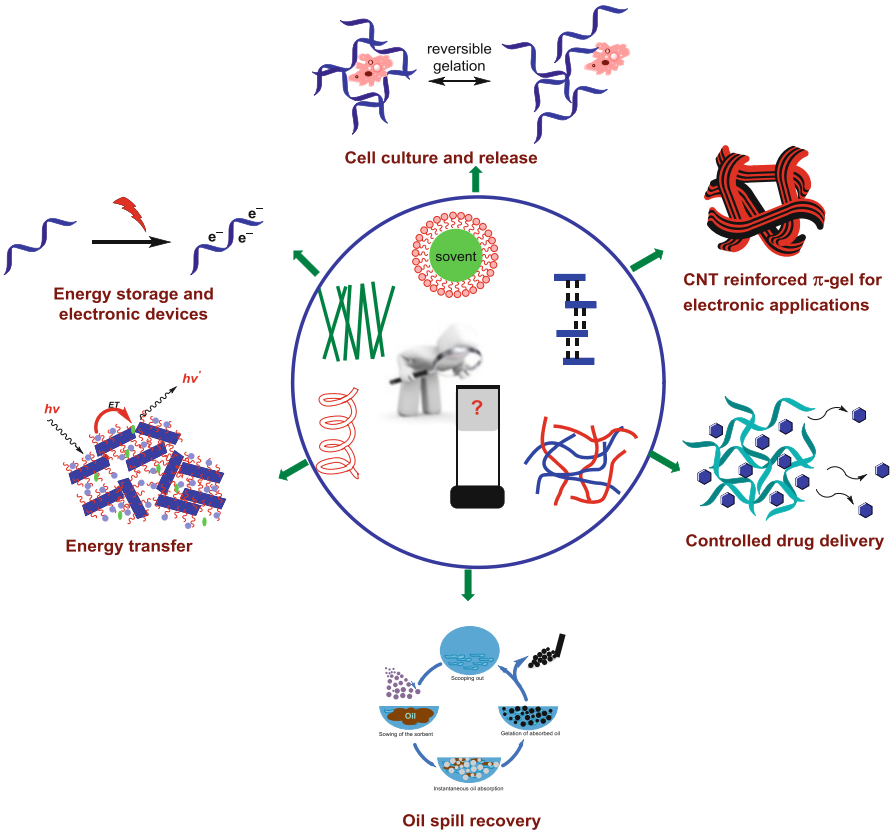

Scheme 10.1 Applications of self-assembled supramolecular gel

thermoreversible and thixotropic behavior, which are frequently used for the fabrication of smart soft devices. In addition, proper design of supramolecular architecture could furnish various stimuli responsive materials such as pH, light exposure, sound, ionic strength, metal ion, biochemical, etc. (Hirst et al. 2008; Ariga et al. 2006). Apart from these gels, metallogels are special type of gels derived by the coordinate bond formation or interaction of molecules having the tendency to self-assemble with metal ions (Pan et al. 2017; Tam and Yam 2013). Potential applications of supramolecular soft gel in various fields are given in Scheme 10.1. Nowadays, metallogels are gaining researchers' attention because of their potential in fabricating advanced electronic devices. In this chapter, we discuss the energy and environmental applications of self-assembled soft materials and their future perspectives.

10.2 Self-Assembly and Low-Molecular-Weight Gelators

Self-assembly is a process, which constructs well-organized structures of different levels of complexity starting from various small molecular building blocks with the help of multiple intermolecular interactions such as electrostatic, hydrophobic, solvophobic, host-guest, charge-transfer, metal ion to ligand coordination, hydrogen bonding, CH-π interaction, anion-π interaction, cation-π interaction, π-π stacking, and dipolar interactions, in large scale (Mohmeyer and Schmidt 2005; Ariga et al. 2008; Komarov et al. 2012; Sangeetha and Maitra 2005; Raeburn and Adams 2015; Stupp and Palmer 2014; Zhang and Wang 2011; Hanabusa and Suzuki 2014). Amphiphiles displaying various degrees of noncovalent driving forces furnish self-assembled nano- or microstructures including nanotubes, nanofibers, micelles, vesicles, and gels. Hence a thorough understanding of the role of noncovalent interactions in the fabrication of self-assembled architectures could precisely generate a wide variety of functional materials. Extensive research work has been carried out to investigate the driving force for self-assembly that facilitates the molecular design suitable for the fabrication of complex functional architectures. Zang et al. have reviewed the synthesis of amphiphiles with various topologies and functions, which are effectively used in the fabrication of supramolecular materials by controlling their self-assembly and disassembly behavior (Zhang et al. 2011). Wang et al. have summarized the development in supramolecular engineering which employs the self-assembly of various amphiphilic and supra-amphiphilic building blocks to construct hierarchical complex structures and smart self-assemblies (Wang et al. 2012).

A number of strategies including the changes in environmental conditions such as pH, temperature, solvent polarity, etc. and usage of locally applied stimuli like light and catalytic action of enzymes have been developed to control and direct the self-assembly process. Few of them have been discussed in this section. Shi and co-workers reported the fabrication of trimeric and tetrameric architectures from dodecylamine-adipic acid mixed solution into self-assemblies like vesicles, bilayers, and ringlike and chain-like aggregates, etc. under the synergistic effect of electrostatic interaction and hydrogen bonding (Shi et al. 2015). The topologies and the self-assemblies of these oligomeric structures were tuned by switching "on" and "off" the hydrogen bonding via pH variation and CO_2 stimulus (Shi et al. 2015). Hamley and co-workers have discussed the recent research progress on self-assembling peptide conjugates and polymer-peptide conjugates (Hamley and Castelletto 2017). They have highlighted the developments in the design, application of bioactive peptide conjugates, and the essential role of molecular self-assembly (Hamley and Castelletto 2017). Roy et al. reported the formation of self-assembled transmembrane Cl^- channel from furamide derivatives with the help of the intermolecular hydrogen bonding capacity (Roy et al. 2018).

Gels are complex soft materials, playing a vital role in our day-to-day life. Many of these commercial gels are prepared from polymeric materials which remain as either entangled biopolymers or covalently cross-linked networks. However, low-

molecular-weight gels (LMWGs) have gained enormous attention due to the existence of dynamic and reversible assembly in supramolecular materials in contrast to conventional covalent polymers. LMWGs are obtained by the self-assembly of a low-molecular-weight gelator (LMWG) in appropriate solvents into a three-dimensional network immobilizing the solvent. A large variety of compounds which includes amphiphiles, cationic and anionic surfactants, carbohydrates, functionalized amino acids, oligopeptides, and dendrimers were used to generate LMWGs (Raeburn et al. 2015). Depending on the gelator's self-organizing tendency and nature of solvent used, LMWG can be categorized into organogelator and hydrogelator; if the gelator is capable of self-organizing in organic solvents to form a viscoelastic material, it is termed as an organogelator, while if the gelator is able to self-assemble in water to form a viscoelastic material, it is termed as a hydrogel. However, the key driving force in molecular self-assembly to form gel is the cooperative operation of hydrogen bonding and other interactions such as ionic, π-π, van der Waals forces, etc. (Estroff and Hamilton 2004). Gelator design parameters involve the critical balance in hydrophilic and hydrophobic forces with the cooperative effect of other forces. A fine-tuning of hydrophilic and hydrophobic units in a gelator substantially influences the gelation process. For example, 1,3 (*R*):2,4(*S*)-dibenzylidene-D-sorbitol (DBS) undergoes self-assembly into a 3D network at relatively low concentration in a variety of nonpolar organic solvents and polymer melt. DBS can be transformed into a hydrogelator by introducing hydrophilic groups such as -COOH (DBS-COOH) and -$CONHNH_2$ (DBS-$CONHNH_2$), which assist its self-assembly in aqueous environment (Okesola and Smith 2016; Cornwell et al. 2013). Knani and Alperstein have discussed the molecular interactions governing the self-assembly of DBS, DBS-COOH, and DBS-$CONHNH_2$ by using molecular modeling studies (Fig. 10.1) (Knani and Alperstein 2017).

Ajayaghosh and co-workers have reported the hybrid π-conjugated gel formation by the self-assembly of oligo(*p*-phenylene vinylene)s (OPV) via physical interactions with carbon nanotubes (CNTs) (Srinivasan et al. 2008). In this system, the molecular self-assembly of OPV is stimulated by CNTs through physical interaction in relatively hydrophobic solvents. The complete dispersion of CNTs in OPV gel resulted in the formation of supramolecular tapes. This OPV-CNT composite gel system has π-conjugated unit; CNTs and an aromatic solvent furnished the optoelectronic properties. In addition, the physical cross-link between the CNT and gelator enhances the stability of the gel without affecting the electronic properties and enables it as an optoelectronic material (Fig. 10.2).

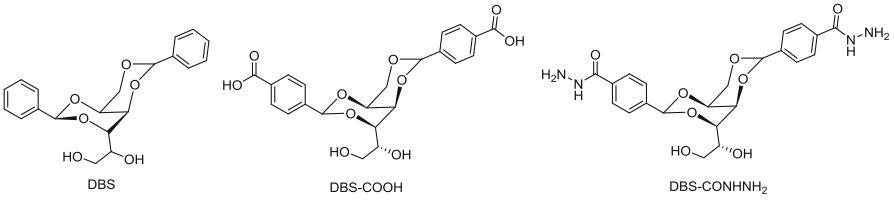

Fig. 10.1 Chemical structure of DBS, DBS-COOH, and DBS-$CONHNH_2$ molecules

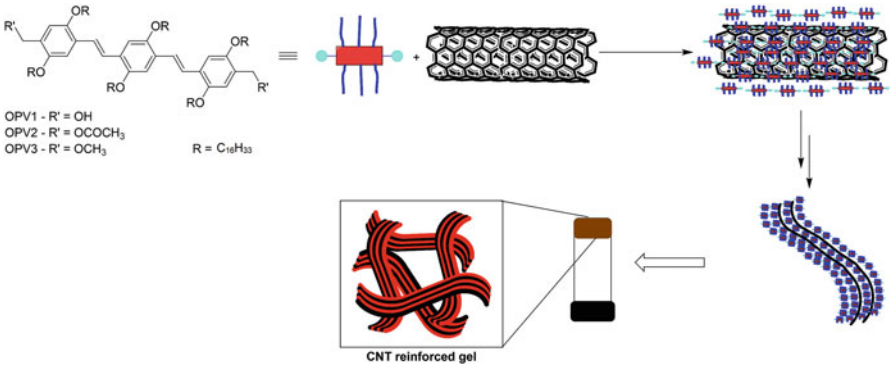

Fig. 10.2 Chemical structures of OPV derivatives and schematic representation of OPV-CNT gel formation. (Srinivasan et al. 2008)

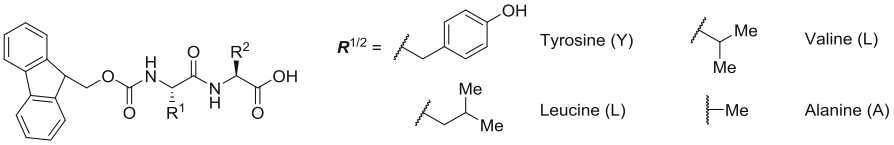

Fig. 10.3 Structures of Fmoc-based aromatic peptide amphiphiles forming hydrogels in presence of salts. (Roy et al. 2012)

Roy et al. have demonstrated that the presence of salts in fluorenylmethoxycarbonyl (Fmoc)-protected aromatic dipeptide amphiphiles directly influences the molecular self-assembly and thereby controls the material properties like stiffness and charge-transfer properties without the need of chemical redesign parameter (Fig. 10.3) (Roy et al. 2012).

Stereogenic centers in chiral LMWGs are found to influence the formation and stabilization of interwoven helical fibrous networks (Edwards and Smith 2014; Aggeli et al. 2001; Smith 2009). In general, enantiomerically pure LMWG exhibits strong gelation. Novel functional soft materials can be designed by understanding the properties of supramolecular gels and chirality relation. Although the supramolecular assemblies can be constructed by mixing enantiomers with different molar ratios, usually the racemates are not good gelators (Shen et al. 2014). Only a few racemic gelators are reported for which the major driving force for self-assembly remains unexplored (Shen et al. 2014; He et al. 2011). Stoddart and co-workers have shown that racemate ***rac***-Δ, obtained by equimolar mixing of pure enantiomers of naphthalenediimide-based gelator (***R***-Δ and ***S***-Δ) in dichloroethane (DCE), self-assembles into interwoven fibrous network in which hydrogen bonding drives the columnar stacking of the triangles in an alternating ***R***-Δ/***S***-Δ fashion and forms the organogel, whereas enantiopures ***R***-Δ and ***S***-Δ do not form fibrous aggregates (Liu et al. 2016). DFT calculations confirm the existence of multiple [C-H···O]

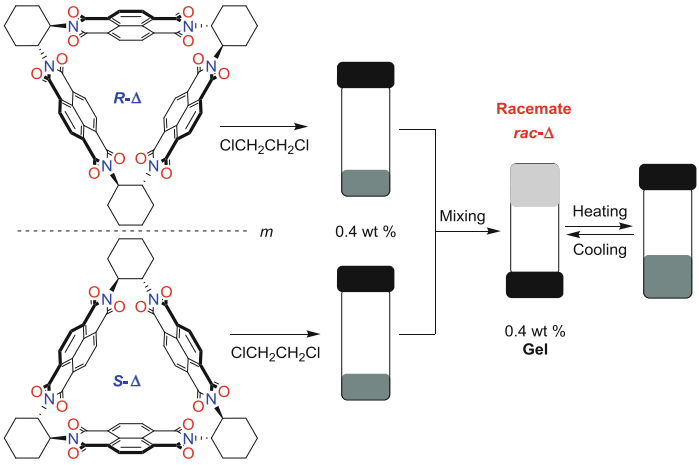

Fig. 10.4 Structural formulas of **R**-Δ and **S**-Δ. (Liu et al. 2016)

interactions acting cooperatively in a supramolecular context, which is further supported by NMR spectral analysis (Fig. 10.4) (Liu et al. 2016).

A detailed discussion on the rheological aspect of gel is crucial for the construction of soft materials. Generally, LMWGs are solid-like, although they are formed with very low gelator concentrations (George and Weiss 2006) and are potentially used in a wide range of areas, including sensing, energy storage, catalysis, drug delivery, optoelectronics, tissue engineering scaffolds, wound healing, wastewater treatment, oil spill recovery, etc. (Fig. 10.5) (Sangeetha et al. 2005; Diaz et al. 2011; Bisoyi and Li 2016; Hirst et al. 2008; Fichman and Gazit 2014). This chapter mainly focuses on research progress of self-assembled soft nanomaterials in energy and environmental applications.

10.3 Applications of Soft Nanomaterials

10.3.1 Water Treatment

In the recent past, scarcity of safe water is considered as a great concern to nature though water is an abundant natural resource, as its quality has been diminished by the discharge of hazardous wastes such as heavy metals, organic dyes, pharmaceuticals, petroleum products, fertilizers, etc. into the environment by the action of various industrial processes. Discharging these effluents as untreated into water resources creates accumulation of various hazardous organic and inorganic toxins in living organisms through food chains and causes damage to genetic material causing health-related issues. Key current methodology available to combat water pollution is the adsorption of dissolved organic/inorganic pollutants onto solid

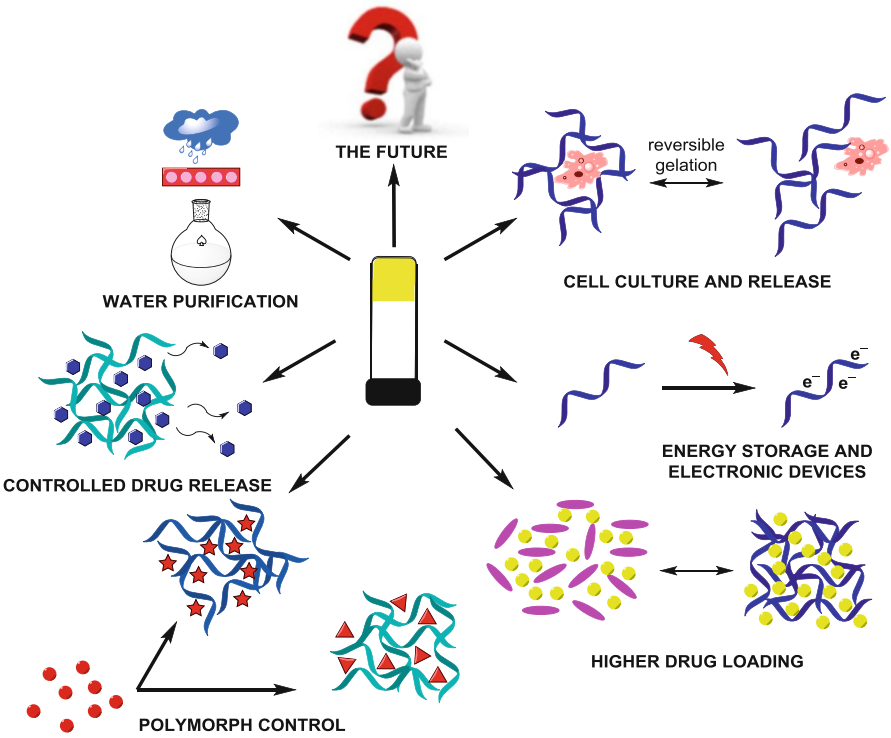

Fig. 10.5 Cartoon showing some of the potential uses of low-molecular-weight gelators. (Sangeetha et al. 2005; Diaz et al. 2011; Bisoyi et al. 2016; Hirst et al. 2008; Fichman et al. 2014)

materials such as activated carbon, zeolites, chitosan, mineral clays, and waste biomatter, because of the advantages associated with this technique such as simplicity, ease of operation and handling, regeneration, and economic feasibility (Gupta and Suhas 2009; Babel 2003). However, there are limitations such as lack of selectivity, generation of large amounts of toxic sludge, low pollutant uptake, and costly regeneration processes. This has initiated a significant interest in the development of smart materials and self-assembled gel-phase materials displaying stimuli-responsive behavior to external stimuli, for environmental remediation (Okesola and Smith 2016).

10.3.1.1 Supramolecular Gels for Oil Spill Recovery

Generally, marine pollution originates from the discharge of crude oil and petrochemicals either accidentally or intentionally resulting in the wastage of valuable nonrenewable resources, long-term adverse environmental impacts to marine ecosystem, human health hazards due to consumption of oil polluted seafoods, toxic oil

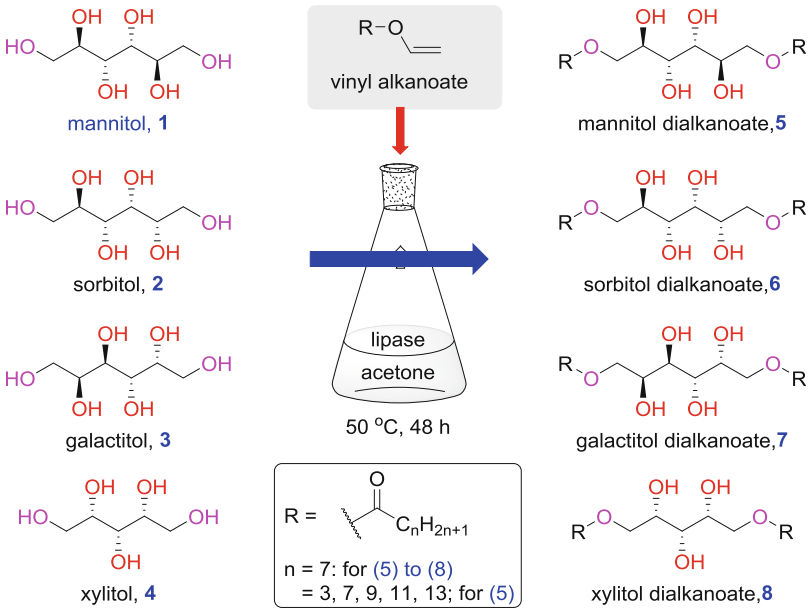

Scheme 10.2 Synthesis of sugar-based amphiphiles enzymatically using Novozyme 435. (Jadhav et al. 2010; Samatch et al. 2016)

residue, and the accumulation of volatile hydrocarbons in the stratosphere (Gong et al. 2014). Although various methods such as mechanical recovery, use of dispersants and solidifiers, burning, and bioremediation are available for oil spill remediation, these approaches are found to be often ineffective, not economically suitable for large-scale applications, or generate toxic residues that can bioaccumulate through food webs. Low-molecular-weight organogels (LMWGs) are considered as eco-friendly, easily synthesizable at low cost, thermoreversible facilitating oil recovery, recyclable, and reusable (Liu et al. 2011). Hence such LMWGs can serve as phase-selective gelators (PSGs) to congeal oil from oil water mixture by immobilizing the oil within the entangled 3D fibrous network formed via self-assembly. Several research works have been carried out by projecting PSGs as possible sorbents for oil spill recovery.

Bhattacharya and co-workers have reported the phase-selective gelation of hydrocarbon-based fuels or solvents exhibited by *N*-lauroyl-L-alanine from a two-phase mixture (Liu et al. 2011). John and co-workers have synthesized environmentally benign, nontoxic, and biodegradable PSGs from eco-friendly and cheap renewable resources and sugar alcohols, such as mannitol, sorbitol, and vinyl esters of fatty acids via enzymatic catalysis (Scheme 10.2) (Jadhav et al. 2010; Samatch et al. 2016). These PSGs are proved to be effective in selective gelation of the crude oil from oil-water mixture through the phase-selective gelation study.

Mukherjee and Mukhopadhyay have developed an eco-friendly galactose-based PSG (Scheme 10.3), which is capable of gelling various fuel oils from an oil-water

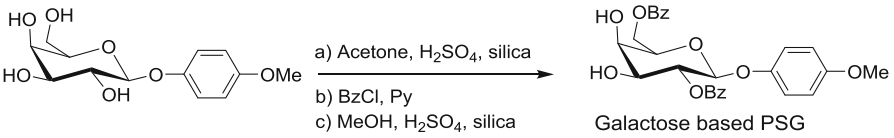

Scheme 10.3 Synthesis of a galactose-based gelator. (Mukherjee and Mukhopadhyay 2012)

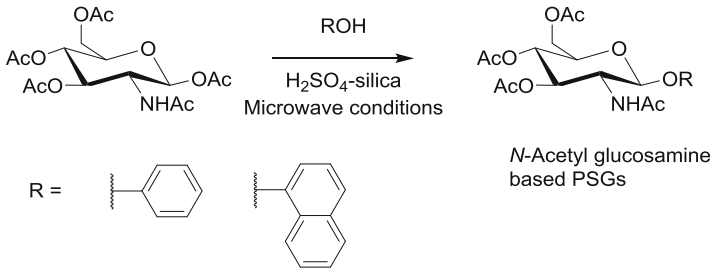

Scheme 10.4 Synthesis of *N*-acetyl glucosamine-based PSGs. (Mukherjee et al. 2014)

mixture, and have demonstrated the recoverability and reusability of both oil and gelator after the gelation (Mukherjee and Mukhopadhyay 2012). Interestingly, they have also demonstrated the effective removal of crystal violet dye from its aqueous solution either by adsorbing the dye in toluene using the PSG xerogel or via phase-selective gelation (Mukherjee and Mukhopadhyay 2012).

Instantaneous selective gelation of oil from oil-water mixture is considered as the essential character of PSGs, which is required to prevent the oil spreading in sea or river water quickly. In order to meet this requirement, Fang and co-workers have synthesized eco-friendly *N*-acetyl glucosamine-based PSGs from per-*O*-acetylated glucosamine (Scheme 10.4) (Mukherjee et al. 2014). The solution of PSG in THF was capable of gelating petrol selectively and efficiently from petrol/water mixture (0.8:2) within 50 s and diesel within 45 s from diesel/water mixture at 0–5 °C (Mukherjee et al. 2014). Further investigations have illustrated that these PSGs are reusable and biodegradable, their efficiency remains unaltered with time and temperature, and recoverable nature of both oil and gelator enables them as potentially suitable materials to combat oil spill recovery (Mukherjee et al. 2014).

Chaudhuri and co-workers have synthesized naphthalenediimide-based PSGs from naphthalene dianhydride, *n*-dodecylamine, and phenylalanine (Scheme 10.5). Molecular self-assembly of naphthalenediimide-based PSGs facilitates the strong supramolecular gelation of heavy crude oil from the biphasic mixture of oil and water instantaneously (Datta et al. 2018). Further investigations have shown that these PSGs are suitable for congealing of oil practically at low temperatures at which the oil exists as highly dense and viscous form (Datta et al. 2018).

Das and co-workers have prepared terminally protected tripeptide-based PSGs, consisting of both natural and synthetic β-amino acids which self-assemble to form fibrillar network capable of immobilizing oils selectively from biphasic mixture of

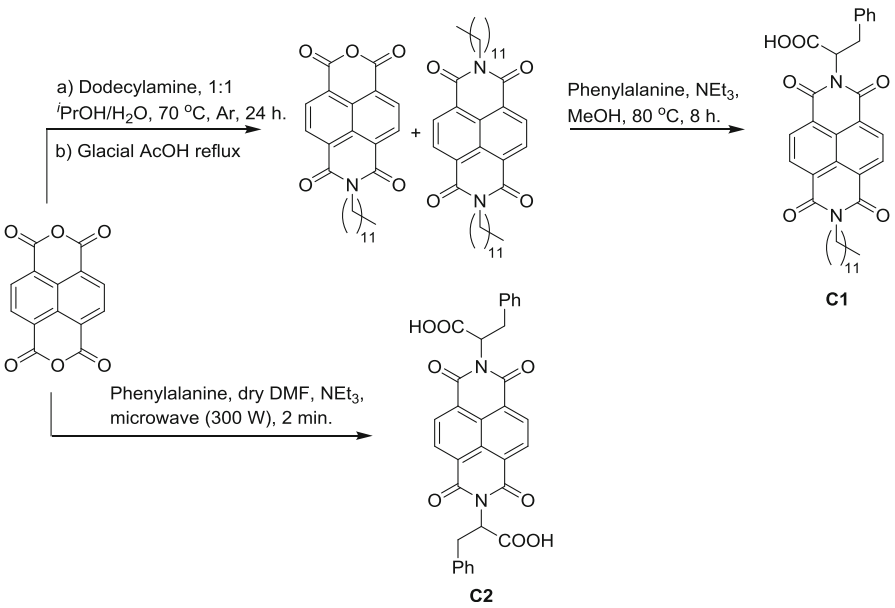

Scheme 10.5 Synthesis of naphthalenediimide-based PSGs, C1 and C2. (Datta et al. 2018)

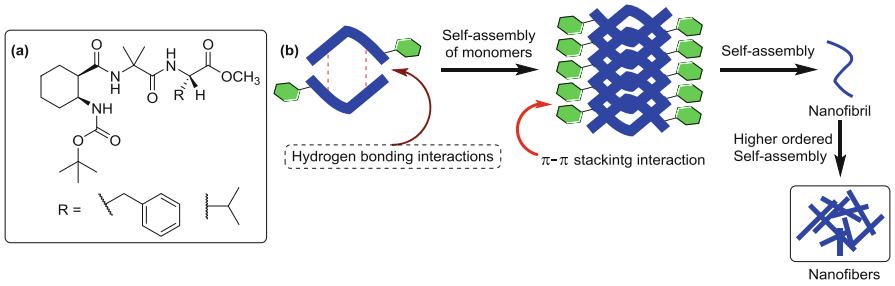

Fig. 10.6 (**a**) Molecular structure of β-amino acid-based peptide gelator. (**b**) Schematic representation of gelation mechanism. (Konda et al. 2014)

oils and brine (Fig. 10.6) (Konda et al. 2014). The potential applicability of these PSGs for oil recovery was demonstrated by adding a hot solution of tripeptide-based PSG in diesel to a biphasic mixture of diesel-brine solution, and the resultant stable gel which floats on the surface of brine solution was distilled to recover the immobilized diesel (Fig. 10.7) (Konda et al. 2014).

Though PSGs are potentially suitable for oil spill recovery, their practical usage is restricted by various factors such as stability of gelator in the corrosive seawater, necessity for either heating-cooling cycle or a water-miscible carrier solvent for their introduction, gelation tendency, and the toxicity of the residual gelator for marine life (Prathap and Sureshan 2012; Vibhute et al. 2016). Uniform distribution of the gelator over spilled oil is another major challenge in using PSGs for oil spill

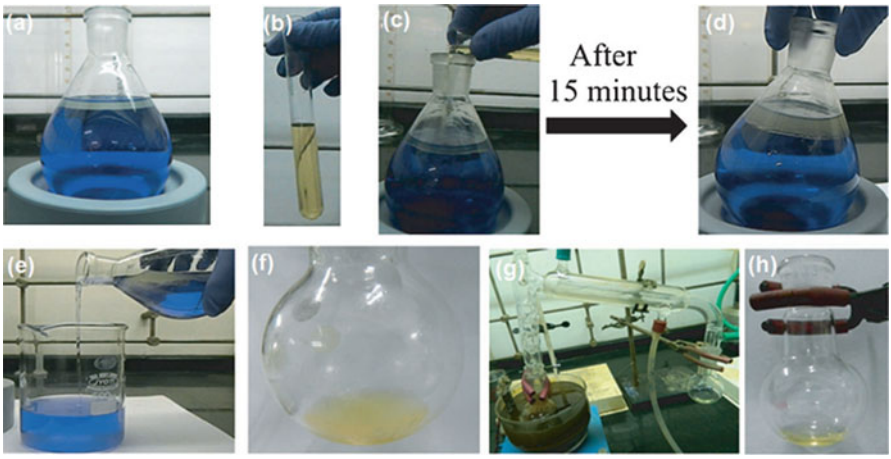

Fig. 10.7 Schematic representation of oil recovery by PSGs: (**a**) biphasic mixture (diesel (20 mL) + aqueous solution of NaCl and $CuSO_4$ (270 mL)), (**b**) hot solution of PSG in diesel, (**c**) addition of warm PSG solution to the biphasic mixture, (**d**) selective gelation of diesel, (**e**) separation of diesel gel from water, (**f–h**) recovery of diesel from diesel gel by vacuum distillation. (Konda et al. 2014)

Scheme 10.6 (**a**) Synthesis of mannitol-based gelators. (**b**) Mechanism of gelation. (Prathap and Sureshan 2012)

recovery. In order to overcome these limitations, recently, Sureshan and co-workers have designed and synthesized nontoxic, cheap, biodegradable, and environmentally benign mannitol-based PSG which can be sprayed aerially in a non-persisting carrier to congeal oil selectively from oil-water mixture at very low concentration (Scheme 10.6) (Prathap and Sureshan 2012). Compared to other PSGs, this mannitol-based gelator was found to possess high gelation efficiency and stability in seawater (Prathap and Sureshan 2012).

Even though the above gelator can form stable gel in oil-water mixture, it has been shown to form a discontinuous and nonuniform gel due to poor diffusion of gelator molecules upon dispersing the finely ground solid gelator over oil-water

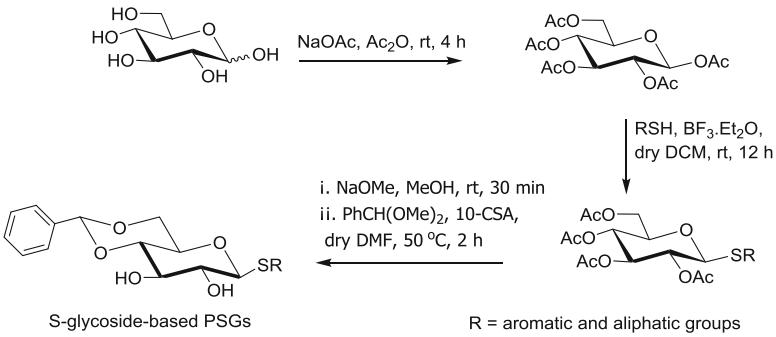

Scheme 10.7 Synthesis of S-glycoside-based PSGs. (Vibhute et al. 2016)

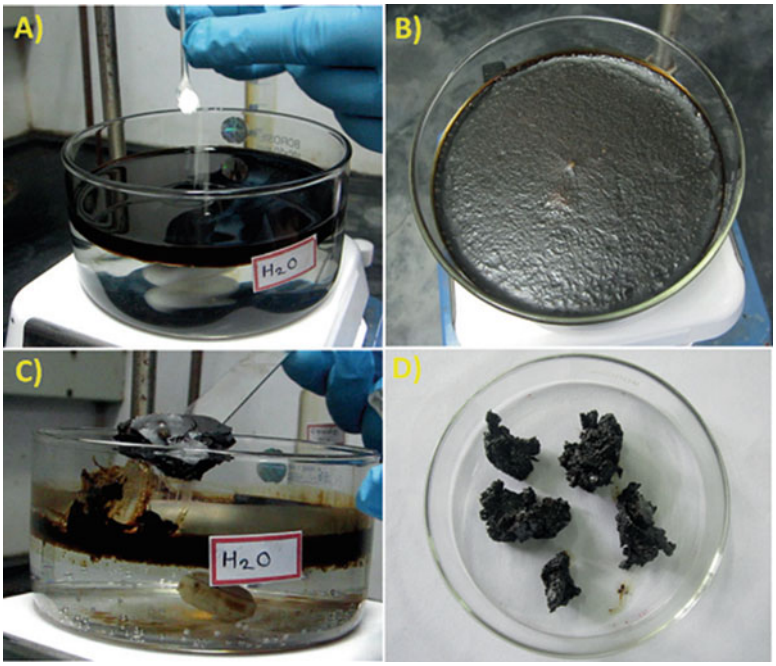

Fig. 10.8 Schematic representation of oil recovery using S-glycoside-based PSGs: (**a**) spreading of gelator powder over a layer of crude oil on water, (**b**) gelation of crude oil layer, (**c**) removal of crude oil gel with a spatula, (**d**) removed crude oil gel. (Vibhute et al. 2016)

mixture (Vibhute et al. 2016). To overcome this drawback, the same group has synthesized S-glycoside-based PSGs which formed stable gel by congealing crude oil and nonpolar liquids selectively in a biphasic system of water and oil (Scheme 10.7) (Vibhute et al. 2016). It was observed that spraying a fine powder of S-glycoside-based PSGs on either benzene-water or diesel-water mixture can congeal all benzene or diesel, respectively, from the biphasic mixture and the gel thus formed was strong enough to handle with a spatula (Fig. 10.8) (Vibhute et al. 2016).

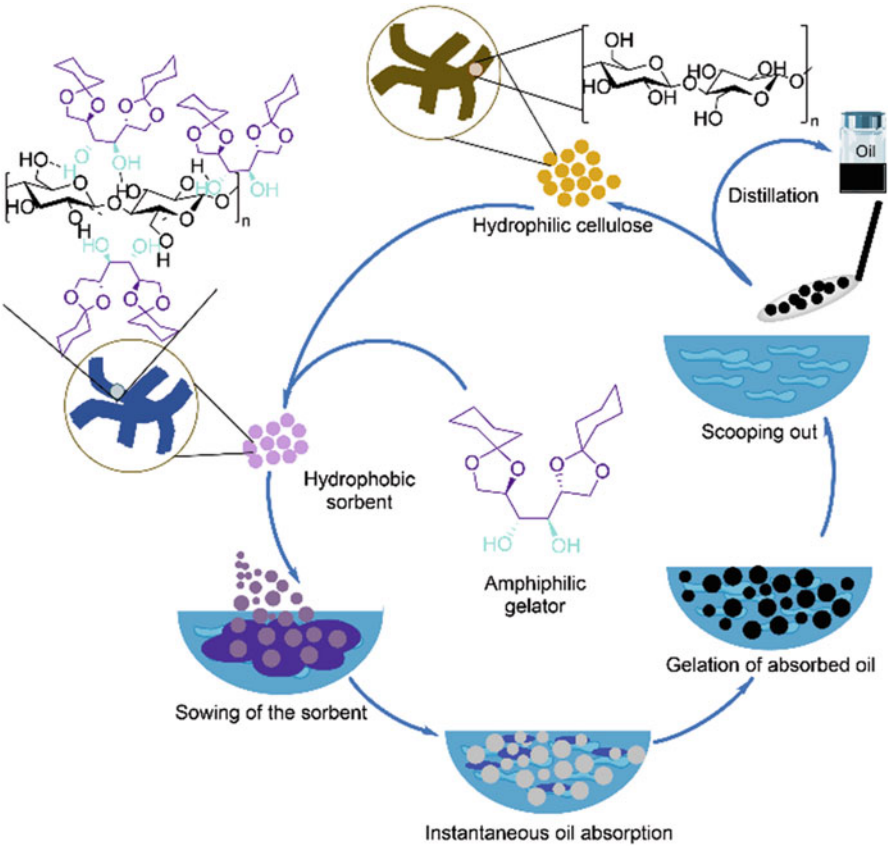

Fig. 10.9 Schematic representation of oil recovery using eco-friendly cellulose-based sorbent. (Prathap and Sureshan 2017)

Recently, Sureshan and co-workers have developed an efficient and cheap cellulose-based sorbent material by impregnating cellulose with an economically viable and biocompatible sugar-based gelator, 1,2:5,6-di-*O*-cyclohexylidene-mannitol, which enhances the hydrophobicity and oleophilicity favoring the oil immobilization within the self-assembled fibrillar network of gelator (Prathap and Sureshan 2017). The reported cellulose-based sorbent material displayed immediate absorption of oil selectively from the biphasic mixture, detachment of gelator from the cellulose matrix, and uniform distribution in the oil phase followed by the immobilization of oil within the self-assembled fibrous network (Fig. 10.9) (Prathap and Sureshan 2017). The oil uptake capacity of the newly developed cellulose-based sorbent material with various crude oils was found to be more than the other known sorbents (Prathap and Sureshan 2017).

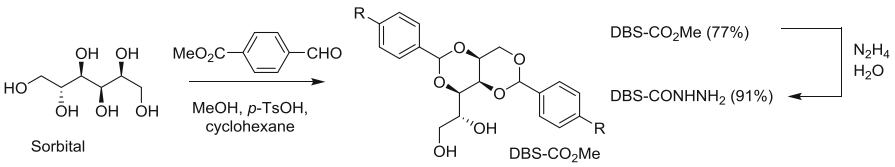

Scheme 10.8 Synthesis of DBS-$CONHNH_2$ from sorbitol. (Okesola and Smith 2013)

A recently reported PSG based on deep eutectic solvent (DES) obtained by mixing the melt of lauric acid and N-methylacetamide (1:2) with a fusion point of 20 °C displayed oil spill recovery behavior even without the use of economically challenging multistep organic synthesis (Cui et al. 2017). However, a wide variety of compounds such as protected sugar alcohols, functionalized peptides and amino acids, and amphiphilic fatty acids were used for the construction of PSGs; their practical application as oil spill recovery material has to be fine-tuned.

10.3.1.2 Supramolecular Gels for Wastewater Management

Effluents from various industrial operations such as dying, electroplating, mining, pharmaceutical, etc. are considered as the major threat to the society owing to the discharge of hazardous metal ions and dyes into aqueous environment causing bioaccumulation and disorders in immune and reproductive systems. Hence, it is essential to perform wastewater treatment before discharging them into environment to minimize the pollution. PSGs can be used to remove dye from water as they are capable of gelling one solvent in preference to another from the solvent mixture. Okesola and co-workers have synthesized hydrazide-based hydrogelator from dibenzylidene sorbitol (DBS) (Scheme 10.8), which can be effectively used to separate dyes by adsorption phenomenon (Okesola and Smith 2013). Selective adsorption of methylene blue (MB) in basic medium and acidic blue (AB25) and naphthol blue black (NBB) in acidic medium has been explored (Okesola and Smith 2013).

Díaz and co-workers have reported the synthesis of tetrapeptide-based gelators from *N*-Boc-protected azobenzene-based amino acids (Fig. 10.10). This class of compounds displayed phase-selective gelation behavior in response to ultrasound (Bachl et al. 2015). This phase-selective gelation property was utilized to remove the oil as well as toxic dyes from aqueous solution (Bachl et al. 2015).

Efficient and rapid separation of dyes and other metallic contaminants is practically possible by fabricating PSGs that adsorb dyes selectively and form a stable gel. In order to achieve selective and effective removal of dyes from biphasic mixture, Yu and co-workers have synthesized imidazolium-based PSG, *N*-cetyl-*N*′-carboxymethyl imidazolium bromide (Scheme 10.9), that self-assemble into stacked bilayer of microplatelets with the potential to adsorb anionic dyes such as Eosin Y and Methyl Orange selectively and aid in rapid removal of anionic dyes from wastewater (Cheng et al. 2015).

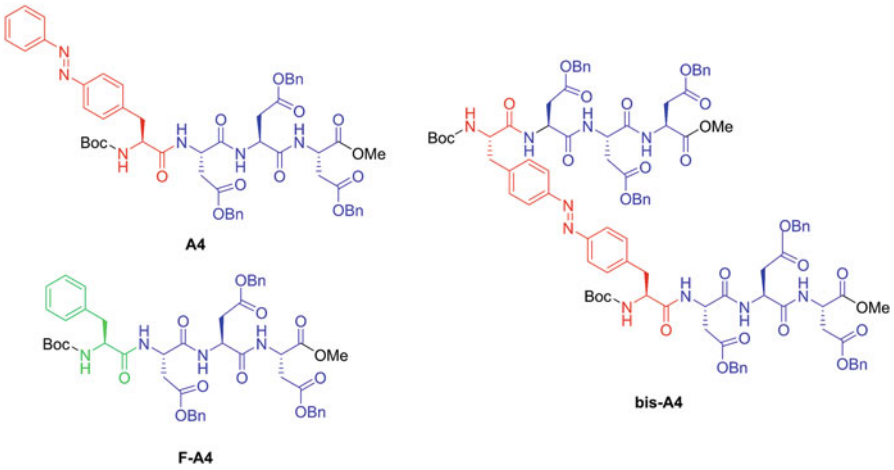

Fig. 10.10 Structure of peptide gelators. (Bachl et al. 2015)

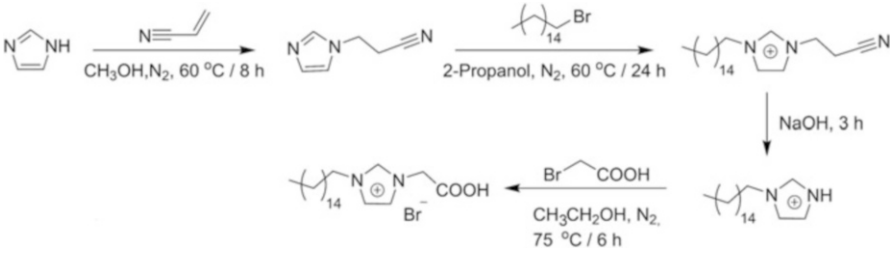

Scheme 10.9 Synthesis of *N*-cetyl-*N*′-carboxymethyl imidazolium bromide. (Cheng et al. 2015)

Fig. 10.11 Chemical structure of peptide gelators. (Nandi et al. 2017; Basu et al. 2017)

Banerjee and co-workers have developed a peptide-based hydrogelator which forms thermoreversible hydrogel in phosphate buffer capable of absorbing both anionic and cationic organic dyes like Brilliant Blue (BB), Congo Red (CR), Malachite Green (MG), Rhodamine B (RB), etc. and inorganic metal ions such as Ni^{2+} and Co^{2+} from aqueous environment (Nandi et al. 2017). They also demonstrated the practical applicability of the hydrogel in treating toxic industrial effluent efficiently at cheap price (Fig. 10.11) (Nandi et al. 2017; Basu et al. 2017). Peptide gelator shown in Fig. 10.11 can be practically used for absorbing oils, organic solvents, and toxic dyes from wastewater (Fig. 10.11) (Nandi et al. 2017; Basu et al. 2017).

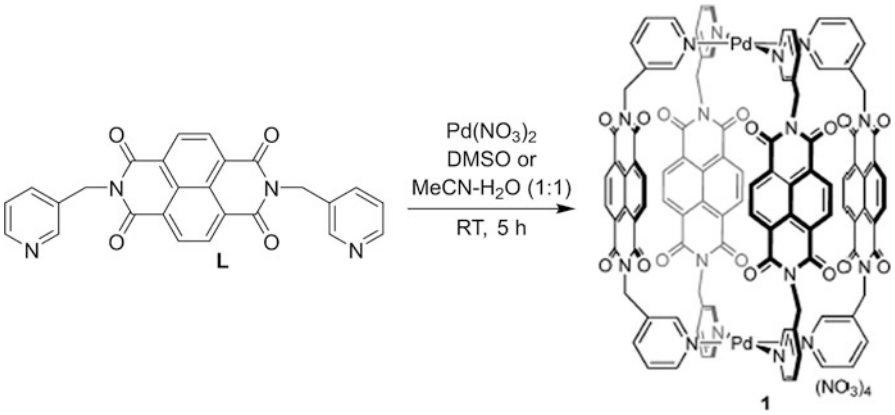

Scheme 10.10 Synthesis of self-assembled metallogelator. (Ganta and Chand 2018)

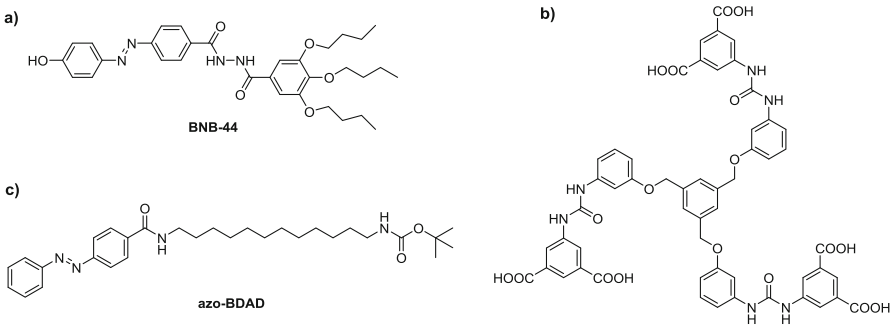

Fig. 10.12 Chemical structure of gelators: (**a**) *N*-(3,4,5-tributoxyphenyl)-*N*′-4[(4-hydroxyphenyl) azophenyl] benzohydrazide; (**b**) hydrogelator, tris-urea; (**c**) azobenzene-based gelator. (Ran et al. 2017; Takeshita et al. 2017; Zhang et al. 2017)

A cylindrical drum-shaped self-assembled Pd_2-L_4-type coordination cage complex, prepared from the ligand *N*,*N*′-Bis(3-pyridylmethyl)naphthalenediimide and $Pd(NO_3)_2$, displayed thixotropic nature and chemical-stimuli-responsive behavior such as response to anionic guests like halides (Scheme 10.10) (Ganta and Chand 2018). Stimuli-responsive behavior of the metallogel is utilized for the removal of aromatics as well as anionic dyes such as Acid Blue 93 and Methyl Orange from the aqueous solution containing the mixture of cationic and anionic dyes (Ganta and Chand 2018).

Ran et al. have explored the possibility of using the thermoreversible phase-selective gelator, *N*-(3,4,5-tributoxyphenyl)-*N*′-4[(4-hydroxyphenyl)azophenyl] benzohydrazide, to treat wastewater by entrapping and releasing the aromatic solvents and dyes from aqueous environment (Fig. 10.12a) (Ran et al. 2017). Takeshita et al. have developed a dendritic supramolecular hydrogelator as an effective adsorbent to purify contaminated water by selectively adsorbing cationic dyes

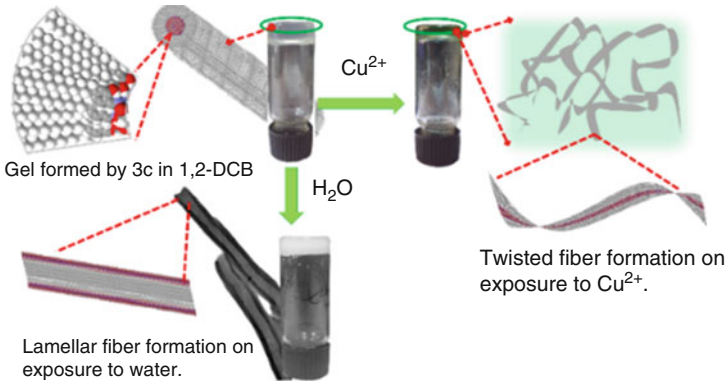

Fig. 10.13 Pictorial representation of morphological transition triggered by $Cu^{2+}$and water. (Lalitha et al. 2017)

such as Rhodamine 6G (R6G) and Methylene Blue (MB) (Fig. 10.12b) (Takeshita et al. 2017). Similarly, Qu and co-workers have designed and synthesized azobenzene-based PSG for the effective removal of Rhodamine B, a cationic dye from polluted water (Fig. 10.12c) (Zhang et al. 2017).

Pal and co-workers have employed an eco-friendly pathway to prepare porous graphite carbon (PGC) materials from calcium alginate by annealing it at 200 °C for 2 h followed by carbonization under nitrogen atmosphere for 1 h at 900 °C. The black char residue thus obtained was then washed with water repeatedly and used to remove sulfide efficiently from wastewater either by adsorption or oxidation at alkaline conditions (Edathil et al. 2017). Literature survey on the chemical structure and the physicochemical properties of chitosan, an abundant natural amino polysaccharide, suggests that it can be used either as such or after conjugating with magnetic materials, as green adsorbent in the wastewater treatment (Nisticò et al. 2017). Recently, Nagarajan and co-workers have developed glucono-appended cardanol (GAC)-based LMOGs and utilized them as metal ion-absorbing material. The chiral molecular packing of GAC to form tubules, which upon exposure to various metal ions, generated metal ion adsorbed ordered structure through an in situ morphological transition with or without change in phase (Fig. 10.13) (Lalitha et al. 2017).

10.3.2 Energy Transfer in Supramolecular Gel

Supramolecular materials use molecular self-assembly as a component to form various complex architectures that cannot be derived by other methods. The fundamental concept involved in the construction of a supramolecular architecture is weak intermolecular forces. The strong electronic communication throughout the self-

assembled supramolecular architecture was achieved by the reversible weak intermolecular interaction. The charge transport in supramolecular architecture determines the molecular device performance. However, the construction of soft supramolecular conducting and semiconducting organic materials is considered as the major challenge in molecular electronic devices because of their enhanced electronic properties, potential for tunable characteristics, and low cost of production.

10.3.2.1 Molecular Gels as Stimuli-Responsive Photonics

Among the several molecular gels, photonic gels are one of the most important because of their periodic structure in dielectric materials, which allows strong interaction with light of wavelength of the same scale. Recently, efforts have been devoted to the study, development, and applications of green photonics and smart photonics. Photonic molecular gels used to develop photonics technology that can conserve energy and create renewable energy. In this line, light-activated molecular gels were derived from 4-amino-1,8-naphthalimide and an acridine-based energy donor. Molecular self-assembly of gelator furnished a fibrillar structure with orthogonal assembly of both chromophores. Orthogonally self-assembled material displayed emission from the naphthalimide-based acceptor upon irradiation of the acridine-derived donor with a significant Stokes shift of ca. 200 nm, which can be used for light harvesting. Energy transfer in gel form and xerogel was identified by fluorescence spectroscopy and confocal laser scanning microscopy. By applying the pH as external stimuli, the light-harvesting process can be switched off/on by addition of HCl or NaOH, respectively, which results in the development of stimuli-responsive photonic soft materials (Felip-León et al. 2016).

10.3.2.2 Molecular Gel Electrolytes

Recently, liquid and solid electrolytes were widely used for energy capture and storage technology. However, the inherent limitations associated with the use of liquid and solid electrolytes for energy applications probe the researchers to develop gel electrolytes. Gel electrolytes are having vital technological importance related to the energy storage problem. Dibenzylidene sorbitol (DBS) and its derivatives were identified as suitable candidates for immobilization of the electrolyte. In particular, methyl-substituted DBS (MDBS) and dimethyl-substituted DBS (DMDBS) displaying higher T_{gel}, thermal stability, and viscoelastic behavior were identified as optimal substances to solidify polar electrolytes. Raghavan and co-workers demonstrated the use of DBS derivative in the construction of lithium-ion batteries (Basrur et al. 2013). Solid-like electrolyte generated from DBS derivative possesses

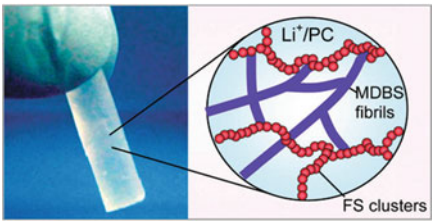

Fig. 10.14 Schematic representation of the synergistic interaction between fumed silica (FS) in Li^+/propylene carbonate (PC) and MDBS and the resulting free-standing gel. (Basrur et al. 2013)

high "liquid-like" ionic conductivity, electrochemical stability window, and good interfacial stability against Li ions (Fig. 10.14).

Lai and Chen have reported gel electrolytes comprising DBS in poly(ethylene glycol) (PEG) containing iodide-based redox couples (Okesola et al. 2015). The chain length of PEG influences the ionic mobility and conductivity of the electrolyte, thereby one can tune its performance. The biological application of DBS organogel-based electrolytes was further explored in biosensing. A detailed review by Smith and co-workers demonstrated the efficiency and industrial application of DBS and its derivatives (Okesola et al. 2015).

10.3.2.3 Molecular Gels for Artificial Light Harvesting

Molecular gels formed by noncovalent interactions are reversible in nature, which could facilitate energy-transfer processes by combining appropriate energy donors and energy acceptors in different molar ratios. Several groups have discussed the use of self-assembled supramolecular gels for energy transfer. Light-harvesting hybrids have gained much importance as they are considered as potential mimics of photosynthetic systems. Self-assembled Al(III)-4-*tert*-butylpyridine (TBP) gel electrolyte acts as a quasi-solid-state electrolyte for dye-sensitized solar cells (DSSCs). The formation of metal-organic gel network induces the gelation process and tailors the performance by penetrating well into the TiO_2 photoanode film. This investigation opens up extended scopes of molecular gels in energy-related fields (Fig. 10.15) (Dong et al. 2017).

In this line, George and co-workers have constructed a light-harvesting hybrid by using aminoclay (AC) and anionic dyes (tetracarboxylate of coronene and perylene), which utilizes covalent, semi-covalent, and noncovalent interactions. A schematic representation of the self-assembly and energy transfer in the clay/dye hybrid gels is depicted in Fig. 10.16 (Rao et al. 2012)

In 2003, Ajayaghosh and co-workers have studied the light-harvesting application of oligo(phenylenevinylene)s (OPVs) in self-assembled molecular gels. Here, Rhodamine B acts as an energy acceptor, which upon mixing with OPV derivatives and fabricating as gel in cyclohexane and chloroform (16:1) produced a light-harvesting device. The indirect excitation of donor followed by the amplified

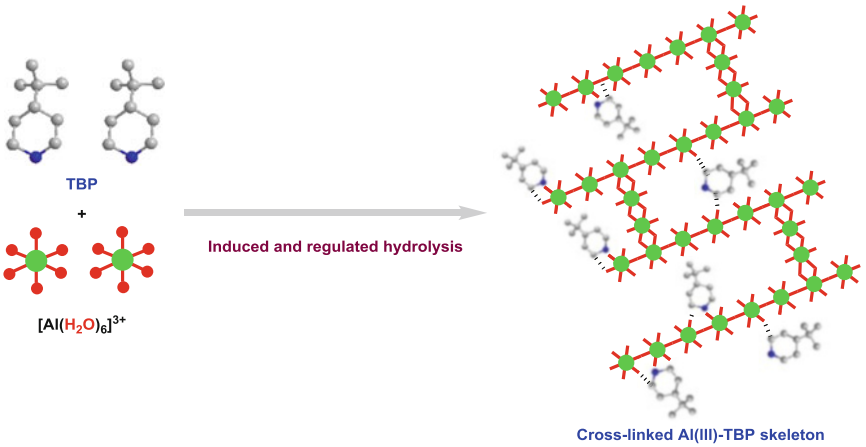

Fig. 10.15 Schematic diagram of possible formation of Al(III)-TBP gel, inset is the photograph of liquid electrolyte before (left) and after (right) addition of Al^{3+}. The red, blue, green, and gray spheres stand for the H_2O molecule, N, Al, and C atoms, respectively. (Dong et al. 2017)

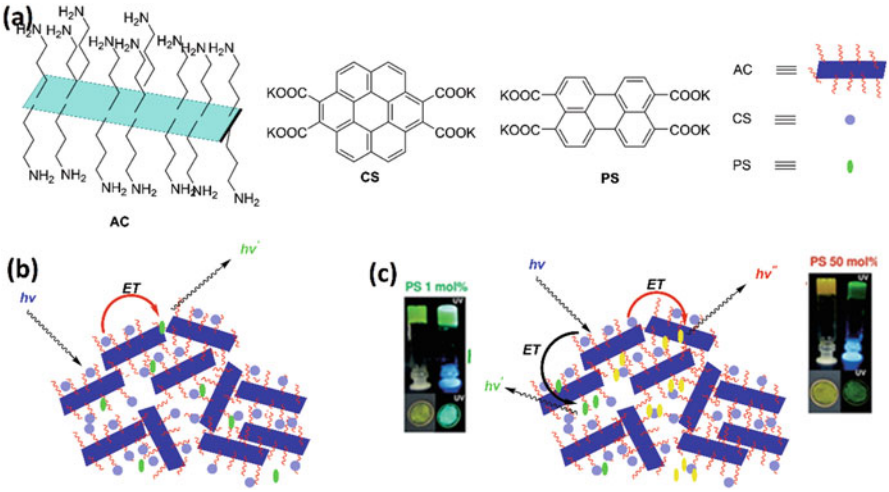

Fig. 10.16 (**a**) Chemical structure of a single layer of aminoclay (AC) and anionic dyes (CS and PS). (**b**) Schematic representation of the self-assembly and energy transfer in clay/dye hybrid gels. (**c**) Schematic representation of the energy transfer from CS to isolated PS in clay-dye hybrid gels and films. (Rao et al. 2012)

emission of the energy acceptor exhibited efficient energy hopping from the donor to the acceptor by FRET (Fig. 10.17) (Ajayaghosh et al. 2003)

On both basic and applied research aspects, π-conjugated materials are vibrant systems in which a wide variety of concepts as well as flexible devices have been

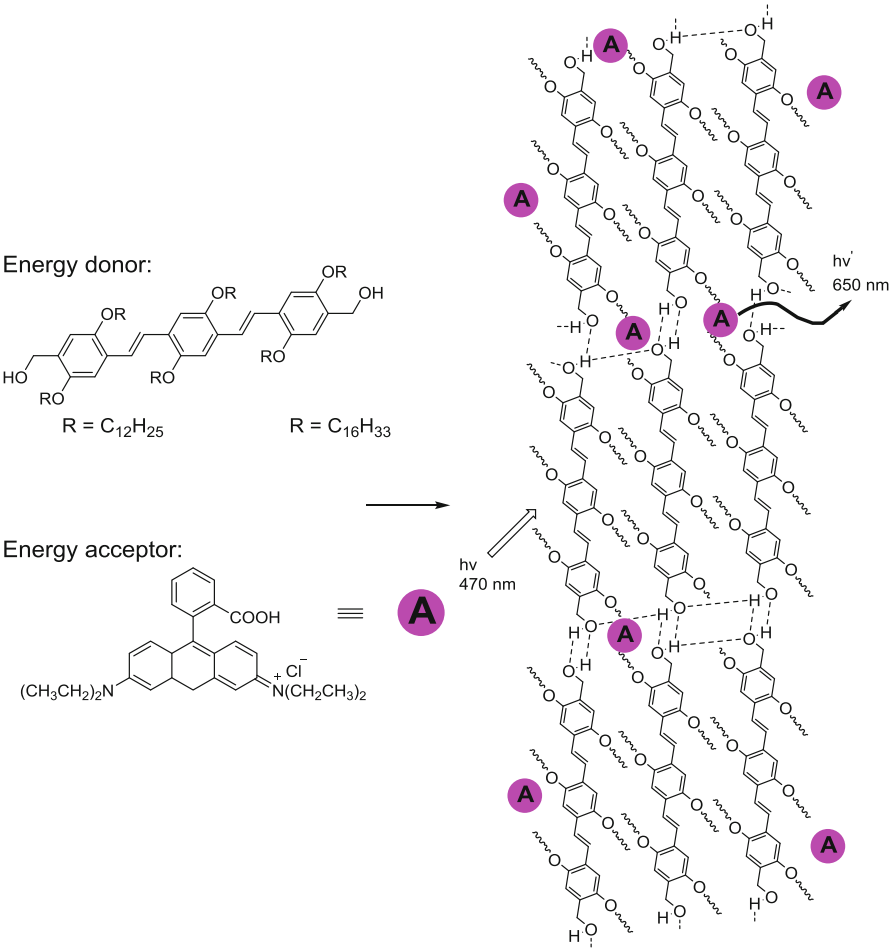

Fig. 10.17 Probable self-assembly of Rhodamine B dispersed in OPV gel. (Ajayaghosh et al. 2003)

developed. In order to replace the conventional inorganic semiconductors, major electronic industries worldwide, such as Intel Corporation, Samsung Electronics, Qualcomm, BASF, DuPont, Merck, Renesas Electronics, and STMicroelectronics to name a few, are now involved in developing efficient source of chemicals/methodologies for organic semiconductor applications. The performance of a semiconductor critically depends on the efficiency with which charge carriers move within the assembled π-conjugated system. Recently Nagarajan and co-workers have synthesized π-conjugated sugar fatty acid esters using enzyme catalysis that self-assemble into gel through H-bonding, π-π interaction, and van der Waals forces. Linseed oil trapped in the self-assembled 3D fibrous network of π-conjugated sugar fatty acid esters and its corresponding graphene incorporated version undergoes

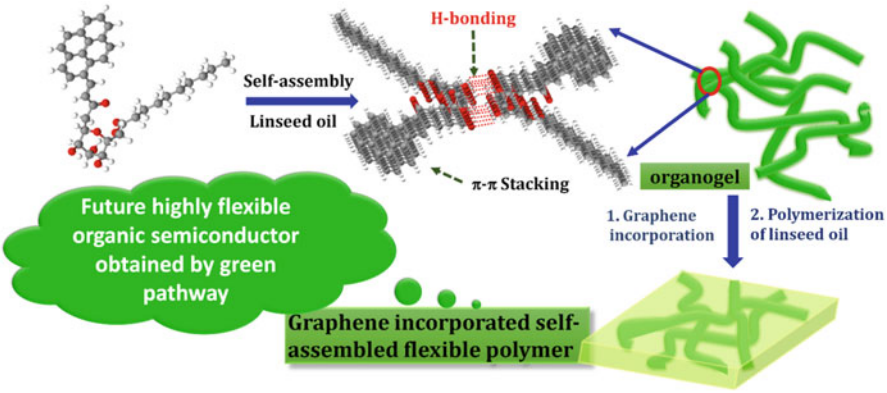

Fig. 10.18 Schematic representation of the formation of self-assembled flexible polymer. (Muthusamy et al. 2016)

polymerization to give hierarchically assembled material (Fig. 10.18). The flexible conducting material thus developed could find potential applications in electrical, mechanical, and optical fields where organic semiconductors were routinely used (Muthusamy et al. 2016).

10.4 Conclusion and Perspectives

In summary, molecular gels act as excellent platforms for environmental and energy applications. The reversible nature of gels achieved via the alteration in self-assembly phenomenon could be used as molecular switches. The practical applications associated with the molecular gels such as removal of dyes, aromatic compounds, toxic metal ions, anions, hydrocarbons and crude oil need to be fine-tuned. The formation of nanofibers can be transformed into conducting architectures or metallic nanowires via doping and annealing procedure. Phase change associated with stimuli-responsive behavior can be used for tuning the electronic behavior at the molecular level. In the future, along with the significant effort on the understanding on the molecular level self-assembly, thermodynamics, rheology, and flow kinetics, supramolecular soft gels will definitely provide a new direction to fabricate tunable functional materials. In particular, the stimuli-responsive behavior of self-assembled soft materials could be exploited to provide a soft electronic switch, optoelectronic devices, photovoltaic cells, ion channels, battery components, semiconductors, and other advanced functional materials.

Acknowledgments SN thanks the Department of Science and Technology (IFA11-CH-04 and #SB/FT/CS-024/2013), India and Board of Research in Nuclear Science (#37(1)/20/47/2014), and Department of Atomic Energy, India, for financial support. S. N. thanks the National Institute of Technology, Warangal for infrastructure facilities and RSM intramural research fund.

References

Aggeli A, Nyrkova IA, Bell M, Harding R, Carrick L, McLeish TCB, Semenov AN, Boden N (2001) Hierarchical self-assembly of chiral rod-like molecules as a model for peptide β-sheet tapes, ribbons, fibrils, and fibers. Proc Natl Acad Sci 98(21):11857–11862. https://doi.org/10.1073/pnas.191825019

Ajayaghosh A, George SJ, Praveen VK (2003) Gelation-assisted light harvesting by selective energy transfer from an oligo(p-phenylenevinylene)-based self-assembly to an organic dye. Angew Chem Int Ed 42(3):332–335. https://doi.org/10.1002/anie.200390109

Amabilino DB, Smith DK, Steed JW (2017) Supramolecular materials. Chem Soc Rev 46:2404–2420. https://doi.org/10.1039/c7cs00163k

Ariga K, Li J, Fei J, Ji Q, Hill JP (2006) Nanoarchitectonics for dynamic functional materials from atomic-/molecular-level manipulation to macroscopic action. Adv Mater 28:1251–1286. https://doi.org/10.1002/adma.201502545.

Ariga K, Hill JP, Lee MV, Vinu A, Charvet R, Acharya S (2008) Challenges and breakthroughs in recent research on self-assembly. Sci Technol Adv Mater 9(1):014109. https://doi.org/10.1088/1468-6996/9/1/014109

Babel S (2003) Low-cost adsorbents for heavy metals uptake from contaminated water: a review. J Hazard Mater 97(1–3):219–243. https://doi.org/10.1016/S0304-3894(02)00263-7

Bachl J, Oehm S, Mayr J, Cativiela C, Marrero-Tellado JJ, Díaz DD (2015) Supramolecular phase-selective gelation by peptides bearing side-chain azobenzenes: effect of ultrasound and potential for dye removal and oil spill remediation. Int J Mol Sci 16(5):11766–11784. https://doi.org/10.3390/ijms160511766

Basrur VR, Guo J, Wang C, Raghavan SR (2013) Synergistic gelation of silica nanoparticles and a sorbitol-based molecular gelator to yield highly-conductive free-standing gel electrolytes. ACS Appl Mater Interfaces 5(2):262–267. https://doi.org/10.1021/am301920r

Basu K, Nandi N, Mondal B, Dehsorkhi A, Hamley IW, Banerjee A (2017) Peptide-based ambidextrous bifunctional gelator: applications in oil spill recovery and removal of toxic organic dyes for waste water management. Interf Focus 7(6):20160128. https://doi.org/10.1098/rsfs.2016.0128

Bhattacharya S, Maitra U, Mukhopadhyay S, Srivastava A (2006) Advances in molecular hydrogels. Mol. Gels Mater. with Self-Assembled Fibrillar Networks. pp 613–647. https://doi.org/10.1007/1-4020-3689-2_18

Bisoyi HK, Li Q (2016) Light-driven liquid crystalline materials: from photo-induced phase transitions and property modulations to applications. Chem Rev 116(24):15089–15166. https://doi.org/10.1021/acs.chemrev.6b00415

Cheng N, Hu Q, Guo Y, Wang Y, Yu L (2015) Efficient and selective removal of dyes using imidazolium-based supramolecular gels. ACS Appl Mater Interfaces 7(19):10258–10265. https://doi.org/10.1021/acsami.5b00814

Cornwell DJ, Okesola BO, Smith DK (2013) Hybrid polymer and low molecular weight gels – dynamic two-component soft materials with both responsive and robust nanoscale networks. Soft Matter 9:8730–8736. https://doi.org/10.1039/C3SM51967H

Cui Y, Li MC, Wu Q, Pojman JA, Kuroda DG (2017) Synthesis-free phase-selective gelator for oil-spill remediation. ACS Appl Mater Interfaces 9(39):33549–33553. https://doi.org/10.1021/acsami.7b10009

Dastidar P, Roy R, Parveen R, Ganguly S, Majumder J, Paul M (2017) Designing soft supramolecular materials using intermolecular interactions. Monogr Supramol Chem 37–74. https://doi.org/10.1039/9781788010276-00037

Datta S, Samanta S, Chaudhuri D (2018) Near instantaneous gelation of crude oil using naphthalene diimide based powder gelator. J Mater Chem A 6(7):2922–2926. https://doi.org/10.1039/C7TA10103A

Díaz DD, Kühbeck D, Koopmans RJ (2011) Stimuli-responsive gels as reaction vessels and reusable catalysts. Chem Soc Rev 40(1):427–448. https://doi.org/10.1039/C005401C

Dong Y-J, Rao H-S, Cao Y, Chen H-Y, Kuang D-B, Su C-Y (2017) In situ gelation of Al(III)-4-tert-butylpyridine based metal-organic gel electrolyte for efficient quasi-solid-state dye-sensitized solar cells. J Power Sources 343:148–155. https://doi.org/10.1016/j.jpowsour.2017.01.051

Draper ER, Adams DJ (2017) Low-molecular-weight gels: the state of the art. Chem 3:390–410. https://doi.org/10.1016/j.chempr.2017.07.012

Edathil AA, Pal P, Banat F (2017) Alginate derived porous graphitic carbon for highly efficient remediation of sulfide from wastewater. J Environ Chem Eng 5(2):1998–2009

Edwards W, Smith DK (2014) Enantioselective component selection in multicomponent supramolecular gels. J Am Chem Soc 136(3):1116–1124. https://doi.org/10.1021/ja411724r

Estroff LA, Hamilton AD (2004) Water gelation by small organic molecules. Chem Rev 104 (3):1201–1218. https://doi.org/10.1021/cr0302049

Felip-León C, Díaz-Oltra S, Galindo F, Miravet JF (2016) Chameleonic, light harvesting photonic gels based on orthogonal molecular fibrillization. Chem Mater 28(21):7964–7972. https://doi.org/10.1021/acs.chemmater.6b03137

Fichman G, Gazit E (2014) Self-assembly of short peptides to form hydrogels: design of building blocks, physical properties and technological applications. Acta Biomater 10(4):1671–1682. https://doi.org/10.1016/j.actbio.2013.08.013

Fujita N, Shinkai S (2006) Design and function of low molecular-mass organic Gelators (LMOGs) bearing steroid and sugar groups. Mol. Gels Mater. with Self-Assembled Fibrillar Networks. pp 553–575. https://doi.org/10.1007/1-4020-3689-2_16

Ganta S, Chand DK (2018) Multi-stimuli-responsive metallogel molded from a Pd_2L_4 -type coordination cage: selective removal of anionic dyes. Inorg Chem 57(7):3634–3645. https://doi.org/10.1021/acs.inorgchem.7b02239

George M, Weiss RG (2006) Molecular organogels. Soft matter comprised of low-molecular-mass organic gelators and organic liquids. Acc Chem Res 39(8):489–497. https://doi.org/10.1021/ar0500923

Gong Y, Zhao X, Cai Z, O'Reilly SE, Hao X, Zhao D (2014) A review of oil, dispersed oil and sediment interactions in the aquatic environment: influence on the fate, transport and remediation of oil spills. Mar Poll Bull 79:16–33. https://doi.org/10.1016/j.marpolbul.2013.12.024

Gupta VK, Suhas (2009) Application of low-cost adsorbents for dye removal – a review. J Environ Manag 90(8):2313–2342. https://doi.org/10.1016/j.jenvman.2008.11.017

Hamley IW, Castelletto V (2017) Self-assembly of peptide bioconjugates: selected recent research highlights. Bioconjug Chem 28(3):731–739. https://doi.org/10.1021/acs.bioconjchem.6b00284

Hanabusa K, Suzuki M (2014) Development of low-molecular-weight gelators and polymer-based gelators. Polym J 46(11):776–782. https://doi.org/10.1038/pj.2014.64

He Y, Bian Z, Kang C, Gao L (2011) Self-discriminating and hierarchical assembly of racemic binaphthyl-bisbipyridines and silver ions: from metallocycles to gel nanofibers. Chem Commun 47(5):1589–1591. https://doi.org/10.1039/C0CC03192E

Hirst AR, Escuder B, Miravet JF, Smith DK (2008) High-tech applications of self-assembling supramolecular nanostructured gel-phase materials: from regenerative medicine to electronic devices. Angew Chem Int Ed 47(42):8002–8018. https://doi.org/10.1002/anie.200800022

Jadhav SR, Vemula PK, Kumar R, Raghavan SR, John G (2010) Sugar-derived phase-selective molecular gelators as model solidifiers for oil spills. Angew Chem Int Ed 49(42):7695–7698. https://doi.org/10.1002/anie.201002095

Knani D, Alperstein D (2017) Simulation of DBS, DBS-COOH, and DBS-$CONHNH_2$ as hydrogelators. J Phys Chem A 121(5):1113–1120. https://doi.org/10.1021/acs.jpca.6b11130

Komarov PV, Mikhailov IV, Alekseev VG, Khizhnyak SD, Pakhomov PM (2012) Self-assembly and gel formation processes in an aqueous solution of L-cysteine and silver nitrate. J Struct Chem 53(5):988–1005. https://doi.org/10.1134/S002247661205023X

Konda M, Maity I, Rasale DB, Das AK (2014) A new class of phase-selective synthetic β-amino acid based peptide gelator: from mechanistic aspects to oil spill recovery. ChemPlusChem 79 (10):1482–1488. https://doi.org/10.1002/cplu.201402120

Krishnan AS, Roskov KE, Spontak RJ (2010) Nanostructured organogels via molecular self-assembly. Adv Nanomater 2:791–834. https://doi.org/10.1002/9783527628940.ch26

Lalitha K, Sridharan V, Maheswari CU, Vemula PK, Nagarajan S (2017) Morphology transition in helical tubules of a supramolecular gel driven by metal ions. Chem Commun 53:1538–1541. https://doi.org/10.1039/C6CC09120B

Lehn J-M (1985) Supramolecular chemistry: receptors, catalysts and carriers. Science 227 (4689):849–856

Lehn J-M (1990) Perspectives in supramolecular chemistry – from molecular recognition towards molecular information processing and self-organization. Angew Chem Int Ed 29 (11):1304–1319. https://doi.org/10.1002/anie.199013041

Lehn J-M (2004) Supramolecular chemistry: from molecular information towards self-organization and complex matter. Rep Prog Phys 67:249–265. https://doi.org/10.1088/0034-4885/67/3/R02

Lin Y, Mao C (2011) Bio-inspired supramolecular self-assembly towards soft nanomaterials. Front Mater Sci 5:247–265. https://doi.org/10.1007/s11706-011-0141-5

Liu K, He P, Fang Y (2011) Progress in the studies of low-molecular mass gelators with unusual properties. Sci China Chem 54:575–586. https://doi.org/10.1007/s11426-011-4250-x

Liu Z, Sun J, Zhou Y, Zhang Y, Wu Y, Nalluri SKM, Wang Y, Samanta A, Mirkin CA, Schatz GC, Stoddart JF (2016) Supramolecular gelation of rigid triangular macrocycles through rings of multiple C-H. . .O interactions acting cooperatively. J Org Chem 81(6):2581–2588. https://doi.org/10.1021/acs.joc.6b00281

Mohmeyer N, Schmidt HW (2005) A new class of low-molecular-weight amphiphilic gelators. Chemistry 11(3):863–872. https://doi.org/10.1002/chem.200400716

Mukherjee S, Mukhopadhyay B (2012) Phase selective carbohydrate gelator. RSC Adv 2:2270–2273. https://doi.org/10.1039/C2RA00036A

Mukherjee S, Shang C, Chen X, Chang X, Liu K, Yu C, Fang Y (2014) *N*-acetylglucosamine-based efficient, phase-selective organogelators for oil spill remediation. Chem Commun 50:13940–13943. https://doi.org/10.1039/C4CC06024E

Muthusamy K, Sridharan V, Maheswari CU, Nagarajan S (2016) Lipase catalyzed synthesis of fluorescent glycolipids: gelation studies and graphene incorporated self-assembled sheet formation for semiconductor applications. Green Chem 18:3722–3731. https://doi.org/10.1039/C6GC00347H

Nandi N, Baral A, Basu K, Roy S, Banerjee A (2017) A dipeptide-based superhydrogel: removal of toxic dyes and heavy metal ions from waste water. Biopolymers 108(1):10–12. https://doi.org/10.1002/bip.22915

Nisticò R, Franzoso F, Cesano F, Scarano D, Magnacca G, Parolo ME, Carlos L (2017) Chitosan-derived iron oxide systems for magnetically guided and efficient water purification processes from polycyclic aromatic hydrocarbons. ACS Sustain Chem Eng 5(1):793–801. https://doi.org/10.1021/acssuschemeng.6b02126

Okesola BO, Smith DK (2013) Versatile supramolecular pH-tolerant hydrogels which demonstrate pH-dependent selective adsorption of dyes from aqueous solution. Chem Commun 49:11164–11166. https://doi.org/10.1039/C3CC45969A

Okesola BO, Smith DK (2016) Applying low-molecular weight supramolecular gelators in an environmental setting – self-assembled gels as smart materials for pollutant removal. Chem Soc Rev 45:4226–4251. https://doi.org/10.1039/C6CS00124F

Okesola BO, Vieira VMP, Cornwell DJ, Whitelaw NK, Smith DK (2015) 1,3:2,4-Dibenzylidene-D-sorbitol (DBS) and its derivatives – efficient, versatile and industrially-relevant low-molecular-weight gelators with over 100 years of history and a bright future. Soft Matter 11:4768–4787. https://doi.org/10.1039/C5SM00845J

Pan M, Wei Z, Xu Y, Su C (2017) Coordination assembly of metal-organic materials. Prog Chem 29:47–74. https://doi.org/10.7536/PC161222

Prathap A, Sureshan KM (2012) A mannitol based phase selective supergelator offers a simple, viable and greener method to combat marine oil spills. Chem Commun 48:5250–5252. https://doi.org/10.1039/C2CC31631E

Prathap A, Sureshan KM (2017) Organogelator–cellulose composite for practical and eco-friendly marine oil-spill recovery. Angew Chem Int Ed 56(32):9405–9409. https://doi.org/10.1002/anie.201704699

Raeburn J, Adams DJ (2015) Multicomponent low molecular weight gelators. Chem Commun 51:5170–5180. https://doi.org/10.1039/C4CC08626K

Ran X, Li Y, Gao Q, Qiu W, Guo L (2017) A smart phase-selective gelator for recycling aromatic solvents, the removal of toxic dyes, and molecular delivery. Asian J Org Chem 6(1):95–101. https://doi.org/10.1002/ajoc.201600480

Rao KV, Datta KK, Eswaramoorthy M, George SJ (2012) Light-harvesting hybrid assemblies. Chemistry 18(8):2184–2194. https://doi.org/10.1002/chem.201103601

Roy S, Javid N, Frederix PWJM, Lamprou DA, Urquhart AJ, Hunt NT, Halling PJ, Ulijn RV (2012) Dramatic specific-ion effect in supramolecular hydrogels. Chemistry 18(37):11723–11731. https://doi.org/10.1002/chem.201201217

Roy A, Gautam A, Malla JA, Sarkar S, Mukherjee A, Talukdar P (2018) Self-assembly of small-molecule fumaramides allows transmembrane chloride channel formation. Chem Commun 54:2024–2027. https://doi.org/10.1039/C7CC08693H

Samateh M, Vidyasagar A, Jadhav SR, John G (2016) Sugar based amphiphiles: easily accessible and efficient crude oil spill thickening agents. RSC Adv 6(109):107598–107605. https://doi.org/10.1039/C6RA21871G

Sangeetha NM, Maitra U (2005) Supramolecular gels: functions and uses. Chem Soc Rev 34 (10):821–836. https://doi.org/10.1039/B417081B

Shen Z, Wang T, Liu M (2014) Tuning the gelation ability of racemic mixture by melamine: enhanced mechanical rigidity and tunable nanoscale chirality. Langmuir 30(35):10772–10778. https://doi.org/10.1021/la502799j

Shi L, Sun N, Zheng L (2015) Controlled topologies and self-assembly behaviors of oligomeric supra-amphiphiles. Chem Commun 51(86):15700–15703. https://doi.org/10.1039/C5CC06445G

Smith DK (2008) Molecular gels – nanostructured soft materials. Org Nanostruct 111–154. https://doi.org/10.1002/9783527622504.ch5

Smith DK (2009) Lost in translation? Chirality effects in the self-assembly of nanostructured gel-phase materials. Chem Soc Rev 38(3):684–694. https://doi.org/10.1039/B800409A

Srinivasan S, Babu SS, Praveen VK, Ajayaghosh A (2008) Carbon nanotube triggered self-assembly of oligo(p-phenylene vinylene)s to stable hybrid π-gels. Angew Chem Int Ed 47 (31):5746–5749. https://doi.org/10.1002/anie.200801000

Stupp SI, Palmer LC (2014) Supramolecular chemistry and self-assembly in organic materials design. Chem Mater 26(1):507–518. https://doi.org/10.1021/cm403028b

Sundararajan PR (2016) Physical aspects of polymer self-assembly. 2016. https://doi.org/10.1002/9781118994405

Takeshita J, Hasegawa Y, Yanai K, Yamamoto A, Ishii A, Hasegawa M, Yamanaka M (2017) Organic dye adsorption by amphiphilic tris-urea supramolecular hydrogel. Chem Asian J 12 (16):2029–2032. https://doi.org/10.1002/asia.201700708

Tam AYY, Yam VWW (2013) Recent advances in metallogels. Chem Soc Rev 42:1540–1567. https://doi.org/10.1039/c2cs35354g

Vibhute AM, Muvvala V, Sureshan KMA (2016) Sugar-based gelator for marine oil-spill recovery. Angew Chem Int Ed 55(27):7782–7785. https://doi.org/10.1002/anie.201510308

Wang C, Wang Z, Zhang X (2012) Amphiphilic building blocks for self-assembly: from amphiphiles to supra-amphiphiles. Acc Chem Res 45(4):608–618. https://doi.org/10.1021/ar200226d

Weiss RG (2014) The past, present, and future of molecular gels. What is the status of the field, and where is it going? J Am Chem Soc 136:7519–7530. https://doi.org/10.1021/ja503363v

Zamboulis A, Dautel O, Moreau JJE (2015) Synthetic self-assembly strategies and methods. Sol-Gel Handb 1–3:121–164. https://doi.org/10.1002/9783527670819.ch04

Zhang S (2003) Fabrication of novel biomaterials through molecular self-assembly. Nat Biotechnol 21(10):1171–1178. https://doi.org/10.1038/nbt874

Zhang X, Wang C (2011) Supramolecular amphiphiles. Chem Soc Rev 40(1):94–101. https://doi.org/10.1039/B919678C

Zhang Z, Zhang S, Zhang J, Zhu L, Qu D (2017) Solvent-dependent self-assembly and morphological transition of low-molecular-weight azobenzene organogel. Tetrahedron 73 (33):4891–4895. https://doi.org/10.1016/j.tet.2017.05.027

Chapter 11
Application of Nanoparticles for Self-Cleaning Surfaces

Sivaraman Somasundaram and Vignesh Kumaravel

Contents

S. Somasundaram (✉)
Department of Chemistry, Kongju National University, Gongju, Republic of Korea
e-mail: sivaraman79@gmail.com; sivaraman79@kongju.ac.kr

V. Kumaravel (✉)
Department of Environmental Science, School of Science, Institute of Technology Sligo, Ash lane, Co. Sligo, Ireland
e-mail: vignesh134@gmail.com; Kumaravel.Vignesh@itsligo.ie

R. Saravanan et al. (eds.), *Emerging Nanostructured Materials for Energy and Environmental Science*, Environmental Chemistry for a Sustainable World 23,
https://doi.org/10.1007/978-3-030-04474-9_11

Abstract Self-cleaning in one of the most significant applications in the recent years to repel the contaminants like dirt, toxic pollutants, and microbes from any kind of surface. Hydrophobic and hydrophilic coatings are commonly used to fabricate a self-cleaning surface. Nanoparticles play a vital role in the design of self-cleaning glasses/goggles, windows, paints, building materials, medical devices, fabrics, and corrosion resistance materials. The basic principles, various applications, and key findings of hydrophobic/super-hydrophobic and hydrophilic/super-hydrophilic coated substrates are briefly discussed in this chapter. The utilization of different self-cleaning products available in the market is also highlighted. Moreover, the future challenges are described to fabricate an eco-friendly, cost-effective, highly stable, and durable self-cleaning surface.

11.1 Self-Cleaning Surfaces

Every human being's dream is to have a dirt-free clean surface. Self-cleaning is one of the most attractive properties of a surface, which can repel all the contaminants (dirt, pollutants, microbes) through the action of rolling-off water drops. Self-cleaning characteristic can be introduced into any kind of surface by controlling its wettability (Liu and Jiang 2012). Self-cleaning surfaces have a wide range of applications in domestic, industry, agriculture, and military (Parkin and Palgrave 2005). The utilization of a self-cleaning surface is smart and laborsaving and offers a healthy environment. Two important technologies are available to fabricate the self-cleaning surfaces (Blossey 2003) via the action of water. The former one by rolling water droplets (hydrophobic) and the latter by sheeting water (hydrophilic) that carries away the dirt. Moreover, hydrophilic coatings have an additional property that they can chemically break down the adsorbed dirt/pollutant on the surface under sunlight irradiation (Parkin and Palgrave 2005). The materials, mechanisms involved in the formation of self-cleaning coatings, applications, and future challenges are discussed briefly in this chapter.

11.2 Wettability of Surfaces

Thomas Young's equation is the fundamental for all wetting phenomena:

$$\gamma_{sg} - \gamma_{sl} = \gamma_{lg} \cos\theta \tag{11.1}$$

where γ represents the surface tension per unit area between the solid (s), liquid (l), and gas (g) phases and θ is intrinsic contact angle of the drop. It should be noted that Young's equation is only valid for ideal solid surfaces, which is chemically

Table 11.1 The classification of the wettability of a surface

WCA	Wettability by water	Wettability by nonpolar liquids
$\theta > 150°$	Super-hydrophobic	Super-oleophobic
$\theta > 90°$	Hydrophobic	Oleophobic
$0° < \theta < 90°$	Hydrophilic	Oleophilic
$\theta < 10° = 0$	Super-hydrophilic	Super-oleophilic

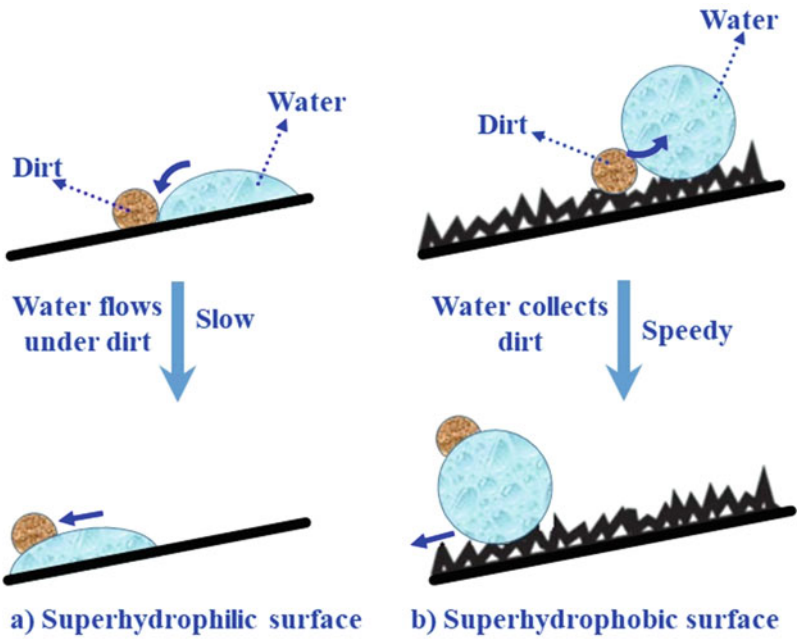

Fig. 11.1 The schematic representation of self-cleaning process in super-hydrophobic and super-hydrophilic surfaces. (Modified from Nishimoto and Bhushan (2013) with permission of The Royal Society of Chemistry)

homogeneous, inert, rigid, and smooth. Based on the water contact angle (WCA), the wettability of a surface is classified as shown in Table 11.1 (Zhang et al. 2012; Martines et al. 2005).

The schematic demonstration of self-cleaning property in super-hydrophobic and super-hydrophilic surfaces is displayed in Fig. 11.1.

The contact angle ($\boldsymbol{\theta}$) of the liquid drop over the surface determines the wettability. The relationship between the contact angle and the wettability properties is shown in Fig. 11.2. The surface with WCA lesser than 90° is called as a hydrophilic (wettable surface). Likewise, the surface with WCA greater than 90° is known as hydrophobic (non-wettable surface) (Parkin and Palgrave 2005). Fluoropolymers or silane coupling agents (to increase the WCA up to 120°) can be used to further enhance the wettability of a surface (Shafrin and Zisman 1964; Coulson et al. 2000).

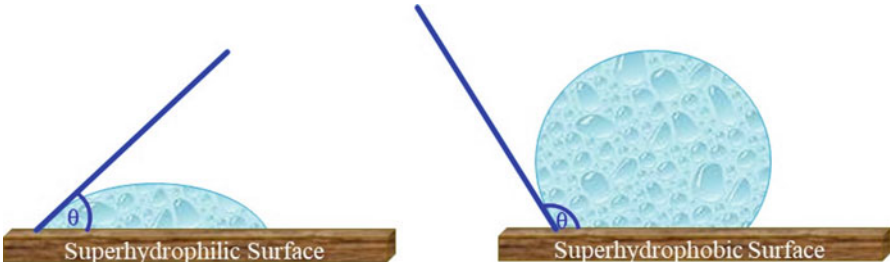

Fig. 11.2 Schematic of the relationship between WCA and wettability. (Modified from Banerjee et al. (2015) with permission from Elsevier)

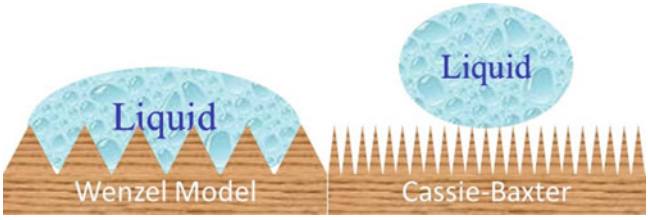

Fig. 11.3 Schematic of Wenzel and Cassie-Baxter models for wettability. (Modified from S. Banerjee, arXiv preprint arXiv:0808.1460 (2008), https://arxiv.org/pdf/0808.1460.pdf)

The surface structure or tropology should be considered to achieve the high values of the WCA (nearly 180°). The effect of surface tropology on the wettability can be easily understood by Wenzel (1936a, b) equation, which describes that the apparent contact angle θ_{app} of the drop on the rough surface is related to Young's intrinsic angle θ on the smooth surface by $\theta_{app} = \mathrm{r} \cos \theta$. Here, r is roughness factor. It is defined as the ratio of geometric surface area to the actual surface area:

$$r = \frac{\text{Geometric surface area}}{\text{Actual surface area}} \tag{11.2}$$

The wettability property of a rough surface by Wenzel (1936a, b) and Cassie-Baxter (1944) models is shown in Fig. 11.3. Wenzel model deals with the homogeneous surface, whereas the Cassie-Baxter model defines about the heterogeneous surface. Generally, the surface area of a rough surface is higher than that of a smooth surface. Based on the Wenzel model for a rough surface, the liquid droplet contacts with the entire surface and sinks completely into the cavities on the surface. The apparent contact angle "θ_{app}" of a liquid droplet on a rough surface is related to the true contact angle "θ" of the droplet on a smooth surface and the roughness factor "r":

$$\cos \theta_{app} = r \cos \theta_s \tag{11.3}$$

The Wenzel equation predicts that the wettability of a surface depends on the nature of the corresponding surface. For a homogeneous surface, the wettability increases with increase of the surface roughness (Banerjee et al. 2015). Nevertheless, Wenzel model cannot satisfactorily explain the concept with the heterogeneous surfaces.

To define this, the rough surface can be simply assumed as heterogeneous, which composed of air and solid (Cassie and Baxter 1944). According to the Cassie-Baxter model, it is postulated that a liquid droplet does not penetrate completely into the surface cavities. This model proposes that the spreading of a liquid droplet on a rough surface destroys the solid-vapor interface and creates solid-liquid and liquid-vapor interfaces. The correlation between the apparent contact angle "θ_{app}" and the true contact angle for a liquid droplet on a rough surface is defined as:

$$\cos\theta_{app} = f_s \cos\theta_s + f_v \cos\theta_v \tag{11.4}$$

where "f_s" and "f_v" are the area fractions of the liquid droplet in contact with the solid surface and the vapor trapped in the cavities on the rough surface, respectively. "θ_s" and "θ_v" are the contact angles of the liquid in solid and liquid, respectively. If one of the surfaces is air, the cosine of the contact angle is -1 and $f_s + f_s = 1$; in this case, the Cassie-Baxter equation states as:

$$\cos\theta_{app} = -1 + f_s(1 + \cos\theta_s) \tag{11.5}$$

11.3 Bioinspired Self-Cleaning Surfaces

Nature is the inspiration for many researchers in the world to advance the artistic self-cleaning functional structures. The lotus leaf is referred as the sign of purity in Asian countries for more than 2000 years. The botanists Barthlott and Neinhuis from Bonn, Germany, studied the structural features of lotus leaf. They found that the micro-/nano-roughness and waxy surface chemistry are the main reasons for non-wettability (Fig. 11.4). Water drips off this rough surface and takes along the powder-like pollutants (Blossey 2003; Barthlott and Neinhuis 1997; Von Baeyer 2000). Instead of investigating the fundamental mechanisms on this surface, they perceived the value of this natural self-cleaning phenomenon for real-world applications. Mimicking the lotus leaf effect, they started to establish a group of companies to develop different products (such as paints, roof tiles, etc.) for self-cleaning applications.

Figure 11.5 displays the schematic of various bioinspired self-cleaning surfaces reported in the literature. Functional materials and surfaces are created by understanding the phenomenon of self-cleaning property found in the living nature (bioinspired process).

Fig. 11.4 The photograph of a sphere-shaped water droplet on a non-wettable lotus leaf. (Reprinted from Blossey and Bosio (2002) with permission from Springer Nature)

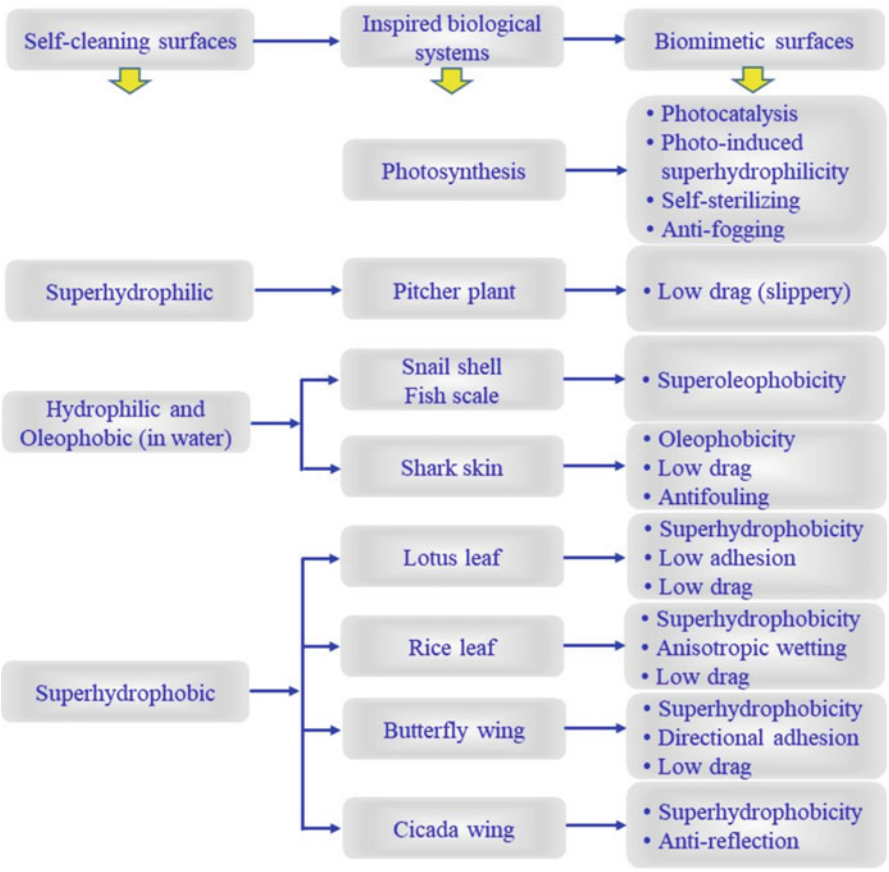

Fig. 11.5 Summary of biomimetic self-cleaning applications inspired by biological systems. (Modified from Nishimoto and Bhushan (2013) with permission of the Royal Society of Chemistry)

11.4 Fabrication of Self-Cleaning Surfaces

In this section, various approaches on the fabrication self-cleaning surfaces are briefly discussed.

11.4.1 Hydrophobic and Super-hydrophobic Coatings

Hydrophobic/super-hydrophobic coatings can clean the surfaces by the droplet flow. The aesthetic self-cleaning phenomenon found in the lotus leaf inspired to describe the fact that, though the lotus leaf grows from the muddy water, it remains clean, untouched by dirt and other contaminants. Studies revealed these surfaces are macroscopically smooth and exhibits microscopic roughness (Fig. 11.6) on different scale lengths for the super-hydrophobicity (Parker and Lawrence 2001; Herminghaus 2000; Ball 1999). These findings are beneficial for the fabrication of various biomimetic super-hydrophobic surfaces inspired by nature. There are two major types of surface microstructures in plant leaves for the super-hydrophobicity: (i) hierarchical micro- and nanostructures and (ii) unitary micro-line structures. The textured surface

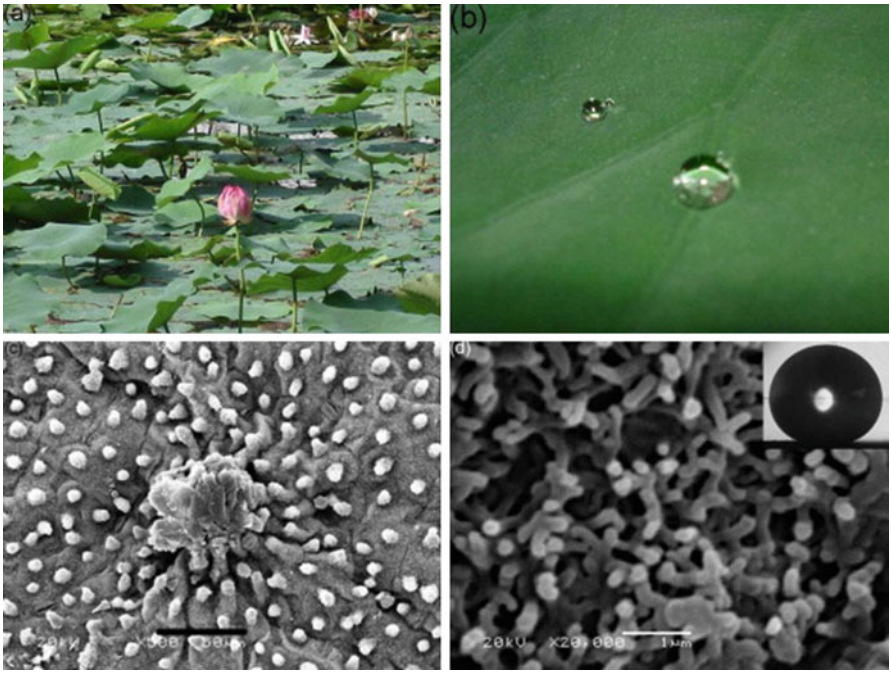

Fig. 11.6 Photographs and SEM images of lotus leaf. (Reprinted from Guo and Liu 2007) with permission from Elsevier)

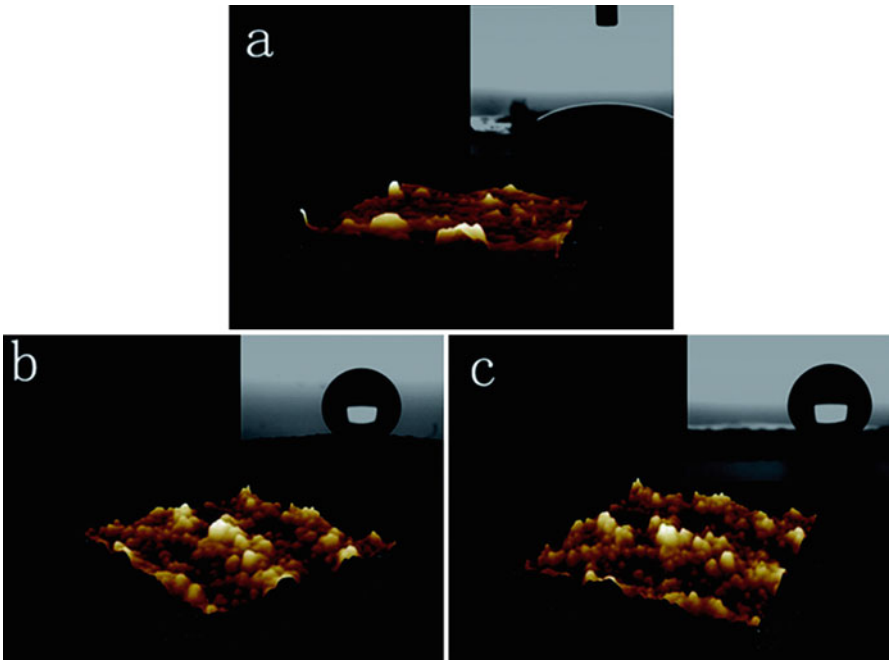

Fig. 11.7 AFM images of (**a**) pure PA, (**b**) TiO_2-coated PA, (**c**) TiO_2-/PVA-coated PA fabrics. (Reprinted from Zhou et al. (2017) with permission from the Royal Society of Chemistry)

with a WCA of 162° supports the lotus leaf to possess super-hydrophobicity. By inspiration from this fascinating hierarchical structure, Sun et al. (2005) successfully imitated a super-hydrophobic surface using lotus leaf as a template using nanoscale-casting technique. Taro leaf template (WCA 159°) was also used to produce super-hydrophobic surfaces with polystyrene film (Chen et al. 2007).

Similarly, Ramee and Chinese watermelon leaves exhibit a unitary structure, which is different from the surfaces of lotus with hierarchical structures. The surface morphologies of the both leaves are similar and exhibit a WCA of ~159°. This discovery clearly states that the hierarchical structure is not the only necessary condition to exhibit super-hydrophobicity. Recently, Saharudin et al. (2018) fabricated eco-friendly super-hydrophobic glass coating using oil palm fuel ash and polydimethylsiloxane. A WCA of $156 \pm 1°$ was achieved, and the coating was stable in the acid-base environment. Nano-TiO_2-coated polyamine-6 (PA) self-cleaning fabrics were synthesized through UV radiation-assisted ultrasonic bath method. The self-cleaning fabrics showed excellent photocatalytic and antibacterial activities. AFM images of pure PA (WCA 33°), TiO_2-coated PA (WCA 153°), and TiO_2/polyvinyl alcohol/PA (WCA 154°) coated fabrics are shown in Fig. 11.7. The high WCA and super-hydrophobicity of TiO_2-coated fabrics are ascribed to the micro-sized surface roughness.

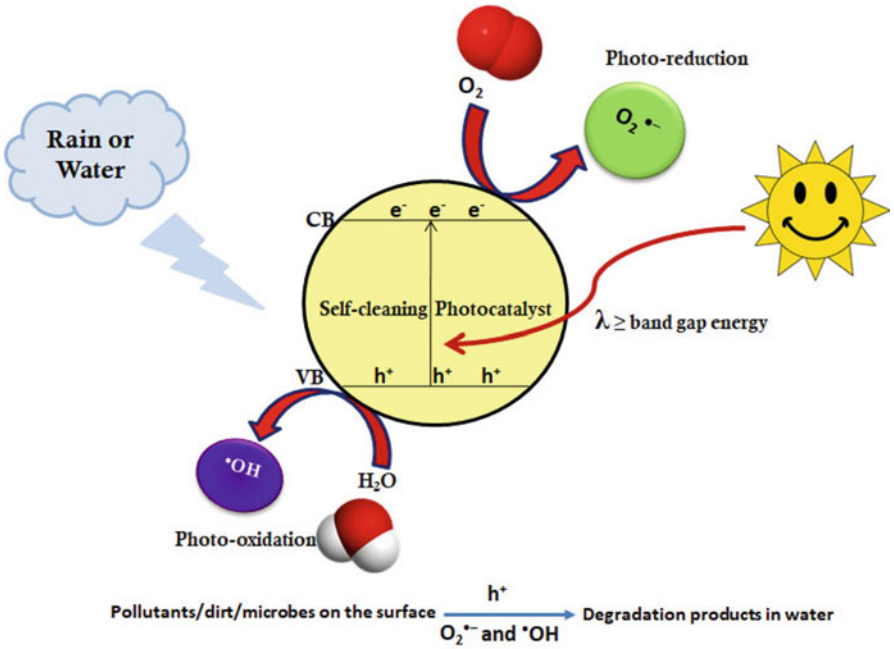

Fig. 11.8 The schematic for the mechanism of photocatalysis on a self-cleaning surface

The aforementioned super-hydrophobic properties found in nature motivate the researchers to develop technologies to make surfaces with low surface energy and to control the surface morphology on a micron/nanometer scale. There are two techniques that have been used to produce hydrophobic and super-hydrophobic surfaces: (1) making a rough surface from a low surface energy material and (2) modifying a rough surface with a material of low surface energy.

11.4.2 Hydrophilic and Super-hydrophilic Coatings

Hydrophilic coatings chemically break down dirt and other impurities when exposed to sunlight. This process is called as "photocatalysis" which is inspired from the photosynthesis of plants. The schematic for the mechanism of photocatalysis on a self-cleaning surface is illustrated in Fig. 11.8. When the surface is irradiated by light with energy higher than the band gap energy, reactive oxygen species (ROS) such as holes (h^+), superoxide radical ($O_2^{\bullet-}$), and hydroxide radical (•OH) are formed. The dirt/pollutant/microbes attached on the surface are completely degraded by the action of ROS. The degraded products are easily rolled out from the surface under rainfall or cleaning with water.

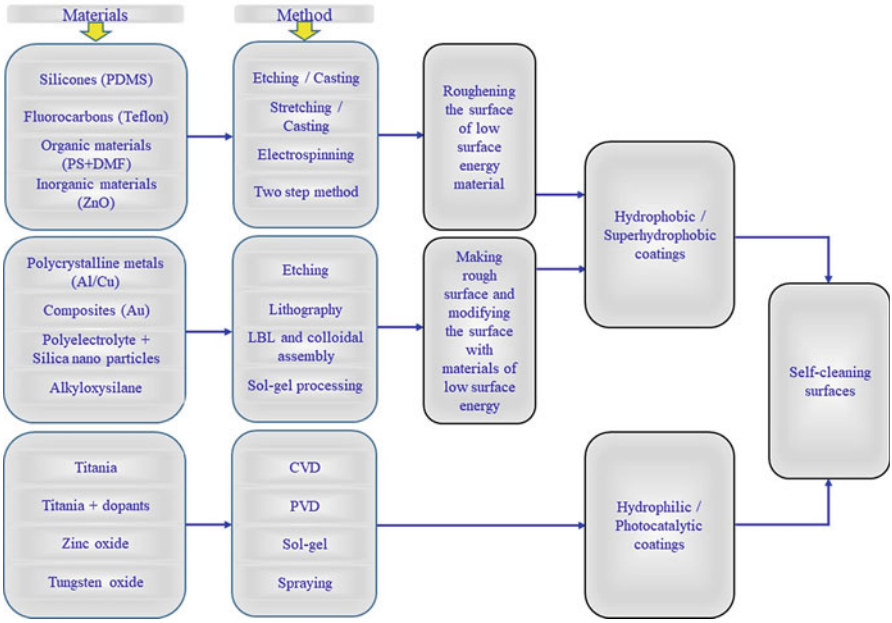

Fig. 11.9 A flowchart of materials and methods used to fabricate the self-cleaning surfaces. (Modified from Ganesh et al. (2011) with permission of the Royal Society of Chemistry)

Figure 11.9 briefly summarizes the various fabrication techniques of hydrophobic and hydrophilic coatings. Developments are under progress in advancing the hydrophilicity of self-cleaning coatings.

11.5 Applications of Nanoparticles in Self-Cleaning Surfaces

Self-cleaning surfaces have a wide range of applications in numerous fields such as textile, automobile, optical, marine, and aerospace industries. Self-cleaning coatings can also be employed in windows, solar modules, and paints. Based on this technology, some products have been commercialized for self-cleaning applications. Pilkington group of companies introduced the first self-cleaning glass (15-nm-thick nanocrystalline TiO2 film; Pilkington Activ™). In recent times, self-cleaning glasses like Radiance Ti™, SunClean™, and BioClean™ are available in the market. Lotusan, a German-based company, commercialized self-cleaning paint, and they are now commonly available in Europe. Cardinal Glass Industries, Saint-Gobain, and PPG industries are also producing self-cleaning products. A summary of recently reported hydrophilic and hydrophobic materials is given in Table 11.2.

Table 11.2 A summary of the key findings of recently developed hydrophilic and hydrophobic coatings

Material	Method	Self-cleaning action	WCA	References
Fe-TiO_2	Sol-gel	Super-hydrophilic with antifogging	2	Duan et al. (2018)
TiO_2/Sb/SnO_2	Solvothermal and ball milling	Super-hydrophilic	3–5.6°	Hu et al. (2018)
Polycrystalline anatase TiO_2	DC magnetron sputtering	Super-hydrophilic	0–5°	Lee and Park (2017)
3D TiO_2 microsphere arrays	Solvothermal	Super-hydrophilic	7°	Sadhu et al. (2017)
3-triethoxysilylpropylamine (KH550) and TiO_2 on PV modules	Hydrothermal	Super-hydrophilic	<10°	Zhong et al. (2017)
Polysiloxane resin/TiO_2	Hydrothermal	Super-hydrophobic	152°	Li et al. (2018)
TiO_2/SiO_2/perfluoro (2-methylpent-2-ene)	Atmospheric pressure plasma	Hydrophobic	140°	Mertens et al. (2017)
Ag doping indium tin oxide	Vapor-liquid-solid (VLS) growth	Super-hydrophobic	151°	Min et al. (2018)
Acrylonitrile-styrene-acrylate/ TiO_2/methacryloxypropyl-trimethoxysilane	Ultrasonication and compression molding	Hydrophobic	113°	Qi et al. (2017)
Cu nanoparticles	Selective laser melting	Super-hydrophobic	~160°	Wang et al. (2018)
ZnO/1H,1H,2H,2H-perfluorooctyltriethoxysilane/ polystyrene	Sonochemical	Super-hydrophobic	~163°	Wang et al. (2017)

11.5.1 Photocatalytic Self-Cleaning Surfaces

Photo-induced hydrophilic surfaces have commercialized for the self-cleaning property in various applications such as fabrics, paints, glass, tiles, and cement (Table 11.3).

Transparent TiO_2 thin films were used in tiles and glass windows to construct the building with photocatalytic self-cleaning property (Chun et al. 2009; Smitha et al. 2010; Radeka et al. 2014; Ke et al. 2014; Midtdal and Jelle 2013). The solar light irradiation activates the photocatalyst to induce the self-cleaning effect (Fig. 11.10).

Lu et al. (2015) fabricated per-fluorooctyltriethoxysilane ($C_{14}H_{19}F_{12}O_3Si$)-coated TiO_2 nanoparticles paint to use on both hard (metal or glass) and soft (cotton or paper) materials to create a self-cleaning surface.

Table 11.3 The commercial applications of photocatalytic self-cleaning surfaces

Substrate	Application	References
Tile	Kitchen, bathroom, building roof, and walls	Mills et al. (2003) and Xie and Lin (2007)
Plastic/ polycarbonate	Automotive industry and buildings	Tung and Daoud (2011) and Kapridaki et al. (2014)
Glass	Mirrors for vehicles and indoor uses, windows, tunnels, road lights, and vehicles	Parkin and Palgrave (2005), Tricoli et al. (2009), Yaghoubi et al. (2010), Takata et al. (2005), Watanabe et al. (1999), and Wang et al. (1997)
Textile/fiber/ cotton	Hospital garments, medical devices, household appliances, interior furnishing, and protective clothing	Qi et al. (2006), and Tung and Daoud (2011)

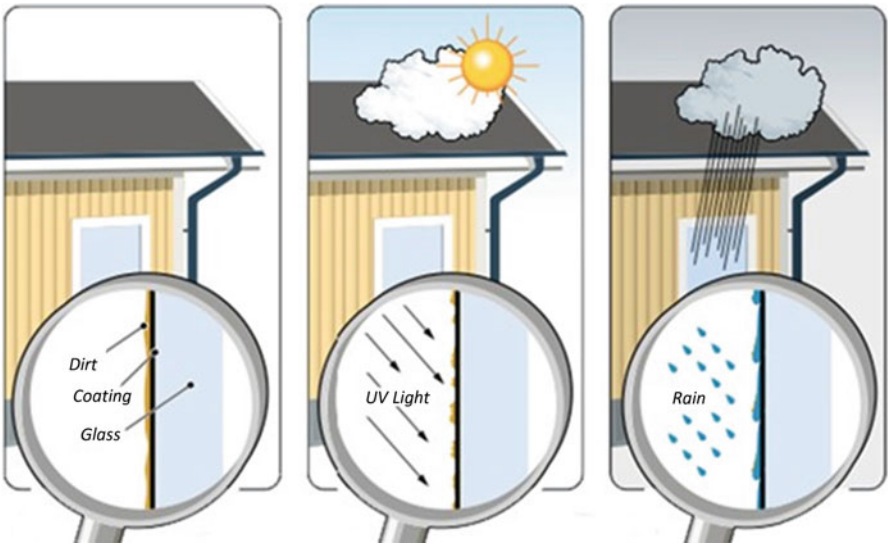

Fig. 11.10 Schematic for the mechanism of photocatalytic self-cleaning surfaces: (1) accumulation of dirt on the surfaces. (2) Solar or UV light activation of photocatalytic coating and degradation of dirt/pollutants on the surface. (3) Washing off the degraded dirt/pollutants from the surface by rainfall. (Reprinted from Midtdal and Jelle (2013) with permission from Elsevier)

11.5.2 Photocatalytic Self-Cleaning Construction Materials

Studies revealed that the self-cleaning effect of TiO_2 could be improved by water flow or rainfall. Hence, one of the best applications of self-cleaning TiO_2 surfaces is the construction materials because these could be exposed to abundant sunlight and rainfall. Later in the 1990s, a wide range of hydrophilic self-cleaning coatings such as cement, tiles, tent materials, glass, aluminum siding, and plastic films were commercialized (Parkin and Palgrave 2005; Bai 2005; Murugan et al. 2013).

Hydrotech™, a photo-induced super-hydrophilicity technology introduced by TOTO Ltd. (a Japanese company). This technology uses sunlight to break down the dirt/pollutants that can be washed away with water. It could be effectively used in building materials, coatings, and paints for constructions. High processing temperatures are required to fabricate the photocatalytic TiO_2-coated self-cleaning glazing products in commercial applications. Etacheri et al. (2011) developed a visible-light-active, oxygen-rich, and thermally stable TiO_2 (900 °C) anatase. Thermally stable photocatalytic materials are more favorable to fabricate the self-cleaning building materials. Italcementi, an Italian company, is actively focusing on self-cleaning cements. They have commercialized a range of products such as TX Aria™, TX ACtive™, and TX Arca™. Fifteen percent of urban surfaces in the Milan City contain TX Active®, which could reduce 50% of the pollution. A German-based cement supplier (Heidelberg cement technology center) produces the popular self-cleaning photocatalytic cement TioCem™, which reduces the air pollution (Spasiano et al. 2015).

The surface of the national opera hall in China has the self-cleaning glass coated with TiO_2 nanoparticles that can prevent from the dirt formation (Bai 2005). A TiO_2 white cement was employed to construct "Sports City's cricket stadium" in Dubai and "Dives In Misericordia Church" in Rome. In Japan, a wide range of eco-friendly self-cleaning windows and roof tiles are being applied. Similarly, in automotive industries, self-cleaning coating with antifogging property is used to develop clean and glare-free windows, automotive mirrors, and headlight mirrors. Lee et al. (2010) reported smart windows with self-cleaning, antireflection, and wetting properties. These windows are enough flexible, stretchable, as well as mechanically tunable optical transparent. Wrinkled polydimethylsiloxane (PDMS) films with the combination of replica molding and nano-porous anodic aluminum oxide were employed to fabricate the smart windows.

11.5.3 Antireflection Self-Cleaning Materials

11.5.3.1 Super-hydrophilic Antireflection Coatings

TiO_2 nanoparticles can easily be coated on transparent substrates such as glass and plastic to obtain a self-cleaning property. Nevertheless, these coatings always enhance the surface reflection of the transparent substrate owing to the large refractive index n of TiO_2 (2.52 and 2.76 for anatase and rutile, respectively). To avoid this, the self-cleaning antireflective coatings are generally fabricated with a mixture of SiO_2 and TiO_2. SiO_2 layer can provide a porous structure with low refractive index, whereas TiO_2 nanoparticles on the SiO_2 surface can deliver the super-hydrophilic self-cleaning function.

11.5.3.2 Super-hydrophobic Antireflection Coatings

Super-hydrophobic antireflection coatings with high reflectivity have been broadly applied in traffic lights and solar cells (Manca et al. 2009; Li et al. 2010a, b). Dai et al. (2010) reported the subwavelength Si nano-wire arrays with super-hydrophobicity, self-cleaning, and antireflection property via a galvanic wet etching method. The subwavelength nano-wires exhibited polarization-independent and omnidirectional antireflection properties (diffuse reflectance is 2.51% and the wavelength-averaged specular is 0.06%). A moth-eye-like poly (ethyleneterepthalate) film-coated TiO_2 nanoparticles were fabricated by Nakata et al. for self-cleaning antireflective surfaces (Nakata et al. 2011). The film showed a high transmittance in the range of 76–95%, no light absorption in the range of 400–800 nm, and a stable super-hydrophilicity after 18 days of prolonged UV irradiation.

Antireflection is also observed in the insect eyes and wings, which is beneficial for camouflage. For instance, cicada wings have super-hydrophobic and antireflection characteristics. Bio-mimicking the functionalities of cicada wings and moth eyes, Min et al. fabricated multifunctional optical coatings using a bioinspired template technique (Min et al. 2008).

11.5.4 Self-Cleaning Cloths

In the textile industry, the self-cleaning mechanism has been successfully applied in a wide range of fabrics in recent days.

11.5.4.1 Self-Cleaning Cloths Using TiO_2

Another significant application of TiO_2 is self-cleaning in fabrics (Tung and Daoud 2011). The coffee and red wine stains on cotton fabrics could be easily removed by TiO_2 nano-sols under UV radiation (Abidi et al. 2009). Besides, TiO_2 nanosol coating showed excellent UV protection to the cotton fabric. Bedford et al. found that cellulose acetate and TiO_2-coated fabrics could retain their self-cleaning activity after several staining and washing (2010).

TiO_2-SiO_2-coated fabrics were tested for its self-cleaning performance (Fig. 11.11) toward the decolorization of red wine stains (Yuranova et al. 2006). Pakdel et al. (2013) carried out a similar approach. They reported that TiO_2-SiO_2 with 30:70 molar ratio displayed the optimum efficiency in stain removal.

Wang et al. (2009) fabricated porous Au/TiO_2/SiO_2 nanocomposite-coated fabrics to improve the visible-light-assisted self-cleaning performance. The red wine and coffee stains on the nanocomposite-coated fabrics were completely removed after 20 h of visible-light irradiation. Au loading may increase the electron transfer

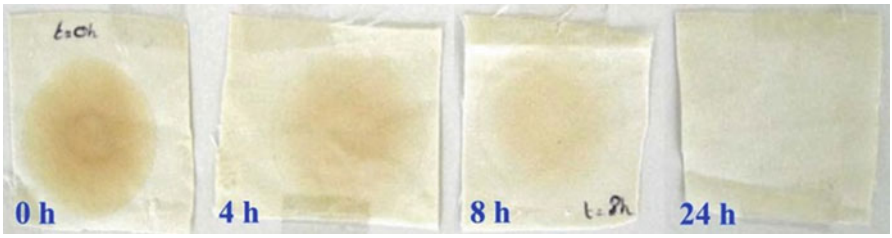

Fig. 11.11 Photographs of red wine stains removal on TiO_2-SiO_2-coated cotton fabric during 0 h, 4 h, 8 h, and 24 h of light irradiation. (Modified from Yuranova et al. (2006) with permission from Elsevier)

Fig. 11.12 Photograph of super-hydrophobic-coated self-cleaning umbrella. (Reprinted from Gould (2003) with permission from Elsevier)

(via surface plasmon resonance) and visible light absorption and decrease the photo-induced electron hole recombination.

11.5.4.2 Super-hydrophobic Self-Cleaning Cloths

Pollutants or dirt particles on the super-hydrophobic fabrics can be quickly removed from the surface while the water rolls off. The photograph of a super-hydrophobic self-cleaning umbrella is shown in Fig. 11.12. Ramarathnam et al. mimicked the self-cleaning activity of lotus leaves to super-hydrophobic self-cleaning textiles by decorating the cotton fibers with reactive SiO_2 nanoparticle monolayers and non-fluorinated polymers (2007). Alike the lotus effect, the dirt was removed from the fabric surface when water droplets were rolled over the textiles.

A wide range of super-hydrophobic self-cleaning products to resist spills, repel and release stains, and resist static are developed by Nanotex (https://www.nanotex.com/). TiO_2, tetra(4-carboxyphenyl)porphyrin (TCPP), and trimethoxy(octadecyl) silane (OTMS)-coated fabrics showed excellent self-cleaning performance (Afzal

et al. 2014). TiO_2 with OTMS showed a WCA of 156° and exhibited superior photocatalytic activity for the degradation of methylene blue dye upon visible light irradiation.

11.5.5 Antifogging Self-Cleaning Surfaces

The surface of cold windshields, eyeglasses, safety glasses, and ski goggles are commonly influenced by fogging. By studying the interaction of liquids with the glass surfaces, fogging can be controlled effectively. There are two ways to solve the fogging using nanoparticles: (a) super-hydrophilic and (b) super-hydrophobic.

11.5.5.1 Antifogging by Super-hydrophilicity

The self-cleaning TiO_2 porous surfaces prepared by Zorba et al. (2010) showed stable super-hydrophilicity without UV light activation. These surfaces demonstrated self-cleaning, antifogging, and high transmittance (from near-UV to IR). Li et al. (2009) reported highly stable and durable biomimetic super-hydrophilic surfaces with antifogging and antireflective properties on silica substrates. The photographs of TiO_2-coated and TiO_2-uncoated automotive mirrors are shown in Fig. 11.13.

Lee et al. synthesized multifunctional TiO_2/SiO_2 thin-film coated surfaces with antifogging, super-hydrophilicity, antireflection, and self-cleaning properties through layer-by-layer deposition technique (2006). The antifogging activity of super-hydrophilic TiO_2/SiO_2 composite film with 0.5 wt% polyethylene glycol was studied. The WCA of the surface was changed from 15 to 3° within 0.16 s (Wang et al. 2011). TiO_2 and reduced graphene oxide (RGO) nanocomposite was exploited as super-hydrophilic antifogging material with a WCA of 4.2° during the

Fig. 11.13 Photographs of antifogging automotive side view mirror: uncoated (left) and coated (right) with TiO_2. (Reprinted from Zhang et al. (2012) with permission of the Royal Society of Chemistry)

Fig. 11.14 Photograph of super-hydrophilic-coated antifogging mirrors. (Reprinted from Gould (2003) with permission from Elsevier)

broadband light irradiation (Zhu et al. 2014). The photograph of super-hydrophilic-coated antifogging mirror is displayed in Fig. 11.14.

Xue et al. (2015) and Koch and Barthlott (2009) synthesized corrosion resistance, super-hydrophilic, and antifogging CeO_2 films by one-step electrodeposition method. The island and micro-cracks on the CeO_2 surface cause the fast spreading of water droplets based on the capillary effect. The transparent multifunctional ZnO nano-rod films fabricated using a hydrothermal method (Kwak et al. 2011). ZnO nano-rod films showed excellent antifogging activity with super-hydrophilicity, high transmittance, and antireflection properties.

11.5.5.2 Antifogging by Super-hydrophobicity

The super-hydrophilic antifogging surfaces may fail under violent fogging conditions. This could be rectified by the application of super-hydrophobic surfaces. Mosquito compound eyes have excellent antifogging and antireflection functionalities, and thus even a tiny fog drop cannot stay on its surface. This is beneficial for mosquito to fly easily even in watery and gloomy environment. Being inspired by this natural creation, researchers developed multifunctional super-hydrophobic antifogging surface using fluoroalkylsilane (FAS) through a soft lithography method (Gao et al. 2007). Wen et al. fabricated an antifogging surface with the help of polyvinylidene fluoride (PVDF) polymer and ZnO (2014).

11.5.6 Sensors

Carbon nanoparticles are commonly employed in bio-imaging and optoelectronic devices. Yuan et al. (2011) designed a high sensitive super-hydrophobic self-cleaning infrared nano-sensor using carbon nanoparticle via a low-cost flame method. This nano-sensor was fabricated by transferring the carbon nanoparticles to an optical transparent and flexible PDMS layer, which showed a sharp photo-response in approximately 68 ms. Song et al. (2010) developed a self-organized TiO_2 nanotube layers for the high-sensitivity immunoassays through the anodization of Ti-foils. The high sensitive fluorescence sensor was found to be recyclable after a short UV treatment, suggesting the self-cleaning property of TiO_2.

Except proteins, almost all the size separation devices with small pore openings have the membrane clogging issue. Roy et al. (2010) successfully designed free-standing and self-cleaning TiO_2 nano-channel membranes for the size-selective protein separation. TiO_2 anatase membrane structures (with both sides opening) were synthesized by a single-step Ti-foil anodization. The membranes clogs can easily be removed due to the self-cleaning property of TiO_2. A self-cleaning and thermo-responsive hydrogel membrane was fabricated for implantable optical glucose biosensors to control the host response (Gant et al. 2010). Quartz crystal-coated-ZnO nano-rod was studied (Joo et al. 2009) to detect the thiol vapor for natural gas fuel cells. The adsorbed thiol molecules could be easily removed by exposing the materials under UV light irradiation to induce the self-cleaning action of ZnO.

11.5.7 Solar Cells

Dust particles and other organic pollutants may reduce the efficiency of solar cells up to 30%. This could be rectified by the use of self-cleaning coating in solar cells (Fig. 11.15). Zhu et al. (2010) reported nano-dome solar cell devices with effective antireflection and light trapping over a wide spectral range. After modification with

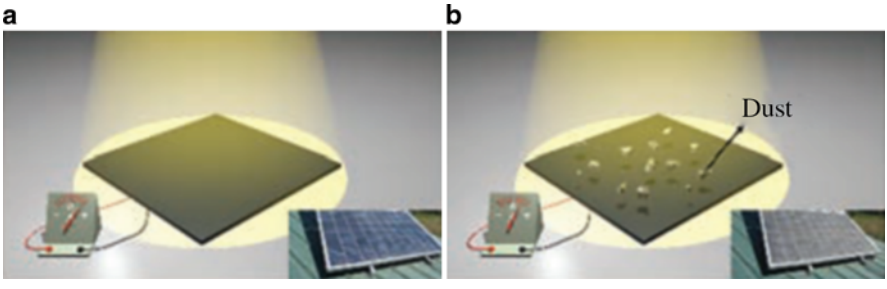

Fig. 11.15 The photographs and schematic of (**a**) clean and (**b**) dust contaminated solar cell panels. (Reprinted from Xu et al. (2016) with permission from Royal Society of Chemistry)

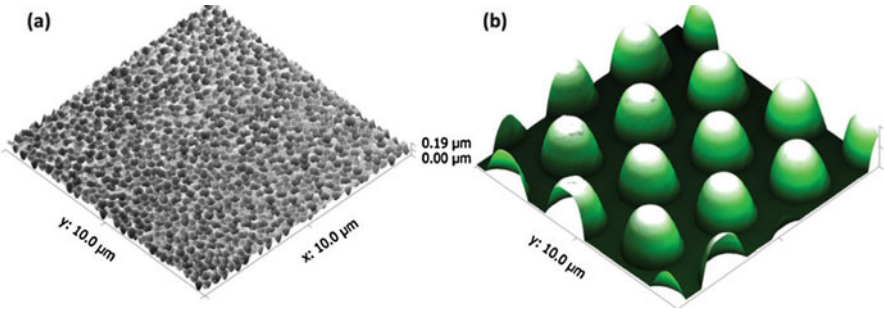

Fig. 11.16 (**a**) SEM and (**b**) AFM images of self-cleaning micromorph solar cell substrates. (Reprinted from Liu et al. (2017) with permission from Royal Society of Chemistry)

hydrophobic molecules, nano-dome solar cells showed super-hydrophobic self-cleaning properties, which exhibits higher power efficiency than the flat-film solar cells.

A micromorph silicon solar cell was designed on a glass substrate via plasma-enhanced chemical vapor deposition method to induce self-cleaning and antireflective properties. (3-mercaptopropyl)trimethoxysilane was used as a silane coupling agent. The hierarchical surface was composed of micro-cone arrays and nano-spits (Fig. 11.16). The surface displayed a WCA of 136° with 4.7% solar cell conversion efficiency. Lin et al. (2016) fabricated Si solar cell surface containing of hierarchical nano-rods and honeycomb nano-walls (HNWs). The as-synthesized Si solar cells achieved a conversion efficiency of 5.2%. Besides, the efficiency of the solar cell was not remarkably changed after 6 weeks of outdoor exposure. This might be ascribed to the self-cleaning action (repels pollutants and dust) of hierarchical nano-morphology (Fig. 11.17).

11.5.8 Other Applications

In addition to the aforementioned applications, self-cleaning surfaces are also used for antibacterial, flame retardant, biotechnology, shielding, and water treatment.

In biotechnology, controlling of DNA and proteins droplets and minimizing its contamination are the most important tasks. Spotting techniques require specific wetting properties of the substrate. Commonly available glass substrates are mildly hydrophobized. “Doughnut effect” is a trouble and unfavorable ringlike structure formation on the glass substrates. This is attributed to the drying of DNA or protein droplets. Studies were reported on the use of hydrophilic/hydrophobic coating on the substrates to overcome such problems (Blossey and Bosio 2002; Deegan et al. 1997; McHale et al. 1998). Antimicrobial activity of TiO_2 is one of the significant applications in the food industries and the medical field to avoid the microbial infection. Antimicrobial TiO_2 nanoparticles were used in construction materials for

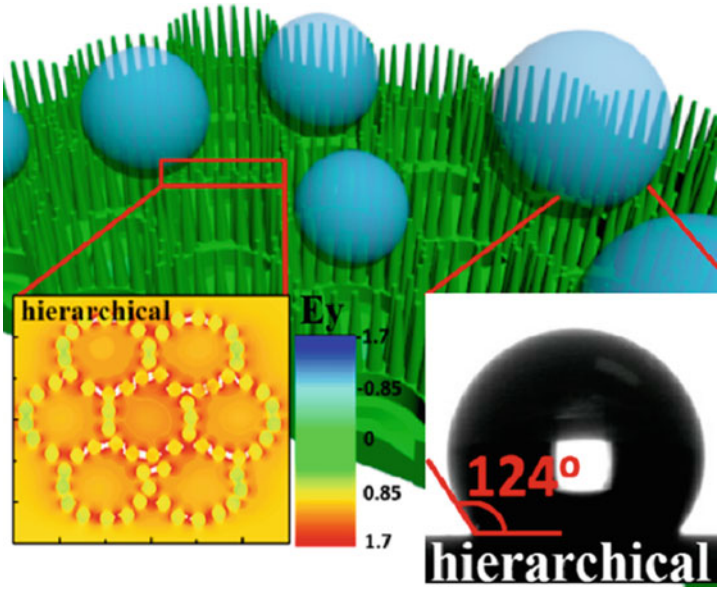

Fig. 11.17 Schematic representation of hierarchical self-cleaning solar cell surface with nano-rods and honeycomb nano-walls morphology. (Reprinted from Lin et al. (2016) with permission from American Chemical Society)

both indoor and outdoor applications (Chen and Poon 2009; Amezaga-Madrid et al. 2002). Thin films of photocatalyst-coated ceramics have been commercialized by companies like TOTO, Karpery, and Biocera, which are functioning as antimicrobial and deodorizing agents (Mills and Lee 2002).

An electro-catalytic membrane reactor with self-cleaning function was developed for industrial wastewater treatment (Yang et al. 2011). The reactor demonstrated superior performance in the treatment of oily water as compared with conventional membrane filtration. Flower-like $Mg(OH)_2$ nanocomposites were prepared by Cao et al. (2010) through an amino acid-assisted hydrothermal method. $Mg(OH)_2$ nanocomposites showed superior super-hydrophobicity with flame retardant effects.

Dunnill et al. (2009) designed a sulfur-doped TiO_2 self-cleaning film with antibacterial activity under white light illumination. The sulfur incorporation in TiO_2 enhanced the photocatalytic activity and photo-induced super-hydrophilic property. Murugan et al. (2013) reported that visible-light-assisted self-cleaning property of TiO_2 building materials was improved by doping of metal ions such as Ni^{2+} and Fe^{3+} into. Metal dopants could improve the efficiency via oxygen vacancies, creating of new energy levels and hybridization with TiO_2 orbitals. Tetraethylorthosilane (TEOS)-modified TiO_2 nanoparticles were coated on ceramic tiles to construct a visible-light-active self-cleaning surface (Zhang et al. 2013). These coated tiles showed superior photocatalytic activity and hydrophilicity under visible light irradiation due to the small particle size, large surface area, and high surface roughness.

TiO_2 nanoparticle-coated cotton, polyester, polyamide, and cellulose fibers have been designed for photocatalytic and self-cleaning textiles (Montazer and Pakdel 2011; Galkina et al. 2014; Marques et al. 2006; Pasqui and Barbucci 2014; Uddin et al. 2007). Materials such as carboxylic acid (Radetić 2013) and multiwalled carbon nanotubes (MWCNTs) (Karimi et al. 2014) are used to achieve the functionalization of TiO_2-coated fabrics. These fabrics showed high antibacterial activity (Doud 2004; Daoud et al. 2005), improved stain removal capability, superior abrasion resistance, UV blocking capability, and high stability several washings (Qi et al. 2011).

A commercially available photocatalyst-based paint (CristalACTiV™) removes the NOx up to 0.5 g/m^2/day (www.cristalactiv.com). Another similar category paint, StoClimansan-Color™ (interior paint), degrades the organic pollutants including CO under the light irradiation (www.climasan.com).

11.6 Challenges and Future Outlook

Tremendous research works have been executed the laboratory. However, they often fail when transformed to commercialization for real-time application due to many difficulties and several reasons. The primary concern is to avoid the "peel off' of self-cleaning coatings from substrates. More studies should be carried out to improve the mechanical stability and durability of the coatings. The coatings should not have any air gaps, and the surface should not be cracked or scratched when the coating is removed. The chemical or molecular interactions of coating with water droplet, dirt, and other pollutants should be studied in detail.

A wide range of TiO_2-based self-cleaning products is commercially available. Nevertheless, the fundamental investigations are required to understand the mechanisms to extend the absorption range into the visible region, enhance the self-cleaning efficacy, and expand their application in various fields. Designing multifunctional materials is a big impetus for human beings. The blend of more than one function into a unique composite is sensational path way to design the novel multifunctional self-cleaning surfaces.

Aging and decay are the biggest challenges to be faced in all the self-cleaning or contamination-free surfaces. This is not as relevant for biotechnology applications because the surfaces often be used for analytic purposes and hence designed as disposables. Studies should be performed to design antimicrobial and ultraclean reusable surfaces in the medical field. The use of self-cleaning surfaces in outdoor applications is a different problem yet. For instance, an advertised product lost its promised self-cleaning activity too rapidly and not justifying the initial investment.

In the future, self-cleaning surfaces with self-healing ability would be one of the significant research motivations. Nature is being an inspiration by providing different solutions to achieve efficient multifunctional integration. Hence, interdisciplinary researches in the area of science and engineering are much required to design and commercialize multifunctional smart self-cleaning surfaces. Moreover, the self-

cleaning coatings should be eco-friendly, highly durable, and stable and should not pollute the eco-system if it is aged.

11.7 Summary

The applications of nanoparticles to fabricate the self-cleaning surfaces (hydrophobic/hydrophilic/super-hydrophobic/super-hydrophobic) have been summarized briefly in this chapter. The basic principles and the important aspects of super-hydrophilic and super-hydrophobic self-cleaning surfaces have been described. Self-cleaning surfaces have a broad range of applications in various fields such as antifogging, cotton fabrics, antimicrobial, paints, building materials, tiles, sensors, and solar cells. There are several self-cleaning products that are commercialized in the market. However, aging and decay are the two major concerns for the self-cleaning surfaces. More studies should be carried out in the future to develop cost-effective, highly durable, and mechanically stable self-cleaning surfaces. We hope that the information presented here may be beneficial for the researchers who are working in various fields.

Acknowledgments Sivaraman Somasundaram is grateful to Energy Technology Development Program of the Korea Institute of Energy Technology Evaluation and Planning (KETEP) for their financial grants from the Ministry of Trade Industry and Energy, Republic of Korea (No.20163010012200).

References

Abidi N, Cabrales L, Hequet E (2009) Functionalization of a cotton fabric surface with titania nanosols: applications for self-cleaning and UV-protection properties. ACS Appl Mater Interfaces 1(10):2141–2146. https://doi.org/10.1021/am900315t

Afzal S, Daoud WA, Langford SJ (2014) Superhydrophobic and photocatalytic self-cleaning cotton. J Mater Chem A 2(42):18005–18011. https://doi.org/10.1039/C4TA02764G

Amezaga-Madrid P, Nevarez-Moorillon GV, Orrantia-Borunda E, Miki-Yoshida M (2002) Photo-induced bactericidal activity against Pseudomonas aeruginosa by TiO_2 based thin films. FEMS Microbiol Lett 211(2):183–188. https://doi.org/10.1111/j.1574-6968.2002.tb11222.x

Bai C (2005) Ascent of nanoscience in China. Science 309(5731):61–63. https://doi.org/10.1126/science.1115172

Ball P (1999) Engineering shark skin and other solutions. Nature 400:507–509. https://doi.org/10.1038/22883

Banerjee S, Dionysiou DD, Pillai SC (2015) Self-cleaning applications of TiO_2 by photo-induced hydrophilicity and photocatalysis. Appl Catal B Environ 176:396–428. https://doi.org/10.1016/j.apcatb.2015.03.058

Barthlott W, Neinhuis C (1997) Purity of the sacred lotus, or escape from contamination in biological surfaces. Planta 202(1):1–8. https://doi.org/10.1007/s004250050096

Blossey R (2003) Self-cleaning surfaces–virtual realities. Nat Mater 2(5):301–306. https://doi.org/10.1038/nmat856

Blossey R, Bosio A (2002) Contact line deposits on cDNA microarrays: a 'twin-spot effect'. Langmuir 18(7):2952–2954. https://doi.org/10.1021/la0114732

Cao H, Zheng H, Yin J, Lu Y, Wu S, Wu X, Li B (2010) $Mg(OH)_2$ complex nanostructures with superhydrophobicity and flame retardant effects. J Phys Chem C 114(41):17362–17368. https://doi.org/10.1021/jp107216z

Cassie ABD, Baxter S (1944) Wettability of porous surfaces. Trans Faraday Soc 40:546–551

Chen J, Poon CS (2009) Photocatalytic construction and building materials: from fundamentals to applications. Build Environ 44(9):1899–1906. https://doi.org/10.1016/j.buildenv.2009.01.002

Chen H, Yuan AQ, Tang JX, Gong HF, Liu YJ, Wang ZX, Shi P, Zhang JD, Chen X (2007) A novel preparation of polystyrene film with a superhydrophobic surface using a template method. J Phys D Appl Phys 40(11):3485. https://doi.org/10.1088/0022-3727/40/11/033

Chun HY, Park SS, You SH, Kang GH, Bae WT, Kim KW, Park JE, Öztürk A, Shin D (2009) Preparation of a transparent hydrophilic TiO_2 thin film photocatalyst. J Ceram Process Res 10 (2):219–223

Coulson SR, Woodward I, Badyal JP, Brewer SA, Willis C (2000) Super-repellent composite fluoropolymer surfaces. J Phys Chem B 104(37):8836–8840. https://doi.org/10.1021/jp0000174

Dai YA, Chang HC, Lai KY, Lin CA, Chung RJ, Lin GR, He JH (2010) Subwavelength Si nanowire arrays for self-cleaning antireflection coatings. J Mater Chem 20(48):10924–10930. https://doi.org/10.1039/C0JM00524J

Daoud WA, Xin JH, Zhang YH (2005) Surface functionalization of cellulose fibers with titanium dioxide nanoparticles and their combined bactericidal activities. Surf Sci 599(1–3):69–75. https://doi.org/10.1016/j.susc.2005.09.038

Deegan RD, Deegan RD, Bakajin O, Dupont TF, Huber G, Nagel SR, Witten TA et al (1997) Capillary flow as the cause of ring stains from dried liquid drops. Nature 389:827–829. https://doi.org/10.1038/39827

Duan Z, Zhu Y, Ren P, Jia J, Yang S, Zhao G, Xie Y, Zhang J (2018) Non-UV activated superhydrophilicity of patterned Fe-doped TiO2 film for anti-fogging and photocatalysis. Appl Surf Sci 452:165–173. https://doi.org/10.1016/j.apsusc.2018.05.029

Dunnill CW, Aiken ZA, Kafizas A, Pratten J, Wilson M, Morgan DJ, Parkin IP (2009) White light induced photocatalytic activity of sulfur-doped TiO_2 thin films and their potential for antibacterial application. J Mater Chem 19(46):8747–8754. https://doi.org/10.1039/B913793A

Etacheri V, Seery MK, Hinder SJ, Pillai SC (2011) Oxygen rich titania: a dopant free, high temperature stable, and visible-light active anatase photocatalyst. Adv Funct Mater 21 (19):3744–3752. https://doi.org/10.1002/adfm.201100301

Galkina OL, Sycheva A, Blagodatskiy A, Kaptay G, Katanaev VL, Seisenbaeva GA, Kessler VG, Agafonov AV (2014) The sol–gel synthesis of cotton/TiO_2 composites and their antibacterial properties. Surf Coat Technol 253:171–179. https://doi.org/10.1016/j.surfcoat.2014.05.033

Ganesh VA, Raut HK, Nair AS, Ramakrishna S (2011) A review on self-cleaning coatings. J Mater Chem 21(41):16304–16322. https://doi.org/10.1039/c1jm12523k

Gant RM, Abraham AA, Hou Y, Cummins BM, Grunlan MA, Coté GL (2010) Design of a self-cleaning thermoresponsive nanocomposite hydrogel membrane for implantable biosensors. Acta Biomater 6(8):2903–2910. https://doi.org/10.1016/j.actbio.2010.01.039

Gao X, Yan X, Yao X, Xu L, Zhang K, Zhang J, Yang B, Jiang L (2007) The dry-style antifogging properties of mosquito compound eyes and artificial analogues prepared by soft lithography. Adv Mater 19(17):2213–2237. https://doi.org/10.1002/adma.200601946

Gould P (2003) Smart, clean surfaces. Mater Today 6(11):44–48. https://doi.org/10.1016/S1369-7021(03)01131-3

Guo Z, Liu W (2007) Biomimic from the superhydrophobic plant leaves in nature: binary structure and unitary structure. Plant Sci 172(6):1103–1112. https://doi.org/10.1016/j.plantsci.2007.03.005

Herminghaus S (2000) Roughness-induced non-wetting. Europhys Lett 52(2):165–170. https://doi.org/10.1209/epl/i2000-00418-8

Hu Y, Zhong H, Wang Y, Lu L, Yang H (2018) TiO2/antimony-doped tin oxide: highly water-dispersed nano composites with excellent IR insulation and super-hydrophilic property. Sol Energy Mater Sol Cells 174:499–508. https://doi.org/10.1016/j.solmat.2017.09.027

Joo J, Lee D, Yoo M, Jeon S (2009) ZnO nanorod-coated quartz crystals as self-cleaning thiol sensors for natural gas fuel cells. Sensors Actuators B Chem 138(2):485–490. https://doi.org/10.1016/j.snb.2009.03.017

Kapridaki C, Pinho L, Mosquera MJ, Maravelaki-Kalaitzaki P (2014) Producing photoactive, transparent and hydrophobic SiO_2-crystalline TiO_2 nanocomposites at ambient conditions with application as self-cleaning coatings. Appl Catal B Environ 156:416–427. https://doi.org/10.1016/j.apcatb.2014.03.042

Karimi L, Zohoori S, Amini A (2014) Multi-wall carbon nanotubes and nano titanium dioxide coated on cotton fabric for superior self-cleaning and UV blocking. New Carbon Mater 29 (5):380–385. https://doi.org/10.1016/S1872-5805(14)60144-X

Ke S, Cheng X, Wang Q, Wang Y, Pan Z (2014) Preparation of a photocatalytic $TiO_2/ZnTiO_3$ coating on glazed ceramic tiles. Ceram Int 40(6):8891–8895. https://doi.org/10.1016/j.ceramint.2014.01.027

Koch K, Barthlott W (2009) Superhydrophobic and superhydrophilic plant surfaces: an inspiration for biomimetic materials. Phil Trans R Soc A 367(1893):1487–1509. https://doi.org/10.1098/rsta.2009.0022

Kwak G, Jung S, Yong K (2011) Multifunctional transparent ZnO nanorod films. Nanotechnology 22(11):115705. https://doi.org/10.1088/0957-4484/22/11/115705

Lee M-K, Park Y-C (2017) Super-hydrophilic anatase TiO2 thin film in-situ deposited by DC magnetron sputtering. Thin Solid Films 638:9–16. https://doi.org/10.1016/j.tsf.2017.07.046

Lee D, Rubner MF, Cohen RE (2006) All-nanoparticle thin-film coatings. Nano Lett 6 (10):2305–2312. https://doi.org/10.1021/nl061776m

Lee SG, Lee DY, Lim HS, Lee DH, Lee S, Cho K (2010) Switchable transparency and wetting of elastomeric smart windows. Adv Mater 22(44):5013–5017. https://doi.org/10.1002/adma.201002320

Li Y, Zhang J, Zhu S, Dong H, Jia F, Wang Z, Sun Z, Zhang L, Li Y, Li H, Xu W (2009) Biomimetic surfaces for high-performance optics. Adv Mater 21(46):4731–4734. https://doi.org/10.1002/adma.200901335

Li X, Du X, He J (2010a) Self-cleaning antireflective coatings assembled from peculiar mesoporous silica nanoparticles. Langmuir 26(16):13528–13534. https://doi.org/10.1021/la1016824

Li Y, Zhang J, Yang B (2010b) Antireflective surfaces based on biomimetic nanopillared arrays. Nano Today 5(2):117–127. https://doi.org/10.1016/j.nantod.2010.03.001

Li C, Sun Y, Cheng M, Sun S, Hu S (2018) Fabrication and characterization of a TiO2/polysiloxane resin composite coating with full-thickness super-hydrophobicity. Chem Eng J 333:361–369. https://doi.org/10.1016/j.cej.2017.09.165

Lin CA, Tsai ML, Wei WR, Lai KY, He JH (2016) Packaging glass with a hierarchically nanostructured surface: a universal method to achieve self-cleaning omnidirectional solar cells. ACS Nano 10(1):549–555. https://doi.org/10.1021/acsnano.5b05564

Liu K, Jiang L (2012) Bio-inspired self-cleaning surfaces. Annu Rev Mater Res 42:231–263. https://doi.org/10.1146/annurev-matsci-070511-155046

Liu D, Wang Q, Shen W, Wang D (2017) Self-cleaning antireflective coating with a hierarchical texture for light trapping in micromorph solar cells. J Mater Chem C 5:103–109. https://doi.org/10.1039/C6TC03152H

Lu Y, Sathasivam S, Song J, Crick CR, Carmalt CJ, Parkin IP (2015) Robust self-cleaning surfaces that function when exposed to either air or oil. Science 347(6226):1132–1135. https://doi.org/10.1126/science.aaa0946

Manca M, Cannavale A, De Marco L, Arico AS, Cingolani R, Gigli G (2009) Durable superhydrophobic and antireflective surfaces by trimethylsilanized silica nanoparticles-based sol− gel processing. Langmuir 25(11):6357–6362. https://doi.org/10.1021/la804166t

Marques PA, Trindade T, Neto CP (2006) Titanium dioxide/cellulose nanocomposites prepared by a controlled hydrolysis method. Compos Sci Technol 66(7–8):1038–1044. https://doi.org/10.1016/j.compscitech.2005.07.029

Martines E, Seunarine K, Morgan H, Gadegaard N, Wilkinson CDW, Riehle MO (2005) Superhydrophobicity and superhydrophilicity of regular nanopatterns. Nano Lett 5 (10):2097–2103. https://doi.org/10.1021/nl051435t

McHale G, Rowan SM, Newton MI, Banerjee MK (1998) Evaporation and the wetting of a low-energy solid surface. J Phys Chem B 102(11):1964–1967. https://doi.org/10.1021/jp972552i

Mertens J, Hubert J, Vandencasteele N, Raes M, Terryn H, Reniers F (2017) Chemical and physical effect of SiO2 and TiO2 nanoparticles on highly hydrophobic fluorocarbon hybrid coatings synthesized by atmospheric plasma. Surf Coat Technol 315:274–282. https://doi.org/10.1016/j.surfcoat.2017.02.040

Midtdal K, Jelle BP (2013) Self-cleaning glazing products: a state-of-the-art review and future research pathways. Sol Energy Mater Sol Cells 109:126–141. https://doi.org/10.1016/j.solmat.2012.09.034

Mills A, Lee SK (2002) A web-based overview of semiconductor photochemistry-based current commercial applications. J Photochem Photobiol A Chem 152(1–3):233–247. https://doi.org/10.1016/S1010-6030(02)00243-5

Mills A, Lepre A, Elliott N, Bhopal S, Parkin IP, O'Neill SA (2003) Characterisation of the photocatalyst Pilkington Activ™: a reference film photocatalyst? J Photochem Photobiol A Chem 160(3):213–224. https://doi.org/10.1016/S1010-6030(03)00205-3

Min WL, Jiang B, Jiang P (2008) Bioinspired self-cleaning antireflection coatings. Adv Mater 20 (20):3914–3918. https://doi.org/10.1002/adma.200800791

Min K, Choi KS, Jeon WJ, Lee DK, Oh S, Lee J, Choi JY, Yu HK (2018) Hierarchical Ag nanostructures on Sn-doped indium oxide nano-branches: super-hydrophobic surface for surface-enhanced Raman scattering. RSC Adv 8:12927–12932. https://doi.org/10.1039/c8ra01510d

Montazer M, Pakdel E (2011) Functionality of nano titanium dioxide on textiles with future aspects: focus on wool. J Photochem Photobiol C Photochem Rev 12(4):293–303. https://doi.org/10.1016/j.jphotochemrev.2011.08.005

Murugan K, Subasri R, Rao TN, Gandhi AS, Murty BS (2013) Synthesis, characterization and demonstration of self-cleaning TiO_2 coatings on glass and glazed ceramic tiles. Prog Org Coat 76(12):1756–1760. https://doi.org/10.1016/j.porgcoat.2013.05.012

Nakata K, Sakai M, Ochiai T, Murakami T, Takagi K, Fujishima A (2011) Antireflection and self-cleaning properties of a moth-eye-like surface coated with TiO_2 particles. Langmuir 27 (7):3275–3278. https://doi.org/10.1021/la200438p

Nishimoto S, Bhushan B (2013) Bioinspired self-cleaning surfaces with superhydrophobicity, superoleophobicity, and superhydrophilicity. RSC Adv 3(3):671–690. https://doi.org/10.1039/C2RA21260A

Pakdel E, Daoud WA, Wang X (2013) Self-cleaning and superhydrophilic wool by TiO_2/SiO_2 nanocomposite. Appl Surf Sci 275:397–402. https://doi.org/10.1016/j.apsusc.2012.10.141

Parker AR, Lawrence CR (2001) Water capture by a desert beetle. Nature 414:33–34. https://doi.org/10.1038/3510218

Parkin IP, Palgrave RG (2005) Self-cleaning coatings. J Mater Chem 15(17):1689–1695. https://doi.org/10.1039/b412803f

Pasqui D, Barbucci R (2014) Synthesis, characterization and self cleaning properties of titania nanoparticles grafted on polyester fabrics. J Photochem Photobiol A Chem 274:1–6. https://doi.org/10.1016/j.jphotochem.2013.08.017

Qi K, Daoud WA, Xin JH, Mak CL, Tang W, Cheung WP (2006) Self-cleaning cotton. J Mater Chem 16(47):4567–4574. https://doi.org/10.1039/B610861J

Qi K, Wang X, Xin JH (2011) Photocatalytic self-cleaning textiles based on nanocrystalline titanium dioxide. Text Res J 81(1):101–110. https://doi.org/10.1177/0040517510383618

Qi Y, Xiang B, Tan W, Zhang J (2017) Hydrophobic surface modification of TiO2 nanoparticles for production of acrylonitrile-styrene-acrylate terpolymer/TiO2 composited cool materials. Appl Surf Sci 419:213–223. https://doi.org/10.1016/j.apsusc.2017.04.234

Radeka M, Markov S, Lončar E, Rudić O, Vučetić S, Ranogajec J (2014) Photocatalytic effects of TiO_2 mesoporous coating immobilized on clay roofing tiles. J Eur Ceram Soc 34(1):127–136. https://doi.org/10.1016/j.jeurceramsoc.2013.07.010

Radetić M (2013) Functionalization of textile materials with TiO_2 nanoparticles. J Photochem Photobiol C Photochem Rev 16:62–76. https://doi.org/10.1016/j.jphotochemrev.2013.04.002

Ramaratnam K, Tsyalkovsky V, Klep V, Luzinov I (2007) Ultrahydrophobic textile surface via decorating fibers with monolayer of reactive nanoparticles and non-fluorinated polymer. Chem Commun 43:4510–4512. https://doi.org/10.1039/B709429A

Roy P, Dey T, Lee K, Kim D, Fabry B, Schmuki P (2010) Size-selective separation of macromolecules by nanochannel titania membrane with self-cleaning (declogging) ability. J Am Chem Soc 132(23):7893–7895. https://doi.org/10.1021/ja102712j

Sadhu S, Gupta P, Poddar P (2017) Physical mechanism behind enhanced photoelectrochemical and photocatalytic properties of superhydrophilic assemblies of 3D-TiO2 microspheres with arrays of oriented, single-crystalline TiO2 nanowires as building blocks deposited on fluorine-doped tin oxide. ACS Appl Mater Interfaces 9:11202–11211. https://doi.org/10.1021/acsami.6b15420

Saharudin KA, Basiron N, Chun LK, Sreekantan S, Kumaravel V, Abdullah TK, Ahmad ZA (2018) Improved super-hydrophobicity of eco-friendly coating from palm oil fuel ash (POFA) waste. Surf Coat Technol 337:126–135. https://doi.org/10.1016/j.surfcoat.2017.11.070

Shafrin EG, Zisman WA (1964) In: Fowkes FM (ed) Contact angle, wettability and adhesion, advances in chemistry series, vol 43., Chapter-9. American Chemical Society, Washington, DC, pp 145–167. https://doi.org/10.1021/ba-1964-0043.ch009. isbn:9780841200449

Smitha VS, Manjumol KA, Baiju KV, Ghosh S, Perumal P, Warrier KG (2010) Sol–gel route to synthesize titania-silica nano precursors for photoactive particulates and coatings. J Sol-Gel Sci Technol 54(2):203–211. https://doi.org/10.1007/s10971-010-2178-9

Song YY, Schmidt-Stein F, Berger S, Schmuki P (2010) TiO_2 nano test tubes as a self-cleaning platform for high-sensitivity immunoassays. Small 6(11):1180–1184. https://doi.org/10.1002/smll.200902116

Spasiano D, Marotta R, Malato S, Fernandez-Ibanez P, Di Somma I (2015) Solar photocatalysis: materials, reactors, some commercial, and pre-industrialized applications: a comprehensive approach. Appl Catal B Environ 170:90–123. https://doi.org/10.1016/j.apcatb.2014.12.050

Sun M, Luo C, Xu L, Ji H, Ouyang Q, Yu D, Chen Y (2005) Artificial lotus leaf by nanocasting. Langmuir 21(19):8978–8981. https://doi.org/10.1021/la050316q

Takata Y, Hidaka S, Cao JM, Nakamura T, Yamamoto H, Masuda M, Ito T (2005) Effect of surface wettability on boiling and evaporation. Energy 30(2–4):209–220. https://doi.org/10.1016/j.energy.2004.05.004

Tricoli A, Righettoni M, Pratsinis SE (2009) Anti-fogging nanofibrous SiO_2 and nanostructured SiO_2-TiO_2 films made by rapid flame deposition and in situ annealing. Langmuir 25(21):12578–12584. https://doi.org/10.1021/la901759p

Tung WS, Daoud WA (2011) Self-cleaning fibers via nanotechnology: a virtual reality. J Mater Chem 21(22):7858–7869. https://doi.org/10.1039/C0JM03856C

Uddin MJ, Cesano F, Bonino F, Bordiga S, Spoto G, Scarano D, Zecchina A (2007) Photoactive TiO2 films on cellulose fibres: synthesis and characterization. J Photochem Photobiol A Chem 189(2–3):286–294. https://doi.org/10.1016/j.jphotochem.2007.02.015

Von Baeyer HC (2000) The lotus effect. The sciences. J N Y Acad Sci 40(1):12–15. https://doi.org/10.1002/j.2326-1951.2000.tb03461.x

Wang R, Hashimoto K, Fujishima A, Chikuni M, Kojima E, Kitamura A, Shimohigoshi M, Watanabe T (1997) Light-induced amphiphilic surfaces. Nature 388(6641):431–432. https://doi.org/10.1038/41233

Wang R, Wang X, Xin JH (2009) Advanced visible-light-driven self-cleaning cotton by Au/TiO2/SiO2 photocatalysts. ACS Appl Mater Interfaces 2(1):82–85. https://doi.org/10.1021/am900588s

Wang JJ, Wang DS, Wang J, Zhao WL, Wang CW (2011) High transmittance and superhydrophilicity of porous TiO2/SiO2 bi-layer films without UV irradiation. Surf Coat Technol 205(12):3596–3599. https://doi.org/10.1016/j.surfcoat.2010.12.033

Wang X, He Y, Liu X, Zhu J (2017) Synthesis of hierarchical flower-like particles and its application as super-hydrophobic coating. Powder Technol 319:408–414. https://doi.org/10.1016/j.powtec.2017.07.005

Wang X, Liu J, He Y, Wang Y (2018) Selective laser melting of ink-printed (SLM-IP) copper (Cu) nanoparticles (NPs) for facile controllable fabrication of super-hydrophobic surface. Surf Coat Technol 347:84–91. https://doi.org/10.1016/j.surfcoat.2018.04.080

Watanabe T, Nakajima A, Wang R, Minabe M, Koizumi S, Fujishima A, Hashimoto K (1999) Photocatalytic activity and photoinduced hydrophilicity of titanium dioxide coated glass. Thin Solid Films 351(1–2):260–263. https://doi.org/10.1016/S0040-6090(99)00205-9

Wen M, Wang L, Zhang M, Jiang L, Zheng Y (2014) Antifogging and icing-delay properties of composite micro-and nanostructured surfaces. ACS Appl Mater Interfaces 6(6):3963–3968. https://doi.org/10.1021/am405232e

Wenzel RN (1936a) Surface roughness and contact angle. Ind Eng Chem 28(8):1466–1467

Wenzel RN (1936b) Resistance of solid surfaces to wetting by water. Ind Eng Chem 28(8):988–994

Xie TH, Lin J (2007) Origin of photocatalytic deactivation of TiO_2 film coated on ceramic substrate. J Phys Chem C 111(27):9968–9974. https://doi.org/10.1021/jp072334h

Xu Q, Zhao Q, Zhu X, Cheng L, Bai S, Wang Z, Meng L, Qin Y (2016) A new kind of transparent and self-cleaning film for solar cells. Nanoscale 8:17747–17751. https://doi.org/10.1039/C6NR03537J

Xue M, Peng N, Ou J, Wang F, Li X, Li W (2015) Hierarchically nanostructured CeO_2 films with superhydrophilicity and corrosion resistance by coupling of surface topography and oxygen vacancies. Mater Chem Phys 160:406–412. https://doi.org/10.1016/j.matchemphys.2015.05.007

Yaghoubi H, Taghavinia N, Alamdari EK (2010) Self cleaning TiO_2 coating on polycarbonate: surface treatment, photocatalytic and nanomechanical properties. Surf Coat Technol 204(9–10):1562–1568. https://doi.org/10.1016/j.surfcoat.2009.09.085

Yang Y, Li J, Wang H, Song X, Wang T, He B, Liang X, Ngo HH (2011) An electrocatalytic membrane reactor with self-cleaning function for industrial wastewater treatment. Angew Chem Int Ed 50(9):2148–2150. https://doi.org/10.1002/anie.201005941

Yuan L, Dai J, Fan X, Song T, Tao YT, Wang K, Xu Z, Zhang J, Bai X, Lu P, Chen J (2011) Self-cleaning flexible infrared nanosensor based on carbon nanoparticles. ACS Nano 5(5):4007–4013. https://doi.org/10.1021/nn200571q

Yuranova T, Mosteo R, Bandara J, Laub D, Kiwi J (2006) Self-cleaning cotton textiles surfaces modified by photoactive SiO_2/TiO_2 coating. J Mol Catal A Chem 244(1–2):160–167. https://doi.org/10.1016/j.molcata.2005.08.059

Zhang L, Dillert R, Bahnemann D, Vormoor M (2012) Photo-induced hydrophilicity and self-cleaning: models and reality. Energy Environ Sci 5(6):7491–7507. https://doi.org/10.1039/c2ee03390a

Zhang P, Tian J, Xu R, Ma G (2013) Hydrophilicity, photocatalytic activity and stability of tetraethyl orthosilicate modified TiO_2 film on glazed ceramic surface. Appl Surf Sci 266:141–147. https://doi.org/10.1016/j.apsusc.2012.11.117

Zhong H, Hu Y, Wang Y, Yang H (2017) TiO2/silane coupling agent composed of two layers structure: a super-hydrophilic self-cleaning coating applied in PV panels. Appl Energy 204:932–938. https://doi.org/10.1016/j.apenergy.2017.04.057

Zhou S, Wang F, Balachandran S, Li G, Zhang X, Wang R, Liu P, Ding Y, Zhang S, Yang M (2017) Facile fabrication of hybrid PA6-decorated TiO2 fabrics with excellent photocatalytic,

antibacterial, UV light-shielding, and super hydrophobic properties. RSC Adv 7:52375–52381. https://doi.org/10.1039/C7RA09613E

Zhu J, Hsu CM, Yu Z, Fan S, Cui Y (2010) Nanodome solar cells with efficient light management and self-cleaning. Nano Lett 10(6):1979–1984. https://doi.org/10.1021/nl9034237

Zhu J, Cao Y, He J (2014) Facile fabrication of transparent, broadband photoresponse, self-cleaning multifunctional graphene–TiO_2 hybrid films. J Colloid Interf Sci 420:119–126. https://doi.org/10.1016/j.jcis.2014.01.015

Zorba V, Chen X, Mao SS (2010) Superhydrophilic TiO_2 surface without photocatalytic activation. Appl Phys Lett 96(9):093702. https://doi.org/10.1063/1.3291667

Chapter 12
Metal and Metal Oxide-Based Nanomaterials for Electrochemical Applications

Chiranjita Goswami, Bhugendra Chutia, and Pankaj Bharali

Contents

Abstract The development of nanotechnology marked a new era in the field of catalysis. The fascinating electronic, structural, and magnetic properties of the nanomaterials arising from its shape, size, and unusually high surface-to-volume ratio make them unique from the bulk materials. These properties facilitate various chemical reactions including fuel cell and other electrochemical reactions for energy and environmental applications. In the recent years, fuel cells have emerged as alternative energy sources to meet the ever-increasing energy demands. Thus, designing suitable catalyst to boost the rate of the reactions associated with fuel cells or other energy storage devices has become very crucial. Different types of electrochemical reactions include oxygen reduction reaction (ORR), oxygen evolution reaction (OER), hydrogen evolution reaction (HER), and electrooxidation of small organic molecules like methanol, ethanol, formic acid, etc. On the other hand electrochemical CO_2 reduction to various value-added products is a promising strategy to address the atmospheric CO_2 levels. Herein, we have mainly emphasized the catalytic behavior of different types of morphology and size-dependent

Chiranjita Goswami and Bhugendra Chutia have been contributed equally to this chapter.

C. Goswami · B. Chutia · P. Bharali (✉)
Department of Chemical Sciences, Tezpur University, Napaam, Assam, India
e-mail: pankajb@tezu.ernet.in

R. Saravanan et al. (eds.), *Emerging Nanostructured Materials for Energy and Environmental Science*, Environmental Chemistry for a Sustainable World 23,
https://doi.org/10.1007/978-3-030-04474-9_12

nanomaterials toward electrochemical reduction of oxygen and CO_2 and electrooxidation of formic acid and ethanol.

12.1 General Introduction

One of the most interesting subfields of nanoscience is the "nanocatalysis." Promotion, control, steering, and enhancement of chemical reactions by varying the size, morphology, chemical composition, dimensionality, charge state of the catalyst, or the reaction center are the fundamental aims of nanocatalysis. Different nanocatalytic systems include nanowires, ultrathin films, or clusters. The chemical and physical properties of these nanocatalytic systems are generally controlled by quantum size effects. They also provide new prospects for an atom-by-atom design, modification and control of chemical activity, specificity, and selectivity (Landman and Heiz 2007). Nanocatalysts or nanomaterial-based catalysts are the heterogeneous catalyst having particles in the range 1–100 nm (Singh and Tandon 2014). They exhibit attractive electronic, optical, and magnetic properties which vary significantly from their bulk counterparts. These novel properties of the nanomaterials facilitate promising applications in many fields such as nanocatalysis, nanofabrication, nanobiology, and nanodevice (Wang et al. 2009b). Different types of nanoparticles (NPs) include metallic NPs, metal oxide NPs, carbon NPs, etc. Metallic NPs usually refers to the pieces of metal forming nanoclusters of size in the nanometer scale. The very high catalytic activity and selectivity of the metallic NPs make them suitable for catalyzing chemical reactions like electrochemical reactions, oxidation reactions, reduction reactions, coupling reactions, etc. Metal oxide NPs find extensive applications in industries as an active component, promoter, or support. Its unique physical and chemical properties can be attributed to the presence of high density of defect sites and their sizes in the nanometer range (Wang and Gu 2015). Both metallic and metal oxide NPs find use as catalysts in fuel cell and other electrochemical reactions. Researchers, in the recent years, adopted various synthetic methods for developing highly active monodisperse NPs for fuel cell reactions (Mazumder et al. 2010b).

Increasing energy demands have stimulated intense research on alternative energy conversion and storage systems with high efficiency, low cost, and environmental benignity (Lewis and Nocera 2006; Bard and Fox 1995; Liang et al. 2011). A significant amount of research is being conducted on fuel cells as a clean, alternative energy source (Delacote et al. 2009). Fuel cells are electrochemical devices that directly convert chemical energy into electrical energy with high efficiency and low emission of pollutants (Steele and Heinzel 2001; Carrette et al. 2000; Brett et al. 2010). Different types of fuel cells include solid oxide fuel cells (SOFCs), molten carbonate fuel cells (MCFC), alkaline fuel cell (AFC) types, phosphoric-acid fuel cell (PAFC), and polymeric-electrolyte-membrane fuel cell (PEMFC). They consist

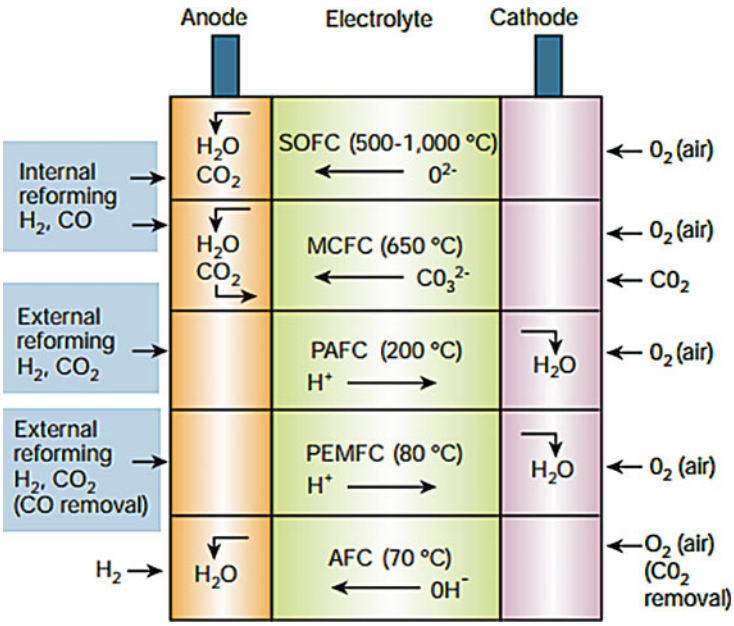

Fig. 12.1 Summary of different types of fuel cells with its basic components. (Adapted from Steele and Heinzel 2001)

of an electrolyte medium sandwiched between two electrodes, i.e., the anode and the cathode, as shown in Fig. 12.1. The anode facilitates electrochemical oxidation of fuel, while the cathode promotes electrochemical reduction of oxidant. The oxidation reaction takes place at the anode (+ve) and involves the liberation of electrons (e.g., $O^{2-} + H_2 = H_2O + 2e^-$ or $H_2 = 2H^+ + 2e^-$). These electrons travel round the external circuit producing electrical energy by means of the external load and arrive at the cathode (−ve) to participate in the reduction reaction (e.g., $½\ O_2 + 2e^- = O^{2-}$ or $½\ O_2 + 2H^+ + 2e^- = H_2O$). Ions generated during oxidation or reduction are transported from one electrode to the other through the ionically conductive but electronically insulating electrolyte. The electrolyte also serves as a barrier between the fuel and oxidant. The successful conversion of chemical energy into electrical energy in a primitive fuel cell was first demonstrated over 160 years ago. However, despite the attractive system efficiencies and environmental benefits associated with fuel cell technology, it has proved difficult to develop the early scientific experiments into commercially viable industrial products. These problems have often been associated with the lack of appropriate materials or manufacturing routes that would enable the cost of electricity per kWh to compete with the existing technology (Steele and Heinzel 2001).

Again, carbon dioxide (CO_2) is an extremely troubling greenhouse gas released mainly from the excessive use of fossil fuels. The CO_2 emission problems have drawn rigorous attention for more than 30 years. The amount of CO_2 gas produced

on the Earth should be equal to the amount consumed for the concentrations of CO_2 in atmosphere to promote a sustainable society. Decreasing CO_2 emissions and further regenerating CO_2 into carbonaceous fuels and chemicals by mimicking the photosynthesis process of green plants would be an excellent method to relieve our demands on high-polluting fossil energy and provide indispensable resources for industrial applications (Shakun et al. 2012; Arora et al. 2011; Zhang et al. 2018). A promising way to address the ever-increasing concentration of CO_2 in the atmosphere is the electrochemical reduction of CO_2. This chapter has extensively reviewed the advantageous applications of nanomaterials as electrocatalysts for various oxidation and reduction reactions that take place on electrode surface. Special emphasis has been paid to the electrochemical reduction of oxygen and CO_2 and electrooxidation of formic acid and ethanol.

12.2 Oxygen Reduction Reaction

Among the fuel cell reactions, oxygen reduction reaction (ORR) at cathode is a very important reaction. Pt/C is proved to be the best catalyst for both in acidic and basic conditions. However, due to cost, abundance and deactivation phenomena associated with Pt have stimulated researchers to search for other options to develop cost-effective, commercially exploitable catalysts. Pt alloying with other metals (to minimize the Pt content), development of non-platinum catalysts, use of promoters, and utilization of different carbon supports are among the various alternatives that have been employed in recent years to overcome the disadvantages associated with Pt catalysts.

ORR at cathode surface is a multi-electron reaction that proceeds via several elementary steps (Shao et al. 2006a). In aqueous solutions on Pt electrodes, it appears to occur in two pathways: (i) a "direct" four-electron reduction, wherein four electrons are transferred in concert:

$$O_2 + 4H^+ + 4e^- \rightarrow 2H_2O \tag{12.1}$$

and (ii) a "series" pathway that involves H_2O_2 as the intermediate:

$$O_2 + 2H^+ + 2e^- \rightarrow H_2O_2 + 2H^+ + 2e^- \rightarrow 2H_2O \tag{12.2}$$

A series four-electron reduction involves the transfer of two electrons to form peroxide, which, without leaving the electrode's surface, is further reduced to H_2O with the exchange of an additional two electrons and two protons. There are three possible first steps in the ORR: (i) splitting of the O-O bond upon adsorption on two Pt sites (S) in a bridge configuration, $O_2 + 2S \rightarrow O^* + O^*$; (ii) formation of the superoxide anion, $O_2 + 2S + e^- \rightarrow O^{2-}$; and (iii) simultaneous electron and proton

transfer, $O_2 + 2S + (H^+ + e^-) \rightarrow HO_2$. Identifying the first step would clarify the pathway of the ORR that takes place on catalytically active metal surfaces.

In the effort to minimize the Pt content, which is the best reported catalyst for ORR, recent attempts to improve the performance of Pt-based catalysts have focused in forming alloy with other metals. Recent reports have also suggested that controlling the composition, size, and shape of the materials has a dramatic catalytic effect. Markovic et al. reported that the ORR activity of Pt is higher on the (100) faces than on the (111) faces in H_2SO_4 (Markovic et al. 1995). Moreover, a cubic shape exposing (100) surfaces was found to benefit a number of catalytic systems (Narayanan and El-Sayed 2004; Wang et al. 2008). Murray and co-workers reported similar work on cubic Mn-Pt nanocrystals and studies of their ORR activity (Kang and Murray 2010).

Recently, Sun and co-workers reported an advanced organic-phase synthesis of thin FePt and CoPt alloy nanowires (NWs) for enhanced catalysis of the ORR (Guo et al. 2013). Electrochemical studies showed that these NWs were active catalysts for the ORR. The specific activity and the mass activity of the 2.5-nm-wide FePt NWs reached 1.53 mA cm^{-2} and 844 mA mg^{-1} Pt at 0.9 V (vs. reversible hydrogen electrode, RHE; 0.2 mA cm^{-2} and 110 mA mg^{-1} Pt at 0.95 V), while those of the benchmark Pt catalyst reached 0.32 mA cm^{-2} and 155 mA mg^{-1} Pt at 0.9 V (0.080 mA cm^{-2} and 35 mA mg^{-1} Pt at 0.95 V). The annealed 6.3-nm-wide FePt NWs showed an even higher specific activity of 3.9 mA cm^{-2} at 0.9 V and 0.46 mA cm^{-2} at 0.95 V. In another report, they have developed a unique approach for synthesizing core/shell structured Pd/FePt nanoparticles (NPs) with a 5 nm Pd core and a FePt shell whose thickness is tunable from 1 to 3 nm and demonstrated that the ORR catalysis of the Pd/FePt NPs is dependent on the FePt shell thickness and that the thin (1 nm or less) FePt shell which is both active and durable for ORR in 0.1 M $HClO_4$ solution (Mazumder et al. 2010a). Moreover, Sun and his group has also reported the synthesis of core/shell nanorods (NRs) to provide a further enhancement of ORR catalysis. They have developed a controlled synthesis of 20×2 nm NRs of FePtM (M = Cu, Ni) and studied their acid stability and found that these thin FePtM NRs, especially FePtCu NRs, are much more stable in acid solution. When treated with acetic acid and etched electrochemically in 0.1 M $HClO_4$, these ternary alloy NRs were converted into core/shell FePtM/Pt NRs with Fe and M (especially Cu) being preserved in the NR cores. These core/shell NRs combine 1D shape and core/shell effects on catalysis and indeed show much higher activity and durability for the ORR (Zhu et al. 2013a). The same group has also very recently explored Co/CoO and metal ferrite nanoparticles for ORR in alkaline medium (Guo et al. 2012; Zhu et al. 2013b).

The specific activity of the ORR on Pt nanoparticles decreases with decreasing particle size, with a maximum in mass activity for particles with a diameter of 3 nm. The ORR activity roughly correlates with the proportion of the terrace sites. The active sites for the ORR are only located on the terrace sites of the nanoparticles which correlates well to the earlier theoretical predictions (Perez-Alonso et al. 2012). Adzic and co-workers have recently examined the effects of the thickness of the Pt shell, lattice mismatch, and particle size on specific and mass activities from the

changes in effective surface area and activity for ORR induced by stepwise Pt-monolayer depositions on Pd and Pd_3Co nanoparticles (Wang et al. 2009a). The results suggest that moderately compressed (111) facets are most conducive to ORR on small nanoparticles and indicate the importance of concerted structure and component optimization for enhancing core/shell nanocatalysts' activity and durability. In another report they have demonstrated a new approach to synthesize highly active electrocatalysts for the ORR with ultra-low Pt content. The synthesis involves placing a small amount of Pt, the equivalent of a monolayer, on carbon-supported niobium oxide nanoparticles (NbO_2 or Nb_2O_5) (Sasaki et al. 2008). Rotating disk electrode measurements showed that the $Pt/NbO_2/C$ electrocatalyst has three times higher Pt mass activity for the ORR than a commercial Pt/C electrocatalyst. The observed high activity of the Pt deposit is attributed to the reduced OH adsorption caused by lateral repulsion between PtOH and oxide surface species. To enhance and optimize nanocatalyst performance and durability for the ORR in fuel cell applications, Abruna and co-workers described a new class of Pt-Co nanocatalysts composed of ordered Pt_3Co intermetallic cores with a two- to three-atomic-layer-thick platinum shell (Wang et al. 2013). These nanocatalysts exhibited over 200% increase in mass activity and over 300% increase in specific activity when compared with the disordered Pt_3Co alloy nanoparticles as well as Pt/C. Recent efforts in ORR electrocatalysis have focused on decreasing the Pt content in fuel cell electrocatalysts or replacing it with less expensive materials. In an approach to synthesize Pt-free electrocatalysts for ORR, Adzic and co-workers have reported the application of Pd-Fe alloy nanoparticles and showed that it has a very high activity for the ORR (Shao et al. 2006b). Recent reports on ORR over various non-platinum-based electrocatalysts, such as Pd-V with different compositions (Ang and Walsh 2010), monodisperse Pd-Cu alloy nanoparticles (Kariuki et al. 2010), Pd-Fe nanoleaves (Zhang et al. 2011), and PdCo (111) surface alloy (Son and Takahashi 2012), show that there are great possibilities for exploitation of Pd-based alloy/intermetallic catalysts for fuel cell applications.

In the recent years, cerium oxide (CeO_2, also known as ceria) has been extensively used as an "active support" for its unique characteristics such as high reactivity and hardness, high oxygen storage capability, strong ultraviolet radiation absorption ability, high oxygen ionic conductivity, as well as its high stability at high temperature. These properties make CeO_2- and CeO_2-based materials widely applicable in gas sensors, polishing materials, luminescent materials, ultraviolet (UV)-shielding materials, solid oxide fuel cells (SOFCs), and so on (Bharali et al. 2012; Liu et al. 2013; Phoka et al. 2009; Reddy et al. 2007). Owing to the existence of Ce^{4+}/Ce^{3+} redox couple, CeO_2 has also been used as a promoter in several reactions such as CO oxidation, ORR, elimination of toxic gases (SO_2, CO, and NO_x), selective hydrogenation of unsaturated aldehydes, etc. (Bharali et al. 2013; Reddy et al. 2008). CeO_2 has been synthesized by many researchers by various methods such as deposition precipitation (DP) method (Liu et al. 2010), hydrothermal method (Liu et al. 2016; Yousaf et al. 2017), precipitation, impregnation method (Ou et al. 2011; He et al. 2015), microwave method (Mondal et al. 2016), etc. Figure 12.2 presents typical XRD profiles and HRSEM and TEM images of CeO_2-modified Ni catalysts.

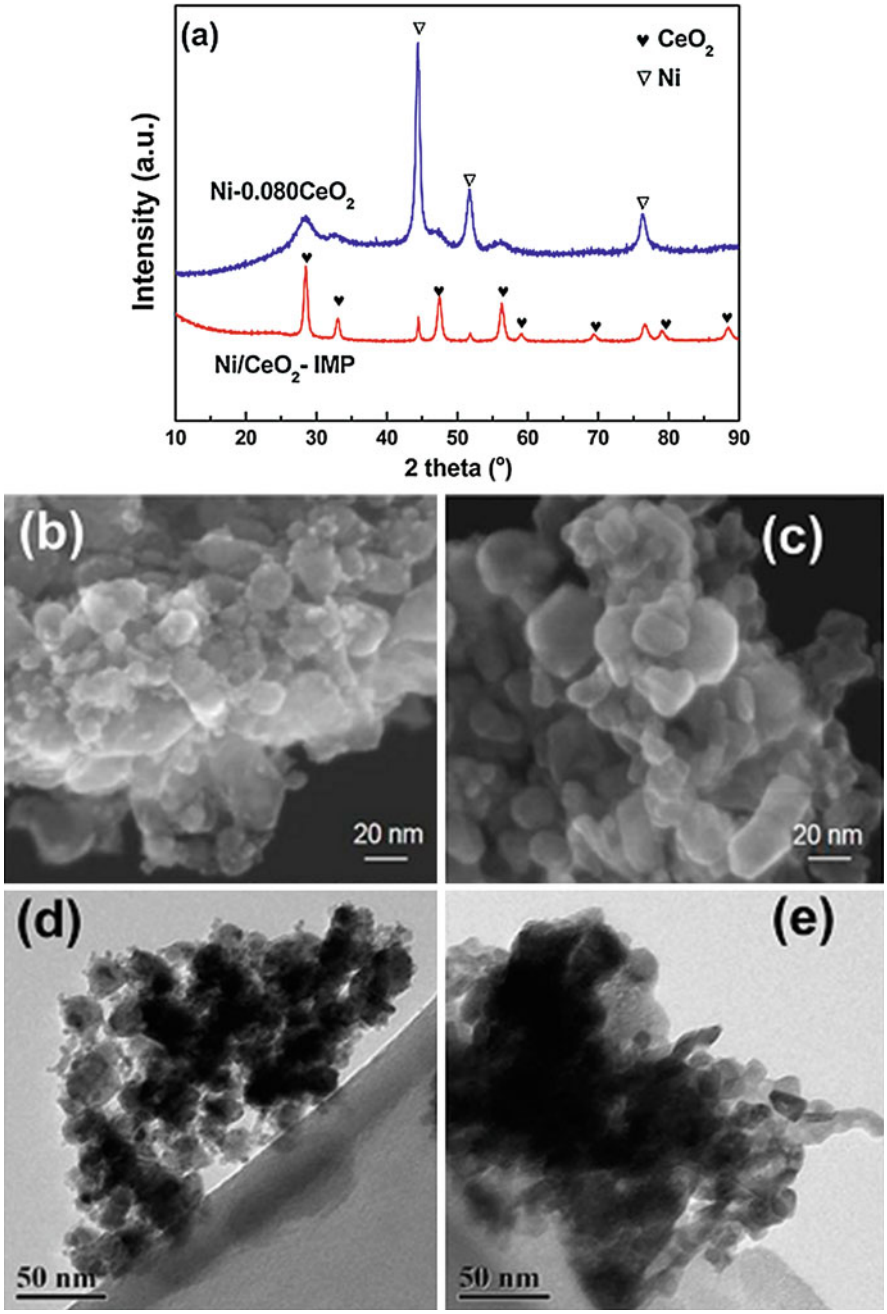

Fig. 12.2 (**a**) XRD profiles for Ni-0.080 CeO_2 and Ni/CeO_2-IMP; HRSEM images for the following: (**b**) Ni/CeO_2−IMP; (**c**) Ni-0.080 CeO_2; and TEM images for the following: (**d**) Ni/CeO_2−IMP; (**e**) Ni-0.080 CeO_2. (Adapted from He et al. 2015)

Liu et al. reported the structural and optical properties of CeO_2 prepared by precipitation method and found that increase in the calcination temperature from 550 to 1050 °C results in complete removal of water and impurities at about 750 °C (Liu et al. 2013). Also, the absorption spectrum in the range 372–395 nm is responsible for its application in UV filter materials. Electrocatalysts based on transition metal oxide (metal = Ir, Mn, Fe, Co, etc.) have been emerged as inexpensive alternatives to precious Pt-based materials with outstanding ORR performance (Osmieri et al. 2016; Osgood et al. 2016).

Metal catalysts sometimes undergo dissolution, agglomeration, and sintering during the course of reaction, thereby lowering catalytic activity and stability (Cao et al. 2010). Thus, to prevent agglomeration and for proper dispersion, the use of an ideal support is necessary (Chen et al. 2011). In this context, carbon-based materials have gain much attention as catalyst supports in many reactions due to its high specific surface areas, high chemical resistivity, high porosity, superior mechanical strength, excellent electron conductivity, and relative chemical inertness. These reactions include chemical and enzymatic biomass transformations, reactions in fuel cell and metal air batteries, etc. The reason behind wide use of carbon-based materials as catalyst supports is the ease of its fabrication in different physical forms and shape (Lam and Luong 2014; Sun et al. 2010). Liu and co-workers have successfully synthesized highly dispersed MnO_x-CeO_2/KB catalyst by a continuous two-step process and found that the as-synthesized sample shows much higher durability and better ORR activity as compared to that of commercial Pt/C due to synergistic effect (Chen et al. 2015). In a similar study, Co_3O_4-CeO_2/KB was synthesized to study the electrocatalytic reduction of oxygen in Al-air batteries via a two-step hydrothermal method. It was reported that the ORR activity of Co_3O_4/KB was significantly increased after CeO_2 incorporation, which even outperformed Pt/C catalyst in alkaline electrolyte. Moreover, the reaction favored a four-electron pathway due to the synergistic effect between CeO_2 and Co_3O_4, and the Co_3O_4-CeO_2/KB exhibited a higher working voltage plateau than CeO_2/KB and Co_3O_4 /KB (Liu et al. 2010). In the recent years, cobalt oxide-based electrocatalysts prepared by various methods were found to be very effective towards ORR. Carbon sphere/Co_3O_4 nanocomposites were designed and employed as an electrocatalyst in Li/air batteries (Park et al. 2013). The air electrode having carbon sphere/Co_3O_4 nanocomposite was found to have low overpotential, moderately stable reversibility, and high capacity during the charge/discharge process than that of commercial Co_3O_4 and plain carbon spheres. It has also revealed that the low electronic conductivity of Co_3O_4 might be compensated by stabilizing the contact between the carbon spheres and the Co_3O_4. These results have made the carbon sphere/Co_3O_4 nanocomposite a promising candidate for Li/air batteries with an air electrode of elevated active surface area. In the same year, Kim and co-workers implemented a combined solvothermal process, followed by thermal treatment and polyol process to synthesize porous flowerlike Co_3O_4 microspheres/Cu nanocomposites for its use in Li/air batteries (Yang et al. 2013). The synthesized nanocomposites having 3D mesoporous structure was found to be highly stable and capable bifunctional catalysts. Moreover, during charge/discharge process, the cobalt oxide-based catalysts

exhibited enhanced activity as compared to that of Vulcan XC-72. The cells having this catalyst have the advantage of reversible charge/discharge process. Li and group adopted one-step replica approach to synthesize high surface area mesostructured Co_3O_4/C composites and applied for ORR (Wang et al. 2014). The Co_3O_4 nanoparticles were dispersed homogeneously in the mesoporous carbon substrates. Relatively high electrocatalytic activity as well as durability was observed during ORR using the mesostructured Co_3O_4/C composites. Moreover, the reduction of oxygen followed a four-electron pathway. The best electrochemical activity was observed when a Co loading of 4.3% was used, which can be attributed to the existence of Co^{3+}/Co^{2+} redox couples along with the conductive nature of the carbon substrate.

Again, Lu et al. synthesized a highly effective non-noble metal catalyst via facile one-step hydrothermal method to study ORR (Lu et al. 2015). During the synthesis of the catalyst, the reduction of graphene oxide (GO) followed by doping of nitrogen to the Co_3O_4 nanoparticles was done simultaneously to obtain an exclusive hierarchical structure, i.e., nitrogen-doped reduced graphene oxide/carbon nanotube/Co_3O_4 hybrids (N-rGO/CNT/Co_3O_4). The space effects of Co_3O_4 nanoparticles and CNTs as well as the synergism between nitrogen doping and the active components were responsible for the better electrocatalytic performance and high durability of N-rGO/CNT/Co_3O_4 hybrid toward ORR. In addition, this hybrid was also found to be well resistant toward methanol crossover effects making it a potential electrocatalysts in the field of fuel cells and other energy conversion devices. Recently, Shao and co-workers adopted a simple pyrolysis method for preparing non-precious metal catalysts encapsulating Co nanoparticles into thin N-doped carbon nanotubes, denoted by Co@NSCNTs (Song et al. 2017).

The catalyst, i.e., Co@NSCNTs was found to exhibit good catalytic activity, high durability, favorable four-electron selectivity, and excellent methanol tolerance which can be attributed to the synergistic effect between the C-N meshwork having N-doped carbon nanotubes and the encapsulated metal particle clusters. Figure 12.3 shows the electrochemical measurement plots of Co@NSCNTs and Pt/C. It can be seen that no apparent reduction peak appeared in the cyclic voltammograms of the two catalysts in N_2-saturated atmosphere. However, an obvious reduction peak was observed for Co@NSCNTs at about 0.77 V relative to the reversible hydrogen electrode (RHE) O_2-saturated atmosphere which is comparable to the cathodic current density of commercial Pt/C. Again, the number of electrons transferred during the reaction was calculated to be 3.94 for Co@NSCNTs, which is very close to 4. This suggests that the synthesized catalyst follow direct four-electron pathway.

Graphene is considered as one of the most promising matrix for incorporating numerous nanomaterials due to its high surface area and conductivity, which eventually increases the structural stability of the nanomaterials. Considering the effectiveness of graphene, Huang and group reported the synthesis of Co_3O_4 nanocubes by incorporating reduced graphene oxide (RGO) to obtain RGO@Co_3O_4 nanohybrid via a single-step hydrothermal method to study ORR. The glassy carbon electrode modified using RGO@Co_3O_4 nanohybrid having 4 wt% graphene oxide,

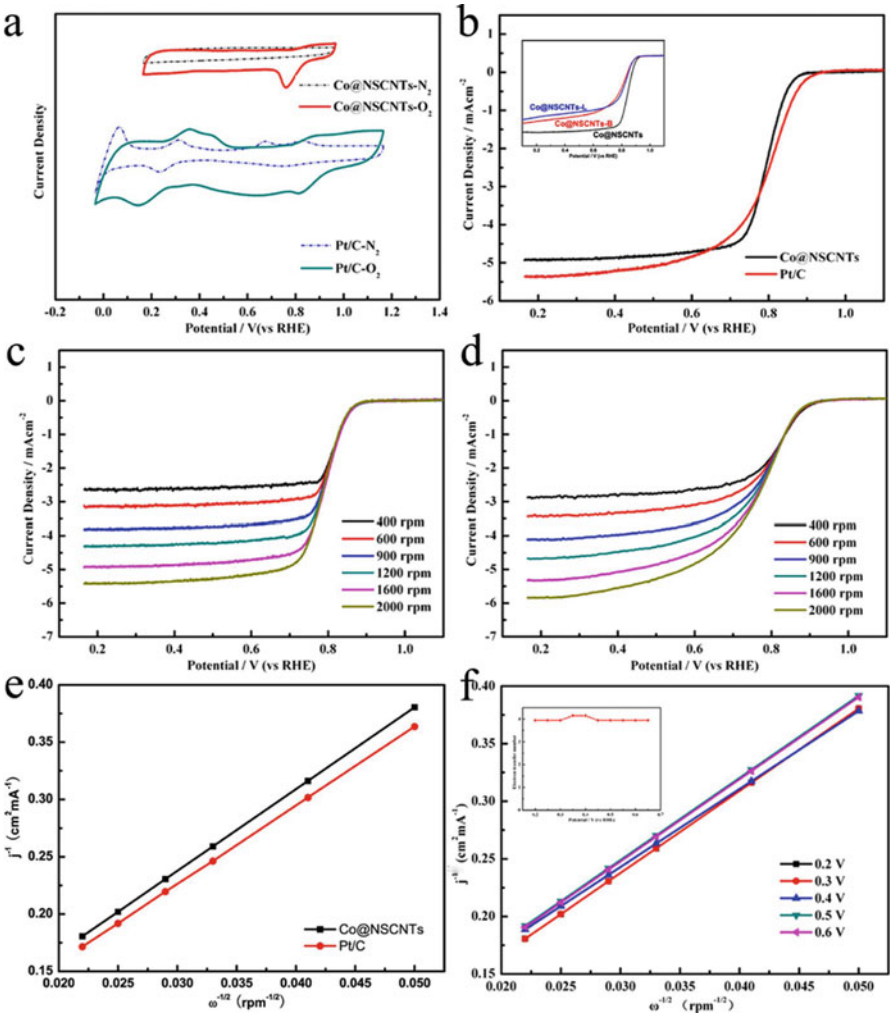

Fig. 12.3 (**a**) Cyclic voltammetry (CV) in 0.1 M KOH aqueous solution saturated with N_2 or O_2 at a sweep rate of 50 mV s^{-1}. (**b**) Linear sweep voltammograms (LSVs) of Co@NSCNTs and Pt/C at 1600 rpm in O_2-saturated 0.1 M KOH (inset: LSVs of Co@NSCNTs, Co@NSCNTs-B, and Co@NSCNTs-L). (**c**, **d**) Linear sweep voltammetry of Co@NSCNTs and Pt/C in O_2-saturated 0.1 M KOH with a sweep rate of 5 mV s^{-1} at different rotation rates indicated. (**e**) Koutecky-Levich (K-L) plots of Co@NSCNTs and Pt/C catalysts at 0.3 V (vs. RHE). (**f**) K-L plots of Co@NSCNTs at different potentials. (Adapted from Song et al. 2017)

exhibited excellent electrocatalytic activity as compared to commercial Pt/C and other modified electrodes in alkaline medium. This enhanced electrocatalytic behavior of the nanohybrid toward ORR is due to the synergistic coupling between Co_3O_4 nanocubes and RGO. The synthesized nanohybrid also exhibited good methanol tolerance when a concentration of 0.5 M methanol was used during ORR (Shahid

et al. 2017). In another report, hierarchical porous three-dimensional (3D) graphene frameworks were synthesized by a one-pot pyrolysis method. The resulting nanocrystals were doped with heteroatoms such as boron and nitrogen. Rapid thermolysis of the cobalt-oleate complex stimulated by large literal sheets of graphene nanomeshes leads to the formation of Co_3O_4 nanocrytals. The synthesized bifunctional electrocatalyst was found to be superior to the commercial Pt/C toward ORR and OER in terms of current density, stability, methanol tolerance, and onset potential (Wang et al. 2017).

12.3 Electrochemical CO_2 Reduction

Electrocatalytic reduction of CO_2 to useful intermediates or fuels such as formic acid, carbon monoxide, hydrocarbons, and alcohols is a promising strategy to address the issue of high atmospheric CO_2 levels (Ma et al. 2016; Appel et al. 2013; Shan et al. 2017; Cai et al. 2017a; Yin et al. 2016; Klinkova et al. 2016; Gao et al. 2017; Jhong et al. 2013; Zhao et al. 2017).

Although the electroreduction of CO_2 to value-added products has promise, the high overpotential of this reaction and low activity of the currently known catalysts still hamper this process from becoming close to commercialization. Monometallic or bimetallic nanoparticles of copper (Ma et al. 2016; Appel et al. 2013), silver (Shan et al. 2017), palladium (Cai et al. 2017b; Yin et al. 2016; Klinkova et al. 2016), platinum (Cai et al. 2017a), and nickel (Zhao et al. 2017) can be used as an active component in fabrication of electrocatalysts for CO_2 reduction. However, it is noted that Cu and Ni catalysts in comparison with Pd catalysts are less stable with respect to CO poisoning or formation of selective CO and formate as products. Especially, electroreduction of CO_2 into formic acid is of particular interest, as formic acid can be used as a fuel in direct formic acid fuel cells (Yu and Pickup 2008) and is used today in the synthesis of fine chemicals such as pharmaceuticals (Szmant 1989; Mura et al. 2012) and as a preservative and antibacterial agent (Hietala et al. 2016).

Formate and formic acid are the main products of CO_2 electroreduction on post-transition metals, such as Pb, Hg, Tl, In, Sn, Cd, and Bi; however, previously reported electroreduction studies using these materials have required very negative potentials relative to the equilibrium potential to achieve good product selectivity (Chaplin and Wragg 2003; Zhang et al. 2014). Figure 12.4 shows transmission electron micrographs of six Pd/C catalysts with different sizes. The NPs are uniformly deposited on carbon support, and typical Pd(111) plane with the characteristic lattice spacing of 0.23 nm is observed.

Figure 12.5 shows the applied potential dependence of faradaic efficiency and current density for CO production over Pd NPs. All the faradaic efficiencies for CO production first increase with applied potential, despite the size of Pd NPs. The competitive HER is facile at low overpotentials, and CO_2 reduction is prone to occur with increased applied potential. However, the faradaic efficiency decreases at high applied potentials, which is probably caused by the limited mass transport of CO_2 in

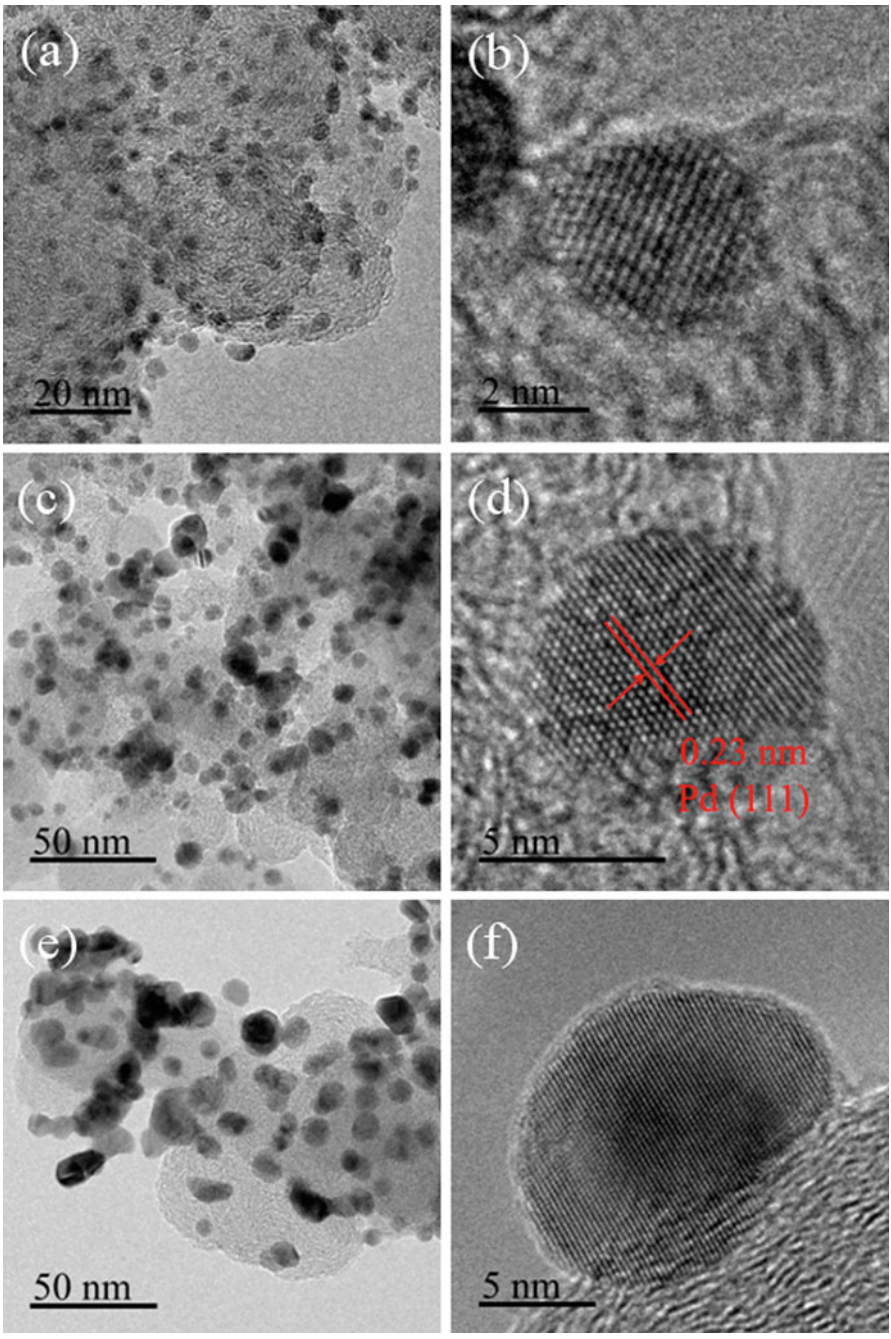

Fig. 12.4 TEM and HRTEM images of (**a**, **b**) 3.7, (**c**, **d**) 6.2, and (**e**, **f**) 10.3 nm Pd. (Adapted from Gao et al. 2015)

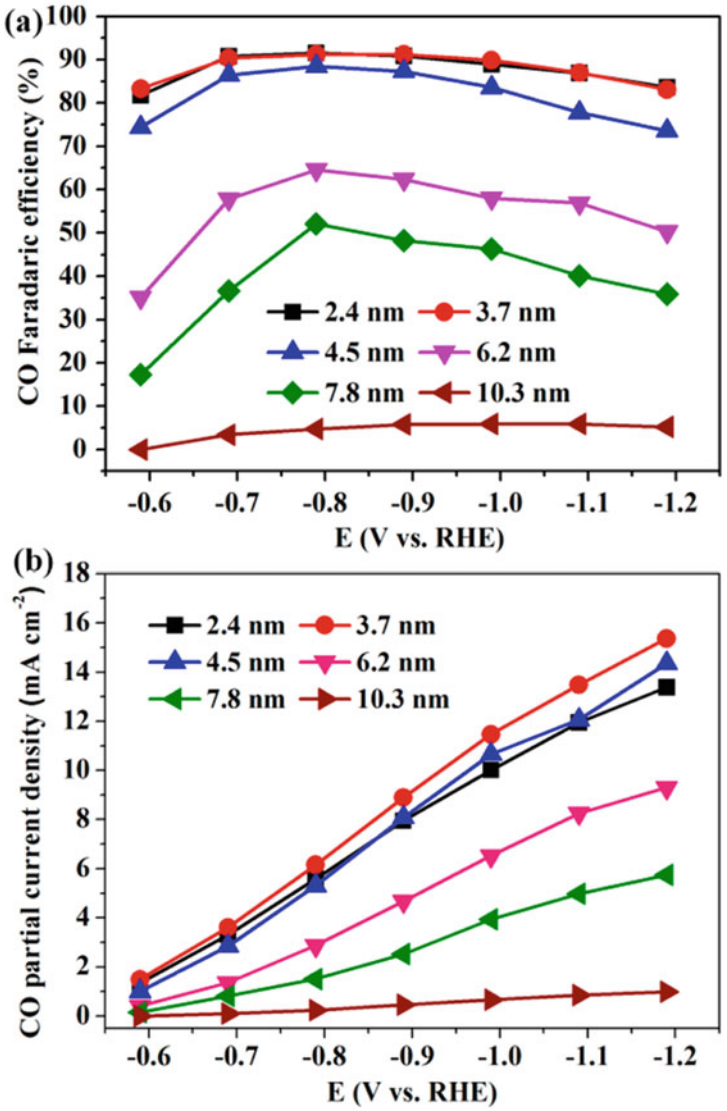

Fig. 12.5 Applied potential dependence of (**a**) faradaic efficiencies and (**b**) current densities for CO production over Pd NPs with different sizes. (Adapted from Gao et al. 2015)

0.1 M $KHCO_3$ solution. On 2.4 and 3.7 nm Pd, all the faradaic efficiencies at different potentials exceed 80%, and the maximum value of 91.2% is reached at −0.89 V (vs. RHE), which is much higher than that over Pd wire electrode (<6%). The faradaic efficiencies for CO production over 2.4 and 3.7 nm Pd are also comparable to those over Au and Ag NPs.

Among inorganic strategies, only through the use of Pd electroreduction of CO_2 to formate have potentials close to the equilibrium potential been obtained; indeed, these results come impressively close to the performance of formate dehydrogenase enzymes (Armstrong and Hirst 2011). Currently, Pd nanoparticles (NPs) used in the selective reduction of CO_2 to formate have been limited to low current densities: specifically, only sub-mA/cm^2 geometric current densities have been reported at near-equilibrium potential (Stalder et al. 1984; Podlovchenko et al. 1994). Recently, Pd NP-based electrocatalysts with near-quantitative faradaic efficiency, impressive geometric current densities (10 mA/cm^2 at −0.2 V in 2.8 M $KHCO_3$), and high mass activity have been reported for CO_2 reduction to formate (Min and Kanan 2015). In these otherwise very promising studies, one key challenge remains: over the course of the reaction, performance was lost (Min and Kanan 2015). Thus, although the application of Pd NPs shows great promise for energy-efficient electroreduction of CO_2, further understanding has to be developed for the factors that affect their stability and high selectivity. It has been proposed that the reduction of stability of Pd nanocatalysts in formate synthesis originates from CO poisoning (Min and Kanan 2015). While at high overpotentials CO_2 steadily reduces to CO, at low overpotential, CO is only forming in trace amounts, and yet this is sufficient for catalyst surface poisoning (Hori et al. 1994). Two proposed multistep mechanisms of electrochemical reduction of CO_2 to formic acid include the following.

Mechanism 1:

$$CO_2 + H^+\,(aq) + e^- + * \rightarrow COOH* \tag{12.3}$$

$$COOH* + H^+\,(aq) + e^- \rightarrow HCOOH \tag{12.4}$$

Mechanism 2:

$$CO_2 + H^+\,(aq) + e^- + * \rightarrow HCOO* \tag{12.5}$$

$$HCOO* + H^+\,(aq) + e^- \rightarrow HCOOH \tag{12.6}$$

Additionally, the competing electrochemical reduction of CO_2 to CO proceeds as follows:

$$COOH^*/HCOO* + H^+\,(aq) + e^- \rightarrow CO* + H_2O \tag{12.7}$$

$$CO* \rightarrow CO + * \tag{12.8}$$

where * represents either a vacant surface catalytic active site or intermediate species adsorbed on the active site. The production of formic acid is proposed to proceed through either a proton/electron pair transfer to form a carboxyl (COOH*) (reaction 12.3) or a formate (HCOO*) intermediate (reaction 12.5). Next, the COOH* (reaction 12.4) or HCOO* (reaction 12.6) can be reduced to HCOOH with a subsequent

proton/electron pair transfer. Importantly, reaction (12.7) leads to the formation of CO species bound to the active site: this in turn poisons the surface of the catalyst (Armstrong and Hirst 2011; Stalder et al. 1984; Podlovchenko et al. 1994; Min and Kanan 2015). Furthermore, it has previously been shown that the more favored intermediate for CO evolution is COOH* (Gao et al. 2015). The surface of the electrode can be reactivated by short oxidative treatment (Min and Kanan 2015). More desirably, though, CO poisoning would be reduced, and the selectivity toward formic acid synthesis, by designing a catalyst that would stabilize the formation of intermediates that reduce to HCOOH (steps 12.3 −12.6) and inhibit the formation of intermediate bound CO (steps 12.7 and 12.8). In order to attain optimum physico-chemical characteristics of the electrocatalysts for the realization of the efficient electrocatalytic CO_2 reduction and their resistance to CO poisoning, it is utmost vital toward development of newer electrocatalysts.

12.4 Electrooxidation of Formic Acid

Since 1960s, researchers are enormously attracted toward the development of direct fuel cells (DFCs) using small organic molecules such as formaldehyde (HCHO), ethanol (CH_3OH), formic acid (HCOOH), etc. due to their possible electrochemical oxidation (Lamy et al. 2002; Selvaraj et al. 2009). Among various DFCs, direct formic acid fuel cells (DFAFCs) find extensive application in emergency power-generating devices, portable electronic devices, and electrical vehicles because of having several merits like high power density in low temperatures, higher theoretical electromotive force, low fuel crossover through the nafion membrane, improved security, as well as the rapid oxidation kinetics. In DFAFCs, liquid formic acid is used as a fuel. The repulsive interaction that occurs during dissociation of formic acid into formate ions is the sole reason of limited fuel crossover in DFAFCs. The theoretical value of electromotive force for DFAFCs was found to be higher than that of hydrogen and methanol fuel cell and is equal to 1.48 V (Lesiak et al. 2016; Jiang et al. 2014; Wang et al. 2004; Bhowmik et al. 2017). Both Pd and Pt metals are considered as suitable electrocatalyst for the oxidation of formic acid. However, the high availability and low price along with enhanced catalytic activity of Pd at comparatively low potential make it the best monometallic electrocatalyst for formic acid oxidation (FAO).

Electrocatalytic FAO takes place via two simple pathways, mechanisms of which are summarized below (Wang et al. 2015; Klinkova et al. 2017):

(i) Dehydrogenation process (also known as direct pathway) involves the formation of CO_2 via simple oxidation of formic acid. It is a two-step proton/electron transfer process which supports the formation of an active intermediate, i.e., HCOO* on the catalyst surface.

$$HCOOH \rightarrow H^+ (aq) + e^- + HCOO^* \quad (12.9)$$

$$HCOO^* \rightarrow CO_2 + H^+ (aq) + e^- \quad (12.10)$$

(ii) Dehydration process (also known as indirect pathway) involves the strong adsorption of CO species on the catalyst surface (especially on Pt) via COOH* intermediate formation that eventually oxidized to CO_2.

$$HCOOH \rightarrow H^+ (aq) + e^- + COOH^* \quad (12.11)$$

$$COOH^* \rightarrow CO^* + OH^* \quad (12.12)$$

$$CO^* + OH^* \rightarrow CO_2 + H^+ + e^- \quad (12.13)$$

The primary disadvantage of Pt catalysts is that they are more vulnerable to CO poisoning effects because the FAO reaction on Pt surface follows the indirect pathway, while Pd-based catalysts are free of CO poisoning as they follow dehydrogenation, i.e., the direct pathway (Zhou et al. 2011). Moreover, in case of Pt catalysts, it has also been observed that the formation of CO intermediate lead to the degradation of the catalyst surface as well as its dissolution particularly in the acidic medium after a few electrocatalytic cycles (Orilall et al. 2009).

Palladium-based transition metal catalysts like Ni (Du et al. 2010; Li et al. 2011), Co (Morales-Acosta et al. 2010), Zn (Fathirad et al. 2016), Pb (Jana et al. 2016), etc. are the commonly used electrocatalysts for FAO. Yin and co-workers synthesized nanoporous $Pd_{57}Ni_{43}$ alloy nanowires with a pore size of 3–6 nm, by chemically dealloying Ni from $Pd_{25}Ni_{75}$ nanowires and applying as electrocatalyst for FAO which exhibits better activity compared to Pd/C (Du et al. 2010). Figure 12.6 represents the cyclic voltammograms of Pd/C, the $Pd_{25}Ni_{75}$, and the nanoporous

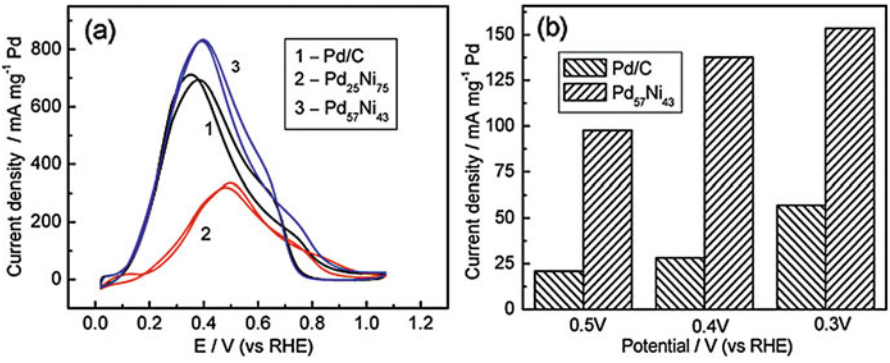

Fig. 12.6 (**a**) Cyclic voltammograms of the Pd/C, the $Pd_{25}Ni_{75}$, and nanoporous $Pd_{57}Ni_{43}$ alloy nanowires in a solution of 0.5 M HCOOH and 0.5 M H_2SO_4 at a scan rate of 50 mVs^{-1}, (**b**) polarization current density of the Pd/C and nanoporous $Pd_{57}Ni_{43}$ alloy nanowires in 0.5 M HCOOH and 0.5 M H_2SO_4 solution at different potentials for 15 min. (Adapted from Du et al. 2010)

$Pd_{57}Ni_{43}$ alloy nanowires along with the polarization current densities of Pd/C and nanoporous $Pd_{57}Ni_{43}$ alloy nanowires. The enhanced stability and durability of the catalyst are mainly due to the high surface area and modulation of its surface properties by Ni. Again, in the same year, Arriaga and group synthesized multi-walled carbon nanotubes (MWCNTs) supported PdCo and Pd catalysts via low-temperature impregnation method to investigate the FAO in acidic medium (Morales-Acosta et al. 2010). The electrochemical measurements revealed more current density and more negative shift in the onset potential with extra stability in acidic media for PdCo/MWCNTs than that attained with Pd/XC72 and Pd/MWCNTs. The current density for PdCo/MWCNTs is three times higher than that of Pd/MWCNTs. Yu and co-workers evaluated electrocatalytic FAO by synthesizing a series of Pd-Ni alloys with different compositions supported on MWCNTs via ultrasonic-assisted chemical reduction (Li et al. 2011). Pd-Ni/MWCNTs were reported as the best catalyst for FAO. The improved performance is attributed to the higher electroactive surface area along with modification in the electronic structure due to Ni doping. Morphology-dependent Pd_3Pb intermetallic nanoparticles are reported to be very active toward FAO and ethanol oxidation in KOH and $HClO_4$ (Jana et al. 2016). Among various morphologies of Pd_3Pb, the flowerlike structure exhibited excellent stability and electrocatalytic activity toward FAO. The mass activity and current density were 2.4 and 2.5 times greater than that of the benchmark Pd/C for FAO. Another study investigated catalytic activity of Vulcan XC-72R carbon-supported bimetallic palladium-zinc nanoalloys toward FAO, synthesized in various atomic ratios using sonochemical process (Fathirad et al. 2016). Compared to Pd/VC catalyst, the Pd_nZn/VC catalyst exhibited better performance toward FAO which is due to the synergistic effect between Pd and Zn. The activities of different catalysts in terms of current densities toward FAO follow the order $Pd_2Zn > Pd_3Zn > Pd_1Zn$.

It has been found that transition metal oxides can act as noble electrocatalyst support materials that not only improves the electrocatalytic activity but also diminishes the effects of CO poisoning over the catalyst surface (Uribe et al. 2004). In the recent decade, researchers are attracted toward the study of effect of CeO_2 on different catalytic systems for its unusual properties which were already mentioned earlier. Xing and group studied the effect of CeO_x on the Pd/C catalyst synthesized via microwave-assisted ethylene-glycol reduction method, toward FAO (Feng et al. 2012). The incorporation of CeO_x in the Pd/C catalyst not only enhances the catalytic activity and stability but also increases the rate of reaction which can be confirmed from the Tafel plots. Electrochemical measurements showed that during FAO, the peak current for $PdCeO_x$/C was approximately 1.67 times the peak current for Pd/C catalyst. This promotional effect is due to the electronic effect, large electrochemical surface area of the $PdCeO_x$/C catalyst, and the presence of oxygen-rich species created by CeO_x. In another study, Habibi and Delnavaz reported the fabrication of reduced graphene oxide-based Pt/CeO_2 nanoparticles on carbon-ceramic electrode (Pt/CeO_2/RGO/CCE) by a two-step electrodeposition method for FAO (Habibi and Delnavaz 2015). The Pt/CeO_2/RGO/CCE nanocomposites were reported to be superior in terms of their electrocatalytic

activity than that of other three electrocatalysts, namely, Pt/CCE, Pt-CeO_2/CCE, and Pt/RGO/CCE. This enhanced electrocatalytic behavior is attributed to the synergistic effect of CeO_2 with Pt to form Pt-CeO_2 nanoparticles.

Recently, Peter and co-workers synthesized Pt/CeO_2 nanoboxes by adopting a simplistic low-temperature aqueous-phase method to investigate the effect of various parameters like thickness of CeO_2 shell, shape and size of CeO_2 nanoboxes, amount of Pt loading, and the type of linkage between Pt nanoparticles and the surface of CeO_2 on the electrocatalytic FAO (Ramani et al. 2017). The catalytic activity was found to be exceptionally high due to the existence of exposed active sites in the smallest Pt/CeO_2 nanoboxes (50 nm) as well as its optimal shell thickness. Apart from the size and the shape, the structure of the oxide support plays a significant role in increasing the activity of the catalyst.

Figure 12.7 shows TEM images at various stages of the synthesis of Pt-supported CeO_2 nanoboxes (Ramani et al. 2017). Moreover, Jiang et al. studied the electrochemical FAO using TiO_2-supported Pd-Ni catalysts synthesized by hydrothermal method (Jiang et al. 2017). The Pd_2Ni_3-TiO_2 showed the best electrocatalytic activity, mass activity, as well as durability as compared to that of commercial Pd/C and Pd/TiO_2 catalysts. This improved electrocatalytic activity of Pd_2Ni_3-TiO_2 catalyst can be ascribed to the exceptional three-dimensional structures and alloying effect occurred during FAO reaction.

12.5 Electrooxidation of Ethanol

Direct alcohol fuel cells (DAFCs) have noteworthy advantages over several other types of fuel cells, since they do not require a fuel reformer and comprise high operating efficiency, excellent volumetric energy density, and the fewest environmental issues (Lamy et al. 2002; Antolini and Gonzalez 2010a, b). Ethanol, with its high energy density, likely production from renewable sources and ease of storage and transportation, is almost the ideal combustible for fuel cells wherein its chemical energy can be converted directly into electrical energy (Liang et al. 2011). Furthermore, compared with methanol, ethanol is less toxic and more convenient, has a higher energy density, and appears to fulfill most fuel requirements for low-temperature fuel cells (Yang et al. 2010). Even though platinum and platinum-based catalysts show a high efficiency toward ethanol electrooxidation (Kowal et al. 2009), the high cost and limited natural abundance of platinum prevent the commercial development of direct ethanol fuel cells (DEFCs). In addition, nanostructures of Pt are highly prone to segregation during long-term operation. This leads to the reduction in the number of active sites on Pt, which drastically decreases its efficiency for alcohol electrooxidation (Shrestha et al. 2011; Brouzgou et al. 2012). Besides, during the electrooxidation of alcohols, the major carbonaceous intermediate, CO, gets adsorbed on the active Pt sites and arrests the long-term activity of the catalyst (Kobayashi et al. 2003; Vigier et al. 2006). However, at a high overpotential, the activation of water generates oxygen-containing species such as

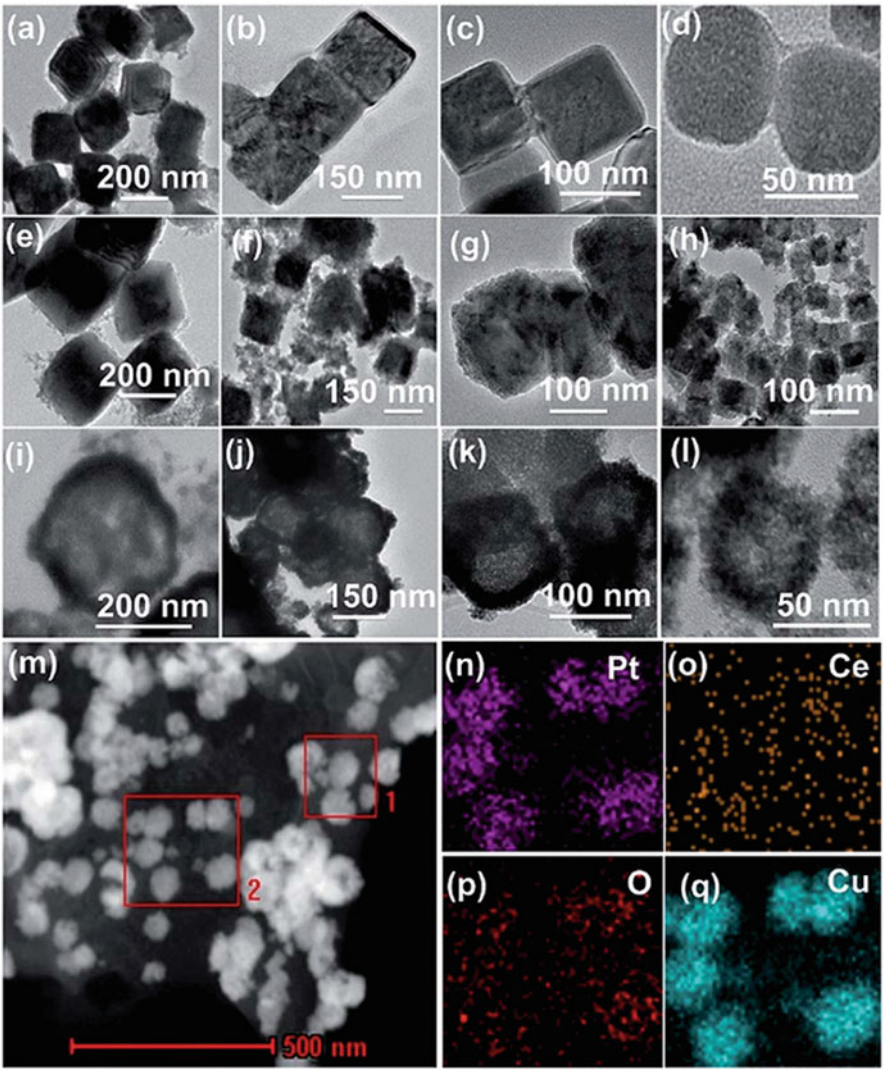

Fig. 12.7 TEM images at various stages of the synthesis of Pt-supported CeO_2 nanoboxes (200, 150, 100, and 50 nm). (**a–d**) TEM images of Cu_2O_NCs, (**e–h**) Cu_2O@CeO_2 CS-NCs, and (**i–l**) Pt/CeO_2_NBs. (**m**) Elemental mapping of Pt/CeO_2_NBs (50 nm) in the area in box 2; (**n–q**) area of mapping of Pt, Ce, O, and Cu, respectively. (Adapted from Ramani et al. 2017)

OH, which can oxidize the adsorbed CO on the Pt surface. Hence, one of the major challenges in DEFC research is the development of efficient and cost-effective catalysts, which can provide oxygenated species at lower overpotentials for oxidative removal of adsorbed CO (Kobayashi et al. 2003; Vigier et al. 2006).

The oxidation mechanism of ethanol on platinum electrodes can be decomposed into five different reactions as shown below in Scheme 12.1 (Colmati et al. 2008).

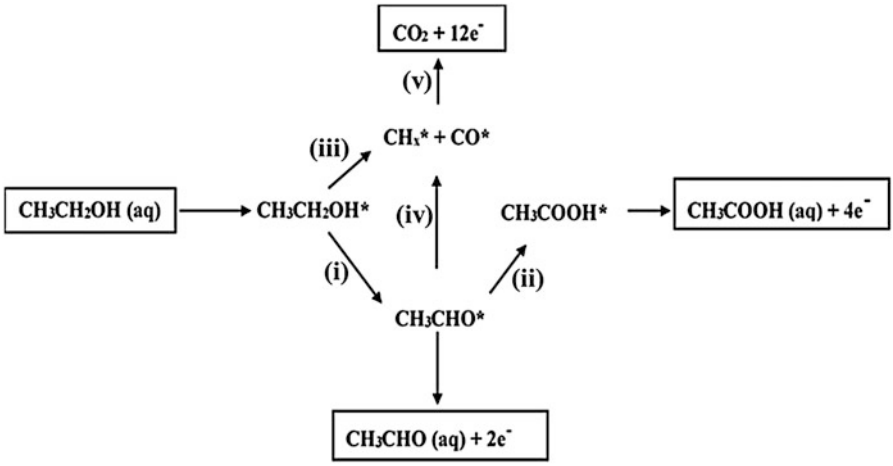

Scheme 12.1 The oxidation mechanism of ethanol on platinum electrodes. (Adapted from Colmati et al. 2008)

Reaction (i) is the oxidation of CH_3CH_2OH to CH_3CHO transferring two electrons. CH_3CHO can, in turn (step ii), be oxidized to CH_3COOH, transferring two additional electrons. CH_3COOH can be considered as a final product since its oxidation is very difficult. In fact, CH_3COOH is stable on platinum electrodes at potentials where oxygen evolves. However, in the formation of CH_3COOH, only four electrons are transferred, and, therefore, the energy density to yield CH_3COOH from CH_3CH_2OH is then lower than that obtained for the complete oxidation of methanol. Reactions (iii) and (iv) represent the routes that allow the transfer of 12 e^-. Both reactions involve the cleavage of the C-C bond in the molecule to yield adsorbed CO and other fragments. These additional fragments, whose identification is not trivial, are probably further oxidized to yield also adsorbed CO. The final oxidation of the adsorbed CO to CO_2 is difficult (reaction v), since it requires the additional transfer of an oxygen atom to the adsorbed CO molecule. Therefore, developing electrocatalysts for ethanol oxidation to CO_2 that break the C-C bond has been a major challenge in electrocatalysis. The existing electrocatalysts can accomplish that only at extreme positive potentials, which renders them unsuitable for direct ethanol fuel cells.

Pt-based alloys with suitable metals such as Pd, Ru, Rh, Au, Sn, Ni, Ir, Os, Cu, etc., which effectively provide electronic suitability to make the oxygenated species available for reaction at lower overpotentials are explored (Léger et al. 2005; Zhong et al. 2008). Lamy et al. reported that PtSn/C bimetallic carbon-supported materials are more active than Pt-Ru/C electrocatalysts for ethanol oxidation. The current density was higher, and the overpotential for ethanol oxidation was less positive on PtSn/C in comparison to that of pure Pt/C electrode. However, the electrooxidation of ethanol on PtSn/C yields almost only partially oxidized products, acetaldehyde and acetic acid, i.e., the presence of Sn does not improve the conversion of ethanol to

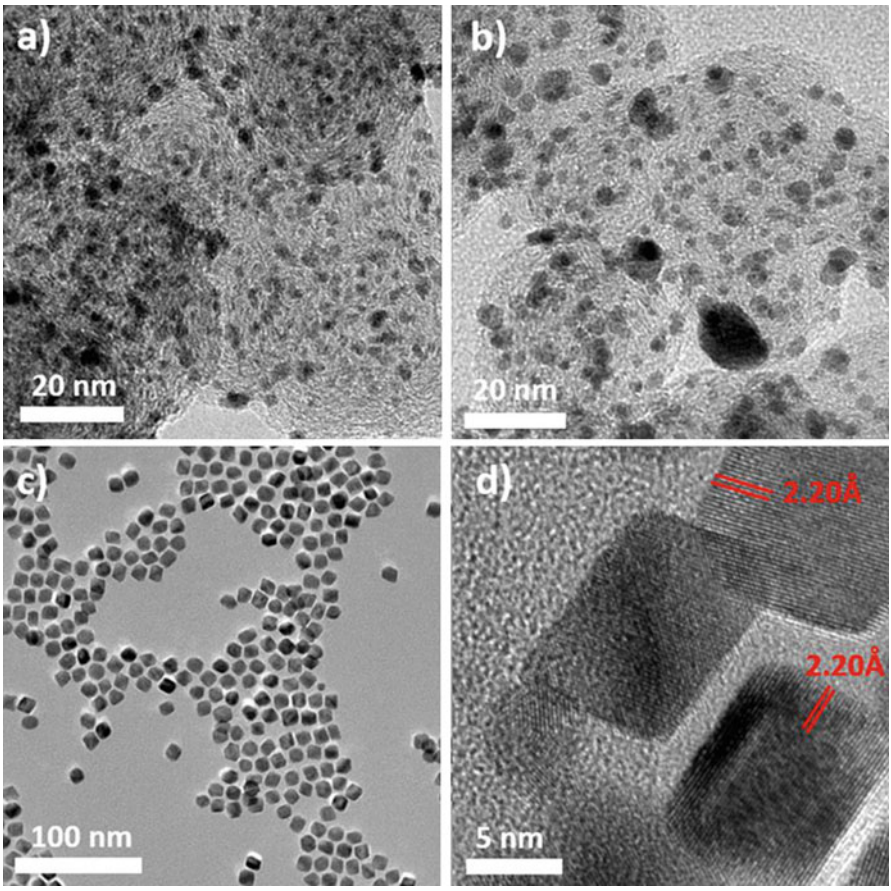

Fig. 12.8 TEM images of Pt/C (**a**), conventional Pt_2Ni/C (**b**), and octahedral $Pt_{2.3}Ni/C$ (**c**) and HRTEM images of octahedral $Pt_{2.3}Ni$ with 10 nm edge length (**d**). (Adapted from Sulaiman et al. 2017)

CO_2 (Lamy et al. 2004). The octahedral Pt-Ni/C nanocatalyst has been employed toward ethanol electrooxidation and observed that it is ca. 4.6 and 7.7 times more active than conventional Pt-Ni/C and commercial Pt/C catalysts, respectively. In situ infrared spectroscopic results showed that the acetic acid/CO_2 absorbance peak intensity on octahedral Pt-Ni/C was 7.6 and 1.4 times higher as compared to commercial Pt/C and conventional Pt-Ni/C, respectively, at 0.75 V (Sulaiman et al. 2017). Figure 12.8 presents the TEM images of Pt/C, conventional Pt_2Ni/C, and octahedral $Pt_{2.3}Ni/C$ employed in the studies.

Gonzalez and co-workers reported a study to investigate the influence of the composition of Pt-Rh/C catalysts on the CO_2 yields. They have showed that Pt-Rh/C catalysts enhance the total ethanol oxidation with respect to pure Pt/C by driving the reaction via the CO_2 route by using differential electrochemical mass spectrometry

technique. The faradaic current efficiency for the oxidation of ethanol to CO_2 was increased from 0.08 on pure Pt/C to 0.5 on the $Pt_{47}Rh_{53}$/C catalyst at 0.7 V vs. RHE. It was concluded that electronic effects play a key role in the mechanism of ethanol oxidation on Pt-Rh/C electrodes (Bergamaski et al. 2008). Moreover it is known that the oxidation of ethanol is a structure-sensitive reaction. Therefore, the final products of the oxidation will depend on the surface structure of the electrode. Additionally, the composition of the electrolyte can also change the reactivity of the electrode. Normally, the presence of strong adsorbing anions on the electrode surface hinders the interaction of the reacting molecules with the surface, resulting in a diminution of the current densities. Colmati et al. reported the effect of the structure of the electrode surface, as well as the effect of the competitive adsorption of the anion of the supporting electrolyte, in the catalytic activity of platinum single crystal electrodes for ethanol oxidation (Colmati et al. 2008).

In another approach to enhance the alcohol electrooxidation activity, various promoters have been introduced for fabrication of electrocatalysts, e.g., metal oxides-, carbides-, and nitrides-promoted electrocatalysts (Rao et al. 2011; Ham and Lee 2009). Among these various promoters, metal oxides are considered as the best due to their low cost. Metal oxides provide suitable functional groups which strongly interact with small Pt crystallites, thereby circumventing their random growth and agglomeration during device operation for longer duration. Metal oxides such as WO_3, CeO_2, RuO_2, V_2O_5, Nb_2O_5, MoO_x, TiO_2, and MnO_2 show immense promise in promoting Pt/C for electrooxidation of alcohols (Antolini and Gonzalez 2010a, b; Meher and Rao 2012; Suffredini et al. 2006; Justin and Rao 2009; Justin et al. 2010). In a recent report, Ranga Rao and co-workers studied the synthesis of tunable morphologies of MnO_2 and its influence in promoting Pt/C for methanol and ethanol electrooxidation reactions in acidic medium (Meher and Rao 2013). The cyclic voltammetry studies revealed higher current response and lower overpotential by the MnO_2-nanorod-modified Pt/C as compared to the MnO_2-microcube-modified Pt/C and bare Pt/C during the electrooxidation reaction as presented in Fig. 12.9. The chronopotentiometry and chronoamperometry analyses showed lower alcohol oxidation overpotential and longer polarization time/stability for MnO_2-nanorod-modified Pt/C as compared to the MnO_2-microcube-modified Pt/C and bare Pt/C. Further, in CO stripping voltammetry study, the MnO_2-nanorod-modified Pt/C showed higher current response and stronger negative shift in the CO electrooxidation potential.

Silva et al. performed a similar study on the ethanol oxidation reaction using SnO_2@Pt/C core/shell structures as electrocatalysts (Silva et al. 2010). They have reported that the electrochemical profile for SnO_2@Pt/C in an acidic medium was almost the same as the typical electrochemical behavior for Pt in an acidic medium. Furthermore, the mass current peak densities for ethanol oxidation were observed to be 50% higher on SnO_2@Pt/C than on commercial PtSn/C E-tek. They have observed that the current mass density for ethanol oxidation on SnO_2@Pt was 2.3 times of that for the same process on the commercial material at 0.5 V. In another very outstanding work, Adzic and co-workers reported that ternary $PtRhSnO_2$/C electrocatalyst by depositing platinum and rhodium atoms on carbon-supported tin

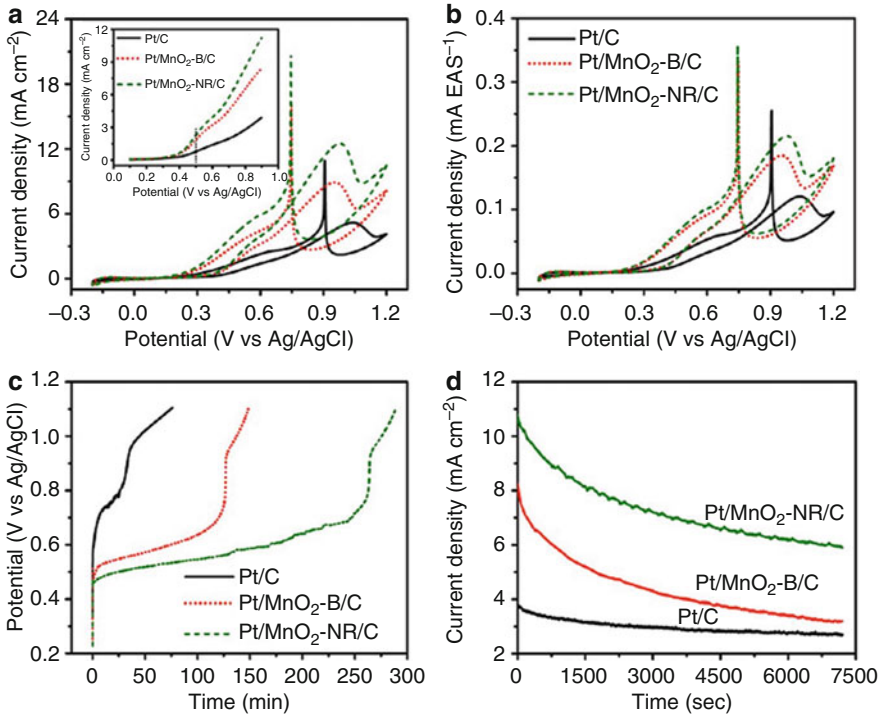

Fig. 12.9 (**a**, **b**) Comparative cyclic voltammograms of Pt/C, Pt/MnO_2-B/C, and Pt/MnO_2-NR/C sample electrodes in 0.5 mol L^{-1} H_2SO_4 + 1 M CH_3CH_2OH solution at a scan rate of 20 mV s^{-1}: graphs in panels **a** and **b** show the current response with respect to geometrical area of the electrode (in cm^2) and per unit electroactive surface area (in m^2) of the catalyst samples, respectively; (**c**) chronopotentiometry profiles of the sample electrodes at a current density of 15 mA cm^{-2}; and (**d**) chronoamperometry profiles of the sample electrodes at an applied potential of 0.9 V. (Adapted from Meher and Rao 2013)

dioxide nanoparticles oxidizes ethanol with high efficiency which holds great promise for resolving the impediments to developing practical direct ethanol fuel cells (Kowal et al. 2009). This electrocatalyst effectively splits the C-C bond in ethanol at room temperature in acid solutions, facilitating its oxidation at low potentials to CO_2. The ternary $PtRhSnO_2$/C exhibits higher activity for EEO than that of $PtSnO_2$/C, highlighting the importance of the Rh component.

12.6 Conclusions and Future Perspectives

Over the last few decades, extensive research on nanocatalysis is being employed for the advancement of fuel cell technology. Because of their unique catalytic, magnetic, and synergistic and adsorptive properties, they can maximize electrode activity in

fuel cell processes. With the growing research interest and with the progress of material science and nanotechnology, researchers have prepared nanocatalysts with fairly controlled size, shape, composition, and structure. The need for highly active fuel cell catalysts for practical applications has encouraged researchers in developing monodisperse NPs of non-precious metal and their oxides as well as NPs comprising alloys and composite NPs. Despite the electrifying progress in fuel cell catalyst developments, plentiful issues still remain. In general, the activity and stability of these catalysts are still lower than those of a Pt-based catalyst. A more fundamental and comprehensive understanding is essential in designing alternative and innovative routes to Pt-free catalysts for practical fuel cell applications.

Platinum and other noble metals severely restrict the commercialization and unitization of electrochemical energy conversion systems. For making commercially viable regenerative fuel cells, extensive research over the past decades has focused on mounting alternative electrocatalysts, including non-noble metal catalysts. These electrocatalysts comprise of non-noble metals and alloys, carbon materials, quinone and derivatives, metal-N complex on carbon matrices, doped carbonaceous materials, transition metal macrocyclic compounds, transition metal chalcogenides, transition metal carbides, transition metal oxides (TMOs), and mixed transition metal oxides (MTMOs) with perovskites, spinel oxide structures. TMOs and MTMOs with different stoichiometric or even nonstoichiometric compositions have recently attracted growing research interest worldwide. Benefiting from their astonishing synergistic and electrochemical properties, TMOs and MTMOs play significant roles for low-cost and environmentally friendly energy storage/conversion technologies.

In the past decades, although there has been astonishing development for metal/alloy and metal oxide-based ORR, HER, and OER catalyst, the electrical properties of these catalysts still need to be improved. The superior intrinsic electrical conductivity is fundamentally appreciated for the better electrochemical activity of catalysts. Novel carbon-based nanostructures being electrical conductive has the potential to decrease the overall cost of PEMFCs. Furthermore, carbon materials with high chemical and physical properties can also function as the supports for nanostructure catalysts, which can prevent the relocation and accumulation of the nanostructures, and improve catalytic performance through the synergistic assistance. It seems still very challenging to acquire ORR electrocatalysis with noteworthy performance in acidic media than alkaline media. The forthcoming research effort can be focused on these aspects:

1. Development and modification of metal and metal oxide-based electrocatalysts that could function particularly in acidic electrolytes.
2. Doping or alloying with first-row transition metal ions to reduce the bandgap and enhance electronic conductivity.
3. Designing 3D hierarchical nanostructures to increase the electrochemically active surface area, reviewing the interplay mechanism between the metal and metal oxide, and transforming metal oxides to increase the interactions and, thus, the chemical and electrochemical stability.

4. To explore novel materials and to improve the catalysts preparation processes retaining stability along with active interfaces.
5. MTMO nanoparticles with tunable pore size and different morphology in association with the functionalized carbon materials.

Furthermore, it is of paramount importance to make efforts for the mechanism study besides the experimental exploration. Many innovative techniques have emerged to rationalize the relationship between material properties and performance, as well as the catalytic mechanism. However, the mechanistic study at the atomic level is seldom, and it might not adequate to conclude the scenario of the catalytic site. Thus, an amalgamation of in situ characterization techniques and theoretical calculations is a requirement to distinctly unveil the catalytic mechanisms. Fundamental understanding of the principles of interfacial electrocatalysis is the key factor to tailor new catalyst structures. In addition, extensive theoretical investigations into the electronic properties, crystal and surface structure, as well as synergetic effects in metal/alloy and MTMO nanomaterials on carbon should be made based on first-principle calculations, which in association with smart experimental strategies will greatly shorten the development process of highly efficient noble metal-free nanomaterials for energy storage and conversion applications.

Acknowledgments The authors thank Tezpur University, Council of Scientific and Industrial Research (CSIR No: 01(2813)/14/EMR-II), New Delhi, and Science and Engineering Research Board (SERB-DST No: SB/FT/CS-048/2014), New Delhi, for generous financial support. CG and BC thank Tezpur University and CSIR, New Delhi, for research fellowship, respectively.

References

Ang SY, Walsh DA (2010) Palladium–vanadium alloy electrocatalysts for oxygen reduction: effect of heat treatment on electrocatalytic activity and stability. Appl Catal B 98(1–2):49–56. https://doi.org/10.1016/j.apcatb.2010.04.025

Antolini E, Gonzalez ER (2010a) Alkaline direct alcohol fuel cells. J Power Sources 195 (11):3431–3450. https://doi.org/10.1016/j.jpowsour.2009.11.145

Antolini E, Gonzalez ER (2010b) Tungsten-based materials for fuel cell applications. Appl Catal B Environ 96(3–4):245–266. https://doi.org/10.1016/j.apcatb.2010.02.039

Appel AM, Bercaw JE, Bocarsly AB, Dobbek H, DuBois DL, Dupuis M, Ferry JG, Fujita E, Hille R, Kenis PJA, Morris RH, Peden CHF, Portis AR, Ragsdale SW, Rauchfuss TB, Reek JNH, Seefeldt LC, Thauer RK, Waldrop GL, Kerfeld CA (2013) Frontiers, opportunities, and challenges in biochemical and chemical catalysis of CO_2 fixation. Chem Rev 113 (8):6621–6658. https://doi.org/10.1021/cr300463y

Armstrong FA, Hirst J (2011) Reversibility and efficiency in electrocatalytic energy conversion and lessons from enzymes. Proc Natl Acad Sci U S A 108(34):14049–14054. https://doi.org/10.1073/pnas.1103697108

Arora VK, Scinocca JF, Boer GJ, Christian JR, Denman KL, Flato GM, Kharin VV, Lee WG, Merryfield WJ (2011) Carbon emission limits required to satisfy future representative concentration pathways of greenhouse gases. Geophys Res Lett 38(5):L05805. https://doi.org/10.1029/2010GL046270

Bard AJ, Fox MA (1995) Artificial photosynthesis: solar splitting of water to hydrogen and oxygen. Acc Chem Res 28(3):141–145. https://doi.org/10.1021/ar00051a007

Bergamaski K, Gonzalez ER, Nart FC (2008) Ethanol oxidation on carbon supported platinum-rhodium bimetallic catalysts. Electrochim Acta 53(13):4396–4406. https://doi.org/10.1016/j.electacta.2008.01.060

Bharali P, Saikia P, Reddy BM (2012) Large-scale synthesis of ceria-based nano-oxides with high CO oxidation activity. Cat Sci Technol 2:931–933. https://doi.org/10.1039/c2cy20024d

Bharali P, Saikia P, Katta L, Reddy BM (2013) Enhancement in CO oxidation activity of nanosized $Ce_xZr_{1-x}O_2$ solid solutions by incorporation of additional dopants. J Ind Eng Chem 19:327–336. https://doi.org/10.1016/j.jiec.2012.08.021

Bhowmik T, Kundu MK, Barman S (2017) Highly efficient electrocatalytic oxidation of formic acid on palladium nanoparticles-graphitic carbon nitride composite. Int J Hydrog Energy 42 (1):212–217. https://doi.org/10.1016/j.ijhydene.2016.11.095

Brett DJ, Kucernak AR, Aguiar P, Atkins SC, Brandon NP, Clague R, Cohen LF, Hinds G, Kalyvas C, Offer GJ, Ladewig B (2010) What happens inside a fuel cell? Developing an experimental functional map of fuel cell performance. ChemPhysChem 11(13):2714–2731. https://doi.org/10.1002/cphc.201000487

Brouzgou A, Song SQ, Tsiakaras P (2012) Low and non-platinum electrocatalysts for PEMFCs: current status, challenges and prospects. Appl Catal B Environ 127:371–388. https://doi.org/10.1016/j.apcatb.2012.08.031

Cai F, Gao D, Si R, Ye Y, He T, Miao S, Wang G, Bao X (2017a) Effect of metal deposition sequence in carbon-supported Pd–Pt catalysts on activity towards CO_2 electroreduction to formate. Electrochem Commun 76:1–5. https://doi.org/10.1016/j.elecom.2017.01.009

Cai F, Gao D, Zhou H, Wang G, He T, Gong H, Miao S, Yang F, Wangb J, Bao X (2017b) Electrochemical promotion of catalysis over Pd nanoparticles for CO_2 reduction. Chem Sci 8 (4):2569–2573. https://doi.org/10.1039/c6sc04966d

Cao A, Lu R, Veser G (2010) Stabilizing metal nanoparticles for heterogeneous catalysis. Phys Chem Chem Phys 12(41):13499–13510. https://doi.org/10.1039/c0cp00729c

Carrette L, Friedrich KA, Stimming U (2000) Fuel cells: principles, types, fuels, and applications. ChemPhysChem 1(4):162–193. https://doi.org/10.1002/1439-7641(20001215)1:4<162::AID-CPHC162>3.0.CO;2-Z

Chaplin RPS, Wragg AA (2003) Effects of process conditions and electrode material on reaction pathways for carbon dioxide electroreduction with particular reference to formate formation. J Appl Electrochem 33(12):1107–1123. https://doi.org/10.1023/b:jach.0000004018.57792.b8

Chen X, Wu G, Chen J, Chen X, Xie Z, Wang X (2011) Synthesis of "clean" and well-dispersive Pd nanoparticles with excellent electrocatalytic property on graphene oxide. J Am Chem Soc 133 (11):3693–3695. https://doi.org/10.1021/ja110313d

Chen J, Zhou N, Wang H, Peng Z, Li H, Tang Y, Liu K (2015) Synergistically enhanced oxygen reduction activity of MnO_x–CeO_2/Ketjenblack composites. Chem Commun 51 (50):10123–10126. https://doi.org/10.1039/c5cc02343b

Colmati F, Tremiliosi-Filho G, Gonzalez ER, Berná A, Herrero E, Feliu JM (2008) Surface structure effects on the electrochemical oxidation of ethanol on platinum single crystal electrodes. Faraday Discuss 140:379–397. https://doi.org/10.1039/b802160k

Delacote C, Bonakdarpour A, Johnston CM, Zelenay P, Wieckowski A (2009) Aqueous-based synthesis of ruthenium–selenium catalyst for oxygen reduction reaction. Faraday Discuss 140:269–281. https://doi.org/10.1039/b806377j

Du C, Chen M, Wang W, Yin G (2010) Nanoporous PdNi alloy nanowires as highly active catalysts for the electro-oxidation of formic acid. ACS Appl Mater Interfaces 3(2):105–109. https://doi.org/10.1021/am100803d

Fathirad F, Afzali D, Mostafavi A (2016) Bimetallic Pd–Zn nanoalloys supported on Vulcan XC-72R carbon as anode catalysts for oxidation process in formic acid fuel cell. Int J Hydrog Energy 41(30):13220–13226. https://doi.org/10.1016/j.ijhydene.2016.05.098

Feng L, Yang J, Hu Y, Zhu J, Liu C, Xing W (2012) Electrocatalytic properties of $PdCeO_x$/C anodic catalyst for formic acid electrooxidation. Int J Hydrog Energy 37(6):4812–4818. https://doi.org/10.1016/j.ijhydene.2011.12.114

Gao D, Zhou H, Wang J, Miao S, Yang F, Wang G, Wang J, Bao X (2015) Size-dependent electrocatalytic reduction of CO_2 over Pd nanoparticles. J Am Chem Soc 137(13):4288–4291. https://doi.org/10.1021/jacs.5b00046

Gao D, Zhang Y, Zhou Z, Cai F, Zhao X, Huang W, Li Y, Zhu J, Liu P, Yang F, Bao X, Wang G (2017) Enhancing CO_2 electroreduction with the metal–oxide interface. J Am Chem Soc 139 (16):5652–5655. https://doi.org/10.1021/jacs.7b00102

Guo S, Zhang S, Wu L, Sun S (2012) Co/CoO nanoparticles assembled on graphene for electrochemical reduction of oxygen. Angew Chem 124(47):11940–11943. https://doi.org/10.1002/ange.201206152

Guo S, Li D, Zhu H, Zhang S, Markovic NM, Stamenkovic VR, Sun S (2013) FePt and CoPt nanowires as efficient catalysts for the oxygen reduction reaction. Angew Chem Int Ed 52 (12):3465–3468. https://doi.org/10.1002/anie.201209871

Habibi B, Delnavaz N (2015) Pt–CeO_2/reduced graphene oxide nanocomposite for the electrooxidation of formic acid and formaldehyde. RSC Adv 5(90):73639–73650. https://doi.org/10.1039/c5ra09770c

Ham DJ, Lee JS (2009) Transition metal carbides and nitrides as electrode materials for low temperature fuel cells. Energies 2(4):873–899. https://doi.org/10.3390/en20400873

He L, Liang B, Li L, Yang X, Huang Y, Wang A, Zhang T (2015) Cerium-oxide-modified nickel as a non-noble metal catalyst for selective decomposition of hydrous hydrazine to hydrogen. ACS Catal 5(3):1623–1628. https://doi.org/10.1021/acscatal.5b00143

Hietala J, Vuori A, Johnsson P, Pollari I, Reutemann W, Kieczka H (2016) Formic acid. Ullmann's encyclopedia of industrial chemistry. Wiley, New York, pp 1–22. https://doi.org/10.1002/14356007.a12_013.pub3

Hori Y, Wakebe H, Tsukamoto T, Koga O (1994) Electrocatalytic process of CO selectivity in electrochemical reduction of CO_2 at metal electrodes in aqueous media. Electrochim Acta 39 (11–12):1833–1839. https://doi.org/10.1016/0013-4686(94)85172-7

Jana R, Subbarao U, Peter SC (2016) Ultrafast synthesis of flower-like ordered Pd_3Pb nanocrystals with superior electrocatalytic activities towards oxidation of formic acid and ethanol. J Power Sources 301:160–169. https://doi.org/10.1016/j.jpowsour.2015.09.114

Jhong HR, Ma S, Kenis PJA (2013) Electrochemical conversion of CO_2 to useful chemicals: current status, remaining challenges, and future opportunities. Chem Eng 2:191–199. https://doi.org/10.1016/j.coche.2013.03.005

Jiang K, Zhang HX, Zou S, Cai WB (2014) Electrocatalysis of formic acid on palladium and platinum surfaces: from fundamental mechanisms to fuel cell applications. Phys Chem Chem Phys 16(38):20360–20376. https://doi.org/10.1039/c4cp03151b

Jiang S, Yi B, Zhao Q, Yu H, Shao Z (2017) Palladium–nickel catalysts based on ordered titanium dioxide nanorod arrays with high catalytic performance for formic acid electro-oxidation. RSC Adv 7(19):11719–11723. https://doi.org/10.1039/c7ra00194k

Justin P, Rao GR (2009) Enhanced activity of methanol electro-oxidation on Pt–V_2O_5/C catalysts. Catal Today 141(1–2):138–143. https://doi.org/10.1016/j.cattod.2008.03.019

Justin P, Charan PHK, Rao GR (2010) High performance Pt–Nb_2O_5/C electrocatalysts for methanol electrooxidation in acidic media. Appl Catal B Environ 100(3–4):510–515. https://doi.org/10.1016/j.apcatb.2010.09.001

Kang Y, Murray CB (2010) Synthesis and electrocatalytic properties of cubic Mn−Pt nanocrystals (nanocubes). J Am Chem Soc 132(22):7568–7569. https://doi.org/10.1021/ja100705j

Kariuki NN, Wang X, Mawdsley JR, Ferrandon MS, Niyogi SG, Vaughey JT, Myers DJ (2010) Colloidal synthesis and characterization of carbon-supported Pd−Cu nanoparticle oxygen reduction electrocatalysts. Chem Mater 22(14):4144–4152. https://doi.org/10.1021/cm100155z

Klinkova A, De Luna P, Dinh CT, Voznyy O, Larin EM, Kumacheva E, Sargent EH (2016) Rational design of efficient palladium catalysts for electroreduction of carbon dioxide to formate. ACS Catal 6(12):8115–8120. https://doi.org/10.1021/acscatal.6b01719

Klinkova A, De Luna P, Sargent EH, Kumacheva E, Cherepanov PV (2017) Enhanced electrocatalytic performance of palladium nanoparticles with high energy surfaces in formic acid oxidation. J Mater Chem A 5:11582–11585. https://doi.org/10.1039/c7ta00902j

Kobayashi T, Otomo J, Wen CJ, Takahashi H (2003) Direct alcohol fuel cell—relation between the cell performance and the adsorption of intermediate originating in the catalyst-fuel combinations. J Power Sources 124(1):34–39. https://doi.org/10.1016/S0378-7753(03)00622-0

Kowal A, Li M, Shao M, Sasaki K, Vukmirovic MB, Zhang J, Marinkovic NS, Liu P, Frenkel AI, Adzic RR (2009) Ternary Pt/Rh/SnO_2 electrocatalysts for oxidizing ethanol to CO_2. Nat Mater 8 (4):325. https://doi.org/10.1038/nmat2359

Lam E, Luong JH (2014) Carbon materials as catalyst supports and catalysts in the transformation of biomass to fuels and chemicals. ACS Catal 4(10):3393–3410. https://doi.org/10.1021/cs5008393

Lamy C, Lima A, LeRhun V, Delime F, Coutanceau C, Léger JM (2002) Recent advances in the development of direct alcohol fuel cells (DAFC). J Power Sources 105(2):283–296. https://doi.org/10.1016/S0378-7753(01)00954-5

Lamy C, Rousseau S, Belgsir EM, Coutanceau C, Léger JM (2004) Recent progress in the direct ethanol fuel cell: development of new platinum–tin electrocatalysts. Electrochim Acta 49 (22–23):3901–3908. https://doi.org/10.1016/j.electacta.2004.01.078

Landman U, Heiz U (eds) (2007) Nanocatalysis. Springer, eBook ISBN: 978-3-540-32646-5. https://doi.org/10.1007/978-3-540-32646-5

Léger JM, Rousseau S, Coutanceau C, Hahn F, Lamy C (2005) How bimetallic electrocatalysts does work for reactions involved in fuel cells?: example of ethanol oxidation and comparison to methanol. Electrochim Acta 50(25–26):5118–5125. https://doi.org/10.1016/j.electacta.2005.01.051

Lesiak B, Mazurkiewicz M, Malolepszy A, Stobinski L, Mierzwa B, Mikolajczuk-Zychora A, Juchniewicz K, Borodzinski A, Zemek J, Jiricek P (2016) Effect of the Pd/MWCNTs anode catalysts preparation methods on their morphology and activity in a direct formic acid fuel cell. Appl Surf Sci 387:929–937. https://doi.org/10.1016/j.apsusc.2016.06.152

Lewis NS, Nocera DG (2006) Powering the planet: chemical challenges in solar energy utilization. Proc Natl Acad Sci U S A 103(43):15729–15735. https://doi.org/10.1073/pnas.0603395103

Li R, Wei Z, Huang T, Yu A (2011) Ultrasonic-assisted synthesis of Pd–Ni alloy catalysts supported on multi-walled carbon nanotubes for formic acid electrooxidation. Electrochim Acta 56(19):6860–6865. https://doi.org/10.1016/j.electacta.2011.05.097

Liang Y, Li Y, Wang H, Zhou J, Wang J, Regier T, Dai H (2011) Co_3O_4 nanocrystals on graphene as a synergistic catalyst for oxygen reduction reaction. Nat Mater 10(10):780–786. https://doi.org/10.1038/nmat3087

Liu CW, Wei YC, Wang KW (2010) Promotion of ceria-modified Pt–Au/C cathode catalysts for oxygen reduction reaction by H_2-induced surface segregation. Chem Commun 46 (14):2483–2485. https://doi.org/10.1039/b920212a

Liu IT, Hon MH, Teoh LG (2013) Structure and optical properties of CeO_2 nanoparticles synthesized by precipitation. J Electron Mater 42(8):2536. https://doi.org/10.1007/s11664-013-2617-9

Liu K, Huang X, Wang H, Li F, Tang Y, Li J, Shao M (2016) Co_3O_4-CeO_2/C as a highly active electrocatalyst for oxygen reduction reaction in Al-air batteries. ACS Appl Mater Interfaces 8 (50):34422–34430. https://doi.org/10.1021/acsami.6b12294

Lu H, Huang Y, Yan J, Fan W, Liu T (2015) Nitrogen-doped graphene/carbon nanotube/Co_3O_4 hybrids: one-step synthesis and superior electrocatalytic activity for the oxygen reduction reaction. RSC Adv 5(115):94615–94622. https://doi.org/10.1039/c5ra17759f

Ma S, Sadakiyo M, Heima M, Luo R, Haasch RT, Gold JI, Yamauchi M, Kenis PJ (2016) Electroreduction of carbon dioxide to hydrocarbons using bimetallic Cu–Pd catalysts with different mixing patterns. J Am Chem Soc 139(1):47–50. https://doi.org/10.1021/jacs.6b10740

Markovic NM, Gasteiger HA, Ross PN Jr (1995) Oxygen reduction on platinum low-index single-crystal surfaces in sulfuric acid solution: rotating ring-Pt (hkl) disk studies. J Phys Chem 99 (11):3411–3415. https://doi.org/10.1021/j100011a001

Mazumder V, Chi M, More KL, Sun S (2010a) Core/shell Pd/FePt nanoparticles as an active and durable catalyst for the oxygen reduction reaction. J Am Chem Soc 132(23):7848–7849. https://doi.org/10.1021/ja1024436

Mazumder V, Lee Y, Sun S (2010b) Recent development of active nanoparticle catalysts for fuel cell reactions. Adv Funct Mater 20(8):1224–1231. https://doi.org/10.1002/adfm.200902293

Meher SK, Rao GR (2012) Polymer-assisted hydrothermal synthesis of highly reducible shuttle-shaped CeO_2: microstructural effect on promoting Pt/C for methanol electrooxidation. ACS Catal 2(12):2795–2809. https://doi.org/10.1021/cs300473e

Meher SK, Rao GR (2013) Morphology-controlled promoting activity of nanostructured MnO_2 for methanol and ethanol electrooxidation on Pt/C. J Phys Chem C 117(10):4888–4900. https://doi.org/10.1021/jp3093995

Min X, Kanan MW (2015) Pd-catalyzed electrohydrogenation of carbon dioxide to formate: high mass activity at low overpotential and identification of the deactivation pathway. J Am Chem Soc 137(14):4701–4708. https://doi.org/10.1021/ja511890h

Mondal AK, Liu H, Li ZF, Wang G (2016) Multiwall carbon nanotube-nickel cobalt oxide hybrid structure as high performance electrodes for supercapacitors and lithium ion batteries. Electrochim Acta 190:346–353. https://doi.org/10.1016/j.electacta.2015.12.132

Morales-Acosta D, Ledesma-Garcia J, Godinez LA, Rodríguez HG, Alvarez-Contreras L, Arriaga LG (2010) Development of Pd and Pd–Co catalysts supported on multi-walled carbon nanotubes for formic acid oxidation. J Power Sources 195(2):461–465. https://doi.org/10.1016/j.jpowsour.2009.08.014

Mura MG, Luca LD, Giacomelli G, Porcheddu A (2012) Formic acid: a promising bio-renewable feedstock for fine chemicals. Adv Synth Catal 354(17):3180–3186. https://doi.org/10.1002/adsc.201200748

Narayanan R, El-Sayed MA (2004) Shape-dependent catalytic activity of platinum nanoparticles in colloidal solution. Nano Lett 4(7):1343–1348. https://doi.org/10.1021/nl0495256

Orilall MC, Matsumoto F, Zhou Q, Sai H, Abruna HD, DiSalvo FJ, Wiesner U (2009) One-pot synthesis of platinum-based nanoparticles incorporated into mesoporous niobium oxide−carbon composites for fuel cell electrodes. J Am Chem Soc 131(26):9389–9395. https://doi.org/10.1021/ja903296r

Osgood H, Devaguptapu SV, Xu H, Cho J, Wu G (2016) Transition metal (Fe, Co, Ni, and Mn) oxides for oxygen reduction and evolution bifunctional catalysts in alkaline media. Nano Today 11(5):601–625. https://doi.org/10.1016/j.nantod.2016.09.001

Osmieri L, Videla AHM, Armandi M, Specchia S (2016) Influence of different transition metals on the properties of Me–N–C (Me= Fe, Co, Cu, Zn) catalysts synthesized using SBA-15 as tubular nano-silica reactor for oxygen reduction reaction. Int J Hydrog Energy 41(47):22570–22588. https://doi.org/10.1016/j.ijhydene.2016.05.223

Ou DR, Mori T, Fugane K, Togasaki H, Ye F, Drennan J (2011) Stability of ceria supports in $PtCeO_x$/C catalysts. J Phys Chem C 115(39):19239–19245. https://doi.org/10.1021/jp205640k

Park CS, Kim KS, Park YJ (2013) Carbon-sphere/Co_3O_4 nanocomposite catalysts for effective air electrode in Li/air batteries. J Power Sources 244:72–79. https://doi.org/10.1016/j.jpowsour.2013.03.153

Perez-Alonso FJ, McCarthy DN, Nierhoff A, Hernandez-Fernandez P, Strebel C, Stephens IE, Nielsen JH, Chorkendorff I (2012) The effect of size on the oxygen electroreduction activity of mass-selected platinum nanoparticles. Angew Chem Int Ed 51(19):4641–4643. https://doi.org/10.1002/anie.201200586

Phoka S, Laokul P, Swatsitang E, Promarak V, Seraphin S, Maensiri S (2009) Synthesis, structural and optical properties of CeO_2 nanoparticles synthesized by a simple polyvinyl pyrrolidone (PVP) solution route. Mater Chem Phys 115(1):423–428. https://doi.org/10.1016/j.matchemphys.2008.12.031

Podlovchenko BI, Kolyadko EA, Lu S (1994) Electroreduction of carbon dioxide on palladium electrodes at potentials higher than the reversible hydrogen potential. J Electroanal Chem 373 (1–2):185–187. https://doi.org/10.1016/0022-0728(94)03324-2

Ramani S, Sarkar S, Vemuri V, Peter SC (2017) Chemically designed CeO_2 nanoboxes boost the catalytic activity of Pt nanoparticles toward electro-oxidation of formic acid. J Mater Chem A 5 (23):11572–11576. https://doi.org/10.1039/c6ta06339j

Rao GR, Justin P, Meher SK (2011) Metal oxide promoted electrocatalysts for methanol oxidation. Catal Surv Jpn 15(4):221–229. https://doi.org/10.1007/s10563-011-9124-x

Reddy BM, Bharali P, Saikia P, Khan A, Loridant S, Muhler M, Grünert W (2007) Hafnium doped ceria nanocomposite oxide as a novel redox additive for three-way catalysts. J Phys Chem C 111:1878–1881. https://doi.org/10.1021/jp068531i

Reddy BM, Bharali P, Saikia P, Park S-E, van den Berg MWE, Muhler M, Grünert W (2008) Structural characterization and catalytic activity of nanosized $Ce_xM_{1-x}O_2$ (M = Zr and Hf) mixed oxides. J Phys Chem C 112:11729–11737. https://doi.org/10.1021/jp802674m

Sasaki K, Zhang L, Adzic RR (2008) Niobium oxide-supported platinum ultra-low amount electrocatalysts for oxygen reduction. Phys Chem Chem Phys 10(1):159–167. https://doi.org/10.1039/B709893F

Selvaraj V, Grace AN, Alagar M (2009) Electrocatalytic oxidation of formic acid and formaldehyde on nanoparticle decorated single walled carbon nanotubes. J Colloid Interface Sci 333 (1):254–262. https://doi.org/10.1016/j.jcis.2009.01.020

Shahid MM, Rameshkumar P, Basirun WJ, Juan JC, Huang NM (2017) Cobalt oxide nanocubes interleaved reduced graphene oxide as an efficient electrocatalyst for oxygen reduction reaction in alkaline medium. Electrochim Acta 237:61–68. https://doi.org/10.1016/j.electacta.2017.03.088

Shakun JD, Clark PU, He F, Marcott SA, Mix AC, Liu Z, Otto-Bliesner B, Schmittner A, Bard E (2012) Global warming preceded by increasing carbon dioxide concentrations during the last deglaciation. Nature 484(7392):49–54. https://doi.org/10.1038/nature10915

Shan C, Martin ET, Peters DG, Zaleski JM (2017) Site-selective growth of AgPd nanodendrite-modified Au nanoprisms: high electrocatalytic performance for CO_2 reduction. Chem Mater 29 (14):6030–6043. https://doi.org/10.1021/acs.chemmater.7b01813

Shao MH, Liu P, Adzic RR (2006a) Superoxide anion is the intermediate in the oxygen reduction reaction on platinum electrodes. J Am Chem Soc 128(23):7408–7409. https://doi.org/10.1021/ja061246s

Shao MH, Sasaki K, Adzic RR (2006b) Pd−Fe nanoparticles as electrocatalysts for oxygen reduction. J Am Chem Soc 128(11):3526–3527. https://doi.org/10.1021/ja060167d

Shrestha S, Liu Y, Mustain WE (2011) Electrocatalytic activity and stability of Pt clusters on state-of-the-art supports: a review. Catal Rev Sci Eng 53(3):256–336. https://doi.org/10.1080/01614940.2011.596430

Silva JCM, De Souza RFB, Parreira LS, Neto ET, Calegaro ML, Santos MC (2010) Ethanol oxidation reactions using SnO_2@Pt/C as an electrocatalyst. Appl Catal B Environ 99 (1–2):265–271. https://doi.org/10.1016/j.apcatb.2010.06.031

Singh SB, Tandon PK (2014) Catalysis: a brief review on nano-catalyst. J Energy Chem Eng 2 (3):106–115

Son DN, Takahashi K (2012) Selectivity of palladium–cobalt surface alloy toward oxygen reduction reaction. J Phys Chem C 116(10):6200–6207. https://doi.org/10.1021/jp2094615

Song A, Yang W, Yang W, Sun G, Yin X, Gao L, Wang Y, Qin X, Shao G (2017) Facile synthesis of cobalt nanoparticles entirely encapsulated in slim nitrogen-doped carbon nanotubes as oxygen reduction catalyst. ACS Sustain Chem Eng 5(5):3973–3981. https://doi.org/10.1021/acssuschemeng.6b03173

Stalder CJ, Chao S, Wrighton MS (1984) Electrochemical reduction of aqueous bicarbonate to formate with high current efficiency near the thermodynamic potential at chemically derivatized electrodes. J Am Chem Soc 106(12):3673–3675. https://doi.org/10.1021/ja00324a046

Steele BCH, Heinzel A (2001) Materials for fuel-cell technologies. Nature 414:345–352. https://doi.org/10.1038/35104620

Suffredini HB, Tricoli V, Vatistas N, Avaca LA (2006) Electro-oxidation of methanol and ethanol using a Pt–RuO_2/C composite prepared by the sol–gel technique and supported on boron-doped diamond. J Power Sources 158(1):124–128. https://doi.org/10.1016/j.jpowsour.2005.09.040

Sulaiman JE, Zhu S, Xing Z, Chang Q, Shao M (2017) Pt–Ni octahedra as electrocatalysts for the ethanol electro-oxidation reaction. ACS Catal 7(8):5134–5141. https://doi.org/10.1021/acscatal.7b01435

Sun Z, Wang X, Liu Z, Zhang H, Yu P, Mao L (2010) Pt−Ru/CeO_2/carbon nanotube nanocomposites: an efficient electrocatalyst for direct methanol fuel cells. Langmuir 26 (14):12383–12389. https://doi.org/10.1021/la101060s

Szmant HH (1989) Organic building blocks of the chemical industry. Wiley, New York ISBN: 978-0-471-85545-3

Uribe FA, Valerio JA, Garzon FH, Zawodzinski TA (2004) PEMFC reconfigured anodes for enhancing CO tolerance with air bleed. Electrochem Solid-State Lett 7(10):A376–A379. https://doi.org/10.1149/1.1795633

Vigier F, Rousseau S, Coutanceau C, Leger JM, Lamy C (2006) Electrocatalysis for the direct alcohol fuel cell. Top Catal 40(1–4):111–121. https://doi.org/10.1007/s11244-006-0113-7

Wang J, Gu H (2015) Novel metal nanomaterials and their catalytic applications. Molecules 20(9):17070–17092. https://doi.org/10.3390/molecules200917070

Wang X, Hu JM, Hsing IM (2004) Electrochemical investigation of formic acid electro-oxidation and its crossover through a nafion® membrane. J Electroanal Chem 562(1):73–80. https://doi.org/10.1016/j.jelechem.2003.08.010

Wang C, Daimon H, Onodera T, Koda T, Sun S (2008) A general approach to the size- and shape-controlled synthesis of platinum nanoparticles and their catalytic reduction of oxygen. Angew Chem Int Ed 47(19):3588–3591. https://doi.org/10.1002/anie.200800073

Wang JX, Inada H, Wu L, Zhu Y, Choi Y, Liu P, Zhou W-P, Adzic RR (2009a) Oxygen reduction on well-defined core−shell nanocatalysts: particle size, facet, and Pt shell thickness effects. J Am Chem Soc 131(47):17298–17302. https://doi.org/10.1021/ja9067645

Wang D, Xie T, Li Y (2009b) Nanocrystals: solution-based synthesis and applications as nanocatalysts. Nano Res 2(1):30–46. https://doi.org/10.1007/s12274-009-9007-x

Wang D, Xin HL, Hovden R, Wang H, Yu Y, Muller DA, DiSalvo FJ, Abruna HD (2013) Structurally ordered intermetallic platinum–cobalt core–shell nanoparticles with enhanced activity and stability as oxygen reduction electrocatalysts. Nat Mater 12(1):81–87. https://doi.org/10.1038/nmat3458

Wang Y, Cui X, Chen L, Wei C, Cui F, Yao H, Shi J, Li Y (2014) One-step replication and enhanced catalytic activity for cathodic oxygen reduction of the mesostructured Co_3O_4/carbon composites. Dalton Trans 43(10):4163–4168. https://doi.org/10.1039/c3dt53192a

Wang L, Zhai JJ, Jiang K, Wang JQ, Cai WB (2015) Pd–Cu/C electrocatalysts synthesized by one-pot polyol reduction toward formic acid oxidation: structural characterization and electrocatalytic performance. Int J Hydrog Energy 40(4):1726–1734. https://doi.org/10.1016/j.ijhydene.2014.11.128

Wang C, Zhao Z, Li X, Yan R, Wang J, Li A, Duan X, Wang J, Liu Y, Wang J (2017) Three-dimensional framework of graphene nanomeshes shell/Co_3O_4 synthesized as superior bifunctional electrocatalyst for zinc–air batteries. ACS Appl Mater Interfaces 9(47):41273–41283. https://doi.org/10.1021/acsami.7b13290

Yang L, Kinoshita S, Yamada T, Kanda S, Kitagawa H, Tokunaga M, Ishimoto T, Ogura T, Nagumo R, Miyamoto A, Koyama M (2010) A metal–organic framework as an electrocatalyst for ethanol oxidation. Angew Chem Int Ed 122(31):5476–5479. https://doi.org/10.1002/ange.201000863

Yang W, Salim J, Ma C, Ma Z, Sun C, Li J, Chen L, Kim Y (2013) Flowerlike Co_3O_4 microspheres loaded with copper nanoparticle as an efficient bifunctional catalyst for lithium–air batteries. Electrochem Commun 28:13–16. https://doi.org/10.1016/j.elecom.2012.12.007

Yin Z, Gao D, Yao S, Zhao B, Cai F, Lin L, Tang P, Zhai P, Wang G, Ma D, Bao X (2016) Highly selective palladium-copper bimetallic electrocatalysts for the electrochemical reduction of CO_2 to CO. Nano Energy 27:35–43. https://doi.org/10.1016/j.nanoen.2016.06.035

Yousaf AB, Imran M, Uwitonze N, Zeb A, Zaidi SJ, Ansari TM, Manzoor S (2017) Enhanced electrocatalytic performance of Pt_3Pd_1 alloys supported on CeO_2/C for methanol oxidation and oxygen reduction reactions. J Phys Chem C 121(4):2069–2079. https://doi.org/10.1021/acs.jpcc.6b11528

Yu X, Pickup PG (2008) Recent advances in direct formic acid fuel cells (DFAFC). J Power Sources 182(1):124–132. https://doi.org/10.1016/j.jpowsour.2008.03.075

Zhang Z, More KL, Sun K, Wu Z, Li W (2011) Preparation and characterization of PdFe nanoleaves as electrocatalysts for oxygen reduction reaction. Chem Mater 23(6):1570–1577. https://doi.org/10.1021/cm1034134

Zhang S, Kang P, Meyer TJ (2014) Nanostructured tin catalysts for selective electrochemical reduction of carbon dioxide to formate. J Am Chem Soc 136(5):1734–1737. https://doi.org/10.1021/ja4113885

Zhang W, Hu Y, Ma L, Zhu G, Wang Y, Xue X, Chen R, Yang S, Jin Z (2018) Progress and perspective of electrocatalytic CO_2 reduction for renewable carbonaceous fuels and chemicals. Adv Sci 5(1):1700275. https://doi.org/10.1002/advs.201700275

Zhao Z, Chen Z, Lu G (2017) Computational discovery of nickel-based catalysts for CO_2 reduction to formic acid. J Phys Chem C 121(38):20865–20870. https://doi.org/10.1021/acs.jpcc.7b06895

Zhong CJ, Luo J, Njoki PN, Mott D, Wanjala B, Loukrakpam R, Lim S, Wang L, Bin Fang B, Xu Z (2008) Fuel cell technology: nano-engineered multimetallic catalysts. Energy Environ Sci 1 (4):454–466. https://doi.org/10.1039/b810734n

Zhou ZY, Kang X, Song Y, Chen S (2011) Butylphenyl-functionalized palladium nanoparticles as effective catalysts for the electrooxidation of formic acid. Chem Commun 47(21):6075–6077. https://doi.org/10.1039/c1cc11235j

Zhu H, Zhang S, Guo S, Su D, Sun S (2013a) Synthetic control of FePtM nanorods (M= Cu, Ni) to enhance the oxygen reduction reaction. J Am Chem Soc 135(19):7130–7133. https://doi.org/10.1021/ja403041g

Zhu H, Zhang S, Huang YX, Wu L, Sun S (2013b) Monodisperse $M_xFe_{3x}O_4$ (M= Fe, Cu, Co, Mn) nanoparticles and their electrocatalysis for oxygen reduction reaction. Nano Lett 13 (6):2947–2951. https://doi.org/10.1021/nl401325u

Chapter 13
Nanobiotechnology Approach for the Remediation of Environmental Hazards Generated from Industrial Waste

Mounika Gudeppu, Krishnapriya Madhu Varier, Arulvasu Chinnasamy, Sumathi Thangarajan, Jesudas Balasubramanian, Yanmei Li, and Babu Gajendran

Contents

The original version of this chapter was revised. A correction to this chapter can be found at https://doi.org/10.1007/978-3-030-04474-9_14

Authors Mounika Gudeppu and Krishnapriya Madhu Varier have equal contribution and are designated as co-first authors.

M. Gudeppu · J. Balasubramanian
Department of Pharmacology and Environmental Toxicology, Dr. ALM PGIBMS, University of Madras, Chennai, India

K. M. Varier
Department of Medical Biochemistry, Dr. ALM PGIBMS, University of Madras, Chennai, India

Department of Zoology, University of Madras, Chennai, India

A. Chinnasamy
Department of Zoology, University of Madras, Chennai, India

S. Thangarajan
Department of Medical Biochemistry, Dr. ALM PGIBMS, University of Madras, Chennai, India

Y. Li · B. Gajendran (✉)
Department of Biology and Chemistry, The Key Laboratory of Chemistry for Natural Products of Guizhou Province and Chinese Academy of Sciences, Guiyang, Guizhou, China

State Key Laboratory of Functions and Applications of Medicinal Plants, Guizhou Medical University, Guiyang, China
e-mail: babug1986@gmail.com

R. Saravanan et al. (eds.), *Emerging Nanostructured Materials for Energy and Environmental Science*, Environmental Chemistry for a Sustainable World 23,
https://doi.org/10.1007/978-3-030-04474-9_13

Abstract Various environmental hazards occurring in present days are the results of population explosion, industrial pollution, unsafe agricultural practices, and several miscellaneous reasons. Hence, remediation process becomes very crucial in limiting the pollution. The process of treatment of contaminated environmental media, i.e., soil and water, in order to remove the toxicants present in it is called as "remediation/environmental remediation." "Bioremediation" is a process of swabbing contaminated media with biological agents/microbes or naturally extracted chemicals. Bioremediation depending on site of application is further categorized into ex situ bioremediation, in situ bioremediation, phytoremediation, and permeable reactive barrier (PRB). However, if the percentage of contaminant is higher in the media, microbes used for bioremediation will get digested by toxicants/contaminants resulting in the ineffectiveness to remove the bacteria. While the usage of nanoparticles in bioremediation process is one of the key factors for reducing the limitations of this technique, the combination/addition of nanoparticles along with biological agents and applying on the contaminated media can give better results than individual bioremediation techniques. Nanoparticles due to their specific physical and chemical properties possess high reactivity with contaminated area. Nanomaterials are used in different forms in bioremediation process like nanoiron, nanofibers, nanorods, nanotubes, nanoribbons, nanocomposites, nanoporous materials, nanofoam, and nanocrystalline materials. Due to the powerful potential executed by the combination of nanoparticles and biological agents in bioremediation, their usage in future gets widened.

13.1 Introduction

"Population explosion" throughout the world is the main causative factor for global warming and pollution at present. The demand for the natural energy resources like air, water, and land is increasing day by day due to rapid increase of population. In order to meet these growing demands of natural resources, there is a rapid expansion of industrialization with regard to food, health care, and transport which are necessary to the human livelihood. Increased population is also one of the respective factors for deforestation which stands as a primary cause of pollution. Unsafe agricultural practices employed by using toxic chemicals, pesticides, and fertilizers to increase the yield, for meeting demand of food by people, are primary factors for soil pollution. Release of industrial effluents like harmful chemicals, radioactive waste, and organic sludge, contact of water with heavy metals, and dumping of industrial waste and residential waste into open oceans/rivers lead to "water pollution" (Naushad et al. 2016; Awual et al. 2016). The releases of toxic gaseous materials from industries and vehicles are resulting in "air pollution." Due to this, environmental hazards occur very subsequently. "Environmental hazard" is a generic term, represented as a "situation" or "state of events," which causes threat to surrounding material environment and leads to negative impact on human health and ecosystem. These environmental hazards can be categorized into different types based on its incidences (Vidali 2001):

- Chemical hazards
- Physical hazards
- Biological hazards
- Phychosocial hazards
- Mechanical hazards

13.1.1 Chemical Hazards

Chemical hazards are defined by the agencies like European Union chemical regulations and globally harmonized systems. These hazards were caused by toxic chemical substance which causes significant damage to the environment. Chemical hazards may be instant or distant. Instant chemical hazards occur due to the sudden release of toxic gases/chemicals into the atmosphere and cause acute detrimental health effects to the livelihood of the living beings. For example, in 2017 about 100 people was hospitalized, due to liquefied petroleum gas (LPG) discharged at Republic of Ghana (West Africa) (Harris and Current 2012). Distant chemical hazards develop slowly, upon deposition of toxic chemicals in the ecosystem. Initially, toxic chemicals get eliminated by photolysis (sunlight), by hydrolysis (water), or by organisms (biological elimination). These processes neutralize many reactive/poisonous substances. But, on subsequent deposition, these chemicals cause toxic damage during long-term exposure. For instance, anoxic (total depletion of

oxygen) conditions can be developed in the aquatic ecosystems due to the spillage of tanker truck chemicals. Spillage of these chemicals causes increased biological oxygen demand (BOD) and eutrophication, leading to environmental hazard (Harris and Current 2012).

13.1.2 Physical Hazards

Physical hazards can occur with or without contact of a human being. These physical hazards were widely caused due to ergonomic hazards, radiation, heat stress, cold stress, and vibration hazards. According to the Health and Safety at Work Act 1974 (HASAW/HSW) established by the UK health and safety regulation, "health, safety and welfare should be ensured and protected" in workplace by all their employees. Machines in industries including manufacturing and mining stand in first place in causing occupational hazards. According to the US Bureau of Labor Statistics (2008), about 64,170 cases were reported due to machine-related injuries. Many were retained from work due to several health problems including the risk of HIV infections. Similarly, in the health-care sectors, hospital nurses have potential exposure to various toxic gases like formaldehyde (in renal dialysis units, during transfer of biological tissue for pathology) and ethylene oxide (for sterilizing medical instruments). These toxic gases cause several infections, abortions, eye irritation, dermatitis, etc. Hence, the National Institute for Occupational Safety and Health (NIOSH) and Occupational Safety and Health Administration (OSHA) have set some standards which limit the exposure of people working in health care prone toward the exposure of toxic gases. Along with these noises, electricity, temperature, lighting, vibrating machinery, and air pressure were described as few causes for physical hazards (Harris and Current 2012).

13.1.3 Biological Hazards

Biological hazards also described as biohazards refer to biological substances which cause significant health risk to living organisms, primarily to that of human. These biological substances may include several toxic materials, which were produced naturally or accidentally in domestic places. Hence, these biohazard incidences may be natural or occupational. According to the recent survey (2017) carried out by the National Hazard Exposure Worker Surveillance (NHEWS), 19% of workers who work in the areas of biological materials reported that about 75% of workers were exposed to human bodily matter (blood, tissues, feces, urine, saliva, breast milk, vomit, etc.), 18% of workers were exposed to animal products (blood, milk, eggs, meat, skins, bones, and offal), 12% of workers were exposed to live animals (mammals, fish, invertebrates, birds, and their urine/feces), 3.4% were exposed to biohazard waste like sewage and rubbish, and 2.8% were exposed to laboratory

cultures. According to the occupational scale statistics, >70% of health professionals, 56% of community and personal service workers, 43% of farmers and farm managers, 31% of professionals, and 20% of laborers and miscellaneous were exposed to these biological hazards (Gelati et al. 2017).

13.1.4 Psychosocial Hazards

According to the World Health Organization (WHO), psychosocial hazards were defined as work-related stress/occupational stress indicating the stress at work associated with mental and physical health problems of workers like heart diseases, depression, and musculoskeletal disorders. However, these are little devoid of environmental hazards as they were mainly related to psychological imbalance of the individuals due to work process (Ng and Jeffery 2003).

13.1.5 Mechanical Hazards

Mechanical hazards are the result of entanglement of people with ungraded mobile parts of machine. From the dangerous moving/mobile parts of machinery like point of operation (cutting, shaping, boring, etc.), power transmission apparatus (belts, couplings, connecting rods, gears, etc.), and other moving parts (reciprocating, rotating, transverse moving parts and auxiliary parts of machine), workers should take necessary precautions to safeguard themselves. However, these mechanical hazards are not caused due to any environmental toxic substance (Abrams 2001).

13.2 Introduction to Remediation

Environmental remediation is carried out on various environmental media, i.e., water and soil/sediments. Water remediation includes surface water as well as groundwater; soil remediation includes topsoil, subsoil, and sediment. These two types of remediation (soil and water) are conducted depending upon the type and extent of the pollution (Environmental Remediation. IAEA.org). Water remediation is a process of removing contaminants from water. Surface water in lakes, rivers, and streams can be contaminated by the release of waste materials in the drainage system, industrial effluents, and of other waste materials from other sources. Groundwater can be contaminated by leaching of pollutants through the soil and sediment above it and may also be because of industrial practices like drilling or mining in search of natural gas and oil (Verma and Jaiswal 2016).

Soil remediation is a process of revitalizing the soil. Soil contamination can be caused due to several factors like improper processing of residential and industrial

waste material, chemical spillage due to industrial activity, and usage of fertilizers and pesticides which results in loosing soil fertility and further leads to soil contamination.

Based on the type of treating the contaminated soil, remediation process can be categorized into two types as follows:

- In situ remediation – is a method of treating contamination without removing soil. The materials used to treat contamination (amendments like household items – molasses, vegetable oil, etc.) were dumped into the wells, formed artificially for the purpose to treat soil and underground water (Folch et al. 2013).
- Ex situ remediation – is a method wherein the soil/sediment is excavated into some huge containers/tanks and it was treated by mixing amendments into it. Then the soil was exposed to be treated and stirred. After treating, soil is replaced to its original site (Philp and Atlas 2005).

In situ/ex situ remediation can be carried out by different methods which were mentioned below (Helena et al. 2013):

- Excavation
- Pump and heat
- Thermal desorption
- Solidification and stabilization
- Oxidation
- Nanoremediation
- Soil vapor extraction
- Bioremediation

Among the abovementioned methods, bioremediation is considered to be as an easy and natural method to treat huge amount of samples.

13.3 Bioremediation

Bioremediation is a process in which microbes or naturally extracted products were used for swabbing the contaminated media like soil, water, and subsurface material/ground material. The word "bioremediation" indicates "bio" which means biological agents and "remediation" which means reversing. Depending upon the site of application, the principles which were used, advantages and limitations of the method, and the solutions employed to overcome the limitations, bioremediation process is broadly categorized into two categories:

- Ex situ bioremediation technique
- In situ bioremediation technique

13.3.1 Ex Situ Bioremediation

This technique is mainly employed to excavate pollutants from polluted sites and treated/processed by subsequently transporting them to other sites of treatment. This method is executed mainly based on the depth of pollution, expenditure for treating, type of pollutant, degree of pollution, geographical location, and geology of polluted site (Philp and Atlas 2005).

Ex situ bioremediation techniques are further divided into the following catagories:

13.3.1.1 Biopile

Biopile-mediated ex situ bioremediation is a cost-effective method and promotes effective degradation (Whelan et al. 2015). It involves pilling of ground and excavating the polluted soil, subsequently treated with nutrients and microorganisms. Aeration, irrigation, nutrients, leachate collection systems, and a treatment bed are the main components of this technique. At polluted sites, biopile bioremediation limits the volatilization of low molecular weight (LMW) pollutants, thus preventing the air from contamination by the toxic gases which are volatized. Extreme polluted environments such as very cold regions can also be remediated by this method (Silva-Castro et al. 2015; Gomez and Sartaj 2014). An experiment was conducted recently, for a period of 94 days, in a highly polluted area containing total petroleum hydrocarbon (TPH) as a main toxicant. Biopile method was employed to treat TPH. In the study, different rates of microbial consortia from 3 to 6 ml/m^3 and mature compost of 5% and 10% were applied, and all the procedures were performed in low-temperature conditions, using response surface methodology (RSM) based on factorial design of experiment (DOE) tone. All the results obtained in the contaminated area were compared with controls. When compared to control with 48% average TPH removal, contaminated area/bioaugmented and biostimulated groups showed 90.7% reduction, indicating the synergistic interaction between bioaugmentation and biostimulation. Dias et al. (2015) also conducted a study for 50 days and reported the reduction of TPH concentration by 71%. This was achieved by the prior treatment of contaminated soil samples prior to biopile formation, followed by biostimulation with fish meal. Biopile bioremediation is also feasible for clay and sandy soil samples (Chemlal et al. 2013; Akbari and Ghoshal 2014).

Microbial activities and contaminant availability for biodegradation can be widened by the amalgamation of heating system (Fig. 13.1) into biopile design, and the time duration of biopile can be shortened (Aislabie et al. 2006). From the study conducted by Sanscartier et al. (2009), the biopile design with humidified atmosphere can have very low final TPH concentration, compared to the heated and passive biopiles due to the optimum moisture content, reduced leaching, and minimal volatilization of LMW contaminants. Biopile design can be used to treat large volume of polluted soil in a limited space, and it can be scaled up to a pilot system (Chemlal et al. 2013). However, biopile design efficiency can be improved by sieving and aeration of contaminated soil before processing it (Delille et al. 2008).

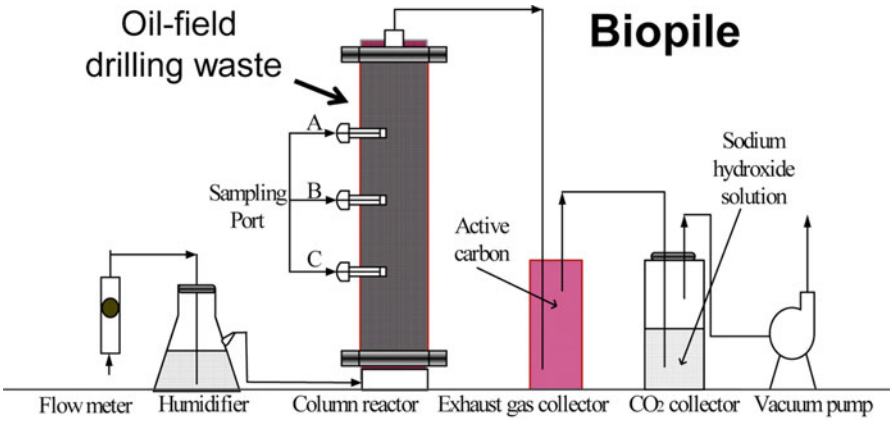

Fig. 13.1 Schematic diagram representing biopile mechanism. (Copyright received)

Natural bulking agents like straw, sawdust, wood chips, or barks and other organic materials were used in a biopile construct (Rodríguez-Rodríguez et al. 2010). When compared to other bioremediation techniques, biopile systems have certain limitations like cost of maintenance and operation, lack of power supply especially at remote sites, and so on. Because contaminated soil pile was distributed uniformly by using an air pump in a biopile design, an optimum heating of air is required during biopile bioremediation, because microorganisms are thermolabile; this may inhibit their degradation capacity (Sanscartier et al. 2009).

Windrows

This method is prominently characterized by periodic tuning of piled polluted soil, to increase the degradation activities of indigenous and/or transient hydrocarbonoclastic bacteria in polluted area. Rate of bioremediation can be increased by addition of water which increases aeration in the contaminated soil. Periodic tuning of polluted soil is also helpful for uniform distribution of pollutants, nutrients, and microbes and is thus accomplished through assimilation, biotransformation, and mineralization (Barr 2002). Windrow treatment is advantageous when compared to biopile method, because periodic tuning removes high amount of hydrocarbons. However, it also depends upon the basic type of the soil which was reported to be more friable (Coulon et al. 2010). In spite of its advantage, the method has its own limitation; it cannot be applied to soil polluted with toxic volatiles, because previous reports implicated the release of CH_4 (greenhouse gas) due to the development of anaerobic zone within piled polluted soil, subsequently leading to reduced aeration (Hobson et al. 2005).

Bioreactor

Bioreactor is a container/vessel where raw materials are converted into specific products by undergoing several series of biological reactions. Depending on the mode of operation, there are several modes of bioreactors like batch, fed-batch, sequencing batch, continuous, and multistage. Inside the bioreactor, polluted samples (dry/slurry) are subjected to optimize bioprocess parameters like temperature, pH, agitation and aeration rates, and substrate inoculum concentrations. These are few major advantages in employing this method. Due to the hold in controlling process parameters, bioreactor method consumes less time when compared to others.

Controlled bioaugmentation, nutrient addition, and increased pollutant bioavailability are other miscellaneous advantages of bioreactor which were considered as limiting factors in other bioremediation techniques (Fig. 13.2). Hence, when compared to others, bioreactor-based bioremediation is an efficient method in processing pollutants. Volatile organic compounds like benzene, toluene, ethylbenzene, and xylenes (BTEX) are used to treat polluted soil or water. The flexibility in opting bioreactor design allows maximal biological degradation and minimal abiotic loss (Mohan et al. 2004). Core bacterial communities involved in bioremediation process can be characterized, and microbial population dynamics can be tracked in crude oil-polluted soil slurry in short- or long-term operations (Chikere et al. 2012; Zangi-Kotler et al. 2015). Sewage sludge can also be used as biostimulant or bioaugmenting agent. As it is an enclosed system, genetically modified microorganisms (GEM) can be used for bioaugmentation, and they get destroyed before treated soils return into the field for land filling, thus ensuring no foreign gene escape into the environment after bioremediation. Biosurfactant usage is insignificant due to efficient mixing in bioreactor operations (Mustafa et al. 2015). Numerous experiments have been carried out at a time by one factor at

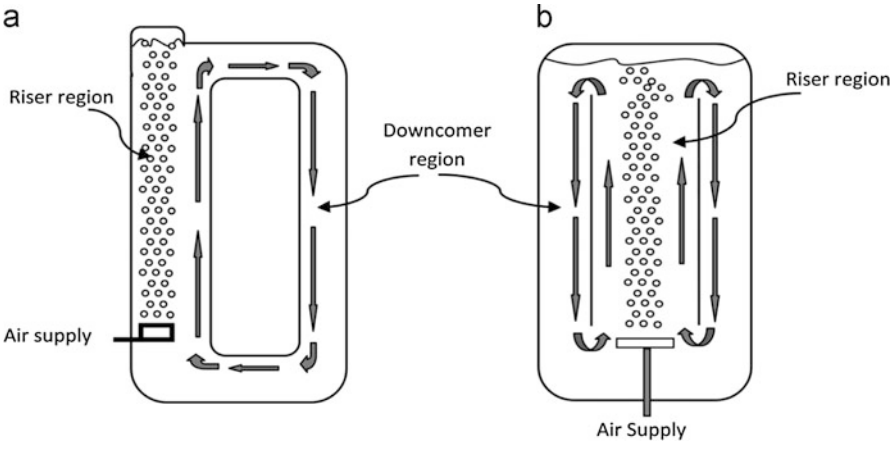

Fig. 13.2 Bioreactor. (Copyright received)

a time (OFAT) approach, i.e., controlling all operating conditions at a time and thus less time-consuming. Design of experiment (DoE) tone registers the optimal range of parameters used as a set of independent variables (controllable and uncontrollable factors) over a specific region (Mohan et al. 2007). For designing optimized conditions, understanding the microbiological processes is of great importance (Piskonen et al. 2005). However, the method has its own disadvantages; firstly more man power is required as it is an ex situ technique and volume of sample to be treated is too large (Philp and Atlas 2005). Secondly, if any parameter is not controlled optimally, it becomes a limiting factor which reduces microbial activity and makes the process less effective. Availability of most suitable design is of paramount importance as pollutants are likely to respond differently to different bioreactors.

Land Farming

Among all other bioremediation techniques, land farming is the simplest and the most cost-effective method. It can be considered as both ex situ and in situ bioremediation techniques depending on the site of treatment. The selection of ex or in situ method depends on the depth of pollution. However, polluted soil excavation is common in land farming. If excavated soil is treated on site, it can be considered as in situ; and if it is treated away from the site, it is considered to be ex situ. Bioremediation might be preceded without excavation, if pollutant lies 1 m below the ground surface. However, if it lies 1.7 m below the ground level, the soil must be transported to ground surface for efficient bioremediation (Nikolopoulou et al. 2013). Excavated polluted soil was applied carefully on a fixed layer support above the ground surface for aerobic biodegradation of pollutant to occur by autochthonous microorganisms (Philp and Atlas 2005; Paudyn et al. 2008; Volpe et al. 2012; Silva-Castro et al. 2015). Activity of autochthonous microorganisms can be stimulated by tillage mechanism. Tillage is an agricultural practice in which soil is prepared by mechanical agitation by employing various methods like digging, stirring, and overturning. Tillage enhances aeration, addition of nutrients (nitrogen, phosphorus, and potassium), and irrigation. For a soil containing increased heterotrophs, optimal diesel-degrading bacterial counts, and appropriate biological activity, remediation process can be employed with tillage and irrigation, and further nutrient addition is not required (Silva-Castro et al. 2015). In a field trial conducted by Paudyn et al. (2008), 80% removal of contaminant (diesel) was achieved by aeration using rototilling technique in a period of 3 years in the remote areas of Canadian Arctic location. This demonstrates that aeration plays a crucial role in cold regions. Land farming is mainly undertaken in hydrocarbon-polluted sites including polyaromatic hydrocarbons (Silva-Castro et al. 2012; Cerqueira et al. 2014). This technique is complied with government regulations and can be used in any climatic conditions or locations (Besaltatpour et al. 2011). Suitable land farming design should be constructed with an impermeable liner to prevent leaching of pollutant into neighboring areas during bioremediation operation (Da Silva et al. 2012). However, land farming bioremediation technique is very simple to design and

implement, low capital input is required, and large volume of polluted soil can be treated with minimum environmental impact and energy requirement (Maila and Colete 2004). The method has its own limitations, like requirement of large operating space, reduction of microbial activities due to unfavorable climatic conditions, expensive due to excavation, and reduced efficacy in removal of inorganic pollutants (Khan et al. 2004; Maila and Colete 2004). In hot (tropical) climatic regions, removal of toxic volatiles from the polluted soil is not possible as it requires the specific mechanism of volatilization. Due to the abovementioned limitations, the method is less efficient and time-consuming when compared to other ex situ bioremediation techniques. However, the major advantage is that they don't require any extensive preliminary assessment of polluted site prior to remediation; thus preliminary study is less time-consuming, less laborious, and cost-effective. This technique can allow the modifications of biochemical and physicochemical conditions and parameters for its efficiency. If polluted soils are excavated, the soil porosity can be reduced which is a key factor for transportation of soil.

Under buildings, inner sites, and working sites, ex situ bioremediation is unlikely to be used (Philp and Atlas 2005). There will be a disruption in soil structure in this method which likely affects surrounding sites, prone to disturbances. An extensive engineering is required for any ex situ bioremediation technique, and large space is required for its operation. However, the bioremediation technique is faster, controllable, and employed to a wide range of pollutants (Prokop et al. 2000) (Fig. 13.3).

13.3.2 In Situ Bioremediation

This method involves treating polluted substances at the site of pollution. Moreover, it is not involved with any excavation of soil thus ensuring no disturbance or alteration in the soil structure. Ideally, it is less expensive as there is no excavation

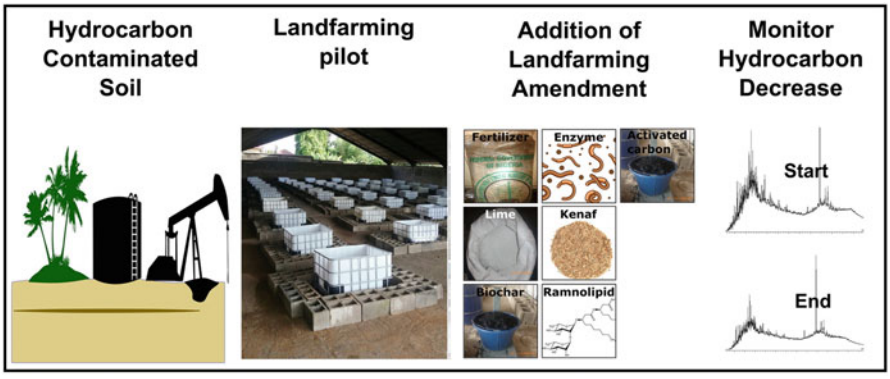

Fig. 13.3 Land farming. (Copyright received)

process required, but cost of installation of equipment for on-site treatment is of major concern. Bioventing, biosparging, and phytoremediation are few such in situ bioremediation techniques. The method is successfully used to treat chlorinated solvents, dyes, heavy metals, and hydrocarbon-polluted sites (Folch et al. 2013; Kim et al. 2014; Frascari et al. 2015; Roy et al. 2015). Few crucial environmental conditions are to be of vital concern in the implementation of this method like status of electron acceptor, moisture content, nutrient availability, pH, soil porosity, and temperature for the method to be successful (Philp and Atlas 2005).

13.3.2.1 Bioventing

This technique works by increasing the activities of indigenous microbes achieved by controlled stimulation of airflow, thus delivering oxygen to unsaturated (vadose) zone in order to increase bioremediation. For the successful microbial transformation of pollutants to harmless state, specific amendments were provided to the site by adding nutrients and moisture (Philp and Atlas 2005). This method is specific and effective in restoring sites polluted with light spilled petroleum products (Höhener and Ponsin 2014). Stimulation of airflow is a rate-limiting factor for this method. A study was conducted by Sui and Li (2011) for 200-day time period, in order to evaluate the air injection rate efficacy in removing pollutants from the site. A toluene-contaminated area was chosen for the experiment to carry out. Two different air injection rates (81.504 and 407.52 m^3/day) were chosen in the study. It was observed that air injection rate/airflow rate has no significant role in increasing the biodegradation rate or in making pollutant biotransformation more effective. This happens because of initial saturation of air (by high or low air injection rate) in the subsurface for oxygen demand during biodegradation. However, lower injection rate may show significant increase in biodegradation. Hence, it is demonstrated that air injection rate is also a basic parameter along with pollutant dispersal, redistribution, and surface loss. Similar experiment was carried out by Frutos et al. (2010) in phenanthrene-contaminated soil and reported the lower involvement of air injection rate in making the method successful. Low air injection rate is more likely effective and economical for bioventing in diesel-polluted clayey soil (Thomé et al. 2014). Rayner et al. (2007) reported that microbioventing using nine small injection rods (0.5 m apart) under identical conditions was effective in removing considerable amount of hydrocarbons from sub-Antarctic hydrocarbon-polluted site which was compared with single-well bioventing method. Compared to microbioventing method, single bioventing was ineffective as it lacks in uneven distribution of oxygen which causes decreased biodegradation. Bioventing design is to encourage aeration in unsaturated zone, and it can also be used for anaerobic bioremediation in treating vadose zone polluted with chlorinated compounds (Mihopoulos et al. 2000, 2002; Shah et al. 2001). In spite of bioventing that depends on enhancing microbial degradation process at vadose zone by optimum air injection, soil vapor extraction (SVE) maximizes volatile organic compound volatilization through vapor extraction (Magalhães et al. 2009). However, both the techniques (microbial degradation and

SVE) use identical equipments. They differ slightly in configuration, philosophical design, and operation significantly (Diele et al. 2002). The rate of airflow is higher in SVE when compared to that of bioventing (Baker and Moore 2000).

13.3.2.2 Bioslurping

Bioslurping method is a combination of vacuum-enhanced pumping, soil vapor extraction, and bioventing for soil and groundwater remediation by providing indirect provision of oxygen (Gidarakos and Aivalioti 2007). Many free products can be recovered such as light nonaqueous phase liquids (LNAPLs) which are present in capillary, unsaturated, and saturated zones. Volatile and semi-volatile organic compounds in the contaminated soil can also be remediated by this process. The free products are removed by the system called "slurp" which is used in free product layer in order to draw up liquids (free products and soil gas) by pumping mechanism. Thus, LNAPLs move upward to the surface and get separated from water and air (Kim et al. 2014). The microbial activity in this technique is reduced due to excessive soil moisture which limits air permeability and decreases oxygen transfer rate. However, the technique is less expensive as it requires minimal storage, treatment, and disposal costs (Philp and Atlas 2005) (Fig. 13.4.).

13.3.2.3 Biosparging

This method is highly similar to bioventing. In bioventing to stimulate microbial activities, the air is injected into soil subsurface in order to remove pollutants, whereas in biosparging, the air is injected on to saturated zone, which causes upward movement of volatile organic compounds to the unsaturated zone for promoting biodegradation. Soil permeability and pollutant biodegradability are two major factors for achieving effective removal of pollutants by biosparging. Soil permeability determines the bioavailability of pollutant to microorganisms, and pollutant biodegradability determines the effectiveness of method (Philp and Atlas 2005). Biosparging promotes degradation of pollutants by in situ air sparging (IAS) technique which involves high airflow rates to achieve pollutant volatilization. The method is mostly employed on treating aquifers contaminated with petroleum products specifically diesel and kerosene.

13.3.2.4 Phytoremediation

Phytoremediation mainly depends on the use of plants in polluted sites to mitigate toxic effects of pollutants by physical, biochemical, biological, chemical, and microbiological interactions. Based on the pollutant type (elemental or organic), several mechanisms like accumulation or extraction, degradation, filtration, stabilization, and volatilization were employed in phytoremediation. Extraction,

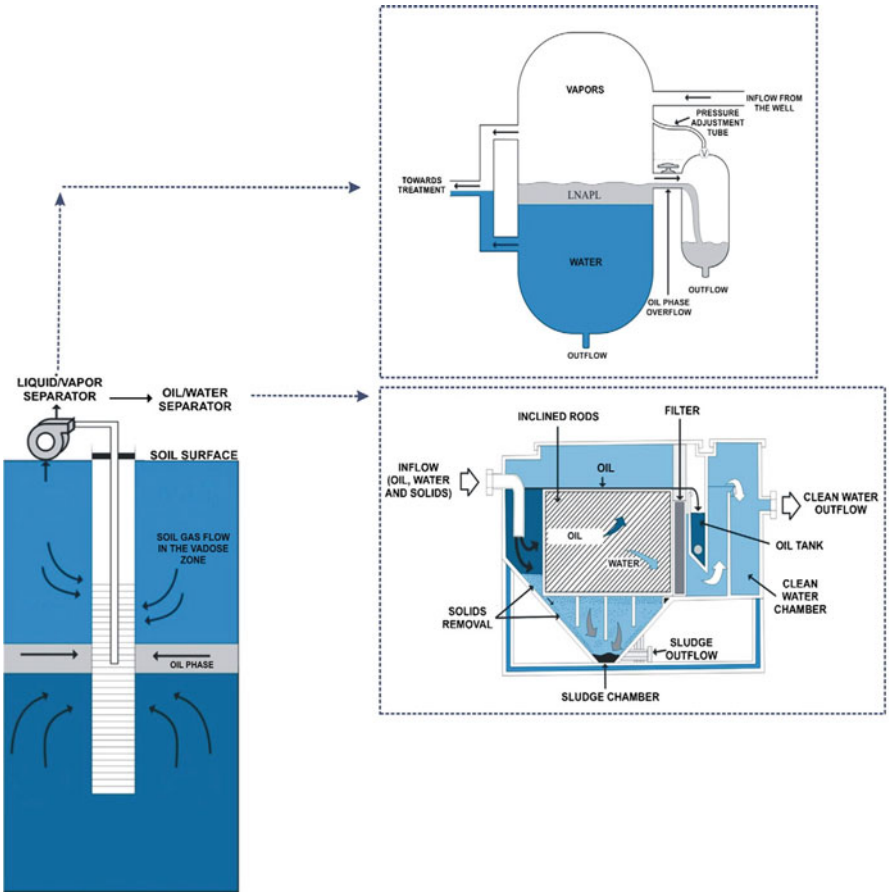

Fig. 13.4 Bioslurping unit. (Copyright received)

transformation, and sequestration methods are used to remove elemental pollutants (toxic heavy metals and radionuclides). Degradation, rhizoremediation, stabilization, and volatilization process are employed to remove organic pollutants (hydrocarbons and chlorinated compounds) (Meagher 2000; Kuiper et al. 2004). Root system, which may be fibrous or tap depending on the depth of pollutant, above ground biomass which should not be available for animal consumption, toxicity of pollutant to plant, plant survival and its adaptability to prevailing environmental conditions, plant growth rate, site monitoring, and, above all, time required to achieve the desired level of cleanliness are the important factors to be considered in choosing a plant as a phytoremediator. The chosen plant should also be resistant to several disease and pests (Lee 2013). Efficiency of phytoremediation process is primarily dependent on native plants growing in the polluted sites by bioaugmentation with endogenous or exogenous plant rhizobacteria or by biostimulation. Plant growth-promoting rhizobacteria (PGPR) enhance biomass production, and tolerance of plants to heavy metals and other unfavorable soil (edaphic) conditions was enhanced

Table 13.1 Plants with phytoremediation property

Plant	Nature of pollutant	Mechanism of removal
Ludwigia octovalvis	Gasoline	Biosurfactant-enhanced rhizodegradation
Aegiceras corniculatum	Brominated diphenyl ethers	Biostimulated degradation
Spartina maritime	As, Cu, Pb, and Zn	Bioaugmented rhizoaccumulation
Arundo donax	Cd and Zn	Rhizofiltration
Eichhorina crassipes (water hyacinth)	Heavy metals	Rhizofiltration
Phragmites amboinicus	PAHs	Rhizodegradation
Sparganium sp.	Polychlorinated biphenyls	Biostimulated rhizodegradation
Amaranthus paniculatus	Ni	Phytoaccumulation
Rhizophora mangle	TPH	Phytoextraction and phytostimulation
Populus deltoides x nigra and Arabidopsis thaliana	Ag	Phytoaccumulation
Carex pendula	Pb	Rhizofiltration

on inoculation of *Brassica napus L.* and *Festuca ovinia L.* (Yancheshmeh et al. 2011; de-Bashan et al. 2012; Grobelak et al. 2015). In addition to phytoremediation of metal-contaminated estuaries with *Spartina maritima*, bioaugmentation with endogenous rhizobacteria resulted in increased plant subsurface biomass, metal accumulation, and enhanced metal removal (Mesa et al. 2015). The plants used in employing phytoremediation are mentioned in Table 13.1.

13.3.2.5 Permeable Reactive Barrier (PRB)

Due to its design and mechanism of pollutant removal, the technique is mostly perceived as a physical method which is employed to remediate contaminated groundwater (Thiruvenkatachari et al. 2008; Obiri-Nyarko et al. 2014). Several mechanisms like degradation, precipitation, and sorption were used for pollutant removal in PRB technique. The role of microorganisms mostly enhances the efficacy of PRB (Philp and Atlas 2005), a permanent or semipermanent reactive barrier made up of a zero-valent iron which is submerged in the trajectory of polluted groundwater (García et al. 2014; Zhou et al. 2014). Pollutants get trapped and undergo series of reactions when polluted water flows through the barrier under its natural ingredient resulting in clean water in the flow (Thiruvenkatachari et al. 2008; Obiri-Nyarko et al. 2014). The barriers are reactive enough to trap pollutants through a method which is passive with little energy input, inexpensive, readily available, and accessible (De Pourcq et al. 2015). Type of media used, which is influenced by pollutant type, biogeochemical and hydrogeological conditions, environmental and health influence, mechanical stability, and cost decide the effectiveness of the technique

Table 13.2 Pollutants removed by permeable reactive barrier (PRB) technique

Reactive material	Nature of pollutant	Mechanism of pollutant removal
Clay	Cs-137	Sorption
Oxygen reactive composed and clinoptilolite	NH_4-N	Ion exchange and biological nitrification
Natural pyrite (FeS_2)	Cs(VI)	Sorption
Zero-valent iron coupled with polyhydroxybutyrate	1,2-Dichloroethane	Biological degradation
Mixture of zero-valent iron, zeolite, and activated carbon	Landfill leachate	Biodegradation
Bio-barrier (*Arthrobacter viscosus*)	Polyaromatic hydrocarbons	Biodegradation
Bio-barrier (*Trametes versicolor*, white-rot fungi)	Orange G dye	Biodegradation
Organic substrates and zero-valent iron (ZVT)	Heavy metals (Al, Zn, and Cu)	Precipitation
Granular oxygen-capturing materials (ZVI powder, sodium citrate, and inorganic salts) and granular activated carbon	Nitrate and nitrite	Biodegradation
Bioaugmented bio-barrier (*Mycobacterium* sp. and *Pseudomonas* sp. immobilized bead) PRB	Benzene, toluene, ethylbenzene, and xylene (BTEX)	Biodegradation
Granular iron	Chlorinated volatile organic compounds (VOC)	Degradation

(Obiri-Nyarko et al. 2014; Liu et al. 2015). Pollutants removed by phytoremediation technique are listed in Table 13.2.

13.4 Introduction to Nanomaterials (NMs)

In the twenty-first century due to industrial revolution, cleaning up the contaminants of environment has become a challenging task. Technologies which are eco-friendly, sustainable, and economically adoptable properties must be employed to execute it. Nanobioremediation is one such new emerging technique for remediation of pollutants using biosynthetic nanoparticles. Nanobioremediation is a subject of "nanotechnology" which is considered as an area for extensive research, and also it was often referred to as the "'Next Industrial Revolution." The concept of nanotechnology was initially postulated by "Richard Feynman" in 1959 (Roco 2005). Nanotechnology has a very good potential to revolutionize existing technologies used in various sectors like chemical, electronic, and biological sciences and also includes pollution control.

Remediation methods which were employed should possess a high sustainability in reducing the toxic concentrations, as well as in minimizing the ancillary environmental impacts like greenhouse gas emissions, waste generation, and natural resource consumptions. Bioremediation is a sustainable method to treat the contaminants by using microbes. However, long-term employment of this method may not be effective if the area of treatment is highly contaminated as high concentrations of toxic materials serve as an inhibitory effect for the existence of microorganisms. Hence, necessary steps should be taken for preventing the death of microorganisms. Integration of nanomaterials and bioremediation has been considered to have additive potential of efficacy and sustainability in cleaning up of environmental pollutants.

13.4.1 Nanomaterials

Nanomaterials are the substances which are constituted of individual particles sized between 1 and 100 nm (according to nanoscale measurement – a length scale which measures nanoparticles applicable to nanotechnology). According to the European Commission:

> A nanomaterials is natural, incidental or synthesized substance which comprises of particles which are in the form of unbound state or aggregate or agglomerate and for 50% or greater than 50% of particles were in the number size distribution and one or more external dimensions is in the size range of 1–100 nm. Due to their applications in environment, health, safety, or competitiveness, the number size distribution may be replaced by a threshold between 1% and 50%.

For synthesizing nanomaterials, detailed assessments should be made regarding their physical and chemical properties. The physical properties include size, shape, specific surface area and ratio of height and width, micelle formation capacity, number size distribution, surface of particles (smooth or bumpy), structure of the crystals formed, and any crystal defects and dissolution pattern. On the other hand chemical properties like composition, its purity and impurities or additives, molecular structure, surface chemistry, adhesion toward water molecules or oils and fats, and its state of being – solid, liquid, or gas – are also important. Considering these physical and chemical properties, nanomaterials should be prepared.

13.5 Applications of Nanomaterials

Nanomaterials (NMs) have a wide variety of applications like:

- Their usage in manufacturing process like products and health care such as filters, insulations, lubricants, additives, etc.
- NMs in the form of enzymes, nanozymes which are emerging artificial enzymes, can be employed for a wide variety of applications like biosensing, bioimaging, tumor diagnosis, antibiofouling, etc.

- NM usage in patients gives us UV protection and improves ease of cleaning.
- NM usage in filters can be used for removal of numerous microorganisms.
- They are also used in insulation technologies mostly in asbestos-based insulation for human safety.
- NMs are also used in lubricants and additives to reduce the friction in moving parts.
- Self-assembling NMs and anisotropic NMs were also used to repair worn and corroded parts.

Along with these mentioned above, there are many more miscellaneous applications of NMs, as it is an emerging branch of area in research (Fig. 13.5).

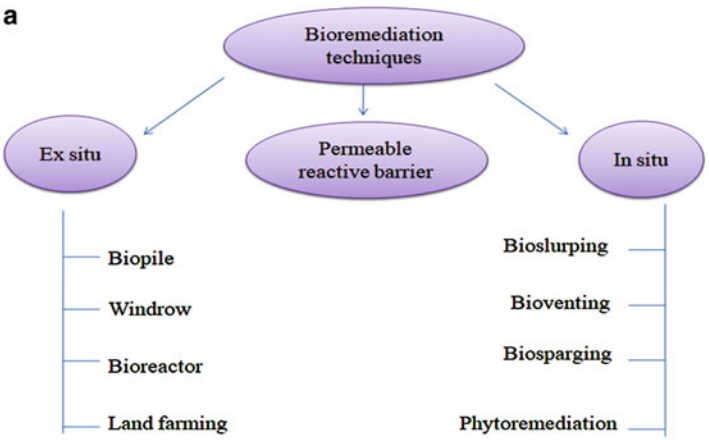

Fig. 13.5a Categorization of bioremediation techniques

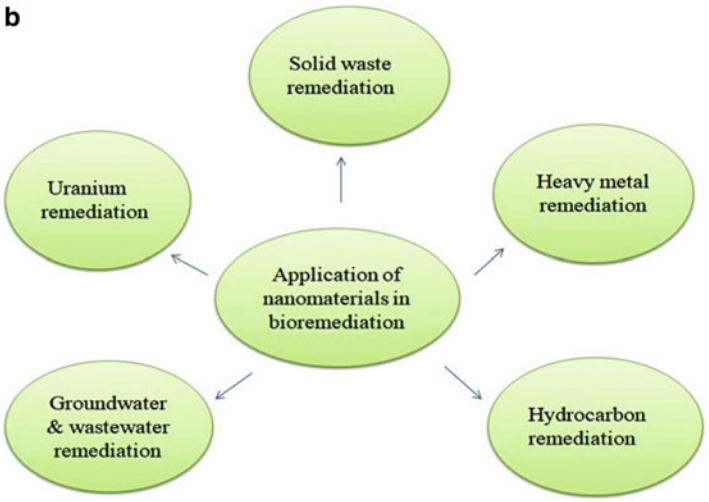

Fig. 13.5b Applications of nanomaterials in bioremediation

13.6 Science of Bioremediation with Nanomaterials

The main advantage in using NMs in bioremediation process is that larger amount of the nanomaterial will come into contact with surrounding material in a specific area, as nanomaterial possess increased surface area per unit mass. Thus, nanomaterials will have a higher reactivity with the surrounding material of contaminated area. "Plasmon resonance phenomenon" is another specific property exhibited by nanoparticles (NPs). This phenomenon depends upon the shape and size of the contaminated material concerned; various metallic and nonmetallic NPs of different shapes and sizes were used. For example, single-metal NPs, bimetallic NPs, carbon-based NPs, etc. were used, because (i) NPs, because of its lower size and higher surface area, get easily diffused into contamination zone as it is not possible with microparticles, (ii) they have higher reactivity toward redox-amenable contaminants, and (iii) they show quantum effect; hence less activation energy is required to make chemical reactions feasible. For instance, carbon tetrachloride (CT) coating of NMs with some reactants like oxides of titanium, carbon, etc. shows better results. Oxide coating of NMs increases the reactivity with carbon tetrachloride and breaks into methane, carbon monoxide or benzoquinone, trichloroethane, and other chlorinated aliphatic hydrocarbons (Nurmi et al. 2005). TiO_2 nanotubes which are used in laboratory purposes degrade pentachlorophenol (PCP) by photoelectrolytic reaction (Quan et al. 2005). Single-metal NPs are also used in the form of biocatalysts for reductive dechlorination. In detoxifying chlorinated compounds, palladium (Pd^0) mixed with microorganism *Shewanella oneidensis* was used. Pd gets deposited with *S. oneidensis* and charged with H^+ radicals in addition to different substrates such as hydrogen, acetate, and formate as electron donors in a bioreductive assay containing Pd(II). When this charged Pd comes in contact with chlorinated compounds, H^+ radical on Pd^0 reacts catalytically with PCP products resulting in the elimination of chlorine molecule from chlorinated compounds (de Windt et al. 2005). NPs are also used to immobilize microbial cells, and they degrade or biorecover specific chemicals. Some kinds of microorganisms like *Pseudomonas delafieldii* were coated with external magnetic field (Fe_3O_4) and functionalized with ammonium oleate. Thus, this microbe wire gets separated from bulk solution and gets recycled for treatment of some substrate (contaminant). These magnetic field-treated microbial cells were added to bioreactor at a high biomass concentration and then utilized to desulfurize organic sulfur from fossil fuel (dibenzothiophene), and their effect will be directly proportionate to non-NP-coated cells (Shan et al. 2005). These nanomaterial-coated microbes will be applied for recycling solid wastes, groundwater, wastewater, and petroleum products like hydrocarbons and uranium and for heavy metal pollution remediation. Hence, nanomaterials have a very good ability to abate pollution production and could potentially catalyze most revolutionary changes in the field of environment in forthcoming decades.

Nanomaterials are used in different forms in bioremediation process like:

(i) Nanoiron and its derivatives
(ii) Dendrimers
(iii) Nanocrystals, carbon nanotubes, and so forth
(iv) Single-enzyme nanoparticles
(v) Engineered polymeric nanoparticles for hydrophobic contaminant bioremediation
(vi) Engineered polymeric nanoparticles for soil remediation
(vii) Biogenic uraninite nanoparticle usage in uranium remediation
(viii) Bioremediation (phytoremediation) of heavy metal particles of *Noaea mucronata*

13.6.1 Nanoiron and Its Derivatives

Arsenic (As) is a predominant constituent due to the contamination of groundwater either from natural or anthropogenic sources, which results in adverse effects on human health and ecosystem. Prolonged exposure toward inorganic As-containing drinking water causes arsenicosis, a deteriorating and disabling disease which was characterized by pigmentation and lesions over the skin and patches on the palm of hands and soles on feet. It also culminates potentially into fatal disease like skin and internal cancers (Shankar et al. 2005). This anoxic groundwater can be bioremediated by using nanoscale zero-valent iron (NZVI) and its derivatives as a colloidal reactive barrier material (Kanel et al. 2005, 2006). Iron forms a reactive wall in contaminated ground plume path which degrades the toxic organic and inorganic compounds. The accepted limit of arsenic in drinking water is 10 microgram/L, and it is considered to be contaminating water if it ranges greater than this limit. Engineered nanoparticles (NPs) like TiO_2NPs, zero-valent iron NPs, carbon nanotubes, and iron oxide NPs are used currently to remove heavy metals from drinking water. These NPs possess enhanced removal efficiency of Arsenic at nanometer scale in contaminated water by employing an adsorption method. "Adsorption" is a method which is employed by NPs to remove Arsenic, wherein adsorbents, i.e., magnetic nanoparticles (MNPs) mixed in the water/soil where contamination is present, get adhered/adsorbed to MNPs described as "surface complexation phenomenon," and there are four types in it:

(a) Bidentate mononuclear edge-sharing
(b) Bidentate binuclear corner-sharing
(c) Monodentate mononuclear corner-sharing
(d) Tridentate hexanuclear corner-sharing

As(III) is highly toxic, when compared to As(V). During drying process, the adsorbed Arsenic species over MNPs [a mixed-valent iron (II, III) oxide] may result in complex surface redox reactions. However, the reversible reaction, i.e., reductions

of adsorbed As(V) to As(III) on MNPs, is also possible whose mechanism is not known. Hence, the potential redox transformation of MNPs associated with Arsenic, an underlying mechanism, is yet to be elucidated. These mechanisms can be useful further in safer disposal of MNP sludge produced in the process of Arsenic removal. The X-ray adsorption near-edge structure (XANES), extended X-ray absorption fine structure (EXAFS), X-ray photoelectron spectroscopy (XPS), batch sorption experiments, and thermodynamic calculations are techniques employed to detect the level of Arsenic adsorption mechanisms by MNPs.

13.6.2 Dendrimers in Bioremediation

"Dendrimer" is a Greek word where "dendri" means "a branch of tree" and "meras" a part of tree." Dendrimers are widely branched and macromolecules are monodispersed. A dendrimer is a typical polymer which has a large size (a large molecule) with smaller molecules linked inside together. These dendrimers have a controlled composition and architecture consisting of three components, i.e., a central core, interior branch cells/radial symmetry, and terminal branch cell/peripheral symmetry (Fig. 13.6). As dendrimers are relatively large molecules with small interlinks; several void spaces exist inside. These void spaces are used by NPs for their interaction with dendrimer and thus form "dendrimer NP composites" which are used to enhance catalytic activity. These types of dendrimer NP composites are used for water and dye treating industries due to their higher reactivity surface area and less toxicity. For example, PAMAM dendrimers (Guo et al. 2012) are efficient and anxious water treatment agents. In case of removal of organic pollutants, a

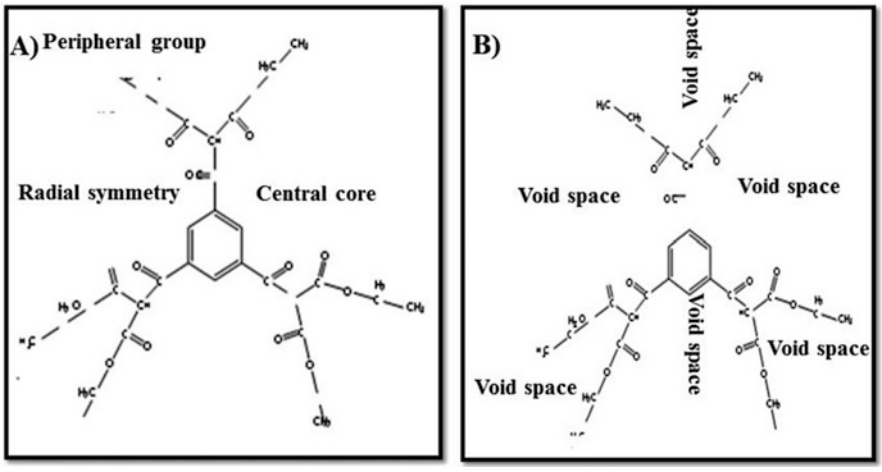

Fig. 13.6 The structure of dendrimer. (**a**) Dendrimer architecture and (**b**) void spaces in dendrimer structure

simple filtration unit, i.e., TiO_2 porous ceramic filters, where pores were impregnated with an alkylated poly(propylene imine) dendrimers, poly(ethylene imine) hyperbranched polymers, or ß-cyclodextrins, was used (Fig. 13.6).

13.6.3 Nanocrystals, Carbon Nanotubes, and So Forth Used in Bioremediation

The specific and tunable properties of carbon nanotubes (CNTs) and nanocrystals which were synthesized basically from carbon enable new technologies for a broad range of environmental applications: high-flux membranes, depth filters, sorbents, antimicrobial agents, environmental sensors, pollution prevention strategies, and renewable energy technologies (Mauter and Elimelech 2008). For example, ethylbenzene is a prominent toxicant which contaminates air, drinking water, as well as groundwater. Exposure to this toxicant leads to adverse effects in living beings. In aqueous form, ethylbenzene is easily absorbed by human via the skin and gastrointestinal tract (GIT). However, in humans high rate of absorption, about 64%, occurred through inhalation. The absorption, distribution, metabolism, and excretion (ADME parameters) rate of ethylbenzene is higher contributing to its toxicity, and because of its higher lipophilic character, the accumulation in fat tissue is seen more often in humans. Ethylbenzene gets biotransformed (metabolized) into mandelic acid and phenylglyoxylic acid (metabolites) which were excreted in urine. Frequent exposure to ethylbenzene may lead to hepatotoxicity, teratogenicity, mutagenicity, reproductive toxicity, and embryotoxicity.

Removal of ethylbenzene from aqueous solution is achieved by various kinds of CNTs like single-walled CNTs (SWCNTs), multiwalled CNTs (MWCNTs), and hybrid CNTs (HWCNTs) on the implementation of the mechanism of absorption. In removal of ethylbenzene, efficacy of SCNTs is higher compared to MCNTs and HWCNTs. Hence, SCNTs were considered as more efficient and rapid adsorbents for the removal of ethylbenzene and possessing good potential applications for maintaining high-quality water. Therefore, SCNTs can be effectively used for cleaning up of environmental pollution to prevent ethylbenzene-borne diseases (Bina et al. 2012).

Besides ethylbenzenes, CNTs in combination with other substances were used for miscellaneous pollution monitoring applications. Recently, cyclodextrins (CDcohexamethylene/toluene-diisocyanate), polyurethanes, and CNT-modified equivalents have been developed and applied successfully to remove organic contaminants from water to very low levels. Organic pollutants like p-nitrophenol and inorganic pollutants like cadmium (Cd^{2+}) and palladium (Pd^{2+}) in water were removed by calixarenes, thiacalixarenes, and CNT-based polymeric materials. CNTs immobilized by calcium alginate (CNTs/CA) were prepared and used to remove copper contamination in water. About 69.9% of copper was adsorbed onto CNTs/CA even at lower pH of 2.1 indicating their efficiency (Li et al. 2010). Nickel

contamination in aqueous system can be removed by MWCNTs (Kandah and Meunier 2007), and magnetic MWCNT nanocomposites were applied to remove dye from water (Gong et al. 2009).

13.6.4 Single-Enzyme NPs in Bioremediation

Enzymes are the combination of proteins which are highly specific and effective, and they mainly function as biocatalysts in bioremediation. But due to their instability and short catalytic life span, their usefulness was limited and cost-effective when compared to synthetic catalysts. As they are more prone to oxidative reactions, they lose their efficiency as biocatalysts. In order to increase their efficiency, stability, longevity, and reusability, clubbing them with magnetic iron NPs is necessary; thus its easy to separate the enzymes from reactants or products on application of magnetic field. MNPs and enzymes were clubbed to each other by conjugation reactions, and the resultant products are MNPs, NP-enzyme conjugates, wherein enzymes can be separated magnetically, thus making enzymes more productive. For example, two enzymes (trypsin and peroxides) having different catabolic activities were used in uniform core-shell magnetic nanoparticles (MNPs). Upon continuous observation, it is indicated that the lifetime and activity of enzymes increase from few hours to weeks, and MNP-enzyme conjugates are more stable, efficient, and economical. The MNPs act as shield for the enzymes preventing them from oxidation (Qiang et al. 2007).

13.6.5 Engineered Polymeric NPs for Bioremediation of Hydrophobic Contaminants

Polycyclic aromatic hydrocarbons (PAHs), hydrophobic contaminants on sorption with the soil, limit their solubilization rate and mobility. On the other hand, their bioavailability can be reduced by their sequestration by sorption to soil followed by partitioning in nonaqueous phase liquids (NAPLs). In an atmosphere with hydrophobic organic contamination like phenanthrene (PHEN), employment of nanonetwork particles can show an increased effective solubility and enhances their release from the contaminated aquifer material. A specific precursor chain, i.e., poly(ethylene)glycol-modified urethane acrylate (PMUA), has been developed in order to enhance the bioavailability of PMUA. These PMUA combined with NPs show increased mineralization rate of PHEN crystals in aqueous media. In a model of NAPL (hexadecane), it was observed that PHEN, which was sorbed on aquifer material, was dissolved in the presence of aquifer media. Thus, from reports obtained by the recent observations, PMUA particles in spite of enhancing the release of sorbed and NAPL-sequestered PHEN, they also increase their mineralization rate.

The contaminants adsorbed to PMUA particles have great accessibility toward the bacteria and enhance their in situ biodegradation rate in remediation process, through the means of natural attenuation of contaminants. Bioreactors can be used to recycle the extracted NPs by soil washing remediation schemes. PMUA-NP (PMUA combined with nanoparticles) properties were stable even in the heterogeneous active bacterial population, enhancing their reusability once after PHENs bounded to particles were degraded by the bacteria (Tungittiplakorn et al. 2005).

13.6.6 Engineered Polymeric NPs for Soil Remediation

The polynuclear aromatic hydrocarbons (PAHs) are hydrophobic organic groundwater contaminants, which are strongly adsorbed to the soil particles and are difficult to remove. Hence, for remediating these contaminants, amphiphilic polyurethane NPs (APUNPs) have been employed. These APUs were prepared by polyurethane acrylate anionomer (UAA) or poly(ethylene glycol)- modified urethane acrylate (PMUA) precursor chains which can be emulsified and cross-linked in aqueous system, resulting in particles with a colloidal size of 17–97 nm as measured by the dynamic light scattering principle. Due to their confined particle size, these APUs will enhance the PAH desorption and their transportation, as similar to the activity of surfactant micelles. But the individual cross-linked precursor chains in APU particles would not be free to get adsorbed on to the soil surface, as like surface-active components of micelles. APU particles are highly stable and individual in the aqueous phase. To obtain the desired properties, APU particles need to be engineered. APU particles can be designed in such a way that they possess hydrophobic interior regions which confer to have a high affinity for PHEN and hydrophilic surface which promotes the particle mobility in soil. The affinity of APU particles for their specific contaminants like PHEN can be regulated by modifying the size of hydrophobic segment used in the chain synthesis. By regulating the charge density or by the size of water-soluble chains which are residing on the particle surface, the mobility of colloidal APU suspensions in soil is controlled. The access toward the controlling of particle properties ensures the potential toward the synthesis of various kinds of optimized NPs, and their usage on contaminant type and soil condition was enhanced (Tungittiplakorn et al. 2004).

13.6.7 Biogenic Uraninite NPs and Their Significance in Uranium Remediation

Biogenic uraninite particles are produced naturally or through engineered process such as bioremediation, which serves as an important key factor in controlling the release of uranium to (sub)oxic pore waters by oxidative dissolution process. This

uraninite dissolution is profoundly dependent on the dissolved oxygen, carbonate, and solutes such as calcium (Ca^{2+}). But, the concentration of these solutes varies accordingly with the time and space, in complex and heterogeneous subsurface environments. Thus, biogenic uraninite due to their finite particular size, biological origin, and important bioremediation strategies became a great interest to geoscientists. From the recent research reports, the chemical and structural complexities of these important natural NMs were understood, and their uses in bioremediation of subsurface uranium(VI) contamination were evaluated. However, in spite of the incredible tiny size of biogenic uraninite NPs, remaining properties like molecular-scale structure, energetic, and surface area were similar and comparable to coarser-particle, abiotic, stoichiometric UO_2 (uranium oxide) (Bargar et al. 2008).

13.6.8 Bioremediation (Phytoremediation) of Heavy Metal Pollution by NPs

In the last two decades, heavy metal accumulation has become one of the prominent factors in causing environmental pollution (Alqadami et al. 2017). A great effort was undertaken to minimize this pollution sources and remediate the polluted soil and water resources. An experiment was conducted in a field which support the growth of native accumulator plants, but deposited with dried waste pool of lead mines. The concentration of heavy metals was determined by flame absorption atomic spectroscopy and found excess when compared with natural soil. The other toxic metals like Cu, Zn, and Ni were also found to be high in contaminated soil. From the experimental results, it was observed six dominant vegetations, namely, *Gundelia tournefortii*, *Centaurea virgata*, *Reseda lutea*, *Scariola orientalis*, *Elaeagnus angustifolia*, and *N. mucronata*, accumulated heavy metals. From the study, it was concluded *N. mucronata* belonging to *Chenopodiaceae* is the best lead (Pb) accumulator when compared to others, and it also has good zinc (Zn), copper (Cu), and nickel (Ni) accumulation. *R. Lutea* is the best iron (Fe) accumulator in the soil. *M. vulgaris* is also the best cadmium (Cd) accumulator. Thus the above experimental results show severalfold decrease in the levels of heavy metals during 3 days of bioremediation (Mohsenzadeh and Chehregani Rad 2012).

13.7 Conclusion

The salient features of NMs contribute to the degradation of waste and toxic material by the action of microorganisms and also help in enhancing their efficiency by protecting them from contaminants which make them nonreactive. The various types of NMs include metal NMs, oxide NMs, carbon NMs, polymer NMs, and nanocomposite and biological NMs. Phytoremediation was also a prominent method

in the removal of toxic heavy metals from the contaminated soil and aqueous systems. Due to their power potential of making bioremediation process efficient, NM usage can be widened in the future and will play a crucial role in sustainable development.

Bioremediation techniques are diverse and have proven effective in restoring sites with different types of pollutants. Microorganisms have a vital role in bioremediation. Hence, their diversity, abundance, and community structure in polluted environments present a great insight into the fate of any bioremediation technique provided other environmental factors, which can impede microbial activities, are maintained at an optimal range. Molecular techniques (such as genomics, metabolomics, proteomics, and transcriptomics) have contributed toward better understanding of microbial identification, functions, and metabolic and catabolic pathways, in this way overcoming the limitations associated with microbial culture-dependent methods. The future application of NP-linked bioremediation is with respect to the application of engineered polymeric NPs and single-enzyme NPs in soil pollution and hydrophobic contaminants in water, respectively. Thus NP bioremediation paves a wider dimension for future pollution and for alleviating its adverse effects.

References

Abrams HK (2001) A short history of occupational health. J Publ Health Pol 22(1):34–80. https://doi.org/10.2307/3343553

Aislabie J, Saul DJ, Foght JM (2006) Bioremediation of hydrocarbon contaminated polar soils. Extremophiles 10:171–179. https://doi.org/10.1007/s00792-2005-0498-4

Akbari A, Ghoshal S (2014) Pilot-scale bioremediation of a petroleum hydrocarbon-contaminated clayey soil from a sub-Arctic site. J Hazard Mater 280:595–602. https://doi.org/10.1016/j.jhazmat.2014.08.016

Alqadami AA, Naushad M, ALOthman ZA, Ghfar AA (2017) Novel metal–organic framework (MOF) based composite material for the sequestration of U (VI) and Th (IV) metal ions from aqueous environment. ACS Appl Mat Interfaces 9:36026–36037. https://doi.org/10.1021/acsami.7b10768

Awual MR, Hasan MM, Eldesoky GE, Khaleque MA, Rahman MM, Naushad M (2016) Facile mercury detection and removal from aqueous media involving ligand impregnated conjugate nanomaterials. Chem Eng J 290:243–251. https://doi.org/10.1016/j.cej.2016.01.038

Baker RS, Moore AT (2000) Optimizing the effectiveness of in situ bioventing: at sites suited to its use, bioventing often is a quick, cost-effective soil remediation method. Pollut Eng 32(7):44–47. https://doi.org/10.1007/s11274-016-2137-x

Bargar JR, Bernier-Latmani R, Giammar DE, Tebo BM (2008) Biogenic uraninite nanoparticles and their importance for uranium remediation. Elements 4(6):407–412. https://doi.org/10.2113/gselements.4.6.407

Barr D (2002) Biological methods for assessment and remediation of contaminated land: case studies. Constr Ind Res Info Assoc, London https://www.brebookshop.com/samples/139819.pdf

Besaltatpour A, Hajabbasi M, Khoshgoftarmanesh A, Dorostkar V (2011) Land farming process effects on biochemical properties of petroleum-contaminated soils. Soil Sediment Contam Int J 20:234–248. https://doi.org/10.1080/15320383.2011.546447

Bina B, Pourzamani H, Rashidi A, Amin MM (2012) Ethylbenzene removal by carbon nanotubes from aqueous solution. J Publ Health Pol 1–8. https://www.hindawi.com/journals/jeph/2012/817187

Cerqueira VS, Peralba MR, Camargo FAO, Bento FM (2014) Comparison of bioremediation strategies for soil impacted with petrochemical oily sludge. Int Biodeterior Biodegrad 95:338–345. https://doi.org/10.1016/j.ibiod.2014.08.015

Chemlal R, Abdi N, Lounici H, Drouiche N, Pauss A, Mameri N (2013) Modeling and qualitative study of diesel biodegradation using biopile process in sandy soil. Int Biodeterior Biodegrad 78:43–48. https://doi.org/10.1016/j.ibiod.2012.12.014

Chikere CB, Chikere BO, Okpokwasili GC (2012) Bioreactor-based bioremediation of hydrocarbon-polluted Niger Delta marine sediment, Nigeria. 3 Biotech 2:53–66. https://doi.org/10.1007/s13205-011-0030-8

Coulon F, Al Awadi M, Cowie W, Mardlin D, Pollard S, Cunningham C, Risdon G, Arthur P, Semple KT, Paton GI (2010) When is a soil remediated? Comparison of biopiled and windrowed soils contaminated with bunker-fuel in a full-scale trial. Environ Pollut 158:3032–3040. https://doi.org/10.1016/j.envpol.2010.06.001

Delillea D, Duvala D, Pelletier E (2008) Highly efficient pilot biopiles for on-site fertilization treatment of diesel oil contaminated sub-Antarctic soil. Cold Reg Sci Technol 54(1):7–18. https://doi.org/10.1016/j.coldregions.2007.09.003

da Silva LJ, Flávia Chaves Alves FC, de França FP (2012) A review of the technological solutions for the treatment of oily sludges from petroleum refineries. Waste Manag Res 30 (10):1016–1030. https://doi.org/10.1177/0734242X12448517

De Pourcq K, Ayora C, García-Gutiérrez M, Missana T, Carrera J (2015) A clay permeable reactive barrier to remove Cs-137 from groundwater: column experiments. J Environ Radioact 149:36–42. https://doi.org/10.1016/j.jenvrad.2015.06.029

de Windt W, Aelterman P, Verstraete W (2005) Bioreductive deposition of palladium (0) nanoparticles on Shewanella oneidensis with catalytic activity towards reductive dechlorination of polychlorinated biphenyls. Environ Microbiol 7(3):314–325. https://doi.org/10.1111/j.1462-2920.2005.00696.x

de-Bashan LE, Hernandez J-P, Bashan Y (2012) The potential contribution of plant growth-promoting bacteria to reduce environmental degradation-a comprehensive evaluation. Appl Soil Ecol 61:171–189. https://doi.org/10.1016/j.apsoil.2011.09.003

Dias RL, Ruberto L, Calabró A, Balbo AL, Del Panno MT, Mac Cormack WP (2015) Hydrocarbon removal and bacterial community structure in on-site biostimulated biopile systems designed for bioremediation of diesel-contaminated Antarctic soil. Polar Biol 38:677–687. https://doi.org/10.1007/s00300-014-1630-7

Diele F, Notarnicola F, Sgura I (2002) Uniform air velocity field for a bioventing system design: some numerical results. Int J Eng Sci 40:1199–1210. https://doi.org/10.1016/S0020-7225(02)00015-0

Folch A, Vilaplana M, Amado L, Vicent R, Caminal G (2013) Fungal permeable reactive barrier to remediate groundwater in an artificial aquifer. J Hazard Mater 262:554–560. https://doi.org/10.1016/j.jhazmat.2013.09.004

Frascari D, Zanaroli G, Danko AS (2015) In situ aerobic co-metabolism of chlorinated solvents: a review. J Hazard Mater 283:382–399. https://doi.org/10.1016/j.jhazmat.2014.09.041

Frutos FJG, Escolano O, García S, Mar Babín M, Fernández MD (2010) Bioventing remediation and ecotoxicity evaluation of phenanthrene-contaminated soil. J Hazard Mater 183:806–813. https://doi.org/10.1016/j.jhazmat.2010.07.098

García Y, Ruiz C, Mena E, Villaseñor J, Cañizares P, Rodrigo MA (2014) Removal of nitrates from spiked clay soils by coupling electrokinetic and permeable reactive barrier technologies. J Chem Technol Biotechnol 90:1719–1726. https://doi.org/10.1002/jctb.4488

Gelati TR, Bonow CA, do Couto AM, de Almeida MCV, Roloff DIT, Cezar-Vaz MR (2017) Physical, chemical and biological hazards to port workers and their potential to cause respiratory disorders. Cogitare Enferm 22(2):e49371. https://doi.org/10.5380/ce.v22i1.49371

Gidarakos E, Aivalioti M (2007) Large scale and long term application of bioslurping: the case of a Greek petroleum refinery site. J Hazard Mater 149:574–581. https://doi.org/10.1016/j.jhazmat.2007.06.110

Gomez F, Sartaj M (2014) Optimization of field scale biopiles for bioremediation of petroleum hydrocarbon contaminated soil at low temperature conditions by response surface methodology (RSM). Int Biodeterior Biodegrad 89:103–109. https://doi.org/10.1016/j.ibiod.2014.01.010

Gong JL, Wang B, Zeng GM (2009) Removal of cationicdyes from aqueous solution using magnetic multi-wall carbon nanotube nanocomposite as adsorbent. J Hazard Mater 164 (2–3):1517–1522. https://doi.org/10.1016/j.jhazmat.2008.09.072

Grobelak A, Napora A, Kacprzak M (2015) Using plant growth promoting rhizobacteria (PGPR) to improve plant growth. Ecol Eng 84:22–28. https://doi.org/10.1016/j.ecoleng.2015.07.019

Guo R, Guo X, Yu D, Hu J (2012) Application research in water treatment of PAMAM dendrimer. Chem Ind Eng Prog 31:671–675 http://en.cnki.com.cn/Article_en/CJFDTotal-HGJZ201203039.html

Harris JR, Current RS (2012) Machine safety: new & updated consensus standards. Prof Saf 57 (5):50–57 http://www.asse.org/professionalsafety/pastissues/057/05/F1Har_0512.pdf

Helena IG, Celiadias-Ferreira, Alexandra BR (2013) Overview of in situ and ex situ remediation technologies for PCB-contaminated soils and sediments and obstacles for full-scale application. Sci Total Environ 445–446:237–260. https://doi.org/10.1016/j.scitotenv.2012.11.098

Hobson AM, Frederickson J, Dise NB (2005) CH4 and N2O from mechanically turned windrow and vermin composting systems following in-vessel pre-treatment. Waste Manag 25:345–352. https://doi.org/10.1016/j.wasman.2005.02.015

Höhener P, Ponsin V (2014) In situ vadose zone bioremediation. Curr Opin Biotechnol 27:1–7. https://doi.org/10.1016/j.copbio.2013.08.018

Kandah MI, Meunier JL (2007) Removal of nickel ions from water by multi-walled carbon nanotubes. J Hazard Mater 146(1–2):283–288. https://doi.org/10.1016/j.jhazmat.2006.12.019

Kanel SR, Manning B, Charlet L, Choi H (2005) Removal of arsenic (III) from groundwater by nanoscale zero-valent iron. Environ Sci Technol 39(5):1291–1298. https://doi.org/10.1021/es048991u

Kanel SR, Greneche JM, Choi H (2006) Arsenic (V) removal from groundwater using nano scale zero-valent iron as a colloidal reactive barrier material. Environ Sci Technol 40(6):2045–2050. https://doi.org/10.1021/es0520924

Khan FI, Husain T, Hejazi R (2004) An overview and analysis of site remediation technologies. J Environ Manag 71:95–122. https://doi.org/10.1016/j.jenvman.2004.02.003

Kim S, Krajmalnik-Brown R, Kim JO, Chung J (2014) Remediation of petroleum hydrocarbon-contaminated sites by DNA diagnosis-based bioslurping technology. Sci Total Environ 497:250–259. https://doi.org/10.1016/j.scitotenv.2014.08.002

Kuiper I, Lagendijk EL, Bloemberg GV, Lugtenberg BJJ (2004) Rhizoremediation: a beneficial plant-microbe interaction. Mol Plant-Microbe Interact 7:6–15. https://doi.org/10.1094/MPMI.2004.17.1.6

Lee JH (2013) An overview of phytoremediation as a potentially promising technology for environmental pollution control. Biotechnol Bioprocess Eng 18:431–439. https://doi.org/10.1007/s12257-013-0193-8

Li Y, Liu F, Xia B (2010) Removal of copper from aqueous solution by carbon nanotube/calcium alginate composites. J Hazard Mater 177(1–3):876–880. https://doi.org/10.1016/j.jhazmat.2009.12.114

Liu Y, Mou H, Chen L, Mirza ZA, Liu L (2015) Cr(VI)-contaminated groundwater remediation with simulated permeable reactive barrier (PRB) filled with natural pyrite as reactive material: environmental factors and effectiveness. J Hazards Mater 298:83–90. https://doi.org/10.1016/j.jhazmat.2015.05.007

Magalhães SMC, Jorge RMF, Castro PML (2009) Investigations into the application of a combination of bioventing and biotrickling filter technologies for soil decontamination processes—a

transition regime between bioventing and soil vapour extraction. J Hazard Mater 170:711–715. https://doi.org/10.1016/j.jhazmat.2009.05.008

Maila MP, Colete TE (2004) Bioremediation of petroleum hydrocarbons through land farming: are simplicity and cost-effectiveness the only advantages? Rev Environ Sci Bio Technol 3:349–360. https://doi.org/10.1007/s111157-004-6653-z

Mauter MS, Elimelech M (2008) Environmental applications of carbon-based nanomaterials. Environ Sci Tech 42(16):5843–5859. https://doi.org/10.1021/es8006904

Meagher RB (2000) Phytoremediation of toxic elemental organic pollutants. Curr Opin Plant Biol 3:153–162. https://doi.org/10.1016/S1369-5266(99)00054-0

Mesa J, Rodríguez-Llorente JD, Pajuelo E, Piedras JMB, Caviedes MA, Redondo-Gómez S, Mateos-Naranjo E (2015) Moving closer towards restoration of contaminated estuaries: bioaugmentation with autochthonous rhizobacteria improves metal rhizoaccumulation in native Spartina maritima. J Hazard Mater 300:263–271. https://doi.org/10.1016/j.jhazmat.2015.07.006

Mihopoulos PG, Suidan MT, Sayles GD (2000) Vapor phase treatment of PCE by lab-scale anaerobic bioventing. Water Res 34:3231–3237. https://doi.org/10.1016/S0043-1354(00)00023-3

Mihopoulos PG, Suidan MT, Sayles GD, Kaskassian S (2002) Numerical modeling of oxygen exclusion experiments of anaerobic bioventing. J Contam Hydrol 58:209–220

Mohan SV, Sirisha K, Rao NC, Sarma PN, Reddy SJ (2004) Degradation of chlorpyrifos contaminated soil by bioslurry reactor operated in sequencing batch mode: bioprocess monitoring. J Hazard Mater 116:39–48. https://doi.org/10.1016/j.jhazmat.2004.05.037

Mohan SV, Sirisha K, Rao RS, Sarma PN (2007) Bioslurry phase remediation of chlorpyrifos contaminated soil: process evaluation and optimization by Taguchi design of experimental (DOE) methodology. Ecotoxicol Environ Saf 68:252–262. https://doi.org/10.1016/j.ecoenv.2007.06.002

Mohsenzadeh F, Chehregani RA (2012) Bioremediation of heavy metal pollution by nano-particles of *Noaea Mucronata*. Int J Biosci Biochem Bioinforma 2:85–89 https://profs.basu.ac.ir/chehregani/upload_file/art.5554.pdf

Mustafa YA, Abdul-Hameed HM, Razak ZA (2015) Biodegradation of 2,4-dichlorophenoxyacetic acid contaminated soil in a roller slurry bioreactor. Clean-Soil Air Water 43:1115–1266. https://doi.org/10.1002/clen.201400623

Naushad M, Ahamad T, Sharma G, Alam MM, ALOthman ZA, Alshehri SM, Ghfar AA (2016) Synthesis and characterization of a new starch/SnO_2 nanocomposite for efficient adsorption of toxic Hg^{2+} metal ion. Chem Eng J 300:306–316. https://doi.org/10.1016/j.cej.2016.04.084

Ng DM, Jeffery RW (2003) Relationships between perceived stress and health behaviors in a sample of working adults. Health Psychol 22(6):638–642. https://doi.org/10.1037/02786133.22.6.638

Nikolopoulou M, Pasadakis N, Norf H, Kalogerakis N (2013) Enhanced ex situ bioremediation of crude oil contaminated beach sand by supplementation with nutrients and rhamnolipids. Mar Pollut Bull 77:37–44. https://doi.org/10.1016/j.marpolbul.2013.10.038

Nurmi JT, Tratnyek PG, Sarathy V (2005) Characterization and properties of metallic iron nanoparticles: spectroscopy, electrochemistry, and kinetics. Environ Sci Techn 39(5):1221–1230. https://doi.org/10.1021/es049190u

Obiri-Nyarko F, Grajales-Mesa SJ, Malina G (2014) An overview of permeable reactive barriers for in situ sustainable groundwater remediation. Chemosphere of polychlorinated biphenyls. Environ Microbiol 7(3):314–325. https://doi.org/10.1016/j.chemosphere.2014.03.112

Paudyn K, Rutter A, Rowe RK, Poland JS (2008) Remediation of hydrocarbon contaminated soils in the Canadian Arctic by land farming. Cold Reg Sci Technol 53:102–114. https://doi.org/10.1016/j.coldregions.2007.07.006

Philp JC, Atlas RM (2005) Bioremediation of contaminated soils and aquifers. In: Atlas RM, Philp JC (eds) Bioremediation: applied microbial solutions for real-world environmental cleanup. American Society for Microbiology (ASM) Press, Washington, DC, pp 139–236

Piskonen R, Nyyssönen M, Rajamäki T, Itävaara M (2005) Monitoring of accelerated naphthalene-biodegradation in a bioaugmented soil slurry. Biodegradation 16:127–134 https://link.springer.com/article/10.1007/s10532-004-4893-9

Prokop G, Schamann M, Edelgaard I (2000) Management of contaminated sites in western Europe. European Environment Agency, Copenhagen https://www.eea.europa.eu/publications/Topic_report_No_131999

Qiang Y, Sharma A, Paszczynski A, Meyer D (2007) Conjugates of magnetic nanoparticle-enzyme for bioremediation, vol 4. Proceedings of the 2007 NSTI Nanotechnology Conference and Trade Show. pp 656–659

Quan X, Yang S, Ruan X, Zhao H (2005) Preparation of titania nanotubes and their environmental applications as electrode. Environ Sci Technol 39(10):3770–3775. https://doi.org/10.1021/es048684o

Rayner JL, Snape I, Walworth JL, Harvey PM, Ferguson SH (2007) Petroleum–hydrocarbon contamination and remediation by microbioventing at sub-Antarctic Macquarie Island. Cold Reg Sci Technol 48:139–153. https://doi.org/10.1016/j.coldregions.2006.11.001

Roco MC (2005) The emergence and policy implications of converging new technologies integrated from the nanoscale. J Nanopart Res 7(2–3):129–143 https://link.springer.com/article/10.1007/s11051-005-3733-0

Rodríguez-Rodríguez CE, Marco-Urrea E, Caminal G (2010) Degradation of naproxen and carbamazepine in spiked sludge by slurry and solid-phase Trametes versicolor systems. Bioresour Technol 101:2259–2266. https://doi.org/10.1016/j.biortech.2009.11.089

Roy M, Giri AK, Dutta S, Mukherjee P (2015) Integrated phytobial remediation for sustainable management of arsenic in soil and water. Environ Int 75:180–198. https://doi.org/10.1016/j.envint.2014.11.010

Sanscartier D, Zeeb B, Koch I, Reimer K (2009) Bioremediation of diesel-contaminated soil by heated and humidified biopile system in cold climates. Cold Reg Sci Technol 55:167–173. https://doi.org/10.1016/j.coldregions.2008.07.004

Shah JK, Sayles GD, Suidan MT, Mihopoulos PG, Kaskassian SR (2001) Anaerobic bioventing of unsaturated zone contaminated with DDT and DNT. Water Sci Technol 43:35–42 http://wst.iwaponline.com/content/43/2/35

Shan G, Xing J, Zhang H, Liu H (2005) Biodesulfurization of dibenzothiophene by microbial cells coated with magnetite nanoparticles. Appl Environ Microbiol 71(8):4497–4502. https://doi.org/10.1128/AEM.71.8.4497-4502.2005

Shankar S, Shankar U, Shikha (2005) Arsenic contamination of groundwater: a review of sources, prevalence, health risks, and strategies for mitigation. Sci World J 1–18. https://www.hindawi.com/journals/tswj/2014/304524

Silva-Castro GA, Uad I, Gónzalez-López J, Fandiño CG, Toledo FL, Calvo C (2012) Application of selected microbial consortia combined with inorganic and oleophilic fertilizers to recuperate oil-polluted soil using land farming technology. Clean Techn Environ Policy 14:719–726. https://doi.org/10.1007/s10098-011-0439-0

Silva-Castro GA, Uad I, Rodríguez-Calvo A, González-López J, Calvo C (2015) Response of autochthonous microbiota of diesel polluted soils to land- farming treatments. Environ Res 137:49–58. https://doi.org/10.1016/j.envres.2014.11.009

Sui H, Li X (2011) Modeling for volatilization and bioremediation of toluene-contaminated soil by bioventing. Chin J Chem Eng 19:340–348. https://doi.org/10.1016/S1004-9541(11)60174-2

Thiruvenkatachari R, Vigneswaran S, Naidu R (2008) Permeable reactive barrier for groundwater remediation. J Ind Eng Chem 14:145–156. https://doi.org/10.1016/j.jiec.2007.10.001

Thomé A, Reginatto C, Cecchin I, Colla LM (2014) Bioventing in a residual clayey soil contaminated with a blend of biodiesel and diesel oil. J Environ Eng 140:1–6. https://doi.org/10.1061/(ASCE)EE.1943-7870.0000863

Tungittiplakorn W, Lion LW, Cohen LW, Kim JY (2004) Engineered polymeric nanoparticles for soil remediation. Environ Sci Technol 38(5):1605–1610. https://doi.org/10.1021/es0348997

Tungittiplakorn W, Cohen C, Lion LW (2005) Engineered polymeric nanoparticles for bioremediation of hydrophobic contaminants. Environ Sci Technol 39(5):1354–1358 https://www.ncbi.nlm.nih.gov/pubmed/15787377

Verma JP, Jaiswal DK (2016) Book review: advances in biodegradation and bioremediation of industrial waste. Front Microbiol 6:1–2. https://doi.org/10.3389/fmicb.2015.01555

Vidali M (2001) Bioremediation an overview. Pure Appl Chem 73(7):1163–1172 https://www.iupac.org/publications/pac/2001/pdf/7307x1163.pdf

Volpe A, D'Arpa S, Del Moro G, Rossetti S, Tandoi V, Uricchio VF (2012) Fingerprinting hydrocarbons in a contaminated soil from an Italian natural reserve and assessment of the performance of a low-impact bioremediation approach. Water Air Soil Pollut 223:1773–1782. https://doi.org/10.1007/s11270-011-0982-7

Whelan MJ, Coulon F, Hince G, Rayner J, McWatters R, Spedding T, Snape I (2015) Fate and transport of petroleum hydrocarbons in engineered biopiles in polar regions. Chemosphere 131:232–240. https://doi.org/10.1016/j.chemosphere.2014.10.088

Yancheshmeh JB, Khavazi K, Pazira E, Solhi M (2011) Evaluation of inoculation of plant growth-promoting rhizobacteria on cadmium uptake by canola and barley. Afr J Microbiol Res 5:1747–1754. https://doi.org/10.5897/AJMR10.625

Zangi-Kotler M, Ben-Dov E, Tiehm A, Kushmaro A (2015) Microbial community structure and dynamics in a membrane bioreactor supplemented with the flame retardant dibromoneopentyl glycol. Environ Sci Pollut Res Int 22:17615–17624. https://doi.org/10.1007/s11356-015-4975-8

Zhou D, Li Y, Zhang Y, Zhang C, Li X, Chen Z, Huang J, Li X, Flores G, Kamon M (2014) Column test-based optimization of the permeable reactive barrier (PRB) technique for remediating groundwater contaminated by landfill leachates. J Contam Hydrol 168:1–16. https://doi.org/10.1016/j.jconhyd.2014.09.003

Correction to: Nanobiotechnology Approach for the Remediation of Environmental Hazards Generated from Industrial Waste

Mounika Gudeppu, Krishnapriya Madhu Varier, Arulvasu Chinnasamy, Sumathi Thangarajan, Jesudas Balasubramanian, Yanmei Li, and Babu Gajendran

Correction to: Chapter 13 in: R. Saravanan et al. (eds.), *Emerging Nanostructured Materials for Energy and Environmental Science,* Environmental Chemistry for a Sustainable World 23, https://doi.org/10.1007/978-3-030-04474-9_13

The original version of this chapter was revised; the affiliation for Arulvasu Chinnasamy and Sumathi Thangarajan had been interchanged.

The affiliations have been updated now as:

A. Chinnasamy
Department of Zoology, University of Madras, Chennai, India

S. Thangarajan
Department of Medical Biochemistry, Dr. ALM PGIBMS, University of Madras, Chennai, India

The updated version of this chapter can be found at https://doi.org/10.1007/978-3-030-04474-9_13

R. Saravanan et al. (eds.), *Emerging Nanostructured Materials for Energy and Environmental Science*, Environmental Chemistry for a Sustainable World 23, https://doi.org/10.1007/978-3-030-04474-9_14

Index

R. Saravanan et al. (eds.), *Emerging Nanostructured Materials for Energy and Environmental Science*, Environmental Chemistry for a Sustainable World 23,
https://doi.org/10.1007/978-3-030-04474-9